

Lecture Notes in Electrical Engineering 482

Limin Jia

Yong Qin

Jianguo Suo

Jianghua Feng

Lijun Diao

Min An

*Editors*

# Proceedings of the 3rd International Conference on Electrical and Information Technologies for Rail Transportation (EITRT) 2017

Electrical Traction

# Lecture Notes in Electrical Engineering

Volume 482

## Board of Series editors

Leopoldo Angrisani, Napoli, Italy  
Marco Arteaga, Coyoacán, México  
Bijaya Ketan Panigrahi, New Delhi, India  
Samarjit Chakraborty, München, Germany  
Jiming Chen, Hangzhou, P.R. China  
Shanben Chen, Shanghai, China  
Tan Kay Chen, Singapore, Singapore  
Rüdiger Dillmann, Karlsruhe, Germany  
Haibin Duan, Beijing, China  
Gianluigi Ferrari, Parma, Italy  
Manuel Ferre, Madrid, Spain  
Sandra Hirche, München, Germany  
Faryar Jabbari, Irvine, USA  
Limin Jia, Beijing, China  
Janusz Kacprzyk, Warsaw, Poland  
Alaa Khamis, New Cairo City, Egypt  
Torsten Kroeger, Stanford, USA  
Qilian Liang, Arlington, USA  
Tan Cher Ming, Singapore, Singapore  
Wolfgang Minker, Ulm, Germany  
Pradeep Misra, Dayton, USA  
Sebastian Möller, Berlin, Germany  
Subhas Mukhopadhyay, Palmerston North, New Zealand  
Cun-Zheng Ning, Tempe, USA  
Toyoaki Nishida, Kyoto, Japan  
Federica Pascucci, Roma, Italy  
Yong Qin, Beijing, China  
Gan Woon Seng, Singapore, Singapore  
Germano Veiga, Porto, Portugal  
Haitao Wu, Beijing, China  
Junjie James Zhang, Charlotte, USA

**\*\* Indexing: The books of this series are submitted to ISI Proceedings, EI-Compendex, SCOPUS, MetaPress, Springerlink \*\***

*Lecture Notes in Electrical Engineering (LNEE)* is a book series which reports the latest research and developments in Electrical Engineering, namely:

- Communication, Networks, and Information Theory
- Computer Engineering
- Signal, Image, Speech and Information Processing
- Circuits and Systems
- Bioengineering
- Engineering

The audience for the books in LNEE consists of advanced level students, researchers, and industry professionals working at the forefront of their fields. Much like Springer's other Lecture Notes series, LNEE will be distributed through Springer's print and electronic publishing channels.

For general information about this series, comments or suggestions, please use the contact address under "service for this series".

To submit a proposal or request further information, please contact the appropriate Springer Publishing Editors:

**Asia:**

China, *Jessie Guo, Assistant Editor* (jessie.guo@springer.com) (Engineering)

India, *Swati Meherishi, Senior Editor* (swati.meherishi@springer.com) (Engineering)

Japan, *Takeyuki Yonezawa, Editorial Director* (takeyuki.yonezawa@springer.com)  
(Physical Sciences & Engineering)

South Korea, *Smith (Ahram) Chae, Associate Editor* (smith.chae@springer.com)  
(Physical Sciences & Engineering)

Southeast Asia, *Ramesh Premnath, Editor* (ramesh.premnath@springer.com)  
(Electrical Engineering)

South Asia, *Aninda Bose, Editor* (aninda.bose@springer.com) (Electrical Engineering)

**Europe:**

*Leontina Di Cecco, Editor* (Leontina.dicecco@springer.com)  
(Applied Sciences and Engineering; Bio-Inspired Robotics, Medical Robotics, Bioengineering; Computational Methods & Models in Science, Medicine and Technology; Soft Computing; Philosophy of Modern Science and Technologies; Mechanical Engineering; Ocean and Naval Engineering; Water Management & Technology)

(christoph.baumann@springer.com)  
(Heat and Mass Transfer, Signal Processing and Telecommunications, and Solid and Fluid Mechanics, and Engineering Materials)

**North America:**

*Michael Luby, Editor* (michael.luby@springer.com) (Mechanics; Materials)

More information about this series at <http://www.springer.com/series/7818>

Limin Jia · Yong Qin · Jianguo Suo  
Jianghua Feng · Lijun Diao  
Min An  
Editors

Proceedings of the 3rd  
International Conference  
on Electrical and Information  
Technologies for Rail  
Transportation (EITRT) 2017

Electrical Traction

*Editors*

Limin Jia  
School of Traffic and Transportation  
Beijing Jiaotong University  
Beijing  
China

Jianghua Feng  
CRRC Zhuzhou Institute Co., Ltd.  
Zhuzhou  
China

Yong Qin  
Beijing Jiaotong University  
Beijing  
China

Lijun Diao  
Beijing Jiaotong University  
Beijing  
China

Jianguo Suo  
CRRC Zhuzhou Locomotive Co., Ltd.  
Zhuzhou  
China

Min An  
University of Salford  
Manchester  
UK

ISSN 1876-1100                      ISSN 1876-1119 (electronic)  
Lecture Notes in Electrical Engineering  
ISBN 978-981-10-7985-6              ISBN 978-981-10-7986-3 (eBook)  
<https://doi.org/10.1007/978-981-10-7986-3>

Library of Congress Control Number: 2017963532

© Springer Nature Singapore Pte Ltd. 2018

This work is subject to copyright. All rights are reserved by the Publisher, whether the whole or part of the material is concerned, specifically the rights of translation, reprinting, reuse of illustrations, recitation, broadcasting, reproduction on microfilms or in any other physical way, and transmission or information storage and retrieval, electronic adaptation, computer software, or by similar or dissimilar methodology now known or hereafter developed.

The use of general descriptive names, registered names, trademarks, service marks, etc. in this publication does not imply, even in the absence of a specific statement, that such names are exempt from the relevant protective laws and regulations and therefore free for general use.

The publisher, the authors and the editors are safe to assume that the advice and information in this book are believed to be true and accurate at the date of publication. Neither the publisher nor the authors or the editors give a warranty, express or implied, with respect to the material contained herein or for any errors or omissions that may have been made. The publisher remains neutral with regard to jurisdictional claims in published maps and institutional affiliations.

Printed on acid-free paper

This Springer imprint is published by the registered company Springer Nature Singapore Pte Ltd. part of Springer Nature  
The registered company address is: 152 Beach Road, #21-01/04 Gateway East, Singapore 189721, Singapore

# Committees

## Honorary Chairs

Liu Youmei, Academician, China  
Ding Rongjun, Academician, China  
Qian Qingquan, Academician, China  
Shi Zhongheng, Academician, China  
Zhang Xinning, Professor, China  
Satoru Sone, Professor, Tokyo University, Japan

## General Chairs

Prof. Jia Limin, State Key Laboratory of Rail Traffic Control and Safety, Beijing Jiaotong University, China  
Prof. Gong Ming, CRRC Institute Co. Ltd., China

## Program Committee Chairs

Prof. Liu Zhigang, Beijing Jiaotong University, China  
Prof. Qin Yong, State Key Laboratory of Rail Traffic Control and Safety, Beijing Jiaotong University, China  
Prof. LI Yaohua, Institute of Electrical Engineering, Chinese Academy of Sciences, China  
Mr. Chang Zhenchen, CRRC Changchun Railway Vehicles Co. Ltd., China  
Mr. Sun Bangcheng, CRRC Institute Co. Ltd., China  
Mrs. Liang Jianying, National Engineering Laboratory for High-speed Train, CRRC Qingdao Sifang Co. Ltd., China

Mr. Shi Tianyun, The Center of National Railway Intelligent Transportation System Engineering and Technology, China Academy of Railway Sciences, China  
Prof. Chen Tefang, National Engineering Laboratory for High-Speed Railway Construction, China  
Prof. Min An, University of Salford, UK  
Prof. Dr.-Ing Zhong Li, Fern Universität in Hagen, Germany  
Prof. Dr.-Ing. Holger Hirsch, Universität Duisburg-Essen, Germany  
Prof. Lothar H. Fickert, Vienna University of Technology, Austria  
Prof. Suleiman M. Sharkh, University of Southampton, UK

## **Organizing Committee Chairs**

Mr. Suo Jianguo, The State Key Laboratory of Heavy Duty AC Drive Electric Locomotive Systems Integration, CRRC Zhuzhou Locomotive Co. Ltd., China  
Prof. Qin Yong, State Key Laboratory of Rail Traffic Control and Safety, Beijing Jiaotong University, China  
Mr. Liu Changqing, National Engineering Laboratory for System Integration of High-speed Train, CRRC Changchun Railway Vehicles Co. Ltd., China  
Mr. Deng Xiaojun, National Engineering Laboratory for High-speed Train, CRRC Qingdao Sifang Co. Ltd., China  
Mr. Fan Yunxin, The State Key Laboratory of Heavy Duty AC Drive Electric Locomotive Systems Integration, CRRC Zhuzhou Locomotive Co. Ltd., China  
Mr. Feng Jianghua, National Engineering Research Center of Converting Technology, China  
Mr. Shi Tianyun, The Center of National Railway Intelligent Transportation System Engineering and Technology, China Academy of Railway Sciences, China  
Prof. Chen Weirong, State Key Laboratory of Traction Power, Southwest Jiaotong University, China  
Mr. Sun Bangcheng, CRRC Institute Co. Ltd., China  
Prof. Min An, University of Salford, UK  
Prof. Diao Lijun, Beijing Jiaotong University, China  
Prof. Zuo Mingjian, University of Electronic Science and Technology of China, China  
Prof. Ren Xiaochun, State Key Laboratory of Rail Transit Engineering Informatization, China  
Prof. Yu Zhiwu, National Engineering Laboratory for High-Speed Railway Construction, China

## Technical Program Committee Members

Prof. Jia Limin, State Key Laboratory of Rail Traffic Control and Safety, Beijing Jiaotong University, China

Prof. Li Yaohua, Institute of Electrical Engineering, Chinese Academy of Sciences, China

Prof. GaoShibin, Southwest Jiaotong University, China

Prof. Chai Jianyun, Tsinghua University, China

Prof. Fang Youtong, Zhejiang University, China

Ms. Zhao Minghua, Changchun Bombardier Railway Vehicles Co. Ltd., China

Mr. Li Jun, CRRC Changchun Railway Vehicles Co. Ltd., China

Prof. Wang Litian, China Railway Electrification Survey and Design Institute Co. Ltd., China

Mr. Cai Changjun, Guangzhou Metro Corporation, China

Prof. Gong Ming, CRRC Institute Co. Ltd., China

Prof. Liu Baoming, China CNR Qingdao Sifang Locomotive & Rolling Stock Research Institute, China

Prof. Liu Zhigang, Beijing Jiaotong University, China

Prof. Qin Yong, State Key Laboratory of Rail Traffic Control and Safety, Beijing Jiaotong University, China

Prof. Li Ping, The Center of National Railway Intelligent Transportation System Engineering and Technology, China Academy of Railway Sciences, China

Prof. Ren Xiaochun, State Key Laboratory of Rail Transit Engineering Informatization, China

Prof. Jiang Jiuchun, Beijing Jiaotong University, China

Prof. Yang Zhongping, Beijing Jiaotong University, China

Prof. Buchheit Karlheinz, Experts of Siemens, Germany

Prof. Clave Roberts, University of Birmingham, UK

Prof. Ing. Kyandoghere Kyamakya, Universität Klagenfurt, Germany

Prof. Jianqiao Ye, Mechanical Engineering Department of Engineering, Lancaster University, UK

Prof. Mark Hooper, Faculty of Engineering and Computing, Coventry University, UK

Prof. Dr.-Ing Zhong Li, Fern Universität in Hagen, Germany

Prof. Dr.-Ing. Holger Hirsch, Universität Duisburg-Essen, Germany

Prof. Rui Chen, Loughborough University, UK

Prof. Satoru Sone, Tokyo University, Japan

Prof. Simon Wang, School of Aeronautical and Automotive Engineering, Loughborough University, UK

Prof. Tung-Chai Ling, University of Birmingham, UK

Prof. Wolfgang A. Halang, Fern Universität in Hagen, Germany

Prof. Zhongqing Su, Hong Kong Polytechnic University, Hong Kong

Dr. Tatsuhiko Fujihira, Fuji Electric, Japan

Dr. Paramjit Singh, Bombardier (Singapore) Pte Ltd., Singapore



## **Organizing Committee Members**

Mr. Zhao Jiangnong, The State Key Laboratory of Heavy Duty AC Drive Electric

Locomotive Systems Integration, CRRC Zhuzhou Locomotive Co. Ltd., China

Prof. Qin Yong, State Key Laboratory of Rail Traffic Control and Safety, Beijing Jiaotong University, China

Prof. Min An, University of Salford, UK

Prof. Diao Lijun, Beijing Jiaotong University, China

Prof. Xu Chunmei, Beijing Jiaotong University, China

Dr. Chen Xiaoqing, State Key Laboratory of Rail Traffic Control and Safety, Beijing Jiaotong University, China

Dr. Xie Zhengyu, State Key Laboratory of Rail Traffic Control and Safety, Beijing Jiaotong University, China

Mr. Xie Zhe, National Engineering Research Center of Converting Technology, China

Prof. Dr. Wolfgang A. Halang, Fern Universität in Hagen, Germany

Prof. Dr.-Ing Zhong Li, Fern Universität in Hagen, Germany

# Contents

<b>Study on Catenary Current Harmonic and Traction Characteristics of New Type Electric Multiple Unit</b> . . . . .	1
Haibo Zhao and Ruijing Ouyang	
<b>Research on Optimization Strategy of Forced Convection Heat Dissipation for Super Capacitor Energy Storage Power Supply</b> . . . . .	9
Jun Zhang, Zhongcheng Jiang, Jixiong Jiang, JingJing Chen and Li Zhou	
<b>Mechanism of Rectified Output Voltage Spike in Isolated Converter Under Wide Input Voltage</b> . . . . .	21
Chunhui Miao, Huiqing Du and Fei Xiao	
<b>Distributed Energy-Saving Dynamic Matrix Control of Multi-locomotive Traction Heavy Haul Train</b> . . . . .	29
Xiukun Wei and Jinglin Zhang	
<b>Research of Hybrid Energy Pack for Rail Transit</b> . . . . .	37
Yejun Mao, Yuan Long, Shengcai Chen and Xiangyuan Xiao	
<b>Instantaneous Voltage PIR Closed-Loop Control for the Auxiliary Inverter</b> . . . . .	49
Xuefu Cao, Yong Ding, Ruichang Qiu, Yun Kang and Yang Yu	
<b>Comparative Study of Two Control Strategies for Capacitor Voltage Balancing in Three-Level Boost Converter for Photovoltaic Grid-Connected Power System</b> . . . . .	59
Yiming Chen, Zhencong Li, Shuping Yang, Wen Xu and Lingling Xie	
<b>A Resonant Push–Pull DC–DC Converter</b> . . . . .	67
Shiyang Yuan, Zhe Tang, Jiyun Tian and Hui Cao	
<b>Distribution Network Planning Considering DG Under Uncertainty</b> . . . . .	79
Yanfei Liu and Hui Zhou	

<b>Reliability Evaluation of Inverter Based on Accelerated Degradation Test</b> .....	89
Xinghui Qiu and Jianwei Yang	
<b>Analysis and Elimination of Early Failure of CNC Grinding Machine</b> .....	103
Yulong Li, Genbao Zhang, Yongqin Wang, Xiaogang Zhang and Yan Ran	
<b>Reliability Fuzzy Comprehensive Evaluation of All Factors in CNC Machine Tool Assembly Process</b> .....	115
Xiaogang Zhang, Genbao Zhang, Xiansheng Gong, Yulong Li and Yan Ran	
<b>A Compacted Brushless Dual Mechanical Port Electrical Machine Model</b> .....	125
Shaowei Wang and Zhenghao Wang	
<b>A Measurement Design for Pantograph Contact Force</b> .....	133
Yuan Zhong, Pengfei Zhang and Jiqin Wu	
<b>Cooperative Control of Voltage Equalization for Multiple Supercapacitors</b> .....	145
Ying Yang, Yanlin Zhang, Yejun Mao, Junmin Peng and Fangrong Wu	
<b>Research on Electromagnetic Environment Safety of High-Speed Railway Catenary</b> .....	155
Huijuan Sun, Jun Liu and Can He	
<b>Application Study of Active Noise Control Technology for Rail Transit Vehicles</b> .....	163
Xiaobo Liu, Jian Xu, Zhongcheng Jiang and Xianfeng Wang	
<b>DC Auto-Transformer Traction Power Supply System for DC Railways Application</b> .....	175
Miao Wang, Xiaofeng Yang, Lulu Wang and Trillion Q. Zheng	
<b>An Optimized Method for the Energy-Saving of Multi-metro Trains at Peak Hours Based on Pareto Multi-objective Genetic Algorithm</b> .....	185
Muhan Zhu, Yong Zhang, Fei Sun and Zongyi Xing	
<b>Optimized Discrete Model Based Model Reference Adaptive System for Speed Sensorless Control</b> .....	197
Shaobo Yin, Yuwen Qi, Yi Xue, Huaiqiang Zhang and Dongyi Meng	
<b>NPV Control Method by Injecting Zero Sequence Voltage for Three Level NPC Inverter</b> .....	205
Bo Gong and Yang Liu	

**Analysis on the Vehicle Network Harmonic Oscillation and Its Influencing Factors of China’s Electrified Railway** . . . . . 213  
 Yue Xu, Peng Lin, Shihui Liu, Fei Lin and Zhongping Yang

**Impact of Rail Transit System on Grid Power Quality** . . . . . 223  
 Zerong Li, Lei Han, Dejing Che and Qingxia Wang

**A Torque Command Generated Method of Re-adhesion Control Based on Slip Acceleration** . . . . . 231  
 Long Qi, Guohui Li and Chenchen Wang

**Research on Real-Time Simulation Modeling of Four-Quadrant Converter System Based on Basic Components** . . . . . 239  
 Yunxin Fan, Huanqing Zou and Jin Fu

**Robust  $H_{\infty}$  Control of Single-Sided Linear Induction Motor for Low-Speed Maglev Trains** . . . . . 251  
 Yifan Shen, Dawei Xiang and Jingsong Kang

**Online Fault Diagnosis of the Hybrid Electrical Multiple Unit Traction Converter** . . . . . 259  
 Lei Wang, Mengzhu Wang, Yujia Guo, Ruichang Qiu and Lijun Diao

**Characterization and Variable Temperature Modeling of SiC MOSFET** . . . . . 271  
 Mengzhu Wang, Yujia Guo, Lei Wang, Guofu Chen and Ruichang Qiu

**Calculation Analysis on Traction Motor Temperature Rise of EMU Vehicles Based on Fuzzy Neural Network** . . . . . 281  
 Jianying Liang, Shaoqing Liu, Chongcheng Zhong and Jin Yu

**Predictive Current Control for Three-Phase Asynchronous Motor with Delay Compensation** . . . . . 293  
 Yaru Xue, Jian Zhou, Yuwen Qi, Huaiqiang Zhang and Yong Ding

**Predictive Direct Power Control of Three-Phase PWM Rectifier Based on Linear Active Disturbance Rejection Control** . . . . . 301  
 Kunpeng Li

**Discussion on the Energy Efficiency and Electrotechnical Questions of Urban Cable Car System** . . . . . 309  
 Lothar Fickert, Ziqian Zhang, Cunyuan Qian and Yanyun Luo

**Test and Regression Analysis of Dynamic Shutdown Characteristic of High Power Thyristor** . . . . . 317  
 Zhihao Zhang, Liqun Zhang, Zeng Shou, Yifang Jin and Yuhao Tan

**Research on Mode-Switchover Process and Protective Circuit of Dual Power Supply System for Regional Express Electric Multiple Unit** . . . . . 327  
Ruijing Ouyang, Haibo Zhao and Long Qi

**Synergetic Control Design of EMU Parallel Motor** . . . . . 335  
Chenhao Zhang, Tao Wang, Jikun Li and Kaidan Xue

**Research on Thermal Management System of Lithium Iron Phosphate Battery Based on Water Cooling System** . . . . . 341  
Liye Wang, Lifang Wang, Yuan Yue and Yuwang Zhang

**Performance Comparison of Battery Chargers Based on SiC-MOSFET and Si-IGBT for Railway Vehicles** . . . . . 351  
Yun Kang, Zhipo Ji, Chun Yang, Ruichang Qiu and Xuefu Cao

**A Research on VIENNA Rectifier Based on SVPWM Algorithm with Expected Voltage** . . . . . 359  
Changjun Guo, Gang Zhang and Xibin Bai

**Research of Induction Motor Model Considering the Variation of Magnetizing Inductance** . . . . . 369  
Yujie Chang, Yi Xue, Yang Guo, Jing Tang, Dongyi Meng and Hui Wang

**Auxiliary Inverter of Urban Rail Train—Oscillation Suppression Method of Induction Motor Load** . . . . . 379  
Hui Wang, Zhigang Liu, Shaobo Yin, Dongyi Meng and Yujie Chang

**Improved Voltage Model Based Flux Observer Design for Traction Induction Motor** . . . . . 387  
Dongyi Meng, Lijun Diao, Shaobo Yin, Yujie Chang and Hui Wang

**Design of Median Machine in Battery Test System** . . . . . 395  
Jianan Chen, Jiuchun Jiang and Jingxin Li

**The Research on Bi-Directional DC/DC Converter for Hybrid Power System** . . . . . 405  
Guodong Liu, Zhipo Ji, Ruichang Qiu and Xiang Wang

**Experimental Study the Electric Braking Anti-skid Performance of Electric Multiple Units** . . . . . 415  
Baomin Wang, Xiang Gao, Yongfong Song, Yi Zhou and Yang Lu

**Performance Test and Evaluation Technology Research of Photovoltaic Power and Energy Storage Generation System** . . . . . 427  
Na Li, Kai Bai, Zhi Li, Jian-ming Dong, Jin Zong and Yu Gong

**Research on Ice-Melting Technology of Urban Rail Transit Catenary Based on Energy Cycle** . . . . . 443  
Jian Liu, Gang Zhang, Fengjie Hao, Zhigang Liu and Xibin Bai

**The Key Design and Control of Single-Sided Linear Induction Motors (SLIMs) Based on Serial Equivalent Model (SEM) . . . . .** 453  
 Jiangming Deng, Qibiao Peng, Tefang Chen and Laisheng Tong

**A Controller Based on Electric-Charger Balance Theory for Front-End Converters . . . . .** 463  
 Yisheng Yuan, Xianglong Mei, Pan Zhou and Jiyun Tian

**Research on Energy Management for Hybrid EMU . . . . .** 475  
 Rongjia He, Chen Zhang, Ruichang Qiu and Lijun Diao

**Anti-circulation Strategy of the Hybrid Traction Power Supply Device Used in Urban Rail Transit . . . . .** 483  
 Lu Ming, Gang Zhang, Fengjie Hao and Xibin Bai

**Comparison of Harmonics Between SVPWM and SHEPWM . . . . .** 491  
 Ruizheng Ni, Miao Sha, Jia Xiaoguang, Yong Ding and Jie Chen

**Parameters Offline Identification of Induction Motor in High-Power Converter System . . . . .** 501  
 Miao Sha, Lailai Shen, Jie Chen and Jing Tang

**Research on Construction Method of “Train-Traction Network” Harmonic Model for High-Speed Railway . . . . .** 511  
 Guorui Zhai, Lingmin Meng and Jie Chen

**Research on Unbalanced Load Suppression Method of Auxiliary Inverter . . . . .** 519  
 Yong Ding, Linghang Huang and Jie Chen

**Hierarchical Control and Harmonic Suppression of a Vehicular Based Microgrid System . . . . .** 529  
 Shuguang Wei, Hailiang Xu, Qiang Gao and Xiaojun Ma

**Research on Vector Control of Long-Primary Permanent Magnet Linear Synchronous Motor Based on Voltage Feed-Forward Decoupling . . . . .** 543  
 Zheng Li, Ruihua Zhang, Yumei Du and Qiongquan Ge

**The LCL Filtering Scheme of High Power Four-Quadrant Converter Used in Urban Rail Transit . . . . .** 553  
 Dongsheng Xu, Gang Zhang, Fengjie Hao and Zhiqiang Hu

**Performance and Thermal Analysis of Five-Phase Linear Induction Motor Optimal Control . . . . .** 563  
 Tao Tong, Jinlin Gong, Yadong Gao and Nicolas Bracikowski

**Thermoelectric Coupling Analysis and Thermal Protection for Busbar Trunking System . . . . .** 571  
 Xiaodong Yin, Tao Tong, Yujiang Li, Jinlin Gong and Xiaohui Wang

**Simulation of Short-Circuit Fault Occurring on Subway Train . . . . .** 585  
Lei Sun, Mingli Wu, Jixing Sun and Shaobing Yang

**Research on Vehicle’s Combination Dashboard Diagnostic Protocol Stack . . . . .** 597  
Yanming Li, Feng Gao, Yongliang Ni and Tingting Wu

**Optimization and Scheduling Strategy of Energy Storage in Urban Rail Traction Power Supply System . . . . .** 611  
Wei Ma, Wei Wang and Ruonan Hu

**Hierarchical Control Strategy of On-board DC Microgrid. . . . .** 621  
Luming Chen, Zili Liao, Hailiang Xu and Xiaojun Ma

**Design and Simulation of Switched Reluctance Motor Control System . . . . .** 631  
Chengling Lu, Gang Zhang, Chengtao Du, Junhui Cheng and Congbing Wu

**Isolated Transit Signal Priority Control Strategy Based on Lane-by-Lane Vehicle Detection Scheme . . . . .** 639  
Jun Deng and Liang Cui

**Analysis of the Effect of a Color Image Encryption Algorithm . . . . .** 653  
Yukun Guo

**Novel Affine Projection Sign Subband Adaptive Filter . . . . .** 661  
Qianqian Liu and Haiquan Zhao

**Research on Redundancy and Fault-Tolerant Control Technology of Levitation Join-Structure in High Speed Maglev Train . . . . .** 671  
Mingda Zhai, Xiaolong Li and Zhiqiang Long

**Short-term Passenger Flow Forecasting Based on Phase Space Reconstruction and LSTM . . . . .** 679  
Yong Zhang, Jiansheng Zhu and Junfeng Zhang

**Application of Improved Gaussian-Hermite Moments in Intelligent Parking System . . . . .** 689  
Xing He, Lin Wang and Zhongyou Zuo

**Research on Optimization of Passenger Volume Flow Monitoring Through the Metro Network Video Surveillance Technology . . . . .** 701  
Yuekun Zhang, Feng Xu, Tianxiang Mao and Bing Han

**Adaptive Locomotive Headlamp System Based on Monocular Vision . . . . .** 717  
Juan Gong

**Influence Analysis of the Grounding Grid of Communication Tower Base on Lightning Signal** ..... 727  
 Jin Yang and Zhiyu Li

**Simulation Model of Direct Power Supply System with Return Wire in Tunnel Section** ..... 739  
 Zhiming Liu, Jiangjian Xie, Zhixin Wang and Jin Yang

**Application of Moving Average Filter to Train’s Active Control System** ..... 749  
 Xu Wang, Jiabin Ji and Peida Hu

**The Simulation of the Longitudinal Force of Heavy Haul Trains** ..... 759  
 Shize Huang, Qiyi Guo, Liangliang Yu, Yue Liu and Fan Zhang

**Nash Bargaining Game of Cloud Resource Provision in Cooperative Market** ..... 771  
 Xiaoqing Zhang

**Research on the Method of Calculating Train Congestion Index Based on the Automatic Fare Collection Data** ..... 781  
 Wenxuan Zhang and Jinjin Tang

**Research on Shortest Paths-Based Entropy of Weighted Complex Networks** ..... 793  
 Zundong Zhang, Zhaoran Zhang, Weixin Ma and Huijuan Zhou

**Train-Mounted Head-up Display System Based on Digital Light Processing Technology** ..... 801  
 Ai-jun Su

**An Effective Detection Algorithm of Zebra-Crossing** ..... 809  
 Zu Sheng Chen and Dao Fang Zhang

**A Node Pair Entropy Based Similarity Method for Link Prediction in Transportation Networks** ..... 817  
 Zundong Zhang, Weixin Ma, Zhaoran Zhang and Huijuan Zhou

**Transfer Domain Class Clustering for Unsupervised Domain Adaptation** ..... 827  
 Yunxin Fan, Gang Yan, Shuang Li, Shiji Song, Wei Wang and Xinpeng Peng

**Nodes Deployment of Wireless Sensor Networks for Underground Tunnel Environments** ..... 837  
 Cuiran Li, Jianli Xie, Wei Wu, Yuhong Liu and Anqi Lv

**Application of DBN for Assessment of Railway Intelligent Signal System Reliability** ..... 845  
 Zhengjiao Li, Bai-gen Cai, Shaobin Li, Jiang Liu and Debiao Lu



**Key-Point Feature Detection Method for Surrounding-Field-of-View Image Applications** . . . . . 857  
 Mai Jiang, Qi cheng Yan and Cheng tao Cai

**The Analysis of the Communication Distance in Wireless Optical Communications for Trains** . . . . . 865  
 Tairan Zhang, Jianghua Feng, Jiabo Xiao and Jun Tang

**The Research on Route Search Based on Heuristic Strategy** . . . . . 871  
 Cheng Wang, Shaobin Li, Yan Li, Ziwei Liu and Huiyong Liu

**Active Compensation Method for Long Time Delay and Packet Loss in Networked Control System** . . . . . 879  
 Wei Fu, Xianyi Yang and Ning Li

**Urban Rail Transit Platform Passenger Alighting and Boarding Movement and Experiment Research** . . . . . 889  
 Yang Li and Yanhui Wang

**Research on Running Curve Optimization of Automatic Train Operation System Based on Genetic Algorithm** . . . . . 899  
 Hao Liu, Cunyuan Qian, Zhengmin Ren and Guanlei Wang

**Research on Tram Detector Location Based on Vehicle–Infrastructure Communication** . . . . . 915  
 Huang Yan, Dongxiu Ou, Ziyan Chen and Yang Yang

**Research on Real-Time Performance of Train Communication Network Based on HaRTES** . . . . . 927  
 Luyao Bai, Lide Wang, Jie Jian, Ping Shen, Chuan Yue and Xingyuan Wei

**Data Cache in Mobile Environment Based on Extensible Markup Language** . . . . . 935  
 Jiusheng Du, Luyao Ma and Zheng Hou

**Fully Automatic Operation System in Urban Rail Transit Is Applying in China** . . . . . 943  
 Fei Yan, Bo Liu, Yao Zhou, Chunhai Gao and Tao Tang

**Discrete Fuzzy Model Optimal Identification Based Approach for High Speed Train Operation** . . . . . 951  
 Kunpeng Zhang and Chunlan An

**Research on GIS Database Construction and Application for UGV in the Campus Traffic Environment** . . . . . 959  
 Mingtao Wu, Yanhui Wang and Xiaofeng Li

**Research on Algorithm of Correlation Denoising Based on Wavelet Transform** . . . . . 969  
 Lei Yang, Feng Xue, Hong hai Wang and Hua wei Cheng

**Distributed Simulation Modeling and System Construction for the Networked Operation of Urban Railway System** . . . . . 977  
Jiaping Feng, Xi Jiang, Feifan Jia and Chi Zhang

**Automatic Train Control with Actuator Saturation Using Contraction Theory** . . . . . 989  
Yue Li

**Linear Quadratic Optimal Control of Passenger Flow in Urban Rail Transfer Stations** . . . . . 999  
Huijuan Zhou, Qiang Zhang, Yanwei Feng, Yu Liu and Guorong Zheng

**RUL Prediction for Bearings Based on Fault Diagnosis** . . . . . 1013  
Dong Yan and Xiukun Wei

**Two-Objective Optimization Reinforcement Learning Used in Single-Phase Rectifier Control** . . . . . 1021  
Ande Zhou, Bin Liu, Yunxin Fan and Libing Fan

**Optimization Design and Research of LEACH Algorithm in Large Region of Rail Transportation** . . . . . 1035  
Chongjun Liu, Kuangang Fan, Pingchuan Liu and Gaoxing Ding

# Study on Catenary Current Harmonic and Traction Characteristics of New Type Electric Multiple Unit

Haibo Zhao and Ruijing Ouyang

**Abstract** Harmonic characteristics of catenary current and traction characteristics play so important role in the traction systems of electric multiple unit (EMU). Throughout the track and measurement of a new type EMU, this paper is aimed to analyze the harmonic characteristics of catenary current by Fourier transform method and figure out the curve of traction characteristics by electric power method. Test results indicate that the catenary current of the new type EMU are in low harmonic, whether the EMU is at the state of traction or braking. When the input power of EMU is above 5 MW, harmonic content of the catenary current is below 1% and total harmonic distortion rate is less than 3%. At the same time, equivalent disturbance current is below 1.5 A and power factor is above 0.98. In addition, the new type EMU has the similar traction characteristics as other EMUs.

**Keywords** EMU · Catenary current · Harmonic characteristics  
Traction characteristics

## 1 Introduction

According to UIC, until April 1st 2017, the whole world altogether have 24 countries and areas own EMU, and beyond the border the number is 2452 standard vehicles, China has surpass 2500 standard vehicles, which accounts for the global total above 50%, simultaneously in running mileage, Chinese high-speed-railway mileage is 22,000 km, accounts for the global total above 60%, Chinese EMU from the technology to the digestion absorption, innovates from the scientific research to the independent research and development, passes through several years, have already made belonged to own EMU brand.

With rapid development of high-speed railway mileage and EMU, the relationship between EUM and become more prominent, specially to entire

---

H. Zhao (✉) · R. Ouyang  
CRRC Changchun Railway Vehicles Co. Ltd., Qingyin Road no. 435, Changchun, China  
e-mail: zhaohaibo@cccar.com.cn

© Springer Nature Singapore Pte Ltd. 2018

L. Jia et al. (eds.), *Proceedings of the 3rd International Conference on Electrical and Information Technologies for Rail Transportation (EITRT) 2017*, Lecture Notes in Electrical Engineering 482, [https://doi.org/10.1007/978-981-10-7986-3\\_1](https://doi.org/10.1007/978-981-10-7986-3_1)

high-speed-railway power supply system is obvious day by day [1], when beginning of mainline from Wuhan to Guangzhou and Beijing to Shanghai, the accident of influence of led to catenary power supply exceptionally both happened, therefore, controlling EMU harmonic ratio effectively is important [2]. This paper is for the purpose of by measuring and calculating new type EMU harmonic, and expounding by application harmonic suppression measure, EMU harmonic ratio conform to the correlation requirement, simultaneously has not influence to its traction characteristic, and satisfied utilization request [3].

## 2 Harmonic of Traction Unit

Figure 1 shows a single traction unit of EMU a lot of electric power and electronic component are massively used in traction converter, therefore created frequency spectrum to be widely, between 3 and 200 Hz, simultaneously massive EMU are running, it is easy to lead to harmonic oscillation between EMU and catenary of power supply, and in specific frequency band harmonic current resonating as well as the resonant overvoltage, finally caused to EMU and the power supply devices be breakdown and overburning accident, therefore we must control EMU harmonic effectively.

The limit of EMU converter power module's switching frequency and controlling of the whole traction converters is key point and the difficulty of solve harmonic question [4], now following two methods are usually deal with this issue:

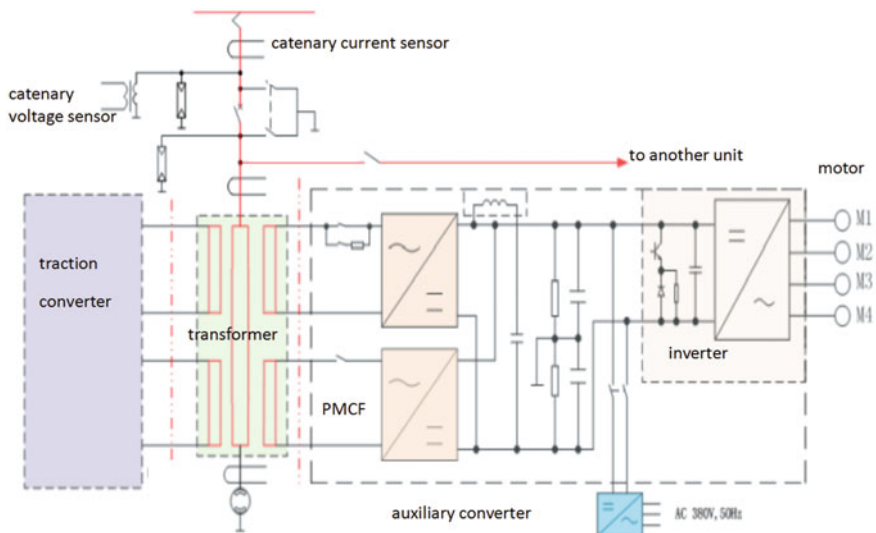


**Fig. 1** EMU Main electrical diagram

- Reducing harmonic through three level ways or harmonic filter on the electric circuit hardware [5];
- Based on the mean current feedback, based on the original side current feedback which two kind of optimization transient current control strategies, and using in the converter control software control strategy and the Carrier Phase-Shifted control technology and so on the way reduces the overtone, and one or all methods are applied in engineering practice for most economical and the finest control effect [6].

### 3 Computational Methods

#### 3.1 Catenary Current Harmonic Computational Method

Catenary current can be expressed in frequency domain by periodic function as [7]:

$$f(t) = f(t + kT) \quad (1)$$

Then it is represented by Fourier's series as:

$$f(t) = a_0 + \sum_{k=1}^{\infty} [a_k \cos(k\omega_1 t) + b_k \sin(k\omega_1 t)] \quad (2)$$

$$\begin{cases} a_0 = \frac{2}{T} \int_0^T f(t) dt \\ a_k = \frac{2}{T} \int_0^T f(t) \cos(k\omega_1 t) dt \\ b_k = \frac{2}{T} \int_0^T f(t) \sin(k\omega_1 t) dt \end{cases} \quad (3)$$

It can be further simplified as:

$$f(t) = A_0 + \sum_{k=1}^{\infty} [A_{km} \cos(k\omega_1 t + \psi_k)] \quad (4)$$

$$\begin{cases} A_0 = a_0 \\ A_{km} = \sqrt{a_k^2 + b_k^2} \\ \psi_k = \arctan\left(-\frac{b_k}{a_k}\right) \end{cases} \quad (5)$$

Equivalent disturbing current equation [8]:

$$J_p = \sqrt{\sum_{n=1}^{100} (S_n^2 \times I_n^2)} \quad (6)$$

where:

$J_p$  Equivalent disturbing current, A;

$I_n$  RMS of n sub-harmonic current, A;

$S_n$  The international telegram inquiry board stipulated static appraisal co-coefficient.

Power factor computational formula is:

$$\lambda = \frac{P}{U \times I} \times 100\% \quad (7)$$

where:

$\lambda$  power factor;

$U$  RMS of catenary voltage, kV;

$I$  RMS of catenary current, A;

$P$  active power, kW.

### 3.2 Computation of Traction Force at the Wheel Rim

Traction force at rim can be calculated as:

$$F = \frac{3.6N \sum_{i=1}^n P_i \eta_m \eta_g}{nv} \quad (8)$$

where:

$N$  Total number of traction motors, and  $N = 16$ ;

$n$  Number of measured traction motors;

$P_i$  The  $i$ th motor of active power, kW;

$V$  Instantaneous velocity, km/h;

$m$  Motor efficiency, and is 0.947;

$g$  Gear efficiency, and is 0.975.

## 4 Test Results and Analysis

Before experiments starts officially, EMU must run continually at least 30 min, so temperature of axis and each revolution partial condition close to actual utilization condition. EMU will run at full traction and full brake, carries on the continual sampling to various operating modes data [9].

The following data must be recorded during test procedure:

- (1) EMU catenary voltage, V;
- (2) EMU catenary current, A;
- (3) EMU velocity, km/h;
- (4) traction motor input voltage, V;
- (5) traction motor input current, A.

### 4.1 Test Results Analyze

EMU start running at straight track and accelerate to 350 km/h, Fig. 2 is EMU's RMS and frequency spectrum of catenary current in this process, and catenary current rises reposefully after EMU start, until EMU enter the permanent power stage, at that time the catenary current stabilizes about 460 A, and velocity probably is 160 km/h, in the harmonic components, the third subharmonic contents is highest, but content does not pass 0.6%.

As shown in Fig. 3, we can see that power factor rises with active power's rising during EMU's accelerating, namely the power is bigger, the power factor is higher. When the power surpasses 5 MW, the power factor reaches above 0.98.

Figure 4 shows the relationship among primary current distortion factor, Equivalent disturbing current and active power map, RMS of catenary current to be bigger (traction power to be bigger), primary current distortion factor to be lower. When the power surpasses 5 MW, primary current distortion factor below 3%, equivalent disturbing current below 1.5 A.

### 4.2 Traction Characteristic

As shown in Fig. 5, the traction characteristic divides into two areas, namely constant force area and constant power area. In constant force area, traction force along with the speed ascension slow drop. This is consistent with the speed change tendency of the adhesion characteristics of the EMU.

In high speed area, because the motor voltage or the power limit, output power invariable, the force of traction assumes the hyperbolic curve relations along with the speed ascension to drop. The constant power area beginning is probably 160 km/h.

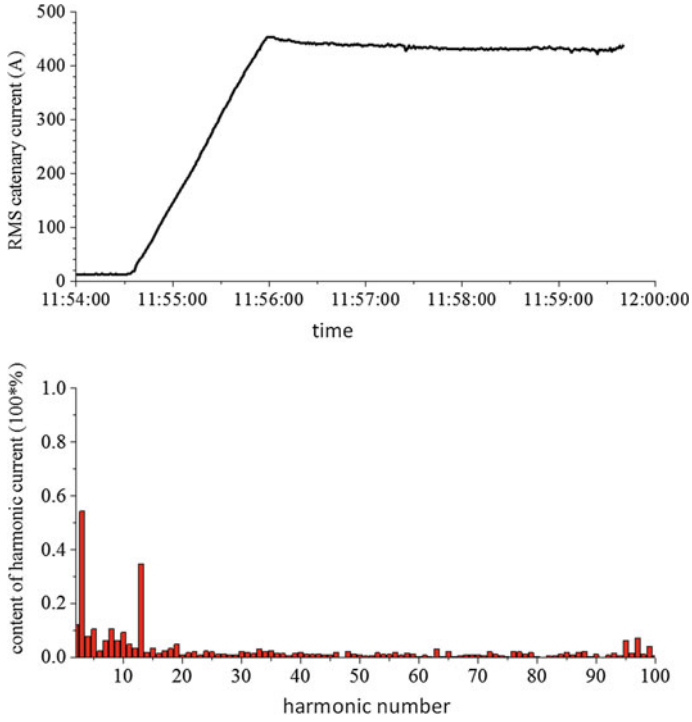
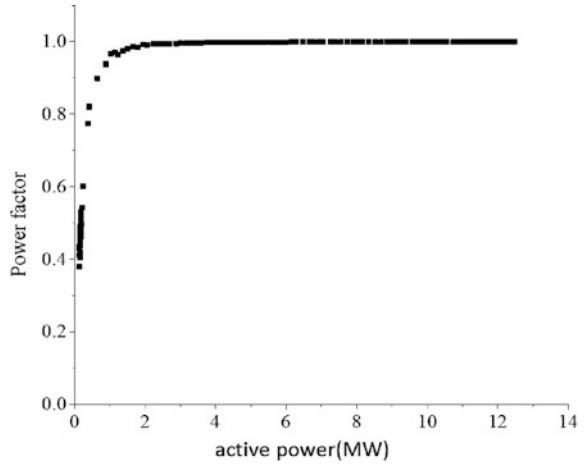


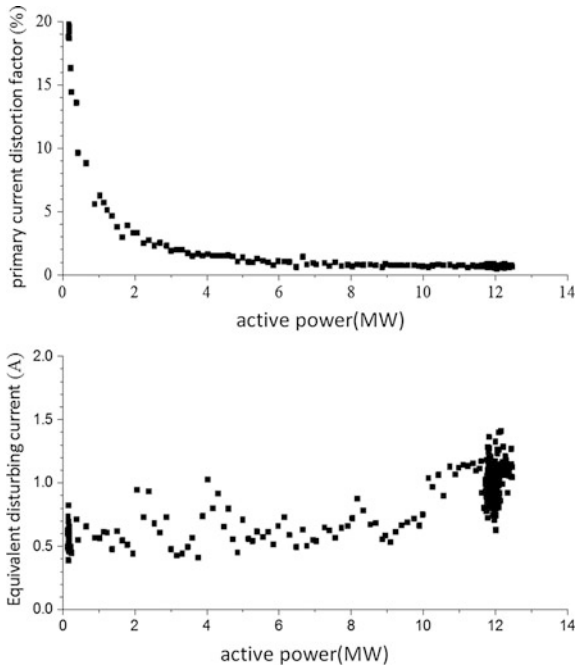
Fig. 2 Catenary current and the frequency spectrum (full traction)

Fig. 3 Relation of power factor with active power (full traction)

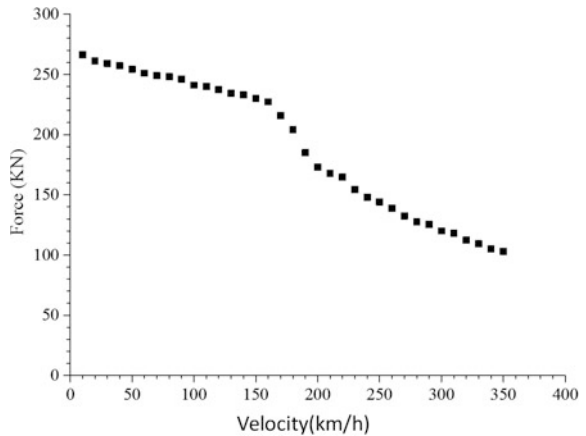




**Fig. 4** Relationship among primary current distortion factor, equivalent disturbing current and active power (full traction)



**Fig. 5** Traction characteristic



## 5 Conclusion

New type EMU uses Carrier Phase-Shifted control technology effective control harmonic, regardless of in traction operating mode and brake operating mode, when the power surpassed 5 MW, the catenary current harmonic components is lower, total harmonic distortion rate of the network is less than 3%, the equivalent

disturbing current is below 1.5 A, and the power factor is above 0.98, and the total harmonic disturbing rate of each harmonic is not more than 1%. The new EMU has similar traction characteristics to the previous EMU, including the constant torque and constant power sections. The method taken to suppress harmonics do not affect the traction characteristics of the train.

## References

1. Sainz L, Monjo L, Riera S (2012) Study of the steinmetz circuit influence on AC traction system resonance. *IEEE Trans Power Deliv* 27(4):2295–2303
2. Diao L, Zhao L, Jin Z et al (2017) Taking traction control to task: high-adhesion-point tracking based on a disturbance observer in railway vehicles. *IEEE Ind Electron Mag* 11(1):51–62
3. Wensheng S, Smedley K, Xiaoyun F et al (2011) One-cycle control of induction machine traction drive for high speed railway part II: square wave modulation region. In: 26th annual IEEE applied power electronics conference and exposition, pp 1003–1009
4. Shu-ming L, Dong-xin C, Qiong-lin L et al (2012) The impact of 350 km/h high-speed railway to grid power quality. In: Asia-pacific power & energy engineering conference. IEEE, pp 1–4
5. Wang N, Song W, Feng X (2012) Characteristics analysis and reduction of the high order harmonics of DC-link voltage for railway traction converters. In: International power electronics & motion control conference. IEEE, pp 1926–1931
6. Jingjing D, Zheng Q, Chunxing P (2011) Harmonic analysis method for input current of traction system applied in high-speed electric multiple unit. In: International conference on electronics & optoelectronics. IEEE, pp V1-30–V1-34
7. Husng J, Lu Y, Zhang B (2012) Harmonic current elimination for single—phase rectifiers based carrier phase-shift. In: IEEE-APS topical conference on antennas & propagation in wireless communications. IEEE, pp 152–155
8. Mendes AMS, Rocha RF, Cardoso AJM (2011) Analysis of a railway power system based on four quadrant converters machines & drives conference under faulty conditions. In: IEEE international electric (IEMDC), pp 1019–1024
9. Dolara A, Gualdoni M, Leva S (2012) Impact of high-voltage primary supply lines in the 2\*27.5 kV–50 Hz railway system on the equivalent impedance at pantograph terminals. *IEEE Trans Power Deliv* 27(1):164–175

# Research on Optimization Strategy of Forced Convection Heat Dissipation for Super Capacitor Energy Storage Power Supply

Jun Zhang, Zhongcheng Jiang, Jixiong Jiang, JingJing Chen and Li Zhou

**Abstract** The service life of the super capacitor is very sensitive to the temperature. In order to obtain the optimization strategy of forced convection heat dissipation for super capacitor energy storage power, the main factors affecting the efficiency of forced convection heat dissipation are analysed based on the heat transfer theory, and the main direction of heat dissipation optimization are determined. The numerical heat transfer calculation model is established by the method of computational fluid dynamics. The internal flow field and temperature field distribution characteristics of super capacitor power supply are analysed. And the influence of cold air volume flow rate, air outlet layout and super capacitor heat dissipation structure on the heat dissipation effect is calculated and compared. The results show that the super capacitor heat dissipation structure and air outlet layout are most obvious to the improvement of heat dissipation. The maximum temperature of super capacitor is reduced to 32.62 °C from 68.69 °C through optimization in the same ventilation air volume flow rate and temperature. The improvement effect is very obvious.

**Keywords** Super capacitor · Forced convection · Heat dissipation  
Computational fluid dynamics

## 1 Instruction

Super capacitor is a new energy storage component, which is different from conventional capacitance, its capacity can be thousands farad. It has the advantages of high power density of conventional capacitors and high energy density of battery, fast charge and discharge, and long service life, has developed into a new, efficient,

---

J. Zhang (✉) · Z. Jiang · J. Jiang · J. Chen · L. Zhou  
The State Key Laboratory of Heavy Duty AC Drive Electric  
Locomotive Systems Integration, Zhuzhou 412001, Hunan, China  
e-mail: zjcrre@163.com

© Springer Nature Singapore Pte Ltd. 2018

L. Jia et al. (eds.), *Proceedings of the 3rd International Conference on Electrical and Information Technologies for Rail Transportation (EITRT) 2017*, Lecture Notes in Electrical Engineering 482, [https://doi.org/10.1007/978-981-10-7986-3\\_2](https://doi.org/10.1007/978-981-10-7986-3_2)

practical energy storage device. In recent years, super capacitor has been applied in urban rail vehicles [1]. In order to achieve the long distance continuous operation, the super capacitor energy storage power supply complete charging in a short time at the stop by the high efficient charging and discharging performance.

The super capacitor will produce thermal loss due to its internal resistance during the working process. The heat generated by internal resistance causes the temperature rise. Forced ventilation cooling is usually used to dissipate heat from the super capacitor energy storage. Based on the heat dissipation of super capacitor energy storage power supply, the optimization direction and strategy of forced ventilation heat dissipation are studied in this paper.

## 2 Introduction of Super Capacitor Energy Storage Power Supply

In order to form a large energy storage capacity and a certain working current and voltage, a super capacitor module is usually connected in series and in parallel, as shown in Fig. 1. The super capacitor module is composed of super capacitor monomer, electrode connecting copper, module skeleton, single isolation strip, and module equalizer circuit board. A gap of 3 mm between each monomer is used for ventilation and is separated by isolation strips. The ventilation holes of copper and circuit board correspond to the gap between the module, and the air can pass up and down through these gaps.

Through the layer arrangement of the module, a complete super capacitor energy storage power supply is formed, as shown in Fig. 2. According to the working current and internal resistance of the super capacitor energy storage power, the total heating power is 681 W. The cold air of the air conditioning system in the vehicle passenger compartment is used as the forced convection cooling medium of the super capacitor energy storage power supply.

## 3 Theoretical Analysis

The air conditioning cold air is used in the ventilation cooling of super capacitor energy storage power supply, which is a typical physical process of forced convection heat transfer. Each super capacitor is a heat source. The cold air flows through the gap between each monomer. The heat of the super capacitor is removed through the convective heat transfer between the cold air and the surface of the super capacitor, which is the process of heat dissipation.

The heat calculation formula of convection is given by Newton cooling formula (1) [2].

**Fig. 1** Super capacitor module

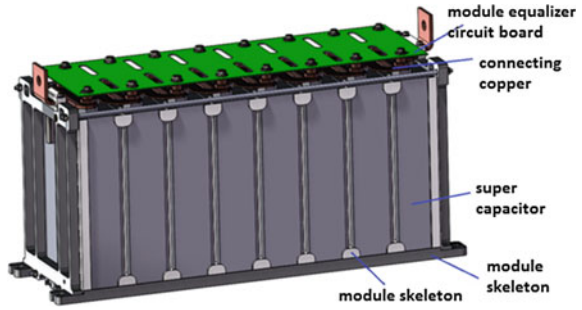
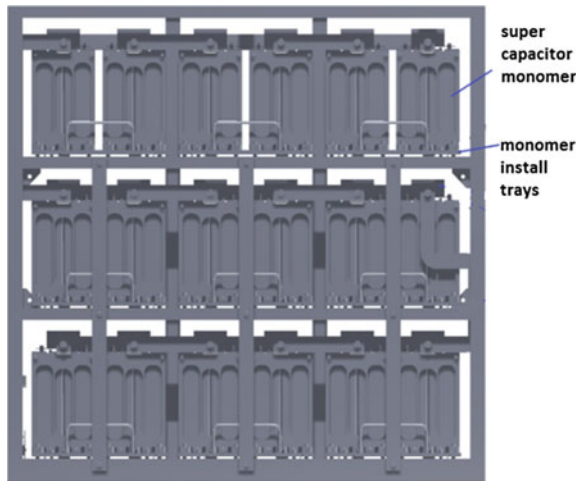


**Fig. 2** Super capacitor energy storage power supply



$$q = h \cdot A \cdot \Delta t \tag{1}$$

where  $q$  is the heat flow through an unit area in an unit time;  $h$  is convective surface heat transfer coefficient;  $\Delta t$  is the mean temperature difference between a solid surface and its surrounding fluid.

The convective surface heat transfer coefficient is a very important parameter. Newton cooling formula only gives its definition formula. Its value is related to many factors, including the physical properties, movement state, phase change, and the shape and size of the solid heat transfer surface [1]. Taking the single-phase forced convection heat transfer as an example, when the high speed flow is excluded, the surface heat transfer coefficient can be expressed as a function which is shown in the formula (1.2) [3].

$$h = f(u, l, \rho, \mu, \lambda, c_p) \tag{2}$$

where  $u$  is the velocity of fluid flow;  $l$  is a characteristic length of solid heat transfer surface;  $\rho$  is the density of the fluid;  $\mu$  is the dynamic viscosity of fluid;  $\lambda$  is the coefficient of thermal conductivity of fluid;  $c_p$  is the specific heat capacity of fluid [4].

From the formula (1), it can be seen that increasing the heat dissipation area and the temperature difference between fluid and solid can improve the efficiency of convection heat dissipation. Because of the limits of the volume and weight of the super capacitor energy storage power supply, the method of enlarging the heat dissipation area will greatly increase the system complexity. Lowering the cooling air temperature can increase the temperature difference between fluid and super capacitor to enhance heat dissipation efficiency. Because the air conditioning system temperature is determined by the HVAC design, reducing the cold air will affect the comfort of passengers. These methods are not desirable.

It can be seen from the formula (2) that convection cooling efficiency can be improved by changing the physical properties of the fluid, increasing the flow velocity of the fluid and changing the geometry dimensions of the object. When the ambient temperature is certain, the physical parameters of the air are constant. If the parameters such as the thermal conductivity of the fluid can be improved by changing the cooling medium, the complexity of the cooling system will be increased, and the system design of the vehicle will be greatly affected. It is almost impossible. When the volume and weight of the energy storage power can not be changed, the characteristic length of convective heat transfer is constant. Therefore, the thermal efficiency of super capacitor can only be improved by increasing the velocity of air flow [5].

Improving the flow velocity of the surface air of the super capacitor can be realized by increasing the air flow and optimizing the local flow characteristics. In this paper, computational fluid dynamics method is used to calculate the three-dimensional temperature field of super capacitor energy storage power, and determine the optimization strategy of super capacitor heat dissipation.

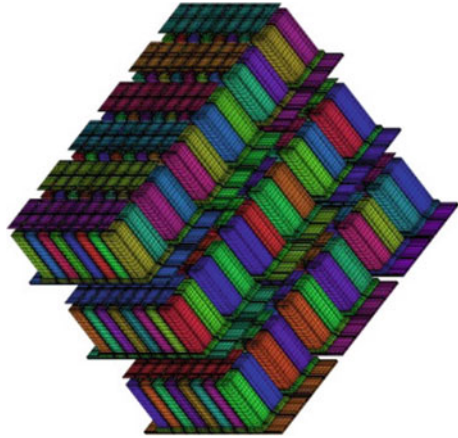
## 4 Numerical Calculation Model

The fluid and solid calculation domain are discretized by hexahedral mesh. The turbulence model is used to simulate. And the commercial computational fluid dynamics software based on the finite volume method is used to calculate [6, 7].

Using the simplified geometric model, a very fine hexahedral calculation grid is established, and the calculation region is discretized. The overall schematic diagram of the grid is shown in Fig. 3, and the fluid domain body grid and partial surface mesh are hidden for visual convenience [8, 9].

The super capacitor energy storage power supply is installed inside the passenger compartment. Both inside and outside of the box are cold air provided by the air conditioning system, the temperature difference between inside and outside is very small. In order to simplify the calculation, the temperature difference between

**Fig. 3** Mesh model of numerical calculation



the inside and outside of the box is ignored, so the convective heat transfer of the inner air and the super capacitor energy storage power supply box wall can be ignored.

The ideal gas is used to calculate, considering the change of air density with the change of temperature, the other physical properties of air are approximately determined as constant. The super capacitor monomer is approximated to be a homogeneous heating body, and its equivalent thermal physical properties are shown in Table 1.

The air inlet of the ventilation system is set to the velocity inlet boundary condition. The inlet velocity is calculated according to the ventilation air flow volume. The inlet air temperature is 20 °C. Pressure export boundary conditions are used for air outlet of the ventilation system. The pressure is 1 ATM. The wall of box is set as no slip adiabatic wall boundary.

Ignoring the transient process of super capacitor temperature, all simulation calculations are steady-state calculation.

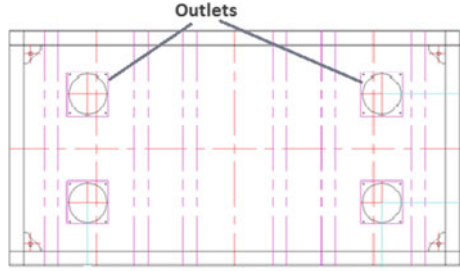
## 5 Calculation Results and Analysis of Initial Scheme

For the initial scheme, the cold air temperature is 20 °C, the cold air volume flow rate is 400 m<sup>3</sup>/h. The air inlet size is 250 mm × 100 mm, the size of each air outlet is 110 mm × 110 mm. The layout of the four air outlets is shown in Fig. 4.

**Table 1** Equivalent physical properties of super capacitor monomer

Physical properties	Density kg/m <sup>3</sup>	Specific heat capacity J/(kg K)	Thermal conductivity W/(m K)
Value	810	2265	0.7

**Fig. 4** The layout of the four air outlets



The simulation model is established, and the numerical solution and post-processing are carried out. The maximum temperature of the super capacitor is 68.69 °C. The highest air temperature is 59.29 °C. The average outlet air temperature is 24.82 °C. Figure 5 is the temperature distribution cloud picture at the symmetrical section. Figure 6 is the velocity distribution cloud picture at the symmetrical section. Figure 7 is the air flow trace picture.

As shown in Fig. 5, the internal temperature distribution in the super capacitor box is very uneven. The highest temperature of the middle two of the third layer module is 68.69 °C. This is obviously not the best working temperature for the super capacitor. The initial scheme should be improved.

As shown in Figs. 6 and 7, the air flow velocity distribution uniformity is very poor. The air velocity is high between the super capacitors in the first layer of super capacitor module, which is low in the second and the third layer. The gap between the super capacitor installation trays is relatively large; the air flow velocity through this gap is very high. In particular, the air velocity between the tray and the wall

**Fig. 5** The temperature distribution cloud picture at the symmetrical section

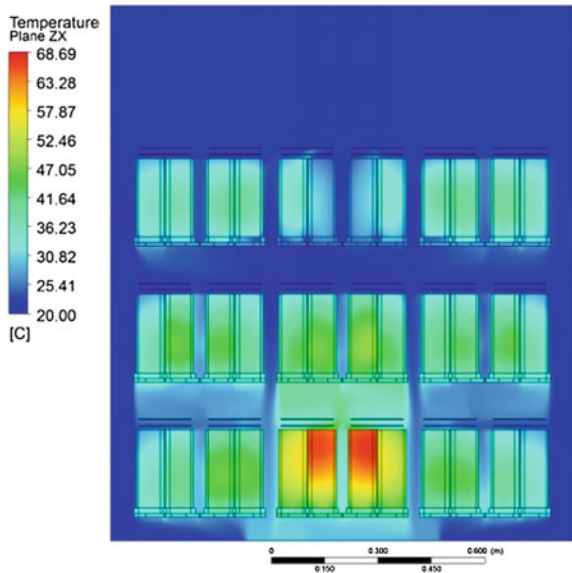




**Fig. 6** The velocity distribution cloud picture at the symmetrical section

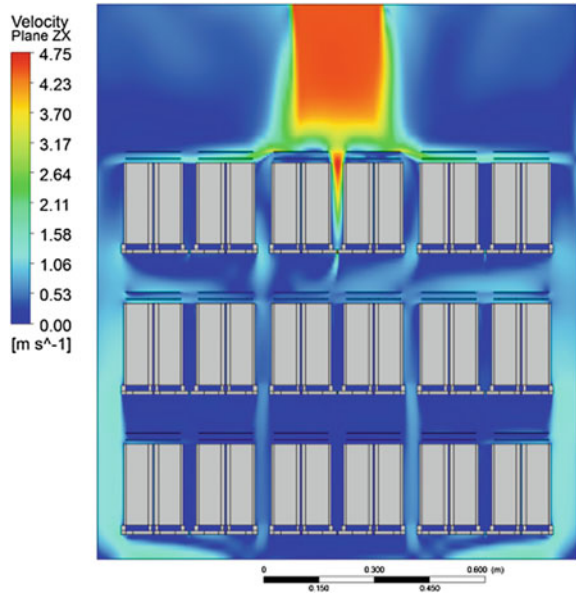
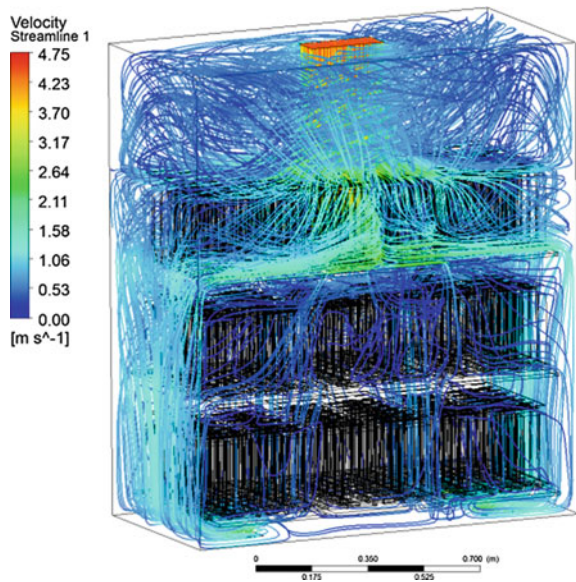


**Fig. 7** The air flow trace picture



surface of the box is very large. Figure 7 is the trace of 500 random selected massless particles from the inlet through the entire fluid domain driven by the velocity vector field. As shown in Fig. 7, the particles flow between the super

capacitor monomers in the second and third layer modules are very few and the flow velocity is very low.

Because the four outlets are located at the bottom of the left and right trays of the third layer module, there is almost no particle flow through the middle tray in the third layer module. The arrangement of the outlet is also the cause of the high temperature of the super capacitor in the third layer module.

According to the mechanism of forced convection heat transfer, the higher the flow velocity on the surface of the high temperature object, the greater the heat transfer in the unit time. The cooling efficiency of the super capacitor can be improved by increasing the flow velocity at the surface of the super capacitor.

According to the analysis of the above calculation results, in order to improve the ventilation and heat dissipation effect of the super capacitor box, reduce the maximum capacitance temperature, can be optimized from the following aspects.

The first, increase the air volume flow rate: by increasing the total air volume flow rate of the heat dissipation, the air velocity in the super capacitor box can be increased, so as to accelerate the convective heat transfer and reduce the maximum temperature of the super capacitor.

The second improve outlet arrangement: Add two air outlets below the intermediate tray in the third layer module. Improve the cooling effect of the intermediate super capacitor in the third layer, thereby reducing the maximum temperature of the super capacitor.

The third, adjust the gap between the trays: by adjusting the gap between the tray and the gap between the tray and the wall of the box, solve the problem of uneven internal velocity distribution, so that the air flow velocity between the super capacitor monomer can be increased under the same air volume flow rate, so as to accelerate the convective heat transfer.

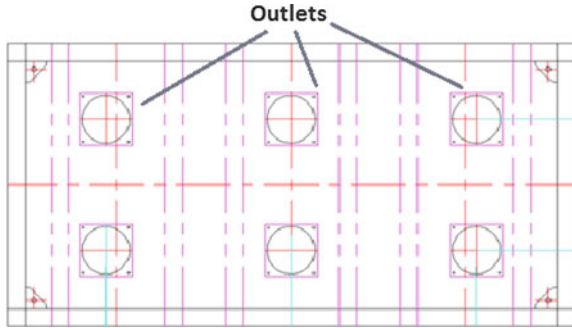
## **6 Effect of Increasing Air Volume Flow Rate**

When the air volume flow rate is increased by half to 600 m<sup>3</sup>/h, the maximum temperature of the super capacitor box is 60.94 °C. The highest air temperature is 57.75 °C. The average outlet air temperature is 23.33 °C. The calculation results show that the heat dissipation efficiency can be improved by increasing the air volume flow rate. But the maximum temperature of the super capacitor is still relatively high. Super capacitor cooling efficiency can still be further improved.

## **7 Effect of Improved Air Outlet Layout**

Add two air outlets below the intermediate tray in the third layer module. The added outlets is in the middle of the original outlets, as shown in Fig. 8.

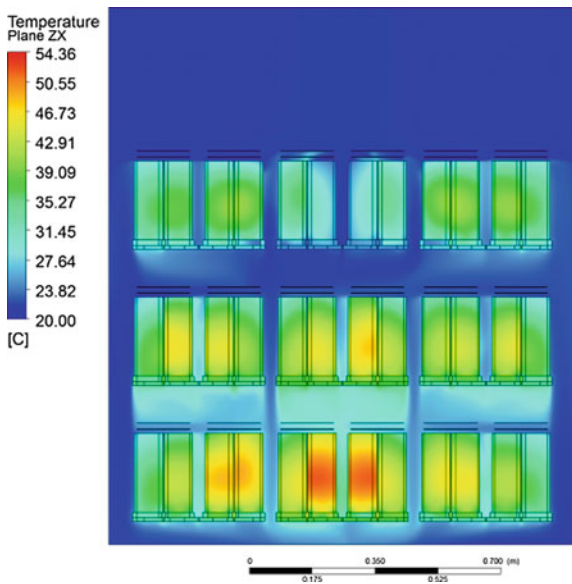
**Fig. 8** Improved air outlet layout



For the improved air outlet layout scheme, the cold air temperature is 20 °C, the cold air volume flow rate is 400 m<sup>3</sup>/h. Through calculation, the internal maximum temperature of the super capacitor is 54.36 °C. The highest air temperature is 50.67 °C. The average outlet air temperature is 25.12 °C. Figure 9 is the temperature distribution cloud picture at the symmetrical section.

Figure 9 shows that the overall temperature distribution is much more uniform than Fig. 4 (initial scheme). And the maximum capacitance of super capacitor also decreased about 14 °C, indicating that the improved outlet layout has obvious effect on heat dissipation. The scheme is better than adding half of the air volume flow rate, and the scheme does not increase the load of the air conditioning system. It is suggested to adopt this improved outlet layout scheme in the project.

**Fig. 9** The temperature distribution cloud picture at the symmetrical section



## 8 Effect of Improvement of Internal Flow Field

In order to improve the uniformity of the velocity field, adjust the gaps to 5 mm between the trays. The gaps between the module trays and the walls are canceled. Improved six outlets layout scheme is adopted. The cold air temperature is 20 °C, the cold air volume flow rate is 400 m<sup>3</sup>/h.

Through calculation, the internal maximum temperature of the super capacitor is reduced to 32.62 °C. The highest air temperature is 30.90 °C. The average outlet air temperature is 25.04 °C. Figure 10 is the temperature distribution cloud picture at the symmetrical section. Figure 11 is the velocity distribution cloud picture at the symmetrical section.

As shown in Fig. 10, the temperature distribution of each super capacitor module is very uniform. The temperature of the first layer super capacitor is the lowest. The temperature of the second and third layer modules increased slightly in turn. The highest temperature is only 32.62 °C. And the improvement effect is remarkable compared with the initial scheme. As shown in Fig. 11, the flow velocity distribution is also very uniform.

**Fig. 10** The temperature distribution cloud picture at the symmetrical section

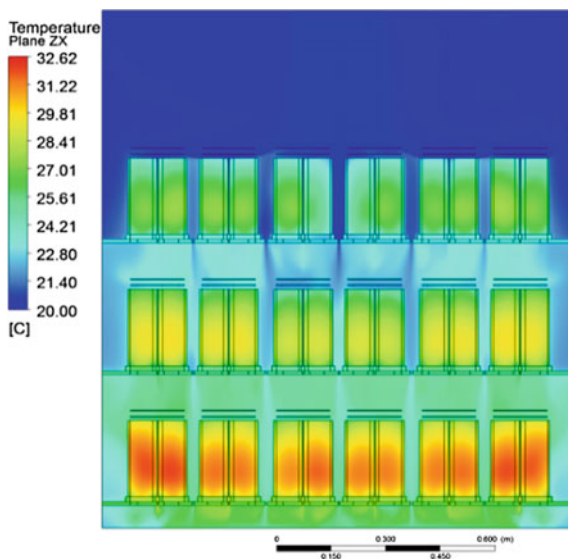
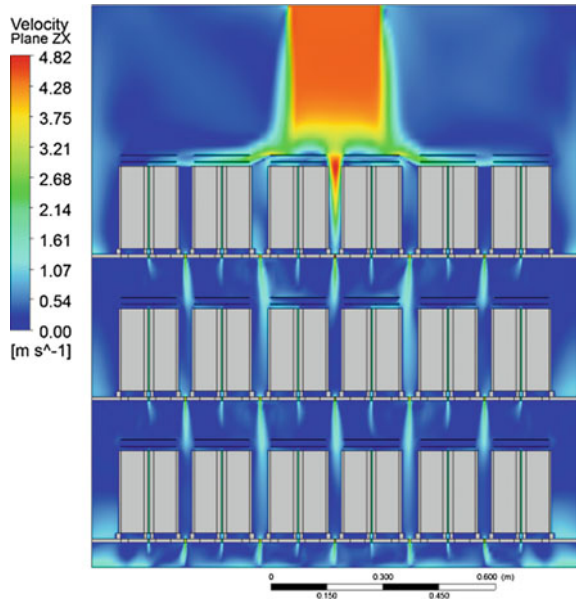


**Fig. 11** The velocity distribution cloud picture at the symmetrical section



## 9 Conclusions

The Comparisons of different forced convection condition are listed in Table 2. Through the research in this paper, it is found that increasing the flow velocity on the surface of super capacitor is an effective way to improve the efficiency of forced ventilation cooling of super capacitor energy storage power. It is not obvious to enhance the heat dissipation efficiency of super capacitors by simply adding the air volume flow rate method. Through optimizing the internal arrangement of the super

**Table 2** Comparisons of different forced convection condition

Convection condition	Maximum temperature °C	Improving temperature difference °C	Remarks
Initial scheme: flow rate 400 m <sup>3</sup> /h	68.69	–	High temperature, uneven distribution
Increasing air volume flow rate to 600 m <sup>3</sup> /h	60.94	7.7	HVAC higher load; uneven temperature distribution
Improved air outlet layout Flow rate 400 m <sup>3</sup> /h	54.36	14.33	Lower temperature More uniform distribution
Improved internal flow field Flow rate 400 m <sup>3</sup> /h	32.62	36	Lowest temperature More uniform distribution

capacitor to change the air flow, and guide more air flow through the super capacitor surface and the gap between the super capacitor monomers, forming more effective air flow is a good way to improve the heat efficiency of super capacitor. In another aspect, through the improvement of the arrangement of the air outlets, changing the uniformity of cooling air flow velocity field has a good effect on the uneven distribution of the temperature field of the super capacitor energy storage power supply.

## References

1. Chen H, Xia H, Yang Z, Li X (2015) Study of output impedance optimization for stationary super-capacity energy storage applied in urban rail power supply system. Society of Instrument & Control Engineers of Japan, pp 900–905
2. Shiming Y, Wenquan T (2006) Heat transfer, 4th edn. Higher Education Press, Beijing, pp 3–12. (In Chinese)
3. Jungeng T (2007) Engineering thermodynamics, 4th edn. Higher Education Press, Beijing, pp 142–145. (In Chinese)
4. Zohuri B, Fathi N (2015) Forced convection heat transfer. Springer International Publishing
5. Dawood HK, Mohammed HA, Sidik NAC, Munisamy KM, Wahid MA (2015) Forced, natural and mixed-convection heat transfer and fluid flow in annulus: a review. *Int Commun Heat Mass Transf* 62:45–57
6. Safaei MR, Goodarzi M, Mohammadi M (2016) Numerical modeling of turbulence mixed convection heat transfer in air filled enclosures by finite volume method. *Intern J Metaphysics* 5(4):307–324
7. Nagendra HR (2015) Transient forced convection heat transfer from an isothermal flat plate. *AIAA J* 11(6):876–878
8. Ortiz C, Skorek AW, Lavoie M, Benard P (2007) Parallel CFD analysis of conjugate heat transfer in a dry-type transformer. *IEEE Trans Ind Appl* 45(4):1530–1534
9. Armando GM, Armando BBJ, Christian VC et al (2010) Analysis of the conjugate heat transfer in a multi-layer wall including an air layer. *Appl Therm Eng* 30(6–7):599–604

# Mechanism of Rectified Output Voltage Spike in Isolated Converter Under Wide Input Voltage

Chunhui Miao, Huiqing Du and Fei Xiao

**Abstract** There exists high rectified output voltage spike in isolated transformer's secondary, especially for the high frequency link auxiliary inverters under wide input voltage. It will lead to increased voltage stress and loss of switching devices, impeding the improvement of system's reliable operation and conversion efficiency. In order to solve the root causes of rectified output voltage spike, the mathematical model of rectifier output voltage is established. Based on the model, the mechanism of voltage spike is explored, deriving two main reasons: one is the wide input voltage, and the other is the resonance between the transformer leakage and the rectifier diode junction capacitor. Consequently, it is more pertinent to address the problem and improve the system's reliability.

**Keywords** Voltage spike · Wide input voltage · High frequency link  
Isolated converter

## 1 Introduction

As the key equipment to ensure stable and comfortable running of rail trains, auxiliary inverter undertakes important task of providing electric power for cooling fans, air compressors, air conditioners, electric heaters, ventilators, information display devices, etc. [1]. The train auxiliary inverter is essentially a converter which transforms direct current into alternating current. As its dc input and ac output are often required for safety isolation on the electrical side, the transformer is widely

---

C. Miao (✉) · F. Xiao  
Naval University of Engineering, PLA, No. 717, Jiefang Road,  
Qiaokou District, Wuhan, Hubei, China  
e-mail: mchcat@189.cn

C. Miao · H. Du  
System Engineering Institute, China State Shipbuilding Corporation,  
No. 1, Fengxian East Road, Haidian, Beijing, China

used because of electrical isolation, voltage adjustment and noise decoupling. According to the different frequencies of the transformers, the auxiliary inverter can be divided into two types: industrial-frequency isolation and high-frequency isolation.

As seen in Fig. 1, the auxiliary inverter has its advantages such as fewer power devices, compact circuit structure, convenient control, high reliability and long lifetime. However, the defects are also significant, including the large and heavy transformer, the large audio noise, the high losses and the uncontrollable zero sequence components [2, 3].

In order to overcome the inherent defects of industrial-frequency isolation type, P. M. Espelage and B. K. Bose proposed a high frequency link energy conversion technique in 1997, whose electrical isolation was performed by using high-frequency-pulse transformer instead of industrial-frequency transformer [4]. The application of the technique has greatly reduced the volume and weight of the transformer, for example, when the frequency of the transformer is increased from 50 to 20 kHz, the volume and weight of the transformer can be reduced to  $1/74 \sim 1/116$  of the industrial-frequency isolated transformer (the former is for the D310-0.08 silicon steel, and the latter is for the ferrite). It can effectively reduce the train load, save the space of the train, improve the travel environment, reduce the energy consumption of the train and improve the dynamic response of the system. Moreover, high frequency topology is more in line with the future trends of the development of semiconductor devices and magnetic materials, contributing to further reduce the volume and weight of passive components, and increase the power density by improving the switching frequency [5]. Therefore, this technology has caused great research interest of the scholars, and some significant research results have been made. At present, the high frequency topology has gradually become the mainstream of train auxiliary inverter topologies [6].

There is a wide variety of high-frequency link topologies, and the most mature topology of the train auxiliary inverter is the fixed dc link inverter as shown in Fig. 2. It's usually constituted by input LC filter, single phase inverter, high-frequency isolated transformer, diode rectifier, middle LC filter, three phase voltage source inverter and three phase LC filter. The whole system contains three stages of power conversion, which are dc to high frequency ac, high frequency ac to dc and dc to low frequency ac.

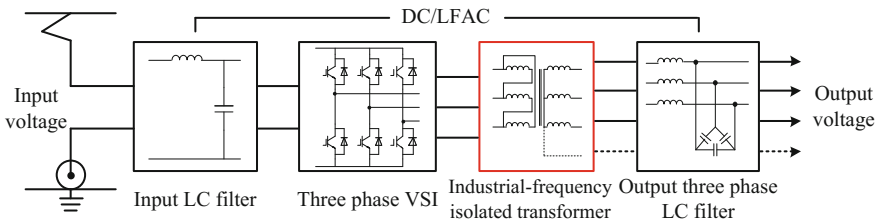


**Fig. 1** Topology of auxiliary inverter with industrial-frequency isolated transformer



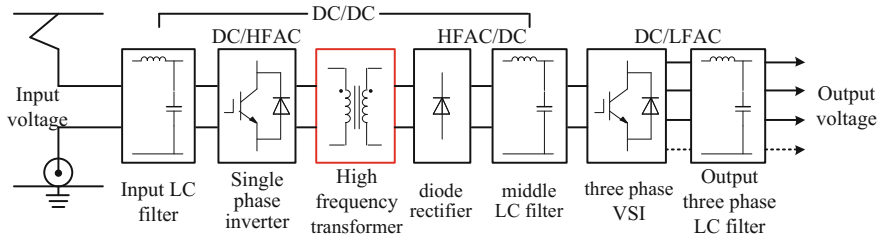


**Fig. 2** Topology of high-frequency fixed DC-link inverter

Despite the lightweight and miniaturized high-frequency transformers is used instead of the industrial-frequency isolated transformer, the system still has the problem of high voltage peak of the rectifier output, which becomes the key factor in safe and reliable operation of the system. In order to solve the problem, previous studies have used the combination of device series, module cascade, passive snubber and active clamp. Although some achievements have been made, the analysis of the mechanism of the output voltage spike is not comprehensive.

To solve the problem of high output voltage spike of fixed dc link Inverter, this paper establishes the mathematical model of the rectifier output voltage. Based on the model, the main reasons for the high voltage spike of the high frequency link auxiliary inverter are analyzed. One is that the system input voltage varies widely, the other is the resonance between the transformer leakage and the rectifier diode junction capacitor.

## 2 Variation Characteristics of the Rectifier Output Voltage Under Wide Input Voltage Range

For the fixed dc link inverter, at the beginning of system design, the ratio of high frequency isolated transformer should be calculated when the intermediate dc voltage  $V_{odc}$  is constant, the power is rated, and the input voltage  $V_{dc-min}$  is minimum. Then the equivalent ratio of the former DC/DC converter should be set to maximum, that  $D_{dc-max} \approx 1.0$ . Take full bridge converter as example to analysis, Eq. (1) can be derived.

$$N = k_a \frac{V_{dc-min} D_{dc-max}}{V_{odc}} \quad (1)$$

Wherein,  $k_a$  is the additional adjustment factor considering the transmission voltage drop,  $k_a < 1.0$ . However, when the transformer in the system is confirmed,  $V_{odc}$  will change linearly with the input voltage. When the system is at the highest input voltage  $V_{dc-max}$ ,  $V_{odc}$  is highest. Its expression is shown as Eq. (2).

$$V_{\text{odc-max}} = \kappa_{\text{in}} \frac{V_{\text{odc}}}{k_a D_{\text{dc-max}}}, \kappa_{\text{in}} = \frac{V_{\text{dc-max}}}{V_{\text{dc-min}}} \quad (2)$$

Equation (2) shows that it is not directly related to the absolute value of the input voltage, which is determined by its range of variation. As shown in Fig. 3, the input voltage variation of the auxiliary inverter is wide [7, 8]. For different voltage rating systems,  $\kappa_{\text{in}}$  is usually 1.8 or 2.0. Therefore,  $V_{\text{odc-max}}$  can be as high as more than  $2V_{\text{odc}}$ . If considering the parasitic oscillations mentioned in the next section, the actual rectifier output voltage spikes will be higher.

### 3 Parasitic Oscillation Mechanism of Transformer's Secondary

In high frequency isolated DC/DC converter, the rectifier diodes take on a very important role. But due to the presence of the junction capacitor, the diodes experience a dynamic transition during switching state. Especially by forward bias switches to reverse bias, the diodes do not shut off immediately, and during that time there exists reverse recovery current, which will cause high frequency resonance between the junction capacitance and the leakage inductance of the transformer, producing a larger voltage overshoot, and causing additional circuit loss. If it is not properly handled, it will seriously threaten the safety of power devices.

In order to analyze the dynamic properties of the diode reverse-recovery process, draw the typical waveform of diode reverse-recovery current, as shown in Fig. 4. In the figure, when  $t = t_0$ , the diode plus voltage is reversed by the forward and the forward current is gradually reduced by the reverse pressure, and its slope is determined by the size of the inverse voltage and the inductance in the circuit. When  $t = t_1$ , forward current drops to zero, but the diode does not restore the

**Fig. 3** Input voltages of systems with different voltage levels

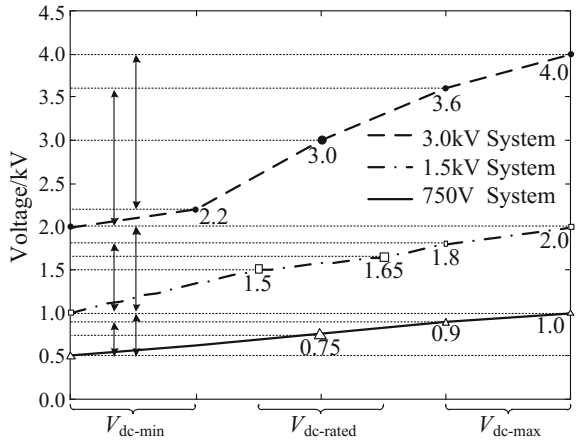
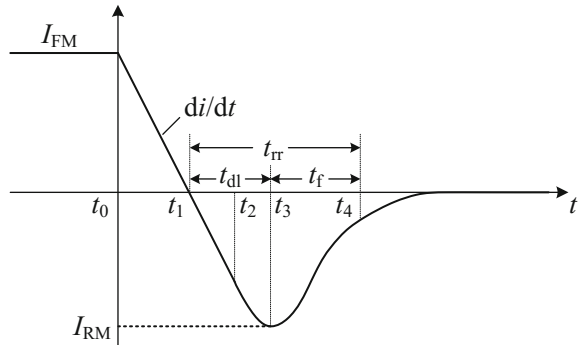


**Fig. 4** Waveform of diode reverse recovery current



reverse blocking ability because PN junction on both sides still has a lot of minority carriers, which are pulled away from the diode under the negative voltage, thus forming the reverse recovery current. When  $t = t_2$ , the minority carriers in the vicinity of the space charge zone are exhausted, and begin to draw down the lower concentrations of the lower concentrations of the space charge. When  $t = t_3$ , the reverse recovery current reaches maximum  $I_{RM}$  and the space charge area begins to widen rapidly, and the diode begins to recover the ability to block the reverse voltage. After  $t > t_3$ , the reverse current drops rapidly, and the current changing rate is close to zero at  $t_4$ , when the diode fully recovers the ability to block the reverse voltage. Wherein, delay time  $t_{dl} = t_3 - t_1$ , current fall time  $t_f = t_4 - t_3$ , and reverse recovery time  $t_{rr} = t_{dl} + t_f$ .

And then based on the reverse recovery characteristics of the diode, the actual turn-off transient of the rectifier diode in the full bridge converter is analyzed. Figure 5a is the simplified circuit of transformer’s secondary, and Fig. 5b is the equivalent circuit of the resonant process, among them,  $u_s$  is the voltage of transformer’s secondary,  $i_s$  is the current of transformer’s secondary,  $L_{ks}$  is the equivalent leakage of transformer’s secondary, and  $i_{rec}$  is rectified output current, which is approximate constant during the analysis process.

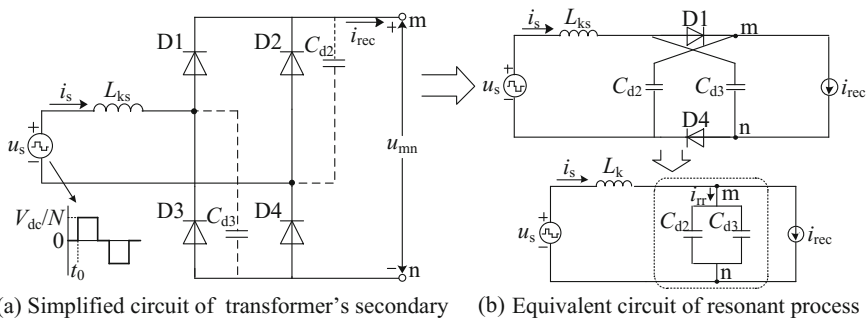


**Fig. 5** Transformer’s secondary simplified circuit and resonant circuit

As seen in Fig. 5, before  $t = t_0$ , the voltage of transformer's secondary  $u_s = 0$ , the current of transformer's secondary  $i_s = 0$ , all the diodes in the rectifier are conducting to provide a circulation circuit for the current  $i_{rec}$ . And the two groups of bridge arms have average current. When  $t = t_0$ ,  $u_s$  increases from 0 to  $V_{dc}/N$ ,  $i_s$  gradually increases from 0 in the slope  $V_{dc}/(NL_{ks})$ , the current flowing through the diode D2 and D3 gradually reduces from  $i_{rec}/2$ . When  $i_s$  increases to  $i_{rec}$ , D2 and D3 stop conducting, and their current reduces to 0, but the reverse recovery current  $i_{rr}$  will flow past the junction capacitance of the diodes between point m and n. In turn, the resonance between the junction capacitor and the transformer leakage induces the m point potential to rise.

The initial state of the resonant circuit is  $u_{mn}(0) = 0$ ,  $i_s(0) = i_{rec}$ , and then the resonance equation can be got as shown in Formula (3).

$$\begin{cases} u_{mn}(t) = \frac{V_{dc}}{N} [1 - \cos(\frac{t}{\sqrt{L_k C_d}})] \\ i_s(t) = i_{rec} + \frac{V_{dc}}{N \sqrt{L_k / C_d}} \sin(\frac{t}{\sqrt{L_k C_d}}) \end{cases} \quad (3)$$

Wherein,  $C_d = (C_{d2}/C_{d3})$ . It is thus obvious that, there will still be oscillation peak which is at least twice of the maximum of ideal rectified output voltage  $V_{rec}$ . Combined with the second chapter, the maximum output voltage peak can be up to  $4V_{odc}$  as shown in Fig. 6. And in order to ensure that the final output ac voltage meets customers' requirement, as a general rule  $V_{odc} > 600$  V, which means that the peak voltage is up to more than 2400 V. If it is not properly handled, it will cause the rectifier diode breakdown, which will seriously affect the reliable operation of the system.

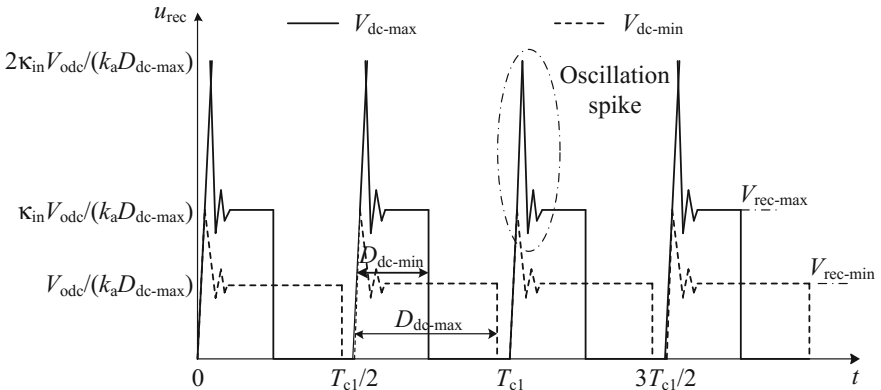


Fig. 6 Typical waveform of rectified output voltage

## 4 Conclusion

As the key equipment of rail trains, train auxiliary inverters usually adopt the high frequency link topologies. While they always have the problem of high rectified output voltage spike in the isolated converters. In order to solve the reliable problems, the mathematical model of rectifier output voltage is established. Based on the model, the mechanism of voltage spike is explored, deriving two main reasons:

- (a) The input voltage of the system varies widely.
- (b) There exists resonance between the transformer leakage and the rectifier diode junction capacitor.

## References

1. Wang Y, Liu W, Yang Z et al (2014) Research on design evaluation of high-speed train auxiliary power supply system based on the AHP. Transportation electrification Asia-Pacific. Beijing, China
2. Versèle C, Deblecker O, Lobry J (2010) Multiobjective optimal design of transformers for isolated switch mode power supplies. In: Power electronics electrical drives automation & motion international symposium on IEEE, pp 1687–1692
3. Martinez C, Lazaro A, Lucena C et al (2013) Improved modulator for losses reduction in auxiliary railway power supplies. In: Applied power electronics conference and exposition. California, USA
4. Espelage PM, Bose BK (1977) High-frequency link power conversion. IEEE Trans Indus Appl IA-13(5):387–394
5. Qian Z, Zhang J, Sheng K (2014) Status and development of power semiconductor devices and its applications. In: Proceedings of the CSEE 34(29):5149–5161. (In Chinese)
6. Pavlovsky M, De Haan SWH, Ferreira JA (2009) Reaching high power density in multikilowatt DC–DC converters with galvanic isolation. IEEE Trans Power Electron 24(3):603–612
7. Maerz A, Bakran MM (2014) Designing a low weight low loss auxiliary converter for railway application. In: PCIM Europe 2014; international exhibition and conference for power electronics, intelligent motion, renewable energy and energy management; proceedings of VDE
8. Vinnikov D, Laugis J, Jalakas T (2007) Development of auxiliary power supplies for the 3.0 kV DC rolling stock. In: Industrial electronics, 2007. ISIE 2007. IEEE international symposium on IEEE, pp 359–364

# Distributed Energy-Saving Dynamic Matrix Control of Multi-locomotive Traction Heavy Haul Train

Xiukun Wei and Jinglin Zhang

**Abstract** Due to the heavy haul train's force condition is far more complex than the ordinary train, broken hook and decoupling situation will become potential danger in the operation of the train. The energy-saving operation of heavy haul train is of great importance for rail transport. In this paper, we will study the distributed co-control of heavy haul train from the aspects of reducing the load-bearing force during the operation of heavy haul train and reducing the energy consumption of heavy haul train. It is of great importance to ensure the safe and stable operation and energy saving operation of heavy haul train. In this paper, simulink is used to build the multi-locomotive multi-particle heavy haul train dynamic model. Based on the dynamic matrix control (DMC) algorithm to establish the multi-locomotive multi-particle heavy haul train dynamic matrix control system, the velocity curve is tracked and controlled. The coupler force, running displacement and energy consumption are obtained. The simulation results are compared with the results which under the PID control system.

**Keywords** Heavy haul train · Multi-locomotive Multi-particle model  
DMC · Simulink

## 1 Introduction

With the gradual improvement of China's railway transport network, transport energy consumption has gradually increased. It reflects the level of rail transport organization and has a direct impact on the cost of rail transport.

The force condition during the operation of the heavy haul train is far more complex. There are potential hazards during the operation of the train, such as

---

X. Wei (✉) · J. Zhang  
State Key Laboratory of Rail Traffic Control and Safety,  
Beijing Jiaotong University, Beijing, China  
e-mail: xkwei@bjtu.edu.cn

breakage, decoupling and so on, which has become an urgent problem to be solved in the heavy rail transport [1, 2]. So it is necessary to carry out detailed research.

## 2 Multi-locomotive Multi-particle Heavy Haul Train Dynamic Model

Multi-locomotive multi-particle heavy haul train dynamic model is a dynamic model that can reflect the actual marshalling situation of train. Each locomotive or vehicle is treated as a particle with length and quality attributes, which are independent of each other but closely linked through the tension between the front and rear vehicles [3].

In multi-locomotive multi-particle heavy haul train dynamic model, the force analysis of each compartment is carried out, and the equation is written to write their state space equation, which is prepared for the establishment of the dynamic model [4–8].

Analyze the force of the first locomotive of the multi-locomotive multi-particle heavy haul train model, which is subject to traction, braking force, resistance, and tension on the coupler, as shown in Fig. 1.

The force equation of the locomotive  $M_0$  is shown in type (1).

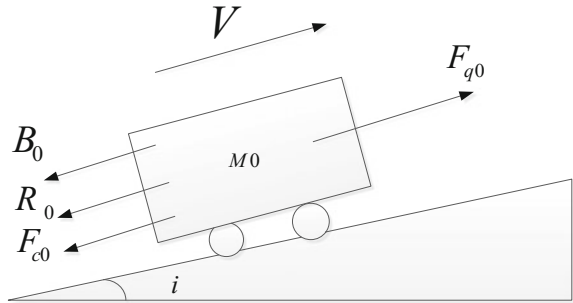
$$M_0 a_0 = F_{q0} - R_0 - B_0 - F_{c0} \quad (1)$$

Among the equation:  $M_0$  is the quality of locomotive, Unit as kg;  $a_0$  is the acceleration of locomotive, Unit as  $m/s^2$ ;  $F_{q0}$  is the traction of locomotive, Unit as N;  $R_0$  is the resultant force of locomotive, Unit as N;  $B_0$  is the braking force of locomotive, Unit as N;  $F_{c0}$  is the Pulling force of locomotive coupler, Unit as N.

Regard the hook as a spring and dampers,  $k_0$  is the elastic coefficient of the spring,  $h_0$  is the damping coefficient of the damper. Then the coupler force is shown in type (2).

$$F_{q0} = k_0(y_0 - y_1) + h_0(v_0 - v_1) \quad (2)$$

**Fig. 1** Force analysis of the first locomotive  $M_0$



Among the equation:  $y_0, y_1$  is the displacement of the locomotive  $M0$  and the wagon  $M1$ , Unit as m;  $v_0, v_1$  is the speed of locomotives and wagons, Unit as m/s.

Let  $x_{0,1}$  represents the displacement of locomotive  $M0$ ,  $x_{0,2}$  represents the speed of locomotive  $M0$ ,  $x_{1,1}$  represents the displacement of wagon  $M1$ ,  $x_{1,2}$  represents the speed of wagon  $M1$ . The coupler force of the locomotive  $M0$  can be expressed as shown in type (3).

$$\begin{aligned} F_{c0} &= k_0(y_0 - y_1) + h_0(v_0 - v_1) \\ &= [k_0 \quad h_0] \begin{bmatrix} x_{0,1} \\ x_{0,2} \end{bmatrix} + [-k_0 \quad -h_0] \begin{bmatrix} x_{1,1} \\ x_{1,2} \end{bmatrix} \end{aligned} \quad (3)$$

Based on the above analysis of locomotive  $M0$ , the state space equation can be established as shown in type (4) and type (5).

$$\dot{X}_0 = \begin{bmatrix} \dot{x}_{0,1} \\ \dot{x}_{0,2} \end{bmatrix} = \begin{bmatrix} 0 & 1 \\ -\frac{k_0}{M_0} & -\frac{h_0}{M_0} \end{bmatrix} \begin{bmatrix} x_{0,1} \\ x_{0,2} \end{bmatrix} + \begin{bmatrix} 0 & 0 & 0 & 0 & 0 \\ \frac{k_0}{M_0} & \frac{h_0}{M_0} & \frac{1}{M_0} & -\frac{1}{M_0} & -\frac{1}{M_0} \end{bmatrix} \begin{bmatrix} x_{1,1} \\ x_{1,2} \\ F_{q0} \\ R_0 \\ B_0 \end{bmatrix} \quad (4)$$

$$Y_0 = \begin{bmatrix} 1 & 0 \\ 0 & 1 \\ k_0 & h_0 \end{bmatrix} \begin{bmatrix} x_{0,1} \\ x_{0,2} \end{bmatrix} + \begin{bmatrix} 0 & 0 & 0 & 0 & 0 \\ 0 & 0 & 0 & 0 & 0 \\ -k_0 & -h_0 & 0 & 0 & 0 \end{bmatrix} \begin{bmatrix} x_{1,1} \\ x_{1,2} \\ F_{q0} \\ R_0 \\ B_0 \end{bmatrix} \quad (5)$$

One locomotive is arranged in the head of the train, another locomotive is arranged in the middle part of the train. According to the state space equation of locomotives and wagons established before, the dynamic model of multi-locomotive multi-particle heavy haul train is established.

The locomotive state space equation is represented by the locomotive module, where  $A_0$  is the system matrix of the state space equation,  $B_0$  is the input matrix and  $C_0$  is the output matrix,  $D_0$  is the direct transfer matrix.

These parameters will be calculated with the input vector  $[x_{1,1} \quad x_{1,2} \quad F_{q0} \quad R_0 \quad B_0]$  of the locomotive, and finally get the output vector  $[x_{0,1} \quad x_{0,2}]$  of the locomotive, that is, the displacement and speed of the locomotive, the coupler force of the locomotive can also output.

### 3 The PID Control System of Multi-locomotive Traction Heavy Haul Train

Put the PID control to the multi-locomotive traction multi-particle heavy haul train dynamic model, the structure shown in Fig. 2.



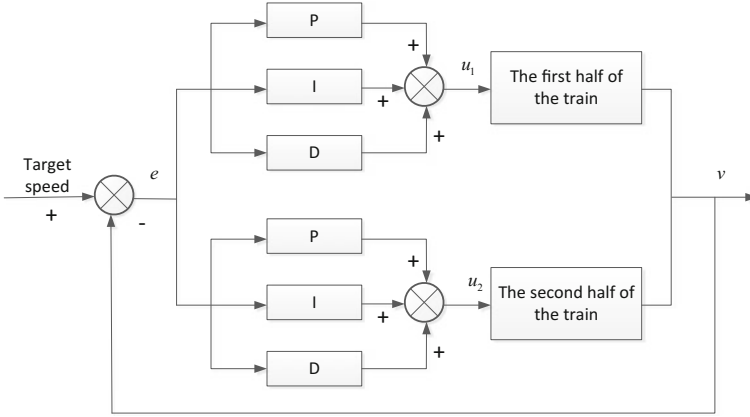


Fig. 2 PID system for multi locomotive traction heavy haul train

In the PID control, the input is the error  $e$  between the actual running speed and the target speed, the output is the control force of the multi-locomotive traction heavy haul train. The input of multi-locomotive traction heavy haul train PID control system is the target speed, the output is the actual speed. Use the PID control system to control the speed and the coupler force during the operating of the heavy haul train.

#### 4 Dynamic Matrix Control System of Multi-locomotive Traction Heavy Haul Train

Discrete the state equation of multi-locomotive multi-particle heavy haul train, then obtain the train running state model of heavy haul train.

To discrete the locomotive  $M0$ . As shown in type (6) and type (7).

$$X_1 = \begin{bmatrix} 0.0044 & 0.0010 \\ -0.7250 & -0.0028 \end{bmatrix} \begin{bmatrix} x_{0,1} \\ x_{0,2} \end{bmatrix} + \begin{bmatrix} 0.9956 & 0.0100 & 0 & 0 & 0 \\ 0.7250 & 0.0072 & 0 & 0 & 0 \end{bmatrix} \begin{bmatrix} x_{1,1} \\ x_{1,2} \\ F_{q0} \\ R_0 \\ B_0 \end{bmatrix} \quad (6)$$

$$Y_0 = \begin{bmatrix} 1 & 0 \\ 0 & 1 \\ 10000000 & 1000000 \end{bmatrix} \begin{bmatrix} x_{0,1} \\ x_{0,2} \end{bmatrix} + \begin{bmatrix} 0 & 0 & 0 & 0 & 0 \\ 0 & 0 & 0 & 0 & 0 \\ -100000000 & -1000000 & 0 & 0 & 0 \end{bmatrix} \begin{bmatrix} x_{1,1} \\ x_{1,2} \\ F_{q0} \\ R_0 \\ B_0 \end{bmatrix} \quad (7)$$

Multi-locomotive traction heavy haul train dynamic matrix control system operation steps are as follows:

- Step 1 to initialize the dynamic matrix control system. The system parameters are set, including model coefficients  $a_i$ , control coefficients  $d_i$ , correction factors  $h_i$ , control matrix  $\mathbf{R}$ , error weight matrix  $\mathbf{Q}$ , optimized time domain length  $P$ , control time domain length  $M$ , and sampling period  $T$ .
- Step 2 import the train state equation model into the system. Import the train running curve.
- Step 3 set the forecast initial value  $\tilde{y}_0(k+i|k), i=1, \dots, N$ . And then correct the predicted value, and then shift the initial value.
- Step 4 detect the actual output of the object and calculate the error value  $e$  while setting the actual output to the predicted initial value and correcting the prediction value.
- Step 5 shift setting the system moment predict initial value. The root shifts the initial value at time.
- Step 6 calculate the control increment  $\Delta u$ . Then calculate and output the prediction value, while feedback the output value to the calculation of the error part of the calculation. Then calculate and output the predicted value.
- Step 7 determine whether to meet the termination conditions. If it is not satisfied, feedback the output to the calculation of the error part of the calculation, to achieve the entire control system cycle operation. If it is satisfied, the calculation result is output and the calculation is terminated.

In this paper, all the simulations select 2 axle weight of 23t HXD3 locomotive; select the C70 wagon and select 17 type coupler.

Simulation results analysis:

#### (1) Coupler force

As can be seen from the figure above, when the slope of the running line changes greatly or the train acceleration changes, it will lead to a corresponding increase in coupler force. The vehicle coupler force output by the PID control system and the vehicle coupler force of the dynamic train control system of heavy haul train do not exceed its minimum failure load. The coupler force output of the DMC system of the heavy haul train is obviously smaller than the output under the PID control. Therefore, when using dynamic matrix control system, heavy haul train in the operation process will be safe and stable (Fig. 3).

#### (2) Speed tracking curve

The velocity tracking curves obtained by the two control systems are compared together, as shown in Fig. 4.

As can be seen from the above figure, the speed of the two control systems are fluctuating in the place where the train acceleration is changed or where the running slope changes greatly. The overall tracking effect is good. When the train running at

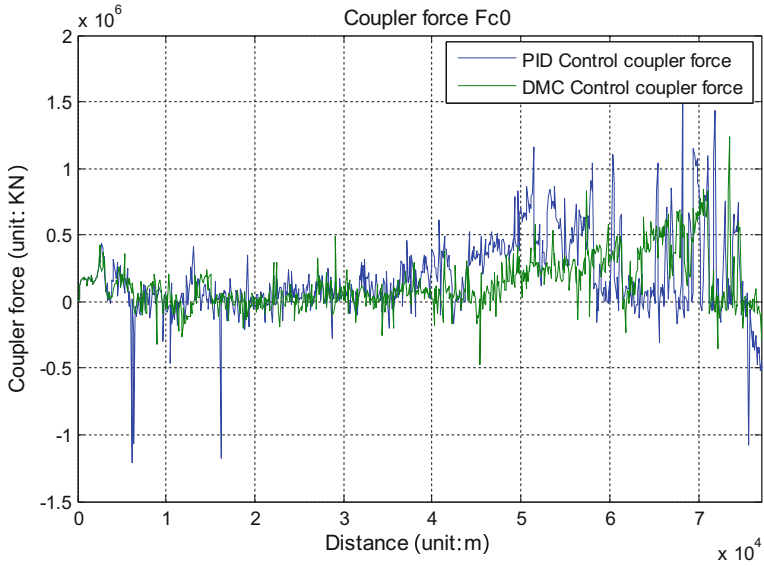


Fig. 3 Coupler force  $F_{c0}$  of locomotive  $M0$  under DMC system and PID control

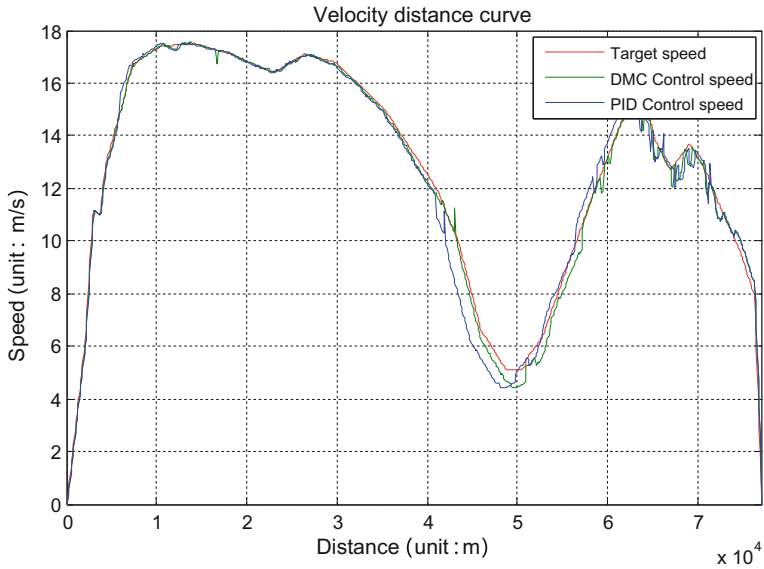


Fig. 4 Speed tracking curve under DMC system and PID control system

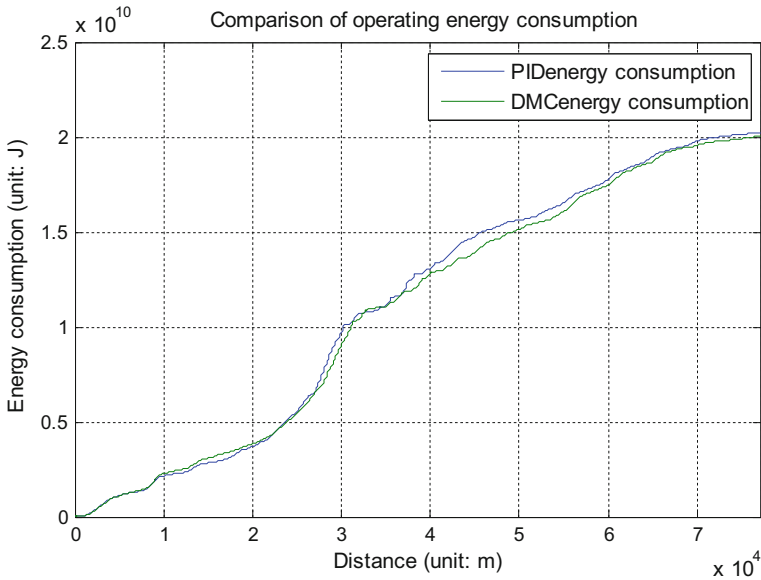


Fig. 5 Energy consumption curve under DMC system and PID control system

40,000 to 50,000 m, due to line slope and line speed change, cause the PID control system on the speed tracking had a large deviation. It can be seen that the tracking speed of the DMC system of heavy haul train is better than that under PID system.

(3) Energy consumption

The energy consumption curves obtained by the two control systems are compared together, as shown in Fig. 5.

As can be seen from the above figure, the energy consumption under PID control system is  $20.216 \times 10^9$ . The energy consumption under DMC system is  $20.054 \times 10^9$ , energy-saving effect is remarkable.

## 5 Conclusion

This paper used simulink to build the multi-locomotive multi-particle heavy haul train dynamic model. The PID control system is established and simulated. At the same time, the dynamic matrix control system of multi-locomotive traction heavy haul train is established based on dynamic matrix control algorithm. The simulation results under the dynamic matrix control system are better than the results under the PID control system.

**Acknowledgements** This work is partly supported by Chinese National Key Technologies R&D program (Contract No. 2013BAG24B03-2). This work is also partly supported by State Key Lab of Rail Traffic Control & Safety (Contract No. RCS2016ZT006).

## References

1. Sun Z, Sun X (1987) Countermeasures for developing heavy haul transportation—dynamics of heavy haul trains and related technical problems. *Railway Trans* 1:91–97 (In Chinese)
2. Zhang H, Zhu J, Ma L (1999) Influence of train speed and heavy load on railway freight cars. *Railway Veh* (2):21 (In Chinese)
3. Cheng L (2014) The application and realization of multi particle dynamics model in the train simulation driving system. Lanzhou Jiaotong University, Lanzhou (In Chinese)
4. Zhu X, Zhenhua X (2011) Dynamic simulation of urban rail transit train based on single point model. *Railway Trans* 33(6):14–19 (In Chinese)
5. Liu R, Golovitcher IM (2003) Energy-efficient operation of rail vehicles. *Transp Res Part A Policy Pract* 37(10):917–932
6. Khmelnitsky E (2000) On an optimal control problem of train operation. *Autom Control IEEE Trans* 45(7):1257–1266
7. Avery RM (1985) A coordinated visual representation of train performance, power, and energy consumption. *IEEE Trans Ind Appl* 21(2):291–294
8. Zhou L, Zujun Y, Shi H (2004) Research on simulation system of train operation line. *J Syst Simul* 16(7):1463–1466 (In Chinese)

# Research of Hybrid Energy Pack for Rail Transit

Yejun Mao, Yuan Long, Shengcai Chen and Xiangyuan Xiao

**Abstract** Low carbon, green and energy-efficient are the important development directions of railway transit. Based on the operational requirements of rail transit and the characteristics of various energy storage components, this paper introduces a new type of E-E hybrid drive technology with super capacitors and batteries, and proposes a new configuration structure of super capacitors and batteries. The power allocation method and the key technical requirements of the technology are described, and the DC/DC voltage control optimization method is proposed for the regenerative braking energy feedback. The energy package scheme can effectively improve the performance of rail transit operation, which can provide reference for other green power drive system design.

**Keyword** Hybrid energy pack · Energy storage power supply · Super capacitor

## 1 Introduction

At present, the energy source for rail transit is mainly from catenary or vehicle internal combustion. The operating conditions of rolling stock are limited by catenary. Meanwhile, with the development of railway electrification and the application of more strict emission standards [1, 2], those rolling stocks powered by internal combustion become less popular. The use of on board power pack can

---

Y. Mao · Y. Long

The State Key Laboratory of Heavy Duty AC Drive Electric  
Locomotive Systems Integration, Zhuzhou, China

Y. Mao · Y. Long · S. Chen

Product Development Centre, CRRC Zhuzhou Electric  
Locomotive Co., Ltd, Zhuzhou, China

X. Xiao (✉)

CRRC ZELC Verkehrstechnik GmbH, 1220 Vienna, Austria  
e-mail: david23301981@gmail.com

© Springer Nature Singapore Pte Ltd. 2018

L. Jia et al. (eds.), *Proceedings of the 3rd International Conference on Electrical and Information Technologies for Rail Transportation (EITRT) 2017*, Lecture Notes in Electrical Engineering 482, [https://doi.org/10.1007/978-981-10-7986-3\\_5](https://doi.org/10.1007/978-981-10-7986-3_5)

effectively solve the problem of internal combustion pollution and it enables rolling stock to operate without catenary. In general, the rolling stock should have the characteristics of long running time, big power under complicated operating environment. Therefore, as the driving power, energy package must have the characteristics of high energy, high power, long life cycle and good environmental adaptability.

There are several types of electric energy storage components, which can be divided into two categories, energy-based and power-based storage components respectively. Energy-based storage components such as lead-acid battery, lithium battery, etc., have the advantages of high energy density, long discharging time, but the disadvantages are low power density, short life cycle [3]. Power-based storage components such as super capacitors, have the advantages of high power density, short response time and long life cycle, but the disadvantages are low energy density, high self-discharging rate [4]. It is not possible to meet all the requirements by a single energy storage component because of the performance limits listed above. Through the application of hybrid energy storage components, based on their own characteristics and taking full advantages of them, rail transit can realize high power traction and braking and achieve green driving in non-electrified zone without pollution and emission.

## 2 Overview of Power Storage Technology

As a power source of rail transit, it should have the characteristics of big capacity, high energy and power density, long life cycle, wide operating temperature range, safety, reliability, environmental friendly and non-pollution, etc.

At present, the main energy storage components are batteries, super capacitors etc. Batteries include lead-acid batteries, alkaline batteries, lithium batteries. Power batteries generally are lithium batteries which have a relatively large energy and power density. The super capacitor is a new type of capacitor which has much bigger capacity compared to conventional capacitor. Although power battery has been widely used on pure electric vehicles and hybrid vehicles, its life and efficiency is affected by the huge current shock, which is a problem recognized widely by the industry. Super capacitor can be quickly charged and discharged with much higher current, but the lower energy ratio of which decides that it is not suitable as a vehicle energy storage alone. Therefore, the combination of power-based super capacitor and energy-based battery is an effective solution for the power source of rail transit.

By combining super capacitor with battery, the hybrid energy pack has the advantages as follows.

- (1) It offsets the deficiencies, and takes advantages of each component. The hybrid energy storage system has the characteristics of high power and energy density, which fulfils the locomotive power requirements.

- (2) It extends the battery life. The super capacitor undertakes the tasks of high power charging or discharging, while the battery works within its power limit, so that the battery is free from the huge current shock which extends its life.
- (3) It utilizes regenerative braking energy. Due to the characteristics of fast charging and discharging the super capacitor can absorb and store the regenerative braking energy which is released during the next traction phase of the vehicle so that the regenerative braking energy is efficiently recycled.
- (4) It has excellent low-temperature characteristics [2]. The capacity of battery decreases sharply when the temperature decreases [5], the attenuation of which may rise more than 70%. By contrast, the attenuation of super capacitor is very small, because the charge transfer occurs mostly on the surface of the active material of the electrode during the charge and discharge processes. Therefore, the application of super capacitor is conducive to enhance the vehicle low-temperature performance.

Table 1 compares the comprehensive performances of mainstream energy storage components in applications [6].

**Table 1** The comprehensive performance comparison of mainstream energy storage components in applications

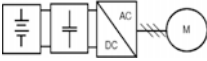
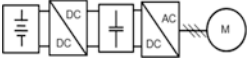
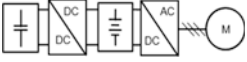
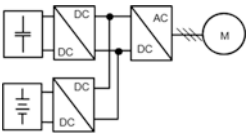
Performance	Super capacitor (9500 F)	Super capacitor (60,000 F)	Lead-acid battery	Phosphoric acid iron battery (LiFePo <sub>4</sub> )	Lithium titanate battery (LTO)
Energy density (Wh/kg)	3	19.49	18.86	56.91	36
Power density (kW/kg)	0.28	0.23	0.02 (1C, 0.5 h)	0.07 (1C, 1 h)	0.2 (5C, 0.2 h)
Power per volume (Wh/L)	1.6	11	45.79	56.61	45.26
Cycle life	>1,000,000 times (monomer 300A, 100%DOD)	>30,000 times (1C, 100% DOD)	>1200 times (1C, 80% DOD)	>3000 times (1C, 100% DOD)	>10,000 times (1C, 100% DOD)
Operating temperature (low/high limit value)	-40 °C	-20 °C	Under 0 °C needs to be heat	Under 0 °C needs to be heat	-25 °C
	+55 °C	+55 °C	+45 °C	+45 °C	+55 °C



## 2.1 Configuration of Energy Storage Components

By combining super capacitors with batteries, we can get a hybrid energy system. There are mainly 4 kinds of combinations, and each has its own characteristics based on the different characteristics of the battery and capacitor [7] as shown in Table 2.

**Table 2** Comparison of different combinations

Framework	Robustness	Configuration	Operation mode	Summary
	<p>The charge and discharge power of the batteries and capacitors cannot be controlled. Large voltage fluctuations on DC side</p>	<p>Both voltage should be configured to DC-Link</p>	<p>Full dynamic of capacitor current, high speed state response</p>	<p>The power and energy of both components cannot be managed effectively due to the different characteristic of them</p>
	<ol style="list-style-type: none"> <li>1. Stable DC voltage</li> <li>2. DC/DC converter runs continuously for long periods of time</li> </ol>	<ol style="list-style-type: none"> <li>1. DC/DC converter is needed</li> <li>2. The voltage of super capacitors is configured to DC-Link</li> </ol>	<ol style="list-style-type: none"> <li>1. Fast state response of super capacitors</li> <li>2. The continuous energy output depends on the battery</li> </ol>	<p>With the rapid increase of the capacity of super capacitors, the DC stability of which is enhanced greatly</p>
	<ol style="list-style-type: none"> <li>1. Stable DC voltage</li> <li>2. DC/DC converter runs intermittently</li> </ol>	<ol style="list-style-type: none"> <li>1. DC/DC converter is needed</li> <li>2. The voltage of batteries is configured to DC-Link</li> </ol>	<p>Energy output mainly depends on batteries, while big power output and regenerative braking depend on super capacitors</p>	<p>Now popular for matching</p>
	<ol style="list-style-type: none"> <li>1. High requirements for the control strategies and synchronization of these two DC/DC converter</li> <li>2. Complex structure affects system stability</li> </ol>	<p>More configuration of DC/DC converter, more complex design</p>	<p>The super capacitors and batteries are output via separate DC/DC converter</p>	<p>Application in part of trams in China [8]</p>

Now, the super capacitor technology products with high capacity are upgraded constantly, 30,000 and 60,000 F and even higher capacity super capacitors are already introduced and applied in the market. The higher the capacity is, the less the change rate of voltage is. Super capacitor with high capacity can effectively stabilize the voltage of DC-Link, response promptly to the power requirement of the vehicle. It plays a more and more important role in power and energy supply in the traction and braking process of the vehicle. Therefore, the second matching scheme in Table 2 has become the development trend of hybrid energy storage system, and will be further developed and applied with the development of super capacitor technology.

### 2.2 Power Configuration Principle

Combined the operational requirements of the rail transit mode with the characteristics of batteries and super capacitors, the power of super capacitors and batteries is managed by DC/DC converter under different operation modes which are described below.

1. Charge the super capacitors with batteries

Since the energy stored in super capacitors is less than that in batteries, the batteries can charge capacitors through a DC/DC converter when the vehicle starts up for operation. The schematic diagram is shown in Fig. 1.

2. Charge both the super capacitors and batteries with the catenary

In the catenary mode, through a charger on board the DC-Link of traction inverter charges the super capacitors as well as the batteries through the DC/DC converter, as shown in Fig. 2.

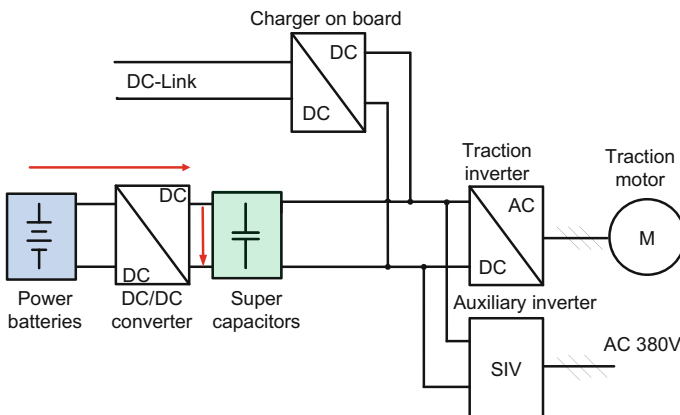


Fig. 1 Operating of charging super capacitors

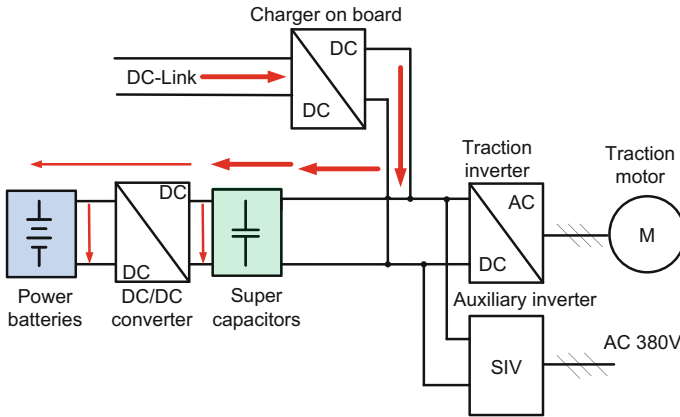


Fig. 2 Operating of charging hybrid energy pack

### 3. Low power traction mode

When the vehicle is in low power traction mode, the traction power can be fulfilled by the batteries only. In this case, the super capacitors are used to stabilize the DC-Link voltage.

While supplying power for traction and auxiliaries, the batteries can also charge the super capacitors when the energy of the latter is too low. See Fig. 3.

### 4. High power traction mode

When the locomotive power increases (e.g. climbing, starting, heavy load running etc.), the batteries and super capacitors output together, and the power of the former is limited by the DC/DC converter. See Fig. 4.

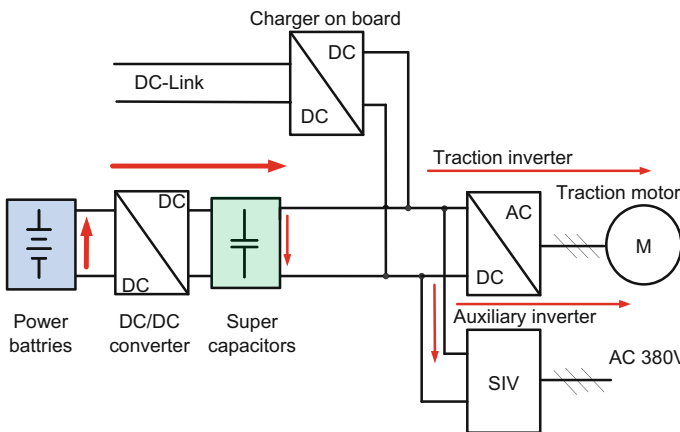


Fig. 3 Operating of low power traction

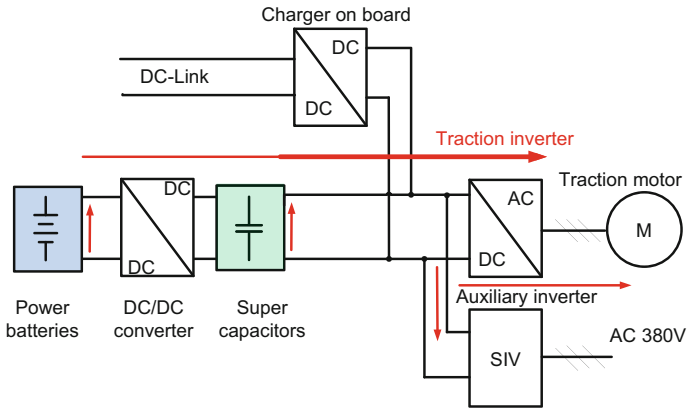


Fig. 4 Operating of high power traction

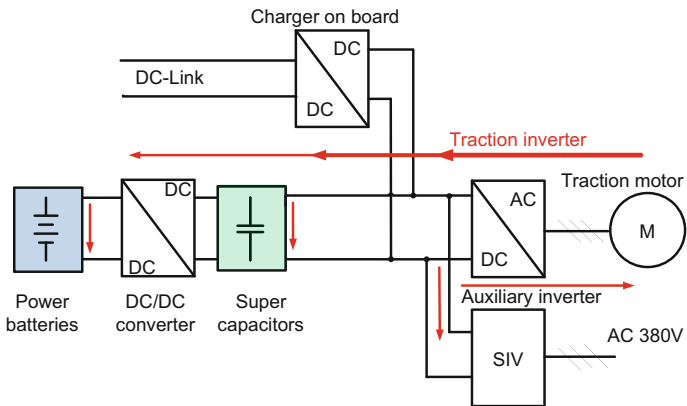


Fig. 5 Operating of regenerative braking

### 5. Regenerative braking

In the regenerative braking mode, energy generated by the traction inverter is directly transmitted to the super capacitors. When the super capacitors are full charged, the batteries will be charged through the DC/DC converter as shown in Fig. 5.

### 2.3 DC/DC Converter

As a core device for the management of super capacitors and batteries, DC/DC converter is responsible for the power and energy management of the whole

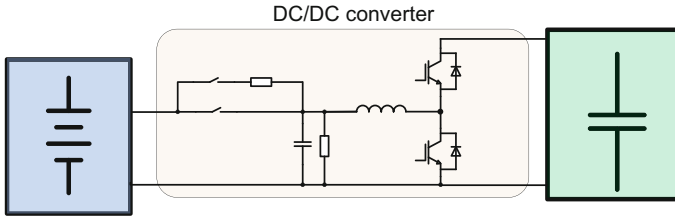


**Fig. 6** Basic topology of DC/DC converter

system [8]. DC/DC converter is a Buck-Boost circuit in principle which is widely used in the field of power electronics, and the basic topology is shown in Fig. 6.

In view of the operating conditions and application requirements of rail transit, the following characteristics of DC/DC converter need to be considered.

1. Wide range of operating voltage

Since the operating voltage of the batteries and super capacitors varies within a few hundred volts, the DC/DC converter must work reliably in normal operating voltage ranges of both the energy components.

2. Bi-directional buck and boost function

Because the voltage range of these two energy components connected to DC/DC converter is very broad and in extreme circumstances the voltage of capacitors may be discharged to 0 V, the DC/DC converter must realize the bi-directional buck and boost function.

3. High efficiency

Since the DC/DC converter needs to run for a long time in the operating process of the vehicle, long term efficient operation becomes particularly important so that energy loss is minimized. Normally, the efficiency of DC/DC converter should be more than 95% under its own operating voltage range.

### 3 Parameter Configuration of Energy Pack

The configuration of super capacitors, batteries and DC/DC converter directly affect the configuration of energy pack and the performance of the whole vehicle. By giving full play to the advantages of each storage component, combining with the vehicle existing main circuit, considering the weight, volume and cost constraints of engineering application, the parameters of super capacitors, batteries and DC/DC converter are selected from the point of view of power cycle and average power of the vehicle [9]. The configuration of parameters for each section is analyzed below.

### 3.1 Configuration of Super Capacitors

#### 1. Voltage of super capacitors in group

Since the super capacitor group is directly connected with the DC-Link, the voltage range of which needs to match the operating voltage range of the vehicle electric system (including traction inverter, traction motor and auxiliary inverter).

#### 2. Power

The power of the super capacitor must at least meet the requirement of the equation below.

$$P_{supercap} = P_{DC\ linkpower} - (P_{battery} \times Efficiency_{DC/DC}) \quad (1)$$

#### 3. Energy

The capacity configuration of super capacitors is often limited by the weight and installation space of the vehicle. The energy decreases (discharging during traction) and increases (recharging during regenerative braking) intermittently when the vehicle runs. So at least the capacity configuration needs to meet the requirements for continuously running of the vehicle.

### 3.2 Configuration of Batteries

#### 1. Voltage of batteries in group

The battery voltage is controlled by DC/DC converter under buck/boost mode. On the one hand, if the voltage of batteries is too low, the operating current of the batteries and DC/DC converter will increase for the same power output; on the other hand, if this voltage is too close to the super capacitors, the switch frequency of DC/DC converter will rise up, which will increase the control difficulty and reduce the reliability and control accuracy. Usually, the voltage ratio of the batteries to DC/DC converter is set to 0.5–0.7.

#### 2. Power

The life and safety of batteries are affected by unexpected large power which has to be limited. Usually, for lead-acid, iron-phosphate batteries, lithium titanate batteries, the charging ratio is respectively selected as 0.2, 1, 3 C, while discharging ratio as 0.2, 0.5, 2 C.

#### 3. Energy

Since the energy of batteries determines the operating time of the vehicle, configuration needs to meet the minimum energy requirements of the whole working conditions of the vehicle.

## 4 Optimization Method of Boost Control

Generally, the output voltage of the Boost circuit (super capacitor terminal) is a fixed value [10]. Under this condition, if the energy of super capacitors and batteries are almost full, the regenerative energy cannot be absorbed effectively while the vehicle is braking, and the brake resistance of the vehicle is required to consume the surplus regenerative braking energy.

Considering the above situations, we choose the boost voltage as a linear change value. The higher the locomotive speed, the lower the boost voltage limit is; contrarily, when the vehicle speed decreases, this limit increase, equal to that the DC-Link voltage varies linearly with the locomotive speed.

Furthermore, the vehicle creates more regenerative braking energy at a high speed, when the super capacitors can absorb more energy. On the other side, the vehicle creates less energy at a low speed when the super capacitors can absorb less energy. By doing so, it can make full use of the super capacitors to absorb the regenerative braking energy, effectively reducing even eliminating the configuration of the braking resistor.

## 5 Running Test

After installation of the energy package on one locomotive, some tests (such as light load, heavy load, low speed and high speed) are carried out according to different operational conditions. The parameters of the tests are shown in Table 3.

Running on the main electrified line, operating under different conditions with different load, the main test results are shown in Table 4.

**Table 3** Main parameters of test system

Definition	Parameter
Locomotive weight	87.4 t
Maximum tractive force	120 kN
Maximum wheel power	300 kW
Rated voltage of battery pack	DC500 V
Capacity of battery pack	285 Ah
Rated voltage of super capacitor pack	DC900 V
Available energy of super capacitor pack	12 kwh
Test line	Main electric locomotive line
Ambient temperature	0–5 °C

**Table 4** Test result

Operating condition	Condition 1 The locomotive pulls the 70 t load and runs continuously at 45 km/h	Condition 2 The locomotive pulls the 600 t load and runs continuously at 10 km/h	Condition 3 The locomotive pulls the 1500 t load and runs in 200 m shunting for an hour with the maximum speed—10 km/h
Continuous tractive force	9.6 KN	23 KN	60 KN
Continuous speed	45 km/h	10 km/h	9 km/h
Maximum speed	65 km/h	10 km/h	10 km/h
Maximum current of battery pack	280 A	280 A	280 A
Maximum current of super capacitor pack	200 A (acceleration)	300 A	300 A
Initial energy	95.2% (energy pack)	70% (batteries) 60% (super capacitors)	100% (energy pack)
Final energy	46% (energy pack)	45% (energy pack)	44% (energy pack)
Distance	45 km	2.5 km	3 km

## 6 Conclusion

At the present, energy storage components are developed and upgraded rapidly, and the power and energy density of which are also enhanced. A single type of energy storage component cannot meet the requirements of large power and high energy for rail transit traction. By combining different energy storage components using respective advantages and offsetting respective disadvantages, and controlling the power and energy by DC/DC converter, the energy pack can effectively fulfil the operational requirements of vehicle thus improve the driving capability.

Currently, the energy package scheme presented above has been applied in Austria for a shunting locomotive and a series of tests have been carried out with good results, which has received widespread attention in the industry.



## References

1. Fan Y, Gao D (2012) Research and development of dual power electric shunting locomotives. *Electric Locomotives Mass Transit Veh* (5):11–15 (in Chinese)
2. Zhang Y (2011) Study on key technology and product simplification of double energy battery electric locomotive. *Electric Locomotives Mass Transit Veh* (3):20–22 (in Chinese)
3. Yu G (2012) Application of Li-ion battery in the field of rail transit vehicle. *Chinese battery industry* (5):299–305 (in Chinese)
4. Jianpu W (2015) Research of onboard energy storage system for urban railway transit vehicle braking. *Electric Drive Locomotives* 4:76–79 (in Chinese)
5. Zhao S, Guo S, Zhao J, Song Y, Nan C (2016) Development on low-temperature performance of lithium ion batteries. *J Chinese Ceramic Soc* 1:19–28 (in Chinese)
6. Chen Q, Liu G, He J, Ma X, Yang R, Hu S, Wu J (2015) Analysis and comparison between standard systems of power battery in China and abroad. *Adv New Renew Energy* (2):151–156 (in Chinese)
7. Miller JM (2011) *Ultracapacitor applications*. Institution of Engineering and Technology, pp 61–75
8. Chen H, Xia H, Yang Z, Li X (2015) Study of output impedance optimization for stationary super-capacitor energy storage applied in urban rail power supply system. In: IEEE 2015 54th annual conference of the society of instrument and control engineers of Japan (SICE), Hangzhou, China, pp 124–129
9. Pen R, Zhang K, Song P, Chen Y, Zhang J (2015) Research on energy management strategy of on-board hybrid power source for trains. *Chinese J Power Sour* (11):64–68 (in Chinese)
10. Huang Z, Yao D, Yang G, Li H, Wu F, Ning X (2016) Study on piecewise control strategy of braking energy regeneration for hybrid power system of electric vehicle. *Mech & Electr Eng Mag* (3):280–286 (in Chinese)

# Instantaneous Voltage PIR Closed-Loop Control for the Auxiliary Inverter

Xuefu Cao, Yong Ding, Ruichang Qiu, Yun Kang and Yang Yu

**Abstract** As an important part of EMU (Electric Multiple Units), the auxiliary power supply system plays an important role in the normal operation of the vehicle. In order to improve the reliability of the auxiliary power supply system, this paper analyses the harmonics of the auxiliary inverter under nonlinear load and suggests that the 6th harmonic voltage components in the DQ synchronous rotating coordinate system can be controlled to achieve the simultaneous control of the 5th and 7th harmonic voltage components in the three-phase static coordinate system. The instantaneous voltage PIR (Proportion Integral Resonance) closed loop control method in DQ synchronous rotating coordinate system is researched to eliminate the voltage aberration caused by harmonics and ensure the quality of output voltage. Finally, the simulation results show that the design has achieved the desired objectives.

**Keyword** Auxiliary inverter · Resonant control · Nonlinear load

## 1 Introduction

With the rapid development of China's rail transportation, EMU has become an important choice for people to travel [1]. The duty of the auxiliary inverter is to provide a stable AC power supply for the medium voltage load on the vehicle including air conditioning unit, air compressor, ventilation device, train wireless, car socket, etc. [2].

---

X. Cao (✉) · R. Qiu · Y. Kang · Y. Yu

School of Electrical Engineering, Beijing Engineering Research Center of Electric Rail Transportation, Beijing Jiaotong University, Beijing 100044, China  
e-mail: 16121414@bjtu.edu.cn

Y. Ding

CRRC Changchun Railway Vehicles CO., LTD., Changchun, China  
e-mail: dingyong@cccar.com.cn

© Springer Nature Singapore Pte Ltd. 2018

L. Jia et al. (eds.), *Proceedings of the 3rd International Conference on Electrical and Information Technologies for Rail Transportation (EITRT) 2017*, Lecture Notes in Electrical Engineering 482, [https://doi.org/10.1007/978-981-10-7986-3\\_6](https://doi.org/10.1007/978-981-10-7986-3_6)

In the 80s of last century, K. P. Gohale introduced the deadbeat control into inverters [3], whose output PWM duty cycle is obtained by the system state equation and the feedback information of voltage and current, because of its sensitivity to the filter circuit parameters, but the anti-disturbance ability of the system is poor; Noue put forward a kind of repetitive control method: the correction signal is assumed that the waveform distortion appearing in the previous period will appear again in the next cycle [4], because of the delay of one power frequency cycle and the existence of periodic delay, but its dynamic characteristics are poor; PID control is one of the most classical and widely used industrial control methods with the advantages of simple control, easy parameter setting, good robustness and high reliability [5], however, the disturbance rejection effect of PID control system under nonlinear load is not good, so it is necessary to add other control methods to suppress the voltage distortion caused by nonlinear load.

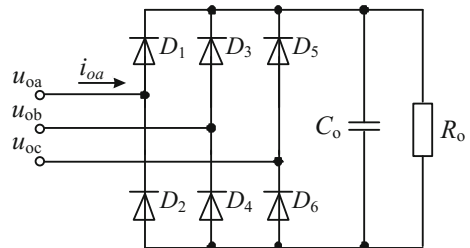
This paper studies the nonlinear load harmonic characteristics of the auxiliary inverter, sets up the auxiliary inverter system model with nonlinear load, and then adopts instantaneous voltage PIR closed loop control method in DQ synchronous rotating coordinate system to control the 5th and 7th harmonics voltage components in the three-phase static coordinate system and improve the output voltage waveform quality of inverter.

## 2 Harmonic Analysis of Auxiliary Inverter Under Nonlinear Load

The main nonlinear loads of the auxiliary inverter of EMU are variable frequency air conditioning units and the chargers, which they are three-phase rectifier load. Figure 1 is the topology of three-phase rectifier type nonlinear load.

Single phase rectifier type nonlinear load is rich in odd harmonics, and the greater the number of harmonics, the smaller the harmonic content [6, 7]. For three-phase rectifier type nonlinear load, because there is no 3rd harmonic and its multiple harmonic paths [8], so the harmonic content of 3rd and multiple times is 0 but the 5th and 7th harmonic content is more. When the harmonic current flows through the output impedance of the inverter, the harmonic voltage drop will occur, which will cause the aberration of the output voltage.

**Fig. 1** The circuit of three phase rectifier load



In three-phase static coordinate system, we can get the output voltage expressions containing 5th and 7th harmonic components as the following formulas.

$$\begin{cases} u_{oa} = \sqrt{2}U_1 \sin \omega t + \sqrt{2}U_5 \sin 5\omega t + \sqrt{2}U_7 \sin 7\omega t \\ u_{ob} = \sqrt{2}U_1 \sin(\omega t - 120^\circ) + \sqrt{2}U_5 \sin 5(\omega t - 120^\circ) + \sqrt{2}U_7 \sin 7(\omega t - 120^\circ) \\ u_{oc} = \sqrt{2}U_1 \sin(\omega t + 120^\circ) + \sqrt{2}U_5 \sin 5(\omega t + 120^\circ) + \sqrt{2}U_7 \sin 7(\omega t + 120^\circ) \end{cases} \quad (1)$$

where  $\omega$  is fundamental angular frequency,  $U_1$  is the effective value of the fundamental positive sequence voltage, and  $U_5$ ,  $U_7$  are the effective values of 5th and 7th harmonic components respectively. The 5th and 7th harmonic voltage vectors are negative sequence component and positive sequence component respectively. We can get the following formulas by the formula (1).

$$\begin{cases} u_{oa} = \sqrt{2}U_1 \sin \omega t + \sqrt{2}U_5 \sin 5\omega t + \sqrt{2}U_7 \sin 7\omega t \\ u_{ob} = \sqrt{2}U_1 \sin(\omega t - 120^\circ) + \sqrt{2}U_5 \sin 5(\omega t + 120^\circ) + \sqrt{2}U_7 \sin 7(\omega t - 120^\circ) \\ u_{oc} = \sqrt{2}U_1 \sin(\omega t + 120^\circ) + \sqrt{2}U_5 \sin 5(\omega t - 120^\circ) + \sqrt{2}U_7 \sin 7(\omega t + 120^\circ) \end{cases} \quad (2)$$

After the Park coordinate transformation of (2), the expressions of the output voltage which contains the 5th and 7th harmonic voltage in the DQ synchronous rotating coordinate system are obtained:

$$\begin{cases} u_{od} = \sqrt{2}U_1 \sin \theta + \sqrt{2}U_5 \sin(6\omega t - \theta) + \sqrt{2}U_7 \sin(6\omega t - \theta) \\ u_{oq} = -\sqrt{2}U_1 \cos \theta + \sqrt{2}U_5 \cos(6\omega t - \theta) - \sqrt{2}U_7 \cos(6\omega t - \theta) \end{cases} \quad (3)$$

According to (3), the fundamental positive sequence voltage component is transformed into the DC component, and the 5th and 7th harmonic voltage components are converted to the 6th harmonic voltage component in the DQ synchronous rotating coordinate system. Therefore, in the DQ synchronous rotating coordinate system, the 6th harmonic voltage components can be controlled to achieve the simultaneous control of the 5th and 7th harmonic voltage components in the three-phase static coordinate system.

### 3 PIR Control in Synchronous Rotating Coordinate System

The instantaneous voltage PI control in synchronous rotating coordinates can realize the control of the static error of the positive sequence fundamental signal [9]. However, the harmonic frequency can not be well controlled, and the system has a poor effect on the nonlinear load. According to the principle of internal model, the resonance controller can be used to restrain the harmonic voltage, and ensure the quality of the output voltage waveform.

According to the analysis under nonlinear load of the auxiliary inverter, the nonlinear load current of the auxiliary inverter is rich in 5th and 7th harmonic current components, which form the corresponding harmonic voltage drop on the output impedance of the inverter, resulting in the distortion of the output voltage and the poor quality of the output voltage waveform. Therefore, the 5th and 7th harmonic voltage should be controlled. Two kinds of resonant controllers in which the 5th (250 Hz) and 7th (350 Hz) harmonics should be designed respectively in the static coordinate system. In the DQ synchronous rotating coordinates, the 5th and 7th harmonics are represented by the 6th harmonic (300 Hz), so there needs to design a harmonic controller for the 6th harmonic.

The transfer function of the PIR controller is:

$$G_{\text{PIR}}(s) = K_p + \frac{K_i}{s} + \frac{2K_r\omega_c s}{s^2 + 2\omega_c s + \omega_n^2} \quad (4)$$

where  $\omega_c$  is used to adjust the controller bandwidth and  $\omega_n$  is used as the controller for the resonant angular frequency to eliminate the specific harmonics.

Figure 2 is the d axis control block diagram of the PIR controlled inverter in the synchronous rotating coordinate system,  $i_{Ld}$  is the filter inductor L and  $i_{Cd}$  is current passing through filter capacitor C. The q axis control block diagram is the same as the d axis analysis method.

The output voltage of the d axis can be obtained according to Fig. 3:

$$u_{od} = G(s)u_{\text{dref}} - Z(s)i_{od} \quad (5)$$

$$G(s) = \frac{G_{\text{PIR}}(s) \cdot G_{\text{pwm}}(s)}{LCs^2 + Crs + 1 + G_{\text{PIR}}(s) \cdot G_{\text{pwm}}(s) - G_{\text{pwm}}(s)} \quad (6)$$

$$Z(s) = \frac{Ls + r}{LCs^2 + Crs + 1 + G_{\text{PIR}}(s) \cdot G_{\text{pwm}}(s) - G_{\text{pwm}}(s)} \quad (7)$$

The derivation of the inverter control amount  $G(s)$  from (6) is shown in Fig. 3.

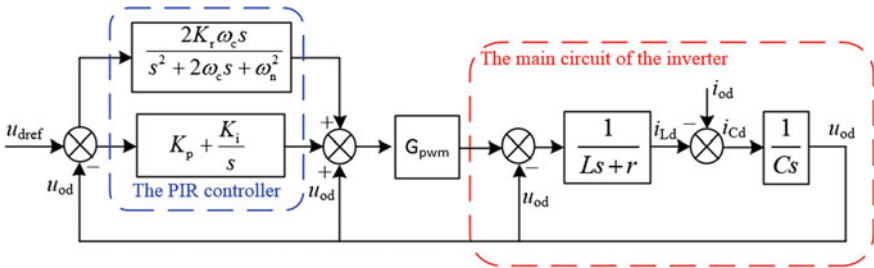
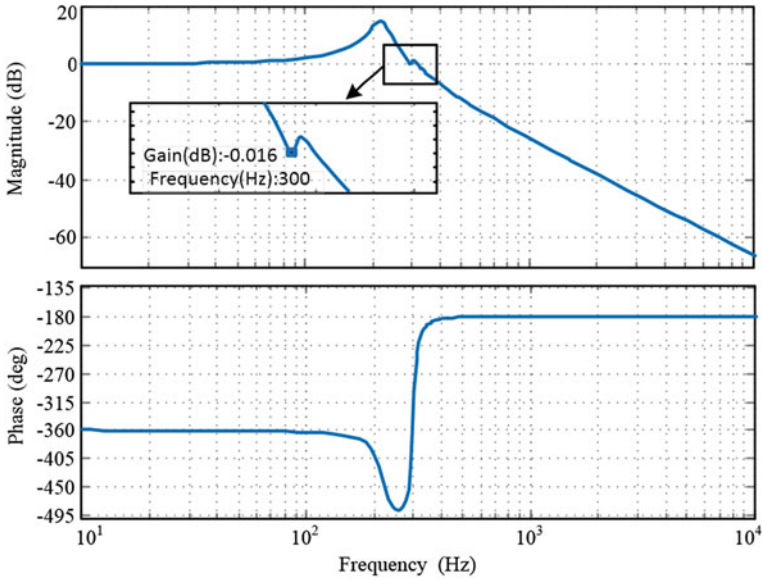


Fig. 2 Block diagram of inverter with PIR controller



**Fig. 3** The bode diagram of  $G(s)$  of inverter with PIR controller

In the DQ synchronous rotating coordinate system, the 5th and 7th harmonics are converted into the 6th harmonic, so we should observe the frequency response at 300 Hz. It can be seen that the magnitude of the control quantity  $G(s)$  is about 1 at the frequency of 300 Hz and the phase angle is 0.

Bode diagrams of the equivalent output impedance  $Z(s)$  of the inverter can be obtained from (7) as shown in Fig. 4.

We can see from Fig. 4 that the equivalent output impedance  $Z(s)$  of the inverter is significantly reduced at 300 Hz.

According to Figs. 3 and 4, it can be concluded that adding PIR controller into the inverter system can inhibit the aberration of output voltage of three-phase rectifier type nonlinear load caused by 5th and 7th harmonic current.

## 4 Simulation Result

This paper using S-Function in Matlab/Simulink, by setting the interrupt similar to DSP with C language, to construct a virtual DSP control system, better simulate main circuit and the discrete control system of the actual operation of the inverter. The simulation parameters are shown in Table 1.

Figure 5 is the output voltage and current waveforms, the inverter with 15 kW three-phase rectifier type nonlinear load by the instantaneous voltage PI control. As it can be seen from Fig. 5, the output voltage waveform is seriously distorted, and the quality of the output voltage waveform is poor.

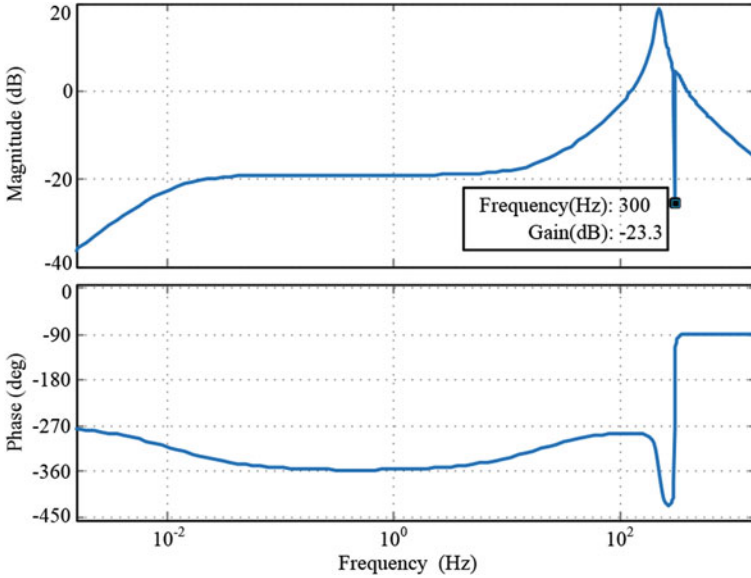


**Fig. 4** The bode diagram of  $Z(s)$  of inverter with PIR controller

**Table 1** Parameters of simulation

Parameters	The setting value	Parameters	The setting value
DC voltage/V	1650	Co/uF	3000
DC filter inductor/mH	0.103	Ro/ $\Omega$	20
DC filter capacitor/uF	2000	Kp	0.7
Power frequency/Hz	50	Ki	0.05
Switch frequency/Hz	1000	Kr	60

Figure 6 is output voltage harmonic analysis distribution with the instantaneous voltage PI closed loop control for a single auxiliary inverter under 15 kW three-phase rectifier type nonlinear load. It can be seen from Fig. 6 that the THD is 9.46% and the 5th harmonic voltage content is 8.99% and the 7th harmonic voltage content is 1.55%.

Figure 7 shows the output voltage and current waveforms of the inverter with the instantaneous voltage PIR closed-loop control. As can be seen from Fig. 7, the output voltage waveform quality has been significantly improved. The output voltage harmonic analysis of the inverter with 15 kW three-phase rectifier type nonlinear load using the instantaneous voltage PIR control is shown in Fig. 8. At this time, the THD is reduced to 2.85%, the 5th harmonic voltage content is reduced to 1.2% and the 7th harmonic voltage content is reduced to 0.5%.

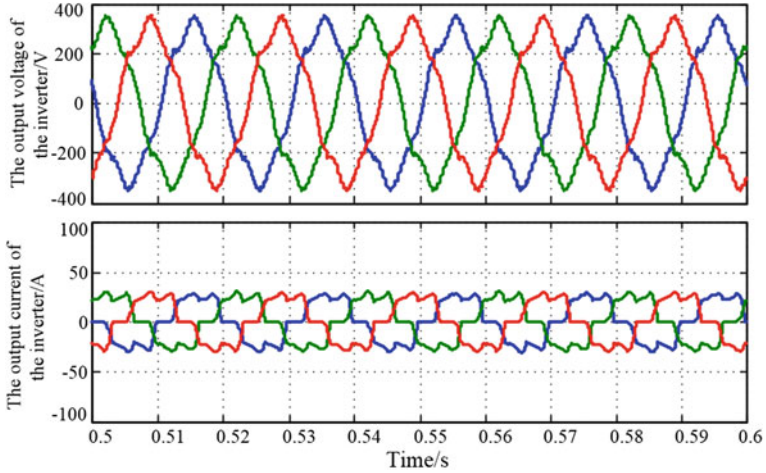


Fig. 5 Simulation waveforms of inverter with PI controller under nonlinear load

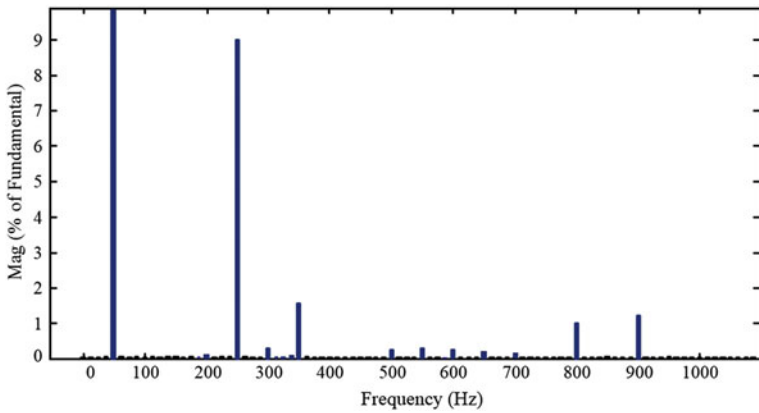


Fig. 6 FFT analysis of inverter with PI controller under nonlinear load

Through the above simulation and analysis, the design of the instantaneous voltage PIR control of single inverter in DQ synchronous rotating coordinate system is stable, and in the case of three-phase rectifier type nonlinear load, it still can guarantee the good quality of the output voltage wave shape.



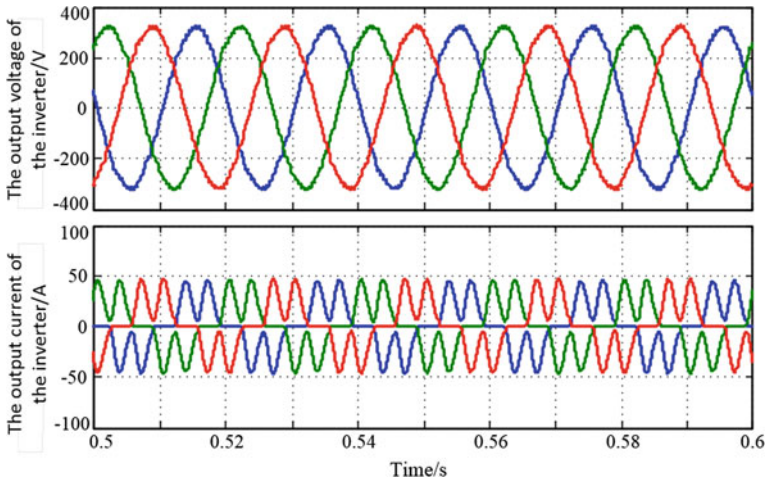


Fig. 7 Simulation waveforms of inverter with PIR controller under nonlinear load

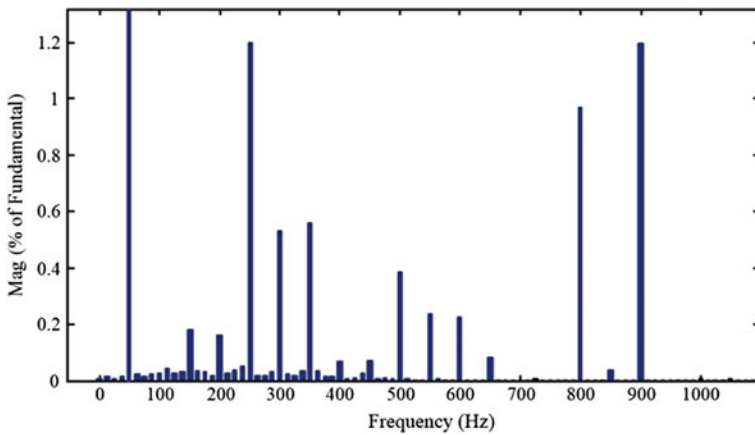


Fig. 8 FFT analysis of inverter with PIR controller under nonlinear load

## 5 Conclusion

In this paper, the harmonic analysis of the three-phase rectifier type nonlinear load such as air conditioner and charger is carried out. It is concluded that the 5th and 7th harmonics are represented by the 6th harmonic (300 Hz) in the DQ synchronous rotating coordinates. In order to realize the accurate tracking of fundamental voltage and the suppression of voltage distortion caused by nonlinear load, the instantaneous voltage PIR closed loop control of DQ synchronous rotating coordinate system is adopted. The auxiliary inverter suppresses 5th and 7th harmonics and the system can run stably.

**Acknowledgements** This work was supported by the China National Science and Technology Support Program under Grant 2016YFB1200502-04, Beijing base construction and personnel training special under Grant Z171100002217025, and the Fundamental Research Funds for the Central Universities under Grant 2016JBM058 and Grant 2016RC038.

## References

1. Li Z, Li Y, Wang P et al (2008) Three-phase PWM inverters with three-phase output transformer and three-phase filter inductor. In: ICEMS 2008. International conference on Electrical Machines and Systems, 2008. IEEE, pp 1116–1121
2. Zhang H, Liu P, Zhang K et al (2000) Three-phase SPWM inverter system based on fuzzy control. Power Electron Motion Control Conf IPEMC 3:1150–1154
3. Chen Y, Smedley K (2005) Parallel operation of one-cycle controlled grid connected three-phase inverters. In: Industry applications conference, 2005. Fortieth IAS annual meeting. conference record of the 2005. IEEE, vol 1, pp 591–598
4. Bon-Ho B, Seung-Ki S (2001) A compensation method for time delay of full digital synchronous frame current regulator of PWM AC drives. In: Industry applications conference, 2001. Thirty-sixth IAS annual meeting. conference record of the 2001 IEEE, pp 1708–1714
5. Yin W, Ma Y (2013) Research on three-phase PV grid-connected inverter based on LCL filter. In: 2013 8th IEEE conference on industrial electronics and applications (ICIEA). IEEE, pp 1279–1283
6. Li ZX, Li YH, Wang P et al (2010) Single-loop digital control of high-power 400-Hz ground power unit for airplanes. IEEE Trans Industr Electron 57(2):532–543
7. Chen Y, Smedley K (2005) Parallel operation of one-cycle controlled grid connected three-phase inverters. In: Industry applications conference, 2005. Fortieth IAS annual meeting. Conference record of the 2005. IEEE, vol 1, pp 591–598
8. Li Z, Li Y, Wang P et al (2008) Three-phase PWM inverters with three-phase output transformer and three-phase filter inductor. In: ICEMS 2008. International conference on electrical machines and systems, 2008. IEEE, pp 1116–1121
9. Guerrero JM, Matas J, de V L et al (2006) Wireless-control strategy for parallel operation of distributed-generation inverters. IEEE Trans Ind Electr 53(5):1461–1470

# Comparative Study of Two Control Strategies for Capacitor Voltage Balancing in Three-Level Boost Converter for Photovoltaic Grid-Connected Power System

Yiming Chen, Zhencong Li, Shuping Yang, Wen Xu and Lingling Xie

**Abstract** The three-level boost converter (TLBC) which is applied in the photovoltaic (PV) grid-connected power generation system has an inherent defect of the midpoint potential shift. This paper compares two control strategies which can solve the problem. They are duty cycle independent control strategy and pulse phase delay control strategy. Then the principles of the two control strategies are analyzed, and in order to carry out simulation experiments more accurately and quickly, the characteristics of the strategies are verified based on the co-simulation of PSIM + Matlab. The results show that the duty cycle independent control strategy has better performance under the condition of the bias voltage is larger.

**Keywords** Duty cycle independent control strategy · Pulse phase delay control strategy · Co-simulation · Three-level boost converter

## 1 Introduction

With the development of new energy technologies, PV grid-connected power generation system has been widely used. Its typical topology consists of Boost converter, three-phase inverter and filter. It is necessary to boost the output voltage of the PV module because it is unstable. Then convert DC into AC power through a three-phase inverter to achieve the purpose of PV grid-connected power generation [1]. In this paper, TLBC is used as the DC boost converter for PV modules. Because TLBC can halve the power device voltage stress compared with the conventional two-level boost converter. Additionally it has several advantages in high voltage applications such as reduced switching losses and lower reverse

---

Y. Chen (✉) · Z. Li · S. Yang · W. Xu · L. Xie  
Zhuhai Power Supply Bureau of Guangdong Power Grid Company,  
Zhuhai 519000 Guangdong Province, China  
e-mail: 14121400@bjtu.edu.cn

© Springer Nature Singapore Pte Ltd. 2018

L. Jia et al. (eds.), *Proceedings of the 3rd International Conference on Electrical and Information Technologies for Rail Transportation (EITRT) 2017*, Lecture Notes in Electrical Engineering 482, [https://doi.org/10.1007/978-981-10-7986-3\\_7](https://doi.org/10.1007/978-981-10-7986-3_7)

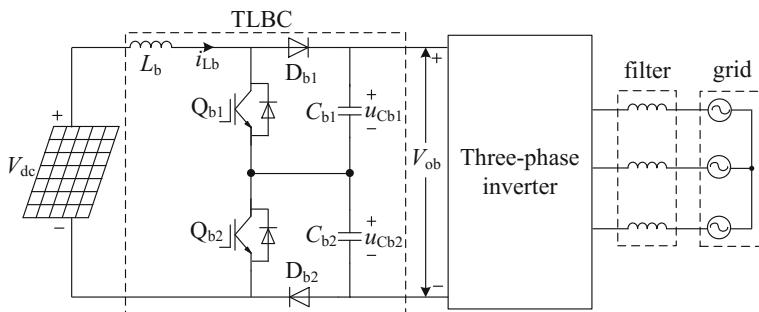


**Fig. 1** Topology of the PV grid-connected power generation system

recovery losses of the diode compared with the conventional boost converters [2–4]. The topology is shown in Fig. 1.

As shown in Fig. 1, the PV grid-connected power generation system consists of a PV modules, a TLBC, a three-phase inverter and a filter. This paper mainly studies the TLBC which consists of an inductor  $L_b$ , two switch tubes  $Q_{b1}$ ,  $Q_{b2}$ , two diodes  $D_{b1}$ ,  $D_{b2}$  and two capacitors  $C_{b1}$ ,  $C_{b2}$ . The duty cycle of the both switch tubes is  $D_{on-b}$ , and the output voltage gain of the converter is  $V_{ob}/V_{dc} = 1/(1 - D_{on-b})$ , when the inductor current are continuous.

There is a problem that the output voltage of the two output filter capacitors is inconsistent in TLBC [4, 5]. There are three reasons for the problem: (1) There is a slight difference between the control circuit and the drive circuit; (2) Turn-on time of the switch tubes cannot be completely equal; (3) The conduction voltage drop and switching characteristics of the two switch tubes cannot be completely consistent. Therefore, the voltage balancing of the two capacitors needs to be controlled under the premise of stabilizing the output voltage  $V_{ob}$ . To achieve effective control of the output voltage  $V_{ob}$  and two capacitance deviation voltage  $\Delta V_{Cb}$ , it is a common method that sample the two capacitor voltages  $u_{Cb1}$ ,  $u_{Cb2}$  separately. The output voltage  $V_{ob}$  is obtained by summing the two capacitor voltages. The subtracting voltage can be obtained by dividing the two capacitor voltages,  $\Delta V_{Cb} = u_{Cb1} - u_{Cb2}$ , then adjust the deviation voltage. According to the different pulse generation methods, It can be divided into duty cycle independent control strategy and pulse phase delay control strategy.

## 2 Analysis of Two Control Strategies for Capacitor Voltage Balancing

### 2.1 The Principle of Duty Cycle Independent Control Strategy

The schematic diagram of the duty cycle independent control strategy is shown in Fig. 2.

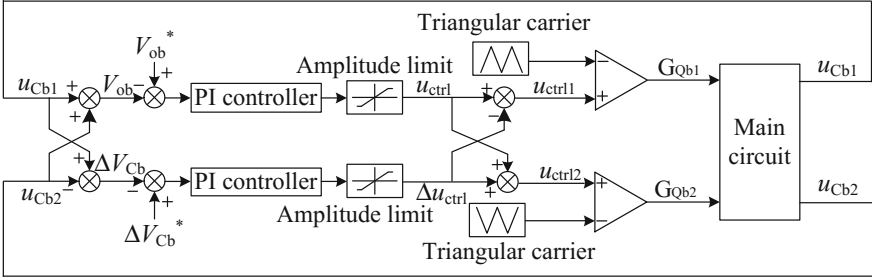


Fig. 2 Schematic diagram of duty cycle independent control strategy

The control strategy is that the output voltage  $V_{ob}$  and deviation voltage  $\Delta V_{Cb}$  are processed separately to obtain output voltage control signal  $u_{ctrl}$  and the deviation voltage control signal  $\Delta u_{ctrl}$  and then the pulse generation unit is adopted to generate two switch pulses  $G_{Qb1}$ ,  $G_{Qb2}$ .

$$\begin{cases} u_{ctrl} = (u_{ctrl1} + u_{ctrl2})/2 \\ \Delta u_{ctrl} = (u_{ctrl2} - u_{ctrl1})/2 \end{cases} \quad (1)$$

$u_{ctrl1}$  and  $u_{ctrl2}$  are the duty ratio of the two switching tubes are  $D_{on-b1}$  and  $D_{on-b2}$ . The phase difference between the two triangular carriers  $u_{tri1}$  and  $u_{tri2}$  is 180 degrees. When the capacitor voltage  $u_{Cb2} < u_{Cb1}$ , regulate  $u_{ctrl2} < u_{ctrl1}$ , and the typical operating waveforms of the TLBC under the duty cycle independent control strategy is shown in Fig. 3.

As the Fig. 3 shows, the principle of the duty cycle independent control strategy is that when the capacitor voltage  $u_{Cb2} < u_{Cb1}$ , regulate  $\Delta u_{ctrl} < 0$ , and  $u_{ctrl2} < u_{ctrl1}$ , so that the duty cycle  $D_{on-b1}$  of the switch tube  $Q_{b1}$  increases and the duty cycle

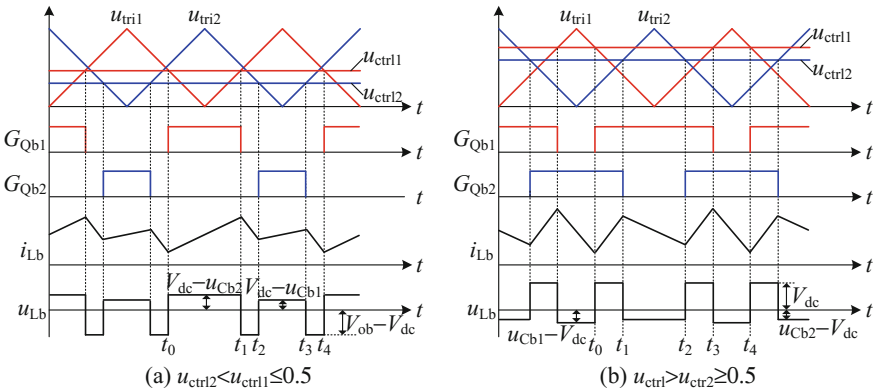


Fig. 3 Typical working waveforms of the TLBC under the duty cycle independent control strategy when  $u_{ctrl2} < u_{ctrl1}$

$D_{on-b2}$  of the switch tube  $Q_{b2}$  decreases. Charging time of the capacitor  $C_{b2}$  is longer and the capacitor  $C_{b2}$  stores more power so that the voltage balance between the two capacitors is achieved. On the contrary, if the voltage  $u_{Cb1}$  is lower than  $u_{Cb2}$ , regulate  $\Delta u_{ctrl} > 0$  to achieve the voltage balance between two capacitors.

### 2.2 The Principle of Pulse Phase Delay Control Strategy

The schematic diagram of the pulse phase delay control strategy is shown in Fig. 4.

As can be seen from Fig. 4, the output voltage control signal  $u_{ctrl}$  and the deviation voltage control signal  $\Delta u_{ctrl}$  are obtained by processing the output voltage  $V_{ob}$  and deviation voltage  $\Delta u_{Cb}$  respectively. Then the two switch tube pulses  $G_{Qb1}$ ,  $G_{Qb2}$  is generated by the logic processing unit and their duty cycles are  $D_{on-b}$  and their phase delay signal is  $\lambda_{pd}$  ( $\lambda_{pd}$  is the ratio of the pulse delay time  $t_{pd}$  and the switching period,  $\lambda_{pd} = t_{pd}/T_{sb}$ ). The typical operating waveforms of the TLBC under the pulse phase delay control strategy is shown in Fig. 5.

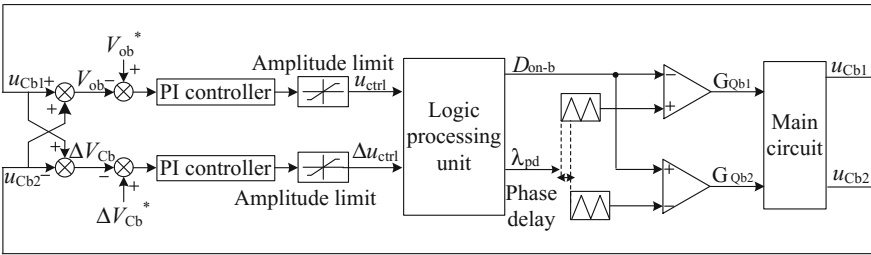


Fig. 4 Schematic diagram of pulse phase delay control strategy

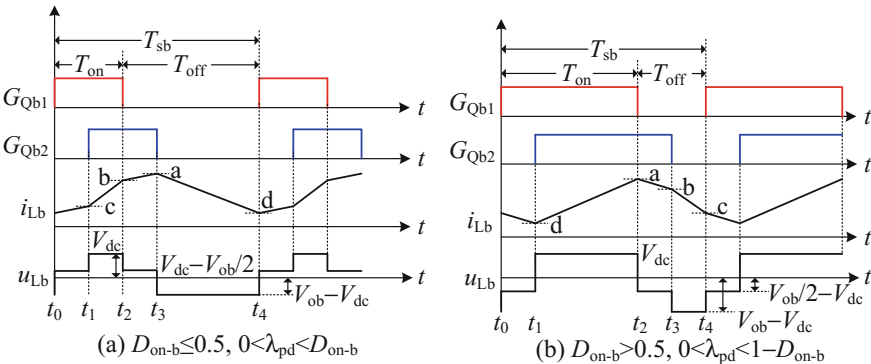


Fig. 5 Typical working waveforms of the TLBC under the pulse phase delay control strategy

It can be seen from Fig. 5 that the pulse phase delay control strategy is under the premise that duty cycles of the two switching tubes are equal. Although the charge time of the two capacitors is equal, the average charging current of them is different, so that one capacitor stores more energy, and the other capacitor stores less energy. Taking Fig. 5a as an example, it can be seen that the average value of the inductor current during  $t_0 \sim t_1$  is obviously smaller than that during  $t_2 \sim t_3$ . The charging current of the capacitor  $C_{b1}$  is significantly higher than that of the capacitor  $C_{b2}$  and capacitor  $C_{b1}$  stores more energy during each switching cycle, so that the voltage on the capacitor  $C_{b1}$  is relatively increased. Thus, we can adjust the phase delay signal  $\lambda_{pd}$  to achieve capacitance voltage balance.

### 3 The Results Based on Co-simulation of PSIM + Matlab

In order to make the simulation results more accurate, this paper use co-simulation of PSIM + Matlab. The specific approach is as follows: use PSIM to build power electronic circuit model and use Matlab to establish a control system model. This method can also improve the simulation efficiency greatly, and shorten the development cycle [6–8]. The simulation model based on PSIM + Matlab co-simulation is shown in Fig. 6.

#### 3.1 Simulation Research on Duty Cycle Independent Control Strategy

In order to verify the adjustment ability of duty cycle independent control strategy, a simulation experiment with unbalanced loads of TLBC is carried out. The main circuit parameter is as follows:  $V_{dc} = 490$  V,  $V_{ob} = 700$  V,  $f_{sb} = 8$  kHz,  $L_b = 2$  mH,  $C_{b1} = C_{b2} = 2267$   $\mu$ F,  $D_{on-b} = 0.3$  and the load resistances are adjusted as needed.

When  $R_{b1} = 55\Omega$ ,  $R_{b2} = 50\Omega$ , the experimental waveform is shown in Fig. 7a. And when  $R_{b1} = 65\Omega$ ,  $R_{b2} = 50\Omega$ , the waveform is shown in Fig. 7b.  $u_{Cb1}$ ,  $u_{Cb2}$  are voltages of the two capacitors,  $u_{ctrl}$  is the output voltage control signal,  $\Delta u_{ctrl}$  is the deviation voltage control signal,  $V_{ob}$  is the output voltage.

It can be seen from Fig. 7a that the two capacitor initial voltage deviation is 31.5 V. After adjustment of 0.05 s, the midpoint potential is balanced and the  $V_{ob}$  fluctuates in the range of  $700 \pm 10$  V during the adjustment process. It can be seen from Fig. 7b that the initial voltage deviation of the two capacitors is 85.8 V. After adjusting of 0.1 s, the midpoint of the potential reaches balance and  $V_{ob}$  fluctuates within the range of  $700 \pm 18$  V during the deviation voltage regulation process.

It is proved that the duty cycle independent control strategy can effectively adjust the large range deviation potential, but the output voltage fluctuates because the duty cycle of the two switches is not same during the adjustment process.

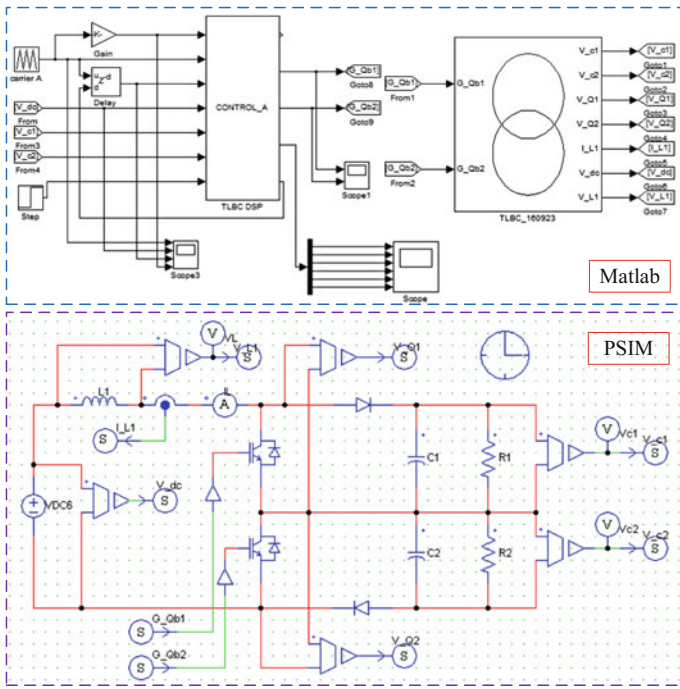


Fig. 6 Co-simulation model of PSIM + Matlab

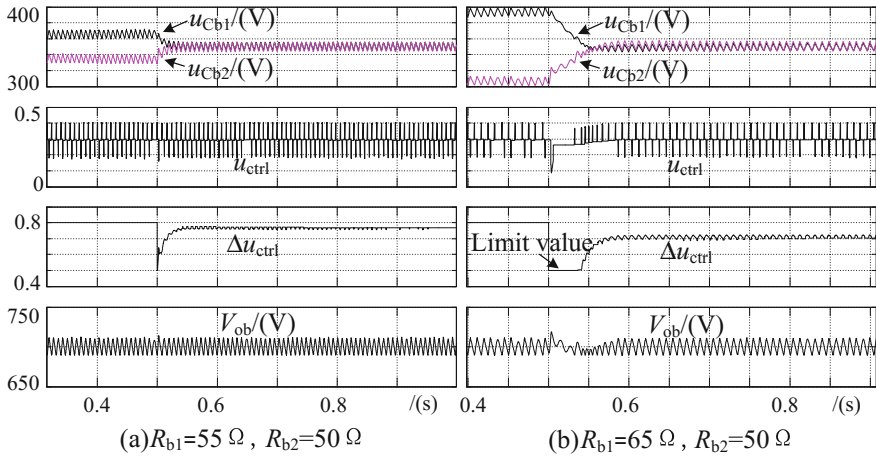


Fig. 7 Waveforms of the system with independent duty control strategy



### 3.2 Simulation Research on Pulse Phase Delay Control Strategy

The pulse phase delay control strategy is simulated based on the same experimental conditions. The experimental waveforms are shown in Fig. 8.

It can be seen from Fig. 8a that the deviation voltage is maintained at 31.8 V when the deviation voltage is not adjusted. After adjustment of 1.8 s, the two capacitor voltages is balanced, and output voltage is relatively stable during the adjustment process. As seen from Fig. 8b, the two capacitor voltage deviation is maintained at 86.1 V when the deviation voltage is not adjusted. After adjustment of 0.25 s, the deviation voltage gradually reduces to 45.5 V and become stability. During the adjustment process, the output voltage fluctuation is very small and the phase delay signal  $\lambda_{pd}$  remains at the limit value, so that the deviation voltage can't be further adjusted.

It is shown that the pulse phase delay control strategy has limited ability to adjust the deviation voltage, but the output voltage is not affected during the adjustment process, and the adjustment process is slower than the other strategy.

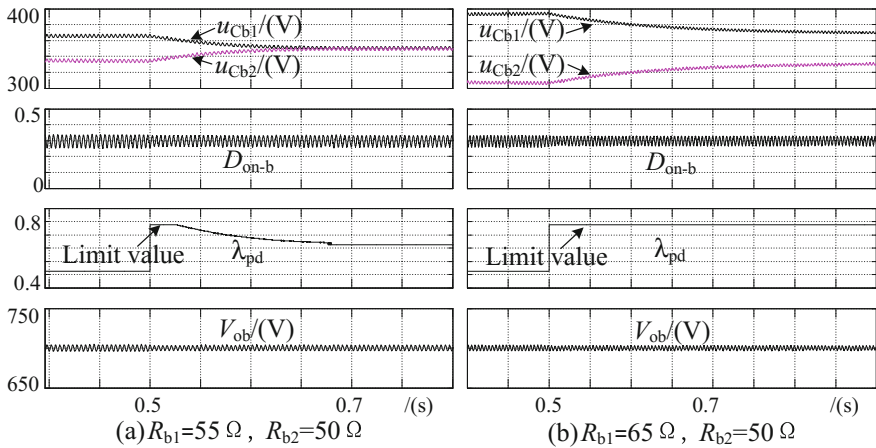


Fig. 8 Waveforms of the system with pulse phase delay control strategy

## 4 Conclusion

The paper mainly contrasts two control strategies that are proposed to suppress the potential shift in TLBC. The conclusions can be drawn from the theoretical analysis and simulation experiments:

1. Both control strategies can make effective adjustment on the midpoint potential when the shift is small.
2. The adjustment range on deviation voltage under duty cycle independent control strategy is larger than the other strategy.
3. The adjustment process of duty cycle independent control strategy is faster than the other strategy, but it will cause the output voltage fluctuations during the deviation voltage regulation processing.

In summary, in the case of smaller deviation voltage, the pulse phase delay control strategy has more advantages; while the midpoint potential shift is larger, the duty cycle independent control strategy is more applicable.

## References

1. Yang C (2014) Research on key technologies of three-level boost for photovoltaic grid-connected power system. Yangzhou University (In Chinese)
2. Krishna R, Soman DE, Kottayil SK et al (2015) Pulse delay control for capacitor voltage balancing in a three-level boost neutral point clamped inverter. *Power Electron Iet* 8(2):268–277
3. Yao G, Ma M, Deng Y, et al (2006) An improved ZVT PWM three level boost converter for power factor preregulator. In: *Power electronics specialists conference, 2007. Pesc. IEEE*, pp 768–772
4. Zhang MT, Jiang Y, Lee FC et al (1995) Single-phase three-level boost power factor correction converter. In: *Applied power electronics conference and exposition, 1995. Apec '95. Conference proceedings. IEEE*, vol. 1, pp 434–439
5. Xia C, Gu X, Shi T et al (2011) Neutral-point potential balancing of three-level inverters in direct-driven wind energy conversion system. *Energy Convers IEEE Trans* 2011 26(1):18–29
6. Li F, Wang Z, Xiao L et al (2016) Simulation of bidirectional energy converter based on PSIM and Matlab. *Electr Switch* 54(3):61–64, 67 (In Chinese)
7. Li J, Wang W, Zhong Y et al (2010) PSIM + Matlab co-simulation method for power electronic system. *Power Electron Technol* 44(5):86–88 (In Chinese)
8. Chen Shuang, Duan Guoyan, Tang Wei et al (2014) Co-simulation of induction motor vector control based on SVPWM. *Manuf Autom* 1:95–97 (In Chinese)

# A Resonant Push–Pull DC–DC Converter

Shiying Yuan, Zhe Tang, Jiyun Tian and Hui Cao

**Abstract** This paper presents a novel topology of a resonant push–pull DC–DC converter. The primary side of the transformer applies a traditional two-transistor push–pull circuit structure, while the secondary side of the transformer includes a circuit of duplex windings and a LC resonant voltage-double structure. The average output voltage of the converter is four times of the voltage-double resonant capacitors. The LC resonance of the voltage-double capacitors and the secondary leakage inductors of the transformer transfers the energy from the primary side to the secondary side. The circuit adopts the strategy of fixing turn-on time and frequency modulation method. All switches and diodes can achieve ZCS (zero current switching). The paper analyses every operation mode in detail. Because of symmetrical working of the secondary upper and lower windings of the transformer, it can be transformed into two-port network to analyze the AC equivalent circuit through fundamental analysis method. And on this basis, the paper deduces the gain characteristic expression of the AC fundamental wave, plots the curve of voltage gain with different frequency ratio  $m$ , excitation inductance/leakage inductance ratio  $h$  and quality factor  $Q$  by MATLAB, and utilizes the voltage gain curve to design the circuit experimental parameters. At last, a sample converter of 20–28 V input/360 V output/rated power 400 W is built and tested. The experimental waveforms verify the correctness of the circuit and validity of the gain model. The experimental conversion efficiency indicates that the switch achieves ZCS to reduce the switching loss of existing push–pull circuit effectively and improve the conversion efficiency. The measured efficiency was 93.5% at rated load.

**Keywords** LC resonance · Push–pull · Voltage-fourfold structure  
ZCS · First harmonic analysis method

---

S. Yuan (✉) · Z. Tang · J. Tian · H. Cao  
East China Jiaotong University (ECJTU), Nanchang, China  
e-mail: 405376417@qq.com

© Springer Nature Singapore Pte Ltd. 2018  
L. Jia et al. (eds.), *Proceedings of the 3rd International Conference on Electrical and Information Technologies for Rail Transportation (EITRT) 2017*, Lecture Notes in Electrical Engineering 482, [https://doi.org/10.1007/978-981-10-7986-3\\_8](https://doi.org/10.1007/978-981-10-7986-3_8)

## 1 Introduction

The traditional push–pull circuit has the advantages of simple structure and drive circuit without isolation. The disadvantages are that the voltage stress of the switch is more than two times of the input voltage, and the switch is hard-switching. Therefore many researches on improved push–pull circuit have been continuously expanding and deepening. A scheme is a soft-switching push–pull circuit of four switches in [1]. The disadvantages are the increase of the number of switches and complex isolated driver circuit. The second scheme is a soft-switching push–pull forward circuit in [2], which achieves the zero current switching and reduces the switching loss, but the disadvantages are that an auxiliary switch which increases isolated driver circuit in the secondary side is necessary and the output filter inductor is retained. The third scheme is a soft-switching three-transistor push–pull converter. Yisheng and Qunfang [3] introduces the basic topology, and the control strategy of main and vice switches is same as two bridge arms of phase shifted full bridge circuit, turn-off currents of main switches are half than the latter, but auxiliary switch could only achieve the zero voltage switching under heavy load conditions. The fourth scheme is LC resonant soft-switching push–pull circuit. Yisheng and Changwei [4] shows that if the resonant period of the secondary LC is less than turn-on time of the switch, the secondary inductor and capacitor will be resonant in multi periods. Under the condition of changing load, the output voltage will appear alternating characteristics of voltage source and current source, and the applicable range is relatively narrow.

This paper presents a novel topology of the resonant push–pull DC–DC converter with a voltage-fourfold structure, which is different from the traditional topologies of LC [4], LCL [5] and LLC [6]. The leakage inductors of transformer as resonant inductors and series resonant capacitors consist of the voltage-double resonant structure. And the voltage-double capacitors of the secondary windings have charging and discharging process on the contrary. The output voltage is four times of the average voltage of each voltage-double capacitor, which is the origin of voltage-fourfold structure. Both of the primary switches and the secondary diodes can achieve ZCS. According to the equivalent model of the circuit based on first harmonic approximation (FHA), the three dimensional curve analysis of the voltage gain variable is performed and the circuit parameters are optimized. An experimental prototype of 400 W is made. The test results verify the feasibility of the circuit and the effectiveness of the gain model.

## 2 Operation Principle

Figure 1 is the voltage-fourfold resonant push–pull circuit. Switch  $Q_1$ ,  $Q_2$  consist of the push–pull structure.  $D_1$ ,  $D_2$  are the parasitic diodes of  $Q_1$ ,  $Q_2$ . And  $C_1$ ,  $C_2$  include the parasitic capacitors and external parallel capacitors of  $Q_1$ ,  $Q_2$ .  $C_{r1}$ ,  $C_{r2}$

are the voltage-double capacitors.  $L_{11}, L_{12}, L_{13}, L_{14}$  are leakage inductors of primary and secondary sides of the transformer. The physical reference directions are shown in Fig. 1.

Before analyzing the principle of the circuit, make the following assumptions:

1. the voltage drop of the switching devices is zero;
2. the number of turns of the transformer TX:  $N_1 = N_2 = N_3/N = N_4/N$ , Where  $N$  is the ratio;  $L_{m1} = L_{m2} = L_m = L_{m3}/N^2 = L_{m4}/N^2$ ; Leakage inductances  $L_{l1} = L_{l2} = L_l = L_{l3}/N^2 = L_{l4}/N^2$  is much less than  $L_m$ ;
3. equivalent capacitances of the two switches  $C_1 = C_2 = C$ ;
4. the voltage-double capacitances  $C_{r1} = C_{r2} = C_r$ , the average voltage is  $U_o/4$ , this is the origin of voltage-fourfold structure.

The key operational waveforms of the circuit are shown in Fig. 2. In one switching period, there are eight operation modes in voltage-fourfold resonant converter, the analysis of each mode is as follows.

- (1) Mode 1 [ $t_0 \sim t_1$ ]: charging and discharging stage of parallel capacitors of the switches

In the moment before  $t_0$ ,  $Q_2$  is turned on, the loop is  $U_i - N_2 - Q_2 - U_i$ , the reverse of the excitation current increases. The excitation current reaches the maximum value of the reverse in the moment of  $t_0$ . At the time, the secondary side has ended resonance, the resonant capacitor voltage is kept constant, the voltage of  $C_{r1}$  reaches the minimum value, the voltage of  $C_{r2}$  reaches maximum value, the resonant current is zero, the winding of the secondary side is open, the primary voltage is clamped by the secondary voltage.

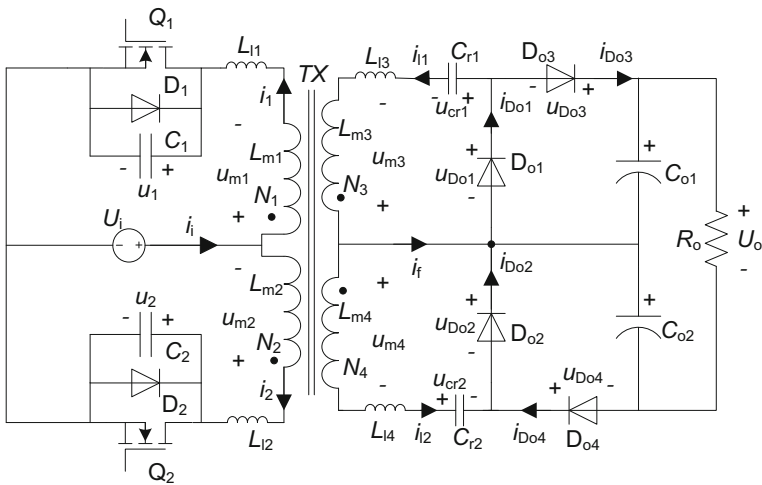


**Fig. 1** Resonant push-pull DC-DC converter with a voltage-fourfold structure

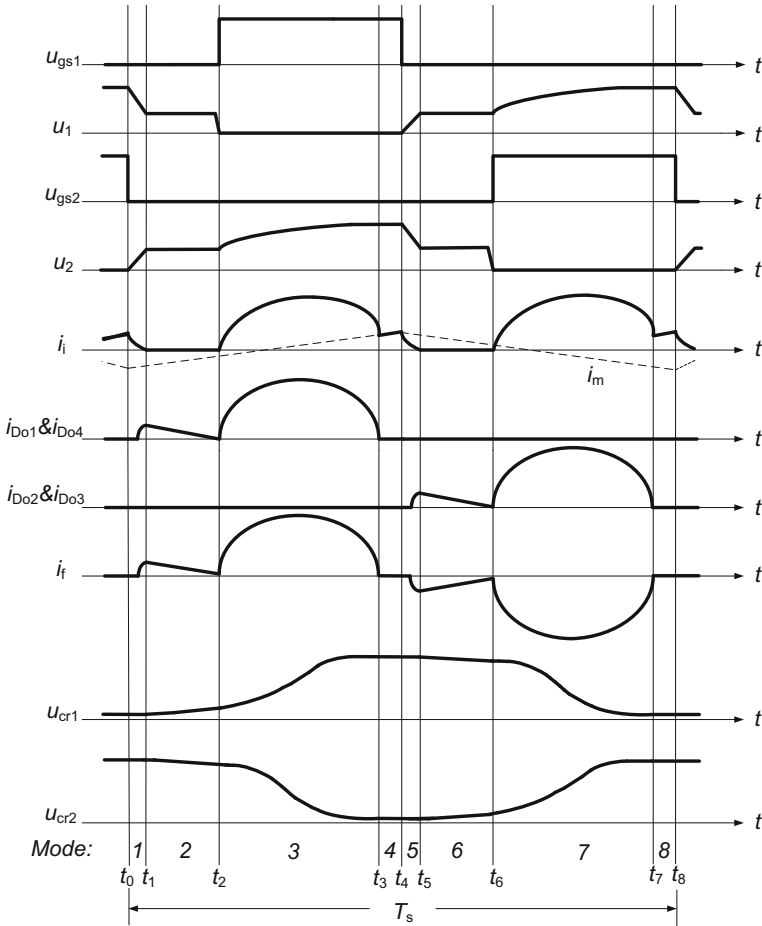


**Fig. 2** Key working waveforms of the converter

In the time  $t_0$ ,  $Q_2$  is turned off, the excitation inductance and leakage inductances of the primary side and  $C_2$ ,  $C_1$  are resonant. During the resonant process, the excitation current charges  $C_2$  to make  $U_2$  rise, and discharges  $C_1$  to make  $U_1$  drop.

$U_{m2}$  has reverse reduction and then has positive increase. Set  $L_{11} = L_{12} = L_1$ , the voltage and node current equations in the primary circuit can be listed:

$$\begin{cases} U_i - u_{m1} - L_1 di_1/dt - u_1 = 0 \\ U_i + u_{m2} - L_1 di_2/dt - u_2 = 0 \\ u_{m1} = u_{m2} = u_m \\ i_1 + i_2 = i_i \\ i_2 - i_1 = I_{mm} \\ i_1 = Cdu_1/dt \\ i_2 = Cdu_2/dt \end{cases} \quad (1)$$

The variables are as follows:

$$\begin{cases} u_1 = 2U_i - I_{mm}(t - t_0)/2C + \frac{I_{mm}}{2} \sqrt{L_1/C} \sin \frac{(t-t_0)}{\sqrt{L_1C}} \\ u_2 = I_{mm}(t - t_0)/2C + \frac{I_{mm}}{2} \sqrt{L_1/C} \sin \frac{(t-t_0)}{\sqrt{L_1C}} \\ u_m = I_{mm}(t - t_0)/2C - U_i \\ i_i = I_{mm} \cos \frac{(t-t_0)}{\sqrt{L_1C}} \\ i_1 = -I_{mm}/2 + \frac{I_{mm}}{2} \cos \frac{(t-t_0)}{\sqrt{L_1C}} \\ i_2 = I_{mm}/2 + \frac{I_{mm}}{2} \cos \frac{(t-t_0)}{\sqrt{L_1C}} \end{cases} \quad (2)$$

In the formula,  $I_{mm}$  is the maximum value of the excitation current.

The leakage inductances are much less than the excitation inductance, so the leakage inductances can be neglected in series. Because this process is very short, it can be considered that the excitation current is kept constant in the process of  $I_{mm}$ .

In the time  $t_1$ ,  $u_1$  is reduced from  $2U_i$  to the platform value;  $u_2$  is increased from 0 to the platform value, and the primary voltage of the transformer rises from  $-U_i$  to the voltage valley value, which is converted from the secondary boundary value of the resonant capacitor  $C_{r1}$ . According to the solutions of the equation group, it is known that the duration of this stage is

$$t_{01} = 2C(U_{cr1} + NU_i)/NI_{mm} \quad (3)$$

(2) Mode 2 [ $t_1 \sim t_2$ ]: resonant stage of the secondary excitation

At the moment  $t_1$ , due to the rise of the voltage of  $C_2$ , the voltage of  $L_{m2}$  rises. When meeting  $u_{m3} > u_{cr1}$ ,  $u_{m4} > U_o/2 - u_{crm}$ ,  $D_{o1}$ ,  $D_{o4}$  are turned on. In the formula,  $u_{cr1}$  is the voltage valley value of the resonant capacitor  $C_{r1}$ , and  $u_{crm}$  is the voltage peak value of the resonant capacitor  $C_{r2}$ . Ideally, according to the symmetry of the circuit, the voltage valley value of the resonant capacitor  $C_{r2}$  is  $u_{cr1}$ , and the peak value of the resonant capacitor  $C_{r1}$  is  $u_{crm}$ .

Therefore, the excitation current is transferred from the primary side to the secondary side, which provides a resonant current for the secondary side. The secondary side begins to resonate, when ignoring the leakage inductors, the resonant loops are  $N_3 - D_{o1} - C_{r1} - N_3$  and  $N_4 - C_{o2} - D_{o4} - C_{r2} - N_4$ . The resonant voltage of  $C_{r1}$  rises, the resonant voltage of  $C_{r2}$  decreases, the both resonant currents decrease. The primary voltage is clamped by the secondary side.  $C_1$ ,  $C_2$ ,  $L_{11}$ ,  $L_{12}$  participate in the resonance, and each current is rapidly reduced to zero due to damping resonance. The voltage and current equations of the two top and bottom winding loops are listed as follows:

$$\begin{cases} L_{m3} di_{D_{o1}}/dt + u_{cr1} = 0 \\ i_{D_{o1}} = C_{r1} du_{cr1}/dt \\ L_{m4} di_{D_{o4}}/dt + U_o/2 - u_{cr2} = 0 \\ i_{D_{o4}} = -C_{r2} du_{cr2}/dt \\ u_{m3} = u_{m4} \end{cases} \quad (4)$$

The variables are as follows:

$$\left\{ \begin{array}{l} i_{D_{o1}} = -\frac{U_{cr1}}{N\sqrt{L_m/C_r}} \sin \omega_c(t-t_1) + \frac{I_{mm}}{N} \cos \omega_c(t-t_1) \\ u_{cr1} = I_{mm} \sqrt{L_m/C_r} \sin \omega_c(t-t_1) + U_{cr1} \cos \omega_c(t-t_1) \\ i_{D_{o4}} = \frac{U_o/2 - U_{crm}}{N\sqrt{L_m/C_r}} \sin \omega_c(t-t_1) + \frac{I_{mm}}{N} \cos \omega_c(t-t_1) \\ u_{cr2} = \frac{U_o}{2} - I_{mm} \sqrt{\frac{L_m}{C_r}} \sin \omega_c(t-t_1) \\ \quad + (U_o/2 - U_{crm}) \cos \omega_c(t-t_1) \frac{U_o}{2} - U_{crm} = U_{cr1} \\ \omega_c = 1/(N\sqrt{L_m C_r}) \end{array} \right. \quad (5)$$

In the formula,  $\omega_c$  is resonant angle frequency of series resonant circuit for this mode. According to the solutions of the equations, the relationship between the peak value and the valley value of the resonant capacitor voltage is  $U_o/2 - U_{crm} = U_{cr1}$ . The primary winding voltage is clamped by the secondary side in  $u_{cr1}/N$ , i.e., it is clamped in  $(U_o/2 - u_{crm})/N$ , and the two are equal. The platforms of  $U_1$ ,  $U_2$  occur.

In the moment  $t_2$ ,  $i_i$  drops to zero. Output diode current  $i_{D_{o1}}$  and  $i_{D_{o4}}$  drop a value of zero or slightly greater than zero, called it  $I_{m1}$ .  $u_{cr1}$  and  $u_{cr2}$  do not change much, and  $u_{cr1}$  is made up to  $U'_{cr1}$  and  $u_{cr2}$  is made down to  $U'_{crm}$  respectively.

At the end of this mode, Q1 is turned on. The duration of this mode is determined by the dead time.

(3) Mode 3 [ $t_2 \sim t_3$ ]: the main resonant stage

In the moment  $t_2$ , Q1 is turned on. The excitation inductors and leakage inductors of the primary and secondary sides and resonant capacitors are resonant together. Secondary loops are  $N_3 - D_{o1} - C_{r1} - L_{l3} - N_3$ ,  $N_4 - C_{o2} - D_{o4} - C_{r2} - L_{l4} - N_4$ . The primary resonant current varies from zero;  $u_1$  decreases and  $u_2$  increases due to resonance. The secondary resonant current varies from zero or a slightly greater than zero. The voltage of charging  $C_{r1}$  rises; the voltage of discharging  $C_{r2}$  drops.

When the primary side is converted to the secondary side, the equations are listed as follows:

$$\left\{ \begin{array}{l} NU_i - u_{cr1} - 2N^2 L_1 di_{D_{o1}}/dt = 0 \\ i_{D_{o1}} = C_{r1} du_{cr1}/dt \\ NU_i + u_{cr2} - U_o/2 - 2N^2 L_1 di_{D_{o4}}/dt = 0 \\ i_{D_{o4}} = -C_{r2} du_{cr2}/dt \end{array} \right. \quad (6)$$

The variables are as follows:

$$\left\{ \begin{array}{l} u_{cr1} = NU_i + I_{m1} N \sqrt{2L_1/C_r} \sin \omega_r(t-t_2) - (NU_i - U'_{cr1}) \cos \omega_r(t-t_2) \\ i_{D_{o1}} = \frac{NU_i - U'_{cr1}}{N\sqrt{2L_1/C_r}} \sin \omega_r(t-t_2) + I_{m1} \cos \omega_r(t-t_2) \\ u_{cr2} = U_o/2 - NU_i - I_{m1} N \sqrt{2L_1/C_r} \sin \omega_r(t-t_2) + (NU_i + U'_{crm} - U_o/2) \cos \omega_r(t-t_2) \\ i_{D_{o4}} = \frac{NU_i + U'_{crm} - U_o/2}{N\sqrt{2L_1/C_r}} \sin \omega_r(t-t_2) + I_{m1} \cos \omega_r(t-t_2) \\ i_f = \frac{2(NU_i - U'_{cr1})}{N\sqrt{2L_1/C_r}} \sin \omega_r(t-t_2) + 2I_{m1} \cos \omega_r(t-t_2) \\ U_o/2 - U'_{crm} = U'_{cr1} \end{array} \right. \quad (7)$$



In the formula,  $\omega_r = 1/(N\sqrt{2L_1C_r})$  is resonant angle frequency of series resonant circuit for this mode.

In the moment  $t_3$ , the resonance of the secondary side ends, and the resonant current is zero. The primary current drops to the excitation current.  $U_2$  rises to a certain value;  $u_{cr1}$  rises to the maximum;  $u_{cr2}$  drops to the minimum. This mode is over, the duration of this mode is

$$t_{23} = \pi N \sqrt{2L_1C_r} \quad (8)$$

(4) Mode 4 [ $t_3 \sim t_4$ ]: the charging stage of the primary excitation inductor

In the moment  $t_3$ , the secondary resonance ends,  $u_{m1}$  is  $U_i$ . The primary excitation winding is charged, the loop is  $U_i - N_1 - Q_1 - U_i$ , the secondary current is zero. The primary current  $i_i$  is the excitation current at this stage:

$$i_i = i_m(t_3) + U_i(t - t_3)/L_m \quad (9)$$

The duration of this mode is a difference between the turn-on time of the switch and the half resonant period of the secondary side.

Four modes in the follow are similar to the first four modes, i.e., the resonant capacitors of the two secondary windings have opposite charging and discharging process. Therefore that won't be said again here.

### 3 DC Gain Characteristics of the Voltage-Fourfold Resonant Converter

The circuit uses the fixed turn-on time to adjust the switching frequency  $f_s$  to control the output voltage. In order to enable the switches and diodes to achieve ZCS,  $f_s$  should be less than the resonant frequency  $f_r$ .

In the design of the circuit, the secondary resonant network ends resonance in advance before the switch is turned off, so the switch is off at the peak of the excitation current. In order to reduce the current and the turn-off switching loss, the durations of mode 4 and mode 8 must be reduced, that is, the half resonant period is close to the turn-on time.

In addition, in mode 2 and mode 6, the excitation current is very small. After the excitation current is transferred to the secondary side, the resonant current is very small, the secondary winding inductance is very large, the energy is basically unchanged, the voltage change of the secondary resonant capacitor is very small, so the function of energy transfer of mode 2 and mode 6 is ignored.

Based on above analyses, the secondary stages of energy transfer, i.e., mode 2 and mode 6, as well as the modes which time are very short, i.e., mode 1, 4, 5, 8, are ignored. So only consider the main stages of energy transfer, namely, mode 3 and mode 7.

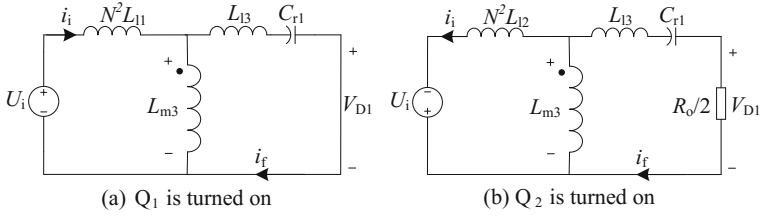


**Fig. 3** Two-port network at different switches terms

In mode 3 and mode 7, the switches  $Q_1$ ,  $Q_2$  are turned on respectively. The primary and secondary windings of the converter in essence are three-port, but due to symmetrical working of upper and lower windings, it can be transformed into two-port network to analyze the AC equivalent circuit through fundamental analysis method. The equivalent models of the two secondary windings are the same. In order to simplify the analysis, when the circuit is stable, only the equivalent model of the upper winding is analyzed.

When  $Q_1$  is turned on, the network diagram of the two-port network is shown in Fig. 3a. When  $Q_2$  is turned on, the network diagram of the two-port network is shown in Fig. 3b.

The total DC gain expression can be deduced

$$G_{dc} = \frac{U_o}{NU_i} = \frac{32mQ \sin(\pi m/2)}{\sqrt{[8mQ(H+1) \sin(\pi m/2)]^2 + \pi^4 [m^2(H+2) - 2(H+1)]^2}} \quad (10)$$

In the above formula,  $h = L_{13}/L_{m3} = L_l/L_m$  is the leakage inductance coefficient.  $Q' = R_{a1}/\sqrt{2L_{l3}/C_{r1}}$  is resonance quality factor  $Q$  is custom quality factor,  $Q = \frac{R_o/2}{\sqrt{2L_{l3}/C_r}}$ .

## 4 Design of Key Circuit Parameters

The key circuit parameters of  $m$ ,  $Q$  and  $h$  are designed by using the voltage-fourfold resonant converter of input DC voltage 20–28 V, output voltage 360 V, rated power 400 W, working frequency of  $f_s = 40$ –80 kHz as an example.

In the actual circuit, due to the line loss and other reasons, the voltage gain is not up to the highest value. Therefore, take  $G_{dc(max)} = 3.7$  here. So the transformer ratio is

$$N = \frac{U_{o(min)}}{U_{i(min)} G_{dc(max)}} = 4.86 \quad (11)$$

At the same time, according to the maximum input voltage, the required minimum voltage gain can be obtained as follows

$$G_{dc(\min)} = \frac{U_{o(\max)}}{NU_{i(\max)}} = 2.65 \quad (12)$$

Based on the total DC gain expression (10),  $Q$  is fixed to 8.3 firstly, then the leakage inductance coefficient  $h$  is desirable for 1/350. In order to ensure that the switch is turned off with a smaller current and the dead time is considered, the maximum operating frequency of the switch should be slightly less than  $f_r$ ,  $T_{\text{on}}$  is desirable for 6.2  $\mu\text{s}$ , so the resonant frequency  $f_r$  of the circuit is desirable for 81 kHz.

According to the custom quality factor  $Q$  and the resonant frequency formula of the circuit in the expression of DC voltage gain, the following equations can be listed:

$$\begin{cases} Q = \frac{R_o/2}{\sqrt{2L_{13}/C_r}} \\ f_r = \frac{1}{2\pi\sqrt{2L_{13}C_r}} \\ R_o = \frac{U_o^2}{P_o} \end{cases} \quad (13)$$

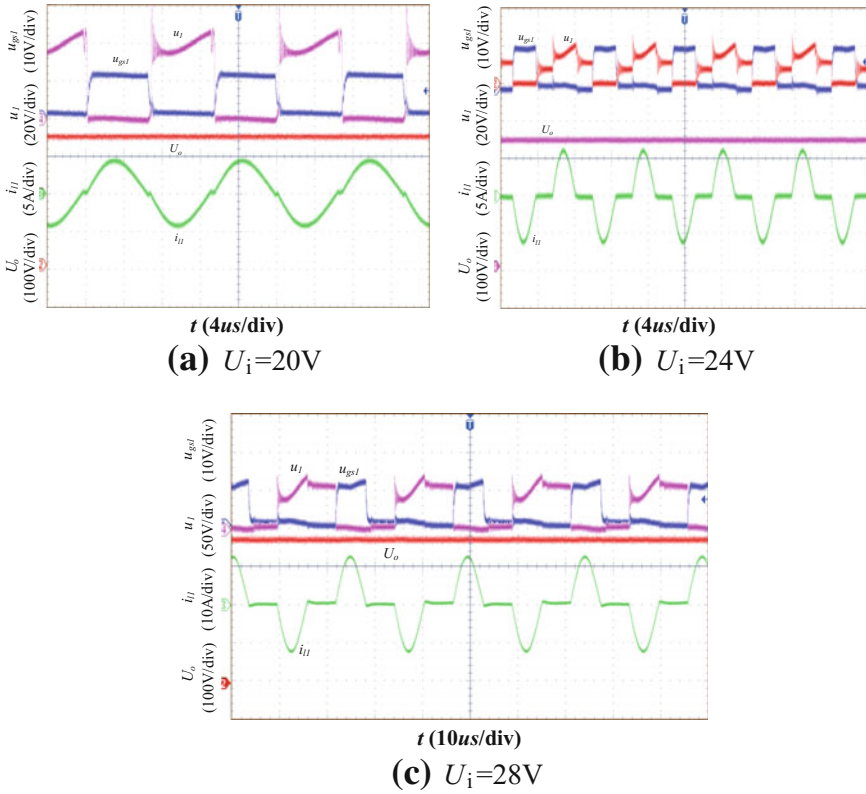
The solutions of the above equations can be obtained,  $R_o = 324 \Omega$ ,  $L_{13} = L_{14} = 19.3 \mu\text{H}$ ,  $C_{r1} = C_{r2} = C_r = 100 \text{ nF}$ , then  $L_{m3} = L_{13}/h = 6.8 \text{ mH}$ ;  $L_{m1} = L_{m3}/N^2 = 288 \mu\text{H}$ ;  $L_{11} = L_{12} = L_{13}/N^2 = 0.8 \mu\text{H}$ .

The circuit selects UC3867 as the driver chip and ETD49 as the core of the transformer. A laboratory prototype with a rated power of 400 W is made according to the above circuit parameters.

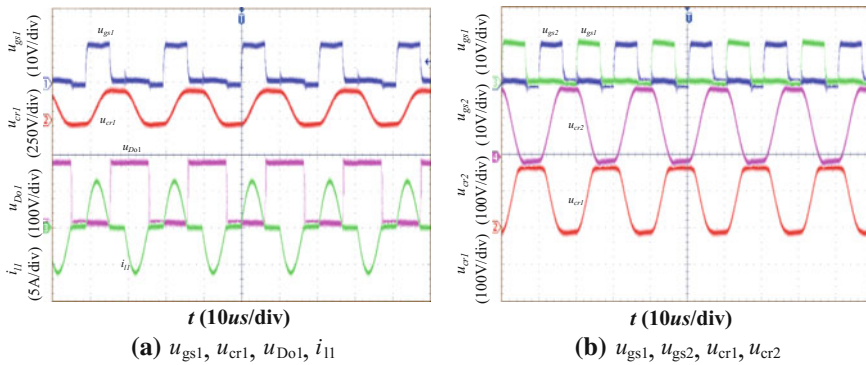
## 5 Experimental Results

Figure 4 shows the test waveforms of the input voltage of 20, 24 and 28 V respectively under rated load conditions. As can be seen from the secondary resonant current waveform in each figure, the excitation current is very small relative to the resonant current, the switch can achieve zero current shutdown; the primary current is resonant from zero, the switch achieves zero current switching; The half of the secondary resonant period is slightly less than the turn-on time of the switch, so the secondary current is resonant in advance, and the diode can achieve zero current shutdown. The switching frequency is adjusted to 77, 48 and 41 kHz.

Figure 5a shows the waveforms of the resonant capacitor voltage  $u_{cr1}$  of the secondary upper winding and the resonant current  $i_{11}$ , as well as the waveform of the diode voltage  $u_{D01}$  under the rated input/nominal load; there is no voltage spike



**Fig. 4**  $u_{gs1}$ ,  $u_{t1}$ ,  $i_{t1}$  and  $U_o$  waveforms at different input voltage with full load



**Fig. 5**  $u_{gs1}$ ,  $u_{gs2}$ ,  $u_{Do1}$ ,  $i_{t1}$ ,  $u_{cr1}$  and  $u_{cr2}$  waveforms at 24 V input voltage with full load

in  $u_{D_{o1}}$  and  $u_{D_{o2}}$ , the voltage of the diode is zero in mode 2, the diode withstands reverse voltage of  $U_o/2$  in mode 6. The circuit is suitable for high voltage output.

In Fig. 5b,  $u_{cr1}$  and  $u_{cr2}$  are similar to trapezoidal wave, and the valley value can be negative, the peak value can be greater than  $U_o/2$ , but its average value is  $U_o/4$ . And the rapid change of the voltage is only in mode 3 and mode 7, which is consistent with the theoretical analysis. The rise and fall of the voltage of  $C_{r1}$  are not synchronized with those of  $C_{r2}$ , but the slopes of the rise and fall of the voltages are the same, the peak and the valley voltage of them are the same and mirror symmetrical.

The measured efficiency under the rated load is 93.5%.

## 6 Conclusion

This paper presents a topology of a resonant push–pull DC–DC converter with a voltage-fourfold structure. The circuit has the following characteristics:

1. The output voltage is 4 times of the average voltage of the voltage-double capacitor, which is voltage-fourfold structure. Its maximum voltage conversion rate is  $4N_s/N_p$ . And it is suitable for large current input and high voltage output.
2. The circuit adopts the secondary LC resonant mode. The switch can be turned on in a wide range of load with zero current and turned off with a small excitation current.
3. The voltage of each rectifier diode is only half of the output voltage. The secondary current is resonant to zero in advance during the turn-on time of the switch. The switch achieves ZCS to reduce the switching loss of existing push–pull circuit effectively and improve the conversion efficiency.
4. Different from the traditional frequency conversion mode, the circuit adopts the frequency conversion mode of fixed conduction time, which makes the result of the fundamental analysis method more accurate and effective.

**Acknowledgements** This work is partially supported by the National Natural Science Foundation of China (No.51467005), the Key Research and Development Plan of Jiangxi Province (20171BBE50018), and the foundation of East China Jiaotong University (No. 14DQ02).

## References

1. Yundong M, Linquan M, Xinbo R et al (2006) Zero-voltage-switching PWM push–pull three-level converter. Proc CSEE 26(23):36–41 (in Chinese)
2. Fanghua Z, Huizhen W, Yangguang Y (2003) ZCS scheme of push–pull forward converter. Power Electron 37(2):60–62 (in Chinese)
3. Yisheng Y, Qunfang W (2012) ZVS three-transistor push–pull DC/DC converter. Proc CSEE 32(33):23–30 (in Chinese)

4. Yisheng Y, Changwei G (2012) Resonant push-pull DC-DC converter. *Electr Power Autom Equip* 32(10):83-87
5. Quanming L, Can Z, Shubo Z, Guohui L, Luowei Z (2013) Constant current LED driver based on LCL-T half bridge resonant converter. *Trans China Electro-technical Soc* 28(12):320-323
6. Haibing H, Wanbo W, Wenjin S, Shun D, Yan X (2013) Optimal efficiency design of LLC resonant converters. *Proc CSAEE* 33(18):48-56

# Distribution Network Planning Considering DG Under Uncertainty

Yanfei Liu and Hui Zhou

**Abstract** With the rise of a new round of energy revolution, the distribution network with distributed generation (DG) has become an important form of the future power grid. However, DG itself has the characteristics of randomness and intermittence, which brings impacts and challenges to the distribution network planning. Based on the uncertainty theory, the fuzzy simulation of DG and load are used to model the distribution network. The model takes the minimum annual investment cost and the minimum cost of network loss as the optimization target. Single parent genetic algorithm based on spanning tree is optimized and verified by 18 node system simulation.

**Keywords** Distribution generation · Network planning · Uncertainty theory  
Genetic algorithm

## 1 Introduction

In recent years, a new type of power network, which is based on distributed power supply and micro grid, has been developed for the new elements of access to power system [1]. However, the increasing of DG, flexible load, electric vehicles and other controllable devices is continued, which also has a negative effect on the distribution network [2]. The planning of the distribution network under a variety of uncertain factors should be reasonable, so as to play full role of DG.

The research of distribution network planning has been developed rapidly, which is mainly reflected in the planning method, the modeling method of uncertain factors, the modeling and optimization algorithm. The objective function of literature [3, 4] are only considering the minimum cost of investment, and did not

---

Y. Liu (✉) · H. Zhou

School of Electrical Engineering, Beijing Jiaotong University,  
No. 3 Shang Yuan Cun, Haidian District, Beijing, China  
e-mail: liuyanfeiaf@163.com

© Springer Nature Singapore Pte Ltd. 2018

L. Jia et al. (eds.), *Proceedings of the 3rd International Conference on Electrical and Information Technologies for Rail Transportation (EITRT) 2017*, Lecture Notes in Electrical Engineering 482, [https://doi.org/10.1007/978-981-10-7986-3\\_9](https://doi.org/10.1007/978-981-10-7986-3_9)

consider other indicators. In [5], distribution network planning is divided into different stages to consider the load change dynamically. In [6], a method based on interval variable correlation affine form is provided. In literature [7], wind power, photovoltaic power generation, storage battery and gas turbine are analyzed, and the comprehensive state power distributed model is established, too. In [8], the charging and discharging state of the electric vehicle polymerization station is considered, and the dynamic optimal scheduling is carried out.

In this paper, the uncertain planning theory and its application are used into the distribution network planning model. The simulation of fuzzy DG and load are established, and the uncertain model of distribution network planning is modeled. The improved partheno genetic algorithm is used to solve the model and verified by an example.

## 2 Uncertainty Theory

Uncertainty theory is the general name of probability theory, credibility theory and trust theory. Randomness, fuzziness and roughness belong to the category of uncertainty. The following definitions and operations are presented in this paper [9].

**Definition 1** *Credibility measure*  $A$  is an aggregate of  $P(\Theta)$ ,  $A^C$  is the opposite aggregate of  $A$ ,  $\sup$  stands for supremum. If  $\text{Pos}$  satisfies the Four Axioms, then  $\text{Pos}$  is named as feasibility measure,  $(\Theta, P(\Theta), \text{Pos})$  is described as feasible space, necessity measure of  $A$  is described as

$$\text{Nec}\{A\} = 1 - \text{Pos}\{A^C\} \quad (1)$$

The credibility measure of  $A$  is

$$\text{Cr}\{A\} = 1/2(\text{Pos}\{A\} + \text{Nec}\{A\}) \quad (2)$$

**Definition 2** *Membership function* Let's assume  $\xi$  is a fuzzy variable in the possibility space  $(\Theta, P(\Theta), \text{Pos})$ , so

$$\mu(x) = \text{Pos}\{\theta \in \Theta | \xi(\theta) = x\}, x \in R \quad (3)$$

is the membership function of  $\xi$ .

If  $x_1, x_2, \dots, x_n$  are independent fuzzy evens which happen in the same time, then the membership function  $\mu(x)$  is the supremum of minimum value of the independent membership function  $\mu_i(x_i)$ , which means

$$\mu(x) = \sup_{x_1, x_2, \dots, x_n \in R} \left\{ \min_{1 \leq i \leq n} \mu_i(x_i) | x = f(x_1, x_2, \dots, x_n) \right\} \quad (4)$$



**Definition 3** *Expected value of fuzzy variable* Let's assume  $\xi$  is a fuzzy variable, which is a function from the possibility space  $(\Theta, P(\Theta), Pos)$  to Real line  $R$ , then

$$E[\xi] = \int_0^{+\infty} C_r\{\xi \geq r\}dr - \int_{-\infty}^0 C_r\{\xi \leq r\}dr \quad (5)$$

is the expected value of  $\xi$ .

### 3 The Uncertainty Simulation of DG and Load

#### 3.1 Wind Power Output Uncertain Model

The output power of wind turbine is mainly related to wind speed, and it can be used to represent the relationship as [10]:

$$P(V) = \begin{cases} 0 & 0 \leq V \leq V_{ci} \text{ or } V_{co} \leq V \\ P_{rated} \cdot \frac{V-V_{ci}}{V_{rated}-V_{ci}} & V_{ci} \leq V \leq V_{rated} \\ P_{rated} & V_{rated} \leq V \leq V_{co} \end{cases} \quad (6)$$

where,  $P_{rated}$  is the rated active power output of wind turbine;  $V_{ci}$ ,  $V_{rated}$ ,  $V_{co}$  is the cutting speed, rated wind speed and cutting speed, respectively.

In general, short-term forecast for output power of large-scale wind turbine, is predicted by the power curve of wind speed and wind machine. Otherwise in the long-term forecast, the wind speed has no randomness, which can be described as fuzzy variables. The trapezoidal fuzzy variables are used to express the wind speed prediction values the Eq. (7).

$$\mu(V) = \begin{cases} \frac{V-S_1}{S_2-S_1} & S_1 \leq V \leq S_2 \\ 1 & S_2 \leq V \leq S_3 \\ \frac{V-S_4}{S_3-S_4} & S_3 \leq V \leq S_4 \\ 0 & \text{others} \end{cases} \quad (7)$$

Thus, if the trapezoidal fuzzy variables  $(S_1, S_2, S_3, S_4)$  and the cutting speed, rated wind speed and cutting speed are given, the wind power output power can be fuzzy simulated.

#### 3.2 Photovoltaic Generation Output Uncertain Model

Ideally, the relationship between the output and the solar radiation intensity is sinusoidal. However, light intensity change is complicated. After extensive

research, the light intensity can approximately obey the Berta distribution of [11], the probability density function is:

$$f(s) = \frac{\Gamma(\alpha + \beta)}{\Gamma(\alpha)\Gamma(\beta)} \left(\frac{s}{s_{\max}}\right)^{(\alpha-1)} \left(1 - \frac{s}{s_{\max}}\right)^{(\beta-1)} \quad (8)$$

where  $\Gamma(\cdot)$  is the Gamma function;  $s$  is the actual light intensity;  $s_{\max}$  is the maximum of light intensity;  $\alpha, \beta$  is the shape parameter of Beta distribution.

Similarly to wind power generation, for the long-term forecast, solar radiation intensity is not random, the output power of the membership function is expressing similarly to the wind power generation. So, the output of photovoltaic can be fuzzy simulated as long as the light intensity of radiation and the trapezoidal fuzzy number are given.

### 3.3 Load Uncertain Model

Most of the papers use the normal distribution model to simulate the load, which reflects the uncertainty of the load. There is a large amount of data base to be fitted by the normal distribution, and sometimes it is not fit for the difference of individual load. In this paper, the trapezoidal fuzzy variable  $\mu(P_L) = (P_{L1}, P_{L2}, P_{L3}, P_{L4})_T$  is similar to the load.

## 4 Grid Planning Model with DG

### 4.1 Grid Planning Model

In this paper, the fuzzy expected value of the investment cost is chosen as the objective function:

$$\min E[f] = \min E\left[\sum C_{ij}n_{ij} + \sum C_{loss}\right] \quad (9)$$

$$st. \begin{cases} P_{is} = U_i \sum_{j \in i} U_j (G_{ij} \cos \theta_{ij} + B_{ij} \sin \theta_{ij}) \\ Q_{is} = U_i \sum_{j \in i} U_j (G_{ij} \sin \theta_{ij} - B_{ij} \cos \theta_{ij}) \end{cases} \quad (10)$$

$$st. \begin{cases} 0 \leq E[P_V] \leq \hat{P}_V \\ 0 \leq E[P_S] \leq \hat{P}_S \\ 0 \leq E[P_L] \leq \hat{P}_L \end{cases} \quad (11)$$

where  $C_{ij}$  is the investment in new routes;  $n_{ij}$  the numbers of lines from node  $i$  to node  $j$ ;  $C_{loss}$  is the cost of operation;  $C_{loss} = \gamma \sum_{i=1}^l \tau_i \tilde{P}_{loss}(x)$ ,  $l$  is the numbers of branch;  $\tau_i$  is the hours of maximum load;  $\tilde{P}_{loss}(x)$  is the fuzzy cost of branches;  $P_{is}$ ,  $Q_{is}$  is the positive and negative power of node  $i$ ;  $U_i$  is the voltage of node  $i$ ;  $j \in i$  indicates node  $j$  and node  $i$  are connected.  $G_{ij}$ ,  $B_{ij}$  is the real and imaginary parts of node admittance matrix of  $Y_{ij}$ ;  $\theta_{ij}$  is the phase-angle difference of the voltage of node  $i$  and node  $j$ ;  $\hat{P}_V$ ,  $\hat{P}_S$  is the limitation of wind and photovoltaic output;  $\hat{P}_L$  is the maximum of load.

## 4.2 Power Flow

Newton Raphson method is used as the basic method to calculate the power flow. And the output of wind, photovoltaic and load are described as trapezoidal fuzzy variables, which replace the digital analog variables into the system. Then, the credibility theory statistical value expectations are used to gain the practical and final results. Steps are as follows:

- (1) Input the original data, including the line parameters, the node load, the wind speed of the wind power DG, the illumination intensity of the DG, the number of years, the number of sampling, the electricity price, etc.;
- (2) Pre-processing of parameters: read the node fuzzy vector, create array variable space;
- (3) Cycle processing: sampling calculation process, each sampling to call the ground state power flow, a series of calculation results;
- (4) Post-processing: indicators of node voltage, phase angle and branch flow expectation, variance, overload and overvoltage of statistics, fuzzy expected current fuzzy objective function of vector case with the values given credibility theory.

## 4.3 Improved Genetic Algorithm

The basic principle of partheno genetic algorithm is: through individual reproduction, to cancel the crossover operator of traditional genetic algorithm, but with the gene exchange operator operating only in one chromosome (recombination operator), including gene transposition, gene translocation and gene inversion [12]. The selection operation can be used in roulette or ranking based on the strategy. Among them, the selection of the operation to achieve the purpose of survival of the fittest, shift operations and reassignment operations are equivalent to binary coded genetic manipulation and genetic mutation in single parent genetic operations.

- (1) Selection operator: the roulette wheel selection mechanism is used, and the optimal hold operation is added to make the algorithm converge globally.
- (2) Shift operator: the father node except the root node is changed. In the father generation, we randomly select a shift point C, disconnect it from the father node A, and then select a new father node of a node B and connect the B and C nodes. In the selection process, B, C can be a node in a different tree, but B cannot be the original father node or descendant of node C, as shown in Fig. 1a.
- (3) Redistribution operator: be similar to shift operation, we choose a redistribution node C from the father nodes randomly, as shown in Fig. 1b, then redistribute all the nodes (node 5 in all, 6, 7) rooted on node C.

### 5 Example Studies

A 10 kV distribution system initial network has 10 nodes and 9 lines, in the future a certain level, increased to 18 node. The network topology and parameters such as node parameters and line parameters are shown in literature [13].

The fuzzy simulation of wind power generation and photovoltaic generation are shown as Fig. 2.

The DG and the load in the form of fuzzy numbers are used to calculate fuzzy power flow. The voltage of some nodes (nodes in 4 as an example) are shown in Fig. 3. The fuzzy power of some branches (branch 1, 4, 14, 22, 26 as examples) are shown in Table 1.

In Fig. 3,  $V_1, V_2, V_3, V_4$  are the four states of the voltage trapezoidal fuzzy quantity respectively, namely  $V_{node4} = [V_1, V_2, V_3, V_4]$ . The voltage fluctuates in the range of  $\pm 3\%$ , the trapezoidal fuzzy variables fluctuates in the range of  $\pm 4\%$ , and when the number of iterations is greater than 25, the node voltage begin to converge.

In Table 1, branch 1 and branch 4 in the existing grid can satisfy the given operation mode and do not overload under normal circumstances; branch 14 and 26 is in a overload situation, so we need to expand these lines; while the t branch line 22 can be removed because of its small effect.

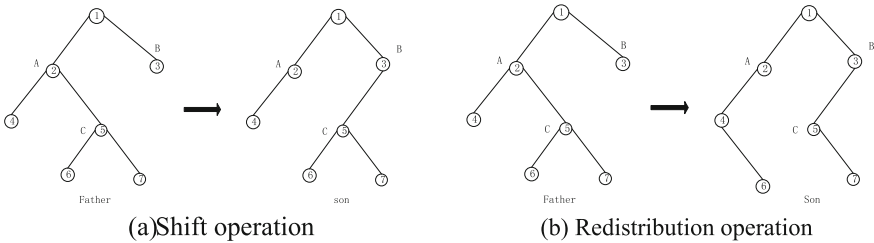


**Fig. 1** Genetic manipulation

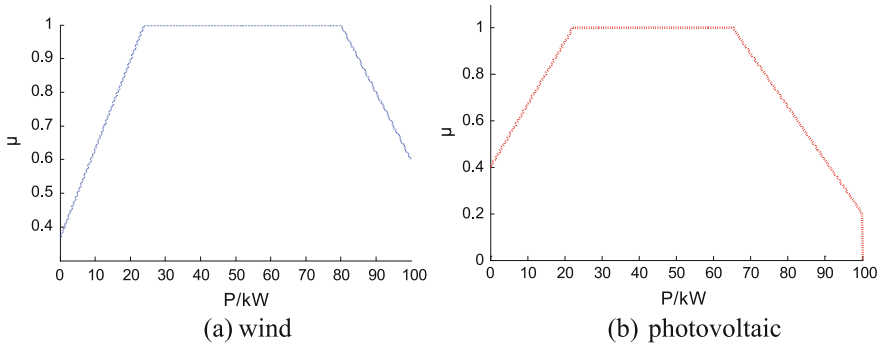


Fig. 2 Membership function of power forecast values of DG

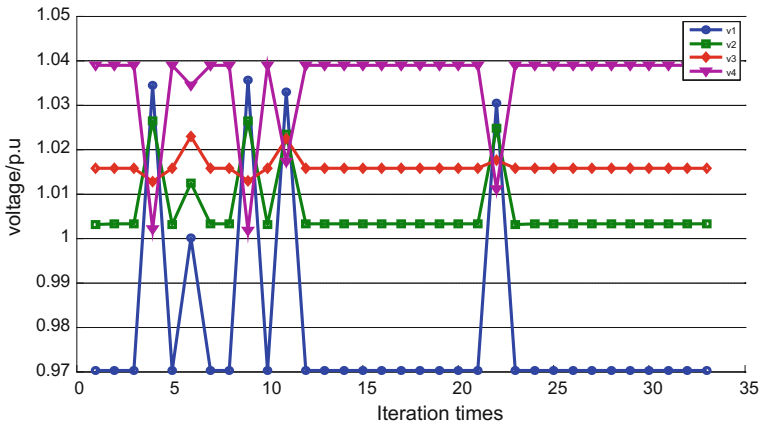


Fig. 3 Fuzzy voltages of node 4

Table 1 Fuzzy active and reactive power of partial branches

Branch	Positive power ( $10^4 \text{kW}$ )	Negative power ( $10^4 \text{Var}$ )
1	[194.33, 210.76, 224.35, 227.32]	[94.12, 102.08, 108.66, 110.10]
4	[172.51, 181.66, 195.47, 202.19]	[83.55, 87.98, 94.67, 97.93]
14	[279.13, 283.04, 291.6302.72]	[135.19, 137.08, 141.23, 146.61]
22	[-33.20, -16.02, 0.48, 14.52]	[-16.08, -7.76, 0.23, 7.03]
26	[220.13, 235.67, 242.56, 248.89]	[106.61, 114.14, 117.48, 120.54]

Finally, a series of optimization under the fuzzy expected value programming method are shown in Table 2. The fuzzy expected value of the total investment cost is about 35 million yuan, the fuzzy expectation value of the network loss is about 600 thousand yuan, and the number of iterations can reach the convergence about 30 times. The wind and photovoltaic generator are connected to the node 4 and 11

**Table 2** Planning results of fuzzy expect programming

Case	Optimizing stringing information	Total investment cost of fuzzy line ( $10^4$ yuan), Network loss cost ( $10^4$ yuan), generations
1	1-11, 4-16(2), 5-12, 6-14(2), 7-8, 7-13(2), 7-15, 8-9, 9-10(2), 10-18, 16-17(2)	[3395.112, 3466.018, 3602.133, 3693.455], [47.01, 52.89, 79.44, 87.67],33
2	1-11, 4-16(2), 6-14(2), 7-8, 7-13(2), 7-15, 8-9, 9-10(2), 10-18, 11-12, 12-13, 16-17(2)	[3321.106, 3467.113, 3608.234, 3759.122], [46.82, 52.33, 77.98, 89.69], 32
3	1-11, 4-16(2), 6-14(2), 7-8, 7-13(2), 7-15, 8-9, 9-10(2), 11-12(2), 16-17(2), 17-18	[3456.011, 3510.689, 3599.016, 3624.561], [48.59, 57.13, 75.04, 86.65], 37
	1-11, 4-16(2), 5-12, 6-14, 7-8, 7-15, 8-9, 9-10(2), 10-18, 11-13, 16-17(2)	[3396.017, 3415.225, 3521.104, 3544.091], [47.27, 54.19, 78.6, 84.31], 35

respectively, then the line 1-11, 5-12, 11-12, 12-13 and 4-16 have different consumption, thus there are diversities of the line extension.

## 6 Conclusion

In this paper, the optimal planning of the distribution network with DG based the uncertainty theory is studied. DG and load are fuzzy proceeded respectively, and then a fuzzy expectation programming are solved by the power flow calculation. Through the comparison of the calculated results of the example, considering the uncertainty factors, the operation cost of the distribution network and network cost are saved greatly. The improved genetic algorithm based on tree structure encoding can quickly find the optimal value, improve the convergence.

## References

1. Zhao MA, Ting AN, Yuwei S (2016) State of the art and development trends of power distribution technologies. Proc CSEE 36(6):1552-1567
2. Zhang LM, Tang W, Zhao Y et al (2010) The integrated evaluation of impact of distributed generation on distribution network. Power Syst Protect Control 38(21):132-135, 140
3. Fuchun H, Mingkai Z (1994) Research on urban power network planning. Autom Electr Power Syst 18(11):57-62
4. Weidong T (1993) New development of foreign power planning. Energy of China 1(6-9):25
5. Zhang W, Cheng H, Cheng Z (2008) Review of distribution network optimal planning. Autom Electr Power Syst 20(5):16-23 (in Chinese)
6. De Figueiredo LH, Stolfi J (2004) Affine arithmetic: concepts and applications. Numer Algorithms 37(1):147-158

7. Tang N (2015) A study on the expansion planning of distribution systems considering distributed generations. Beijing Jiaotong University
8. Zhang H (2015) Dynamic optimal dispatch of active distribution network with electric vehicle aggregators. School of Electrical and Electronic Engineering
9. Liu BD, Zhao RQ, Wang G (2003) Uncertain programming with applications. Tsinghua University Press, Beijing
10. Karaki SH, Chedid RB, Ramadan R (1999) Probabilistic performance assessment of autonomous solar-wind energy conversion systems. *IEEE Trans Energy Convers* 14(3):766–772
11. Abouzahr I, Ramakumar R (1991) Loss of power supply probability of stand-alone photovoltaic systems: a closed form solution approach. *IEEE Trans Energy Convers* 6(1):1–11
12. Maojun L (2002) Theory and application of partheno genetic algorithm. Hunan University
13. Wang X (1990) Optimal planning of power system. China Water Power Press, Beijing

# Reliability Evaluation of Inverter Based on Accelerated Degradation Test

Xinghui Qiu and Jianwei Yang

**Abstract** In order to evaluate the reliability of the inverter, this paper adopted sequence and stress accelerated degradation test of a certain type of inverter. Take the voltage as the accelerated stress, setting 0.8 as the linear growth proportion coefficient of stress levels, through the detection of the inverter IGBT collector emitter voltage state and diode voltage to judge the wear condition of the inverter. The accelerated model is obtained through analyzing the test data, and the model parameters are estimated by the least square method. At the same time, the reliability of the inverter is evaluated, and the reliability curve is obtained. Finally, the reliability at the normal stress level is solved through accelerate model. In order to evaluate the effectiveness of Bayes reliability analysis of inverter, the Monte Carlo simulation about accelerated test is done, simulation results and evaluation results are similar. It shows that the accelerated degradation testing data is valid. The evaluation method can be used to evaluate the reliability of other power electronic devices in the rail transit vehicle.

**Keywords** Accelerated degradation test · Inverter · Inverse power law model  
Bayes reliability

## 1 Introduction

Urbanization is the inevitable trend of development in China, railway transit vehicle carrying an important historical mission as the key equipment on the road of urbanization. As a power electronic device, traction inverter is an important part of the traction system. To ensure the stable operation of the train, it is necessary to evaluate the reliability of traction inverter in advance. The electronic device in the

---

X. Qiu (✉) · J. Yang  
School of Mechanical Electronic and Vehicle Engineering, Beijing University  
of Civil Engineering and Architecture, No. 1 Zhanlanguan Road,  
Xicheng District, Beijing, People's Republic of China  
e-mail: Qiuxh1025@163.com



railway transit railway has a long life, it is difficult to obtain enough data. Thus, the accelerated degradation test is adopted to research this problem.

Many researches [1–5] analyzed the reliability and the wear-out failure of electronic device in the railway transit vehicle. Xiao et al. [6–8] used accelerated degradation test to evaluate the reliability of some products, through managing the environment temperature and reliability change with time, more accurate results were obtained. In the Bayes reliability field, Zhu and Jia [9, 10] evaluated the reliability of bearing and other parts under the circumstance of extremely small sample and minimal failure data. Trabelsi [11] analyzed the fault diagnosis of the IGBT modules in the voltage source inverter, a new control system can increase the efficiency of the inverter has been found. Czerny et al. [12–14] conclude that the longer the time of temperature swing is, the smaller the failure cycling number is. And a new method to evaluate the reliability of inverter has been presented.

This article put forward a method of evaluating the reliability of inverter using the accelerated degradation test. Meantime, the Bayes method is adopted to estimate the failure rate. In order to analysis the effectiveness of the reliability evaluating of the inverter, the Monte Carlo simulation about the accelerated degradation test of inverter is operated.

## 2 Accelerated Degradation Test

Figure 1 shows the layout of accelerated degradation test with inverter, it consist of three parts, the first part is the power system with 220 V alternating current and the load converter, it provides the needed voltage that input to the test inverter, also monitoring the IGBT collector emitter voltage and the forward voltage of the diode to decide the inverter is failure or not. The second part is the control system. It consists of the PC et al. It can achieve the object that improve the voltage

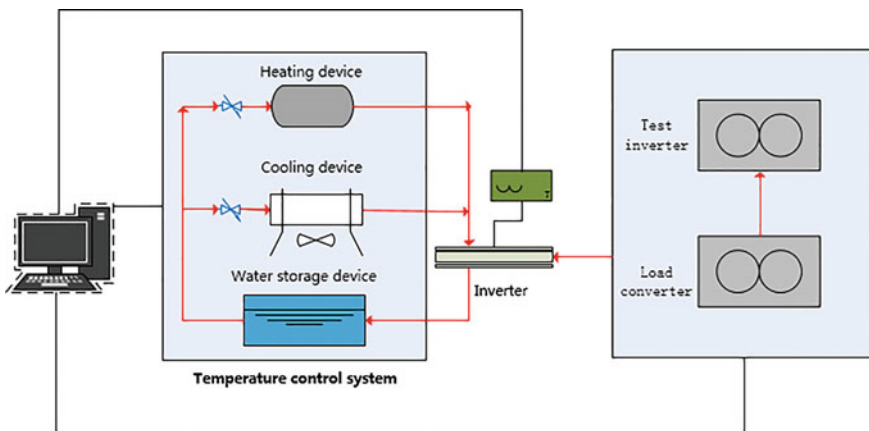


Fig. 1 The layout of accelerated degradation test system

accordingly and control the environment temperature. The third part is the water cooling system, it can keep the environment temperature relatively constant, and it can simulate the reality situation closely.

## ***2.1 Testing Program***

The object of the accelerated degradation test is a kind of inverter, the plate size of the inverter is 15.2\*10.2 cm, the rated input voltage of the inverter is 32 V. The main reason that caused the failure of the traction inverter is the wear-out of the switch components, mainly marked by the short circuit and the broken circuit of the IGBT power switches. Taking the overall level of the test into account, voltage is chosen as the acceleration stress of the test, set from scratch, and the scale coefficient of the linear growth stress level is 0.8. To control the cost of the accelerated degradation test and meet the statistical requirements, the test inverter sample is set as 4. In the test, the change of the IGBT collector emitter voltage and the forward voltage is taken as the degradation parameter, and the failure threshold is the change of the IGBT collector emitter voltage is up to 3 V. The censored time of each sub test is set as: [72 205 252 277 300 324 348 372 374].

## ***2.2 Testing Circuit***

To simulate the working circuit of the traction inverter closely, the test circuit is designed as Fig. 2. The unit in the dashed box above is the test inverter, and the unit in the dashed box below is the load converter. The load converter provides the needed voltage to test inverter, this two are connected with the electric fuse, it protects the whole system from abnormal heavy current. The IGBT collector emitter voltage is monitored by the online testing circuit that can tell the inverter is failure or not. The test inverter and the load converter are both controlled by the control board, the control board consists of DSP and PC terminal. The water cooling system makes the whole system a temperature stable state.

## ***2.3 Test Data Processing***

The data processing of the accelerated degradation test is shown as Fig. 3. It shows the voltage variation trend of 4 samples, as time goes on, the value of the voltage variation is continuous increase. It fits the purpose of the accelerated degradation test that the test can accelerate the wear-out of the inverter, and the priori information can be obtained from the test results. According to the results of the accelerated degradation test, the fault type of inverter can be diagnosed as wear-out type failure.

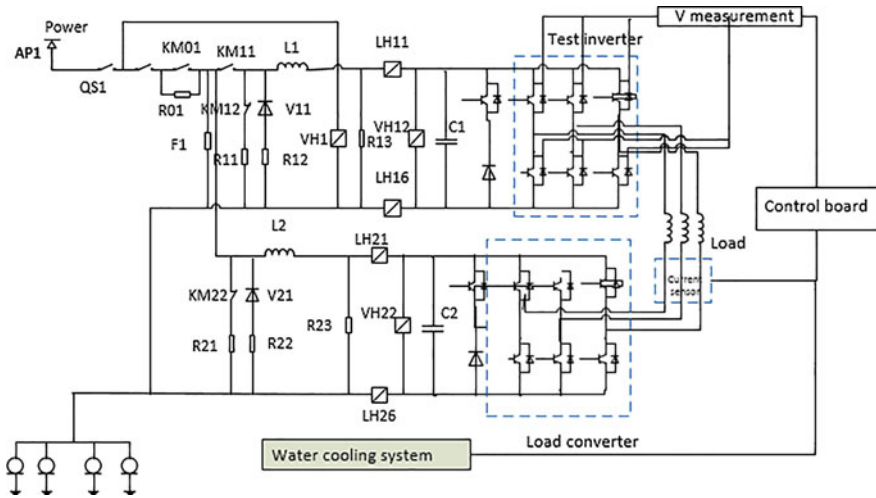


Fig. 2 The circuit of the accelerated degradation test of inverter

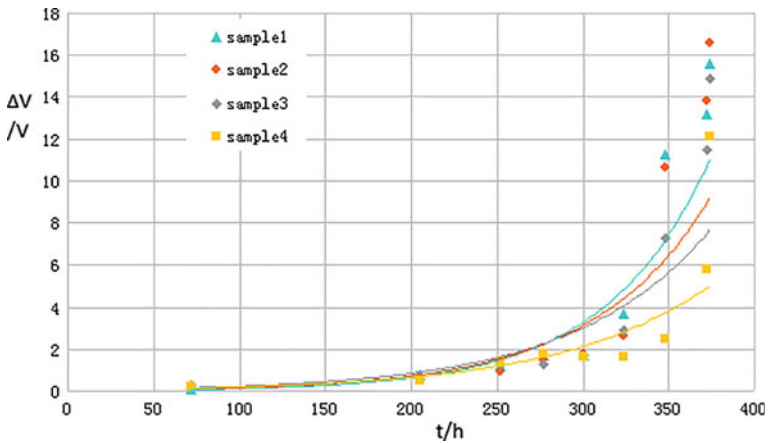


Fig. 3 The data of the accelerated degradation test of inverter

### 3 Analysis of the Acceleration Model

In the accelerated degradation test with electronic equipment, inverse power law model is often adopted to describe the relation between product life and the added stress:

$$\eta(V) = 1/[dV^C] \tag{1}$$

where,  $V$  is the stress,  $\eta(V)$  is the scale parameter, parameter to be estimated  $c$  and  $d$  is irrelative to stress  $V$ . Log on Eq. (1):

$$\ln[\eta(V)] = b_0 + b[\phi(V)] \tag{2}$$

where,  $b_0 = -\ln(d)$ ,  $b = -c$ ,  $\phi(V) = \ln(V)$ .

In the test, the failure mechanism of inverter is high voltage, the voltage that far greater than the rated voltage caused the high temperature of inverter, accelerated the damage of the IGBT module, thus, the fault type of inverter can be also diagnosed as wear-out type failure. It assumed that the life distribution of inverter is two-parameter Weibull distribution  $wei(\theta, \beta)$ ,  $\theta$  is scale parameter,  $\beta$  is the shape parameter. Thus, on the condition of order stress  $V(t) = Kt$ , the cumulative failure probability is:

$$F^*(t) = \exp\left[-\frac{d^m K^{mc}}{c+1} t^{m(c+1)}\right] = 1 - \exp\left[-\left(\frac{t}{\theta}\right)^\beta\right] = G\left[\frac{\ln t - \mu}{\sigma}\right] \tag{3}$$

where,  $G(x) = 1 - \exp[-\exp(x)]$  is the distribution function of standard extreme value distribution, and:

$$\begin{cases} \beta = \frac{1}{\sigma} = m(1+c) \\ \mu = \ln\theta = A + B\ln K \end{cases} \tag{4}$$

where,  $\begin{cases} A = \frac{-m\ln d + \ln(1+c)}{m(1+c)} \\ B = -\frac{c}{1+c} \end{cases}$

There is a set of stress levels:  $k_1 < k_2 < \dots < k_p (p \geq 2)$ , owing to  $\mu_i - \mu_j = B(\ln k_i - k_j)$ ,  $1 \leq i < j \leq p$ , there is  $\theta_i = e^{\mu_i}$ ,  $i = 1, 2, \dots, p$ . And:

$$\theta_p < \theta_{p-1} < \dots < \theta_1 < \theta_2 k_{2,1} < \dots < \theta_p k_{p,1} \tag{5}$$

where,  $k_{i,j} = k_i/k_j$ ,  $i, j = 1, 2, \dots, p$ .

### 4 Parameter Estimation

There are  $n_i$  products in the accelerated degradation test, the ordered stress is  $V_i(t) = k_i t$ . The failure time of the products is  $0 < t_{i1} < t_{i2} < \dots < t_{ir_i} < \tau_{i0}$ ,  $r_i < n_i$ ,  $i = 1, 2, \dots, p$ .  $\tau_{i0}$  is the censored time.  $r_i$  is the number of failed products before the censored time.

Assumed that  $r = \sum_{i=1}^p r_i$ ,  $V = \prod_{i=1}^p \prod_{j=1}^{r_i} t_{ij}$ ,  $\tau = (n_i, r_i, t_{ij}, j = 1, 2, \dots, p)$ , and

$$\tau_i(\beta) = \sum_{j=1}^{r_i} t^{\beta} + ij(n_i - r_i)\tau_{i0}^{\beta}.$$

From the analysis above, the likelihood function is:

$$L(\beta, \theta|\tau) = \beta^r V^{\beta-1} \prod_{i=1}^p \frac{1}{\theta_i^\beta r_i} \exp \left[ -\frac{\tau_i(\beta)}{\theta_i^\beta} \right] \quad (6)$$

According to the Bayes method about the prior distribution [15], it assumed that the prior distribution of  $\theta_j^\beta$  is the inverse  $\Gamma$  distribution  $IG(a_j, b_j)$ , from the prior information, it concludes that  $a_j > 0, b_j > 0$ , thus, the prior distribution is:

$$\pi(\theta_j|\beta) = \frac{\beta b_j^{\alpha_j}}{\Gamma(\alpha_j)} \theta_j^{-(1+\beta\alpha_j)} \exp \left( -\frac{b_j}{\theta_j^\beta} \right) \quad (7)$$

When  $\beta \in (0, 1)$ , the prior distribution of  $\beta$  is beta distribution:

$$\pi_1(\beta) = \frac{1}{B(\alpha_1, \beta_1)} \beta^{\alpha_1-1} (1-\beta)^{\beta_1-1}, 0 \leq \beta \leq 1 \quad (8)$$

When  $\beta \in (1, \infty)$ , the prior distribution of  $\beta - 1$  is  $\Gamma$  distribution  $\Gamma(\alpha_2, \beta_2)$ :

$$\pi_2(\beta) = \frac{\beta_2^{\alpha_2}}{B(\alpha_2, \beta_2)} (\beta-1)^{\alpha_2-1} e^{-\beta_2(\beta-1)}, \beta > 1 \quad (9)$$

From the prior distribution, it can be affirmed that  $\alpha_1 > 1, \beta_1 > 1, \alpha_2 \geq 1, \beta_2 > 0$ . And:

$$\begin{aligned} \frac{\partial^2 \pi_1(\beta)}{\partial \beta^2} &= -\frac{\alpha_1 - 1}{\beta^2} - \frac{\beta_1 - 1}{(\beta - 1)^2} < 0 \\ \frac{\partial^2 \pi_2(\beta)}{\partial \beta^2} &= -\frac{\alpha_2 - 1}{\beta^2} < 0 \end{aligned}$$

From the equation above, the prior distribution about  $\beta$  is both logarithmic convex function. Where,  $B$  is the value space of  $\beta$ , and  $H_p$  is the value space of  $\theta$ , where  $H_p = \{(\theta_1, \dots, \theta_p) | \theta_p < \theta_{p-1} < \dots < \theta_1 < \theta_2 k_{2,1} < \dots < \theta_p k_{p,1}\}$ , it assumed that the prior distribution of  $\beta$  is  $\pi(\beta)$ . According to the Bayes equation, the posterior distribution of  $\beta, \vec{\theta}$  is:

$$g(\beta, \theta|\tau) \propto \pi(\beta) \beta^{r+p} V^{\beta-1} \prod_{i=1}^p \frac{1}{\theta_i^{1+\beta(\alpha_i+r_i)}} \exp \left[ -\frac{\tau_i(\beta) + b_i}{\theta_i^\beta} \right] \beta \in B, \theta \in H_p \quad (10)$$

It is difficult to solve the equation through traditional method, in this article, the Gibbs sampling is used to solve the equation above. The foundation of the Gibbs sampling is the complete posterior distribution that can be sampled.

$\bar{\theta}_{-j} = \{\theta_i, i \neq j, i = 1, 2, \dots, p\}$ , according to Eq. (10), the complete posterior distribution of  $\theta_j$  is:

$$\pi(\theta_j | \beta, \theta_{(-j)}, \tau) = \frac{\beta(b_j + \tau_j(\beta))^{\alpha_j + r_j}}{\Gamma(a_j + r_j)} \frac{1}{\theta_j^{1 + \beta(a_j + r_j)}} \exp\left(-\frac{b_j + \tau_j(\beta)}{\theta_j^\beta}\right) \quad (11)$$

That is:  $(\theta_j | \beta, \theta_{(-j)}, \tau) \sim IG(a_j + r_j, b_j + \tau_j(\beta)) \quad j = 1, 2, \dots, p, \theta_j \in G_j$ , and

$$\begin{aligned} G_1 &= \{\theta_1 : \theta_2 < \theta_1 < \theta_2 k_{2,1}\} \\ G_p &= \{\theta_p : \theta_{p-1} k_{p-1,p} < \theta_p < \theta_{p-1}\} \\ G_i &= \{\theta_i : \theta_{i+1} < \theta_i < \theta_{i-1}, \theta_{i-1} k_{i-1,i} < \theta_i < k_{i+1,i} \theta_{i+1}\} \\ &= \{\theta_i : \max(\theta_{i+1}, \theta_{i-1} k_{i-1,i}) < \theta_i < \min(\theta_{i-1}, k_{i+1,i} \theta_{i+1})\} \end{aligned}$$

The complete posterior distribution of  $\beta$  is:

$$\begin{aligned} &\pi(\beta | \vec{\theta}, \vec{\tau}) \\ &\propto \pi(\beta) \beta^{r+p} V^{\beta-1} \prod_{i=1}^p \frac{1}{\theta_i^{1 + \beta(a_i + r_i)}} \exp\left[-\frac{\tau_i(\beta) + b_i}{\theta_i^\beta}\right], \beta \in B \end{aligned} \quad (12)$$

Make  $\ln\pi(\beta | \vec{\theta}, \tau) = h(\beta)$ , there is:

$$\begin{aligned} \frac{\partial^2 h(\beta)}{\partial \beta^2} &= \frac{\partial^2 \ln \pi(\beta)}{\partial \beta^2} - \frac{r+p}{\beta^2} \\ &\quad - \sum_{i=1}^p \left\{ \sum_{k=1}^{r_i} \left(\frac{t_{ik}}{\theta_i}\right)^\beta \left[\ln \frac{t_{ik}}{\theta_i}\right]^2 + (n_i - r_i) \left(\frac{\tau_{i0}}{\theta_i}\right)^\beta \left[\ln \frac{\tau_{i0}}{\theta_i}\right]^2 \right\} \\ &\quad - \sum_{i=1}^p \frac{b_i}{\theta_i^\beta} [\ln(\theta_i)]^2 \end{aligned}$$

From the analysis above, it can be concluded that  $b_i > 0, i = 1, 2, \dots, p, \tau_{i0} > 0, t_{ik} > 0, k = 1, 2, \dots, r_i, i = 1, 2, \dots, p$ , the concavity of  $\beta$  complete posterior distribution depends on the concavity of  $\pi(\beta)$ , that is the logarithmic convex. The sampling method is as follows:

It assumed that  $(\theta_{k,1}, \theta_{k,2}, \dots, \theta_{k,p}, \beta_k, k = 1, 2, \dots, M_1, M_1 + 1)$  is a sample of parameter  $(\theta_1, \dots, \theta_p, \beta)$ ,  $M_1$  is the abandoned sample capacity. Thus, the estimated value of  $\theta_j, \beta$  can be obtained as follows:

$$\hat{\theta}_j = \frac{1}{M - M_1} \sum_{k=M_1+1}^M \theta_{k,j}, j = 1, 2, \dots, p, \quad (13)$$

$$\hat{\beta} = \frac{1}{M - M_1} \sum_{k=M_1+1}^M \beta_k \tag{14}$$

According to Eqs. (4), (13), (14) and the Markov theorem, the estimation value of m, c and d can be obtained as follows:

$$\begin{aligned} \hat{m} &= \hat{\beta}(1 + \hat{\beta}), \\ \hat{c} &= -\frac{\hat{B}}{1 + \hat{B}}, \\ \hat{a} &= -\ln(\hat{d}) = \ln(1 + \hat{B}) + \frac{\hat{A}}{1 + \hat{B}}, \end{aligned}$$

where,  $\hat{A} = \frac{GH-IM}{EG-I^2}$ ,  $\hat{B} = \frac{EM-IH}{EG-I^2}$ ,  $I = \sum_{i=1}^p A_{r_i} n_i^{-1} \ln(k_i)$ ,

$$G = \sum_{i=1}^p A_{r_i, n_i}^{-1} \ln^2(k_i), H = \sum_{i=1}^p \hat{\mu}_l, M = \sum_{i=1}^p A_{r_i, n_i}^{-1} \hat{\mu}_l \ln(k_i),$$

$E = \sum_{i=1}^p A_{r_i, n_i}^{-1}$ ,  $\hat{\mu}_l = \ln \hat{\theta}_l$ ,  $A_{r_i, n_i}^{-1}$  is the coefficient of variation. Supposed that the estimation of A and B is the normal least square estimation so that the value of the coefficient of variation is 1. Refer to the [16], the acceleration model, the coefficient of the acceleration model and the reliability of inverter under the normal voltage can be obtained as follow:

$$\begin{aligned} \ln \hat{\eta}_V &= -\ln(\hat{d}) - \hat{c} \ln(V), \\ \hat{\tau}_p &= \left(\frac{V}{V_0}\right)^{\hat{c}}, \\ \hat{R}_{V(t)} &= \exp\{-(\hat{d}V^{\hat{c}}t)^{\hat{m}}\}, t > 0 \end{aligned} \tag{15}$$

## 5 Reliability Evaluation of Inverter

From the hypothesis above, the life distribution of inverter is two-parameter Weibull distribution, and the scale parameter and the added stress meet the inverse power law model. From the test data in the second part of this article and the expertise experience, the value of  $\beta$  is larger than 1, according to Eq. (9), the prior distribution of  $\beta-1$  is  $\Gamma(12, 2)$ , the prior distribution of  $\theta_1^\beta, \theta_2^\beta, \theta_3^\beta, \theta_4^\beta$  is  $IG(10, 9 \times 10^{10}), IG(8, 5 \times 10^{10}), IG(5, 8 \times 10^9), IG(3, 4 \times 10^6)$ . In the Gibbs sampling, the iterations are  $M = 1000$ , the initial value is  $\beta = 4.6, \theta_1 = 80, \theta_2 = 30, \theta_3 = 10, \theta_4 = 5$ , after the sampling, the results is  $\hat{\beta} = 6.0206, \hat{\theta}_1 = 54.3507, \hat{\theta}_2 = 41.3841, \hat{\theta}_3 = 29.9559, \hat{\theta}_4 = 11.4457$ , according

to Eq. (15), the estimation value of  $m, c, a$  can be obtained as follows:  $\hat{m} = 0.2385, \hat{c} = 24.2384, \hat{a} = 111.6332$ . And the acceleration model is as follows:

$$\ln \hat{\eta}_V = 111.6332 - 24.2387 \ln V$$

When the inverter works under the rated voltage 32 V, the reliability of inverter at any work time can be described as follows:

$$\hat{R}_V(t) = \exp\{-(111.6332 \times 32^{24.2387} t)^{0.2385}\}$$

The reliability curve of inverter is showed as Fig. 4.

To checkout the evaluation results of the inverter based on the Bayes reliability, the simulation of the accelerated degradation test based on Monte Carlo is thought to be done. The detailed procedure is as follow:

1. Generate the candidate point  $x_{(0)}$ .
2. Given the proposal distribution  $q(x_{(k)}, x_{(k-1)})$ , this distribution refers to the probability of the value of  $x_{(k)}$  transfer to the value of  $x_{(k-1)}$ . This probability is also called alternative probability. Based on the current value  $x_{(k-1)}$ , extract the  $x^*$  from the distribution  $q(x_{(k)}, x_{(k-1)})$ .
3. Compute the accept probability  $\alpha_{accept}$ .

$$\alpha_{accept} = \min\left[1, \frac{p(x^*)q(x^*, x)k - 1}{p(x(k-1))q(x(k-1), x^*)}\right]$$

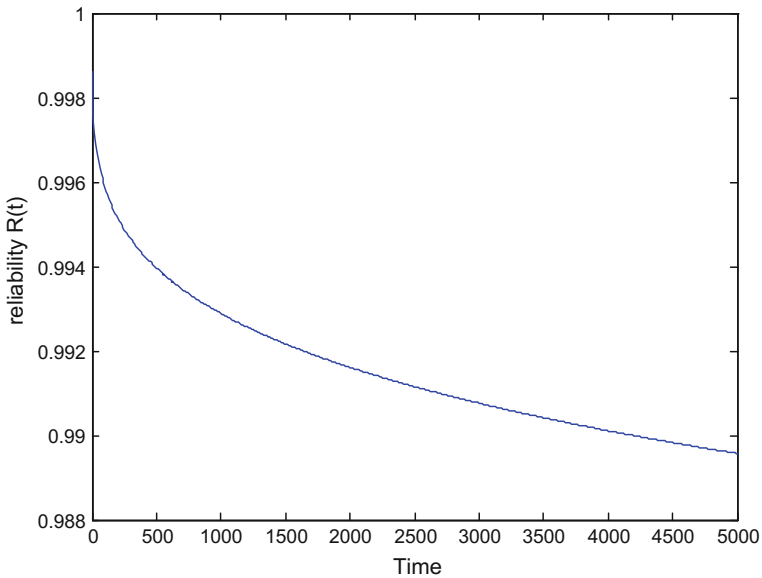


Fig. 4 The reliability curve of inverter



4. Extract the value of  $\alpha'$  from  $[0, 1]$ , if  $\alpha' < \alpha^{accept}$ , then the  $x^*$  is accepted. If not,  $x^*$  is rejected, that is  $x_{(k)} = x_{(k-1)}$ .
5. Repeat the previous step, until the sampling is down.

The simulation of accelerated degradation with inverter is done, the life distribution of inverter is two-parameter Weibull distribution, and the acceleration model is inverse power law model, the simulation scheme is as follows:

The normal stress of the inverter is 32 V, set the scale coefficient as 0.8, the accelerated stress is growing as time goes, the initial value is  $\beta = 4.6$ ,  $\theta_1 = 80, \theta_2 = 30, \theta_3 = 10, \theta_4 = 5$ , the times of the Monte Carlo simulation is 2000. The simulation results are as Fig. 5.

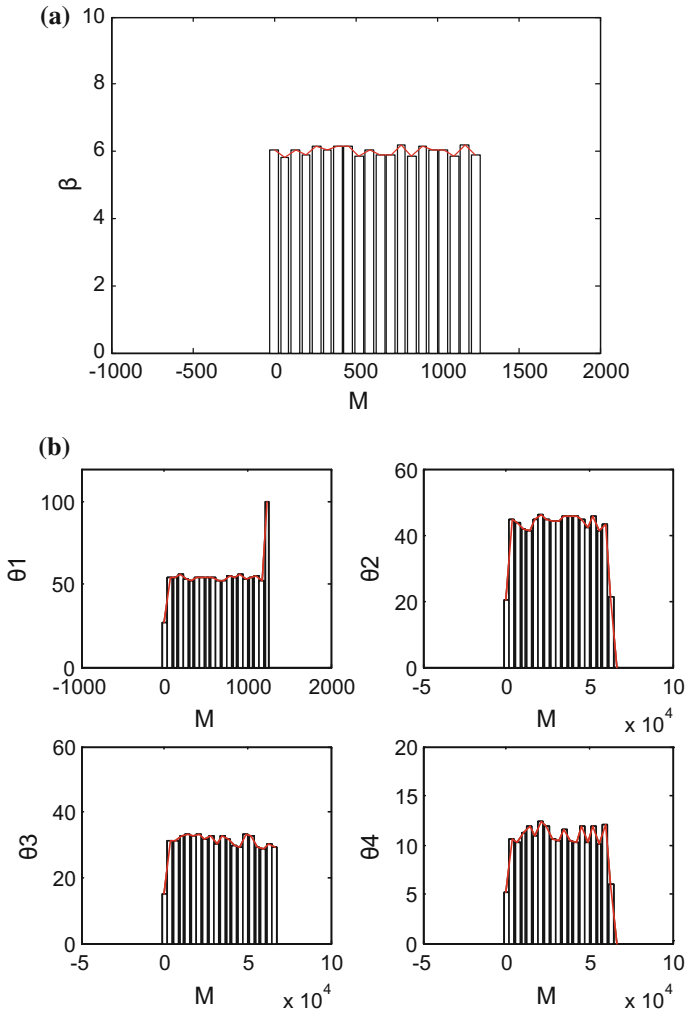
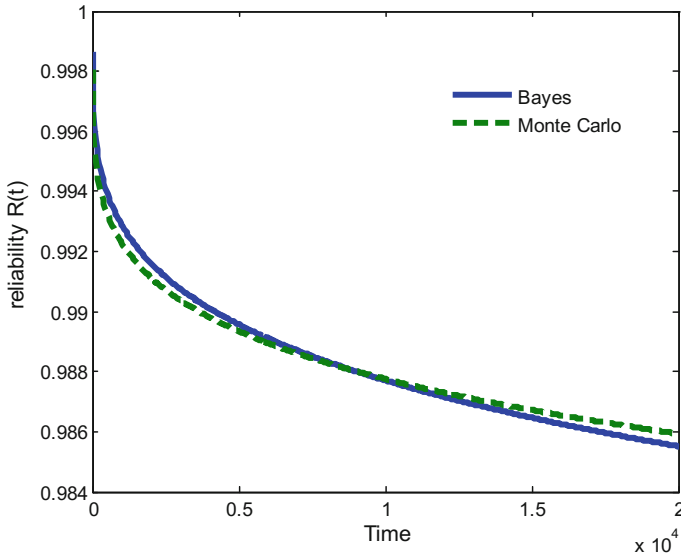


Fig. 5 Monte Carlo simulation results of parameter  $\beta, \theta$



**Fig. 6** The comparison of reliability curve based on Bayes and Monte Carlo method

According to the results of simulation, the average value of  $\beta, \theta$  can be obtained as  $\bar{\beta} = 5.3128, \bar{\theta}_1 = 59.3527, \bar{\theta}_2 = 39.2596, \bar{\theta}_3 = 31.4867, \bar{\theta}_4 = 13.1694$ , put these value into equation of  $\hat{m}, \hat{c}, \hat{a}$  and Eq. (15), the acceleration model is:

$$\ln \hat{\eta}_v = 125.5483 - 23.2571 \ln V$$

As shown above, the reliability of inverter under the normal working voltage 32 V is:

$$\hat{R}_V(t) = \exp\{-(125.5483 \times 32^{23.2571} t)^{0.2015}\}$$

Figure 6 shows the comparison of two reliability curve under the Bayes method and the Monte Carlo simulation. From the curve, it is obviously that the two curves are extremely close. It validates the accuracy of the evaluation method of inverter's reliability.

Several conclusions can be drawn from this article:

1. In the accelerated degradation test, the water cooling system is adopted to maintain the test temperature relatively stable, thus, the failure mechanism of inverter can consistent with practice, during the test, the fault type of inverter can be diagnosed as wear-out type failure. It assumed that the life distribution of inverter is two-parameter Weibull distribution.

2. Combined with Weibull distribution, the acceleration model is analyzed, using the Bayes method, the evaluation method of inverter is obtained, and the reliability curve of inverter is solved through the accelerated degradation test.
3. To checkout the evaluation results of the inverter based on the Bayes reliability, the simulation of the accelerated degradation test based on Monte Carlo is operated. The evaluate results and the simulation results are extremely close. It validates the accuracy of the evaluation method of inverter's reliability. This method can used to evaluate the other electronic equipments' reliability.

**Acknowledgements** This article is sponsored by National Natural Science Foundation of China under grant no. 51175028, Great scholars training project under CIT&TCD20150312, and Beijing outstanding talent training project under 2012D005017000006.

## References

1. Minwu C (2011) The reliability assessment of traction substation of high speed railway by the GO methodology. *Power Syst Protect Control* 39(18):56–61 (in Chinese)
2. Jiankang Z, Xiaohua L, Xia Y (2015) Discussion on protection configuration and setting calculation for 750 kV transformer. *Power Syst Protect Control* 43(9):89–94 (in Chinese)
3. Kaiyi Z, Yifa S, Yongsheng L (2016) Research on transient characteristics of passing neutral section in CRH2 trains traction motor. *Res Develop* 4:38–41
4. Chenxi D, Zhigang L, Song G (2016) Fault diagnosis for traction transformer of high speed railway on the integration of model-based diagnosis and fuzzy petri nets. *Power Syst Protect Control* 44(11):26–32 (in Chinese)
5. Gaofu D, Dan Z, Pengfeng L, Chunchun Z (2016) Study of control strategy for active power filter based on modular multilevel converter. *Power Syst Protect Control* 43(8):74–80 (in Chinese)
6. Yashun W, Chunhua Z, Xun C, Yongqiang M (2009) Simulation-based optimal design for accelerated degradation tests with mixed-effects model. *J Mech Eng* 45(12):108–114 (in Chinese)
7. Kun X, Xiaohui G, Chen P (2014) Reliability evaluation of the O-type rubber sealing ring for fuse based on constant stress accelerated degradation testing. *J Mech Eng* 50(16):62–69 (in Chinese)
8. Yongqiang M (2008) Investigation in lifetime assessment of electron multiplier based on double-stress accelerated degradation test. National University of Defense Technology (in Chinese)
9. Xiang J, Xiaolin W, Bo G (2016) Reliability assessment for very few failure data and zero-failure data. *J Mech Eng* 52(2):182–188 (in Chinese)
10. Dexin Z, Hongzhao L (2013) Reliability evaluation of high-speed train bearing with minimum sample. *J Central South Univ* 44(3):963–969 (in Chinese)
11. Trabelsi M, Boussak M, Benbouzid M (2016) Multiple criteria for high performance real-time diagnostic of single and multiple open-switch faults in ac-motor drives: application to IGBT-based voltage source inverter. *Electr Power Syst Res* 144:136–149
12. Xiaoping D, Yangang W, Yibo W, Haihui L, Guoyou L, Daohui L, Steve J (2016) Reliability design of direct liquid cooled power semiconductor module for hybrid and electric vehicles. *Microelectron Reliab* (in Chinese)

13. Czerny B, Khatibi G (2016) Interface reliability and lifetime prediction of heavy aluminum wire bonds. *Microelectron Reliab* 58:65–72
14. Choi UM, Blaabjerg F, Jorgensen S, Lannuzzo F, Wang H, Uhrenfeldt C, Munk-Nielsen S (2016) Power cycling test and failure analysis of molded intelligent power IGBT module under different temperature swing duration. *Microelectron Reliab*
15. Hamada MS, Wilson AG, Shane Reese C, Martz HF (2008) *Bayesian Reliability*. Springer, pp 51–60
16. China Electronics Standardization Institute (1987) *Reliability Test Table*. National Defense Industry Press, Beijing (in Chinese)

# Analysis and Elimination of Early Failure of CNC Grinding Machine

Yulong Li, Genbao Zhang, Yongqin Wang, Xiaogang Zhang and Yan Ran

**Abstract** The problem of early failure of domestic CNC grinding machine is studied herein. Minitab is used to analyze the machine fault data collected, and the best fitting function about it is obtained. On the basis, the early failure period about the machine is found, and the fault data in the early failure period is also analyzed by FMEA. Meanwhile, the main fault location, fault mode and fault reason in the early failure period of the machine are obtained. Some measures to eliminate the early failure, which are related to the self-made parts, purchased parts and enterprise management, are proposed. These studies lay a foundation for improving the reliability of the series machine.

**Keywords** Grinding machine · Early failure · Reliability

## 1 Introduction

CNC machine tools industry provides the basis technology and equipment for the equipment manufacturing industry and national defense industry, and it is the core of the equipment manufacturing industry [1]. Meanwhile, its development level represents a country level of manufacturing [2]. The early use of machine tools is a critical time for users to judge the quality of the product [3], it is important to improve the reliability of CNC machine tools in this period [4]. So eliminating the early faults is the key for improving the reliability of CNC machine tools. In recent years, domestic and foreign scholars have done a lot of researches. For example, Xiujun Fan [4] obtains the early failure point of the machine tools, and set up a set of technical system to eliminate its early faults. Keller [5, 6] introduces the fuzzy theory to the fault analysis and evaluation of NC machine tools, which makes the fuzzy uncertainty problem be quantified. The problems of the hardware and

---

Y. Li (✉) · G. Zhang · Y. Wang · X. Zhang · Y. Ran  
School of Mechanical Engineering, Chongqing University,  
Chongqing 400044, People's Republic of China  
e-mail: 1004762383@qq.com

software of the CNC system is studied by Haibo Zhang [7], and the reliability growth technology of the system is proposed. Xie [8] uses the extended Weibull model to establish the failure rate curve model and proposes the corresponding parameter estimation method.

However, there are still some deficiencies in these studies. For example, the failure data of machine tools are fitted according to experience, and it lacks the comparison of multiple function fitting data, so it is impossible to confirm that the double Weibull distribution is the best fitting function. Meanwhile, the enterprises lack technology and management methods to improve the reliability about their products. This will reduce the competitiveness of the domestic machine tool.

To solve those problems, a CNC grinding machine is researched herein. The failure data are analyzed by Minitab and the best fitting function is obtained. The early failure period of the machine tool is found. The failure occurred in the early failure period is analyzed, and techniques and methods for improving the reliability of the machine tool are presented.

## 2 Determination of Early Failure Period

Early failures are failures occurring in the early stages of the product, which is caused by the internal design errors, the material, the technical defects, the improper installation and running, and so on. This type of failure must be detected and eliminated as early as possible in order to reduce the failure rate of the machine tools.

### 2.1 The Best Fitting Function

The data used in this paper are from the service center of a machine tool factory in china. The fault frequency table and the probability density plot of the gear grinding machine are obtained and shown respectively in Table 1 and Fig. 1.

**Table 1** Failure frequency table

Group	Lower interval/h	Upper interval/h	Median value/h	Frequency	Probability	Cumulative probability	Sample probability
1	0	1322	661	214	0.862903	0.862903	0.0006527
2	1323	2645	1984	24	0.096774	0.959677	0.0000732
3	2646	3968	3307	5	0.020161	0.979838	0.0000153
4	3969	5291	4630	1	0.004032	0.983871	0.0000031
5	5292	6614	5953	1	0.004032	0.987903	0.0000031
6	6615	7937	7276	2	0.008065	0.995968	0.0000062
7	7938	9260	8599	1	0.004032	1.000000	0.0000031

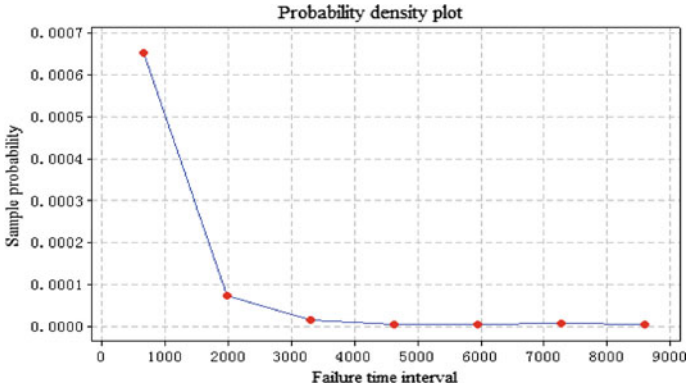


**Fig. 1** Probability density plot

It can be seen that the failure data generally obey exponential distribution, lognormal distribution, Gama distribution or Weibull distribution in Fig. 1. These data are analyzed by Minitab, and the probability plot is shown in Fig. 2.

It can be seen that the P value of the Weibull distribution is the largest in Fig. 2, which indicates that the Weibull distribution is the best fit to the data.

### 2.2 Determination of Early Failure Period

The Weibull fitting of the data is shown in Fig. 3, and it can be seen from the Fig. 3 that the data belong to the double piecewise Weibull function [9].

The reliability about the Weibull function can be expressed as follows [10]:

$$R(t) = \begin{cases} k_1 \exp\left[-(t/\alpha_1)^{\beta_1}\right] & 0 < t \leq t_1 \\ k_2 \exp\left[-(t/\alpha_2)^{\beta_2}\right] & t_1 < t \leq t_2 \\ k_3 \exp\left[-(t/\alpha_3)^{\beta_3}\right] & t_2 \leq t \end{cases} \quad (1)$$

where  $t_1$  is the dividing point between the early failure period and the accidental failure period.

The formula (1) is solved, and the results are as follows:

$$\begin{cases} t_1 = [\beta_1 \alpha_2^{\beta_2} / \beta_2 \alpha_1^{\beta_1}]^{1/(\beta_2 - \beta_1)} \\ t_2 = [\beta_2 \alpha_3^{\beta_3} / \beta_3 \alpha_2^{\beta_2}]^{1/(\beta_3 - \beta_2)} \\ k_2 = \exp[(1 - \beta_2 / \beta_1)(t_1 / \alpha_2)^{\beta_2}] \\ k_3 = \exp[(1 - \beta_3 / \beta_2)(t_2 / \alpha_3)^{\beta_3}] \end{cases} \quad (2)$$

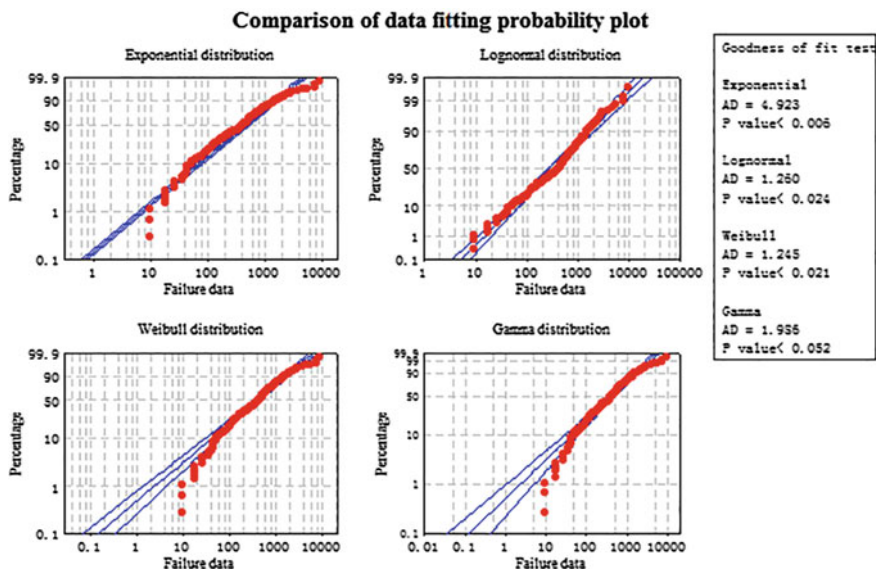


Fig. 2 Comparison of probability plot of data fitting

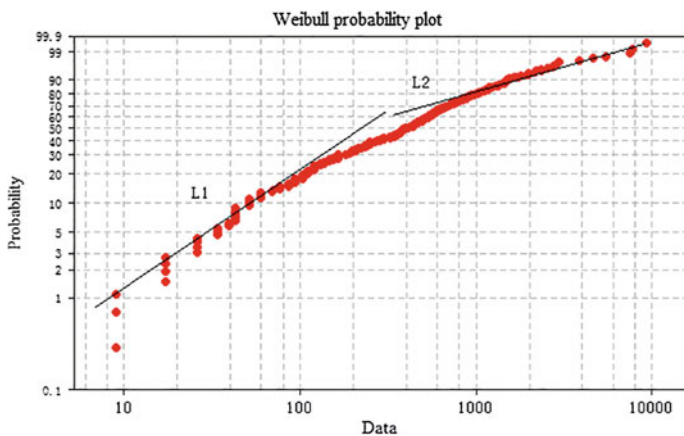


Fig. 3 Weibull data fitting plot

Taking the data into the above formula, and the  $t_1 = 1641$ . It means that the early failure usually occurs about 1641 h after the machine leaves the factory, and it is consistent with the phenomenon reflected by the users.



### 3 Early Failure Elimination Mechanism

The reliability design and analysis technology, and consistency control technique of machining and assembly process have been used as the theoretical foundation of the early failure eliminate mechanism. The reliability test is used as the excitation method of the early failure elimination mechanism, and the reliability management technology is used as its guarantee. Then, improvement measures are put forward to eliminate the defects in the process of design and manufacture [4].

Early failure can not be completely eliminated before it leaves the factory, and some early failures may occur in using the machine. The FMEA is usually used to analysis those failures, and the corresponding improvement measures can be put forward to improve the reliability of products.

## 4 FMEA Analysis of Early Failure

### 4.1 Analysis of Early Failure Location

There are 153 failures occurred in the early failure period of the grinding machine, and those early failures belong to the 8 subsystems, as shown in Table 2. The proportion plot of each subsystem is shown in Fig. 4.

It can be seen from the Table 2 and Fig. 4 that the failures of auxiliary system in the early failure occur most frequently, followed by the electrical system, the bed and so on.

### 4.2 Analysis of Early Failure Mode

Early failure mode frequency table and proportion plot of the machine tools are shown in Table 3 and Fig. 5.

**Table 2** Frequency table of failure location

Location	Frequency	Probability	Location	Frequency	Probability
Diamond wheel device	3	0.0175	Working frame	20	0.1170
Grinding wheel frame	4	0.0234	Bed	26	0.1520
Dresser	6	0.0351	Electrical system	48	0.2807
Column	14	0.0819	Auxiliary system	50	0.2924

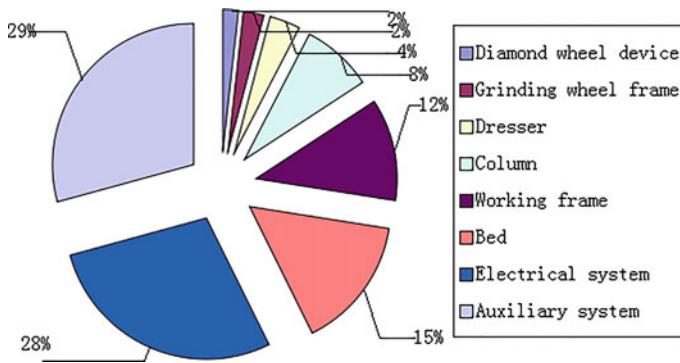


**Fig. 4** Proportion plot of failure location

**Table 3** Failure mode frequency table

Failure mode	Frequency	Probability
Improper stroke	1	0.0046
Program control failure	2	0.0092
Parts or components damage of liquid, gas or oil	3	0.0138
Armor or shield damage	3	0.0138
Liquid, gas and oil blockage	4	0.0183
Can not accurately return to zero	4	0.0183
Improper operation	4	0.0183
Moving parts jitter	5	0.0229
Abnormal sound	5	0.0229
Component damage	8	0.0367
Software deficiency	9	0.0413
Liquid, gas and oil leakage	9	0.0413
Unable to rotate and move	10	0.0459
Machine tool cannot be executed in program instructions	11	0.0505
Spindle disorder	12	0.0550
Work accuracy exceeded	19	0.0872
Operation can not be carried out properly	20	0.0917
Geometric accuracy exceeded	21	0.0963
Parts damage	33	0.1514
Components function loss	35	0.1606

It can be seen from Table 3 and Fig. 5 that the failure modes of the grinding machine mainly are the components function loss, the parts damage, the geometric accuracy exceeded and the operation can not be carried out properly.

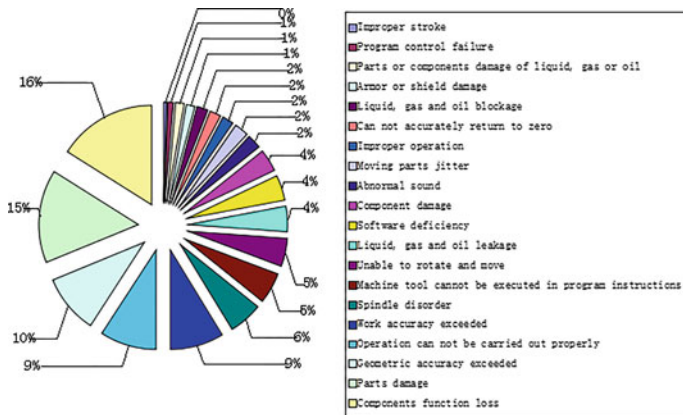


Fig. 5 Failure mode proportion plot

### 4.3 Analysis of Early Failure Cause

The reason why analyzing the failure cause of the machine tools is that finding its defective part so that the measures to improve the reliability are found. Early failure cause frequency table and proportion plot are shown in Table 4 and Fig. 6.

It can be seen from Table 4 and Fig. 6 that the failure causes in early failure of the grinding machine mainly are the component damage, the parts damage, the incorrect operation and the parameter or program error.

Table 4 Failure cause frequency table

Failure cause	Frequency	Probability	Failure cause	Frequency	Probability
Design error	1	0.0068	Loose	5	0.0338
Insufficient cleaning	1	0.0068	Poor connection to the Wiring	7	0.0473
Motor damage	1	0.0068	Poor assembly	8	0.0541
Abrasion	1	0.0068	Improper pressure flow	9	0.0608
Aging	1	0.0068	Parameter or program error	15	0.1014
Improper adjustment	2	0.0135	Incorrect operation	17	0.1149
leakage	3	0.0203	Parts damage	26	0.1757
blocking	4	0.0270	Component damage	42	0.2838
Software or system damage	5	0.0338			

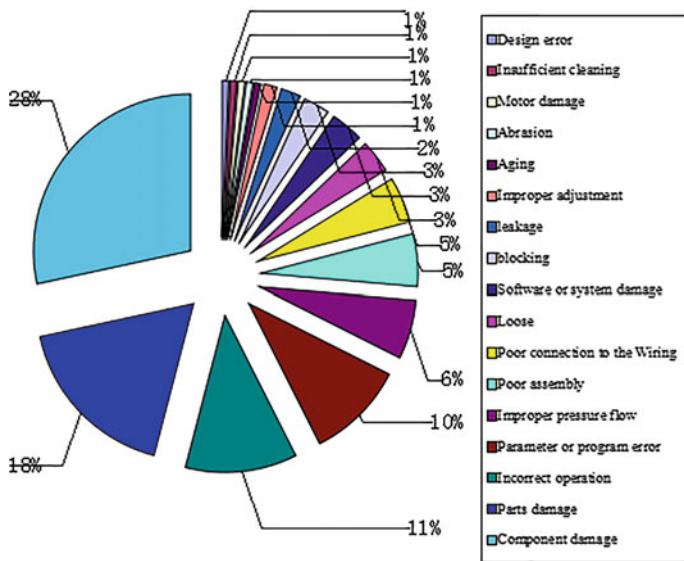


Fig. 6 Failure cause proportion plot

In addition, whether the failure in the early failure period caused by the self-made or purchased parts need to be analyzed. Failure frequency table and proportion plot about them are shown in Table 5 and Fig. 7.

It can be seen from Table 5 and Fig. 7 that the early failure of the grinding machine mainly caused by the purchased parts.

## 5 Suggestions for Shortening Early Failure Period

### 5.1 Early Failure Elimination for Self-Made Parts

In order to eliminate the early failure of the machine tool within the enterprise as much as possible, and it is necessary to control the self-made products. The early failure elimination methods are shown in Table 6.

Table 5 Self-made and purchased parts frequency table

Category	Frequency	Probability
Self-made parts	34	0.2297
Purchased parts	114	0.7703

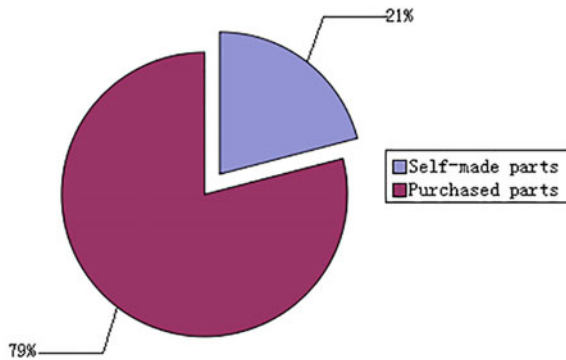


Fig. 7 Self-made and purchased parts proportion plot

Table 6 Early failure elimination method for self made parts

Fault phase	Early failure elimination plan
Design phase	The consistency of the design method of product structure and reliability should be adopted. A reasonable reliability test should also be designed to revise the defect of product structure design
Manufacturing phase	The potential defects of the product should be exposed by environmental stress screening test, and the control measures of processing and assembly process consistency should be formulated
Fault phase	Early failure elimination plan
Assembly phase	The assembly process documents should be formulated by the technology and assembly department. The processing quality of self-made parts should be checked carefully and the cleanliness of the assembly site should be control in the assembly site
Debug phase	The machine tool should be debugged on the premise that the instructions, electrical and programming are known by workers
Using phase	Some reliability analysis tools should be used to put forward some improvement measures for machine tool

### 5.2 Early Failure Elimination for Purchased Parts

Improving the quality of purchased parts plays an important role in shortening the early failure period. Purchased parts should be purchased in fixed manufacturers, and the corresponding inspection instructions of the key purchased parts should be made by quality inspection department. The acceptance strength of purchased parts should be increased to ensure their quality in the inspection process. In addition, the corresponding reliability test platform should be built to verify the reliability of the purchased parts before them enter the factory. At the same time, manufacturers should train the users and assist them to do daily maintenance.

### 5.3 *Improvement Measures for Enterprise Management*

The following suggestions have been proposed to solve the problem of reliability management in enterprises. Firstly, the company should put forward the overall plan for machine tool reliability work in the design phase of the project. Secondly, the company should establish a checklist system to achieve reliability control of design, manufacturing and assembly activities. Thirdly, the company should strengthen the reliability test and evaluation activities in order to analyze and improve the reliability of their products. Fourthly, the degree of involvement of the supplier in the design selection phase should also be improved to ensure the proper selection and use of the purchased parts. Finally, the company should set up the management standard of oil to ensure its quality and cleanliness.

In order to find out the corresponding improvement measures, the FMEA should be used to analyze the early faults which cannot be eliminated before the factory. And the fault location, the reason and the detailed solution should be promptly summarized and sorted to improve the product failure database.

## 6 Conclusions

The empirical fitting distribution of machine failure data is discarded herein, and the best fitting function of the data is obtained by Minitab. The best fitting function is analyzed and the early failure period of the target machine is found. Machine data on early failure period are analyzed by FMEA, and the improvement measures to eliminate the early failure are proposed. These measures also laid a foundation for improving the reliability of the series of machine tool. The method can also be used for other types of machine tool.

**Acknowledgements** This work is supported by the National Nature Science Foundation (China under Grant No. 51575070); National Major Scientific and Technological Special Project for “High-grade CNC Basic Manufacturing Equipment” (China under Grant Nos. 2016ZX04004-005; 2013ZX04012-041); and the Fundamental Research Funds for the Central Universities (No. 106112017CDJXY110006).

## References

1. Wei G (2015) The research on early fault eliminating test technology of machining center. Jilin University (in Chinese)
2. Heng Z (2012) Research of reliability analysis and control technology of CN machine based on element action. Chongqing University (in Chinese)
3. Jia Z, Shen G, Zhongxiang H et al (2008) Life distribution model and control of CNC lathe based on life cycle. Mach Tools Hydraulics 36:164–167 (in Chinese)

4. Fan X, Jingling X, Zhang G et al (2013) Technology of eliminating early failures for NC machine tools. *China Mech Eng* 24(16):2241–2247 (in Chinese)
5. Keller AZ, Beng C, Kara-Zaitri C (1988) Further applications of fuzzy logic to reliability assessment and safety. In: *Reliability in electronics-elected, proceedings of the seventh symposium on reliability in electronics (Electronics'88)*, Aug 29–Sept 2. Budapest, Hung
6. Fleming PV, Kara-Zaitri C, Keller AZ (1997) Reliability analysis of machine tool structures. *J Eng Ind* 99(4):882–888
7. Haibo Z (2006) Research on reliability design and growth technology of CNC system. Jilin University (in Chinese)
8. Xie M, Tang Y, Goh TN (2002) A modified Weibull extension with bathtub-shaped failure rate function. *Reliab Eng Syst Saf* 76(3):279–285 (7)
9. Renyan J, Mingjian Z (1999) Reliability model and operation. Machinery Industry Press (in Chinese)
10. Xiaobo L (2010) Quantitative modeling & application study of failure rate bathtub curve of machine tool. Chongqing University (in Chinese)

# Reliability Fuzzy Comprehensive Evaluation of All Factors in CNC Machine Tool Assembly Process

Xiaogang Zhang, Genbao Zhang, Xiansheng Gong, Yulong Li and Yan Ran

**Abstract** There are many complex factors for the reliability of CNC machine tool assembly process. For this question, reliability factors system of a CNC machine tool assembly process is established by analyzing systematically and comprehensively using 5M1E method. For lots of uncertainties in evaluating the reliability of the CNC machine tool assembly process, a multiple target multi-level fuzzy comprehensive model is established by fuzzy mathematical theory. At the same time, the relationship of common reliability and fuzzy reliability is found, and weights of the various factors are obtained by expert scoring method and AHP method. The overall level of CNC machine tool reliability can be grasped by reliability comprehensive evaluation of its assembly process. Lastly, a certain type of CNC lathe is taken as an example to illustrate the validation of the model.

**Keyword** CNC machine tool · Assembly process · Fuzzy comprehensive evaluation

## 1 Introduction

Defined as the combination of various parts to realize the predetermined functions of products, assembly is an important part of the product quality, and the reliability of assembly process is getting more attention [1]. Beiter, who uses the assembly quality analysis method (Total Quality Management, TQM) to analyze the underlying assembly method of the allied resources in the form of production from the design phase, evaluate the quality of product assembly, and improves assembly quality of products in the design stage [2]. Tsinarakis establishes a multi-assembly manufacturing system model by the Petri-nets technology [3]. According to the

---

X. Zhang (✉) · G. Zhang · X. Gong · Y. Li · Y. Ran  
School of Mechanical Engineering, Chongqing University,  
Chongqing 400044, People's Republic of China  
e-mail: 534592109@qq.com

© Springer Nature Singapore Pte Ltd. 2018

L. Jia et al. (eds.), *Proceedings of the 3rd International Conference on Electrical and Information Technologies for Rail Transportation (EITRT) 2017*, Lecture Notes in Electrical Engineering 482, [https://doi.org/10.1007/978-981-10-7986-3\\_12](https://doi.org/10.1007/978-981-10-7986-3_12)

115



reliability status of products in the assembly workshop, Suzuki et al. proposes the assembly reliability evaluation method, and quantitatively researched the assembly failure rate through the design factors and workshop factors, and improved the corresponding impact factors enhance the reliability level of assembly workshops [4, 5]. Utilizing polychromatic sets and dynamic Bayesian network, Zhang [6, 7] comes up the model of assembly process and technology drove by reliability and analyzes the main factors influencing the reliability of the assembly process, and he also proposes the corresponding control measures and improves the reliability of the product assembly. By human error analysis of a gearbox assembly process, Feilong Zhong studies the human reliability of the transmission assembly process and reveals the weak links in the assembly process and the possible influence of human error, and he also ultimately provides the basis for relevant departments to take measures [8]. The all above studies are just for some influence factors of the assembly process reliability. The research from the perspective of the whole factors of assembly process reliability is required, so 5M1E (Man, Machine, Material, Method, Measurement and Environment) Method is adopted.

5M1E is abbreviation of the six main factors about influencing the quality of products in the theory of TQM. The assembly process of CNC machine tool is a complicated production system. Using 5M1E method, all factors of it are analyzed, and the influencing factors system is established. The comprehensive evaluation model of CNC assembly system reliability is presented by applying the theory of fuzzy mathematics, which can solve the problem of uncertain factors in the analysis process.

## **2 All Influencing Factors Analysis of Assembly Process Reliability**

The assembly process reliability of CNC machine tool is synthetically decided by the six factors, man, machine, material, method, measurement and environment, and any breakdown of these factors will affect the reliability of the whole system.

Therefore, the whole factor structure system is established by researching the reliability influencing factors of the CNC machine assembly process from these six aspects of 5M1E method. Human factors analysis can be presented from two aspects, namely, assembly workers and the support personnel. For assembly workers error analysis, it includes operation error with illness, distracted assembly error etc. Similarly, for the support personnel, management error of management organization and part scheduling error should be considered. The influence factors of machine reliability are mainly considered in the two aspects of assembly machine fault (Clamp fault, Manipulator fault, etc.) and auxiliary machine fault (such as crown block fault, forklift fault). The influencing factors of the material reliability mainly contain defective parts for assembly and without incoming inspection. For methods, unreasonable assembly process and unreasonable operating specifications

are the crucial factors. For measurement, it holds measuring method error, measuring instrument fault and not measured by specification. At last, for environment, the main influencing factors are temperature, humidity, noise, vibration, etc.

Through the above analysis, the structural system influential factors of the reliability of CNC machine tools assembly process is established, as shown in Fig. 1, and the various factors are numbered in the diagram.

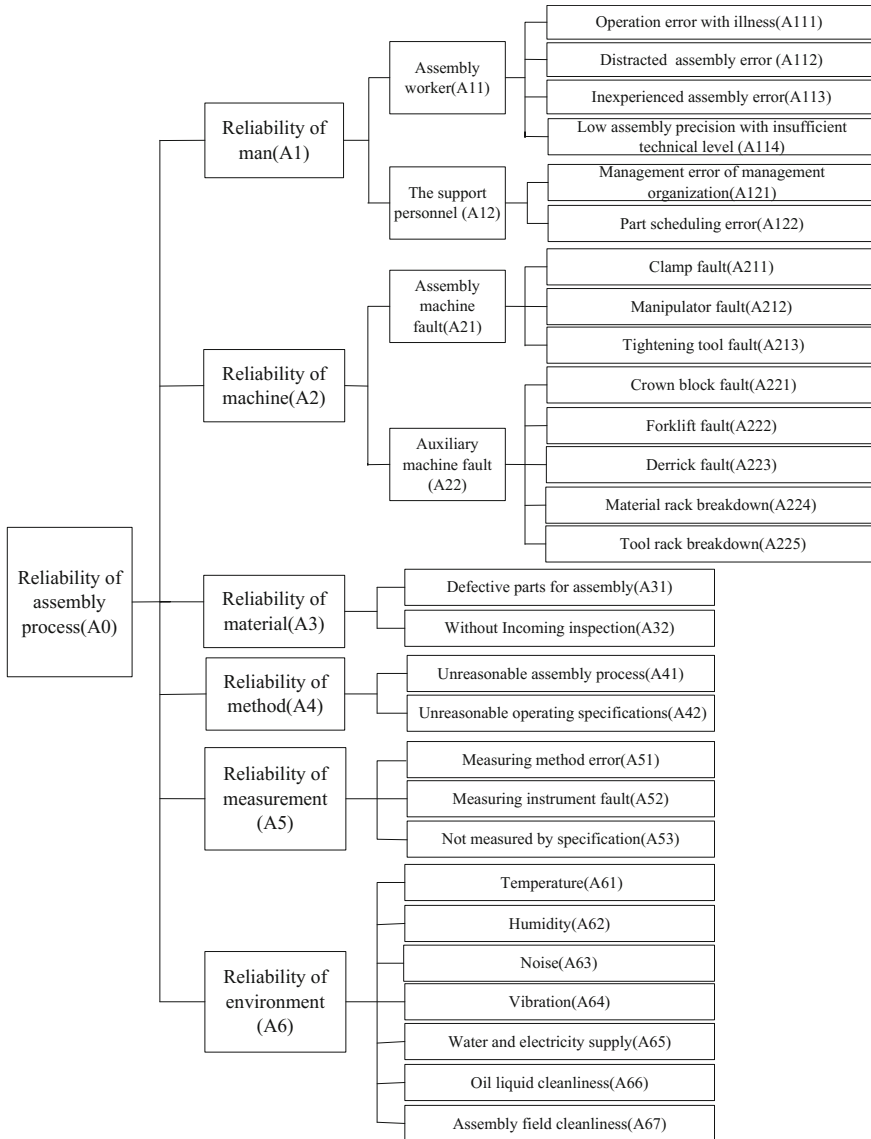


**Fig. 1** The influential factors of the reliability of CNC machine tools assembly process

### 3 Fuzzy Comprehensive Evaluation of Assembly Process

As shown in Fig. 1, the structure of the factors affecting the reliability of CNC machine tools assembly system is arranged in a hierarchy. The assembly system reliability of CNC machine tools is the top layer (set as 0 layer), then the reliability of six factors (man, machine, material, method, measurement and environment) is set as the first layer, and the other layers are set in turn. Meanwhile, the 0 layer is considered as the parent of the first layer, and the first layer is the child, and the other corresponding levels are set as well. As suggested above, the factors structure system affecting the assembly reliability of CNC machine tools is multi-objective and multi-level. Therefore, the fuzzy evaluation of it is a typical multi-objective multilevel comprehensive evaluation process.

#### 3.1 Fuzzy Membership Functions of Assembly System

When studying the dependability of the assembly process, a very important parameter is reliability, but sometimes an accurate number of reliability can't quickly form a clear concept, thus some fuzzy languages are used to describe the work state of CNC assembly system. The evaluation set,  $E = (e_1, e_2, \dots, e_6)$ , in the comprehensive evaluation of the assembly system reliability of CNC machine too, is adopted, and from  $e_1$  to  $e_6$ , is orderly described as highly reliable, very reliable, reliable, unreliable, very unreliable and highly unreliable.

The mathematical model is used to describe the mapping relationship between reliability values and fuzzy reliability languages. The mapping relationship is presented as follows:

$$R(\omega) = e_j, e_j \in E, j = 1, \dots, 6 \tag{1}$$

Thereby,  $\omega$  is used for the system unit,  $E$  for the values space of fuzzy reliability language,  $e_j$  for one value of fuzzy reliability language.

Based on literature [9], "very reliable" is defined as:

$$\mu_{e_2}(R) = \begin{cases} 0 & 0 \leq R \leq a \\ 2\left(\frac{R-a}{1-a}\right)^2 & a \leq R < 0.5(1+a) \\ 1 - 2\left(\frac{R-1}{1-a}\right)^2 & 0.5(1+a) \leq R < 1 - 0.437(1-a) \\ 1 - \left[1 - 2\left(\frac{R-1}{1-a}\right)^2\right]^2 & 1 - 0.437(1-a) \leq R \leq 1 \end{cases} \tag{2}$$

where,  $a(0.5 < a < 1)$  is a parameter and here  $a = 0.7$ .

According to the definition of fuzzy tone factors and Eq. (2), the relationship of membership functions can be obtained as follows:

$$\mu_{e_6} = \mu_{e_1}(1 - R), \mu_{e_4} = \mu_{e_3}(1 - R), \mu_{e_4} = \mu_{e_3}(1 - R) \tag{3}$$

Then, the 6 membership functions of fuzzy can be expressed as follows:

$$\mu_{e_1}(R) = \begin{cases} 0 & 0 \leq R < 0.7 \\ 4\left(\frac{R-0.7}{0.3}\right)^2 & 0.7 \leq R < 0.85 \\ 1 - 2\left(\frac{R-1}{0.3}\right)^2 & 0.85 \leq R \leq 1 \end{cases} \tag{4}$$

$$\mu_{e_2}(R) = \begin{cases} 0 & 0 \leq R < 0.7 \\ 2\left(\frac{R-0.7}{0.3}\right)^2 & 0.7 \leq R < 0.85 \\ 1 - 2\left(\frac{R-1}{0.3}\right)^2 & 0.85 \leq R < 0.87 \\ 1 - \left[1 - 2\left(\frac{R-1}{0.3}\right)^2\right]^2 & 0.87 \leq R \leq 1 \end{cases} \tag{5}$$

$$\mu_{e_3}(R) = \begin{cases} 0 & 0 \leq R < 0.7 \\ \sqrt{2}\left(\frac{R-0.7}{0.3}\right)^2 & 0.7 \leq R < 0.83 \\ 1 - 2\left(\frac{R-0.7}{0.3}\right)^2 & 0.83 \leq R < 0.85 \\ 2\left(\frac{R-1}{0.3}\right)^2 & 0.85 \leq R \leq 1 \end{cases} \tag{6}$$

$$\mu_{e_4}(R) = \begin{cases} 2\left(\frac{R}{0.3}\right)^2 & 0 \leq R < 0.15 \\ 1 - 2\left(\frac{R-0.3}{0.3}\right)^2 & 0.15 \leq R < 0.17 \\ \sqrt{2}\left(\frac{0.3-R}{0.3}\right) & 0.17 \leq R < 0.3 \\ 0 & 0.3 \leq R \leq 1 \end{cases} \tag{7}$$

$$\mu_{e_5}(R) = \begin{cases} 1 - \left[1 - 2\left(\frac{R}{0.3}\right)^2\right]^2 & 0 \leq R < 0.13 \\ 1 - 2\left(\frac{R}{0.3}\right)^2 & 0.13 \leq R < 0.15 \\ 2\left(\frac{0.3-R}{0.3}\right) & 0.15 \leq R < 0.3 \\ 0 & 0.3 \leq R \leq 1 \end{cases} \tag{8}$$

$$\mu_{e_6}(R) = \begin{cases} 1 - 2\left(\frac{R}{0.3}\right)^2 & 0 \leq R < 0.15 \\ 4\left(\frac{0.3-R}{0.3}\right)^2 & 0.15 \leq R < 0.3 \\ 0 & 0.3 \leq R \leq 1 \end{cases} \tag{9}$$

### 3.2 Single-Stage Fuzzy Evaluation

The influence factor gather of a target is set as  $S = \{s_1, s_2, \dots, s_i, \dots, s_m\}$ , and the corresponding remark is set as  $E = \{e_1, e_2, \dots, e_j, \dots, e_n\}$ , and the weight is set as  $W = \{w_1, w_2, \dots, w_i, \dots, w_m\}$ . The weight  $w_i (i = 1, 2, \dots, m)$  is used to describe

the importance of the factor  $s_i (i = 1, 2, \dots, m)$ . The fuzzy relationship  $R$  between the  $S$  and  $E$  is obtained as follows:

$$R = \begin{bmatrix} r_{11} & r_{12} & \cdots & r_{1j} & \cdots & r_{1n} \\ r_{21} & r_{22} & \cdots & r_{2j} & \cdots & r_{2n} \\ \vdots & \vdots & \vdots & \vdots & \vdots & \vdots \\ r_{i1} & r_{i2} & \cdots & r_{ij} & \cdots & r_{in} \\ \vdots & \vdots & \vdots & \vdots & \vdots & \vdots \\ r_{m1} & r_{m2} & \cdots & r_{mj} & \cdots & r_{mn} \end{bmatrix} \quad (10)$$

While  $r_{ij}$  stands for the membership of the factor  $s_i$  with the remark  $e_j$ ,  $R_i = \{r_{i1}, r_{i2}, \dots, r_{ij}, \dots, r_{in}\}$  for the remark set of the factor  $s_i$ .

Thus, the comprehensive evaluation for the objective can be obtained as follows:

$$\begin{aligned} A &= W \cdot R \\ &= (w_1, w_2, \dots, w_i, \dots, w_m) \begin{bmatrix} r_{11} & r_{12} & \cdots & r_{1j} & \cdots & r_{1n} \\ r_{21} & r_{22} & \cdots & r_{2j} & \cdots & r_{2n} \\ \vdots & \vdots & \vdots & \vdots & \vdots & \vdots \\ r_{i1} & r_{i2} & \cdots & r_{ij} & \cdots & r_{in} \\ \vdots & \vdots & \vdots & \vdots & \vdots & \vdots \\ r_{m1} & r_{m2} & \cdots & r_{mj} & \cdots & r_{mn} \end{bmatrix} \\ &= (a_{11}, a_{12}, \dots, a_{1j}, \dots, a_{1n}) \end{aligned} \quad (11)$$

### 3.3 Multistage Multiobjective Comprehensive Fuzzy Evaluation

By the previous method, the comprehensive evaluation value of the same layer of the target can be obtained, and comment set  $A_{gk}$  constructs a new fuzzy matrix  $R_g$ . Thereby,  $A_{gk}$  for comment aggregation of the layer  $g$  and the target  $k, l$  for the factor numbers of target in the layer  $g$ .

$$R_g = \begin{bmatrix} A_{g1} \\ A_{g2} \\ \vdots \\ A_{gl} \end{bmatrix} = \begin{bmatrix} A_{g11} & A_{g12} & \cdots & A_{g1n} \\ A_{g21} & A_{g22} & \cdots & A_{g2n} \\ \vdots & \vdots & \vdots & \vdots \\ A_{gl1} & A_{gl2} & \cdots & A_{gln} \end{bmatrix} \quad (12)$$

The weight set of targets in the layer  $g$  shows as follows:

$$W_g = \{w_{g1}, w_{g2}, \dots, w_{gj}, \dots, w_{gl}\}. \tag{13}$$

The comprehensive assessment of the parent layer  $g - 1$  for the layer  $g$  can be calculated from Eq. (9) as:

$$\begin{aligned} A_{g-1} &= W_g \cdot R_g \\ &= (w_{g1}, w_{g2}, \dots, w_{gj}, \dots, w_{gl}) \begin{bmatrix} A_{g11} & A_{g12} & \dots & A_{g1n} \\ A_{g21} & A_{g22} & \dots & A_{g2n} \\ \vdots & \vdots & \vdots & \vdots \\ A_{gl1} & A_{gl2} & \dots & A_{gln} \end{bmatrix} \\ &= (a_{g-1,1}, a_{g-1,2}, \dots, a_{g-1,n}) \end{aligned} \tag{14}$$

Thus, through layer-by-layer evaluation, the comprehensive assessment of the general target can be acquired as:

$$A_0 = (A_{01}, A_{02}, \dots, A_{0n}). \tag{15}$$

### 3.4 Weight Calculation

In order to minimize the subjective factors of evaluators, experts grading methods (EGM) and the analytic hierarchy process (AHP) are adopted to determine the weight of each evaluation factor [10, 11]. When using EGM, the selection of experts is very important. In order to get more accurate index weight, an experts group, including specialists from the experienced assembly technical staff, assembly process makers, quality inspection personnel and production management, is constructed.

## 4 Case Study

The influence factors structure system of CNC assembly process reliability and the corresponding evaluation method have been given. Hence, the assembly process of a CNC lathe of Baoji Machine Tool Group Co., Ltd., as an example, is used to verify the research.

According to EGM and AHP, the influence factor weights of assembly system reliability of the CNC lathe can be obtained carefully in Table 1.

Based on a large amount reliability data of assembly field, the probabilities and the common reliabilities of various influencing factors can be calculated. Then,

**Table 1** The weights influence factor of assembly system reliability of the CNC lathe

Factor	Weight	Factor	Weight	Factor	Weight
A1	0.3	A42	0.3	A113	0.3
A2	0.2	A51	0.3	A114	0.3
A3	0.2	A52	0.4	A121	0.4
A4	0.1	A53	0.3	A122	0.6
A5	0.1	A61	0.1	A211	0.6
A6	0.1	A62	0.1	A212	0.2
A11	0.7	A63	0.1	A213	0.2
A12	0.3	A64	0.1	A221	0.2
A21	0.6	A65	0.1	A222	0.2
A22	0.4	A66	0.2	A223	0.2
A31	0.6	A67	0.3	A224	0.2
A32	0.4	A111	0.2	A225	0.2
A41	0.7	A112	0.2		

fuzzy reliabilities of influential factors in the bottom layer can be figured out by Eqs. (4)–(9) in Table 2.

Using the above fuzzy synthetic evaluation method, the fuzzy reliability of each parent layer is calculated by the Eqs. (10)–(15), and the final fuzzy reliability of assembly process can also be acquired (see Table 3).

The result shows that the membership degree of assembly process reliability of CNC lathe, for the first level (very reliable) is 0.7913, for the second level (very reliable) is 0.1975, and for the third level (reliable) is 0.2616. According to the maximum membership degree principle, the assembly process reliability of CNC lathe is very reliable and is consistent with the actual situation in the company.

**Table 2** Fuzzy reliabilities of influential factors in the bottom layer

Factor	Fuzzy reliabilities	Factor	Fuzzy reliabilities
A111	(0.944, 0.108, 0.056, 0, 0, 0)	A225	(0.944, 0.108, 0.056, 0, 0, 0)
A112	(0.964, 0.070, 0.036, 0, 0, 0)	A31	(0.564, 0.564, 0.436, 0, 0, 0)
A113	(0.964, 0.070, 0.036, 0, 0, 0)	A32	(0.447, 0.111, 0.778, 0, 0, 0)
A114	(0.778, 0.395, 0.222, 0, 0, 0)	A41	(0.920, 0.154, 0.080, 0, 0, 0)
A121	(0.944, 0.108, 0.056, 0, 0, 0)	A42	(0.964, 0.070, 0.056, 0, 0, 0)
A122	(0.980, 0.040, 0.020, 0, 0, 0)	A53	(0.564, 0.564, 0.436, 0, 0, 0)
A211	(0.444, 0.111, 0.778, 0, 0, 0)	A61	(0.991, 0.018, 0.009, 0, 0, 0)
A212	(0.964, 0.070, 0.036, 0, 0, 0)	A62	(0.991, 0.018, 0.009, 0, 0, 0)
A213	(0.991, 0.018, 0.009, 0, 0, 0)	A63	(0.944, 0.108, 0.056, 0, 0, 0)
A221	(0.998, 0.004, 0.002, 0, 0, 0)	A64	(0.920, 0.154, 0.008, 0, 0, 0)
A222	(0.998, 0.004, 0.002, 0, 0, 0)	A65	(0.998, 0.004, 0.002, 0, 0, 0)
A223	(0.991, 0.018, 0.009, 0, 0, 0)	A66	(0.444, 0.111, 0.778, 0, 0, 0)
A224	(0.991, 0.018, 0.009, 0, 0, 0)	A67	(0.871, 0.436, 0.564, 0, 0, 0)

**Table 3** The fuzzy reliabilities of factors in the parent layer

Factor	Fuzzy reliabilities	Factor	Fuzzy reliabilities
A11	(0.904, 0.175, 0.096, 0, 0, 0)	A3	(0.515, 0.383, 0.573, 0, 0, 0)
A12	(0.966, 0.067, 0.034, 0, 0, 0)	A4	(0.927, 0.140, 0.073, 0, 0, 0)
A21	(0.657, 0.084, 0.492, 0, 0, 0)	A5	(0.778, 0.333, 0.222, 0, 0, 0)
A22	(0.984, 0.030, 0.016, 0, 0, 0)	A6	(0.835, 0.183, 0.340, 0, 0, 0)
A1	(0.923, 0.143, 0.077, 0, 0, 0)	A0	(0.791, 0.198, 0.262, 0, 0, 0)
A2	(0.788, 0.063, 0.301, 0, 0, 0)		

## 5 Conclusion

Using 5M1E method, the whole influential factors of assembly process reliability of CNC machine tools are analyzed, and the influencing factors structure system of reliability is constructed. Then combining the theory of fuzzy mathematics, the multi-objective multi-level fuzzy comprehensive evaluation method of assembly system reliability is established.

Taking a type of CNC lathe in Baoji Machine Tool Group Co., Ltd. as an example, the fuzzy comprehensive evaluation of its assembly process is accomplished, and the result shows its reliability situation is “very reliable”, which is in conformity with the actual situation and verifies the feasibility of the proposed evaluation method.

This method is not just limited to CNC lathe. It can also be applied to other types of CNC machine tool.

**Acknowledgements** This work is partially supported by the National Nature Science Foundation (China under Grant No. 51575070); and National Major Scientific and Technological Special Project for “High-grade CNC Basic Manufacturing Equipment” (China under Grant Nos. 2016ZX04004-005; 2013ZX04012-012).

## References

1. Zhang G, Li D et al (2013) Modularized fault tree modeling and multi-dimensional mapping for assembly reliability. *Comput Integr Manuf Syst* 19(03):516–523 (in Chinese)
2. Beiter KA, Cheldelin B, Ishii K (2000) Assembly quality method: a tool in aid of product strategy, design, and process improvement. In: *Proceedings of ASME design engineering technical conferences*, Sept 10–13. Baltimore MD, pp 1–9
3. Tsinarakis GJ, Tsourveloudisn KP (2005) Studying multi-assembly machine production systems with hybrid timed Petri-nets. In: *Proceedings of the 2005 IEEE international conference on automation science and engineering*, Aug 1–2. IEEE Service Center, Edmonton, Canada. Piscataway, NJ, pp 1–6
4. Suzuki T, Ohashi T, Asano M et al (2003) Assembly reliability evaluation method (AREM). *CIRP Annals Manuf Technol* 52(1):9–12
5. Suzuki T, Ohashi T, Asano M et al (2004) AREM shop evaluation method. *CIRP Ann Manuf Technol* 53(1):43–46



6. Zhang G, Ge H et al (2011) Reliability-driven modeling approach of assembly process. *Trans Chinese Soc Agri Mach* 42(10):192–196 (in Chinese)
7. Zhang G, Liu J et al (2012) Modeling and analysis for assembly reliability based on dynamic bayesian networks. *China Mech Eng* 23(2):211–215 (in Chinese)
8. Feilong Z (2009) Study of human reliability in gearbox assembly process. *Jilin University* (in Chinese)
9. Cui Y, Li T (1991) Fuzzy reliability for CF model. *Syst Eng Theory Pract* 11(6):41–45 (in Chinese)
10. Zhang L, Guo J (2007) Fuzzy comprehensive evaluation of wear status on a type of engine group. *Lubr Eng* 32(10):120–122 (in Chinese)
11. Wang S, Li L (2004) Application of the improved AHP in weighted assessment of engine. *J Civil Aviation Univ China* 22:107–110 (in Chinese)

# A Compacted Brushless Dual Mechanical Port Electrical Machine Model

Shaowei Wang and Zhenghao Wang

**Abstract** A Pole-Modulation Brushless Dual Mechanical Port Machine (PMB-DMPM) model is presented. This model removes brush, the stator and its embedded winding are ordinary, the outer rotor is single-layer concentric cage, and the inner rotor is permanent magnets. By the modulating function of the cage rotor, the stator windings and the permanent magnets of the inner rotor produce a magnetic field individually, whose rotational speed and magnetic pole's number are consistent with each other, and the energy can delivery through the stator, the outer rotor and inner rotor. The simulation results show that the machine model can achieve a good magnetic field modulation effect, and validate the proposed model's feasibility.

**Keywords** Dual mechanical port · Brushless · Model · Energy conversation

## 1 Introduction

In recent years, dual mechanical ports machine has been widely studied in domestic and international institutes. It mainly contains two rotors, with which mechanical parts are connected. Currently there are some types as following: (a) permanent magnet & permanent magnet [1], where the inner rotor is winding, the both sides of the outer rotor's surface are permanent magnets, and the stator is embedded with windings; (b) squirrel cage & squirrel cage [2], where the inner rotor is winding and both sides of outer rotor are squirrel cages; (c) single permanent magnet type [3–7],

---

S. Wang (✉)

Hubei Province Key Laboratory of Intelligent Information Processing and Real-Time Industrial System, College of Computer Science and Technology, Wuhan University of Science and Technology, Huangjiahu Road, Hongshan District, Wuhan City 430065, China  
e-mail: alang\_wsw@126.com

Z. Wang

State Grid Xinxiang Power Supply Company, Xinxiang, Henan Province, China

© Springer Nature Singapore Pte Ltd. 2018

L. Jia et al. (eds.), *Proceedings of the 3rd International Conference on Electrical and Information Technologies for Rail Transportation (EITRT) 2017*, Lecture Notes in Electrical Engineering 482, [https://doi.org/10.1007/978-981-10-7986-3\\_13](https://doi.org/10.1007/978-981-10-7986-3_13)

125

where the inner rotor is windings and the outer rotor is a single layer permanent magnet. All of the inner rotors in (a), (b), (c) adopt windings, and brushes are used to export wire. As result, the high frequency faults of the brush affect the machine's efficiency; (d) Recently Huang Sheng Hua, Wan Shan Ming, Chen Xiao etc. in Huazhong University of Science and Technology have proposed dual mechanical port brushless machine [8]. There are two independent windings in the stator and three windings in the outer rotor, of which two windings are linked in reverse order. The inner rotor is a permanent magnet without brush. However, in order to demolish brushes, increasing the number of motor windings enhances the excessive coupling in the magnetic field, so it results in a more complicated control. In this paper, based on pole modulation theory of concentric cage rotor, we propose a compacted dual mechanical port brushless machine model called Pole-Modulator-Brushless Dual Mechanical Port Machine (PMB-DMPM), where the outer rotor is cage and the inner rotor is permanent magnet. PMB-DMPM can use mixed energy without brushes and simple structure. The paper will explain the feasibility in the term of magnetic field.

## 2 PMB-DMPM Model

### 2.1 PMB-DMPM Structure

As showed in Fig. 1, the proposed PMB-DMPM is divided into three layers: the outer layer is a stator with 3-phases windings, which are the same to ordinary AC stator and it can produce a rotating magnetic field after being electricity-powered; the intermediate layer is outer rotor, whose function is modulating magnetic field; the inner layer is inner rotor made up of permanent magnets. The PMB-DMPM has clear and simple structure without brushes. When it begins running, the stator gets

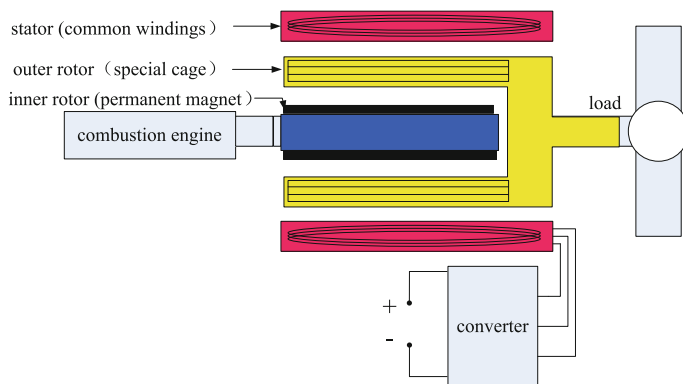


**Fig. 1** Structure of PMB-DMPM

charged, the outer rotor's shaft is driven by the load, and the inner rotor can be connected to other power sources, such as internal combustion engines.

Since the magnetic fields produced by the stator and the inner rotor in PMB-DMPM are two independent rotating magnetic fields with different pole number and speed, in order to make the energy flow, every magnetic field should through the outer rotor produce a rotating magnetic field with the same pole number and speed of another field. The two rotating magnetic fields without direct magnetic coupling can employ the outer rotor to mediate to realize magnetic coupling, and promote the energy transfer between the inner rotor, the outer rotor and the stator. This function of outer rotor is called pole-modulation mechanism.

## 2.2 Pole-Modulation

Some conditions are assumed as following: the stator's surface is smooth, the two magnetic fields in the stator and the inner rotor are independent, and the magnetic fields are sine wave. In the outer-rotor rotating coordinate system, the fundamental MMFs (Magneto Motive Force) generated in the stator windings and the inner rotor are written as:

$$\begin{cases} F_S(x_S, t) = F_{SM} \sin(\omega_{OS}t - P_S x_S) \\ F_I(x_I, t) = F_{IM} \sin(\omega_{OI}t - P_I x_I) \end{cases} \quad (1)$$

where  $\omega_{OS} = P_S \omega_S - P_S \omega_O$ ,  $\omega_{OI} = P_I \omega_I - P_I \omega_O$ ,  $F_S$  is the MMF generated by the stator's windings,  $F_{SM}$  is its amplitude,  $F_I$  is the MMF generated by the inner-rotor permanent magnet,  $F_{IM}$  is its amplitude, both  $F_S$  and  $F_I$  are functions of the position and time,  $x_S$  is the mechanical angle between the location of  $F_{SM}$  and the outer-rotor reference axis,  $x_I$  is the mechanical angle between the location of  $F_{IM}$  and the outer-rotor reference axis,  $P_S$  and  $\omega_S$  are the pole pairs' number and mechanical rotation speed of stator magnet field.  $P_I$  and  $\omega_I$  are the pole pairs' number and mechanical rotation speed of the permanent magnet field,  $\omega_O$  is the mechanical rotation speed of the outer rotor,  $\omega_{OS}$  and  $\omega_{OI}$  are electric rotation speed of the stator magnetic field and the permanent magnet magnetic field under the outer rotor reference coordinate system.

The flux densities are:

$$\begin{cases} B_S(x_S, t) = F_S(x_S, t) \cdot \lambda = B_{SM} \sin(\omega_{OS}t - P_S x_S) \\ B_I(x_I, t) = F_I(x_I, t) \cdot \lambda = B_{IM} \sin(\omega_{OI}t - P_I x_I) \end{cases} \quad (2)$$

$\lambda$  is permeability coefficient,  $B_S$  and  $B_I$  are the flux density of the stator's magnetic field and the inner rotor's magnetic field, respectively. If cage structure is selected for the outer rotor, and  $Q$  represents the number of conducting bars, every bar will cut the two magnetic fields. According to the cutting EMF formula, EMF

can be calculated as follows:

$$E(k, t) = E_S(k, t) + E_I(k, t) = B_S(k, t)l\omega_{OS} + B_I(k, t)l\omega_{OI} \quad (3)$$

where  $E_S(k, t)$ ,  $E_I(k, t)$  represent electromotive forces generated in the stator magnetic field and the inner-rotor magnetic field, respectively.  $B_S(k, t)$  and  $B_I(k, t)$  represent the flux density of stator field and permanent magnetic field at the  $k$ th bar,  $k = 0, 1, 2, \dots, Q - 1$ ,  $l$  is the length of bar. Since

$$\begin{cases} B_S(k, t) = B_{SM} \sin(\omega_{OS}t - \frac{2P_S\pi}{Q} \cdot k) \\ B_I(k, t) = B_{IM} \sin(\omega_{OI}t - \frac{2P_I\pi}{Q} \cdot k) \end{cases} \quad (4)$$

Thus,

$$\begin{cases} E_I(k, t) = B_{IM} \sin(\omega_{OI}t - \frac{2P_I\pi}{Q} \cdot k)l\omega_{OI} \\ E_S(k, t) = B_{SM} \sin(\omega_{OS}t - \frac{2P_S\pi}{Q} \cdot k)l\omega_{OS} \end{cases} \quad (5)$$

To make sure the frequency of  $E_S$  and  $E_I$  are the same, it can be assumed that  $|\omega_{OI}| = |\omega_{OS}|$ .

If  $\omega_{OI} = -\omega_{OS}$ ,

$$\begin{aligned} E_I(k, t) &= B_{IM} \sin(\omega_{OI}t - \frac{2P_I\pi}{Q} \cdot k)l\omega_{OI} \\ &= -B_{IM} \sin(-\omega_{OS}t - \frac{2P_I\pi}{Q} \cdot k)l\omega_{OS} \\ &= B_{IM} \sin(\omega_{OS}t + \frac{2P_I\pi}{Q} \cdot k)l\omega_{OS} \end{aligned} \quad (6)$$

To make EMFs in all cage have the same phase,

$$\omega_{OS}t + \frac{2P_I\pi}{Q} \cdot k = \omega_{OS}t - \frac{2P_S\pi}{Q} \cdot k + 2\pi \cdot k \quad (7)$$

This is,  $Q = P_I + P_S$ .

Therefore, if  $\omega_{OI} = -\omega_{OS}$ ,  $Q = P_I + P_S$ , two magnetic fields in the cage outer rotor can induce two electromotive forces with the same frequency and phase. In order to reduce other unexpected harmonics, the number of cage bars should be integral multiples of  $P_I + P_S$ , and the bars are divided into  $P_I + P_S$  groups, which of them can be connected concentrically.

Further analysis should be made to figure out the relationship mode of the outer-rotor speed, the stator magnetic field rotating speed and the permanent magnet rotor speed. On condition that  $\omega_{OI} = -\omega_{OS}$ , the stator magnetic field rotation speed, the rotation speed of the inner rotor and outer rotor speed should meet the following relationship:

$$P_S\omega_S - P_S\omega_O = -(P_I\omega_I - P_I\omega_O) \quad (8)$$

So, the rotation speed of the outer rotor is:

$$\omega_O = \frac{P_I\omega_I + P_S\omega_S}{P_S + P_I} \quad (9)$$

Another expression

$$n_O = \frac{P_I n_I + 60f_S}{P_S + P_I} \quad (10)$$

$n_I$ ,  $n_O$  represent the rotation speed of the inner rotor and outer rotor (rev/min).  $f_S$  represents stator current frequency.

On the other hand, the stator with tooth shape can generate harmonics magnetic fields beside fundamental magnetic field:

$$\begin{aligned} B_{SZ}(x_S, t) &= B_{S_z} \sin(\omega_{OS}t - P_S x_S) \cdot \sin\left(P_S \frac{Q}{P_S} x_S\right) \\ &= -\frac{B_{SZ}}{2} \left[ \cos(\omega_{OS}t + P_S(\frac{Q}{P_S} - 1)x_S) - \cos(\omega_{OS}t - P_S(\frac{Q}{P_S} + 1)x_S) \right] \\ &= B_{SZ1} + B_{SZ2} \end{aligned} \quad (11)$$

where  $B_{SZ}$  is harmonics magnetic fields. It can clearly be seen that the tooth harmonics can be broken down into  $B_{SZ1}$  and  $B_{SZ2}$ . They are all rotating magnetic fields with constant amplitude. The pole pairs' number of  $B_{SZ1}$  is  $Q - P_S$ , and the rotation direction is opposite to the fundamental magnet field. Therefore when  $Q = P_I + P_S$ , the speed, the number of pole pairs and the direction of  $B_{SZ1}$  are the same to the main magnetic field established by the permanent magnet field. Therefore, the stator can not only generate a fundamental magnetic field, but also can obtain a magnetic field component which keeps the same to the permanent magnet through the harmonic modulation. Similarly, the permanent magnet can not only produce a fundamental magnetic field, but can also obtain a magnetic field component that is the same to the stator's main magnetic field.

In summary, when  $Q = P_I + P_S$  and  $\omega_{OS} = -\omega_{OI}$ , by the cage rotor's modulation, the stator magnetic field and the permanent magnet field can generate the rotating magnetic field consistent with the same pole number and speed between them, and thus the permanent magnet and the stator magnetic field can achieve energy conversion through the cage out rotor.

### 3 The Simulation

To verify the modulation process of PMB-DMPM, PMB-DMPM is constructed in Ansoft Maxwell and the simulation of magnetic field modulation has been conducted. PMB-DMPM's main parameters: the number of slots in stator is 36,  $P_S = 3$ ,  $P_I = 1$ ,  $Q = 20$ , which is divided into  $P_I + P_S = 4$  groups, each group owns 5 bars. The two adjacent groups is connected by a short circuit ring, concentric connection exists within each group, and the sample PMB-DMPM is shown in Fig. 2.

#### 3.1 Magnetic Field Produced by Stator Windings

Removing the permanent magnet of the inner rotor, charging the three-phase AC power, phase A =  $500\sin(2\pi * 40 * t)$  volts in the stator windings, we can get a simulation result. As shown in Fig. 3a and b, there can be clearly seen three pairs of poles in the stator and one pair of poles in the inner rotor. Through FFT analyzing the air gap magnetic field, as shown in Fig. 3c, the magnetic field components get three pairs of poles as predominant; one pair of pole component produced by cage rotor's modulating is subordinated.

#### 3.2 Magnetic Field Produced by Permanent Magnet of Inner Rotor

When the stator winding is powered off and the inner rotor has one pair of permanent magnets, the simulation result is shown in Fig. 4a and b. Obviously a magnetic field with one pair of poles in the core can be seen. By FFT analysis, a

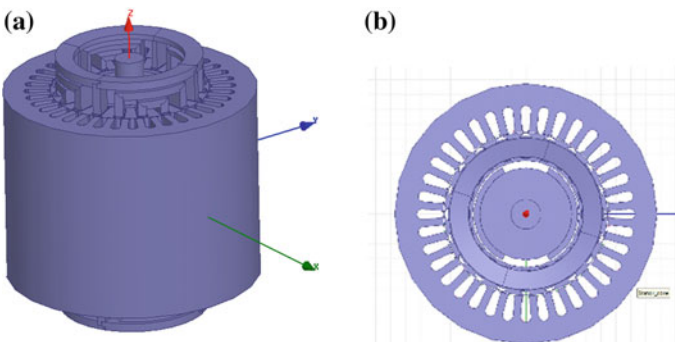
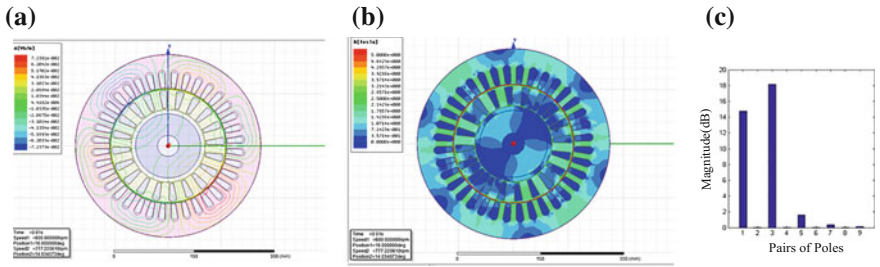


Fig. 2 Sample PMB-DMPM



**Fig. 3** Stator field and its modulation. **a** Flux linkage, **b** flux density, **c** energy of individual field component

magnetic field with 3 pairs of poles is generated by modulation, but the content is not high, as shown in Fig. 4c. Certainly, there are other harmonic components of 5, 7 and 9.

If the stator winding is charged and inner rotor with permanent magnet is rotating, the results are obtained as shown in Fig. 5. There are two magnetic field components: one is one pair of poles, and the other is 3 pairs of poles.

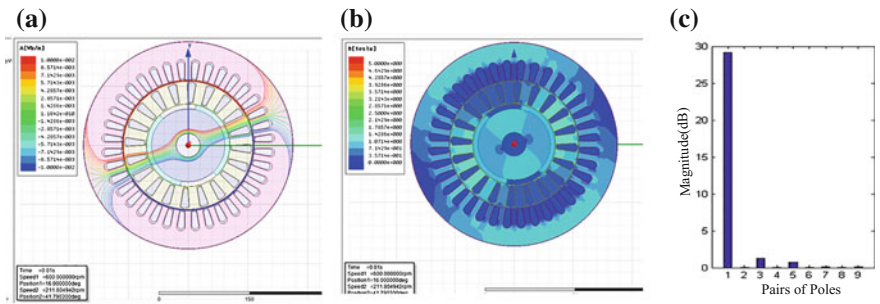


**Fig. 4** The inner rotor magnetic field and its modulation. **a** Flux linkage, **b** flux density, **c** energy of individual field component

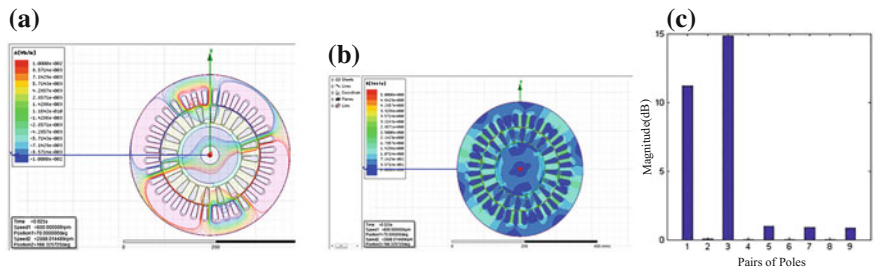


**Fig. 5** Mixing magnetic field and its modulation. **a** Flux linkage, **b** flux density, **c** energy of individual field component



## 4 Conclusions

The biggest advantage of dual mechanical ports motor lies in two features: simple structure and without brushes. Through the modulation of the cage-type outer rotor, the two magnetic fields produced by the stator winding and the inner rotor's magnetic field, can generate a magnetic field component consistent with each other, respectively. As a result, every energy source can transfer in the two magnetic fields, and this process sets the foundation for the running of PMB-DMPM. The construction and the design of PMB-DMPM can be accomplished according to this principle.

**Acknowledgements** This work is sponsored by the Science Funding of Hubei Province's Education Department (No. Q20141111) and the Science Funding of Wuhan University of Science and Technology (No. 2014XG012).

## References

1. Nordlund E (2005) The four-quadrant transducer system [Ph.D.]. Royal Institute of Technology, Stockholm
2. Hoeijmakers MJ, Rondel M (2004) The electrical variable transmission in a city bus. In: IEEE 35th annual power electronics specialists conference, Aachen, Germany, vol 4, pp 2773–2778
3. Xu L, Zhang Y, Wen X (2009) Multi-operational modes and control strategies of dual-mechanical-port machine for hybrid electrical vehicles. *IEEE Trans Ind Appl* 2(45):747–755
4. Zheng P, Liu R, Thelin P et al (2007) Research on the parameters and performances of a 4QT prototype machine used for HEV. *IEEE Trans Mag* 43(1):443–446
5. Zheng P, Liu R, Wu Q et al (2007) Magnetic coupling analysis of four-quadrant transducer used for hybrid electric vehicles. *IEEE Trans Mag* 34(6):2597–2599
6. Liu R, Zhao H, Tong C et al (2009) Experimental evaluation of a radial-radial-magnet compound-structure permanent-magnet synchronous machine used for HEVs. *IEEE Trans Mag* 45(1):645–649
7. Zheng P, Bai J, Tong C et al (2013) Investigation of a novel radial magnetic-field-modulated brushless double-rotor machine used for HEVs. *IEEE Trans Mag* 49:1231–1241
8. Chen X, Pang T, Huang S, Wan S (2013) Control of the dual mechanical port electrical machine and its applications in hybrid electrical vehicle. *Institute of Electrical Engineers of Japan. Trans Electr Electron Eng* 8(1):94–100

# A Measurement Design for Pantograph Contact Force

Yuan Zhong, Pengfei Zhang and Jiqin Wu

**Abstract** Contact force between pantographs and overhead contact line used to evaluate contact quality should be measured properly. Nowadays, force sensors are usually assembled in pantograph head that appearance and dynamic performance of pantograph could be changed and influenced. To solve the problem, the authors designed a rod-type force sensor to replace the pantograph head pivot. At first, it is theoretically analyzed that force sensors can be placed not only in pantograph head but also in frame, and inertial correction is required. Aiming at a domestic pantograph, a force sensor was designed based on calculation. Furthermore, test results show great linearity and accuracy, which is over 90% with only inertial correction of pantograph head that satisfied the requirement of EN50317. With full correction, accuracy of the measurement system can reach 94%.

**Keywords** Force sensor · Contact force measurement · Pantograph

## 1 Introduction

Pantograph and overhead contact line system is to transit power to trains. During working, contact force should be limited in an acceptable range for reliable current collecting. By monitoring contact force, some potential failure may be detected. In addition, site data can be used to verify simulation of pantograph and overhead contact line system. Therefore appropriate measurement should be taken.

According to EN50317 [1], the measurement of contact force shall be carried out on the pantograph using force sensors that shall be located as near as practicable to the contact points. And contact force shall be compensated by temperature and inertia force, barely effected by magnetic field, air flow and mass change.

---

Y. Zhong (✉) · P. Zhang · J. Wu  
Southwest Jiaotong University, 111 North 1st Section, 2nd Ring Road,  
Chengdu, Sichuan, China  
e-mail: zhongyuan@my.swjtu.edu.cn

More importantly, only vertical component of the contact force that be defined as vertical force on all contact points in EN50367 [2] shall be measured.

Cases [3–5] gave applications of load cells to measure contact force of the pantographs. These distinctive designs integrated accelerators with load cells, so that inertia force of pantograph head can be calculated and compensated into contact force. The method using load cell is sound, but paper [5] clearly shows that additional load cells reduce lifting force 50–60%. In addition, pantograph head suspensions are different so measurement design cannot be the same.

In recent years, with the development of measurement technology, new methods were published: Schroeder [6–8] and Bocciolone [9, 10] assembled fiber optic sensor directly onto pantograph head to measure the contact force. It voids the problem of isolation between high voltage condition and low voltage condition. But Bocciolone points out that thermal compensation of FBG sensors is a problem and need further discussion. Japanese researchers [11, 12] measured displacement of pantograph head and upper frame by image processing technology. The results satisfied the requirements of EN50317 with less than 10% error. However it need further discussion when spring of elastic structure is not linear.

Briefly speaking, mentioned methods don't have strong generality. However contact force became more important in pantograph and overhead contact line system, especially when trains' speed increasing. Therefore, it needs a more general force sensor to bring less influence and more accuracy.

## 2 Model Analyses

### 2.1 Force Sensor

Usually to measure force, there are two ways, spring scale and strain gauge. No matter which way, force is reflexed as deformation and measured in Hooke's Law. It assumes that force sensors are connected to pantograph rigidly and only deformation occurs in the deformation zone of force sensors. Then force sensors can be seen as a spring with lumped masses  $m_{01}$  and  $m_{02}$  at both ends and reading can be expressed as  $k_0(x_1 - x_2)$ .

Lumped masses can be got by weighting, and additional fixture of force sensors should be always considered. In this case,  $m_{01}$  and  $m_{02}$  are assumed to be 0.1 kg.

Usually the deformation of force sensors could be very small. The stiffness of force sensors  $k_0$  can be calculated according to force and deformation.

Because stiffness of force sensors is much larger than the one in pantograph mass model. In rough calculation, the stiffness is allowed to be  $10^{10}$  N/m.

## 2.2 Pantograph

In pantograph and overhead contact line system simulation, pantographs are usually be seen as a mass-damping-spring model, as shown in Fig. 1. Parameters in the model can be found in EN50318 [13], shown in Table 1.

According to the model, dynamic equations can be got.

$$m_1\ddot{x}_1 + c_1\dot{x}_1 - c_1\dot{x}_2 + k_1x_1 - k_1x_2 - F_c = 0 \tag{1}$$

$$m_2\ddot{x}_2 - c_1\dot{x}_1 + (c_1 + c_2)\dot{x}_2 - k_1x_1 + (k_1 + k_2)x_2 = 0 \tag{2}$$

To evaluate dynamics of the system, the easiest way is to get its natural frequencies. When damping is not considered, the natural frequencies are respectively 0.24 and 4.68 Hz.

## 3 Sensors in Pantograph

In EN50317, it straightly points out that force sensor should be located as near as practicable to the contact points. Considering zigzag arrangement of overhead contact wires, it is inclined to place force sensors out of contact strips. So in most cases, force sensors were arranged near the suspension.

**Fig. 1** Spring-mass-damping of a pantograph

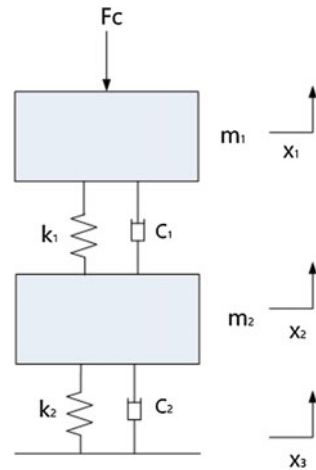


**Table 1** Pantograph parameters given in EN50318

Mass	Unit kg	Spring	Unit N/m	Damping	Unit Ns/m
m1	7.2	k1	4200	c1	10
m2	15	k2	50	c2	90

It is assumed that force sensors are directly assemble to pantograph, and the connection is rigid. In this condition, pantograph collector head is divided into 2 parts. The model of pantograph with force sensors can be got as Fig. 2 shows. When force sensors are assembled in frame, pantograph model is as Fig. 3 shows.

When sensors in pantograph head, dynamic equations can be got:

$$\left(m_1 - m' + \frac{m_0}{2}\right)\ddot{x}_1 + c_0\dot{x}_1 - c_0\dot{x}' + k_0x_1 - k_0x' = F_c \tag{3}$$

$$\left(\frac{m_0}{2} + m'\right)\ddot{x}' - c_0\dot{x}_1 + (c_0 + c_1)\dot{x}' - c_1\dot{x}_2 - k_0x_1 + (k_0 + k_1)x' - k_1x_2 = 0 \tag{4}$$

$$m_2\ddot{x}_2 - c_1\dot{x}' + (c_1 + c_2)\dot{x}_2 - k_1x' + (k_1 + k_2)x_2 = 0 \tag{5}$$

When sensors in the frame, similar equations are present as follow:

$$m_1\ddot{x}_1 + c_1\dot{x}_1 - c_1\dot{x}' + k_1x_1 - k_1x' = F_c \tag{6}$$

$$\left(\frac{m_0}{2} + m'\right)\ddot{x}' - c_1\dot{x}_1 + (c_0 + c_1)\dot{x}' - c_0\dot{x}_2 - k_1x_1 + (k_0 + k_1)x' - k_0x_2 = 0 \tag{7}$$

$$\left(m_2 - m' + \frac{m_0}{2}\right)\ddot{x}_2 - c_0\dot{x}' + (c_0 + c_2)\dot{x}_2 - k_0x' + (k_0 + k_2)x_2 = 0 \tag{8}$$

Force sensors brings one more freedom into the model as well as a very high natural frequency. When sensors are in pantograph head, the 1st and 2nd mode is

**Fig. 2** Model of pantograph with force sensors in collector head

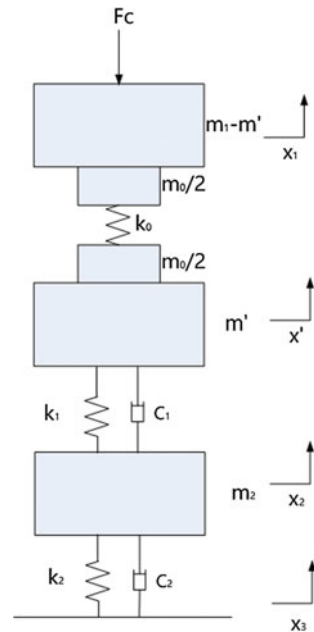
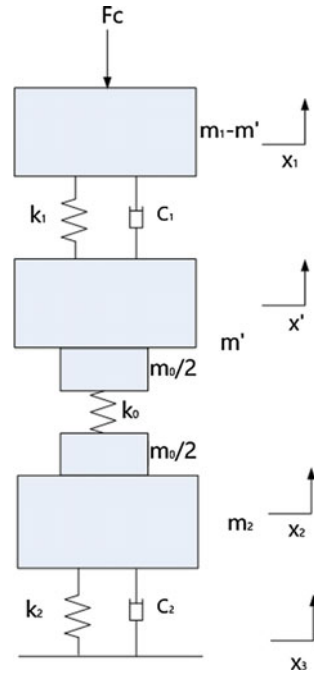


**Fig. 3** Pantograph model with force sensors in frame



0.24 and 4.64 Hz. And when they are assembled in the frame, natural frequencies of the first 2 model is 0.24 and 4.67 Hz, which are more similar to the origin one. It is suggested that assembling force sensors in frame will bring less impact to pantograph dynamic performance. According to literature [5], aerodynamics could bring much more impact to dynamics of the system. These impacts did not be considered in this paper.

Substitute  $F_c = 100 \sin \omega t$  into Eqs. (3)–(5), and set appropriate tolerance, numerical solution can be got by some mature solver. And then reading of force sensors can be calculated as well as inertial correction.

Measured force will changes with  $m'$  and frequencies. As we can see in Fig. 4, max error occurs at natural frequency 4.6 Hz. And as  $m'$  grows, errors become less. Therefore, it was verified that force sensor should be located as near as practicable to the contact points as mentioned in EN50317.

In a similar way, motion of bodies in Fig. 3 can be got. According to Eqs. (6) and (7), measured contact force is

$$F_c = m_1 \ddot{x}_1 + \left( \frac{m_0}{2} + m' \right) \ddot{x}' + k_0 (x' - x_2) \tag{9}$$

According to Eq. (9), inertial force of collector head and partial frame should be used as correction. Figure 5 shows the measured force with changes of  $m'$  and frequency.

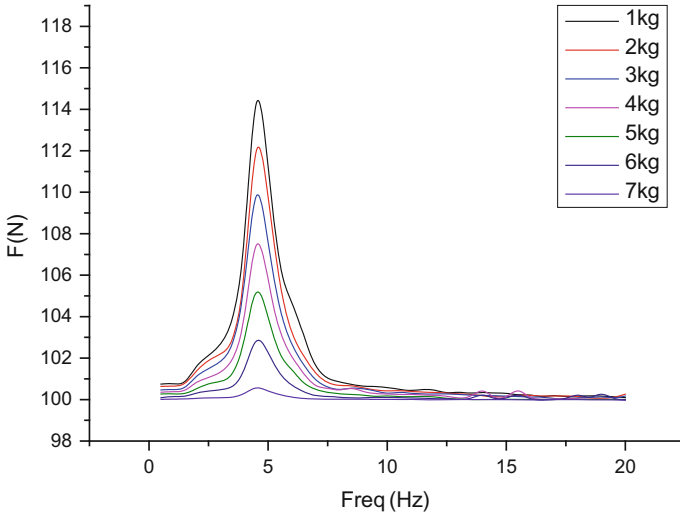


Fig. 4 Measured force when force sensors are in pantograph head

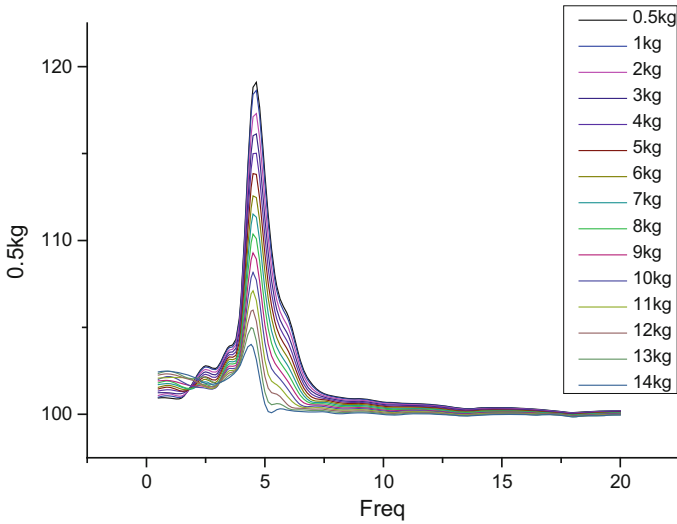


Fig. 5 Measured force when force sensors are in pantograph frame

Measured force changes with frequency. And the max error occurring at natural frequency is slightly greater than the one when force sensors in pantograph head, but is less than 20% which is desirable.

Surprisingly,  $m'$  increases, errors decreased on the contrary. However when  $m'$  is very small, its inertial force can be neglected, then correction become simpler.

According to calculation results, force sensors can be placed in frame and accuracy is acceptable.

## 4 Sensor Design

To minimize aerodynamic effects of force sensor, it is ideal to make the force sensor as the original parts in appearance and weight. In this way, sensors can be daily used as a part of pantograph. And it is helpful for monitoring of pantograph and contact line system.

Considering that there are various kinds of elasticity structure connecting collector head and upper frame as a suspension, it is difficult to get a common solution to replace them. However, pantograph head and frame structure are similar in pantographs. As discussed above, force sensors can get accurate results no matter where they assembled if there are accelerators attached to proper parts of pantograph to get inertial force compensated. The author design a rod-type force sensor to replace the inner axle of collector head pivot in upper frame for following reasons:

- Collector head pivots are widely used in nearly all kinds of pantographs, no matter they are single-arm type, double-arm type or else. Slightly change can make it widespread use.
- The collector head pivot is hollow structure containing 2 pipes. The outer pipe is welding to pantograph frame, and the inner one is detachably connected to pantograph head suspension. Bearings support inner the axle for rotating at end of outer pipe. Pantograph head may rotate during traveling, but mounting plane of the axle is always parallel to contact plane of all strips that vertical component of contact force transferred to the inner pipe.
- Little appearance change makes no aerodynamic performance to pantograph. And weight can be controlled in structure design and material selection, so this design will not affect pantographs.

Considering about the above facts, it is decided to add deform zooms in the pantograph head pivot, and make it as a force sensor. And accelerators are attached on pantograph head and pivot tail.

An example to a certain domestic pantograph is given as follow. The pantograph head is attached to the pantograph head pivot by 4 M6 screws. The original inner pipe is shown in Fig. 6. Because in this case, the distance between the bearing and mounting hole is not enough for a deform zoom, the pivot is lengthened as Fig. 6 shows. However lugs of the suspension can be respectively mirrored and make spare room for the deform zoom. No additional fixed part need in this case.

To maintain the weight, radius of the force sensor center section was reduced. But comparing to the ordinary, the designed sensor is 1.5 kg heavier. Considering the extra weight, natural frequency changed only about 0.06 Hz. The change of nature frequency is very small, so it can be thought that dynamics of the pantograph remains.



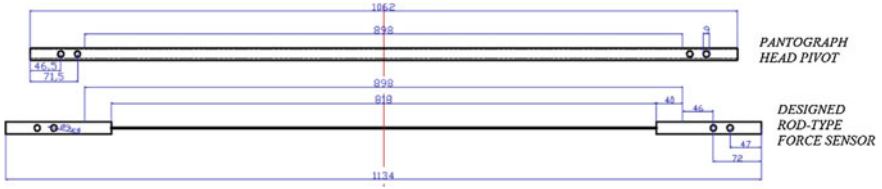


Fig. 6 Designed force sensor

### 5 Measurement Results

To verify, the rod-type force sensor was equipped to the experiment pantograph. Pantograph was limited at 650 mm height and standard force sensor connecting an exciter is mounted over contact point. During the test, uplifting force was changed by air pressure. Results from standard force sensor and designed rod-type force sensor were recorded by computer.

At first, the exciter did not work, and only uplifting force changed. Results from standard force sensor and designed force sensor are shown in Fig. 7. Results shows great linearity and has little difference to the standard sensor.

Then, the vibrate exciter was controlled to do sine wave motion in different frequencies. Force measured by the standard force sensor and the designed force sensor were recorded as well as acceleration of the pantograph head and pivot tails.

Measured force from designed force sensor should be inertial corrected according to Eq. (9). In the design case, suspensions are directly connect to the force sensor, the mass is about 0.8 kg. The inertial force is not remarkable. So in the test, the results were corrected in both ways.

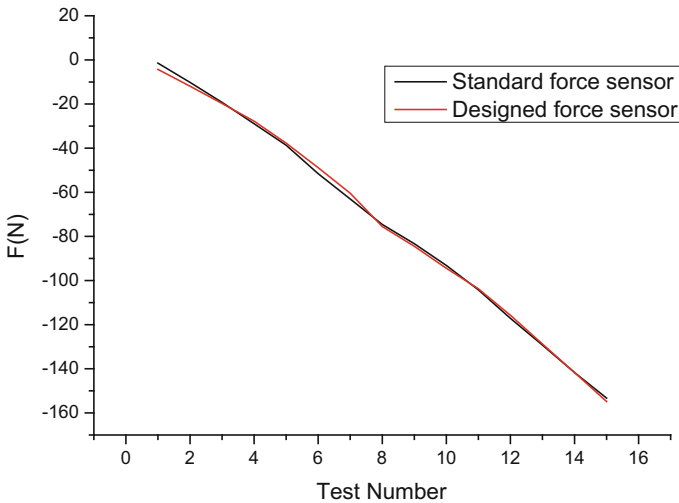
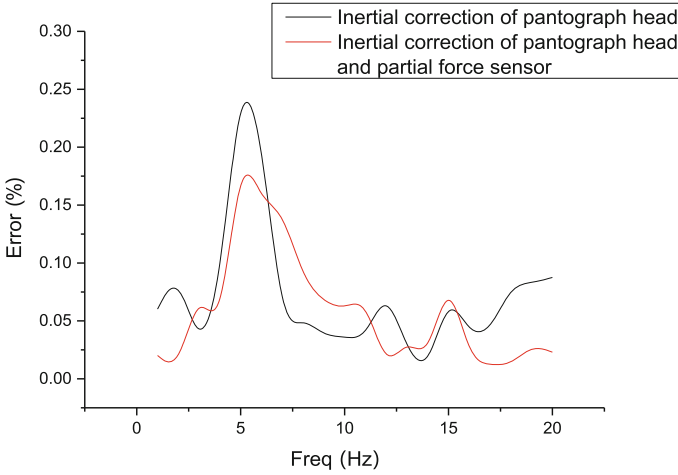


Fig. 7 Measured results from standard and designed force sensor



**Fig. 8** Errors in different frequencies

Take  $\left|1 - \frac{F_{measured}}{F_{applied}}\right|$  as the error in each frequency, Fig. 8 can be obtained.

As we can see, when only inertial correction of pantograph head is taken, errors goes over 20% at the natural frequency of the pantograph about 5 Hz, and then decreases to about 5%. Results with both inertial correction are more smooth and steady that errors are no more than 20%, even at the natural frequency of the pantograph. Test results are similar to simulation results in Sect. 3, it is verified the model to some extent.

According to EN50317, accuracy of contact force measurement system should be calculated as

$$J = \left(1 - \frac{1}{(f_n - f_1)} \sum_{i=1}^{n-1} \left((f_{i+1} - f_i) \left|1 - \frac{F_{measured}}{F_{applied}}\right|\right)\right) \quad (10)$$

The accuracies with partial and full inertial correction are 92.7% and 94.1% respectively. According to EN50317, accuracy should be greater than 90% up to 20 Hz. Therefore with either compensation, the designed force measurement is qualified. And with full compensation, measurement results are better.

## 6 Discussions

In this paper, force sensor is equivalent to a mass-spring model and substitute into a pantograph mass-spring-damping model. By solving its dynamic equations, motion of every parts can be obtained. Base on simulation, force sensors can be placed

anywhere in pantograph and error of contact force measurement system could increase at pantographs' natural frequencies.

Based on these conclusions, a rod-type force sensor was designed to replace pantograph head pivot to get contact force. Test results show that the designed force sensor has great linear and can measure contact force accurately. In line with EN50317, accuracies of the contact force measurement system with partial/full compensation are 92.7% and 94.1% satisfying the requirement 90%. Therefore this system is convinced to be valid and practicable.

However, there are still some problems that need further research. The designed force sensor haven't been applied in site tests. And there is no temperature compensation. Influence from longitude force such as friction was either not considered in the model or tested. In addition, the weight can be further reduced for daily use.

**Acknowledgements** This work was supported by the National Natural Science Foundation of China (U1534209).

## References

1. CENELEC (2012) BS EN 50317:2012 Railway application-current collection systems-requirements for and validation of measurements of the dynamic interaction between pantograph and overhead contact line. BSI, Brussels
2. CENELEC (2012) BS EN 50367:2012 Railway application-current collection systems-technical criteria for the interaction between pantograph and overhead line (to achieve free access). BSI, Brussels
3. PEOSE AG (2017) Measurements on pantographs in line with EN 50317. Swiss [cited 2017 April 10] [http://www.prose.one/DesktopModules/PRO\\_CaseHistory/files\\_ch/4-3\\_000.pdf](http://www.prose.one/DesktopModules/PRO_CaseHistory/files_ch/4-3_000.pdf)
4. Kiessling F, Puschmann R, Schmieder A (2017) Contact lines for electric railways: planning, design, implementation, maintenance, 3rd edn. Wiley
5. Seo SI, Cho YH, Mok JY et al (2006) A study on the measurement of contact force of pantograph on high speed train. *J Mech Sci Technol* 20(10):1548–1556
6. Schroeder K, Ecke W, Kautz M et al (2007) Fiber optical sensor network embedded in a current collector for defect monitoring on railway catenary. In: Fancesco B, Jiri H, Robert AL, Miroslav M (ed) *Proceedings of the SPIE, optical sensing technology and applications*
7. Schröder K, Ecke W, Kautz M et al (2013) An approach to continuous on-site monitoring of contact forces in current collectors by a fiber optic sensing system. *Opt Lasers Eng* 51(2): 172–179
8. Schröder K, Rothhardt M, Ecke W et al (2017) Fibre optic sensing system for monitoring of current collectors and overhead contact lines of railways. *J Sens Sens Syst* 6(1):77
9. Boccione M, Bucca G, Collina A et al (2013) Pantograph–catenary monitoring by means of fibre Bragg grating sensors: results from tests in an underground line. *Mech Syst Signal Process* 41(1–2):226–238
10. Boccione M, Bucca G, Collina A et al (2010) Comparison of optical and electrical measurements of the pantograph-catenary contact force. *Proceedings of SPIE Intern Soc Opt Eng* 7653(1):99–106
11. Koyama T, Ikeda M, Nakamura K et al (2012) Measuring the contact force of a pantograph by image processing technology, pp 189–198

12. Koyama T, Ikeda M, Nakamura K et al (2011) 101 Measuring the contact force of pantograph by line sensor cameras and trapezoid marker. In: The Japan society of mechanical engineers editors: symposium on evaluation and diagnosis
13. CENELEC (2002) BS EN 50318:2002 Railway application-current collection systems-validation of simulation of the dynamic interaction between pantograph and overhead contact line. BSI, Brussels

# Cooperative Control of Voltage Equalization for Multiple Supercapacitors

Ying Yang, Yanlin Zhang, Yejun Mao, Junmin Peng  
and Fangrong Wu

**Abstract** In this paper, a cooperative voltage equalizer is proposed such that the voltages of supercapacitors in the power source achieve consensus. Voltage equalization for supercapacitors in the power source is a crucial issue since unbalanced voltage states would result in inefficiency and acceleration of lifetime decay. As multiple supercapacitors are connected in certain form, the power source can be modeled as a networked system. In this view, voltage equalization problem can be formulated as a consensus problem of multi-agent system. Combining cooperative control theory and Lyapunov method, a distributed controller is designed for each supercapacitor to drive its voltage synchronized to its neighbors in the network. It is proved that under the topology condition that the graph is connected, all voltages of supercapacitors can achieve consensus, i.e., voltage equalization of the power source is achieved. Simulation result has been presented to verify the effectiveness of the proposed controller.

**Keywords** Supercapacitor · Voltage equalization · Consensus  
Cooperative control

## 1 Introduction

Recently, energy storage type tramcar attracts engineers attention due to its traction power source, which is composed by multiple supercapacitors [1]. As an efficient energy storage element, supercapacitor has significant advantages, such as high power density, extremely high cycling capability and environment friendly [2].

---

This work is support by National Natural Science Foundation (NNSF) of China under Grant 61741315 and Natural Science Foundation of Hunan Province under Grant 2017JJ4056.

---

Y. Yang · Y. Zhang · Y. Mao · J. Peng (✉) · F. Wu  
CRRC Zhuzhou Locomotive Co., Ltd., Zhuzhou 412000, Hunan, People's Republic of China  
e-mail: eejmpeng@hotmail.com

In application, multiple supercapacitors are series-connected or parallel-connected together to compose the power source in order to satisfy the voltage requirement. In this view, it can be modeled as a multi-agent system. Due to the different parameters of each supercapacity such as capacity, internal impedance, self-discharge rate and so on, the voltages of supercapacitors are inevitably be different [3]. On account of efficiency and safety, voltage of each supercapacitor should be equalized in application, which is a challenging problem not only in power source that composed by supercapacitors but also by batteries [4]. The key issue of voltage equalization problem is to design control strategy such that the higher voltages are reduced while the lower ones are increased, no matter which type of circuit is employed to carry out the task [5]. In general, voltage equalization strategy is divided into two classes: dissipative and non-dissipative approach. Dissipative equalization mainly focus on consuming the extra energy of some supercapacitors to realize voltage balanced, for the sake of circuit simplicity but with the shortcoming of energy waste [6]. On the other hand, non-dissipative equalization carry out the task by transferring extra energy from higher voltage ones to the lower ones [7], such as DC/DC converters [8], switch capacitor converter [9] and so on. Although non-dissipative equalization has the advantage of efficiency, it increases the hardware cost. Considering reliability and cost, in this paper, we propose the voltage equalizer which is based on dissipative equalization.

In power source, supercapacitors are series-connected or parallel-connected, on the other hand, their states, such as voltage, are transferred throughout CAN BUS. In this view, the voltage equalization problem of power source can be equated with the consensus problem of multi-agent system. To the best of our knowledge, most existing works solve the problem via centralized control. In past decades, distributed control of multi-agent system has attracted intensive attention in the literature, due to its applications in various areas such as formation flight of unmanned aerial vehicles (UAVs), cluster of satellites, automated highway systems [10–12]. Combined graph theory and stability analysis, various controllers for cooperative control of networked systems have been proposed as documented in the reference papers [13, 14] and books [15, 16].

In this paper, the voltage equalization problem of power source which is composed by multiple supercapacitors is transferred into the consensus problem in cooperative control. A distributed voltage equalizer has been designed via graph theory and Lyapunov method to achieve the voltage consensus of all supercapacitors.

The rest of this paper is organized as follows: The voltage equalization problem is formulated as the consensus problem in Sect. 2, a distributed controller is proposed for each supercapacitor to achieve voltage consensus in Sect. 3. Then a numerical example is given in Sect. 4 to illustrate the effectiveness of the proposed controller. Finally, conclusion and future work are given in Sect. 5.

## 2 Problem Formulation

### 2.1 Preliminary

Throughout this paper,  $R^{m \times n}$  denotes the family of  $m \times n$  real matrices.  $M \geq (\leq) 0$  means that  $M$  is a semi-positive(semi-negative) definite matrix,  $M > (<) 0$  means that  $M$  is a positive(negative) definite matrix.

We introduce some graph terminologies that can be found in [10]. A weighted graph is denoted by  $G = (V, \zeta)$ , where  $V = \{1, 2, \dots, N\}$  is a nonempty finite set of  $N$  nodes, an edge set  $\zeta \subseteq V \times V$  is used to model the communications among agents. The neighbor set of node  $i$  is denoted by  $N_i = \{j | j \in V, (i, j) \in \zeta\}$ .  $j \notin N_i$  means there is no information flow from node  $j$  to node  $i$ . A sequence of successive edges in the form  $\{(i, k), (k, l), \dots, (m, j)\}$  is defined as a directed path from node  $i$  to node  $j$ . An undirected path in undirected graph is defined analogously. A directed graph is strongly connected if there is a directed path from every node the every other node. For the undirected graph, it is said to be connected if there is a path from node  $i$  to node  $j$ , for all the distinct nodes  $i, j \in V$ .

A weighted adjacent matrix  $A = [a_{ij}] \in R^{N \times N}$ ,  $a_{ii} = 0, \forall i$  and  $a_{ij} > 0, i \neq j$ , if  $(i, j) \in \zeta$  and 0 otherwise. In undirected graph,  $a_{ij} = a_{ji}$ . Define the in-degree of node  $i$  as  $d_i = \sum_j a_{ij}$  and  $D = \text{diag}\{d_i\} \in R^{N \times N}$  is the in-degree matrix. Then, the Laplacian matrix of graph  $L = D - A$ . Let  $\mathbf{1}_N = [1, 1, \dots, 1]^T \in R^N$ , it is well-known that 0 is the one of eigenvalues of the Laplacian matrix  $L$  associated with the eigenvector  $\mathbf{1}_N$ .

**Lemma 1** *Let the undirected graph be connected, then  $L \in R^{N \times N}, L = L^T \geq 0$  and  $\text{Null}(L) = \text{span}\{\mathbf{1}_N\}$ .*

**Lemma 2** *Let the undirected graph be connected and  $G = \text{diag}\{g_1, \dots, g_N\} \neq 0$ , then  $H = L + G > 0$  (Fig. 1).*

Considering each supercapacitor in the power source as an agent in the networked system, the voltage of agent  $i$  is

$$\dot{v}_i = \begin{cases} \frac{1}{C_i} I & t \notin \bar{d}_i T \\ \frac{1}{C_i} \left( I - \frac{v_i}{R_i} \right) & t \in \bar{d}_i T \end{cases} \quad (1)$$

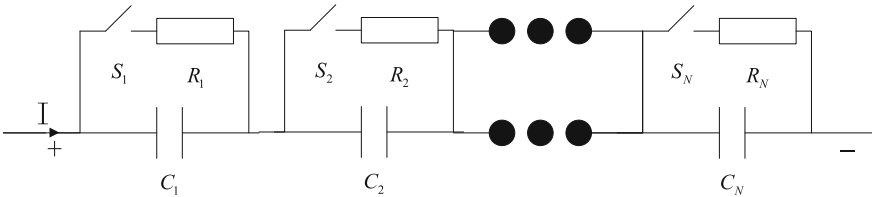


**Fig. 1** Power source together with voltage equalization circuit

where  $v_i \in R$  is the voltage across supercapacitor  $i$ ,  $i = 1, \dots, N$ .  $I$  is the charging or discharging current,  $C_i, R_i$  are the capacity and resistance respectively,  $0 \leq \bar{d}_i \leq 1$  is the duty ratio of the switch  $S_i$  at each period.

*Remark 1* In application,  $C_i$  may be different from the nominal value, as a result, it would be viewed as an unknown constant. The voltage dynamic across each supercapacitor can be formulated as follows with the aid of state space average modeling method.

$$\begin{aligned} \dot{v}_i &= \frac{1}{C_i} I \bar{d}_i + \frac{1}{C_i} \left( I - \frac{v_i}{R_i} \right) (1 - \bar{d}_i) \\ &= -\frac{v_i}{R_i C_i} (1 - \bar{d}_i) + \frac{1}{C_i} I \end{aligned} \quad (2)$$

Let

$$\frac{1}{C_i} \left[ -\frac{v_i}{R_i} (1 - \bar{d}_i) + I \right] = b_i u_i \quad (3)$$

Dynamic model (2) is converted into a first order integrator as follows:

$$\dot{v}_i = g_i u_i \quad (4)$$

where  $u_i$  is the control input to be designed,  $g_i$  denotes the control gain with unknown amplitude.

## 2.2 Control Objective

The control objective of this paper is to design distributed controller  $u_i$  for each agent in the network such that all  $v_i$  reach consensus, such that

$$\lim_{t \rightarrow \infty} \|v_i(t) - v_j(t)\| = 0, \forall i, j \quad (5)$$

Since all voltages achieve consensus, voltage equalization of the each supercapacitor in the power source achieved.

*Remark 2* In application,  $\bar{d}_i$  is the final control signal to be carried out. In the power source,  $u_i$  is designed according to the voltage of itself and its neighbor, i.e.,  $v_i, v_j, \forall i, j \in N_i$ .  $v_i$  and  $v_j$  are transmitted throughout the CAN BUS. As  $u_i$  is designed,  $\bar{d}_i$  can be obtained according to (3).



### 3 Main Result

In this section, a distributed adaptive controller is introduced for each supercapacitor to achieve the voltage equalization objective.

**Theorem 1** *Given a network of  $N$  series connected supercapacitors (4) with fixed communication topology. Under the circumstance that the related undirected  $G = (V, \zeta)$  is connected, then all supercapacitors' voltages achieve consensus, i.e., voltage equalization of the power source is realized if the distributed controller (6) is applied to each supercapacitor in the power source.*

$$u_i = k_i \sum_{j \in N_i} a_{ij} (v_j - v_i) \quad (6)$$

where  $0 \leq k_i \leq \frac{I}{NC_i \bar{v}}$  is the control gain,  $I$ ,  $C_i$  and  $\bar{v}$  are the charging (discharging) current, capacity and the maximum voltage in product instruction,  $N$  is the  $a_{ij}$  is the entry of adjacency matrix related to the digraph  $G = (V, \zeta)$ , which denotes the weight from supercapacitor  $j$  to supercapacitor  $i$ , i.e., the information of the  $j$ th supercapacitor transferred to the  $i$ th supercapacitor throughout the CAN BUS.

*Proof* Define a Lyapunov function component  $V$

$$V = \frac{1}{2} \mathbf{x}^T \mathbf{x} \quad (7)$$

where  $\mathbf{x} = [v_1, \dots, v_N]^T \in R^N$  is the vector of all supercapacitors' voltages. It can be seen that its derivative with respect to time  $t$  along (6) as

$$\dot{V} = -\mathbf{x}^T (L + L^T) \mathbf{x} \quad (8)$$

It can be obtained from Lemmas 1 and 2, matrix  $L + L^T \geq 0$ , thus

$$\dot{V} \leq 0 \quad (9)$$

According to Barabart lemma,  $\mathbf{x} = [x_1, \dots, x_N]^T$  converges to the zero space of matrix  $L + L^T$ . Since  $L = L^T$  when graph is undirected, the null space of  $L$  is  $\mathbf{1}_N = [1, 1, \dots, 1]^T$ , thus,  $v_i \rightarrow v_j, \forall i, j \in V$ .

**Remark 3** The effectiveness of the controller above is proven via taking the derivative of the Lyapunov function  $V$ , then, the semi-positive definite characteristic of graph-related matrix  $L + L^T$  determines the convergence. Theorem 1 indicates that consensus of multiple supercapacitors' voltages can be achieved when distributed controller (6) is applied. But in real system, which is shown in the following figure, the ultimate voltage, i.e., the consensus state is assigned according to the Motor. Therefore, the control objective aforementioned should be extended as follows:

$$\lim_{t \rightarrow \infty} v_i(t) = \lim_{t \rightarrow \infty} v_j(t) = v_0(t), \forall i, j \quad (10)$$

where  $v_0(t)$  is the expected voltage.

**Theorem 2** *Given a network of  $N$  series connected supercapacitors (4) with fixed communication topology. Under the circumstance that the related digraph  $G = (V, \zeta)$  has a spanning tree and at least one supercapacitor can obtain the information of  $v_0(t)$ , then all supercapacitors' voltages achieve consensus, meanwhile, coverage to the desired voltage, i.e., voltage equalization of the power source is realized if the distributed controller (11) is applied to each supercapacitor in the power source.*

$$u_i = k_i \sum_{j \in N_i} a_{ij}(v_j - v_i) + b_i(v_0 - v_i) \quad (11)$$

control gain  $k_i$  is defined as aforementioned, where  $b_i = 1$  if supercapacitor  $i$  can receive the information of  $v_0$ ,  $b_i = 0$  otherwise.

*Proof* Similar to the proof of Theorem 1, the overall system can be written as

$$\dot{\xi} = -(L + B)\xi \quad (12)$$

with  $\xi = [v_1 - v_0, \dots, v_N - v_0]^T \in R^N$ ,  $B = \text{diag}\{b_1, \dots, b_N\} \in R^{N \times N}$ . According to Lemma 2, eigenvalues of matrix  $-(L + B)$  are negative, thus, system (12) is stable, i.e.,  $\xi = [v_1 - v_0, \dots, v_N - v_0]^T \rightarrow 0$ , which completes the proof.

When the graph is directed, under the same positive definite  $V$ , we have the following corollary.

**Corollary** *Given a network of  $N$  series connected supercapacitors (4) with fixed communication topology. Under the circumstance that the digraph  $G = (V, \zeta)$  has a spanning tree and  $v_0(t)$  can be obtained by the root agent, then all supercapacitors' voltages achieve consensus, meanwhile, coverage to the desired voltage, i.e., voltage equalization of the power source is realized if the distributed controller (11) is applied to each supercapacitor in the power source.*

## 4 Simulation

This section will provide a numerical example to illustrate the effectiveness of the proposed controller. Consider a power source that constituted by 4 supercapacitors in series as shown in Fig. 2. The weights of the edges are all set to 1 and thus (Fig. 3).

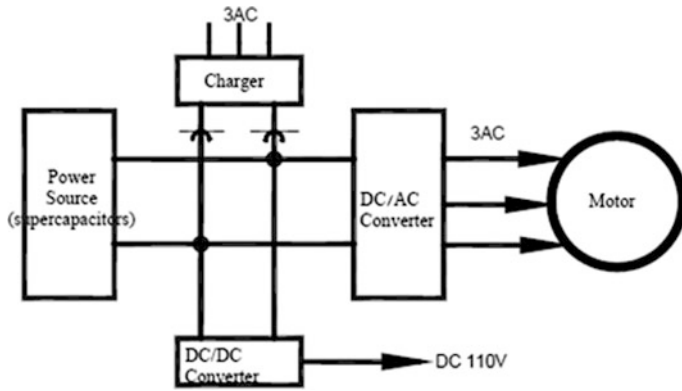


Fig. 2 Structure of traction power source

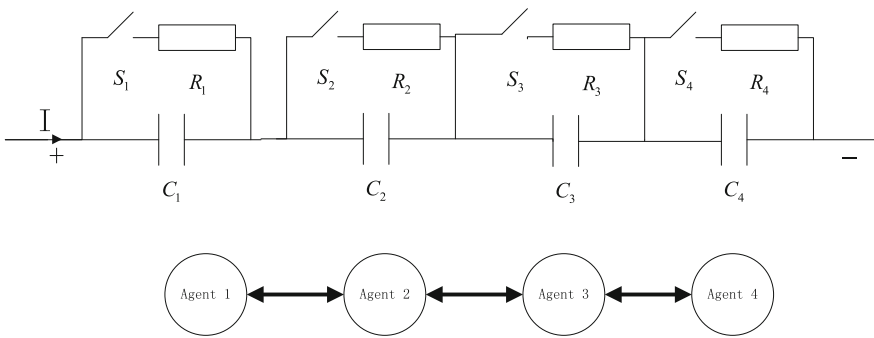


Fig. 3 Example system

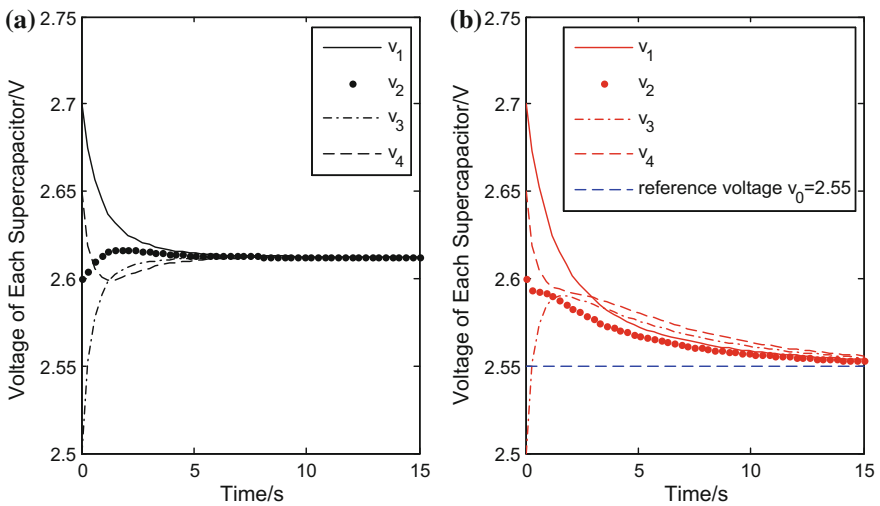


Fig. 4 Voltages of supercapacitors

$$L = \begin{bmatrix} 1 & -1 & 0 & 0 \\ -1 & 2 & -1 & 0 \\ 0 & -1 & 2 & -1 \\ 0 & 0 & -1 & 1 \end{bmatrix}$$

Figure 4a shows that the voltages of all agents (supercapacitors) achieve consensus when the distributed controller in Theorem 1 is applied to each supercapacitor with different initial voltages  $v_1(0) = 2.7$ ,  $v_2(0) = 2.6$ ,  $v_3(0) = 2.5$ ,  $v_4(0) = 2.65$ .

Furthermore, when  $v_0$  is transmitted to one agent (supercapacitor), such as agent 2, controller (11) is proposed for that circumstance. Figure 4b shows that all supercapacitors' voltages are converged to the desired value  $v_0 = 2.55$ .

## 5 Conclusion and Future Work

In this paper, we consider the voltage equalization problem of multiple supercapacitors. Combining Lyapunov method together with graph theory, we construct a Laplacian potential function for analysis. A distributed controller is designed for each supercapacitor, such that the voltages of all supercapacitors achieve consensus under the circumstance that the undirected graph is connected, i.e., voltage equalization of the power source is achieved.

Our future work will consider other equalizer circuits, e.g., non-dissipative equalizer rather than the dissipative equalizer, for efficiency.

## References

1. Allegre AL, Bouscayrol A, Delarue P et al (2010) Energy storage system with supercapacitor for an innovative subway. *IEEE Trans Indust Electron* 57(12):4001–4012
2. Linzen D, Buller S, Karden E et al (2005) Analysis and evaluation of charge-balancing circuits on performance, reliability, and lifetime of supercapacitor systems. *IEEE Trans Ind Appl* 41(5):1135–1141
3. Uno M, Tanaka K (2013) Single-switch multioutput charger using voltage multiplier for series-connected lithium-ion battery/supercapacitor equalization. *IEEE Trans Industr Electron* 60(8):3227–3239
4. Satou D, Hoshi N, Haruna J (2014) Characteristics of cell voltage equalization circuit using LC series circuit in charging and discharging states. In: *Industrial electronics society, IECON 2013—Conference of the IEEE, IEEE*, pp 514–519
5. Liu J, Huang Z, Peng J et al (2015) Distributed cooperative voltage equalization for series-connected super-capacitors. In: *American control conference, IEEE*, pp 4523–4528
6. Wei T, Jia D (2014) Characteristics and design method of supercapacitor modules with voltage equalization circuit. In: *IEEE, conference on industrial electronics and applications, IEEE*, pp 6–11
7. Xu A, Xie S, Liu X (2009) Dynamic voltage equalization for series-connected ultracapacitors in EV/HEV applications. *IEEE Trans Veh Technol* 58(8):3981–3987

8. Hussain A, Lee H, Sul SK (2013) Forward fly-back voltage balancing circuit for series connected super capacitors using digital control. In: International conference on renewable energy research and applications, IEEE, pp 377–382
9. Baughman AC, Ferdowsi M (2008) Double-tiered switched-capacitor battery charge equalization technique. *IEEE Trans Industr Electron* 55(6):2277–2285
10. Shamma J (2007) Cooperative control of distributed multi-agent system. Wiley, Hoboken
11. Cao Y, Yu W, Ren W et al (2012) An overview of recent progress in the study of distributed multi-agent coordination. *IEEE Trans Industr Inf* 9(1):427–438
12. Andreasson M, Dimarogonas DV, Sandberg H et al (2014) Distributed control of networked dynamical systems: static feedback, integral action and consensus. *IEEE Trans Autom Control* 59(7):1750–1764
13. Murray RM (2007) Recent research in cooperative control of multivehicle systems. *J Dyn Syst Meas Control* 129(3):571–583
14. Olfati-Saber R (2006) Flocking on multi-agent dynamic systems: algorithms and theory. *IEEE Trans Autom Control* 51(3):401–420
15. Ren W, Beard R (2008) Distributed consensus in multi-vehicle cooperative control: theory and applications. Springer, London
16. Qu Z (2009) Cooperative control of dynamical systems: applications to autonomous vehicles. Springer, London

# Research on Electromagnetic Environment Safety of High-Speed Railway Catenary

Huijuan Sun, Jun Liu and Can He

**Abstract** The simulation of electromagnetic fields distribution around high-speed railway catenary on the platform by the finite element method. The research is based on simulation models as classification material properties of human body parts, and presents subdivision mesh sub-model method to calculate and simulate the frequency electromagnetic fields around the human, and giving a comprehensive evaluation on the safety of electromagnetic environment around high-speed railway according to national standard limit.

**Keywords** Finite element · High-speed railway catenary · Subdivision mesh sub-model method · Frequency electromagnetic fields

## 1 Introduction

With the increasingly serious environmental problems, traffic transportation and other industry experts believe that high-speed railway as a new transport model in the modern society, has a very distinct advantage. So planning and developing high-speed railway is imperative [1–3]. The development of high-speed railway has caused public concern, therefore it is very important to study the distribution of the frequency electromagnetic field around the high-speed railway platform, and necessary to calculate the electromagnetic radiation on the human body.

Literature [4] measured the electromagnetic changes of the train, there is doubt as to the accuracy due to the impact on the measurement instrument itself; literature [5] studies the relationship between the train material and the low frequency magnetic, but it did not consider the impact of the environment literature [6] by the mirror method to study the different power supply under the contact field of the electric field strength; literature [7] explores biological effects of human under

---

H. Sun · J. Liu (✉) · C. He

School of Electrical and Automation Engineering, East China Jiao Tong University (ECJTU),  
Nan Chang, Jiang Xi, China  
e-mail: ljun930801@163.com

© Springer Nature Singapore Pte Ltd. 2018

L. Jia et al. (eds.), *Proceedings of the 3rd International Conference on Electrical and Information Technologies for Rail Transportation (EITRT) 2017*, Lecture Notes in Electrical Engineering 482, [https://doi.org/10.1007/978-981-10-7986-3\\_16](https://doi.org/10.1007/978-981-10-7986-3_16)

155

the high-voltage transmission line, but it cannot replace the original incentive reasonably.

Based on above-mentioned reasons, the finite element method is used to study the electromagnetic field distribution around the high-speed railway catenary, and subdivision mesh sub-model method is proposed to calculate the electromagnetic radiation around human body. Meanwhile, through analysis of numerical simulation results, to make a comprehensive evaluation of the electromagnetic environment of high-speed railway, which provides the basis for the design of the circuit and the evaluation of the environmental impact.

## 2 High-Speed Rail Platform and Human Body Model

In China, high-speed railway mostly using side platform and AT power supply. Table 1 shows the catenary parameters and the simplified structure drawing of platform is shown in Fig. 1.

In order to investigating whether the electromagnetic field caused by catenary would affect the health of passengers, a more sophisticated human body model is established. The human body are mainly composed of bones, blood, viscera, muscle and other parts, the relative dielectric constant, conductivity and permeability as

**Table 1** Catenary parameters

Name	Line type	Radius (mm)	Voltage (kV)	Current (A)
Line of contact	TCJ-120	6.6	27.5	100
Carrier cable	TCJ-110	5.9	27.5	100
Positive feeder	LJ-185	7.7	-27	-192
Guard line	LJ-70	4.7	0.25	-0.972

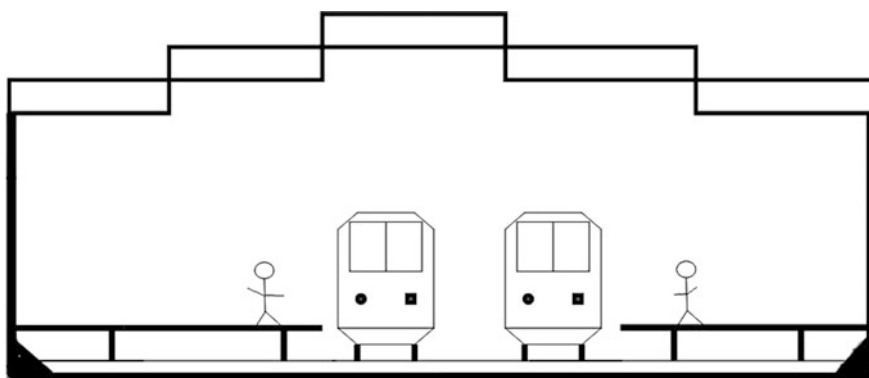


**Fig. 1** The simplified structure drawing of high-speed railway platform

**Table 2** Properties of the human body material parameters

Name of human tissue	Relative dielectric constant	Conductivity	Permeability
Head	500,000	0.045	1
Trunk	9,570,000	0.11	1
Foot	8867.8	0.02	1
Limbs	8,800,000	0.125	1

shown in Table 2. In this paper, the human body consist of limbs, head, trunk and feet, so the dielectric constant and conductivity of each part are replaced by average value.

### 3 Numerical Calculation Method of Electromagnetic Field

#### 3.1 Finite Element Method

The finite element method is a combination of discrete solutions domain as a group of elements. The function of whole is replaced by the approximate function of each unit [8]. The finite element algorithm flow chart is shown in Fig. 2:

The finite element analysis method and the algorithm flow can be realized by ANSOFT finite element analysis software.

#### 3.2 Subdivision Mesh Sub-model Method

The subdivision meshes sub-model method is based on the finite element analysis software that the smaller the length of the mesh is, the more accurate the calculation

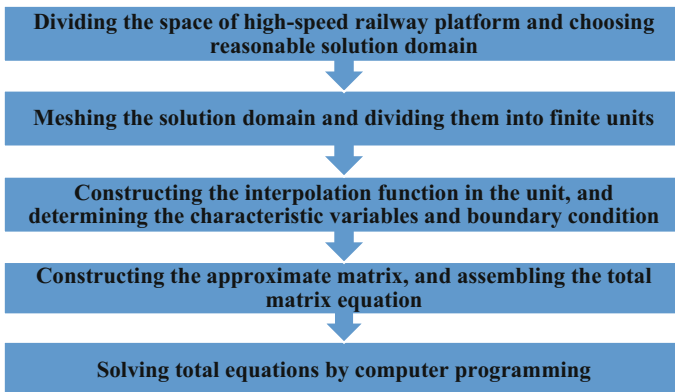


**Fig. 2** Finite element algorithm flow chart



result is. Meanwhile, finding out the equivalent excitation around a certain region in the model, and adding the body of the region, and then finite element calculations are performed to obtain more accurate electromagnetic fields around the human body. Figure 3 shows the specific steps in the below flow chart.

## 4 Numerical Calculation and Analysis of Electromagnetic Fields Around the Human Body

Many countries have their own electromagnetic exposure standards [9]. Table 3 shows the exposure limit of frequency electromagnetic field in China.

### 4.1 Subdivision Mesh Method for Solving Electromagnetic Fields Around Human Body

Excluding external factors, and we select the site without train. Meanwhile extracting 1.5 m long and 2 m wide solution area around the human body, and then meshing it. The region is divided into three dimensions: the grid length is 5, 0.1 and 0.05 m.

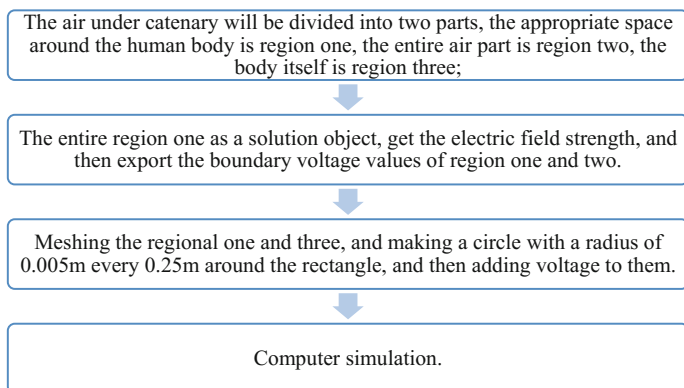


**Fig. 3** Sub model process

**Table 3** Frequency electromagnetic exposure limit

Name	Frequency (Hz)	E (kV/m)	B ( $\mu T$ )	Contact current (mA)
China	50	4	22	0.5

With the decrease of the length of the mesh, the number of grids increases, and the result of grid focusing on the head and feet more obviously. The corresponding electric field intensity and magnetic field intensity distribution as shown in Figs. 4 and 5, respectively.

Figures 4 and 5 show that the electromagnetic field distribution of high-speed railway catenary around human body has the following characteristics: (1) The head and shoulder is close to catenary, and it is easy to accumulate electric charge and form a high electric field, so the electric field intensity around the body is mainly concentrated on the head, shoulders and feet. (2) The internal magnetic field distribution of the human body is uneven, and is mainly concentrated on the legs and feet, and the magnetic field doesn't gather in the head, so the magnetic field of high-speed railway does not harm to the brain.

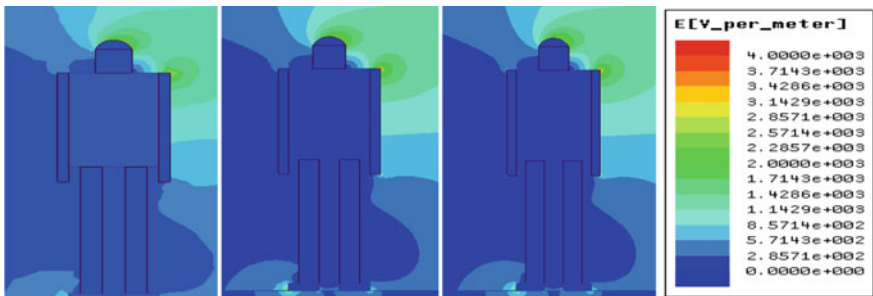


Fig. 4 Distribution of electric field intensity around human body

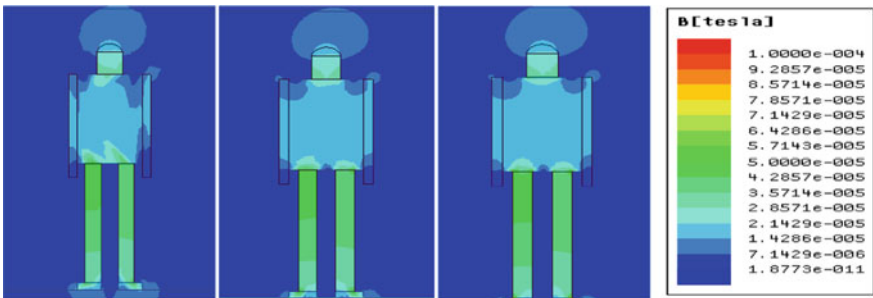


Fig. 5 Distribution of magnetic field intensity around human body

### 4.2 Subdivision Mesh Sub-model Method for Solving Electromagnetic Fields Around Human Body

Meshing the sub-model in Fig. 4 with grid length of 0.05 m. Calculating the potential for the boundary by analytical method, and according to the accuracy and speed of the request, we add a radius of 0.005 m circles as an excitation every 0.25 m in the boundary.

The intensity distribution of the electric field around the human body is shown in Fig. 6. It shows that the electric field was significantly enhanced on the head. And in order to illustrating the superiority over the proposed method, the numerical simulation results of the two methods are exported. The curve graph is shown in Fig. 7, and the maximum electric field intensity on the head is shown in Table 4.

Figure 7 and Table 4 show that the electric field intensity curve obtained by the sub-model method is similar to that of the subdivision grid method, but the value is significantly enhanced, especially in the area near the head. The reason is that the

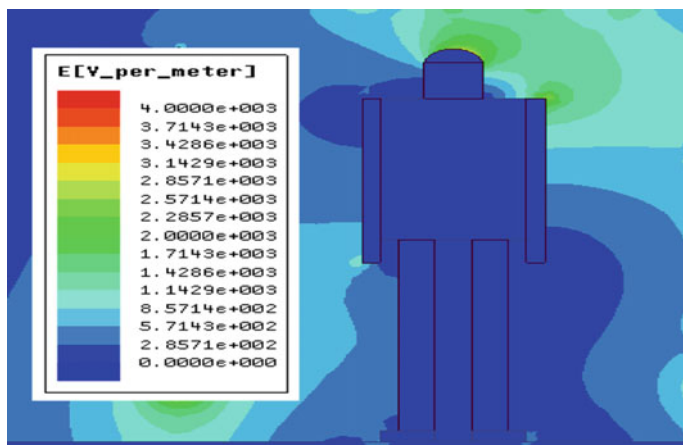


Fig. 6 Distribution of electric field intensity around human body

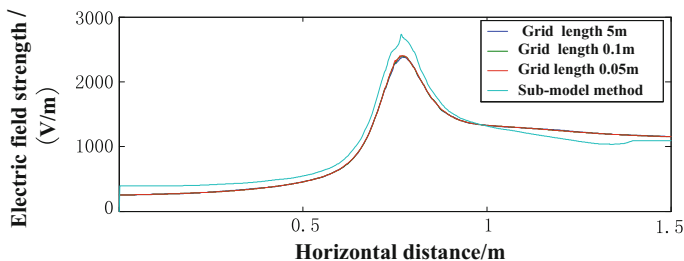


Fig. 7 The electric field intensity at the top of the human body

**Table 4** Maximum intensity of electric field at the top of human under different methods

Method	Electric field intensity (V/m)
Grid length 5 m	2383.966
Grid length 0.1 m	2400.993
Grid length 0.05 m	2402.749
Sub-model	2743.32

sub-model method adds incentives around the human body to reduce the loss of transmission, and avoid the interference from other factors. More agglomeration effect on human charge is attracted, so the electric field strength value is more accurate. Comparing with exposure limit of frequency electromagnetic field in China (shown in Table 3), the value does not exceed the standard limit.

## 5 Conclusion

In this paper, we use the finite element method to calculate and simulate the electromagnetic environment of high-speed railway catenary. The numerical simulation results show that the electromagnetic field generated by high-speed railway catenary does not cause electromagnetic radiation damage to the human. And the subdivision meshes sub-model method proposed to this paper can provide new idea about electromagnetic modeling research in the future.

**Acknowledgements** This work is partially supported by the Fundamental Research Funds for the Jiangxi Science and Technology Support Project (20142BBE50001), Jiangxi Provincial Natural Science Foundation Project (20152ACB20017, 2015BAB216020) and Jiangxi Provincial Science and Technology Project of Education Department (GJJ160525).

## References

1. Shizheng T (2012) Relying on regional advantages and railway advantages to speed up the development of railway logistics enterprises practice and thinking. *Railway Econ Res* 02:16–18 (in Chinese)
2. Mengqiao C, Xufeng Z, Yuhong N (2016) Comparative advantages and tasks of railways in comprehensive transportation system. *Integr Transp* 07:5–11 (in Chinese)
3. Lili S (2013) Heilongjiang Province Qiqihar City Railway Bureau Railway fan-shaped garage and automatic turntable. *Heilongjiang Shi Zhi* 21:321 (in Chinese)
4. Feng Z, Guanghui L, Jiaquan Y, Hui D (2015) Test analysis and modeling of power frequency magnetic-field environment in carriages of electrified trains. *J Southwest Jiaotong Univ* 03:400–404 (in Chinese)
5. Xiquan C, Hailin H, Jie S (2012) Numerical simulation of electromagnetic radiation field strength in traction power network of rail transit. *Sci Technol Eng* 29:7659–7663 (in Chinese)
6. Yongjiang L (2012) Mirror method to calculate the electric field strength of catenary. *Technol Inf* 07:120–121 (in Chinese)

7. Yang G (2015) The research on high voltage transmission line electromagnetic environment and the biological effects of human. N China Electr Power Univ (in Chinese)
8. Zhen WANG, Tiantang YU (2016) Adaptive multi-scale extended finite element method for modeling three-dimensional crack problems. Eng Mech 01:32–38 (in Chinese)
9. Jianfeng H, Zhicheng G, Yingyan L (2006) Values and rationales of limits of power frequency electric and magnetic fields in various countries. High Voltage Technol 04:51–54, 64 (in Chinese)

# Application Study of Active Noise Control Technology for Rail Transit Vehicles

Xiaobo Liu, Jian Xu, Zhongcheng Jiang and Xianfeng Wang

**Abstract** Active noise control (ANC) technology is a powerful complement for the traditional noise reduction technology. Analysed the current situation of noise control for rail vehicles; according to the application range of ANC technology, analysed the application strategy of ANC technology for rail transit vehicles; measured and analysed noise characteristics of an electric locomotive cab under different operating speeds and railway conditions, and proposed the ANC system scheme based on the whole cab space. Through the preliminary simulation calculation, the total sound pressure level in cab can be reduced by 4 dB(A). It provides a new idea for the noise control and comfort design of rail transit vehicles.

**Keywords** Rail transit vehicles · ANC · Electric locomotive cab

## 1 Introduction

Conventional passive noise control techniques work well at higher frequencies above 1 kHz, but are not effective at the low frequency range below 1 kHz, because of the long wavelengths associated with these frequencies. A good approach to controlling low frequency interior cabin noise would be to add an active noise control (ANC) system based on the principle of wave interference. ANC is achieved by introducing an anti-noise sound through a secondary source, it is an active complements for the traditional passive control methods.

---

X. Liu (✉) · Z. Jiang · X. Wang

The State Key Laboratory of Heavy Duty AC Drive Electric Locomotive  
Systems Integration, Zhuzhou 412001, Hunan, China  
e-mail: llyycsr@126.com

X. Liu · Z. Jiang · X. Wang

CRRC Zhuzhou Locomotive Co. Ltd, Zhuzhou 412001, Hunan, China

J. Xu

Northwestern Polytechnical University, Xi'an 710072, China

© Springer Nature Singapore Pte Ltd. 2018

L. Jia et al. (eds.), *Proceedings of the 3rd International Conference on Electrical and Information Technologies for Rail Transportation (EITRT) 2017*, Lecture Notes in Electrical Engineering 482, [https://doi.org/10.1007/978-981-10-7986-3\\_17](https://doi.org/10.1007/978-981-10-7986-3_17)

ANC technology has been applied to many industries, such as in headphones, in aircraft [1], automobiles [2, 3], elevator cabin noise [4], engine noise [5], haul truck noise [6], Heating, Ventilating and Air Conditioning (HVAC) system noise [7], ventilation fan noise in ducts [8], passenger train compartments [9, 10], and locomotive cab [11, 12]. The literature [9] used ANC technology to create local quiet zones at passenger ears position. However, the system is very sensitive to head movements, especially in higher frequencies.

The studies in the literature [11] have further confirmed the application feasibility the ANC in a railway environment and especially in a locomotive cab, The ANC around the driver's ears provides a noise reduction from 3 to 4 dB(A), and main annoying pure tones below 800 Hz are cut. But it consider as ANC is not efficient in the full cab space, rather than only around the driver's head.

This paper firstly analyzes main problems of noise control of railway vehicles at present. Put forward the application strategy of ANC technology for railway vehicle from three aspects: the local zones, the ducts of HVAC system and the large space zones. Measured and analyzed noise characteristics of an electric locomotive cab under different operating speeds and railway conditions, and proposed the ANC system scheme based on the cab space. The preliminary results show that the ANC system designed can effectively reduce the low-frequency noise below 300 Hz, which can reduce the total sound pressure level in the cab by 4 dB(A).

## 2 Noise Control for Rail Vehicles

Although many measures have been taken to reduce vibration and noise of vehicles, it is still difficult to achieve the ideal technical design requirements (1) The faults of production process, such as pipeline sealing, door sealing problems and so on, caused noise increase in local position, furthermore, the sound pressure level has a certain difference at different positions in passenger compartment [13]; (2) Improper handling on the interior noise, such as secondary noise induced by air duct structure and air supply mode of HVAC system, results the noise in passenger compartment is difficult to be effectively controlled; (3) The elastic vibration of lightweight body increases the vibration coupling between car body and equipment, the vibration from car body and equipment caused structure borne radiation; (4) With the trains speed increasing and the continuous improvement of the vibration isolation measures of the operation track, the wheel polygon and the track corrugation period are shortened in some extent, these vibration caused by the polygon is transferred to the car body through the suspension system, which increases the car body structure borne noise.

In order to effectively control noise, many measures has been taken, such as surface spraying or pasting damping material, using sound insulation mat, aluminum honeycomb panel, composite floor, and so on. These measures have a good effect in the processing of high frequency noise, but there are obvious deficiencies in the low frequency noise and structural borne noise.

### 3 ANC Application Strategy for Rail Vehicles

#### 3.1 ANC for Local Zones

ANC control for local zones includes active headphones and active headsets. They, undoubtedly, are the most successful application of ANC. Active headset system is the most widely used noise control methods at present, which is fit for the driver's seats and the passenger's seats. Compared to the active headphones, there is not oppression and weight for wearing headphones.

An active headset system [14] is actually two independent ANC systems that are used to reduce the noise of the left and right ears, respectively. In order to facilitate the head activities, the error sensor is usually far from the ear or eardrum position, but this arrangement is no guarantee minimum noise at the eardrum, to solve this problem, the virtual error sensing technology is used, that is, using the actual error sensor to predict sound pressure of the cancelling noise point (virtual error sensor position).

It should be noted that, considering the presence of the head, the zone surrounded by the active headset formed a diffraction field, which has a significant impact on system performance, such as, the stability of the adaptive algorithm. In order to obtain a good acoustic performance, it is necessary to measure the acoustic transmission impedance on site.

#### 3.2 ANC Control for Air Duct Noise of HVAC

Another successful application for ANC technology is pipeline noise control, such as, air-conditioning, industrial ventilation systems and engine exhausts.

The ANC of pipeline noise has been one of the focuses. The pipeline sound field is a relatively small bounded sound field, the low frequency sound waves below the pipeline cut-off frequency are propagated in plane waves form, the arrangement of the secondary sound source is simple, and the single-channel system can achieve a certain noise reduction effect, so that the sound field analysis were greatly simplified.

Figure 1 shows noise spectrum comparison curves of HVAC air supply before and after installed in vehicle. According to Fig. 2, the differences of the noise peaks of the air supply lied on mainly after 250 Hz. Especially, the high frequency after 1000 Hz, the noise amplitudes have significant decline, because the sound absorption of porous insulation materials outside the duct surface. But for the frequencies below 1000 Hz, the noise amplitudes have a little difference, which is the application effective frequency range of the ANC methods.



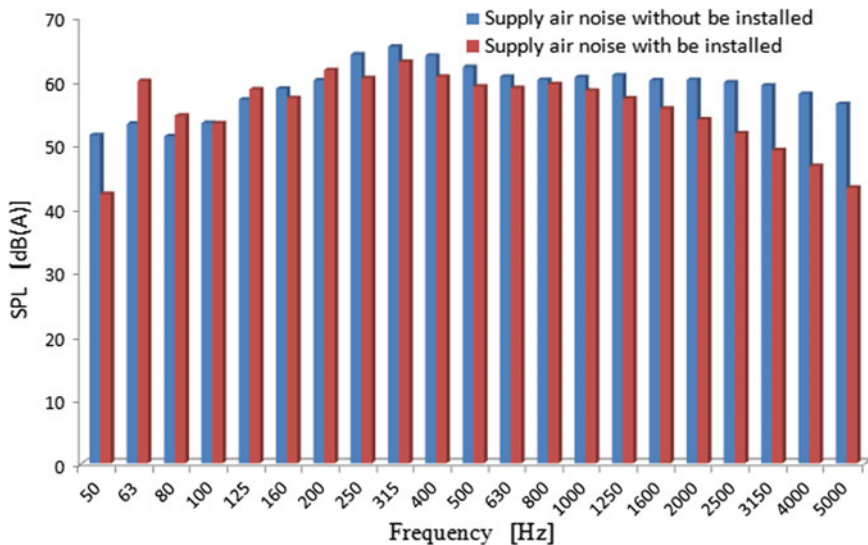


Fig. 1 Sound pressure spectrum of HVAC supply air before and after installed

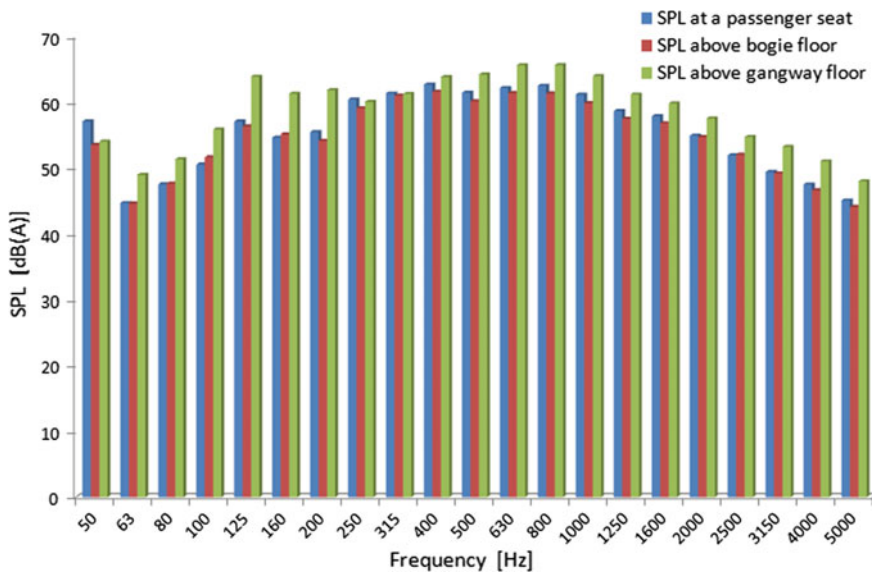


Fig. 2 The SPL spectrum above the floor of the bogie, passenger seat and gangway position

### 3.3 ANC Control for Space Zones

Space zones refers to the entire passenger compartment zone or the driver cab zone, ANC take the entire space zone as an acoustic cavity, the secondary sound source layout inside the space zone, decline the acoustic energy of the entire zone to minimum. Noise can be produced either from inside noise sources like the ventilation, air-conditioning systems, structure-borne sound, or from outside noise sources like the wheel-rail interaction, the propulsion or hydraulic systems, brakes, compressor and aerodynamics.

Figure 2 shows the sound pressure spectrum measured at 1.6 m above the floor of a subway train bogie, 1.2 m above a passenger seat and 1.6 m above the gangway floor center. It can be seen from this figure that the whole noise energy is very wide, the band amplitude is mainly prominent in the 50 Hz, 125 Hz and 250–1000 Hz, especially, at the gangway position, the overall noise level is higher than the other two positions, mainly because the gangway is the channel to connect two vehicles. One reason is its sound insulation relatively weak, another is the seal not strict. From the noise characteristics of the passenger compartment, the noise of the subway passenger compartment has obvious broadband characteristics, and there is obvious regional difference in the space distribution of sound energy. Therefore, it is extremely complex to achieve a wide range control effect by used ANC system in passenger compartments.

## 4 ANC Application for an Electric Locomotive Cab

Compared to the subway passenger compartment, the space zones of electric locomotive cab is a relatively small space, it is a good transition space of applying ANC system from local zones to large space zones. If the ANC system succeeded in the locomotive cab, then it can be used to the larger space.

### 4.1 Noise Characteristics of an Electric Locomotive Cab

The sound field inside a real locomotive cab is generated both by outside sources, including wheel/rail noise, mechanical equipment noise, and in inside sources, including air supply noise of HVAC system, structure-borne noise by vibrations of interior panels. In railway, the sound pressure level in a driver cab must be less than 78 dBA at 80 km/h. Due to the customer's requirements, the noise requirements in the cab are becoming more stringent, requiring vehicle manufacturers adopt more efficient low-sound design measures to reduce noise in cab.

In order to obtain the noise characteristics of the electric locomotive driver's cab, the noise data in driver's cab were collected in a servicing electric locomotive. The

test uses three acoustic sensors, located respectively at the main driver's head position (P1), the vice driver's head position (P2) and the center position behind two drivers (P3). Acquisition speed are two typical operating speed conditions: 70 km/h for freight locomotive and 90 km/h for passenger locomotive, Acquisition conditions are also two typical operating environments, that is, in free fields and tunnels. Figures 3 and 4, respectively, show the sound pressure spectrum at three points at 70 km/h and 90 km/h. From the noise data collected can be seen (1) The interior noise peak frequencies are mainly low frequency below 200 Hz; (2) with the train speed increasing, the new peak also appears between 200 and 300 Hz.

Figure 5 shows the noise characteristics at P1 when the train through a continuous tunnel and intermittently through tunnels and the open line at 70 km/h speed. Compared to Fig. 3, when the train running in a tunnel, or intermittently through tunnels, the driver's cab noise has no obviously change, mainly due to the cab floor, side walls, partition walls, as well as the driver cab doors are made of steel panels, sound-absorbing material and interior panels, which has a good sound insulation performance, if the seals are good at every connecting position, even in the tunnel, there is little airborne noise transmission from outside space field.

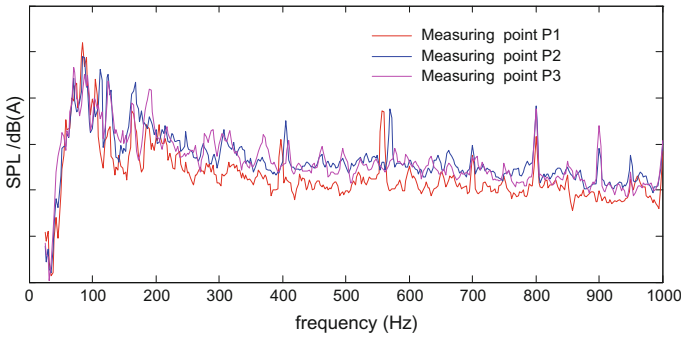


**Fig. 3** On the open section at 70 km/h

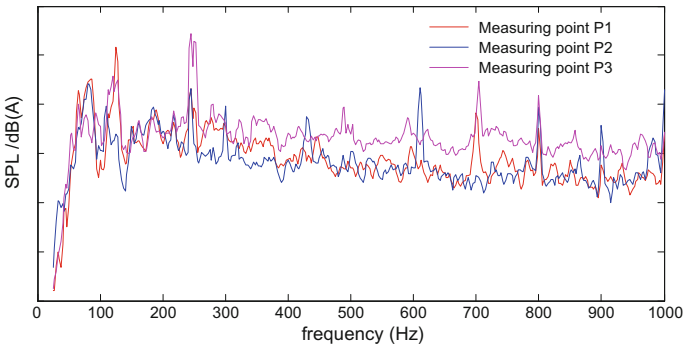


**Fig. 4** On the open section at 90 km/h

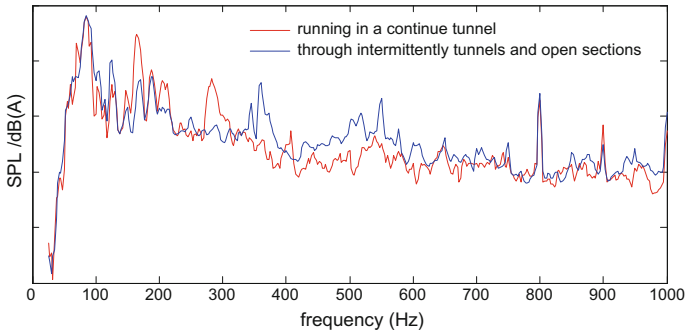


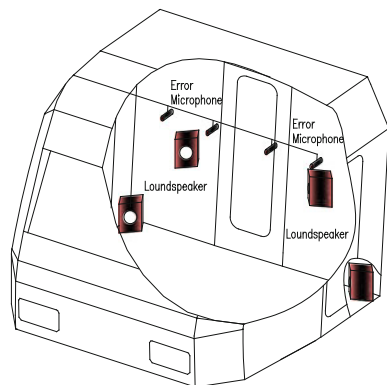
**Fig. 5** Train running in tunnels at 70 km/h

The measuring data confirm the feasibility of the application of the ANC in a railway environment and especially in the cabin of a locomotive. But, at the same time, there are difficulties in control: the ANC control in the cab inevitably has some problems such as frequency bandwidth, time-varying spectrum and space distribution, and so on.

### 4.2 ANC System Scheme for an Electric Locomotive Cab

Figure 6 shows the  $4 \times 4$  layout scheme of error microphones and loudspeakers for a locomotive cabin. 4 error sensors are located above two drivers' ears, the microphone head pointed to the rear of the driver cab. 4 secondary sound sources are located in the rear wall of the cab, two of which are located in two corner positions on the floor, other two loudspeakers installed in partition wall behind the seats, about 0.75 m from the floor. Four secondary sound sources are all faced to front of the cab.

**Fig. 6** Layout scheme of error microphones and loudspeakers for a Locomotive cabin



### 4.3 Effect of ANC System in Electric Locomotive Cab

A preliminary calculation is carried out by using feed forward filtered-x least mean square (FxLMS) algorithm, an adaptive filter algorithm most commonly used. The basic structure of the adaptive active feed forward control system is shown in Fig. 7  $p(t)$  is the primary signal produced by the noise source.  $x(t)$ ,  $y(t)$  and  $e(t)$  are the reference signal, secondary signal and error signal, respectively.

Define the transfer function of the controller is  $W(z)$ , and the transfer function of reference path, primary path and secondary path are  $H_r(z)$ ,  $H_p(z)$  and  $H_s(z)$  whose impulse response are  $h_r(n)$ ,  $h_p(n)$  and  $h_s(n)$ , respectively. Then, the adaptive feed forward control system showed as Fig. 7 can be represented as a system block diagram in discrete domain illustrated in Fig. 8. Corresponding with Fig. 8,  $x(n)$  is the reference signal input into the filter;  $e(n)$  is residual noise downstream measured by an error microphone;  $d(n)$  is undesired primary noise at the position of the error microphone;  $y(n)$  is the output of filters which can be approximated as actual sound generated by the secondary source; and  $s(n)$  is in fact the cancelling signal at the position of the error microphone.

The signal received by the error sensor can be expressed as

$$e(n) = d(n) + s(n) = d(n) + r^T(n)W(n) \tag{1}$$

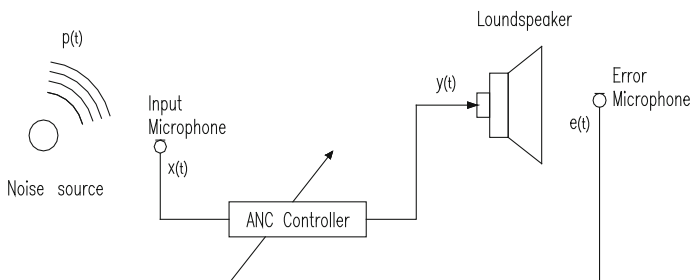


Fig. 7 Schematic diagram of adaptive active feed forward control system

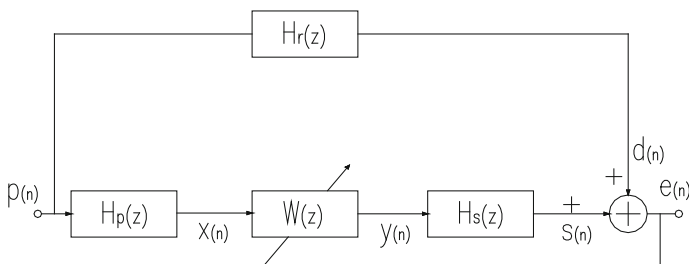


Fig. 8 Simplified diagram of discrete domain adaptive feed forward control system

where  $\mathbf{W}(n)$  is the weight coefficient of the filter, and  $\mathbf{r}^T(n)$  is filtered-x signal vector, the index  $T$  stands for transpose, whose relationship with the reference signal vector  $\mathbf{X}(n)$  is

$$\mathbf{r}(n) = \mathbf{X}(n) * h_s(n) \quad (2)$$

The control target of the ANC system usually chooses the minimum mean square error criterion, thus the objective function of the control system is represented as

$$J(n) = E[e^2(n)] \quad (3)$$

where  $E(\cdot)$  is time averaging of independent variable.

Substituting Eq. (1) into Eq. (3) gives

$$J(n) = E[d^2(n)] + 2\mathbf{P}^T\mathbf{W} + \mathbf{W}^T\mathbf{R}\mathbf{W} \quad (4)$$

where  $\mathbf{P} = E[d(n)\mathbf{r}(n)]$ ,  $\mathbf{R} = E[\mathbf{r}(n)\mathbf{r}^T(n)]$ .

Using the steepest descent algorithm, which updates the coefficient vector in the negative gradient direction with step size  $\mu$

$$\mathbf{W}(n+1) = \mathbf{W}(n) - \mu\nabla(n) \quad (5)$$

where  $\mu$  is the convergence coefficient (or step size) that controls the stability and convergence speed of the algorithm.  $\nabla(n)$  is the gradient of mean square error. In practical application, in order to simplify the calculation and meet the real-time requirements of the system, the gradient of square of a single sample  $e(n)$  is generally taken as an estimate of the mean square error  $\nabla(n)$ . Thus, the instantaneous estimate of the mean square error gradient at time  $n$ ,  $\hat{\nabla}(n)$ , can be expressed as

$$\hat{\nabla}(n) = \frac{\partial e^2(n)}{\partial \mathbf{W}} = 2e(n)\mathbf{r}(n) \quad (6)$$

Substituting Eq. (6) into Eq. (5) can obtain the iteration formula of the weight vector

$$\mathbf{W}(n+1) = \mathbf{W}(n) - 2\mu e(n)\mathbf{r}(n) \quad (7)$$

Typical results are shown in Fig. 9, the total noise reduction achieved in the cabin cavity is around 4 dB(A). It notes that the cancellation of sound at low below 300 Hz frequencies is quite effective, especially for the frequency below 200 Hz.

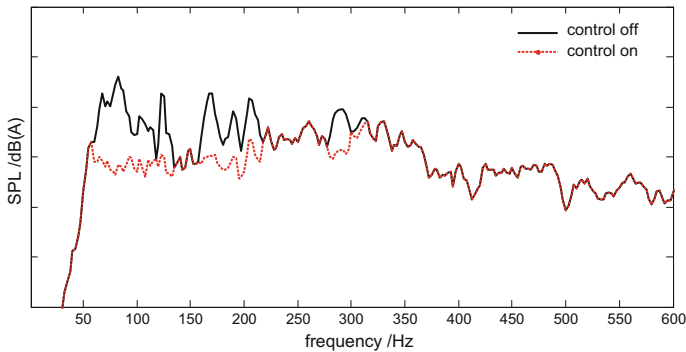


**Fig. 9** Noise reduction achieved by using ANC system

## 5 Conclusion and Application Prospect

The noise of low-speed rail vehicles is mainly in the middle and low frequency, such as electric locomotive cabs, passenger compartments. Obviously, the ANC technology is very suitable. But the ANC control in the space zone inevitably has some problems such as frequency bandwidth, time-varying spectrum and space distribution. It is extremely complex to achieve a wide range control effect by using ANC system in these space zones.

This paper put forward the application strategy of ANC technology of railway vehicle from three aspects: the local zones, the ducts of HVAC system and the large space zone. According to the noise characteristics of an electric locomotive cab under different operating conditions, the ANC system scheme of the whole cab space is proposed. The preliminary results show that the ANC system designed can effectively reduce the low-frequency noise in the driver's cab below 300 Hz, and can reduce the total sound pressure level in the cab by 4dBA.

To further verify the ANC system noise reduction effect, the follow-up work is to complete the test verification in the laboratory and in a real locomotive cab.

## References

1. Johansson S (2000) Active control of propeller-induced noise in aircraft: algorithms & methods. Blekinge Institute of Technology
2. Couche J (1999) Active control of automobile cabin noise with conventional and advanced speakers. Virginia Polytechnic Institute and State University
3. Kang WP, Moon HR, Lim J (2014) Analysis on technical trends of active noise cancellation for reducing road traffic noise. *Journal of Emerging Trends in Computing and Information Sciences* 5(4):286–291
4. Landaluz J, Portilla I, Pagalday JM et al (2003) Application of active noise control to an elevator cabin. *Control Engineering Practice* 11(12):1423–1431

5. Zhang L, Pan J, Qiu X (2013) Integrated passive and active control of engine noise. In: Proceedings of the 20th international congress on sound & vibration, Bangkok, Thailand
6. Lin Z, Zhang L, Qiu X et al (2014) An integrated passive and active control system for reducing haul truck noise. In: Inter Noise 2014. Australian Acoustical Society 2014:1–8
7. Gelin LJ (1997) Active noise control: a tutorial for HVAC designers. *ASHRAE J* 39(8):43
8. Prezelj J, Čudina M (2011) A secondary source configuration for control of a ventilation fan noise in ducts. *Strojnikivestnik-J Mech Eng* 57(6):468–476
9. Rutger Kastby C (2013) Active control for adaptive sound zones in passenger train compartments. Stockholm, Sweden
10. Botto MA, Sousa JMC, da Costa JMGS (2005) Intelligent active noise control applied to a laboratory railway coach model. *Control Eng Pract* 13(4):473–484
11. Loizeau T, Poisson F (2006) Acoustic active control inside a locomotive cabin. In: 7th World congress on railway research, Montreal, Canada
12. Johnson TM, Hanson CE, Ross JC et al (2009) Development of passive and active noise control for next generation locomotive cabs. In: Inter noise
13. Liu XB, Liu J (2016) Study on acoustic management process and key technology for railroad vehicle. *Noise Vib Control* 36(6):82–86 (in Chinese)
14. Garcia-Bonito J, Elliott SJ, Boucher CC (1997) Generation of zones of quiet using a virtual microphone arrangement. *J Acoust Soc Am* 101(6):3498–3516



# DC Auto-Transformer Traction Power Supply System for DC Railways Application

Miao Wang, Xiaofeng Yang, Lulu Wang and Trillion Q. Zheng

**Abstract** In DC railways, the running rails are used as the return path for traction current, which inevitably leads to stray current and rail potential issues with poor insulation. However, the effects of existing solutions are limited, so DC auto-transformer (DCAT) traction power supply system (TPSS) is analyzed in this paper to solve the problems of stray current and rail potential fundamentally. Compared with the existing TPSS (E-TPSS), the mathematical analysis and simulation results show that DCAT-TPSS may solve both stray current and rail potential issues, which further reduce the voltage drop and power loss of power supply lines additionally.

**Keywords** DC railways · DCAT traction power supply system  
Stray current · Rail potential

## 1 Introduction

Nowadays, with the economic development and the growing of population, rail transit systems play a more and more important role in transportation. In DC railways, the running rails act as the return path of traction current. However, the running rails are not totally isolated from the ground, so a part of current leaks to the ground, which causes stray current issue. The stray current results in the electric potential difference between the rails and the ground, which is called rail potential [1–4]. The stray current will not only cause serious corrosion of the underground structures such as reinforced concrete, but also reduce the service life of the pipelines, such as oil and natural gas pipelines, resulting in greater economic losses. Meanwhile, the rail potential will also threaten the safety of passengers and the safe operation of DC railways.

---

M. Wang · X. Yang (✉) · L. Wang · T. Q. Zheng  
School of Electrical Engineering, Beijing Jiaotong University,  
No. 3 Shang Yuan Chun, Hai Dian District, Beijing, China  
e-mail: xfyang@bjtu.edu.cn

The main solutions for DC railways to reduce stray current and rail potential include: (1) improving the supply voltage level; (2) strengthening the insulation between the rails and the ground; (3) reducing the rail resistance; (4) establishing stray current collection network; (5) adopting the drainage protection method, the cathodic protection method and other protective means to protect the corrosion objects; (6) setting the rail over-voltage protection devices (OVPD) [5–8]. Although these methods may reduce stray current and rail potential, the costs are too high while the effects are limited. So the stray current and rail potential issues still cause huge economic losses. The fundamental reason for the limited effects of these methods is that the running rails always act as the return path of traction current, and it's essential to propose a new structure of traction power supply system (TPSS) to solve the problems fundamentally.

In order to solve the above mentioned issues, the fourth-rail DC railway system has been used in practice [9, 10]. But it requires additional provision for the fourth rail, whereas the cost is high. The fourth-rail DC railway system needs to improve the train's design additionally, so it doesn't get a wide range of promotion. Reza Fotouhi [11] proposed a DC booster circuit to reduce stray current and rail potential in DC railways, by using DC booster circuit to transfer the traction current from the rail to the return line. This method requires additional provision of the return line and a number of the booster circuits, meanwhile each booster requires two bulky inductors and eleven switches. All switches are operating in the hard switching mode, and there is dead time interval between the switching operating modes. During the dead time interval, the traction current still goes through the rail like the existing TPSS (E-TPSS). Qunzhan Li [12] proposed a single-phase AC TPSS to replace E-TPSS for urban rail transit. With higher power supply voltage, the insulation level between the train and tunnels is higher. What's more, the train's traction drive system needs to be improved greatly with DC power supply changed to AC power supply.

Compared with these systems' problems in terms of power density, efficiency, cost, reliability and so on, Trillion Q. Zheng [13] proposed DC auto-transformer (DCAT) TPSS. DCAT-TPSS uses DCAT to transfer the traction current from the rail to the negative feeder, thus reduces stray current and rail potential fundamentally. DCAT-TPSS is verified through the mathematical analysis and simulation in this paper, by comparing with E-TPSS based on grounded scheme. The results show that DCAT-TPSS not only solves both stray current and rail potential issues, but also reduces the voltage drop and power loss of power supply lines.

## 2 Configuration and Principle of DCAT-TPSS

Figure 1 shows the general configuration of DCAT-TPSS, which adds the negative feeder and several DCATs compared with E-TPSS. Figure 2 shows the configuration of DCAT, which is comprised of two capacitors and one energy transfer module (ETM). The ETM is responsible for balancing the voltage across of

capacitors. The ETM may adopt the resonant cell (including the resonant capacitor and the resonant inductor) to transfer the energy, as shown in Fig. 2b, or the DC inductor, as shown in Fig. 2c, and the principles of ETM have been introduced in [13, 14]. Moreover, DCAT's terminals (i.e. HPT, MPT and LPT) are connected to the contact line (or the third rail), the rail and the negative feeder respectively.

In DCAT-TPSS, DCAT is used as a step-up converter in the substation side and a step-down converter in the train side, when the train runs under traction condition. Therefore, the voltage level of power supply lines increases, the voltage drop and power loss of power supply lines decreases, and the power supply distance of the substations can be further extended. What's more, the train's voltage level remain unchanged in DCAT-TPSS, which means the existing trains may be used in DCAT-TPSS directly without any improvement.

As shown in Fig. 1, substation1 and substation2 supply the energy to the train together, and by installing four DCATs, the rail can be divided into three sections: section I, section II and section III. Figure 3 shows the current distribution of DCAT-TPSS when the train is running on section II. No matter which section the train is running on, DCAT will transfer the total traction current from the rail to the

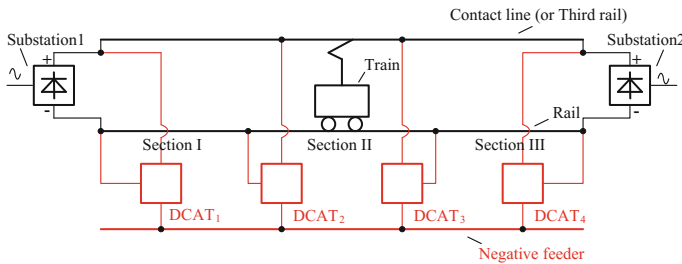


Fig. 1 General configuration of DCAT-TPSS

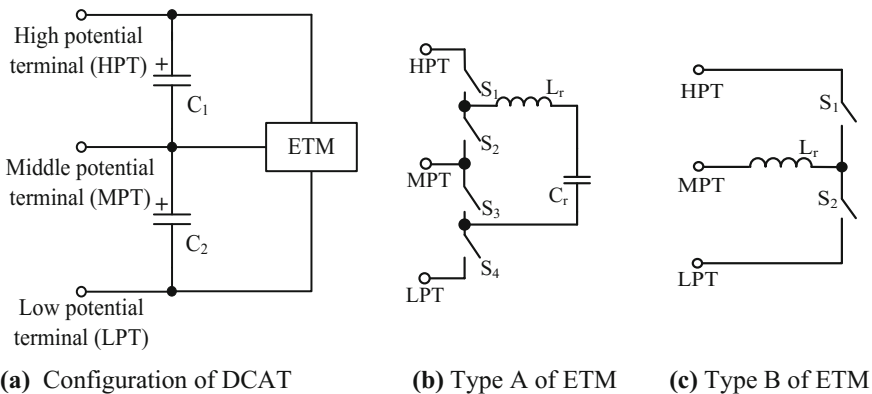
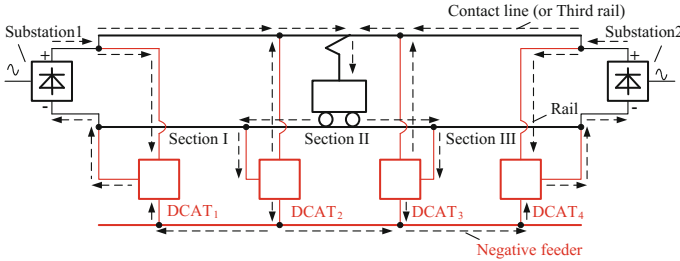


Fig. 2 Configuration of DCAT and ETM



**Fig. 3** The current distribution of DCAT-TPSS when the train is running on section II

negative feeder. Thus the traction current only exists in the section which the train is running on, and the current of the section which no train is running on is zero. So DCAT-TPSS may solve the problems of stray current and rail potential fundamentally.

### 3 Mathematical Analysis of DCAT-TPSS and E-TPSS

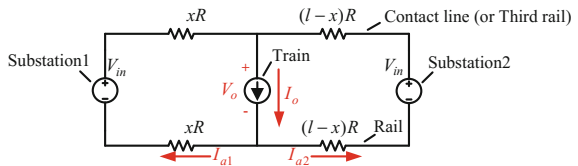
To compare DCAT-TPSS and E-TPSS, this paper will discuss rail potential, stray current, leakage charge, voltage drop and power loss of power supply lines based on grounded system (i.e. the negative terminal of the substations is grounded).

Figures 4 and 5 show the equivalent model of E-TPSS and DCAT-TPSS respectively. In these models, the substations are equivalent to voltage sources  $V_{in}$ , and the train is equivalent to current source  $I_o$ . The distance between the substations is  $l$ , and the distance between the train and the substation1 is  $x$ . The resistance per unit length of the rail, the contact line and the negative feeder is  $R$ . What's more, by installing  $N + 1$  DCATs, the rail of DCAT-TPSS can be divided into  $N$  sections, and the train runs on section  $N_1 + 1$  (i.e. the running section).

#### 3.1 Rail Potential

Based on the equivalent models of E-TPSS and DCAT-TPSS, the rail potential gets the maximum value  $V_{max}$  at position of the train, and the rail potential gets the

**Fig. 4** The equivalent model of E-TPSS



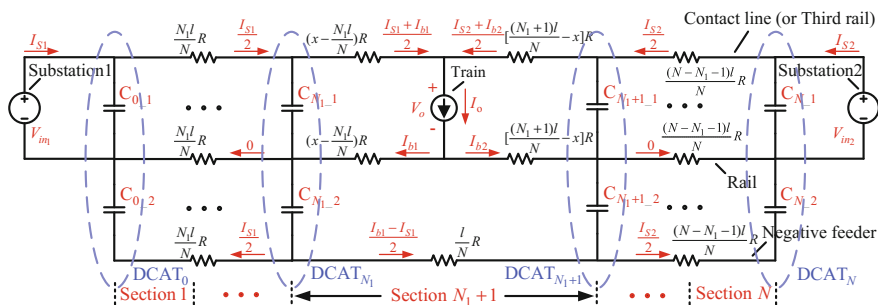


Fig. 5 The equivalent model of DCAT-TPSS

minimum value (i.e. 0) at position of the substations. From the equivalent models, the maximum rail potential value of E-TPSS and DCAT-TPSS can be described as

$$V_{E-TPSS_{max}} = \frac{lR I_o}{4} \tag{1}$$

$$V_{DCAT-TPSS_{max}} = \frac{lR I_o}{4N} \tag{2}$$

So the maximum rail potential ratio of DCAT-TPSS to E-TPSS is expressed as

$$\frac{V_{DCAT-TPSS_{max}}}{V_{E-TPSS_{max}}} = \frac{1}{N} \tag{3}$$

### 3.2 Stray Current

Because the rail potential causes the voltage difference between the rail and the ground, under the resistance  $R_G$  between the rail and the ground, the leakage current  $I_G$  will gather together continuously, and cause the stray current issue. From the equivalent models, the maximum stray current value of E-TPSS and DCAT-TPSS can be described as

$$I_{E-TPSS_{max}} = \frac{l^2 R I_o}{16 R_G} \tag{4}$$

$$I_{DCAT-TPSS_{max}} = \frac{l^2 R I_o}{16 N^2 R_G} \tag{5}$$

So the maximum stray current ratio of DCAT-TPSS to E-TPSS is expressed as

$$\frac{I_{DCAT-TPSS_{max}}}{I_{E-TPSS_{max}}} = \frac{1}{N^2} \tag{6}$$

### 3.3 Leakage Charge

According to the analysis of the stray current, the sum of the leakage currents equals to the sum of the maximum stray currents on the left and right sides of the train. For simplified analysis, it is assumed that the train runs from the substation1 to the substation2 at a constant speed  $v$ , and the sum of the leakage charges of E-TPSS and DCAT-TPSS can be calculated as

$$Q_{E-TPSS} = \int_0^{\frac{l}{v}} I_{G\_E-TPSS\_sum} dt = \frac{l^3 RI_o}{12vR_G} \quad (7)$$

$$Q_{DCAT-TPSS} = \sum_{N_1=0}^{N-1} \int_{\frac{N_1 l}{Nv}}^{\frac{(N_1+1)l}{Nv}} I_{G\_DCAT-TPSS\_sum} dt = \frac{l^3 RI_o}{12N^2 v R_G} \quad (8)$$

So the leakage charge ratio of DCAT-TPSS to E-TPSS is expressed as

$$\frac{Q_{DCAT-TPSS}}{Q_{E-TPSS}} = \frac{1}{N^2} \quad (9)$$

### 3.4 Voltage Drop and Power Loss of Power Supply Lines

Based on the equivalent models of E-TPSS and DCAT-TPSS, the average voltage drop and power loss of power supply lines can be expressed as

$$\Delta V_{E-TPSS\_avg} = \frac{1}{l} \int_0^l \Delta V_{E-TPSS} dx = \frac{lRI_o}{3} \quad (10)$$

$$\Delta P_{E-TPSS\_avg} = \frac{1}{l} \int_0^l \Delta P_{E-TPSS} dx = \frac{lRI_o^2}{3} \quad (11)$$

$$\Delta V_{DCAT-TPSS\_avg} = \frac{1}{N} \sum_{N_1=0}^{N-1} \left( \frac{N}{l} \int_{\frac{N_1 l}{N}}^{\frac{(N_1+1)l}{N}} \Delta V_{DCAT-TPSS} dx \right) = \frac{(N+3)lRI_o}{12N} \quad (12)$$

$$\Delta P_{DCAT-TPSS\_avg} = \frac{1}{N} \sum_{N_1=0}^{N-1} \left( \frac{N}{l} \int_{\frac{N_1 l}{N}}^{\frac{(N_1+1)l}{N}} \Delta P_{DCAT-TPSS} dx \right) = \frac{(N+3)lRI_o^2}{12N} \quad (13)$$

So the average voltage drop ratio and power loss ratio of DCAT-TPSS to E-TPSS are expressed as

$$\frac{\Delta V_{\text{DCAT-TPSS}_{\text{avg}}}}{\Delta V_{\text{E-TPSS}_{\text{avg}}}} = \frac{\Delta P_{\text{DCAT-TPSS}_{\text{avg}}}}{\Delta P_{\text{E-TPSS}_{\text{avg}}}} = \frac{N + 3}{4N} \tag{14}$$

From the mathematical analysis of DCAT-TPSS and E-TPSS, DCAT-TPSS can solve the rail potential, stray current and leakage charge issues effectively compared with E-TPSS, and reduce the voltage drop and power loss of the power supply lines additionally, which means DCAT-TPSS can improve power distance and power efficiency of the substations.

Compared with E-TPSS, if the rail is divided into  $N$  sections in DCAT-TPSS, it can be concluded as: (1) the maximum rail potential ratio is  $1/N$ ; (2) the maximum stray current ratio is  $1/N^2$ ; (3) the leakage charge ratio is  $1/N^2$ ; (4) the average voltage drop ratio and power loss ratio are  $(N + 3)/4$ . As can be seen in Fig. 6, with increasing the number  $N$  of sections (i.e. add one to the number of DCATs), the effect of DCAT-TPSS will be better. With comprehensive consideration of the effect and the cost of DCAT-TPSS, the recommended number of sections is 3 to 5 under the different distance between the substations.

### 4 Simulation Results

In order to validate the above mathematical analysis, build DCAT-TPSS as shown in Fig. 1, and E-TPSS in Matlab software, which are based on grounded system. DCAT's EMT adopts the type A (i.e. the resonant cell), and the main parameters of DCAT-TPSS and E-TPSS are given in Table 1. To simplify the analysis, all the components are assumed ideal.

**Fig. 6** The ratio of DCAT-TPSS to E-TPSS

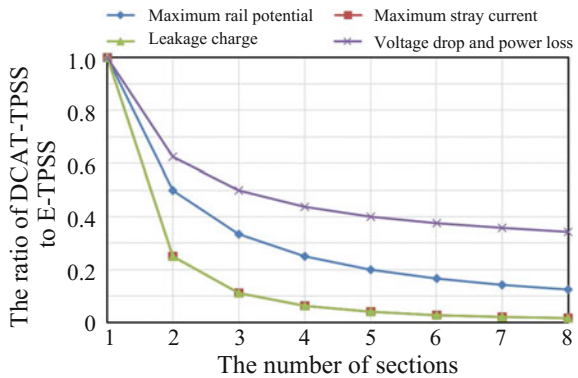


**Table 1** Simulation parameters of DCAT-TPSS and E-TPSS

	Parameters
$V_{in}$	750 V
$I_o$	2000 A
$R$	30 mΩ/km
$R_G$	15Ω km
$l$	3 km
$v$	120 km/h
The number of DCAT	4

Figure 7 shows the comparison about the rail potential and stray current, when the train is running on the midpoint of the rail. The rail potential at position of the train achieves the maximum value, and the stray current at position of the substations achieves the maximum value. Figure 8 shows the comparison about the sum of leakage currents, leakage charge, voltage drop and power loss, when the train runs from the substation1 to the substation2. The sum of leakage currents, the voltage drop and power loss achieve the maximum value when the train is running at midpoint of the rail, and the leakage charge achieves the maximum value when the train is running at right substation (i.e. the end of the travel).

The simulation results are consistent with the mathematical results, which proves the correctness of the mathematical analysis. The simulation results show that DCAT-TPSS can effectively solve the problems of rail potential and stray current, and reduce the voltage drop and power loss of the power supply lines.

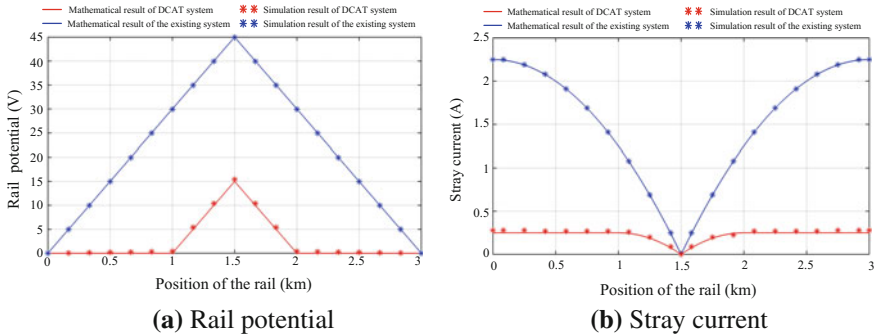


**Fig. 7** Comparison when the train is running on the midpoint of the rail



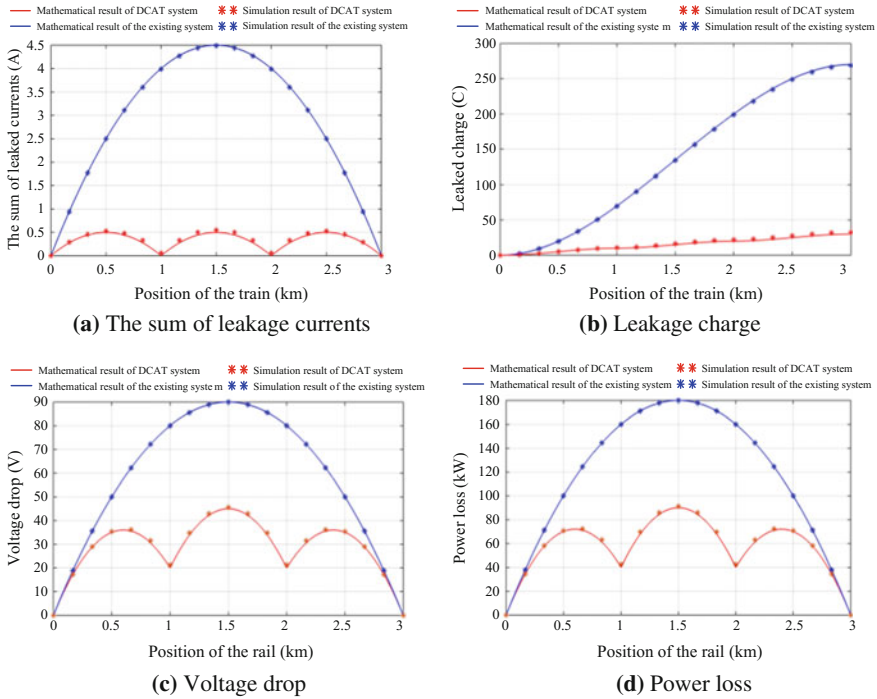


Fig. 8 Comparison when the train runs from the substation1 to the substation2

## 5 Conclusion

DCAT-TPSS has been described and demonstrated in this paper. Mathematical analysis and simulation results show that, DCAT-TPSS may solve rail potential and stray current issues by transferring the traction current from the rail to the negative feeder, and reduce the voltage drop and power loss additionally with the voltage level of power supply lines doubling, which effectively proves that DCAT-TPSS has a promising application prospect in DC railways.

**Acknowledgements** This work was supported by the Fundamental Research Funds for the Central Universities (2017JBM057).

## References

1. Ibrahim A, Elrayyah A, Sozer Y, De De Abreu-Garcia JA (2017) DC railway system emulator for stray current and touch voltage prediction. *IEEE Trans Ind Appl* 53(1):439–446
2. S-Y Xu, Li W, Wang Y-Q (2013) Effects of vehicle running mode on rail potential and stray current in DC mass transit systems. *IEEE Trans Veh Technol* 62(8):3569–3580

3. Tzeng Y-S, Lee C-H (2010) Analysis of rail potential and stray currents in a direct-current transit system. *IEEE Trans Power Deliv* 25(3):1516–1525
4. Charalambous CA, Aylott P (2014) Dynamic stray current evaluations on cut-and-cover sections of DC metro systems. *IEEE Trans Veh Technol* 63(8):3530–3538
5. Cotton I, Charalambos C, Aylott P, Ernst P (2005) Stray current control in DC mass transit systems. *IEEE Trans Veh Technol* 54(2):722–730
6. Liu YC, Chen JF (2005) Control scheme for reducing rail potential and stray current in MRT systems. *IEE Proc—Electr Power Appl* 152(3):612–618
7. Paul D, Guest Author (2016) DC stray current in rail transit systems and cathodic protection. *IEEE Ind Appl Mag* 22(1):8–13
8. Zaboli A, Vahidi B, Yousefi S, Hosseini-Biyouki MM (2017) Evaluation and control of stray current in DC-electrified railway systems. *IEEE Trans Veh Technol* 66(2):974–980
9. Jin J, Allan J, Goodman CJ, Payne K (2004) Single pole-to-earth fault detection and location on a fourth-rail DC railway system. *IEE Proc-Electr Power Appl* 151(4):498–504
10. Zhang Y (2011) Technology of traction power supply for the fourth traction return rail of transit. *Mod Urban Trans* 4:8–10 (in Chinese)
11. Fotouhi R, Farshad S, Fazel SS (2009) A new novel DC booster circuit to reduce stray current and rail potential in DC railways. *2009 Compat Power Electron*:457–462
12. Li Q (2015) Industrial frequency single-phase AC traction power supply system and its key technologies for urban rail transit. *J Southwest Jiaotong Univ* 50(2):199–207 (in Chinese)
13. Zheng TQ, Yang X, You X (2016) DC auto-transformer based traction power supply system for urban rail transit. *Urban Rapid Rail Trans* 29(3):91–97 (in Chinese)
14. Sano K, Fujita H (2008) Voltage-balancing circuit based on a resonant switched-capacitor converter for multilevel inverters. *IEEE Trans Ind Appl* 44(6):1768–1776

# An Optimized Method for the Energy-Saving of Multi-metro Trains at Peak Hours Based on Pareto Multi-objective Genetic Algorithm

Muhan Zhu, Yong Zhang, Fei Sun and Zongyi Xing

**Abstract** Urban rail train starts and brakes frequently in its movement. It is important to improve the utilization efficiency of electric energy and reduce the traction energy consumption in the field of metro transit. At peak hours, the overlap time between two trains in the same power supply interval is longer and there is much more renewable energy generated by the train's braking due to a large increasement in passenger flow and the number of departure. In this paper, a method based on pareto multi-objective genetic algorithm is proposed to optimize energy consumption. By optimizing the stopping time of trains in each station, train schedule is optimized and the regenerative braking energy can be used more efficiently.

**Keywords** Train energy-saving · Multi-objective optimization  
Genetic algorithm · Train timetable optimization

## 1 Introduction

Urban rail transit traction energy consumption occupies a larger proportion in the social power consumption demand. Considering subway train's traction performance and its characteristic of frequent start and stop, energy-saving slope and regenerative braking [1, 2] can greatly improve the utilization efficiency of electricity. At present, the research on regenerative braking energy mainly includes installing energy absorption device [3], designing and developing contravariant feedback device [4, 5], optimizing metro train's timetable and so on. The optimization of train schedule has gained many achievements which is both economical and practical.

---

M. Zhu · Y. Zhang (✉) · F. Sun · Z. Xing  
School of Automation, Nanjing University of Science and Technology,  
No 200 Xiao Lin Wei Xuanwu District, Nanjing 210094, China  
e-mail: 34445721@qq.com

© Springer Nature Singapore Pte Ltd. 2018  
L. Jia et al. (eds.), *Proceedings of the 3rd International Conference on Electrical and Information Technologies for Rail Transportation (EITRT) 2017*, Lecture Notes in Electrical Engineering 482, [https://doi.org/10.1007/978-981-10-7986-3\\_19](https://doi.org/10.1007/978-981-10-7986-3_19)

Yang et al. [6] took stop time as the control variable, the maximization of overlap time as the objective function, established an integer programming model and used genetic algorithm to solve this problem. PeñaAlcaraz et al. [7] adopted the method of mixed integer programming to optimize the off-peak hours train schedules. Nasri et al. [8] took stop time as the optimized object, established an objective function aimed at maximizing the exchange of energy between two trains and built an optimal model combined with genetic algorithm. Feng Jia et al. [9] established a kind of schedule optimization model considering the regenerative energy, an adjusted energy saving model based on passenger flow volume, a traction energy consumption and transport efficiency assessment model respectively and illustrated the result based on some cases. This paper adopts Pareto multi-objective genetic algorithm and builds an energy-saving optimization model of multi-trains at peak hours.

## 2 Pareto Multi-objective Genetic Algorithm

### 2.1 Multi-objective Optimization

The optimal control for train's energy saving is a typical multi-objective optimization problem, it's mathematical model can be described as:

$$\begin{cases} \text{Min}F(x) = [f_1(x), f_2(x), f_3(x), \dots, f_n(x)] \\ \text{s.t.} \begin{cases} h_i(x) = 0, 0 \leq i \leq I \\ g_j(x) \leq 0, 0 \leq j \leq I \end{cases} \end{cases} \quad (1)$$

where  $x = [x_1, x_2, \dots, x_l]$  are control variables;  $F(x)$  are optimization objectives;  $h_i(x)$  and  $g_j(x)$  are equation constraint and inequation constraint.

### 2.2 Pareto Non-dominated Solution

$x \in S$  are feasible solutions of multi-objective optimization problem, if and only if there doesn't exist any  $y \succ x$  in  $S$ , which means  $x$  are non-dominated individuals in  $S$ ,  $x$  are the Pareto non-dominated solutions [10] for multi-objective optimization problem.

### 2.3 NSGA-II Algorithm

NSGA-II [11] is an improved algorithm based on NSGA. The algorithm steps are listed below.

- Step 1: Initialize parameters.
- Step 2: Generate initial population randomly.
- Step 3: Solve fitness value.
- Step 4: Do non-dominated sorting and calculate individual's congestion distance
- Step 5: Select elite individual and merge them with parent population.
- Step 6: Do crossover and mutation operations and obtain a new population.
- Step 7: If the interaction has not reached the maximum times, go back to step 4, if not, finish the interaction calculation.

### 3 Multi-train Energy-Saving Optimization Model

Multi-train's movement at peak hours is a complicated problem [12]. To simplify the energy-saving problem, we need to make the following assumptions:

- The regenerative braking electricity energy can only be used by the accelerated trains in the same power supply interval.
- The power supply system of two lines is separated, trains in one line don't use the braking energy generated by other trains in different lines.
- Trains running in the same direction between two stations share the same running time and stop time.
- All the trains in one line share a same model, we suppose that train's weight equals to a constant and ignore the change of passengers on the train.

#### 3.1 Model of Train's Movement

At peak hours, adjacent trains can run cooperatively and utilize the regenerative braking energy to an extreme through optimizing trains' stop time under the condition of keeping the running time between intervals constant. In the same power supply interval, the longer the overlap time of two trains is, the more energy generated by trains in braking state can be utilized by other tractive trains.

In the same traction power supply interval, the running situations of former and latter trains can be divided as follows:

(1) Situation 1

The former train accelerates to drive out of the station and the latter train brakes to drive into the station. There are four cases in this situation:

- Case 1: The former train has ended up accelerating, while the latter train has not yet started braking, the overlap time is zero.
- Case 2: The former train has not yet started accelerating, while the latter train has ended up braking, the overlap time is zero.
- Case 3: The time that former train stops accelerating is earlier than the time that latter train stops braking. This case is shown in Fig. 1.
- Case 4: The time that latter train stops braking is earlier than the time that former train stops accelerating. This case is shown in Fig. 2

**Fig. 1** Former train stops accelerating earlier than latter train stops braking

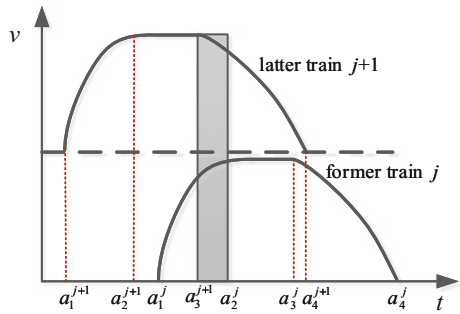
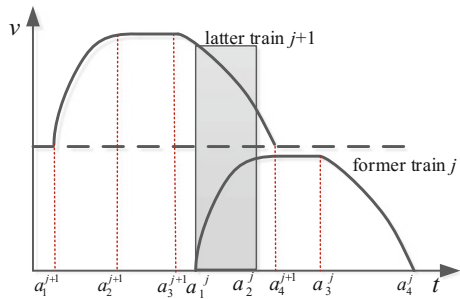


**Fig. 2** Latter train stops braking earlier than former train stops accelerating



The calculating formula of overlap time for situation 1 is summarized as follows:

$$F_1 = \begin{cases} 0 & a_2^j \leq a_3^{j+1} \\ \min[T_z^{j+1}, (a_2^j - a_3^{j+1})] & a_1^j < a_3^{j+1} \leq a_2^j \\ \min[T_a^j, (a_4^{j+1} - a_1^j)] & a_3^{j+1} < a_1^j \leq a_4^{j+1} \\ 0 & a_4^{j+1} \leq a_1^j \end{cases} \quad (2)$$

where  $F_1$  is the overlap time of adjacent trains in case 1,  $a_1^j$  and  $a_2^j$  are the time that the  $j$ th train starts and stops accelerating,  $a_3^j$  and  $a_4^j$  are the time that the  $j$ th train starts and stops braking,  $T_a^j$  and  $T_z^j$  are the accelerating and braking time of the  $j$ th train.

(2) Situation 2

The second situation is the former train brakes to drive into the station and the latter train in different interval accelerates to drive out of the station. There are also four cases in this situation.

- Case 1: The former train has ended up braking, while the latter train has not yet started accelerating, the overlap time is zero.
- Case 2: The former train has not started braking, while the latter train has stopped accelerating, the overlap time is zero.
- Case 3: The former train stops braking earlier than the latter train stops accelerating, this situation is shown in Fig. 3.
- Case 4: The latter train stops accelerating earlier than the former train stops braking, this situation is shown in Fig. 4.

**Fig. 3** Former train stops braking earlier than latter train stops accelerating

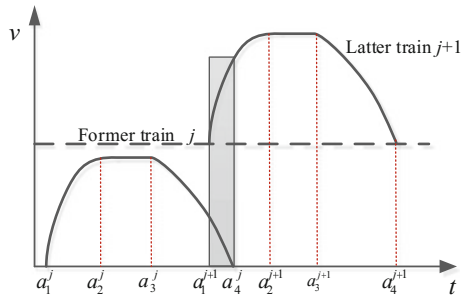
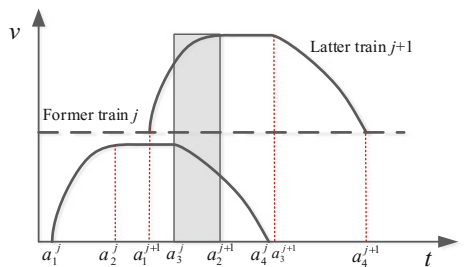


**Fig. 4** Latter train stops accelerating earlier than former train stops braking



Considering these two trains are running in different intervals, they may working in various power supply interval. It is necessary to judge whether these two trains are running in the same interval. The calculating formula of overlap time for situation 2 is summarized as follows,  $\lambda = 1$  signifies these two trains are running in the same power supply interval,  $\lambda = 0$  signifies they are not running in the same power supply interval.

$$F_2 = \begin{cases} 0 & a_4^j \leq a_1^{j+1} \\ \min[T_a^{j+1}, (a_4^j - a_1^{j+1})] \cdot \lambda(j, j+1) & a_3^j < a_1^{j+1} \leq a_4^j \\ \min[T_z^j, (a_2^{j+1} - a_3^j)] \cdot \lambda(j, j+1) & a_1^{j+1} < a_3^j \leq a_2^{j+1} \\ 0 & a_2^{j+1} \leq a_3^j \end{cases} \quad (3)$$

### 3.2 Objective Function and Constraint Condition

Take the utilization amount of regenerative braking energy as the optimization objective and stop time as the control variable. The objective function  $f_1(x)$  is:

$$f_1(x) = \sum_{i=1}^{N-1} \sum_{m=1}^M [F_1(h_i(x), d_m(x)) + \lambda(i, i+1) \cdot F_2(h_i(x), d_m(x))] \quad (4)$$

where  $M$  is the amount of power supply intervals,  $N$  is the amount of trains running in one direction per hour at peak hours.  $h_i$  is the departure interval of the  $i$ th train,  $d_n$  is train's stop time in  $n$ th station.

The objective function  $f_2(x)$  related to total running hours is:

$$f_2(x) = \left[ \sum_{k=1}^K (d_k(x)) + \sum_{j=1}^{K-1} (T_j(x)) \right] \quad (5)$$

where  $d_k$  is train's stop time in  $K$ th station,  $T_j$  is train's running time in  $j$ th interval. In order to ensure train running in the normal working condition, take safety index, accurate parking index, comfort index as the constraint condition.

Constraint condition  $g_1(x)$  related to safety index is:

$$g_1(x) = K\_V = 0 \quad (6)$$

where  $K\_V$  is the flag of speeding,  $K\_V = 0$  signifies not speeding,  $K\_V = 1$  signifies speeding.



Constraint condition  $g_2(x)$  related to stop time is:

$$l_{di} \leq g_2(x) = d_n \leq u_{di} \quad (7)$$

where  $l_{di}$  and  $u_{di}$  are the minimum and maximum value of stop time respectively.

Constraint condition  $g_3(x)$  related to departure interval is:

$$l_h \leq g_3(x) = h_i = \left\lceil \frac{3600}{N} \right\rceil \quad (8)$$

where  $\left\lceil \frac{3600}{N} \right\rceil$  is the integer of departure interval,  $l_h$  is the safe departure interval time.

### 3.3 Solve Optimization Model

The specified steps of solving multi-train energy-saving optimization model based on Pareto multi-objective genetic algorithm are listed below.

- Step 1: Input basic parameters and initialize population.
- Step 2: Solve the fitness value of overlap time and total running time.
- Step 3: Do non-dominated sorting and calculate individual's congestion.
- Step 4: Select elite individual, generate progeny population.
- Step 5: Merge elite population with parent population and obtain a new population
- Step 6: Do crossover and mutation operation, obtain a new generation.
- Step 7: If the interaction has not reached the maximum times, go back to step 2, if not, go to step 8.
- Step 8: Save the most optimal Pareto non-dominated solution.
- Step 9: Obtain new stop time and timetable after optimization.

## 4 Experiment Analysis

Take the data of Guangzhou metro line No. 7 for energy-saving optimization simulation analysis. The selected peak hours is from 7 a.m. to 8 a.m. The power supply interval is divided into 6 sections. The expected departure number of trains in up and down lines is 18 respectively from 7 a.m. to 8 a.m. The related parameters settings is shown in Tables 1 and 2.

The simulation result is shown in Fig. 5 and the comparison of schedule between before and after optimization is shown in Table 3.

**Table 1** Simulation parameters for train’s running

Parameter	Value
Train length (m)	118.32
Maximum speed (km/h)	80
Maximum acceleration (m/s <sup>2</sup> )	1.2
Transfer efficiency of regenerative braking energy	0.7
Simulation time step (s)	0.01

**Table 2** Total running time and stop time settings

Parameter	Total running time	Maximum stop time	Minimum stop time	
			Transfer station	Non-transfer station
Value (s)	1385	60	30	25

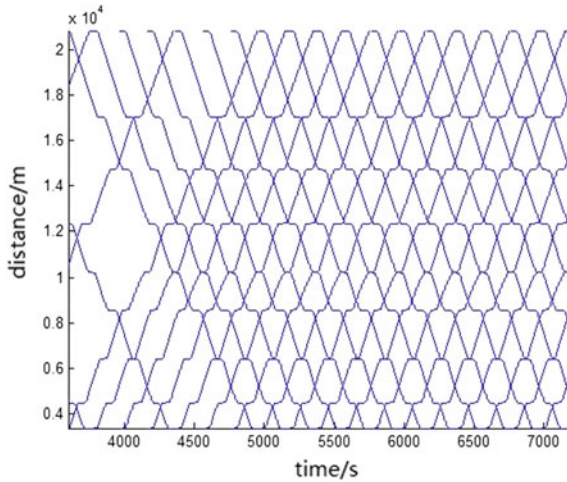


**Fig. 5** Trains running simulation result

As shown in Table 3, after the optimization, stop time in Shibi station reduced from 30 to 29 s, stop time in Hanlong changxi station added from 30 to 31 s, stop time in other stations kept unchanged, the total running time remained unchanged but the total overlap time was 1462 s which had raised 53.6% compared with 952 s before optimization.

**Table 3** Optimal departure timetable

Station	Before optimization (s)				After optimization (s)			
	Arrival	Departure	Stop	Travel	Arrival	Departure	Stop	Travel
Guangzhou south	200	235	35	80	200	235	35	80
Shibi	315	345	30	121	315	344	29	121
Xiecun	466	491	25	133	465	490	25	133
Zhongcun	624	649	25	108	623	648	25	108
Hanxi changlong	757	802	45	132	756	801	45	132
Hezhuang	933	963	30	155	932	963	31	155
Guantang	1118	1153	35	143	1118	1153	35	143
Nancun	1296	1331	35	218	1296	1331	35	218
Daxuecheng south	1549	1584	35		1549	1584	35	80
Running time	1385				1385			
Overlap time	952				1462			

**Table 4** Relations between departure interval and overlap time

Departure interval (s)	200	163	120
Initial total overlap time (s)	952	1911	4963
Initial average overlap time (s)	52.9	86.9	165.4
Optimal overlap time (s)	1462	2121	5495
Average optimal overlap time (s)	81.2	96.4	183.2
Optimization rate	53.5%	10.9%	10.8%

Analyze the influence factor of the utilization of regenerative energy, we can draw a conclusion that the departure interval affects the utilization. Departure interval is inversely proportional to the number of departure in per hour. The change of departure interval can result in a corresponding changing in timetable (Table 4).

Take the data in metro line No. 7 as an example, analyze the relations between departure interval and overlap time.

When the departure interval reduced from 200 to 163 s, the total overlap time raised from 1462 to 2121 s, when departure interval reduced from 200 to 120 s, the total overlap time raised from 2121 to 5495 s. departure interval has a great influence to the total overlap time. The comparison between each train’s average overlap time before and after optimization is shown in Fig. 6.

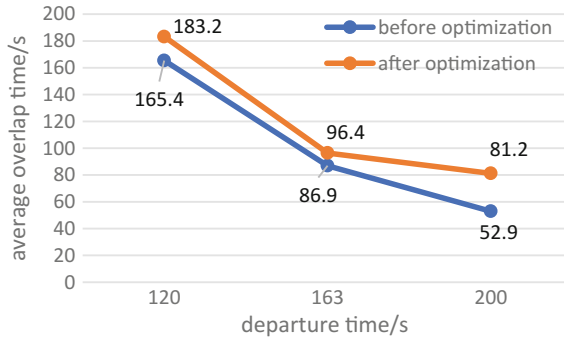


**Fig. 6** Comparison of each train's average overlap time before and after optimization

## 5 Conclusion

This paper proposed a method for multi-train energy saving based on Pareto multi-objective genetic algorithm. The approach of optimizing train's timetable is easy to operate and this method can make the best of regenerative braking energy and reduce total energy consumption in the process of train's running. The simulation result indicates the rationalization and feasibility of this optimization method.

**Acknowledgements** This work is supported by National Key R&D Program of China under Grant (2016YFB1200402) and Guang Zhou science and technology plan project (No. 201604030061).

## References

1. Jian Y, Fayang L (2011) Review of the utilization of vehicular braking energy in urban railway transportation. *J Railway* 11:27–32 (in Chinese)
2. Shili L, Wenji S, Jingxian H (2014) Simulation on regenerative braking energy and utilization of rail transit vehicle. *J Mass Trans* 17(5):59–63,67 (in Chinese)
3. Bo L (2004) Research and implementation of braking-energy recovery system based on pure electric vehicle. School of Computer Science and Technology, TsingHua University, Beijing (in Chinese)
4. Qirui Z, Daqian B (2012) Application of regenerative braking energy injected-grid device for subway. *J Power Electron* 9(46):61–64 (in Chinese)
5. Bochamnikov YV, Tobias AM, Roberts C et al (2007) Optimal driving strategy for traction energy saving on DC suburban railways. *J IET Electric Power Appl* 1(5):675
6. Yang X, Li X, Gao Z et al (2013) A cooperative scheduling model for timetable optimization in subway systems. *J IEEE Trans Intell Transp Syst* 14(1):438–447
7. Peña-Alcaraz M, Fernández A, Cucala AP et al (2012) Optimal underground timetable design based on power flow for maximizing the use of regenerative-braking energy. *J Proc Inst Mech Eng Part F: J Rail Rapid Trans* 226(4):397–408

8. Nasri A, Fekri Moghadam M, Mokhtari H (2010) Timetable optimization for maximum usage of regenerative energy of braking in electrical railway systems. In: SPEEDAM 2010. IEEE
9. Jia F (2014) Train behavior optimization of urban rail transit system considering energy saving. Beijing Jiaotong University, Beijing (in Chinese)
10. Haichuan T (2012) Energy-efficient multi-train control in metro transit system. Southwest Jiaotong University, Chengdu (in Chinese)
11. Fang W, Yunqing R (2016) Fast construction method of pareto non-dominated solution for multi-objective decision making problem. *J Syst Eng Theor Pract* 36(2):454–463 (in Chinese)
12. Deb K, Jain H (2012) Handling many-objective problems using an improved NSGA-II procedure. *Evol Comput* 22(10):1–8

# Optimized Discrete Model Based Model Reference Adaptive System for Speed Sensorless Control

Shaobo Yin, Yuwen Qi, Yi Xue, Huaiqiang Zhang and Dongyi Meng

**Abstract** In this paper, an improved inductive motor model reference adaptive system (MRAS) is proposed based on an optimized full-order adaptive observer. By using of an optimized discrete model of induction motor, the proposed method can be applied to the condition of low switching frequency. The rotor speed is calculated by an adaptive scheme and used as the feedback signal for vector control. The simulation results show that the modified version of MRAS enables accurate and stable performance of speed sensorless control.

**Keywords** Traction inverter · Sensorless control · Vector control  
Discrete model

## 1 Introduction

Speed sensorless vector control technique has the advantage of reducing the hardware cost and increasing the robustness of system [1]. While the flux observation and speed estimation are the key points of speed sensorless control. The orientation of the flux will affect the performance of the control system, where the flux observation plays the most important role [2].

Thus far, there are so many schemes for speed sensorless control of induction motor. Such as the open loop speed estimation based on motor dynamic model [3], model reference adaptive system (MRAS) [4, 5], rotor speed estimation through high frequency signal injection [6], extend Kalman Filter method [7] and sliding

---

S. Yin (✉)

School of Electrical Engineering, Beijing Engineering Research Center for Electric Rail Transportation, Beijing Jiaotong University, Beijing 100044, China  
e-mail: 15117395@bjtu.edu.cn

Y. Xue

Shanghai Railway Administration Dispatch Place, Shanghai 200071, China

Y. Qi · H. Zhang · D. Meng

CRRC Changehun Railway Vehicles Co., Ltd, Changehun 130062, China

© Springer Nature Singapore Pte Ltd. 2018

L. Jia et al. (eds.), *Proceedings of the 3rd International Conference on Electrical and Information Technologies for Rail Transportation (EITRT) 2017*, Lecture Notes in Electrical Engineering 482, [https://doi.org/10.1007/978-981-10-7986-3\\_20](https://doi.org/10.1007/978-981-10-7986-3_20)

197

mode control [8]. Most of these strategies are based on the motor model in continuous domain, which are not suitable for low switching frequency control period. In general, traction inverters have low switching frequency, as well as the control algorithm. Then first-order Euler discrete method will not be applicable because it will cause instability during the high speed range.

In this paper, an improved MRAS by using of optimized discrete model is proposed, which maintains stable in high speed region and achieves good performance of speed sensorless control in the condition of low switching frequency. The simulation results are given based on the actual metro traction system for validation.

## 2 Control Strategy of Speed Sensorless

Speed sensorless control for traction motor can be shown in Fig. 1. Unlike conventional vector control, speed information for speed sensorless vector control is not obtained by mechanical speed sensor, but by mathematical model. Therefore, accurate speed estimation is the key to speed sensorless vector control.

## 3 Speed Adaptive Flux Observer

As shown in Fig. 2, the adaptive state observer estimates the states and the rotor speed  $\hat{\omega}_r$ , by regulating the value of  $\hat{\omega}_r$  in the matrix  $\hat{A}$  to eliminate the error

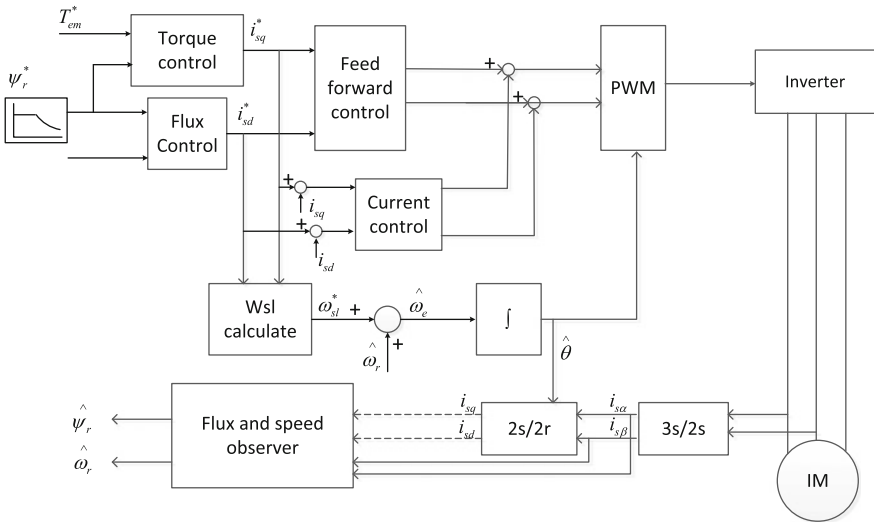


Fig. 1 Speed sensorless vector control block diagram of traction system

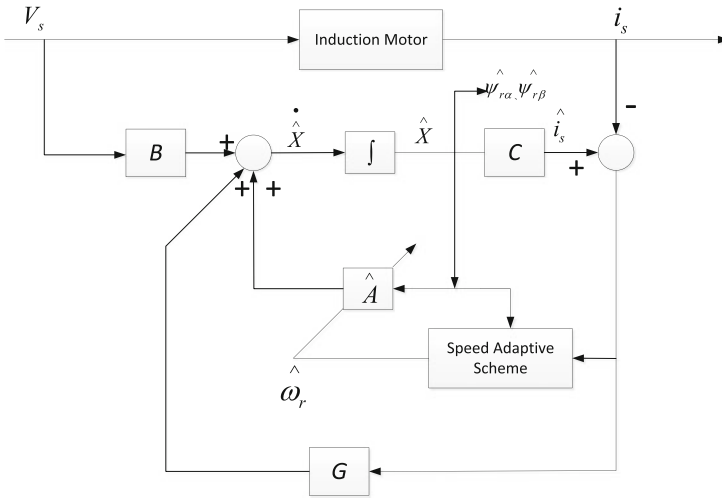


Fig. 2 Block diagram of adaptive flux observer

between actual stator current  $i_s$  and estimated stator current  $\hat{i}_s$ . The adaptive scheme for estimating the rotor speed is added to the observer. By using of Lyapunov theory, we can get the equation of the adaptive scheme.

### 3.1 Flux Observer of Induction Motor

In the stationary reference frame, the induction motor can be described by the following state equation:

$$\dot{X} = AX + BV_s \tag{1}$$

where  $X = [i_{s\alpha} \ i_{s\beta} \ \psi_{r\alpha} \ \psi_{r\beta}]^T$ ,  $V_s = [U_{s\alpha} \ U_{s\beta} \ 0 \ 0]^T$

$i_{s\alpha}, i_{s\beta}, U_{s\alpha}, U_{s\beta}$ , are the  $\alpha$  and  $\beta$  components of stator current and voltage, respectively.

The coefficients of the state equation can be expressed as



$$A = \begin{bmatrix} \frac{L_r^2 R_s + L_m^2 R_r}{L_r(L_m^2 - L_s L_r)} & 0 & \frac{-L_m R_r}{L_r(L_m^2 - L_s L_r)} & \frac{-L_m \omega_r}{(L_m^2 - L_s L_r)} \\ 0 & \frac{L_r^2 R_s + L_m^2 R_r}{L_r(L_m^2 - L_s L_r)} & \frac{L_m \omega_r}{(L_m^2 - L_s L_r)} & \frac{-L_m R_r}{L_r(L_m^2 - L_s L_r)} \\ \frac{L_m R_r}{L_r} & 0 & \frac{-R_r}{L_r} & -\omega_r \\ 0 & \frac{L_m R_r}{L_r} & \omega_r & \frac{-R_r}{L_r} \end{bmatrix} \quad (2)$$

$$B = \begin{bmatrix} \frac{1}{\sigma L_s} & 0 \\ 0 & \frac{1}{\sigma L_s} \\ 0 & 0 \\ 0 & 0 \end{bmatrix}$$

where,  $\psi_{r\alpha}$ ,  $\psi_{r\beta}$  are the  $\alpha$  and  $\beta$  components of rotor flux;  $R_s$ ,  $R_r$  are the stator and rotor resistances;  $L_s$ ,  $L_r$  are the stator and rotor self inductances;  $L_m$  is the mutual inductance;  $\sigma$  is the leakage coefficient and  $\sigma = 1 - L_m^2/(L_s L_r)$ ; and  $\omega_r$  is the motor angular frequency.

Then the state observer for estimating the stator current and the rotor flux can be written as:

$$\frac{d}{dt}(\hat{X}) = \hat{A}\hat{X} + BV_s + G(\hat{i}_s - i_s) \quad (3)$$

By replacing the actual speed  $\omega_r$  with estimated speed  $\hat{\omega}_r$  in state equation A to get the new state equation  $\hat{A}$  which is used for rotor speed and flux observation.

To make the adaptive observer stabilize in usual operation, the feedback gain matrix G is calculated to make sure that observer poles is as  $k$  times ( $k \geq 1$ ) as the poles of the induction motor, as shown in (4).

$$G = \begin{bmatrix} (k-1)(\frac{1}{\tau_r} + \frac{1}{\tau'_\sigma}) & (k-1)\hat{\omega}_r \\ -(k-1)\hat{\omega}_r & (k-1)(\frac{1}{\tau_r} + \frac{1}{\tau'_\sigma}) \\ \frac{r_\sigma}{k_r}((k^2-1)(1-k_1) - (k-1)(1 + \frac{\tau'_\sigma}{\tau_r})) & -\frac{r_\sigma}{k_r}(k-1)\hat{\omega}_r\tau'_\sigma \\ \frac{r_\sigma}{k_r}(k-1)\hat{\omega}_r\tau'_\sigma & \frac{r_\sigma}{k_r}((k^2-1)(1-k_1) - (k-1)(1 + \frac{\tau'_\sigma}{\tau_r})) \end{bmatrix} \quad (4)$$

where  $\tau_r = \frac{L_r}{R_r}$ ,  $k_r = \frac{L_m}{L_r}$ ,  $r_\sigma = R_s + k_r^2 R_r$ ,  $k_1 = k_r L_m / (r_\sigma \tau_r)$ ,  $\tau'_\sigma = \sigma L_s / r_\sigma$

### 3.2 Optimized Discrete Model for Adaptive Scheme

It can be seen from (3) that the  $\hat{\omega}_r$  is included in the matrix  $\hat{A}$  of the state observer, so the following scheme for the speed estimation can be derived by using Lyapunov's theory [9] as

$$\hat{\omega}_r = k_p(e_{isz}\hat{\psi}_{r\beta} - e_{is\beta}\hat{\psi}_{rx}) + k_i \int (e_{isz}\hat{\psi}_{r\beta} - e_{is\beta}\hat{\psi}_{rx})dt \quad (5)$$

where  $e_{isz} = i_{sz} - \hat{i}_{sz}$ ,  $e_{is\beta} = i_{s\beta} - \hat{i}_{s\beta}$ .  $k_p$  and  $k_i$  are PI parameters of speed estimation.

By discretizing the equations of stator current and rotor flux in the stator and rotor coordinate systems, respectively, the optimized discrete model can be achieved like:

$$\begin{bmatrix} \hat{i}_{sz}(k+1) \\ \hat{i}_{s\beta}(k+1) \\ \hat{\psi}_{rx}(k+1) \\ \hat{\psi}_{r\beta}(k+1) \end{bmatrix} = \begin{bmatrix} 1 + T_s \frac{L_s^2 R_s + L_m^2 R_r}{L_r(L_s^2 - L_m^2 - L_s L_r)} & 0 & T_s \frac{-L_m R_r}{L_r(L_s^2 - L_s L_r)} & T_s \frac{-L_m \hat{\omega}_r(k)}{(L_s^2 - L_s L_r)} \\ 0 & 1 + T_s \frac{L_s^2 R_s + L_m^2 R_r}{L_r(L_s^2 - L_s L_r)} & T_s \frac{L_m \hat{\omega}_r(k)}{(L_s^2 - L_s L_r)} & T_s \frac{-L_m R_r}{L_r(L_s^2 - L_s L_r)} \\ \frac{L_m R_r}{L_r} T_s \cos(\hat{\omega}_r(k) T_s) & -\frac{L_m R_r}{L_r} T_s \sin(\hat{\omega}_r(k) T_s) & (1 - \frac{T_s R_r}{L_r}) \cos(\hat{\omega}_r(k) T_s) & -(1 - \frac{T_s R_r}{L_r}) \sin(\hat{\omega}_r(k) T_s) \\ \frac{L_m R_r}{L_r} T_s \sin(\hat{\omega}_r(k) T_s) & \frac{L_m R_r}{L_r} T_s \cos(\hat{\omega}_r(k) T_s) & (1 - \frac{T_s R_r}{L_r}) \sin(\hat{\omega}_r(k) T_s) & (1 - \frac{T_s R_r}{L_r}) \cos(\hat{\omega}_r(k) T_s) \end{bmatrix} \\ \times \begin{bmatrix} \hat{i}_{sz}(k) \\ \hat{i}_{s\beta}(k) \\ \hat{\psi}_{rx}(k) \\ \hat{\psi}_{r\beta}(k) \end{bmatrix} + \begin{bmatrix} \frac{T_s}{\sigma L_s} & 0 \\ 0 & \frac{T_s}{\sigma L_s} \\ 0 & 0 \\ 0 & 0 \end{bmatrix} \begin{bmatrix} U_{sz}(k) \\ U_{s\beta}(k) \end{bmatrix} + G \begin{bmatrix} i_{sz}(k) - \hat{i}_{sz}(k) \\ i_{s\beta}(k) - \hat{i}_{s\beta}(k) \end{bmatrix} \quad (6)$$

By using (5) and (6), estimated  $\hat{\omega}_r$  and rotor flux are obtained. The accuracy of  $\hat{\omega}_r$  plays an important role in the output torque of induction motor. While the optimized discrete model improves the discrete accuracy, and can estimate the rotor speed with less error, then good performance of speed sensorless control can be achieved.

**Table 1** Main parameters of the traction induction motor

Parameters	Value
Rated line voltage $V_N$	550 V
Rated stator current $I_N$	240 A
Rated power $P_N$	180 kW
Rated stator frequency $f_N$	77 Hz
Stator self-inductance $L_s$	0.01076 H
Rotor self-inductance $L_r$	0.01076 H
Magnetizing inductance $L_m$	0.010184 H
Stator resistance $R_s$	0.027027 $\Omega$
Rotor resistance $R_r$	0.028424 $\Omega$

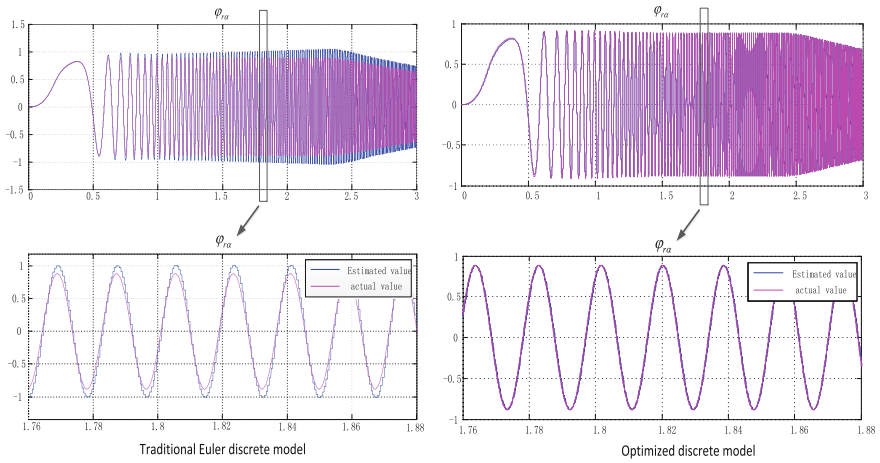


Fig. 3 Observation results of rotor flux

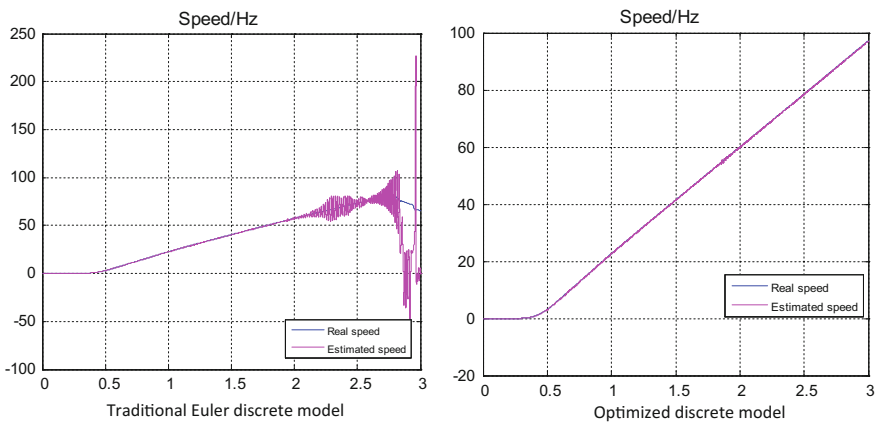
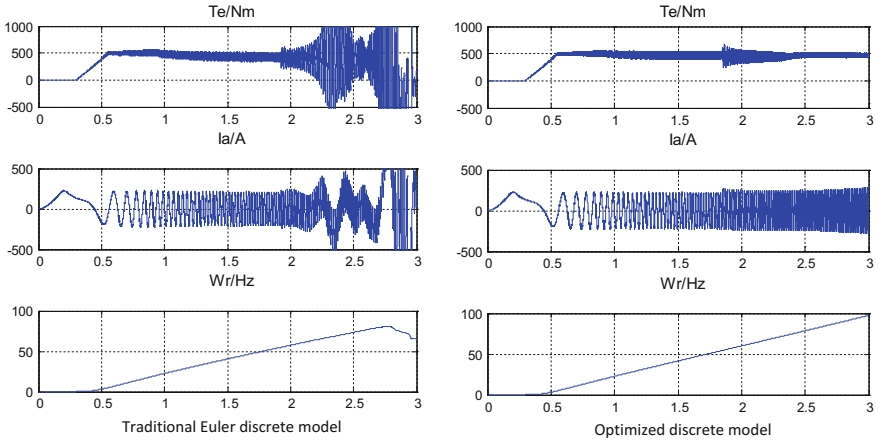


Fig. 4 Estimated and measured rotor speed

### 4 Simulation Results

In order to verify the proposed speed sensorless control strategy, a simulation model was built in MATLAB/Simulink based on an actual traction motor, and the main parameters are given in Table 1. The modulation method adopts hybrid method [10]. The simulation results are shown in Figs. 3, 4 and 5.

A constant torque command of 500 Nm is given to the motor. Then the motor speed up from 0 to 100 Hz.



**Fig. 5** Vector control using estimated speed

From Fig. 3, compared to the results of traditional first-order forward Euler model, the observed rotor flux of  $\hat{\psi}_{rx}$  obtained by optimized discrete model is close to the actual value of  $\hat{\psi}_{rx}$ . And from the enlarged view of observation results, the waveforms of rotor flux is smooth and sinusoidal, from low speed to high speed, the discrete adaptive model achieves a good result.

From the Fig. 4, based on the traditional Euler discrete model, the estimated rotor speed calculated by the purposed speed adaptive scheme becomes unstable during high speed range, while under the same conditions, the optimized discrete model maintains stable and get the rotor speed accurately during the whole speed range.

By replacing the measured speed with the estimated speed using optimized discrete model, the vector control strategy shows good performance as shown in Fig. 5. The output torque is stabilized in about 500 Nm, there is no phenomenon of reduced or elevated torque compared to the results of traditional Euler discrete model, and the stator current and actual rotor speed are stable during the acceleration process.

## 5 Conclusion

This paper used modified version of the model reference adaptive system to estimate the actual speed accurately. There is little influence on torque performance when the estimated speed is used for vector control. The optimized discrete model is stable in the whole speed region for speed sensorless control compared to traditional Euler discrete model. The simulation results verify the validity of the proposed method.

**Acknowledgements** This work was supported by the China National Science and Technology Support Program under Grant 2016YFB1200502-04 and the Fundamental Research Funds for the Central Universities under Grant 2016JBM058 and Grant 2016RC038.

## References

1. Finch JW, Giaouris D (2008) Controlled AC electrical drives. *IEEE Trans Ind Electron* 55(2): 481–491
2. Diao LJ, Sun Dn, Dong K, Zhao LT, Liu ZG (2013) Optimized design of discrete traction induction motor model at low switching frequency. *IEEE Trans Power Electron* 28(10):4803–4810
3. Kumar R, Das S, Syam P et al (2015) Review on model reference adaptive system for sensorless vector control of induction motor drives. *IET Electr Power Appl* 9(7):496–511
4. Teja AVR, Chakraborty C, Maiti S et al (2012) A new model reference adaptive controller for four quadrant vector controlled induction motor drives. *IEEE Trans Ind Electron* 59(10): 3757–3767
5. Benlaloui I, Drid S, Chrifi-Alaoui L et al (2015) Implementation of a new MRAS speed sensorless vector control of induction machine. *IEEE Trans Energy Convers* 30(2):588–595
6. Caruana C, Asher GM, Sumner M (2006) Performance of HF signal injection techniques for zero-low-frequency vector control of induction machines under sensorless conditions. *IEEE Trans Ind Electron* 53(1):225–238
7. Bensiali N, Etien E, Benalia N (2015) Convergence analysis of back-EMF MRAS observers used in sensorless control of induction motor drives. *Math Comput Simul* 115:12–23
8. Comanescu M, Xu L (2006) Sliding-mode MRAS speed estimators for sensorless vector control of induction machine. *IEEE Trans Ind Electron* 53(1):146–153
9. Maes J, Melkebeek JA (2000) Speed-sensorless direct torque control of induction motors using an adaptive flux observer. *IEEE Trans Ind Appl* 36(3):778–785
10. Diao LJ, Tang J, Loh PCA et al (2017) An efficient DSP-FPGA-based implementation of hybrid PWM for electric rail traction induction motor control. *IEEE Trans Power Electron*

# NPV Control Method by Injecting Zero Sequence Voltage for Three Level NPC Inverter

Bo Gong and Yang Liu

**Abstract** The relationship of the zero sequence voltage and the neutral point voltage (NPV) is studied based on SPWM, in this paper. A new NPV control scheme by injecting a simple zero sequence voltage is proposed. The presented method does not require large collection of current and voltage signals, so it is very easy to implement. And the validity of the NPV control method is verified based on Matlab platform.

**Keywords** Zero sequence voltage · NPV · Control scheme · SPWM

## 1 Introduction

The NPV imbalance is an inherent problem of Neutral Point Clamped (NPC) three-level inverters. Many control methods are used to maintain the NPV balance [1–3]. Most of them are based on SVPWM and SPWM [4, 5]. For SVPWM, four types vectors are defined: large vectors, medium vectors, small vectors, and zero vectors. There are two redundant states positive and negative for each small vector, they have the same effect on the synthetic voltage vector, but their effect on the MPV is the opposite. So, the positive small vector and negative small vector are selected for NPV control [6]. But there are many combinations of switch states, resulting in very complex computation. For SPWM, usually, the NPV is controlled by superimposing the zero sequence component to the modulation wave [7]. The bias term and an offset are added to command voltage for synthesizing two auxiliary waves. Two auxiliary waves are used to balance the NPV [8]. However, the methods need a lot of parameters.

In this paper, the relationship of the zero sequence voltage and the NPV is discussed, and a NPV control scheme by injecting a simple zero sequence voltage based on SPWM is proposed. The zero sequence voltage used in this paper is very

---

B. Gong (✉) · Y. Liu

Wuhan Institute of Marine Electric Propulsion, CSIC, Wuhan, China  
e-mail: 151701728@163.com

© Springer Nature Singapore Pte Ltd. 2018

L. Jia et al. (eds.), *Proceedings of the 3rd International Conference on Electrical and Information Technologies for Rail Transportation (EITRT) 2017*, Lecture Notes in Electrical Engineering 482, [https://doi.org/10.1007/978-981-10-7986-3\\_21](https://doi.org/10.1007/978-981-10-7986-3_21)

205

easy to implement with few parameters of the systems, Simulation results based on Matlab platform show that the balance of NPV can be maintained well by using the proposed method.

## 2 Instantaneous Volatility of NPV Analysis

The NPV unbalance can be represented as

$$dU_c = U_{c1} - U_{c2} = \frac{i_a t_{ao} + i_b t_{bo} + i_c t_{co}}{C} \tag{1}$$

where  $t_{ao}, t_{bo}, t_{co}$  are the zero state time,  $t_{jo}(j = a, b, c)$  can be represented as

$$t_{jo} = \begin{cases} 1 - u_j & (u_j \geq 0) \\ 1 + u_j & (u_j < 0) \end{cases} \tag{2}$$

As shown in Fig. 1, a voltage modulation wave cycle is divided into six ranges.

Assumed the injected zero sequence component is  $u_z$ , then in range I, the instantaneous volatility of NPV can be expressed as

$$\begin{aligned} \Delta U_c &= \frac{i_a(1 - u_a - u_z) + i_b(1 + u_b + u_z) + i_c(1 - u_c - u_z)}{C} \\ &= \frac{m \times I_m}{C} \times \left[ -\frac{\cos \varphi}{2} - \cos\left(2 \times \omega t - \frac{4\pi}{3} - \varphi\right) \right] + \frac{2 \times I_m \times u_z}{C} \times \sin\left(\omega t - \frac{2\pi}{3} - \varphi\right) \end{aligned} \tag{3}$$

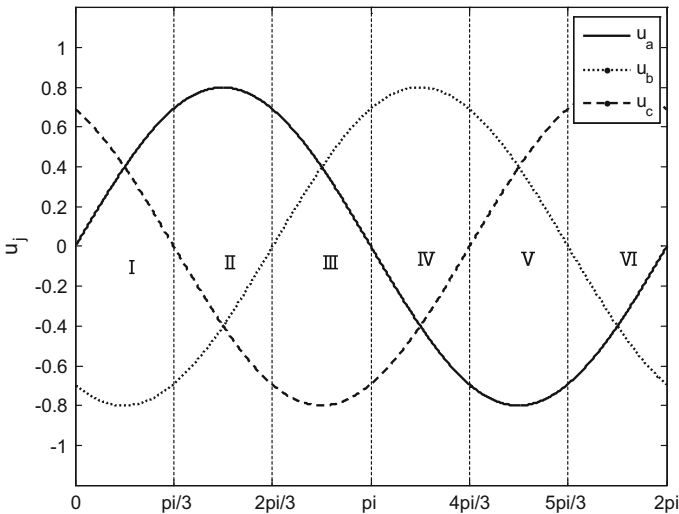


Fig. 1 SPWM range distribution

Following the same method, the NPV transient expression by injecting zero-sequence component in other ranges are shown as below (Table 1).

Therefore, NPV can be controlled by selecting the appropriate zero sequence voltage.

### 3 NPV Balance Control Method

A new SPWM scheme based on adding simple a zero sequence signal to the modulation waves is proposed in this paper for NPV balance control. Maintaining the NPV can be accomplished by changing the amplitude and phase of the zero sequence signal. In the scheme, the modulation waves are changed. The zero sequence signal  $u_z$  is expressed by following expressions:

$$u_z = \frac{8 \times K \times u_a \times u_b \times u_c \times (u_a - u_b) \times (u_b - u_c) \times (u_c - u_a)}{3\sqrt{3} \times m^5} \tag{4}$$

Let  $K$  be the changing coefficient,  $u_z$  should be limited within  $[-m/4, m/4]$  to prevent excessive changes in the modulated wave, therefore, the range of  $K$  is  $[-1, 1]$ . The greater the  $K$  is, the better the NPV control effect is.

The changed modulation waves are

$$\begin{cases} u_a = m \sin \omega t + u_z \\ u_b = m \sin(\omega t - \frac{2}{3}\pi) + u_z \\ u_c = m \sin(\omega t - \frac{4}{3}\pi) + u_z \end{cases} \tag{5}$$

The changed modulation waves are shown in Fig. 2.

**Table 1** The instantaneous volatility of neutral point voltage

Range	Instantaneous volatility of neutral point voltage
I	$\frac{m \times I_m}{C} \times [-\frac{\cos \varphi}{2} - \cos(2 \times \omega t - \frac{4\pi}{3} - \varphi)] + \frac{2 \times I_m \times u_z}{C} \times \sin(\omega t - \frac{2\pi}{3} - \varphi)$
II	$\frac{m \times I_m}{C} \times [\frac{\cos \varphi}{2} + \cos(2 \times \omega t - \varphi)] - \frac{2 \times I_m \times u_z}{C} \times \sin(\omega t - \varphi)$
III	$\frac{m \times I_m}{C} \times [-\frac{\cos \varphi}{2} - \cos(2 \times \omega t - \frac{2\pi}{3} - \varphi)] + \frac{2 \times I_m \times u_z}{C} \times \sin(\omega t - \frac{4\pi}{3} - \varphi)$
IV	$\frac{m \times I_m}{C} \times [\frac{\cos \varphi}{2} + \cos(2 \times \omega t - \frac{4\pi}{3} - \varphi)] - \frac{2 \times I_m \times u_z}{C} \times \sin(\omega t - \frac{2\pi}{3} - \varphi)$
V	$\frac{m \times I_m}{C} \times [-\frac{\cos \varphi}{2} - \cos(2 \times \omega t - \varphi)] + \frac{2 \times I_m \times u_z}{C} \times \sin(\omega t - \varphi)$
VI	$\frac{m \times I_m}{C} \times [\frac{\cos \varphi}{2} + \cos(2 \times \omega t - \frac{2\pi}{3} - \varphi)] - \frac{2 \times I_m \times u_z}{C} \times \sin(\omega t - \frac{4\pi}{3} - \varphi)$



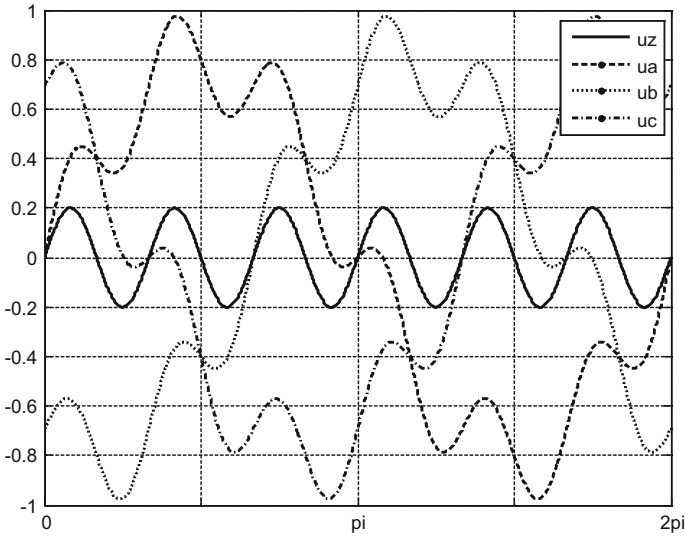


**Fig. 2** The changed modulation waves and zero sequence signal

## 4 Simulation Results

To verify the effectiveness of the proposed method, a NPV control model is built based on Matlab. To make the NPV unbalance, a resistor is connected in parallel to  $C_2$ . The NPV control works at 0.2 s in the simulation.

As shown in Fig. 3,  $dU_c$  shift away from zero at first, when the control method works at 0.2 s, the regulation of NPV balance works quickly. And  $dU_c$  is controlled to be zero. The modulation index is 0.8 in Fig. 3a, b, but  $K$  is different. In Fig. Figure 3a,  $K = 1$ , and in Fig. 3b,  $K = 0.5$ , it is clearly that the greater the  $K$  is, the better the NPV control effect is, which is the same as the theoretical analysis. In Fig. 3c, the modulation index is 0.4, and  $K = 1$ , the NPV is controlled to be balance quickly even at low modulation index, it is proved that this control method is effective at different modulation index.

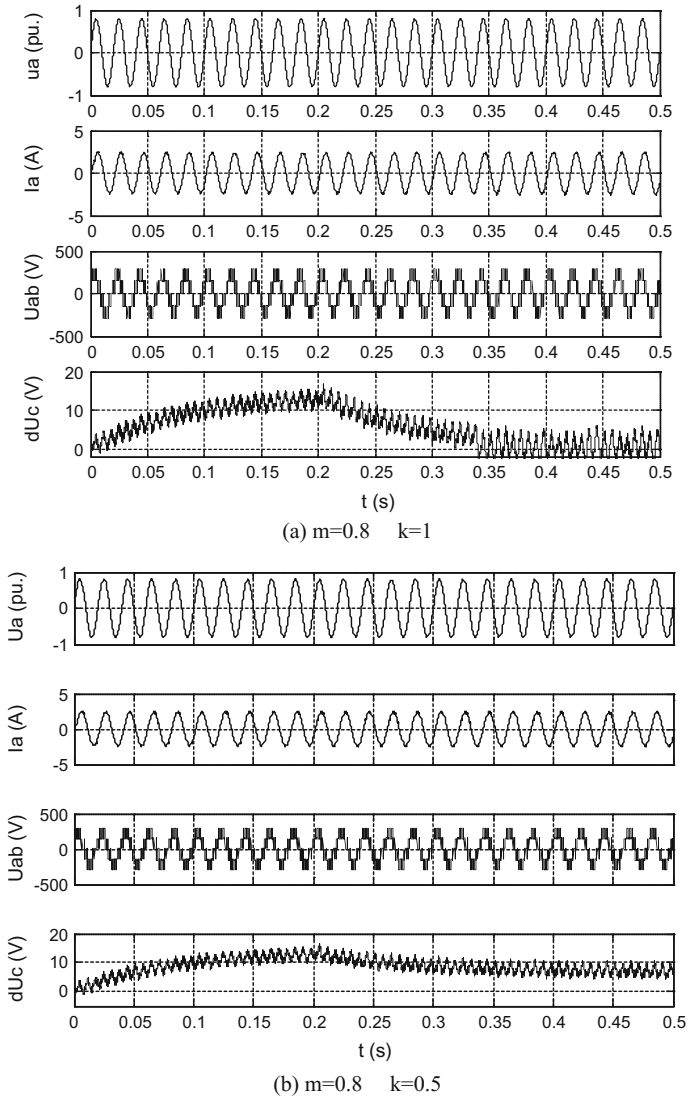


Fig. 3 Control results at different modulation indexes

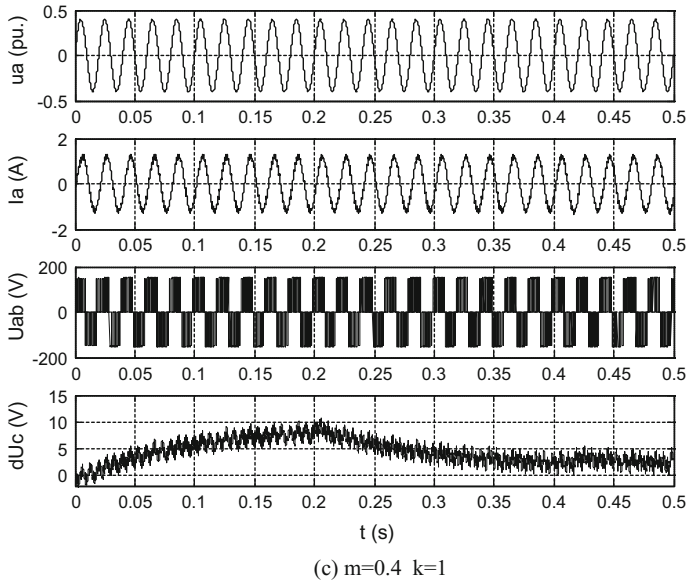


Fig. 3 (continued)

## 5 Conclusions

In this paper, a simple zero sequence voltage injecting method is proposed to maintain the NPV balance. Compared to other zero-sequence signal injection neutral point voltage control method, the present method does not require a large collection of current and voltage signals, so it is very easy to implement, and the simulation results show the effectiveness of the proposed method.

## References

1. Mekhilef S, Kadir MN (2010) Voltage control of three-stage hybrid multilevel inverter using vector transformation. *IEEE Trans Power Electron* 25(10):2599–2606
2. Alemi P, Jeung Y, Lee D (2015) DC-link capacitance minimization in T-type three-level AC/DC/AC PWM converters. *IEEE Trans Ind Electron* 62(3):1382–1391
3. Lee J, Lee K (2016) Time-offset injection method for neutral-point AC ripple voltage reduction in a three-level inverter. *IEEE Trans Power Electron* 31(3):1931–1941
4. Cobreces S, Bordonau J, Salaet J, Bueno EJ, Rodriguez FJ (2009) Exact linearization nonlinear neutral-point voltage control for single-phase three-level NPC converters. *IEEE Trans Power Electron* 24(10):2357–2362
5. Deng Y, Harley RG (2015) Space-vector versus nearest-level pulse width modulation for multilevel converters. *IEEE Trans Power Electron* 30(6):2962–2974

6. Zhu R, Wu X, Tang Y (2015) Duty cycle-based three-level space-vector pulse-width modulation with overmodulation and neutral-point balancing capabilities for three-phase neutral-point clamped inverters. *IET Power Electron* 8(10):1931–1940
7. Yongdong L, Chenchen W (2010) Analysis and calculation of zero-sequence voltage considering neutral-point potential balancing in three-level NPC converters. *IEEE Trans Ind Electron* 57(7):2262–2271
8. Qiang S, Wenhua L, Qingguang Y, Zhonghong W (2003) A neutral-point potential balancing algorithm for three-level NPC inverters using analytically injected zero-sequence voltage. In: *Proceedings of the 8th IEEE annual conference on applied power electronics*, pp 228–233

# Analysis on the Vehicle Network Harmonic Oscillation and Its Influencing Factors of China's Electrified Railway

Yue Xu, Peng Lin, Shihui Liu, Fei Lin and Zhongping Yang

**Abstract** With the rapid development of China's electrified railway, vehicle network harmonic oscillation attracts more attention. The four-quadrant converter is an important part of the traction drive system. Based on its main circuit and control strategy, different vehicle network harmonic oscillation are classified by the mechanism and frequency into mediate-frequency harmonic oscillation and high-frequency harmonic oscillation. Their control loop transfer function are established separately and their main influencing factors are analyzed. Use the main circuit parameters of China's electrified railway to establish a Simulink model. Analyze current wave and its FFT result to compare the harmonic oscillation situation. The simulation results verify the correctness of the analysis.

**Keywords** Four-quadrant converter · Vehicle network · Electrified railway Harmonic oscillation · Influencing factors

## 1 Introduction

Traction converter in high-speed train traction drive system mainly uses pulse width modulation. With the large-scale use of high-speed trains, phenomenon of substation tripping, arrester burned, train outage and other accidents caused by harmonic oscillation have occurred sometimes. In 2009, CRH2 EMU run in Hefei to Longcheng line, where 850 Hz oscillation occurred [1]. In 2011, in Xuzhou East—Bengbu South pilot section of the Beijing-Shanghai high-speed railway, CRH380

---

Y. Xu · P. Lin  
CRRC Qingdao Sifang CO., Ltd., No. 88 Jinhongdong Road,  
Chengyang District, Qingdao, China

S. Liu (✉) · F. Lin · Z. Yang  
School of Electrical Engineering, Beijing Jiaotong University,  
No. 3, Shang Yuan Cun, Beijing, China  
e-mail: 16117399@bjtu.edu.com

in the test process occurred 4750 Hz grid voltage oscillation [2]. Analysis of oscillation and its influencing factors is meaningful to avoid such accidents.

The research on the harmonic oscillation in the vehicle network is generally analyzed in both trains and traction networks. In the domestic and international research, the traction network model is mainly considered as the Thevenin equivalent circuit model [3, 4], so the traction network model as a high-speed train power supply is represented by the ideal infinite voltage source and the impedance in series. High-speed train traction drive system is composed of traction transformer, four quadrant converter, inverter and multiple motors. The support capacitor in the middle DC side of the system is large. It is generally believed that the post-inverter harmonics do not affect the forefront, so we focus on the impact of the four quadrant converter [5–8].

The oscillation frequency is distributed in each frequency band, some are the converter harmonic characteristics frequency, and some are caused by improper converter control parameters [10–14]. In this paper, based on the analysis of the four-quadrant converter, China's electrified railway vehicle network harmonic oscillation and its influencing factors are analyzed from two aspects, mediate frequency (between power frequency and switching frequency), and high frequency (above switching frequency). And the correctness of the analysis is verified by the simulation.

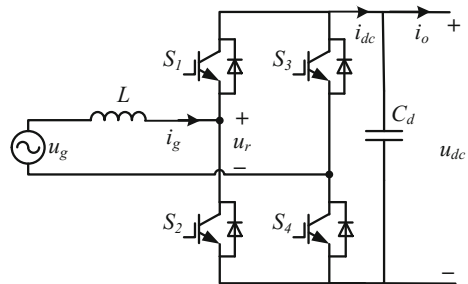
## 2 Circuit Model

### 2.1 Topology of Four-Quadrant Converter

Considering the isolation effect of the DC link of the traction converter, the single-phase four quadrant converter is considered as the key link of the coupling between the high-speed train traction drive system and the traction network. At the same time, the strong nonlinearity of the system determines the complexity of its harmonic components.

Figure 1 is the main circuit structure of four-quadrant converter. Where,  $S_1$ – $S_4$  are semiconductor switching devices;  $L$  is ac-side inductor;  $C_d$  is dc support

**Fig. 1** Main circuit structure of four-quadrant converter



capacitor;  $u_g$  is grid voltage,  $u_r$  is converter ac-side voltage;  $i_g$  and  $i_o$  are respectively the grid current and load current;  $u_{dc}$  and  $i_{dc}$  are respectively the dc output voltage and dc current [14].

### 2.2 Control Strategy of Single-Phase 4Q Converter

The current control strategy [15] of single-phase 4Q converter has been shown in Fig. 2.  $U_d^*$  is for the DC-link voltage command, and  $U_d$  is represented for the DC output voltage sampled value, and the current command ( $i_m^*$ ) amplitude is derived from the PI controller output, and the current command phase is from the input voltage source sampled value.

## 3 Mediate-Frequency Harmonic Oscillation

### 3.1 Theoretical Analysis

Considering the digital control delay, the transfer function block diagram in discrete domain can be derived as Fig. 3 [16].

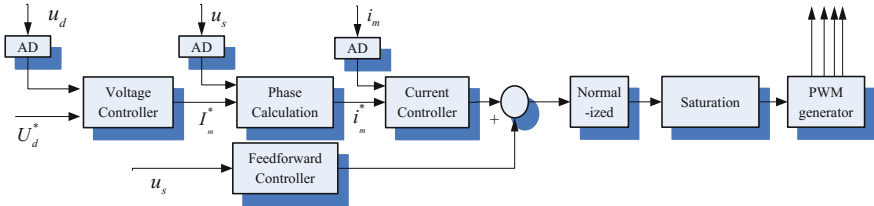


Fig. 2 4Q converter double-loop control strategy

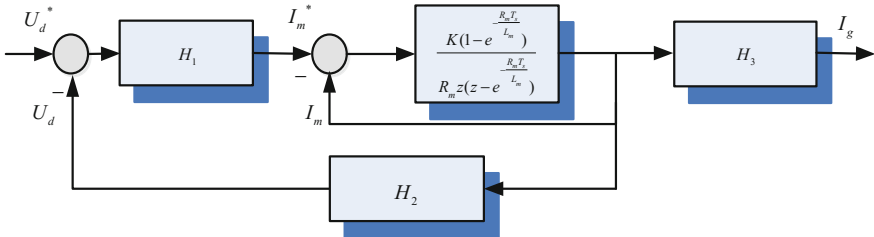


Fig. 3 Transfer function in z-domain of railway power system

$$H_1(z) = \frac{(2K_p + K_i T_s)z + K_i T_s - 2K_p}{2(z - 1)} \quad (1)$$

$$H_2(z) = \frac{(MU_d \sin \varphi - \omega L_m I_m) \cos \varphi T_s R_L (z + 1)}{\sin \varphi [(R_L T_s M + 4R_L U_d C_d + 2T_s U_d)z + R_L T_s M - 4R_L U_d C_d + 2T_s U_d]} \quad (2)$$

$$H_3(z) = \frac{T_s^2 (z + 1)^2}{(4L_g C_g + \cos \varphi_1 T_s^2)z^2 + (-8L_g C_g + 2 \cos \varphi_1 T_s^2)z + 4L_g C_g + \cos \varphi_1 T_s^2} \quad (3)$$

The current loop proportional coefficient  $K$  is the most important parameters.

### 3.2 Simulation Analysis

Use the main circuit in China as shown in Table 1 to establish a Simulink model.

For the nominal loaded simulation model, with gradually increasing  $K$ , the simulation waves and FFTs have been shown in Figs. 4 and 5.

When the sampling frequency of the digital control is 1250 Hz, if the gain of the current loop reaches the critical value of the bifurcation, the current waveform has obvious 200 Hz harmonic. When the digital control sampling frequency is 5000 Hz, the current loop gain of 800 Hz harmonics appear in current waveform bifurcation critical value.

The mediate-frequency harmonic oscillation generated by the four quadrant converter is mainly related to the current loop proportional coefficient of the transient current control strategy, the harmonic oscillation frequency is positively correlated with the switching frequency.

**Table 1** Main circuit parameter of a CRH<sub>2</sub> EMUs 4Q converter and line parameter in China

Meaning	Symbol	Value
Voltage source RMS	$U_m$	150 V
DC-link voltage command	$U_d^*$	300 V
AC side inductance	$L_m$	7 mH
DC-link capacitance	$C_d$	3.3 mF
Nominal resistance load	$R_L$	200 $\Omega$
Switching frequency	$f_{ss}$	5 kHz
Line equivalent inductance	$L_S$	0.1 mH
Line equivalent resistance	$R_S$	0.01 $\Omega$



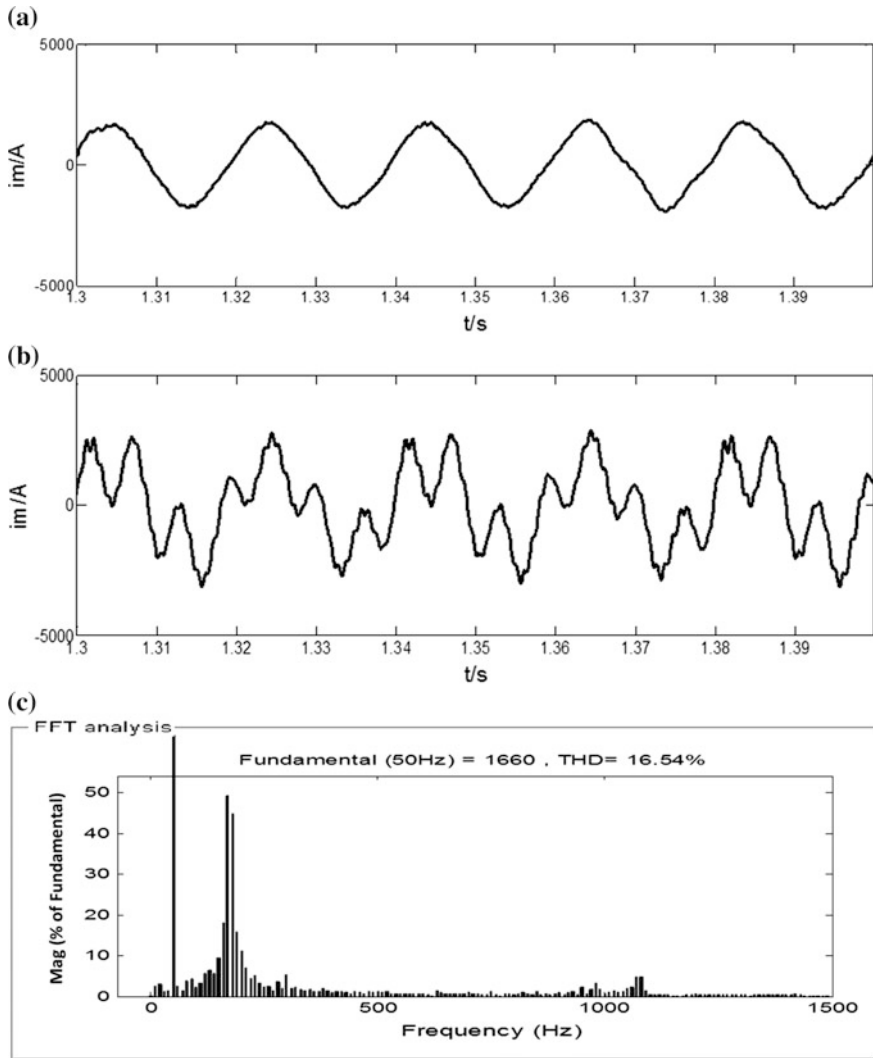


**Fig. 4** AC-side current waves and FFT results of current wave when the sampling frequency of the digital control is 1250 Hz. **a** AC-side current waves with nominal load when the gain of the current loop below the critical value of the bifurcation **b** AC-side current waves with nominal load when the gain of the current loop above the critical value of the bifurcation **c** FFT results of current wave when the gain of the current loop above the critical value of the bifurcation

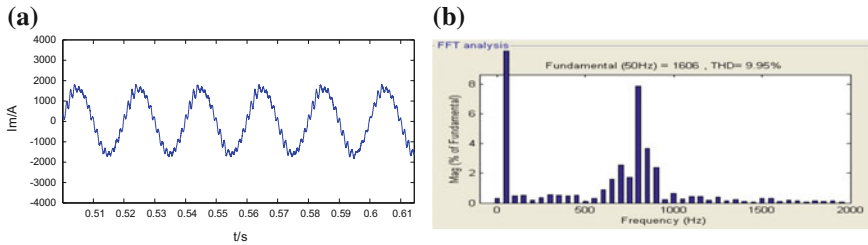


**Fig. 5** AC-side current waves and FFT results of current wave when the sampling frequency of the digital control is 5000 Hz **a** AC-side current waves with nominal load when the gain of the current loop above the critical value of the bifurcation **b** FFT results of current wave when the gain of the current loop above the critical value of the bifurcation

## 4 High-Frequency Oscillation

The pulse rectifier is not a linear element. In the process of switching, the voltage and current in the AC side will contain the harmonic multiple times of the switching frequency. A harmonic current flows into the traction network, and a certain oscillation circuit is formed with the traction network and the traction substation, making the traction substation or train terminal voltage and current amplitude increased significantly.

There are many factors influencing high frequency harmonics.

### 4.1 Multiplex Technology

The multiplex technology of the converter is one of the important factors.

The multiplex technology of the converter refers to the way through the transformer coupling of a number of the same structure of the converter unit in series or parallel way combination. Each unit converter uses a common modulation wave, the phase of the triangular carrier phase of each unit rectifier is staggered with the same phase angle, namely the carrier phase shifting strategy.

When the multiplex technology is used properly, the harmonic content will be reduced. It is obviously from Fig. 6 that the multiplex technology will change the harmonic band. Harmonic frequency shift may also make high frequency oscillation easier to occur.

In practical applications, due to the delay caused by signal transmission and other reasons, carrier phase shift angle will have deviation. It will also affect the harmonic content. In some particular harmonic frequencies, the effect is serious.

From Table 2, it is clearly that if multiple control strategies are applied accurately, the harmonic content will be ideal and it is less likely to occur oscillation. However, once carrier phase shift angle exists gross errors, some particular harmonic content will rise very high, and due to harmonic frequency band is several times of the switching frequency, it is very easy to trigger oscillation.

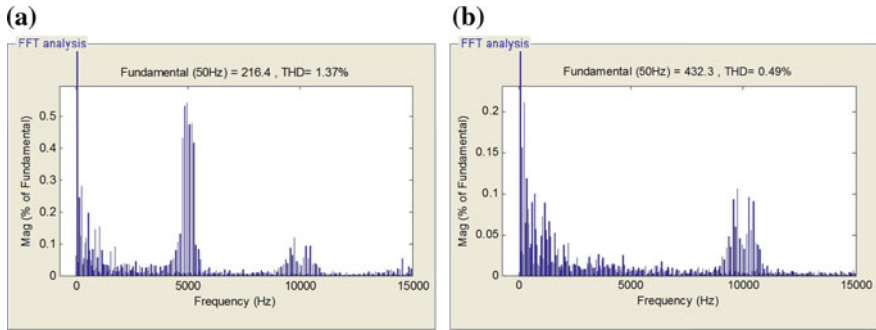


**Fig. 6** FFT results of current wave **a** when double-converter **b** when quadruple-converter

**Table 2** Under certain circumstances, the harmonic content before and after optimization

Conditions	Content of 45th harmonic (%)	Content of 47th harmonic (%)
Carrier phase shift angle exists gross errors	11.3	11.5
Optimize multiple control strategies	0.05	0.28

### 4.2 Other Factors

There are also some other factors to affect high-frequency oscillation.

The harmonic band is mainly concentrated in the 2 times and 4 times of switching frequency. The change of switching frequency will affect the distribution of harmonic band. After detection and check the inherent frequency of the traction network, adjusting the value of the switching frequency can make the harmonic wave of the converter avoid the inherent frequency of the traction network.

Too small transformer inductance will lead to increased harmonic content, and too large inductance will increase transformer volume. Meeting the basic functions of the converter, considering the transformer volume within a reasonable range, increasing transformer inductance in an appropriate area can make current better.

## 5 Conclusion

Based on the model of four quadrant converter, this paper analyzes the influencing factors problem of vehicle network oscillation of the China electrified railway from the following two aspects, mediate frequency and high frequency.

By reasonable setting the current loop parameters, the medium oscillation can be effectively reduced. High frequency harmonic oscillation has many influence factors. The multiplex strategy can effectively reduce the harmonic content and change

the harmonic frequency band to higher frequency. However, if the phase angle is not set properly, it will lead to the rise of harmonic content. Some particular harmonic is very easy to trigger oscillation.

Simulation analysis verifies the specific impact of these factors. These analyses are meaningful to the analysis of the vehicle network oscillation of China's electrified railway.

**Acknowledgements** This work was supported by a grant from the Major State Basic Research Development Program of China (973 Program: 2011CB711100).

## References

1. Xi C, Fei L, Yang Z (2013) Analysis of high frequency oscillations in the power supply line of the high speed train. *Trans China Electrotech Soc* S2:354–359
2. Liu J, Yang Q, Zheng TQ (2012) Harmonic analysis of traction networks based on the CRH380A series EMUs accident. In: *IEEE transportation electrification conference and expo (ITEC)*, Dearborn, MI, pp 1–6
3. Fernandez E, Paredes A, Sala V, Romeral L (2017) Control and modulation techniques applied to converters with impedances networks for traction systems. *IEEE Lat Am Trans* 15(1):21–30
4. Liu Z, Zhang G, Liao Y (2016) Stability research of high-speed railway EMUs and traction network cascade system considering impedance matching. *IEEE Trans Ind Appl* 52(5):4315–4326 (Sept–Oct 2016)
5. Cheng X, Song W, Feng X (2016) Finite control-set model predictive current control of five-phase permanent-magnet synchronous machine based on virtual voltage vectors. *IET Electr Power Appl*:2016. ISSN 1751-8660
6. Zhou X, Yang C, Cai T (2016) A model reference adaptive control/PID compound scheme on disturbance rejection for an aerial inertially stabilized platform. *J Sens* 2016:1. ISSN 1687-725X
7. Lin Z, Su B, Xu B (2016) Application of deadbeat control method in Co-phase traction power supply system. In: *Control conference (CCC) 2016 35th Chinese*, pp 10198–10203. ISSN 1934-1768
8. Chang GW, Lin H-W, Chen S-K (2004) Modeling characteristics of harmonic currents generated by high-speed railway traction drive converters. *IEEE Trans Power Delivery* 19(2):766–773 (April 2004)
9. Chang GW, Lin H-W, Chen S-K (2004) Modeling characteristics of harmonic currents generated by high-speed railway traction drive converters. *IEEE Trans Power Delivery* 19(2):766–773 (April 2004)
10. Lee H, Lee C, Jang G, Kwon S (2006) Harmonic analysis of the korean high-speed railway using the eight-port representation model. *IEEE Trans Power Delivery* 21(2):979–986 (April 2006)
11. Lian Q, Lin F, Wei S, Yang Z, Sun H (2015) Analysis of nonlinear oscillation of four-quadrant converter in high-speed trains based on discrete model. In: *Industrial electronics society, IECON 2015—41st annual conference of the IEEE, Yokohama, Japan*, pp 002124–002129
12. Wang H, Mingli W, Sun J (2015) Analysis of low-frequency oscillation in electric railways based on small-signal modeling of vehicle-grid system in dq frame. *IEEE Trans Power Electron* 30(9):5318–5330

13. Brenna M, Foiadelli F, Zaninelli D (2011) New stability analysis for tuning PI controller of power converters in railway application. *IEEE Trans Ind Electron* 58(2):533–543
14. Lin F, Liu S, Yang Z et al (2016) Analysis of nonlinear oscillation of four-quadrant converter based on discrete describing function approach. 13(17)
15. Zheng J, Feng X, Xie W, Zhang J (2009) The transient current control for single phase PWM rectifiers. *Power Electron* 43(12):2–3
16. Liu S, Yang Z, Lin F et al (2016) Medium-frequency oscillation analysis in high-speed railway system considering power supply system with LCL model. In: *IECON 2016—conference of the IEEE industrial electronics society*. IEEE, pp 3470–3475

# Impact of Rail Transit System on Grid Power Quality

Zerong Li, Lei Han, Dejing Che and Qingxia Wang

**Abstract** As the issues of energy security, environmental degradation and traffic jam becoming more prominent, the rail transit is experiencing an unprecedented prosperity. However, rail transit is a special load system with “four-non” features which can cause the decline in power quality of grid, so it is more important to solve the power quality problems. In this paper, the basic structure of the public power grid and the power supply system of rail transit are introduced firstly. The types and characteristics of main loads are summarized, and the influence factors and potential hazards of the power quality problems are analyzed entirely. Finally, some solutions are proposed to solve each kind of power quality problems.

**Keywords** Power quality · Rail transit · Harmonic · SVG

## 1 Introduction

As the issues of energy security, environmental degradation and traffic jam are becoming more prominent, China’s transportation system will have a crucial period in reducing energy consumption, accelerating mode transformation and transportation system modernization in the next five to ten years [1–3]. Meanwhile, the foreign market is the ‘development blue sea’ of China’s rail transit equipment. As a transportation means of green environmental protection and large capacity, rail transit equipment will be the pioneer in the “One Belt and One Road” strategy which government is implementing energetically. There will be a huge demand market along the “One Belt and One Road” and its radiation areas. It can be seen that whether construction speed or construction scale, China’s urban rail transit is experiencing an unprecedented prosperity.

---

Z. Li (✉) · L. Han · D. Che · Q. Wang  
China Electric Power Research Institute, No. 15, Xiaoying Rd(E), Qinghe,  
Haidian District, Beijing, China  
e-mail: csee\_lizerong@163.com

However, rail transit is a special load system, and its “four non” features, namely, non-linear, non-sinusoidal, asymmetrical and non-continuous, will cause decline in power quality of grid. When it’s serious, it can cause relay protection device incorrect manipulation, trigger system resonance, small and medium-sized generator rotor damage, or even large area blackout [4]. Under the background of the active development of smart grid in China and in the social construction for resource saving and environment-friendly, it is more important to solve the power quality problems [5].

Therefore, in this paper, the basic structure of the public power grid and the power supply system of rail transit are introduced. Then, the types and characteristics of main loads are summarized, and the influence factors and potential hazards of the power quality problems were analysed entirely. Finally, the corresponding solutions are proposed for each kind of power quality problems and the power quality of electric grid is improved effectively.

## **2 Power Supply System and Main Loads of Rail Transit**

### ***2.1 Public Grid and Traction Power System***

As a special user of urban grid, rail transit obtains the electricity from urban grid directly, without the need for separate power plant. Its power supply methods include centralized, distributed and hybrid power supply. As shown in Fig. 1, the urban rail transit uses 110/35 kV set of power supply mode.

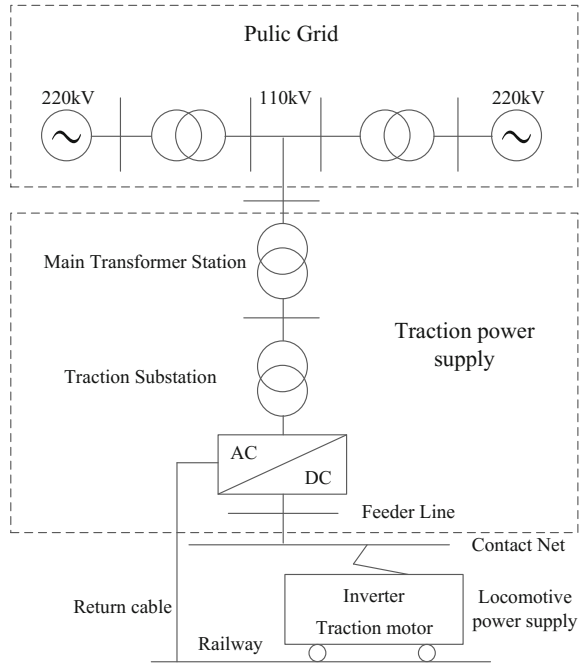
In Fig. 1, three phase currents are firstly introduced from the urban grid. Secondly, the voltage is reduced from 110 to 35 kV in the 110/35 kV main transformer station by the main transformer. Thirdly, the power is supplied by the 35 kV medium voltage ring to the full traction substation and the lower voltage transformer. Centralized power supply is conducive to the rail transit to be an independent system, and easy to manage and operating [6]. This power supply way is widely used in the world, such as Shanghai, Guangzhou, Nanjing, Hong Kong and Teheran metro.

### ***2.2 Main Loads***

The rail transit power supply system mainly includes traction loads and power illumination loads. The traction load is an electric vehicle for rail transit, and the power illumination load is mainly used for communication, signal, ventilation, air conditioning, lighting and so on.

The traction load is usually powered by DC traction power supply system which voltage level is 750 V or 1500 V. The DC traction power supply system includes traction substation, traction network (contact network or contact rail), electric motor unit, reflux rail, etc. The traction substation converts 35 kV medium voltage to

**Fig. 1** Power supply system of urban mass transit



1500 VDC or 750VDC by the rectifier unit, then supplies the power for the running electric motor unit through traction network and reflux through the rail. The single-set rectifier unit of traction substation adopts three-phase bridge type 12 pulse rectifier mode, and two sets of rectifier units are parallel operation on the same bus to constitute equivalent 24 pulse rectifier.

Power illumination system are usually powered by 380/220 V voltage grade as shown in Fig. 2. Low voltage distribution and lighting system adopt three-phase four-wire distribution mode, and use TN-S ground protection system.

There are more kinds of power illumination loads, including conventional loads such as lighting, escalator and motor loads such as water supply and drainage device, air conditioner and ventilation system. There are also some systems which more sensitive to the power quality such as master control system, control system and signal system.

### 3 Power Quality Problems in Rail Transit

#### 3.1 Harmonics

The traction power supply system adopts the rectifier unit to provide DC power to the train, therefore the harmonics are generated inevitably. The frequency of



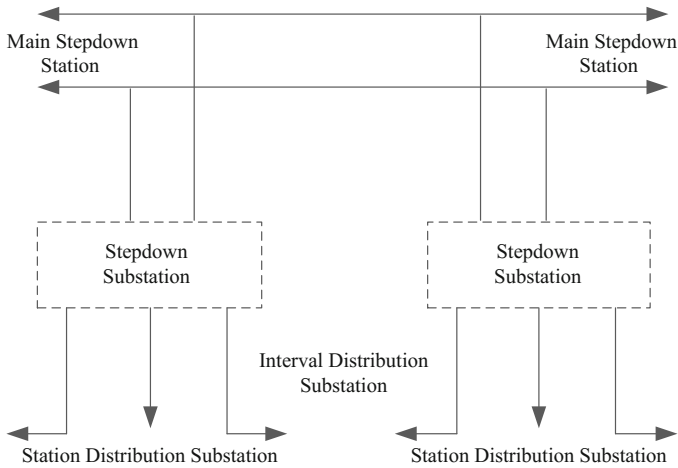


**Fig. 2** Power illumination supply system

harmonic current in the rectifier unit is related to the output pulse number of the rectifier unit. In ideal conditions, the harmonic current generated in the high voltage side of the rectifier unit is  $k \times (P \pm 1)$  times ( $P$  is the pulse number of the rectifier unit,  $k$  is positive integer). The simulation waveform and harmonic spectrum as shown in Fig. 3. The higher pulse number of the rectifier unit, the less lower-order harmonics, and the smaller impact on the system.

Some of factors can generate harmonics such as fluctuation of the power supply, commutation of the rectifier diode, changing of the main loads, starting or braking of the train, switching of the supply arm, and change of the vehicle, etc.

Low power illumination loads mainly include the ventilation air conditioning in station, escalators, drainage, ventilation, fire control and the lighting loads of each station, interval, substation, etc. There are a lot of frequency conversion loads which can generate amount of harmonics in 5 or 7 times, and more frequency conversion equipment will be used in future to reduce the energy consumption of the rail transit system.

The harmonic current can increase the copper loss of the transformer and make the transformer heat grow up [8]. The harmonic voltage can increase the hysteresis loss and vortex loss of the power transformer. The harmonics can increase the dielectric loss of the cable and the power loss on the transmission line, and cause the temperature of transmission line to high and accelerate the insulation aging. The influence of harmonics on the capacitor is mainly to make the capacitor resonate, which lead to harmonic current magnify and result in damage of capacitor.

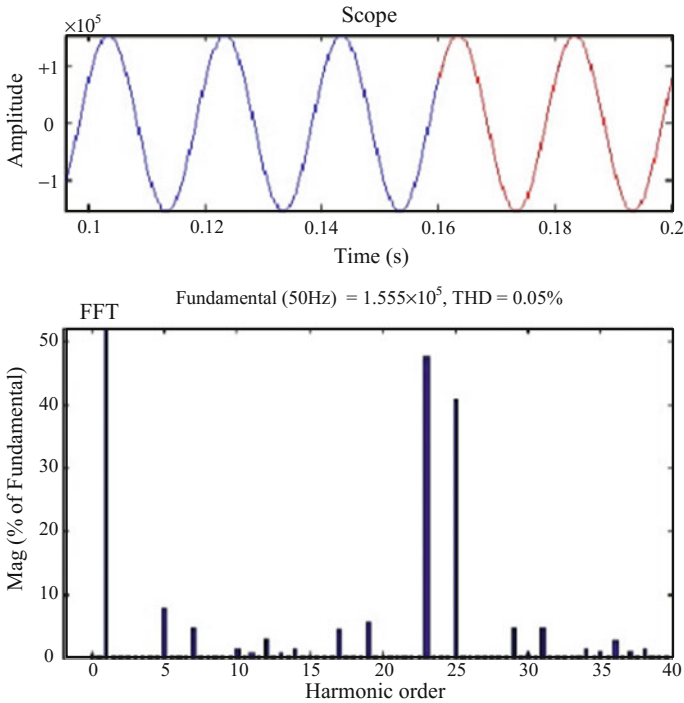


Fig. 3 Waveform and harmonic spectrum

### 3.2 Reactive Power

The reactive power of the system is mainly from main transformer, traction load, cable and power illumination loads. In the rail transit power supply system, electric locomotive power supplied by 24 pulse rectifier unit. The rectifier unit have higher power factor (typically 0.9 above) which follows load condition change. And various transformers will consume certain perceptual reactive power in the system. A large number of cable can also generate reactive power.

The higher reactive power can reduce the power factor of the power supply and distribution system and the voltage of contact network, and increase the loss of lines and equipment. This can cause the voltage instability, and then damage to the electrical equipment. Thus power companies have set up a series of penalties for reactive power as shown in Table 1.

According to the prescribed standards, excess reactive power will lead to additional economic spending. It is not allowed to ignore the harm of reactive power problems, and is urgent to solve the reactive power problems.

**Table 1** Penalties for reactive power set up by power companies

No.	Power factor of average monthly	Electricity bills needed to pay (%)
1	Below the calibration 0.05	+2.5
2	Below the calibration 0.1	+5
3	Higher than the calibration 0.05	-1.5
4	Equal to the calibration	-2.5

## 4 Management Strategy of Power Quality

### 4.1 Harmonic Suppression Strategy

The major methods of reducing the harmonic content of power system is to adopt multi-pulse rectifier circuit, active filter, passive filter and three-phase power factor correction circuit. To the rail transit system, its general approaches mainly include:

- (1) Suppress the harmonics by changing the power supply mode of the power supply system. For instance, adopting three-level power supply mode to isolate higher-order harmonic, and the step-down transformer (0.4 kV from 35 kV) plays an isolation and restrain role of higher-order harmonic caused by the traction rectifier equipment.
- (2) Increase the number of pulsations of the rectifier to reduce and suppress low frequency harmonic. From Figs. 4 and 5, we can see that after adopting 24-pulse rectifier, the main harmonic frequencies increase form  $12k \pm 1$  to  $24k \pm 1$ , and THD decreases form 3.57–2.11%.

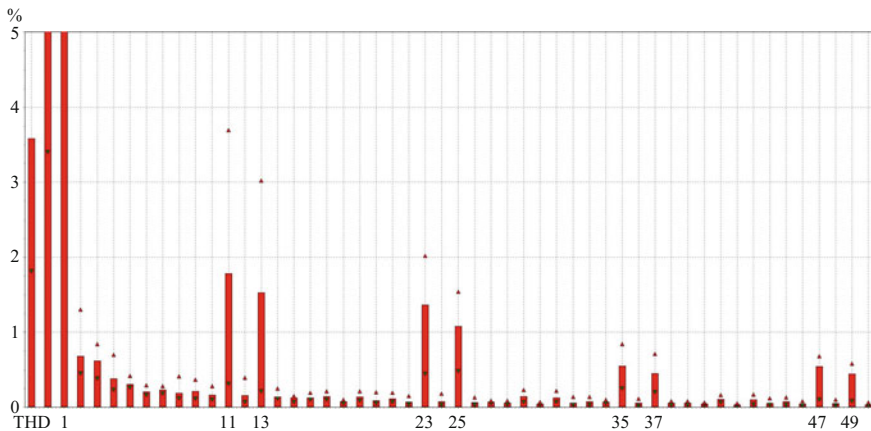


**Fig. 4** Measured harmonic spectrum of 12-pulse rectifier

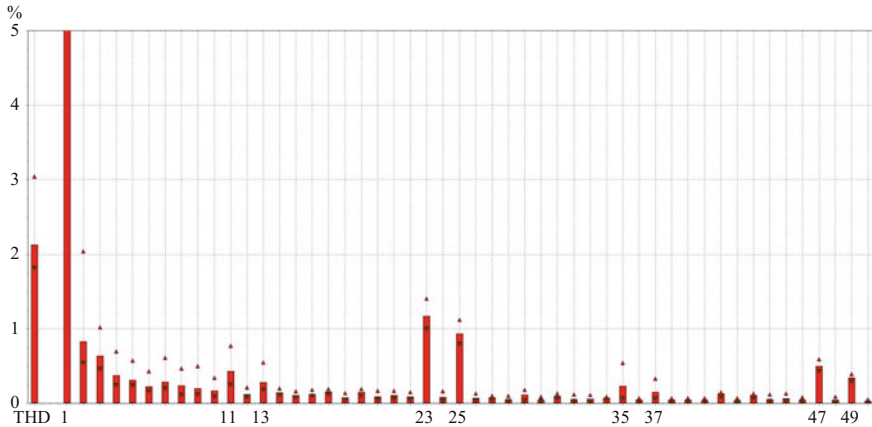


**Fig. 5** Measured harmonic spectrum of 24-pulse rectifier

- (3) Install a filter at the harmonic source to absorb the harmonics of the harmonic source. But it's just suitable for the condition when the output power is particularly high.
- (4) Increase the harmonic suppression circuit in the 0.4 kV low voltage system to eliminate the high harmonics.

## 4.2 Reactive Compensation Strategy

With the principles of cost savings, energy saving and consumption reducing, based on the change characteristics of the subway load during day time, the ideal compensation scheme should be able to track the change of the load, random timing compensation, maintaining voltage stability, so as to meet the biphasic compensation of reactive power in rail transit power supply system.

The capacity of reactive power compensation device in the traction substation should be reasonable set, otherwise, there will be frequent changes of the reactive power between sensibility and tolerance, and lead to the public power grid accident and cause damage.

At present, compensation ways usually used in China are: the shunt reactor is selected according to the maximum perceptual compensation capacity in the system light load condition; the parallel capacitor is selected according to the maximum capacitive compensation capacity.

In order to make up for the deficiency of static reactive compensation, the dynamic reactive compensation is used at present. Dynamic reactive compensation devices include: synchronous camera, saturation resistor, static synchronous compensator, active power filter, etc. [9]. In contrast, a better method of reactive

compensation is to use dynamic reactive compensation technology SVG (Static Var Generator). As the third reactive compensation technology, the SVG has many advantages such as high reliability, good safety, low loss, high efficiency operation, and its power factor compensation value can be to 0.95 ~ 1.

## 5 Conclusions

Rail transit system will be the pioneer in the “One Belt and One Road” strategy which is implemented energetically by the government. The power quality problem is an important factor in its development and should not be allowed to ignore. In this paper, the influence factors and potential hazards of the power quality problems are analyzed entirely. And the corresponding solutions of problems are summarized to improve the power quality of electric grid effectively.

## References

1. Wang Y, Li K, Xu X et al (2014) Transport energy consumption and saving in China. *Renew Sustain Energy Rev* 29(7):641–655
2. Tian Y, Zhu Q, Lai KH et al (2014) Analysis of greenhouse gas emissions of freight transport sector in China. *J Transp Geogr* 40:43–52
3. Huo H, Wang M, Zhang X et al (2012) Projection of energy use and greenhouse gas emissions by motor vehicles in China: policy options and impacts. *Energy Policy* 43(3):37–48
4. Qian C, Qi J, Li G et al (2007) Harmonic Calculation and Analysis of Currents in 24-Pulse Rectifier Transformer [J]. *Transformer*, 44(12): 1–7, 47(in Chinese)
5. Terciyanlı A, Acik A, Cetin A et al (2010) Power quality solutions for light rail public transportation systems fed by medium-voltage underground cables. *IEEE Trans Ind Appl* 48(3):1017–1029
6. Elisa C (2011) Assessing the potential of railway station redevelopment in urban regeneration policies: an Italian case study. In: 2011 international conference on green building and sustainable cities. *Procedia Eng* 21:1096–1103
7. Xu X, Chen B (2009) Research on power quality control for railway traction power supply system. In: Pacific-Asia conference on circuits, communications and systems, 2009, PACCS09. IEEE, pp 306–309
8. Mc Eahern A, Grady WM, Monerief WA (1995) Revenue and harmonics: an evaluation of some proposed rate structures. *IEEE Trans Power Delivery* 10(1):474–482
9. Lee SY, Wu CJ (2000) Reactive power compensation and load balancing for unbalanced three-phase four-wire system by a combined system of an SVC and a series active filter. In: *Electric power applications, IEE proceedings, IET*, 147(6):563–578

# A Torque Command Generated Method of Re-adhesion Control Based on Slip Acceleration

Long Qi, Guohui Li and Chenchen Wang

**Abstract** This paper proposes a new method of generating torque command for re-adhesion control by analyzing the mechanical equations of electric motor and train. The method of torque command is based on designing the reference slip acceleration without requiring a lot running control parameters and running test, so that the slip acceleration of the train in slip/skid state is negative and the amount of slip velocity can be theoretically determined. The effectiveness of the proposed method has been confirmed by the numerical simulation with high utilization ratio of adhesion force.

**Keywords** Re-adhesion control · Slip acceleration · Adhesion characteristic  
Torque command for re-adhesion

## 1 Introduction

With the increasing of speed, the requirements for the safety of high-speed EMU become more and more important. If the train has a slip/slide phenomenon without adhesion control, it will lead to a consumption of both the rails and the wheels. So it is important to study the adhesion control strategy of high-speed EMU. Good adhesion utilization can improve the acceleration performance of train, shorten braking distance, at the same time also can reduce slip/slide phenomenon, avoid serious abrasion of wheel and rail, prolong the service life and improve the sitting comfort.

When control device detecting slip/slide phenomenon, the increase of creep speed can be restrained by adjusting torque command. So it is important to choose a

---

L. Qi (✉) · G. Li  
CRRC Changchun Railway Vehicles Co., Ltd., Qingyin Road No. 435,  
Changchun, Jilin, China  
e-mail: qilong\_crcc@126.com

C. Wang  
School of Electrical Engineering, Beijing Jiaotong University, Beijing, China

© Springer Nature Singapore Pte Ltd. 2018

L. Jia et al. (eds.), *Proceedings of the 3rd International Conference on Electrical and Information Technologies for Rail Transportation (EITRT) 2017*, Lecture Notes in Electrical Engineering 482, [https://doi.org/10.1007/978-981-10-7986-3\\_24](https://doi.org/10.1007/978-981-10-7986-3_24)

231

suitable motor torque instruction value. References [1] and [2] describe traditional adhesion control strategy, according to motor torque of slip/slide and determining re-adhesion motor torque, the value is proportional to the torque of slip/slide. References [3] and [4] present an adhesion control strategy which is based on the tangential force estimation. And then the estimated load torque multiply a certain percentage to determine re-adhesion motor torque, used to suppress slip/slide.

In order to implement re-adhesion and obtain high utilization rate of adhesion, the above two strategies both need a large number of test to adjust the proportion parameter to determine the re-adhesion motor torque command value. For this reason, this paper proposes an adhesion control strategy based on creep acceleration. Through the design reference creep acceleration value determining re-adhesion motor torque instruction value, it can guarantee the creep speed decline rapidly and realize re-adhesion, improve the utilization rate of adhesive. Simulation result verifies the correctness and effectiveness of the proposed method.

## 2 Adhesion Mechanism of Wheel and Rail

### 2.1 Adhesion Characteristics

The ultimate power of trains is traction force. Studies have shown that only there is a certain degree relative tangential movement in train wheel and rail contact, train can produce its own forward traction. Define the speed of relative tangential movement for creep speed  $v_s$ , its value is wheel speed  $v_d$  and vehicle speed  $v_t$  difference, namely

$$v_s = v_d - v_t \quad (1)$$

Tangential force coefficient is defined as the ratio of wheel traction and vertical load.

$$\mu(v_s) = \frac{F_s}{W \cdot g} \quad (2)$$

where  $\mu(v_s)$  is the tangential force coefficient,  $F_s$  for the wheel traction force,  $W$  for the axle weight,  $g$  for the acceleration of gravity.

Trains can achieve the maximum traction force which is restricted by adhesion conditions. When the condition of wheel/rail and train speed under certain conditions, there is a maximum tangential force coefficient  $\mu_{\max}$  namely adhesion coefficient:

$$\mu_{\max} = \frac{F_{\max}}{W \cdot g} \quad (3)$$

The relationship between tangential force coefficient and the creep speed is called adhesion properties, as shown in Fig. 1. Curve shows that with the increase of creep speed in the adhesive area, tangential force coefficient increases, but when the creep speed is greater than the adhesion coefficient corresponding with creep speed, the train will enter into slip area from the adhesion area, then tangential force coefficient will drop rapidly with the increase of creep speed, which resulted in the traction reduction between the wheel and rail.

### 2.2 Model of Wheel and Rail

$$\text{Train motion equation } M \frac{dv_t}{dt} = F_s - F_d \tag{4}$$

where  $M$  is train weight,  $F_d$  is basic resistance for train motion.

$$\text{Motor rotation equation } J_m \frac{d\omega_m}{dt} = T_m - T_L \tag{5}$$

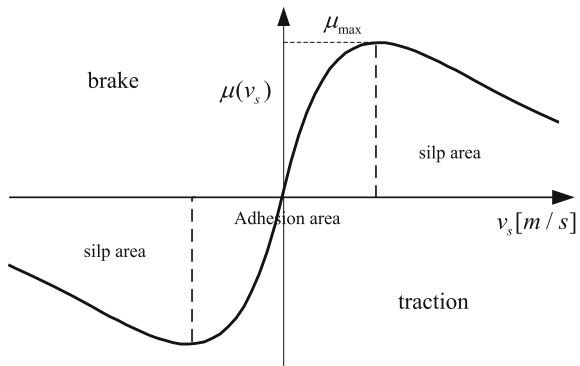
In (5),  $J_m$  is the moment of inertia converted to the motor side,  $\omega_m$  is motor angular speed,  $T_m$  is motor output torque,  $T_L$  is motor load torque.

$$\text{Wheel rotation equation } J \frac{d\omega_d}{dt} = T - F_s r \tag{6}$$

$J$  is the moment of inertia converted to the wheel side,  $\omega_d$  is wheel angular speed,  $T$  is driving torque,  $r$  is wheel radius. The traction force can be converted into the motor load torque:

$$T_L = \frac{1}{R_g} \mu(v_s) \cdot W \cdot g \cdot r \tag{7}$$

**Fig. 1** Adhesion characteristic curve





### 3 Control Strategy Based on Creeping Acceleration

#### 3.1 Determination of Motor Torque Command Value

The motor rotation Eq. (5) is expressed by train acceleration and creep acceleration:

$$T_m = T_L + J_m \frac{R_g}{r} (\dot{v}_t + \dot{v}_s) \quad (8)$$

$\dot{v}_t$  is train acceleration,  $R_g$  is gear ratio,  $\dot{v}_s$  is creep acceleration. After slipping, in order to achieve re-adhesion, the creep acceleration should be of negative value, so motor torque should be satisfied

$$T_m < T_L + J_m \frac{R_g}{r} \dot{v}_t \quad (9)$$

$$T_m^{ref} = \hat{T}_L + J_m \frac{R_g}{r} (\hat{v}_t + v_s^{ref}) \quad (10)$$

$T_m^{ref}$  is motor torque command value for re-adhesion,  $\hat{T}_L$  is load torque,  $\hat{v}_t$  is train acceleration,  $v_s^{ref}$  is reference creep speed.

The load torque can not be obtained directly, so the disturbance observer is introduced to estimate the load torque

$$\hat{T}_L = \frac{a}{s+a} (T_m - J_m s \omega_m) \quad (11)$$

To sum up, it can be concluded that the value of the creep speed can be obtained by design, and the torque command value of the adhesion motor can be obtained by satisfying (9) to restrain the increase of creep speed.

#### 3.2 Design of Reference Creep Acceleration

Taking into account the actual operation of the train, there is a limit to the degree of slip, therefore, the adhesion characteristic curve can be approximately linearized within the allowable slip range. The load torque expression is:

$$T_L = T_{l0} + K_{ls} * v_s \quad (12)$$

$T_{l0}$  is load torque initial value,  $K_{ls}$  is the slope of the slip area for the load torque. The Eqs. (10) (12) is brought into Eq. (5)

$$K(\dot{v}_t + \dot{v}_s) = \hat{T}_L + K(\hat{v}_t + v_s^{ref}) - (T_{l0} + K_{ls} * v_s) \quad (13)$$

$K = J_m \frac{R_g}{r}$ , differential equation of creep speed:

$$\dot{v}_s + \frac{K_{ls}}{K} * v_s + \left( \frac{T_{l0} - \hat{T}_L}{K} - v_s^{ref} \right) = 0 \quad (14)$$

If the instant creep speed  $v_{s0}$  is detected, expressions of creep speed versus time:

$$v_s(t) = v_{s0} + \frac{K}{K_{ls}} v_s^{ref} (1 - e^{-\frac{K_{ls}}{K} t}) \quad (15)$$

$$\text{Average creep acceleration } \bar{\dot{v}_s} = \frac{\Delta v_s}{\Delta t} \quad (16)$$

The expression of creep acceleration is obtained by Eqs. (15, 16)

$$v_s^{ref} = \frac{K_{ls}}{K} \frac{\Delta v_s}{1 - e^{-\frac{K_{ls}}{K} \Delta t}} \quad (17)$$

Form (17) reference creep acceleration can be designed by setting the creep speed drop  $\Delta v_s$  and  $\Delta t$ .

## 4 Simulation Verification

### 4.1 Simulation Conditions

The train model parameters are shown in Table 1. Use the adhesion control strategy shown in Fig. 2. The adhesion control device uses the wheel circumference acceleration as the slip criterion, and determines the current slip condition by comparing with the slip speed threshold of the wheel circumference acceleration. Set the creep acceleration threshold  $2.6 \text{ m/s}^2$ . The simulation parameter settings are shown in Table 2 including dry road conditions and wet road conditions. And

**Table 1** Setting of simulation model parameters

Converted moment of inertia $J_m$ (kg m <sup>2</sup> )	5.813
Wheel radius $r$ (m)	0.43
Gear ratio $R_g$	5.64
Train weight $M$ (kg)	21250
Axle weight $W$ (kg)	10000
Gravitational acceleration $g$ [m/s <sup>2</sup> ]	9.8

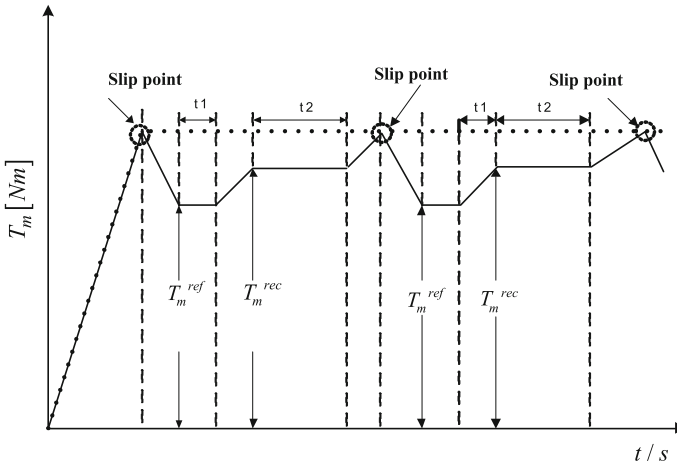


Fig. 2 Adhesion control strategy

Table 2 Simulation of road condition parameters

Condition	a	b	c	d	$v_s, \mu_{max}$
Dry	0.54	1.2	1	1	(1.21, 0.2862)
Wet	0.54	1.2	0.4	0.4	(1.21, 0.1145)

$T1(\Delta t) = 100 \text{ ms}$ ,  $\Delta v_s = 0.15 \text{ m/s}$ . In the simulation, the adhesion characteristic curve is shown in the expression (18):

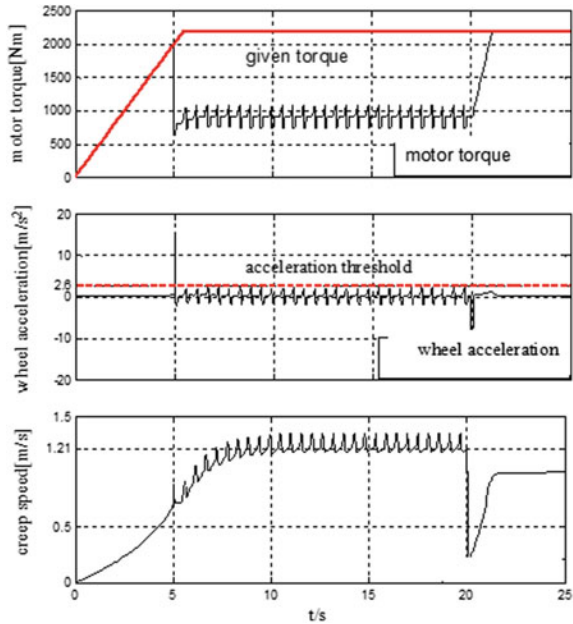
$$\mu = c * \exp(-a * v_s) - d * \exp(-b * v_s) \tag{18}$$

### 4.2 Simulation Result Analysis

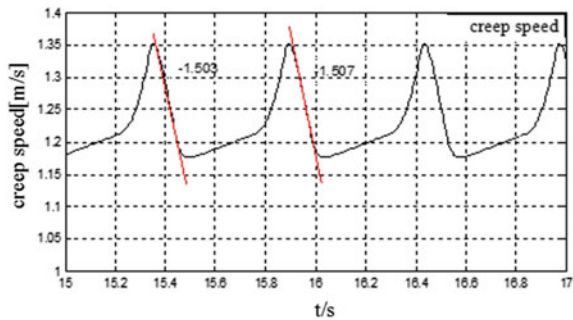
In Fig. 3, when  $t = 5 \text{ s}$ , from the dry road into the wet road, the wheel acceleration increases rapidly. When the wheel acceleration is greater than the set of slip threshold  $2.6 \text{ m/s}^2$ . The train has the tendency of slip running, and the motor torque is decreased under the adhesion control, the tendency of slip running is suppressed.

Figure 4 is a local enlargement of the creep speed under wet condition. Re-adhesion motor torque is maintained within 100 ms, creep speed is shown in accordance with formula (15). The creep speed is detected when value is 1.35 m/s. After falling, the creep velocity is approximately 1.2 m/s. Reentering the adhesive area and introducing average creeping acceleration at the same time as an index to evaluate the correctness of the adhesion control strategy. From the diagram, the actual descent slope is  $1.503 \text{ m/s}^2$ . The theoretical values are approximately

**Fig. 3** Motor torque, wheel acceleration and creep speed curve



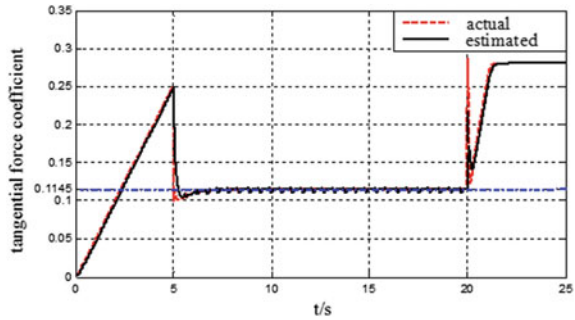
**Fig. 4** Local amplification curve of creep velocity



consistent with the average creep acceleration  $1.5 \text{ m/s}^2$ , and the results prove the feasibility and effectiveness.

Figure 5 is the actual rail surface tangential force coefficient and disturbance observer of the tangential force coefficient changes with time, can be seen from the figure accuracy of disturbance observer. At the same time the adhesion coefficient in the wet conditions of tangential force coefficient can reach 0.1145 of the current road conditions, and can basically keep unchanged, so that the train run on the rail surface near the maximum adhesion force, make full use of the rail surface adhesion. The simulation results show that the wet road adhesion utilization rate reached 99%.

**Fig. 5** Tangential force coefficient



## 5 Conclusion

Based on the analysis of adhesion characteristic and adhesion mechanism, this paper proposed a torque command generated method of re-adhesion control based on slip acceleration. There is no need to adjust the scale parameters through a large number of tests, so that the train can quickly achieve adhesion and obtain high adhesion utilization. Finally, based on the Matlab/Simulink simulation platform. The correctness and feasibility of the proposed method are proved.

## References

1. Li Y (2011) Research on optimum creep control method. Southwest Jiao Tong University, Sichuan (in Chinese)
2. Li J, Ma J, Peng H (2002) Basic principle and method of locomotive adhesion control. *Locomotive Electr Drive* (6):4–8 (in Chinese)
3. Kadowaki S (2007) Anti-slip re-adhesion control based on speed-sensorless vector control and disturbance observer for electric commuter train—series 205-5000 of the East Japan Railway company. *54(4):2007–2008*
4. Shimizu Y, Kadowaki S (2009) Evaluation and discussion of disturbance observer-based anti-slip/skip re-adhesion control for electric train. *169(4):55–64*

# Research on Real-Time Simulation Modeling of Four-Quadrant Converter System Based on Basic Components

Yunxin Fan, Huanqing Zou and Jin Fu

**Abstract** In the field of real time HiL (hardware-in-Loop) simulation of rail transportation traction electric drive system, in order to solve the problems that real-time simulation model, based on the equation of equivalent circuit state, occupies too many resources of system and lacks universality, and it is difficult to achieve on-line adjustment of variables. This paper presents the analysis and modeling of the basic components such as inductor, resistor, capacitor, four-quadrant convertor and so on. It realizes the real-time simulation of the four quadrant converter system. What's more, the feasibility and effectiveness of the simulation model are verified by comparing the real-time simulation results with the experimental data.

**Keywords** Four-quadrant converter system · Real-time simulation Inductor · Resistor · Capacitor · Four quadrant convertor

## 1 Introduction

With the improvement of the intelligent and complicated degree of modern rail transit vehicles, real-time simulation in the development process becomes an important means to save cost and improve efficiency. In particular, the development of the four-quadrant converter controller or inverter controller in the traction electric drive system is usually done through the real time HiL (hardware-in-Loop) simulation, which involves the real-time simulation model of the main circuit [1–7], that is, the simulator simulates main circuit's input and output signals of traction electric drive system through calculating the real time simulation model to complete the testing process with the controller. In a complete main circuit of traction drive system, high-power power electronic switching devices are used in rectifier and inverter, which make the relationship between input and output electrical parameters

---

Y. Fan · H. Zou (✉) · J. Fu  
CRRC Zhuzhou Locomotive Co., Ltd., Zhuzhou 412001, China  
e-mail: zhq1875@163.com

© Springer Nature Singapore Pte Ltd. 2018

L. Jia et al. (eds.), *Proceedings of the 3rd International Conference on Electrical and Information Technologies for Rail Transportation (EITRT) 2017*, Lecture Notes in Electrical Engineering 482, [https://doi.org/10.1007/978-981-10-7986-3\\_25](https://doi.org/10.1007/978-981-10-7986-3_25)

239

more complex. Therefore, in the process of simulation modeling or system analysis, the main circuit is divided into four quadrant converter system and the motor side subsystem generally.

At present, there are two main methods to establish simulation model of four quadrant converter system. One is to use the basic model of Matlab’s SimPowerSystems toolbox to build a simulation model based on the circuit structure of the emulated object [1, 2]. The advantage of the above-mentioned method is that it’s easy to build the simulation model according to the different circuit topology, but the real-time simulation is difficult to realize because the real-time code program takes up too many system resources. Therefore, the disadvantage of using Matlab’s SimPowerSystems to build the simulation model is that the system resources are occupied more and it’s difficult to achieve real-time calculation. The other is that based on different conduction states of four quadrant converter, we can also establish the equivalent circuit state description equation, to get simulation method of four quadrant converter system mathematical model [3–5]. Although this approach is easy to achieve real-time and take up less system resources, it lacks universality. In other words, the original model is no longer applicable when the simulation system circuit structure changes, so we must establish a new simulation model.

In order to solve the above problems, this paper takes the inductor, resistor, capacitor and four-quadrant converter in the equivalent circuit of four-quadrant converter system (Fig. 1) as the basic components, carrying on the simulation modeling respectively, and then combines them based on Kirchhoff law of voltage and current, according to the circuit topology, to achieve real-time simulation for four quadrant converter system.

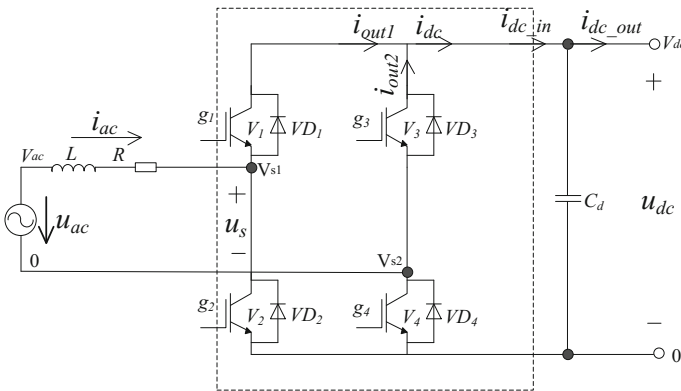


Fig. 1 Equivalent circuit diagram of single four quadrant converter system

## 2 Modeling Analysis of Basic Components

### 2.1 Inductor Modeling Analysis

The relationship between the voltage and current of the linear inductor is shown below.

$$u_L(t) = L \frac{di_L(t)}{dt} \quad (1)$$

The Forward Euler method is used to discretize the continuous state equation. Namely, assuming that the inductor voltage is constant at  $t_1$  to  $t_2$ , Eq. (1) can be written as follows,

$$i_L(t_2) = \frac{1}{L} \int_{t_1}^{t_2} u_L(t) dt + i_L(t_1) = i_L(t_2) = \frac{(t_2 - t_1)}{L} u_L(t_1) + i_L(t_1) \quad (2)$$

### 2.2 Resistor Modeling Analysis

The relationship between the voltage and current of the linear resistor is shown below.

$$u_R(t) = i_R(t)R \quad (3)$$

### 2.3 Capacitor Modeling Analysis

The relationship between the voltage and current of the linear capacitor is shown below.

$$i_C(t) = C \frac{du_C(t)}{dt} \quad (4)$$

The Forward Euler method is used to discretize the continuous state equation. Assuming that the capacitor current is constant at  $t_1$  to  $t_2$ , Eq. (4) can be written as follows,

$$u_C(t_2) = \frac{(t_2 - t_1)}{C} i_C(t_1) + u_C(t_1) \quad (5)$$



## 2.4 Four-Quadrant Converter Modeling Analysis

Based on the simulation of system level, the dynamic characteristics of high-power power electronic devices and their absorption circuits in the converter can be neglected. Therefore, IGBT and diodes are regarded as ideal switching devices during simulation modeling of four quadrant converters.

Considering that the structure of each four quadrant converter is identical, a single four quadrant converter system is analyzed and modeled. As shown in Fig. 1,  $i_{ac}$  is defined as its AC-side input current,  $i_{dc}$  is defined as its DC-side output current,  $i_{out1}$  is the output current for the bridge arm 1,  $i_{out2}$  is the output current for the bridge arm 2, the DC-Link positive busbar potential is  $V_{dc}$ . The negative potential is 0, the potential difference between the positive and negative busbar of the DC-Link is  $u_{dc}$ . The midpoint potential of the bridge arm 1 is  $V_{s1}$ , the midpoint potential of the bridge arm 2 is  $V_{s2}$ , the middle point potential difference between the two arms is the output voltage  $u_s$ .  $g_1, g_2, g_3, g_4$  respectively represent control signals of  $V_1, V_2, V_3, V_4$ , 1 means on, and 0 means off. At the same time, the positive reference terminal potential of the AC power supply  $u_{ac}$  is defined as  $V_{ac}$ , while the negative reference terminal potential is 0.

From the composition of the four-quadrant converter, it is not difficult to see that when  $g_1, g_2, g_3, g_4$  are all 0,  $V_1, V_2, V_3, V_4$  in the block state are not involved in the work, the four quadrant converter is equivalent to diode Rectifier. Therefore, according to the state of  $g_1, g_2, g_3, g_4$  control signal, the four-quadrant converter is divided into the switching state ( $V_1, V_2, V_3, V_4$  involved) and the blocked state ( $V_1, V_2, V_3, V_4$  in blocked state) for modeling and simulation.

### 2.4.1 Modeling Analysis of Switching State ( $V_1, V_2, V_3, V_4$ Involved in the Work)

In the following sections, we first analyze the relationship between the main outputs and inputs when a single bridge in different conduction states (not including the bridge short-circuit conditions  $g_1 = 1, g_2 = 1, g_3 = 1, g_4 = 1$ ). Then the main outputs of four quadrant converter is calculated by  $i_{dc} = i_{out1} + i_{out2}$  and  $u_s = V_{s1} - V_{s2}$ .

#### (a) simulation of bridge arm 1

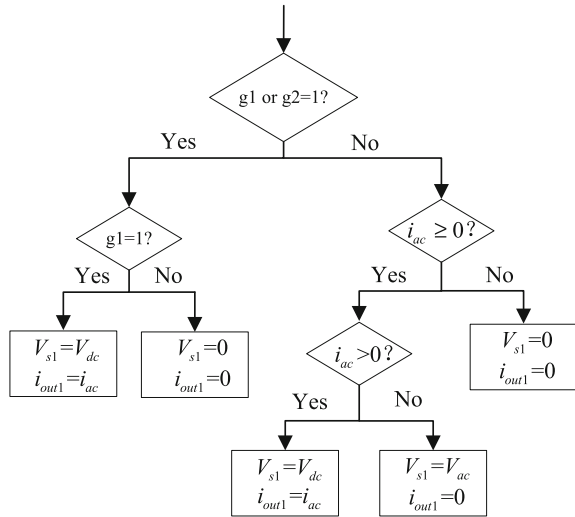
The inputs of bridge arm 1 include  $i_{ac}, V_{dc}, V_{ac}, g_1, g_2$ , the DC-Link negative busbar potential 0. The outputs include  $V_{s1}, i_{out1}$ .

According to the relationship between the main inputs and outputs of the bridge arm 1, the simulation program execution flow chart can be written as follows (Fig. 2),

#### (b) simulation of bridge arm 2

The inputs of bridge arm 2 include  $i_{ac}, V_{dc}, g_3, g_4$ , the AC power supply negative reference terminal potential 0. The outputs include  $V_{s2}, i_{out2}$ .

**Fig. 2** Simulation program execution flow chart of bridge arm 1



According to the relationship between the main inputs and outputs of the bridge arm 2, the simulation program execution flow chart can be written as follows (Fig. 3),

**2.4.2 Simulation Analysis of Blocked State**  
**( $V_1, V_2, V_3, V_4$  in the Blocked State)**

When  $g1 = 0, g2 = 0, g3 = 0, g4 = 0$  and all IGBTs of the four-quadrant converter are in the cut-off state, the four-quadrant converter is equivalent to the diode rectifier, as shown in Fig. 4. Before analyzing the working status of the rectifier, we should define the inputs and outputs first. The inputs include  $i_{ac}, u_{ac}, u_{dc}$ . The outputs include  $u_s, i_{dc}$ .

**Fig. 3** Simulation program execution flow chart of bridge arm 2

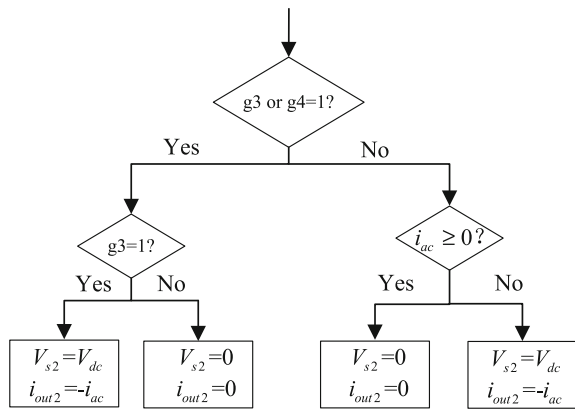
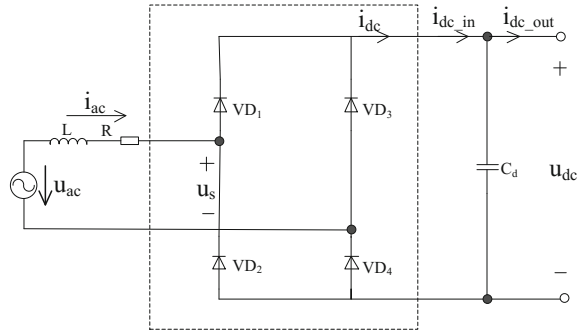


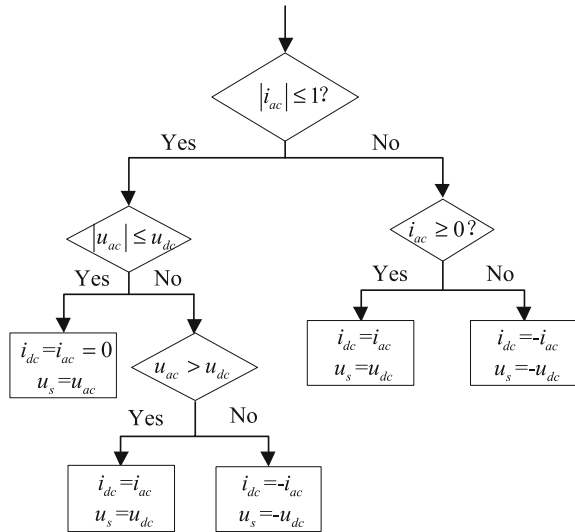
**Fig. 4** Equivalent diode rectifier circuit diagram



According to the relationship between the inputs and outputs, we can write the four-quadrant converter blocked state simulation program execution flow chart as Fig. 5.

According to the bridge arms 1 and 2 simulation program execution flow chart, the relationship between bridge arm 1 outputs and bridge arm 2 outputs  $i_{dc} = i_{out1} + i_{out2}$ ,  $u_s = V_{s1} - V_{s2}$ , and Simulation program execution flow chart of blocked state ( $V_1, V_2, V_3, V_4$  in the blocked state), we can write simulation program execution flow chart Fig. 6 of four quadrant converter.

**Fig. 5** Simulation program execution flow chart of four-quadrant converter blocked state



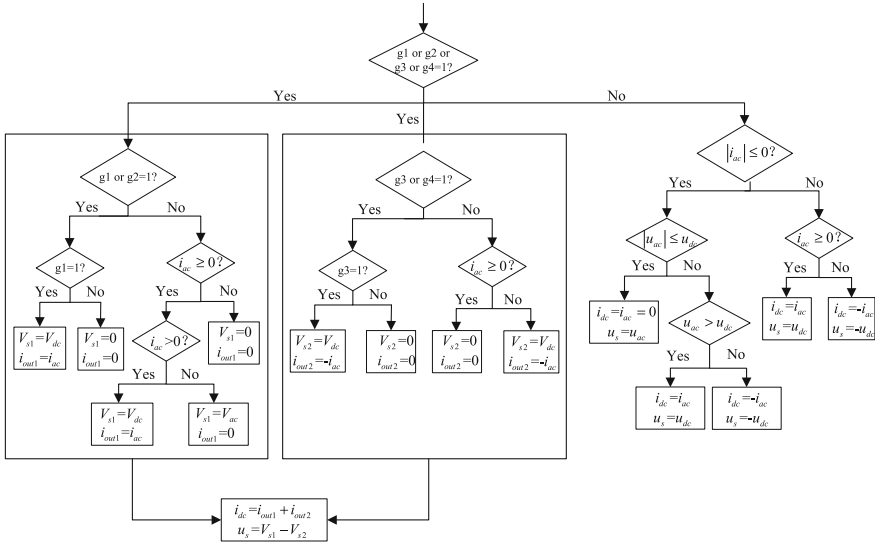


Fig. 6 Simulation program execution flow chart of four-quadrant converter

### 3 Simulation Modeling of Four-Quadrant Converter System

According to equivalent circuit topology of single four quadrant converter system in Fig. 1 and Kirchhoff voltage and current law, we can obtain,

$$u_L = u_{ac} - u_R - u_s \tag{6}$$

$$i_{cd} = i_{dc} - i_{dc-out} \tag{7}$$

It is easy to construct the simulation model of single four quadrant converter system by using the Eqs. (6), (7) and the resistor, inductance, capacitance and four quadrant converter models.

In this paper, inductors and capacitors use forward Euler algorithm to construct model. Because the convergence domain of forward Euler algorithm is relatively small, in a simulation calculation step of processor, there may be no stable numerical solution. We can calculate cyclically N times in a simulation step of processor. Namely, reduce the simulation step and extend convergence region to solve the problem. According to the actual parameters of the traction drive system, based on the simulation operation of processors, if the simulation step of processors is 40 μs, the number of cycles can be taken 20 times.

### 4 Real-Time Simulation of the System

The basic models of four-quadrant converter, capacitor, inductor and resistor are used to compose the main circuit simulation model of the HX<sub>D</sub>1 locomotive grid-side converter system as shown in Fig. 7, according to the Kirchhoff voltage and current law. Combining the four quadrant converter control algorithm, real-time simulation of the system is carried out. The four-quadrant control algorithm uses the following transient current control algorithm [8].

$$I_{ac}^* = K_p(U_{dc}^* - u_{dc}) + \frac{1}{T_i} \int (U_{dc}^* - u_{dc})dt + \frac{U_{dc} \times I_{dc}}{U_{ac}} \quad (8)$$

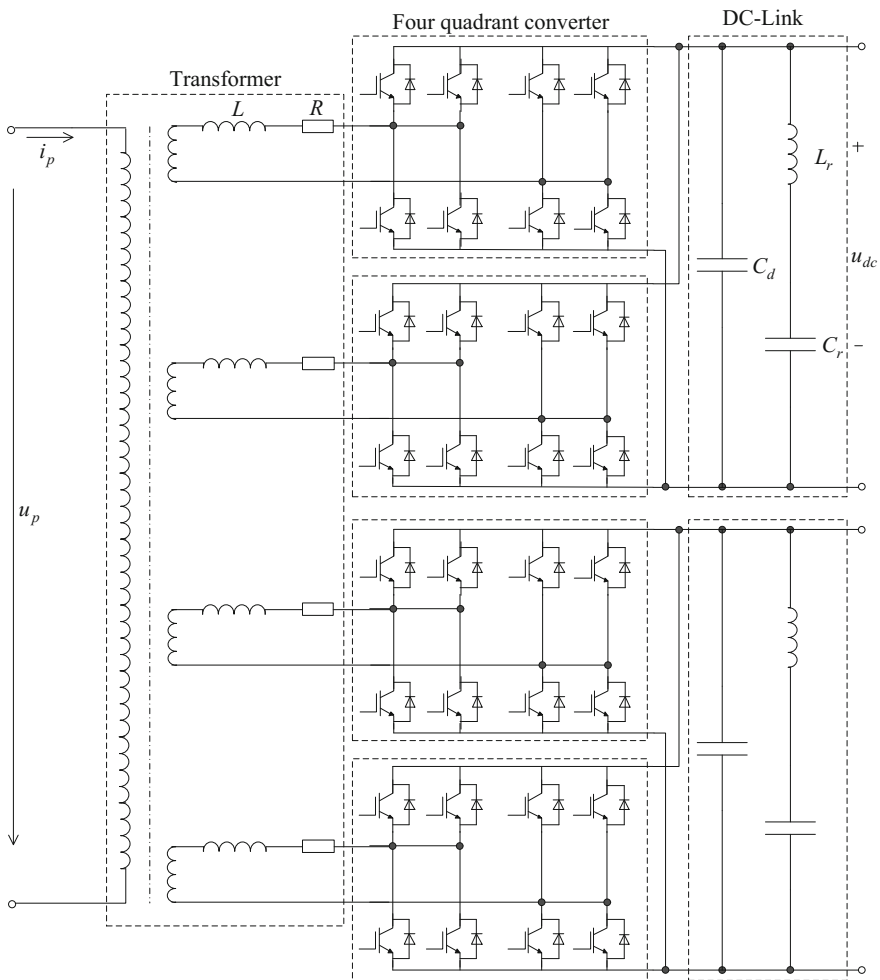


Fig. 7 The main circuit diagram of the HXD1 locomotive grid-side converter system

$$u_s^*(t) = u_{ac}(t) - \omega LI_{ac}^* \cos \omega t - RI_{ac}^* \sin \omega t - K[I_{ac}^* \sin \omega t - i_{ac}(t)] \quad (9)$$

$K_P$  and  $T_i$  are the regulator parameters of voltage loop  $PI$  in (8) and (9).  $K$  is the proportional regulator parameters of current loop.

Simulation modeling uses MATLAB software, while the real-time calculation hardware adopts dSPACE standard component system platform. The hardware resources are shown in Fig. 8. In the hardware simulator, the network side subsystem model is calculated by the processor. The switch signal of the controller is processed by the DS5203 interface card. The current and voltage of each device are output by DS2102. In the controller, 4QC control algorithm is operated by the processor, DS5203 is responsible for issuing converter signals controlling converter, and the DS2004 collects the current, voltage and other signals of the electrical equipment.

### 5 Comparison of Simulation and Experimental Data

The simulation calculation data were collected on the dSPACE hardware platform, comparing with the test data of the HX<sub>D</sub>1 locomotive in the rolling test bench. The test data include transformer primary voltage and current, input voltage and current of four quadrant converter and DC-Link voltage. It can be seen from Table 1,

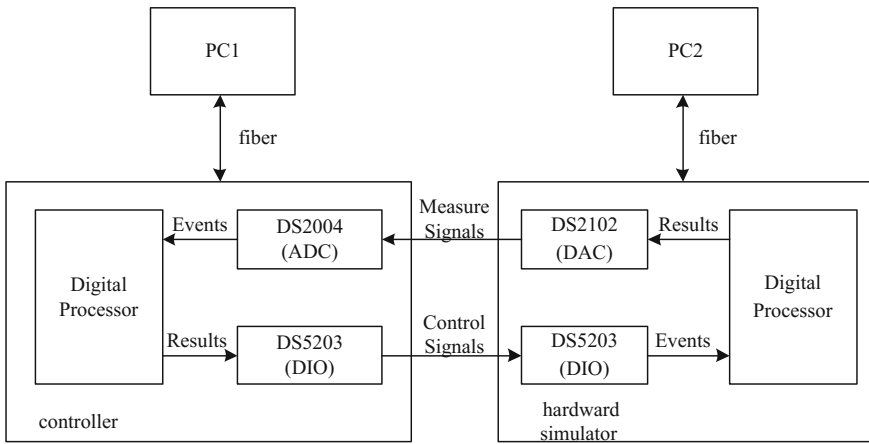
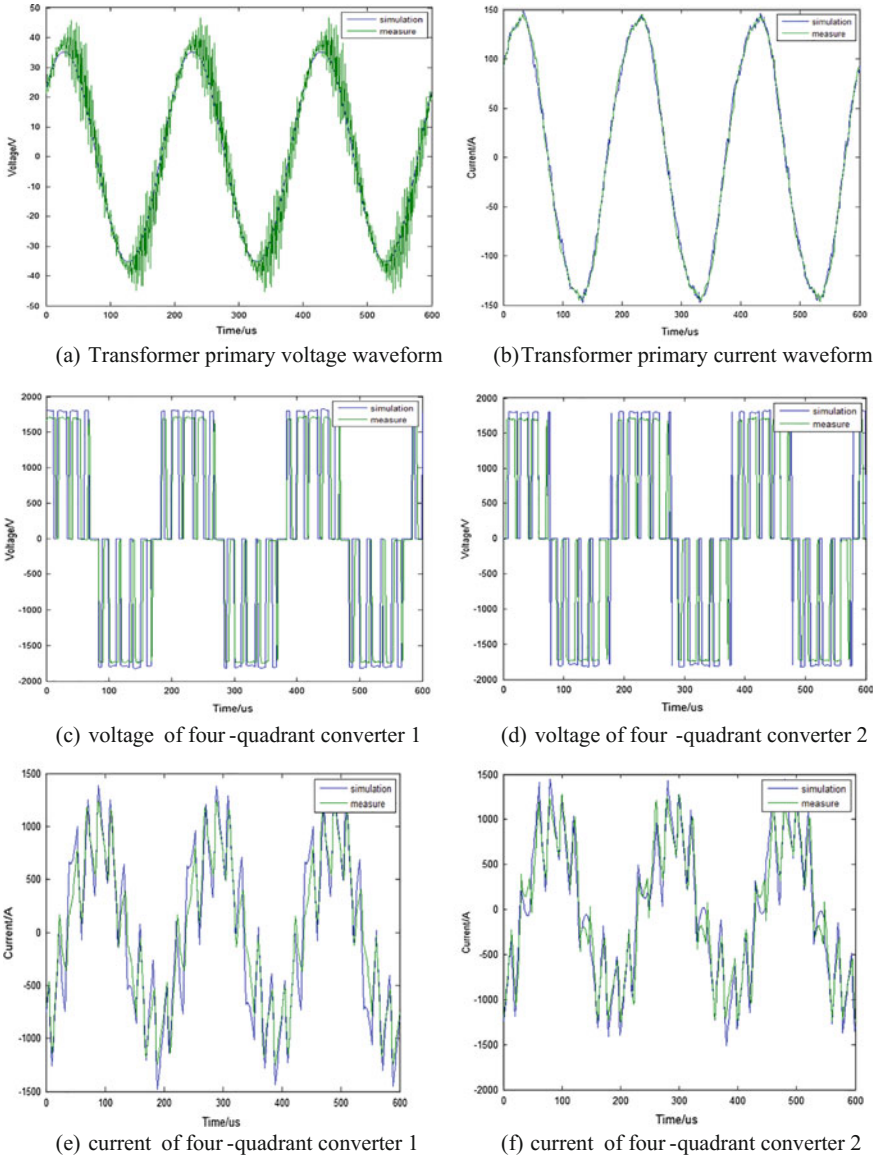


Fig. 8 dSPACE hardware and monitoring terminal diagram

Table 1 Comparison of main data during locomotive traction operation

	Transformer primary			4QC1		4QC2		DC-link
	Voltage	Current	Power factor	Voltage	Current	Voltage	Current	Voltage
Measure	28.31	106.20	0.99	1260	748	1241	759	1726
Simulation	28.68	105.89	0.99	1268	740	1297	729	1798

locomotive measured power is 2783 kW, simulation data is 2720 kW, and power error is less than 2%. From the comparison of data in Fig. 9, it can be seen that the simulation data are basically consistent with the measured data. Among them, in the DC-Link voltage comparison of (c) and (d) in Fig. 9, the setting simulation



**Fig. 9** Main data waveform of locomotive grid-side converter system, **a** Transformer primary voltage waveform, **b** transformer primary current waveform, **c** voltage of four-quadrant converter 1, **d** voltage of four-quadrant converter 2, **e** current of four-quadrant converter 1, **f** current of four-quadrant converter 2

DC-Link voltage is higher than the actual value for the sake of intuitive comparison. In Fig. 9 simulation modeling of (a) uses the ideal voltage source, not taking the impedance and distributed capacitance of the catenary into account, so there is a difference from the test data.

## 6 Conclusion

In this paper, the basic components of the equivalent circuit of four quadrant converter system are analyzed and modeled to achieve a real-time simulation of four-quadrant converter system. And the real-time simulation results are compared with the test data to verify the feasibility and effectiveness of the model. The simulation method takes up less system resources, requires a smaller simulation step, is easy to implement real-time, and can easily adjust the parameters online. At the same time, because the simulation model of the basic unit has the universality, we can easily form a different system simulation model for real time simulation.

## References

1. He H-X, Shen H-P, Wang J (2009) Simulation demo platform of main circuit for AC drive electric locomotive based on Matlab GUI. *High Power Converter Technol* 4:31–33 (in Chinese)
2. Gu C-J, Wei W, He Y (2013) Real time simulation of high-speed EMU traction drive system based on RT-LAB. *J Mech Electr Eng* 30(2):218–222 (in Chinese)
3. Ding R, Gui W, Chen G (2008) HiL simulation of electric locomotive AC drive system. *China Railway Sci* 29(4):96–102 (in Chinese)
4. Cui H, Ma Z, Han K, Feng X (2011) Research on the real-time simulation of the traction drive system in electric multiple units. *China Railway Sci* 32(7):94–100 (in Chinese)
5. Dai P, Zhu H-S, Li J-J, Fu X (2012) Design of power drive real-time simulation system based on FPGA. *Power Electron* 46(9):69–71 (in Chinese)
6. Cao Z, Böcker J et al (2010) State of the art of real-time hardware-in-the-loop simulation technology for rail vehicles. In: *Proceedings of the PCIM Europe Conference, Nuremberg, Germany*
7. Böcker J, Sun M et al (2012) High fidelity hybrid hardware-in-the-loop simulator with FPGA and processor for AC railway traction. In: *Proceedings of the PCIM China Conference, Beijing, China*
8. Zou R (2003) Simulation study on transient current control of four quadrant converter. *Electr Drive Locomotive* 2003(6):17–20 (in Chinese)



# Robust $H^\infty$ Control of Single-Sided Linear Induction Motor for Low-Speed Maglev Trains

Yifan Shen, Dawei Xiang and Jingsong Kang

**Abstract** The single-sided linear induction motor has been used widely in low-speed maglev trains. In this paper, an  $H^\infty$  control strategy under field orientation has been proposed to reduce the end effects and enhance the dynamic performance of the control system. First, the mathematic model of the SLIM is established. Then, the model is simplified, the end effects are attributed to the uncertainty of the system and the design is turned into an  $H^\infty$  mixed-sensitivity optimal design. After that, an  $H^\infty$  method based on internal model principle is proposed, by which a speed controller is designed finally. Simulation results indicate that a system with an  $H^\infty$  controller has much better performance than that with a traditional PI controller.

**Keywords** SLIM ·  $H^\infty$  control · Internal model principle

## 1 Introduction

Single-sided Linear Induction Motor (SLIM) has been developed and widely used in many areas these years. Compared to Rotary Induction Motor, SLIM has a simpler structure, requires less maintenance and doesn't need mechanical rotary-to-linear converters [1]. Currently, most low-speed maglev trains have adopted SLIM as their traction drives. In contrast with the rotary induction motor, the SLIM has several unique features known as the End Effects [2], which are relevant with the velocity of the motor.

Currently, the most commonly-used method of control strategy for the SLIM is the scalar control [2]. It doesn't require the accurate orientation of the field, which simply the control strategy considerably. Many optimization methods for the scalar control have been proposed to alleviate the end effects [2–4]. The Field Oriented

---

Y. Shen · D. Xiang · J. Kang (✉)

School of Electronics and Information Engineering, Tongji University,  
Shanghai, China

e-mail: kjs@tongji.edu.cn

© Springer Nature Singapore Pte Ltd. 2018

L. Jia et al. (eds.), *Proceedings of the 3rd International Conference on Electrical and Information Technologies for Rail Transportation (EITRT) 2017*, Lecture Notes in Electrical Engineering 482, [https://doi.org/10.1007/978-981-10-7986-3\\_26](https://doi.org/10.1007/978-981-10-7986-3_26)

251

Control (FOC), which has been widely-used for high performance Rotary Induction Motors and accepted as an effective method, has also been adopted as the control strategy for the SLIM and proved available [5, 6]. The FOC achieves a better dynamic performance, in contrast to the scalar control. In this paper, an  $H^\infty$  control strategy based on internal model principle for the FOC is proposed. An  $H^\infty$  speed controller is designed to reduce the sensitivity of the control system, which lowers the end effects and boosts the dynamic performance. The simulation is conducted and indicates a much better performance of the  $H^\infty$  Controllers in comparison with the traditional PI controllers.

## 2 Mathematical Model of the SLIM

The SLIM used in this research consists of a long linor and a short primary. The primary, which is designed to carry the carriage, is movable while the linor is fixed as the rail. The equations of the SLIM on d-axis and q-axis with the consideration of the end effects are shown as below [6, 7], where the  $L_m$  denotes the mutual inductance,  $L_{lr}$  and  $L_{ls}$  denote the leakage inductance of the primary and the linor.  $R_s$  and  $R_r$  denote the resistance of the primary and the linor.  $i_{ds}$ ,  $i_{qs}$ ,  $i_{dr}$  and  $i_{qr}$  denote the current of the primary and the linor on d-axis and q-axis.  $v_{ds}$  and  $v_{qs}$  can be explained in the same way.  $\omega_s$  denotes the angular velocity of the d-q reference frame and  $\omega_r$  denotes the electrical angular velocity of the linor.

$$\begin{cases} v_{ds} = R_s i_{ds} + R_r f(Q)(i_{ds} + i_{dr}) + p\varphi_{ds} - \omega_s \varphi_{qs} \\ v_{qs} = R_s i_{qs} + p\varphi_{qs} + \omega_s \varphi_{ds} \\ 0 = R_r [i_{dr} + f(Q)(i_{ds} + i_{dr})] + p\varphi_{dr} \\ 0 = R_r i_{qr} + (\omega_s - \omega_r)\varphi_{dr} \end{cases} \quad (1)$$

$$\begin{cases} \varphi_{ds} = L_{ls} i_{ds} + L_m [1 - f(Q)](i_{ds} + i_{dr}) \\ \varphi_{qs} = L_{ls} i_{qs} + L_m (i_{qs} + i_{qr}) \\ \varphi_{dr} = L_{lr} i_{dr} + L_m [1 - f(Q)](i_{ds} + i_{dr}) \\ 0 = L_{lr} i_{qr} + L_m (i_{qs} + i_{qr}) \end{cases} \quad (2)$$

$$\begin{cases} F_e = \frac{3\pi}{2\tau} p_n (\varphi_{ds} i_{qs} - \varphi_{qs} i_{ds}) \\ F_e - F_m = mpv \end{cases} \quad (3)$$

In the above equations,  $Q = \frac{DR_r}{(L_m + L_r)v}$ ;  $f(Q) = \frac{1-e^{-Q}}{Q}$ ;  $\omega_r = \frac{\pi v}{\tau}$

According to the equations above, the expression of the thrust force can be derived as:

$$F_e = \frac{3\pi}{2\tau} p_n \frac{L_m [1 - f(Q)]}{L_{lr} + L_m [1 - f(Q)]} \left[ \varphi_{dr} i_{qs} - \frac{L_{lr}^2}{L_r} \frac{f(Q)}{1 - f(Q)} i_{ds} i_{qs} \right] \quad (4)$$

As is shown in the equations above, the coefficient,  $f(Q)$ , represents the measurement of the end effects. It ranges from 0 to 1, in accordance with the velocity of the SLIM. The higher the velocity is, the larger the value of  $f(Q)$  would be.

### 3 Robust $H^\infty$ Control of the SLIM

According to the Eq. (4), the coefficients of the current in the expression of the thrust force are no longer constants. However, considering that the SLIM for the low-speed maglev train operates at a low speed under most circumstances and its acceleration is also limited at  $1 \text{ m/s}^2$ , the coefficient change caused by end effects is limited and slow. Therefore, the change could be attributed to the unconstructed uncertainty of the control system, which could be handled properly and effectively by the  $H^\infty$  method.

#### 3.1 $H^\infty$ Control Theory

A standard  $H^\infty$  problem could be represented by the following state-space equations [8]:

$$\begin{cases} \dot{x} = Ax + B_1w + B_2u \\ z = C_1x + D_1u \\ y = C_2x + D_2u \end{cases} \quad (5)$$

where ‘ $u$ ’ is the control input, ‘ $w$ ’ is the exogenous input, ‘ $y$ ’ is the measurement output, ‘ $z$ ’ is the control output. ‘ $x$ ’ is the state vector of the plant. The state-space equation of the controller  $K$  can be represented as:

$$\begin{cases} \dot{\varepsilon} = A_K\varepsilon + B_Ky \\ u = C_K\varepsilon + D_Ky \end{cases} \quad (6)$$

where ‘ $\varepsilon$ ’ is the state vector for the controller. The goal of the  $H^\infty$  method is to find a controller  $K$  that stabilizes the plant and keeps the  $H^\infty$  norm of the transfer function  $T_{zw}$  below a given constant.

#### 3.2 Design of the $H^\infty$ Speed Controller

The speed of the low-speed maglev is constrained by the upper limit of the velocity at 120 km/h, where  $f(Q)$  ranges from 1 to 0.1411. In this case, the plant of the control system has been given by Eq. (4). The plant consists of two parts.

The second part, represented as  $\frac{L_{lr}^2}{L_r} \frac{f(Q)}{1-f(Q)} i_{ds} i_{qs}$ , is positively correlated with  $f(Q)$ . Considering that the maximum value of  $f(Q)$  is 0.1411, which is much less than 0.5, the value of  $\frac{f(Q)}{1-f(Q)}$  would be small. Therefore its impact on the thrust force would be minute, which can be ignored reasonably. Hence the model of SLIM can be represented in Fig. 1a, where  $K_b$  stands for  $\frac{3\pi}{2\tau} p_n \frac{L_m[1-f(Q)]}{L_{lr} + L_m[1-f(Q)]} \varphi_{dr}$ .

The plant without the consideration of disturbance, denoted by  $P_A(s)$ , can be represented as:

$$P_A(s) = \frac{v}{i_{ds}} = \frac{3\pi}{2\tau} p_n \frac{L_m[1-f(Q)]}{L_{lr} + L_m[1-f(Q)]} \varphi_{dr} \frac{1}{ms} \tag{7}$$

In this case, the nominal model of the plant, denoted by  $P(s)$ , is set as:

$$P(s) = \frac{v}{i_{ds}} = \frac{F_e}{ms} = \frac{3\pi}{2\tau} p_n \frac{L_m}{L_{lr} + L_m} \varphi_{dr}^* \frac{1}{ms} \tag{8}$$

A simplified scheme of the control system is shown in Fig. 1b, where the uncertainty of the plant is represented as the multiplicative uncertainty:

Since the stator current can follow the given value rapidly as long as the parameters of the current loop controller are set properly, the transfer function of the current loop can be regarded as 1, which would simplify the design greatly.

The  $H^\infty$  mixed sensitivity approach is adopted here. The scheme of the  $H^\infty$  mixed sensitivity strategy is presented in Fig. 2a, where the transfer function  $W_1$  and  $W_2$  are the weighting functions.

In the  $H^\infty$  mixed sensitivity approach, the  $H^\infty$  norm of the system is:

$$\|T_{zw}\|_\infty = \left\| \begin{matrix} W_1 S \\ W_2 T \end{matrix} \right\|_\infty \tag{9}$$

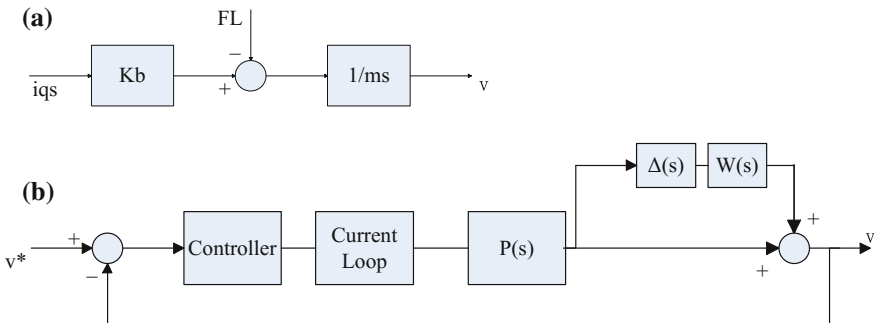


Fig. 1 The simplified plant and control system

where S stands for  $\frac{1}{1+PK}$ , and T stands for  $\frac{PK}{1+PK}$ . The goal of the approach is to constrain the H $\infty$  norm of the system to be below 1 while the controller K stabilizes the system. The weighting function of the multiplicative uncertainty can be derived from the inequality below:

$$\left| \frac{P_A(j\omega)}{P(j\omega)} - 1 \right| \leq |W_2(j\omega)| \tag{10}$$

In order to reduce the effect from the exogenous input ‘w’ on the measurement output ‘y’, the ‘S’, sensitivity of the system, should be minimized, which could be contrary to the stability of the system. Therefore, a compromised method is proposed, which is to add a weighting function  $W_1$  to the system. Considered that the exogenous input has a larger gain in low frequency, the weighting function  $W_1$  should be designed to be low-pass.

According to the internal model theory [9], in order to eliminate the static error, either the controller or the plant is required to contain an internal model of the input command signal. Also, the controller is required to contain the internal model of the disturbance signal whether the plant contains it or not. In this case, the command signal, speed, is a constant value when steady, so the internal model could be regarded as 1/s, which has already been contained by the plant according to Eq. (7). The wind disturbance can also be regarded as 1/s in the same way. By putting the internal model of the disturbance into the controller beforehand, the requirement for zero static error can be met properly. The design based on internal model principle is shown in Fig. 2b.

The most widely-used internal model for the controller is the integrator. However, the poor dynamic performance of the integrator could jeopardize the performance of the whole controller. Hence a novel method is proposed in this

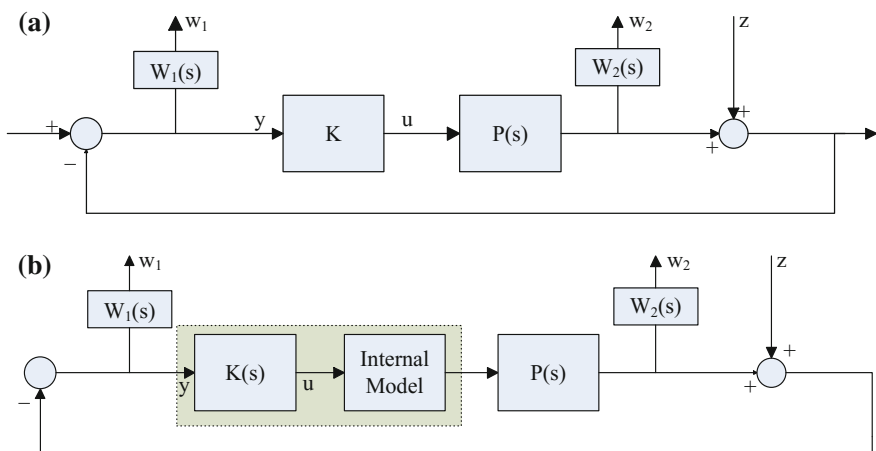


Fig. 2 Mixed-sensitivity approach based on internal model principle

paper, which is to replace the integrator with a PI controller as the internal model. The PI will be placed in the ‘Internal Model’ part in Fig. 2b. In this way, the controller will perform much more satisfactorily.

### 3.3 Simulation Study

The complete scheme of the control system is shown below (Fig. 3).

The data and parameters for the simulations are shown below:

$$R_s = 0.0897\Omega; R_r = 0.09\Omega; L_m = 0.032H; L_{ls} = 6 \times 10^{-4}H,$$

$$L_{ls} = 5 \times 10^{-4}H; p_n = 6; m = \frac{10000}{3}kg$$

The weighting functions are chosen as:  $W_1 = 0.022$ ;  $W_2 = (6/s + 0.01)$ .

The derived  $H_\infty$  controller is:  $K = \frac{64.5s^2 + 9.04s + 1.05}{s^2 + 11.39s^2 + 12.93s - 0.03} \cdot (80 + \frac{55}{s})$

Two simulations are conducted in this paper to examine the steady-state and the dynamic performance of the  $H_\infty$  control system separately. In the first simulation, a step signal is imposed on the control system as the speed signal. The simulation aims to verify if the static error has been eliminated. The results are shown below. Figure 4a shows the speed error over time, and Fig. 4b shows the thrust force.

As we can see from the results, the speed follows the given signal and the static error has been eliminated as planned, which indicates the effectiveness of the internal model planted inside the controller.

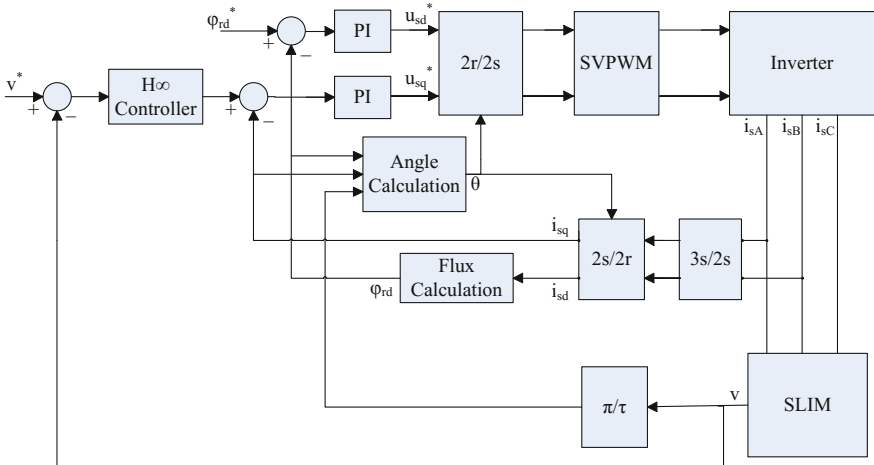
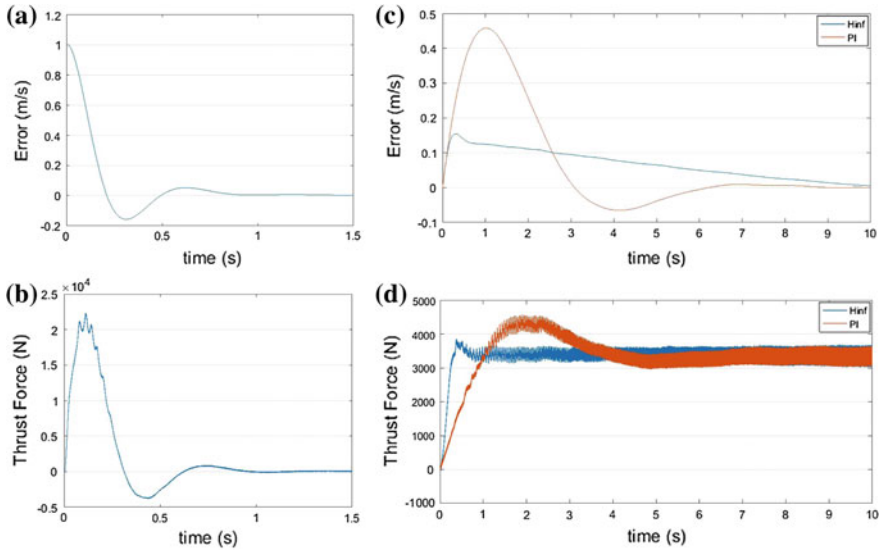


Fig. 3 The complete scheme of the control system



**Fig. 4** The error and thrust force of an  $H^\infty$ -controlled system and a PI-controlled system

The second simulation is a comparison between a  $H^\infty$  speed Controller and a traditional PI speed controller. A ramp signal is imposed on the system. The slope of the ramp is set as 1, which simulates the acceleration of the maglev. Figure 4c shows the errors of the speed from two control systems, where the orange curve denotes the PI controlled system and the blue curve denotes the  $H^\infty$  controlled system. Figure 4d shows the thrust force of two systems.

It is demonstrated that a control system with a  $H^\infty$  controller has much better performance than that with a traditional PI controller. The simulation results claim the superiority and the practicability of the  $H^\infty$  control strategy. The thrust force tends to divergence in Fig. 4d because of the rising of the speed. However, according to Fig. 4b, the thrust force is stable when the speed stops rising and becomes a constant.

## 4 Conclusion

In this paper, an  $H^\infty$  control strategy under field orientation has been proposed to reduce the end effects and enhance the dynamic property of the control system. The mathematic model of the SLIM is established and the end effects are considered. After the simplification of the model, the end effects are attributed to the uncertainty of the system and a mixed-sensitivity optimization is conducted. A speed controller is designed by an  $H^\infty$  method based on internal model principle. The traditional internal model, an integrator, is replaced by PI to enhance the dynamic property. The simulation indicates the superiority and the practicability of the  $H^\infty$  controller.

**Acknowledgements** This study was funded by the National Key R&D Program of China (2017YFB1200900) and Research on Simulation Verification and Design Optimization of Key Technologies for High Speed Maglev Transportation System (2016YFB1200602-02).

## References

1. Tong L, Ma Y, Xu R (2003) Medium and low speed maglev technology applicable to urban mass transit. *Electr Locomotives Mass Transit Veh* 26(5):4–6 (in Chinese)
2. Deng J, Chen T, Tang J, Tong L (2013) Optimum slip frequency control of Maglev single-sided linear induction motors to maximum dynamic thrust. *Proc CSEE* 33(12):123–130 + 194 (in Chinese)
3. Yu H, Fahimi B (2009) A novel control strategy of linear induction motor drives based on dynamic maximum force production. In: 2009 IEEE vehicle power and propulsion conference (VPPC), pp 98–102
4. Lu C, Dawson GE, Eastham TR (1993) Dynamic performance of a linear induction motor with slip frequency control. In: 1993 Canadian conference on electrical and computer engineering (Cat. No.93TH0590-0), 1057-60 vol 2
5. Yu H, Fahimi B (2009) Maximum force/ampere control of linear induction motor drives in field weakening region. In: 2009 IEEE international electric machines and drives conference (IEMDC), pp 592–597
6. da Silva EF, dos Santos EB, Machado PCM, de Oliveira MAA (2003) Dynamic model for linear induction motors. In: IEEE proceedings of ICIT 2003, vol 1. Maribor (Slovenia), pp 478–482
7. Deng J, Tang J (2015) An improved state filter for end-effect cross control of single-sided linear induction motors. *Proc CSEE* 35(23):6179–6187 (in Chinese)
8. Attaianese C, Tomasso G (2001)  $H^\infty$  control of induction motor drives. *IEE Proc-Electr Power Appl* 148(3):272–278
9. Francis BA, Wonham WM (1976) The internal model principle of control theory. *Automatica* 12(5):457–465



# Online Fault Diagnosis of the Hybrid Electrical Multiple Unit Traction Converter

Lei Wang, Mengzhu Wang, Yujia Guo, Ruichang Qiu and Lijun Diao

**Abstract** In this paper, the signatures and the diagnosis approach of the failure of switching devices in Hybrid Electrical Multiple Unit (HEMU) traction converter (TC) are developed. In this paper, the distorted voltage and current with such failures are treated as disturbance exerted over normal voltage and current without failures, and a special analytical failure model is built for the expression of voltage and current disturbance. Combined with the failure model, this paper proposes a novel reasoning process to locate malfunctioning switching device. The reasoning process is based on object-oriented colored Petri Net (OOCPN). Digitalized failure signatures are taken as inputs into the OOCPN reasoning machine, what stimulates the brain activities during fault diagnosis of an expert.

**Keywords** Analytical failure model · Switching device failure · Cascading and coupling interaction · Online fault reasoning · Object-oriented Petri Net

## 1 Introduction

With the development of traction converter (TC) technology of passenger and freight EMU, the integration degree of the equipment has been increased, along with the complexity of the converter's power circuit. Originated from such tendency, the fault diagnosis of power circuit in the presence of switching device failures has been more and more indispensable. The increasing complexity of power circuit has been making it harder for the diagnosis process to locate malfunctioning switching device. Take the TC of Hybrid Electrical Multiple Unit (HEMU) as an example, with the supply from external diesel power package, the TC consists of two cascaded subsystems, i.e. the Grid Converter Module (GCM) and the Traction

---

L. Wang (✉) · M. Wang · Y. Guo · R. Qiu · L. Diao  
School of Electrical Engineering, Beijing Jiaotong University,  
No. 3 Shangyuancun, Haidian District, Beijing 100044, China  
e-mail: leiwang@bjtu.edu.cn

Converter Module (TCM). The power circuit of GCM and TCM is coupled with a common DC-Link (as is shown in Fig. 1).

To diagnose power circuit failures caused by malfunctioning switching devices, conventional diagnosis approaches aim at generally diagnosing switching device failures or specially diagnosing the failures in certain specific circuit layouts [1]. in Refs. [2–5], the failure is diagnosed directly with recognizing the variations of IGBT conduction resistance, of gate current dynamic characteristic, and of gate voltage; in Refs. [6–9], the failure is diagnosed indirectly with signatures extracted with frequency components, with wavelet sets, with high-order spectrum analysis, and with self-defined functions, which demands higher real-time computing capability. The efficiency and effectiveness of such approaches for specific circuit layouts remain to be testified, when they are applied to diagnose other layout.

In Fig. 1, the input ports of GCM in TC are connect to diesel power package, which is simplified as voltage source  $e_A$  through  $e_C$ . Between such input ports and the power package, are the parasitic resistance of  $R_1$  through  $R_3$ , and the AC filtering inductance  $L_1$  through  $L_3$ . In Fig. 1,  $i_A$  through  $i_C$  are current inputs of GCM, and  $i_U$  through  $i_W$  are current outputs of TCM.  $U_{dc}$  is the DC voltage across the mutual coupling port.

To build an efficient failure model is the prerequisite of fault diagnosis and malfunctioning device locating after power circuit failure. After that, the diagnosis process could be carried out, with failure analysis scheme and based on the data from the failure model. In the following part of this paper, both the proposed analytical fault model and a novel automatic failure reasoning scheme will be introduced in detail.

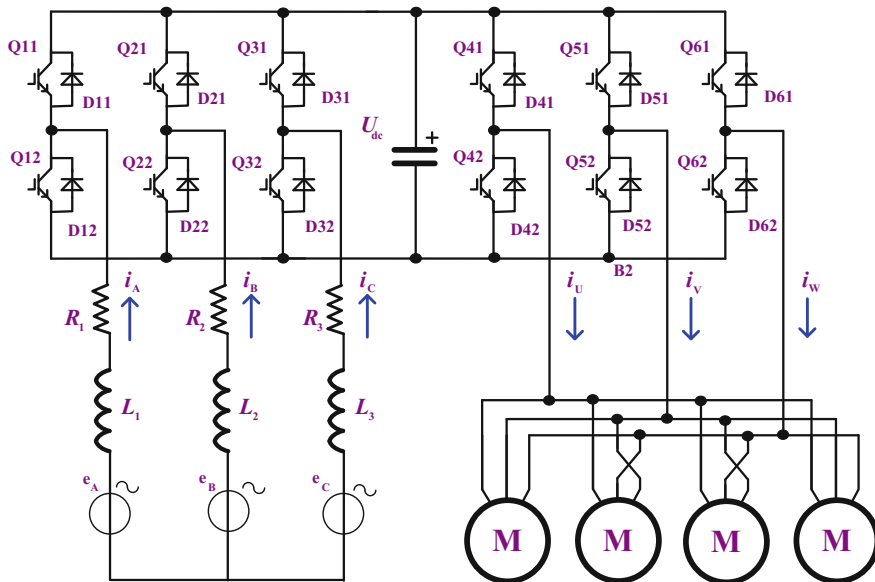
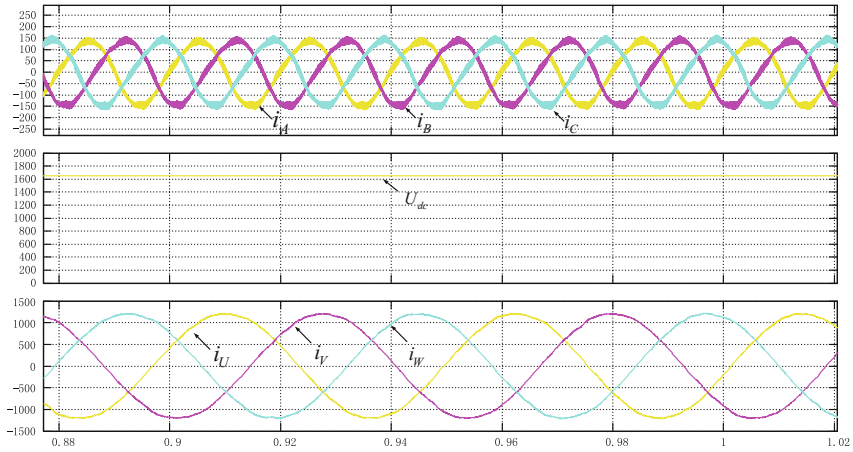
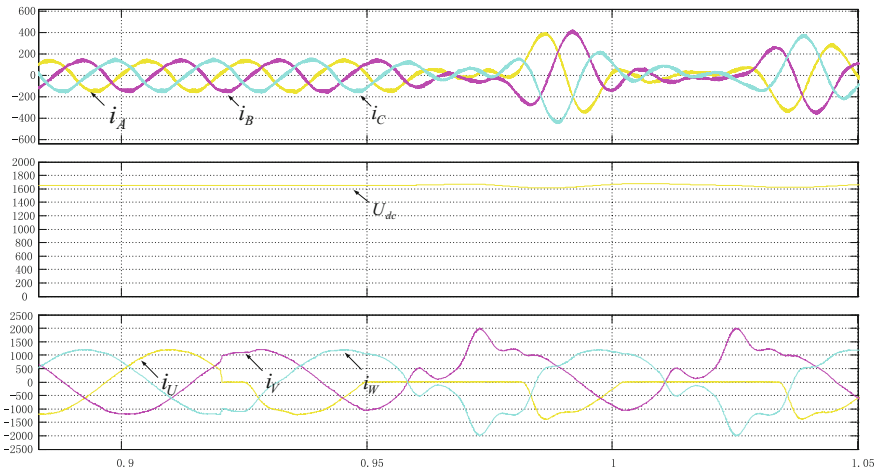


Fig. 1 The power circuit layout of TC in HEMU with diesel power package supply



(a) With no IGBT failures



(b) With a broken IGBT of Q41 in TCM

Fig. 2 The waveforms of  $i_A \sim i_C$ ,  $U_{dc}$ ,  $i_U \sim i_W$ , with and without IGBT failure

## 2 The Fault-Disturbance Model Considering Internal Cascading and Mutual Coupling

The characteristic waveforms of current inputs and outputs are given in Fig. 2, when there is no IGBT failures and when one IGBT is broken. In order to describe the distortion condition of  $i_U \sim i_W$ ,  $U_{dc}$  and  $i_A \sim i_C$ , and to describe the interactions among the current and voltage distortions, the distortion of  $i_U \sim i_W$  and  $i_A \sim i_C$  are treated as input disturbance into GCM and TCM. By such means, an analytical cascaded failure model of GCM + TCM + traction motors is built.

## 2.1 The Analytical Failure Model of TCM + Traction Motor, with Disturbance Input

At first, we denote the failure model of TCM + traction motor as in Eq. (1)

$$X_1' = A_1 X_1 + B_1 U_1 \quad (1)$$

In a failure model, the state vector  $X_1$  in Eq. (1) should be  $X_1 = (\Delta i_U \ \Delta i_V \ \Delta i_W)^T$ , where  $\Delta i_U \sim \Delta i_W$  are current output disturbance of TCM.

$$X_1 = (\Delta i_{qs} \ \Delta i_{ds})^T, U_1 = (\Delta U_{dc})^T \quad (2)$$

and

$$A_1 = \begin{pmatrix} \frac{R_s L_r}{L_m^2 - L_s L_r} & \frac{\omega_r L_m^2}{L_m^2 - L_s L_r} - \omega_e \\ \frac{-\omega_r L_m^2}{L_m^2 - L_s L_r} - \omega_e & \frac{R_s L_r}{L_m^2 - L_s L_r} \end{pmatrix}$$

$$B_1 = \begin{pmatrix} \frac{L_r M_U}{(L_m^2 - L_s L_r)} \\ 0 \end{pmatrix} \quad (3)$$

In view of the transformation from stationary 3-phase coordinates to rotary 2-phase coordinates [10], it gives

$$Y_1 = (\Delta i_U \ \Delta i_V \ \Delta i_W)^T \quad (4)$$

where  $\Delta i_U \sim \Delta i_W$  are the current output distortions and

$$(\Delta i_{qs} \ \Delta i_{ds})^T = C_1 (\Delta i_U \ \Delta i_V \ \Delta i_W)^T \quad (5)$$

where

$$C_1 = \frac{2}{3} \begin{pmatrix} \cos(\omega_e t) & \cos(\omega_e t - \frac{2}{3}\pi) & \cos(\omega_e t + \frac{2}{3}\pi) \\ \sin(\omega_e t) & \sin(\omega_e t - \frac{2}{3}\pi) & \sin(\omega_e t + \frac{2}{3}\pi) \end{pmatrix} \quad (6)$$

$C_1$  is not square, so the inverse matrix of  $C_1$  could not be derived easily.

and Eq. (7) shows the mutual coupling relationship between DC-link voltage distortion ( $\Delta U_{dc}$ ) and AC current distortions ( $\Delta i_U \sim \Delta i_W$ ).

$$T_m = \frac{3}{2} \left( \frac{P}{2} \right) (\Psi_{ds} \quad -\Psi_{qs}) \begin{pmatrix} i_{qs} \\ i_{ds} \end{pmatrix} \quad (7)$$

$$\Delta T_m = \frac{3}{2} \left(\frac{P}{2}\right) (\Psi_{ds} + \Delta\Psi_{ds} \quad -\Psi_{qs} - \Delta\Psi_{qs}) \begin{pmatrix} i_{qs} + \Delta i_{qs} \\ i_{ds} + \Delta i_{ds} \end{pmatrix} - T_m \quad (8)$$

Equation (7) is the expression of  $T_m$  under normal performance, and Eq. (8) is that with IGBT failure. In Eq. (8),  $\Delta\Psi_{ds}$  and  $\Delta\Psi_{qs}$  is the projection on d-axis and q-axis of the stator flux distortion, while the d-axis and q-axis are the vertical and horizontal axis, respectively.

Taking into account that the magnetic inertia of the motor is much larger than its electric inertia, then  $\Delta\Psi_{ds}$  and  $\Delta\Psi_{qs}$  are basically zero, so Eq. (9) gives:

$$\Delta T_m = \frac{3}{2} \left(\frac{P}{2}\right) (\Psi_{ds} \quad -\Psi_{qs}) \begin{pmatrix} \Delta i_{qs} \\ \Delta i_{ds} \end{pmatrix} \quad (9)$$

hence

$$\Delta T_m = \left(\frac{P}{2}\right) (\Psi_{ds} \quad -\Psi_{qs}) \begin{pmatrix} \cos(\omega_e t) & \cos(\omega_e t - \frac{2}{3}\pi) & \cos(\omega_e t + \frac{2}{3}\pi) \\ \sin(\omega_e t) & \sin(\omega_e t - \frac{2}{3}\pi) & \sin(\omega_e t + \frac{2}{3}\pi) \end{pmatrix} \begin{pmatrix} \Delta i_U \\ \Delta i_V \\ \Delta i_W \end{pmatrix} \quad (10)$$

Here we assume that

$$\begin{cases} \Delta i_U = \sqrt{2}I \sin(\omega_e t + \theta_1) \\ \Delta i_V = \sqrt{2}I \sin(\omega_e t + \theta_1 - \frac{2}{3}\pi) \\ \Delta i_W = \sqrt{2}I \sin(\omega_e t + \theta_1 + \frac{2}{3}\pi) \end{cases} \quad (11)$$

where  $I$  is the effective value of the output current distortion,  $\Delta T_m$  is derived by substituting Eq. (11) into Eq. (12):

$$\Delta T_m = \frac{3P}{2\sqrt{2}} (\Psi_{ds} \quad -\Psi_{qs}) \begin{pmatrix} I \sin \theta_1 \\ I \cos \theta_1 \end{pmatrix} \quad (12)$$

With distorted mechanical torque output ( $T_m$ ), the TCM active power  $P_m$  is also distorted accordingly, as is shown in Eq. (13).

$$\Delta P_m = \Delta T_m * \Omega_r \quad (13)$$

Such conclusion could be confirmed by waveforms in Fig. 3. In Fig. 3, Q41 is broken on 0.92 s, and the waveform of  $T_m$  fluctuates along with  $\Delta i_U \sim \Delta i_W$ , in the same frequency.

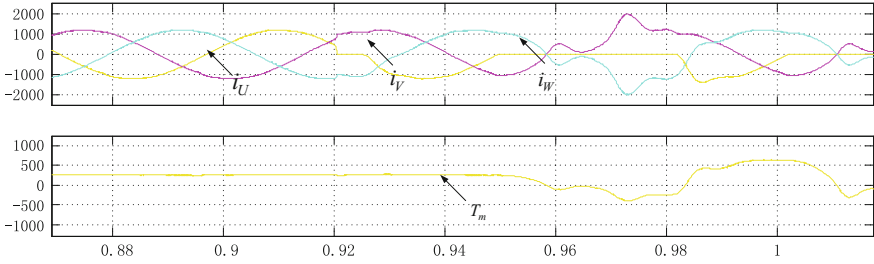


Fig. 3 The waveforms of  $i_U \sim i_W$  and  $T_m$ , after Q41 of TCM is broken

### 2.2 The Fundamental Failure Signatures of TC Considering Internal Cascading and Mutual Coupling

As for the effect on  $U_{dc}$ , by ignoring  $R_s$  and  $R_g$ , and with an average modulation depth of  $M_m$  and  $M_{A \sim C}$ , it gives

$$\Delta U'_{dc} \approx -\frac{K}{R_L L_g} \Delta U_{dc} \tag{14}$$

In Eq. (14),  $K$  is a constant conversion factor. Given that  $L_g$  can be considered constant, so  $\Delta U_{dc}$  is uniquely determined by  $R_L$ , i.e., by the torque output of the motive car. What's more, Eq. (14) implies that with accurate voltage control scheme of GCM, the power circuit failure of TCM distorts  $U_{dc}$  much more seriously.

As for  $R_L$ , it gives

$$R_L = \frac{U_{dc}^2}{NT_m \Omega_r} = \frac{U_{dc}^2}{P_m} \tag{15}$$

In Eq. (15),  $N$  is the number of traction motors connected to TCM,  $T_m$  is mechanical torque output of a single traction motor, and  $\Omega_r$  is mechanical rotor angular velocity of traction motors.  $NT_m \Omega_r$  equals the active power  $P_m$  that TCM absorbs from or feeds into DC-link, in traction or braking stage, respectively. In traction stage,  $P_m > 0$ , hence  $R_L > 0$ , and in braking stage  $R_L < 0$ .

Figure 2 shows the waveforms of  $i_A \sim i_C$ ,  $U_{dc}$ ,  $i_U \sim i_W$ , with and without IGBT failure. In Fig. 2a, TC operates normally without any malfunctioning switching device; in Fig. 2b, the Q41 of TCM breaks on 0.92 s.

The effect on  $\Delta U_{dc}$  from  $\Delta i_A \sim \Delta i_C$  on  $\Delta U_{dc}$  is greatly suppressed by voltage closed-loop control scheme of GCM [11], while  $U_{dc}$  is still subject to certain slight distortion in Fig. 2b. However, the effect of such distortion is further suppressed and finally eliminated by the voltage feedforward scheme of TCM, that the output current  $i_U \sim i_W$  shows no distortion is a good proof of this. In Fig. 2b,  $\Delta U_{dc}$  is serious owing to the distortion of  $\Delta i_U \sim \Delta i_W$ , what can be partly explained with Eq. (14) and (15).

Current and voltage distortions increase the electrical and thermal stress of the sound switching devices left in PCM and TCM greatly, making it a must to detect switching device failure as soon as the failure has occurred. If the control unit of TC fails to recognize such power circuit failures and to locate malfunctioning switching devices, other switching previously sound will be damaged, resulting in greater loss.

### 3 The Automatic Fault Reasoning with OOC PN Model and Digitalized Current/Voltage Signatures

Being an effective tool for dealing with discrete time dynamic processes, Petri Net is also applicable completely in fault diagnosis of IGBT breakdown [12]. The transitions of colored tokens in OOC PN simulates natural brain activities what occur during fault reasoning by a field expert, and the stability of the reasoning process is higher because of the discrete logic deduction process [13].

Based on the analysis above, the current input and output as well as the voltage of DC-link are capable of acting as excellent fault signatures because they are seriously and directly affected by power circuit faults. Since that OOC PN only takes digital token inputs, the currents and voltage must be coded into digital quantities. Such digitalization could be carried out with normalized average which are compared with corresponding hysteresis thresholds, as is shown in Eq. (16).

$$sig_{dc} = \begin{cases} 1, & \overline{U_{dc}^*} > thres(U_{dc}) \\ 0, & \overline{U_{dc}^*} < thres(U_{dc}) \end{cases} \quad (16)$$

In Eq. (16),  $sig_x$  is the digitalized signature of  $i_x$ , where  $x$  could be  $A \sim C$  or  $U \sim W$ .  $\overline{i_x^*}$  is the normalized average of  $i_x$ , and  $thres(i_x)$  is the hysteresis threshold of  $i_x$ ;  $sig_{dc}$  and  $\overline{U_{dc}^*}$  are the digitalized signature and normalized average of  $U_{dc}$ , respectively, and  $thres(U_{dc})$  is the hysteresis threshold of  $U_{dc}$ . The normalized average values are derived with Eq. (17), where  $i_{dx}$  and  $i_{qx}$  are the d-axis and q-axis projection in rotary 2-phase coordinate system of  $i_x$ ,  $x = A \sim C, U \sim W$ .  $U_{nom}$  is the nominal DC voltage of DC-link, and is 1650 V for a TC of HEMU.

$$\overline{i_x^*} = \frac{i_x}{\sqrt{i_{dx}^2 + i_{qx}^2}}, \overline{U_{dc}^*} = \frac{U_{dc}}{U_{nom}} \quad (17)$$

The mapping relations between malfunctioning IGBTs and digitalized fault signatures are listed in Table 1. The current and voltage disturbance under power circuit failures make it harder to realize accurate diagnosis [14]. To solve such problem, we carry out the diagnosis process with a reasoning machine, so the effect from such disturbance will be eliminated by iterative reasoning.

**Table 1** The correspondence between malfunctioning IGBT and digitalized fault signature

IGBT with Failure	$sig_{A\sim C}, sig_{DC}/sig_{U\sim W}, sig_{DC}$	IGBT with Failure	$sig_{A\sim C}, sig_{DC}/sig_{U\sim W}, sig_{DC}$
Q11/Q41	1, -1, 1, 0/-1, 1, -1, 1	Q22/Q52	-1,-1,1,0/1,1,-1,1
Q12/Q42	-1, 1, -1, 0/1, -1, 1, 1	Q31/Q61	-1,1,1,0/1,-1,-1,1
Q21/Q51	1, 1, -1, 0/-1, -1, 1, 1	Q32/Q62	1,-1,-1,0/-1,1,1,1

The reasoning machine with OOCPN layout is shown in Fig. 4. Here is the definition of a color token of the OOCPN:

{Cg,Ct, Cmid,Cgf, Ctf, Fun}

Cg records the IGBT identifier of GCM that has been diagnosed to be malfunctioning. Ct records the IGBT identifier of TCM that has been diagnosed to be malfunctioning. Cgm keeps information of current signatures of GCM (i.e.  $sig_{A\sim C}$ ), Ctm keeps information of current signatures of TCM (i.e.  $sig_{U\sim W}$ ); Cmid keeps information of voltage signature of TCM (i.e.  $sig_{DC}$ ); Fun is the functional attribute of the token, and it project Cgm, Ctm, Cmid to Cg and Ct.

With OOCPN reasoning machine, we realize field diagnosis of Q11 and Q41 failures on a DSPF2812 platform. In Fig. 5a, b, a rising edge of the end mark

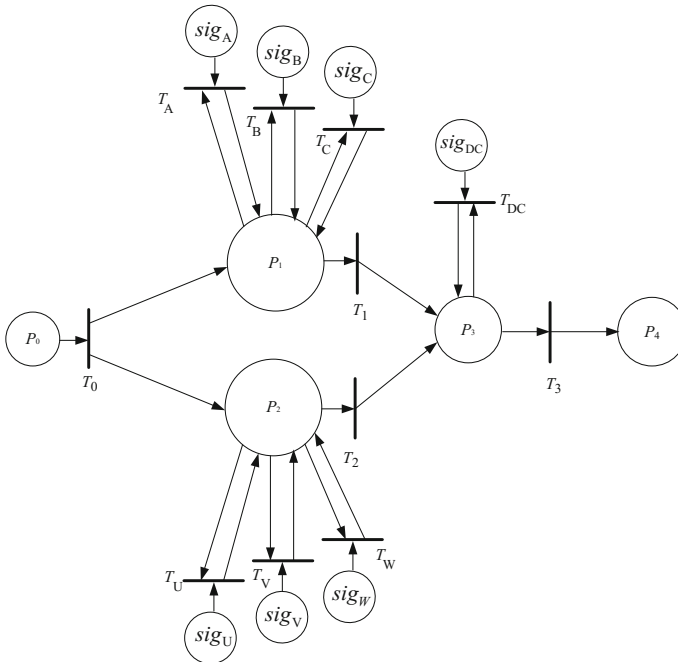
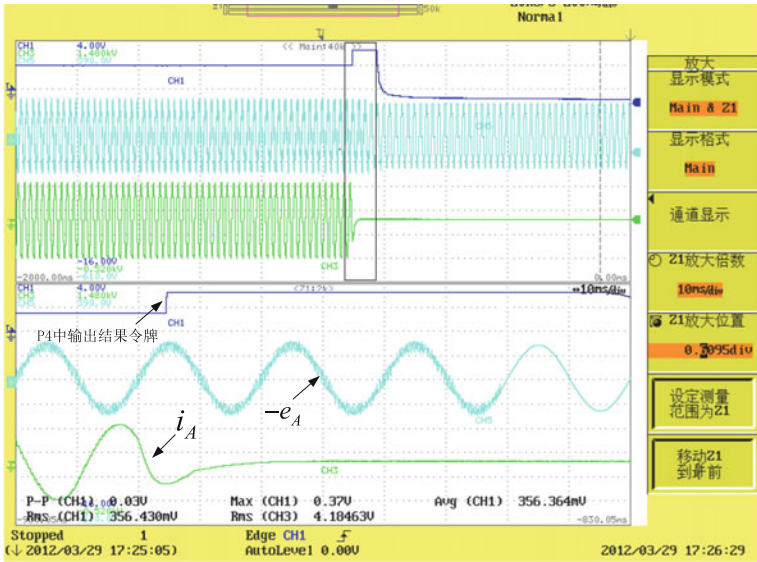
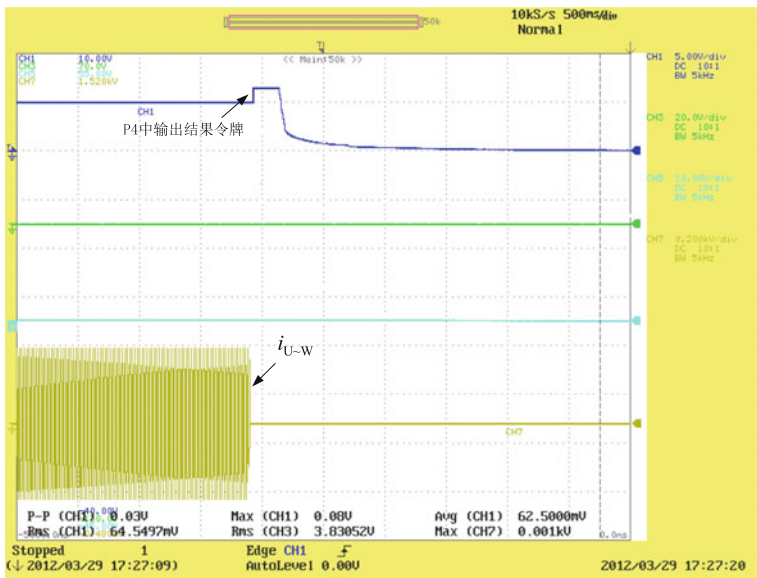


**Fig. 4** The fault reasoning machine based on OOCPN





(a) The Q11 of GCM is broken



(b) The Q41 of TCM is broken

Fig. 5 Waveform after diagnosis with IGBT failure in power circuit of TC

implies that a token result has been obtained by the OOC PN reasoning machine. For malfunctioning Q11 and Q41. In both cases, the malfunctioning IGBT is successfully diagnosed. The token results are as follows:

With malfunctioning Q11:

$\{\{Q11\}, \{0\}, \{0\}, \{1, -1, 1\}, \{0\}, \text{Fun}\}$ .

With malfunctioning Q41:

$\{\{0\}, \{Q41\}, \{1\}, \{0\}, \{1, -1, 1\}, \text{Fun}\}$ .

It should be noted that 3.3 and 3.5 ms is consumed by the diagnosis process for GCM and TCM, respectively, and such consumption is cost mostly by normalization and averaging process. In Fig. 5a, b, it can be observed that the current inputs or outputs of TC are interrupted on the arriving of a diagnosis result, to protect the sound IGBTs left.

## 4 Conclusions

The cascading and coupling relationship of sub-systems in TC of HEMU makes it difficult for conventional diagnosis approaches to recognize malfunctioning switching devices in the power circuit. In this paper, the fault signatures of switching device failures are reconfigured with an analytical fault model, which takes into consideration the inner coupling and mutual interactions among the GCM and TCM of TC. With such fault model, the current inputs, the current outputs, and the voltage across DC-link of TC are selected as basic fault signatures. Digitalized signatures derived with the currents and voltage are put into an OOC PN reasoning machine for malfunctioning switching device location. The diagnosis process proposed and exemplified in this paper is testified with experimental results, and it is hoped that such process will provide reference to some similar system.

**Acknowledgements** This work was supported by the Fundamental Research Funds for the Central Universities of China (No.E16JB00160/2016JBM062/2016JBM058) and The National Key Research and Development Program of China (2016YFB1200504-C-02).

## References

1. Lei R, Zheng W, Gong C, Shen Q (2015) Fault feature extraction techniques for power devices in power electronic converters: a review. *Proc CSEE* 35(12):3089–3101
2. Celaya JR, Saxena A, Vashchenko V et al (2011) Prognostics of power MOSFET. In: *The 23th international symposium on power semiconductor devices and ICs*. IEEE, San Diego, CA, pp 160–163
3. Xiong Y, Cheng X, Shen ZJ et al (2008) Prognostics and warning system for power-electronics modules in electronic, hybrid electric, and fuel-cell vehicles. *IEEE Trans Ind Electr* 55(6):2268–2276
4. Zhou S, Zhou L, Sun P (2013) Monitoring potential defects in an IGBT module based on dynamic changes of the gate current. *IEEE Trans Power Electr* 28(3):1479–1487

5. Rodriguez-Blanco MA, Claudio-sanchez A, Theilliol D et al (2011) A failure-detection strategy for IGBT based on gate-voltage behavior applied to a motor drive system. *IEEE Tran Ind Electr* 58(5):1625–1633
6. Han X, Wang Y, Cui J (2008) Fault diagnosis of power electronic circuits based on wavelet radical basis function network. *Microelectronics* 38(3):309–311
7. Hu Q, Wang R, Zhan Y (2008) Fault diagnosis technology based on SVM in power electronics circuit. *Proc CSEE* 28(12):107–111
8. Zhang X (1996) Time series analysis. Tsinghua university press, Beijing, pp 11–13
9. Ma H, Mao X, Xu D (2005) Parameter identification of DC/DC power electronic circuits based on hybrid system model. *Proc CSEE* 25(10):50–54
10. Bimal KB (2011) Modern power electronics and AC drives. Prentice Hall PTR
11. Jiang J, Holtz J (2001) An efficient braking method for controlled AC drives with a diode rectifier front end. *IEEE Trans Ind Appl* 37(5):1299–1307
12. Oikonomou N, Holtz J (2008) Closed-loop control of medium-voltage drives operated with synchronous optimal pulsewidth modulation. *IEEE Trans Ind Appl* 44(1):115–123
13. Wang L (2011) Study on the fault diagnosis and protection of energy-fed supply system in urban mass transit. Doctoral Dissertation, Beijing Jiaotong University
14. Wang L, Li Y, Liu Z (2012) The fault diagnosis method of urban rail transit traction power supply system based on topology analysis and backward reasoning of OOC PN. *China Railway Sci* 33(4):52–59

# Characterization and Variable Temperature Modeling of SiC MOSFET

Mengzhu Wang, Yujia Guo, Lei Wang, Guofu Chen  
and Ruichang Qiu

**Abstract** Silicon power semiconductor device is difficult to meet the requirements of high temperature, high pressure and high frequency. Among them, the MOSFET which has the fast switch speed and the simple driving circuit, become the most popular object in SiC power electronic devices. In this paper, we choose the C2M0160120D chip of CREE company, establishing a complete model. And the static characteristics of SiC MOSFET under different temperature points are simulated. The switching characteristics of SiC MOSFET under different driving resistances are analyzed and compared with the experimental results, and the accuracy of the model is verified in this paper.

**Keywords** SiC MOSFET · Simulation model · Pspice · Characteristic analysis

## 1 Introduction

Si and GaAs, as the representative of the traditional semiconductor devices, can only work under 200 °C, and they can't meet the new requirements of the development of modern electronic technology [1]. Since 1990s, with the outstanding performance advantages of band gap, breakdown field strength, thermal conductivity and saturation electron drift rate, the third generation wide band gap semiconductor material, represented by SiC and GaN, have become the research focus. At present, SiC MOSFETs have a very good application in the civil power substation and transmission field, the aerospace field, and the new energy field, such as PV inverter, hybrid/electric vehicles, rail vehicles, wind power [2].

---

M. Wang (✉) · Y. Guo · L. Wang · R. Qiu  
School of Electrical Engineering, Beijing Jiaotong University,  
No. 3 Shangyuancun, Haidian District, Beijing 100044, China  
e-mail: 16121530@bjtu.edu.cn

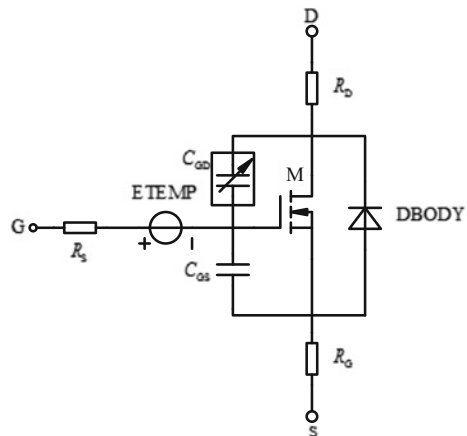
G. Chen  
State Key Laboratory of Advanced Power Transmission Technology,  
Global Energy Interconnection Research Institute, Beijing, China

With the wide use of SiC MOSFET, it is very important to use a model of the device to evaluate performance. Therefore, obtaining a precise and concise model is the key to simulate exactly of the device characteristics. The MOSFET device model can be divided into physical model and equivalent circuit model [3]. According to the structure diagram of the SiC MOSFET, the circuit schematic diagram and the physical equations of the model, a SiC MOSFET model based on the physical level was established in Ref. [4]. However, this method has a large amount of calculation. It is suitable for the research at the physical level and the analysis of the intrinsic characteristics of the device, but industrial applications. Taking SiC MOSFET CMF20120D chip of CREE company as an example, a variable temperature parameter PSpice model was built in Ref. [5]. The model was tested under different voltage, current and temperature conditions. It was turned out that the model was accurate and had a high reference value [6–8]. But the way, modeling of temperature controlled voltage source, is very complex and easy to make mistakes. In this paper, we use ABM (Analog Behavioral Modeling) simulation behavior model to improve the modeling method. Gate-drain capacitance  $C_{GD}$  is an important factor to affect the switching characteristic of SiC MOSFET, and the method in Ref. [6] has a poor accuracy. In this paper, based on the establishment of the SiC MOSFET model of MOS3, we make a thorough inquiry of modeling  $C_{GD}$ .

## 2 Variable Temperature Modeling of SiC MOSFET

Figure 1 shows the SiC MOSFET PSpice model that needs to be established in this paper. M and DBODY are used to describe the basic characteristics of N channel MOSFET with Model Editor in PSpice software. The temperature dependent voltage source *E*TEMP, is employed to describe the static characteristics of SiC MOSFET. CGD and CGS are used to describe the dynamic characteristics.

**Fig. 1** PSpice model of SiC MOSFET



### 2.1 Temperature Compensation Modeling of on-State Resistance

Basic unit M only sets up a model at a single temperature (25 °C). In order to improve the accuracy of the model, we will build a model of temperature compensation of on-state resistance  $R_{ds}$ . From the datasheet of C2M0160120D, we can know that the value of  $R_{ds}$  increases with temperature. To simplify the modeling process, We combine the drain and source resistance into  $R_{ds(on)}$ , and we use the second-order fit method for its mathematical treatment

$$R_{ds(on)}(T) = R_{ds(on)}(T_{25}) \cdot \left[ 1 + TC_1 \cdot (T - T_{25}) + TC_2 \cdot (T - T_{25})^2 \right] \quad (1)$$

Through the data points extraction and curve fitting, we can get the formula of on-state resistance

$$R_{ds(on)}(T) = 0.0024 \cdot \left[ 1 + 0.1309 \cdot (T - T_{25}) + 0.0016 \cdot (T - T_{25})^2 \right] \quad (2)$$

where  $R_{ds(on)}(T_{25})$  is the typical  $R_{ds(on)}$  value at 25 °C, we take 160 mΩ,  $T$  is the temperature point in simulations,  $TC_1$  and  $TC_2$  are fitting coefficients.

Place the temperature compensation resistor in the circuit, and test the  $R_{ds(on)}$  of SiC MOSFET with the condition of  $U_{GS} = 20 \text{ V}, I_D = 10 \text{ A}$ .

As is shown in Fig. 2b, the blue line that Model Editor default is far away from the trend of On-Resistance versus Temperature in datasheet. The red line can describe the on-state resistance with temperature changes better.

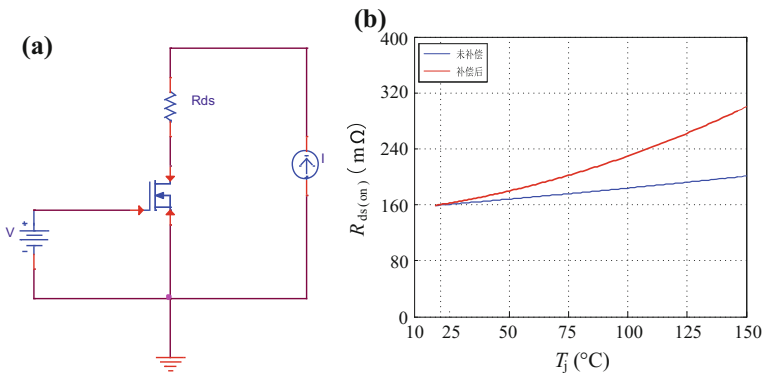


**Fig. 2** a Test circuit of drain-source on-state resistance, b before and after the compensation of on-resistance versus temperature

## 2.2 Modeling of Temperature Control Voltage Source

In this paper, ABM (Analog Behavioral Modeling) is used to model the temperature control voltage source. ABM is an extension of the controlled source. It calls mathematical formulas or look-up tables to describe the device, without the need to design specific circuit [9].

In PSpice, the default threshold voltage change rate is  $-1\text{Mv}/^\circ\text{C}$ , which isn't match with the actual device threshold voltage variation.  $E_{\text{TEMP}}$  is used to compensate for the change of threshold voltage caused by temperature change. It proposed in Ref. [10]. Simple linear fitting can't perfectly represent the curve of Threshold Voltage vs. Temperature. So we use the three order function and three order fitting to the  $E_{\text{TEMP}}$  modeling,

$$E_{\text{TEMP}} = VT_3 \cdot (T - T_{25})^3 + VT_2 \cdot (T - T_{25})^2 + VT_1 \cdot (T - T_{25}) \quad (3)$$

where  $T$  is the temperature point in simulations,  $VT_1$ ,  $VT_2$  and  $VT_3$  are fitting coefficients. The ABM model used in this paper is simpler, and the improved formula is

$$E_{\text{TEMP}} = VT_3 \cdot T^3 + VT_2 \cdot T^2 + VT_1 \cdot T \quad (4)$$

## 2.3 Modeling of Gate-Source Capacitance

The capacitance between several poles affect the switching characteristics of SiC MOSFET. It is almost independent of temperature, but sensitive to voltage parameters. So, in this paper, temperature factors will not be considered, and mainly discuss the modeling of  $C_{\text{GD}}$  which has a significant influence on the switching characteristics of the device. Two modeling methods of  $C_{\text{GD}}$  will be explored in this paper.

### 2.3.1 Sub Circuit Modeling Method

Figure 3a shows the sub circuit of nonlinear capacitance, it uses two diodes in series to describe the nonlinear capacitance [11]. Diode has PN junction capacitance effect. In the reverse bias state, the capacitance decreases as the voltage increases, which conform to the changing trend of  $C_{\text{GD}}$ . We can reasonably configure the parameters of two diodes to accurately simulate the changes in capacitance.

When the device is in off-state,  $U_{\text{GD}} < 0$ ,  $D_{\text{GD1}}$  and  $D_{\text{GD2}}$ , in series, are used to describe the changes in  $C_{\text{GD}}$ . When the device is in the on-state,  $U_{\text{GD}} > 0$ , fixed capacitance  $CGD_{\text{MAX}} = C_{\text{GD}}$ . In this way, the sub circuit can accurately describe the nonlinear variable capacitance  $C_{\text{GD}}$ .

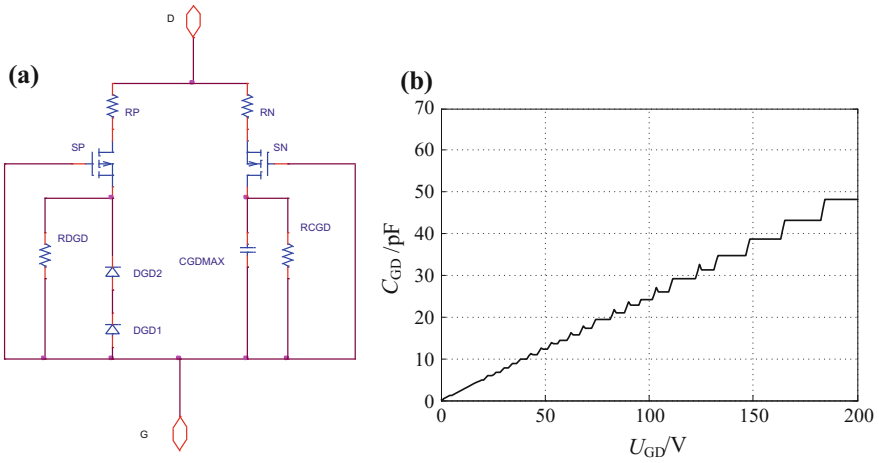


**Fig. 3** **a** The sub circuit of nonlinear capacitance. **b** The test simulation curve of diode’s capacitance

The waveform of the capacitance with voltage is shown in Fig. 3b. In the simulation process, the running speed is slow and the simulation curve is not easy to converge, which is prone to error. The capacitance value increases with the  $U_{GD}$  value, which is far from the actual one. Diode parameters can only be set by trial and error, which has poor accuracy.

**2.3.2 Descriptive Statement Modeling Method**

$C_{GD}$  is nonlinear before the device is fully turn on, and it is a fixed value after the opening. It needs to describe the nonlinear variation of the capacitance value, which is expressed in  $C_g$ . Because measure capacitance directly is hard, referring to the formula (6), when  $dU_{GD}/dt$  is linear to 1, the  $i_g - t$  change can be used to replace the description of  $C_g - U_{GD}$  change.

$$i_g = C_g \cdot \frac{dU_{GD}}{dt} \tag{6}$$

Use the diode charge formula to derive the junction capacitance formula (7),

$$C_{JO} = \frac{Q_D(m-1)}{\varphi_D \left[ \left(1 - \frac{U_{GD}}{\varphi_D}\right)^{1-m} - 1 \right]}, m \neq 1 \tag{7}$$

Define  $a = \frac{Q_D(m-1)}{\varphi_D}$ ,  $b = \varphi_D$ ,  $c = 1 - m$ . Optimize the formula (7) so that the variable capacitor  $C_g$  only works when the  $C_{GD}$  is less than zero. We can get the fitting function (8).



$$\begin{cases} C_{GD} = \frac{a}{\left(1 + \frac{|U_{GD}|}{b}\right)^c}, & U_{GD} < 0 \\ C_{GD} = a, & U_{GD} > 0 \end{cases} \quad (8)$$

According to the fitting formula and using statement modeling method of Model Editor, we can build  $C_{GD}$  sub circuit module.

Figure 4 shows the simulation results.

As is shown, when  $U_{GD} < 0$ , the capacitance value decreases with the increase of voltage. When  $U_{GD} > 0$ , the capacitance value keeps constant. Therefore, this model can accurately simulate the nonlinear capacitance  $C_{GD}$  in SiC MOSFET.

The above two models respectively use diode and voltage control current source to complete the modeling of  $C_{GD}$ . There is a great deal of uncertainty in parameter setting by using diode modeling. So we select the second method by using VCCS to the modeling in this paper.

### 3 Characteristics Verification

#### 3.1 Static Characteristics Verification

Compare the simulation results with the characteristic curves (solid lines) provided in datasheet as shown in Fig. 5.

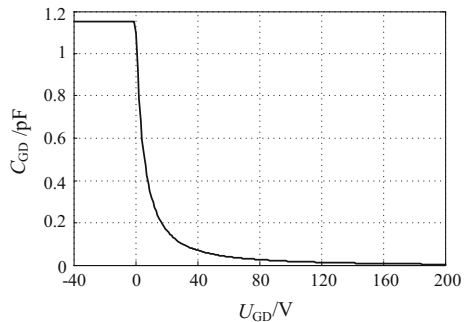
Figure 6 shows the output characteristic of SiC MOSFET. The proposed model fits the datasheet well.

#### 3.2 Dynamic Characteristics Verification

In this paper, the dynamic characteristics are verified by double pulse test (Fig. 7).

The test circuit uses a double pulse gate drive mode. The drive voltage is  $-5/19$  V. The drain-source voltage is 600 V. The load inductance is 5  $\Omega$ , 10  $\Omega$ , 20  $\Omega$ ,

**Fig. 4** Test simulation curve of sub circuit of  $C_{GD}$



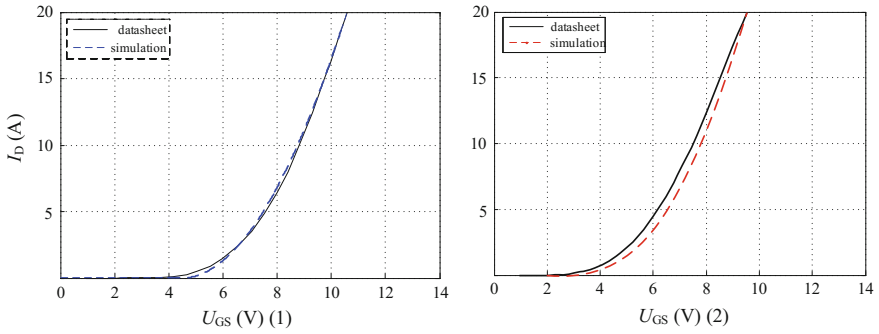


Fig. 5 Compare of transfer characteristic between simulation and datasheet on 25 °C and 150 °C

Fig. 6 Compare of output characteristic between simulation and datasheet

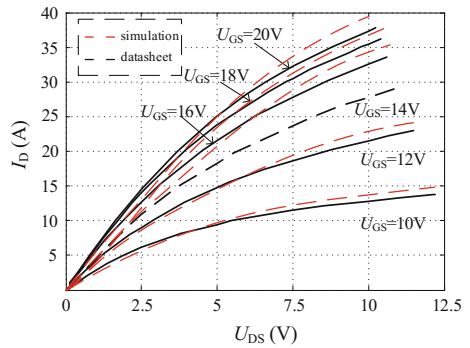
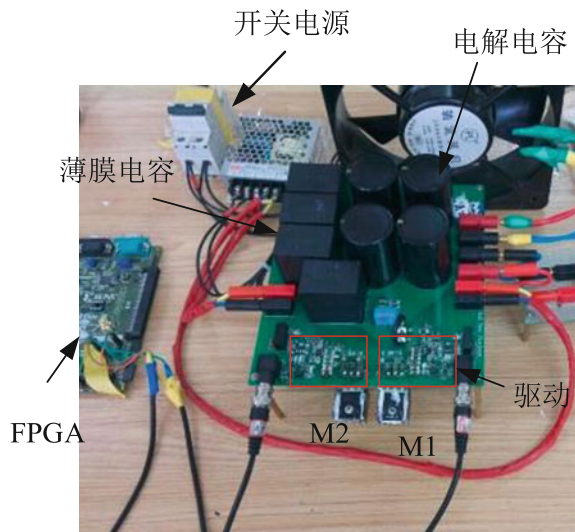


Fig. 7 The material object of circuit



30 Ω. Observe the on-state and off-state simulation waveform of SiC MOSFET on different drive resistances, and compare to the experimental result.

Due to the fast switching speed of the SiC MOSFET, it requires wider band gap of current and voltage probes. We use the 100 MHz bandwidth voltage probe and 120 MHz current probe in this paper.

The test results are as follows,

(1) The driving resistance is set to 5 Ω. The moment the device turn on (Fig. 8)

The driving resistance is set to 5Ω. The moment the device turn off (Fig. 9).

Above the pictures, the prior is simulation waveform. The latter is the experimental waveform. The blue line represents the change in drain-source voltage with time, and the red line represents the change in drain current with time.

From the simulation and experimentation results can be seen, the model built in this paper can fit the waveforms of current and voltage in the turn-on and turn-off time of SiC MOSFET C2M0160120D.

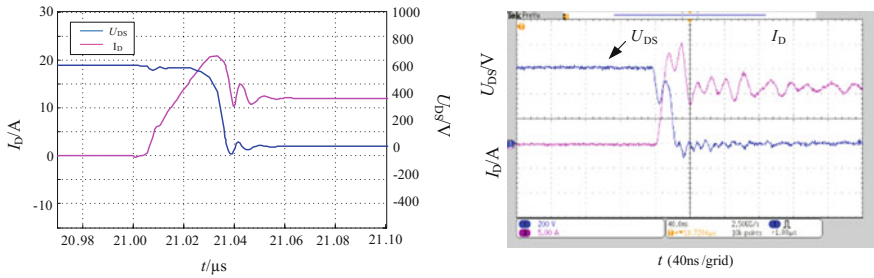


Fig. 8 The comparison between simulation and experiment when the drive turn-on and resistance is 5 Ω

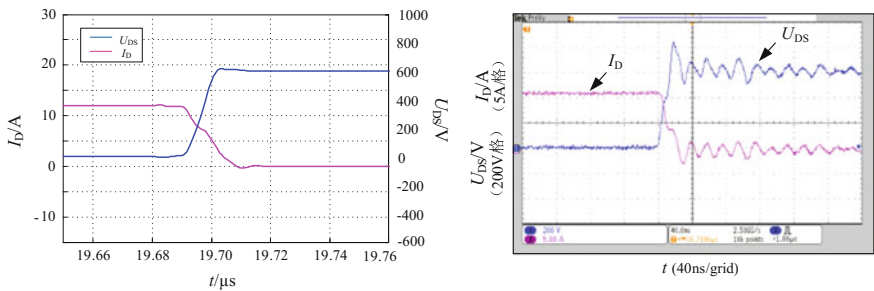


Fig. 9 The comparison between simulation and experiment when the drive turn-off and resistance is 5 Ω

## 4 Conclusion

This paper focuses on the establishment of the simulation model based on SiC MOSFET C2M0160120D in Pspice. When modeling temperature-controlled voltage sources, we use the ABM module to simplify the modeling process. On the basis of the previous modeling methods, the model is further improved in this paper. Test the static characteristics of the model at different temperatures, the simulation results are in good agreement with the data provided in datasheet. Two models respectively use diode and voltage control current source to complete the modeling of  $C_{GD}$ . After the comparison, we select the second method by using VCCS to the modeling in this paper. Build the test circuit by the dynamic model and test switching characteristics under different driving resistance. Compare the simulation result with experiment. It verifies the correctness of the dynamic model.

**Acknowledgements** This work was supported by the Fundamental Research Funds for the Central Universities of China (No. E16JB00160/2016JBM062/2016JBM058) and The National Key Research and Development Program of China (2016YFB1200504-C-02).

## References

1. Jiang W (2015) Development and application of silicon carbide power electronic devices. *China High Tech Enterp* 36:1–3 (in Chinese)
2. Wang L, Zhu P (2014) Overview of application of SiC power devices in power electronics. *J Nanjing Univ Aeronaut Astronaut* 46(4):524–532 (in Chinese)
3. Cheng S (2001) MOSFET modeling in electronic device simulation software. Hunan University (in Chinese)
4. Kraus R, Castellazzi A (2015) A physics-based compact model of SiC power MOSFETs. *IEEE Trans Power Electr* PP(99):0885–8993
5. Sun K, Wu H, Lu J et al (2013) Modeling of SiC MOSFET with temperature dependent parameters. *Proc CSEE* 33(3):37–43 (in Chinese)
6. Kumar K, Bertoluzzo M, Buja G (2015) Impact of SiC MOSFET traction inverters on compact-class electric car range. In: *Power electronics, drives and energy systems (PEDES)*, Mumbai, India, pp 1–6
7. Ozdemir S, Acar F, Selamogullari US (2015) Comparison of silicon carbide MOSFET and IGBT based electric vehicle traction inverters. In: *International conference on electrical engineering and informatics*, Bali, Indonesia
8. Cui Y, Chinthavali M, Tolbert LM (2012) Temperature dependent Pspice model of silicon carbide power MOSFET. In: *Applied power electronics conference and exposition*, Orlando, Florida, USA, pp 1698–1704
9. orctn101 Analog behavioral model using PSpice. [www.cadence.com](http://www.cadence.com)
10. Lu J, Sun K, Wu H et al (2013) Modeling of SiC MOSFET with temperature dependent parameters and its applications. In: *IEEE applied power electronics conference and exposition —Apec*, Long Beach, California, USA, pp 540–544
11. Zhao B, Zhou Z, Xu Y et al (2015) Study on the PSpice model of SiC MOSFETs applied in the electric vehicle (in Chinese)

# Calculation Analysis on Traction Motor Temperature Rise of EMU Vehicles Based on Fuzzy Neural Network

Jiaying Liang, Shaoqing Liu, Chongcheng Zhong and Jin Yu

**Abstract** As a major consideration during the traction system design procedure, the traction motor temperature rise is also deemed as an important physical parameter for evaluating performance of the traction motor over the course of long-term service. Due to the operating conditions, ambient temperature and other factors, it is difficult to accurately assess the traction temperature rise during the designing process of traction system. On a basis of extensive data analysis on traction motor temperature rise tests, this paper first adopts the Heuristic method of Sequential Forward Selection to determine main factors that cause the traction motor's temperature rises in various operating conditions. Then the fuzzy neural network calculation models of traction motor temperature rise is established under different working conditions. Training these fuzzy neural networks with sample data from route test to obtain the traction motor temperature rise calculation model under full operating conditions and the whole climate environment. Taking actual parameters of a certain type EMU (Electric Multiple Units) of the Beijing—Shanghai line as the object, this paper compares the temperature variation of the traction motor obtained from the simulation calculation with the experimental data in a way to justify the correctness and validity of the selected method.

**Keywords** Fuzzy neural network · EMU · Traction motor · Temperature rise

## 1 Introduction

At present, the three-phase asynchronous motor is commonly adopted by the EMU vehicles in China as the power driving system. Such motor is powered by VVVF converters and the current features abundant high-order harmonics. During the running process, the traction motor speed and working conditions frequently vary with the operating demands, making the iron core circuit saturation of the motor

---

J. Liang · S. Liu · C. Zhong · J. Yu (✉)  
CRRC Qingdao Sifang Co., Ltd, Qingdao 266111, China  
e-mail: yujin@cqsf.com

© Springer Nature Singapore Pte Ltd. 2018

L. Jia et al. (eds.), *Proceedings of the 3rd International Conference on Electrical and Information Technologies for Rail Transportation (EITRT) 2017*, Lecture Notes in Electrical Engineering 482, [https://doi.org/10.1007/978-981-10-7986-3\\_29](https://doi.org/10.1007/978-981-10-7986-3_29)

281

changes accordingly and thus the rise of loss and temperature; meanwhile, the improvement of maximum running speed and start-up performance of EMU vehicles brings about more stringent requirements on the motor temperature rise. Therefore, all EMU vehicles are equipped with specific temperature inspection system on each traction motor and real-time inspection on iron core temperature of each traction motor is carried out to ensure running reliability of the motor.

In the designing of the traction system, the traction motor temperature rise is always deemed as a major performance parameter, and it is crucial to accurately calculate the temperature rise according to the established design plan. At present, the traction motor temperature rise is finally determined by simulation calculation as well as the bench test of trial specimen at the design phase. The bench test of trial specimen can produce the final results. However, the design plan is usually optimized according the results in combination with designing experience, and the verification process is a lengthy one; usually the finite element method is adopted in simulation calculation for the temperature rise of the three-phase asynchronous motor. However, due to frequent change of VVVF inverter power supply, running environment and working conditions, it is difficult obtain accurate calculation results through the traditional finite element method. The asynchronous motor temperature rise and temperature distribution have been extensively researched both at home and abroad [1–5].

As a combination of fuzzy logic system and neural network, the fuzzy neural network features the research and generalization ability of complex nonlinear system from the neural network and fully utilization of system experience and knowledge from the fuzzy logic system, making itself a powerful tool for dealing with uncertainties and nonlinear complex problems. Therefore, it has drawn wide attention of researchers of various fields [6–8] and also gradually applied to the rail transit field.

This paper presents a calculation method for traction motor temperature rise of EMU vehicles based on fuzzy neural network. It first adopts the Heuristic method on the basis of numerous historical data to determine the factors affecting temperature rise in different working conditions and the change rule. Taking the affecting factors as model parameters of fuzzy neural network, then the fuzzy neural network calculation model of traction motor temperature rise in various working conditions is established. Learn with track test data by the error back-propagation and gradient descent method to determine the link weight of the fuzzy neural network and parameters of fuzzy membership function, and the calculation model of traction motor temperature rise is finally established. The method used in this paper not only can make full use of the existing historical data, but also has some reasoning abilities in the temperature rise calculation process.

## 2 Factors Analysis on Traction Motor Temperature Rise

According to the principle of energy conservation, heat generated by the traction motor in the unit of time should be equal to the sum of the heat dissipated from the object and the heat absorbed by the object at the same time [9], i.e.,

$$cG \frac{d(\Delta\tau)}{dt} + \alpha A \Delta\tau = p$$

where,

$c$  specific heat capacity of the object;

$G$  object mass;

$\Delta\tau$  temperature rise of the object surface relative to the surrounding medium;

$\alpha$  surface radiation coefficient;

$A$  surface radiating area;

$$\frac{d(\Delta\tau)}{dt} + \frac{A}{C} \Delta\tau = \frac{p}{C}$$

where,

$\Lambda = \alpha A$ , object thermal conductance;

$C = cG$ , object thermal capacity.

$$\Delta\tau = e^{-\int \frac{\Lambda}{C} dt} \left[ \int \frac{p}{C} e^{-\int \frac{\Lambda}{C} dt} dt + D \right]$$

$A$ ,  $C$  and  $p$  are time functions and difficult to determine, furthermore, the generation and propagation of heat are affected by factors such as load current, ambient temperature, running speed and inlet and outlet wind pressure of ventilation system. It is difficult to determine the current temperature rise of traction motor using the traditional analytical method or the finite element method.

In order to calculate the traction motor temperature rise more accurately, firstly it is necessary to accurately identify the factors that affect the temperature rise of the motor under the current working conditions, and then select the appropriate method such as fuzzy neural network to determine to what extent that the temperature is influenced by each factor so that the motor temperature rise can be calculated.

There are many working conditions over the course of running, such as start-up speed, constant speed running, coasting, braking and parking. With the change of train running conditions, the factors affecting the temperature rise of traction motor and the degree will change greatly. Therefore, the influencing factors should be analyzed separately for different train running conditions. In this paper, the following methods are used to search the fundamental factors of motor temperature rise under various working conditions:

- (1) To determine the potential factors of motor temperature rise: Consider all the following possible parameters: running time  $Tr$ , ambient temperature  $T$ , difference between the motor and ambient temperature  $R$ , running speed  $V$ , motor power  $P$ , current  $I$ , voltage  $U$ , frequency  $f$ , and inlet and outlet wind pressure of

ventilation system  $P_v$ , and create a feature set  $S = \{Tr, AT, TD, V, P, I, U, f, P_v\}$  and corresponding motor temperature rise  $TR_m$ . These factors have different effects on the temperature rise of the motor under different running conditions. Some may have no significant influence and there may be a strong correlation between some factors. Too many factors will complicate the analysis process affecting the accuracy and efficiency of calculation. In this point, it is necessary to screen out the most fundamental factors;

- (2) To adopt the Heuristic method of Sequential Forward Selection to determine the fundamental factors of the traction motor temperature rise under the working condition [10]. The heuristic search method selects one factor that minimizes root-mean-square error from these factors at one time according to the following method, and the final selection set are the fundamental factors under such condition:

- ① Set a feature set  $S = \{U_1, U_2, \dots, U_k\} = \{Tr, AT, TD, V, P, I, U, f, P_v\}$ ,  $k = 9$ , the initial set of fundamental factors is set to  $I$  be empty  $I = \{\}$ ;
- ② Select a subset  $S_i$  in turn from the feature set  $S$ , together with the set  $I$ , to constitute a new fundamental factor set  $I = \{I, S_i\}$ ; together with temperature rise  $TR_m$  to create the training and testing set  $D_i = [ITR_m]$ . By different sampling intervals, separate training sample  $Trn\_data$  and testing sample  $Chk\_data$  from  $D_i$ .
- ③ Train and test  $Trn\_data$  and  $Chk\_data$  samples with the fuzzy neural network;
- ④ Calculate the temperature rise error of the motor generated by each type of factor combinations under the influence of training and testing samples, and summarize root-mean-square of errors  $e_r$ ;
- ⑤ Select the combination with the minimum error from various sets  $I$  as an optimum solution for the search as well as a fundamental factor  $I$ , save the optimum solution  $I_0 = I$  and corresponding errors  $e_{r0}$  and then update the set  $S = \{S_1, S_2, \dots, S_k\}$ ;  $k = k - 1$ ;
- ⑥ Repeat the above process②–⑤; when the corresponding error to various combinations during this search is no longer reduced, that is,  $e_r < e_{r0}$ , stop searching, and the current set  $I$  is deemed as the fundamental factors of traction motor temperature rise under such working condition.

Via the above-mentioned method, the fundamental factors of traction motor temperature rise under the start-up condition can be determined as shown in Fig. 1. Through the heuristic search method, the minimum root-mean-square error of the motor temperature rise comes from the factor combination of “temperature difference, power, speed, time and wind pressure” and thus this combination is the fundamental factor during the start-up stage.

The same method can be adopted to obtain the fundamental factors of the traction motor temperature rise under different working conditions as shown in Table 1 below.



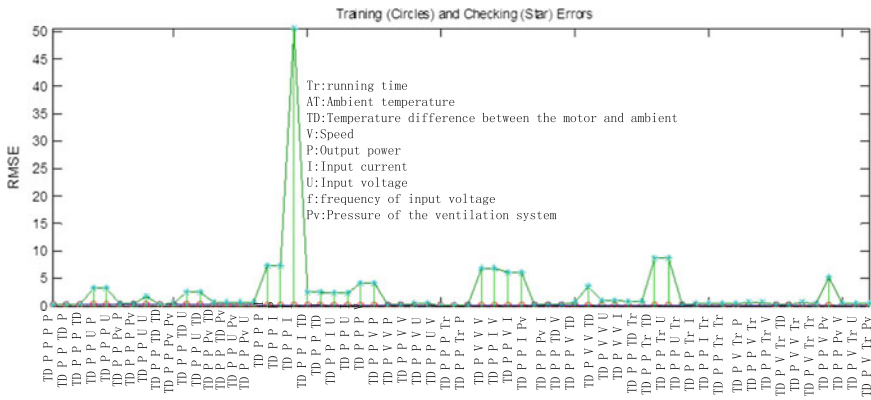


**Fig. 1** Fundamental factors analysis results of the traction motor temperature rise during the EMU start-up phase

**Table 1** Fundamental factors analysis results of the traction motor temperature rise under various working conditions of the EMU

Train operation condition	Fundamental factors of the traction motor temperature rise
Start-up stage	Running time, speed, temperature difference, power, wind pressure of ventilation
Constant speed running	Running time, speed, temperature difference, power, wind pressure of ventilation
Coasting	Running time, speed, temperature difference, wind pressure of ventilation
Braking	Running time, speed, temperature difference, power, wind pressure of ventilation
Stopping	Stopping time, temperature difference, wind pressure of ventilation

### 3 Calculation Model of Traction Motor Temperature Rise of EMU Vehicles Based on Fuzzy Neural Network

On the basis of factors analysis of temperature rise, the temperature rise calculation model based on the fuzzy neural network under different conditions are established [10], and the calculation model during the start-up stage is as follows (Fig. 2),

The model is divided into five layers. The first layer is the input layer, and the fundamental factors obtained from the search, i.e., temperature difference, ventilation wind pressure, speed, running time and power are inputs into the system;

The fuzzification of the input variables is realized at the second layer. Determine the membership function  $\mu_i^j$  for each input corresponding to language variables of the fuzzy set and calculate the corresponding degree of membership. This paper adopts the bell-shaped membership function  $\mu_i^j = e^{-(x_i - c_{ij})^2 / \sigma_{ij}^2}$ ,  $i = 1, 2, \dots, 5$  is the input variable dimension, and  $j = 1, 2, 3$  is fuzzy language variable dimension,

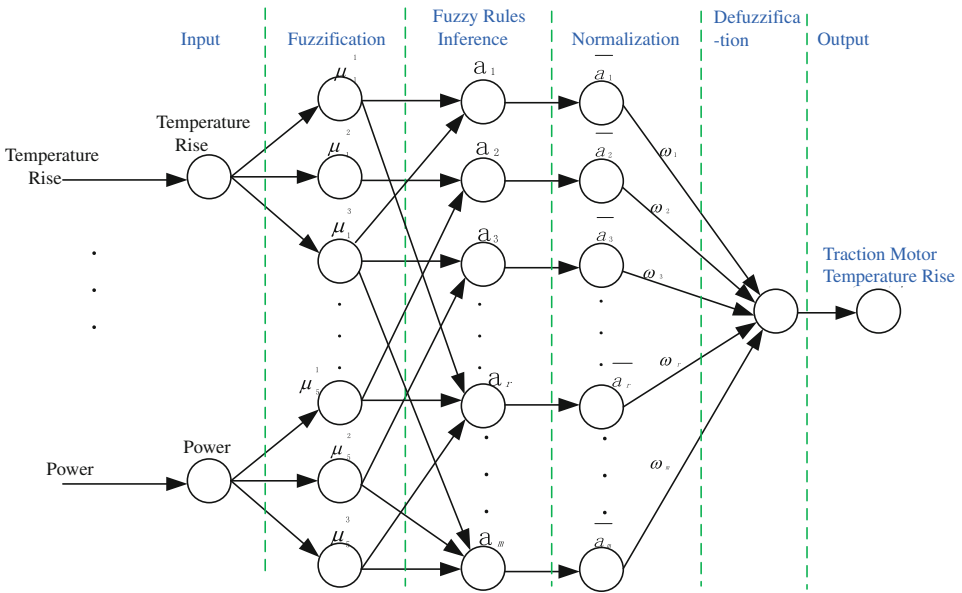


**Fig. 2** Fuzzy neural network model of the traction motor temperature rise during the EMU start-up

all of which are divided into B (big), M (medium) and S (small).  $c_{ij}$  and  $\sigma_{ij}$  are the function center and width respectively;

The fuzzy rules are set at the third layer to accomplish the fuzzy reasoning calculation accordingly. Each node of this layer represents a rule, match the antecedent of the fuzzy rules, calculate the applicability of each fuzzy rule  $\alpha_j = \min\{\mu_1^{k_1}, \mu_2^{k_2}, \mu_3^{k_3}, \mu_4^{k_4}, \mu_5^{k_5}\}$ ,  $k_1, k_2, k_3, k_4, k_5 \in \{1, 2, 3\}$ ,  $j = 1, 2, \dots, m$ , and  $m$  belongs to the rule number,  $m < 3^5$ ;

There are totally five groups of fuzzy language variables at the start-up stage with three kinds of values for each group. Therefore, the system will have at most  $3^5 = 243$  fuzzy rules.

The normalization process is achieved in the fourth layer,  $\bar{\alpha}_j = \alpha_j / \sum_{i=1}^m \alpha_i$ ;

The fifth layer deals with defuzzification calculation,  $y = \sum_{j=1}^m \omega_j \bar{\alpha}_j$ , and the output is the temperature rise of the traction motor.

The whole model has three groups of parameters to be determined by the test sample data via the corresponding optimization algorithm, namely each membership function center  $c_{ij}$ , width  $\sigma_{ij}$  and weighting coefficient  $\omega_j$ . This paper adopts the following method to determine these parameters:

- (1) Based on the statistical analysis of the experimental data and the variation range of each fundamental factor, the membership function ( $c_{ij}$  and  $\sigma_{ij}$ ) of each fuzzy set language variable is roughly determined, and the weighting coefficient  $\omega_j$  is randomly assigned;

- (2) Extract two groups of data of corresponding working conditions at different periods and on different lines from historical data to serve as learning and checking samples;
- (3) Apply the corresponding learning sample data to the input end of the model to perform the above-mentioned model processing calculation (fuzzification, fuzzy inference, defuzzification) and the output is the current motor temperature rise. Then the error is calculated via a comparison with the sample data;
- (4) Adopt the error back-propagation algorithm (BP algorithm) to adjust each weighting coefficient  $\omega_k$ , membership function  $c_{ij}$  and  $\sigma_{ij}$ . In order to prevent the network from becoming “premature”, the weighting coefficient  $\omega_k$  is optimized by the momentum factor gradient descent method;

① Set the variable of error generated at the output layer in the Step t iterative process against the rule k **to be**  $e_{k,t}$ , then

$$\omega_{k+1,t} = \omega_{k,t} - \beta_1 e_{k,t}$$

② Transmit each  $e_{k,t}$  along the reverse path for passing fuzzy neural network information to the input end, set the error variable generated at some fuzzification layer to be  $e_{(ij),t}$ , and the corresponding membership function parameter  $c_{ij}$  and  $\sigma_{ij}$  are learned and adjusted according to the following algorithm;

$$c_{(ij)+1,t} = c_{(ij),t} - \beta_2 e_{(ij),t}$$

$$\sigma_{(ij)+1,t} = \sigma_{(ij),t} - \beta_3 e_{(ij),t}$$

- (5) Repeat Step (3)–(4), to complete the learning of temperature rise calculation model of the fuzzy neural network;
- (6) Test the feasibility of the model with checking samples. If the sample error occurs within the acceptable range, the modeling process is completed, and the model can be applied to calculation of the traction motor temperature rise. In case of bigger error, repeat the above Step (1)–(5) until the result is satisfactory

The checking results of the traction motor temperature rise calculation model at the start-up stage established in this paper are shown in the following (Fig. 3).

The checking sample contains iron core temperatures of four traction motors on a certain type EMU. As is shown in the figure: affected by nearby environment of the motor itself, and the differences of motor parameters, the temperature rise differences of different motors under different working conditions can reach 10 °C. See the following figure for calculation errors of the model (Fig. 4):

For the checking sample data, the calculation error  $\pm$  is 3 °C, and for all the testing data under the same working conditions, the maximum error is  $\pm 5$  °C. Therefore, the established temperature rise calculation model can be used to calculate the temperature rise of the traction motor.

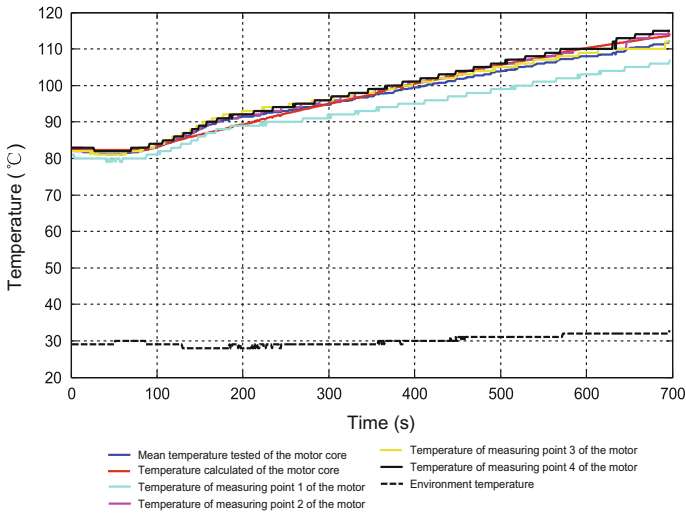


Fig. 3 Calculation results of the traction motor temperature rise model during the EMU start-up

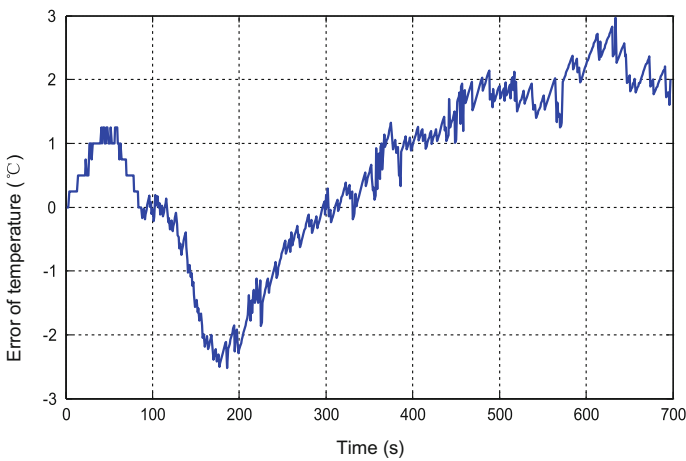


Fig. 4 Error made by the temperature rise model compared with the track test

Establish the calculation model of the traction motor temperature rise under each working condition by following the above methods, through which the corresponding motor temperature rise to the traction system design plan can be calculated and evaluated.

### 4 Test Verification

In order to verify the feasibility of the method adopted in this paper, based on the actual parameters from the traction system of a certain type EMU and the line between Xuzhou East and Bengbu, which is a segment of the Beijing—Shanghai line, we simulate and calculate the electrical performance parameters of this type of EMU during its running process on Beijing—Shanghai line. Adopt the calculation model of the traction motor temperature rise established in this paper to calculate real-time motor temperature rise according to the following methods:

- (1) According to the historical data of the local meteorological service, the maximum temperature of the regional line is 36 °C in the past two years, and the ambient temperature is set at 36 °C in calculation to determine the temperature difference;
- (2) Carry out statistical analysis on the inlet and outlet wind pressure of the motor ventilation system according to the historical test data, and the typical inlet and outlet wind pressure curve varying with the EMU speed is obtained from the start-up stage to the braking and parking process as shown in the following (Fig. 5):
- (3) Running speed, running time and power of traction motor during the running process of a certain type EMU are obtained through traction calculation. Based on the above wind pressure and speed curve, the wind pressure at the current speed is obtained through linear interpolation;
- (4) Call the corresponding calculation model of the traction motor temperature rise according to the current working conditions, load the information reflecting the traction motor temperature rise at the corresponding working conditions such as time, speed, temperature difference, power, and wind pressure of ventilation system onto the calculation model to obtain the motor temperature rise at current period.

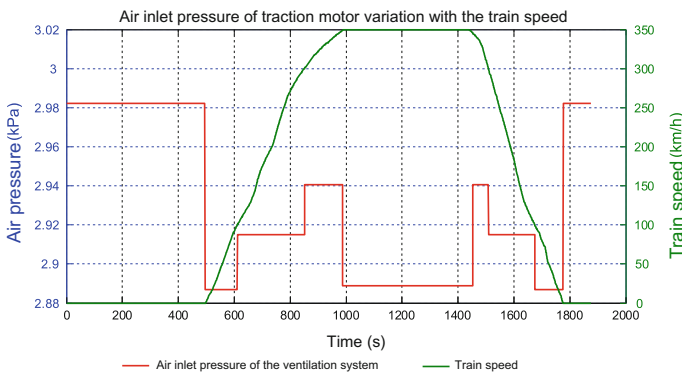
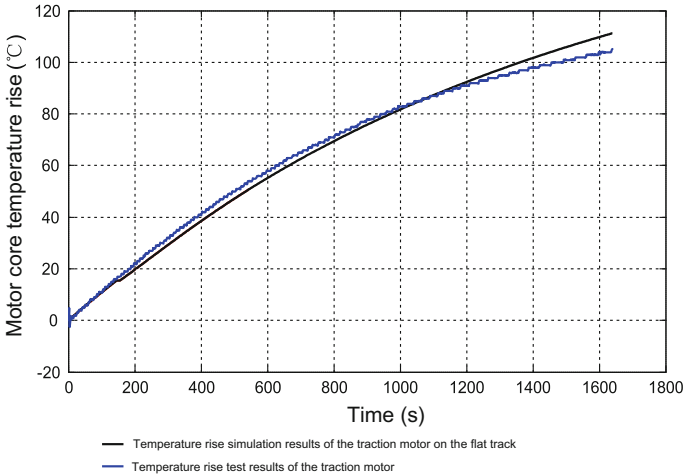


Fig. 5 Wind pressure varied with the EMU velocity



**Fig. 6** Core temperature rise calculation results of the traction motor of a certain type EMU

- (5) Repeat the above Step (3)–(4) to the end. The temperature rise variation curve of the traction motor during the whole running process can be obtained as shown in the following (Fig. 6).

For the purpose of comparison, the figure also shows the test results of EMU traction motor temperature rise. When the motor heat is about to reach the equilibrium period, the model calculation result is slightly greater than the test results, with the maximum error of about 7 °C. According to the above historical data of the traction motor temperature rise, it can be seen that as the temperature rise difference of each motor of the same EMU can reach about 10 °C under the same working condition, the calculation result of the model is acceptable in the actual design process. Therefore, the fuzzy neural network model of the traction motor temperature rise established in this paper is feasible.

## 5 Conclusions

As for the problem that it is difficult to calculate the accurate motor temperature rise during the designing process of the EMU traction system, this paper starts with an extensive research of the test data and different working conditions to determine the fundamental factors of motor temperature rise under different working conditions with the heuristic search method of Sequential Forward Selection; on this basis, the artificial intelligence technology is adopted to establish the fuzzy neural network models of EMU motor temperature rise under different working conditions in a way to accurately calculate the traction motor temperature rise resulting from EMU

traction system designing plan. Through a comparison with the test results of a certain type EMU, it can be concluded that the error generated by calculation model established in this paper is acceptable and the model can be applied to temperature rise calculation of EMU traction motors.

## References

1. Maximini M, Koglin HJ (2004) Determination of the absolute rotor temperature of squirrel cage induction machines using measurable variables. *IEEE Trans Energy Convers* 19(1): 34–39
2. Kral C, Habetler TG, Harley RG (2004) Rotor temperature estimation of squirrel-cage induction motors by means of a combined scheme of parameter estimation and a thermal equivalent mode. *IEEE Trans Ind Appl* 40(4):1049–1056
3. Calculation and analysis of 3D temperature fields of medium size high voltage asynchronous motor based on coupled field. *Electric Machines Control* 15(1):73–78. (Ch)
4. Xie Y, Liweili L (2008) Calculation and analysis of temperature field for induction motors with broken bars fault. *Trans China Electrotechnical Soc* 23(10):33–399. (Ch)
5. Yang M, Zhang P (2013) Dynamic thermal characteristic and its discrete algorithm of stator windings of the asynchronous motor. *Proc CSEE* 33(24):121–126. (Ch)
6. Huang Z, Wei X, Liu Z (2012) Fault diagnosis of railway track circuits using fuzzy neural network. *J China Railway Soc* 34(11):54–59. (Ch)
7. Dong H, Liu Y, Li X, Yan J (2013) Study on high-speed train atp based on fuzzy neural network predictive control. *J China Railway Soc* 35(8):58–62. (Ch)
8. Dai W, Lou H, Yang A (2009) An overview of neural network predictive control for nonlinear systems. *Control Theory Appl* 26(5):521–530. (Ch)
9. Yunqiu T (2016) *Electromechanics*, 5th edn. China Machine Press, Beijing
10. Cai Z, Xu G (2004) *Artificial intelligence and its application*, 3rd edn. Tsinghua University Press, Beijing

# Predictive Current Control for Three-Phase Asynchronous Motor with Delay Compensation

Yaru Xue, Jian Zhou, Yuwen Qi, Huaiqiang Zhang and Yong Ding

**Abstract** High performance control method which is able to improve the current inner loop performance is required in order to avoid the problem of the parameter setting of PI controller in vector control. And it will take time for controller to sample and calculate so there is a delay in the processing of the prediction model. Therefore, the paper proposes a model prediction current control with a delay compensation strategy for asynchronous motor drive. Firstly, the current prediction model under the rotating coordinate system is built using the asynchronous motor equation and the basic framework of current model predictive control is established based on the field orientation strategy. Also, the future trajectory of the current is predicted based on the linear fitting method. Then, aimed at a delay problem existing in the current predictive control, the paper proposes the delay compensation strategy to improve the adverse effects caused by a delay. And the simulation results verify the feasibility of the compensation strategy.

**Keywords** Current model predictive control · A delay · Asynchronous motor  
Delay compensation

---

Y. Xue (✉)

School of Electrical Engineering, Beijing Jiaotong University,  
No. 3 Shang Yuan Cun, Hai Dian District, 100044 Beijing, China  
e-mail: 16117403@bjtu.edu.cn.jp

J. Zhou

Fifth Institute of Electronics, Ministry of Industry and Information Technology,  
Guangzhou, China  
e-mail: 15126058@bjtu.edu.cn

Y. Qi · H. Zhang · Y. Ding

CRRC Changchun Railway Vehicles Co., Ltd., Changchun, China  
e-mail: jiechen@bjtu.edu.cn

© Springer Nature Singapore Pte Ltd. 2018

L. Jia et al. (eds.), *Proceedings of the 3rd International Conference on Electrical and Information Technologies for Rail Transportation (EITRT) 2017*, Lecture Notes in Electrical Engineering 482, [https://doi.org/10.1007/978-981-10-7986-3\\_30](https://doi.org/10.1007/978-981-10-7986-3_30)



## 1 Introduction

The vector control, as a mainstream control method of the asynchronous motor drive, has many advantages: a wide speed adjustment range and high steady precision [1]. However, the PI controller and modulation module employed in vector control is complex and redundant and improper PI parameter settings even may contribute to the control system overshoot and oscillation. While, the model predictive control doesn't need PI controller and voltage modulation module. Besides, the stability of algorithm is good, the control thought is simple, and it is apt to deal with the nonlinear constraints [2].

Holtz and Stadtfeld came up with the prediction control based on the linear fitting of the current trajectory in 1983 and introduced MPC algorithm into asynchronous motor control for the first time [3–5]. In the current model predictive control proposed by Holtz, the control algorithm is simple and intuitive, but the method is based on the motor electromotive force model that contains differential loop, so the model is more easily disturbed by the environment [6]. Also, it takes a period of time for the controller to sample and calculate the optimal vector in practical application. And the optimal vector can't be used until the next sampling instant so there is a delay, affecting the control performance of algorithm [7]. Aimed at the problems above, this paper establishes a current prediction model and proposes a delay compensation strategy in order to improve the adverse effects caused by a delay.

## 2 The Mathematical Equation of Current Prediction Model

The current model predictive control system is described in Fig. 1: the field current instruction  $i_{sd}^*$  can be obtained by a given flux signal  $\psi_r^*$  and the torque current component  $i_{sq}^*$  is calculated by the combination of the traction instruction  $T_c^*$  and the given flux instruction  $\psi_r^*$ . Then the controller will put the current instruction and the actual d and q axis currents into the prediction model, the current error can be obtained from predictive algorithm and optimal switch state of the next moment can be obtained by optimization of the flux vector, leading the actual current to track the instruction value.

The paper uses the discrete state equation under d-q synchronous rotating coordinate system as the current prediction model. And the state equation under d-q synchronous rotating coordinate system for asynchronous motor is shown in (1.1).

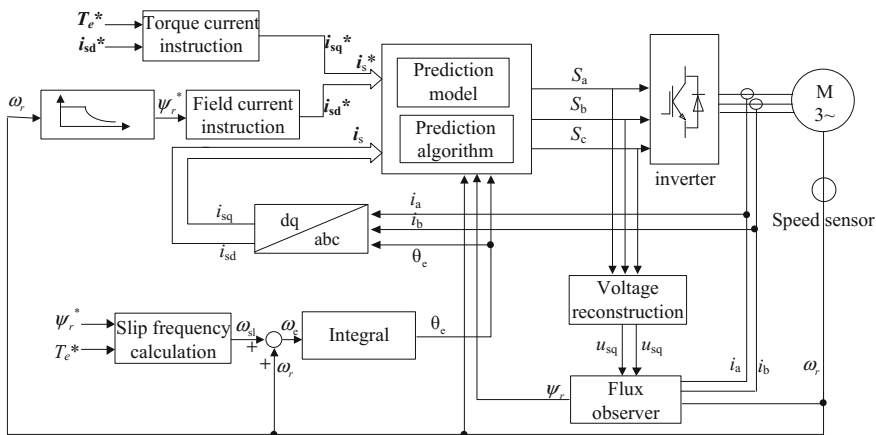


Fig. 1 Current model predictive control diagram of induction machine

$$\begin{cases} \frac{di_{sd}}{dt} = -\frac{R_s L_r^2 + R_r L_m^2}{\sigma L_s L_r^2} i_{sd} + \omega_e i_{sq} + \frac{L_m}{\sigma L_s L_r T_r} \psi_{rd} + \frac{L_m}{\sigma L_s L_r} \omega_r \psi_{rq} + \frac{u_{sd}}{\sigma L_s} \\ \frac{di_{sq}}{dt} = -\omega_e i_{sd} - \frac{R_s L_r^2 + R_r L_m^2}{\sigma L_s L_r^2} i_{sq} + \frac{L_m}{\sigma L_s L_r T_r} \psi_{rq} - \frac{L_m}{\sigma L_s L_r} \omega_r \psi_{rd} + \frac{u_{sq}}{\sigma L_s} \\ \frac{d\psi_{rd}}{dt} = \frac{L_m}{T_r} i_{sd} - \frac{1}{T_r} \psi_{rd} + (\omega_e - \omega_r) \psi_{rd} \\ \frac{d\psi_{rq}}{dt} = \frac{L_m}{T_r} i_{sq} - \frac{1}{T_r} \psi_{rq} - (\omega_e - \omega_r) \psi_{rq} \end{cases} \quad (1.1)$$

Let's suppose that  $T_s$  is the discrete sampling period of controller. Then use the Forward Euler method to discrete the stator current and the current prediction model used in the paper is as follows:

$$\begin{aligned} i_{sd}[k+1] &= \left(1 - \frac{R_s L_r^2 + R_r L_m^2}{\sigma L_s L_r^2} T_s\right) i_{sd}[k] + \omega_e T_s i_{sq}[k] \\ &+ \frac{L_m T_s}{\sigma L_s L_r T_r} \psi_{rd}[k] + \frac{L_m \omega_r T_s}{\sigma L_s L_r} \psi_{rq}[k] + \frac{T_s}{L'_s} u_{sd}[k] \end{aligned} \quad (1.2)$$

$$\begin{aligned} i_{sq}[k+1] &= -\omega_e T_s i_{sd}[k] + \left(1 - \frac{R_s L_r^2 + R_r L_m^2}{\sigma L_s L_r^2} T_s\right) i_{sq}[k] \\ &- \frac{L_m \omega_r T_s}{\sigma L_s L_r} \psi_{rd}[k] + \frac{L_m T_s}{\sigma L_s L_r T_r} \psi_{rq}[k] + \frac{T_s}{L'_s} u_{sq}[k] \end{aligned} \quad (1.3)$$

### 3 The Algorithm Design of Current Model Prediction Control

The prediction control considers the motor and inverter as a whole system and the current as control target in order to implement the direct control of current vector. It is well-known that two-level inverter generates eight kinds of space voltage vectors at most and after the different voltage vectors are applied to induction motor, the current vector will generate corresponding change [8]. Based on linear fitting method, the future trajectory of the current in several sampling periods can be predicted as follows: supposing when it is at  $t_k$ , the actual value of current vector is  $\mathbf{i}(t_k)$ , and the target value is  $\mathbf{i}^*(t_k)$ , then the current at  $t(t > t_k)$  can be described as follows:

$$\mathbf{i}^*(t) = \mathbf{i}^*(t_k) + \left. \frac{d\mathbf{i}^*(\tau)}{d\tau} \right|_{\tau=t_k} \Delta t \quad \mathbf{i}(t) = \mathbf{i}(t_k) + \left. \frac{d\mathbf{i}(\tau)}{d\tau} \right|_{\tau=t_k} \Delta t \quad (1.4)$$

where,  $\Delta t = t - t_k$ .

Different voltage vector actions can generate different current slopes, which can be described as  $d\mathbf{i}^*(\tau, m)/d\tau|_{\tau=t_0}$ ,  $m = 0, 1, \dots, 7$  in which  $m$  represents the different voltage vectors. So the current error between the real current and the target value at  $t$  moment under different voltage vector actions is as follows:

$$\begin{aligned} \Delta \mathbf{i}(t, m) &= \mathbf{i}^*(t) - \mathbf{i}(t) = \mathbf{i}^*(t_k) + \left. \frac{d\mathbf{i}^*(\tau)}{d\tau} \right|_{\tau=t_k} \Delta t - \left( \mathbf{i}(t_k) + \left. \frac{d\mathbf{i}(\tau, m)}{d\tau} \right|_{\tau=t_k} \Delta t \right) \\ &= (\mathbf{i}^*(t_k) - \mathbf{i}(t_k)) + \left( \left. \frac{d\mathbf{i}^*(\tau)}{d\tau} \right|_{\tau=t_k} - \left. \frac{d\mathbf{i}(\tau, m)}{d\tau} \right|_{\tau=t_k} \right) \Delta t \end{aligned} \quad (1.5)$$

If we define the following equations:

$$\mathbf{e}(t_k) = \mathbf{i}^*(t_k) - \mathbf{i}(t_k) \quad \mathbf{e}'(t_k, m) = \left. \frac{d\mathbf{i}^*(\tau)}{d\tau} \right|_{\tau=t_k} - \left. \frac{d\mathbf{i}(\tau, m)}{d\tau} \right|_{\tau=t_k} \quad (1.6)$$

$$\begin{aligned} \mathbf{i}(t_k) &= \mathbf{i}_d + j\mathbf{i}_q \quad \mathbf{i}^*(t_k) = \mathbf{i}_d^* + j\mathbf{i}_q^* \\ \mathbf{e}'(t_k, m) &= \mathbf{e}'_d + j\mathbf{e}'_q \quad \mathbf{e}(t_k) = \mathbf{e}_d + j\mathbf{e}_q \end{aligned} \quad (1.7)$$

Combine (1.5) (1.6) and (1.7), we can obtain the modulus of the current error:

$$\begin{aligned} |\Delta \mathbf{i}(t, m)|^2 &= (\mathbf{e}_d + \mathbf{e}'_d \Delta t)^2 + (\mathbf{e}_q + \mathbf{e}'_q \Delta t)^2 \quad m = 0, 1, \dots, 7 \\ &= a(t_k, m) \Delta t^2 + b(t_k, m) \Delta t + c(t_k) \end{aligned} \quad (1.8)$$

We can discover from (1.8) that the modulus of current error trajectory is a parabola as shown in Fig. 2a, and the time to get to that error again from the moment of  $t_k$  can be obtained as follows:

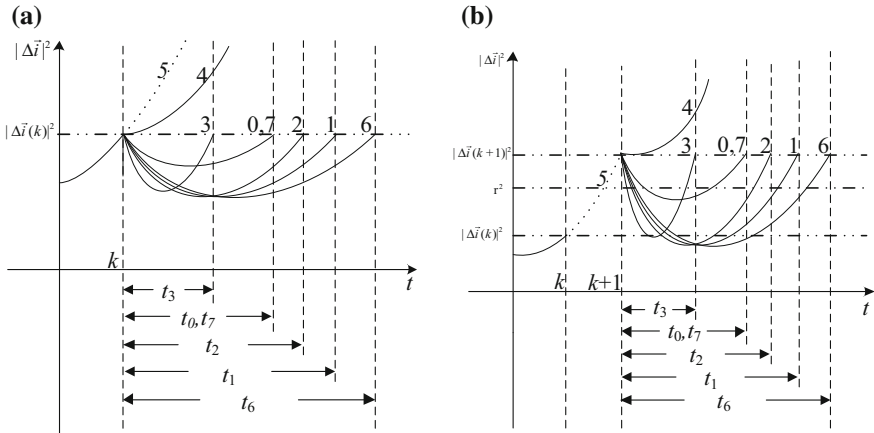


Fig. 2 Current error trajectories. **a** Under different voltage vectors. **b** With a delay compensation

$$\Delta t(m) = -\frac{b(t_k, m)}{a(t_k, m)} \tag{1.9}$$

The 0–7 corresponds to eight different voltage vectors,  $t_0, t_1, \dots, t_7$  corresponds to the time when the current once again reaches the error. In order to reduce the switching frequency of inverter as far as possible, voltage vector generated by the new switch state should be able to reduce current error and keep the time to get back to current error again as long as possible. At the same time, ensure the opening times of each switching tube are as small as possible and define the switching frequency as  $n_m$ . Then the problem of finding the optimal switch vector can be described as the following optimization problem:

$$\min_m J_1(m) = \min_m \frac{n_m}{\Delta t(m)} \quad m = 0, 1, \dots, 7 \tag{2.0}$$

### 3.1 A Delay Compensation Strategy

Considering that the sampling time and calculation time of controller cannot be ignored in the practical operation, the calculated optimal vector is not adopted during the  $[t_k, t_{k+1}]$  until the next sampling moment  $t_{k+1}$ , so there is a delay for the predictive control. To compensate for this delay, when it is at  $t_k$ , the controller needs to give the voltage vector of  $t_{k+1}$  moment on the asynchronous machine. As shown in Fig. 2b, at  $t_k$ , suppose that voltage vector acted on the inverter has been obtained at  $t_{k-1}$  and the optimal voltage vector is 5 vector during the  $[t_k, t_{k+1}]$ . Then use the prediction model in (1.2) and (1.3) to calculate the current vector  $i[t_{k+1}]$  of  $t_{k+1}$  moment under the 5 voltage vector action. Next, the controller determines the

current error  $|\Delta i(k+1)|^2$  between the current vector  $\mathbf{i}[t_{k+1}]$  and the target current vector at this moment. In order to assess the current tracking, the paper introduces the concept of the error limit, a given error range. As in Fig. 2b, suppose that the error limit is  $r^2$ , if the current error modulus exceeds  $r^2$ , it means that the current error modulus is too large so that the original voltage vector is not suitable any more. Then the controller puts the  $\mathbf{i}[t_{k+1}]$  into the prediction model to choose the optimal switch combination and at  $t_{k+1}$  moment, the optimal switch combination is added to the inverter to generate the corresponding voltage vector that actions on the motor. Otherwise, there is no need to change the voltage vector and the switch does not operate.

## 4 Simulation Results

In order to verify the effectiveness of the compensation strategy, the prediction control system is established by Simulink/s-function. The motor parameters used in the paper are shown in Table 1 and the simulation parameters are set as follows: the simulation is the fixed-step and the simulation step is 2us; for the comparison of each control algorithm in convenient, the d axis component of the target current is set to about 30% of the rated peak current, which is 2 A; the error limit is 0.2 A<sup>2</sup>; the time of dead area is 4us; and the simulation employs the advanced voltage rotor flux observer [9].

The paper simulates the control effect of current model prediction algorithm under the sampling frequency of 20 k. Target torque instruction is 9 N m, the motor startups with load and maintains stable at the speed of 200 r/min. Besides, the simulation comparison results between the situation with a delay and the situation with compensation are as follows (Figs. 3 and 4):

The steady-state tracking effect of the d axis and q axis currents and the control effect of torque are given in the four figures above. With a delay, the tracking effect of d axis and q axis currents gets worse and the current error modulus is near 1 A<sup>2</sup>; the corresponding current harmonics of a phase reaches 10.03%; the average torque ripple is expanded to about  $\pm 1.6$  N m. After adopting the delay compensation strategy, the tracking effect of d axis and q axis currents are better than before compensation, the maximum value of current error is below 1 A<sup>2</sup> and the corresponding current harmonic of a phase is reduced to 8.63%. Also, the average torque ripple is reduced to  $\pm 1.3$  N m, torque burr and the current harmonic decrease more

**Table 1** The motor parameters

Rated voltage/frequency: 380 V/50 Hz	Stator resistance: 3.024 $\Omega$
Rated current: 5 A	Rotor resistance: 2.397 $\Omega$
Rated power: 2.2 kW	Mutual inductance: 0.3323 H
Rated speed: 1420 r/min	The leakage inductance of stator: 0.0117 H
Number of pole-pairs: 2	The leakage inductance of rotor: 0.0122 H

compared with the simulation before compensation. The simulation results suggest that the delay compensation strategy improves the negative effects of a delay on the motor torque and the current tracking (Fig. 5).

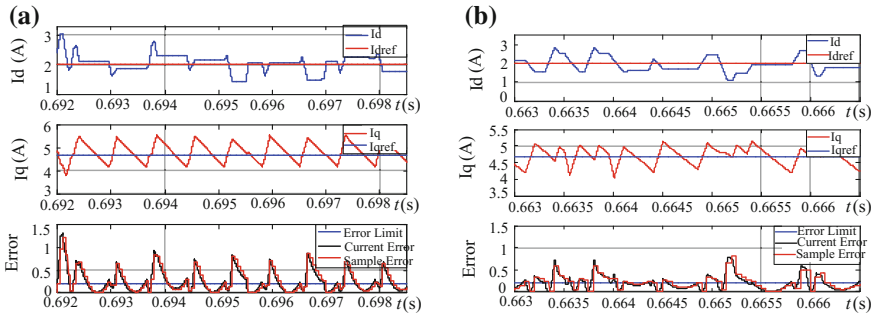


Fig. 3 D and q axis currents. a With a delay. b With compensation

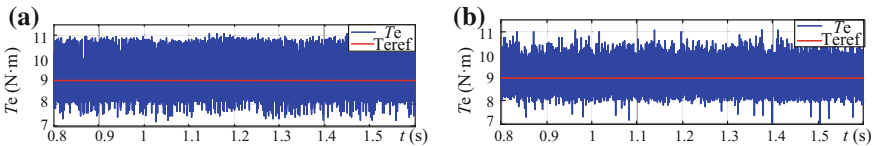


Fig. 4 Torque steady-state effect. a With a delay. b With compensation

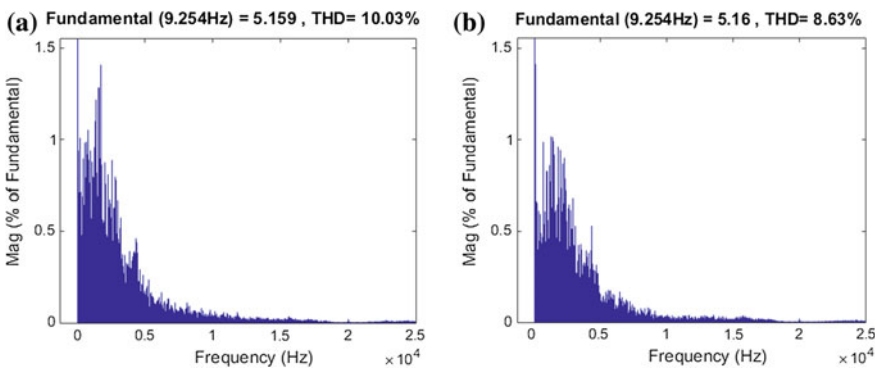


Fig. 5 The FFT analysis of current of a phase. a With a delay. b With compensation

## 5 Conclusion

The model predictive current control for asynchronous motor drive is simple and does not need the parameter setting of PI controller, but when the MPC algorithm operates actually, there is a delay problem, which leads the control effect of algorithm to get worse, even resulting in the system out of control. So aimed at the delay problem in prediction control, the paper adopts a delay compensation strategy. By simulation, it is discovered that compensation algorithm can effects very well: the torque output ripple and current harmonic are reduced to a less level than before compensation and the tracking of d axis component and q axis component of stator current is very good.

**Acknowledgements** This work was supported by National Science and Technology Support Program under Grant 2016YFB1200502-04 and 2016YFB1200504-C-02, Beijing Science and Technology major program Z17111000210000 and School level project 2016JBM058.

## References

1. Telford D, Dunnigan MW, Williams BW (2000) A comparison of vector control and direct torque control of an induction machine. *Power Electron Spec Conf* 1:421–426
2. Yilin Z (2012) Research on model predictive current control of inverter supplied induction machine. Huazhong University of Science and Technology. (in Chinese)
3. Holtz J (2016) Advanced PWM and predictive control—an overview. *IEEE Trans Ind Electron* 63(6):3837–3844
4. Holtz J (2011) Power electronics-A continuing challenge. *IEEE Ind Electron Mag* 5(2):6–15
5. Xin Q, Xiaomin Z, Xianghua M (2013) Induction motor predictive control algorithm. *J Mach Control* 17(3):62–69. (in Chinese)
6. Holtz J (1992) Pulsewidth modulation—a survey. *Power Electron Spec Conf* 1:11–18
7. Yongchang Z, Suyu G (2016) Predictive current control for permanent magnet synchronous motor with delay compensation. *J Electr Eng* 11(3):13–20. (in Chinese)
8. Holtz J, Quan J, Schmitt G (2003) Design of fast and robust current regulators for high power drives based on complex state variables. *Ind Appl Conf* 3:1997–2004
9. Dana S, Wenli L, Lijun D (2011) Improved voltage model flux observer design of induction machine. *J Beijing Jiaotong Univ* 35(2):94–98. (in Chinese)

# Predictive Direct Power Control of Three-Phase PWM Rectifier Based on Linear Active Disturbance Rejection Control

Kunpeng Li

**Abstract** A dual closed loop for PWM rectifier, consisted of an inner instantaneous power loop and an outer dc-bus voltage loop, is presented in this paper. The inner loop adopts predictive direct power control (PDPC) and the outside one adopts linear active disturbance rejection control (LADRC) strategy. In order to achieve the expected switching voltage vectors, the instantaneous power values are forced to be equal to references at the next sampling instance in PDPC. The state space form can be established according to instantaneous active power balance equation, and then the generalized disturbance can be compensated. And the instantaneous active power reference can be achieved by LADRC structure. Finally, the presented structure is tested by simulation in Matlab/Simulink environment. And simulation results verified the feasibility and the effectiveness of the proposed system.

**Keywords** Rectifier · Instantaneous power · Predictive power control  
Linear active disturbance rejection control

## 1 Introduction

For the reason that three-phase PWM rectifier represents some merits, such as low harmonic distortion of ac-side current, near-unity power factor, and high-quality dc-bus voltage, the three-phase PWM rectifier has been widely applied in the past few years. Some researches on predictive direct power control (PDPC) technique for the converter have been proposed in recent years [1–3]. In PDPC strategy, instantaneous active and reactive powers are regarded as controlled variables, and the expected switching voltage vectors of rectifier are decided by instantaneous power tracking errors within a fixed sampling period. The advantages of this

---

K. Li (✉)

School of Automation and Electrical Engineering, Tianjin University of Technology and Education, No. 1310, Dagu South Road, Hexi District, Tianjin, China  
e-mail: likunpeng\_87@163.com

© Springer Nature Singapore Pte Ltd. 2018

L. Jia et al. (eds.), *Proceedings of the 3rd International Conference on Electrical and Information Technologies for Rail Transportation (EITRT) 2017*, Lecture Notes in Electrical Engineering 482, [https://doi.org/10.1007/978-981-10-7986-3\\_31](https://doi.org/10.1007/978-981-10-7986-3_31)

301



scheme, compared to the other control methods proposed in [4, 5], are faster response, lower sensitivity to structure parameters, more satisfied dynamic performances. However, there exists error because that the components of power source are assumed constant over a switching period in [1]. And a high sampling frequency is necessary to achieve satisfied properties for the reason that a sophisticated dynamic look-up table (LUT) has been adopted in [2] and [3]. Therefore, to solve these problems, a novel PDPC algorithm combined with space vector modulation (SVM) technology was proposed in this paper. Moreover, the instruction value of instantaneous active power of tradition PDPC structure is usually provided from the outer PI dc-bus voltage controller. The expected performances of controlled system are limited to realize because of the drawbacks of PI controller, including that (a) control effects are over-dependent on process model; (b) control parameters are difficulty to be set; (c) time delay exists in the controller. Besides, some uncertain disturbances cannot be compensated fast enough.

Active disturbance rejection control (ADRC) was proposed by Prof. Han [6]. The main structures of ADRC include a tracking differentiator (TD), an extended state observer (ESO) and a nonlinear state error feedback (NLSEF). Although this structure is able to achieve better performances than PI controller, it is still complex and difficult to use in practice. To this, LADRC used linear ESO and linear SFF was proposed in [7, 8]. These researches have proved that the performances of LADRC are sometimes superior to ADRC.

Predictive direct power control of three-phase PWM rectifier based on LADRC was proposed in this paper. The inner instantaneous power controller adopted predictive control method and the outer dc-bus voltage controller adopted LADRC strategy. Finally, the presented structure was tested by simulation in Matlab/Simulink environment. By contrasting to the other predictive control methods, the simulation results verified the feasibility and the effectiveness of the proposed system.

## 2 Model-Based PDPC-LADRC

In the stationary reference frame  $\alpha - \beta$ , voltage equations are described as follows,

$$\begin{bmatrix} L_1 \frac{di_\alpha}{dt} \\ L_1 \frac{di_\beta}{dt} \end{bmatrix} = \begin{bmatrix} -R_1 & 0 \\ 0 & -R_1 \end{bmatrix} \begin{bmatrix} i_\alpha \\ i_\beta \end{bmatrix} - \begin{bmatrix} 1 & 0 \\ 0 & 1 \end{bmatrix} \begin{bmatrix} v_\alpha \\ v_\beta \end{bmatrix} + \begin{bmatrix} 1 & 0 \\ 0 & 1 \end{bmatrix} \begin{bmatrix} e_\alpha \\ e_\beta \end{bmatrix} \quad (1)$$

Where  $e_{\alpha,\beta}$  and  $i_{\alpha,\beta}$  are ac power source voltage vectors and ac-side current vectors in  $\alpha\beta$  coordinates, respectively.  $v_{\alpha,\beta}$  are switching voltage vectors of rectifier in  $\alpha\beta$  coordinates, respectively.  $R_1$ ,  $L_1$ ,  $C$ , and  $R_L$  represent line resistance, filter inductance, dc-bus capacitor and load respectively. Meanwhile the relationship of power-source voltage vectors  $e_{\alpha,\beta}$  and their derivative values are deduced as following equation:

$$\begin{cases} \dot{e}_\alpha = -\omega \cdot e_\beta \\ \dot{e}_\beta = \omega \cdot e_\alpha \end{cases} \quad (2)$$

Where  $\omega$  is angular frequency of ac power source voltage.

According to the instantaneous reactive power theory, the controlled instantaneous power variables are defined as follows:

$$\begin{cases} p = e_\alpha i_\alpha + e_\beta i_\beta \\ q = e_\beta i_\alpha - e_\alpha i_\beta \end{cases} \quad (3)$$

Where  $p$  and  $q$  are instantaneous active power and reactive power of rectifier, respectively. Combining with Eqs. (1) and (2), the derivations of Eq. (3) are finally made out as follows:

$$\begin{cases} \dot{p} = -\omega q - \frac{R_1}{L_1} p - \frac{1}{L_1} e_\alpha v_\alpha - \frac{1}{L_1} e_\beta v_\beta + \frac{\|e_{\alpha\beta}\|^2}{L_1} \\ \dot{q} = \omega p - \frac{R_1}{L_1} q - \frac{1}{L_1} e_\beta v_\alpha + \frac{1}{L_1} e_\alpha v_\beta \end{cases} \quad (4)$$

Where  $\|e_{\alpha\beta}\|$  is module of the vectors  $e_{\alpha\beta}$ . By analyzing the Eq. (4), the vectors  $v_{\alpha,\beta}$  can be decoupled. Meanwhile, considering of the discrete property of rectifier operation, the instantaneous power variables vary during each sampling period  $T_s$ . Substituting descending difference for differential, which is described as  $\dot{p} = \frac{\Delta p}{T_s} = \frac{p_{k+1} - p_k}{T_s}$ ,  $\dot{q} = \frac{\Delta q}{T_s} = \frac{q_{k+1} - q_k}{T_s}$ . The instantaneous active and reactive powers are forced to be equal to their reference values at the  $(k+1)$ th sampling instance. And then the expecting switching voltage vectors  $v_{\alpha,\beta}^*$  in the proposed PDPC strategy are calculated as follows,

$$\begin{cases} v_\alpha^* = \frac{L_1}{\|e_{\alpha\beta}\|^2} \left[ \omega \cdot X - \frac{R_1}{L_1} \cdot Y + \frac{\|e_{\alpha\beta}\|^2}{L_1} e_\alpha - \frac{\delta p}{T_s} e_\alpha - \frac{\delta q}{T_s} e_\beta \right] \\ v_\beta^* = \frac{L_1}{\|e_{\alpha\beta}\|^2} \left[ -\omega \cdot Y - \frac{R_1}{L_1} \cdot X + \frac{\|e_{\alpha\beta}\|^2}{L_1} e_\beta - \frac{\delta p}{T_s} e_\beta + \frac{\delta q}{T_s} e_\alpha \right] \end{cases} \quad (5)$$

Where  $\delta p = p_{\text{ref}} - p_k$ ,  $\delta q = q_{\text{ref}} - q_k$ ,  $X = p e_\beta - q e_\alpha$ ,  $Y = p e_\alpha + q e_\beta$ ,  $p_{\text{ref}}$ , and  $q_{\text{ref}}$  are instantaneous active and reactive power references, respectively.

In Eq. (5), the instantaneous reactive power reference is equal to zero, i.e.,  $q_{\text{ref}} = 0$ , for unity power factor operation of three-phase voltage source PWM rectifier. However, the instantaneous active power reference  $p_{\text{ref}}$  should be achieved by the outer dc-bus voltage controller. Finally, the expecting switching states can be achieved with the help of space vector modulation (SVM) technology.

In order to achieve the high quality dc-bus voltage, a outer dc-bus voltage controller based on the LADRC method is adopted in this paper. As the switching losses of the PWM rectifier are neglected, the law of energy conservation can be expressed as

$$p = p_{dc} = u_{dc} \times C \times \frac{du_{dc}}{dt} = \frac{C}{2} \frac{du_{dc}^2}{dt} + \frac{u_{dc}^2}{R} \stackrel{v=u_{dc}}{=} \frac{C}{2} \dot{v} + \frac{v}{R} \quad (6)$$

According to the strategy of the inner instantaneous power controller, the second derivative of  $v$  can be calculated by the variation of instantaneous active power between two successive sampling instances, as follows

$$\ddot{v} = \frac{2\dot{p}}{C} - \frac{4p}{RC^2} + \frac{4v}{R^2C^2} = \frac{2}{C} \frac{p_{k+1} - p_k}{T} - \frac{4p_k}{RC^2} + \frac{4v}{R^2C^2} = b \cdot p_{ref} + f \quad (7)$$

Where  $f = -\frac{2}{TC}p_k - \frac{4p_k}{RC^2} + \frac{4v}{R^2C^2}$  named as generalized disturbance, is a unknown combination of the unknown dynamics and the external disturbances of PWM rectifier. The variables  $b = \frac{2}{TC}$ ,  $p_{ref}$ , and  $v$  are denoted as gain, input and output of LADRC, respectively. Then the central idea of linear extended state observer (LESO) is to estimate the generalized disturbance and compensate it quickly. So the estimated variable of generalized disturbance can be used in control to reject itself more quickly. Then the control law can be chosen as follows

$$p_{ref} = (-\hat{f} + u_o)/b \quad (8)$$

Where  $\hat{f}$  are estimated value of  $f$ . If the design structure of LESO is proper, i.e.,  $\hat{f} = f$ , substituting Eqs. (8) to (7), then the outer dc-bus voltage model becomes a pure second-order integral system, i.e.,  $\ddot{v} = u_o$ . The above integral system can be controlled through a integral-differential (PD) controller (i.e., LSEF), described by

$$u_o = k_p(v - z_1) + k_d z_2 \quad (9)$$

Where  $k_p$  and  $k_d$  are proportional coefficient and differential coefficient of the PD controller, respectively,  $z_1$  and  $z_2$  are observations of  $v$  and its first-order derivative, respectively.

By the way, the chosen observations also illustrate that the square of dc-bus voltage and its first-order derivative are seemed as state variables. This is the central idea of TD and the purpose of TD is to solve the contradictory between quickness and overshoot.

The LESO can be designed as the following state-space form:

$$\begin{cases} \dot{z} = \mathbf{A}z + \mathbf{B}u + \mathbf{L}(y - \hat{y}) \\ \hat{y} = \mathbf{C}z \end{cases}, \quad \mathbf{A} = \begin{bmatrix} 0 & 1 & 0 \\ 0 & 0 & 1 \\ 0 & 0 & 0 \end{bmatrix}, \quad \mathbf{B} = \begin{bmatrix} 0 \\ b \\ 0 \end{bmatrix}, \quad \mathbf{C} = \begin{bmatrix} 1 \\ 0 \\ 0 \end{bmatrix}^T, \quad \mathbf{L} = \begin{bmatrix} \beta_1 \\ \beta_2 \\ \beta_3 \end{bmatrix} \quad (10)$$

Where  $z = [z_1, z_2, z_3]^T$ ,  $z_i (i = 1, 2, 3)$ , are the outputs of the LESO, and they are the estimations of the system states  $v, \dot{v}$  and  $f$ , respectively.  $L$  is the gain matrix of the LESO,  $\beta_i (i = 1, 2, 3)$  which are the observer gains, can be calculated by the bandwidth method.

Finally, it can be seen that the proper estimations of the system states of LADRC can be easily determined.

### 3 Simulation Based PDPC-LADRC

The schematic diagram of the proposed PDPC-LADRC for three-phase PWM rectifier is shown in Fig. 1. In this paper, three control algorithms of three-phase PWM rectifier have been contrasted in MATLAB/Simulink environment. And they are (a) PDPC-LADRC, proposed in this paper (b) PDPC-PI (c) LUT (Look-Up-Table)-PDPC-PI, presented in [2], respectively.

Simulation parameters are designed as follows: the amplitude and frequency of ac voltage  $e_s$  are 85 V and 50 Hz. Switch frequency is 5 kHz, filter inductance  $L$  is 4 mH, line resistance  $R_1$  is 0.5  $\Omega$ , dc-bus capacitor  $C$  is 2200  $\mu\text{F}$ , dc-bus voltage reference is 300 V. Simulation duration is 0.8 s and load mutate from 100 to 60  $\Omega$  at 0.4 s.

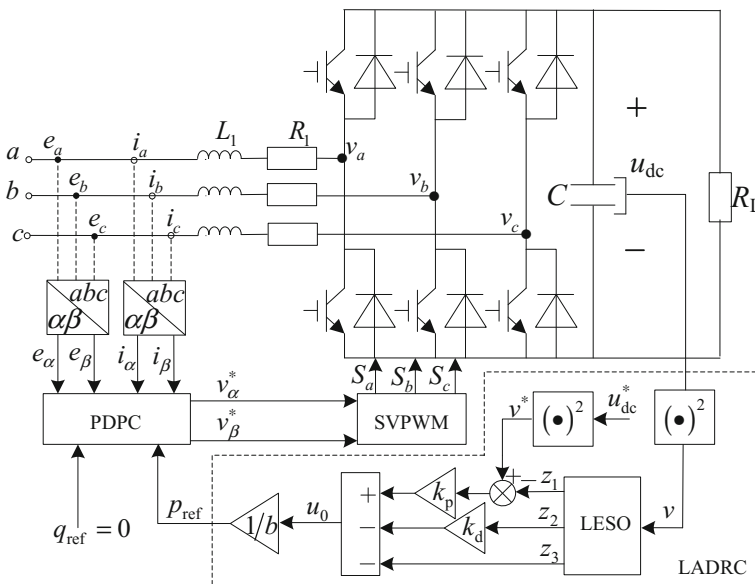


Fig. 1 Structure of the proposed PDPC-LADRC

Simulation results of dc-bus voltage are described in Fig. 2a, c, e. It can be seen the static and dynamic characteristics of the dc-bus voltage of the proposed PDPC-LADRC is the best one than the other two. Total harmonic distortion (THD) of ac current simulation results are described in Fig. 2b, d, f. From these three pictures, the ac currents are nearly sinusoidal waveforms except LUT-PDPC-PI system (THD = 26.51%). Though the THD value of ac current in PDPC-LADRC (2.38%) is larger than the PDPC-PI's (2.26%), the former didn't appear to be much different from the later. Meanwhile it is much easier to design filter in PDPC-LADRC and PDPC-PI structures, because that their current harmonics mainly tend to centre on the switching frequency.

Simulation waveforms of power source voltage and ac current are shown in Fig. 3a, c, e. From these three pictures, the ac current is always aligned with the power source voltage in each phase in these three structures. Figure 3b, d, f show the simulation results of instantaneous active power and its reference value and instantaneous reactive power. In every figure, the variable  $p$  is nominal 900 W in the first stage and 1500 W in the last process, and  $q$  is nominal 0Var within the whole process. Meanwhile both instantaneous active power and reactive power can track their references, respectively. But the instantaneous powers of PDPC-PLUT-PI have more obvious oscillation than the others.

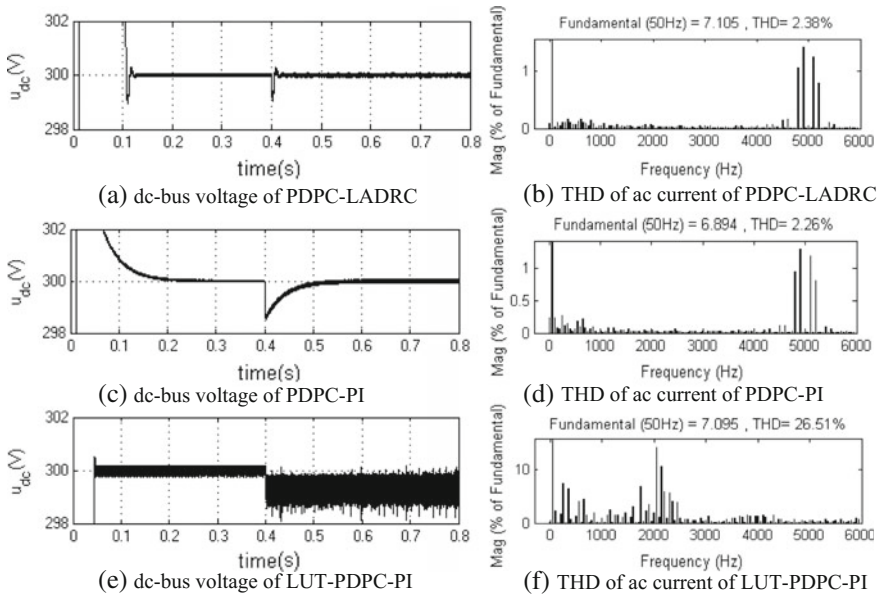


Fig. 2 Simulation results of dc-bus voltage and ac current

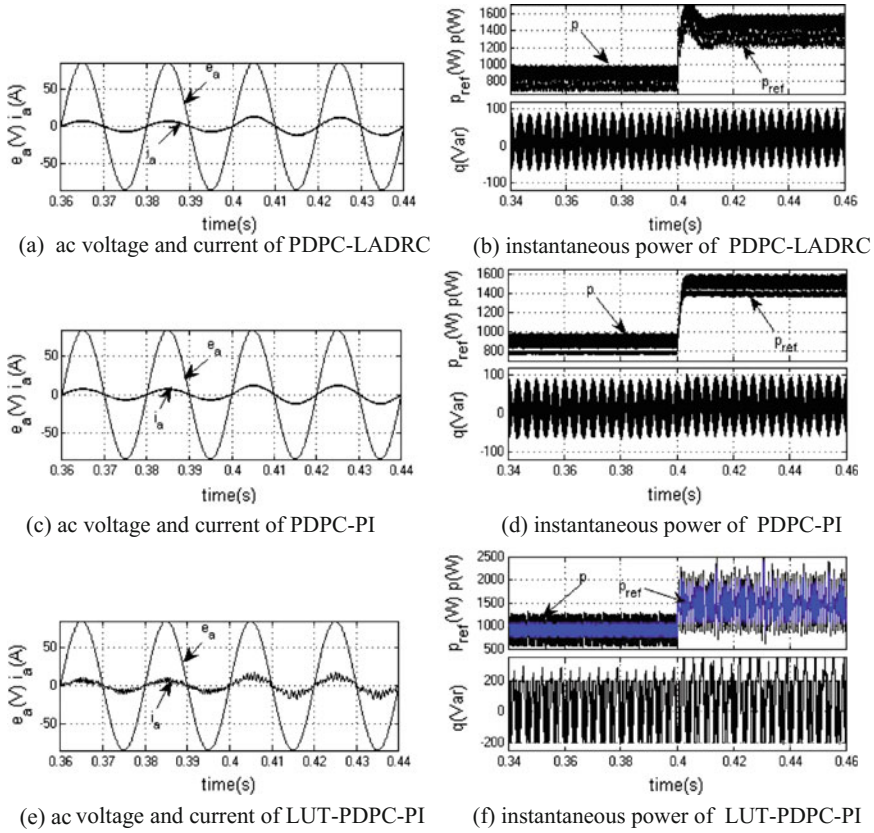


Fig. 3 Simulation waveforms of ac current and voltage and instantaneous power

### 4 Conclusion

This paper has proposed a PDPC-LADRC for three-phase PWM rectifier. The stationary coordinate without angle measurement is used in this paper, and the components of switching voltage can be calculated by the predictive algorithm of the instantaneous active and reactive powers. In order to realize fixed switching frequency, the SVM technology is adopted instead of LUT in proposed PDPC-LADRC algorithm. The simulation results illustrate that the PDPC-PI had much better static and dynamic performances than LUT-PDPC-PI. And not only that, the fixed switching frequency is easier to realize than unfixed switching frequency in practice. Meanwhile a LADRC structure is applied to replace PI controller, and the simulation results have proved excellent performances of the proposed PDPC-LADRC, compared to PDPC-PI.

## References

1. Abdelouahab B, Jean-paul G, Fateh K (2010) Predictive direct power control of three-phase pulsewidth modulation (PWM) rectifier using space-vector modulation(SVM). *IEEE Trans Power Electron* 25(1):228–236
2. Brando G, Dannier A, Del Pizzo A, Di Noia LP, Spina I (2015) Quick and high performance direct power control for multilevel voltage source rectifiers. *Electr Power Syst Res* 121:152–169
3. Ma J, Song W, Feng X (2016) A model predictive direct power control of single-phase three-level PWM rectifiers. *Proc CSEE* 36(4):1098–1105 (in Chinese)
4. Leng Y, Yang H, Wang Z (2017) A method of suppressing low-frequency oscillation in traction network based on two-degree-of-freedom internal model control. *Power Sys Technol* 41(1):258–264 (in Chinese)
5. Omar FR, Angelica MT, Irwin ADD, Ilse C, Nancy V, Ciro N, Ernesto B (2016) Controllability of rectifiers and three point hysteresis line current control. *Control Eng Pract* 55:212–225
6. Han J (1998) Active disturbance rejection controller and its applications. *Control Decis* 13(1): 19–23 (in Chinese)
7. Tan W, Fu C (2016) Linear active disturbance-rejection control: analysis and tuning via IMC. *IEEE Trans Ind Electron* 63(4):2350–2359
8. Li J, Xia Y, Qi X, Gao Z (2017) On the necessity scheme and basis of the linear-nonlinear switching in active disturbance rejection control. *IEEE Trans Ind Electron* 64(2):1425–1435

# Discussion on the Energy Efficiency and Electrotechnical Questions of Urban Cable Car System

Lothar Fickert, Ziqian Zhang, Cunyuan Qian and Yanyun Luo

**Abstract** Due to the convenience and low cost of cable car system construction, its application in urban public transport becomes more interesting. In the past, cable car systems were commonly used in non-urban areas, but now its application in urban areas requires more expert consideration. From the point of view of electrotechnical aspects, this paper studies the problems that may arise from the application of the cable car systems in urban areas, mainly from the aspects of energy efficiency, electromagnetic interference and electric corrosion. Also the technical compatibility of cable car systems with the high voltage transmission lines, photovoltaic plants and wireless communications is analyzed.

**Keywords** Cable car · Energy efficiency · Electromagnetic interference  
Stray current

## 1 Introduction

Cable car systems for public transport are planned and publicly discussed in many cities [1–4]. Since similar questions arise repeatedly, it is in the interest of all participants (city administrations, manufacturers, residents, and operators) that these questions are objectively dealt with at a high professional level. The focus is mainly about defining terms and key figures that can be used in planning procedures and standards. Planners, administrators and manufacturers need common criteria in order to be able to assess urban cable car projects and to implement them efficiently.

---

L. Fickert · Z. Zhang  
Department for Electrical Power Systems, Graz University of Technology,  
Inffeldgasse 18 A, 8010 Graz, Austria

C. Qian (✉) · Y. Luo  
Institute of Rail Transit, Tongji University, Building H112,  
No. 4800 Cao'an Road, Jiading District, Shanghai 201804, China  
e-mail: tjqcy@126.com

© Springer Nature Singapore Pte Ltd. 2018

L. Jia et al. (eds.), *Proceedings of the 3rd International Conference on Electrical and Information Technologies for Rail Transportation (EITRT) 2017*, Lecture Notes in Electrical Engineering 482, [https://doi.org/10.1007/978-981-10-7986-3\\_32](https://doi.org/10.1007/978-981-10-7986-3_32)



## 2 Energy Consumption of Urban Cable Car System

In order to compare the energy efficiency of different transport modes, the energy is mostly related to passenger kilometers in terms of kWh/Pers km (Fig. 1).

In this context, however, it should be noted that, according to a study [5], the apparent energy efficiency increases with the number of kilometers covered by the passenger. Since the unit “energy consumption per passenger kilometer” is a length dependent or speed-dependent variable, for urban traffic with relatively short lengths and low average speeds, therefore, the energy consumption per person transported is the most adequate measure.

The values for the energy consumption of different vehicles’ types in passenger transport and public passenger transport vary very strongly. The standard values for different vehicles are shown below. The energy consumption here refers to the final energy and takes into account only the pure driving energy (without system related energy consumption, for example for buildings and other related structures) (Table 1).

As a result, a standard values of 0.29 kWh/per person can be used for 3S-cableways.

**Fig. 1** Cable car in London. Reprinted from ref. [1], with kind permission from THOMAS/TELFORD LTD



**Table 1** Standard values of power consumption [6, 7]

Vehicle	Power consumption	
	kWh/(Pers km)	kWh/Pers
Private motor vehicle	0.4–0.6	3–4.5
Private electric vehicle	0.2	1.5
Bus (LPG)	0.1–0.15	1.23
Metro	0.02–0.05	0.74
Tram	0.07–0.08	0.40
Cable car	0.11	0.29

### **3 Technical Compatibility of Urban Cable Car System with Rail Transit**

#### **3.1 General**

The technical compatibility of an urban cable car system with conventional rail transit depends on the type of electrical power supply of the transport modes. For this reason, the different modes of transport are considered separately below.

#### **3.2 Tram**

The electrical power supply of trams is usually carried out using DC. In this case, particular attention must be paid to stray-current corrosion. As a result, stray currents can result in the ground, which in the case of unfavorable grounding and potential equalization conditions may cause longtime damage to metallic structures. This current effect can lead to corrosion and material removal in the area of building foundations, grounding and potential equalization systems and other metallic parts.

In order to prevent this potential danger, special attention should be paid to the appropriate design of the grounding systems when planning the cable car system. In addition, an electrical separation, and a correctly dimensioned and adjusted cathodic corrosion protection can be helpful.

The minimum distances between the cableway ropes and the overhead contact lines of the tram must be determined individually for the specific case on the basis of a corresponding calculation.

#### **3.3 Metro**

Similar to the tram, the electrical power supply of the Metro is also provided with DC. Regarding the influence, the following two cases can be distinguished.

- (1) The Metro rails are not isolated from ground: in this case, the DC current forms a flow field between the point of current transfer from the traction vehicle into the rails and the connection point of the return conductor at the infeeding point. This can result in a longitudinal DC voltage drop and consequently generate leakage currents in the cable car systems.
- (2) The Metro rails are isolated from the ground: The insulation in this case prevents a possible current flow and accompanying longitudinal DC voltage drops in the ground, so that no or only slight corrosion phenomena can occur. In this case, the metro is negligible in terms of corrosion risk.

With regard to the electrotechnical compatibility of an urban cable car system with the Metro, no special precautions have to be taken in the case of the planning and construction of the cable car system for case 2 (rails are isolated from the ground).

In case 1 (rails are not isolated from the ground), stray current result from the ohmic influence. These currents cause DC corrosion and material removal, which in the long term causes static mechanics endangering.

In order to prevent this potential hazard, special attention should be paid to the appropriate design of the grounding system when planning and constructing the urban cable car system.

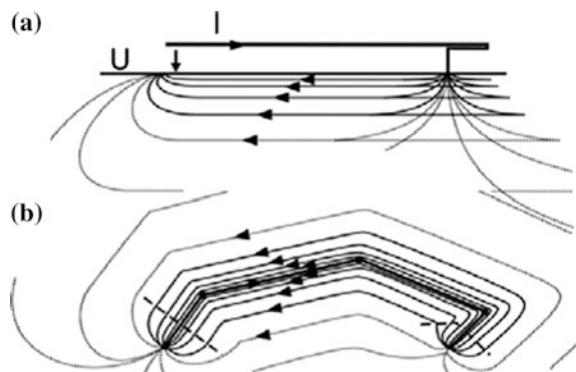
### 3.4 Railways

In Austria, electric trains mostly operate with AC at a frequency of 16.7 Hz or in many regions of the world they operate with AC at a frequency of 50/60 Hz. DC operation is also common in some European countries. As shown in Fig. 2, in the case of an AC supply, the return current in the ground is bundled by the effect of the magnetic field under the supply lines (driving wire, reinforcing lines, rails) and generally follows the route of the active conductor (“hot conductor”). However, if other conductor constructions, such as, for example, urban cable car systems, run in the vicinity and parallel to those return current paths, some proportion of the current will pass into and cause undesired currents flow.

## 4 Technical Compatibility of Urban Cable Car System with High Voltage Cables

In principle, influences are caused by high voltage lines, which are realized either as high voltage overhead lines or, more and more often in urban areas, as high voltage cable car system, on their operating state (in normal and fault operation).

**Fig. 2** Current distribution in the ground (**a** side view, **b** top view)



For the consideration of the technical compatibility of an urban cable car system with high voltage systems (see Fig. 3, used for a high voltage overhead line for illustrative reasons), the following cases have to be differentiated.

- Influencing in normal operation (three-phase operation).
- Influencing in the faulty operation (single-pole faults/multipolar faults/cross-country faults).

When a cableway rope is geographically close to a high voltage overhead line, as shown in Fig. 4, inductive influences can occur due to the magnetic coupling, whereby a short parallel section can be regarded as less problematic than a longer parallel routing of the two equipment.

A survey calculation can be carried out as follows:  
 Calculation of the induced voltage in the cableway rope:

$$U_{\mu} = l \cdot Z'_{v\mu} \cdot I_v \tag{1}$$

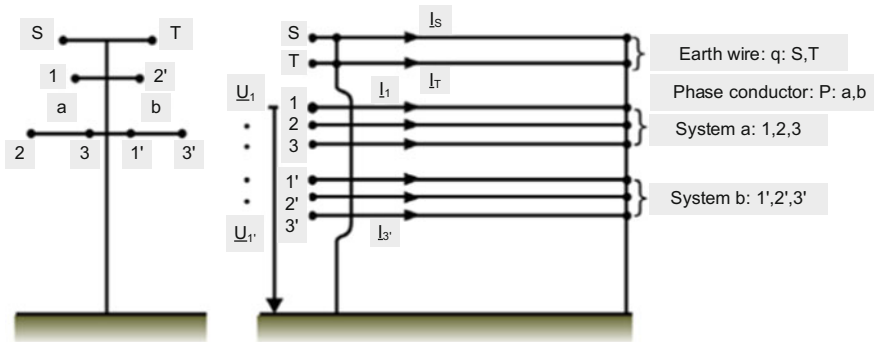


**Fig. 3** Schematic representation of double-circuit high voltage overhead line with a grounding conductor. Reprinted from ref. [8], with kind permission from L. Fickert

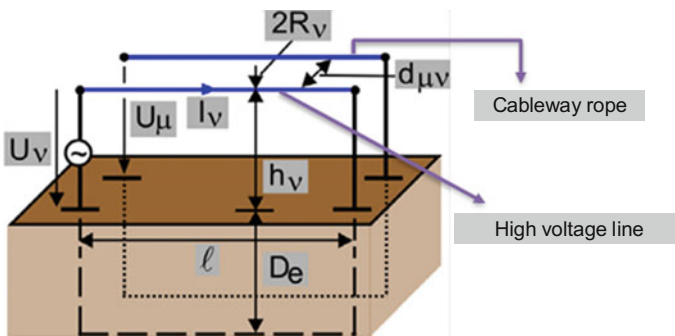


**Fig. 4** Model of a high voltage line parallel with a cableway rope. Reprinted from ref. [8], with kind permission from L. Fickert

Approximation for the specific coupling impedance:

$$\underline{Z}'_{v\mu} = \frac{j\omega\mu_0}{2\pi} \cdot \ln\left(\frac{D_e}{d_{v\mu}}\right) \quad (2)$$

The dangers lie in the current load of the cableway ropes, roller and traction wheels, and in the occurring contact voltages, which can lead to damage in technical equipment, if certain threshold values are exceeded, and even to ventricular fibrillation of persons in the worst case. This point is particularly important in view of the large number of people present in public transport.

For each specific case, however, a corresponding calculation has to be made. A reduction in the inductive coupled voltages is possible or a critical distance can be determined, through the determination of reduction factors and the line structure (cables, overhead lines, number of systems). Based on this calculation, the necessary measures for the planning and construction of the cable car systems can then be derived.

## 5 Technical Compatibility of Urban Cable Car System with Photovoltaic System

The influence of urban cable car systems on photovoltaic plant by means of (partial) shading effects of by cabins can be shown in the sense of an energetic consideration on the basis of the following example. The following assumptions are made in the sense of a worst case estimate:

- Full (100%) shadow effect (can be mitigated by streak effects).
- A fully intransparent cabin (without glass, without spreading effects) throws a shadow with  $(4 \times 4) \text{ m}^2$ , every 30 s and a speed of 4 m/s (in reality, a gondola with glass windows is partially light-permeable).
- There is a complete breakdown of the current output of the PV panels.

With an assumed overlap period of 1 s. and an assumed efficiency of the photovoltaic plant of  $\eta = 15\%$ , the loss in the supply of electrical energy for a gondola can be calculated:

$$1 \frac{\text{kW}}{\text{m}^2} \cdot 16 \text{ m}^2 \cdot 0.15 \cdot 1 \text{ sek.} = 2.4 \text{ kW s} \quad (3)$$

Loss of electrical energy per direction and day (12 operating hours, passage of a cabin every 30 s):

$$12 \cdot \frac{3600 \text{ sek.}}{30 \text{ sek.}} \cdot 2.4 \text{ kW s} = 3456 \text{ kW s} = 0.96 \text{ kWh} \quad (4)$$

With regard to the compatibility of an urban cable car system with photovoltaic plant, a review of the legal situation (“right of claim to sunlight” by photovoltaic system owners) is recommended. This repeated short-term shading effect possibly results in unacceptable grid retroactive effects, a closer examination of this situation is recommended.

## **6 Technical Compatibility of Urban Cable Car System with Antenna Equipment**

Since the height of urban cable car system is comparable to the construction height of power lines, urban cable car system (with the exception of directional microwave radio links) generally do not cause interference with communication and radar systems.

In the area of airports, however, the ILS land system could be influenced by the horizontal cableway ropes. Furthermore, a shading of directional microwave radio links through the cabin is possible, but this can be avoided by suitable planning.

The supply of the cabins with WLAN service is basically conceivable. The required antennas do not have to be installed in each cabin, but can also be mounted on the masts. Regarding interference from other communication systems, the same restrictions apply as for the installation of WLAN equipment in buildings.

With regard to the compatibility of an urban cable car system with antenna system, it is therefore advisable to clarify or take into account the position of the ILS land system and microwave radio links in the planning of the cable car system.

## **7 Conclusions**

This paper makes a comprehensive study of the problems that may be encountered by the application of urban cable car system in electrotechnical aspects, and gives the corresponding recommendations. From the point of view of the energy consumption per passenger, the urban cable car system is the most efficient public transport system. As for the technical compatibility with Metro, tram and railway systems, the electrotechnical influence on the urban cable car system are mainly restricted to the electromagnetic interference and stray currents. With respect to the technical compatibility with high voltage overhead lines, the dangers may lie in the current loadings and also in occurring contact voltages in the cableway ropes, roller and traction wheels in the worst case. As for the compatibility with a photovoltaic system and antenna equipment, the block of light and microwave radio links may be the most important problem.

**Acknowledgements** This work is partially supported by the National “Twelfth Five-Year” Pillar program for Science & Technology—the interoperability Comprehensive Evaluation Integrative Platform and Demonstration for Urban Rail Transit (No.2015BAG19B02).

## References

1. Randall M (2013) Delivering the Emirates air line, London–Britain’s first urban cable car. *Proc Inst Civ Eng—Civ Eng*, November 166(4):162–169. Thomas Telford Ltd
2. Fiedler J (2016) Urban cable—a policy option. *J Traffic Transp Eng* 4:247–250
3. Cordoba DZ, Stanley J, Stanley JR (2014) Reducing social exclusion in highly disadvantaged districts in Medellín, Colombia, through the provision of a cable-car. *Soc Incl*, 2(4)
4. Miller P, Birchall M, McCormick F (2014) Delivering the Emirates air line, London, UK: design and construction of the steel main towers. *Proc Inst Civ Eng Struc Build* 167(10):570–580
5. Frey, Schopf, Winder (2014) Energy-Efficient New Mobility in Vienna, TU Wien
6. Energy Efficient Mobility <http://www.umweltbundesamt.at/umweltsituation/energie/effizienz/effizienzverkehr/>, 2016-03-23
7. Passenger car occupancy rate for private car use <http://www.forschungsinformationssystem.de/servlet/is/79638/>
8. Fickert L (2014) Electrical Energy Systems 1, Script TU Graz

# Test and Regression Analysis of Dynamic Shutdown Characteristic of High Power Thyristor

Zhihao Zhang, Liqun Zhang, Zeng Shou, Yifang Jin and Yuhao Tan

**Abstract** This paper focuses on thyristor in the aspects of its junction temperature, its zero  $di/dt$ , its forward current  $I_T$  and its reverse voltage  $V_r$ , and presents in-depth study of internal factors which cause commutation failure of the valve. This paper puts forward the optimal configuration approach to the factors above, reduces various improvement measures to induce thyristor turn off time. A physical test platform of the shutdown characteristics is built. By testing the shutdown characteristics of thyristor, the linear regression analysis method is used to get the fitting formula of the thyristor turn off time.

**Keywords** High power thyristor · Dynamic shutdown characteristic  
Regression analysis

## 1 Introduction

The inherent dynamic shutdown process of high power thyristor in converter valve affects the probability of commutation failure greatly. A lot of research has been done on the high power thyristor commutation failure at home and abroad, while very few research work is carried around the converter valve equipment itself, and fewer has considered the inherent actual off time of converter valve. References [1, 2] analyze the cause of commutation failure; References [3, 4] analyze the

---

Z. Zhang (✉) · Y. Tan  
Beijing KeDong Electric Power Control System Co., Ltd,  
Haidian District, Beijing 100192, China  
e-mail: 87887803@qq.com

L. Zhang  
Shenyang Institute of Computing Technology Co., Ltd,  
Cas, Dongling District, Shenyang 110168, China

Z. Shou · Y. Jin  
State Grid Liaoning Electric Power Supply Co., Ltd,  
Hepign District, Shenyang 110006, China



influence factors of commutation failure; Ref. [5, 6] present the evaluation criterion of commutation failure; Ref. [7, 8] present the detection method of commutation failure; Ref. [9] presents some recovery measures for commutation failure; in Ref. [10], the failure detection, fault recovery and protection of the phase transition are simulated, combined with specific HVDC (High Voltage Direct Current) transmission project; Ref. [11] studies the commutation failure of multi-infeed HVDC system.

In all the research results above, the minimum turn off angle of the converter valve is defined as a fixed value (around  $8^\circ$ ), without taking operating conditions into consideration. However, in actual operation, the dynamic relationship between valve turn off time and the operation conditions determines the occurrence of converter valve commutation failure directly, and determines the control margin of the turn off angle indirectly. Therefore, It is of practical significance to study the dynamic shutdown characteristics of thyristor.

## 2 Main Factors Affecting the Thyristor Shutdown Process

The residual carrier density of the N base region inside a thyristor is determined by junction temperature  $T_j$ , forward on-state current  $I_F$ , rate of current decrease  $di/dt$ , reverse voltage  $V_{rr}$  during turn off and carrier lifetime  $\tau$  of the conduction time.

(1) Thyristor forward on-state current  $I_F$  and current drop rate  $di/dt$

Before turn off, the thyristor is in steady state, and the stored charge can be approximately written:

$$Q_F = K_0 \tau_P I_F \quad (1)$$

In Eq. (1),  $K_0 = a_{npn}$ ,  $a_{npn}$  is current gain of npn transistor. Thus, the value of the stored charge depends on the forward on-state current  $I_F$  and also on N-band minority lifetime  $\tau_P$  and current gain of npn transistor  $a_{npn}$ .

When the voltage at the two ends of the thyristor is changed from positive to reverse, the forward on-state current  $I_F$  is decreasing at a rate of  $di/dt$ . Induction electromotive force in the loop inductance  $L$  hinders the reduction of the forward on-state current. The thyristor maintains a positive turn-on-state. The  $di/dt$  is entirely determined by the external reverse voltage  $V_{rr}$  and the loop inductance  $L$ .

$$\frac{di}{dt} = -\frac{V_{rr}}{L} \quad (2)$$

Given that  $t_1$  is the starting point for turn-off of thyristor. When the current is zero, the stored charge  $Q_{t1}$  has been reduced to:

$$Q_{t1} = Q_F \frac{\tau_P}{t_1} (1 - e^{-\frac{t_1}{\tau_P}}) = K_0 \tau_P I_F (1 - e^{-\frac{t_1}{\tau_P}}) \quad (3)$$

When the loop inductance is small,  $di/dt$  is larger. So  $t_1 = \tau_p$  and  $Q_{t1} \approx Q_F$ . When the loop inductance is big,  $di/dt$  is less and  $\tau_p = t_1$ , so  $Q_{t1}$  changed into:

$$Q_{t1} = Q_F \frac{\tau_p}{t_1} = K_0 \tau_p^2 \frac{di}{dt} \tag{4}$$

For a small current drop rate, the stored charge at zero current is independent of the original forward current  $I_F$ , only associated with  $di/dt$ . When the current drop rate is large and the current is zero, the stored charge is only related to the forward current  $I_F$ .

The current drop rate  $di/dt$  of the converter valve is varied when the thyristor is off, closely relating to external circuit. Because of the leakage resistance, when the converter valve is off, the equivalent shutdown circuit has a series inductance. Figure 1 shows equivalent circuit of thyristor commutation process.

As is shown in Fig. 1:

$$L_u \frac{di_1}{dt} - L_u \frac{di_3}{dt} = L_u \frac{di_1}{dt} - L_u \frac{d(I_d - i_1)}{dt} = u_{ab}(t) \tag{5}$$

Assume that the flat wave reactor of the DC system is infinite, Eq. (5) gives:

$$\frac{di_1}{dt} = \frac{u_{ab}(t)}{2L_\mu} \tag{6}$$

Using commutation failure to analysis how  $I_F$  and  $di/dt$  influent thyristor turn-off time in PSCAD. Increase the  $I_F$  under 1–10% conditions, the changes in relevant factors are shown in Fig. 2.

As is shown in Fig. 2, the turn off time of the thyristor  $t_q$  increases with  $I_F$ . However, the magnitude of increase was not proportional to  $I_F$ , but less. In addition, the decrease of  $di/dt$  is basically the same as that of the system running off angle. Since that the trigger angle  $\beta$  remains unchanged; run off angle decreases; cause change phase angle  $\mu$  increases; the current drop time is prolonged;  $di/dt$  decreases and the decrease amplitude is consistent with decreasing range of  $\gamma$ .

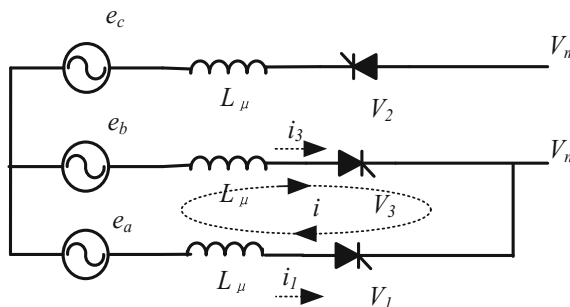


Fig. 1 Valve 1 and valve 3 commutation process equivalent circuit

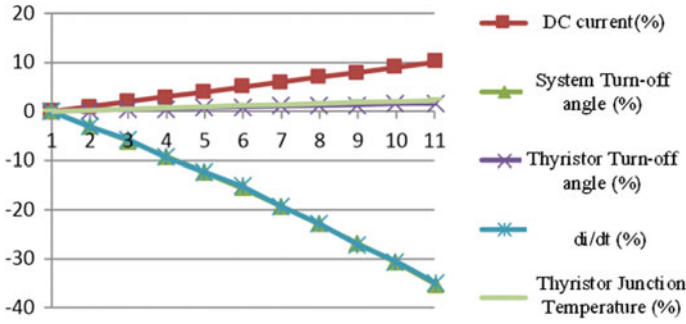


Fig. 2 The influence of the forward current and the current drop rate on the turn off time of thyristors

Now, both  $I_F$  and  $di/dt$  influence the turn-off time of Thyristor. Equation (4) shows that The reduction of  $di/dt$  reduces  $Q_{t1}$ , which is beneficial to shorten the turn-off time of thyristor. Therefore, under the positive and negative feedback combined action of  $I_F$  and  $di/dt$ , the turn-off time of the thyristor has increased, but amplitude is not large. It seems that the influence of  $I_F$  on turn-off time is greater than  $di/dt$ .

(2) Thyristor reverse recovery charge  $Q_{RR}$

In the forward conduction stage of thyristor, there are a large number of carriers in the N1 base region and the P2 base region. When turned off, the current through thyristor is reduced to 0 and then inversely increased and a part of the accumulation carrier of the base region is removed by the reverse current.

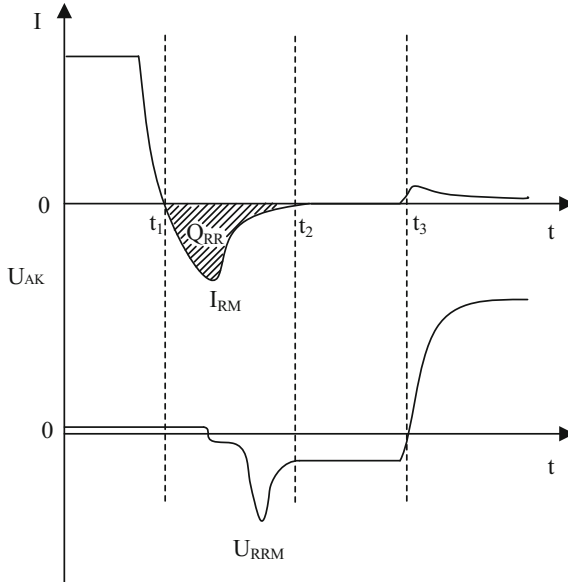


Fig. 3 Turn-off characteristics of thyristor

The reverse recovery current that flows through the thyristor enables the anode junction J1 junction to recover. During this time, the storage charge of the device is reduced by a total value of  $Q_{rr}$ .  $Q_{rr}$  is not equal to the reverse recovery charge  $Q_{RR}$  (shadow area in Fig. 3). Because in the recovery stage, the injection of carriers into the base region continues. Therefore, the remaining storage charge  $Q_{t2}$  at  $t_2$  is:

$$Q_{t2} = Q_{t1} - Q_{rr} \tag{7}$$

After  $t_2$ , the thyristor restores the reverse blocking state. The reverse recovery current is reduced to near the peak  $I_{RRM}$  of the thyristor off state current. The remaining stored charge  $Q_{t2}$  disappears by the combination of holes and electrons:

$$Q(t) = Q_{t2}e^{\frac{-t}{\tau_p}} \tag{8}$$

At  $t_3$ , the remaining charge of the thyristor base is:

$$Q_{t3} = Q_{t2}e^{\frac{-(t_3-t_2)}{\tau_p}} \tag{9}$$

If  $Q_{t3}$  is not enough to cause a positive trigger, i.e.  $Q_{t3} = Q_{off}$ , the thyristor shutdown process is completed. So:

$$t_3 - t_2 = \tau_p \ln\left(\frac{Q_{t2}}{Q_{off}}\right) \tag{10}$$

Equation (10) can be used as a simple approximate formula for estimating the turn off time of thyristors. It is assumed that  $I_{off}$  by  $Q_{off}$  is just less than the current  $I_H$  needed to maintain conduction and  $Q_{t2} = Q_F$ . Then the turn-off time of thyristor  $t_q$  is:

$$t_q = \tau_p \ln\left(\frac{I_F}{I_{off}}\right) \tag{11}$$

$I_{off}$  can approximate the thyristor current  $I_H$ . In effecting on turn-off time, the change of forward current and holding current are more sensitive than minority carrier lifetime  $\tau_p$ .

(3) Thyristor junction temperature  $T_j$

Thyristor junction temperature  $T_j$  can calculate following Eq. (12).

$$T_j = T_C + P_j \times R_{\theta JC} \tag{12}$$

$T_C$  is the average value of inlet temperature and outlet temperature;  $P_j$  is the total loss of each thyristor;  $R_{\theta JC}$  is the thermal resistance between thyristor junction and coolant.

The thyristor on-state loss is the product of on-current and corresponding ideal on-state voltage:

$$P_{V1a} = \frac{N_t \times I_d}{3} \left[ U_0 + R_0 \times I_d \times \left( \frac{2\pi - \mu}{2\pi} \right) \right] \quad (13)$$

$U_0$  is the independent part of current of the average on-state voltage drop in a thyristor;  $R_0$  is a resistor that determines the average slope of the thyristor's on-state characteristics.  $I_n$  is effective value of  $N$  subharmonic current of DC bridge.

Equation (14) is for direct current smoothing. When the square root and the value of the DC side harmonic current are both more than 5%, use Eq. (14).

$$P_{V1b} = \frac{N_t \times I_d \times U_0}{3} + \frac{N_t \times R_0}{3} \left( I_d^2 + \sum_{n=12}^{n=48} I_n^2 \right) \left( \frac{2\pi - \mu}{2\pi} \right) \quad (14)$$

The thyristor diffusion loss is the additional conduction loss of thyristor. It is produced during the full turn-on of the thyristor silicon wafer.

$$P_{V2} = N_t \times f \times \int_0^{t_1} [u_b(t) - u_a(t)] \times i(t) dt \quad (15)$$

$u_b(t)$  is the thyristor transient on-state voltage;  $u_a(t)$  is the average value of thyristor transient on-state voltage;  $i(t)$  is the transient value of current flowing through thyristor;  $t_2$  is the turn-on time.

$$t_2 = \frac{\frac{2}{3}\pi + \mu}{2\pi f} \quad (16)$$

The turn-off loss of thyristor:

$$P_{V3} = Q_{rr} \times f \times \sqrt{2} \times U_{V0} \times \sin(\alpha + \mu + 2\pi \times f \times t_0) \quad (17)$$

$$t_0 = \sqrt{\frac{Q_{rr}}{(di/dt)_{i=0}}} \quad (18)$$

Substituting Eq. (13), (14), (15) and (16) into Eq. (12), it gives:

$$T_j = T_C + [P_{V1a} + P_{V1b}] + P_{V2} + P_{V3} + P_{V4} \times R_{\theta JC} \quad (19)$$

From Eq. (19), we can reduce the thyristor junction temperature  $T_j$  by reducing  $R_0$ ,  $Q_{rr}$ , and  $R_{\theta JC}$ . Thus, the turn-off time of the thyristor  $t_q$  is reduced.

(4)  $dv/dt$  of applying the forward voltage

The magnitude of the recovery current depends not only on the value of the remaining charge, but also on the value of the  $dv/dt$ . If the forward recovery current is too large, the thyristor will be re converted to the turn-on-state and can not achieve a positive recovery.

In the process of positive recovery when the thyristor is turned off, as time goes on, partial blocking of the forward voltage was gradually resumed. But its ability to tolerate positive  $dv/dt$  is limited. The displacement current caused by  $dv/dt$  can be the trigger condition for thyristor from blocking state to on-state. Near zero current, the triggering of residual carriers is very significant and the anode voltage of the thyristor is very low when the switch is turned on. Thus, the recovery time and the maximum turn-on voltage of the thyristor are significantly increased with the increase of temperature and  $dv/dt$ .

(5) Reverse voltage  $V_{rr}$

When J1 junction begins to withstand reverse pressure, the lower the reverse voltage is, the longer the turn off time is, the more detrimental to the thyristor shutdown and to remove all the remaining carriers stored there. At the same turn-off angle, for contravariant operation of thyristor valve, the lower the voltage at the turn off time, the more detrimental to the thyristor recovery, the more likely to reverse failure. Minimum shutoff angle test is used to verify the valve’s inverter operating capability.

### 3 Fitting and Analysis of Dynamic Turn off Characteristics

Figure 4 shows a simple and effective sine half wave test circuit. C is energy storage capacitor. L is the inverting commutation inductor. When C is charged to an equal scaled off voltage, the thyristor then flows through sinusoidal half wave current. When such current is zero, the voltage on the capacitor C is reversed due to the small loss of the thyristor and almost equal to the charge voltage. So, at this

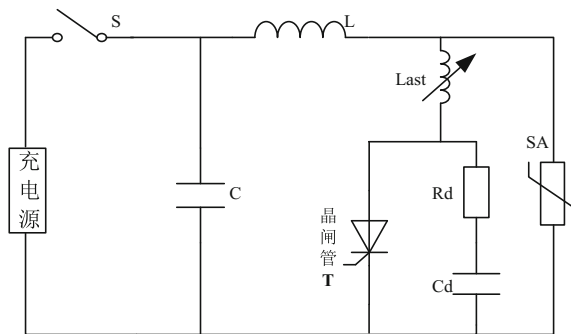
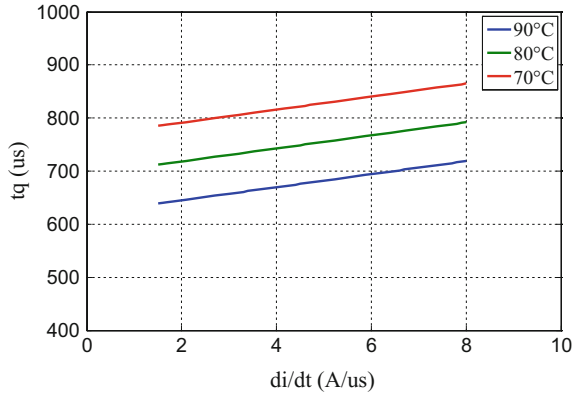


Fig. 4 Sine half-wave turn-off test circuit



**Fig. 5** Fitting curves of turn-off time of 5 kA thyristors with di/dt at different temperatures

time, the circuit parameters are equal to the proportion of reduction, and di/dt can be equal to the actual value.

According to the measured data, the three independent variables of  $I_F$ , di/dt and  $T_j$  can explain thyristor turn-off time  $t_q$ . The observed relation curve shows that there is a linear correlation between independent variable and dependent variable. So, use multiple linear regression analysis method for analysis.

$$t_q = f\left(\frac{di}{dt}, T_j, V_{rr}, I_T\right) = \beta_0 + \beta_1 \frac{di}{dt} + \beta_2 T_j + \beta_3 V_{rr} + \beta_4 I_T \quad (20)$$

With the multiple sets of raw data from device data sheet, modeling with MATLAB and perform multiple linear regression analysis. Regression analysis can obtain fitting regression formula:

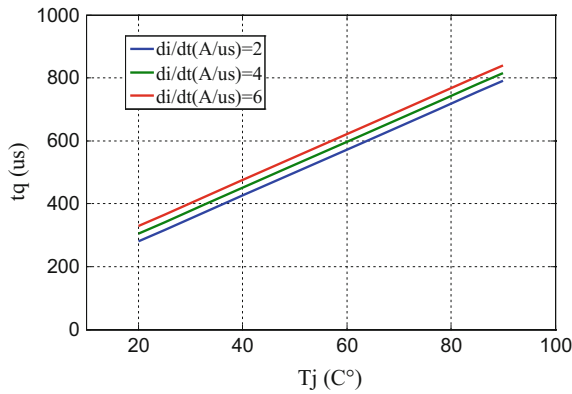


**Fig. 6** Fitting curves of turn off time of 5 kA thyristors with junction temperature under different di/dt

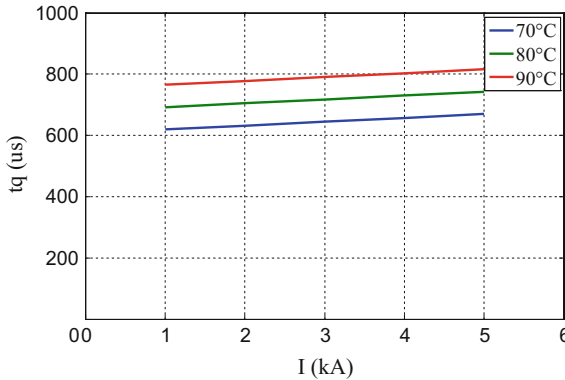


Fig. 7 Fitting curves of turn off time of 5 kA thyristors with current in different temperatures

$$t_q = 45.5171 + 12.2907 \frac{di}{dt} + 7.3048T_j + 0V_{rr} + 12.7380I_F \tag{21}$$

Figure 5 through Fig. 7 show the fitting results of turn-off time of a 5 kA thyristor with different di/dt and with temperatures. It implies that Eq. (21) can accurately calculate the turn off time of the thyristor. The data is basically consistent with the original test data and consistent with theoretical analysis result (Fig. 6).

### 4 Conclusion

In this paper, the shutdown process of thyristor was analyzed, and the factors that influence thyristor turn off were analyzed in detail. Built a dynamic shutdown characteristics of the simulation and physical platform, also established a turn-off time fitting regression equation. Through the actual operation of the thyristor to study, it is concluded that the thyristor shut-off process is determined by the reverse recovery characteristic of the thyristor and the external circuit parameters.

**Acknowledgements** This work was supported by National Power Grid Corp science and technology project: Study on Ultra High Voltage Bypass Impedance Topology.

### References

1. Zheng B, Ricai G (2003) The development of interconnected power grid China. Power Grid Technol 27(2):1-3



2. Chao Z (2004) The role of HVDC transmission in the development of China's power grid. *High Voltage Technol* 30(11):11–12
3. Shang C (2006) Application and application of UHV transmission technology in China southern power grid. *High Voltage Technol* 32(1):35–37
4. Fang X, Zhong S, Chen Z et al (2006) Study on access system of Zhuzhou converter station in Zhuzhou  $\pm 800$  kV HVDC project. *China Electr Power* 39(3):50–54
5. Yinbiao S (2005) Development and implementation of UHV transmission in China. *China Electr Power* 38(11):1–8
6. Wang M (2003) Application of modern new technology in HVDC. *Int Electr* 7(2):32–34
7. Liu H, Xu Z (2002) Review of reliability of world long - distance high - capacity HVDC project. *High Voltage Apparatus* 38(3):26–28
8. Wang W (2004) HVDC engineering technology. China Electric Power Press, Beijing
9. Yang X, Chen H, Jin X (2006) Research on dynamic recovery characteristics of HVDC transmission system. *High Voltage Technol* 32(9):11–14
10. Ren Z, Chen Y, Zhensheng L et al (2004) Probabilistic analysis of commutation failure of HVDC transmission system. *Autom Electr Power Syst* 28(24):19–22
11. Zheng C, Huang L, Lin G et al (2011) RTO simulation of  $\pm 800$  kV UHVDC commutation failure and its subsequent control and protection characteristics. *Power System Technol* 35(4):14–20

# Research on Mode-Switchover Process and Protective Circuit of Dual Power Supply System for Regional Express Electric Multiple Unit

Ruijing Ouyang, Haibo Zhao and Long Qi

**Abstract** This paper firstly puts forward the integrated traction equipment proposal of dual power supply system. Then it analyzes the catenary-pantograph relationship, the mode-switchover process and the risk of incorrect connection between the main circuit and power, then taking these as a measure, assesses the current collection and protective proposal according to the economic and industrial factors etc. Finally, on the basis of it, the preferred proposal is given.

**Keywords** Regional express EMU · Dual power supply mode  
Mode-switchover · Current collection · Protection

## 1 Introduction

In recent years, as the commuting requirements between megacity and satellite city are increasing gradually, the city rail connecting main line railway and urban railway is developing rapidly. The suburban region, within one hour commuting circle, 50–80 km far from central area, is the transition area of AC and DC power supply. The dual power supply mode regional express ( $V_{\max}$  ranges from 120 to 160 km/h) which can join the above two power supply system effectively and run from the central area to the suburban directly, has both advantages of two power supply systems, according to the economic and technical factors.

In order to adapt to two power supply systems, the AC and DC traction equipments on the dual mode vehicle have to be integrated effectively, to improve the system economy and practicability to the greatest extent. Secondly, need to meet the current collection requirements of the two power supply systems. At last, it must switch quickly and safely. The above aspects will be researched on in this paper.

---

R. Ouyang (✉) · H. Zhao · L. Qi  
General R&D Department, National Railway Engineering Research Center,  
CRRC Changchun Railway Vehicle Co., Ltd, No.435, Qingyin Road,  
Changchun, Jilin Province, China  
e-mail: ouyangruijing@cccar.com.cn

## 2 The Integrated Proposal of the Traction Equipment

The traction main circuit of the vehicle is mainly composed by current collection equipment (mainly two kinds: current collector and pantograph), protective equipment (main circuit breaker), and traction equipment (includes the transformer, converter and motor) etc. Due to the limit of installing room, weight and cost, the DC power is lined to converter DC-link of dual mode vehicle directly or after the treatment, so the DC-AC parts is able to be shared by two sets of the traction system (as shown in Fig. 1), this proposal is mainly used for the traction equipment of the dual or multiple mode vehicles [1].

## 3 Factors Impact on the Proposal of Current Collection and Protective Equipment

After the integration of the traction main equipments, the following three factors impacting on the current collection and protective equipment should be considered.

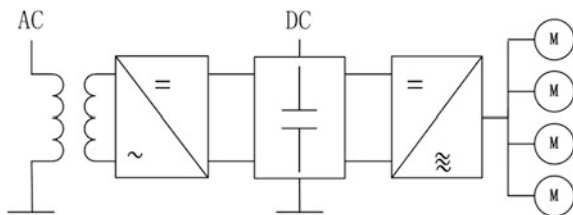
### Factor 1: The Catenary-Pantograph/Rail-Collector Relationship

It is the most simple proposal that the separate specified current collection equipments are equipped for each power supply system, but the integration of the current collection equipment is the developing direction, considering the economic and installing room aspects etc. For the integration of the current collection, the following key aspects should be considered: power voltage, current, the quality of current collection, gauge and pull-out value.

Issues should be faced in the integration:

1. Gauge and pull-out value
  - (a) The pantographs can't be shared due to different upper gauge and pull-out value [2];
  - (b) Pantograph and current collector can't be shared;
  - (c) The current collectors can't be shared due to different gauge.
2. When high-speed EMU runs in DC mode, the higher current and speed, and the higher pantograph dynamic behaviour is needed, so pantographs have to be connected in parallel to meet the quality of current collection.

**Fig. 1** Integrated proposal of traction equipment



Main circuit of Eurostar EMU mentioned in literature [3] is shown in Fig. 2. Rise one pantograph for AC catenary, rise two for DC catenary and use current collector for the third rail.

**Factor 2: Power Supply Mode-Switchover**

There two main mode-switchover proposals:

- (1) Ground breaker switchover proposal (hereinafter abbreviated as Switch 1)  
 When vehicle stops at the station, the neutral section is connected to the adjacent power section by opening and closing the corresponding breakers to switch power supply. It is the example in JR Kuroiso Station [4–6] as shown in Fig. 3a. And there are ten mode-switchover parts in JR network, only one uses SWITCH 1, and the other nine use the following proposal.
- (2) On-board breaker switchover proposal (hereinafter abbreviated as Switch 2, shown in Fig. 3b).

The neutral section is non-electric part, vehicle passes neutral section by inertia, and completes the switchover process. This proposal has more applications in Japan, Germany, and Spain etc. [3], and is the main research object of this paper.

The switchover time is the important index of Switch 2 which is the dynamic process, at the same initial speed, the shorter switchover time, the shorter non-electric part need to be set, and the less speed will loss. In the switchover process, pantograph’s up-down action and main switch’s rotating action should

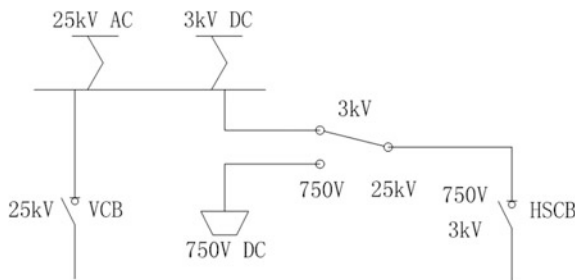


**Fig. 2** Main circuit of Eurostar EMU

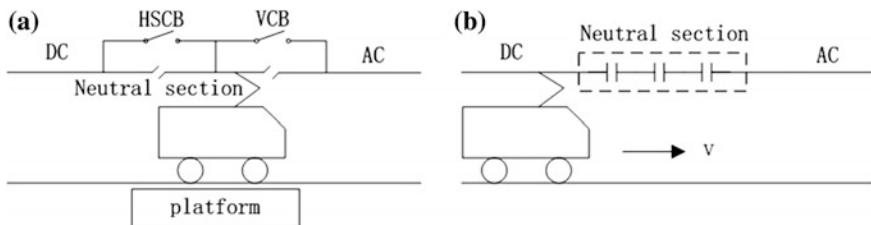


**Fig. 3** a Ground and b on-board breaker switchover

complete. Switchover process can be classified as three kinds according to the pantograph's action: up&down, up/down and no up&down. The switchover time of them decreases in turn.

### **Factor 3: Risk of Incorrect Connection Between the Main Circuits**

Risk 1: The high voltage power connects to the low voltage loop, which will cause over-voltage damage to the low voltage devices. it is usual case that AC power is connected to DC loop.

Risk 2: The low frequency power connects to the high frequency loop, which will cause over-current damage to the coils. It is usual case that DC power connects to AC loop which is transformer primary side generally.

Methods to reduce risk: improve the reliability of the executive devices; increase the reliability of control system; add protective equipment.

## **4 Compare and Analyze the Proposals of Current Collection and the Protective Equipment**

The proposals of current collection and protective equipment will be assessed according to the factors summarized above. The different parts of these proposals are the integrated program of current collection and the protective equipment and the type of switch need to be added for the programs.

### **4.1 *Separate Pantograph Proposal***

**Main circuit proposal 1** (hereinafter abbreviated as Main 1, as shown in Fig. 4a): To Optimize factor 1, separate pantograph and the protective will be equipped for the AC and DC loop. Of which P: pantograph, F: arrester, TV: voltage transformer, TA: current transformer, VCB: vacuum circuit breaker, HSCB: high-speed circuit breaker, HS: Isolating switch, L: filter reactor.

Factor 2: Lower one pantograph, and raise another one, main circuit switchover is realized by pantograph's up&down. The switchover time is longest.

Factor 3: Risk 1: The triggering condition is that raising the DC pantograph in AC area, and the devices and lines designed according to DC insulation will all be broken. It is the main risk.

The power supply voltage mode signal on the current position which is provided by the signalling system [hereinafter abbreviated as the voltage mode (signalling)] is added as the precondition of raising pantograph; Add on-board voltage detector which can output the voltage mode signal [hereinafter abbreviated as the voltage mode (on-board)], therefore, add a voltage detecting procedure after raising the pantograph on original circuit, add a TV(DC) and HS, and the circuit and equipment all meet high voltage isolation requirement of the AC power supply, the added devices are shown in the region enclosed by the dotted line in the Fig. 4a HS must

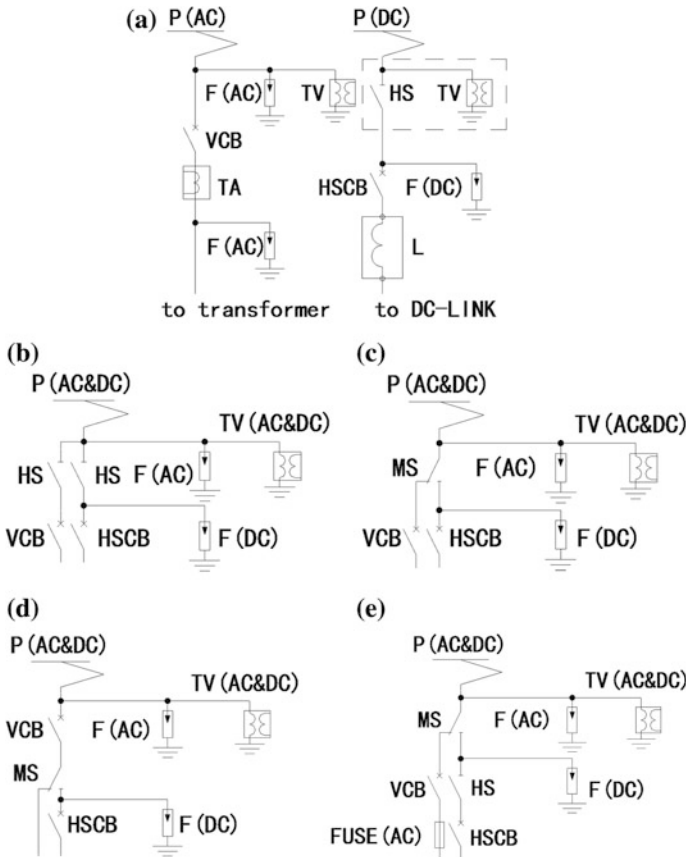


Fig. 4 Proposed main circuit proposals 1-5 (a-e)

be open before raising pantograph, and doesn't close unless input voltage is correct; In order to reduce the risk of the incorrect action of pantograph caused by the incorrect output of control signal, electric interlock is set, which guarantees two pantographs can't be raised at the same time.

Risk 2: Triggering condition is that raising the AC pantograph in DC area and VCB closing by mistake (the DC mode signals given and the voltage value is higher than the AC working lowest voltage), after the contact is closed, transformer primary side will occur short circuit, and VCB can't cut off this current.

### 4.2 The Integrated Pantograph Proposal

To optimize Factor 2, no up&down and up/down program are preferred whose switchover time is shorter. Therefore, it is necessary to integrate the current collection equipment, and the following aspects should be considered:

**Voltage:** use AC insulator to meet insulating requirement; **Gauge:** use the AC pantograph head profile which should also meet DC gauge requirement; **Current:** use two or four metal dipping contact strips and increase the diameter of the jumper wire between the components to stand the high current in DC mode; **Dynamic behaviour:** use the airbag usually used on AC pantograph as the driving element, and alternate between the corresponding static contact force by controlling the valve on the plate according to the voltage type (on-board).

EMU shown in Fig. 2 raises or lowers the pantograph in switchover process, the corresponding mode is the up/down.

Obviously, using one shared dual mode pantograph on vehicle will cause the weight of head to increase, which may deteriorate dynamic behaviour. But it is still able to guarantee some quality of current collection indexes (mean contact force and percentage of arcing) meeting criterion requirements in condition of the max speed less than 160 km/h. Therefore, it doesn't need pantographs to be connected in parallel like Fig. 2, the corresponding switchover is no up&down.

Then, let's discuss some proposals of single dual mode pantograph using on dual mode vehicle.

Factor 1: It can meet current collection requirements under the specified speed level, although it isn't the optimal one.

Factor 2: The switchover time is shortest.

The first two factors will not change in the following proposals, so no more discussion for them.

Factor 3: Because the shared pantograph is used, the main switch is set after the pantograph to switch between two loops. It becomes the key factor used to assess the following proposals, which will be analyzed in detail as below:

**Main circuit proposal 2** (hereinafter abbreviated as Main 2), as shown in Fig. 4b.

The difference between Main 1: use one shared pantographs and one shared TV (AC&DC). Add HS to isolate the loop, which is realized by the pantograph in Main 1.

Risk 1: Two HS must be open before raising pantograph, after raising, the voltage type (on-board) and the voltage type (signalling) are given to enable HS(AC and DC loop) to close. Electric interlock between two loops is set. This risk equals to Main 1.

Risk 2: The triggering condition is that the AC loop HS closes in DC power supply and VCB closes by mistake. It equals to Main 1.

**Main circuit proposal 3** (hereinafter abbreviated as Main 3), as shown in Fig. 4c.

The difference between Main 2: Two HS are integrated into one three-position contact (one input, two output) MS. It can reduce the installing room and cost.

Risk 1: MS must be on the AC position before rising pantograph. Original electric interlock is replaced by mechanical interlock. The risk is a little lower than Main 1.

Risk 2: The triggering condition is that MS is on the AC position in DC power supply and VCB closes by mistake. The risk is little higher than Main 2.

**Main circuit proposal 4** (hereinafter abbreviated as Main 4), as shown in Fig. 4d.

The difference between Main 3: VCB is moved from AC loop to main loop between MS and pantograph.

Risk 1: VCB is open in default if there is no control signal, so raising pantograph don't need to interlock with VCB status, the risk of incorrect connection is reduced obviously. MS must be in the correct position before closing VCB.

Risk 2: The triggering condition is that MS switch is on the AC position in DC input and VCB closes by mistake. The risk equals to Main 2.

New problem of high voltage devices: P (AC&DC), MS and TV (AC&DC) mentioned above are all based on reliable AC products of main line railway, and do a simple modification on them. They are reliable and economical.

But in this proposal, if VCB need to cut off the DC large current, the special design [5, 7] is required, it is still far away from the on-broad application. More difficulty is that VCB need to protect both AC and DC loop, and two mode has two different voltages, frequency and braking current, it is nearly impossible in technology. Therefore, the feasible method is that VCB works in the large DC current and HSCB brakes the DC current. Only some Japanese companies have product performance, but the technology is still in the locked status, the cost of researching and developing independently is high, considering the small quantity of products, the cost of one piece product is higher. It is very important that VCB should coordinate with HSCB during working in DC mode, and VCB will jump automatically if its control signal is cut off, it equals to VCB cut off DC current directly. The braking arc energy is very high, and VCB may explode. The system complexity of system will reduce the reliability on the contrary.

**Main circuit proposal 5** (hereinafter abbreviated as Main 5), as shown in Fig. 4e.

The difference between Main 3: add the protective equipment, HS and FUSE (AC), in AC and DC loop.

Risk 1: The risk of circuit before FUSE (AC) is same as Main 3. Add HS to reduce the loss of incorrect connection. HS will close with 3 s delay after MS switching to DC position. If AC power is connected incorrectly, which will cause F (DC) over-voltage break, and occur short circuit to earth, and breaker of power side will trip. If there is no power, HS can't close, and protect the following circuit. It is better to link the MS, HS and F (DC) by the copper bar.

Risk 2: The risk of the circuit before FUSE (AC) is same as Main 3. If the DC power connect to transformer primary side, and it will occur short circuit to earth, the FUSE (AC) is melted, so as to protect the circuit. FUSE (AC) should stand the normal working current in AC mode, and melt in short circuit to realize the protective function.



## 5 Conclusion

After the comprehensive comparison, the proposed main circuit mode 5 is the optimal and reliable. It uses shared pantograph working both in DC and AC mode and max speed is less than 160 km/h, coordinating between the quality of current collection and switchover time; it uses the three-position main switch to complete switchover between AC and DC loops, there is mechanical interlock to reduce the risk of incorrect connection; It is important to set hardware protective proposal, adding fuse over-current protection in AC loop, and adding isolating switch over-voltage protection in DC loop, which can effectively reduce the damage caused by incorrect connection, and be easy to repair. The new devices should be developed from the AC product are reliable, and have much successful applications. This proposal is reliable, stable, economic, and its safety risk is in control.

## References

1. Qian L (2015) A study on some problems of traction power supply system selection of regional rail transit. Southwest Jiaotong University, ChengDu (in Chinese)
2. EN 50388. Railway applications-power supply and rolling stock-technical criteria the coordination between power supply (substation) and rolling stock to achieve interoperability
3. Qian L (2003) The world's high-speed railway technology. China Railway Press, Beijing (in Chinese)
4. Central Reconstruction Engineering Consulting Co., Ltd. (2013) Japan subway association. Japan AC-DC switching operation and AC-DC EMU technology. Chongqing Rail Transit (Group) Co., Ltd., Chongqing. (in Chinese)
5. Jia S, Shi Z, Zhu T (2017) Investigations on high-speed actuator of vacuum DC circuit breaker. High Voltage Apparatus 57(3):12–16 (in Chinese)
6. Wang Z (2004) Power supply switching scheme for dual-current vehicle passing the pantograph neutral section. Urban Mass Transit 19(6):128–132 (in Chinese)
7. Franck CM (2011) HVDC circuit breakers: a review identifying future research needs. IEEE Trans Power Deliv 26(2):998–1007

# Synergetic Control Design of EMU Parallel Motor

Chenhao Zhang, Tao Wang, Jikun Li and Kaidan Xue

**Abstract** It is of great practical significance and wide application prospect to study the high performance multi-induction motor control strategy and control system by using advanced synergetic control theory. Combined with the principle of motor vector control and synergetic control, a parallel motor vector control system based on synergetic controller is designed. The system is more suitable for high-order, nonlinear systems than traditional vector control methods. The method not only can simplify the algorithm, but also can simplify the circuit structure, that is, to eliminate the traditional method of PI regulator, with better steady-state and dynamic performance. This paper verifies the above conclusion by stimulations in MATLAB/Simulink.

**Keywords** Parallel motor · Vector control · Synergetic control · EMU

## 1 Introduction

Due to space and cost constraints, high-speed EMU will generally use the bogie control mode, that is, a traction converter to drive the two parallel traction motor on the bogie. Under the control of the bogie, the wheel speed of the two wheels is the same, but due to friction and depreciation and other factors, there must be a difference between the two wheels, resulting in two motor speed different, and the torque is not the same. Therefore, if you do not take the appropriate control strategy, when the motor torque is greater than the adhesion torque the wheels will be idle or slippery. It will affect the passenger travel comfort, reduce the performance of high-speed EMU. Therefore, it is necessary to study the control method of asynchronous motor parallel operation mode. At present, the control of parallel motor adopts vector control method based on average rotor flux orientation [1, 2].

---

C. Zhang (✉) · T. Wang · J. Li · K. Xue  
School of Electrical Engineering, Southwest Jiaotong University (SWJTU),  
Chengdu, China  
e-mail: 798418587@qq.com

In this paper, the synergetic controller instead of the PI regulator to achieve the control of the parallel motor.

In the Sect. 2, the design of the motor synergetic controller and the design of the whole parallel motor control system is introduced. The Sect. 3 introduces the simulation results. The Sect. 4 mainly analyses the conclusion.

The parameters of CRH2 EMU are used to simulate the parameters. The simulation results show that the parallel motor vector control system with synergetic controller has good dynamic and steady state characteristics.

## 2 Synergetic Control Design of EMU Parallel Motor

### 2.1 Mathematical Description of Synergetic Control

Synergetic control is a kind of universal and very suitable control method for high-order and nonlinear systems. The nonlinear controller designed according to the synergetic control theory has good dynamic performance and steady-state characteristics [3].

The mathematical description is as follows [4–6]:

Assume the state equation of n-dimensional nonlinear system:

$$\dot{x} = f(x, u, t) \quad (1)$$

where  $x$  is the state vector,  $u$  is the control variable,  $t$  is the time, and  $f$  is the non-linear function.

First select the macro variable that defines the controlled system. A macro variable consisting of a system state variable that can be expressed as:

$$\Psi = \Psi(x, t) \quad (2)$$

The goal of synergetic control is to make the system converge in a finite time and remain at the manifold  $\Psi = 0$ :

$$\Psi = \Psi(x, t) = 0 \quad (3)$$

After defining the macro variable, the control variables of the system can be solved according to the expected manifold dynamic equation. The expected dynamic equation of the manifold is as follows:

$$T\dot{\Psi} + \Psi = 0, T > 0 \quad (4)$$

Derived according to the above formula:

$$T \frac{d\Psi}{dx} f(x, u, t) + \Psi = 0 \quad (5)$$

## 2.2 Design of Induction Motor Synergetic Controller

Combined with the state equation of the induction motor and the theory of synergetic control, set  $x_1 = \omega_r$ ,  $x_2 = \psi_{rd}$ ,  $x_3 = \psi_{rq}$ ,  $x_4 = i_{sd}$ ,  $x_5 = i_{sq}$ :

$$\begin{aligned}
 \dot{x}_1 &= \frac{n_p^2 L_m}{J L_r} (x_2 x_5 - x_3 x_4) - \frac{n_p}{J} T_L \\
 \dot{x}_2 &= -\frac{1}{T_r} x_2 + \omega_{sl} x_3 + \frac{L_m}{T_r} x_4 \\
 \dot{x}_3 &= -\frac{1}{T_r} x_3 - \omega_{sl} x_2 + \frac{L_m}{T_r} x_5 \\
 \dot{x}_4 &= \frac{L_m}{\sigma L_s L_r T_r} x_2 + \frac{L_m}{\sigma L_s L_r} \omega_r x_3 - \frac{R_s L_r^2 + R_r L_m^2}{\sigma L_s L_r^2} x_4 + \omega_s x_5 + \frac{u_{sd}}{\sigma L_s} \\
 \dot{x}_5 &= \frac{L_m}{\sigma L_s L_r T_r} x_3 - \frac{L_m}{\sigma L_s L_r} x_1 x_2 - \frac{R_s L_r^2 + R_r L_m^2}{\sigma L_s L_r^2} x_5 - \omega_s x_4 + \frac{u_{sq}}{\sigma L_s} \\
 \sigma &= 1 - \frac{L_m^2}{L_s L_r} \quad T_r = \frac{L_r}{R_r}
 \end{aligned} \tag{6}$$

where

- $R_s$  stator resistance
- $L_s$  stator self-inductance
- $R_r$  rotor resistance
- $L_r$  rotor self-inductance
- $L_m$  mutual inductance
- $n_p$  pole pairs
- $\omega_s$  rotor frequency
- $\omega_r$  rotor frequency

Combined with the design steps of the synergetic controller, the principle of the three-phase asynchronous motor and the equation of state, we select the stator current  $x_4 = i_{sd}$ ,  $x_5 = i_{sq}$  as the control variable and select two macro variables as follows:

$$\begin{cases} \Psi_1 = x_1 - x_{1ref} \\ \Psi_2 = x_2 - x_{2ref} \end{cases} \tag{7}$$

The purpose of synergetic control is to stabilize the macro variables in the system at  $\Psi = \Psi(x, t) = 0$ , which is a invariant manifold:

$$\begin{cases} T_1 \dot{\Psi}_1 + \Psi_1 = T_1 \dot{x}_1 + (x_1 - x_{1ref}) = 0 \\ T_2 \dot{\Psi}_2 + \Psi_2 = T_2 \dot{x}_2 + (x_2 - x_{2ref}) = 0 \end{cases} \tag{8}$$

Combine Eq. (6), we obtain:

$$\begin{cases} T_1 \left( \frac{n_p^2 L_m}{J L_r} (x_2 x_5 - x_3 x_4) - \frac{n_p}{J} T_L \right) + (x_1 - x_{1ref}) = 0 \\ T_2 \left( -\frac{1}{T_r} x_2 + \omega_{sl} x_3 + \frac{L_m}{T_r} x_4 \right) + (x_2 - x_{2ref}) = 0 \end{cases} \quad (9)$$

Solve the Eq. (9), the control variables are:

$$\begin{cases} i_{sd} = \frac{L_r}{L_m R_r} \left( \frac{\psi_{rdref} - \psi_{rd}}{T_2} + \frac{\psi_{rd}}{T_r} \right) \\ i_{sq} = \frac{J L_r}{n_p^2 L_m \psi_{rd}} \left( \frac{\omega_{rref} - \omega_r}{T_1} + \frac{n_p}{J} T_L \right) \end{cases} \quad (10)$$

### 2.3 Simulation of Circuit Diagrams and Parameters

Simulation of the circuit as shown in Fig. 1. In order to make the system gets good performance, the control of the current using the CHBPWM (Current Hysteresis Band PWM) control method. And the motor parameters using CRH2 EMU parameters for simulation (Table 1).

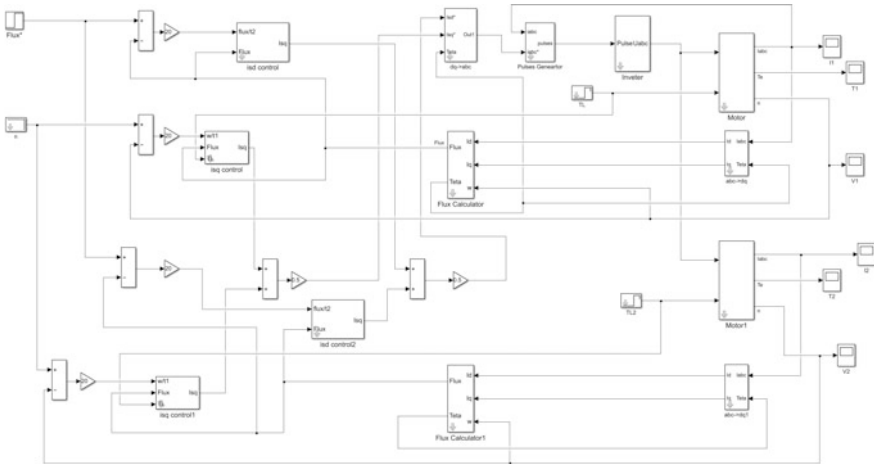


Fig. 1 Simulation circuit diagram in MATLAB

Table 1 CRH2 EMU motor parameters

Stator resistance $R_s(\Omega)$	0.144
Stator self-inductance $L_s(H)$	0.034265
Stator resistance $R_r(\Omega)$	0.146
stator self-inductance $L_r(H)$	0.034142
Mutual inductance $L_m(H)$	0.032848
Pole pairs $n_p$	2

### 3 Simulation Results

We set the experimental simulation conditions as shown in the Tables 2 and 3, the simulation results shown in the Figs. 2 and 3.

Combined with the conclusion of the relevant literature, this paper compares the performance of the synergetic controller with the PI regulator in the parallel motor control system [7], as shown in the following (Table 4).

**Table 2** Simulation conditions when load torque is balanced

Time	0–0.5 s	0.5–1 s	1–1.5 s	1.5–2 s
Motor 1 torque (N·m)	0	0	450	300
Motor 1 rotating speed (rpm)	1500	1000	1000	1000
Motor 2 torque (N·m)	0	0	450	300
Motor 2 rotating speed (rpm)	1500	1000	1000	1000

**Table 3** Simulation conditions when load torque is unbalanced

Time	0–0.5 s	0.5–1 s	1–1.5 s	1.5–2 s
Motor 1 torque (N·m)	0	0	400	350
Motor 1 rotating speed (rpm)	1500	1000	1000	1000
Motor 2 torque (N·m)	0	0	350	350
Motor 2 rotating speed (rpm)	1500	1000	1000	1000

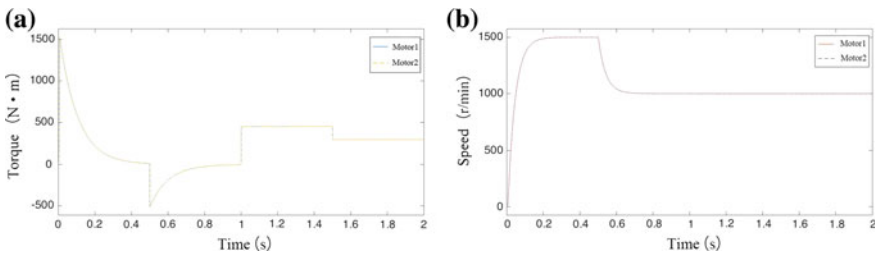


**Fig. 2** Torque and speed waveform of the motor when the load torque is balanced

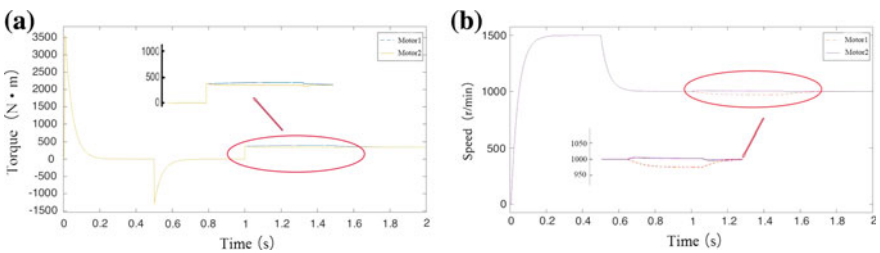


**Fig. 3** Torque and speed waveform of the motor when the load torque is unbalanced

**Table 4** Error comparison of two control methods for parallel motor torque unbalance

Error Method	Maximum speed error (n/min)	Steady state speed error (n/min)	Maximum torque error (N·m)	Steady state torque error (N·m)
PI regulator	75	5–10	100	0–5
Synergetic controller	30	0	50	0

## 4 Conclusions

As it is shown in the output waveform diagram, when the parallel motor load torque is balanced, the actual value of the output coincides well with the given value, and there is no difference between the two motor data. The above results prove the method can achieve good control of torque and speed. When the load torque is not balanced, it can be seen from the waveform diagram that the output torque of the two motors is very close to the given value. It can be seen that the parallel motor system under the synergetic control can stabilize the operation of the two motors when the torque change quickly, and the speed is not much different from the given value, which shows that the synergetic control is an effective method for EMU parallel motor.

**Acknowledgements** This work is supported by National Natural Science Foundation (NNSF) of China under Grant 51477146.

## References

1. Wang R, Wang Y, Dong Q, He Y, Wang Z (2006) Study of control methodology for single inverter parallel connected dual induction motors based on the dynamic model. In: 37th IEEE power electronics specialists conference, Jeju, pp 1–7
2. Fei X, S L, Li Y (2013) The weighted vector control of speed irrelevant dual induction motors fed by the single inverter. *IEEE Trans Power Electron* 28(12):5665–5672
3. Niu M, Wang T, Zhang Q, He X, Zhao M (2016) A new speed control method of induction motor. In: 35th Chinese control conference (CCC), Chengdu, pp 10140–10143
4. Son T-D, Heo T-W, Santi E, Monti A (2004) Synergetic control approach for induction motor speed control. In: 30th annual conference of IEEE industrial electronics society, IECON 2004, pp 883–887
5. Kolesnikov, Veselov G (2000) Modern applied control theory: synergetic approach in control theory. Tsure Press, Moscow-Taganrog, Russia
6. Knyazeva H (1998) What is synergetic? *Indian Sci Cruiser* 12(1):17–23
7. Li W, Hu A, Nie Z (2006) The simulation research on vector control of parallel-connected induction motors. *J Electric Mach Control* 01:102–106 (in Chinese)

# Research on Thermal Management System of Lithium Iron Phosphate Battery Based on Water Cooling System

Liye Wang, Lifang Wang, Yuan Yue and Yuwang Zhang

**Abstract** This paper analyzes the heat generation mechanism of lithium iron phosphate battery. The simulation and analysis of the battery thermal management system using water cooling is carried out. A cooling plate model in the thermal management system of water cooled battery was established. According to the simulation results of the cooling plate, Designed and developed a water cooled battery thermal management system. The experimental results show that the water cooling system has a better cooling effect, which can reduce the temperature gradient inside the battery box. All batteries are working in a stable environment, which is conducive to maintaining the consistency of the battery pack.

**Keywords** Lithium iron phosphate battery · Battery thermal management Temperature · Simulation

## 1 Introduction

In order to meet the needs of electric vehicle power in the process of using, the battery has been seried connection for battery pack, battery chemical reaction will bring high heat load to the battery pack when more than 100 batteries in use [1]. when the vehicle driving process, if the heat has not been in a timely manner to take away, it will certainly affect the working performance of battery life, and may even bring great danger to traffic safety, and the low temperature properties of lithium iron phosphate battery is poor. how to make the battery can work in low temperature environment is a very challenging problem [2–5]. This also makes the battery thermal management system become an integral part of electric vehicles.

---

L. Wang (✉) · L. Wang · Y. Zhang  
Key Laboratory of Power Electronics and Electric Drive, Institute  
of Electrical Engineering, Chinese Academy of Sciences, Beijing, China  
e-mail: wangliye@mail.iee.ac.cn

Y. Yue  
School of Electrical Engineering & Automation, Tianjin University, Tianjin, China

© Springer Nature Singapore Pte Ltd. 2018

L. Jia et al. (eds.), *Proceedings of the 3rd International Conference on Electrical and Information Technologies for Rail Transportation (EITRT) 2017*, Lecture Notes in Electrical Engineering 482, [https://doi.org/10.1007/978-981-10-7986-3\\_36](https://doi.org/10.1007/978-981-10-7986-3_36)



The battery thermal management system mainly involves two aspects: ① Ensure that the battery is in the optimum operating temperature range (generally from 20 to 50 °C), ② Ensure that the temperature gradient between the batteries is as low as possible (generally less than 2 °C). An ideal battery should work in a temperature range that allows the battery's performance and life to reach its optimum performance [6, 7]; In addition, the uniformity of temperature and the uneven temperature will have a serious impact on the performance of the battery. Mainly due to the uneven temperature between the battery units, which will lead to different charging and discharging behavior, and then affect the balance between the battery cells, and ultimately will reduce the battery life [8–10].

## 2 Heat Generation Mechanism of Lithium Ion Batteries

Lithium ion batteries can absorb and release heat during charge and discharge, the heat is mainly composed of the following parts: reaction heat, polarization heat, Joule heat and side reaction heat. the side reaction heat for lithium ion batteries in the proportion is very small, generally not be considered.

The energy emitted in the electrochemical reaction of the battery can be expressed by Gibbs free energy:

$$\Delta G = \Delta H - T \cdot \Delta S \quad (1)$$

$\Delta G$  is Gibbs free energy change,  $\Delta H$  is Enthalpy change for battery reaction,  $T$  is Absolute temperature,  $\Delta S$  is Entropy change in the reaction of a battery. In formula (1),  $T \cdot \Delta S$  the amount of heat corresponding to the electrochemical reaction in the battery can be expressed in the form of reactive heat  $Q_r$ :

$$Q_r = T \cdot \Delta S = T \left( -\frac{\partial \Delta G}{\partial T} \right) \quad (2)$$

Under the condition of constant temperature and pressure, when the system changes, the reduction of Gibbs free energy of the system is equal to the maximum non expansion work done outside, and if the non expansion work is only the electricity work, then:

$$\Delta G = -nFE_e \quad (3)$$

$n$  is the stoichiometric coefficient of the electron in the oxidation or reduction of the electrode,  $F$  is Faraday constant  $96485.3383 \pm 0.0083$  C/mol,  $E_e$  is Electromotive force for batteries. Based on (2) and (3) can be obtained:

$$Q_r = nFT \left( \frac{\partial E_e}{\partial T} \right) \tag{4}$$

The internal battery polarization exist at the same time, accompanied by the polarization of the reaction heat, it is heat loss due to battery polarization. the polarization will cause the battery to the actual voltage deviates from its theoretical electromotive force, because of the electrochemical reaction of atomic diffusion and movement need energy. The polarization reaction heat pe-unit time of a battery during charging and discharging can be indicated as follows:

$$Q_{pd} = I_d^2 R_{pd} = I_d^2 (R_{td} - R_e) \tag{5}$$

$$Q_{pc} = I_c^2 R_{pc} = I_c^2 (R_{tc} - R_e) \tag{6}$$

$Q_{pd}$  and  $Q_{pc}$  is polarization heat per unit time when the battery is discharged and charged,  $I_d$  and  $I_c$  is current for battery discharge and charging,  $R_{pd}$  and  $R_{pc}$  is the polarization internal resistance respectively when the battery is discharged and charged,  $R_{td}$  and  $R_{tc}$  is the total internal resistance when the battery is discharged and charged,  $R_e$  is The resistance inside the battery.

The heat generated by the current flowing through the battery’s internal resistance is called Joule heat, and the Joule heat per-unit time of the charge and discharge of the battery can be expressed as follows:

$$Q_J = I_d^2 R_e \tag{7}$$

$$Q_J = I_c^2 R_e \tag{8}$$

### 3 Simulation of Cooling Plate Structure of Water Cooled Battery Thermal Management System

In this paper, the simulation model of cooling plate is established in the pre-processing software Gambit, and Fig. 1 is the geometric model of the cooling plate, in which the diameter of the copper tube inside the cooling plate is 6 mm, and the vertical distance between the pipes is 20 mm. Because the cooling liquid flow along the inner wall of the copper pipe, copper mesh quality will directly affect the convergence speed and the precision of the results of the simulation, in the grid, using all hexahedral mesh division of the structure.

Use the software Fluent to simulation of transient simulation of cooling plate, the speed of entrance and outlet pressure boundary conditions, the flow is always 4.5 L/min entrance, entrance temperature is 283 K, temperature 308 K, heat flow generated by the cooling plate on both sides of the battery discharge is  $500 \text{ Wm}^{-2}$ ,

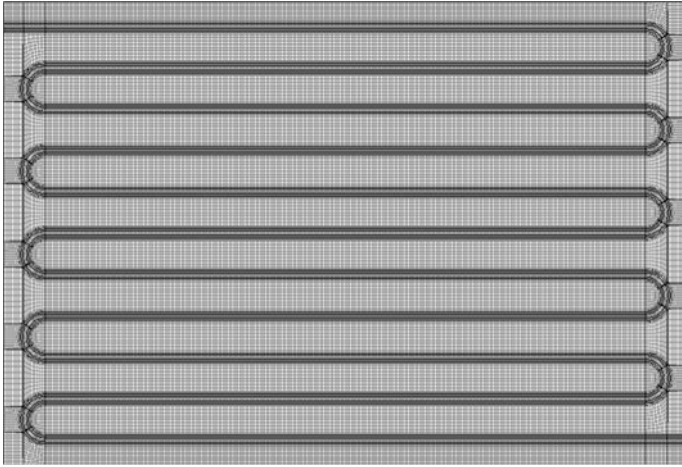


**Fig. 1** Geometric model of heating plate and grid

using RNG turbulence model to simulate the vortex tube. Application of PISO algorithm to solve the pressure and velocity coupling problem, the time step is 0.002 s, calculate the 10,000 step (20 s), single iteration times up to 50 times. The maximum, minimum, mean temperature and standard deviation of temperature are monitored in simulation. When the residuals converge below  $10 e^{-6}$ , the monitoring parameters are stable and the difference between the inlet and outlet mass flow rates is less than 1/10 of the minimum residuals, the calculation convergence is considered.

As shown in Fig. 2, the cloud chart shown on the left shows the simulation results with vertical distance of 20 mm, and the result on the right is 30 mm. It can

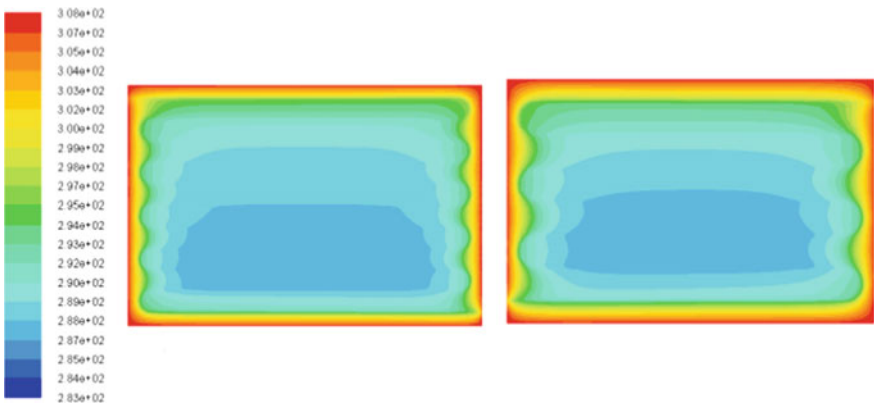


**Fig. 2** Simulation results of vertical distance of different pipes are compared with the diameter of 6 mm (left: 20 mm, right: 30 mm)

be seen that the lowest temperature occurs in the middle and lower parts of the cooling plate, which is mainly caused by the entry of coolant from the bottom of the cooling plate. the temperature range is slightly larger than the left image right, the cooling effect is slightly better than the latter; because in the simulation, the entrance flow is a fixed value, when the diameter is larger, although the total volume of the cooling liquid is increased, but the entrance rate is reduced, thus affecting the convective heat transfer ability of the cooling liquid, when the diameter is small, it will have better cooling effect.

To measure the cooling effect of cooling plate not only depends on the minimum temperature, more important is the cooling plate surface average temperature and temperature gradient, the average temperature can reflect the comprehensive effect of cooling plate, and the temperature gradient will directly affect the battery life. Figure 3 show the standard cooling plate surface temperature difference of the above two kinds of structure, it is obvious that when the pipe vertical distance is small, the temperature standard deviation is smaller 5.25 K, and when the vertical distance is large, the temperature standard deviation is 5.86 K. Obviously, from the point of view of temperature gradient, the optimal cooling structure obtained by

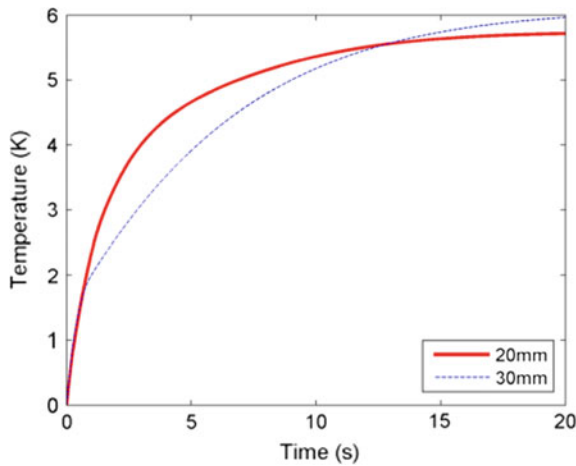


**Fig. 3** Comparison of the standard deviation of the surface temperature of the cooling plate with different pipe distance

**Table 1** Average temperature and temperature difference of cooling plate surface under different geometrical structure

Structure	4/20 mm	4/30 mm	6/20 mm	6/30 mm	8/20 mm	8/30 mm
Average temperature (K)	291.3	291.3	292.2	292.8	293.1	293.5
Standard deviation of temperature (K)	5.25	5.86	5.72	5.97	6.02	6.21
Heat transfer rate (W)	2652	2042	2627	2238	2683	2192

qualitative analysis of cloud images is not optimal. As shown in Table 1, in the same diameter under the condition when the vertical distance between the pipeline and the average temperature difference is not obvious, but the vertical distance is, the temperature of the standard deviation is greater, indicating that the system can provide the external flow and pressure reduction, small diameter can improve the velocity. In order to obtain better cooling effect.

The above data and comprehensive analysis, taking into account the brass in national standard GB-T1803-2007 the smallest diameter 6 mm, the cooling system in the actual selection of diameter 6 mm tube, vertical distance between channels is still 20 mm.

## 4 Water Cooled Battery Thermal Management System

The structure of a water-cooled battery thermal management system is shown in Fig. 4 The size of the battery is consistent with the thermal management system of the water cooled battery. The twelve batteries form a battery module and are divided into three rows in the battery case. On both sides of the cooling plate of each row of the battery core, cooling plate is U type pipe, the pipe size and arrangement based on the simulation results, the pipeline on each side of a coin, so that they are connected with each other by brazing, the cooling liquid flows from the bottom of the right side of the pipeline, the pipeline flow from the upper left side. In order to ensure the uniform surface temperature of each cooling plate, the import and export of cooling liquid in the battery module on both sides. The tube of the battery case is composed of a short copper tube, a three pass joint and a two pass joint, and the structure is convenient for the expansion and assembly of the battery module.

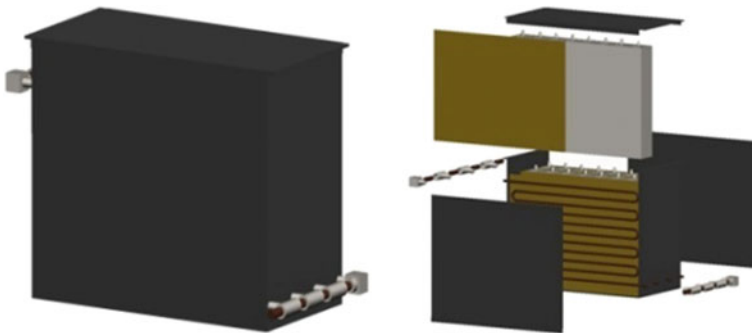


**Fig. 4** The mechanical structure of the battery thermal management system

## 5 Experimental Research on Cooling Effect of Battery Thermal Management System

The installation position of the temperature sensor battery thermal management system is shown in Fig. 5, the charging and discharging experiments of different magnification of twelve pieces of lithium iron phosphate battery: 20A or 40A charging, discharge and discharge of 60A or 40A. Comparing the temperature of the battery surface when the water cooling system is switched on and off (only by the natural convection between the tank and the air). The temperature sensor is a digital temperature sensor DS18B20, with an accuracy of 0.5 °C. In addition, because of the poor consistency of the twelve batteries, in order to prevent excessive charge and discharge, the voltage of any single battery reaches the threshold of charging and discharging (charging 3.65 V, discharging 2.5 V).

Figure 6a, b are the temperature contrast of battery charge at 40A and discharge at 40A, thin lines for liquid cooling when the temperature change curve, coarse dashed line temperature changes the liquid cooling, the temperature sensor accuracy is only 0.5 °C, the temperature curves are ladder. In addition, because the temperature rise of the battery surface is approximately linear, in order to compare the temperature changes of the water cooling system when it is turned on and off, the starting point of the temperature curve is moved to 15 °C.

As shown in Fig. 6a, the temperature changes in the battery box when charging at 40A. When the water cooling system is closed, the starting temperature of 40A charging is 17 °C, and the charging starting temperature of the water cooling system is 16 °C. Similar to the 20A charging test, the electric water pump is switched on to cool the battery box twenty minutes before the charging stop. It can

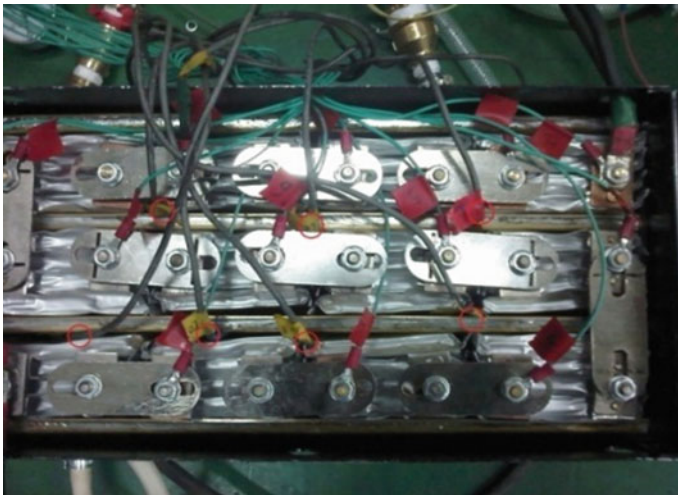
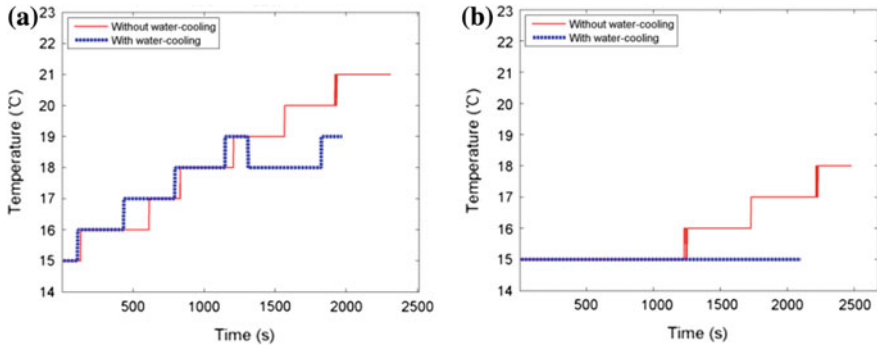


Fig. 5 Installation position of temperature sensor



**Fig. 6** Comparison of temperature variation during 40A charge and 40A discharge

be seen from the figure, when the battery 40A charging the cooling system makes the surface temperature of the battery, but also reduces the rate of temperature rise.

As the 40A discharge and charging process, the battery heat generation rate is not the same, in order to make the experiment itself more meaningful, in the process of 40A discharge, the electric water pump has been switched on to cool the battery. When the water cooling system is on and off, the battery surface temperature is 32 and 27 °C at the beginning of the discharge. Can be seen from Fig. 6b, in the water cooling system is turned on, the battery surface temperature is kept constant until the discharge stop. After adding the water cooling system, the temperature distribution inside the battery box is more balance.

## 6 Conclusion

Based on the above analysis, the battery thermal management system of water cooling and the cooling effect is good, especially in the 40A charge and discharge is more obvious, and it can reduce the temperature gradient inside of the battery case, the batteries are all working in a stable environment, conducive to maintain consistency of battery pack, and water cooling system need the cooling liquid in the heat dissipated in time to ensure the cooling effect, in actual use, can be installed in the water tank to strengthen fan forced convection on the surface of the box body heat, which can effectively reduce the cooling liquid to reach the purpose of temperature.

**Acknowledgements** This study is sponsored by the National Key Research and Development Program of China (2016YFB0101800), National Science Foundation program of China (51677183), Science and Technology Program of SGCC (Operation Safety and Interconnection Technology for Electric Infrastructure).

## References

1. Wei C, Zheng L, Cai X, Wei X (2016) Variable step-size control method of large capacity battery energy storage system based on the life model. *Trans China Electrotechnical Soc* 31(14):58–66. (in Chinese)
2. Zhaobin D, Zeng C, Lin G, Yunhua X, Ping H, Yaopeng H (2015) Energy-storage battery optimal configuration of mobile power source for power supply ensuring of users. *Trans China Electrotechnical Soc* 30(24):215–221. (in Chinese)
3. Ze C, Mengnan D, Tiankai Y, Lijie H (2014) Extraction of solar cell model parameters based on self-adaptive chaos particle swarm optimization algorithm. *Trans China Electrotechnical Soc* 29(9):245–252. (in Chinese)
4. Cao S, Song C, Lin X, Xia Y (2014) Study of PCS's control strategy for battery energy storage grid-connected system. *Power Syst Protection Control* V42(24):93–98. (in Chinese)
5. Sang B, Tao Y, Zheng G, Hu J, Yu B (2014) Research on topology and control strategy of the super-capacitor and battery hybrid energy storage. *Power Syst Protection Control* V42(2):1–6. (in Chinese)
6. Wang W, Xue J, Ye J et al (2014) An optimization control design of battery energy storage based on SOC for leveling off the PV power fluctuation. *Power Syst Protection Control* V42(2):75–80. (in Chinese)
7. Guo G et al (2010) Three-dimensional thermal finite element modeling of lithium-ion battery in thermal abuse application. *J Power Sources* 195:2393–2398
8. Cheng L, Ke C, Fengchun S (2009) Research on thermo-physical properties identification and thermal analysis of EV Lithium-ion battery. In: *Vehicle power and propulsion conference, VPPC'09, IEEE*
9. Yang K, Li DH, Chen S, Wu F (2009) Thermal behavior of nickel/metal hydride battery during charging and discharge. *J Thermal Anal Calorimetry* 95(2):455–459
10. Battery test manual for plug-in hybrid electric vehicles. U.S. Department of Energy, Idaho National Laboratory, pp 5–9



# Performance Comparison of Battery Chargers Based on SiC-MOSFET and Si-IGBT for Railway Vehicles

Yun Kang, Zhipo Ji, Chun Yang, Ruichang Qiu and Xuefu Cao

**Abstract** New type semiconductors, for instance, SiC-based switching devices, have many performance advantages over Si-based devices, including faster switching and lower power dissipation. In this paper, a research of an application of SiC-based MOSFET in a battery charger for railway vehicles is introduced, focusing on the performances of the charger. This battery charger is designed based on a silicon-IGBT-based charger. The new SiC-based battery charger has the same input and output rating with the original charger, but there's an increase of switching frequency from 15 to 50 kHz. Therefore, a comparison between the two chargers from the aspects of efficiency, volume and power density is provided in this paper. It can provide some technical support for the design and application of high-power-density battery chargers in the auxiliary power system of railway vehicles.

**Keywords** SiC · Auxiliary power system · Battery charger · Performance comparison

## 1 Introduction

The main function of a battery charger in auxiliary power system is to supply power for loads that work at 110 V DC, and to charge the battery, which would work as the power source for the loads when the vehicle is separated from the overhead lines. The main part of a battery charger is a high-frequency isolated DC/DC

---

Y. Kang (✉) · R. Qiu · X. Cao

Beijing Engineering Research Center of Electric Rail Transportation, School of Electrical Engineering, Beijing Jiaotong University, Beijing 100044, China  
e-mail: 16121468@bjtu.edu.cn

Z. Ji

Beijing Spacecrafts, Beijing, China

C. Yang

Wuhan Zhongyuan Electronics Group Co., LTD., Wuhan, Hubei, China

© Springer Nature Singapore Pte Ltd. 2018

L. Jia et al. (eds.), *Proceedings of the 3rd International Conference on Electrical and Information Technologies for Rail Transportation (EITRT) 2017*, Lecture Notes in Electrical Engineering 482, [https://doi.org/10.1007/978-981-10-7986-3\\_37](https://doi.org/10.1007/978-981-10-7986-3_37)

converter, thus the application of new type wide-bandgap semiconductors in the converter of a battery charger is one of the hotspots in current study, as well as the application of soft-switching technology. Represented by silicon carbide and gallium nitride, new types of semiconductors have characteristics of wide bandgap, high critical breakdown electric field, high thermal conductivity, small dielectric constant, high saturation drift speed and other prominent advantages [1], attracting researchers' attention.

Compared with Si IGBT, SiC MOSFET has a lower threshold voltage, lower parasitic capacitance, shorter turn-on and turn-off time [2]. In addition, the reverse recovery current from the body diode of SiC MOSFET as well as turn-off tail current is zero [3]. As a result, the reverse recovery loss can be neglected, thus the efficiency, switching frequency, and reliability of the system can be improved.

## 2 The Design of the Charger Using SiC MOSFET

In this paper, the topology of the SiC-MOSFET-based battery charger is designed as Fig. 1. It consists of a precharge circuit, a three-phase rectifier circuit, a high-frequency full-bridge DC/DC converter and an output filter circuit. The pre-charge circuit is to avoid a high instantaneous voltage change if the equipment was put into operation with an initial input of zero voltage [4]. This voltage change may cause system protection to go wrong.

The rated output power of the charger is designed to be 15 kW, and the DC voltage peak after the rectification of input is 618 V, and the maximum current in MOSFETs is 45.8 A after calculation. Taking the margin into account, the CREE 1200 V/120 A SiC MOSFET half-bridge module is chosen in this design.

Because of the use of SiC MOSFET which has the advantage of fast switching, low switching loss and zero reverse recovery loss, the disadvantage of the bipolar control strategy that it leads to higher switching loss can be made up. Therefore, there's no need to adopt other complex control strategies, and the simplest bipolar control strategy is used in this paper for experiment [5].

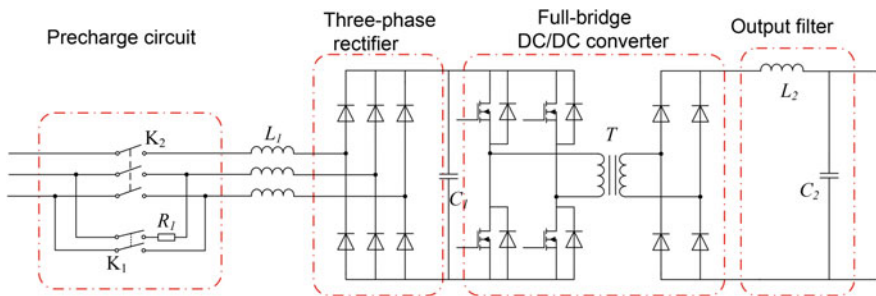


**Fig. 1** The topology of the SiC-based charger

The main processor of the control system is DSP TMS320F28335 which can easily implement the control function. Ideally speaking, the duty of drive pulses can be modified from 0 to 0.5. However, dead time should be considered because of the turn-on and turn-off delay time of switching devices and the delay time error between the two sets of drive pulses. The maximum of duty is determined to be 0.44 at last.

### 3 Comparison Between the SiC Charger and the Si Charger

The SiC-based charger is designed based on the original Si-based charger, so the topologies, control units and basic demands of the both are the same. The differences between the chargers are component parameters. Table 1 gives a comparison of parameters of the two chargers.

#### 3.1 Efficiency Comparison of the Two Chargers

Si IGBT modules used in the Si-based charger are the Infineon FF150R12KE3G. According to the datasheets, parameters for loss calculation are listed as Table 2.

Assuming the current in IGBTs or MOSFETs keeps constant when these devices are in the on state, the loss in a cycle can be calculated as the Eq. (1) [6, 7].

$$\left\{ \begin{array}{l} P_{IGBT.on(loss)} = V_{CES}I_{CE}D \\ P_{MOSFET.on(loss)} = R_{DS(on)}I_{DS}^2D \\ P_{off(loss)} = I_{CES}U_{avg}(1 - D) \\ P_{drive(loss)} = f_sQ_gV_{gs} \\ P_{switch(loss)} = f_s(E_{on} + E_{off}) \\ P_{s\_loss} = P_{on(loss)} + P_{off(loss)} + P_{switch(loss)} + P_{drive(loss)} \end{array} \right. \quad (1)$$

**Table 1** Charger parameter table

	SiC-based charger	Si-based charger
Rated output power (kW)	15	15
Rated input power (V)	380 AC	380 AC
Rated output voltage (V)	110	110
Switching frequency (kHz)	50	15
Filter inductance (μH)	15	50
Filter capacitance (μF)	100	200

**Table 2** Loss calculation parameter table

	FF150R12ME3G	CAS120M12BM2
On-resistance $R_{ds(on)}$ ( $\Omega$ )	–	0.013
Collector-emitter saturation voltage $V_{CES}$ (V)	1.7	–
Collector-emitter current $I_{CES}$ or drain current $I_{DSS}$ (A)	0.005	0.0008
Turn-on energy loss $E_{on}$ (J)	0.005	0.0023
Turn-off energy loss $E_{off}$ (J)	0.009	0.001

In these equations,  $I_{CE}$  and  $I_{DS}$  are average current in IGBTs or MOSFETs when they are in the on state, and  $U_{avg}$  is the DC output of the three-phase rectifier. Losses of a single SiC MOSFET or Si IGBT at different operating frequencies at full load are shown in Fig. 2.

From Fig. 2 we can see that the loss of Si IGBTs is much higher than the loss of SiC MOSFETs at the same working frequency. Even when SiC MOSFETs work at 50 kHz, the loss is two thirds of the loss of Si IGBTs at 20 kHz. The theoretical losses of the chargers are shown in Table 3, indicating that the efficiency of the SiC-based charger is 1.79% higher than the Si-based charger. The increase in switching frequency causes losses of other components to alter. The secondary-side rectifier diode loss is increased by one more times, while the filter inductor loss and the transformer loss are reduced by almost 2/3.

Put in 38% of full load, 65% of full load and full load respectively to perform power loss experiments. Input power and output waveforms are recorded as Fig. 3. According to the records, the SiC-based charger efficiency at different loads can be summarized as Table 4.

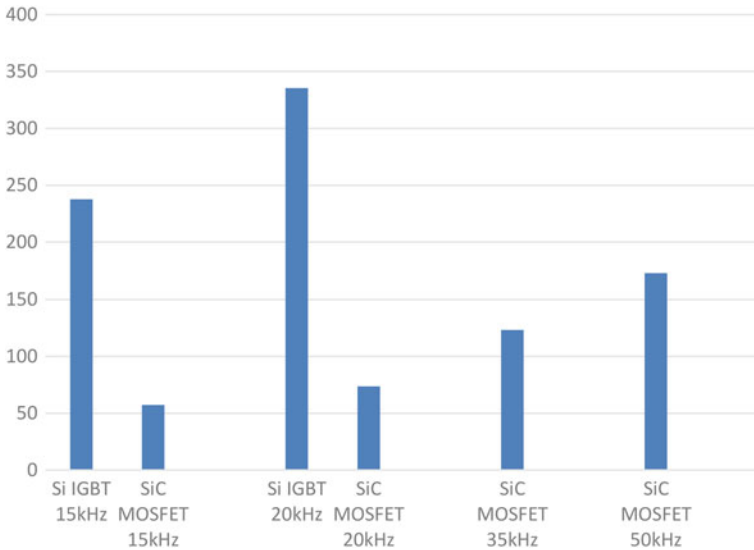


**Fig. 2** Switching device loss comparison at full load

**Table 3** Comparison of main device loss of the chargers (theoretical)

Loss (W)	SiC charger (50 kHz)	Si charger (15 kHz)
Three-phase filter inductors	20	20
Three-phase rectifier	36.88	36.88
Input capacitors	3.19	3.19
Main switching devices	690.99	950.72
Transformer	25	80
Secondary-side rectifier	95.9	45.9
Filter inductors	10	34
Filter capacitors	5.27	3.14
Total	887.23	1173.83
Efficiency	94.42%	92.74%

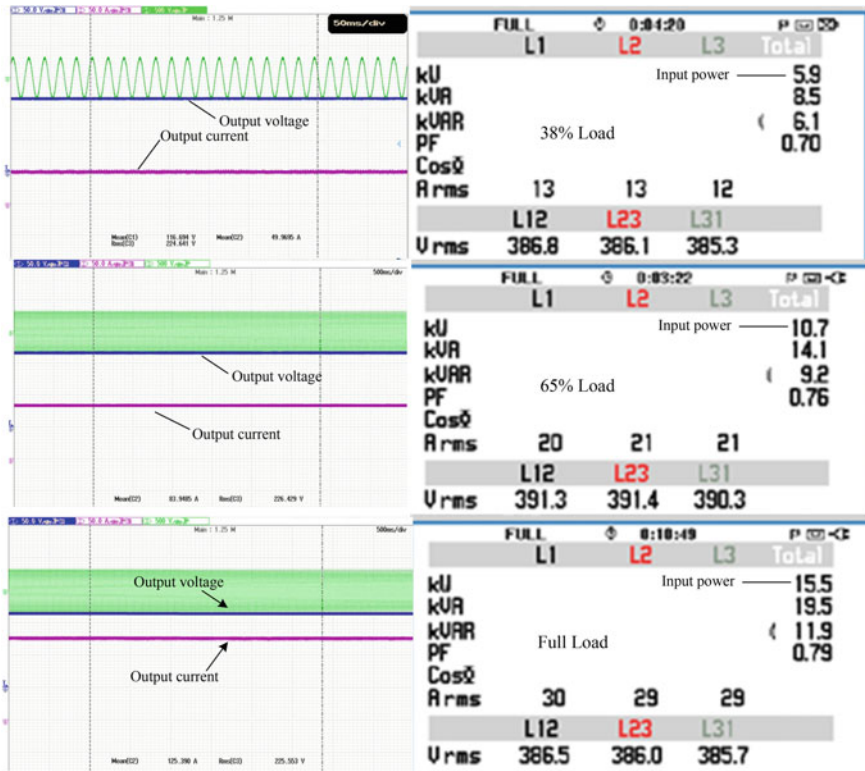


**Fig. 3** SiC-based charger power loss experiment records

**Table 4** SiC MOSFET charger efficiency table

Load	Input power (kW)	Output power (kW)	Efficiency (%)
38%	5.9	5.38	91.14
65%	10.7	9.96	93.12
Full	15.5	14.58	94.05

The Si-based charger power loss in different loads can be experimented in the same way as the SiC-based charger, and the comparison of efficiency of the two chargers is shown in Table 5.

According to Table 5, the practical efficiency of Si-based charger is lower than the theoretical efficiency by 0.31%, while the practical efficiency of SiC-based charger is lower than the theoretical one by 0.37%. The SiC-based charger has higher efficiency than the Si-based charger from low load to full load, and it's higher by 1.75% at full load, which is coincident with the theoretical analysis in general.

### 3.2 Power Density and Volume Comparison of the Chargers

The high-frequency isolated transformer and the filter circuit takes up a big part of the charger in volume and weight. Their weight is proportional to the volume approximately, thus a reduction in volume makes a decrease in weight. The application of SiC power devices achieves an increase of switching frequency that reduce the volume and weight of the main passive components such as the transformer, inductors and capacitors [8].

Figure 4 is a shape comparison of real transformers in these chargers. The red transformer used in the Si-based charger is almost twice as much in volume as the yellow transformer used in the SiC-based charger. Table 6 is a volume table of the two chargers.

According to Table 6, the increase of switching frequency leads to the reduction of the volume of magnetic components and capacitors by 33.4%, and the reduction of total volume by 29.4%, indicating that the power density increases by 41.6%. It's obvious that the application of SiC MOSFETs in the battery charger provides higher power density.

**Table 5** SiC/Si charger efficiency comparison table

Load	SiC charger efficiency (50 kHz) (%)	Si charger efficiency (15 kHz) (%)
38%	91.14	90.05
65%	93.12	91.92
Full	94.05	92.43

**Fig. 4** The transformers shape comparison between SiC and Si charger

The transformer in the Si-based charger

The transformer in the SiC-based charger

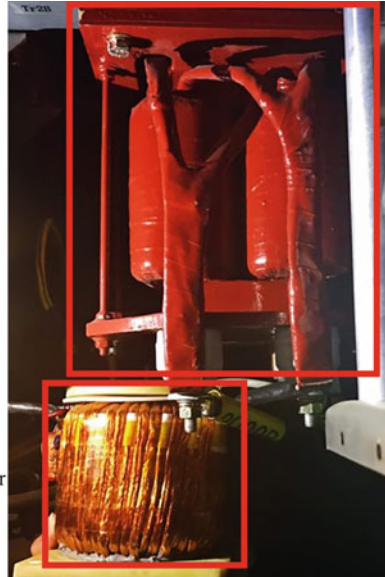


**Table 6** Components volume comparison table

Components	SiC charger	Si charger
Three-phase filter inductors (dm <sup>3</sup> )	5.7	5.7
Rectifier diode modules (dm <sup>3</sup> )	0.096*5	0.096*5
DC-side capacitors (dm <sup>3</sup> )	0.88	0.88
Main switching modules (dm <sup>3</sup> )	0.2*2	0.2*2
The heat sink (dm <sup>3</sup> )	2.27	2.27
High-frequency transformer (dm <sup>3</sup> )	4.2	9.2
Filter inductors (dm <sup>3</sup> )	4.6	7.2
Filter capacitors (dm <sup>3</sup> )	0.22	0.44
Total (dm <sup>3</sup> )	18.75	26.57
Power density (kW/dm <sup>3</sup> )	0.8	0.56

## 4 Conclusion

A new battery charger based on SiC MOSFETs is introduced, and compared with the original charger based on Si IGBTs in this paper. The chargers are compared from the efficiency, volume and power density. Because of the same requirements of these chargers, it's easier to make the comparison by doing the same experiments. From the theoretical analysis and experiment results, it can be concluded that the high-frequency SiC-based charger has the efficiency 1.75% higher while it

takes up the volume 29.4% less than the Si-based charger. The power density of the charger also benefits a lot from the application of SiC devices, and it's improved by 41.6%. SiC-based chargers will have more advantages over Si-based chargers with further refinements of the design and the control strategy.

**Acknowledgements** This work was supported by the China National Science and Technology Support Program under Grant 2016YFB1200504-C-01, Beijing Science and Technology Major Project under Grant Z171100002117011.

## References

1. Li W, Ping Z (2014) Application of new type wide-bandgap SiC power devices in power electronic. *J Nanjing Univ Aeronaut Astronaut* 04:524–532 (in Chinese)
2. Zhao B, Song Q, Liu W (2013) Experimental comparison of isolated bidirectional DC–DC converters based on all-Si and all-SiC power devices for next-generation power conversion application. *IEEE Trans Industr Electron* 61(3):1389–1393
3. Tiwari S, Midtgård OM, Undeland TM (2016) Comparative evaluation of a commercially available 1.2 kV SiC MOSFET module and a 1.2 kV Si IGBT module. In: *Industrial electronics society, IECON 2016-42nd annual conference of the IEEE*, 1093–1098
4. Haijie J (2015) Research and design of lithium battery charger for hybrid EMU. Beijing Jiaotong University, Beijing (in Chinese)
5. Shuai Z, Xiaoyong Z, Fangjun H, Wei X, Qing Z (2014) Design of a EMU battery charger. *High Power Converter Technol* (01):13–16+31. (in Chinese)
6. Van den Bossche A, Stoyanov R, Dukov N, et al (2016) Analytical simulation and experimental comparison of the losses in resonant DC/DC converter with Si and SiC switches. In: *Power electronics and motion control conference (PEMC), IEEE international*. 934–939
7. Calderon-Lopez G, Forsyth AJ (2014) High power density DC-DC converter with SiC MOSFETs for electric vehicles. In: *IET international conference on power electronics, machines and drives. IET*, 1–6
8. Han D, Noppakunkajorn J, Sarioglu B (2014) Comprehensive efficiency, weight, and volume comparison of SiC-and Si-Based bidirectional DC–DC converters for hybrid electric vehicles. *IEEE Trans Veh Technol* 63(7):3001–3010



# A Research on VIENNA Rectifier Based on SVPWM Algorithm with Expected Voltage

Changjun Guo, Gang Zhang and Xibin Bai

**Abstract** At present, more and more power electronic fields have been applied to rectifiers. VIENNA rectifier is a new type of rectifier with wide application prospect. Compared with other rectifiers, VIENNA rectifier has a more simple structure. This kind of simple topology makes VIENNA rectifiers with many of the advantages that other rectifiers do not have. At present, there are many research and control strategies for VIENNA rectifier, in which the voltage space vector control strategy has better control effect. In this paper, a SVPWM modulation algorithm based on expected voltage is proposed for three-level VIENNA rectifier. What's more, the realization of the modulation strategy and simulation results is given in this paper.

**Keywords** SVPWM · VIENNA rectifier · Simulation

## 1 Introduction

In recent years, the world economy is in the rapid development and Chinese economy is also in rapid progress. With the development of economy, people have realized the importance of protecting the environment. Electric energy is a kind of clean energy which promotes the development of electric motor vehicle [1]. Recently, the electric car has been a hot research in the field of power electronics in the world [2]. As a result, the promotion of electric vehicles needs a lot of charging stations, so the establishment of charging stations is a very important link. In this

---

C. Guo (✉) · G. Zhang  
School of Electrical Engineering, Beijing Jiaotong University, Beijing 100044, China  
e-mail: 16121442@bjtu.edu.cn

C. Guo · G. Zhang  
Beijing Engineering Research Center of Electric Rail Transportation, Beijing, China

X. Bai  
China Railway Electrification Bureau Group Co Ltd., Beijing, China

© Springer Nature Singapore Pte Ltd. 2018

L. Jia et al. (eds.), *Proceedings of the 3rd International Conference on Electrical and Information Technologies for Rail Transportation (EITRT) 2017*, Lecture Notes in Electrical Engineering 482, [https://doi.org/10.1007/978-981-10-7986-3\\_38](https://doi.org/10.1007/978-981-10-7986-3_38)

paper, the topology and working principle of three-phase three-level VIENNA rectifier are analyzed [3, 4].

## 2 The Topology of VIENNA Rectifier

A scholar at University of VIENNA has proposed a new type of rectifier topology, so the rectifier called VIENNA rectifier. This kind of three-level rectifier is unique. Each phase of the bridge only contains one switching device. The switch and the other four diodes constitute the bidirectional switch so that current can flow in two directions. The topology of the VIENNA rectifier is shown in Fig. 1.

VIENNA rectifier has many advantages. First of all, the nature of the VIENNA rectifier belongs to the BOOST circuit so that the inductance of the rectifier continues in the BOOST state [5]. What's more, the structure allows the current to remain constant, so there is no zero sequence current in the VIENNA rectifier. Secondly, the maximum voltage drop of the rectifier switching device is only 1/2 of the voltage drop on the bus, which makes the rectifier suitable for working at high voltage. Furthermore, the harmonic current of the rectifier is low, so the power density is much higher than that of the conventional rectifier. Finally, the VIENNA rectifier can also be operated under the condition of unity power factor [6].

## 3 Analysis of the Working Principle of VIENNA Rectifier

According to the previous analysis, we know that each arm of the VIENNA rectifier can be equivalent to a two-way switch. Thus an equivalent simplified model of the VIENNA rectifier can be obtained shown in Fig. 2.

Three bridge arms of the VIENNA rectifier can be equivalent to three bidirectional switches and each arm has two states, so there are 8 types of switching combinations shown in Table 1.

According to Table 1, VIENNA rectifier will have different working states under different three-phase current. Now we take  $i_u < 0, i_v < 0, i_w > 0$  as an example. Then 8 kinds of current path in this state can be shown in Fig. 3.

Fig. 1 The topology of VIENNA rectifier

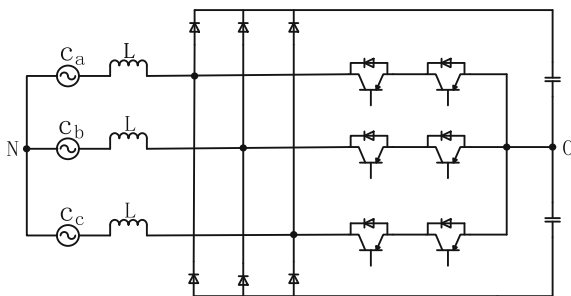


**Fig. 2** Equivalent simplified model of VIENNA rectifier

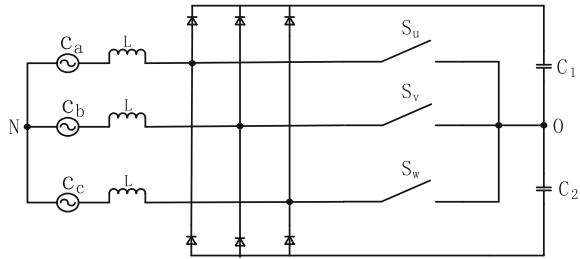


**Table 1** Switch combination state

Switch number	Switch combinations							
Su	0	0	0	0	1	1	1	1
Sv	0	0	1	1	0	0	1	1
Sw	0	1	0	1	0	1	0	1

In fact, the work of the circuit in the state of other current combinations can be drawn from this example.

## 4 A SVPWM Control Algorithm Based on Expected Voltage Auxiliary Judgment

### 4.1 Calculation of Voltage Space Vector

In order to calculate the voltage vector of the desired voltage, calculate the specific plane region of the desired voltage need to be calculated. According to the basic principle of VIENNA rectifier, we can know that there are three different potentials of the rectifier input to the DC neutral point. These three different kinds of potentials are:  $+V_{DC}/2$ ,  $0$ ,  $-V_{DC}/2$ . A function  $k_i$  is used to represent the three level states. It is shown in Eq. 1.

$$K_i = \begin{cases} 1 & u_{sio} = V_{DC}/2 \\ 0 & u_{sio} = 0 \\ -1 & u_{sio} = -V_{DC}/2 \end{cases} \quad (1)$$

The Eq. 2 can be obtained from the structure of VIENNA rectifier.

$$\begin{cases} u_{NO} = \frac{u_{Suo} + u_{Svo} + u_{Swo}}{3} \\ u_{Si} = u_{Sio} - \frac{u_{Suo} + u_{Svo} + u_{Swo}}{3} \end{cases} \quad (2)$$

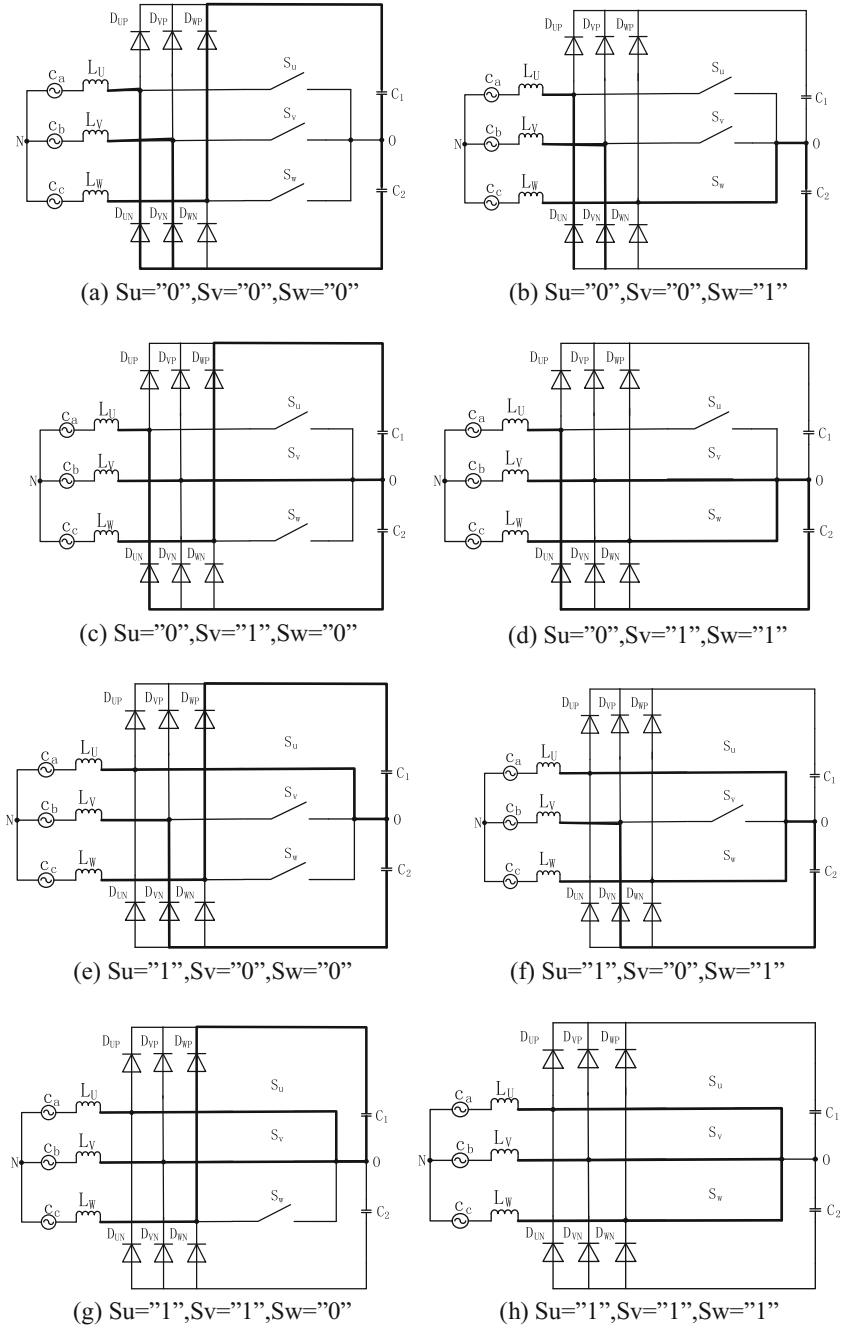


Fig. 3 Current path under different switch combination

Using the coordinate transformation formula, the voltage calculation formula can be deduced which is shown in Eq. 3.

$$\vec{V} = \begin{bmatrix} V_\alpha \\ V_\beta \end{bmatrix} = T_{clarke} \begin{bmatrix} u_{Su} \\ u_{Sv} \\ u_{Sw} \end{bmatrix}, T_{clarke} = \frac{2}{3} \begin{bmatrix} 1 & -\frac{1}{2} & -\frac{1}{2} \\ 0 & \frac{\sqrt{3}}{2} & -\frac{\sqrt{3}}{2} \end{bmatrix} \quad (3)$$

The voltage space vector can be drawn according to the calculated voltage which is shown in Fig. 4.

We divide the vector space plane into 6 large regions. Furthermore, each large area is divided into 6 small regions. When the desired voltage space vector is in the region of B and D, it is easy to calculate the voltage vector and its time. In order to further judge the small area, the SVPWM control algorithm based on the expectation voltage is introduced. In order to determine where the desired voltage is located, we can list the judging conditions of each small area which is shown in Table 2.

In order to further determine when the desired voltage vector is located in a region of the A<sub>1</sub>, A<sub>2</sub>, C<sub>1</sub>, C<sub>2</sub>, the judging conditions of each small area can be listed in Table 3.

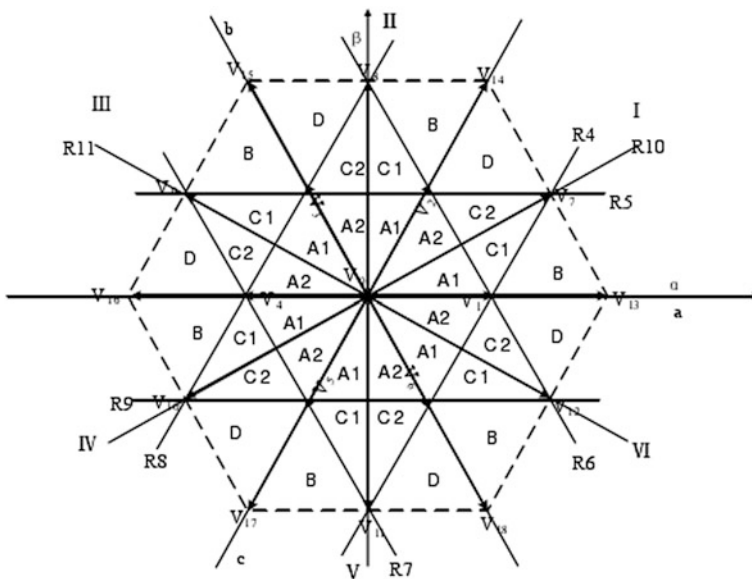


Fig. 4 Voltage space vector

**Table 2** Small area judge condition list

	A	B	D	C
I	$R_6 \leq 0$	$R_4 \leq 0$	$R_5 \geq 0$	Not Conform
II	$R_5 \leq 0$	$R_6 \geq 0$	$R_8 \geq 0$	Not Conform
III	$R_8 \leq 0$	$R_5 \leq 0$	$R_7 \leq 0$	Not Conform
IV	$R_7 \geq 0$	$R_8 \geq 0$	$R_9 \leq 0$	Not Conform
V	$R_9 \geq 0$	$R_7 \leq 0$	$R_4 \leq 0$	Not Conform
VI	$R_4 \geq 0$	$R_9 \leq 0$	$R_6 \geq 0$	Not Conform

**Table 3**  $A_1, A_2, C_1, C_2$  region judgment condition

	$A_1$	$A_2$	$C_1$	$C_2$
I	$R_{10} \leq 0$	$R_{10} \geq 0$	$R_{10} \leq 0$	$R_{10} \geq 0$
II	$V_x \geq 0$	$V_x \leq 0$	$V_x \geq 0$	$V_x \leq 0$
III	$R_{11} \geq 0$	$R_{11} \leq 0$	$R_{11} \geq 0$	$R_{11} \leq 0$
IV	$R_{10} \geq 0$	$R_{10} \leq 0$	$R_{10} \geq 0$	$R_{10} \leq 0$
V	$V_x \leq 0$	$V_x \geq 0$	$V_x \leq 0$	$V_x \geq 0$
VI	$R_{11} \leq 0$	$R_{11} \geq 0$	$R_{11} \leq 0$	$R_{11} \geq 0$

### 4.2 Calculation Time of Each Voltage Space Vector

According to the principle of volt second area equal, the calculation equation can be obtained in 4.

$$\begin{cases} V_x T_x + V_y T_y + V_z T_z = V_{ref} T_s \\ T_x + T_y + T_z = T_s \end{cases} \quad (4)$$

We assume that the desired voltage is located in I-B. Through the analysis of Sect 4.1, it can be calculated that the needed voltage space vectors are V1, V7, V13. Bring the three voltage space vector into the 4, the Eq. 5 can be obtained.

$$\begin{cases} V_1 T_1 + V_7 T_7 + V_{13} T_{13} = V_{ref} T_s \\ T_1 + T_7 + T_{13} = T_s \end{cases} \quad (5)$$

Transform the Eq. 5 into plural form and make the real and imaginary parts correspond to each other. So the Eq. 6 can be obtained.

$$\begin{cases} V_\alpha = \frac{V_{DC}}{3T_s} T_1 \cos 0 + \frac{2V_{DC}}{3T_s} T_{13} \cos 0 + \frac{V_{DC}}{3T_s} T_7 \cos \frac{\pi}{6} \\ V_\beta = \frac{V_{DC}}{3T_s} T_1 \sin 0 + \frac{2V_{DC}}{3T_s} T_{13} \sin 0 + \frac{V_{DC}}{3T_s} T_7 \sin \frac{\pi}{6} \\ T_s = T_1 + T_7 + T_{13} \end{cases} \quad (6)$$

After solving the equations, the time of the three voltage space vector can be shown in Eq. 7.

$$\begin{cases} T_1 = 2T_s - \frac{\sqrt{3}T_s}{V_{DC}} (\sqrt{3}V_\alpha + V_\beta) \\ T_{13} = \frac{\sqrt{3}T_s}{V_{DC}} (\sqrt{3}V_\alpha - V_\beta) - T_s \\ T_7 = \frac{2\sqrt{3}T_s}{V_{DC}} V_\beta \end{cases} \quad (7)$$

### 5 System Simulation of VIENNA Rectifier

The system parameters of the VIENNA rectifier simulation is shown in Table 4.

The system simulation model of VIENNA rectifier is shown in Fig. 5.

When the simulation time is 0.25 s, the load is added into the system. The simulation results are as follows. The DC output waveform of the rectifier is shown in Fig. 6.

As can be seen from the Fig. 6, the output voltage of the rectifier follows the given value well. The voltage and current waveforms on the AC side of the rectifier are shown in Fig. 7.

**Table 4** The system parameters of VIENNA rectifier simulation

Parameter type	Unit	Parameter values
Input voltage	V	380
Grid frequency	Hz	50
Output power	kW	100
Output voltage	V	800
Switching frequency	Hz	10 k

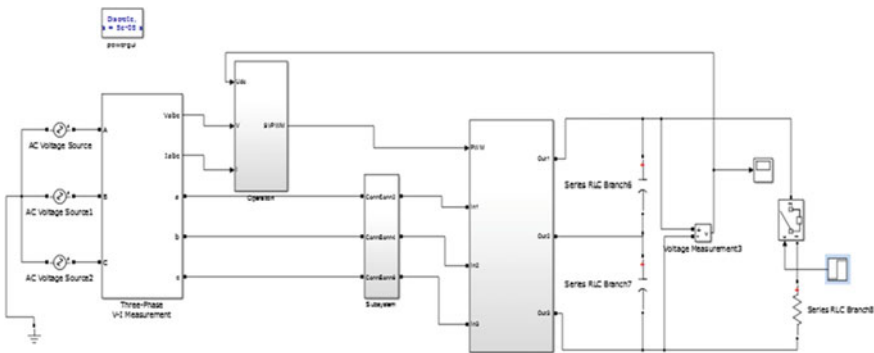


**Fig. 5** The system simulation model of VIENNA rectifier

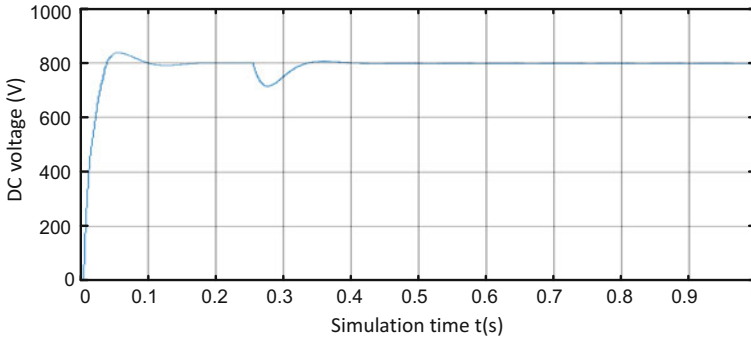


Fig. 6 DC output of the rectifier

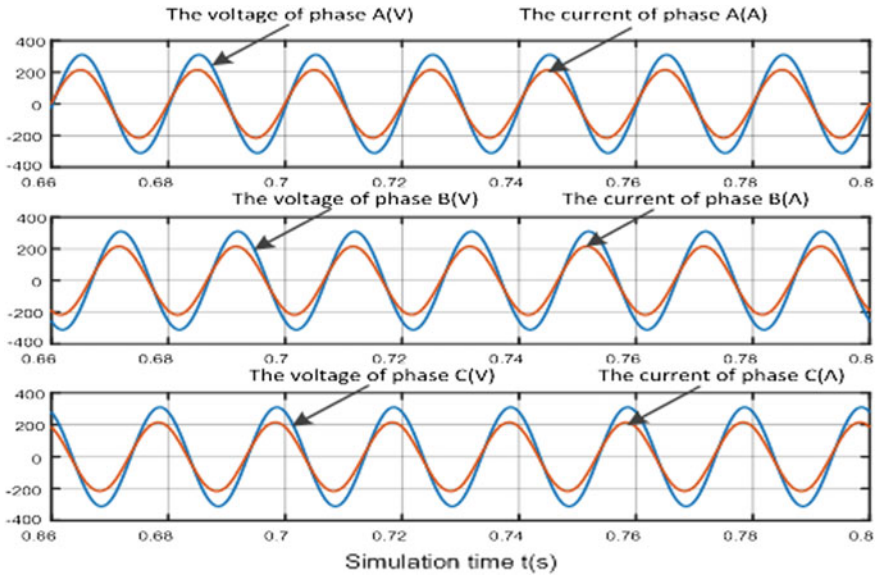


Fig. 7 waveforms of AC voltage and current

As can be seen from Fig. 7, the voltage is in the same phase with the current. The power factor of the system is 1, that is to say the system is operated under unity power factor. In addition, according to the effective value of voltage and current, we can know that the calculated power is 100 kW which is consistent with the design of the system. After the coordinate transformation, the current  $I_d$  and  $I_q$  are shown in Fig. 8.

As can be seen from Fig. 8, the AC current is transformed into a straight line through the coordinate transformation [7]. In addition, the current component of the q axis represents the reactive component whose value is approximate zero. The current component of the d axis represents the active component [8]. When the



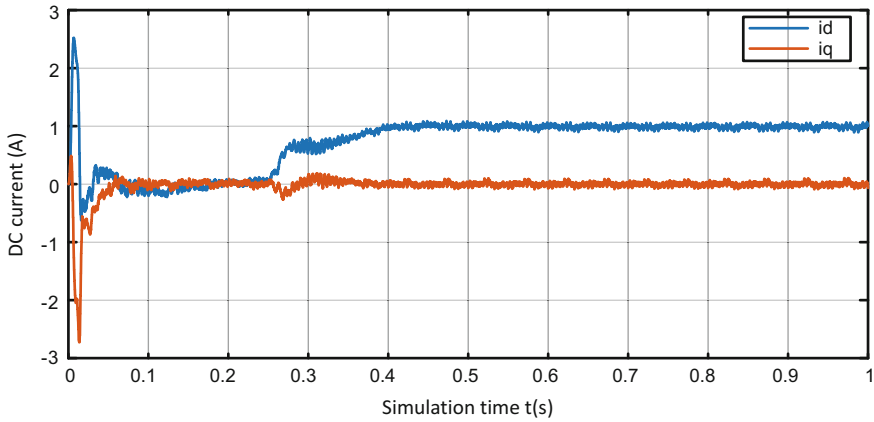


Fig. 8 The current obtained by coordinate transformation

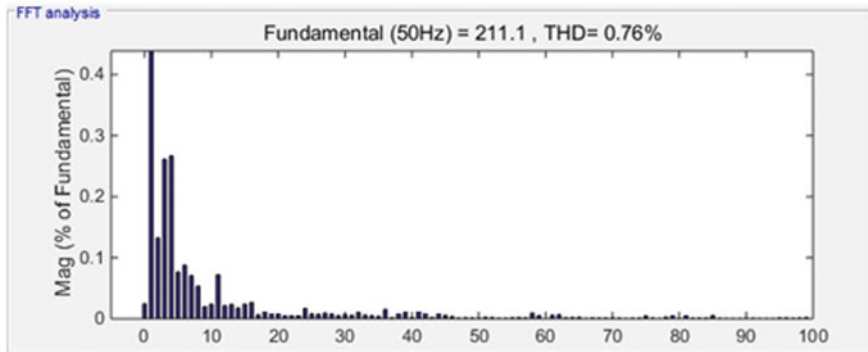


Fig. 9 The results of harmonic analysis by Fourier transform

system is subjected to rated load, its value is 1. Finally, the harmonics by Fourier transform is analyzed. The system simulation of Fourier analysis is shown in Fig. 9.

From the results of Fourier analysis, the SVPWM modulation algorithm based on the expected voltage auxiliary judgment can produce relatively low harmonics in the whole system. Of course, this has a certain relationship with the higher switching frequency during simulation.

## 6 Conclusions

Through the analysis of this paper we can know that the SVPWM modulation strategy based on the expected voltage can be used in three-level VIENNA rectifier. Of course, there are still some deficiencies in this paper. Due to the limited capacity

and the limited time of the author, the simulation model is not good enough in choosing parameter selection and so on. The SVPWM modulation algorithm of VIENNA rectifier still needs to be further improved.

**Acknowledgements** This work was supported by the China National Science and Technology Support Program under Grant 2016YFB1200504-C-01, China National Science and Technology Support Program under Grant 2017YFB1200802.

## References

1. Lee J-S, Lee K-B (2015) Carrier-based discontinuous PWM method for Vienna rectifiers. *IEEE Trans Power Electron* 30(6):2896–2900
2. Friedli T, Hartmann M, Kolar JW (2011) The essence of three-phase PFC rectifier systems—part II
3. Morin CM, Vallières A, Guay B et al (2009) Cognitive-behavior therapy, singly and combined with medication, for persistent insomnia: acute and maintenance therapeutic effects. *JAMA* 301:2005–2015
4. Qiao C, Smedley KM (2002) A general three-phase PFC controller for rectifiers with a parallel-connected dual boost topology. *IEEE Trans Ind Appl* 17(6):925–934
5. Hang L, Zhang H, Liu S, Xie X, Zhao C, Liu S (2015) A novel control strategy based on natural frame for Vienna-type rectifier under light unbalanced-grid conditions. *IEEE Trans Power Electron* 62(3):1353–1362
6. van Wyk JD, Lee FC (2013) On a future for power electronics. *IEEE J Emerg Sel Topics Power Electron* 1(2):59–72
7. Friedli T, Hartmann M, Kolar JW (2014) The essence of three-phase PFC rectifier systems—Part II. *IEEE Trans Power Electron* 29(2):543–560
8. Kolar JW, Friedli T (2013) The essence of three-phase PFC rectifier systems—Part I. *IEEE Trans Power Electron* 28(1):176–198

# Research of Induction Motor Model Considering the Variation of Magnetizing Inductance

Yujie Chang, Yi Xue, Yang Guo, Jing Tang, Dongyi Meng and Hui Wang

**Abstract** Accurate induction motor mathematical model is the cornerstone of the high-performance vector control of motor. Magnetic saturation can easily affect motor parameters, and the relation of magnetic saturation and the motor parameters is important to the establishment of the motor model. This paper derives a mathematical model of induction motor considering the variation of magnetizing inductance, based on the ideal mathematical model and magnetic saturation characteristic of the motor, from no-load test. Then, the motor model proposed and the ideal model in the MATLAB/Simulink Power System Block are respectively applied to the motor control simulation, and the experimental data are compared to verify the feasibility of the model designed.

**Keywords** Induction motor mathematical model · No-load test  
Magnetization curve · Magnetic saturation · Magnetizing inductance

## 1 Introduction

With the more and more maturing control theory of AC induction motor, the motor control technology has been developed from the scale control based on the steady state model of motor to the vector control based on the dynamic model. Grasping the parameters of motor under different operating conditions to get accurate observation of the motor flux linkage is the premise of high-performance vector control of motor.

---

Y. Chang (✉) · J. Tang · D. Meng · H. Wang  
Beijing Engineering Research Center of Electric Rail Transportation,  
School of Electrical Engineering, Beijing Jiao Tong University, Beijing 100044, China  
e-mail: 16121417@bjtu.edu.cn

Y. Xue  
Shanghai Railway Administration Dispatch Place, Shanghai, China

Y. Guo  
CRRC Changchun Railway Vehicles Co., Ltd., Changchun, China

© Springer Nature Singapore Pte Ltd. 2018

L. Jia et al. (eds.), *Proceedings of the 3rd International Conference on Electrical and Information Technologies for Rail Transportation (EITRT) 2017*, Lecture Notes in Electrical Engineering 482, [https://doi.org/10.1007/978-981-10-7986-3\\_39](https://doi.org/10.1007/978-981-10-7986-3_39)

Induction motor is affected by the actual conditions, and the parameters will change. Variation of internal temperature, magnetic saturation and skin effect are the main factors of change of motor parameters [1]. However, there are some assumptions in the establishment of induction motor dynamic mathematical model, and the change of motor parameters is often ignored because of the restriction of numerical analysis methods and tools [2]. It will cause deviation of the parameters in the observer or controller during the actual operation, which leads to dynamic torque oscillation and affects the normal operation of the motor.

Although the motor model in the MATLAB/Simulink Power System Block has been widely used, its parameters are fixed during the simulation and the internal blocks can't be edited, which can't simulate real-time change of the motor parameters and affects the final simulation results.

Therefore, it is important to establish a motor model that can accurately simulate the change of the actual motor parameters. It provides not only a precise simulation module for simulation, but also a more excellent mathematical model for the motor vector control.

At present, motor model based on the magnetic saturation has been studied from many aspects. The author of [3] proposed the mathematical model of the motor with mutual inductance, but the expression of mutual inductance was not given. In [4], the motor model considering the main magnetic saturation was designed, but it was complex, which was not easy to be realized. The author of [5] obtained the relationship among magnetizing inductance, phase voltage and frequency by using the software Ansoft, and proposed motor model considering the magnetizing inductance. The author of [6] got the exponential relationship between magnetizing inductance and frequency from no-load test.

This paper considers magnetic saturation of the motor and ignores other factors. And the motor mathematical model is derived and the magnetic saturation curve is obtained to propose the model considering the variation of the magnetizing inductance, and the feasibility of the model is verified by the comparison with the ideal model.

## 2 Ideal Induction Motor Mathematical Model

The ideal induction motor mathematical model consists of the voltage equation, the flux linkage equation, the torque equation and the motion equation [7].

The voltage equation on the dq axis is shown:

$$\begin{aligned}
 \begin{bmatrix} v_{qs} \\ v_{ds} \\ v_{qr} \\ v_{dr} \end{bmatrix} &= \begin{bmatrix} R_s & & & \\ & R_s & & \\ & & R_r & \\ & & & R_r \end{bmatrix} \begin{bmatrix} i_{qs} \\ i_{ds} \\ i_{qr} \\ i_{dr} \end{bmatrix} + \begin{bmatrix} L_s p & & L_m p \\ L_s p & & L_m p \\ & L_m p & L_r p \\ L_m p & & L_r p \end{bmatrix} \begin{bmatrix} i_{qs} \\ i_{ds} \\ i_{qr} \\ i_{dr} \end{bmatrix} \\
 &+ \begin{bmatrix} 0 & \omega & & \\ -\omega & 0 & & \\ & & 0 & \omega - \omega_r \\ & & \omega_r - \omega & 0 \end{bmatrix} \begin{bmatrix} \Psi_{qs} \\ \Psi_{ds} \\ \Psi_{qr} \\ \Psi_{dr} \end{bmatrix} \tag{1}
 \end{aligned}$$

Where,  $\Psi_{qs}$ ,  $\Psi_{ds}$ : the component of the stator flux linkage on the dq axis,  $\Psi_{qr}$ ,  $\Psi_{dr}$ : the component of the rotor flux linkage on the dq axis,  $R_s$ : stator resistance,  $R_r$ : rotor resistance,  $L_m$ : magnetizing inductance,  $L_s$ : stator inductance,  $L_r$ : rotor inductance,  $\omega_r$ : angular velocity of rotor,  $\omega$ : angular velocity of dq frame,  $p$ : differential operator.

Equation (2) represents the relation of flux linkage and current.

$$\begin{bmatrix} \Psi_{qs} \\ \Psi_{ds} \\ \Psi_{qr} \\ \Psi_{dr} \end{bmatrix} = \begin{bmatrix} L_s & & L_m \\ & L_s & & L_m \\ L_m & & L_r & \\ & L_m & & L_r \end{bmatrix} \begin{bmatrix} i_{qs} \\ i_{ds} \\ i_{qr} \\ i_{dr} \end{bmatrix} \tag{2}$$

Where,  $i_{qs}$ ,  $i_{ds}$ : the component of the stator current on the dq axis,  $i_{qr}$ ,  $i_{dr}$ : the component of the rotor current on the dq axis.

The electromagnetic torque is expressed by Eq. (3).

$$T_e = 1.5n_p(\Psi_{ds}i_{qs} - \Psi_{qs}i_{ds}) \tag{3}$$

Where,  $T_e$  is the electromagnetic torque,  $n_p$  is the pole pair of the motor.

The motion equation of the motor is shown:

$$\frac{d\omega_r}{dt} = \frac{n_p}{2J}(T_e - T_L - F\omega_r) \tag{4}$$

$$\frac{d\theta_r}{dt} = \omega_r \tag{5}$$

Where,  $T_L$  is the load torque,  $F$  is friction coefficient,  $J$  is the rotational inertia,  $\theta_r$  is the rotation angle.

Substituting Eq. (2) into Eq. (1) and transforming, we can get:

$$\begin{bmatrix} \dot{\Psi}_{qs} \\ \dot{\Psi}_{ds} \\ \dot{\Psi}_{qr} \\ \dot{\Psi}_{dr} \end{bmatrix} = \begin{bmatrix} kL_r R_s & -\omega_e & -kL_m R_s & 0 \\ \omega_e & kL_r R_s & 0 & -kL_m R_s \\ -kL_m R_r & 0 & kL_s R_r & -(\omega_e - \omega_r) \\ 0 & -kL_m R_r & (\omega_e - \omega_r) & kL_s R_r \end{bmatrix} \begin{bmatrix} \Psi_{qs} \\ \Psi_{ds} \\ \Psi_{qr} \\ \Psi_{dr} \end{bmatrix} + \begin{bmatrix} v_{qs} \\ v_{ds} \\ v_{qr} \\ v_{dr} \end{bmatrix} \quad (6)$$

It is the motor mathematical model under continuous state.

The first-order forward Euler formula [8] can be expressed as

$$s = \frac{z - 1}{T} \quad (7)$$

Inserting Eq. (7) in Eq. (6), we can get Eq. (8), which is the motor mathematical model under discrete-state.

$$\begin{bmatrix} \Psi_{qs}(k) \\ \Psi_{ds}(k) \\ \Psi_{qr}(k) \\ \Psi_{dr}(k) \end{bmatrix} = \begin{bmatrix} kL_r R_s T + 1 & -\omega_e T & -kL_m R_s T & 0 \\ \omega_e T & kL_r R_s T + 1 & 0 & -kL_m R_s T \\ -kL_m R_r T & 0 & kL_s R_r T + 1 & -(\omega_e - \omega_r) T \\ 0 & -kL_m R_r T & (\omega_e - \omega_r) T & kL_s R_r T + 1 \end{bmatrix} \begin{bmatrix} \Psi_{qs}(k-1) \\ \Psi_{ds}(k-1) \\ \Psi_{qr}(k-1) \\ \Psi_{dr}(k-1) \end{bmatrix} + \begin{bmatrix} v_{qs}(k-1) \\ v_{ds}(k-1) \\ v_{qr}(k-1) \\ v_{dr}(k-1) \end{bmatrix} \quad (8)$$

### 3 Induction Motor Mathematical Model Considering Magnetizing Inductance

#### 3.1 Magnetic Saturation of Induction Motor

The magnetic saturation mainly occurs in the main closed magnetic circuit of induction motor [9]. And its characteristic can be indicated by the magnetization saturation curve, shown in Fig. 1, described by flux linkage and magnetic current of the motor. When the magnetic circuit is not saturated, the magnetization saturation curve changes linearly. When the magnetic circuit is saturated, the flux linkage cannot increase with the same multiple as the current, and the curve is nonlinear.

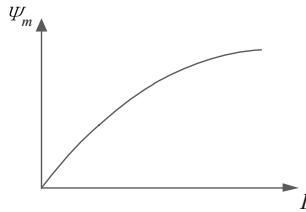


**Fig. 1** Magnetic saturation curve of target motor

With the change of the magnetic saturation, the magnetizing inductance is constantly in flux. Therefore, the magnetizing inductance can be expressed as a function of air-gap flux linkage and current shown in Eq. (9).

$$L_m = \frac{\Psi_m}{I} \tag{9}$$

The point on the magnetization saturation curve indicates magnetizing inductance in the steady state. And the slope of the curve reflects the magnetizing inductance in the transient state.

Therefore, getting the magnetization saturation curve can make obtaining the variation of magnetizing inductance easily and intuitively.

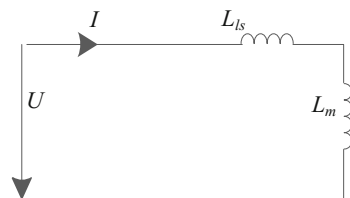
### 3.2 Determination of Magnetizing Saturation Curve

No-load test can obtain the magnetic saturation curve of the target motor. The equivalent circuit diagram of no-load test (irrespective of the iron loss and the stator resistance drop) is shown in Fig. 2.

The stator voltage and current values under different operating conditions are collected, which will be calculated to get the air gap flux linkage value at the rated frequency by Eq. (10).

$$\Psi_m = \frac{U - 2\pi f_n L_{ls} I}{2\pi f_n} \tag{10}$$

**Fig. 2** The equivalent circuit diagram of no-load test



Where,  $U$  represents stator voltage,  $f_n$  represents rated frequency.

The air-gap flux linkage values and stator current values are linearly fitted by interpolation and extrapolation. It is the obtained curve that is the magnetic saturation curve of target motor.

### 3.3 Induction Motor Mathematical Model Considering Magnetizing Inductance

The magnetic saturation curve of target motor is got from no-load test, and according the motor mathematical model under discrete-state shown in Eq. (8), we can establish the induction motor mathematical model considering magnetizing inductance in the dq frame, mainly including coordinate transformation block, flux linkage observation block, mechanical block and magnetic saturation block. The specific block diagram is shown in Fig. 3.

The function of coordinate transformation block is the transformation between ABC frame and dq frame. Flux linkage observation block is the core of the motor mathematical model, which is used to calculate the motor flux linkage, current and electromagnetic torque. Mechanical block is used to analyze the movement of the motor rotor.

The function of magnetic saturation block is to correct the value of magnetic inductance using the magnetization curve. The specific block diagram is shown in Fig. 4.

The realization of the block is as follows:

1. The air gap flux linkage  $\Psi_m$  is calculated from the stator and rotor flux linkage  $\Psi_{qs}$ ,  $\Psi_{ds}$ ,  $\Psi_{qr}$  and  $\Psi_{dr}$ .
2. The calculated air gap flux linkage  $\Psi_m$  is substituted into the magnetic saturation curve model, which contain the curve got from the above section, to obtain the corresponding current value  $I$ .
3. Use Eq. (9) to calculate  $L_m$ .

## 4 Simulation

The motor mathematical model proposed in this paper and motor model in the MATLAB/Simulink power system block are simulated respectively using the simulation model of the motor control system. The experimental data of the actual motor are obtained under the same control condition. And simulation results and experimental data are compared.

The motor parameters used is in Table 1.



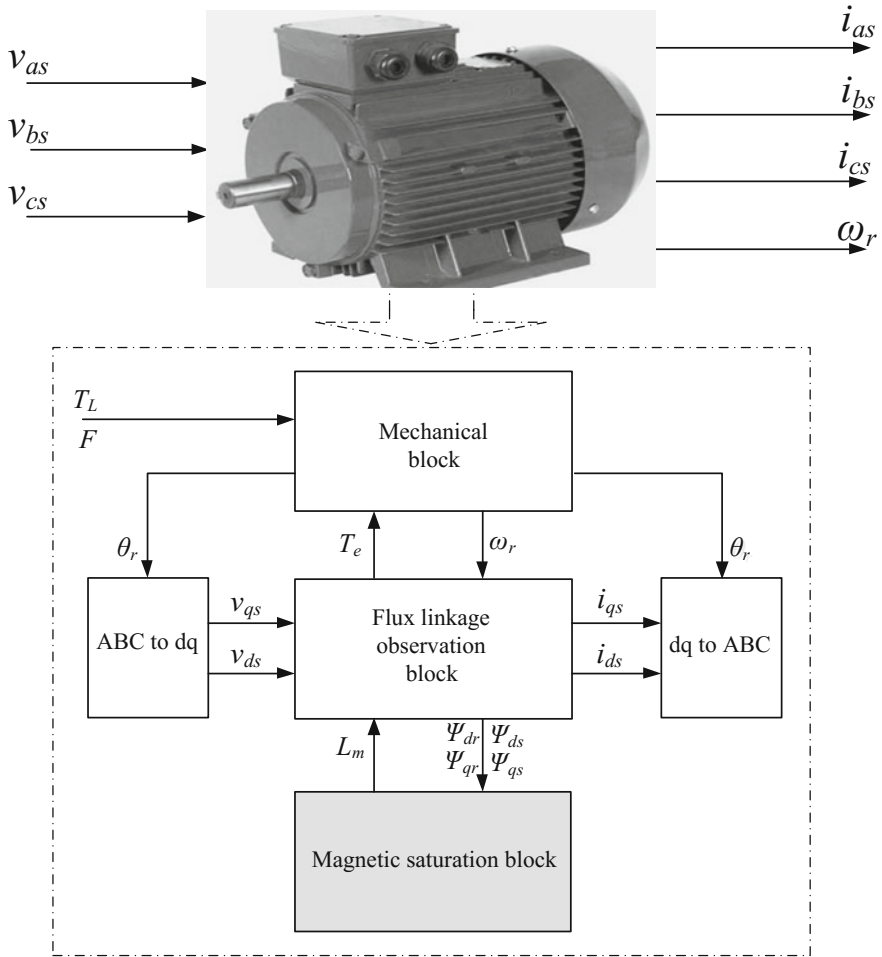


Fig. 3 Block diagram for motor mathematical model

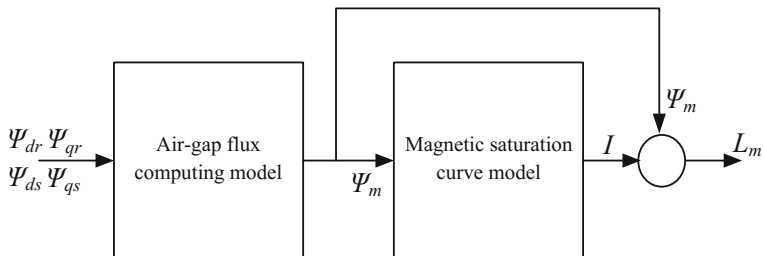
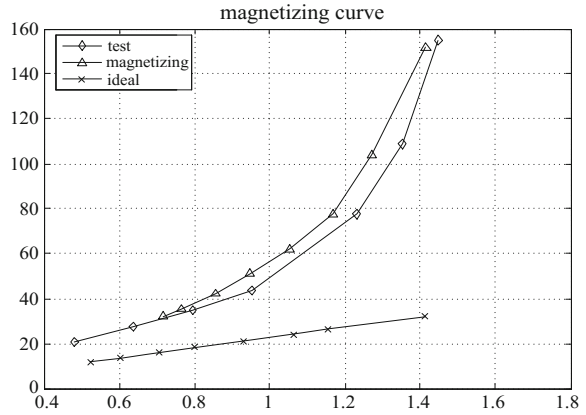


Fig. 4 Block diagram of magnetic saturation block

**Table 1** Parameters of experimental motor

Rated power $P_n$	160 kW	Stator resistance $R_s$	0.233 $\Omega$
RMS line-line voltage $V_{nrms}$	1287 V	Rotor resistance $R_r$	0.103 $\Omega$
Rated frequency $f_n$	84 Hz	Stator leakage inductance $L_{ls}$	1.58 mH
Inertia coefficient $J$	1.5 kg m <sup>2</sup>	Raotor leakage inductance $L_{lr}$	2.076 mH
Number of pole pairs $n_p$	2	Magnetizing inductance $L_m$	43.8 mH

**Fig. 5** Simulation results and experimental data

The waveforms are shown in Fig. 5, including the magnetization curve of the actual motor experiment, that of the motor model considering the magnetizing inductance and that of the motor model in the MATLAB/Simulink block. The horizontal axis is the peak of the flux and the vertical axis is the peak of the current. It can be seen that the motor model considering the magnetizing inductance is better than that in the MATLAB/Simulink block, which verifies the feasibility of the motor model designed in this paper.

## 5 Conclusion

Firstly, this paper analyzes the magnetic saturation characteristic of the induction motor and obtains the magnetization curve of the motor by no-load test. Then, based on the state equation of the motor and the magnetization curve, the mathematical model of the motor considering the variation of the magnetizing inductance under discrete-state is proposed, including coordinate transformation block, flux linkage observation block, mechanical block and magnetic saturation block. Finally, the motor model designed in this paper and the motor model in the MATLAB/Simulink block are applied to the motor control simulation respectively. Compared with the experimental data, it can be seen that the motor model

considering the magnetizing inductance can simulate the motor under the actual working condition, which verifies the feasibility of the mathematical model of the motor.

**Acknowledgements** This work was supported by the National Key Research and Development Program of China (2016YFB1200502-04) and the Fundamental Research Funds for the Central Universities under Grant 2016JBM058 and Grant 2016RC038.

## References

1. Han L (2004) Parameter identification of the asynchronous motor. Zhejiang University. (in Chinese)
2. Li K (2007) Study of high efficient and fast response electric drive system control strategy for electric vehicles. Shandong University. (in Chinese)
3. Moulahoum S, Touhami O, Ibtouen R, Fadel M (2007) Induction machine modeling with saturation and series iron losses resistance. In: IEEE international electric machines & drives conference, 1067–1072
4. Therrien F, Chapariha M, Jatskevich J (2015) Constant-parameter voltage-behind-reactance induction machine model including main flux saturation. IEEE Trans Energy Convers, 90–102
5. Chen G, Liu H, Liu Q et al (2016) Model of induction motor considering the variation of magnetizing inductance. Small Spec Electr Mach (06):23–26+34. (in Chinese)
6. Ilina ID (2017) Enhanced mathematical model used to simulate induction machine operation. Experimental validation. In: 10th international symposium on advanced topics in electrical engineering (ATEE) 164–169
7. Shah HV (2012) A modular Simulink implementation of induction machine model & performance in different reference frames. In: IEEE-international conference on advances in engineering, science and management (ICAESM -2012). 203–206
8. Luo H (2009) Research of full-order observer and speed estimation of induction motor. Huazhong Technology University. (in Chinese)
9. Cárdenas FVC, Kuong JL (2016) A methodology to include magnetic saturation in the modeling of the induction machine. IEEE ANDESCON. 1–4

# Auxiliary Inverter of Urban Rail Train—Oscillation Suppression Method of Induction Motor Load

Hui Wang, Zhigang Liu, Shaobo Yin, Dongyi Meng and Yujie Chang

**Abstract** Suppressing the induction motor load oscillation of auxiliary converter in urban rail train is very important to ensure the quality of train power supply and the operation stability. Firstly, this paper analyzes the energy state of the auxiliary converter. Then, according to the mechanical characteristic curve of the induction motor, the unstable operating area of the motor is discussed. After that, a method based on the inverter output frequency compensation by detecting DC side voltage is proposed, resulting in controlling the energy state and suppress induction motor load oscillation. Finally, the effectiveness and practicability of the method are full verified by simulation and experiments.

**Keywords** Induction motor load · Energy state · Voltage detection  
Frequency compensation · Suppression oscillation

## 1 Introduction

Induction motor load, such as air conditioner, air compressor, is an important part of the rail train auxiliary inverter [1]. Under certain conditions, the induction motor load is likely to oscillate, thus affecting the auxiliary system power supply quality, and the stable operation of the train. The oscillation suppression methods considered from induction motor include: the analysis of inherent instability [2], direct torque optimization control [3], dynamic model of voltage-flux linkage [4], induction motor parameters [5], etc. And the methods considered from inverter include: adjusting the power direction based on the negative sequence of the inverter input current [6], considering the influence of inverter dead time on the operation of induction motor [7], the input impedance of the inverter supply system suppresses the oscillation [8], etc. However, due to the large number and types of

---

H. Wang (✉) · Z. Liu · S. Yin · D. Meng · Y. Chang  
Beijing Engineering Research Center of Electric Rail Transportation,  
School of Electrical Engineering, Beijing Jiaotong University, Beijing 100044, China  
e-mail: 16121528@bjtu.edu.cn

the induction motor load on urban rail train, a suitable oscillation suppression method for engineering application is needed.

In this paper, the reason of the induction motor load oscillation is analyzed through the energy state of the inverter and the mechanical characteristic curve of the induction motor. Then, a method of controlling energy state by detecting the DC side voltage to compensate output frequency is proposed. Finally, it is proved that the method can effectively solve the oscillation phenomenon of the induction motor load, by simulation and experiments.

## 2 Analysis the Energy State of the Auxiliary Converter

In this paper, seven-stage SVPWM is used for modulation. And the energy exchange process between the inverter and the induction motor load is analyzed. Suppose the composite vector is in the third sector for a period of time. The switching states  $S_U$ ,  $S_V$  and  $S_W$  are the conduction states of the three-phase leg of U, V and W respectively. Set the current direction from U phase into, through the V, W phase out. The energy state during this time is as follows (Table 1).

In the “Loop” pattern, both the input current and power are zero. In the “Input” pattern, the current direction is consistent with the definition and the power direction is from inverter to motor. The “Output” pattern is the opposite of “Input” pattern.

To sum up, the input current and power of the inverter are positive, negative, and zero in each carrier cycle. Simplify the model and make further analysis.

As shown in Fig. 1a. When the negative input current increases, the energy of the load is transmitted to the DC side. Because of the effect of inductance  $L$ , the energy is concentrated on the capacitor  $C$ . When  $U_C$  is greater than  $U_S$ , the energy on the capacitor will transmit to the power grid and the load side respectively, as shown in Fig. 1b. The transmission of this energy is stable under normal conditions, but when the induction motor load oscillation occurs, the energy fluctuates sharply, which will lead to the instability of the inverter system.

## 3 Suppressing Oscillation Method

The mechanical characteristic curve of the induction motor load is shown in the following figure.

As the output voltage drops, the torque decreases as well. The intersection “A” between the load torque  $T_L$  and the induction motor’s mechanical characteristic curve is located in the unstable zone, as shown in Fig. 2. Under some special conditions, the flow of unstable energy causes the capacitance voltage and the output voltage to fluctuate, which makes the induction motor load move into the unstable operating area easily and results in oscillation.

Table 1 The energy state of the auxiliary converter

Model	I	II	III	IV	V	VI	VII
$S_U$	0	1	0	1	0	1	0
State $S_V$	0	1	1	1	1	1	0
$S_W$	0	0	0	1	0	0	0
Current loop							
Input current							
Pattern	Loop	Input	Output	Loop	Output	Input	Loop
Power	0	+	-	0	-	+	0

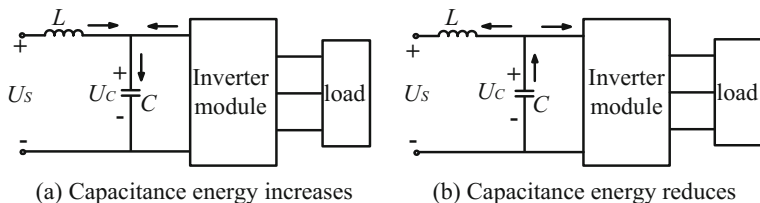
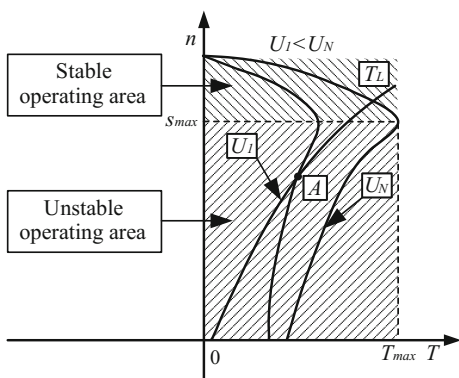


Fig. 1 Energy transfer diagram

Fig. 2 Mechanical characteristics curve of induction motor load



When the induction motor is running in the unstable zone, the power factor and the electromagnetic torque are relatively low. In order to suppress the oscillation, we can consider increasing the active power to improve the electromagnetic torque and induction motor power factor. Ignoring the influence of the loss, the relationship between the inverter output active power and the torque is:

$$P = \omega_m \cdot T_L \tag{1}$$

$$\omega_m = \frac{2\pi f}{p} (1 - s) \tag{2}$$

In Eqs. (1) and (2),  $\omega_m$  and  $T_L$  are the angular speed of rotor and load torque respectively.  $f$  is the output voltage frequency of inverter,  $p$  is numbers of the poles,  $s$  is slip ratio of induction motor.

According to the above two formulas, adjusting the inverter output voltage frequency can change the rotational angular velocity of the induction motor, thus adjusting the inverter output active power. As the analysis in Sect. 2, the DC side voltage and energy state are closely related. So using the scale factor  $k_p$  to realize the output frequency compensation of the inverter by detecting DC side voltage, and then control the inverter energy state and suppress the load oscillation.

$$\Delta f = k_p \Delta U = k_p (U_c - U_s) \tag{3}$$

where  $k_p$  is the frequency adjustment factor,  $U_c$  and  $U_s$  are the capacitance voltage and the network side voltage,  $\Delta f$  is the frequency adjustment.

The steady-state output voltage frequency of the urban rail auxiliary converter is 50 Hz, so the frequency regulation range can't be too large, and the adjustment needs to be limited.

The control diagram for suppressing the induction motor load oscillation is as follows (Fig. 3).

## 4 Simulation and Experiment Results

### 4.1 Simulation Results

The frequency adjustment factor  $k_p$  is 0.067. The induction motor model adopts a three-phase asynchronous induction motor with rated power of 2.2 kW, line voltage of 380 V, frequency of 50 Hz and torque of 14.795 Nm. A harmonic voltage source is added to the input side of the inverter to simulate the oscillation state of the converter. The simulation results are as follows:

At 0.2 s, the induction motor is in the rated operating state, and the motor stator current is in the oscillation state. The oscillation suppression algorithm is added at 0.4 s, and the motor stator current is suppressed after about 0.1 s. As shown in Fig. 4.

As shown in Fig. 5. The oscillation suppression algorithm is added at 0.4 s, and the output torque ripple of the induction motor is also effectively suppressed after

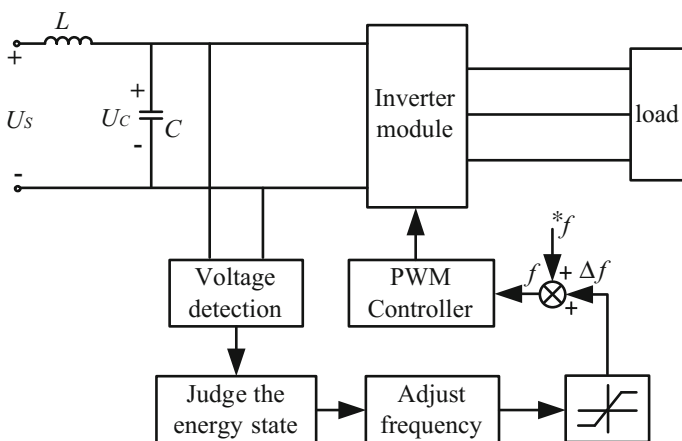
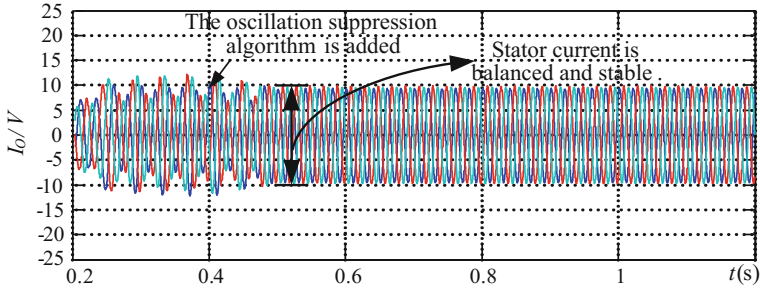
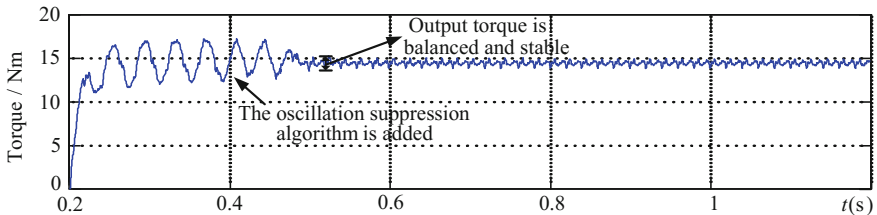


Fig. 3 The control diagram for suppressing the induction motor load oscillation





**Fig. 4** Output current waveform before and after the oscillation suppression



**Fig. 5** Motor torque waveform before and after the oscillation suppression

about 0.1 s. The simulation results show that the oscillation suppression method, based on DC side voltage detection, can suppress the oscillation of induction motor load commendably.

## 4.2 Experiment Results

In order to verify the practicability of the method, experiments are carried out in the train operation, and virtual oscilloscope is used to display the waveform. The large level start of traction motor can cause the voltage on the side of the auxiliary inverter to fluctuate greatly, resulting in the fluctuation of the output voltage of the auxiliary inverter system, and then the induction motor load oscillation phenomenon occurs. At this point, the waveforms is shown below:

According to Fig. 6, the capacitance voltage, the DC voltage and current, the AC voltage and current have a violent oscillation.

The following figure shows the DC voltage, current and AC voltage, current waveforms of the auxiliary inverter after adding the oscillation suppression algorithm for 3 s. It can be seen that the DC voltage and current, the AC voltage and current oscillation of the auxiliary converter has been completely suppressed, and the induction motor load oscillation also disappeared (Fig. 7).

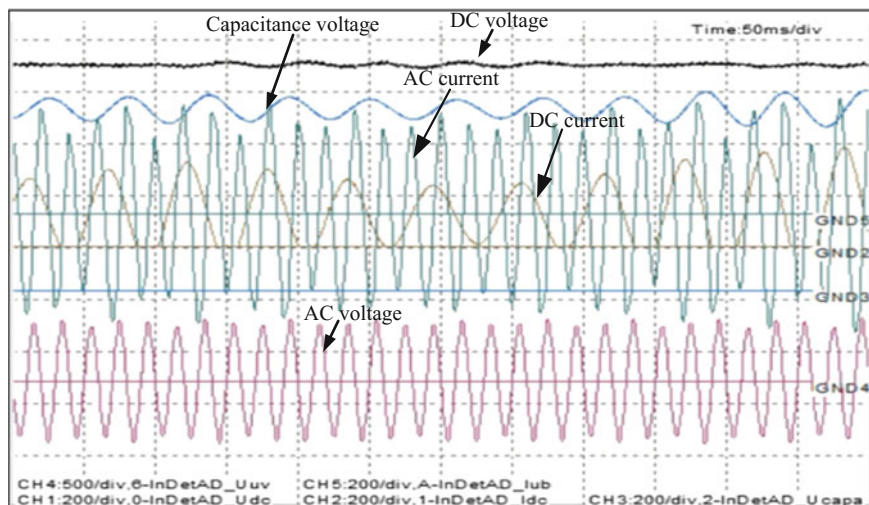


Fig. 6 Voltage and current waveforms when the motor load is oscillating

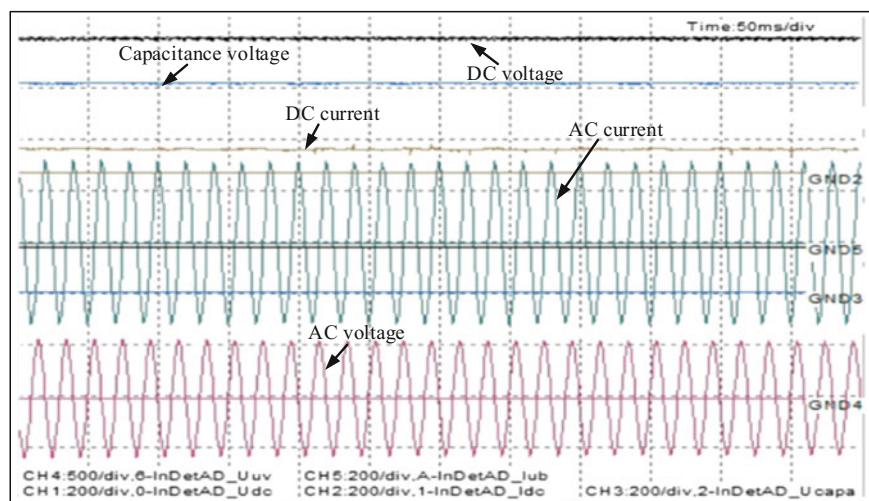


Fig. 7 Voltage and current waveforms after oscillation suppression

## 5 Conclusion

In this paper, the oscillation suppression algorithm is proposed, combining the energy state of urban rail train auxiliary converter and the characteristics of the mechanical characteristic curve of the induction motor load. The algorithm compensates the output frequency by detecting the DC side voltage, and controls the

energy state of the inverter to suppress the oscillation of the induction motor load. Finally the effectiveness and practicability of the method are verified by simulation and experiments.

**Acknowledgements** This work was supported by the China National Science and Technology Support Program under Grant 2016YFB1200504-C-01, Beijing Science and Technology Major Project under Grant Z171100002117011.

## References

1. Gong A (2012) Research on voltage control method of electrical locomotive auxiliary inverter. Beijing Jiaotong University. (in Chinese)
2. Li H, Yang T, Sun C (2003) The low frequency oscillation analysis in the induction motor system fed by an inverter. In: Electrical machines and systems, sixth international conference on ICEMS 2003, vol 2, IEEE, pp 577–580
3. Brando G, Rizzo R (2004) An optimized algorithm for torque oscillation reduction in DTC-induction motor drives using 3-level NPC inverter. In: Industrial electronics, IEEE international symposium on, vol 2, IEEE, pp 1215–1220
4. Islam S, Bakhsh FI, Ahmad S, Iqbal A (2012) Simplified stability analysis of a three-phase induction motor drive system 57(1):1–6
5. Chen H, Bai H, Zhang YW, Shi YH (2010) Stability and damping performance analysis of induction motor. In: International conference on advances in power system control, operation and management, IET pp 1–6
6. Mutoh N, Ueda A, Sakai K, Hattori M (1990) Stabilizing control method for suppressing oscillations of induction motors driven by pwm inverters. *Ind Electron IEEE Trans* 37(1):48–56
7. Guha A, Narayanan G (2016) Small-signal stability analysis of an open-loop induction motor drive including the effect of inverter dead time. *IEEE Trans Ind Appl* 52(1):242–253
8. Kang S, Luo Y, You J, Lv S (2011) The input characteristic and stability analyse of inverter with induction motor. In: IEEE international conference on information and automation, IEEE, pp 568–571

# Improved Voltage Model Based Flux Observer Design for Traction Induction Motor

DongYi Meng, Lijun Diao, Shaobo Yin, Yujie Chang and Hui Wang

**Abstract** In traction control, accurate observation of the flux is critical to achieve high performance control of the motor. This paper first summarizes the commonly used flux observation method, and analyses the working principle and existing problems of the commonly used voltage model flux observer. Then, an improved voltage model flux observer is designed, which series high-pass filter and low-pass filter. The compensation algorithm of amplitude and phase error due to the introduction of the filter is deduced, which eliminates the integral saturation problem caused by DC bias and realizes accurate observation of flux. Finally, the simulation and experimental analysis are carried out to verify the feasibility of the improved voltage model flux observer.

**Keywords** Flux observer · High-pass filter · Low-pass filter

## 1 Introduction

The accuracy of flux observation has always been a key research content in vector control for the motors in traction applications. There are many types of flux observer, including current model observer, voltage model observer, improved voltage model observer, MRAS-based rotor flux observer, full-order state observer, reduced order observer, etc. The latter three observers have higher observation accuracy in theory, but the algorithm is complicated and requires a lot of computing resources. At present, it is more practical to use voltage model observer, current model observer and improved voltage model observer [1].

The current model observer is applicable in the full speed range, but the observation accuracy of the model is affected by the changed motor parameters, e.g., the motor temperature affects the rotor resistance  $R_r$ , magnetic saturation affects the

---

D. Meng (✉) · L. Diao · S. Yin · Y. Chang · H. Wang  
Beijing Engineering Research Center of Electric Rail Transportation,  
School of Electrical Engineering, Beijing Jiaotong University, Beijing 100044, China  
e-mail: 16121500@bjtu.edu.cn

excitation inductance  $L_m$ , which will lead to flux amplitude and phase signal distortion [2, 3]. In contrast, the voltage model observer only requires voltage and current signals, and the algorithm is only related to stator resistance  $R_s$ , affected by the motor parameters change is relatively small, and the algorithm is simple and easy to implement. But the voltage model observer also has its flaws. Firstly, the results of flux observation at low speed are greatly influenced by the change of stator resistance. Secondly, the pure integral part of the model is easy to saturate with DC bias. The former can reduce the influence by adjusting the stator resistance parameters online. The problem of integral saturation due to the sensor measurement, sampling delay, electromagnetic interference and other factors is more significant in the practical application. Therefore, this paper will mainly focus on the latter problems [4].

In this paper, the working principle of the voltage model flux model observer is analysed in detail as well as the factors that affect its observation accuracy. On this basis, the improved voltage model observer is analysed, which series high-pass filters and low-pass filters. Finally, it is verified by simulation and experiment.

## 2 Voltage Model Rotor Flux Observer

### 2.1 Basic Principle

The equivalent circuit of the asynchronous motor can be used to derive the expression of the voltage model rotor flux observer in two-phase stationary coordinates:

$$\begin{cases} \psi_{r\alpha} = \frac{L_r}{L_m} \left[ \int (u_{s\alpha} - R_s i_{s\alpha}) dt - \sigma L_s i_{s\alpha} \right] \\ \psi_{r\beta} = \frac{L_r}{L_m} \left[ \int (u_{s\beta} - R_s i_{s\beta}) dt - \sigma L_s i_{s\beta} \right] \end{cases} \quad (1)$$

Where  $\psi_{r\alpha}, \psi_{r\beta}$  are the flux of the rotor in  $\alpha$  and  $\beta$  axis.  $u_{s\alpha}, u_{s\beta}$  are the voltage of the stator in  $\alpha$  and  $\beta$  axis.  $i_{s\alpha}, i_{s\beta}$  are the current of the stator in  $\alpha$  and  $\beta$  axis.  $L_s, L_r, L_m$  are the stator inductance, converted to the stator side of the rotor inductance, excitation inductance, respectively.

It can be seen from (1) that the voltage model rotor flux observer is essentially a pure integrator, according to its mathematical expression, we can get its schematic as shown in Fig. 1.

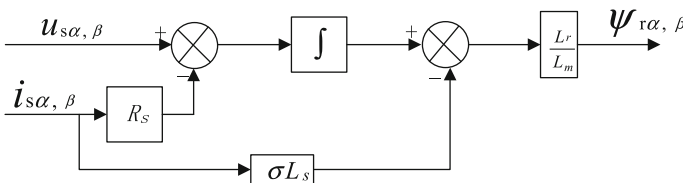


Fig. 1 Schematic diagram of voltage-model flux observer

## 2.2 Analysis of Voltage Model Flux Observer

It can be seen from the (1) that the integral item contains the stator resistance of the motor. When the speed is low, the back electromotive force is low, and the flux observation value is sensitive to the change of the motor stator resistance. In addition, the voltage model flux observer contains pure integrator which means flux observation is achieved by integrating the back electromotive force. When a DC offset is input, saturation occurs under the action of the integrator, resulting in the accuracy of the flux observer being affected.

For the former problem, you can adjust the motor stator parameters online to reduce the impact, it will not be discussed here. For the latter problem, the more common solution is to use the first-order low-pass filter instead of pure integrator [5], the expression is as follows:

$$\frac{\psi s}{u_s - R_s i_s} = \frac{1}{s + \omega_{cL}} \quad (2)$$

The first-order low-pass filter (LPF) method can solve the problem of pure integral saturation due to DC bias, but the LPF can cause the amplitude and phase error of the observed flux linkage, the system performance will have a greater adverse impact [6–8].

## 3 Improved Voltage Model Flux Observer

In order to solve the saturation problem caused by pure integrator, while avoiding the flux amplitude and phase error cause by using the first-order low-pass filter.

In this paper, the first-order high-pass filter (HPF) and the first-order low-pass filter (LPF) in series are used to improve the voltage model flux observer.

The transfer function of the high-pass filter is designed as follows:

$$A_H(s) = \frac{s}{\omega_H + s} \quad (3)$$

The transfer function of the low-pass filter is designed as follows:

$$A_L(s) = \frac{\omega_L}{\omega_L + s} \quad (4)$$

$\omega_L$ ,  $\omega_H$  are low-pass filter, high-pass filter cut-off frequency.

After the filter, the original signal will be distorted in the amplitude and phase, so in the actual control system, compensation link for amplitude and phase is necessary. The derivation of the amplitude and phase compensation formula for the HPF series LPF is derived below.

The transfer function of HPF in the frequency domain can be obtained from the formula (3), its expression is as follows:

$$A_H(\omega) = \frac{1}{1 + \frac{\omega_H}{j\omega}} = \frac{1}{1 - j\frac{\omega_H}{\omega}} \quad (5)$$

Where  $\omega$  is the sync angle frequency.

Then the amplitude gain of HPF is:

$$|A_H(\omega)| = \frac{1}{\sqrt{1 + (\frac{\omega_H}{\omega})^2}} = \frac{|\omega|}{\sqrt{\omega^2 + \omega_H^2}} \quad (6)$$

The phase angle of HPF is:

$$\varphi_H = \arctan(\omega_H/\omega) \quad (7)$$

Similarly, the amplitude and phase expressions of the low-pass filter are as follows:

$$|A_L(\omega)| = \frac{|\omega_L|}{\sqrt{\omega_L^2 + \omega^2}}, \quad \varphi_L = -\arctan(\omega/\omega_L) \quad (8)$$

Assuming that the total amplitude compensation is  $A$ , the total phase compensation is  $P$ , and the total comprehensive compensation is  $C$ , then:

$$A = \frac{\sqrt{(\omega^2 + \omega_L^2)(\omega^2 + \omega_H^2)}}{\omega^2} \quad (9)$$

$$P = e^{-j\varphi_H} e^{-j(\frac{\pi}{2} + \varphi_L)} \quad (10)$$

$$C = AP \quad (11)$$

According to Euler formula:

$$e^{-j\varphi_H} = \cos(\varphi_H) - j \sin(\varphi_H) \quad (12)$$

$$e^{-j(\frac{\pi}{2} + \varphi_L)} = -\sin(\varphi_L) - j \cos(\varphi_L) \quad (13)$$

According to the basic trigonometric formula:

$$\cos(\varphi_H) = \frac{|\omega|}{\sqrt{\omega^2 + \omega_H^2}}, \quad \sin(\varphi_H) = \frac{\omega_H}{\sqrt{\omega^2 + \omega_H^2}} \quad (14)$$

$$\cos(\varphi_L) = \frac{\omega_L}{\sqrt{\omega^2 + \omega_L^2}}, \quad \sin(\varphi_L) = \frac{-|\omega|}{\sqrt{\omega^2 + \omega_L^2}} \tag{15}$$

According to formulas (9)–(15),  $C$  can be derived as follows:

$$C = \left(1 - \frac{\omega_H \omega_L}{\omega^2}\right) - j \frac{(\omega_L + \omega_H)}{\omega} \tag{16}$$

Select the cut-off frequency associated with the synchronization frequency  $\omega$ , make sure that  $\omega_L = \lambda_L \omega$ ,  $\omega_H = \lambda_H \omega$ , Substituting them into Eq. (16), we can get the final compensation:

$$C = (1 - \lambda_H \lambda_L) - j(\lambda_L + \lambda_H) \tag{17}$$

Figure 2 shows the schematic diagram of improved voltage-model flux observer. The stator voltage and stator current were passed through the low-pass and high-pass filter, get back electromotive force, and then add the amplitude and phase compensation measures, after a series of operations, we can get the rotor flux. its expression is as follows:

$$\psi_r = \frac{L_r}{L_m} \left[ \left( \frac{s}{s + \omega_H} \cdot \frac{1}{s + \omega_L} u_s - \frac{s}{s + \omega_H} \cdot \frac{R_s}{s + \omega_L} i_s \right) C - \sigma L_s i_s \right] \tag{18}$$

Where  $C$  is the amplitude and phase compensation, and the voltage and current filters have the same cutoff frequency.

HPF series LPF rotor flux observer eliminates DC bias by high-pass filter, the problem of integral saturation is eliminated by a low-pass filter, real-time compensation measures are added at the same time, which has greatly improved the observation accuracy of the observer.

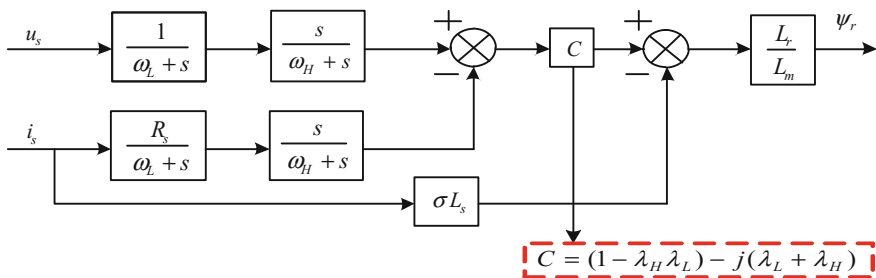


Fig. 2 Schematic diagram of improved voltage-model flux observer



## 4 Simulation and Experiment

The Matlab/Simulink software is used to simulate the flux observer and analyzes it, experiments were carried out, the superiority of the improved voltage type flux observer with HPF series LPF is compared and analyzed.

### 4.1 Simulation Analysis

The simulation uses the same parameters as the actual experimental motor, as shown in the following Table 1.

When a 0.1% nominal DC bias is added to the input signal, the simulation results are shown in Fig. 3 when the common voltage model is used for flux observation.  $\hat{\psi}_{r\alpha}$  is the rotor flux component observed in  $\alpha$  axis, and  $\psi_{r\alpha}$  is the actual rotor flux component in  $\alpha$  axis.

As can be seen from the figure above, the observed flux is significantly deviated from the actual flux. This is due to the fact that the pure integral in the voltage model flux observer is integral and saturated when there is a DC component.

**Table 1** The motor parameters

Rated voltage: 550 V	Stator resistance: 0.0324 $\Omega$
Rated current: 240 A	Rotor resistance: 0.034 $\Omega$
Rated power: 180 kW	Mutual inductance: 10.59 mH
Rated speed: 2255 rpm	Stator leakage inductance: 0.72 mH
Maximum speed: 4242 rpm	Rotor leakage inductance: 0.72 mH
Rated frequency: 77 Hz	Pole pairs: 2
Power factor: 0.855	Maximum torque: 1343 Nm

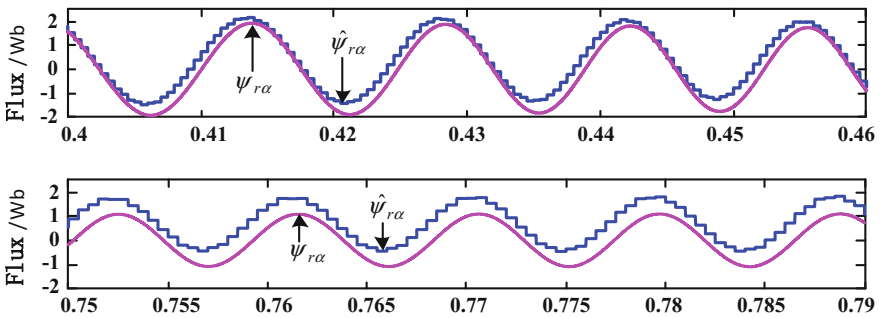


**Fig. 3** Observation waveforms of voltage-model rotor flux observer

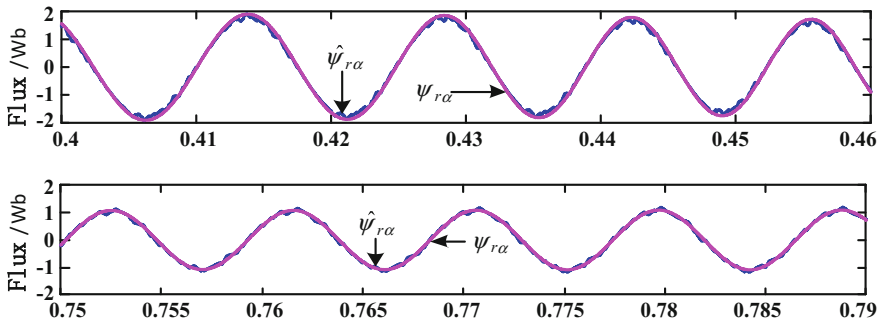


Fig. 4 Observation waveforms of LPF + HPF rotor flux observer

When a 0.1% nominal DC bias is applied to the input signal, the simulation results are shown in Fig. 4 when using the improved voltage model flux observer, which series the high-pass filter and low-pass filter.

Figures 3 and 4 show that the LPF+HPF observer can eliminate the effects of pure integral and DC bias, the optimization effect of the improved flux observation algorithm is verified.

### 4.2 Experimental Results

The experiment in this paper is based on DSP+FPGA control platform. The motor parameters, control methods and so on are the same in simulation.

Figures 5 and 6 shows observation waveform when the motor running at 60, 100 Hz, where figure a is the waveform without load and figure b is the waveform under load.

The figure shows the motor phase current, rotor  $\alpha$  axis flux observation value  $\hat{\psi}_{r\alpha}$  and rotor  $\beta$  axis flux observation value  $\hat{\psi}_{r\beta}$ . We can see that there is no vibration in motor current and the rotor flux is well sinusoidal, it shows a good stability in the whole process.

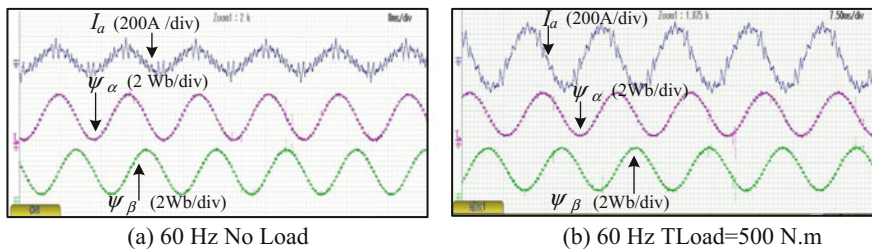
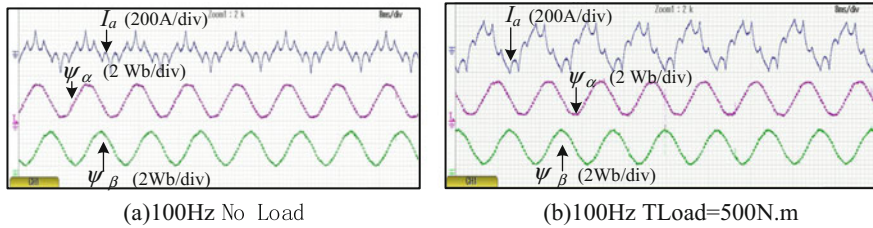


Fig. 5 Observation waveforms of rotor flux under 60 Hz



**Fig. 6** Observation waveforms of rotor flux under 100 Hz

## 5 Conclusion

This paper analyses the working principle and shortcomings of the normal voltage model flux observer. On this basis, an improved voltage model flux observer with HPF series LPF instead of pure integral is designed, which successfully solves the problem of integral saturation of the original voltage model flux observer, so that the observed flux amplitude and phase error are reduced. Simulation and experiment were carried out to verify the advantage of improved voltage model flux observer.

**Acknowledgements** This work was supported by the China National Science and Technology Support Program under Grant 2016YFB1200502-04, Beijing base construction and personnel training special under Grant Z17111000220000, and the Fundamental Research Funds for the Central Universities under Grant 2016JBM058 and Grant 2016RC038.

## References

1. Shaobang X (2007) Research on flux chain observation and SVPWM in modern AC speed control system. MS thesis. QingDao University. (in Chinese)
2. Masala JM, Busawon K, Djemaï M (2014) Speed sensorless flux observer for induction machines. Environmental friendly energies and applications (EFEA). In: 3rd international symposium on IEEE
3. Yuan Z, Lu H, Kerkman RJ et al (2007) Parameter sensitivity analysis of flux observers for induction motors. In: Industry applications conference, 42nd IAS annual meeting. Conference record of the 2007 IEEE. IEEE, 2007:1015–1022
4. Li M-Z, Yang Z-Q, Zhang F (2015) Improved stator flux observer based on voltage model. Micro-motor, 48(6):65–68. (in Chinese)
5. Wei L et al (2001) A new method for eliminating DC bias errors in voltage flux observer. J Tsinghua Univ (Nat Sci Ed) 41(9):51–54 (in Chinese)
6. Stojić D et al (2015) Improved stator flux estimator for speed sensorless induction motor drives. IEEE Trans Power Electron 30(4):2363–2371
7. Seyoum D, Grantham C, Rahman MF (2003). Simplified flux estimation for control application in induction machines. In: Electric machines and drives conference. IEMDC'03. IEEE international. Vol. 2. IEEE
8. Hu H, Li YD, Yi Z (2002) Direct torque control of induction motor for railway traction in whole speed range. In: IECON 02 [Industrial electronics society, IEEE 2002 28th annual conference of the]. Vol. 3. IEEE

# Design of Median Machine in Battery Test System

Jianan Chen, Jiuchun Jiang and Jingxin Li

**Abstract** The three-level structure composed of upper, median and lower machine is applied in battery test system (BTS) in this paper. The median machine in this BTS is designed and realized. CAN bus is used to communicate with each other between the upper and the median machine. RS-485 bus is used between the median and the lower machine. When the upper machine is online, the median machine can parse battery test instructions, store and send them to the lower machine. When the upper machine transits to offline state, the median machine can control the lower machine to continue battery test. When there is not an upper machine in BTS, the median machine can independently create and edit battery test and control the lower computer to complete test.

**Keywords** Median machine · CAN · RS-485 · Battery test system

## 1 Introduction

The 13th Five-Year Plan encourages accelerating development of urban railway system and the construction of an efficient and intensive rail network. With the rapid development of urban railway system, power battery, as the key power unit, will receive unprecedented attention and development. As an important quantitative analysis tool in battery research and diagnostics, battery test system (BTS) also becomes a research focus, especially the power unit and battery state data acquisition unit of BTS are made deep research [1–3]. At present, BTS mainly adopts the two-level structure, in which computer is used as the upper machine and power unit is used as the lower machine [4]. The upper machine is directly connected to the lower machine through communication cable, and the controlling message is

---

J. Chen (✉) · J. Jiang · J. Li  
National Active Distribution Network Technology Research Center,  
Beijing Jiaotong University, No.3 Shangyuancun, Haidian District,  
Beijing 100044, People's Republic of China  
e-mail: 15121394@bjtu.edu.cn

© Springer Nature Singapore Pte Ltd. 2018

L. Jia et al. (eds.), *Proceedings of the 3rd International Conference on Electrical and Information Technologies for Rail Transportation (EITRT) 2017*, Lecture Notes in Electrical Engineering 482, [https://doi.org/10.1007/978-981-10-7986-3\\_42](https://doi.org/10.1007/978-981-10-7986-3_42)

395

directly sent from the upper to lower machine. If communication failure occurs and results in an online-offline transition of the upper machine, BTS will not continue to work. To solve this problem, researchers have proposed a simple median machine based on 51 single-chip microcomputer. However, limited to the memory storage and processing ability, the simple median machine can only maintain the system operation for a short time. In this paper, the three-level structure of BTS is shown in Fig. 1. The median machine is based on a small size, light weight, high reliability and powerful function industrial personal computer (IPC). This median machine can be simply hung or fixed on the cabinet of the lower machine. This ensures the reliable connection between median and the lower machine and avoids the long range communication resulting in the failure. The median machine can also provide friendly GUI to operators and help operators intuitively know the state of the lower machine or operate simply.

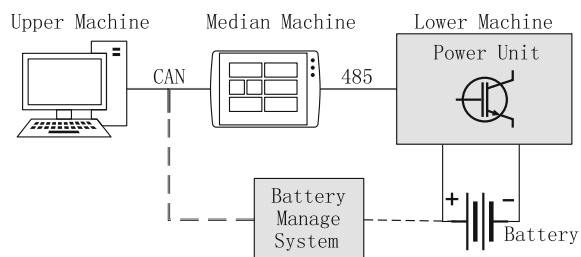
In present, the primary methods of communication between the upper and the median machine are CAN, RS-485, Ethernet and others [5–8]. In some special cases, GSM and other wireless network can also be used [9]. Power battery is mainly applied in railway transit and electrical vehicle and CAN is widely used in this area. The features of CAN are long range, flexible extension and high reliability, which meet the requirement of BTS. Moreover, the power unit of BTS only acquires the status of battery modules. CAN is widely adopted in the battery management system (BMS), which can acquires the status of battery cells. If CAN is used, the upper machine can be connected to the median machine and simultaneously time receive the status of battery cells from BMS. Therefore, CAN is adopted as the communication method between the upper and the median machine in this paper. And RS-485 is adopted as the communication method between the median and the lower machine.

In this paper, the median machine is the intermediate equipment and it is also required to maintain the basic system function when there is no more upper machine working.

## 2 Mechanism of Median Machine

In order to meet the need of three-level BTS, the median machine is requested three functions, including:

**Fig. 1** The structure of three-level BTS



- (a) Receives step instructions from the upper machine, stores, parses and sends to the lower machine one by one, and send the working state of the lower machine back to the upper machine;
- (b) Stores one or more step instructions. When the upper machine transits from online state to offline state, the median machine controls the lower machine to sequentially execute instructions;
- (c) Can be operated to create and edit simple step instructions. When there is not an upper machine, the median machine can independently create or edit step instructions and control the lower machine to complete the battery test.

## ***2.1 Mechanism of Median Machine with Upper Machine Online***

In this paper, CAN bus connected to the median machine adopts CAN 2.0B extension mode and the baud rate is 250 kbps. The CAN messages are comprised of ID and data. In this paper, the definition of message ID is based on SAE J1939 Data Link Layer protocol [10]. The median machine uses event trigger mechanism to response the signal from CAN bus. When a CAN message is detected on bus, an interruption will be triggered to set an acknowledgement flag (ACK flag). The median machine's main function periodically detects every CAN ACK flags. When main function detects an ACK flag set, the sub-function to parse the message will be called. The sub-function acquires the type and parameters of instruction from the message and stores them in the tail of the step instruction queue. Meanwhile, the median machine sends working status and error information of the lower machine to the upper machine according to protocol.

RS-485 bus adopts MODBUS RTU protocol in this paper. According to protocol, bus adopts master-slaver mode to request and response. In this paper, the lower machine is master node and the median machine is slaver node. The lower machine requests reading or writing operation and the median machine response to the lower machine. The lower machine periodically reads step instruction from the median machine and writes working status. The median machine allocates storage space to store the data read or written by the lower machine. The address of these data is listed in a mapping table corresponding to the data ID in MODBUS RTU protocol.

The median machine also allocates storage space to the step instruction queue. The step instruction from the upper machine is stored in the tail of the queue. The median machine is able to create a step instruction in the tail of the queue and edit or delete each one in the queue. When the median machine receives a new step instruction and there are  $N$  steps stored in the queue, the median machine will process the CAN message and store the instruction type and parameter at the  $N + 1$  step position. When the lower machine complete a step, the median machine controls the lower machine to implement the first step instruction in the queue and at the same time the number of remaining steps in the queue  $N$  is reduced by 1.

## ***2.2 Mechanism of Median Machine with Upper Machine Offline***

When the upper machine transits from online state to offline state, the median machine controls the lower machine to execute the battery test step according the step stored in the step queue. The step instruction queue working mechanism is consistent with the above. After the upper machine is offline, the median machine cannot receive a new message and it controls the lower machine to execute the step instructions stored in the memory until the last one completed, and then the system will enter the standby state. After the upper machine offline, the user cannot check the data through the upper machine. Thus, the median machine is requested to display the working state and data. The median machine provides the display screen. The status and data of the lower machine sending to median machine are displayed on the median machine screen in real time.

## ***2.3 Mechanism of Median Machine Without Upper Machine***

In the absence of the upper machine, the median machine needs to be able to independently control the lower machine to complete a series of battery test steps. Since the user cannot create a battery test step through the upper machine, it is necessary to create and edit step instructions through the median machine. Thus, the median machine are requested to provide a human-machine interface to allow user to input instruction and parameter to create new steps and edit the existing ones.

# **3 Program Design of Median Machine**

The median machine in this paper is developed by using TPC1061TI touch screen industrial computer as the platform of Beijing Kunluntongtai Automation Software Technology Co., Ltd. This type of IPC consists of Cortex-A8 CPU, the 10.2 inch LCD screen, build-in 128 M storage space and the communication interface of RS-485 and CAN. The touch screen can meet the hardware request of system. The IPC is programmed by using MCGS configuration software on computer.

## ***3.1 Construction of Communication Device***

In the MCGS configuration software, the parent device and child device for communication device are configured under the page of the communication device, as

shown in Fig. 2. The parent device completes the initialization of the CAN and the RS-485 controller and sets the address, baud rate and other parameters. The child device sets the CAN message ID, data format and RS-485 data ID and other parameters. The status of bus can be obtained to check whether a new communication message is received by reading the status register of parent device. Configuring the data register of child device, the address of the data in the receiver register of communication controller can be set.

As described above, the parent and child devices are built under the MCGS configuration software. As shown in Fig. 3, CAN parent device are created and parameters are configured. The child device is connected to the parent device. According to the CAN protocol, the upper machine sends 6 kinds of controlling messages to the median machine and the median machine sends 21 kinds of state messages to the upper machine. The child devices from “PC\_HC\_1” to “PC\_HC\_6” are used to represent each controlling messages. When the upper machine sends a controlling message, the median machine will automatically store the data in the corresponding receiving register. The message’s data is connected to the variable for further data processing. The child device “HC\_PC” is used to represent the status message sent from the median machine to the upper machine, which will be described below.

RS-485 communication parent and child device are built by the similar method to CAN. RS-485 parent device is created to initialize the controller and parameters are configured. The child device is connected to the parent device and the data ID is configured. According to MODBUS protocol, child device is used to define the permission of each data, which limits the lower machine can only read or both read and write one of data.

Fig. 2 The communication device in MCGS

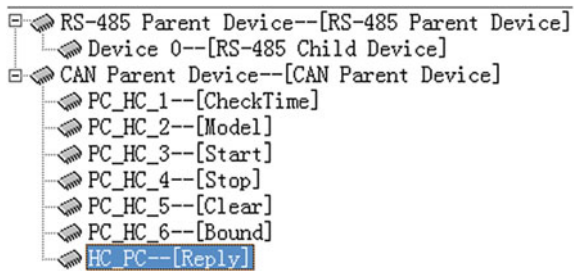


Fig. 3 The parent device of CAN

Device Name	CAN Parent Device
Device Note	CAN Parent Device
Initial State	1 - Start
Minimum Acquisition Period	100ms
Device ID	1
Baud Rate	8 - 250k
Mask Code	0
Mode	2 - 2.0B extended



### 3.2 Data Forwarding

As described above, CAN and RS-485 messages are clearly different. Thus, the parsing script is needed. Meanwhile, the script is needed to call the child device “HC\_PC” when sending message to the upper machine.

Take the CAN message “PC\_HC\_2” for example. When the child device receives a “PC\_HC\_2” message, “PC\_HC\_StartDet” is set 1, which means the median machine receives a new step instruction. Then the script program begins to parse this message. “PC\_HC\_Type” represents the type of step. If the type is constant power charging, “CurStepType\_temp01” is assigned 2. The parameter of this step is given by the variable “PC\_HC\_Para3L” and “PC\_HC\_Para3H”. And “StepType\_temp01” and “StepPara01” are sent to the lower machine via the RS-485 message, which sends the type and parameters of the step. Similarly, the script can be written to forwarding other data.

The program which means median machine sends a status message “HC\_PC\_3” are shown in Fig. 4. This message contains the output current and voltage. These two parameters are floating point number and the length of decimal places is 3, and the variables are allocated 4 bytes. Two values are stored into the 8 byte of the CAN send register by a series of calculations. Then the child device “HC\_PC” is called to send the message whose ID is 0X00020020.

### 3.3 Implementation of Step Queue

As shown in Fig. 5, when the upper machine sends the first controlling message, the 8 bytes of parameters are parsed by the median machine and stored in the variable “StepType01” and “StepPara01”. At the same time, the flag variable “StepConfirm01” is set 1. The value of variable “CurrentStep” is 0 when the median machine is standby and the value is automatically added 1 after receiving the start command. When the variable “StepConfirm01” value is 1 and variable “CurrentStep” value is 1, the median machine will sends the variables

```
HPD1=(C_VoltOut*1000) Mod 256
HPD2=(C_VoltOut*1000) Mod 65536\256
HPD3=(C_VoltOut*1000) Mod 16777216\65536
HPD4=(C_VoltOut*1000)\16777216
HPD5=(C_CurrOut*1000) Mod 256
HPD6=(C_CurrOut*1000) Mod 65536\256
HPD7=(C_CurrOut*1000) Mod 16777216\65536
HPD8=(C_CurrOut*1000)\16777216
!SetDevice(HC_PC,6,"write(131104,0,1,8,1,HPD1,HPD2,HPD3,HPD4,HPD5,HPD6,HPD7,HPD8)")
```

Fig. 4 The segment of sending message HC\_PC\_3

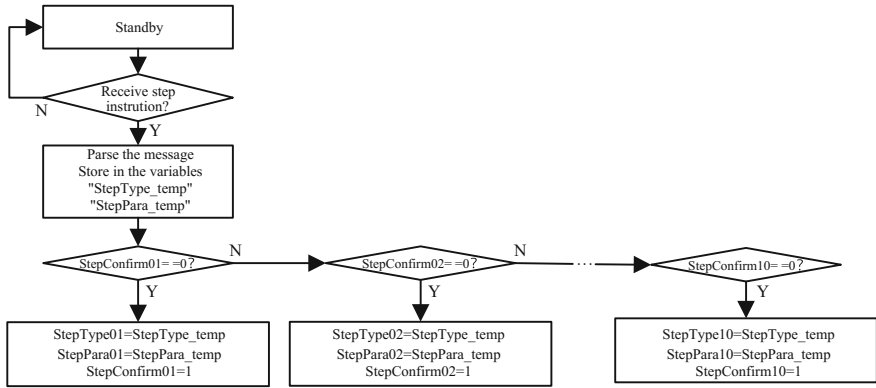


Fig. 5 Working step storage queue

“StepType01” and “StepPara01” values to the lower machine to be executed. After the first step completed, the variable “CurrentStep” value is added 1. Then if the variable “StepConfirm02” value is 1, the second step is executed as the above, otherwise the system is going to be standby and step queue and flag variables are cleared. When the step instruction is being executed, if the upper machine sends a new controlling message, the median machine will sequentially check the value from variables “StepConfirm01” to “StepConfirm10”. If the value from variables “StepConfirm01” to “StepConfirm03” is 1 and “StepConfirm04” is 0, this message will be stored in the variables “StepType04” and “StepPara04” and the variable “StepConfirm04” value is set 1.

### 3.4 Design of Graphical User Interface

Create a new interface, use the tools and the controls provided by MCGS to create a user interface, configure the controls and connect the variables to the controls in order to display the value or to assign the variables. As shown in Fig. 6, when input number to the input box, the value of the variable connected to the input box is assigned. The new value is sent to the lower machine through the RS-485 bus. When the status of lower machine is changed during it working, the value is sent to the median machine through the RS-485 bus. The median machine displays the value of the variable in the display box connected to the variable after the value received.

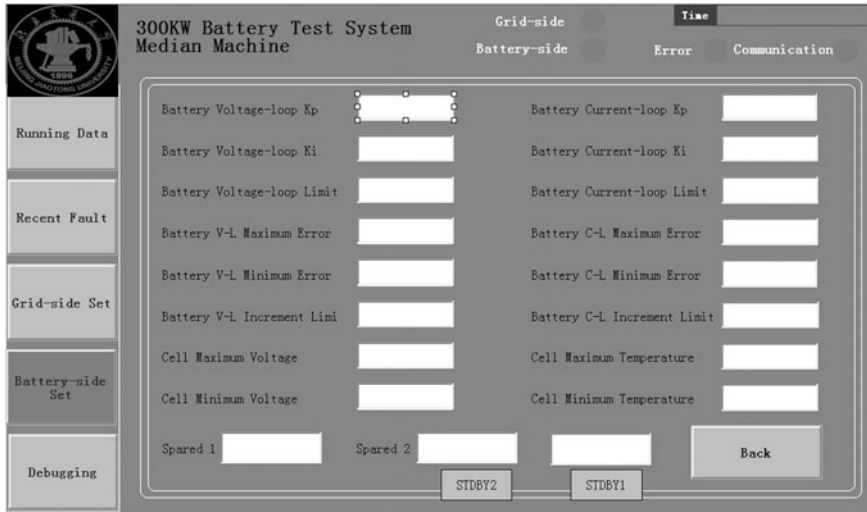


Fig. 6 The median computer's GUI

## 4 Conclusion

In this paper, a three-level structure battery test system is proposed. According to the characteristics and requirements of the BTS, the median machine is designed and implemented. With the addition of the median machine, the reliability of the system is improved, and the system can continue to work when the upper machine is offline and the battery test is carried out according to the preset step. The median machine provides a new method to input step instructions. When the upper machine is not able to be used, the battery test step can be created and edited by the median machine. CAN bus used between the upper machine and the median machine can satisfy the practical application requirements, but also provides a convenient and reliable method for the further expansion of the system. It also provides the research direction for the further development in the future.

**Acknowledgements** This work is supported by Beijing Municipal Science and Technology Project (Z161100002216008).

## References

1. Liu X (2014) Study on data acquisition system of the power battery's test platform. Beijing Jiaotong University, Beijing (in Chinese)
2. Qin Q, Sun Y, Zhong X (2007) Study on battery voltage automatic sampling system. J Suzhou Univ (Eng Sci Ed) 27(6):34–37 (in Chinese)

3. Zhang D (2012) Design and realization of battery management system based on embedded technology. Wuhan University of Technology, Wuhan (in Chinese)
4. Liu J (2009) Design of data acquisition system of HEV power batteries integration test platform. Haerbin University of Science and Technology, Haerbin (in Chinese)
5. Teng Y (2006) The embedded system for battery test. Tianjin University, Tianjin (in Chinese)
6. Zhang W, Zhang W, Mao P et al (2016) Development of photovoltaic grid power system monitoring and control system. *Chin J Power Sources* 40(3):633–637 (in Chinese)
7. Pan Y, Wang Z, Wang H (2011) The methane sensor monitoring and control system based on RS-485 communication. *Microcomput Inf* 27(5):60–62 (in Chinese)
8. Meng F, Wang Y, Yang D et al (2017) Data detecting and communication of rockwell controller and MCGS based on MODBUS protocol. *Electronics World* (2):200–201 (in Chinese)
9. Li B (2014) Design of novel wireless gas monitoring system. *Comput Measur Control* 22 (4):1062–1064 (in Chinese)
10. Society of Automotive Engineers (2006) Data link layer. SAE J1939/21-2006

# The Research on Bi-Directional DC/DC Converter for Hybrid Power System

Guodong Liu, Zhipo Ji, Ruichang Qiu and Xiang Wang

**Abstract** In the hybrid power system, the bidirectional DC/DC converter, as the driving devices for energy storage element, is the core element of hybrid energy storage system and has the function of stabilizing the intermediate DC link voltage. This paper introduces the working principle and the derivation of bidirectional Buck/Boost converter in the process of modeling. A voltage and current double closed loop control system based on load current prediction is designed. When the load changes constantly, the response speed of the system can be improved. Simulation studies using MATLAB/Simulink show that the established model and control strategy can be used for further research.

**Keywords** Hybrid power system · Bi-directional DC/DC converter  
Switching convert modeling · Double closed-loop control system

## 1 Introduction

For hybrid powertrains, the basic requirement for bi-directional DC/DC converters is the ability to achieve two-way flow of energy, and the structure should be as simple as possible to ensure high reliability. Bi-directional Buck/Boost topology has the advantages of simple structure, small number of devices and the device is subjected to less voltage stress [1]. It is suitable for high power. Therefore, the bi-directional Buck/Boost circuit is used as the topology of bi-directional DC/DC converter.

---

G. Liu (✉) · R. Qiu  
School of Electrical Engineering, Beijing Engineering Research Center of Electric Rail Transportation, Beijing Jiaotong University, Beijing 100044, China  
e-mail: 16121481@bjtu.edu.cn

Z. Ji  
Beijing Spacecraft, Beijing 100190, China

X. Wang  
State Key Laboratory of Advanced Power Transmission Technology, Global Energy Interconnection Research Institute, Beijing 102206, China

The mathematical model has important significance for the research on the control system of switching power supply. To ensure that the switching power supply has near ideal performance, it can maintain good output characteristics during the load change process. Therefore, the mathematical model of DC/DC converter is the basis of designing an ideal control system. In order to accordance the complex power requirements in the operation of EMU, the control system based on current prediction is designed on the basis of the voltage and current double closed-loop control strategy. The dynamic response of the system is improved.

## 2 Operation Principle

The working principle of the bi-directional Buck/Boost circuit is shown in Fig. 1 In the Boost operation mode, the bridge upper arm ( $Q_1$ ) is always in off state, and by controlling the on-off of the lower arm ( $Q_2$ ) of the bridge arm, the energy flows from the battery to the middle DC high voltage side, as shown in Fig. 1a. In the Buck operating mode, the bridge arm  $Q_2$  is always switched off, and the energy is transferred from the middle DC side to the battery by controlling the on-off of the upper arm ( $Q_1$ ) of the bridge arm, as shown in Fig. 1b.

## 3 Modeling Research

The DC/DC converter is a nonlinear and time-varying system and the dynamic analysis is complex. In the design of control strategy of DC/DC converter, the dynamic model of DC/DC converter must be analyzed to counteract the influence of low frequency small signal disturbance so as to meet the design requirements of the system [2]. The existing modeling methods are divided into numerical simulation method and analytic modeling method. The accuracy of analytical modeling method is lower than that of numerical modeling method, but it has definite physical meaning, which is easy to study the change of parameter control

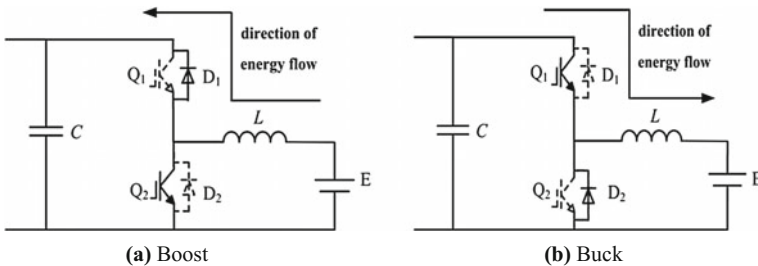


**Fig. 1** Operation principle of bi-directional Buck/Boost converter circuit

characteristics. Small signal model is a kind of analytic modeling method, that is, analytic expression of the system is derived by analytic modeling. What's more, average state space method and switching average model method are Comparatively common [3]. It is a common analytic modeling method to deduce the small signal model of the system by means of the state space averaging method [4]. The expressions obtained by using this method are clear in physical meaning and can be used to study the steady-state and dynamic performance of the system by means of linear analysis in the circuit.

In this paper, the Boost model of Buck/Boost circuit is taken as an example. The Buck/boost Converter operating in the Boost mode has two stages of operation during each switching cycle when the inductor current is continuous. The equivalent circuit is shown in Fig. 2, and each element in the diagram is considered as an ideal device without affecting parasitic parameters.

When the  $Q_2$  is switched off, the state equation of the circuit matrix is as follows:

$$\begin{bmatrix} \dot{i}_L(t) \\ \dot{v}_{dc}(t) \end{bmatrix} = \begin{bmatrix} 0 & -\frac{1}{L} \\ \frac{1}{C} & -\frac{1}{R_L C} \end{bmatrix} \begin{bmatrix} i_L(t) \\ v_{dc}(t) \end{bmatrix} + \begin{bmatrix} \frac{1}{L} \\ 0 \end{bmatrix} v_c(t) \tag{1}$$

When  $Q_2$  is switched on, the state equation of the circuit matrix is as follows:

$$\begin{bmatrix} \dot{i}_L(t) \\ \dot{v}_{dc}(t) \end{bmatrix} = \begin{bmatrix} 0 & 0 \\ 0 & -\frac{1}{R_L C} \end{bmatrix} \begin{bmatrix} i_L(t) \\ v_{dc}(t) \end{bmatrix} + \begin{bmatrix} \frac{1}{L} \\ 0 \end{bmatrix} v_c(t) \tag{2}$$

Under the assumption of low-frequency hypothesis and small ripple [5], the equation of state of is derived from the Eqs. (1) and (2) taking the average value in a switching period and introducing small signal perturbation:

$$\begin{aligned} \begin{bmatrix} \dot{I}_L + \tilde{\dot{i}}_L(t) \\ \dot{V}_{dc} + \tilde{\dot{v}}_{dc}(t) \end{bmatrix} &= (D + \tilde{d}) \left\{ \begin{bmatrix} 0 & 0 \\ 0 & -\frac{1}{R_L C} \end{bmatrix} \begin{bmatrix} I_L + \tilde{i}_L(t) \\ V_{dc} + \tilde{v}_{dc}(t) \end{bmatrix} + \begin{bmatrix} \frac{1}{L} \\ 0 \end{bmatrix} (V_c + \tilde{v}_{dc}(t)) \right\} \\ &+ [1 - (D + \tilde{d})] \left\{ \begin{bmatrix} 0 & -\frac{1}{L} \\ \frac{1}{C} & -\frac{1}{R_L C} \end{bmatrix} \begin{bmatrix} I_L + \tilde{i}_L(t) \\ V_{dc} + \tilde{v}_{dc}(t) \end{bmatrix} + \begin{bmatrix} \frac{1}{L} \\ 0 \end{bmatrix} (V_c + \tilde{v}_{dc}(t)) \right\} \end{aligned} \tag{3}$$

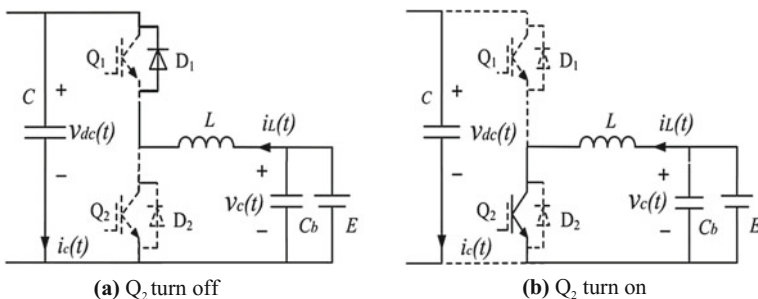


Fig. 2 Work principle of Boost converter

According to the Eq. (3), the state equation of small signal can be obtained when the Boost model is obtained:

$$\begin{bmatrix} \tilde{i}_L(t) \\ \tilde{v}_{dc}(t) \end{bmatrix} = \begin{bmatrix} 0 & -\frac{1-D}{L} \\ \frac{1-D}{C} & -\frac{1}{RC} \end{bmatrix} \begin{bmatrix} \tilde{i}_L(t) \\ \tilde{v}_{dc}(t) \end{bmatrix} + \begin{bmatrix} \frac{1}{L} \\ 0 \end{bmatrix} \tilde{v}_c(t) + \tilde{d} \begin{bmatrix} 0 & \frac{1}{L} \\ -\frac{1}{C} & 0 \end{bmatrix} \begin{bmatrix} I_L \\ V_{dc} \end{bmatrix} \tag{4}$$

In the Boost mode, the AC small signal equivalent model is shown in Fig. 3.

According to the equivalent circuit of AC small signal, the loop equation of KCL and KVL is as follows:

$$\begin{cases} \tilde{v}_c - \tilde{i}_L \cdot sL + (D\tilde{v}_{dc} + \tilde{d}V_{dc}) - \tilde{v}_{dc} = 0 \\ \tilde{i}_L - (D\tilde{i}_L + \tilde{d}I_L) - \tilde{v}_{dc}(sC + \frac{1}{R}) = 0 \end{cases} \tag{5}$$

Obtained by the above formulas:

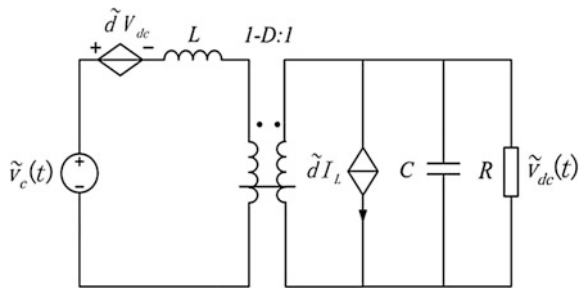
The transfer function ( $G_{id}(s)$ ) of duty cycle ( $\tilde{d}(s)$ ) to inductor current of battery side ( $\tilde{i}_L(s)$ ) is:

$$G_{id}(s) = \left. \frac{\tilde{i}_L(s)}{\tilde{d}(s)} \right|_{\tilde{v}_c(s)=0} = \frac{V_{dc}(\frac{2}{R} + sC)}{LCs^2 + \frac{L}{R}s + (1-D)^2} \tag{6}$$

The transfer function ( $G_{vc}(s)$ ) of the input voltage of battery side ( $\tilde{v}_c(s)$ ) to capacitor voltage of DC bus side ( $\tilde{v}_{dc}(s)$ ) is:

$$G_{vc}(s) = \left. \frac{\tilde{v}_{dc}(s)}{\tilde{v}_c(s)} \right|_{\tilde{d}(s)=0} = \frac{(1-D)}{LCs^2 + \frac{L}{R}s + (1-D)^2} \tag{7}$$

**Fig. 3** AC small signal equivalent model of Boost mode converter





### 4 Double-Loop Control Strategy

In the non-contact mode, the motor starts, accelerates, decelerates, and brakes frequently. Accordingly, the bus voltage varies continuously over a wide range [8]. The core function of the bidirectional DC/DC converter is to maintain the constant voltage of the intermediate DC link. Therefore, the control system should be double-loop control system [6, 7].

For the traditional double closed loop control system, the voltage PI controller can't realize the static tracking of the dynamic command when the load changes constantly. This problem can be alleviated by increasing the integral coefficient in a certain extent. But the response speed of the external voltage loop can't be faster than the current loop, in other words, the integral coefficient can't increase without limitation [8, 9]. Additional inductor current can be estimated in real time by adding additional load, which can improve the performance of the system under conditions of changing load. It can be obtained by calculating the ratio of the power derived from the traction inverter and the auxiliary inverter ( $P_{demand}$ ) to the battery voltage ( $U_{bat}$ ). The control system is reorganized into the traditional double closed loop control system when the estimated load current is severe distorted, which can ensure the system stability. It is shown in Fig. 4.

$G_v(s)$  and  $G_i(s)$  are voltage and current control transfer function;  $Z(s)$  is the output voltage to current pair transfer function;  $G_M(s)$  is the modulation transfer function;  $H_i(s)$  and  $H_v(s)$  are current and voltage sampling transfer functions.

In the double closed loop control system with load current prediction, The predicted current and the actual load current are equivalent to the system disturbance. Therefore, it is only necessary to study the stability of double closed loop control systems. The designing process is as follows:

Transfer function of current inner loop PI controller:

$$G_i(s) = K_{ip} + \frac{K_{ii}}{s} \tag{8}$$

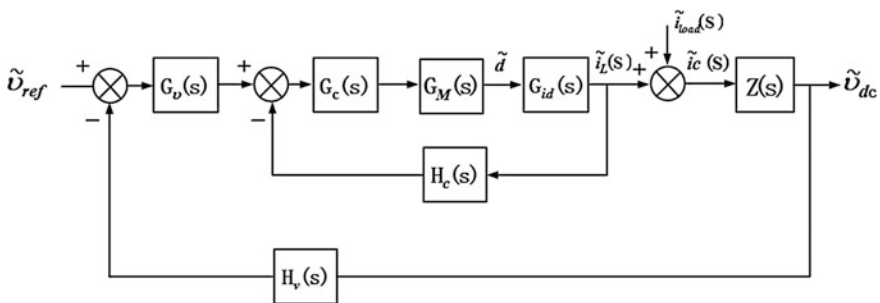


Fig. 4 Diagram of voltage and current double-loop control

The open-loop transfer function of current loop is:

$$G_{io}(s) = G_M(s)H_i(s)G_{id}(s)G_i(s) \tag{9}$$

Take the modulation link  $G_{M(s)} = 1$ , the current sampling link  $H_i(s) = 1$ . The PI parameter of current loop controller is  $K_{ip} = 5$ ,  $K_{ii} = 0.01$ . Substituting the system parameters shown in Table 1 into formula (9), the bode diagram of open-loop transfer function can be obtained, as is shown in Fig. 5.

In the figure, the amplitude margin is infinite, the phase margin is 89.8°, the crossing frequency is 503 Hz, the slope is 20 db/dec, the current inner loop has excellent stability and very large margin of amplitude.

Outer voltage loop PI controller transfer function:

$$G_v(s) = K_{vp} + \frac{K_{vi}}{s} \tag{10}$$

The transfer function of the DC side voltage to the current:

$$Z(s) = \frac{1}{Cs} \tag{11}$$

**Table 1** Parameters of bi-directional DC/DC converter for HEMU

Parameters of IGBT	3300 V/1500 A	Switching frequency	1 kHz
Inductor	4 mH	Capacitor	8000 μF
Low-voltage side	1100 V	High voltage side	1500 V/1750 A

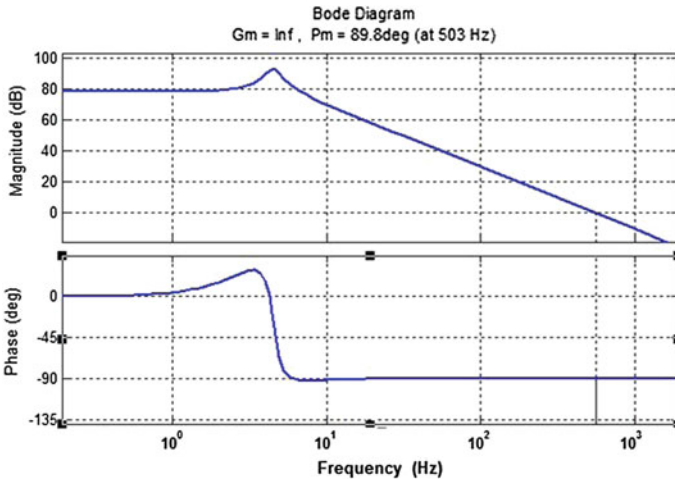


**Fig. 5** Diagram of Boost mode current open-loop transfer function bode

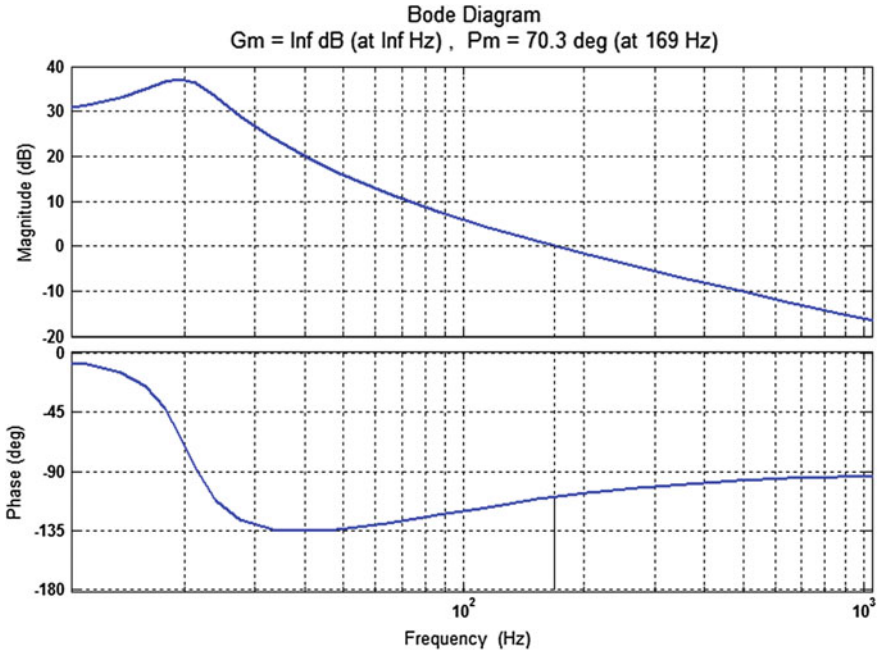


Fig. 6 Bode diagram of close-loop transfer function of Boost inner current loop

The closed-loop transfer function of current loop:

$$G_{ic}(s) = \frac{G_M(s)G_{id}(s)G_i(s)}{1 + G_{io}(s)} \tag{12}$$

The open-loop transfer function of voltage outer loop is:

$$G_{vo}(s) = H_v(s)Z(s)G_{ic}(s)G_v(s) \tag{13}$$

The voltage sampling transfer function  $H_v(s) = 1$ , PI parameter is  $K_{vp} = 0.013$ ,  $K_{vi} = 0.0016$ . The bode diagram of open-loop transfer function is shown in Fig. 6.

The amplitude margin is infinite, the phase angle margin is 70.3°. It is verified that the voltage outer loop is stable and the open loop cut-off frequency is 169 Hz. The inner loop of the control system is fast in response and the outer loop of the voltage is stable.

### 5 Simulation Results

In this paper, a circuit-level simulation model of Buck/Boost converter is built by MATLAB/Simulink simulation. The switching frequency is 1 kHz, and the specific parameters are shown in Table 1. The control part adopts the S-function module.

In the simulation, the two power batteries were used to carry out the back-back test of the power battery. A power battery is discharged as a power source, and a power battery is charged as a load. The DC side voltage is 1500 V. Variations in load are simulated during the simulation. To verify the capability of controlling DC voltage for double closed-loop control system with load current prediction. The simulation result is shown in Fig. 7.

As shown in Fig. 7, DC peak-peak voltage of DC side is less than 5 V and there is no static deviation. The double closed-loop control system achieves excellent voltage regulation performance, and has good dynamic and stability.

The Simulation result that the other conditions are exactly the same as of double closed-loop control system without load current prediction is shown in Fig. 8.

By comparing Figs. 7 and 8, the output voltage ripple is basically the same when the load current is stable. Obviously, the double closed loop control system without load current prediction is unable to track the target voltage without static difference. When the load increases gradually, the output voltage is lower than target voltage.

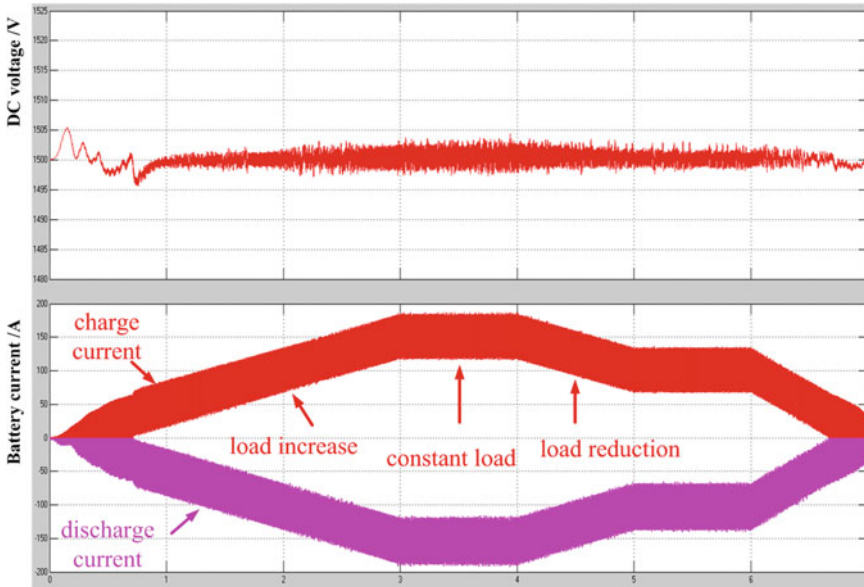
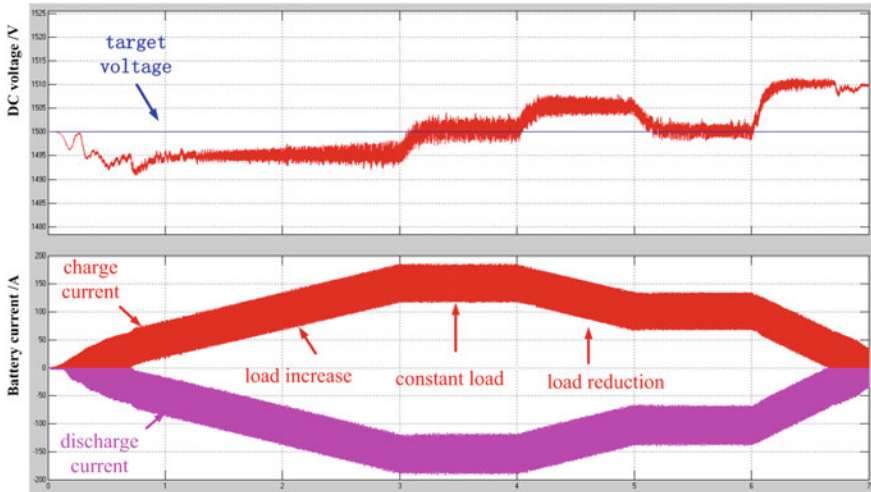


Fig. 7 Simulation result of back to back test of Bi-DC/DC convert



**Fig. 8** Simulation result of back to back test of Bi-DC/DC convert without predictive load current estimation

Conversely, it will be higher. The deviation value is positively correlated with the slope of the load change. The optimization function of the load current prediction in the dynamic process of load fluctuation for the double closed-loop control system is verified.

## 6 Conclusion

In hybrid powertrain, the stability of cascade system consisting inverter and DC/DC convert affects the performance of the whole system. Therefore, the establishment of a reasonable mathematical model is the basis of the design and optimization of the control system. The double closed loop control system using predictive load current estimation can effectively improve the dynamic response of the system when the load changes constantly, stabilizing effectively the DC side voltage. The control method accords with the basic requirements of the hybrid EMU and can be used for further research.

**Acknowledgements** This work was supported by the China National Science and Technology Support Program under Grant 2016YFB1200504-C-01, Beijing major science and technology project under Grant Z171100002117011.

## References

1. Zhang F, Zhu C, Yan Y (2005) The controlled model of bi-directional DC-DC converter. In: Proceedings of the CSEE Uo25 No.11 Jun. 2005. (in Chinese)
2. Gong J, Liu W, Xie S (2010) Modeling and simulation of bi directional DC DC power converter. *Comput Simul* 27(10):263–267 (in Chinese)
3. Xin C (2009) Modeling and simulation of nonideal DC–DC converters. Hefei Polytechnic University. <https://doi.org/10.7666/d.y1509101>. (in Chinese)
4. Xu H (2005) Research on topology and analysis theory of high power bi-directional DC-DC converter. Institute of electrical engineering, Chinese Academy of Sciences, 2005. (in Chinese)
5. Zhang F, Zhu C, Yan Y (2005) Control model of bi-directional DC-DC converter. *Proc Chin Soc Electr Eng*, 25(11):46–49. (in Chinese)
6. Vazquez N, Alvarez J, Aguilar C et al (1998) Some critical aspects in sliding mode control design for the Boost inverter. *Power Electron Congr*, 76–81
7. Pinheiro H, Martins A, Pinheiro J (1993) Single-phase voltage inverters controlled by sliding mode. In: *Brazilian automation control conf*, 1177–1182
8. Luo Y (2005) Study on bi-directional DC/DC converter and battery energy management system. *Huazhong University of Science and Technology*, 2013 25(11):46–49, <https://doi.org/10.7666/d.D410662> (in Chinese)
9. Diaz J, Martin-Ramos JA, Prieto MJ (2004) A double-closed loop DC/DC converter based on a piezoelectric transformer. *Appl Power Electron Conf Exposition*, 2004(3):1423–1428

# Experimental Study the Electric Braking Anti-skid Performance of Electric Multiple Units

Baomin Wang, Xiang Gao, Yongfong Song, Yi Zhou and Yang Lu

**Abstract** When an electric multiple units (EMU) runs on a long heavy downgrade track, electric brake failure may occur during the anti-skid control process, which would result to longer pneumatic braking time, high brake pad temperature and wear, etc. Thus, it is important to determine optimal strategies for the anti-skid control of EMUs through field experiments. In the present study, a method of spraying anti-friction fluid was adopted to simulate rail surface conditions with low adhesion. This would allow low adhesion conditions and enable the EMU to continuously operate on it. Then, control parameters and strategies were constantly adjusted to obtain the optimal glide. The field experiment revealed that it is feasible to reduce electric brake failure times and improve electric power flow by optimizing the anti-skid control strategy.

**Keywords** Electric multiple units · Anti-skid performance · Experimental validation · Electric braking · Control strategy

## 1 Introduction

The formulation of electric braking forces of electric multiple units (EMUs) highly depend on the adhesive force between the wheels and rails, and electric braking power would be affected when sliding occurs. Sliding occurs when the braking

---

B. Wang (✉)

Postgraduate Department, China Academy of Railway Sciences,  
No. 2, Liushu Road, Haidian District, Beijing, China  
e-mail: wangbaomin1982@126.com

B. Wang

School of Mechanical and Electrical Engineering,  
Lanzhou Jiaotong University, Lanzhou, China

X. Gao · Y. Song · Y. Zhou · Y. Lu

Locomotive & Car Research Institute, China Academy  
of Railway Sciences, No. 2, Liushu Road, Haidian District, Beijing, China

© Springer Nature Singapore Pte Ltd. 2018

L. Jia et al. (eds.), *Proceedings of the 3rd International Conference on Electrical and Information Technologies for Rail Transportation (EITRT) 2017*, Lecture Notes in Electrical Engineering 482, [https://doi.org/10.1007/978-981-10-7986-3\\_44](https://doi.org/10.1007/978-981-10-7986-3_44)

force exceeds the maximum wheel-rail adhesive force. The electric braking force can achieve a no sliding transmission in adhesive boundaries. However, in rain, wet and snow environments, it is difficult to obtain stable adhesive forces to improve braking performance [1]. In the previous decades, studies and field experiments have revealed that wheel-rail adhesion can be effectively utilized by installing anti-skid control equipment [2]. However, electric brake failure may occur due to the improper control of anti-skid systems, especially in long heavy downgrade rails. This would induce a series of problems such as pneumatic braking delay and high temperature on the brake pads, which would occur due to low adhesion.

This study is the first time in China to conduct a special experiment to investigate the non-skid performance of electric brake systems. Based on the actual running data of EMUs in different adhesive conditions and control strategies, the influence of anti-skid control system parameters on anti-skid property was analyzed and validated, and the scientific support for the designation of the anti-skid control system of EMUs was provided.

## 2 Electric Anti-skid Control Principle

In the process of controlling anti-skid brake systems, a proper algorithm is introduced to judge the critical stage at which the glide is going to happen based on wheel rotating velocity and acceleration signals, and the regenerative brake force is reduced through the traction convector. This way, the brake force acting on the wheelset would rapidly decrease to a value lower than the adhesive force, preventing the wheel from sliding and restoring wheel-rail adhesion. Then, the exerting braking force is determined through specific conditions to realize the full use of the electric brake force under wheel-rail adhesion.

The primary mission of the electric anti-skid brake system is to judge the occurrence of the slide. At this stage, the criteria used to judge this sliding phenomenon are velocity difference, deceleration, longitudinal slip and deceleration differential. Among these, velocity difference and deceleration are commonly adopted. The principle of velocity difference is that as one wheelset slides, the velocity of its axle would inevitably be lower than the velocity of the non-sliding axle (a pure trail axle of the trailer) [3]. Thus, the difference between the velocity of the sliding axle and the standard velocity of the trailing axle is obtained. When this difference is larger than the default standard value, it is regarded to be sliding. In addition, the deceleration criterion is determined by comparing the reduction ratio of the wheel rotational speed to the default standard values [4]. When a locking slide occurs, the speed of the wheel would abruptly change, the deceleration would correspondingly increase, and a slide is assumed to occur once the deceleration becomes larger than the standard value. Due to the great difference between the wheelset and vehicle, the velocity of the wheelset will change relatively faster, and the deceleration would be faster than the velocity difference. Therefore, the criterion of deceleration was adopted prior in this study.



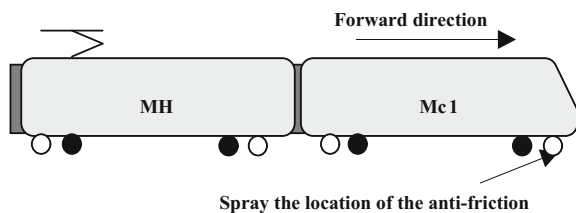
After accomplishing the judgment of the slide, the anti-skid control system will adopt effective strategies to achieve the purpose of controlling the slide. At present, the main methods can be classified as follows: logical threshold control method [5], indirect creep speed method, sliding mode variable structural control method [6], optimal control method [7], and fuzzy control method [8]. Among these methods, the logical threshold control method is not involved with the detailed mathematical model of the system, allowing a convenient way to achieve the control of the nonlinear systems. Thus, it is commonly used in practical applications. The logical threshold control method mainly uses one or several parameters as the controlling threshold, such as velocity difference, deceleration, deceleration difference and longitudinal slip ratio. By setting thresholds closely correlated to the controlling purpose, and based on the relationship between actual measurements and thresholds, the control parameters are adjusted to realize the controlling purposes.

In the present study, the logical threshold control method was implemented to achieve the anti-skid brake system of EMUs, in which the velocity difference and deceleration were used as the criterion for sliding conditions. Furthermore, with the confirmation of the sliding tendency, the electric torque is reduced according to the control of the traction convertor. In addition, the electric torque would be restored timely after the slide to adequately bring into the function of electric braking forces in the process of braking.

### 3 Test Methods

The field experiment was conducted in the Beijing Circuit Railroad. Furthermore, the low adhesive status of the rail surface was induced by spraying different proportions of anti-friction fluid, and the slides were simulated during the electric braking process of the EMU. The anti-friction fluid was paired by water and detergent using ratios of 50 L:0 L, 50 L:4 L, 50 L:8 L and 50 L:16 L. The moving axes were the second, and the third axis of the tested EMU was called Mc1, which corresponds to motor 1 and motor 2, respectively. In the test, Mc1 was the master vehicle, and the water outlet of the anti-friction fluid system was installed towards the moving direction of the first axis. The detailed positions are listed in Fig. 1.

**Fig. 1** The placement where the anti-friction fluid of the EMU was located



In the test, the master hand shank was placed at full traction level, the velocity of the EMU was accelerated from 0 to 160 km/h, and the master hand shank was placed at the maximum brake position of the first section. Consequently, the velocity of the EMU was decreased from 160 to 0 km/h. During this period, the anti-friction fluid was sprayed, and the following data was recorded.

Operating condition (handle level), trailer speed, speed of the EMU axle, given value of every motor car's electric brake, feedback value, sanding instruction, skid mark, pressure of the braking cylinder, output voltage of traction converter, traction motor current, BCU output voltage, net voltage, net flow and other information.

For quantitatively contrasting the non-skid property of the electric brake system under different control strategies, the percentage of electricity utilization (PEU) was introduced. PEU can be defined as the mean value of the ratio of the response value of the electric braking force and the given value, which was expressed by:

$$\text{PEU} = \text{mean} \left( \frac{\text{Feedback value}}{\text{Given value}} \right) \times 100\% \quad (1)$$

## 4 Experimental Results and Analysis for Software Version 0.1 Before Optimization

In the beginning of the experiment, the software version 0.1 was used to monitor the electric brake failure induced by anti-skid control when the EMU ran on a long heavy downgrade rail.

During the test, the EMU was under normal working condition when the running velocity reached 160 km/h, and the governor lever was pulled to the maximum brake position of the first section. In the meantime, the test personnel started to spray clear water on the rails to form the low adhesive state of the rail surface [9]. Figure 2 shows the experimental results of the anti-skid performance experiments with water sprayed on the rail surface. As shown in Fig. 2, the EMU begin to glide at a velocity of 138.9 km/h, and the degree of glides of the second axis was larger than that of the third axis. The PEU of the second axis

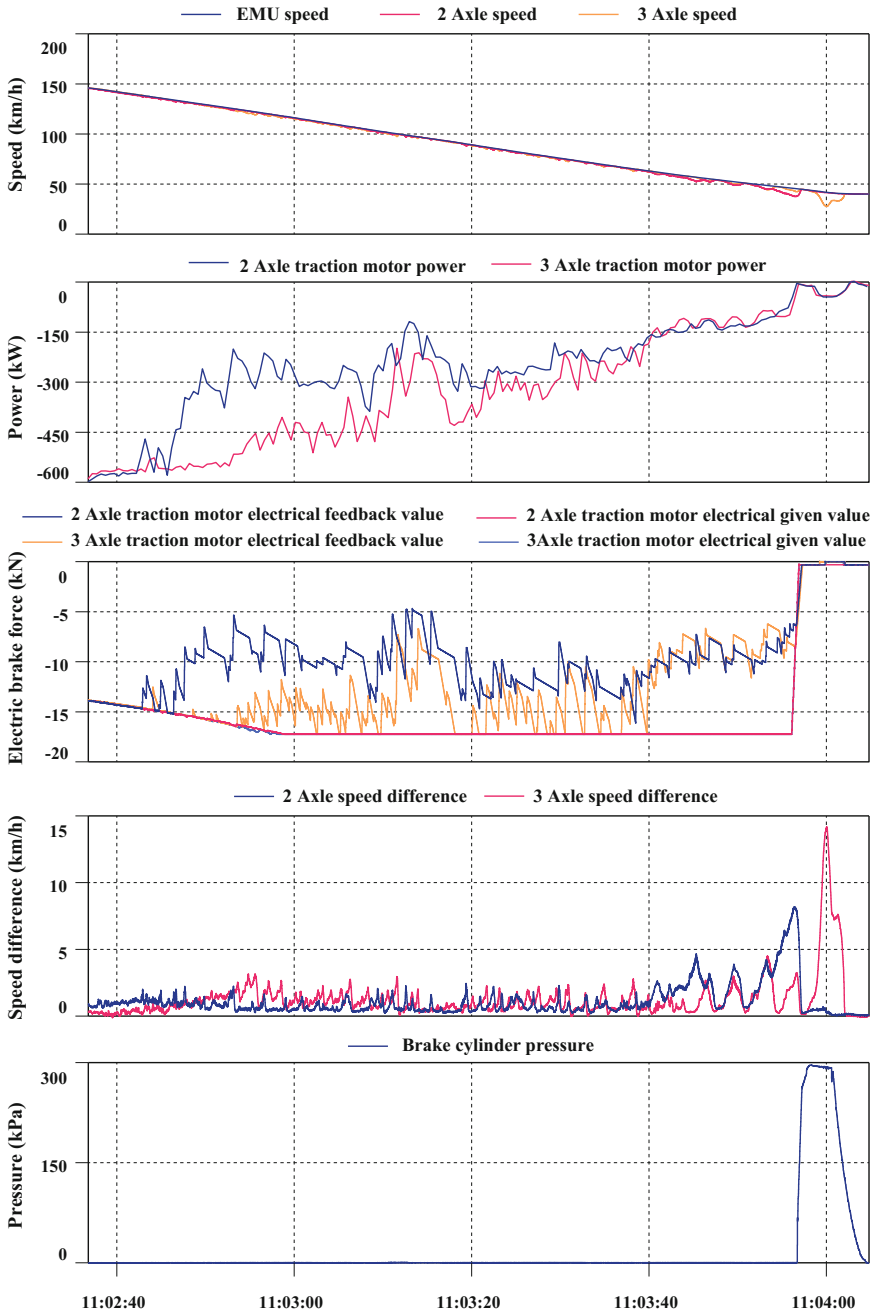


Fig. 2 Experimental results of the anti-skid performance for the non-optimized software version 0.1 (water)

**Table 1** Experimental results of the anti-skid performance by software version 0.1

Anti friction liquid ratio	Test no.	Maximum sliding speed (km/h)		Whether the electric brake was removed (Yes/No)	Velocity (km/h)	PEU of the last three seconds before removing electric brake (%)
		2nd axle	3rd axle			
Clear water	1	8.1	4.1	Yes	45.9	45.3
	2	2.6	3.5	Yes	90.6	33.5
50 L:4 L	1	3.5	3.1	Yes	87.9	39.7
	2	3.1	3.6	Yes	92.5	43.9
50 L:8 L	1	3.2	3.2	Yes	88.8	37.8
	2	2.9	2.8	Yes	115.1	45.9
50 L:16 L	1	3.2	3.3	Yes	100.6	36.2
	2	3.8	4.2	Yes	88.3	40.5

was 62.3% under the speed of 138.9–64.6 km/h, the PEU of the third axis was 86.5%, and the PEU of the first vehicle reached 74.4%. When running speed reached 45.9 km/h, sliding occurred on the second and third axis of the EMU; and when vehicle speed reached 45.9 km/h, the electric brakes of the first vehicle were eliminated and were implemented with the air brakes. The PEU of the electric brake of the second axis was approximately 54.1% within a speed range of 62.8–45.9 km/h, the PEU of the electric brake of the third axis was approximately 50.2%, and the electric brake of the first vehicle reached 52.2%. In the test, the maximum sliding speed of the second and third axis was approximately 8.1 and 4.1 km/h, respectively; and the PEU of the first vehicle before eliminating the electric brakes was 45.3%.

The experimental results against different proportions of anti-friction fluid are summarized in Table 1. Two results are presented for each proportion of anti-friction fluid. As shown in Table 1, the PEUs were all lower than 50% in the three seconds before removing the electric brakes. As the proportion of detergent in the anti-friction fluid increased, the wheel-rail adhesive forces decreased. Consequently, the PEU of the EMU exhibited a descending trend, and the velocity tended to increase when the electric brakes were removed. Accompanied by the removal of the electric brakes and low PEU of the electric braking force, the air brake was implemented, which lead to the severe wear of the brake pad.

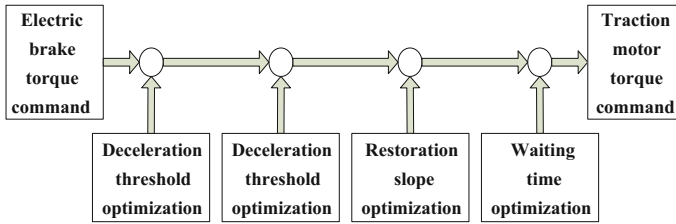


Fig. 3 Optimal control diagram

## 5 The Experimental Results and Analysis for the Software Version v0.1 After Optimization

Aiming at issues that occurred before optimizing the software, the optimized software version 0.2 was confirmed by experimentally adjusting the parameters of the sliding velocity, the action threshold of the deceleration, and unloading ratio of the electric torque and waiting time. The optimal control diagram is shown in Fig. 3.

### 5.1 Experimental Results and Analysis of the Removal of the Sanding Function

Figure 4 shows the experimental results of anti-skid performance when water was sprayed on the rail surface. It can be observed that the second axis of the EMU starts to glide at a velocity of 140.9 km/h. When the running velocity of the EMU was 13 km/h, the hand shank of the driver returned to zero, and there was no condition where the electric braking was removed. Furthermore, the PEU of the second axis was approximately 67.9% at a velocity of 140.9–13.8 km/h. Moreover, the PEU of the third axis was approximately 62.7%, while the PEU of the first vehicle was approximately 65.3%.

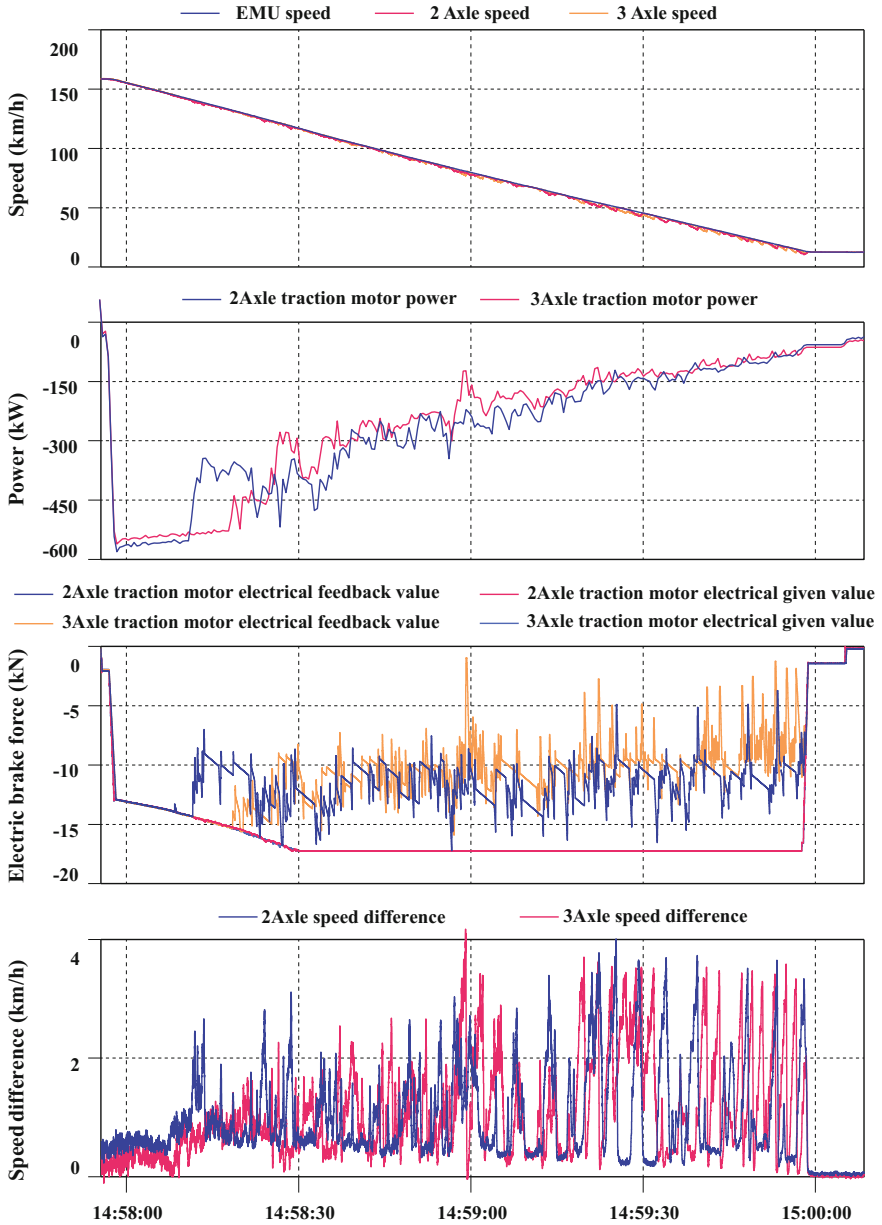


Fig. 4 Experimental results of anti-skid performance using the optimized software version 0.2 (water)

**Table 2** Experimental results of anti-skid performance using version 0.2 after removing the sanding function

Anti friction liquid ratio	Test no.	Maximum sliding speed (km/h)		Whether the electric brake was removed (Yes/No)	PEU of the 1st vehicle (%)
		2nd axle	3rd axle		
Clear water	1	4.0	4.2	No	65.3
	2	5.0	4.3	No	63.3
50 L:4 L	1	4.5	3.8	No	59.2
	2	5.4	4.4	No	50.7
50 L:8 L	1	5.0	4.2	No	52.4
	2	4.9	4.0	No	50.1
50 L:16 L	1	5.2	4.2	No	52.5
	2	5.1	4.2	No	48.1

The experimental results of EMU anti-skid performance against different proportions of anti-friction fluid after removing the sand are listed in Table 2. Two results are presented for each proportional anti-friction fluid. As shown in Table 2, no abscission of electric brake occurred in the first vehicle of the EMU in all experiments, and the PEU was relatively low. Accompanied by the increase in proportion of the detergent in the anti-friction fluid, the wheel-rail adhesive state decreased, and the PEU of the EMU exhibited a descending trend.

### 5.2 Experimental Results and Analysis After Restoring the Sanding Function

Figure 5 presents the experimental results of anti-skid performance after spraying clear water to the rail surface and the sanding function was recovered. As observed in Fig. 4, sanding instructions were given by the control system after judging whether the wheelset entered a gliding state. This was indicated by the gliding symbol, which were lesser, and no electric resection occurred in the whole braking process. The maximum glide speed of the second and third axle was 4.7 and 4.5 km/h, respectively, and the PEU of the first vehicle was 87.2% against a velocity range of 140.5–15.2 km/h.

After restoring the sanding function, the experimental results of EMU anti-skid performance against the different proportions of anti-friction fluid are listed in Table 3. Two results are presented for each proportion of anti-friction fluid. It can

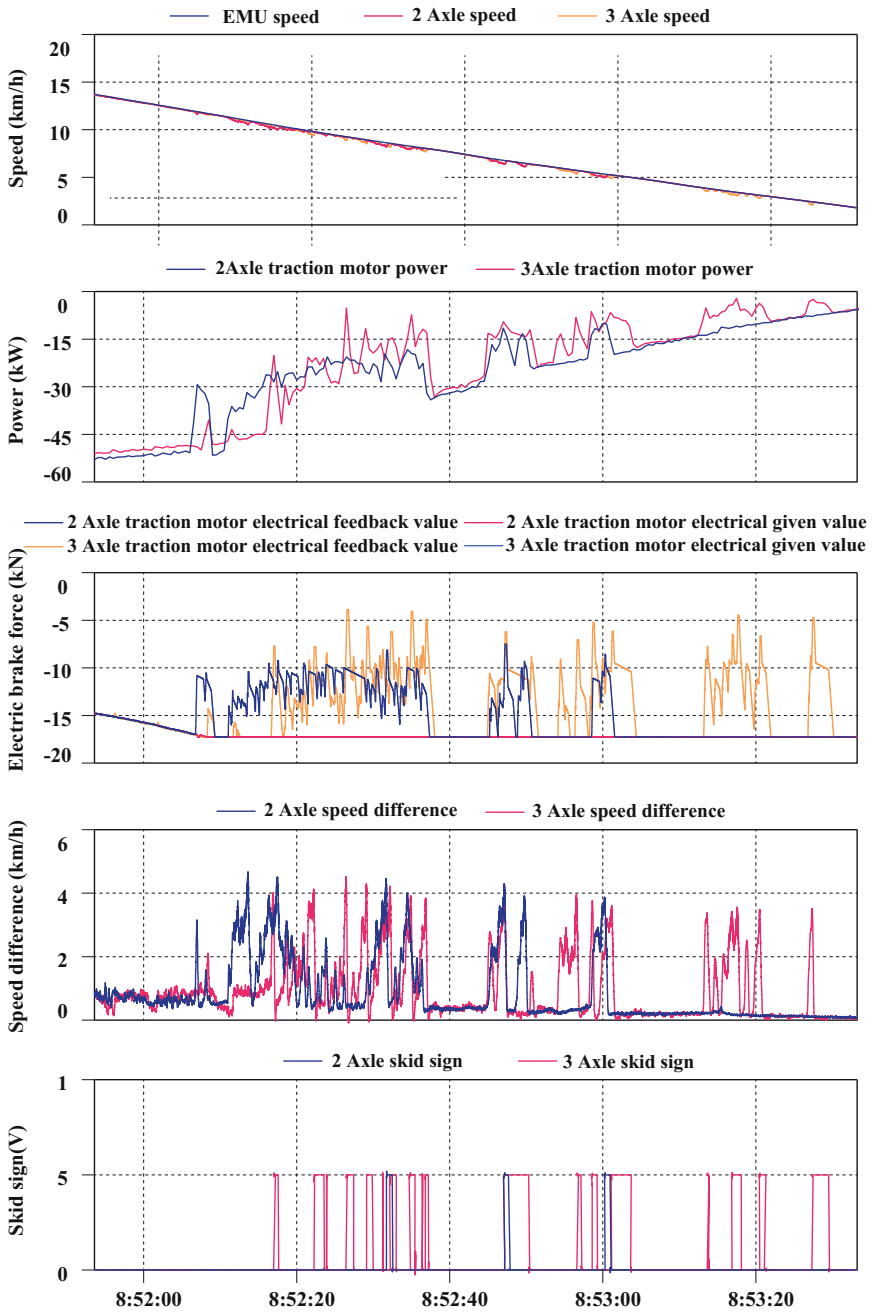


Fig. 5 Experimental results of anti-skid performance using the optimized software version 0.2 after sanding (water)



**Table 3** Experimental results of anti-skid performance using version 0.2 after restoring the sanding function

Anti friction liquid ratio	Test no.	Maximum sliding speed (km/h)		Whether the electric brake was removed (Yes/No)	PEU of the 1st vehicle (%)
		2nd axle	3rd axle		
Clear water	1	4.3	4.2	No	87.2
	2	4.7	4.5	No	82.6
50 L:4 L	1	5.0	3.5	No	75.7
	2	5.3	3.8	No	72.7
50 L:8 L	1	5.0	3.7	No	75.2
	2	5.1	3.7	No	75.3
50 L:16 L	1	5.2	3.9	No	72.4
	2	5.1	3.6	No	77.3

be observed from Table 3 that no phenomenon of the removal of the electric brake simultaneously occurred, because the wheel-rail adhesive state was improved due to the sanding; and the PEU of the first vehicle greatly increased to 87.2%. Moreover, the wheel-rail adhesive force was reduced and the proportion played by the electric braking force tended to decrease along with the proportion of the detergent in the anti-friction fluid. At the same time, it was proven that the sanding method had a good effect on the improvement of adhesion coefficients when the running speed of the EMU was lower than 140 km/h [10].

## 6 Conclusion

Based on these presented experiments, it can be observed that the anti-skid control strategies of the software version (v0.1) without optimization exhibited a relatively poor performance, had a large difference in axle velocity, and the phenomenon of electric brake abscission occurred in each test. Meanwhile, the fluctuation of the torque of the traction motor was relatively large, which was accompanied by the high frequency of depth adjustments. Occasionally, the torque would be reduced to almost zero, which indicates the poor utilization of adhesions. However, with repeated correction and experimental validation over these anti-skid control parameters, the optimized software version (v0.2) can be finally confirmed. In this version, the condition where the EMUs are operated in low adhesive status in the long term was optimized, and the torque of the traction motor is controlled through strategies of quick drop and quick rise, which decreases the risk of removing of the

electric brake. These have been validated by these experiments. In particular, with the implementation of the sanding function, wheel-rail adhesions were significantly improved below the running velocity of 160 km/h, and the performance of electric brakes was obviously enhanced. These experimental results, which aims characterize the anti-skid performance of EMUs, provides important engineering significance for improving the anti-skid control system.

**Acknowledgements** The author would like to thank the Science and Technology Research Programme of China Academy of Railway Science (Grant Nos. 2014YJ089 and 2015YJ121) and the Lan Zhou Jiaotong University Youth Fund (Grant no. 2013020) for their financial support.

## References

1. Huang J, Tang S, Lin P et al (2015) Simulation research on locomotive adhesion control based on rail identification. *Comput Simul* 32(1):206–211 (in Chinese)
2. Zhang L, Wang X, Wang J et al (2015) Development of intercity EMUs brake system. *Electr Drive Locomotives* 245(4):5–9 (in Chinese)
3. Zhao Y, Qiao F (2015) Research of high speed EMU braking anti-skid control problems. *Railway Locomotive Car* 35(4):31–34 (in Chinese)
4. Chen W, Zhou J, Wang X et al (2011) Theory and test of wheel-slid-protection system in brake control of China EMU. *Railway Locomotive Car* 31(5):32–38 (in Chinese)
5. Sun K (2014) Study on dynamic detection system of locomotive adhering-sliding test on rigs [Ph. D]. Beijing Jiaotong University, Beijing. (in Chinese)
6. Wang X (2010) Research on the key technology of anti-skid control for locomotive [Ph. D]. Beijing Jiaotong University, Beijing. (in Chinese)
7. Lai H (2016) Adaptive adhesion control of high speed trains based on RBF network approximation and robust fault tolerance [Ph. D]. Beijing Jiaotong University, Beijing. (in Chinese)
8. Xu Y (2016) Research on the antiskid control of train operation [Ph. D]. Beijing Jiaotong University, Beijing. (in Chinese)
9. Shen P (2012) Experimental study on wheel/rail adhesion characteristic [Ph. D]. Southwest Jiaotong University, Chengdu. (in Chinese)
10. Shen P, Wang W, Zhang H et al (2010) Effect of spraying sand on adhesion characteristic of wheel/rail. *J Mech Eng* 46(16):74–78 (in Chinese)

# Performance Test and Evaluation Technology Research of Photovoltaic Power and Energy Storage Generation System

Na Li, Kai Bai, Zhi Li, Jian-ming Dong, Jin Zong and Yu Gong

**Abstract** In recent years, the capacity of distributed generations has a rapid growth, high penetration of distributed generation technology is facing new problems compared to the traditional distribution network. Therefore, it is necessary to evaluate the grid-connection before the distributed power source is connected to the grid. In this paper, based on the actual distributed photovoltaic and energy storage power generation system, the power control capability and response speed of the hybrid energy storage system are tested, The grid-connection of hybrid energy storage system and photovoltaic power generation system under smooth fluctuation, tracking plan instruction and peak to valley power generation scenario is evaluated, Provide a reference for the follow-up of distributed generations collocation network evaluation technology.

**Keywords** Distributed PV · Energy storage system · Grid-connection  
Coordinated control

## 1 Introduction

China's installed capacity of distributed PV power generation has been growing rapidly in recent years. From the first-quarter of 2017 figures released by National Energy Administration, it shows that national photo-voltaic power generation maintains rapid growth in the first quarter and new installed capacity reaches

---

N. Li (✉) · K. Bai · Z. Li · J. Dong · Y. Gong  
State Grid's Wind Combined with Light Power Generation  
Operation Technology Lab, Beijing 100045, China  
e-mail: qiboer@163.com

N. Li · K. Bai · Z. Li · J. Dong · Y. Gong  
State Grid Jibei Electric Power CO., LTD. Research Institute,  
Beijing 100045, China

J. Zong  
State Grid Jibei Electric Company Limited, Beijing 100045, China

7,210,000 kW. Thereinto, new installed capacity of centralized photo-voltaic power plant is 4,780,000 kW and drops 23% year-on-year. Nevertheless, new installed capacity of distributed PV is 2,430,000 kW with year-on-year growth of 151%. The new installed capacity has the tendency that the speed of centralized photo-voltaic power plants will be reduced and distributed photo-voltaic power generation will be increased. In addition, distributed PV will become the focus [1, 2] in the development of photo-voltaic industry.

Distributed PV appears explosive growth in North of Hebei. As of the end of February 2017, North of Hebei completed distributed photo-voltaic grid with a total of 5854 households, cumulative grid-synchronized capacity of 85,700 kW, the cumulative generating capacity of 9,947,800 kWh, and network capacity of 7,965,800 kWh.

The distributed photo-voltaic power generation is affected by the randomness of natural resources, and its output is characterized by fluctuation and intermittence. High penetration of distributed PV connected to the traditional distribution network is easy to cause the fluctuation and off-limit of distribution network voltage and other conditions [3, 4] influencing the stable operation of power grid. So the performance of distributed photo-voltaic grid needs to be tested and evaluated. Meanwhile, the configuration of battery energy storage system is one of the approaches [5, 6] to address the randomness of distributed PV output.

At present, China has issued the relevant standards on the performance of distributed power grid synchronization. According to the year released, the standards are sorted out as shown in Table 1.

Provisions for test methods and technical regulations of distributed power grid synchronization performance are completely made by Aforesaid standards

**Table 1** Standards of distributed power grid interconnection in China

Year of issuance	Year of execution	Authority	Standard no.	Standard name
2013-11-28	2014-04-01	China Electricity Council	NB/T 32015-2013	Technical rule for distributed resources connected to distribution network
2014-02-20	2014-02-20	Science and Technology Department of State Grid Corporation	Q/GDW 11147-2013	Technical rule for distributed resources connected to distribution network
2016-03-31	2016-03-31		Q/GDW 1480-2015	Technical rule for distributed resources connected to distribution network
2014-09-01	2014-09-01		Q/GDW 11073-2013	Testing and acceptance standards for distributed resources connected to distribution network

(continued)

**Table 1** (continued)

Year of issuance	Year of execution	Authority	Standard no.	Standard name
2014-10-15	2015-03-01	China Electricity Council	NB/T 33011-2014	Testing technical rule for distributed resources connected to distribution network
2014-10-15	2015-03-01		NB/T 33010-2014	Operation and control standards for distributed resources connected to distribution network
2014-10-15	2015-03-01		NB/T 33013-2014	Operation and control standards for distributed source island
2014-10-15	2015-03-01		NB/T 33016-2014	Testing standards for electrochemical energy storage system connected to distribution network
2014-10-15	2015-03-01		NB/T 33015-2014	Technical rule for electrochemical energy storage system connected to distribution network
2014-10-15	2015-03-01			NB/T 33014-2014
2017-03-24	2017-03-24	Science and Technology Department of State Grid Corporation	Q/GDW 11559-2016	Testing standards for micro-grid connected to distribution network
2017-03-24	2017-03-24		Q/GDW 10666-2016	Testing technical rule for distributed resources connected to distribution network
2017-03-24	2017-03-24		Q/GDW 10370-2016	Technical guidance for distribution network
2017-03-24	2017-03-24		Q/GDW 10667-2016	Operation and control standards for distributed resources connected to distribution network

relatively. Depended on in-depth analysis of the above standards and distributed photo-voltaic energy storage power generation system launched in the ‘photo-voltaic and wind joint power generation and operation technical laboratory’ of State Grid Corp, the comprehensive field tests are conducted for the grid synchronization performance. Moreover, this paper analyzes the test method and index of the output of photo-voltaic energy storage under the coordinated control, which provides a reference for test method of grid synchronization and design of index

evaluation pertaining to distributed photo-voltaic energy storage connected to power distribution network.

## 2 Structure and Parameters of Distributed Optical Storage Platform

The distributed optical storage power generation system studied in this paper consists of distributed photo-voltaic power supply, hybrid energy storage system, power distribution system and monitoring and energy management system as well. Of which, 29.4 kW silicon photo-voltaic power generation system atop the roof is connected to PV inverter through header box, and its operation mode is maximum power tracking mode. 30 kW/75 kWh lithium iron phosphate battery energy storage system and 40 kW/10 s super capacitor energy storage system are respectively connected to bi-directional converter whose capacity is 30 kVA. Working in the PQ control mode, reactive power's adjustable range is  $\pm 30$  kVar, and it shall be paralleled to photo-voltaic inverter for networking and then connected to low-voltage 380 V AC bus. Topological structure is as shown in Fig. 1.

### 2.1 Power Control Capability of Energy Storage System

The power control capability of energy storage system includes the active power control capability of charging and discharging, the reactive power control capability of charging and discharging, the active power regulation capability of charging and discharging, and the combined control capability of active and reactive power.

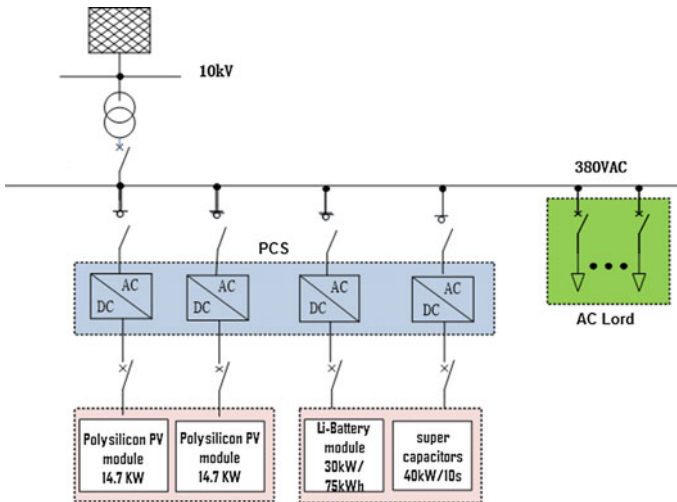


Fig. 1 Main circuit structure of distributed generation system

The measured curves are shown in Fig. 2, and the following six curves are set according to the following conditions:

Figure 2a is the testing charging curve of active power. Reactive power and energy storage system is set to 0, and the active power is from the beginning of 0. Charging reactive power shall be gradually increased to  $-0.25 P$  rated,  $-0.5 P$  rated,  $-0.75 P$  rated,  $-P$  rated, then gradually reduced to  $-0.75 P$  rated,  $-0.5 P$  rated,  $-0.25 P$  rated,  $0 \text{ kW}$  rated. Keep each point at least 30 s;

Figure 2b is the discharge power regulation curve. Storage system of reactive power is set to 0, and the active power is from the beginning of 0. Discharging reactive power shall be gradually increased to  $0.25 P$  rated,  $0.5 P$  rated,  $0.75 P$  rated,  $P$  rated, then gradually reduced to  $0.75 P$  rated,  $0.5 P$  rated,  $0.25 P$  rated,  $0 \text{ kW}$  rated. Keep each point at least 30 s;

Figure 2c is regulation curve of charging and discharging power. Storage system of reactive power is set to 0, and the active power is from the beginning of 0. Active power is regulated to  $0.9 P$  rated,  $-0.9 P$  rated,  $0.8 P$  rated,  $-P$  rated,  $P$  rated,  $-0.8 P$  rated. Keep each point at least 30 s;

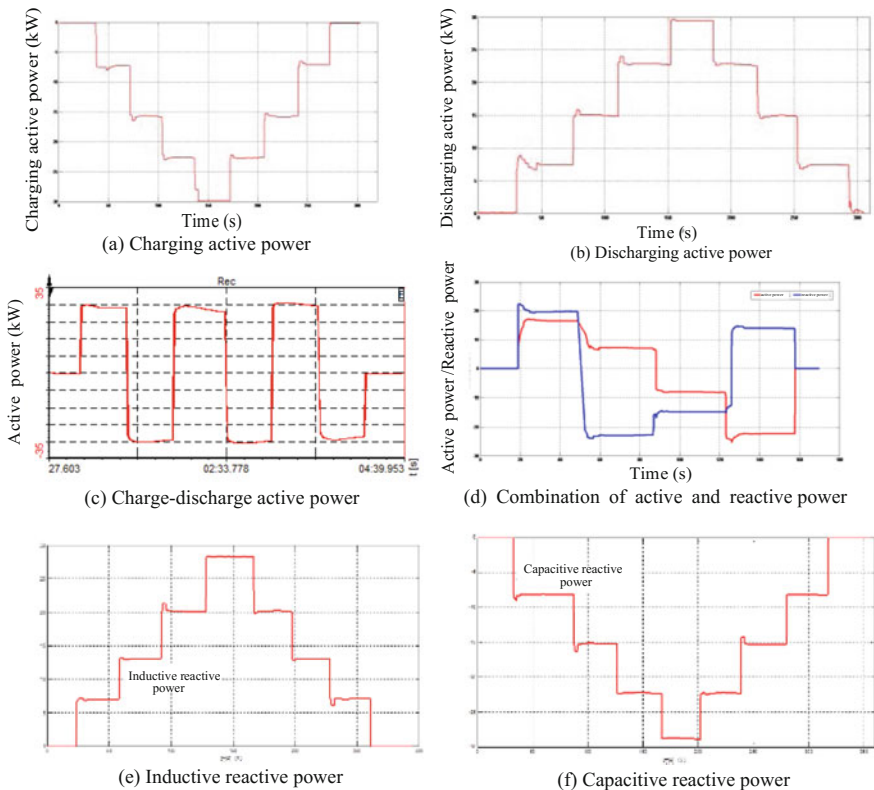


Fig. 2 Power control capability test curve

Figure 2d is regulating combination curve of charging and discharging of the active and reactive power. Storage system of reactive power is set to 0, and active power is 0 hot standby. Active power is regulated to 0.5 P rated, 0.25 P rated, -0.25 P rated -0.75 P rated. At the same time, adjust the reactive power to 0.75 Q rated, -0.75 Q rated, -0.5 Q rated and 0.5 Q rated. Keep each point at least 30 s;

Figure 2e is adjusting curve of sensibility of reactive power. Storage power system is set to 0, and the reactive power is 0, gradually raising the reactive power to -0.25 Q rated, -0.5 Q rated, -0.75 Q rated, -Q rated, and then gradually reducing the reactive power to -0.75 Q rated, -0.5 Q rated, -0.25 Q rated, 0. Keep each point at least 30 s;

Figure 2f is regulating curve of capacitive reactive power. Active power energy storage system is set to 0, and the reactive power is 0, gradually raising the reactive power to 0.25 Q rated, 0.5 Q rated, 0.75 Q rated, Q rated, and then gradually reducing the reactive power to 0.75 Q rated, 0.5 Q rated, 0.25 Q rated, 0. Keep each point at least 30 s.

The test data are analyzed and the corresponding measured values are recorded according to the set values of the above working condition curves, and the power control deviation is calculated. The results are shown in Table 2.

Summary Table 2 shows that the range of the active power control deviation of energy storage system measured is -10.7-8.0%, and the range of the reactive power control deviation is -12.7-4.0%.

## 2.2 Power Response Speed of Energy Storage System

The storage system's response speed is related to whether to meet the requirements of complex response time of energy management system response time. In this paper, charging response time of charging and discharging and charge-discharge conversion time, regulation time of charge-discharge are tested and analyzed. The test results are shown in Table 3.

The adjustment and response time of charging-discharging the is field energy management system sending rated power to charge (discharge) storage system command from the energy storage system beginning to charge (discharge) electric moment to charge (discharge) the electric power reaching 90% of the rated power of energy storage system. Adjustment time is from the charging (discharging) power response time to the energy storage system rated power deviation less than 2%. The final evaluation of adjusting time and charging-discharging response time is to get the maximum in three times' tests. As shown in Table 2, the charging response time of the object under test is 43.7 ms, and the discharge response time is 45.0 ms, and the charging regulation time is 52.2 ms, and the discharge regulation time is 54.1 ms as well.

Charge-discharge conversion time is during the process of energy storage system with a rated power charging, to send rated power of discharge command to the energy storage system. Record the first time from 90% rated power charging to 90%



**Table 2** Test results analysis of power control capability of energy storage system

Parameters measured	Active power setting value (kW)	Measured value of active power (kW)	Active power control deviation (%)	Parameters measured	Reactive power set point (kVar)	The measured value of reactive power (kVar)	Reactive power control derivation (%)
Charging active power	-7.5	-7.3	-2.6	Inductive reactive power	7.5	7.1	-5.3
	-15	-15.4	2.8		15	13.1	-12.7
	-22.5	-23.1	2.8		22.5	20.3	-9.7
	-30	-29.0	3.3		30	28.3	-5.7
	-22.5	-23.1	2.8		22.5	20.3	-9.7
	-15	-15.4	2.8		15	13.1	-12.7
	-7.5	-7.3	-2.6		7.5	7.1	-5.3
Discharging active power	7.5	7.6	1.3	Capacitive reactive power	-7.5	-7.8	4.0
	15	14.8	-1.3		-15	-15.2	1.3
	22.5	22.8	1.3		-22.5	-22.2	-1.3
	30	29.5	-1.6		-30	-28.7	-4.3
	22.5	22.8	1.3		-22.5	-22.2	-1.8
	15	14.8	-1.3		-15	-15.2	1.3
	7.5	7.6	1.3		-7.5	-7.8	4.0
Charge-discharge active power	27	26.6	-1.5				
	-27	-27.5	1.9				
	24	25	4.2				
	-30	-29.5	-1.6				
	30	29.5	-1.6				
	-24	-25	4.2				

(continued)

Table 2 (continued)

Parameters measured	Active power setting value (kW)	Measured value of active power (kW)	Active power control deviation (%)	Parameters measured	Reactive power set point (kVar)	The measured value of reactive power (kVar)	Reactive power control derivation (%)
Combination of active and reactive power	15	16.6	-10.7		22.5	20.2	-9.8
	7.5	7.1	-5.3		-22.5	-22.6	0.4
	-7.5	-8.1	8.0		-15	-14.8	-1.3
	-22.5	-22.4	-0.4		15	14.1	-6.0

**Table 3** Energy storage system time index test result

Charging response time	Max	Discharging response time	Max	Charging adjust time	Max	Discharging adjust time	Max
43.5	43.7	45.0	45.0	51	52.2	54.1	54.1
43.7		44.8		52.2		53.8	
42.4		44.9		51.6		54	

Unit: ms

rated power discharging time. Afterwards, the energy storage system discharges with rated power, and send rated power charging command to energy storage system. Record the second time from 90% rated power discharging to 90% rated power charging. Take the average value of two times and it is the charge discharge conversion time. Take the maximum value from the three results. After testing, charge-discharge conversion time of energy stored system measured is 48.4 ms.

### 3 Performance Test and Analysis of Grid Synchronized Under Coordinated Control of Optical Storage

The existing standards do not make provisions for verification method of optical storage coordination control function. And thus, on the basis of relevant literature [7, 8], and combined with the existing standards, the conditions of energy storage system for stabilizing the output of photovoltaic power fluctuation and output condition of tracking program, and peak load shifting condition are tested and evaluated in this paper.

#### 3.1 Stabilization of Fluctuation of PV Output of Energy Storage System

In order to reduce the influence of distributed PV on the power quality of distribution network, the output power of the parallel network is smoothed. The control strategy of the measured object is to transform the Fourier of the output power of the distributed power supply, and the spectrum of power fluctuation is obtained. With the use of components of super capacitor compensation system and lithium battery energy storage system with the characteristics of large frequency but small amplitude fluctuation, power [8] of super capacitor and lithium battery is determined by the low-pass filtering method.

Through the energy management system, the hybrid energy storage system operation mode is set as smooth output, and the photovoltaic power generation

system generates electricity freely. Using test equipment to collect experimental data, according to formula (1), calculate the 1–10 min fluctuation rates of distributed PV output of hybrid energy storage system before and after the smooth platform.

$$F_{t-1min} = \frac{P_{t-max1} - P_{t-min1}}{P_{gen}} \times 100\% \tag{1}$$

Of which,  $F_{t-1min}$ —fluctuation ratio at t moment 1 min volatility;  $P_{t-1max}$ —maximum power before t moment 1 min (including t moment);  $P_{t-1min}$ —minimum power before t moment 1 min (including t moment);  $P_{gen}$ —equipment power generation. Similarly, fluctuation ratio in 10 min can be calculated.

During the test, the irradiance change is more intense. Figure 3 is the output curve of photovoltaic and hybrid energy storage system, as well as the coordinated control platform in 0.2 s sampling interval. It can be seen that when the photovoltaic power generation system fluctuates rapidly, the energy storage system has the ability of high power charging and discharging in short time, and has the ability of continuous charging and discharging. It can effectively smooth the fluctuations of distributed PV output.

The power fluctuation before and after smoothing is shown in Table 4. The average power fluctuation rate of optical storage power generation system is decreased from 5.41 to 2.26%, and the average 10 min power fluctuation rate is decreased from 24.50 to 6.50%.

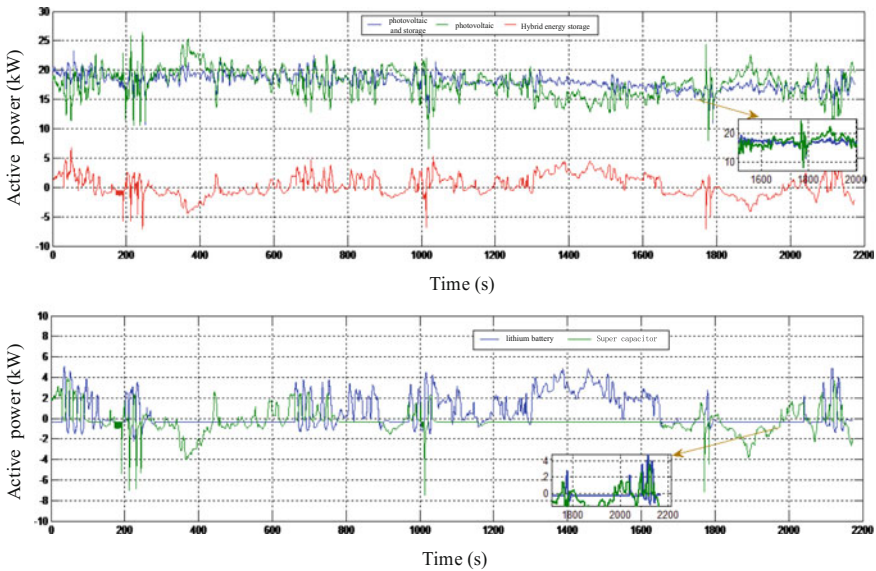


**Fig. 3** Coordinated fluctuation control effect of distributed generation system

**Table 4** 10 and 1 min output volatility

Fluctuation 10 min		Fluctuation 1 min			
Max.		Mean.		Max.	
Pre-smooth (%)	Post-smooth (%)	Pre-smooth (%)	Post-smooth (%)	Pre-smooth (%)	Post-smooth (%)
30.15	7.76	24.5	6.50	17.77	5.90
				5.41	2.26

### 3.2 Output Condition of Tracking Program of Energy Storage System

In the interface of distributed optical storage power system energy management system, set platform operation mode to output tracking program, and send output curve of simulation scheduling tracking program. Power accuracy is calculated by data acquired by testing the equipment comparing output curve of tracking program and actual curve combined power.

Figure 4 shows the output curve of distributed PV and hybrid energy storage system and coordinated control platform within 10 s sampling interval, which is obtained from the output of the simulation tracking program.

Figure 4 is the tracking program output control accuracy. From it, the maximum positive deviation of the tracking program is 0.96 kW, and the maximum value of negative deviation is 0.60 kW, and the overall tracking accuracy of the platform is within the range of  $-5.87\%$ – $6.00\%$  (Table 5).

### 3.3 Working Conditions of Peak Load Shifting of Energy Storage System

The coordinated control function of peak load shifting can simulate the dynamic change of load demand response and reduce the long-term peak-valley difference by taking advantage of energy storage system. Set the platform operation mode into peak load shifting through the interface of energy management system and send the

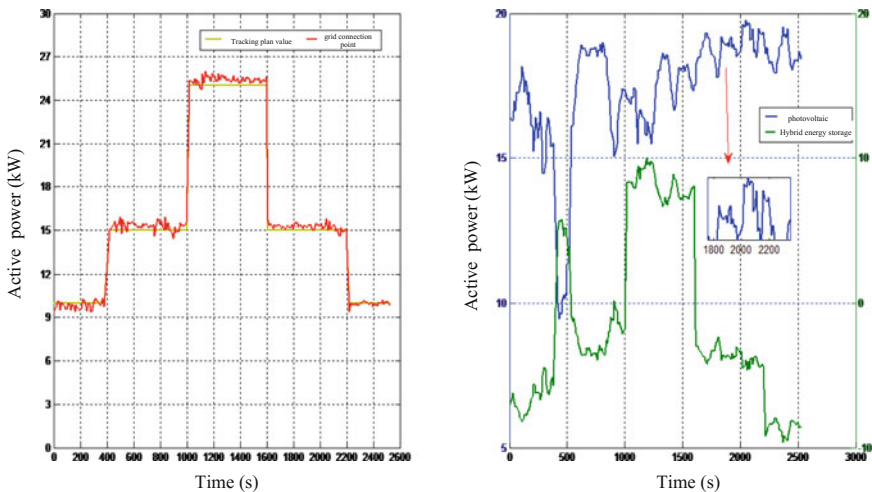


Fig. 4 Tracking plan output effect of distributed generation

**Table 5** Tracking plan output accuracy

Operation mode	Tracking plan output accuracy				
	Maximum positive deviation (kW)	Maximum negative deviation (kW)	Maximum positive deviation (%)	Maximum negative deviation (%)	Average value of deviation control (%)
Generation of tracking plan	0.96	-0.60	6.00	-5.87	1.94

peak-load shifting command of distributed photo-voltaic power generation system and hybrid energy storage system. Peak-load shifting function of platform energy management system is verified by data acquired by testing equipment.

As shown in Fig. 5, during the output process of distributed PV, energy management system automatically switches over to the “peak load shifting” mode. Hybrid energy storage system of super capacitor and lithium battery will maintain 2 h’ state of charging in terms of peak load shifting control strategy.

The test results are shown in Table 6, and the average value of deviation control under the operation of peak load shifting is 2.97%.

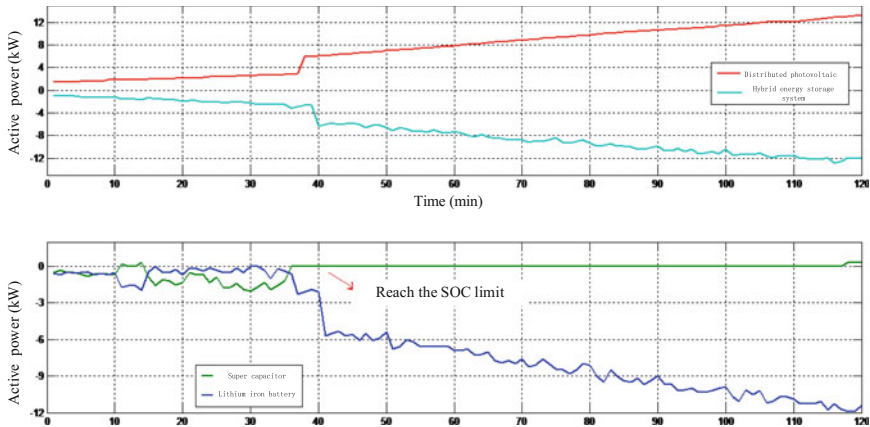


**Fig. 5** Coordinated effect of peak load shifting

**Table 6** Control precision of peak load shifting

Simulated load demand (kW)	Maximum deviation value (kW)	Minimum deviation value (kW)	Platform output average value (kW)	Deviation control average value (%)
14	14.89	14.26	14.42	2.97

## 4 Conclusion

Based on the practical distributed photo-voltaic energy storage power generation system, grid-synchronized performance of hybrid energy storage system and optical storage performance under coordinated control are tested in the paper, and performance of system is evaluated by the proposed index as well. The evaluation results can guide the formulation of operation strategy intended for the distributed generation system, and the main conclusions are as follows:

- (1) The conversion time of charge-discharge of energy storage system tested is 48.4 ms, and response time of it is 43.7–45.0 ms, and adjustment time of it is 52.2–54.1 ms. All are within 100 ms, and thus the system has the ability in fast response to power.
- (2) Smooth fluctuation coordination control function of photo-voltaic energy storage can be evaluated by the power fluctuation of 1 min power and 10 min. The average fluctuation 1 min of power system measured drops from 5.41 to 2.26%, and average fluctuation 10 min decreases from 24.50 to 6.50%, which effectively reduces the amplitude of fluctuation.
- (3) The maximum output positive deviation of tracking program of optical storage distributed power generation system measured is 0.96 kW and its maximum negative deviation is 0.60 kW. Thus, the whole tracking accuracy is in the range of –5.87–6.00%, which provides effective support for distributed load forecasting.
- (4) The evaluation method of grid-synchronized performance is comprehensively sorted out and verified for distributed photo-voltaic power generation system of battery energy storage system.

**Acknowledgements** This work was supported by the Science and Technology Project of State Grid Corporation of China “Research and demonstration of key technologies for distributed energy storage and user side optimal allocation” 5210EF17001C.

## References

1. Yang Cai, Jie Feng, Shanghuan Zhang et al (2014) Allocation method for schedulable microgrid energy storage capacity considering wind/PV power generation. *East China Electric Power* 42(9):1821–1826 (in Chinese)
2. Hao Zhang (2014) Research of economic evaluation for load shifting in distribution network based on energy storage system. North China Electric Power University, Beijing (in Chinese)
3. Wang Chengshan Yu, Bo Xiao Jun et al (2012) Sizing of energy storage systems for output smoothing of renewable energy systems. *Proc CSEE* 32(16):1–8 (in Chinese)
4. Shaobo Lin, Minxi-ao Han, Guopeng Zhao et al (2013) Capacity allocation of energy storage in distributed photovoltaic power system based on stochastic prediction error. *Proc CSEE* 33(4):25–33 (in Chinese)



5. Hidalgo R, Abbey C, Joós G (2010) A review of active distribution networks enabling technologies. In: Power and energy society general meeting, IEEE. IEEE, 2010:1–9
6. Chen H, Cong TN, Yang W et al (2009) Progress in electrical energy storage system: a critical review. *Prog Nat Sci* 19(3):291–312
7. Li X (2012) Fuzzy adaptive kalman filter for wind power output smoothing with battery energy storage system. *IET Renew Power Gener* 6(5):340–347
8. Peng S (2013) Battery energy storage system and its operation and control in the isolated grid based on wind-battery. Shang Hai Jiao Tong University. (in Chinese)

# Research on Ice-Melting Technology of Urban Rail Transit Catenary Based on Energy Cycle

Jian Liu, Gang Zhang, Fengjie Hao, Zhigang Liu and Xibin Bai

**Abstract** When the train is running, if the catenary is heavily covered by ice, there will be arcs between the pantograph and the catenary, resulting in the train to be powered abnormally, even causing major accidents such as catenary breaks and pantograph damage. This paper proposes an ice-melting scheme based on energy cycle which is formed between the medium voltage grid and the icing catenary. The current of the catenary is controlled over the ice-melting current, which produces Joule heat to melt the ice. This paper analyzes the working principle and control strategy of the ice-melting system, calculates the ice-melting current, verifies the effectiveness of the control method and realizes the expected energy cycle by simulation.

**Keywords** Urban rail transit · Catenary · Ice-melting · Energy-fed device

## 1 Introduction

The catenary is an important part of the traction power supply system of urban rail transit, which is a transmission line that drips along the rails to provide electricity for trains. The train is powered by the catenary through the pantograph. Whether the quality of the current is good will affect the train running state.

The phenomenon of catenary icing refers to the water droplets are coagulated to catenary after encountering the cold air. This phenomenon mainly occurs in the early winter and early spring, it is a natural disaster which was formed under the combined effect of temperature, humidity, wind speed and other factors [1].

---

J. Liu (✉) · G. Zhang · F. Hao · Z. Liu  
Beijing Engineering Research Center of Electric Rail Transportation, School  
of Electrical Engineering, Beijing Jiaotong University, 100044 Beijing, China  
e-mail: 16126033@bjtu.edu.cn

X. Bai  
China Railway Electrification Bureau (Group) Co., Ltd, 100036 Beijing, China

At present, the deicing methods of urban rail transit mainly include artificial deicing method, catenary hot-sliding method and thermal ice-melting method [2]. Artificial deicing method is time-consuming and laborious, with low efficiency and a high risk. Catenary hot-sliding method has some damage to the catenary and can not completely remove the ice. The principle of thermal ice-melting method is to apply the current to the catenary, producing heat to melt ice, which is one of the most popular methods [3].

This paper proposes an ice-melting scheme which bases on the energy cycle. In the power dispatching center, a set of ice-melting control device is set up to control the energy-fed device in the substation at both ends of the icing section to operate in the rectifier and inverter state respectively, which forms an energy circulation path between the AC grid and the DC catenary. The catenary current is controlled over the ice-melting current value through the corresponding method, which produces Joule heat to achieve the purpose of melting ice.

## 2 The Structure and Principle of the Energy-fed Device

The energy-fed traction power supply device is shown in Fig. 1, it mainly includes high voltage switch, transformer, low voltage switch, PWM rectifier, DC switch, negative isolation switch [4].

The core of the energy-fed device is the PWM rectifier, which is a power conversion device based on pulse width modulation technology [5]. Its single phase equivalent circuit is shown in Fig. 2.

The mathematical expression of the single-phase equivalent circuit of the PWM rectifier is:

$$e_a - U_a = L \frac{di_a}{dt} \tag{1}$$

In the case of a determined grid voltage  $e_a$  and AC inductance  $L$ , the magnitude and phase of the current  $i_a$  are controlled by the amplitude and phase of  $U_a$ . As is shown in Fig. 3, based on the relative position of the current and voltage of the grid, four typical operating conditions can be obtained:

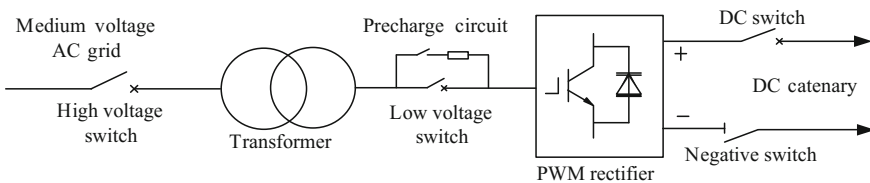


**Fig. 1** Energy-fed traction power supply device

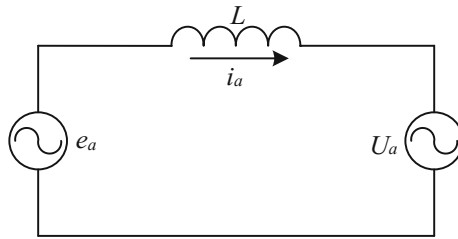


Fig. 2 Single-phase equivalent circuit of PWM rectifier

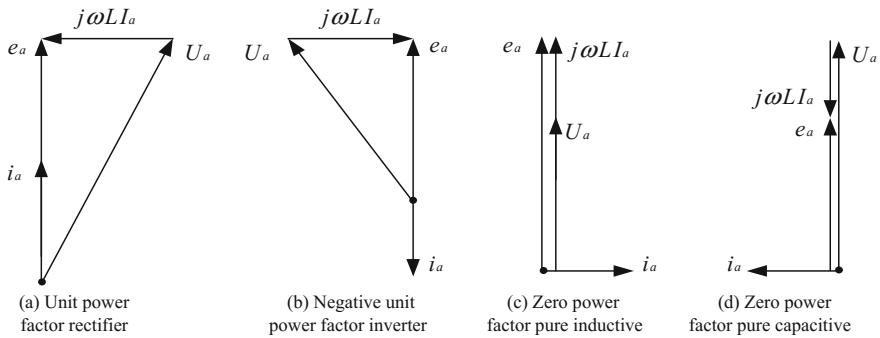


Fig. 3 Phase diagram of PWM rectifier single-phase equivalent circuit

- (a) Unit power factor rectifier operation, which can provide DC power supply, reducing the DC voltage fluctuation;
- (b) Negative unit power factor inverter operation, which can recover the regenerative braking energy of the train;
- (c) Zero power factor pure inductive operation, which can compensate for reactive power, improving the system power factor;
- (d) Zero power factor pure capacitive operation, which can compensate for reactive power, improving the system power factor.

### 3 The Research on Ice-Melting Technology

#### 3.1 The Calculation Method of Ice-Melting Current

Assuming that the ice on the wire is cylindrical, the ice-melting current can be calculated in the following formula [6]:

$$I = \sqrt{\frac{[c_i(273.15 - T_a) + L_F]\rho_i R_i (2R_0 - \frac{\pi}{2} R_i)}{R_e t}} \quad (2)$$

The parameters in the above formula are shown in Table 1.

Introducing the above parameters into Eq. (2), the ice-melting current of contact line is 428 A, the ice-melting current of bearing cable is 412 A. So the catenary current which is simplified as the sum of the contact line current and the bearing cable current is 840 A. When the ice-melting system works, ice-melting current should be less than the rated current.

### 3.2 The Formation of Energy Circulation Path

The wireless multimedia sensor network, composed of sets of sensor nodes around the catenary, collects the information such as air temperature, wind speed and catenary images etc., and then transmits the data to the ice-melting control device in the power dispatch center [7].

The ice-melting control device analyzes and processes the uploaded data to determine the catenary status. When the catenary is covered by ice, the ice-melting control device begins to calculate the icing thickness and the ice-melting current.

The ice-melting control device controls the energy-fed device in the substation at both ends of the icing section to work in the rectifier and inverter state through PSACDA communication network. So the energy circulation is formed between the medium voltage AC grid and the DC catenary, which is shown in Fig. 4.

### 3.3 The Control Strategy of the Energy-fed Device

For the control method of the energy-fed device, the current closed-loop control based on the synchronous rotating coordinate system is the basis of all the control methods [8]. The control block diagram is shown in Fig. 5.

In order to control the DC output of the energy-fed device in the rectifier state to the constant current source, it is necessary to introduce the output of the DC current

**Table 1** The parameters of the ice-melting current calculation formula

Ambient temperature $T_a$	-3 °C	Ice cylinder radius $R_0$	21.9 mm
Ice specific heat $c_i$	2090 J/kg °C	Wire radius $R_i$	6.9 mm
Ice density $\rho_i$	917 kg/m <sup>3</sup>	Icing thickness ( $R_0 - R_i$ )	15 mm
Heat and mass ratio $L_F$	335,000 J/kg	Contact line unit resistance $R_e$	0.1078 Ω/kM
Ice-melting time	60 min	Bearing cable unit resistance $R_e$	0.1119 Ω/kM

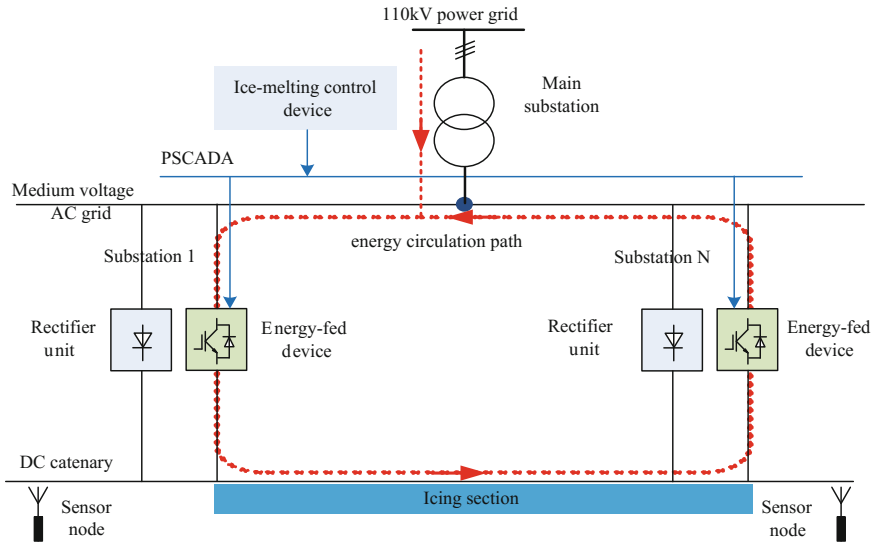


Fig. 4 Energy circulation path of ice-melting system

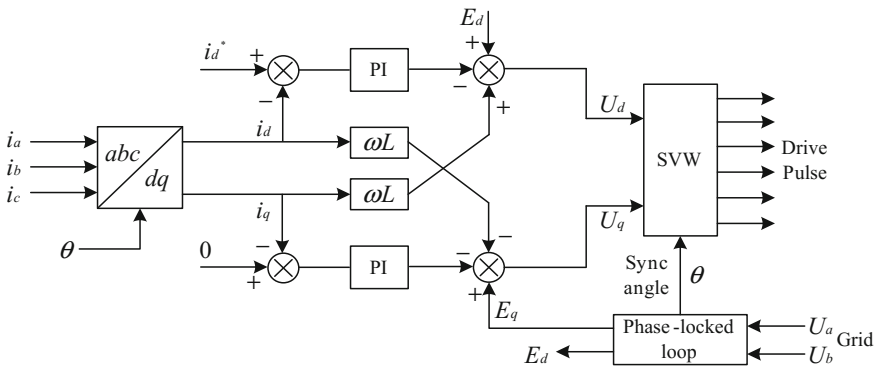


Fig. 5 Current closed-loop control of PWM rectifier

closed-loop as the d-axis current reference, based on dq-axis current closed-loop. The control block diagram is shown in Fig. 6.

The current closed-loop control, shown in Fig. 6, is adopted to control the energy-fed device into the inverter state. The d-axis current  $i_d^*$  is manually given by the controller to run the energy-fed device in the negative unit power factor state.

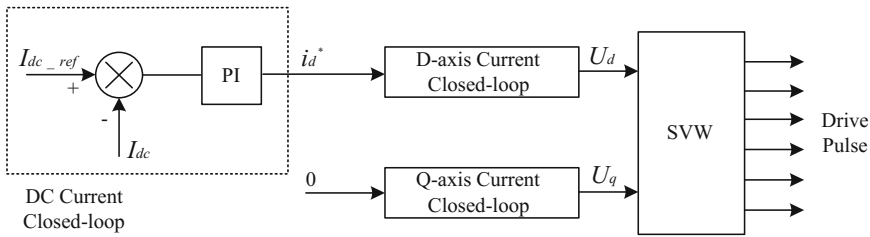


Fig. 6 Closed-loop control diagram for DC current

### 4 Simulation Verification

In order to verify the control strategy of the ice-melting system presented in this paper, the ice-melting test is carried out between the substation 1 and the substation 2. The ice-melting system model which is established under the MATLAB/SIMULINK is shown in Fig. 7, and the main parameters of the model is shown in Table 2.

The waveform of catenary current is shown in Fig. 8. It can be seen that the current is kept at around 840 A. According to the calculation of ice-melting current, the 15 mm ice can be melted at  $-3\text{ }^{\circ}\text{C}$  after 60 min. The ice-melting current value is changing under different meteorological conditions, so it is necessary to adjust the current value to meet the ice-melting requirement, though adjusting the DC current closed-loop given value.

The AC side voltage and current waveform of the energy-fed device in the rectifier state is shown in Fig. 9, and their phase are same. The AC side voltage and current waveform of the energy-fed device in the inverter state is shown in Fig. 10,

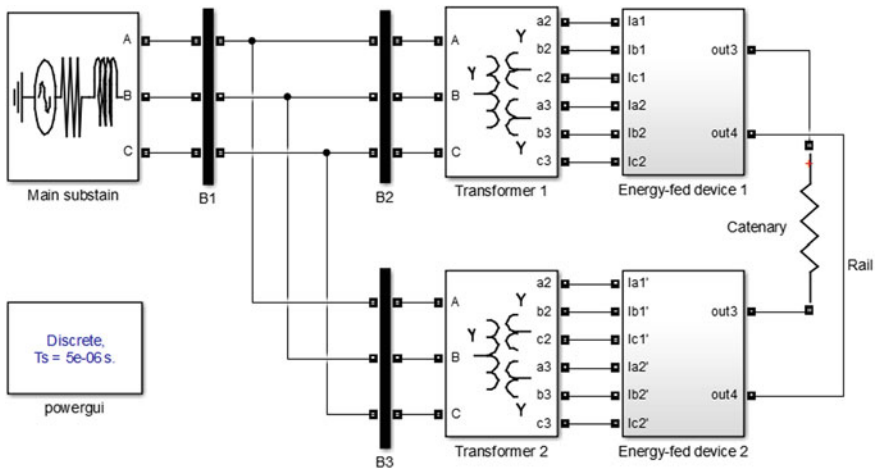
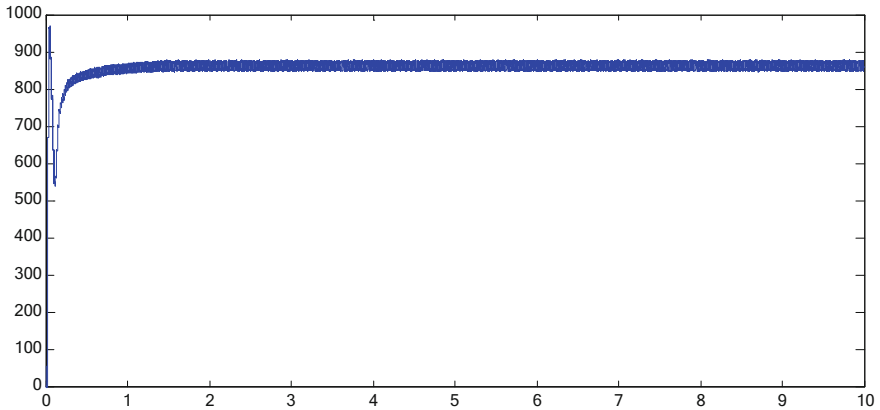


Fig. 7 Simulation model of the ice-melting system

**Table 2** The main parameters of the simulation model

Main substation power	30 MVA	AC grid voltage	35 kV
Catenary rated voltage	1500 V	Catenary resistance	0.1647 Ω
Filter inductance	500 μH	Filter capacitor	0.3 F
Ice-melting current	840 A	Ice-melting time	60 min



**Fig. 8** The waveform of catenary current

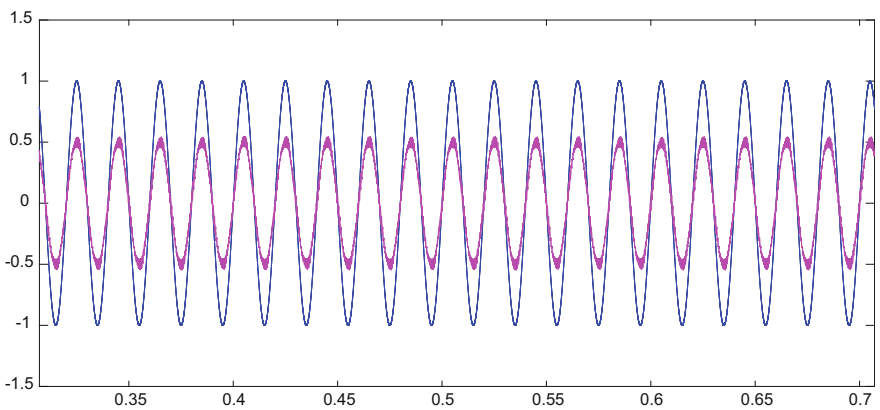


**Fig. 9** AC side voltage and current waveform of the energy-fed device in the rectifier state

and their phase are opposite. Through the energy-fed devices, the energy circulation path is formed between the AC grid and the DC catenary. The ice-melting system can realize the unit power factor operation, which proves that the control strategy proposed in this paper is feasible.



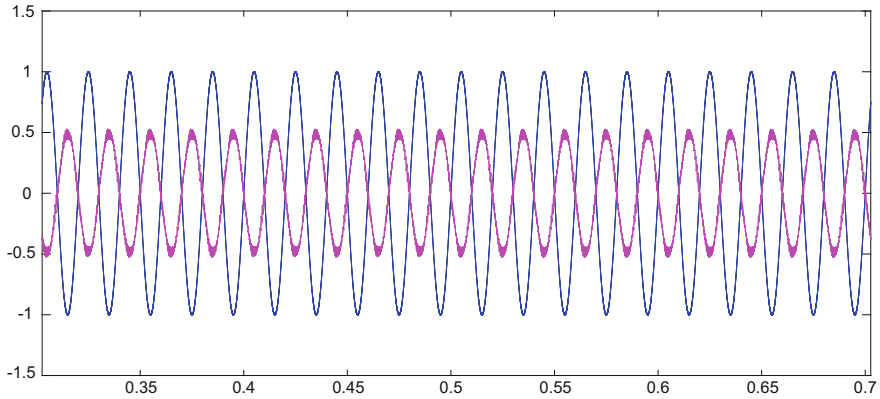


**Fig. 10** AC side voltage and current waveform of the energy-fed device in the inverter state

## 5 Conclusions

This paper introduces the basic structure and working principle of the energy-fed device, and proposes a melting system of urban rail transit catenary based on energy-fed device. This paper introduces the calculation scheme of ice-melting current, puts forward the reasonable ice-melting control strategy, sets up the traction power supply system model, and carries on the MATLAB simulation verification.

The train runs frequently during daytime, so catenary is generally not covered with ice. Due to the train is suspended during the night, there is no current on the catenary, the catenary on the ground is easy to be covered by ice when the weather conditions are bad. Without adding other devices, before the train goes online, starting the ice-melting system can melt the ice to ensure normal operation.

**Acknowledgements** The work was supported by the National Key Research and Development Program 2017YFB1200802 and the Beijing Science and Technology Commission Project Z171100002217025.

## References

1. Zhen Lei (2011) Analysis on the harm and countermeasure of the icing catenary. *Electrification* 03:30–32 (in Chinese)
2. Shao Quandong (2012) Discussion on the deicing method of catenary. *Shanghai Railw Sci Technol* 02:54–56 (in Chinese)
3. Jing Huabing, Nian Xiaohong (2012) Catenary DC ice-melting technology and device development of electrified railway. *Trans China Electrotech Soc* 09:277–284 (in Chinese)
4. Zhang Gang, Liu Zhigang, Mou Fuqiang (2014) Application of Bi-directional converter in urban railway traction power supply system. *Urban Rapid Rail Transit* 04:109–112 (in Chinese)

5. Zhang Xing, Zhang Chongwei (2012) PWM Rectifier and Its Control. Mechanical Industry Press, Beijing (in Chinese)
6. Liu H (2001) Study on the mechanism of icing and deicing of overhead conductor. Huazhong University of Science and Technology, Wuhan
7. Cao Yijun, Dong Xinghui, Cao Nianhong, Hong Wu, Qi Yongtao (2010) Ice monitoring system of overhead transmission line based on image acquisition and recognition technology. *Electr Technol* 08:51–53 (in Chinese)
8. Zhang G (2010) Study on key techniques of energy-fed traction power system for urban mass transit. Beijing Jiaotong University, Beijing. (in Chinese)

# The Key Design and Control of Single-Sided Linear Induction Motors (SLIMs) Based on Serial Equivalent Model (SEM)

Jiangming Deng, Qibiao Peng, Tefang Chen and Laisheng Tong

**Abstract** The Serial equivalent model (SEM) of short-primary linear induction motor (SLIM) was established. Impedance parameters was theoretical analyzed, and primary input frequency, current, power, thrust, factor-efficiency were iteratively calculated. The overall performance of SLIM was evaluated according to given top indicators. Two-dimensional and three-dimensional finite element analysis (FEA) were carried out, and the results were compared to the actual application tests to verify the consistency of design and real get.

**Keywords** Serial equivalent model (SEM) · Short-primary linear induction motor (SLIM) · Engineering applications · Finite element analysis (FEA) Factor-efficiency

## 1 Introduction

As China's first, the world's longest commercial short stator medium-low speed maglev line—Changsha maglev express was put into application, the medium-low speed maglev train with advantages of green, quiet and comfortable, strong climbing ability, small turning radius and low construction cost, reflects the strong adaptability to the environment and higher economy in city rail transportation applications [1]. The Changsha maglev express uses short primary linear induction motor (SLIM, the structure is indicated in Fig. 1) to drive, since SLIM with simple structure and no intermediate transmission device that can directly generate linear movement thrust, has been widely used in the fields of industry applications such as transportation, maglev train, subway/light rail train, piling machine, pumping device, electric vehicle door [2, 3]. Maglev train with no traditional wheel and rail,

---

J. Deng (✉) · Q. Peng · T. Chen · L. Tong  
Zhuzhou Electric Locomotive Limited Company, CRRC, No. 1 Tian Xin Road,  
Shi Feng District Zhuzhou, Hunan Province, China  
e-mail: senmingt@163.com

© Springer Nature Singapore Pte Ltd. 2018  
L. Jia et al. (eds.), *Proceedings of the 3rd International Conference on Electrical and Information Technologies for Rail Transportation (EITRT) 2017*, Lecture Notes in Electrical Engineering 482, [https://doi.org/10.1007/978-981-10-7986-3\\_47](https://doi.org/10.1007/978-981-10-7986-3_47)

and the state of train operation, such as traction and braking, positive and reverse operation, is completely realized by linear motor frequency converter system. The main circuit of the traction system of maglev train consists of traction inverter, linear motor and corresponding control and detection circuit [4]. Due to the special structure of the maglev vehicle, the linear motor in the medium-low speed maglev train with the short length of air gap, terrible electromagnetic load, weight index of strict restrictions, leads to some difficulties for the design and manufacture. Generally, in order to achieve matched traction/braking characteristics, the speed of the maglev train resistance characteristics is calculated firstly, then, the related technical parameters and the design of single motor and traction inverter for obtaining the required traction power and traction characteristics are specified.

Many researches of the design and performance analysis of SLIM have been done around the world, and in those researches also a lot of simulations and measurements are carried out. With those studies, the formation of T-type equivalent circuit and the rotating coordinate vector of two main control modeling ideas have provided experience for design and performance index of SLIM comprehensive assessment.

Combining with the project of top-level requirements, a series of SLIM type equivalent model has been established in this paper, and by using theoretical analysis method, the key design parameters of impedance loop are provided with iteratively calculation of stator frequency, current, power, thrust, efficiency and factor.

## 2 Serial Equivalent Model (SEM)

The linear induction motor is highly similar with the rotating asynchronous motor in principle and basic characteristics, and its electromagnetic design can be continued by using the serial equivalent model (SEM) method [5]. The one phase of SEM considering the end effect and equivalent correcting coefficients of SLIM is shown in Fig. 2.

To evaluate the performance of SLIM, the appropriate formulas to calculate the equivalent resistive and inductive coefficients are shown in Fig. 2, and the motor

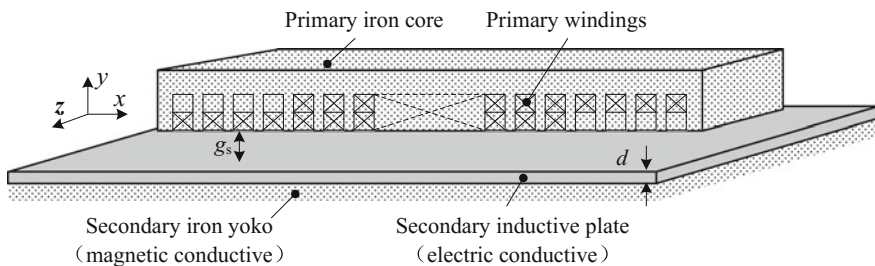
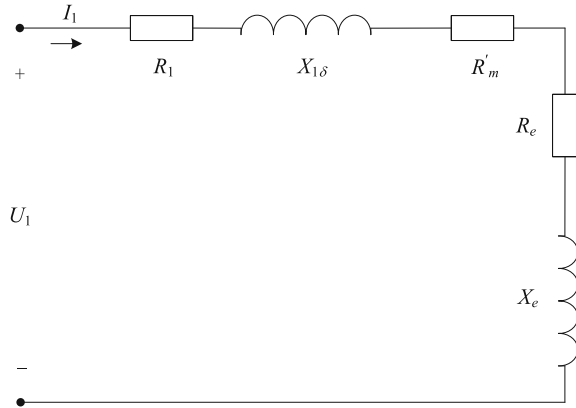


**Fig. 1** Schematic diagram of SLIM

**Fig. 2** SEM of SLIM considering the end effect



current  $I_1$ , thrust  $F_e$  and product of efficiency and factor ( $\eta \cdot \cos\varphi$ ) are then obtained through given voltage.

- (1) The primary winding resistance  $R_1$  is determined by wire material, connection way of series and parallel, turns  $W_1$ , shunt branches and cross sectional area of conductors.
- (2) Primary leakage  $X_{1\delta}$ , is related with windings, core tooth end, core slot leakage, harmonics and other factors, and relationship with the primary frequency  $f_1$  is illustrated as

$$X_{1\delta} = k_\delta \times f_1 \tag{1}$$

In (1),  $k_\delta$ , which value is constant, is the unity coefficient of leakage reactance.

- (3)  $R'_m$  is the equivalent iron loss resistance, and it is related with primary core loss. It has nonlinear characteristic associated with the primary winding frequency, i.e.  $R'_m \propto f_1^{1.3}$ .
- (4) Since the track of the medium-low speed maglev train is consist of two branches of the aluminum inductive plate and the steel guide which are connected in parallel, the secondary equivalent resistance  $R_2$  is

$$R_2 = \frac{R_{al} \cdot R_{fe}}{R_{al} + R_{fe}} \tag{2}$$

where,  $R_{al}$ ,  $R_{fe}$  are the equivalent resistances of secondary inductive plate and secondary iron yoko, respectively.

- (5) Excitation reactance  $X_m$

$$X_m = \frac{4\mu_0 f_1 \tau l_\delta m (W_1 \times k_{dp1})^2}{\pi g'_e K_\mu p} \tag{3}$$

where,  $l_\delta$ ,  $m$ ,  $k_{dp1}$ ,  $g'_e$ ,  $K_\mu$ ,  $p$ ,  $\mu_0$ , are respectively the core thickness, phases, winding coefficient, equivalent electromagnetic air gap, saturation coefficient, pole numbers, the permeability of vacuum.

(6) Quality factor  $G$

$$G = \frac{X_m}{R_2} = \frac{2\mu_0 \cdot \sigma \cdot f_1 \cdot \tau^2}{\pi g'_e} \quad (4)$$

where,  $\sigma$  is the secondary equivalent conductivity.

Make  $s$  represent motor slip, and solve the multiplication of  $s$  and  $G$

$$s \cdot G = \frac{2\mu_0 \cdot \sigma \cdot f_s \cdot \tau^2}{\pi g'_e} \quad (5)$$

Without consideration of the side effect, the synthetic resistance is

$$R_{e0} = \frac{sG}{1 + (sG)^2} \cdot X_m \quad (6)$$

Moreover, the synthetic reactance without considering the side effect is

$$X_{e0} = \frac{1}{1 + (sG)^2} \cdot X_m \quad (7)$$

Further, according to the operation characteristics of SLIM, the transverse edge effect coefficients  $K_p$ ,  $K_q$ , longitudinal end effect coefficient  $D_a$  and  $D_j$  on the synthesis of equivalent parameters (6) and (7) are modified by

$$R_e = R_{e0} K_p \left( 1 + D_a - \frac{D_j K_q}{sG K_p} \right) \quad (8)$$

$$X_e = X_{e0} K_q \left( 1 + D_a + \frac{sG \cdot D_j K_q}{K_p} \right) \quad (9)$$

Thus, in corresponding to Fig. 1, the final equivalent model with consideration of the end effect is assumed to be

$$Z_1 = \sqrt{(R_1 + R'_m + R_e)^2 + (X_e + X_{1\delta})^2} \quad (10)$$

If

$$k_{c1} = (R_1 + R'_m + R_e)^2 \quad (11)$$

Meantime, the sum of reactance is considered to be directly proportional to the two power approximation of frequency  $f_1$ . The expression is expressed in terms of the unity coefficient  $k_{c2}$ . Then, a simplified control model is obtained, as shown in Fig. 3.

Controllable equation is

$$Z_1 = \sqrt{k_{c1} + k_{c2} \cdot f_1^2} \tag{12}$$

Further, considering the DC steady-state voltage  $U_d$ , volatility  $\alpha$ , serial motor number  $N$ , the fluctuation range of line voltage  $U_1$  is

$$\frac{K_u}{N} \times U_d(1 - \alpha) \leq U_1 \leq \frac{K_u}{N} \times U_d(1 + \alpha) \tag{13}$$

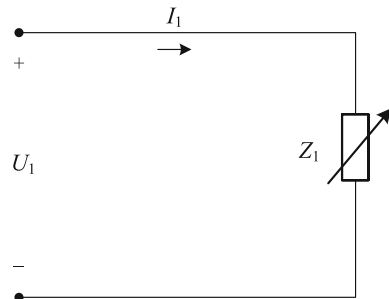
where,  $K_u$  is the voltage adjustment factor.

### 3 Functional Control

Generally, for the reason that motor model is uncertain and the motor parameters are asymmetric and changeable in running process, the recommended control strategy of SLIM in maglev train is not dependent on the motor parameters. Moreover, both theory and experiment analysis have proved that if the slip frequency  $f_s$  of SLIM is constant under the condition that the primary current is constant, the air gap magnetic field and eddy current of secondary plate are also controlled, and the generated thrust is also constant [6, 7].

As we known, after the motor made out, the  $R_e$  is determined. According to the requirements of thrust  $F_e$  and the iteration of speed, the characteristics of  $I_1$  are calculated to check whether the inverter can satisfy the inverter output, and this design process is iterative. The efficiency-factor product illustrates the capacity of the active output of SLIM under given design parameters.

**Fig. 3** Simplified control model



$$\eta \cdot \cos \varphi = \frac{R_e}{\sqrt{k_{c1} + k_{c2} \cdot f_1^2}} \cdot (1 - s) \quad (14)$$

From (14), it indicates that the efficiency-factor product is related to slip and primary frequency.

## 4 Simulation and Experimental Analysis

### 4.1 Two Dimensional (2D)/Three-Dimensional (3D) FEA

According to the design engineering experience, with consideration of non-symmetry characteristics of SLIM, generally, transient field analysis by using two-dimensional or three-dimensional FEA are fulfilled to understand the performance of the output characteristics, the electromagnetic field, temperature field and mechanical strength in high precision [8]. In this paper, a 2D/3D finite element model of SLIM is established and the simulation analysis is carried out, and for comparison, the results of theoretical analysis are also given. The SLIM parameters and control coefficients are listed in Tables 1 and 2.

In simulation, the thrust is only determined by the given current and frequency, and the value of the induced voltage (its value smaller than  $U_1$ ) is obtained and it is suggestively used to correct the simulation error.

### 4.2 Experimental Analysis

The actual motors are assembled on a medium-low speed maglev train. In the experimental study, key data are collected of two conditions with traction and

**Table 1** Technical parameters of SLIM

Parameters	Values	Parameters	Values
Maximum speed (km/h)	100	Rated thrust (kN)	3.1
Rated power (kW)	36	Motor length (mm)	1820
Pole pairs	4	Pole pitch (mm)	202.5
Voltage (V)	220	Lamination width (mm)	220
Starting current (A)	340	Secondary plate width (mm)	244
Winding material	Aluminum	Air gap (mm)	13

**Table 2** Simplified control coefficients

Coefficients	$k_{c1}$	$k_{c2}$	$f_s$ (Hz)
Value	0.01352	$6.089 \times 10^{-5}$	13.69



braking at three operating points (starting, turning, and maximum speed). In the following Figs. 4, 5, 6, 7, 8, 9, 10 and 11,  $U_{uv}$ ,  $U_{vw}$  represent motor U-V and W-V line voltage respectively, and fundamental motor phase current are  $I_u$ ,  $I_w$ .

Figures 4, 5, 6 and 7 show the traction condition of maglev train. As the vehicle accelerates from 0 to 100 km/h, with the increase of voltage, the harmonic current distortion amplitude is also increased, and, the highest starting the current value is gradually decreased from 326 A at starting point to 167 A at the maximum speed point. The turning point speed at 42 km/h, and the corresponding current value is 318 A. Figures 8, 9, 10 and 11 show the braking condition of maglev train (larger ripple in Fig. 8 is the test sensor suffering interference). As the vehicle decelerates from 100 to 15 km/h, with the decrease of voltage, the harmonic current distortion amplitude is also gradually decreased, and the current amplitude climbs from 280 up to 330 A and lasts to the point of air-electricity conversion. The turning point speed is at 85 km/h, and the results are highly accordance to theoretical design. Table 3 shows the statistical results among the theoretical, simulated and experimental ones. As can be seen from Table 3 ( $\varepsilon_i$  ( $i = 1, 2, 3$ ) represent calculated, 2D-FEA, and 3D-FEA deviation from actual measurement correspondingly), all the

**Fig. 4** Traction (0–100 km/h)

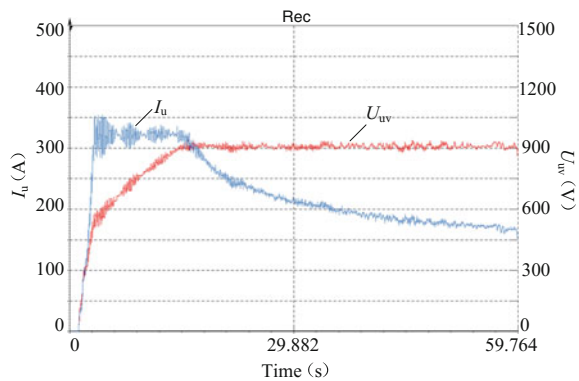


**Fig. 5** Traction (starting point)

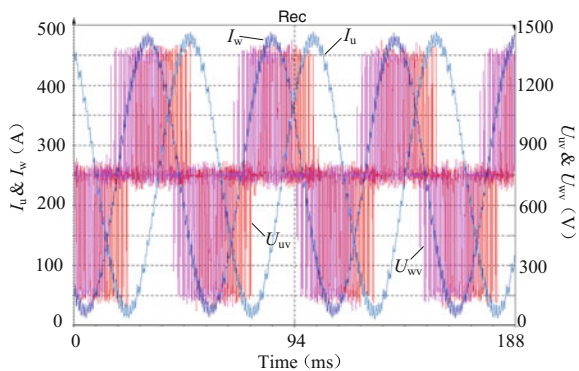


**Fig. 6** Traction (turning point)

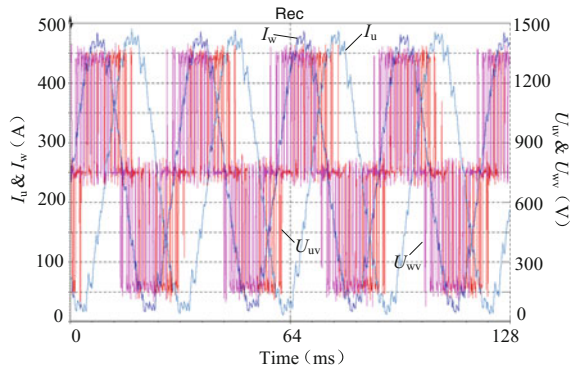


**Fig. 7** Traction (maximum speed point)

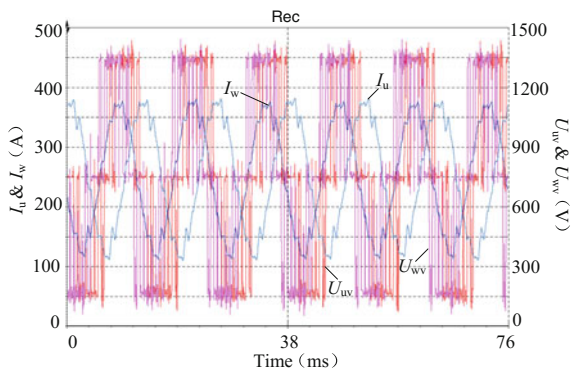
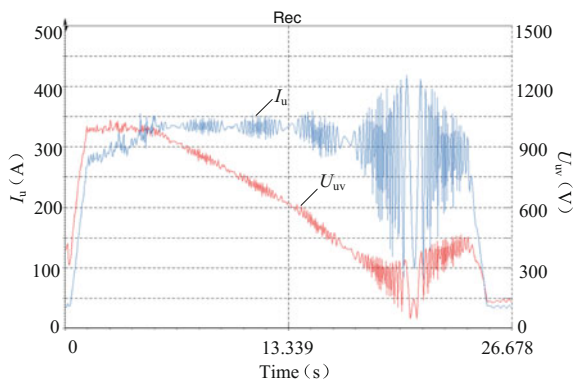


**Fig. 8** Braking (100–0 km/h)



3D-FEA values are larger than the experimental ones in whole speed range, with the maximum deviation of 15%. The 3D-FEA and theoretical values are much closer to real ones in low speed range with the maximum deviation no more than 3.5%, but at maximum speed point, their deviations are over 10%.

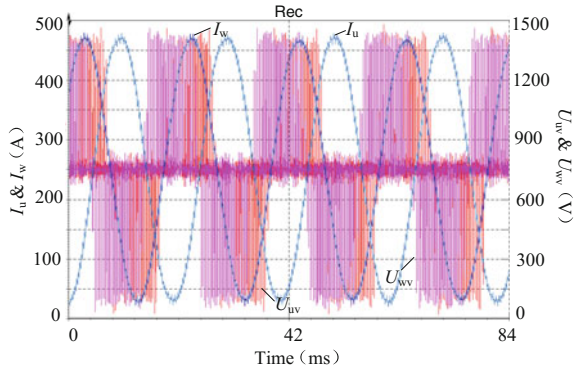


Fig. 9 Braking (generation end point)

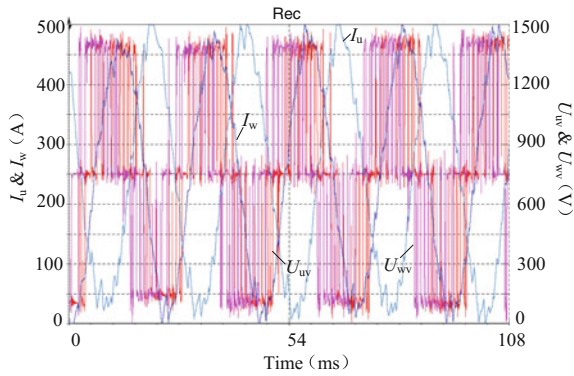


Fig. 10 Braking (turning point)

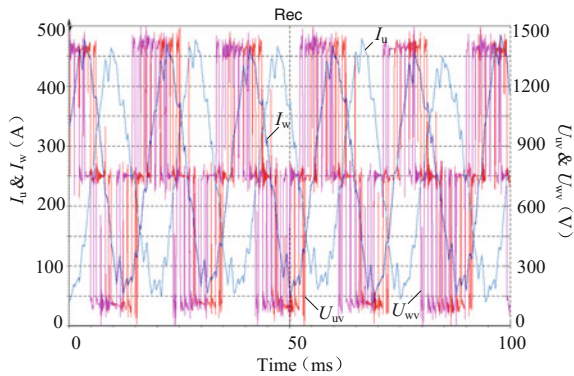


Fig. 11 Braking (maximum speed point)

**Table 3**  $F_e$  results comparison of theory, simulation and actual measurement

Points	Theoretical (kN)	$\varepsilon_1$ (%)	2D-FEA (kN)	$\varepsilon_2$ (%)	3D-FEA (kN)	$\varepsilon_3$ (%)	Experimental (kN)
Starting	3.234	1.32	2.991	-6.297	3.306	3.57	3.192
Turning	3.038	-2.94	2.872	-8.243	3.137	0.224	3.13
Maximum speed	0.737	12.69	0.709	8.409	0.755	15.443	0.654

## 5 Conclusion

The designed size motor is able to meet the traction and braking requirement of 100 km/h speed medium-low speed maglev train. Compared with the simulated and the experimental ones, the theoretical analysis are much simpler by using the simplified SEM. Therefore, one can introduce bias compensation method to improve the analysis accuracy, and make the theory and experiment highly unify. Since the experimental condition is difficult to construct, one can use some measurable variables, such as speed, train weight, and current to indirectly calculate thrust and resistance, and then use the current scan method to reduce the deviation of FEA and experimental results. After doing these, only minimal computational burden is paid to achieve high accuracy simulation analysis.

## References

1. Liu Y, Yang Y (2003) Linear motor driving metro vehicle—a new mode for urban mass transit. *Electr Locomotives Mass Transit Veh* 26(4):4–7 (in Chinese)
2. Fang Y, Li G, Lv G (2006) Linear motor and its application in urban rail transit. *Urban Rapid Rail Transit* 19(1):1–6 (in Chinese)
3. Yan L (2008) Development and application of the maglev transportation system. *IEEE Trans Appl Supercond* 18(2):92–98
4. Liu S, Chang W, Yin L (1997) The running experiment description of Japan maglev train HSST-100. *Electr Drive Locomotive* 6:29–31 (in Chinese)
5. Long X (2006) The theoretical analysis and electromagnetic design of linear induction motor. Science Press, Beijing, pp 103–104 (in Chinese)
6. Alfredo MG, Thomas AL, Donald WN (1998) A new induction motor V/f control method capable of high-performance regulation at low speeds. *IEEE Trans Ind Appl* 34(4):813–821
7. Deng J, Chen T, Tang J et al (2013) Optimum slip frequency control of maglev single-sided linear induction motors to maximum dynamic thrust. *Proc CSEE* 33(12):123–130 (in Chinese)
8. Yang T, Zhou L, Li L (2008) Finite element analysis of linear induction motor for transportation systems. In: *IEEE vehicle power and propulsion conference (VPPC 2008)*. IEEE, Harbin, pp 1–4

# A Controller Based on Electric-Charger Balance Theory for Front-End Converters

Yisheng Yuan, Xianglong Mei, Pan Zhou and Jiyun Tian

**Abstract** Aiming at the problem that between the second harmonic current  $i_{2nd}$  and dynamic response characteristic of the middle bus voltage  $u_b$  of the two stage inverter, the charge balancing controller integrated with the traditional double-loop controller is proposed. The traditional controller operates as load stable to suppress the secondary harmonic current  $i_{2nd}$ , but the load switched by the new controller. Based on the traditional double-loop controller, the design of the voltage-loop controller that meeting requirements of  $i_{2nd}$  is expounded, containing the influence of cross frequency  $\omega_c$  on  $\Delta u_b$  and the final dynamic response time  $t_s$  of  $u_b$ . The working principle of the electric-charge-balancing controller and some other key design issue are described. A prototype of 450 W is built to verify the correctness of the theoretical analysis and the feasibility of the new converter.

**Keywords** Single-phase inverter · Front-end converter · Middle bus voltage Control method dynamic response

## 1 Introduction

The two stage inverter is widely used in the grid or off grid system of new energy sources such as batteries, photovoltaic arrays and fuel cells. In a two-stage type inverter, the adoption of a large middle energy storage electrolytic capacitor  $C_b$  to support the middle bus voltage  $U_b$ , the former and back stage is decoupling. But in the single-phase output system, there are still two problems, the first problem is the output power of the inverter contains the secondary harmonic component [1], which is bound to produce the secondary harmonic voltage component in the bus capacitor; the second problem is that the ripple current is limited strictly in the most

---

Y. Yuan (✉) · X. Mei · P. Zhou · J. Tian  
School of Electrical and Automation Engineering, East China Jiaotong University,  
No. 808 East Shuanggang Street, Economic and Technological Development Zone,  
Nanchang, China  
e-mail: cloudstone\_yuan@aliyun.com

© Springer Nature Singapore Pte Ltd. 2018  
L. Jia et al. (eds.), *Proceedings of the 3rd International Conference on Electrical and Information Technologies for Rail Transportation (EITRT) 2017*, Lecture Notes in Electrical Engineering 482, [https://doi.org/10.1007/978-981-10-7986-3\\_48](https://doi.org/10.1007/978-981-10-7986-3_48)

direct source system [2], which needs to pre stage circuit to suppress the secondary harmonic current component. These two problems through the main circuit with the controller are associated with each other, and mutual constraints.

From the perspective of circuit, increasing the middle bus capacitors [3], adding secondary harmonic LC filter or bidirectional converter in the middle links [4–6], can't only reduce the secondary harmonic component of intermediate bus voltage, and to restrain the DC second harmonic current favorable. However, the circuit is complicated and the power density of the device is reduced.

From the perspective of control to solve the problem is the main research direction. Literature [7, 8] put forward respectively add a band trap in voltage control loop and the current feedback loop, can effectively reduce the harmonic current and speed up the dynamic response but the addition of trap in certain frequencies cause instability of the system.

In literature [9], the method of adding resonant controller in voltage control loop is presented, which can also reduce the second harmonic current on the DC side, but there is no experimental waveform of improve the dynamic characteristics. In literature [10], the feedforward control is introduced to inverter after the band trap added to load current, However, the load current is not the inverter output load current, but the inverter input current, so the inverter needs to increase additional detection devices. In the literature [11], the current feedback channel is added to the duty cycle signal generated by the traditional control, and the secondary harmonic of the duty cycle is weakened, but the parameters are difficult to be adjusted. Literature [12, 13] respectively based on virtual impedance and Reverse current boost model theoretically summarizes different kinds of control method that restrain the secondary harmonic current on DC side. The above method is mainly used in the control loop to reduce the secondary harmonic current on the DC side by adding the link of restraining or eliminating secondary harmonic component which is introduced by the middle bus voltage feedback. It is still based in independent control of the front-end circuit. In the case of the inverter output load switching, middle bus voltage must be in the fall or rise by the controller lagging to callback, reducing the dynamic response. To this, some literature introduce the inverter power or current into the feedforward controller of the front-end circuit to controlling to improve the dynamic characteristics of middle bus voltage. Methods which is the inductor current and capacitor current control by inverter output power feedforward in reference [14–16], speeding up the response of intermediate bus voltage.

In this paper, a new control method that about the front-end stage of single-phase inverter of variable structure based on the charge balance is proposed. Compared with the traditional control method, the method has the advantages of great consideration of constraining the second ripple current  $i_{2nd}$  and the improvement of the dynamic characteristics of the middle bus voltage  $u_b$ . To solve the problem of poor dynamic characteristics of bus voltage of the two stage inverter under the traditional control. This paper analyzes the working principle and the proposed control method, and verified by experiment.

## 2 The Charge Balance Control Strategy of Front-End Circuit

The control block diagram of the front stage circuit is shown in Fig. 1. At the top of the graph is the traditional double loop control algorithm and the charge balance control algorithm is below the graph. The Circuit diagram of two stage inverter is shown in Fig. 2.

Traditional double loop control algorithm in the system work under the steady state. The charge balance control algorithm work under load switch state. Two kinds of algorithm of switching conditions are as follows:

- (1) The admission mechanism of charge balance control algorithm: System load switching action when the system detects the load current of  $I_o$  abnormal fluctuations, then enter the charge balance control algorithm. The output duty cycle  $D_{f(N)}$  is switched to the charge balance control side. At the same time, continue to run the traditional double loop control algorithm, but the duty  $D_{f(N)}$  is not sent to the final output.

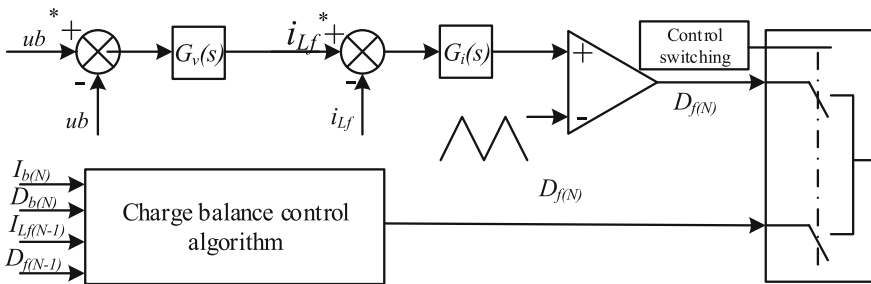


Fig. 1 Block diagram of the front stage circuit

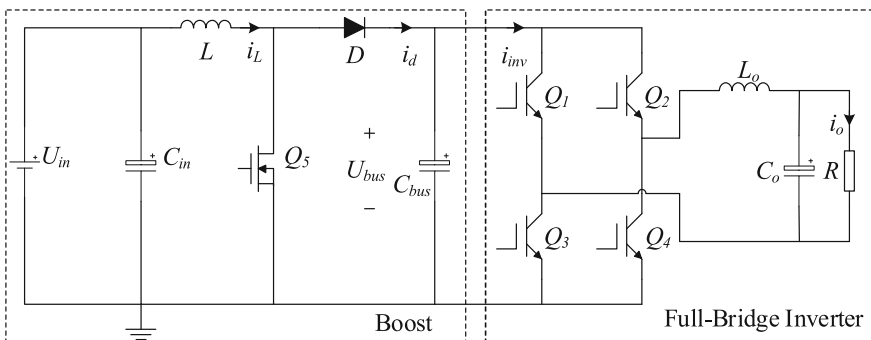


Fig. 2 Circuit diagram of two stage inverter

- (2) The exit mechanism of the charge balance control algorithm: System will quit the mechanism when detect average value of bus voltage recovery to the rated value.

## 2.1 Derivation of Charge Balance Equation

According to Fig. 1, the dynamic equation of DC bus capacitor voltage is

$$C_b \frac{du_b}{dt} = i_f - i_b \quad (1)$$

$i_f$  is the diode current of the Boost circuit, the  $i_b$  is the input current of the full bridge inverter circuit. Ideally, the time to maintain the  $i_f$  the instantaneous value of instantaneous value is equal to the  $i_b$ ,  $u_b$  will don't produce ripple. But it is not so strict in fact, as long as guarantee the average current of  $i_f$  and  $i_b$  are equal in a switching period, it can be considered that satisfy (1), namely  $\Delta u_b$  is zero. Assuming that the switching period of the circuit is  $T_s$ , the charge balance equation of  $C_b$  in the N switching cycle is

$$\Delta u_b = C_b \cdot (I_{f(N)} - I_{b(N)}) \cdot T_s = 0 \quad (2)$$

But in the actual control, the Boost circuit control the average inductor current of  $I_{L_f}$ , rather than the average diode current  $I_f$ . In addition, the bandwidth of the voltage loop is limited, and the current command  $i_{*L_f}$  always lags behind the  $U_b$ . These two points of traditional control result in existing insurmountable defects in dynamic characteristics, including methods that using the band trap.

In addition, the back stage inverter circuit control the inverter inductor current  $I_{L_b}$ , instead of inverter circuit input current  $I_b$ . The current of the front stage circuit and back stage circuit is

$$\begin{cases} I_f = (1 - D_f) \cdot I_{L_f} \\ I_b = D_b \cdot |I_{L_b}| \end{cases} \quad (3)$$

The  $D_f$  represents the duty cycle of the front stage circuit, and the  $D_b$  represents the duty cycle of the back stage circuit. By formula (3) simplifies the charge balance equation is used for control:

$$I_{L_f(N)} \cdot (1 - D_{f(N)}) = |I_{L_b(N)}| \cdot D_{b(N)} \quad (4)$$

It said that by controlling the current  $I_{L_f(N)}$  of front-end circuit and duty ratio  $D_{f(N)}$  in accordance with the above relationship can achieve the charge balance of capacitor charging and discharging, and eliminate fluctuation for unloading.



### 2.2 Duty Ratio of the Acquisition

$I_{Lf(N)}$  and duty ratio  $D_{f(N)}$  in formula (4) are the same rhythm and both interconnected in the Boost circuit,  $D_{f(N)}$  will affect the values of  $I_{Lf(N)}$ . So, the essence of formula (4) is to solve the  $D_{f(N)}$ .

Figure 3 is the  $i_{Lf}$  waveform of the inductor of the Boost circuit in the  $N - 1$  rhythm to  $N + 1$  rhythm. Among them,  $I_{Lf(N-1)}$  and  $I_{Lf(N)}$  was the midpoint of  $N - 1$  rhythm and  $N$  rhythm current rising edge respectively and also the current sampling point of DSP control.

According to the principle of Boost circuit switch:

$$\begin{cases} i'_{n-1} = I_{Lf(N-1)} + \frac{U_{in}D_{f(N-1)}T_s}{2L_f} \\ i_{n-1} = i'_{n-1} - \frac{(U_b-U_{in})(1-D_{f(N-1)})T_s}{L_f} \end{cases} \tag{5}$$

The  $D_{f(N-1)}$  is the  $N - 1$  rhythm duty of front boost circuit,  $i'_{n-1}$  is the peak inductor of front boost circuit current  $i_{Lf}$  when the switch is turned off,  $i_{n-1}$  is the value of the inductor current  $i_{Lf}$  at the end of the  $N - 1$  period of front circuit, but also the initial value of  $i_{Lf}$  when the  $N$  period beginning.

It is deduced that the initial inductor current  $i_{n-1}$  at the  $N$  period is:

$$i_{n-1} = I_{Lf(N-1)} + \frac{(2U_b - U_{in}) \cdot D_{f(N-1)} \cdot T_s}{2L_f} - \frac{(U_b - U_{in}) \cdot T_s}{L_f} \tag{6}$$

The midpoint current  $I_{Lf(N)}$  of the  $N$  period is

$$I_{Lf(N)} = i_{n-1} + \frac{U_{in}D_{f(N)}T_s}{2L_f} \tag{7}$$

Combining the formula (6), (7) to obtain the following relation:

$$\begin{cases} I_{Lf(N)} = K_1 + K_2D_{f(N)} \\ K_1 = i_{n-1} \\ K_2 = \frac{U_{in}T_s}{2L_f} \end{cases} \tag{8}$$

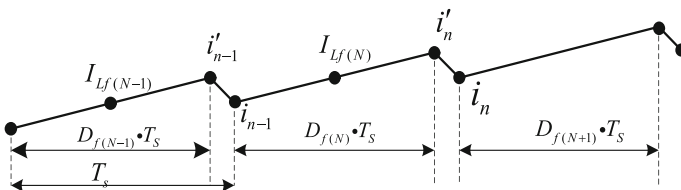


Fig. 3 Boost inductor current waveform

In fact,  $K_1$  is the initial current value of the  $N$  rhythm during sampling current and duty of the  $N - 1$  rhythm,  $K_2$  is the unit current increment coefficient decided by the main circuit parameter.

To solve formula (4) and (8):

$$D_{f(N)} = \frac{(K_2 - K_1) + \sqrt{\delta}}{2K_2} \quad (9)$$

Among these:

$$\delta = (K_1 + K_2)^2 - 4K_2 I_{Lb(N)} D_{b(N)} \quad (10)$$

Formula (10) don't have solution when the  $\delta$  less than 0. Its physical meaning is: when a little rhythm before load added suddenly the current of inverter circuit side increasing rapidly and the Boost circuit diode current is still small,  $C_b$  can't achieve the charge balance at the time.  $\Delta$  should be zero.

$$D_{f(N)} = \frac{K_2 - K_1}{2K_2} \quad (11)$$

In the extreme case of no-load switching load, the  $K_1$  will be zero due to the initial operation of the Boost circuit in CCM,  $D_{f(N)}$  is 0.5. This accord with the requirement of the Boost circuit fast response.

### 2.3 Elimination of Control Error

In the simplified charge balance Eq. (4), the duty cycle  $D_{b(N)}$  of the inverter side can be obtained in real time, but the current  $I_{Lb(N)}$  can't be obtained in real time. That can be simply predict through the following equation:

$$I_{Lb(N)} = I_{Lb(N-1)} + \frac{(D_N - D_{N-1})}{D_{N-1}} \cdot I_{Lb(N-1)} \quad (12)$$

In addition, in order to reduce the error of control, the charge error integral is added into the controller, and the formula (12) is amended as

$$I_{Lf(N)} \cdot (1 - D_{f(N)}) = \sum_{N=1}^N [I_{Lb(N)} \cdot D_{b(N)}] - \sum_{N=1}^{N-1} [I_{Lf(N)} \cdot (1 - D_{f(N)})] \quad (13)$$

This can offset the control errors caused by inaccurate parameters.

## 2.4 The Key Points of Design

### 2.4.1 The Condition of Charge Balance Control

Through the judgment of  $di_o/dt$  of inverter output current. But because the charge balance control is only responsible for the improvement of the dynamic response, in order to avoid the error in the steady state operation,  $di_o/dt$  can't be too small. In fact,  $di_o$  what is the difference between the two rhythm as a condition of judgement, when the output is the sine wave current  $di_o$  should be greater than the crossing zero point what is (the highest derivative at this time) the difference between the two rhythm. Take a circuit as an example, its  $I_o$  is 4 A, output frequency is 50 Hz and switch frequency is 20 kHz.

$$di_o = \sqrt{2} \times 4 \sin\left(\frac{2\pi}{400}\right) = 0.089A \quad (14)$$

In order to prevent interference, this data will be magnified 3 times as a criterion.

In addition, the output voltage instantaneous value  $u_o$  of switching point as a starting control criterion, because the power fluctuation and  $u_b$  fluctuation near zero produced by loaded and unloaded are small.

### 2.4.2 The Condition of Charge Balance Control Exit

The middle bus voltage  $U_b$  Whether is restored to the vicinity of the rating and combined with the threshold conditions to judge exit conditions.  $U_b$  is the average value  $u_b$  in a power frequency cycle. While time threshold conditions can prevent the lack of control. If  $u_b$  can't restore to the vicinity of the rating, system can't withdraw from the charge balance control.

### 2.4.3 Charge Balance Control Parameters

The charge balance control in the dynamic response is derived from the system based charge balance, which has incomparable rapidity. However, according to the formula, it is also affected by the parameters. These parameters include three categories: duty cycle, sampling voltage and current and inductor.

Duty cycle: It can be read in the DSP, but to make up for the 2 factors—delay time and dead time. The former needs to be measured by the drive circuit, and the latter is obtained by the dead zone register.

Voltage and current signals: these signals will have sampling delay, which affecting the sampling accuracy. In the actual design, the precision by reducing the filter capacitor in the sampling circuit can be reduced to 3%.

Inductance: The relationship which composed of inductor magnetic core permeability and current is nonlinear, the inductance will decline when the current is greater than a certain value. In order to reduce the volume and cost of the inductor, it is generally designed to reduce the inductance to the initial value of 70–80% at the peak of the rated current. It can be seen that the change of inductance for the control the most important factor in the above parameters. The method to solve this problem is to make a relation table between inductance and current value in DSP. By looking up the table, we can determine the  $L_f$  value according to detected the inductor current  $i_{L_f}$ .

### 3 Result of Experiment

#### 3.1 Experimental Parameters

A prototype was made in laboratory. The parameters are shown in Table 1. The prototype circuit is controlled by DSP, and the DSP is the TMS320F28335 of TI.

#### 3.2 The Controller of Back Stage Inverter Circuit

The full bridge inverter circuit adopts unipolar modulation and double loop control scheme. As shown in Fig. 4, the outer loop is the loop of the output voltage instantaneous value, the inner loop is a capacitive current loop. Due to the fact that the sampling interference what is capacitance current  $I_C$  is large, the inverter inductor current  $i_{L_b}$  minus the output current  $i_o$ . The control loop only use proportional components because the output voltage and capacitance current are instantaneous variables, integral link is easy to cause oscillation.

**Table 1** System parameters of two stage inverter

Parameters	Numerical value
The input voltage of front stage $U_{in}/V$	100
The output voltage of front stage $U_b/V$	200
Boost inductor $L_f/mH$	1
Middle bus capacitance $C_b/\mu F$	1290
The output voltage of inverter $U_o/V$	110
Output frequency $f/Hz$	50
Output filter inductor $L_f/mH$	1
Output filter capacitance $C_o/\mu F$	10
Load power $P_o/W$	450
System switching frequency $f_s/KHz$	20

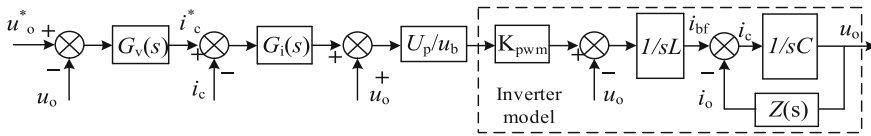


Fig. 4 The block diagram of the double loop control of inverter

Figure 4,  $K_{pwm}$  is the PWM modulation coefficient of the inverter circuit, defined  $K_{pwm} = u_b/U_p$  ( $U_p$  is the peak of the triangular wave,  $u_b$  is input voltage of the inverter). From the internal model of the inverter, it can be seen that there are two interference variable  $u_o$  and  $u_b$ . Therefore, the method of disturbance feed-forward inhibition used in internal control loop to eliminate the interference. On one hand,  $u_o$  introduced to internal feed forward control loop; on the other hand,  $u_b$  introduced into a divider  $U_p/u_b$  to get Reciprocal of  $K_{pwm}$ , finally  $u_o$  and  $u_b$  offset in the feed channel of the system.

The control parameters  $G_v(s) = 0.063$ ,  $G_i(s) = 16$ .

### 3.3 Result of Experiment

Figure 5 is waveforms under the traditional control when the load in the transient and steady-state, that include the inverter output voltage  $u_o$  of inverter, the output current  $i_o$ , the bus voltage  $u_b$ , the front Boost inductor current  $i_{L_f}$ . When the load is increased, the inverter current  $i_o$  changed suddenly, inverter output voltage  $u_o$  almost unchanged, the bus voltage decreased by 50 V, the former Boost inductor current  $i_{L_f}$  slow changes in the transient process. The whole adjusting time is 160 ms.

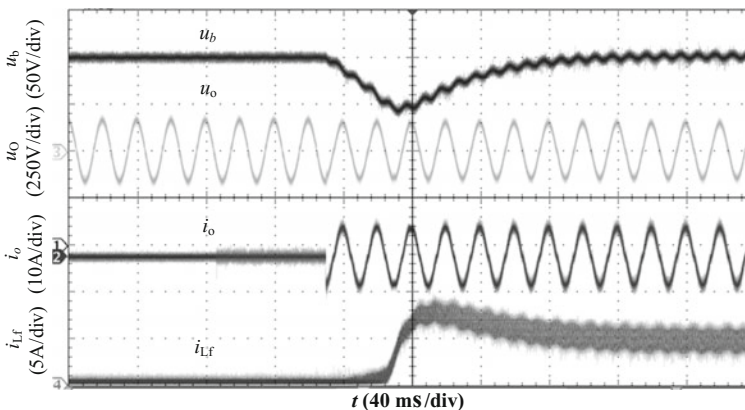
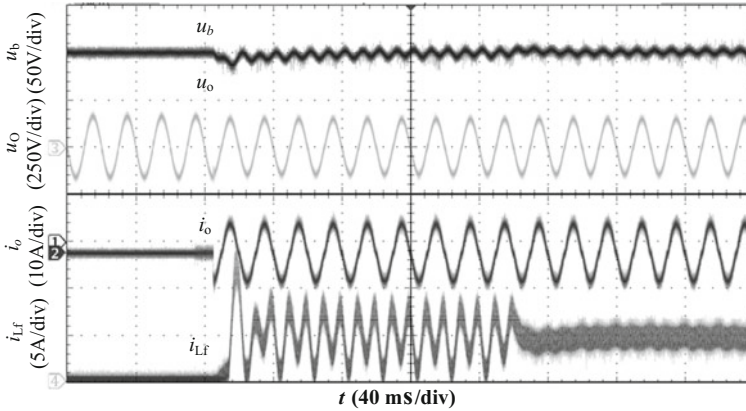


Fig. 5 waveforms using traditional controller



**Fig. 6** waveforms using proposed controller

Figure 6 is waveforms under the electric-charge-balancing controller combined with the traditional double-loop controller when the load in the transient and steady-state, that include the inverter output voltage  $u_o$  of inverter, the output current  $i_o$ , the bus voltage  $u_b$ , the front Boost inductor current  $i_{Lf}$ . When the load is increased, the inverter current  $i_o$  changed suddenly, inverter output voltage  $u_o$  almost unchanged. The front boost inductor current  $i_{Lf}$  changes rapidly and almost no change in the bus voltage  $u_b$ . When switching back to the traditional control structure, bus voltage remained stable and the whole adjustment time is very short.

## 4 Conclusion

An electric-charge-balancing controller combined with the traditional double-loop controller of the two stage inverter is proposed in this paper, that don't influence the suppression of the secondary ripple current, greatly improving the dynamic response ability of bus voltage, reducing the fluctuation of bus voltage and promoting the quality of output voltage of the inverter circuit. This method can be widely used in the control of this kind of inverter.

**Acknowledgements** This work is mainly supported by the National Natural Science Foundation of China (51467005) and the Key Research and Development Plan of Jiangxi Province (20171BBE50018).

## References

1. Jung S, Bae Y, Choi S et al (2007) A low cost utility interactive inverter for residential fuel cell generation. *IEEE Trans Power Electron* 22(6):2293–2298
2. Fontes G, Turpin C, Saisset R, et al (2004) Interactions between fuel cells and power converters influence of current harmonics on a fuel cell stack. *Power Elect Spec Conf* 4729–4735

3. Itoh J, Hayashi F (2010) Ripple current reduction of a fuel cell for a single-phase isolated converter using a DC active filter with a center tap. *IEEE Trans Power Electron* 25(3):550–556
4. Wang R, Wang F, Boroyevich D et al (2011) A high power density single-phase PWM rectifier with active ripple energy storage. *IEEE Trans Power Electron* 26(5):1430–1443
5. Li H, Zhang K, Zhao H (2012) Study on the DC active power filter for high power density single phase converter. *Proc CSEE* 40–47. (in Chinese)
6. Li H, Zhang K, Zhao H (2012) Researches on DC active power filters for high power density single phase converters/proceedings of the Chinese society of electrical engineering (Proceedings of the Chinese Society of Electrical Engineering). *Chinese Soc for Electr Eng* 32(15):40–47
7. Wang C, Li X, G Li (2012) Double stage converter coordinated control of power balance and time delay compensation combination. *Proc CSEE* 32(25):15–22 (in Chinese)
8. Li Z, Xiaoyong R, Xinbo R (2014) Control strategy to improve the bandwidth and reduce the second harmonic current in the two-stage inverter based on virtual impedance. *Trans China Electro Tech Soc* 29(6):136–144
9. Gong C, Chen J, Zhang F (2012) A novel technique of low frequency input current ripple reduction in two-stage DC-AC inverter. *IECON 2012-38th Annual Conference on IEEE Industrial Electronics Society*. IEEE 139–143
10. Zhu G, Ruan X, Wang X et al (2013) Suppression of the second harmonic current and improvement of the dynamic performance for two-stage-single-phase inverters. *Proc CSEE* 33(12):72–80 (in Chinese)
11. Bin L, Jianjun H, Mei S et al (2013) Input ripple current active mitigating for two-stage single-phase inverter based on double channel current feedback. *Electr Technol* 28(8):187–193 (in Chinese)
12. Li Z, Xinbo R, Xiaoyong R (2015) Control method of two level inverter front stage DC converter. *Proc CSEE* 35(3):660–670 (in Chinese)
13. Ji B, Wang J, Zhao J (2013) Reduction of low frequency input current ripple in a non-isolated single phase photovoltaic grid-connectors inverter. *Electro Techn J* 28(7):139–146. (in Chinese)
14. Zhang X, Wen X, Zhao F (2012) A direct power control scheme for Bi-directional buck/boost converters in motor drive systems. *Proc Chinese Soc Electr Eng* 32(33):15–22 (in Chinese)
15. Zhang X, Wen X, Zhao F (2012) Research on the bus capacitor current control scheme for buck/Boost bi-directional converters in motor drive systems. *Proc CSEE* 32(30):23–29 (in Chinese)
16. Hur N, Jung J, Nam K (2001) A fast dynamic DC-link power-balancing scheme for a PWM converter-inverter system. *IEEE Trans Industr Electron* 48(4):794–803

# Research on Energy Management for Hybrid EMU

Rongjia He, Chen Zhang, Ruichang Qiu and Lijun Diao

**Abstract** The operation route of EMU is relatively definite, the operating condition can be predicted and planned, and the applicability of logic threshold is relatively good. Therefore, the rule based on logic threshold energy management strategy is adopted as a control strategy in this paper. Depending on the operating characteristics of hybrid EMU, this paper develop the logic threshold energy management control strategy based on rules considering of integrated fuel consumption, and make the simulation model of specific control method and speed control of diesel generator and battery charge and discharge control, then the hybrid energy management strategy of different mode have been achieved.

**Keywords** Hybrid power system · Energy management control  
The logic threshold management

## 1 Introduction

Hybrid power control strategy not only realizes the best fuel economy, but also takes into account the engine emissions, battery life, driving performance and vehicle costs and other requirements [1–3], should be combined with the characteristics and operating conditions of hybrid vehicle components, the various sub-systems to achieve the best match.

Among the mainstream energy management strategies, the rule based logic threshold management strategy is relatively simple and robust. It is the most widely used energy management strategy. It is based on the train speed, traction torque,

---

R. He (✉) · R. Qiu · L. Diao

School of Electrical Engineering, Beijing Engineering Research Center of Electric Rail Transportation, Beijing Jiaotong University, 100044 Beijing, China  
e-mail: 15121414@bjtu.edu.cn

C. Zhang

Technology Managment Dept, CRRC Zhuzhou Locomotive Co., Ltd.,  
412000 Zhuzhou, China

© Springer Nature Singapore Pte Ltd. 2018

L. Jia et al. (eds.), *Proceedings of the 3rd International Conference on Electrical and Information Technologies for Rail Transportation (EITRT) 2017*, Lecture Notes in Electrical Engineering 482, [https://doi.org/10.1007/978-981-10-7986-3\\_49](https://doi.org/10.1007/978-981-10-7986-3_49)

475



battery, SOC and other variables and set the logical threshold of the comparison results, in accordance with pre-set rules for control [4, 5].

The hybrid system is studied in this paper belongs to the series system. The common control modes are the thermostat mode and the power tracker model [6, 7]. The two control modes are combined based on the single target control of the battery SOC or the engine fuel consumption, using the engine’s efficient area and the battery’s rapid response characteristics, to realise the battery SOC balance control [8] and improve vehicle fuel consumption at the same time in order to achieve the overall efficiency of the best.

## 2 Diesel Generator Speed Control

In the process of controlling the diesel generator speed, it is necessary to consider the DC voltage, output power and fuel consumption and other factors, this paper in the course of the study, combined with the load characteristics and fuel consumption curve, sub-mode to take different diesel generator speed control strategy.

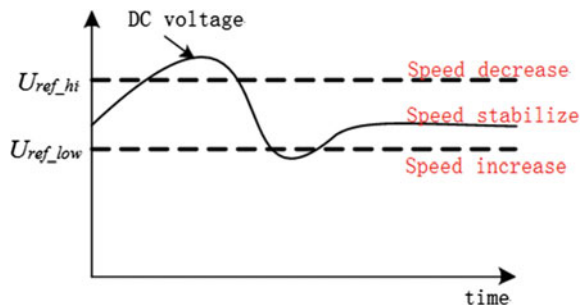
### 2.1 Traction Conditions

In the traction conditions, use the voltage hysteresis based on the speed control method. During the traction process, the power will change, and this change will be reflected in the middle DC voltage, so the diesel generator speed on the power tracking can be achieved indirectly by its output droop characteristics. According to the DC voltage to set a certain width of the hysteresis, the use of voltage hysteresis control method can be achieved under the traction conditions of diesel generator speed automatic adjustment.

The figure below is the voltage hysteresis control of engine speed (Fig. 1).

The DC voltage range of diesel generator sets at different speeds is shown in Fig. 2. At the speed of 1800 rpm, the maximum output power is 330 kW, and the DC voltage range is about 1520–1700 V, satisfying the power and voltage

**Fig. 1** Voltage hysteresis control of engine speed



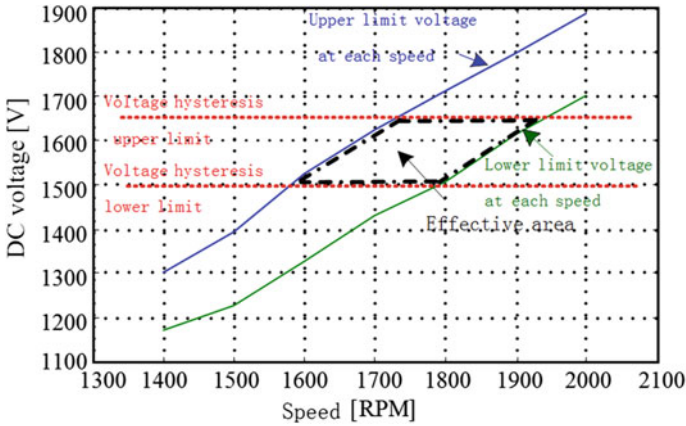


Fig. 2 DC-link voltage ranges with different engine speed of diesel generator

requirements, and at this time the fuel consumption rate is relatively low, 1800 rpm can be considered the ideal speed of diesel generators for traction conditions. According to its voltage range, set the DC voltage hysteresis to be 1500–1650 V.

Traction conditions, the diesel generator speed of the hysteresis loop control simulation waveform is shown in Fig. 3.

It can be seen from the Fig. 3, beginning from the DC voltage of  $A_1, A_2$  below the hysteresis lower limit of 1500 V, the engine speed increases, the DC voltage increases; DC voltage enter into the hysteresis interval in the point of  $B_1, B_2$ , the generator speed remains unchanged; DC voltage of  $C_1$  is higher than the hysteresis ceiling 1650 V, the engine speed decreases, the DC voltage drops, reaching the point  $C_2$  while keeping the speed constant again. With the DC side voltage

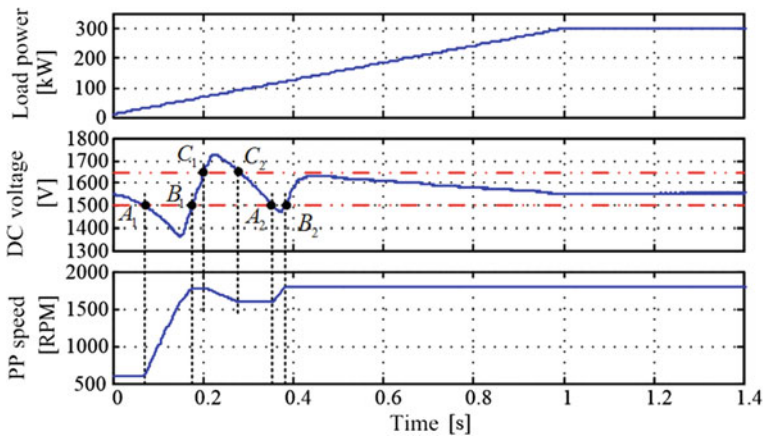


Fig. 3 Simulation result of voltage hysteresis control of engine speed in traction cycle

fluctuating near the 1500–1700 V hysteresis, diesel generator adjust between the speed of 1600–1800 rpm, the final diesel generator speed is stable at 1800 rpm, DC voltage 1550 V, being consistent with the theoretical analysis.

## 2.2 Other Conditions

In the non-traction conditions, use constant speed control. In the case of idling, braking and stopping, the load power of the diesel generator set is known and the change is small. Therefore, the speed of the diesel generator is controlled by the constant speed control method. The control rules are shown in Table 1.

In the idling conditions, considering the straight running conditions only, traction power is small, diesel generator sets may be appropriate to charge the battery, the speed  $N_{chg}$  is a fixed value of 1700 rpm; when the battery SOC to reach the upper limit of charge, the diesel generator set change into the idle state not charging, the speed  $N_{cons}$  down to 1500 rpm.

In the braking conditions, the battery pack absorb the regenerative braking energy of the train, with diesel generator waiting for the speed of 1400 rpm, when the battery failure, operating in pure diesel generator conditions, the same as the idling conditions while not charging.

In the stopping conditions, the APS power is provided in principle by the battery pack. In particular, in the station charging mode, the diesel generator sets the battery charge, the specific control strategy is the same as the idle charge; when the battery SOC reaches the upper limit of the parking charge, the generator set turns to idle at 600 rpm.

According to the logic threshold energy management rule, the operation mode of the system is judged, and then the voltage hysteresis control or constant speed control is selected in different operation modes, the output is the diesel generator speed.

**Table 1** Constant engine speed control rule of diesel generator

Operating conditions		PP speed
Idling conditions	Charging	$N_{chg} = 1700$ rpm
	Not charging	$N_{cons} = 1500$ rpm
Breaking conditions	Normal	$N_{brk} = 1400$ rpm
	Error	$N_{cons} = 1500$ rpm
Stopping conditions	Charging	$N_{chg} = 1700$ rpm
	Not charging	$N_{idling} = 600$ rpm

### 3 Charge and Discharge Control of Power Battery Based on Droop Characteristic

Charge and discharge control of power battery based on droop characteristic, that is, according to the fitted drop voltage formula, figuring out the drop voltage  $U_{drop}$  of the diesel generator at the current speed  $N_{dg}$  when power output  $P_{dg}$  is certain, as the battery target voltage, power battery being equivalent as the load of the diesel generator set, the controlling of the battery charge and discharge can adjust the output power of the generator, through the coordination of the two to achieve energy distribution between the power source.

Taking the diesel generator set as a constant speed of 1800 rpm, the target output power is changed from 240 to 150 kW.

In Simulink using m language to code power battery target voltage control function, simulate the process above; get DC voltage, power battery current, diesel generator output power waveform (Fig. 4).

From the figure above we can see, at the speed of 1800 rpm, the target output power is from 240 to 150 kW, the battery target voltage is from 1550 to 1590 V, diesel generator output power decreases. The simulation shows that the charge and discharge control based on the droop voltage can achieve one-to-one correspondence between the target voltage and the power output of the power pack.

At the speed of 1800 rpm, the load power changed from 210 to 360 kW, requiring the diesel generator output 240 kW, and the simulation waveform is shown in Fig. 5.

In the figure, the target voltage of the battery pack is always constant when the diesel generator speed and target power are constant. Throughout the process, the

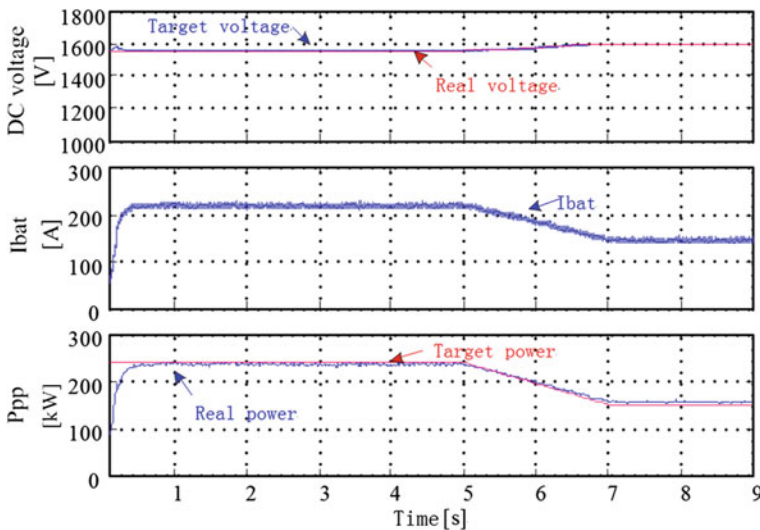


Fig. 4 Simulation result of battery drop control with different diesel power target

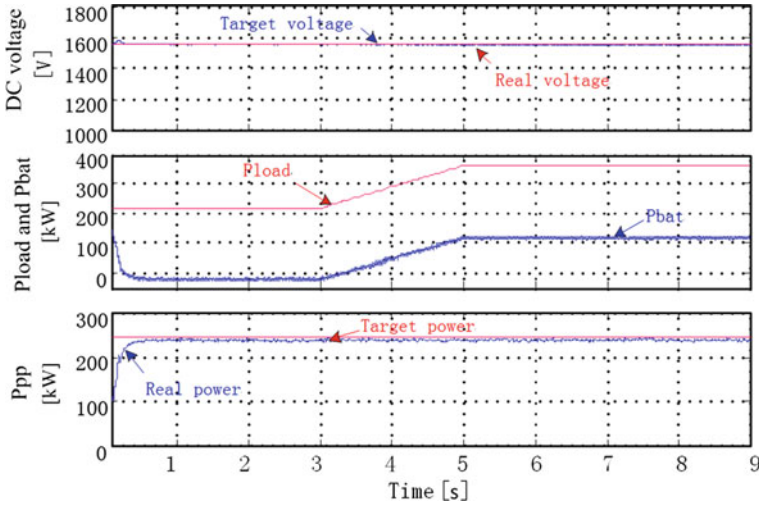


Fig. 5 Simulation result of battery drop control with different load power

DC voltage stabilized at 1550 V, the output power of the diesel generator set is 240 kW, indicating that the charge and discharge control based on the droop characteristic can realize the power distribution of the hybrid system.

When the battery running, besides controlling the DC voltage, using the state of the battery to limit the current, in addition, when in the idling conditions, the diesel generator charging the battery is also used constant voltage control mode. On the base of the droop voltage, according to the current limit set a certain hysteresis bandwidth, to adjust the target voltage and then control the current.

According to the energy management strategy and the above-mentioned power battery control method, get the battery SOC changes in the train running range as shown in Fig. 6.

Mode A/Mode B: The train is in the traction state, the power battery pack discharges, the battery SOC is reduced, the bidirectional DC/DC operates in the Boost mode, and the target voltage is the droop voltage.

Mode C: The train is in the charging mode in the station. When the power battery pack cannot meet the energy require for the traction acceleration, the diesel generator set charges the battery and the target voltage is the drop voltage plus current hysteresis adjustment.

Mode D: The train is in the electric braking mode, the power battery is in the charging state, the battery SOC is increased, the bidirectional DC/DC works in the Buck mode, and the target voltage is fixed.

Mode E: When the battery SOC is below the discharge limit, in order to prevent the battery over discharge, power battery stops discharge.

Mode F: When the battery SOC is above the feedback limit, in order to prevent the battery overcharge, power battery pack stops charging.

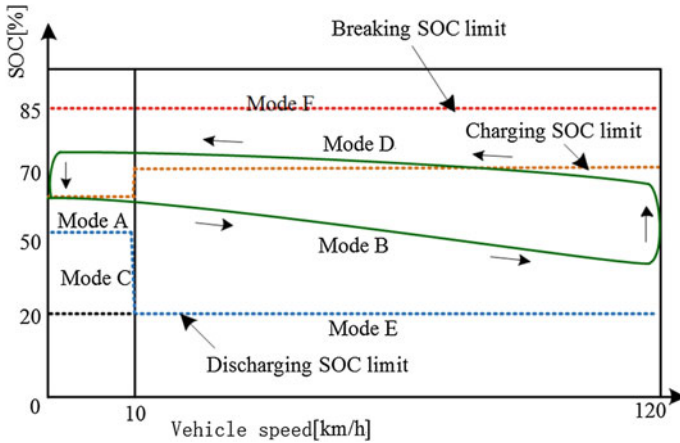


Fig. 6 SOC variation of battery in HEMU operating zone

### 4 Conclusions

The main content of this paper is the research of hybrid energy management and control strategy. Firstly, according to the characteristics of EMU operation, a rule-based logic threshold energy management strategy is proposed, and the generator speed is optimized according to the principle of low fuel consumption. The logic threshold management strategy of integrated fuel consumption is obtained. Then, the control method of hybrid system The design and realization of the voltage hysteresis control of the diesel generator speed and the charge and discharge control of the power battery and the load management control based on the droop characteristics are realized, and the energy distribution inside the power source is realized and verified by simulation.

**Acknowledgements** This work was supported by the China National Science and Technology Support Program under Grant [2017YFB1200802, 2016YFB1200504-C-01] and the Fundamental Research Funds for the Central Universities under Grant 2016JBM058 and Grant 2016RC038.

### References

1. Shu H, Qin D, Hu J (2001) Research on status and development trend of hybrid electric vehicle control strategy. *J Chongqing Univ (Natural Science Edition)* (06):28–31. (in Chinese)
2. Yu H, Tarsitano D, Hu X, Cheli F (2016) Real time energy management strategy for a fast charging electric urban bus powered by hybrid energy storage system. *Energy* 112:322–331
3. Zhang LP, Qi BN, Zhang RS, Liu JC, Wang LQ (2016) Powertrain design and energy management of a novel coaxial series-parallel plug-in hybrid electric vehicle. *Sci China (Technological Sciences)* (04):618–630

4. Yuan H, Zhao Y, Yao J (2011) Management strategy of fuel cell car energy optimization based on dynamic logic rules. *High-tech Commun* 21(4):428–433. <https://doi.org/10.3772/j.issn.1002-0470.2011.04.017>. (in Chinese)
5. Liu Y, Hu J (2016) Research on control strategy of hybrid electric vehicle energy management system. *Inform Technol* (9):121–125,129. <https://doi.org/10.13274/j.cnki.hdztj.2016.09.032>. (in Chinese)
6. Zhang X, Tian Y, Zhang X (2012) Research on power system modeling and energy management of hybrid locomotive. *J China Railway* 34(5):20–25. <https://doi.org/10.3969/j.issn.1001-8360.2012.05.004>
7. Gu Z, Wang S, Li J (2006) Research on Multi-objective control energy management strategy for hybrid electric vehicles. *J Beijing Inst Technol* 26(6):487–491. <https://doi.org/10.3969/j.issn.1001-0645.2006.06.005>
8. Kong Q (2009) Research on energy management strategy and soc estimation of hybrid electric vehicle. *Shan Dong Univ*. <https://doi.org/10.7666/d.y1561831>

# Anti-circulation Strategy of the Hybrid Traction Power Supply Device Used in Urban Rail Transit

Lu Ming, Gang Zhang, Fengjie Hao and Xibin Bai

**Abstract** In urban rail transit, when the train running, the AC voltage fluctuates, which resulting in the instability of DC side voltage of the rectifier unit. The hybrid traction power supply consists of a 12-pulse rectifier unit and a four-quadrant converter device (4QC). Aiming at the problem of circulation between the rectifier unit and the 4QC unit of the hybrid traction power supply device, the possible causes of the circulation are analyzed. The output voltage characteristics and basic structure and the working principle of the hybrid power supply device are studied. Then putting forward the corresponding anti-circulation strategy, and through simulation and test to verify its effectiveness. And the strategy adjusts the voltage value automatically according to the actual situation without manual operation, which is very practical.

**Keywords** Urban rail transit · The hybrid power supply device  
Anti-circulation

## 1 Introduction

With the continuous expansion of urban rail transit in China, urban railways play an increasingly important role in alleviating urban traffic congestion and energy conservation [1]. There is DC output voltage fluctuations in the 24-pulse and 12-pulse rectifier, and the energy can only be transmitted from AC to DC. When the urban rail train regenerative braking, the excess energy generated will make the traction net voltage soared, resulting in reduced regenerative braking capacity of the train or even regenerative braking failure [2].

---

L. Ming (✉) · G. Zhang · F. Hao  
School of Electrical Engineering, Beijing Engineering Research Center of Electric Rail Transportation, Beijing Jiao Tong University, Beijing 100044, China  
e-mail: 16121502@bjtu.edu.cn

X. Bai  
China Railway Electrification Bureau (Group) Co., Ltd, Beijing 100036, China



The hybrid traction power supply consists of a 12-pulse rectifier unit and a four-quadrant converter device (4QC). The four-quadrant converter device can operate either in a rectified state (providing energy to the DC catheters) or in an inverting state (the excess regenerative braking energy is fed back to the AC grid). At the same time, the device can also reactive power compensation to the AC medium voltage, and improve the system power factor [3].

## 2 The Hybrid Power Supply Device

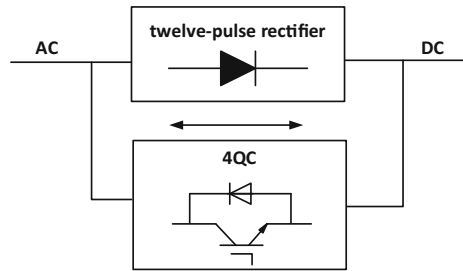
As shown in Fig. 1, the hybrid traction power supply device consists of a 12-pulse rectifier unit and a four-quadrant converter device (4QC).

Figure 2 shows the main circuit of 12-pulse rectifier unit, which consists of a three-winding phase-shifting transformer TR, two three-phase rectifier bridge RCT1 and RCT2, balanced reactor  $L_p$  [4].

Figure 3 is the PWM rectifier schematic diagram considering for the line impedance.  $U_a, U_b, U_c$  is the fundamental voltage of the midpoint of each phase bridge relative to the AC power source neutral point N [5].

The PWM rectifier unit adopts the current decoupling control based on the synchronous rotating coordinate system. The double closed-loop control structure (voltage outer ring and the current inner ring) and the space vector modulation (SVPWM) are used.

**Fig. 1** The equivalent circuit diagram of no-load test



**Fig. 2** The main circuit diagram of 12-pulse rectifier unit

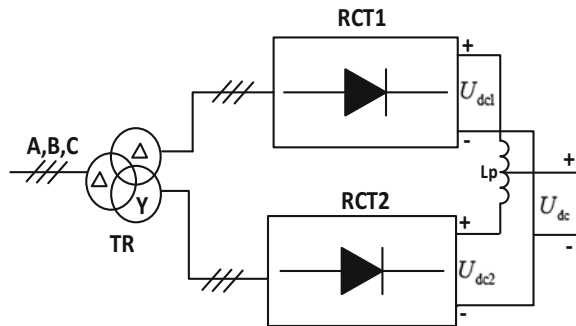
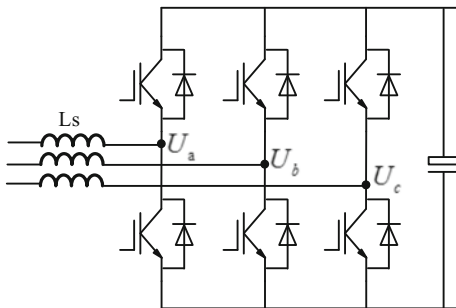


**Fig. 3** PWM rectifier schematic diagram



### 3 Output Characteristics of the Hybrid Traction Power Supply Device

#### 3.1 Output Characteristics of the 12-Pulse Rectifier

The 12-pulse rectifier output characteristic curve is shown in Fig. 4.

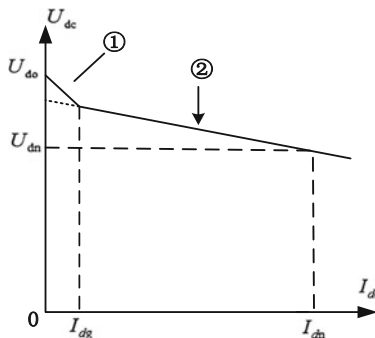
Bounded with the critical current  $I_{dg}$ , the output characteristic curve is divided into ① and ② two curves, ① for the two rectifier bridge in the push-pull work output curve; ② for the two rectifier bridge in parallel work output curve [6].

The output characteristic curve is curve ① when the load current  $I_{dc}$  is less than the critical current  $I_{dg}$ . The output characteristic curve is curve ② when the load current  $I_{dc}$  is greater than the critical current  $I_{dg}$ . The voltage  $U_{do}$  is called the ideal no-load DC voltage when curve ② reverse to zero current.

#### 3.2 Output Characteristics of 4QC

The output characteristics control of 4QC is outer ring control, the main function is to detect actual DC output voltage and DC output current of the PWM unit. Using

**Fig. 4** Outer characteristics of twelve-pulse rectifier



closed-loop control to achieve unified instructions current  $i_d^*$  of the PWM rectifier. The ultimate goal is to make the entire four-quadrant converter unit in accordance with a given output characteristic curve [7].

The two basic output characteristics of 4QC are: regulation characteristics, droop characteristics. The droop characteristic is shown in Fig. 5.

In Fig. 5, ① is rectification and ② is inversion.  $U_k$  is the no-load DC voltage,  $I_{dm-}$  is the maximum inverter DC current,  $I_{dm+}$  is when the DC current of maximum rectifier power. In general, the device runs as constant power curve when DC current exceed  $I_{dm-}$  and  $I_{dm+}$ .

## 4 Strategy of Anti-circulation

### 4.1 Reason of Circulation

According to the external characteristics introduced in Chap. 3, the 4QC unit behaves as a droop characteristic and works with the 12-pulse rectifier unit [8].

When the four-quadrant converter unit's no-load voltage is lower than the 12-pulse rectifier unit no-load voltage, the 12-pulse rectifier unit work in rectification state while the four-quadrant converter unit in the inverter work, resulting in energy cycle between the two units. That is, as shown in Fig. 6, the circulation.

In the actual system, when the train brake, four-quadrant converter unit work in the inverter state, the DC current generated by the catenary brake into AC power, and sent to the pressure ring network. The control system of 4QC unit receives measurement parameters of the sensors, and calculate real-time 12-pulse rectifier unit ideal no-load voltage  $U_{do}$  according to (1):

$$U_{do} = U_{abc} \times k_1 \times k_2 \tag{1}$$

where,  $U_{do}$  is the ideal no-load voltage of 12-pulse rectifier unit,  $U_{abc}$  is the grid voltage of AC side,  $k_1$  is transformer ratio for the rectifier unit side,  $k_2$  is coefficient between rectifier unit no-load voltage  $U_{do}$  and transformer secondary side voltage.

Fig. 5 Droop characteristics of 4QC

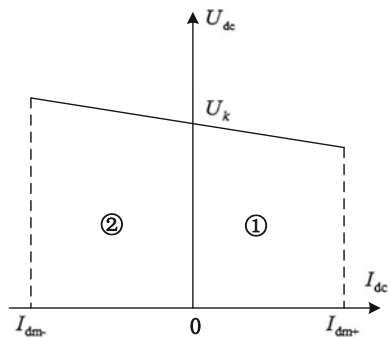
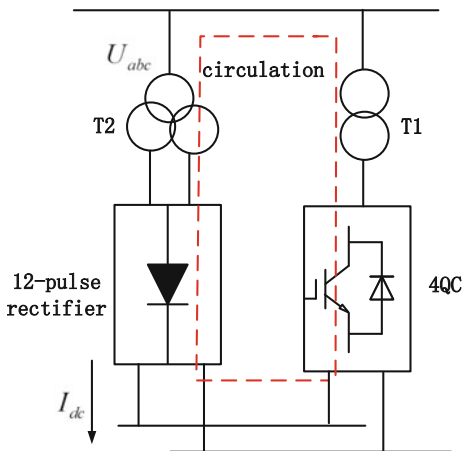


Fig. 6 Circulation diagram



When the train running, the AC voltage fluctuates, which resulting in the instability of DC side voltage of the rectifier unit. In the original system, the 4QC unit has a fixed inverter turn-on voltage (no-load voltage). When the ideal no-load voltage of rectifier unit is higher than the no-load voltage of 4QC unit, it will occur circulation.

### 4.2 Strategy of Anti-circulation

When the hybrid power supply is in the rectified state, the 12-pulse rectifier unit and the 4QC supply power to the load at the same time. Figure 7 shows the outer characteristic curve between the 4QC unit and the 12-pulse rectifier unit.

Where each symbol has the following meaning:

- ① is the DC output characteristic curve of the energy-fed device;
- ② is the DC output characteristic curve of the 12-pulse rectifier unit.

4QC unit use double closed-loop control and Space Vector Pulse Width Modulation (SVPWM),  $U_{dc-ref}$  is the DC voltage reference. According to the outer characteristic curve of the 4QC unit and the diode rectifier, there is a linear relationship between the no-load voltage of the 4QC unit and the DC voltage reference. According to the droop characteristics:

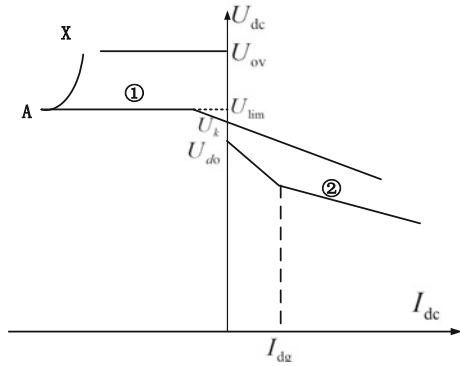
$$U_{dc-ref} = U_k - R_{dp}I_{dc} \tag{2}$$

In order to ensure load balancing, the two no-load voltage should maintain consistency:

$$U_k = U_{do} = U_{abc} \times k_1 \times k_2 \tag{3}$$

So that the no-load DC voltage  $U_k$  of the 4QC unit is always following the no-load voltage  $U_{do}$  of the 12-pulse rectifier unit. Then put this  $U_k$  into the voltage

**Fig. 7** Outer characteristic mating curve



loop, and through a series of PI adjustment and decoupling, and the required drive pulse is generated.

This control strategy can ensure that inverter turn-on voltage of 4QC unit is always changing with the 12-pulse rectifier unit ideal no-load voltage, thus preventing circulation. And the strategy adjusts the voltage value automatically according to the actual situation without manual operation, it's very practical.

### 5 Simulation

Using Matlab/Simulink to build a hybrid power supply device model, including a set of 12 pulse rectifier and a four-quadrant converter unit. The simulation circuit is shown in Fig. 8.

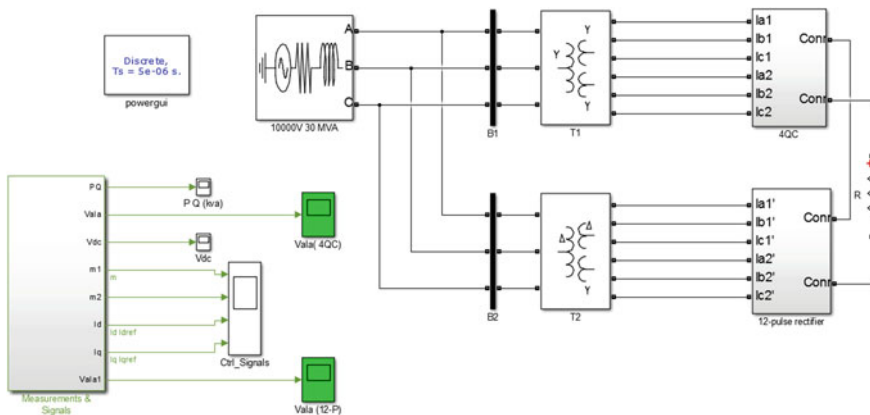


**Fig. 8** MATLAB simulation model

There is a set of contrast simulations to verify the effectiveness of anti-circulation strategy. Figure 9 is the fault AC current waveform before using of anti-circulation strategy. It can be seen from Fig. 1, the voltage and current of 12-pulse rectifier unit is in phase, it works in the rectified state; And the voltage and current of 4QC unit is in inversion, it works in the inverter state. There is circulation between the two units.

With the anti-circulation strategy, the AC current is shown in Fig. 10.

It can be seen that the voltage and current is both in phase in 12-pulse rectifier unit and 4QC unit, and the two units supply power to the load at the same time. This anti-circulation strategy can effectively prevent the circulation.

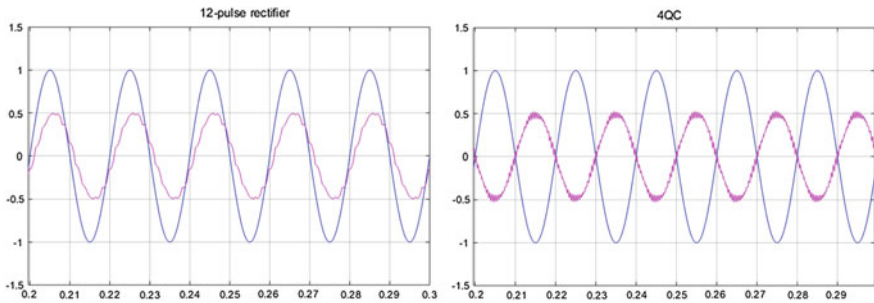


Fig. 9 A-phase AC voltage and current waveform (circulation)

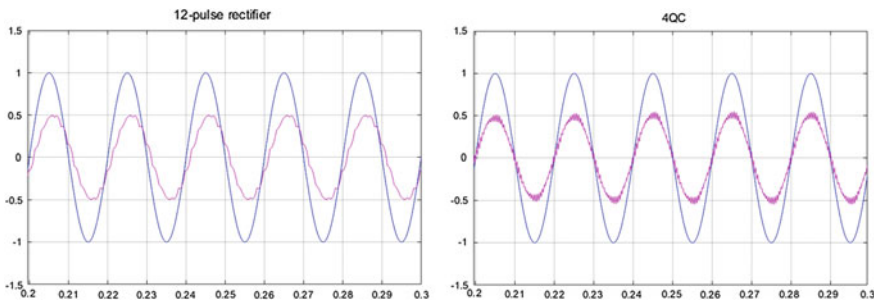


Fig. 10 A-phase AC voltage and current waveform

## 6 Conclusion

In this paper, the structure and external characteristics of the hybrid traction power supply system are introduced. The working principle and the cause of the circulation are introduced. An anti-circulation method is proposed and its feasibility is verified by Matlab.

**Acknowledgements** The work was supported by the National Key Research and Development Program 2017YFB1200802 and the Beijing Science and Technology Commission project Z171100002217025.

## References

1. Luo R (2009) Design on Monitory Platform for Novel Traction Supply System of Urban Rail Transportation. Beijing Jiaotong University, Beijing (in Chinese)
2. Quan H (2013) Research on key techniques and performance optimization of hybrid traction power equipment for urban rail transit. Beijing Jiaotong University, Beijing (in Chinese)
3. Quan H, Zhang G (2013) Urban rail transit hybrid traction power system with energy feedback. *J Beijing Jiaotong University* 37(2):92–98 (in Chinese)
4. Wang N, Wei X (2003) Line side harmonic current analysis in 24-pulse traction rectifier substation of city track. *Transformer* 40(1):1–7 (in Chinese)
5. Shi-you ZHU (2013) Study of urban rail reactive power compensation strategy based on energy-fed traction power supply equipment. *Adv Technol Electr Engineering Energy* 32(2):16–19 (in Chinese)
6. Li L (2017) Simulation and application of external characteristics curve of 24-pulse rectifier in urban rail transit. *Res Urban Rail Transit* 10(15):52–55 (in Chinese)
7. Zhang G (2010) Study on key techniques of energy-fed traction power system for urban mass transit. Beijing Jiaotong University, Beijing (in Chinese)
8. Lu (2015) Control method and application of energy-fed traction power supply device. Proceedings of the 2015 International Conference on Electrical and Information Technologies for Rail Transportation (in Chinese)

# Comparison of Harmonics Between SVPWM and SHEPWM

Ruizheng Ni, Miao Sha, Jia Xiaoguang, Yong Ding and Jie Chen

**Abstract** The traction system of rail transit has the characteristics of low switching frequency and wide speed range, and generally adopts “asynchronous modulation + synchronous modulation + square wave” full-speed range pulse width modulation strategy. In order to realize the smooth transition from asynchronous modulation to square wave modulation, many excellent modulation methods have been developed in the past 30 years. This paper focusses on researching the space vector pulse width modulation and the specific harmonic elimination pulse width modulation. The principle of the two methods and its harmonic calculation methods are introduced, two methods have different advantages, people should choose their own modulation as needs. Simulation proves the feasibility of the modulation strategy.

**Keywords** Rail transit · Space vector pulse width modulation · Specific harmonic elimination

## 1 Introduction

In the synchronous modulation area, the commonly used modulation methods are: the middle 60° modulation, SVPWM, SHEPWM [1]. The middle 60° modulation method is modulation only in the middle 60° region of each half-wave period,

---

R. Ni (✉) · J. Chen

School of Electrical Engineering, Beijing Engineering Research Center  
of Electric Rail Transportation, Beijing Jiaotong University, 100044 Beijing, China  
e-mail: 16121504@bjtu.edu.cn

R. Ni · J. Xiaoguang

Global Energy Interconnection Research Institute, Beijing, China

M. Sha · Y. Ding

CRRC Changchun Railway Vehicles CO., LTD, Changchun, China

J. Xiaoguang

State Key Laboratory of Advanced Power Transmission Technology, Beijing, China

© Springer Nature Singapore Pte Ltd. 2018

L. Jia et al. (eds.), *Proceedings of the 3rd International Conference on Electrical and Information Technologies for Rail Transportation (EITRT) 2017*, Lecture Notes in Electrical Engineering 482, [https://doi.org/10.1007/978-981-10-7986-3\\_51](https://doi.org/10.1007/978-981-10-7986-3_51)



the advantage of this modulation method is that the switching frequency and the switching losses can be significantly reduced, while ensuring the symmetry of the output waveform, and the middle  $60^\circ$  modulation method is simple and easy to implement. But its harmonics in the output voltage are obvious, especially low-frequency harmonics, so this method gradually replaced by other excellent modulation methods. SVPWM modulation is in the view of the three-phase inverter system and the motor as a whole, establishing the relationship of inverter switch state and the voltage space vector, by controlling the switching state of the inverter, the stator flux of the motor is approximated to the ideal circular trajectory [2, 3]. The advantage of SHEPWM is that its pulses have the characteristics of half-wave symmetry and even symmetry in quarter-cycle, so the output voltage contains only odd-order sinusoidal harmonic components, and the symmetrical three-phase traction motor does not contain the harmonics of multiple of 3rd, so the minimum number of harmonics in the output voltage is 5th harmonic. In addition, the higher the switching frequency, the more low-order harmonics can be eliminated [4]. Although the above-mentioned optimization modulation method has some differences in the implementation, but the purpose is same basically, that is to reduce the harmonic current. Harmonic distortion and pulsating torque are also generated by the harmonic current, so decreasing the harmonics of current is the main purpose of a variety of new PWM technology research.

## 2 Harmonic Loss Analysis

In the voltage source inverter system, we are more interested in the current. However, if the influence of the harmonic current is taken into account, the harmonic characteristics of the modulation must be analyzed [5, 6]. Ignoring reactance other than  $L$  in circuit, the harmonic current size of myopia is inversely proportional to the number of harmonics, so the Weighted Harmonic Distortion:

$$WTHD = \frac{1}{V_1} \sqrt{\sum_{n=2}^{\infty} \left(\frac{V_n}{n}\right)^2} \quad (1)$$

Figure 1 shows the a, b phase voltage and a-b line voltage, ripple current sketch in a carrier period of three-phase voltage source inverter. Within the time intervals  $T_1$ ,  $T_2$ ,  $T_3$ , the ripple current is defined as follows:

$$\Delta i_{ab}(t) = -\frac{e_{ab}}{L_\sigma} t \quad 0 \leq t \leq T_1 \quad (2)$$

$$\Delta i_{ab}(t) = \left(\frac{2V_{dc} - e_{ab}}{L_\sigma}\right)(t - T_1) - \frac{e_{ab}}{L_\sigma} T_1 \quad T_1 \leq t \leq T_1 + T_2 \quad (3)$$

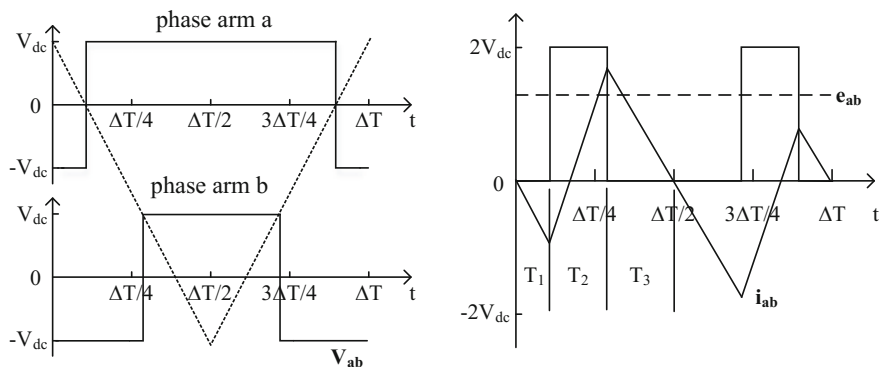


**Fig. 1** Two-phase bridge arm ripple current of three-phase inverter

$$\Delta i_{ab}(t) = -\frac{e_{ab}}{L_{\sigma}}(t - T_1 - T_2) + \left(\frac{2V_{dc} - e_{ab}}{L_{\sigma}}\right)T_2 - \frac{e_{ab}}{L_{\sigma}} \quad (4)$$

$$T_1 T_2 \leq t \leq T_1 + T_2 + T_3$$

In the above equations,  $L_{\sigma}$  is the load between the phase a and phase b of the triangular connection, and  $e_{ab}$  is the internal average electromotive force of the load in any one switching cycle. Combined with the following two equations:

$$T_1 + T_2 + T_3 = \Delta T/2 \quad (5)$$

$$\Delta i_{ab}(t) = -\frac{e_{ab}}{L_{\sigma}}T_3 + \left(\frac{2V_{dc} - e_{ab}}{L_{\sigma}}\right)T_2 - \frac{e_{ab}}{L_{\sigma}}T_1 = 0 \quad (6)$$

Solve the above equations with the following results:

$$T_1 = (1 - u_1)\Delta T/4 \quad (7)$$

$$T_2 = (u_1 - u_2)\Delta T/4 \quad (8)$$

$$T_3 = (1 + u_2)\Delta T/4 \quad (9)$$

In the above formula,  $u_1 = e_a/V_{dc}$ ,  $u_2 = e_b/V_{dc}$ .

The rms value of the current ripple at this time can be organized into the following form:

$$(\Delta i_{ab}^2) = \left(\frac{V_{dc}}{L_{\sigma}}\right) \frac{\Delta T^2}{48} [(u_2 - u_1)^2 + (u_2 - u_1)^3 + (u_2 - u_1)(u_2^3 - u_1^3)] \quad (10)$$

### 3 SVPWM Modulation Principle and Harmonic Analysis

SVPWM is an overall consideration from the perspective of the motor and the inverter, by selecting the appropriate switch state, to control the voltage space vector trajectory, and then control the induction motor stator flux trajectory [7, 8]. Because of its advantages of lower total distortion compared with SPWM and the high utilization rate of DC voltage, it becomes the basic control method of voltage inverter. SVPWM use the combination of adjacent two vector and zero vector to approximate the output voltage vector [9, 10]. For the voltage vector  $U$ , voltage space vector rotation angle  $\theta$ , switching period  $\Delta T$ , vector  $U_1$  action time  $t_1$ , vector  $U_2$  action time  $t_2$ , then:

$$U * \Delta T = U_1 * t_1 + U_2 * t_2 \quad (11)$$

Solve the above equations with the following results:

$$t_1 = \frac{\sqrt{3}U}{U_{dc}} * \Delta T * \sin(60^\circ - \theta) \quad (12)$$

$$t_2 = \frac{\sqrt{3}U}{U_{dc}} * \Delta T * \sin \theta \quad (13)$$

Neglecting the fluctuation of the network voltage frequency, it is considered that the system is in steady state, that is, the  $U$  calculation does not change in the harmonic calculation process, and does not include the turn-on delay of the switch tube, the resulting dead time and the minimum pulse width under the premise of the influence of Eq. (10) on a positive half cycle, the total harmonic loss of space vector modulation is calculated.

$$I_{ab}^2 = \left( \frac{V_{dc}}{L_\sigma} \right) \frac{\Delta T^2}{48} \left[ \frac{3}{2} M^2 - \frac{4\sqrt{3}}{\pi} M^3 + \frac{9}{8} \left( \frac{3}{2} - \frac{9}{8} \cdot \frac{\sqrt{3}}{\pi} \right) M^4 \right] \quad (14)$$

As can be seen from the above equation, the overall harmonic loss of the SVPWM is related to the DC bus voltage  $V_{dc}$ , the load  $L_\sigma$ , the switching period  $\Delta T$ , and the modulation ratio  $M$ .

### 4 SHEPWM Modulation Principle and Harmonic Analysis

Typical optimization synchronous modulation pulse of SHEPWM is shown in Fig. 2, the figure is the trigger pulse waveform for the  $N = 4$ , where  $N$  is the number of switching angle in a quarter of the fundamental wave period,

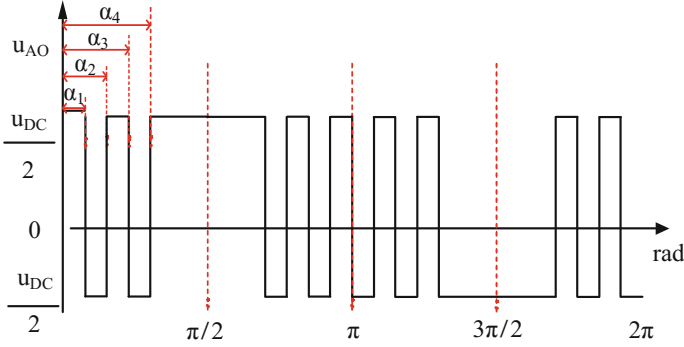


Fig. 2 Typical pulses of optimized synchronous PWM strategy

four switching angles can eliminate three specific harmonic components [6]. If there are more switching angles in the illustrated waveform, more harmonic components can be eliminated. According to the related research results of SHEPWM, there are two possible distributions of 0–60° and 0–90° in the switching angle, and the harmonic performance of the switch angle 0–90° is better than that of the switching angle 0–60°, so this article studies only on the switch angle 0–90° distribution.

Figure 2 shows the output voltage under the pulse only contains odd-order sinusoidal harmonic components, and because the symmetrical three-phase traction motor does not contain the harmonics of multiple of 3rd, so its Fourier series can be written as:

$$u_n = \sum_{n=1,5,7\dots}^{\infty} U_n \sin(n\omega_e t) \tag{15}$$

$$U_n = \mp \frac{2U_{dc}}{n\pi} \left[ 1 + 2 \sum_{i=1}^N (-1)^i \cos n\alpha_i \right] \tag{16}$$

where  $n$  is the number of harmonics,  $U_n$  is the magnitude of the  $n$ th harmonic,  $U_{DC}$  is DC voltage,  $N$  is the number of switch angles,  $\omega_e$  is the frequency of fundamental,  $\alpha_i$  is the  $i$ th switch angle. In the formula (16), the four switching angles are unknown. To solve the four switching angles, four equations are needed, removing the fundamental voltage equation, which can eliminate three specific harmonics. And then can calculate the each harmonic voltage amplitude, Divide to  $U_1/\omega_e(L_{ls} + L_{lr})$  to get a single current harmonic amplitude per unitary value.

$$I_{n(pi)} = \frac{U_n}{nU_1} \tag{17}$$

**Fig. 3** Single harmonic current per unit value of SHEPWM

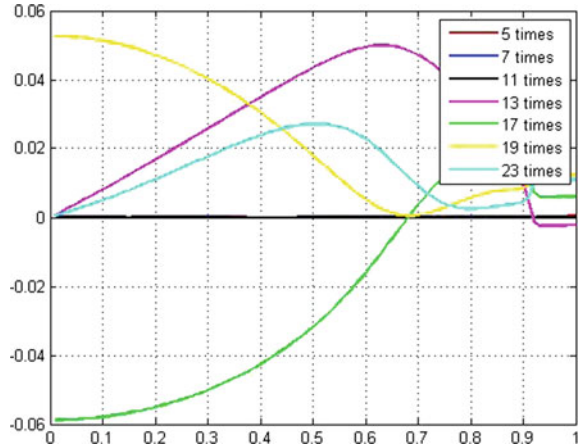
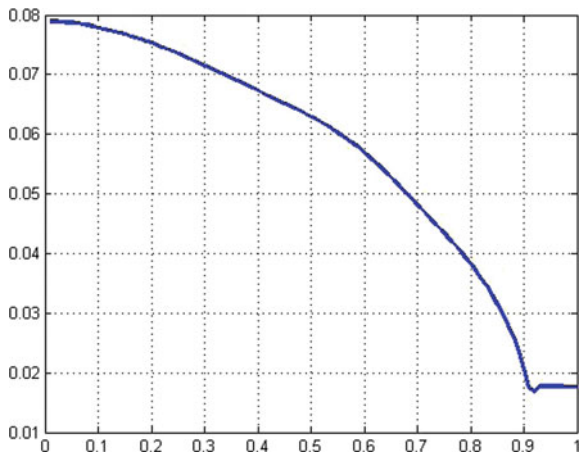


**Fig. 4** SHEPWM weighted harmonic distortion



The graph (Fig. 3) shows the single harmonic current of SHEPWM. It is consistent with the previous formula. When the number of switching angle is 4, you can eliminate 5,7,11 harmonic. There are many paper mention that SHEPWM can eliminate the specified low-order harmonics, but the high harmonics content is increased, which is the reason why the 13, 17, 19th harmonic amplitude is higher [4]. According to the formula (1) can be seen SHEPWM weighted total harmonic distortion (WTHD) increased with the increase in modulation depth of the situation, the results shown in Fig. 4, the WTHD decreases with the increase of the modulation depth and becomes stable after the modulation depth is greater than 0.9, and the minimum value of the weighted harmonic distortion appears at a modulation depth slightly greater than 0.9.

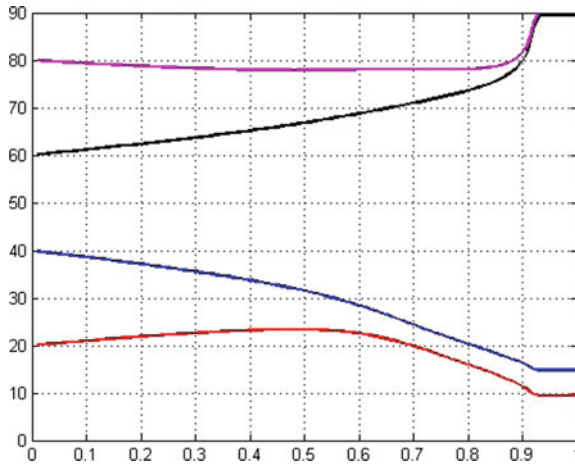


Fig. 5 9-pulse SHEPWM switch angle distribution

### 5 SHEPWM Switching Principle and Simulation Verification

EMU traction inverter switching frequency is generally 500 Hz, the maximum switching frequency of 1 kHz. In this paper, the hybrid pulse width modulation strategy of “asynchronous modulation +15 pulse synchronous modulation +9, 7, 5, 3 pulse SHEPWM + single pulse modulation” is used in the full speed range.

When switching between different modes, the voltage and current will have a certain jitter, the timing of switching between different modulation modes should take into account two factors, first the maximum switching frequency should be less than 1 kHz, so the 15-pulse synchronous modulation to 9-pulse SHEPWM switching frequency limit of 66.7 Hz, followed by the full use of the impact of

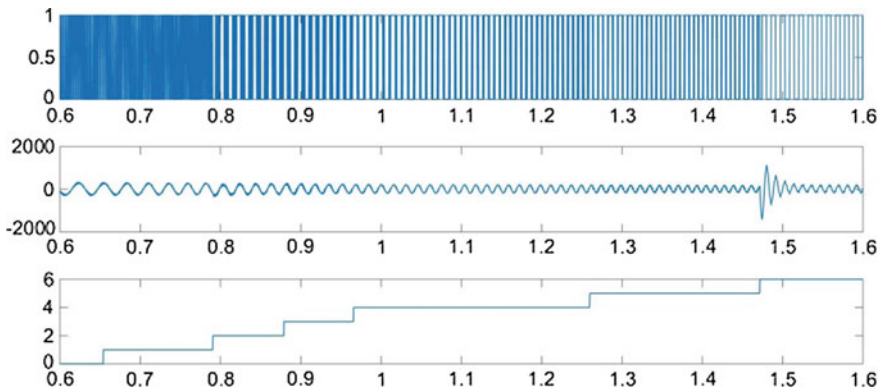


Fig. 6 Full-speed range of mixed pulse-width modulation

modulation depth, It can be seen from Fig. 4 that the *WTHD* of the 9-pulse SHEPWM decreases as the modulation depth increases, and from Fig. 5 to know the modulation depth of 0.9 or so switching angle changes are obvious, then the switch should avoid the interval of this modulation depth. The other switching should also consider these two factors, no longer elaborate here.

Figure 6 shows the simulation waveforms for switching between adjacent modes in the full modulation range, starting from top to bottom as trigger pulse, current waveform, switching flag, the switch flag is switched from left to right in accordance with the full-speed range modulation strategy, simulation results can be seen, the process of switching the motor current is basically stable, a serious jitter appearance in the switch from 3-pulse SHEPWM to Square wave, and it cannot be eliminate in many test, but it soon vanish after two or three periods.

## 6 Conclusion

According to the above analysis, SVPWM and SHEPWM have different advantages and disadvantages. SVPWM is the analysis of the motor from the overall performance, which is more convenient to control, less hardware resources and easy to implement, but its harmonic performance is worse than SHEPWM. SHEPWM harmonic performance is better, especially in the case of the number of switching angle is more, but SHEPWM cannot be calculated in real time, and switch angle data need to take up more memory resources. So it have higher requirements for the hardware. In the choice of modulation methods should weigh the advantages and disadvantages of the two, according to their own needs.

**Acknowledgements** This work was supported by National Key R&D plan under Grant 2016YFB1200502-4 and 2017YFB1200802, Beijing Science and School level project 2016RC038.

## References

1. Chenchen W, Minglei Z, Xiaojie Y (2012) Research on the PWM Method of high-power ac electric locomotive. *Trans China Electrotech Soc* 27(2):173–178 (in Chinese)
2. Rathore R, Holtz H, Boller T (2013) Generalized optimal pulsewidth modulation of multilevel inverters for low-switching-frequency control of medium-voltage high-power industrial ac drives. *IEEE Trans Industr Electron* 60(10):4215–4224
3. Narayanan G, Ranganathan VT (1999) Synchronised PWM strategies based on space vector approach. Part 1: Principles of waveform generation. *IEEE Proc Power Appl* 146(3):267–275
4. Minglei Z, Qiang L, Xiaojie Y, Chenchen W, Jian W (2014) Research on SHEPWM-based switching strategy of multi-mode modulation. *J China Railw Soc* 34–39 (in Chinese)
5. Holmes DG, Lipo TA (2010) Pulse width modulation for power converters: principles and practice. Post & Telecom Press
6. Dong K, Liu Z (2015) Research on key control techniques and performance optimization of traction drive system for EMUs. Bei Jing Jiaotong University, U266-533/65 (in Chinese)

7. Mirafzal B, Saghaleini M, Kaviani AK (2011) An SVPWM-based switching pattern for stand-alone and grid-connected three-phase single-stage boost inverters. *IEEE Trans Power Electron* 26(4):1102–1111
8. Gupta AK, Khambadkone AM (2006) A space vector PWM scheme for multilevel inverters based on two-level space vector PWM. *IEEE Trans Ind Electron* 53:1631–1639
9. Malinowski M, Jasinski M, Kazmierkowski MP (2004) Simple direct power control of three-phase PWM rectifier using space-vector modulation (DPC-SVM). *IEEE Trans Industr Electron* 51(2):447–454
10. Chen Y, Tong Y, Jin X (2007) A novel algorithm of SVPWM harmonic analysis based on PWM rectifier. *Proc Chinese Soc Electr Eng* 27(13):76–80 (in Chinese)



# Parameters Offline Identification of Induction Motor in High-Power Converter System

Miao Sha, Lailai Shen, Jie Chen and Jing Tang

**Abstract** Currently the induction motor control system uses vector control widely. If the motor parameters adopted in vector control algorithm do not match with the actual motor parameters, there will be a significant impact on the control performance. Therefore, it is necessary to identify parameters before running an induction motor whose parameters are unknown and provide precise initial value for the online identification. This paper investigates a method with DC experiment, single phase AC short-circuit experiment and no-load experiment to identify the parameters of an induction motor. And the compensation of the output voltage which results from dead time, turn-on and turn-off delay and drop voltage of IGBTs and Diodes is studied in this paper. Identified results in both simulations and experiments are given to validate the method.

**Keywords** Parameters identification · Induction motor · Matlab/Simulink

## 1 Introduction

The induction motor has the advantages of simple structure, convenient maintenance, high reliability and low production cost, so it is widely applied in the industrial field and our daily life [1]. However, motor parameters are unknown in some situations. And the control performance of induction motor vector control will be poor if the parameters adopted in control system do not match with the actual motor parameters [2].

Since vector control has been widely used, the parameters identification of motor has become a hot topic among researchers. The traditional motor test puts forward

---

M. Sha (✉)

CRRC Changchun Railway Vehicles CO., LTD, Changchun, China  
e-mail: shamiao@cccr.com.cn

L. Shen · J. Chen · J. Tang

School of Electrical Engineering, Beijing Engineering Research Center of Electric Rail Transportation, Beijing Jiaotong University, 100044 Beijing, China

© Springer Nature Singapore Pte Ltd. 2018

L. Jia et al. (eds.), *Proceedings of the 3rd International Conference on Electrical and Information Technologies for Rail Transportation (EITRT) 2017*, Lecture Notes in Electrical Engineering 482, [https://doi.org/10.1007/978-981-10-7986-3\\_52](https://doi.org/10.1007/978-981-10-7986-3_52)

501

parameters measurement method which can be used in small power motors [3], those are, locked rotor test and no-load test. However, this method is limited in high-power induction motors and it is difficult to complete the locked rotor test of motors in some field environments.

The foundation of parameters identification is based on the stator voltage equation, the rotor voltage equation, stator flux equation and rotor flux equation [4]. The identification methods are using the stator winding current, the DC bus voltage and the motor frequency etc. to determine the motor parameters according to a certain algorithm or model observer. These methods vary in terms of the way they are controlled and the hardware system, but the fundamentals will not change.

This paper investigates a method with DC experiment, single phase AC short-circuit experiment and no-load experiment to identify the parameters of an induction motor offline. In DC experiment, voltage loss is largely avoided because of the way of voltage subtraction and the stator resistance is identified. In single phase AC short-circuit experiment, the single-phase signal is injected to the motor, therefore the bridges of phases B and C are shorted without electromagnetic torque and the rotor resistance and stator and rotor leakage are identified. In no-load experiment, the magnetizing inductance is identified through the  $v/f$  control mode. Identified results in both simulations and experiments are given to validate the method.

## 2 DC Experiment

The stator resistance can be identified by applying dc excitation to the stator winding. The control block diagram of DC experiment is shown in Fig. 1. Stator current is sampled by current sensor while stator voltage is calculated by DC side voltage and inverter switch function.  $D$  represents duty ratio of PWM wave.

Because of high DC voltage of inverter, DC voltage cannot be directly applied to the motor. As a result, the command current is a dc value and the control signals of the bridges of phases B and C are identical. The equivalent circuit diagram of DC experiment is shown in Fig. 2. The voltage applied to the motor is adjusted by chopping control.

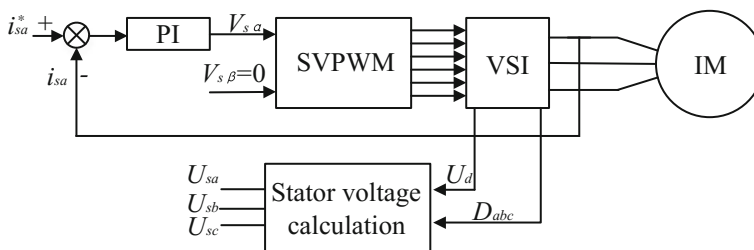
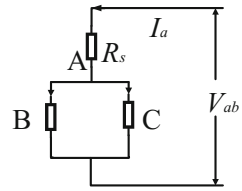


**Fig. 1** The control block diagram of DC experiment

**Fig. 2** The equivalent circuit diagram of DC experiment



In DC experiment, The PWM wave duty ratio will be greatly influenced by the dead time, turn-on and turn-off delay and drop voltage of Diodes or IGBTs. Therefore, stator current and duty ratio under rated and half rated current are measured respectively. The value of the stator resistance is calculated by voltage subtraction as shown in Eq. (1).

$$R_s = \frac{2 U_d(D_1 - D_2)}{3 I_{a1} - I_{a2}} \tag{1}$$

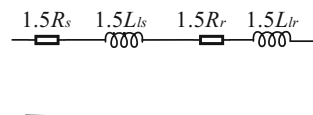
### 3 Single Phase AC Short-Circuit Experiment

The electromagnetic phenomenon of induction motor in single-phase sinusoidal signal is the same with the electromagnetic phenomenon in three-phase sinusoidal signal. However, there will be no rotating magnetic field and electromagnetic torque under the single-phase sinusoidal signal, the rotational speed of the motor is zero [5]. The control block diagram is the same as that in DC experiment. Because the excitation inductance is much larger than the rotor leakage inductance, the magnetizing branch is considered as an open circuit, and the equivalent circuit diagram is shown in Fig. 3.

It is generally considered that the drop voltage of IGBTs and Diodes are the same, which means  $U_{IGBT} = U_{DIODE}$ . When voltage and current are positive,  $U_{AB} = U_{DIODE} - 2U_{IGBT}$ . After the analysis of different sign symbols of voltage and current, a conclusion can be drawn from this: Due to the influence of IGBTs and Diodes, the motor terminal voltage drops  $2U_{IGBT}$  during the positive half cycle of the current and increases  $2U_{IGBT}$  during the negative half of the current. Equation 2 can be obtained by equal area method [6]:

$$2U_{IGBT} \cdot \frac{T_s}{2} = U_{IGBT} T_s = \frac{U_m}{\omega} (\cos 0 - \cos \pi) = \frac{2U_m}{\omega} \Rightarrow U_m = \pi U_{IGBT} \tag{2}$$

**Fig. 3** The equivalent circuit diagram of single phase AC short-circuit experiment



It means that the sinusoidal voltage whose frequency and phase is the same with the current signal is superimposed on the fundamental voltage. As a result, the superimposed voltage should be subtracted after the reconstructed voltage is obtained.

The driving signals, calculated by DSP, to be used to turn on or turn off IGBTs has a non-negligible delay and the turn-on and turn-off delay are usually not equal. In field environments, the delay can be measured once by comparing the actual motor voltage with DSP PWM signals respectively and be named as  $t_{on}, t_{off}$  (Fig. 4).

The relation between the actual output voltage of the motor and the given pulse driving signal can be expressed in Fig. 5, which can be summarized as follows:

1. When the current is positive, the time of the actual phase voltage reduces  $t_d + t_{on} - t_{off}$  compared to the ideal phase voltage;
2. When the current is negative, the time of actual phase voltage increases  $t_d + t_{on} - t_{off}$  compared to the ideal phase voltage.

After the reconstructed voltage is compensated with the analysis shown above and the current are measured in a sinusoidal period, the rotor resistance and stator, rotor leakage are identified in Eq. 3:

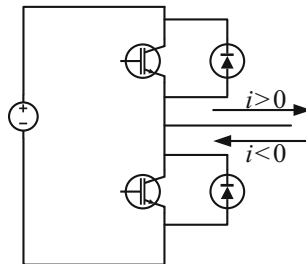


Fig. 4 Schematic diagram of the single-phase inverter

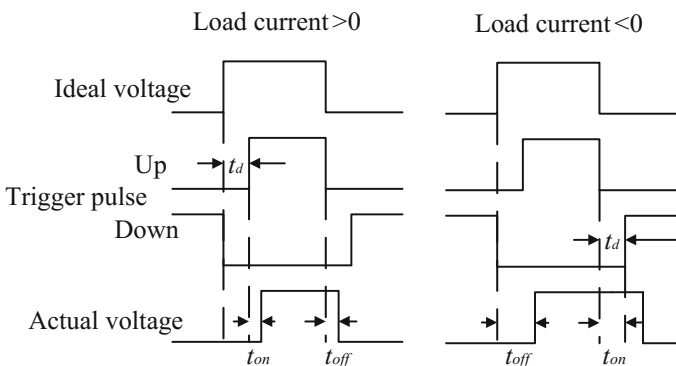


Fig. 5 The impact of dead time and turn-on and turn-off delay to output voltage

$$\begin{cases} Z_{eq} = \frac{V_{ab}}{I_a} \\ R_{eq} = Z_{eq} \cos \theta \\ X_{eq} = \sqrt{Z_{eq}^2 - R_{eq}^2} \\ R_r = R_{eq} - R_s \\ L_{ls} = L_{lr} = 0.5L_{eq}/\omega \end{cases} \quad (3)$$

In Eq. 2, the fundamental amplitudes of voltage ( $V_{ab}$ ) and current ( $I_a$ ) and the included angle  $\theta$  between them are obtained by Fourier analysis.

### 4 No-Load Experiment

The no-load experiment under  $v/f$  control is used to identify the excitation inductance. The induction motor can start with small current and high electromagnetic torque under  $v/f$  control.

The control block diagram of the no-load experiment is as shown in Fig. 6, and the  $v/f$  curve is given directly. Because the motor is no-load and the speed is close to the synchronous speed, the rotor branch is ignored. The equivalent circuit is shown in Fig. 7.

The fundamental amplitude of current and voltage is obtained by Fourier analysis, and then the magnetizing inductance is identified by Eq. 4.

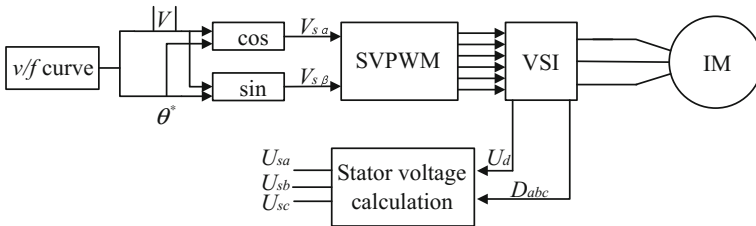
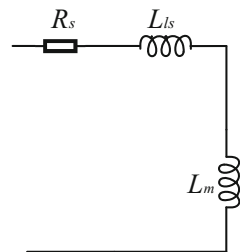


Fig. 6 The control block diagram of no-load experiment

Fig. 7 The equivalent circuit diagram of no-load experiment



$$\begin{cases} Z_{eq} = \frac{V_{am}}{I_a} \\ X_{eq} = \sqrt{Z_{eq}^2 - R_s^2} \\ L_m = \frac{X_{eq}}{2\pi f} - L_{ls} \end{cases} \quad (4)$$

Because the no-load voltage which is the rated voltage is relatively high, the compensation of output voltage can be ignored.

## 5 Simulation and Experiment

The simulation parameters of the model used in MATLAB/SIMULINK are shown in Table 1 and the waveforms are shown below.

In DC experiment, the bridges of phases B and C are short-circuited and  $V_{ab}$  is equal to the mean value of the output pulse. The duty ratio in each switching cycle is same and very small.

In single phase AC short-circuit experiment, the electromagnetic torque and the motor speed are zero.

In no-load experiment, the harmonic of the current of phase A is very large; there are electromagnetic torque ripples (Figs. 8, 9 and 10).

The results of simulation are shown in Table 2 and the value of rotor resistance in simulation has larger difference with the set value because the magnetizing branch is ignored in single phase AC short-circuit experiment.

The experiment platform is based on a traction converter of hybrid multiple units. The results of experiments are shown in Table 3 and they are essentially in agreement with the results of simulation. It is proved that this method using for the parameters identification of induction motor has some practical significance.

**Table 1** The simulation parameters of the model

Motor parameters		Inverter parameters	
Rated power	160 kW	$U_d$	900 V
Rated line voltage	1287 V	Switching frequency	1000 Hz
Rated frequency	84 Hz		
$R_s$	0.223 $\Omega$	Simulink configuration	
$R_r$	0.103 $\Omega$	Simulation type	discrete
$L_{ls} = L_{lr}$	1.828 mH	Solver type	Tustin
$L_m$	43.8 mH	Sample time	2e-6 s

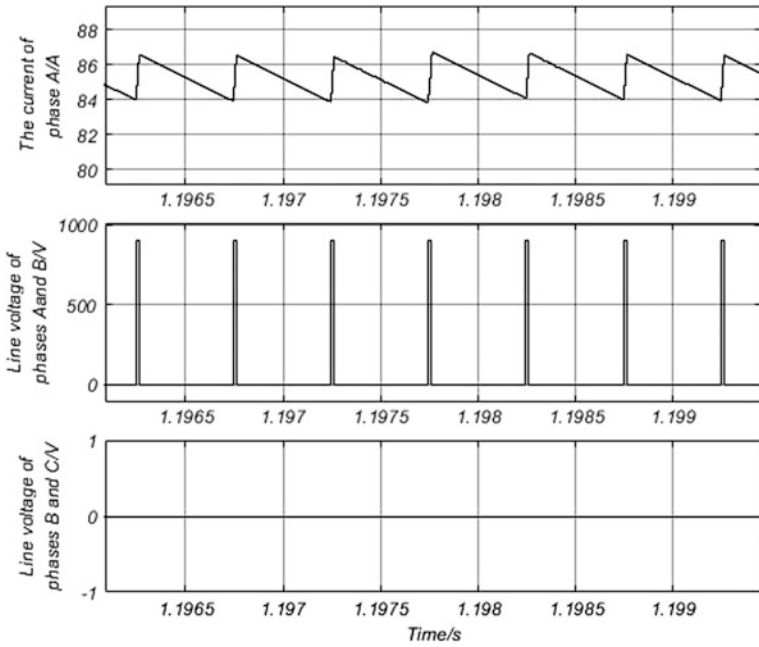


Fig. 8 The simulation waveforms of DC experiment

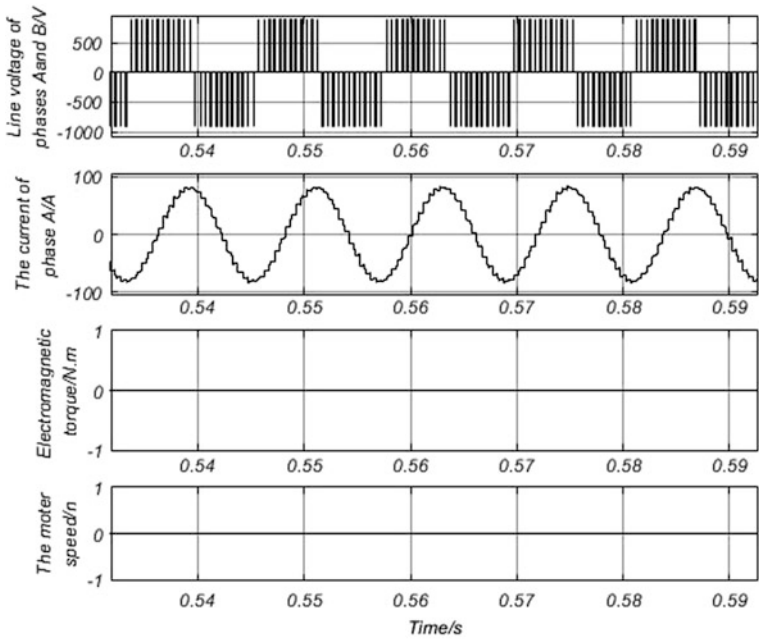
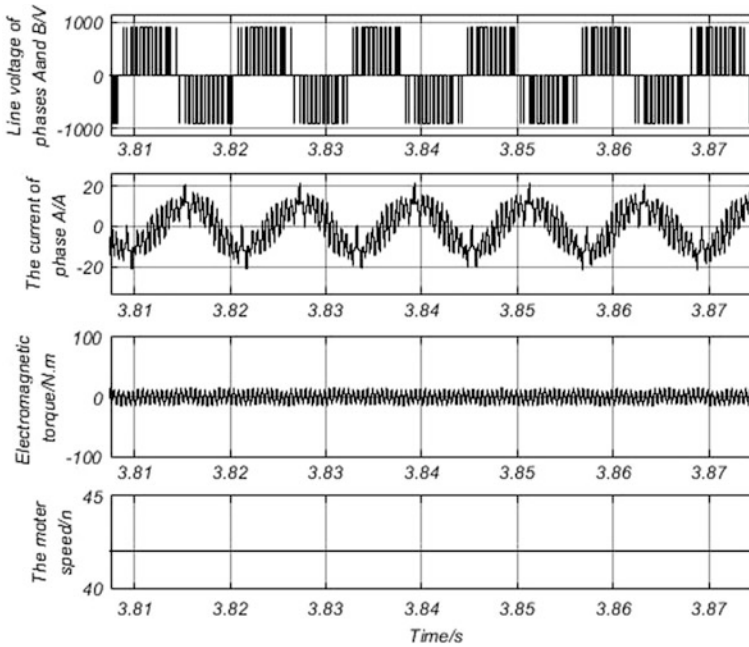


Fig. 9 The simulation waveforms of single phase AC short-circuit experiment



**Fig. 10** The simulation waveforms of no-load experiment

**Table 2** The identified parameters and errors of simulation

Parameters	Simulation value	Set value	Error (%)
$R_s$	0.226 $\Omega$	0.223 $\Omega$	1.35
$R_r$	0.0958 $\Omega$	0.103 $\Omega$	-6.99
$L_{ls} = L_{lr}$	1.8 mH	1.828 mH	-1.53
$L_m$	43.9 mH	43.8 mH	0.23

**Table 3** The identified parameters and errors of experiments

Parameters	Experiment value	Set value	Error (%)
$R_s$	0.21 $\Omega$	0.223 $\Omega$	-5.83
$R_r$	0.0955 $\Omega$	0.103 $\Omega$	-7.20
$L_{ls} = L_{lr}$	1.85 mH	1.828 mH	6.67
$L_m$	45.9 mH	43.8 mH	4.79

## 6 Conclusions

This paper investigates a method to identify the parameters of induction motor, which can be applied to high-power motor without the rotor locked. Besides, the compensation of the output voltage which results from dead time, turn-on and turn-off delay and drop voltage of IGBTs and Diodes is studied in each experiment



respectively. Identified results in both simulations and experiments are given to prove that the method can be applied to the field environment.

**Acknowledgements** This work was supported by National Key R&D plan under Grant 2016YFB1200502-4 and 2017YFB1200802, Beijing Science and School level project 2016RC038.

## References

1. Han L (2004) Detection and identification of motor parameters. Zhejiang University (in chinese)
2. Yanhui H, Yue W, Zhaoan W (2011) Improved algorithm for off-line identification of induction motor parameters. *Trans Electrotech Soc* (06):73–80 (in chinese)
3. Tang Y (1981) *Electromechanics-Mechanical and electrical energy conversion*. Mechanical Industry Press (in chinese)
4. Chrzan PJ, Klaassen H (1996) Parameters identification of vector-controlled induction machines. *Electr Eng* 79(1):39–46
5. Duan L (2012) Research on motor parameters identification for asynchronous motor vector control inverter. Shanghai Jiao Tong University, 77 (in chinese)
6. Liu H (2008) Research on off-line parameters tuning and parameters identification of induction motors. Beijing Jiaotong University, 90 (in chinese)
7. Yin W, Ma Y (2013) Research on three-phase PV grid-connected inverter based on LCL filter. *Industrial Electronics and Applications (ICIEA), 2013 8th IEEE Conference on*. IEEE, 2013: 1279–1283
8. Li ZX, Li YH, Wang P et al (2010) Single-Loop digital control of high-power 400-Hz ground power unit for airplanes. *IEEE Trans Industr Electron* 57(2):532–543

# Research on Construction Method of “Train-Traction Network” Harmonic Model for High-Speed Railway

Guorui Zhai, Lingmin Meng and Jie Chen

**Abstract** Network-side converter of high-speed train produces high harmonics in the modulation process, which are injected into traction network in the course of the operation which may cause resonance. In order to analyze the resonant characteristics of the traction drive system, it is necessary to construct the “train–traction network” harmonic model.

**Keywords** Harmonic resonance · High-speed train modeling · Traction network modeling

## 1 Introduction

Nowadays, there are many studies on the harmonic resonance of high-speed railway, including the construction of harmonic model of high-speed train, the construction of harmonic model of traction network, and the suppression of harmonic resonance of traction drive system and so on. The joint simulation model of the locomotive and the traction network is built by using PSCAD/EMTDC, and then the resonant characteristics of traction network are studied [1]. The traction network transmission line is equivalent to  $\pi$ -type circuit, the harmonic model of the traction network is obtained [2]. The modeling methods proposed in the literatures provide the idea for the research of this paper. In this paper, the harmonic current generated by the high-speed train is subjected to double Fourier analysis to obtain the composition of the harmonic current, and the harmonic model of the train is constructed. According to Multi-conductor transmission line principle, the traction network is reduced and equivalent to T-type circuit, then it will get the traction

---

G. Zhai (✉)  
CRRC Changchun Railway Vehicles CO., LTD, Changchun, China  
e-mail: zhaiguorui@163.com

L. Meng · J. Chen  
School of Electrical Engineering, Beijing Engineering Research Center of Electric Rail Transportation, Beijing Jiaotong University, 100044 Beijing, China

network model and complete the “train–traction network” model construction. Finally, the simulation model is used to verify the effectiveness of the modeling method.

## 2 High-speed Train Modeling

The high harmonics of high-speed train injected into the traction network is mainly generated in the PWM modulation process of the network-side converter. Therefore, this paper uses the network-side converter instead of the electric locomotive to carry on the research.

The network-side converter topology is shown in Fig. 1, the converter uses a double frequency unipolar-PWM modulation. The carrier is a positive and negative alternating bipolar triangular wave  $U_c$ . The modulated waves are two sine waves  $U_s$  and  $-U_s$  with a phase difference of 180 degree. The output PWM wave after modulation is a pulse sequence that changes in sinusoidal law. Figure 2 shows the waveforms of the switch drive signal and the rectifier bridge AC side voltage.

Double Fourier analysis of the higher harmonics of the network-side converter is carried out. First assuming that (1) the DC side voltage of the PWM rectifier is constant; (2) regardless of the dead time of the switching device and the switching loss problem; (3)  $x(t) = \omega_c t + \theta_c, y(t) = \omega_s t + \theta_s$ .

Then the equations of the modulation waves for the bridge arm  $a$  and  $b$  can be respectively expressed as:

$$U_s(t) = M \cos(\omega_s t + \theta_s) = M \cos y \tag{1}$$

$$-U_s = -M \cos(\omega_s t + \theta_s) = -M \cos y \tag{2}$$

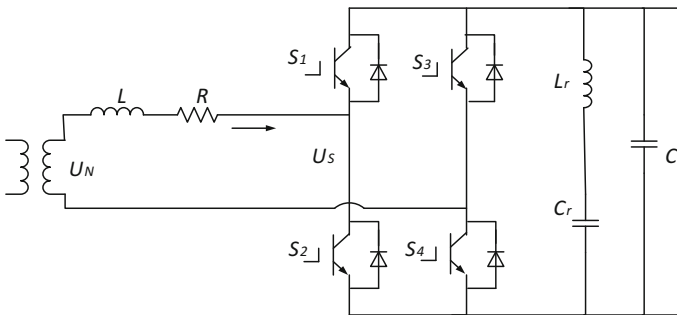
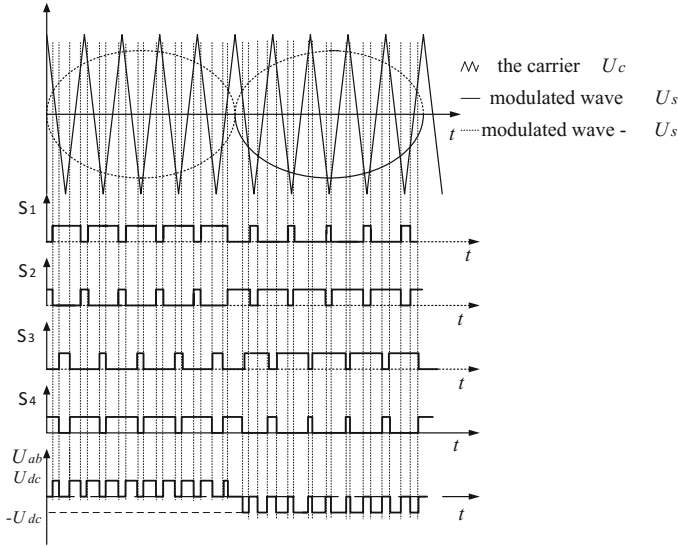


Fig. 1 Network-side converter topology



**Fig. 2** The waves of switch drive signal and bridge arm voltage  $U_{ab}$  in double frequency unipolar-PWM modulation

In a carrier period  $[-\pi, \pi]$ , we get the following carrier equation.

$$U_c(t) = \begin{cases} \frac{2}{\pi}(x + \frac{\pi}{2}) & x \in [-\pi, 0] \\ -\frac{2}{\pi}(x - \frac{\pi}{2}) & x \in [0, \pi] \end{cases} \quad (3)$$

where  $\omega_c$  is the carrier angular frequency,  $\theta_c$  is the phase offset angle of the carrier,  $\omega_s$  is the modulation wave angular frequency,  $\theta_s$  is the phase offset angle of the modulation wave.  $M$  is the modulation ratio.

Calculate the turn-off point and the turn-on point of the switching devices for bridge arm  $a$  and the bridge arm  $b$  in the carrier cycle  $[-\pi, \pi]$ .

The formula of double Fourier analysis can be expressed as:

$$\begin{aligned} f(x, y) = & \frac{A_{00}}{2} + \sum_{n=1}^{\infty} (A_{0n} \cos ny + B_{0n} \sin ny) \\ & + \sum_{m=1}^{\infty} (A_{m0} \cos mx + B_{m0} \sin mx) \\ & + \sum_{m=1}^{\infty} \sum_{n=-\infty}^{\infty} [A_{mn} \cos(mx + ny) + B_{mn} \sin(mx + ny)] \end{aligned} \quad (4)$$

The calculation results are substituted into the coefficient expression of the double Fourier analysis. The coefficients of the Fourier analysis expression can be obtained.

Finally, the Fourier analysis expression of the bridge arm voltage  $U_{ab}(t)$  can be expressed as:

$$\begin{aligned}
 U_{ab}(t) = & U_a(t) - U_b(t) = U_{dc}M\cos(\omega_s t + \theta_s) \\
 & + \frac{4U_{dc}}{\pi} \sum_{m=1}^{\infty} \sum_{\substack{n=-\infty \\ n \neq 0}}^{\infty} \frac{1}{m} J_n\left(m\frac{\pi}{2}M\right) \cos\left(\frac{\pi}{2}m\right) \sin\left(\frac{\pi}{2}n\right) \\
 & \cdot \cos[m(\omega_c t + \theta_s) + n(\omega_s t + \theta_s)]
 \end{aligned} \tag{5}$$

The grid voltage only contains the fundamental wave, the bridge arm voltage acts as a harmonic source to produce harmonic currents on the AC side of the network-side converter. Therefore, when analyzing the resonant characteristics of the traction network, the locomotive can be equivalent to the harmonic current source as shown in Fig. 3.

### 3 Traction Network Modeling

High-speed railway generally use AT power supply, the AT traction power supply network structure is complex, and it is difficult to build the model and analyze directly. Therefore, it is necessary to reduce the traction network according to the principle of multi-conductor transmission line. The reduction process is shown in Fig. 4.

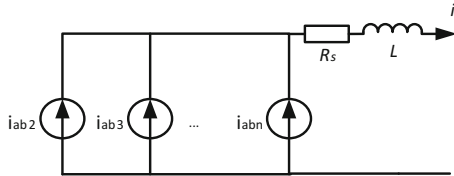


Fig. 3 Locomotive harmonic current source model

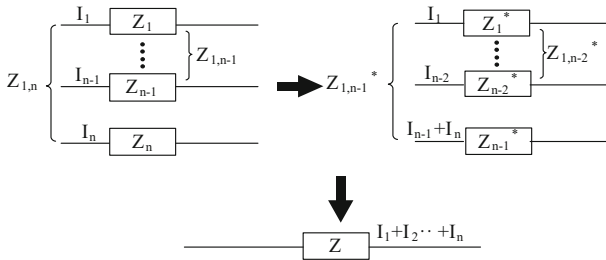


Fig. 4 Schematic diagram of reduction process of multi-conductor transmission line

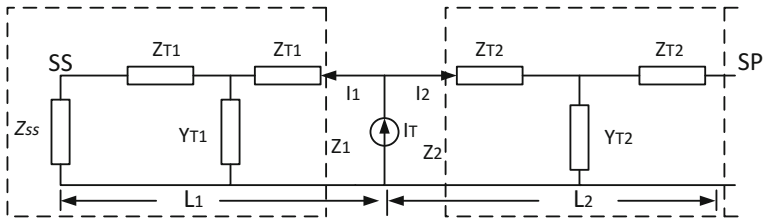


Fig. 5 Traction network impedance model

By the reduction, the number of transmission line ports can be reduced continuously, and ultimately the unit length equivalent impedance  $Z$  and the unit length to ground admittance  $Y$  of the traction network can be gotten.

The traction network is considered as a uniform transmission line, the traction network on both sides of the locomotive is equivalent to T-type circuit. The traction network impedance model is shown in Fig. 5.

In Fig. 5, SS (TPSS) denotes a traction power supply substation, SP denotes a sectioning post, and  $Z_{SS}$  indicates the equivalent impedance of the traction substation and the external power supply. According to the series-parallel relationship of the impedance in Fig. 5, the formula of the traction network impedance model on the left side of the locomotive can be described as:

$$Z_1 = Z_u \frac{Z_{SS} \cosh \gamma L_1 + Z_u \sinh \gamma L_1}{Z_{SS} \sinh \gamma L_1 + Z_u \cosh \gamma L_1} \tag{6}$$

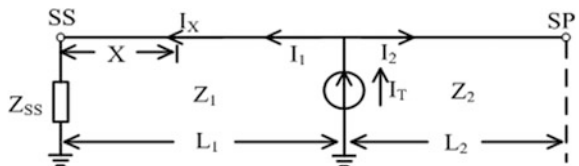
The formula of the traction network impedance model on the right side of the locomotive can be described as:

$$Z_2 = Z_u \frac{\cosh \gamma L_2}{\sinh \gamma L_2} \tag{7}$$

where  $L_1$  represents the distance between the locomotive and the traction substation,  $L_2$  represents the distance between the locomotive and the sectioning post,  $Z_u$  is the characteristic impedance of the transmission line, and  $\gamma$  is the propagation constant of the transmission line.

The locomotive is equivalent to a harmonic current source  $I_T$ , analyzing the traction network resonance characteristics. The model is shown in Fig. 6.

Fig. 6 “train-traction network” equivalent model



At a distance of  $x$  km from the traction substation, the current  $I_x$  of the traction network transmission line can be calculated in the following way.

$$I_x = I_1 \frac{(Z_{ss} \sinh \gamma X + Z_u \cosh \gamma X) \cosh \gamma L_2}{Z_{ss} \sinh \gamma L + Z_u \cosh \gamma L} \quad (8)$$

Define the magnification of the harmonic current in the traction network as the harmonic gain  $A_x$ , using the value  $A_x$  to describe the severity of the resonance.

$$A_x = I_x / I_1 = \frac{(Z_{ss} \sinh \gamma X + Z_u \cosh \gamma X) \cosh \gamma L_2}{Z_{ss} \sinh \gamma L + Z_u \cosh \gamma L} \quad (9)$$

The greater the value of  $A_x$  is, and the more serious the impact of resonance is.

#### 4 “Train-Traction Network” Joint Simulation

According to the construction of the “train-traction network” model, discuss the influencing factors of the resonance characteristics of traction network. The observation point of the harmonic current is at the traction substation.

First we can change the length of the traction network, and the distance between the traction substation and the sectioning post is set to 8, 16 and 25 km respectively. The locomotive is located at the sectioning post. The harmonic current gain at the observation point is calculated by simulation. The simulation results are shown in Fig. 7.

The simulation results show that the distance between the traction substation and the sectioning post is farther away, the resonant frequency is lower and the value of the harmonic current gain is smaller.

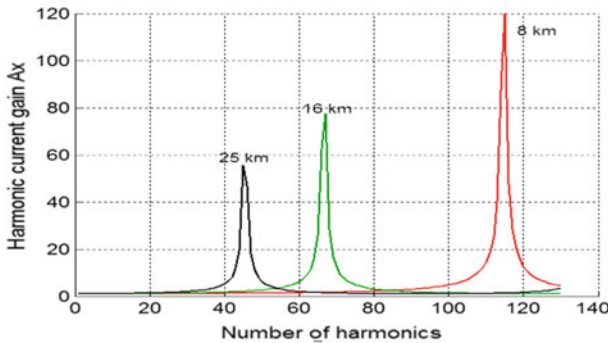


**Fig. 7** The harmonic current gains at the observation point when the traction network length is 8, 16 and 25 km respectively

And then we set the length of the traction network to 25 km, and change the position of the locomotive in the traction network. The distance between the locomotive and the traction substation is set to 5, 15, 20 and 25 km. The harmonic current gain at the observation point is calculated through simulation. The simulation results are shown in Fig. 8.

The simulation results show that when the length of the traction network is fixed, the farther the locomotive is from the traction network, the greater the value of the harmonic current gain at resonance is.

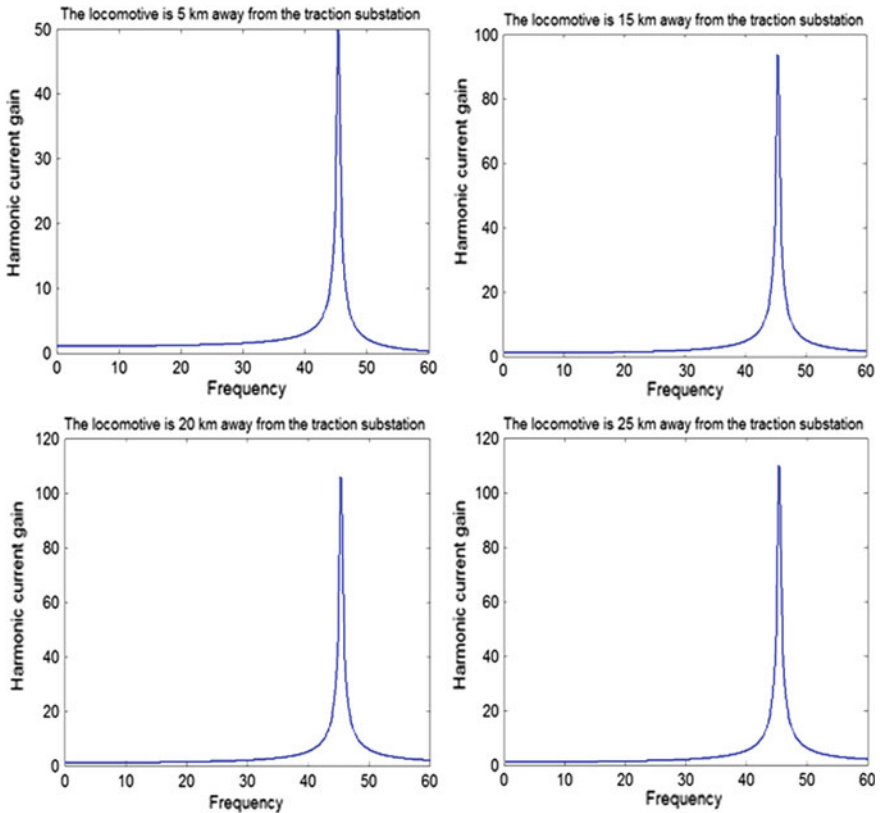


**Fig. 8** The harmonic current gains at the observation point when the distance between the locomotive and the traction substation is 5, 15, 20 and 25 km



## 5 Conclusions

Through the analysis of the high-order harmonics generated by the network-side converter of the high-speed train, it is found that the harmonic current of the network-side converter is related to the operating conditions of the locomotive, which is independent of the impedance of the traction network, so the locomotive is equivalent to the harmonic current source. The traction network is simplified through the reduction and its impedance model is obtained. The “train-traction network” model is jointly simulated, and the simulation results show that the length of the traction network and the position of the locomotive in the traction network are the influencing factors of the resonant characteristics of the traction network.

**Acknowledgements** This work was supported by National Key R&D plan under Grant 2016YFB1200502-4 and 2017YFB1200802, Beijing Science and School level project 2016RC038.

## References

1. Li HQ, Wang XR, Xu JJ (2014) Harmonic simulation analysis of traction power supply system based on train-network coupling system. 42(20):116–122 (in Chinese)
2. Yang Z, Liu Z (2011) Modelling and characteristic analysis of harmonic in high-speed railway traction network based on PSCAD/EMTDC platform. *Power Sys Technol* 35(5):70–75 (in Chinese)
3. Haitao HU, Zhengyou HE, Zhang M et al (2012) Series resonance analysis in high-speed railway all-parallel at traction power supply system. *Proc CSEE* 32(13):1371–1377 (in Chinese)
4. Cui H, Song W, Ge X et al (2016) High-frequency resonance suppression of high-speed railways in China. *Iet Elect Sys Trans* 6(2):88–95 (in Chinese)
5. Lee H, Lee C, Jang G et al (2006) Harmonic analysis of the korean high-speed railway using the eight-port representation model. *IEEE Trans Power Deliv* 21(2):979–986
6. Brenna M, Capasso A, Falvo MC et al (2011) Investigation of resonance phenomena in high speed railway supply systems: Theoretical and experimental analysis. *Electr Power Syst Res* 81(10):1915–1923
7. Yuen KH, Pong MH, Lo WC, et al (1999) Modeling of electric railway vehicle for harmonic analysis of traction power-supply system using spline interpolation in frequency domain. In: *Applied Power Electronics Conference and Exposition, 1999. Apec '99. Fourteenth. IEEE*, vol 1, pp 458–463
8. Lee H, Lee C, Cho H et al (2004) Harmonic analysis model based on PSCAD/EMTDC for Korean high-speed railway. *J Electrochem Soc* 131(8):1773–1776

# Research on Unbalanced Load Suppression Method of Auxiliary Inverter

Yong Ding, Linghang Huang and Jie Chen

**Abstract** This paper focuses on how to suppress the effect of unbalanced load on the output voltage distortion of the auxiliary inverter. The auxiliary inverter in this paper uses a split-capacitor inverter topology with a midline inductor to suppress the effect of unbalanced load. In this paper, the auxiliary inverter is split into three independent single-phase inverters, respectively, to control the fundamental impedance of each single-phase inverter to obtain excellent output voltage waveform. Each single-phase inverter control system uses voltage and current double-loop control strategy, the voltage outer ring with a new resonant controller, not only can inhibit the unbalanced load on the auxiliary inverter output voltage distortion, and can balance the split capacitor voltage. Finally, a virtual DSP system based on S-Function is constructed. The simulation results show that the new resonant controller can suppress the effect of unbalanced load on the output voltage distortion of the auxiliary inverter.

**Keywords** Auxiliary inverter · Unbalanced load · Split capacitor inverter  
New resonant controller

## 1 Introduction

With the rapid development of China's economy, urban rail transit technology has entered a period of rapid development. The auxiliary inverter is the core part of the rail transit auxiliary power supply system. Its function is to provide 380/220 V AC voltage to a stable medium voltage load of the urban rail transit train. Due to the rapid development of urban rail transit, the medium-pressure load of urban rail

---

Y. Ding (✉)  
CRRC Changchun Railway Vehicles CO., LTD, Changchun, China  
e-mail: dingyong@cccar.com.cn

L. Huang · J. Chen  
School of Electrical Engineering, Beijing Engineering Research Center of Electric Rail Transportation, Beijing Jiao Tong University, Beijing 100044, China

© Springer Nature Singapore Pte Ltd. 2018

L. Jia et al. (eds.), *Proceedings of the 3rd International Conference on Electrical and Information Technologies for Rail Transportation (EITRT) 2017*, Lecture Notes in Electrical Engineering 482, [https://doi.org/10.1007/978-981-10-7986-3\\_54](https://doi.org/10.1007/978-981-10-7986-3_54)

transit train is complicated, including both conventional load and other load such as unbalanced load, which is a significant challenge for the output voltage waveform of auxiliary inverter.

Under unbalanced load conditions, if the three-phase inverter as a whole, the use of coordinate transformation method in the DC closed-loop control is difficult to obtain excellent output characteristics.

At present, the field of rail transit commonly used auxiliary inverter for the three-phase four-wire inverter, commonly used four typical topologies, such as the output connected  $\Delta/Y_0$  transformer inverter, the output connected NET inverter, split-capacitor inverter [1] and four-leg inverter [2], these four structures have their own advantages and disadvantages. If the three-phase four-wire inverter is split into three independent single-phase inverters, then the control method of the single-phase inverter is used to control the fundamental impedance of each single-phase inverter, it will get good output voltage waveforms.

There are many commonly used single-phase inverter control methods, such as PID control [3], Deadbeat control [4], double closed-loop control, proportional resonance control [5, 6], repetitive control [7], which have their own advantages and disadvantages. Considering the advantages and disadvantages of various control methods, it can be concluded that the proportional resonant controller has a strong ability to suppress unbalanced load, and the stability and dynamic performance of the controller are excellent. However, due to the poor attenuation of the controller DC bias and the existence of a large phase angle hysteresis, a new type of resonant controller is needed, which both have the excellent characteristics of the original controller, and the good attenuation ability of DC bias, also its phase angle lag is small, and it is easy to design its parameters.

## 2 Construction of Auxiliary Inverter Model and Analysis of Output Waveform Distortion

The paper adds neutral inductor to the split-capacitor inverter which combined with four-leg inverter and split-capacitor inverter characteristics, as shown in Fig. 1. The neutral inductor can effectively suppress the ripple current flowing through the filter capacitor and the supporting capacitor, it can increase the life of the capacitors and the ability of the inverter with unbalanced load, and because the neutral inductor is small and light, it can reduce the axle weight and improve the auxiliary inverter power density.

The output voltage waveform of the auxiliary inverter is the standard sine wave under the ideal condition, but the output voltage waveform will be distorted to be non-standard sine wave due to many factors such as unbalanced load effects, and other factors.

Unbalanced load will cause the three-phase output voltage of the auxiliary inverter unbalanced, the main person of unbalanced three-phase output voltage is

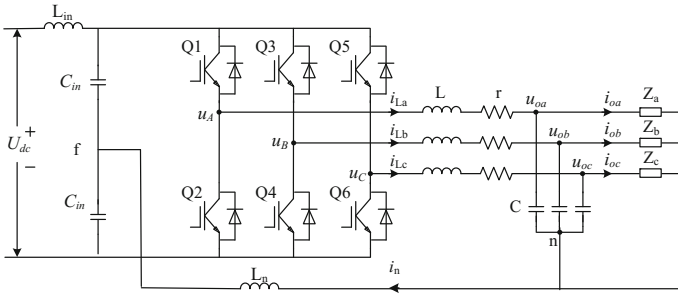


Fig. 1 Split-capacitor inverter with neutral inductor

the voltage drop across the auxiliary inverter equivalent output impedance caused by three-phase unbalanced currents.

Assuming there is no neutral inductor, Fig. 1 is converted to a conventional split-capacitor inverter.

When the load is balanced load, the inverter bridge output voltage is:

$$\begin{bmatrix} u_A \\ u_B \\ u_C \end{bmatrix} = \frac{U_{dc}}{2} \begin{bmatrix} m_a \cos \omega t \\ m_b \cos(\omega t - \frac{2\pi}{3}) \\ m_c \cos(\omega t + \frac{2\pi}{3}) \end{bmatrix} \tag{1}$$

where  $m_a \sim m_c$  for the modulation degree. Assuming that the load of the auxiliary inverter is switched from the balanced load to the unbalanced load at time t, the a-phase load and the b-phase load are  $Z_a = Z_b = Z$ , and the phase load is  $Z_c = 0$ . According to Kirchhoff's law, it finds the f-point potential as:

$$u_f = \frac{U_{dc}}{2} - \frac{U_m}{2\omega Z C_{in}} \sin\left(\omega t + \frac{2}{3}\pi\right) \tag{2}$$

Equation (2) shows that when the load is unbalanced load, the voltage at point f will be superimposed on the amount of AC, so you can get the inverter bridge output voltage:

$$\begin{bmatrix} u_A \\ u_B \\ u_C \end{bmatrix} = \begin{bmatrix} \frac{U_{dc}}{2} m_a \cos \omega t - \frac{U_m m_a}{4\omega Z C_{in}} \sin(2\omega t + \frac{2}{3}\pi) - \frac{U_m m_a}{4\omega Z C_{in}} \sin \frac{2}{3}\pi \\ \frac{U_{dc}}{2} m_b \cos(\omega t - \frac{2\pi}{3}) - \frac{U_m m_b}{4\omega Z C_{in}} \sin(2\omega t + \frac{2}{3}\pi) - \frac{U_m m_b}{4\omega Z C_{in}} \sin \frac{4}{3}\pi \\ \frac{U_{dc}}{2} m_c \cos(\omega t + \frac{2\pi}{3}) - \frac{U_m m_c}{4\omega Z C_{in}} \sin(2\omega t + \frac{4}{3}\pi) \end{bmatrix} \tag{3}$$

According to Eq. (3), we can see that the unbalanced load produces an unbalanced voltage drop across the equivalent output impedance of the inverter, results in the inverter bridge output voltage imbalance component and the output voltage distortion.

Above mentions that the neutral inductor can effectively suppress the ripple current flowing through the filter capacitor and the supporting capacitor, and it can also increase the ability of the inverter with unbalanced load.

After the introduction of midline inductance, according to Eq. (2), n point potential can be expressed as:

$$u_n = u_f + L_n \frac{di_n}{dt} = \frac{U_{dc}}{2} - \frac{U_m}{Z} \left( \frac{1}{2\omega Z C_{in}} - \omega L_n \right) \sin \left( \omega t + \frac{2}{3}\pi \right) \quad (4)$$

Comparing with Eqs. (2) and (4), the presence of the neutral inductor can reduce the amount of AC at the n-point potential and reduce the unbalanced component of the output voltage of the inverter bridge.

If the neutral inductor value satisfies the following condition:

$$L_n = \frac{1}{2\omega^2 Z C_{in}} \quad (5)$$

According to Eq. (4), the n-point potential is  $U_{dc}/2$ , which improves the output voltage quality of the inverter bridge, and reduces the imbalance of the output voltage of the inverter bridge caused by the unbalanced load.

As shown in Fig. 2, the figure is the output voltage waveforms with the neutral inductor and without the neutral inductor under the open loop condition with unbalanced load, modulation using SPWM modulation, the system parameters shown in Table 1.

The waveform shows that the auxiliary inverter output voltage will be serious imbalanced with unbalanced load; adding the neutral inductor to the inverter, it can better suppress the output voltage imbalance with a small unbalanced load. However, with the neutral inductor, it cannot completely suppress the output voltage imbalance phenomenon, there is also a slight imbalance phenomenon, because the neutral inductor cannot eliminate the unbalanced voltage drop across

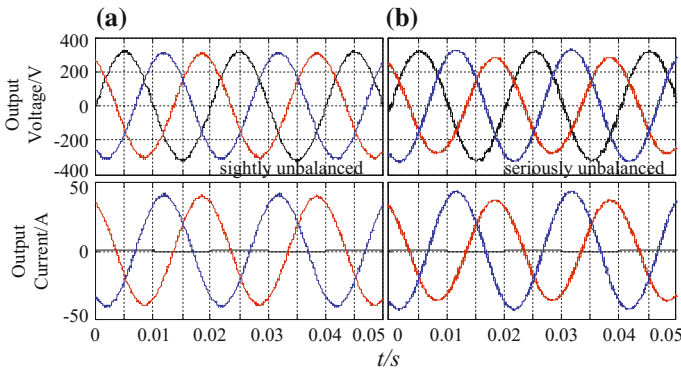


**Fig. 2** Waveforms of two structures in open loop with unbalanced load

**Table 1** Parameters of system

Sampling frequency/Hz 10 k	Rated frequency/Hz 50
Filter inductor/mH 1.5	Switching frequency/Hz 5 k
Filter capacitor/ $\mu$ F 20	Filter inductance parasitic resistance/ $\Omega$ 0.027
Neutral inductor/mH 2	Support capacity/ $\mu$ F 1100
First order PADE parameter/ $a$ $1.33e^4$	Rated power/kVA 5
Input voltage/V 700	Rated output voltage/V 220

the auxiliary inverter equivalent output impedance, it need to improve the control method to reduce the equivalent output impedance of the inverter, so that it can eliminate unbalanced voltage drop.

### 3 Design of Auxiliary Inverter Control System

The new resonant controller is expressed as:

$$G_R(s) = \frac{K_{pr}s^2 + K_{ir}s}{s^2 + 2\omega_c s + \omega_o^2} \tag{6}$$

Equation (6) shows that, the new resonant controller DC bias attenuation capability is good;

The three-phase four-wire auxiliary inverter is divided into three independent single-phase inverter. The single-phase inverter control system generally adopts the double closed-loop control strategy. This paper selects the inductor current inner ring voltage outer ring double closed-loop control strategy, and the voltage feed-forward is introduced to eliminate the negative feedback effect of the output voltage, as shown in Fig. 3.

According to the internal model principle [8], if the controller contains the internal model of the input function, it can suppress the impact of load disturbance, and realize the effect of the no static error tracking of the command. The input function under unbalanced load condition is the sine function of the fundamental frequency. Therefore, as adding a fundamental frequency new resonant controller to the  $G_v$ , it is possible to realize the effect of the no static error tracking of the fundamental command and suppress the unbalanced load. In the current inner loop

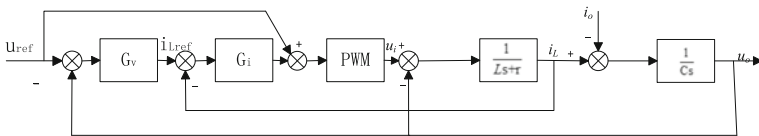


**Fig. 3** The control block of voltage and current double-loop control

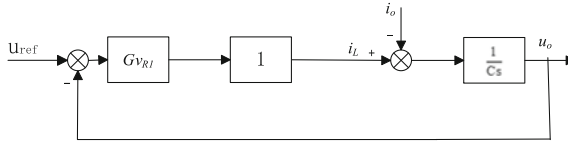


Fig. 4 Simplified inverter control block diagram

bandwidth condition, the current loop can be equivalent to the unit gain, Fig. 4 shows a simplified auxiliary inverter control block diagram.

Figure 4 shows the system voltage outer ring closed loop transfer function is:

$$H_c = \frac{K_{pr1}s + K_{ir1}}{Cs^2 + (2\omega_{c1}C + K_{pr1})s + \omega_o^2C + K_{ir1}} \tag{7}$$

In this paper, the fundamental frequency new resonant controller parameters are:  $K_{ir1} = 90$ ,  $\omega_{c1} = 0$ ,  $K_{pr1} = 0.0606$

Figure 5 shows the controller voltage outer loop closed loop transfer function bode diagram. The voltage fundamental wave frequency gain of the controller outer ring loop is 0.00121 dB, there is almost no steady-state error; the phase difference is  $-0.0124^\circ$ , the phase difference is small, so that the phase lag is small. Figure 6 shows that the voltage outer ring bandwidth is 167.197 Hz, it is to meet the voltage requirement of the outer ring bandwidth.

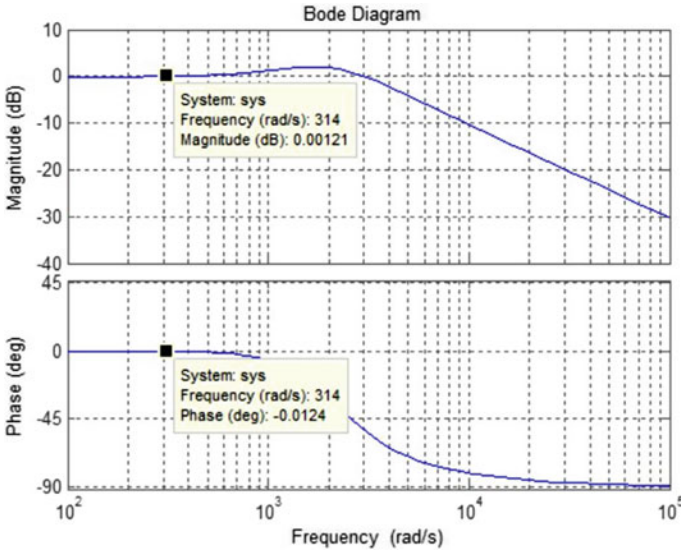


Fig. 5 Controller voltage outer ring closed loop transfer function bode graph

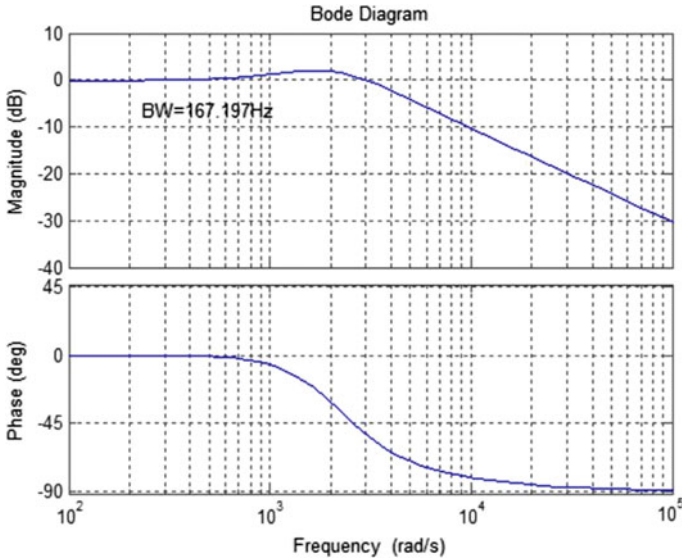


Fig. 6 Controller voltage outer ring closed loop transfer function bode graph

Through the above analysis, it can be obtained that if the voltage outer ring control selects the fundamental frequency new resonant control, the bandwidth of the voltage outer ring control system is wide, the high frequency component decays rapidly, the dynamic performance is good, the stability is good, there is almost no steady-state error, the voltage outer ring tracking command voltage ability is good, and the unbalanced load is eliminated.

### 4 Simulation Result

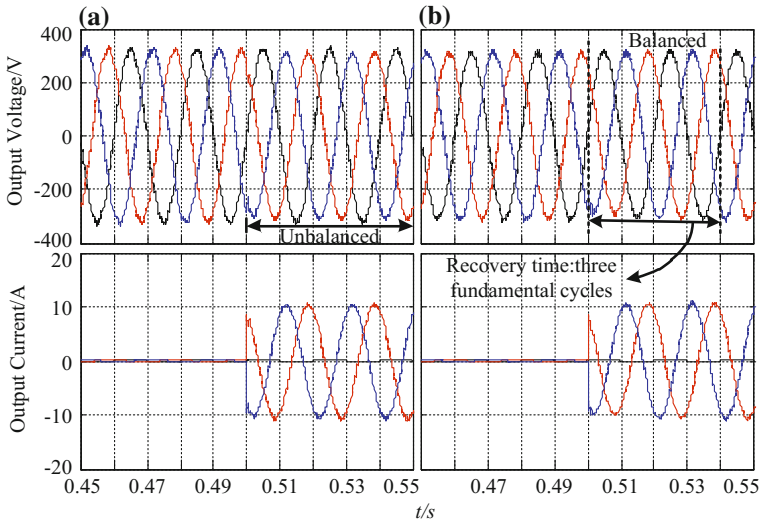
The virtual DSP system including interrupt program, AD sampling, control algorithm and PWM pulse generation is constructed by S-Function. The above mentioned new resonant control attenuation of the DC component of the ability is very strong, so select the common PID controller with the contrast, the system is still double closed loop control system, only use the PID controller to replace the new resonant controller, control system parameters as shown in Table 2.

Figure 7a for the use of PID controller and load for the unbalanced load of the three-phase voltage simulation waveform, in order to facilitate the analysis, it

Table 2 Parameters of simulation system

$K_{pr1}$	0.0606	PID controller $K_p$	0.011
$K_{ir1}$	90	PID controller $K_i$	1.2
Current loop $K_p$	5.35	PID controller $K_d$	0.0001





**Fig. 7** Voltage and current waveform with instantaneous imbalanced load. **a** PID strategy. **b** The improved resonant controller strategy

increases unbalanced load. As can be seen from Fig. 7a, after loading, the output voltage imbalance is serious and the PID controller suppressing unbalanced load capacity is weak.

Figure 7b is a three-phase voltage simulation waveform with a new resonant controller and unbalanced load. Compared with Fig. 7b, it can be seen that the output voltage remains balanced after loading, which shows that the new resonant controller can reduce the auxiliary inverter output base impedance, and inhibit unbalanced load.

## 5 Conclusion

Unbalanced load affects the auxiliary inverter output voltage quality greatly, unbalanced load will lead to the auxiliary inverter three-phase output voltage imbalance, the main reason of the three-phase output voltage imbalance is the different voltage drop caused by the three-phase unbalanced current across the equivalent output impedance of the auxiliary inverter. In this paper, it proposes a circuit topology that a neutral inductor is added to a split-capacitor inverter. The midline inductance can effectively suppress the ripple current flowing through the filter capacitor and the supporting capacitor, which can increase the capacitor life and increase the ability to suppress unbalance load of the inverter.

Based on this topology, an auxiliary inverter voltage and current double-loop control system is proposed for the unbalanced load characteristics of the auxiliary

inverter. A new type of resonant control is used to maximize the ability to adapt to the unbalanced load of the auxiliary inverter. In order to further verify the circuit topology and the performance of the control system proposed in this paper, a virtual DSP simulation module based on S-Function is constructed, and the simulation of unbalanced load characteristics is constructed. The simulation and theoretical analysis are consistent, which can verify the effectiveness of the method.

**Acknowledgements** This work was supported by National Key R&D plan under Grant 2016YFB1200502-4 and 2017YFB1200802, Beijing Science and School level project 2016RC038.

## References

1. Hornik T, Zhong Q (2012) Parallel PI voltage–H-infinity current controller for the neutral point of a three-phase inverter. *Indust Electr, IEEE Trans*
2. Ryan MJ, De DR, Lorenz RD (2001) Decoupled control of a four-leg inverter via a new 4x4 trans formation matrix. *Power Electr, IEEE Trans on* 16(5):694–701
3. Ryan MJ, Brumsickle WE, Lorenz RD (1997) Control topology options for single-phase UPS inverters. *Industry Applications, IEEE Transactions on*, 33(2):493–501
4. Mattavelli P (2005) An improved deadbeat control for UPS using disturbance observers. *Indust Electr, IEEE Trans* 52(1):206–212
5. Hasanzadeh A, Onar O C, Mokhtari H, et al (2010) A proportional-resonant controller-based wireless control strategy with a reduced number of sensors for parallel-operated UPSs. *IEEE Trans Power Deliv* 25(1): 468-478
6. Guo S, Liu D (2010) Proportional-resonant based high-performance control strategy for voltage-quality in dynamic voltage restorer system. *Power Electronics for Distributed Generation Systems (PEDG), 2010 2nd IEEE International Symposium on*. 721–726
7. Hornik T, Zhong QC (2011) A current-control strategy for voltage-source inverters in microgrids based on h(infinity) and repetitive control. *IEEE Trans Power Electron* 26(3): 943–952
8. Francis BA, Wonham WM (1975). *Applied Mathematics & Optimization* (2):170–194

# Hierarchical Control and Harmonic Suppression of a Vehicular Based Microgrid System

Shuguang Wei, Hailiang Xu, Qiang Gao and Xiaojun Ma

**Abstract** This paper presents a hierarchical control and harmonic suppression strategy for a vehicular based microgrid system, which is utilized as an ac mobile power station supplying both pulse power loads (PPLs) and nonlinear loads (NLs). In order to reduce the impact of the PPLs on the microgrid, a hybrid storage system consisted of battery and super-capacitor was designed to be paralleled with the diesel generator through a dc bus. Hence, the stability of the dc-bus voltage can be enhanced. And the size of the generator turbine can thus be dramatically decreased. To reinforce the uninterrupted operation capability of the power station, the vehicular microgrid was hierarchically controlled in two levels, i.e., the system level and converter level. Moreover, an improved vector control was proposed to deal with the current harmonics introduced by the NLs. The effectiveness and feasibility of the proposed control were initially verified by simulation results.

**Keywords** Vehicular based microgrid · Hybrid storage system  
Pulse power loads (PPLs) · Hierarchical control · Harmonic suppression

## 1 Introduction

Nowadays, mobile power stations (MPSs) are widely used as emergency power in remote areas or fieldwork places, duo to its highlighted merits, such as maneuverability and flexibility, reduction of cables, variation of voltage classes, etc. Nevertheless, the utilized ac mobile power stations are mainly based on diesel or gasoline based generator turbines, which have several limits summarized as follows.

Firstly, the dynamic loading capability of the diesel-based station is not so satisfactory. As the inertia of the power station is relatively small, the network is considerably sensitive to power fluctuation. For instance, when a high power

---

S. Wei · H. Xu (✉) · Q. Gao · X. Ma  
Army Academy of Armored Forces, No. 21, Beijing Fengtai District, China  
e-mail: xuhl@zju.edu.cn

electrical machine is suddenly loaded or unloaded, power/voltage fluctuations may occur in the network. Secondly, the light load drive phenomenon is quite conspicuous. There are so many electric equipment behaving as pulse power loads (PPLs), such as the pulse radar and other military monitoring and communicating equipment, whose instantaneous power is often more than twice of their average one. If no power buffer modules are involved, the existing diesel-based stations will have to be designed according to the instantaneous power, resulting in a substantial increase in the size and weight of the mobile station. Thirdly, as for sensitive loads, the power quality requirement is strict. However, as with traditional mobile power stations, the voltage unbalance, the harmonic distortion and other typical grid faults are usually not considered.

Recently, microgrid technologies have been developed rapidly and widely utilized in decentralized electricity supply and residential grids, which presents alternative topologies and control approaches for the MPSs. For instance, in [1], a model based on mixed integer linear programming was presented for the optimization of a hybrid renewable energy system with battery energy storage systems in residential microgrids. The demand response (DR) of available controllable appliances was coherently considered in the proposed optimization problem but with reduced calculation burdens. In [2], to address the tie-line power fluctuations caused by intermittent renewable energy resources, a hierarchical control configuration was proposed to control and manage DR resources and other grid resources such as conventional battery storage. In [3], an integrated energy management controller was explored for a dc microgrid that improves power supply resilience in wireless communication networks. In [4], a multi-timescale cost effective power management algorithm was proposed for islanded MG operation targeting generation, storage, and demand management. To be generic and to consider various microgrid configurations, an optimal management model was presented for a smart-house with a V2G system, a set of manageable domestic devices and two renewable sources [5].

In this paper, a hierarchical control and harmonic suppression strategy for a vehicular microgrid system was put forward. The operation modes and the mode transition mechanism of the microgrid system were discussed in detail. To improve the power quality, a harmonic control method was also proposed. Simulation studies were carried out to demonstrate the effectiveness and feasibility of the proposed control.

## 2 Vehicular Microgrid Configuration

The topology of the vehicular microgrid system is depicted in Fig. 1. Compared with the conventional diesel-based power station, the proposed one utilizes a hybrid storage system consisting of a battery and a super-capacitor as a power buffer, which is paralleled with the diesel generator turbine through a dc bus. As shown in Fig. 1, the output tree-phase voltages and currents of the diesel generator are firstly

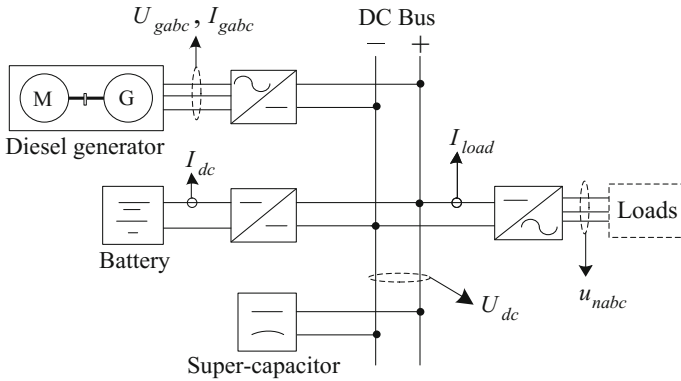


**Fig. 1** Topology diagram of the vehicular based microgrid system

transformed into dc components via an AC/DC converter, to ensure the turbine’s operation state always around its optimal fuel oil consuming curves. Meanwhile, in order to take the advantages of the high energy diversity and high power densities of the hybrid energy storage system, the battery is connected to the dc bus through a bidirectional DC/DC converter, while the latter one is paralleled directly with the dc bus. Then the electric power is provided for the loads as ac form via a modularized DC/AC inverter.

Adopting this topology, the diesel generator can be controlled to output the average load power, while the hybrid storage system is designed to supplement the pulse power of the loads. Additionally, as with small power load condition, since the efficiency of the diesel generator would be relatively low if fired, the hybrid storage system can be set to operate independently to satisfy the whole power demand with the generator turbine shut down. Hence the pulse load disturbance on the diesel generator can be reduced to a large extent. And the stability of the system’s output voltage can also be enhanced. With this design, the size of the generator turbine can be designed to the average load power level, which contributes to reduce the generator turbine’s volume and weight.

### 3 Hierarchically Control Strategies

The vehicular microgrid is hierarchically controlled in two levels, i.e., the system level and micro-source level. In the system level, the vehicular microgrid is arranged to operate in four modes, with their corresponding energy management strategies designed. Whereas in the micro-source level, three kinds of converters need to be controlled respectively to realize the alternative operation targets.

### 3.1 System Level–Operation Modes

According to the load condition and the battery's state of charge (SOC), the vehicular microgrid system is arranged to operate in four alternative modes, described as follows.

**Mode I**—Heavy load and battery discharging model. When the load power is more than 30% of the diesel generator's rating power and the SOC of the battery is higher than is threshold  $SOC_{min}$ , the diesel generator is turned on and outputs the average power, while the hybrid storage system plays the role of peak load shifting. Herein the DC/DC converter works in its boost mode, as analyzed in next part of this section. It needs to be pointed out that the definition of heavy load is not unalterable. Actually, it depends on the proportion of hybrid storage system power (especially the battery power) over the generator power. It is indisputable that Model I is the main operation model of the vehicular microgrid system. And during this model, the power station can output the maximum instantaneous power.

**Mode II**—Heavy load and battery charging model. When the load power is more than 30% of the diesel generator's rating power and the SOC of the battery is lower than  $SOC_{min}$ , the diesel generator is controlled preferentially to meet the load power demand. If there is surplus power in the diesel generator, the battery is charged until its SOC value reaching the upper limit, i.e.,  $SOC_{max}$ . During this process, the DC/DC converter works in its buck mode, as analyzed in Part B of this section.

**Mode III**—Light load and battery charging model. In this situation, the load power is less than 30% of diesel generator's rating power. And the state of charge (SOC) of the battery is lower than is threshold  $SOC_{min}$ . Then the diesel generator has to be turned on and outputs the whole power, which includes the load power and battery charging power.

**Mode IV**—Light load and battery discharging model. It occurs when the load power is less than 30% of the diesel generator's rating power. During such operation mode, the diesel generator turbine is shut down, leaving the hybrid storage system outputs all the demanded power. This model conserves the fuel oil and increases the efficiency of the system.

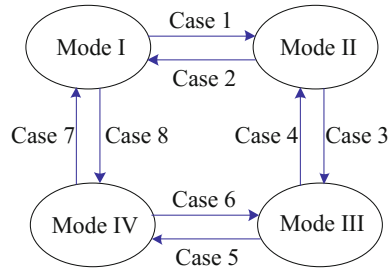
As above mentioned, there are four operation modes in the vehicular microgrid system. Hence it is an important thing to determine the mode transition conditions to realize self-adaptive mode control. The adaptive mode transition mechanism is displayed in Fig. 2, with the transition conditions of Case 1 to Case 8 summarized as follows.

Case 1—The load is heavy and the SOC of the battery is lower than  $SOC_{min}$ ;

Case 2—The load is heavy and the SOC of the battery reaches its upper limit, i.e.,  $SOC_{max}$ ;

Case 3—The load jumps to be light and the SOC of the battery is still lower than  $SOC_{min}$ ;

**Fig. 2** The adaptive mode transition mechanism of the vehicular microgrid system



- Case 4—The load returns to be heavy and the SOC of the battery remains lower than  $SOC_{min}$ ;
- Case 5—The load keeps to be light and the SOC of the battery reaches its upper limit, i.e.,  $SOC_{max}$ ;
- Case 6—The load keeps to be light and the SOC of the battery is lower than  $SOC_{min}$ ;
- Case 7—The load jumps to be heavy and the SOC of the battery is more than  $SOC_{min}$ ;
- Case 8—The load jumps to be light and the SOC of the battery is more than  $SOC_{min}$ .

Theoretically, there are other four transition conditions that are not shown in Fig. 2. For instance, the conditions for the transition mechanism between Mode I and Mode III. Since such cases usually do not occur in a real mobile station, they are not further discussed herein.

### 3.2 Micro-Source Level–Converter Control

#### 3.2.1 AC/DC Converter

The AC/DC converter is arranged to be worked in two patterns according to the station’s operation modes, i.e., power control and voltage control. When the vehicular microgrid is operating in Mode I, the diesel generator is set to output the average load power, while the DC/DC converter takes charge of the dc bus voltage. Hence power control is assigned for the AC/DC converter, as depicted in Fig. 3a. When the vehicular microgrid is operating in Modes II and III, the DC/DC converter loses the control of the dc bus voltage, and the diesel generator takes over the stability of the network. In this case, voltage control is assigned for the AC/DC converter, as depicted in Fig. 3b. The variables appearing in Fig. 3 are defined as follows.

$U_{gabc}, I_{gabc}$  three phase voltage and current of the generator;  
 $U_g$  magnitude of the three phase voltage in synchronous rotating coordinate;  
 $\omega_g, \theta_g$  angular frequency and position angle of  $U_{gabc}$ ;  
 $P_g, Q_g$  output active and reactive powers of the generator;  
 $L_g, R_g$  input inductance and resistance of AC/DC converter;  
 $V_{dc}$  dc bus voltage;  
 \* reference value.

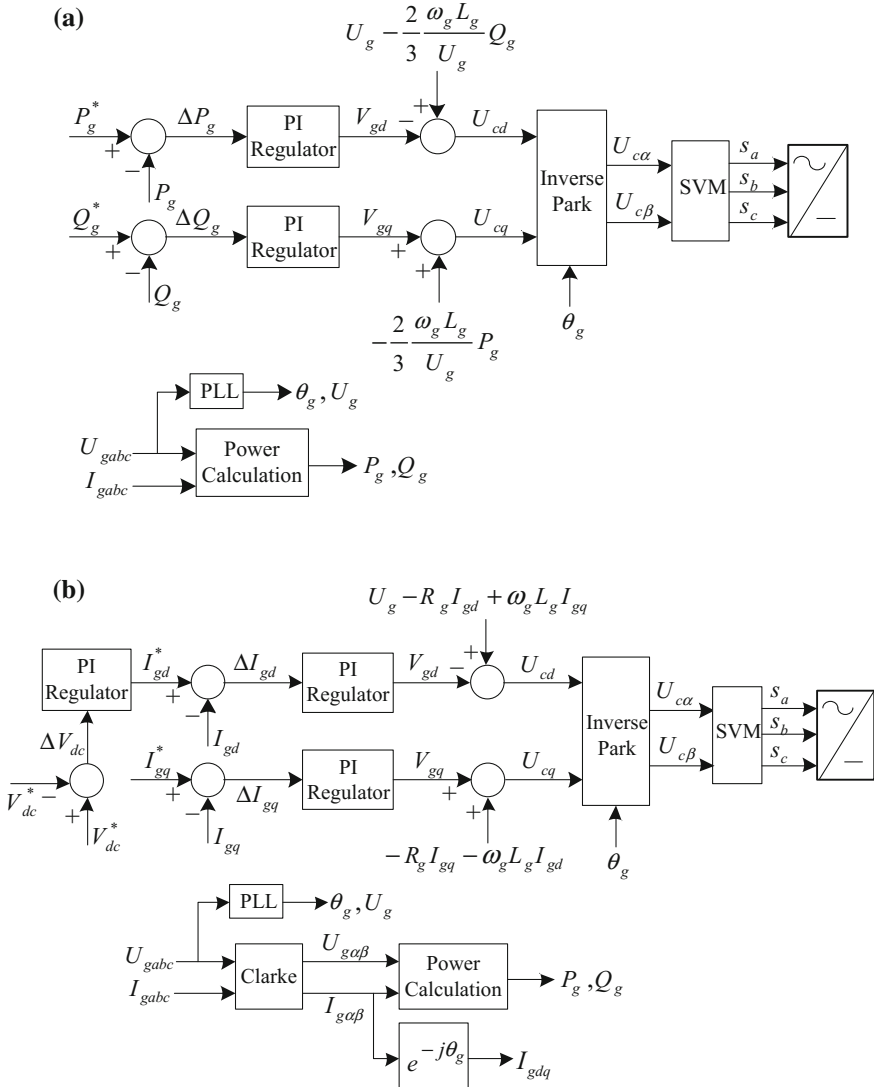


Fig. 3 Control diagram of the AC/DC converter: a power control; b voltage control



### 3.2.2 DC/DC Converter

As aforementioned, the function of the DC/DC converter is to charge or discharge the battery according to its SOC value. Correspondingly, the DC/DC converter can be controlled to operate in Boost or Buck model, as illustrated in Fig. 4. Since the control process has been reported by many papers [6–8]. It will not be discussed in detail duo to space limitation.

### 3.2.3 DC/AC Inverter

In the view of suppressing the voltage harmonics introduced by nonlinear loads, an improved vector control is put forward for the DC/AC inverter, as shown in Fig. 5. At the beginning, the three phase voltage reference is set as (1), with  $\omega_1$ ,  $\omega_0$ ,  $M$  being the fundamental angular frequency, initial angular frequency (usually set as zero) and magnitude of the phase voltage, respectively. Then the voltage is transferred into positive synchronous rotating coordinate so as to be regulated with the improved vector control.

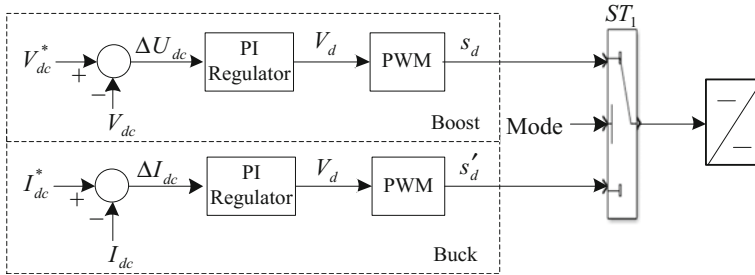


Fig. 4 Control diagram of the DC/DC converter

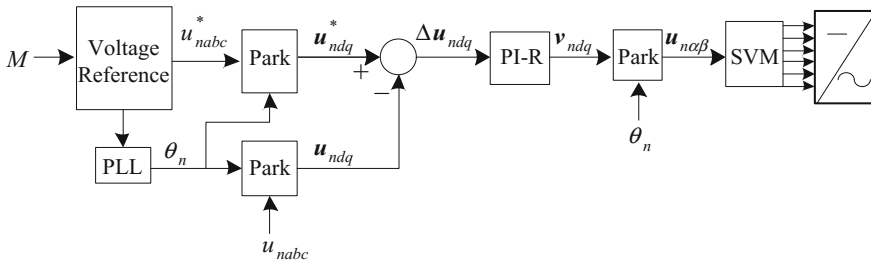


Fig. 5 Control diagram of the DC/AC inverter

$$\begin{cases} u_{na}^* = M \cdot \sin(\omega_1 \times t + \omega_0) \\ u_{nb}^* = M \cdot \sin(\omega_1 \times t + \omega_0 - 2\pi/3) \\ u_{nc}^* = M \cdot \sin(\omega_1 \times t + \omega_0 + 2\pi/3) \end{cases} \quad (1)$$

It has been proved that in the positive synchronous rotating coordinate both the fifth and seventh order harmonics behave as six order harmonics, though their rotating directions are opposite [9–11]. In order to suppress the voltage harmonics, a proportional integral plus resonant (PI-R) regulator is utilized herein to replace the conventional PI regulator. The transfer function of the PI-R is expressed as (2), with  $K_p$ ,  $K_i$ ,  $K_r$  being the proportional, integral and resonant parameters, respectively;  $\omega_c$  is the cutoff frequency of the resonant regulator.

$$G_{\text{PI-R}}(s) = K_p + \frac{K_i}{s} + \frac{K_r s}{s^2 + 2\omega_c s + (6\omega_1)^2} \quad (2)$$

The steady and transient response of the PI-R regulator has been investigated in detail in [9, 10]. Thereby no further theoretical analysis will be carried out in this paper. However, the effectiveness of the proposed control can be verified by simulation tests.

## 4 Simulation Verifications

In order to demonstrate the effectiveness and feasibility of the proposed ac vehicular microgrid and its control strategies, a simulated test rig with the structure of Fig. 1 is set up in the Matlab/Simulink environment. An ac programmable power (APP) with its power climbing rate limited is substitute for the diesel generator turbine so as to simplify the modeling process. The APP is rated of 60 kW. And the rated voltage of the dc bus is 600 V. The fully charge voltage of the super-capacitor is 658 V and its capacitor is 3.3 F. The parameters of the Lithium-Ion battery are shown in Tab. 1. Tests were performed into three steps with the results and analysis shown as follows.

**Table 1** Parameters of the Lithium-Ion battery

Nominal voltage	400 V
Rated capacity	30Ah
Maximum capacity	30Ah
Fully charge voltage	465 V
Internal resistance	0.133 $\Omega$
Capacity @nominal voltage	27.1Ah
Exponential zone	432.1 V, 1.5Ah

### 4.1 Nominal Operation with PPLs

Test was firstly carried out during nominal operation with the PPLs, which were simulated by step loads. And the results are shown in Fig. 6. In the figure, from top to down, the waveforms stand for three-phase output voltages of the DC/AC inverter, three-phase output currents of the DC/AC inverter (i.e., the load current), dc bus voltage, output current of the AC/DC converter (equal to the output current of the generator), output current of super-capacitor, output current of battery and SOC of battery, respectively.

At the beginning of the simulation, the load power is 21 kW, more than 30% of the generator's rated power. Consequently, Mode I is selected automatically. As analyzed above, during this operation mode, the AC/DC converter is operated in power control strategy and the generator turbine outputs all the average load power, while the hybrid storage system monitors the pulsation of the dc bus. At 0.2 s, the load power jumps up to 60 kW, but still in the power control range of the generator system. As can be seen from the current waveform of super-capacitor, i.e.,  $I_{sc}$  in the figure, at the very moment, the super-capacitor responds firstly and outputs the transient step load power, whereas the generator turbine outputs the average load power gradually. Since no significant voltage pulsation occurs in the dc bus and the SOC of the battery is 80%, the battery is not charged or discharged during the process, as shown in the waveform of the battery current, i.e.,  $I_{bat}$ . At 0.25 s, the load power jumps down back to 21 kW, and similarly, the super-capacitor responds quickly and helps to maintain the three-phase output voltages of the DC/AC inverter, as shown in  $u_{nabc}$ . At 0.3 s and 0.35 s, the same loading and unloading process repeats again and the similar results are thus obtained.

The test results in Fig. 6 initially verify the effectiveness of the proposed topology. Pulsed power load tests were also carried out in the simulation. Since the results are similar to those of Fig. 6 and the space is limited, these waveforms are not shown here.

### 4.2 Mode Transition Mechanism Test

In order to validate the feasibility of the proposed mode transition mechanism, test was then performed with mode transitions. The simulation results are shown in Fig. 7, where Fig. 7a, b are the transition processes of Mode I to Mode II and Mode III to Mode IV, respectively.

In Fig. 7a, at the beginning, the load power is 43 kW, more than 30% of the generator's rated power. Hence, the system is operated in Mode I. At 0.2 s, the SOC of the battery is monitored to be lower than 40%. According to the transition mechanism, the operation model should be transited from Mode I to Mode II automatically. As shown in Fig. 7a, the battery is charged with a constant current of 30A. Correspondingly, the equal average outputting current of the generator turbine

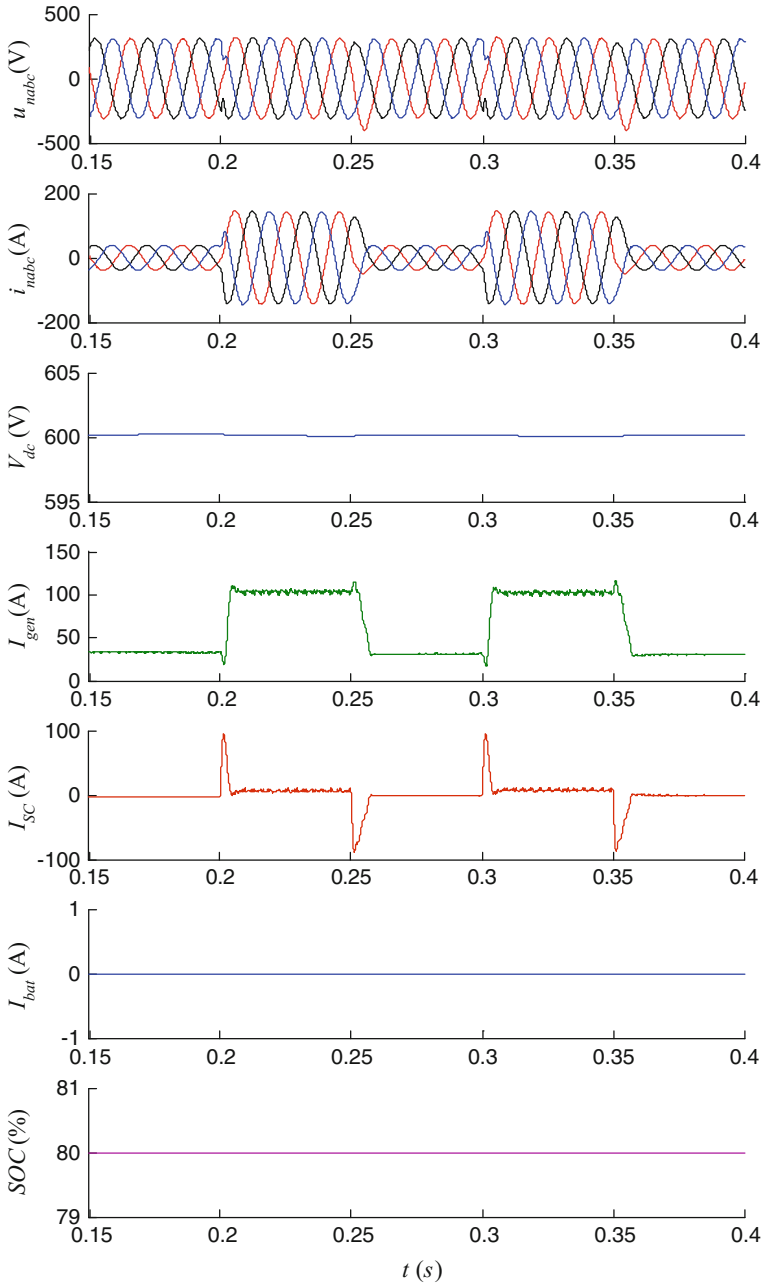


**Fig. 6** Simulation results of Mode I with load power step changes

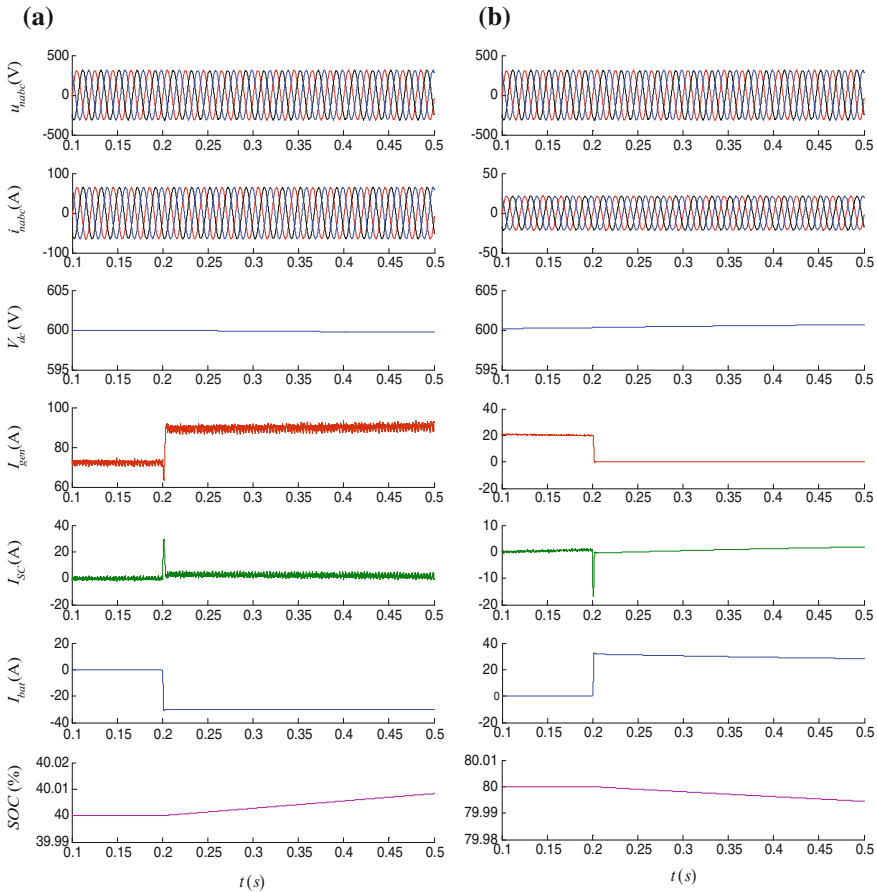


**Fig. 7** Simulation results of mode transition mechanism test: **a** Mode I to Mode II; **b** Mode III to Mode IV

is climbed up from 72 to 92 A. Consequently, the SOC of the battery starts to rise up, as can be seen from the waveform of SOC.

In Fig. 7b, when the simulation starts, the load power is 10 kW, lower than 30% of the generator’s rated power. At the same time, the battery is charged and its SOC is very oncoming the value of 80%. With no doubt, the station is set to operate in Mode III at the beginning. At 0.2 s, the SOC of the battery is observed to be equal to 80%. According to the transition mechanism, since the load power is still low at the moment, the operation model of the system should be transited from Mode III to Mode IV. As shown in Fig. 7b, the transition process is smoothness and self-adaptive. The battery outputs the whole load power and correspondingly, the SOC of the battery starts to dip, as can be seen from the waveform. To be the most importance thing, the three-phase output voltages of the DC/AC inverter keeps throughout sine and balanced all over the process, as shown in the waveforms of

$u_{nabc}$ . Other mode transition processes were also carried out. And likewise, the waveforms are not given herein for space limitation. Nevertheless, the reasonableness and feasibility are initially verified by the simulation results.

### 4.3 Harmonic Suppression Test

The proposed harmonic suppression control was finally performed with NLs. The results are shown in Fig. 8, in which during the time of 0.1–0.2 s with the conventional vector control, while during the time of 0.2–0.3 s with the proposed control. The FFT results of the three-phase output voltages of the DC/AC inverter are then presented in Fig. 9. Based on Figs. 8 and 9, it is obviously that the three-phase output voltages of the DC/AC inverter would be harmonically distorted if no corresponding measures were taken. However, when the proposed harmonic control works, the fifth and seventh order harmonics are suppressed in large measure, as shown in Fig. 9. Finally, the quality of the output voltage is improved, which is very meaningful to the sensitive equipment connected to the microgrid.

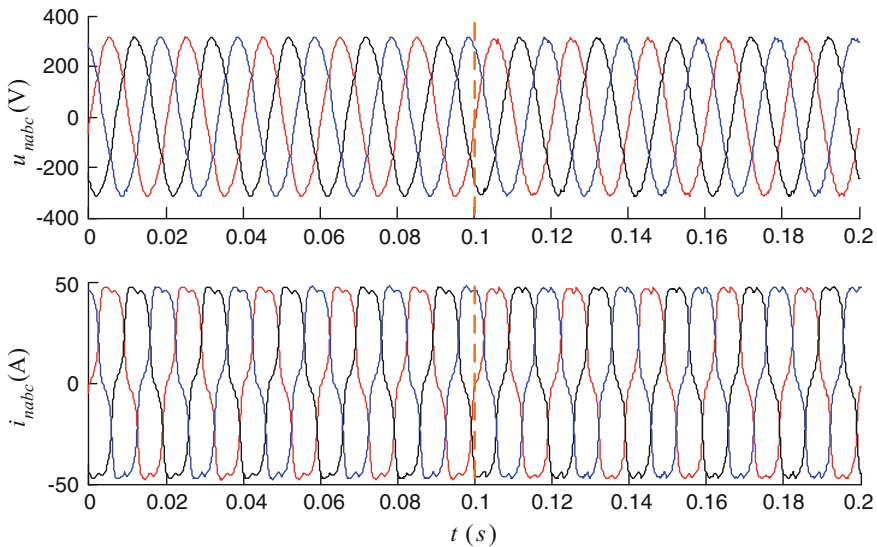


**Fig. 8** Simulation results of the conventional vector control and proposed harmonic control

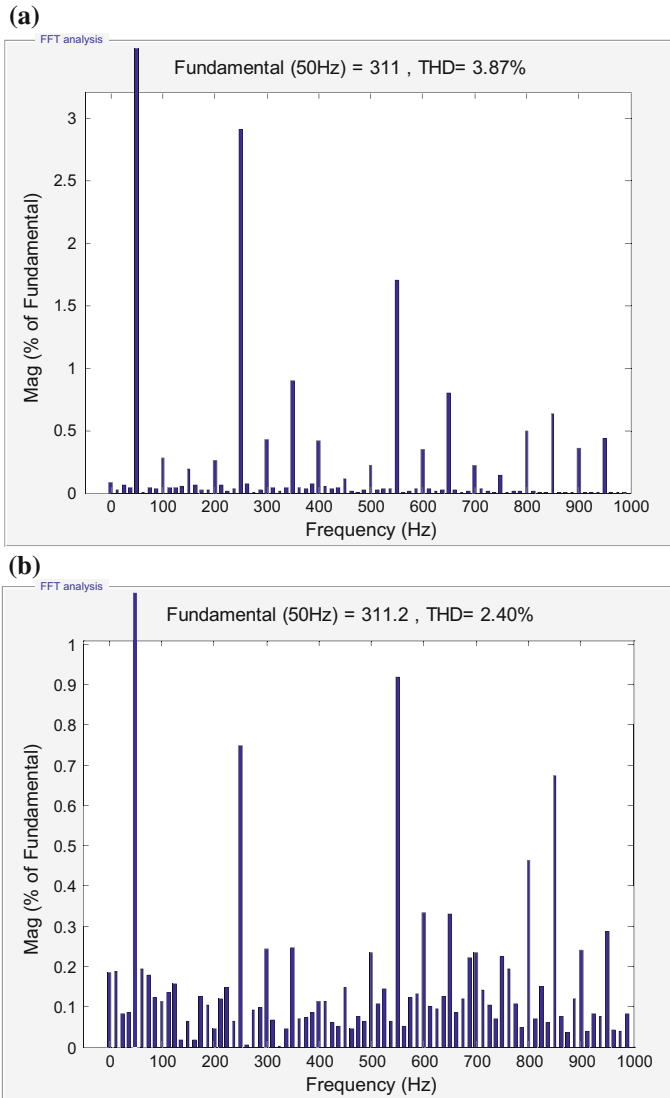


**Fig. 9** FFT of the three-phase output voltages of the DC/AC inverter. **a** Conventional vector control; **b** proposed harmonic control

## 5 Conclusion

A hierarchical control and harmonic suppression strategy for a vehicular based microgrid system is proposed, which is structured as an ac mobile power station simultaneously supplying for pulse power loads (PPLs) and nonlinear loads (NLs). The novel topology adopts a hybrid storage system as a buffer, which consists of a

battery and a super-capacitor and paralleled with the diesel generator through a dc bus. In the system control level, the vehicular microgrid is arranged to operate in four alternative modes. According to the load condition and the battery's state of charge, the operation modes can be transited automatically. The control strategies of the AC/DC convertor and the DC/DC converter are designed and analyzed. A harmonic suppression control for the DC/AC inverter is presented so as to eliminate the voltage harmonics caused by nonlinear loads. It is verified by simulation results that adopting this design, the stability of the output voltage stability can be improved. And the size of the generator turbine can be decreased to a large extent. To be the most importance thing, the three-phase output voltages of the DC/AC inverter keeps strictly sine throughout the whole operation, which is very important to the grid-connected sensitive equipment.

**Acknowledgements** This work was supported in part by the National Natural Science Foundation of China (No. 51507190) and the China Postdoctoral Science Foundation (No. 2017T100831).

## References

1. Atia R, Yamada N (2016) Sizing and Analysis of Renewable Energy and Battery Systems in Residential Microgrids. *IEEE Trans Smart Grid* 7(3):1204–1213
2. Wang D, Ge S, Jia H et al (2014) A demand response and battery storage coordination algorithm for providing microgrid tie-line smoothing services. *IEEE Trans Sustain Energy* 5(2):476–486
3. Kwon Y, Kwasinski A, Kwasinski A (2016) Coordinated Energy Management in resilient microgrids for wireless communication networks. *IEEE J Emerg Sel Top Power Electr* 4(4):1158–1173
4. Pourmousavi SA, Nehrir MH, Sharma RK (2015) Multi-timescale power management for islanded microgrids including storage and demand response. *IEEE Trans Smart Grid* 6(3):1185–1195
5. Igualada L, Corchero C, Cruz-Zambrano M et al (2014) Optimal energy management for a residential microgrid including a vehicle-to-grid system. *IEEE Trans Smart Grid* 5(4):2163–2172
6. Li W, He X (2011) Review of Nonisolated high-step-up dc/dc converters in photovoltaic grid-connected applications. *IEEE Trans Industr Electron* 58(4):1239–1250
7. Grbovic PJ, Delarue P, Moigne PL et al (2010) A bidirectional three-level DC–DC converter for the ultracapacitor applications. *IEEE Trans Industr Electron* 57(10):3415–3430
8. Gualous H, Gustin F, Berthon A et al (2010) DC/DC converter design for supercapacitor and battery power management in hybrid vehicle applications—Polynomial control strategy. *IEEE Trans Industr Electron* 57(2):587–597
9. Xu H, Hu J, He Y (2012) Operation of wind-turbine-driven DFIG systems under distorted grid voltage conditions: analysis and experimental validations. *IEEE Trans Power Electron* 27(5):2354–2366
10. Hu J, Xu H, He Y (2013) Coordinated control of DFIG's RSC and GSC under generalized unbalanced and distorted grid voltage conditions. *IEEE Trans Industr Electron* 60(7):2808–2819
11. Zandzadeh MJ, Vahedi A (2014) Modeling and improvement of direct power control of DFIG under unbalanced grid voltage condition. *Int J Electr Power Energy Syst* 59(7):58–65



# Research on Vector Control of Long-Primary Permanent Magnet Linear Synchronous Motor Based on Voltage Feed-Forward Decoupling

Zheng Li, Ruihua Zhang, Yumei Du and Qiongquan Ge

**Abstract** The dynamic response characteristics of current loop in vector control system is closely related to the realization of vector control strategy. In the system model of multiple motors connected in series (which consists of coupled section, uncoupled section and feeder cable), the inductance and resistance of uncoupled section and feeder cable are taken into consideration in this paper. Due to the ignoring of current coupling problem of d-q axis in traditional PI current regulator, the dynamic performance of the system is poor. To solve this problem, a modified PI regulator based on voltage feed-forward decoupling is applied to build the control system of permanent magnet linear synchronous motor (PMLSM). The model of traditional PI current regulator and the model of modified PI current regulator are built respectively and compared with each other in Matlab/Simulink. The simulation results verify the correctness and effectiveness of PI current regulator with voltage feed-forward decoupling, and indicate that this improved control system has better dynamic and static characteristic than traditional control system.

**Keywords** Motor drives · PMLSM · Vector control · Voltage feed-forward decoupling

## 1 Introduction

PMLSM has many advantages, such as simple structure, high thrust force and low mechanical loss. It has been widely used in high-performance AC servo systems [1]. At present, vector control is usually used to realize the independent control of drive motor thrust and excitation flux in PMLSM.

---

Z. Li · R. Zhang (✉) · Y. Du · Q. Ge

Key Laboratory of Power Electronics and Electric Drive, Institute of Electrical Engineering, Chinese Academy of Sciences, No. 6 Beiertiao, Zhongguancun, Beijing, China  
e-mail: ruihuazh@mail.iee.ac.cn

Z. Li

University of Chinese Academy of Sciences (UCAS), Beijing, China

© Springer Nature Singapore Pte Ltd. 2018

L. Jia et al. (eds.), *Proceedings of the 3rd International Conference on Electrical and Information Technologies for Rail Transportation (EITRT) 2017*, Lecture Notes in Electrical Engineering 482, [https://doi.org/10.1007/978-981-10-7986-3\\_56](https://doi.org/10.1007/978-981-10-7986-3_56)

543

Vector control was first proposed by experts in Blanche, Germany, company of SIEMENS in 1971 [2]. The basic idea is based on the coordinate transformation and the motor torque/thrust equations. At first, vector control was developed for asynchronous motors. With the development of vector control and other types of AC motors, the application of vector control became widespread. Vector control is also transplanted into permanent magnet linear synchronous motor (PMSM). The direct control of thrust and excitation flux of the drive motor is realized by controlling the d-q axis components of the stator current [3], in d-q rotating coordinate system.

At present, the traditional PI current regulator is usually used to control the d-q axis respectively. However, the current coupling problem of d-q axis is usually ignored, which leads to the poor dynamic performance of system. In order to solve this problem, this paper designed a modified current regulator which adopted voltage feed-forward decoupling, and simulation model was built up in Matlab/Simulink. The experiment results verify the feasibility and effectiveness of voltage feed-forward decoupling, and indicate that this improved control system has better dynamic and static characteristic than traditional control system.

## 2 Theoretical Analysis

### 2.1 *The Mathematical Model*

#### 2.1.1 The Mathematical Model of PMLSM

PMLSM is a complex system with high order, strong coupling and nonlinearity [4]. When establishing the mathematical model, the internal parameters can be simplified in ideal conditions. The assumptions are made as follows:

- Ignore the saturation effect of magnetic circuit, both of hysteresis loss and eddy current loss are regardless in the iron core.
- Rotor without damping winding.
- Stator three-phase winding symmetry, the incoming current is three-phase sinusoidal current.
- The PMLSM air gap is distributed equally; namely, the quadrature axis inductance is equal to direct axis inductance.
- The magnetic potential produced in the air gap varies according to the sine law; ignore the higher harmonic potential.
- The permanent magnet is stable and does not occur demagnetization; the parameters of the motor do not vary with the external conditions such as temperature.

In the middle speed maglev trains, the long-primary linear motor is usually used to drive the maglev train. Being laid along the track, the stator section and the cable connecting the stator section is very long. Therefore, when establishing the mathematical model of the system, the impedance of the uncoupled section, leakage

inductance and leakage resistance of the feeding cable are taken into consideration. In the maglev train, multiple long-primary PMLSM are usually connected in series. Then, the equivalent circuit diagram of the total power system can be obtained, as shown in Fig. 1.

As shown in Fig. 1,  $R_k$  is the resistance of feeder cable,  $L_k$  is the inductance of feeder cable,  $R_s$  is the resistance of stator winding,  $L_s$  is the inductance of stator winding,  $I_s$  is the stator current,  $U$  is the voltage of the whole electric power system.

According to Fig. 1, based on the basic theory of motor and principle of coordinate transformation, the mathematical model of the drive motor of the permanent magnet maglev train can be shown as following equations, in d-q rotating coordinate system:

Voltage equations:

$$\begin{cases} u_{sd} = R i_{sd} + \frac{d\psi_d}{dt} - \frac{\pi v}{\tau} \psi_q \\ u_{sq} = R i_{sq} + \frac{d\psi_q}{dt} + \frac{\pi v}{\tau} \psi_d \end{cases} \quad (1)$$

where  $R = NR_s + R_k$ ,  $L_d = L_{sd} + L_{kd}$ ,  $L_q = L_{sq} + L_{kq}$ .

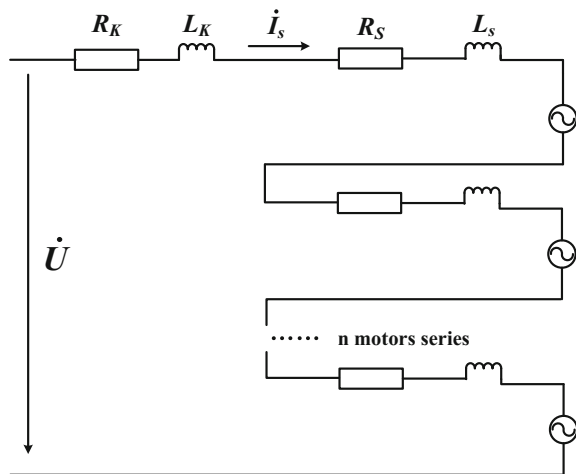
Flux linkage equations:

$$\begin{cases} \psi_d = L_d i_{sd} + \psi_f \\ \psi_q = L_q i_{sq} \end{cases} \quad (2)$$

Electromagnetic force equations:

$$F_x = \frac{3\pi}{2\tau} n_p [\psi_f i_{sq} + (L_d - L_q) i_{sd} i_{sq}] \quad (3)$$

Fig. 1 The equivalent circuit diagram of multiple PMLSM series



The equations of motion:

$$F_x - F_d(v) = m \frac{dv}{dt} \quad (4)$$

where  $u_{sd}, u_{sq}$  are the stator voltage components in d-q reference frame;  $i_{sd}, i_{sq}$  are stator current components;  $L_{kd}, L_{kq}$  are feeder cable inductance components;  $L_{sd}, L_{sq}$  are stator inductance components;  $L_d, L_q$  are total inductance components;  $R_{kd}, R_{kq}$  are feeder cable resistance components;  $R_{sd}, R_{sq}$  are stator resistance components;  $R_d, R_q$  are total resistance components;  $R_s$  is stator resistance;  $\psi_d, \psi_q$  are stator magnetic flux linkage components in d-q frame;  $\psi_f$  is the magnetic flux linkage of permanent magnetic motor;  $\tau$  is the pole pitch in meter;  $v$  is the speed of rotor in meter per second;  $F_x$  is the horizontal thrust of motor;  $F_d(v)$  is the equivalent resistance force;  $n_p$  is the number of polar logarithm;  $N$  is the number of motors in series.

The synchronous speed of motor is shown as:

$$v = 2\tau f \quad (5)$$

$$\omega_r = \frac{\pi}{\tau} v \quad (6)$$

where  $\omega_r$  is the synchronous angular frequency.

According to the mathematical model in d-q rotating coordinate system, the equation of state of the electric current is obtained:

$$\begin{cases} \frac{di_{sd}}{dt} = \frac{u_{sd}}{L_d} - \frac{R}{L_d} i_{sd} + \frac{\pi v}{\tau} \frac{L_q}{L_d} i_{sq} \\ \frac{di_{sq}}{dt} = \frac{u_{sq}}{L_q} - \frac{R}{L_q} i_{sq} - \frac{\pi v}{\tau} \frac{L_d}{L_q} i_{sd} - \frac{\pi v}{\tau} \frac{\psi_f}{L_q} \end{cases} \quad (7)$$

According to the formula (7), there is a coupling term between the d-q axis current equations,  $L_q i_{sq} \pi v / \tau$  and  $L_d i_{sd} \pi v / \tau$ . It is a coupling of d-q axis caused by the inductance parameter  $L$  and the speed  $v$ .

### 2.1.2 The Voltage Feed-Forward Decoupling Unit

Due to the inductance of the feeder cable was led into consideration, the value of coupling term in formula (7) becomes larger. In addition, the coupling effect becomes stronger with the increasing of speed. The coupling term has great influence in the middle and high speed zone [5]. A part of the output voltage of traditional PI regulator is used to counteract the back electromotive force, the other part is used to control the d-q axis current [6]. Then, the regulation time is increased, the regulation accuracy and the dynamic performance of the system are reduced. To solve this problem, the state feedback of  $i_{sd}, i_{sq}$  and  $v$  are set as input of the voltage feed-forward decoupling unit. Then it passes through the output of the

d-q axis current regulator and works with the voltage feed-forward decoupling unit, as compensation voltage, to realize the decoupling control of d-q axis current loop.

Defining the  $u'_{sd}, u'_{sq}$  as:

$$\begin{cases} u'_{sd} = u_{sd} + \frac{\pi v}{\tau} L_q i_{sq} \\ u'_{sq} = u_{sq} - \frac{\pi v}{\tau} (L_d i_{sd} + \psi_f) \end{cases} \tag{8}$$

where  $u'_{sd}, u'_{sq}$  represents the voltage components after compensation in d-q reference frame respectively.

Putting formula (8) into formula (7), we get:

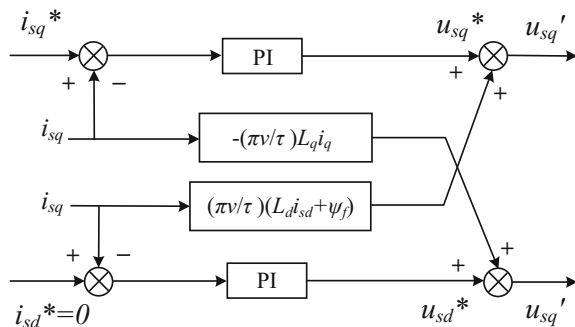
$$\begin{cases} \frac{di_{sd}}{dt} = \frac{u'_{sd}}{L_d} - \frac{R_s}{L_d} i_{sd} \\ \frac{di_{sq}}{dt} = \frac{u'_{sq}}{L_q} - \frac{R_s}{L_q} i_{sq} \end{cases} \tag{9}$$

According to formula (9), the parameters after coupling compensation can be calculated, as  $u'_{sd}$  and  $u'_{sq}$ . Then, the given item,  $u^*_{sd}$  and  $u^*_{sq}$  does not contain the coupling term anymore. The block diagram of the voltage feed-forward decoupling method is shown as Fig. 2.

### 2.2 The Vector Control System of PMLSM Based on Voltage Feed-Forward Decoupling

PMLSM vector control system consists of two closed-loops: outer PI speed closed-loop and inner PI current closed-loop. Transformed by Clarke and Park, the stator three-phase current is changed into two-phase rotating currents,  $i_{sd}$  and  $i_{sq}$ . The two currents are used as feedback values of the current loop to be compared with the given values [7]. The received signal is passed through the PI regulator, which is used as a compensation value for d-q axis voltage. The feedback current and

**Fig. 2** Control block diagram of current regulator with voltage feed-forward decoupling



feedback speed are input into the voltage feed-forward decoupling model, and then, the voltage signal is obtained through the Park inverse transformation. The voltage signal is input to the SVPWM control algorithm module to obtain the pulse signal, so as to realize the control of PMLSM. In the use of  $i_{sd} = 0$  vector control method, the stator current vector is located on q-axis, without any d-axis component. Namely, the stator current is used to generate thrust, and excitation flux of the drive motor is only proportional to the amplitude of the stator current. Under vector control with  $i_{sd} = 0$ , the control system becomes simple, the thrust fluctuation is small and wider range of speed control can be obtained [8].

After adding the voltage feed-forward decoupling unit, the dynamic performance of PMLSM vector control system is improved. The block diagram of the current controller with voltage feed-forward decoupling is shown as Fig. 3. The part inside dotted line is the voltage feed-forward decoupling unit.

### 3 Simulation Results and Analysis

According to Fig. 3, the vector control simulation model of PMLSM with traditional current regulator and modified current regulator based on voltage feed-forward decoupling is established in Matlab/Simulink. Except for the decoupling unit, other structures and parameters are consistent. The simulation parameters of PMLSM are given in Table 1.

Started at a given speed of 20 m/s. At 10 s, the given speed was increased to 25 m/s. Then, at 25 s, the given speed was reduced to 20 m/s. The acceleration is 0.5 and  $-0.5 \text{ m/s}^2$  in raising speed and decelerating speed processes, respectively.

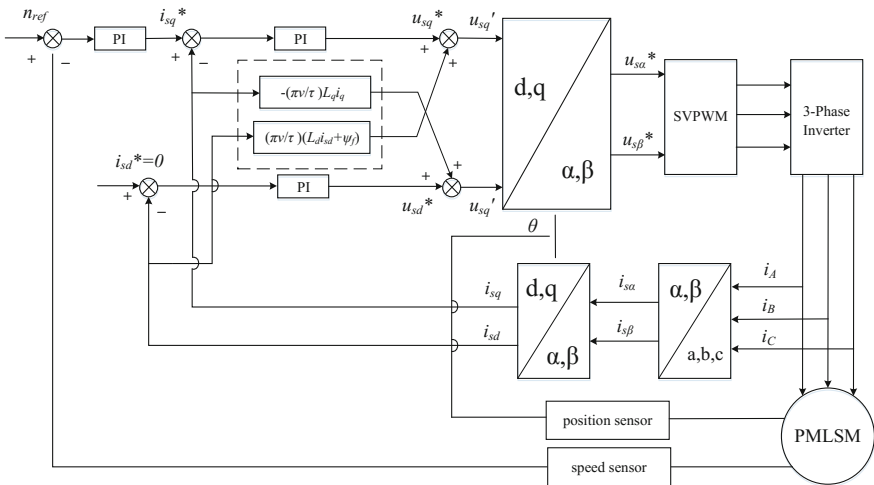


Fig. 3 Block diagram of PI regulator with voltage feed-forward decoupling

**Table 1** Motor parameters

Parameters	Value
Stator resistance $R_s$	0.985 $\Omega$
D-axis induction $L_d$	5.25 mH
Q-axis induction $L_q$	12 mH
Pole pitch $\tau$	0.196 m
Flux linkage $\Psi_f$	0.1827 Wb

The simulation results are shown below. The simulation waveforms of two control system are given as Figs. 4, 5, 6, 7 and 8.

As shown in Fig. 4, the motor can be stabilized at a given speed after the adjustment time and has a good tracking effect on the given speed.

As shown in Fig. 5, the adjustment time of traditional PI current regulator with adjustment time of modified PI current regulator are compared. The dynamic response time of traditional PI current regulator and the modified one are 1.1 and 0.8 s respectively. And the time motor taking to reach the steady state are 3.5 and 2.8 s respectively. Figure 5 implies that, after compensation, both of dynamic response time and the steady state time are shorter than before.

Figure 6 shows that the d-axis current remains near zero values throughout the operation, and there almost has no fluctuation, consistent with the control strategy mentioned in this paper.

As shown in Fig. 7, the three-phase current has little fluctuation when the motor starts. As the speed tends to steady state, the three-phase current will reach the corresponding stability. Everytime the speed changes, three-phase current can reach steady state quickly.

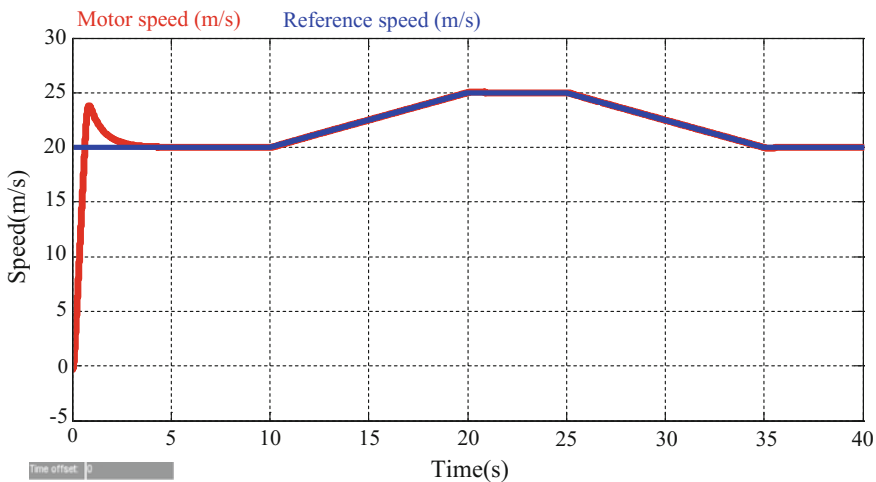


**Fig. 4** Speed of modified control method system

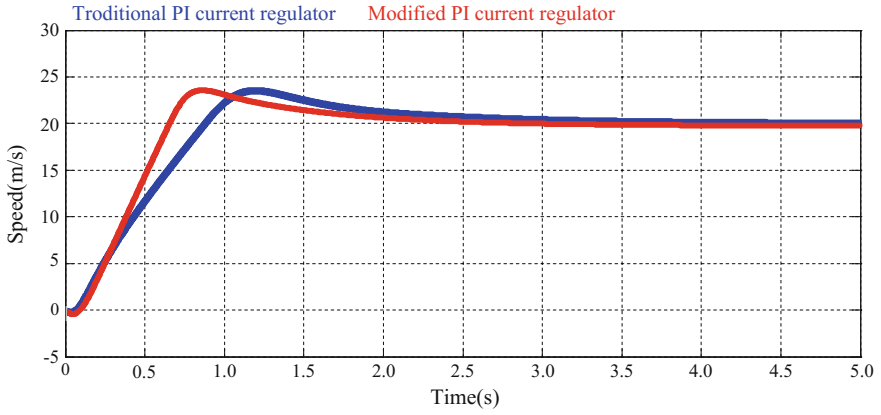


Fig. 5 Speed to time curve

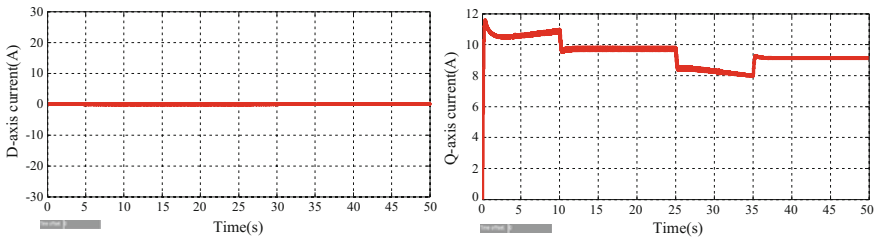


Fig. 6 D-q axis current to time curve

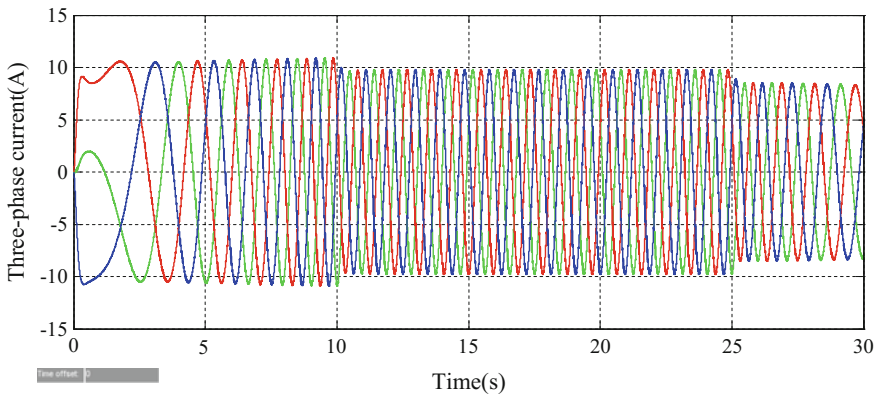
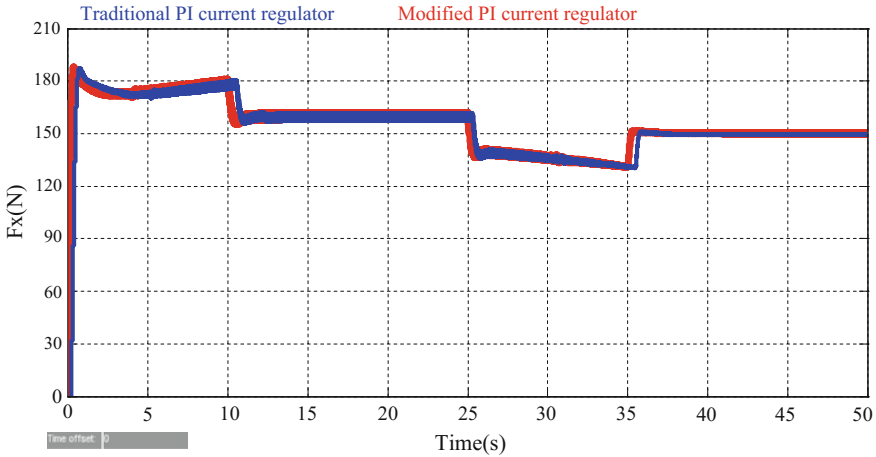


Fig. 7 Three-phase current to time curve





**Fig. 8** Thrust to time curve

Compared the red curve in Fig. 8 with Fig. 6, it shows that the horizontal thrust is linearly proportional to the quadrature component of stator current of motor. Almost all the parts of stator current are applied to producing the horizontal thrust of motor. The direct axis armature reaction is small, which is consistent with the theoretical analysis. Compared the two curves in Fig. 8, the dynamic response time of modified PI current regulator, after compensation, is faster than before.

The experimental results prove the correctness of control strategies. It shows that the current regulator with voltage feed-forward decoupling has faster response speed and better dynamic performance than the traditional PI current regulator.

## 4 Conclusion

In this paper, the effect of the inductance and resistance of uncoupled section and feeder cable in the system model of multiple motors connected in series is taken into consideration. Aiming to improve the dynamic performance of system caused by the ignoring of current coupling problem of d-q axis in traditional PI current regulator, a modified PI regulator with voltage feed-forward decoupling unit is presented. The experiment results indicate the feasibility and effectiveness of the modified regulator. This improved control system has faster responding speed, higher adjustment accuracy, better dynamic and static characteristic than traditional control system.

**Acknowledgements** This work was supported by National Key R&D Program of China (2016YFB1200601)

## References

1. Kosaka M, Uda H (2009) Parameters identification for interior permanent synchronous motor driven by sensorless control. *J Low Freq Noise, Vib Act Control* 28(4):269–293
2. Xuezheng C (2009) Analysis on different rotor structure synchronous motor vector control. *Intelligent computation international conference technology and automation (ICICTA) 2009*:143–147
3. Jiang H (2014) Research on driving motor and control strategy of permanent magnet hybrid maglev train. *J Southwest Jiaotong University* (in Chinese)
4. Zhang K, Qin B, Wang X, Liang F, Cao C (2016) Research on vector control of metro permanent magnet synchronous motor based on voltage feed-forward decoupling. *J Hunan Univ Technol* 05:22–26 (in Chinese)
5. Deng R, Tang J, Xian Y (2013) Decoupling control of current loops for permanent magnet synchronous motor based on feedforward compensation. *Power Electr* 06:68–70 (in Chinese)
6. Yang B, Deng F (2016) Research on vector control system of permanent magnet synchronous motor based on voltage Feed-forward current controller (04):64–66 (in Chinese)
7. Bian Y, Zhuang H, Zhang Y (2015) Decoupling control current loops for permanent magnet synchronous motor based on voltage feedforward. *Micromotors* 07:68–72 (in Chinese)
8. Liu T, Tan Y, Wu G (2009) Simulation of PMSM vector control system based on Matlab/Simulink. *Int Conf Meas Technol Mechatron Autom (ICMTMA) 2009*:343–346

# The LCL Filtering Scheme of High Power Four-Quadrant Converter Used in Urban Rail Transit

Dongsheng Xu, Gang Zhang, Fengjie Hao and Zhiqiang Hu

**Abstract** The regenerative braking energy of the train can be fed back to the medium voltage AC grid by using the high power four-quadrant converter, which has a good energy saving effect. But the traditional single-inductor filter is very large in size. In order to suppress the current harmonics, and reduce the volume and cost of the filter, the LCL filtering scheme of the large power four-quadrant converter for rail transit is introduced in this paper. The design method of LCL filter parameters is presented, and the damping control methods are studied. The filtering effect and stability of the proposed filter are verified by simulation.

**Keywords** LCL filter · Passive damping · Active damping

## 1 Introduction

Urban rail transit is mainly composed of subway, light rail and tram. Because of its advantages of safety, comfort, large capacity, fast operation, energy saving and environmental protection, it has become the solution to the increasingly serious problem of urban congestion. At present, China has entered a rapid development of city rail transit period.

The power consumption of urban rail transit is large, and the power used for traction power supply accounts for more than 40% of the total energy consumption. When the train is in the braking state, the motor is in the power generation state, and this energy is fed back to the DC power grid through the inverter. This energy has to be dissipated or exploited in some way, otherwise it will cause excessive voltage on the DC grid. Based on the high power four quadrant converter technology,

---

D. Xu (✉) · G. Zhang · F. Hao  
School of Electrical Engineering, Beijing Engineering Research Center of Electric Rail Transportation, Beijing Jiaotong University, Beijing 100044, China  
e-mail: 13291115@bjtu.edu.cn

Z. Hu  
Beijing Subway Operation Co., Ltd., Beijing 100044, China

the medium voltage energy feedback device can return the regenerative braking energy of the train back to the medium voltage AC grid. However, the four quadrant converter will bring harmonic problems. In order to meet the harmonic requirements of the grid, higher inductance is needed to eliminate the harmonic when using the traditional single-inductor filter. Due to the limited space of the transformer substation, the problem of volume and weight brought by the large inductance cannot be solved properly. Therefore, the existing filtering scheme needs to be optimized, and the volume and weight can be reduced by optimizing the scheme to reduce inductance values.

In order to reduce the cost and volume of the equipment, the traditional single-inductor filtering scheme is optimized and an optimization scheme using the LCL filter instead of the L filter is proposed in this paper. LCL filter is studied from parameter design, damping method and stability, and the performances of various damping methods are compared by simulation.

## 2 LCL Filter Parameters Design

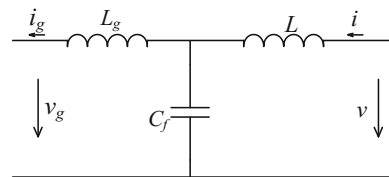
The circuit diagram of the single-phase LCL filter is shown in Fig. 1. These three parameters will be designed separately in the following [1, 2].

### 2.1 Design of Converter Side Inductance

First of all, the current ripple of the converter side must be limited. Higher switch stress and power loss will be caused by excessive current ripple. Therefore, when designing the filter parameters, not only the harmonic need to meet the requirements, but also the current ripple of the converter side is limited.

In order to limit the current ripple at the converter side, it is necessary to study the variation law of the inductance current at the side of the converter. When the maximum value is found, the amplitude of the current ripple can be limited. For the LCL filter, the current ripple at the converter side is mainly determined by the value of the converter side inductance  $L$ . The relation between the maximum current ripple and inductance is derived, as shown in the formula (1). The maximum current ripple is 30% of the peak current to determine the value of  $L$ .

**Fig. 1** Single phase LCL filter circuit



$$L \geq \frac{v_{dc}T}{4\sqrt{3}\Delta i_{\max}} \tag{1}$$

### 2.2 Design of Filter Capacitor

The filter capacitor of the LCL filter will generate reactive power. The greater the value of the filter capacitor, the greater the reactive power. Therefore, when designing the filter capacitor, the reactive power generated by the capacitor needs to be limited to less than 5% of the rated power of the converter. The voltage drop on the grid side inductance is ignored in the design. Therefore, the capacitor voltage is equal to the grid phase voltage, and the value of the filter capacitor can be obtained, as shown in the formula (2).

$$C_f \leq 5\% \frac{P_n}{3e_n^2\omega} \tag{2}$$

where  $e_n$  is RMS of power grid phase voltage.

### 2.3 Design of Grid Side Inductance

The grid side is equivalent to a short circuit and the converter is equivalent to a harmonic power supply in considering the higher harmonic state. Then we can draw a single-phase equivalent circuit for high harmonics, as shown in Fig. 2. Thus, the relation between the harmonic current attenuation can be obtained, as shown in the formula (3), and  $\gamma$  equals the ratio of the two inductance. By choosing the value of  $i_g/i$ , the value of the inductance of the grid side  $L_g$  can be determined. The value of  $i_g/i$  is generally around 20%.

$$\frac{i_g}{i} = \frac{1}{|\gamma(1 - \omega^2LC_f) + 1|} \tag{3}$$

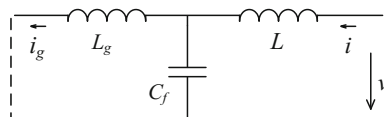


Fig. 2 Equivalent circuit of single phase LCL filter

### 2.4 LCL Filtering Effect Analysis

According to the design method of the previous section, the LCL filter parameters can be obtained. The final design result is that the converter side inductance is 137  $\mu\text{H}$ , the filter capacitor is 700  $\mu\text{F}$ , and the grid side inductance is 55  $\mu\text{H}$ . According to the circuit, the transfer function between  $I_g$  and  $V$  of the L filter and the LCL filter is shown in the formula (4) respectively. Then, the Bode diagram of the two filters can be drawn, as shown in Fig. 3.

$$\begin{cases} G_1(s) = \frac{I_g(s)}{V(s)} = \frac{1}{Ls} \\ G_2(s) = \frac{I_g(s)}{V(s)} = \frac{1}{L_g L C_f s^3 + (L_g + L)s} \end{cases} \quad (4)$$

According to Fig. 3, the attenuation rate of the LCL filter is obviously faster in the high frequency section, so the LCL filter can work even the total inductance is reduced.

### 3 LCL Damping Method

According to the amplitude-frequency characteristic of the LCL filter, the resonance spike can be seen at the 960 Hz. The control block of the current inner loop is shown in Fig. 4. The open-loop transfer function of the current inner loop is shown in Eq. (5).

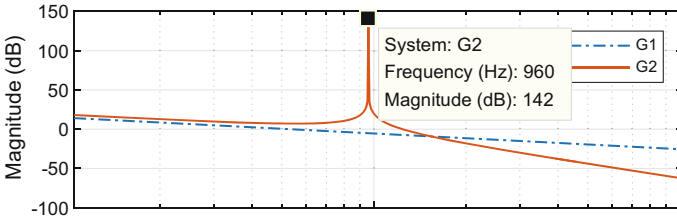


Fig. 3 Bode diagram of L and LCL filters

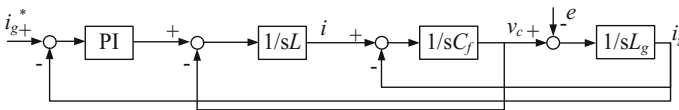


Fig. 4 Block diagram of current inner loop system with no damping

$$G_{o2} = \frac{K(1 + s)}{L_g L C_f s^4 + (L_g + L)s^2} \tag{5}$$

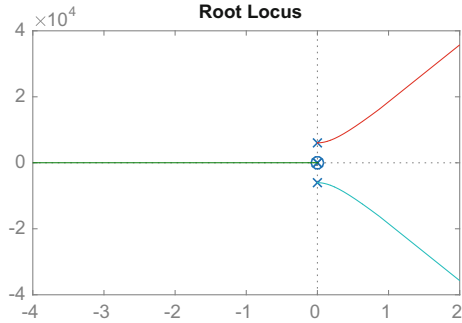
The root locus of the system can be drawn according to formula (5), as shown in Fig. 5 [3]. It shows that regardless of the value of the open-loop gain, the poles are always on the right side of the imaginary axis, so the system is unstable. Therefore, it is necessary to add damping to the control system in order to make the system stable [4, 5].

### 3.1 Passive Damping

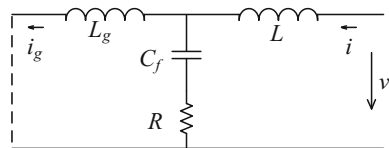
The simplest way to increase system damping is adding resistors in the loop of the filter, which is called passive damping. The common passive damping method is to add series resistance in the filter capacitor branch, and the single-phase equivalent circuit for high harmonics is shown in Fig. 6.

The control block diagram of the inner loop can be obtained from the circuit, as shown in the Fig. 7. According to Fig. 7, the open-loop transfer function at this time can be obtained, as shown in the formula (6), and the root locus of the system can be obtained, as shown in the Fig. 8a. Therefore, the system can be stabilized by selecting proper open-loop gain.

**Fig. 5** Root locus of system with no damping



**Fig. 6** Circuit diagram of series resistance of capacitor branches



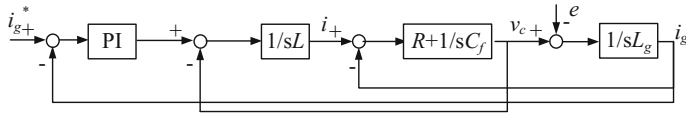


Fig. 7 Block diagram of current inner loop system with passive damping

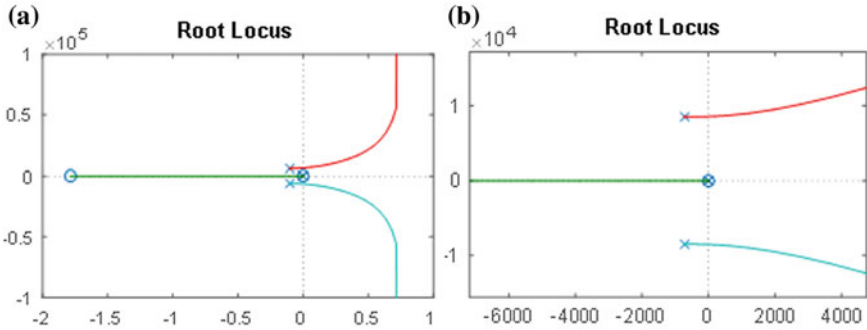


Fig. 8 Root locus of system with passive damping and active damping

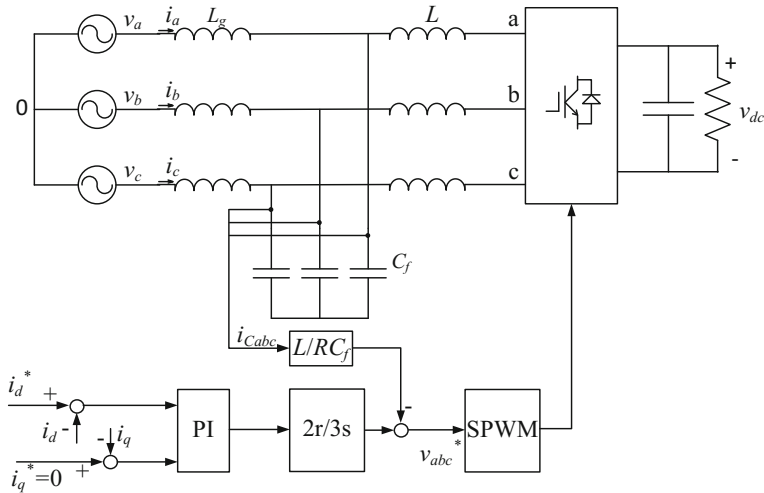


Fig. 9 Structure diagram of current inner loop system with active damping

$$G_{o3} = \frac{K[C_f R s^2 + (C_f R + 1)s + 1]}{L_g L C_f s^4 + C_f R(L_g + L)s^3 + (L_g + L)s^2} \tag{6}$$



### 3.2 Active Damping

Passive damping method can increase system damping and restrain resonance effectively, but it also increases loss. The method of increasing damping by correcting the control system is called active damping [6].

Figure 10 is a system block diagram of an active damping method [7, 8]. The concrete implementation method can be got according to the diagram, as shown in Fig. 9 [9]. After feeding back the capacitor current, the open-loop transfer function of the system can be obtained according to the system block diagram of active damping method, as shown in the formula (7). The root locus of the system can be drawn, as shown in Fig. 8b, which shows that the system remains stable by selecting the proper open-loop gain.

$$G_{o4} = \frac{K(1+s)R}{L_gLC_f s^4 + L_gLs^3 + (L_g + L)Rs^2} \tag{7}$$

## 4 Simulation Result Analysis

The converter simulation model using L filter and LCL filter is built by MATLAB/Simulink. Figure 11a is the grid current harmonics using 300 μH single inductor filter. Figure 11b is the grid current harmonics using LCL filter without damping. Figure 11c is the grid current harmonics using LCL filter with passive damping. Figure 11d is the grid current harmonics using LCL filter with active damping. The LCL filter parameters are the same as the parameters above.

When using LCL filter without damping, system loses its stability. But LCL filter with damping has better filtering effect comparing with L filter, and both damping methods can guarantee the stability of the system. Compared with the active damping method, the passive damping method is better in resonance suppression.

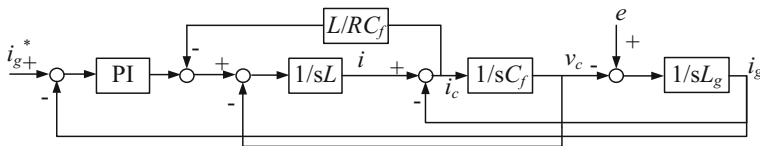


Fig. 10 Block diagram of current inner loop system with active damping

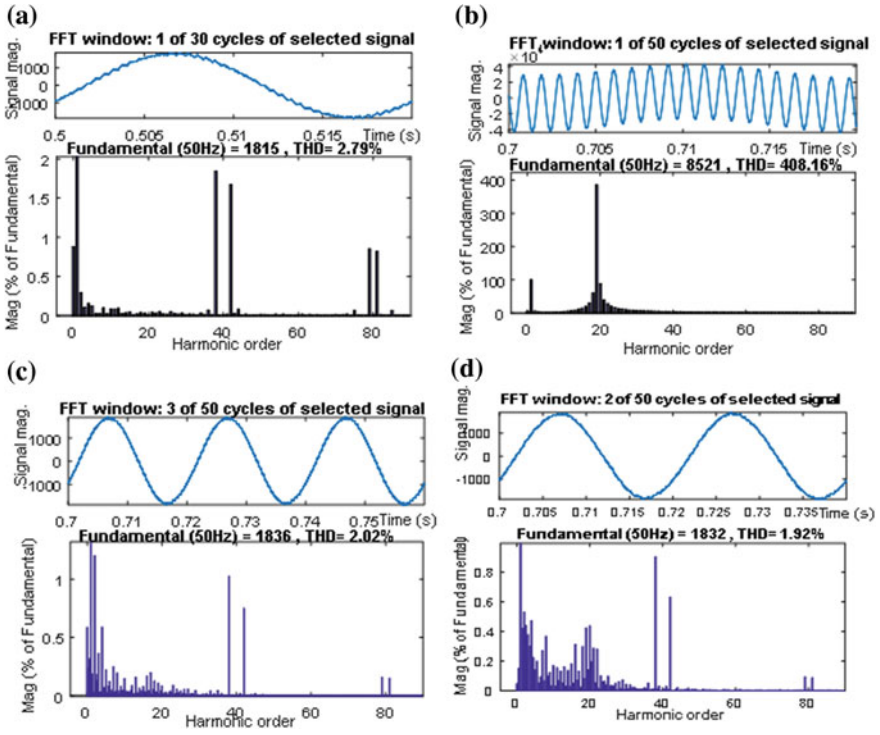


Fig. 11 The grid current harmonics of different filter

## 5 Conclusion

In this paper, the LCL Filtering Scheme of High Power Four-quadrant Converter is introduced. The LCL filter and the traditional single-inductor filter are compared from the point of view of transfer function. Then, according to the resonance phenomenon of LCL filter, a passive damping method and an active damping method are proposed to increase the system damping. The stability of each damping method is analyzed from the point of the root locus. Finally, the simulation results show that the LCL filter has a better filtering effect, and the proposed damping schemes are effective.

**Acknowledgements** This research was supported by National Key R&D Program of China 2017YFB1200800 and the Beijing Science and Technology Commission project Z1711000 02117011.

## References

1. Liserre M, Dell'Aquila, Blaabjerg B (2002) Stability improvements of an LCL-filter based three-phase active rectifier: 2002 IEEE 33rd Annual IEEE Power Electronics Specialists Conference. Proceedings (Cat. No.02CH37289)
2. Liserre M, Blaabjerg F, Hansen H (2004) Design and control of an LCL-filter-based three-phase active rectifier. *IEEE T IND APPL* 41(5):1281–1291
3. Freijedo FD, Rodriguez-Diaz E, Golsorkhi G, et al (2017) A Root-locus design methodology derived from the impedance/admittance stability formulation and its application for lcl grid-connected converters in wind turbines. *IEEE T Power Electr* 32(10):8218–8228
4. Xin Z, Wang X, Loh PC, et al (2017) Grid-current-feedback control for LCL-filtered grid converters with enhanced stability. *IEEE T Power Electr* 32(4):3216–3228
5. Wu W, Liu Y, He Y, et al (2017) Damping Methods for resonances caused by LCL-filter-based current-controlled grid-tied power inverters: an overview. In *Transactions on Industrial Electronics, IEEE*, p 1
6. Huang Q, Rajashekara K (2017) Virtual RLC active damping for grid-connected inverters with LCL filters. In *Applied Power Electronics Conference and Exposition (APEC), IEEE*, pp 424–429
7. Wang X, Bao C, Ruan X, et al (2014) Design considerations of digitally controlled LCL-filtered inverter with capacitor-current-feedback active damping. *IEEE J Emerg Sel Top Power Electr* 2(4):972–984
8. Saïd-Romdhane MB, Naouar MW, Slama-Belkhodja I, et al (2017) Robust active damping methods for LCL filter-based grid-connected converters. *IEEE T Power Electr* 32(9):6739–6750
9. Sanatkar-Chayjani M, Monfared M (2016) Stability analysis and robust design of LCL with multituned traps filter for grid-connected converters. *IEEE T Ind Electron* 63(11):6823–6834

# Performance and Thermal Analysis of Five-Phase Linear Induction Motor Optimal Control

Tao Tong, Jinlin Gong, Yadong Gao and Nicolas Bracikowski

**Abstract** Linear motors are featured with direct linear motion, but it has a low torque density due to the presence of edge effects. The torque density of five-phase linear induction motor can be improved by injecting high order harmonics of the magnetic field. The purpose of the paper is to present the optimal control strategy of a five-phase linear induction motor based on a rotor-flux-oriented control scheme, which promoted the performance of linear induction motor. The proposed control scheme is confirmed using finite element modeling and experimental tests. And the temperature distribution of the LIM shows temperature rise of the motor under this strategy is within the specified range.

**Keywords** Linear induction motor · Finite element method · Temperature

## 1 Introduction

As the advantages of simple structure, high acceleration and less mechanical loss between transmission parts for the linear induction motor (LIM), its technology and research have been developed rapidly in recent decades [1]. An increasing number of scientific research institutions, universities joined the ranks of LIM research, while more companies began to develop, manufacture and use the technology of

---

T. Tong (✉) · J. Gong  
School of Electrical Engineering, Shandong University, No.17923 Jingshi Road,  
Li Xia District Jinan, China  
e-mail: 441445952@qq.com

Y. Gao  
Zhejiang Huayun Electric Power Engineering Design & Consulting Co.,Ltd,  
No.1 Huadian Nong, Hangzhou, Zhejiang, China  
e-mail: gyd.zj@163.com

N. Bracikowski  
IREENA Laboratory, University of Nantes, No.1 Tourville, Nantes, France  
e-mail: nicolas.bracikowski@ec-lille.fr

LIM 错误!未找到引用源。. Induction motors are used for application requiring high power, such as trains (Maglev), naval propulsion, and roller coaster. They can also be found in some kinds of machine-tools or sliding doors. The electromagnetic device to be optimally sized in this paper is a 5-phase LIM, which is designed for the railway system application. For this application, the static part is the aluminum plate with back-iron which is installed on the ground, while the moving part is represented by the coils and laminations primary which are installed on the train. With the development of power electronic technology, the control technology of multi-phase machines ( $>3$ ) has attained significant proportions in the last decade [2]. Compared to classical wye-coupled three phase machines, these machines have more degrees of freedom than the minimum necessary, thus allowing a rotating field even with one opened phase [3]. In fact, even in normal working conditions with multi-leg Voltage Source Inverters (VSI), it is possible to take advantage of the numerous control strategies. Recent works and developments support the prospect of future more widespread applications, especially in low voltage and high power applications, such as electric vehicles, railway traction and all-electric ships [4].

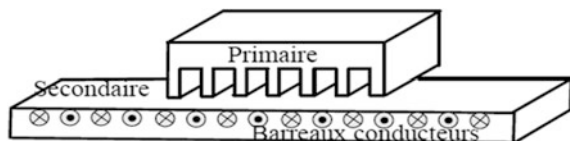
For induction machines, it has been shown that, for given RMS current, it is possible to increase the torque density by imposing non-sinusoidal airgap magnetic flux density and corresponding harmonic currents. Obtains with eleven phases induction machine 14% improvement of torque with third harmonic injection and up to 27% with injection of harmonics up to 9th harmonics [5]. This paper presents the torque improvement control strategy of a five phases linear induction motor using injection of the both first and the third harmonic current. The ratio between the first and the third harmonic is decided by parameters and constraints of the LIM.

## 2 Model of Five Phases LIM System

### 2.1 Basic Structure of Five Phases LIM

The linear induction motor LIM generally adopts the short stator technology, the stator coil (primary coil) is installed on the vehicle, and the rotor part is installed on the guide rail. The structure of LIM is shown in the Fig. 1. The LIM consists of two parts, the primary and the secondary. The LIM consists of two parts, the primary and the secondary. The primary is constituted by several slots, which coiled a winding around a steel lamination. A slippery magnetic field is created by the current of winding in the air gap, which induces a voltage in the secondary. A thrust is produced by the interaction between the current and magnetic field in the

Fig. 1 The structure of LIM



secondary. Different from the three phases LIM, five phases machines have more degrees of freedom than the minimum necessary [6], thus allowing a rotating field even with one opened phase.

The 2D Finite element methods (FEM) of the five phases LIM shows in Fig. 2, and the structure of model is parameterized. It is hard to analyze the model of LIM because of the end effects in the longitudinal direction, so a high quality of LIM is modeled to satisfy the calculation accuracy. A pretty mesh of LIM is shown in Fig. 2.

### 2.2 Control Strategies of LIM

The primary coil of the LIM is set on the vehicle [7], and the running condition and speed of the train are controlled by the driver of the train, so it is called the train driving. Unlike three phases machine, both first and third current harmonics can be used to produce a constant torque in the five phases machine. When the motor is running in one or three harmonic currents, the electromagnetic torque ( $T_e$ ) of a multiphases machine can be written as follows:

$$T_e = \frac{pN}{2} \left( \frac{M_1^2}{L_{R1}} I_{S1d} I_{S1q} + 3 \frac{M_3^2}{L_{R3}} I_{S3d} I_{S3q} \right) \tag{1}$$

where  $p$  is the pole pairs;  $N$  is the number of phases;  $M_{1,3}$  is the mutual inductance;  $L_{R1,3}$  is the rotor self-inductance of rotors; and  $I_{S1d}$ ,  $I_{S1q}$ ,  $I_{S3d}$ , and  $I_{S3q}$  are the component of the stator current vector in d and q directions.

For a given RMS value of the applied current, a coefficient ( $r$ ) is introduced to express the distribution between the fundamental and third harmonic [6]. The optimal distribution  $r$  is the ratio of the injected fundamental and third harmonic currents as (2), and by optimizing the value, the optimum torque can be obtained with a constant RMS of the current.

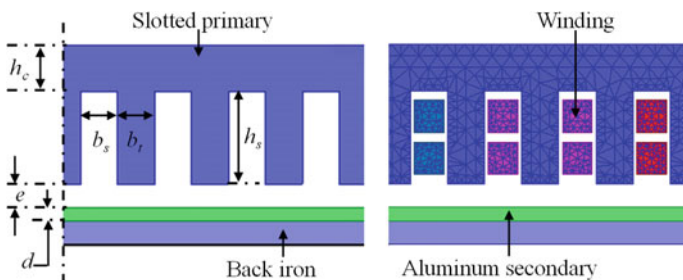


Fig. 2 Basic structure of the five-phase LIM and mesh representation using 2D-FEM

$$I_{RMS} = \sqrt{(I_1^2 + I_3^2)/2} \tag{2}$$

$$I_1 = \sqrt{2} \times \sqrt{1 - r^2} \times I_{RMS}, I_3 = \sqrt{2} \times r \times I_{RMS}$$

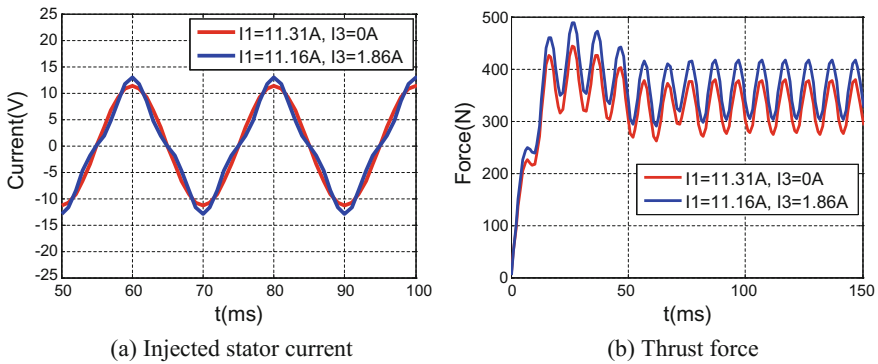
where  $I_{1,3}$  is the peak value of the first and third stator harmonic currents, and  $I_{RMS}$  is the RMS value of the injected stator current.

Figure 3 shows the performance of five phases LIM with different current injections simulated by 2D FEM. The injection with a third current harmonic produces 10.78% more thrust force with the same RSM current value. In conclusion, when to keep the injection current RMS value constant, the thrust force can be improved by optimizing the ratio of injected currents between fundamental and third harmonic.

### 3 Thermal Analysis of LIM

The temperature of a motor in the work condition is an important parameter, which has a close relationship with the output and life of the motor. In the analysis of thermal model, to facilitate the simulation conveniently, several basic assumptions and boundary conditions are come up combined with the actual motor conditions [8]:

- (1) Ignore the radiation effect of the motor, the thermal conductivity and heat dissipation coefficient of each motor`s part of the motor are constant regardless of the temperature`s change.
- (2) The outer insulation paint of the winding coil is evenly distributed, and is tightly wound on the surface of the iron core, and ignore the error caused by the insulating layer between the copper wires (means the winding coil can be equivalent to a whole consisting of enamelled copper wire). The internal parts of the motor are contacted well with each other, and the heat is completely conducted at the contact surface and the thermal resistance is neglected.



**Fig. 3** Five-phase LIM performance with the first and third harmonic current injections, **a** injected stator current, **b** thrust force

- (3) The transient change of the relative moving displacement of the stator and rotor equivalently when the motor is running is treated by changing the heat dissipation coefficient properly.

To construct a thermal model, it is not only necessary to quantify the different heat reservoirs, but also need to distinguish the boundary conditions and the heat transfer modes. The losses have been worked out in the electromagnetism model, and they are imported to the thermal model as the heat reservoirs to analyse the temperature distribution of the motor. The heat reservoirs are mainly consisted of core loss and copper loss, and through the finite element software coupling import. There are three types of heat dissipation: heat conduction, convection and radiation. Figure 4 shows the principle of coupling between the two models.

Thermal conduction is determined by the properties of material. It exists in the primary, secondary and coil so long as there is a temperature difference in the same solid. Thermal convection exists on all the interface with the air on the solid, and radiation exists on the space outside of heat reservoir. Thermal convection and radiation are both determined by the temperature difference.

As we know, the convection around the busbar is a problem of natural convection in large spaces. The convection coefficient of each side of the busbar is shown in Table 1.

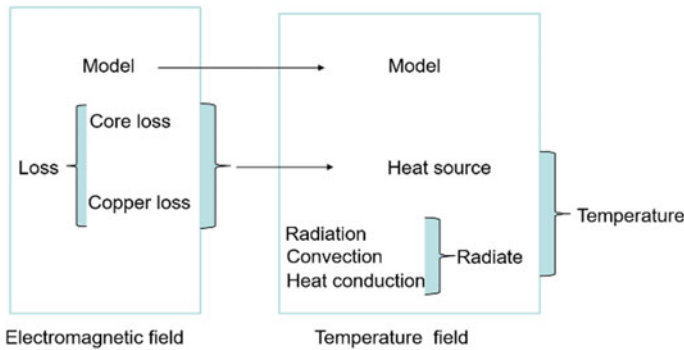


Fig. 4 Principle of coupled magnetic-thermal field analysis

Table 1 Convection coefficients of each surfaces

Material	Location	Convection(W/m <sup>2</sup> °C)
Primary	Top face	8.2
	Air gap face	15.5
	Side face	8.5
Secondary	Air gap face	15.5
	Outside face	6.3
	Bottom face	5.5
Coils	Inside	3.2
	Outside	15.5

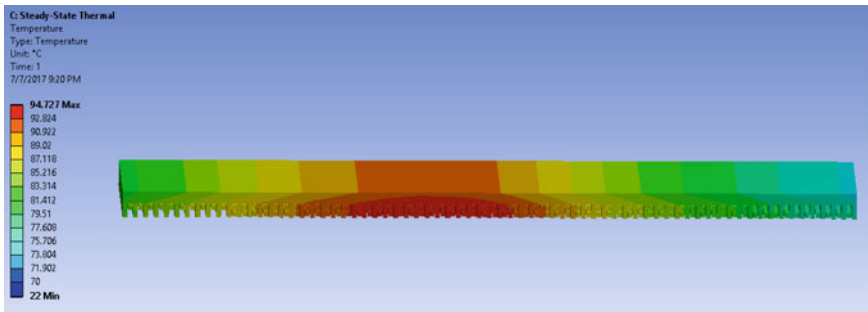


In the coupling analysis of the temperature and electromagnetic field, the loaded radiation coefficient of the conductor is 0.66 as the peripheral space reference temperature is 22 °C.

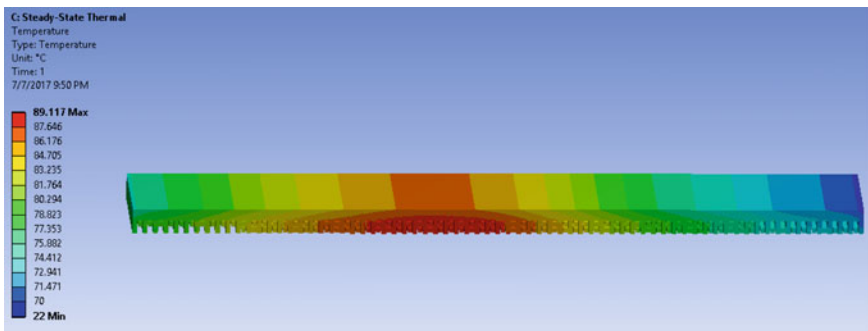
Figure 5 shows temperature distribution in the primary of five phases LIM. The maximum temperature with a third current harmonic is more than 4 °C lowers than with only first current harmonic. The average temperature with a third current is also about 5 °C lowers under the same RSM current value. It is because the injection with a third current harmonic produces a higher thrust force as mentioned previously, and has a higher the current utilization.

### 4 Experiment Validation

The simulation results are validated by a prototype which is shown in Fig. 6. The secondary is a composite type, while the primary fixed in the guide device, and the base is made of marble.



(1) The injection with only first current harmonic



(2) The injection with a third current harmonic

**Fig. 5** Temperature distribution in the primary of five phases LIM (1) The injection with only first current harmonic (2) The injection with a third current harmonic



**Fig. 6** Prototype of the five phases LIM

The control system of the prototype is based on DSP, which can input either ratio of current injection. Applying a different harmonic current to the motor and adjusting the load so that the motor is running at the rated speed [9, 10], the data of thrust and temperature is available by using a speedometer and a thermometer.

The difference of the thrust force between the simulation and the experiment is 23.2% of the measured result, which is due to the influence of friction and temperature. The results of software simulation are close to the results of the prototype experiment. It shows that the optimized control strategy performs better in terms of temperature.

## 5 Conclusion

Five-phase motor has a robust characteristic. Based on the 2D FEM, a five phases LIM is studied about its thrust force with an optimized control strategy as it can be controlled the same as rotating machine. To study the influence of the injection with a third current harmonic on the motor temperature, a thermal model is then modelled and coupled with the magnetic model. In the end, the simulation result is compared with the experimental result. The comparison shows that the multi-phase LIM have a better performance with a small amount third current harmonic injected.

In the future, the optimal distribution ratio between the first and the third harmonic current would be studied with a constant RMS value of current to get a better performance for different sizes of LIM.

**Acknowledgements** This work was supported by the National Natural Science Foundation of China under grant #51307099.

## References

1. Gong JL, Gillon F, Brochet P (2010) Magnetic and thermal 3D finite element model of a linear induction motor. In: Vehicle Power and Propulsion Conference, IEEE pp 1–6
2. Gong JL, Gillon F, Brochet P Comparison of optimized control strategies of a high-speed traction machine with five phases and Bi-Harmonic electromotive force. In: IEEE Transactions on Magnetics, vol 99, pp 1–1
3. Bojoi R, Cavagnino A, Tenconi A, Tassarolo A, Vaschetto S (2015) Multiphase electrical machines and drives in the transportation electrification. In: 1st International Forum on Research and Technologies for Society and Industry Leveraging a better tomorrow (RTSI), IEEE, Turin, pp 205–212
4. Abdelkhalik A, Masoud M, Barry W (2010) Eleven-phase induction machine: steady-state analysis and performance evaluation with harmonic injection. IET Electr Power Appl 4 (8):670–685
5. Gong JL, Gillon F, Brochet P Proposal of a kriging output space mapping technique for electromagnetic design optimization. Electromagnetic Field Computation IEEE, 2017:1–1
6. Huang LY, Huang XZh (2013) Numerical calculation of temperature field for tubular linear motor based on finite element method. Trans China Electrotech Soc 2:132–138
7. Ye Y, Lu Q (2011) Research and development of linear motor technology in China during recent decade. The 8th Symposium on Linear Drives for Industry Applications (LDIA2011). Eindhoven, Netherlands, 2011
8. Editors of Wikipedia. Radiation [G/OL]. Wikipedia. 2017. <https://en.wikipedia.org/wiki/Radiation>
9. Gong JL, Wang XH (2015) Multi-objective optimal design of a linear induction motor using efficient global optimization. Trans China Electrotech Vol. 30, (24):32–37
10. Barrero F, Duran MJ (2016) Recent advances in the design, modeling and control of multiphase machines—Part 1. IEEE Trans Ind Electron 63(3):449–458

# Thermoelectric Coupling Analysis and Thermal Protection for Busbar Trunking System

Xiaodong Yin, Tao Tong, Yujiang Li, Jinlin Gong and Xiaohui Wang

**Abstract** Generators with water-cooled stators and water-cooled rotor windings are often with aluminum conductor flat wires, which are close to the surrounding steel frame structure (SFS). The magnetic fields, generated by the strong alternating current in the busbar, can lead to eddy current losses in the steel structure and reduce its life cycle costs. In this paper, the influence on the SFS by the busbar is analyzed by using the finite element method. Firstly, the temperature distribution of the SFS is obtained through the coupled analysis of both magnetic field and the thermal field. Secondly, the thermal-protection measures are proposed and optimal designed in order to protect the SFS from overheating.

**Keywords** Thermal-protection measure · Thermoelectric coupling Busbar · Finite element model

## 1 Introduction

Dual water inner cooled generator is widely used in the thermal power plants, due to the advantages of simple auxiliary system, easily operation and low cost of maintenance [1].

Many researches [1–9] can be found in literature, most of them concerns the temperature rise or the heat dissipation problem of the busbar trunking, and the measures of isolated enclosed bus are studied and continually improved [7]. However, the influence of the busbar, the bar aluminum conductor flat wire, on the

---

X. Yin (✉) · Y. Li  
Shandong Electric Power Engineering Consulting Institute Corp., Ltd.,  
No. 106 Minziqian Road, Li Xia District Jinan, China  
e-mail: yinxiaodong@sdepci.com

T. Tong · J. Gong · X. Wang  
School of Electrical Engineering, Shandong University, No.17923 Jingshi Road,  
Li Xia District Jinan, China  
e-mail: 441445952@qq.com

surrounding Steel frame structure is out of concern, which has important effect on the life cycle costs of the steel. What's more, the equipment in the room is easy to repair and replace, so this thermal safeguard can reduce maintenance costs significantly in the long run [1].

The methods used to analyze the busbar trunking system are varied, such as the analytical method, semi-analytical method, and the numerical method (finite element method-FEM). For the reason of the rapidity, the analytical approach is preferred. However, with the development of computer capacity, the numerical methods are largely employed, such as multi-physical finite element method.

The analysis of the busbar is carried out by a fusion of a typical multi-physical topic, the electro-magnetic and the thermal field analysis are often coupled together [8, 10]. The mechanical analysis is also sometimes coupled [2]. In this paper, the magnetic field and the temperature distribution of the busbar and the surrounding SFS are analyzed using the coupled magnetic-thermal finite element method.

In this paper, the study is divided three parts. In the first part, the basic structure of the steel frame and the busbar of bare flat wire are introduced and then the magnetic field is analyzed using FEM. The flux density and losses distribution are figured out. In the second part, the temperature distribution of the SFS is obtained, thanks to the coupled magnetic-thermal model. In the third part, the thermal-protection measures are proposed and optimal designed using output space-mapping technique in order to protect the SFS from local overheating.

## 2 Magnetic Field Analysis Using Finite Element Method

### 2.1 Bare Aluminum Conductor and Steel Frame Structure

Figure 1 gives the basic structure of the surrounding STS, in which the blue ones are of U-shape steel (U-steel) and used to fix the bare conductors. There are six conductors, the front three is used as neutral point three of them are connected together with a neutral point and the other three ones are another three is used as power outlet busbar and transmit power. The six conductors carry nominated current of 12,500 A of 50 Hz, and the eddy currents are induced in surrounding STS and U-steel. In this part, the distribution of the magnetic field in the surrounding STS and the U-steel are analyzed using FEM and the losses are then calculated.

### 2.2 Flux Density Distribution

The flux density distribution is analyzed using FEM. The numerical model consists of 2,963,051 elements, and it takes 13 h for one analysis with steady state solver. Figure 2 shows the flux density distribution in the whole model of SFS (a) and in

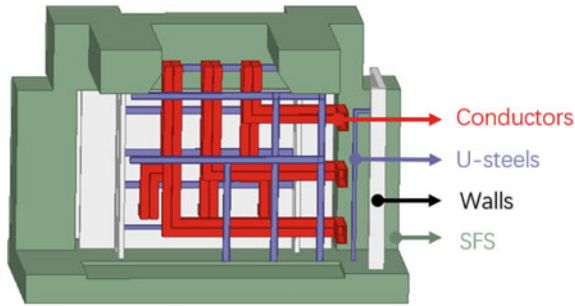


**Fig. 1** The layout of six busbar and the steel structure basic structure of the busbar trunking system

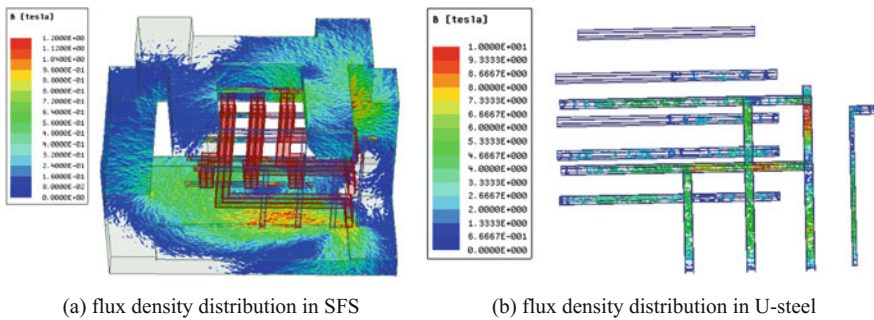


**Fig. 2** Flux density distribution by FEM, **a** flux density distribution in SFS, **b** flux density distribution in U-steel

the U-steel (b). The flux density is heavy in two places, one is the top right corner and the other is the bottom. Important eddy current and generate markedly losses, due to the magnetic field. The distribution of the magnetic field brought Important eddy current and generate markedly losses.

### 2.3 Losses Analysis

Two types of losses are concerned in the model: The Joule losses in the bare conductors and the eddy current losses in the SFS. The Joule losses in the bare conductors can be calculated as follows:

$$P_J = I^2 \frac{\rho l}{S} \tag{1}$$

where  $I$  is the current in the conductors;  $\rho$  is the resistivity of aluminum;  $l$  and  $S$  are the length and the section area of the conductors respectively. The Joule losses  $P_J$  is 8.052 kW.

For the calculation of losses in the SFS using FEM, ignoring the influence of space charge and displacement current, the permeability of the medium is considered to be linear. The basic equation of eddy current field is as follow [11]:

$$\nabla \times \frac{1}{\mu}(\nabla \times \mathbf{A}) = \mathbf{J}_s - \sigma_e \frac{\partial \mathbf{A}}{\partial t} \tag{2}$$

where  $\mu$  is the relative permeability of the material,  $\sigma_e$  is the conductivity of the eddy current conductor region,  $J$  is the current density.

The losses (including the Joule losses and eddy current losses) of the unit length of the conductor and the steel are calculated as follows:

$$q = \int \frac{J^2}{\sigma} dS \tag{3}$$

The result calculated in this step will be the unit heat reservoir load for the next step of temperature field analysis, which is the linkage between the electromagnetic filed and the temperature field.

The losses distribution in the model is shown in Fig. 3, and it is coherent with the flux density distribution in Fig. 2. The Joule losses and the eddy current losses are obtained using FEM are shown in Table 1.

The Joule losses  $P_J$  obtained by FEM is close to the value obtained by analytical approach, and therefore the finite element model is validated. The total losses of FEM could be considered as heat reservoirs and injected into thermal model in the next part.

Fig. 3 Losses distribution

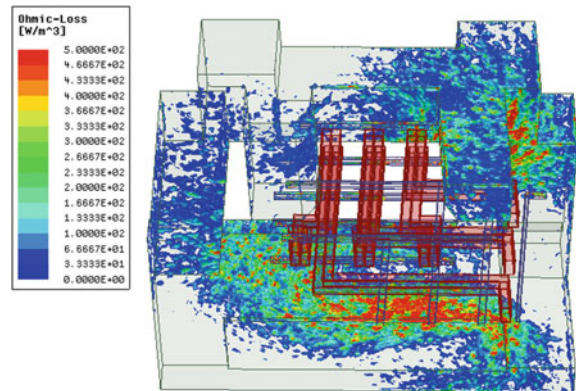


**Table 1** Losses in the model

Type of losses	Unit	Value
Joule losses $P_j$	kW	8.03
Eddy current losses in SFS $P_{e1}$	kW	18.74
Eddy current losses in U-steel $P_{e2}$	kW	6.28

### 3 Thermal Analysis Using Finite Element Method

#### 3.1 Basic Equation in Temperature Field

The purpose of the thermal model is to estimate the temperature distribution. To construct a thermal model, not only it is necessary to quantify the different heat reservoirs, but also need to distinguish the boundary conditions and the heat transfer modes. Three types of heat transfer modes occur in the model: radiation, conduction and convection.

Radiation is the emission or transmission of energy in the form of waves or particles through space or through a material medium [12]. Steels could convert heat by themselves, and there is a dynamic heat balance between the air and steel, and we can build their mathematical model by convection and radiation. The coefficient of radiation is decided by the Law of Stefan-Boltzmann [4]:

$$q_1 = \frac{A_i \sigma (T_i^4 - T_0^4)}{\frac{1}{\varepsilon_i} + (A_i/A_0)(\frac{1}{\varepsilon_0} - 1)} = \varepsilon \sigma (T_i^4 - T_0^4) \tag{4}$$

where  $A_i$ ,  $T_i$  and  $\varepsilon_i$  are the area, temperature and emissivity of the outer surface of the main conductor, while  $A_0$ ,  $T_0$  and  $\varepsilon_0$  are the area, temperature and emissivity of the inner surface of the shielded housing respectively.

Thermal conduction is the transfer of heat by microscopic collision of particles and movement of electrons within a body. The time rate of heat transfer through a material is proportional to the negative gradient in the temperature and to the area, which is known as Fourier’s law.

$$\vec{q} = -k \nabla T \tag{5}$$

where  $\vec{q}$  is the local heat flux density;  $k$  is the material’s conductivity;  $\nabla T$  is the temperature gradient.

Convection is the transfer of heat from one place to another by movement of fluids. The basic relationship for heat transfer by convection is expressed in (6)

$$\dot{Q} = hA(T_a - T_b) \tag{6}$$

where  $\dot{Q}$  is the heat transferred per unit time;  $A$  is area of the object;  $h$  is the heat transfer coefficient;  $T_a$  is the object’s surface temperature and  $T_b$  is the fluid temperature.



### 3.2 Coupled Magnetic-Thermal Model Analysis

The coupled magnetic-thermal model is presented in this part. The two models are coupled together through the eddy current losses and the joule losses. The same meshes are constructed in the both models. Figure 4 shows the principle of coupling between the two models. The losses in different part of the model are injected in the thermal models as heat reservoir. The modes of heat transfer and the corresponding coefficients are set up in the thermal model, and the temperature distribution is finally obtained.

### 3.3 Temperature Distribution

Thermal conduction is the main way of heat transfer in solids, which is determined by the properties of material. It exists in the conductors, steels and walls so long as there is a range of temperature in the same solid. Thermal convection exists on all the interface with the air on the solid, and radiation exists on the space outside of heat reservoir. Thermal convection and radiation are both determined by the temperature difference as (4) and (6).

As we know, the convection around the busbar is a problem of natural convection in large spaces. And it can be calculated by (4). The convection coefficient of each side of the busbar is shown in Table 2.

In the coupling analysis of the temperature and electromagnetic field, the loaded radiation coefficient of the conductor is 0.66 as the peripheral space reference temperature is 27 °C.

Figure 5 shows temperature distribution in the model. The U-steel of the top right corner has the maximum temperature, and it reaches up to 75.3 °C. For the STS, the bottom, the top right corner and the bottom left corner has higher

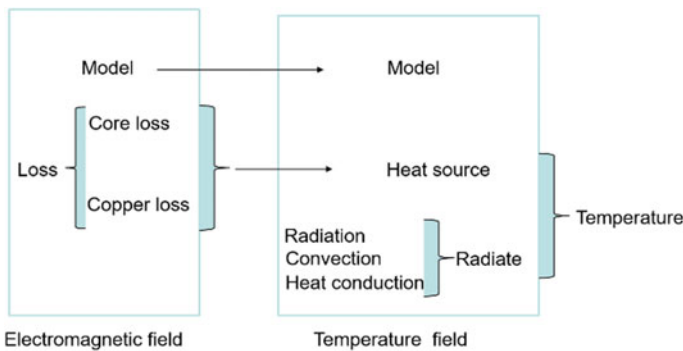


Fig. 4 Principle of coupled magnetic-thermal field analysis

**Table 2** Convection coefficients of outer surfaces

Material	Location	Convection(W/m <sup>2</sup> °C)
<i>conductors</i>	<i>Top face</i>	3.16
	<i>Bottom face</i>	6.54
	<i>Side face</i>	5.97
<i>steels</i>	<i>Top face</i>	5.79
	<i>Bottom face</i>	9.23
	<i>Side face</i>	8.12
Concrete	<i>Near the room</i>	6.32
	<i>away from the room</i>	3.22

temperature which is about 56 °C. Thermal-protection measures should be taken to extend service life, especially for the U-steel.

For the working current greater than 4000 A, the steel structure loss may be close to or exceed the loss of the conductor itself, which is confirmed in our simulation, and these losses cause steel overheating, personal safety and electrical appliances work properly [13]. And we see the allowable temperature as shown in the Table 3. 80 °C is the limiting temperature for the steel in the concrete while 70 °C for the steel in the busbar room. The maximum temperature in the busbar room is higher than the allowable limitation. What’s more, the allowable temperature in Table 3 is the data for a safety operation instead of an economical program to power plant. So, Actions should be taken to decrease the losses and lower the temperature of busbar system.

After grasp the relationship between the busbar and the thermal effect of the surrounding steel, a protection measure is come up with the function of inquiring and applying. Several FEM experiments show that thin plates made by aluminum are the best choice in thermal protecting.

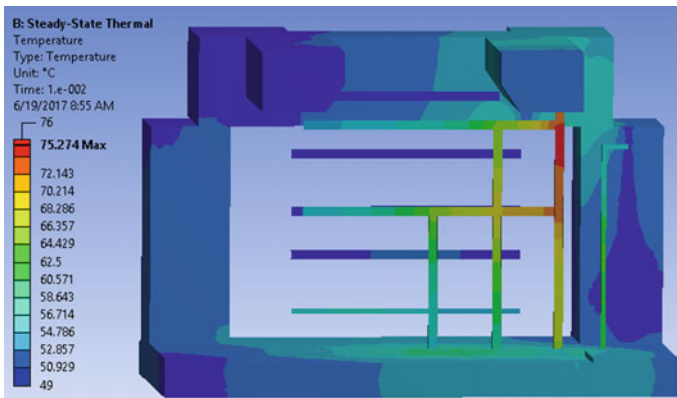


**Fig. 5** Temperature distribution

**Table 3** The allowable temperature for steel

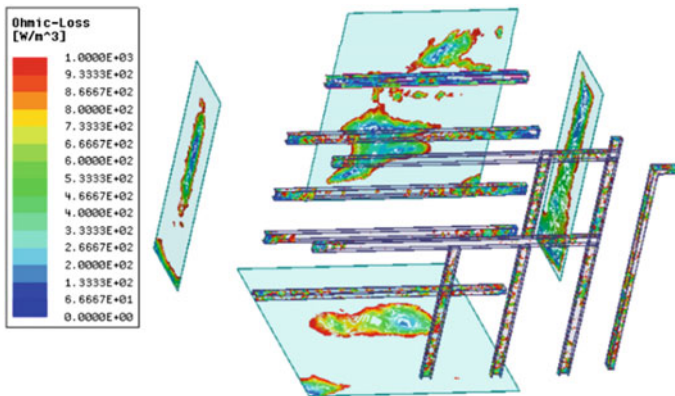
Position of the steel	Allowable temperature(°C)
Available to people	70
Unavailable to people	100
Steel in the concrete	80

### 4 Thermal-Protection

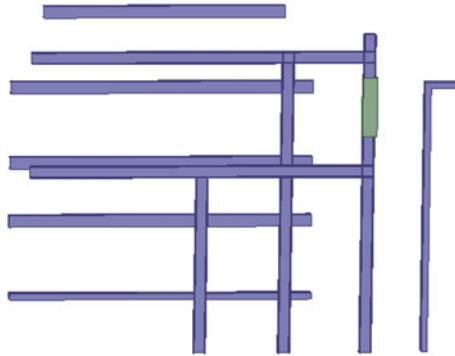
The thermal-protection measures are presented in this part. According to the analysis of the temperature distribution in the model, the aluminium sheets are mounted to the places of the SFS with high temperature, i.e. the bottom, the top right corner, the bottom left corner, and the back position, which is shown in Fig. 5. The effects of the aluminum sheets are that it can reduce the influence of the magnetic field from bare conductors, and reduce the temperature of SFS. The U-shape aluminum ring is installed outside U-steel, which is shown in Fig. 7. The losses due to the magnetic field can be partly induced in the thermal-protection devices which can be easily reinstalled and changed.

Figure 6 shows the location of SFS protection. Due to the thin physical structure and good performance of thermal conductivity, the temperature in aluminum sheets is not the highest. They can dissipate heat rapidly even though it produces the high heat density. So, the SFS protection is applied to decrease the overall temperature of the busbar room.

As the SFS protection has a satisfactory effect to decrease the overall temperature, the maximum temperature in U-steel keeps a high temperature. The U-shape retaining ring is presented in the Fig. 7. It has a same structure but a bigger than U-steel, which can be stuck in the steel outside exactly.



**Fig. 6** SFS protection



**Fig. 7** U-steel protection

The temperature distribution in the SFS and in the U-steel is shown in Fig. 8. Compared to Fig. 5b, the area with a high temperature of the SFS and the maximum temperature are both reduced. The maximum temperature of the U-steel is obviously decreased with the application of the thermal-protection measures.

Combining the measure with SFS and U-steel protection, the temperature has reduced both the overall and partial of the busbar room. The above method has a significant effect on the thermal protection and can be optimized to get a better performance.

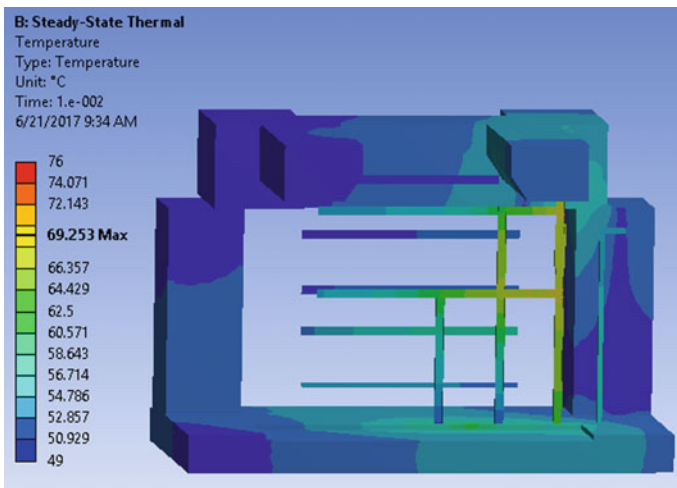


**Fig.** Temperature distribution with thermal protection

## 5 Optimal Design of Thermal-Protection Devices

### 5.1 Optimization Problem

The thermal-protection devices are optimal designed in this part using space-mapping technique. The optimization problem is presented in (7). It consists of four design geometrical variables:  $l$ ,  $w$ , and  $h$  are the length, width and thickness of the aluminum sheets;  $e$  is the thickness of the retaining ring for the U-steel. The maximum temperature of the SFS is taken as the constraint and should less than  $65\text{ }^\circ\text{C}$ ; The objective function is to minimize the cost of the aluminum sheets.

$$\begin{aligned} & \min_{l,w,h,e} \text{cost} \\ \text{s.t.} \quad & T_{\text{temperature}} \leq 65\text{ }^\circ\text{C} \\ \text{with} \quad & l \in [1500, 4000], w \in [2000, 4000], h \in [3, 10], e \in [10, 25] \end{aligned} \quad (7)$$

### 5.2 Space-Mapping Optimization Technique

Optimal design of electromagnetic devices using FEM is a time-consuming process, especially for a 3D one. The space-mapping optimization technique allows benefiting both from the rapidity of the analytical model (coarse model) and the accuracy of the FEM by aligning them. The flowchart of the basic mapping optimization process is presented in Fig. 1. The optimization is carried out with the coarse model and the results are then validated with the fine model. When the stop criterion is satisfied, the algorithm stops, otherwise the optimization continues with the modified coarse model using an updated mapping function.

Classically, the computationally cheaper and coarse model is denoted by  $c(z) \in \mathbb{R}^m$  with  $z \in Z \subset \mathbb{R}^n$ , the computationally expensive and fine model is denoted by  $f(x) \in \mathbb{R}^m$ . The nonlinear constraints of the coarse and fine models are  $k_c(x)$  and  $k_f(x)$ , respectively. The optimization problem is expressed as:

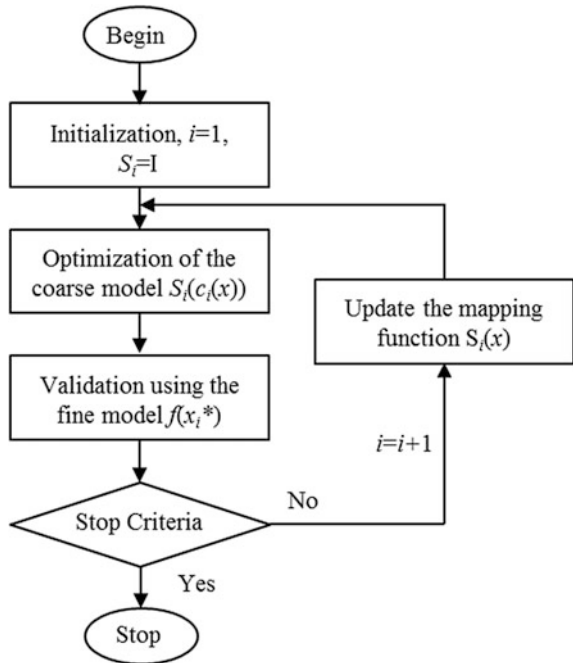
$$x^* = \arg \min_{x \in X} \|f(x) - y\| \text{ s.t. } k_f(x) \leq 0 \quad (8)$$

where  $y \in \mathbb{R}^m$  denotes a vector of design specification and can be zero in the case of minimization,  $x^*$  is optimal solution. This problem is hard to solve due to time-expensive model and is replaced by:

$$x_i^* = \arg \min_{x \in X} \|S_i(c(x)) - y\| \text{ s.t. } K_i(k_c(x)) \leq 0 \quad (9)$$

where  $S_i$  and  $K_i$  are respectively the mapping for the objective and constraint function (Fig. 9).

**Fig. 9** Flowchart of the space-mapping technique



### 5.3 Coarse Model

A set of 30 points in the parameter space is selected using Latin Hypercube sampling technique. The selected points are then evaluated using the 3D FEM (fine model), and the objective and constraint function values are obtained. For each objective and constraint function, a Kriging surrogate model is fitted over the sampling set. In this study, the Kriging model is chosen for its short simulation time (less than one second), rather than its accuracy.

### 5.4 Optimization Results

For the three techniques, the Matlab’s sequential quadratic programming (SQP) routine is used to solve the optimization on Kriging model. The optimal sizing problem was successfully tackled by the three low evaluation budget optimization techniques. The optimization results by SQP are shown on the Table 4.

**Table 4** Losses in the model

Variable	Initial design	OSM
$l$ (mm)	2500	2330
$w$ (mm)	3000	2823
$h$ (mm)	6	6.4
$e$ (mm)	16	13.3
3D FEM evaluation	–	9
Time (h)	8	72

## 6 Conclusion

In this paper, the eddy current losses are quantitatively calculated using FEM, the temperature distribution is figured out through the magneto-thermal modeling. The thermal-protective measures both for the steel frame structure and the U-steel are proposed to shield the eddy current losses, and the effectiveness is validated by the decrease of the maximum temperature both in SFS and U-steel and thus can extend the life cycle cost, which is very important to the thermal power plant.

## References

1. Keikko T, Kotiniitty J, Korpinen L (2000) Calculations of magnetic fields from indoor distribution substation busbars. In: Proceedings of the IEEE Power Engineering Society Transmission and Distribution Conference, vol 4. IEEE, Washington, pp 2309–2314
2. Xu S, Jin XL, Pang F, Shen J, Ma BL, Zhang XY (2005) A finite element analysis of 3D eddy current field for heavy current bus bar bridge System. *J Shanghai Jiaotong Univ* 12:2097–2101
3. Yan LJ, Zhang Y (2008) Calculation for temperature rise of large current closed bus. *High Voltage Engineering* 01:201–203
4. Ding B, Xu YL, Yang N, Dan SH (2010) Finite element analysis of coupled magneto-fluid-thermal field for large current enclosed bus bar. *High Volt Appar* 08:31–34
5. Hwang CC (1998) Analysis of electromagnetic and thermal fields for a bus duct system. *Electr Power Syst Res* 45(1):39–45
6. Wu AB, Zhang GG, Wang JH, Chen DG, Geng YS (2002) Analysis of thermal capacity for busbar trunking system by coupled magneto-fluid-thermal field calculation. *Adv Technol Electr Eng Energy* (03):62–66
7. Ho SL, Li Y, Lo EWC (2003) Analyses of three-dimensional eddy current field and thermal problems in an isolated phase bus. *IEEE Trans on Magn* 39(3):1515–1518
8. Km SW, Km HH, Hahn SC (2002) Coupled finite element analytic technique for prediction of temperature rise in power apparatus [J]. *IEEE Trans on Magn* 38(2):921–924
9. Zheng CY (2003) The eddy heat problem of the fixing bolt in the low voltage high current busbar frame. *Electric Drive* 06:52–54
10. Wu AB, Wang JH, Geng YS (2003) Finite element analysis of coupled magneto-thermal fields for compact busbar trunking system. *High Volt Appar* (04):7–10
11. Sheng JN (1991) Numerical analysis of engineering electromagnetic fields. Xi'an JiaoTong University Press, Xi'an

12. Editors of Wikipedia. Radiation [G/OL]. Wikipedia. 2017. <https://en.wikipedia.org/wiki/Radiation>
13. Ge DF (1989) Handbook of electrical design for power engineering. China Electric Power Press, Beijing



# Simulation of Short-Circuit Fault Occurring on Subway Train

Lei Sun, Mingli Wu, Jixing Sun and Shaobing Yang

**Abstract** Recently, with the large-scale development of subway, the safety of subway operation is attracting universal attention of the society. A short-circuit fault is a serious accident that threatens the safety of subway operation. The existing research focuses on the short-circuit fault occurring on the overhead line, but research on the short-circuit fault occurring onboard the subway train is rare. In this paper, a MATLAB/Simulink short-circuit fault model is built based on actual parameters of the subway train and the DC traction power supply system with MATLAB/Simulink platform. The currents of several branches are investigated through the simulation. The simulation result provides useful data when verifying the stability of electrical equipment and the accuracy of relay protection.

**Keywords** DC traction power supply system · Subway train · Short-circuit fault

## 1 Introduction

Nowadays, the safety of subway operation is becoming more and more important. Short-circuit fault is a frequent accident in the DC transit system. It may lead to serious hazards in the DC transit system [1]. Short-circuit fault may occur onboard the train. When a short-circuit fault occurring, the current surge can seriously damage the electrical equipment, and even endanger the person's safety. In order to verify the accuracy of relay protection, the short-circuit fault occurring onboard the train should be studied. The simulation model is built and the current waveforms are investigated in this paper [2]. Through the simulation results, the characteristics of the short-circuit fault are analyzed.

---

L. Sun · M. Wu (✉) · J. Sun · S. Yang  
School of Electrical Engineering, Beijing Jiaotong University, 100044 Beijing, China  
e-mail: mlwu@bjtu.edu.cn

## 2 DC Traction Power Supply System and Subway Train

In a conventional traction substation, the input voltage is normally AC 35 kV and the output voltage is DC 1500 V. The DC traction power supply network consists of the feeder, the overhead line, rails, the return wire and the subway train. The schematic diagram of the DC traction power supply system is shown in Fig. 1.

### 2.1 Rectifier Unit

The rectifier unit includes transformers and rectifiers. The AC voltage presented on the secondary side of the rectifier transformer is converted to DC by an AC/DC rectifier, and the 1500 V DC voltage can be obtained on the DC side of the rectifier. In order to improve power supply quality and reduce the DC voltage ripple factor, the multi-pulse rectifier is widely used. The rectifier unit develops from the earlier 6-pulse rectifier to the 12-pulse and 24-pulse rectifier [3]. In the DC traction power supply system, the axial double-split four-winding three-phase transformer is used, which is shown in the Fig. 2.

The 12-pulse rectifier consists of a rectifier transformer and two sets of parallel three-phase-bridge rectifier circuits. Rectifier transformer's two secondary windings are set to a triangle ( $\Delta$ ) and a star (Y) connection. Two rectifying bridges are run in parallel, and the equivalent 12-pulse rectifying voltage can be generated [4].

The schematic diagram of the 12-pulse rectifier circuit is shown in Fig. 3.

Two 12-pulse rectifier units of the same capacity combine a 24-pulse rectifier. One of them has  $+7.5^\circ$  phase-shifting in its primary side and the other  $-7.5^\circ$ . Two rectifier transformers and four groups of three-phase-bridge rectifier circuits form a 24-pulse rectifier unit, whose schematic diagram is shown in Fig. 4.

**Fig. 1** Schematic diagram of the DC traction power supply system

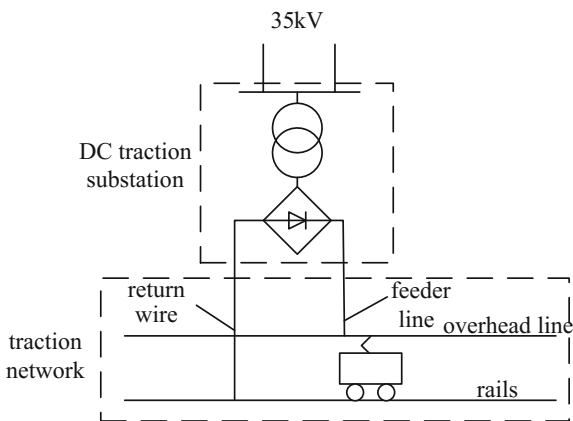


**Fig. 2** Diagram of axial double-spilt four-winding transformer

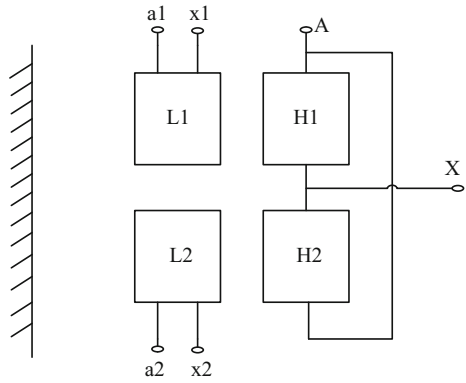


**Fig. 3** Schematic diagram of the 12-pulse rectifier unit

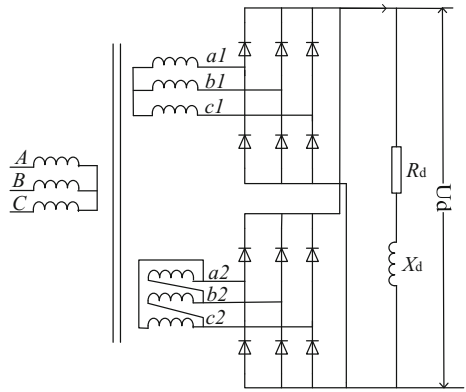
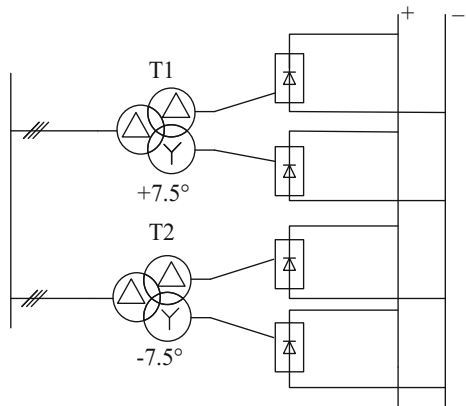


**Fig. 4** Schematic diagram of 24-pulse rectifier unit



### 2.2 DC Traction Network

DC traction network includes the overhead network, the return network and other components. The overhead line used as the positive electrode of traction net, through which the train can get electricity [5]. Return network is usually replaced by rails. There are a small number of subways using separate return network laying next to the rail. Return network used as the negative electrode of traction net, is the current reflow device [6–8].

The schematic diagram of the traction network is shown in Fig. 5.

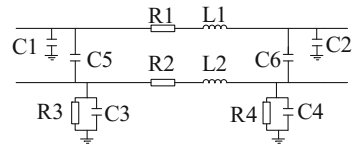
- R1 resistance of overhead line
- R2 resistance of rail
- R3, R4 resistances of rail to ground
- L1 inductance of overhead line
- L2 inductance of rail
- C1, C2 capacitances of overhead line to ground
- C3, C4 capacitances of rail to ground
- C5, C6 capacitances of overhead line to rail.

### 2.3 Subway Train

From the circuit diagram of subway train, it can be seen that Mc1 car’s electrical equipment includes a battery, a VVVF inverter and a motor. Mp1 car’s electrical equipment includes an auxiliary power box, two VVVF inverters and two motors. In M1 car, there is an auxiliary power box, two VVVF inverters and two motors. Pantograph installed in Mp1 car get electricity from the overhead line. The pantograph transmits power to the electrical equipment. Through cables, the pantograph is connected to electrical equipment. The normal electricity need of the electrical equipment can be guaranteed.

The circuit diagram of subway train is shown in Fig. 6.

**Fig. 5** Simplified circuit diagram of traction network



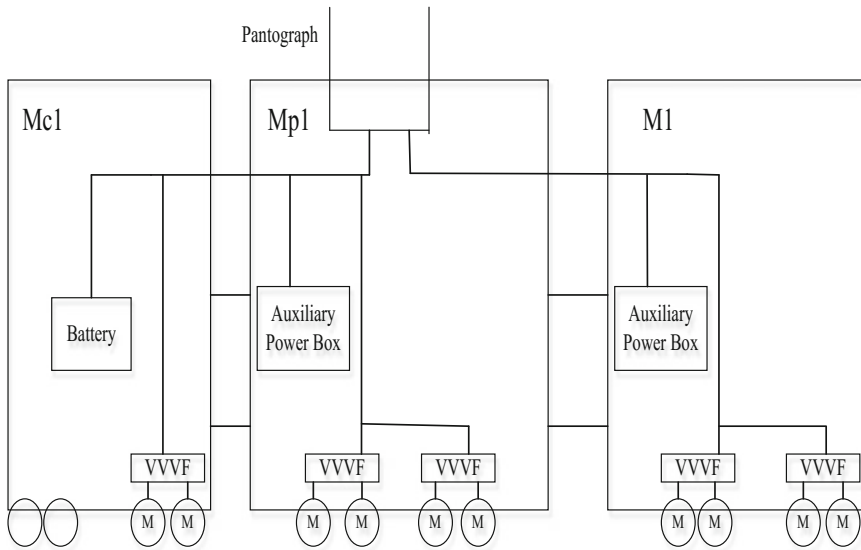


Fig. 6 Simplified circuit diagram of subway train

### 3 Parameters of Traction Network and Subway Train

According to the transformer design book, parameters of rectifier transformer used in an actual traction substation are summarized in Table 1. According to the traction network design book, parameters of the traction network are summarized in Table 2.

According to design book of the subway train, parameters of the subway train are summarized in Table 3.

When simulating the short-circuit fault of subway train, the train has no traction power, VVVF and the motor do not work. That branch can be ignored.

### 4 Schematic Diagram of Short-Circuit Fault Test

In the simulation of short-circuit fault test, only one substation is in operation. The subway train is 2.075 km away from the substation. The short-circuit point is located between inverter's large inductance and the high-speed breaker. The short-circuit point will be directly connected to the rail. The current of the feeder line and several branches of the subway train will be measured [9]. The schematic diagram of short-circuit fault test is shown in Fig. 7.

**Table 1** Parameters of 24-pulse rectifying transformer

Capacity	Connection mode	Primary rated voltage	Secondary rated voltage	Short-circuit loss	Percentage of short-circuit voltage	No-load loss	Percentage of no-load current
3300 kVA	Dy11d0/ Dy1d2	35 kV	1180 V	20200 w	8%	6000 w	1%

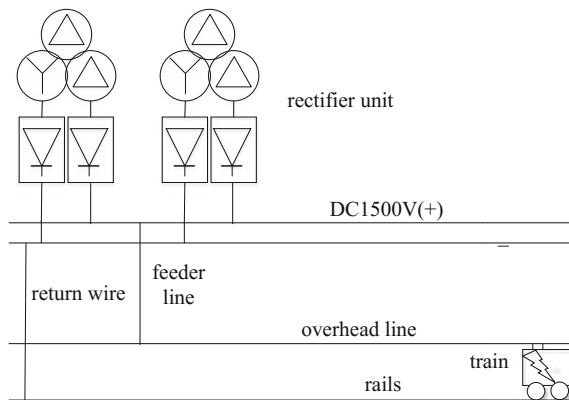
**Table 2** Parameters of the traction network

R1	R2	R3, R4	L1	L2	C1, C2	C3, C4	C5, C6
0.0136 Ω/km	0.020 Ω/km	20 Ω/km	2.533 mH/km	2.33 mH/km	3.7825 nF/km	13.77 nF/km	4.25 nF/km

**Table 3** Parameters of the subway train

Filter reactor and its resistance on the traction branch	Shunt capacitor and its resistance on the traction branch	Reactor on the auxiliary branch	Shunt capacitor and its resistance on the auxiliary branch	On-resistance and forward voltage drop of the clamp diode
8 mH, 55 mΩ	4000 uF, 0.6 mΩ	5 mH	3 mF, 0.9 mΩ	0.00028 Ω, 1.78 V

**Fig. 7** Schematic diagram of short-circuit fault test



## 5 Simulation Model

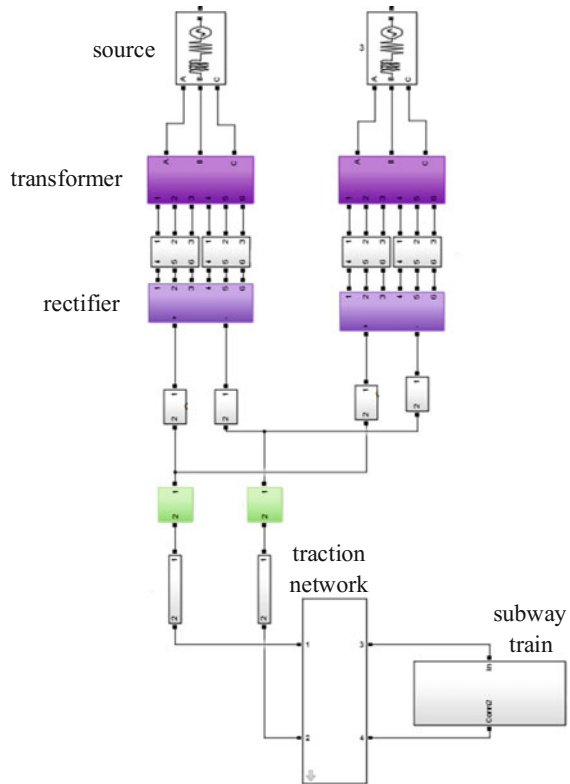
Based on the former analysis of the DC traction power supply system and subway train, this paper uses MATLAB/Simulink platform to build the short-circuit fault test model.

The simulation diagram of entire system is shown in Fig. 8. The simulation diagram of subway train is shown in Fig. 9.

## 6 Simulation Results

Through the parameter settings, short-circuit fault occurs at 0.5 s later after the simulation starting. When the simulation is finished, the waveforms of current can be observed.

**Fig. 8** Simulation schematic diagram of the entire system



The current of the feeder is shown in the Fig. 10.

When the short-circuit fault occurs, the current of feeder line increases exponentially, the steady-state value is about 16784 A.

The current of branch which has a short-circuit fault is shown in Fig. 11.

As shown in the figure, the current shows a upward trend of oscillation due to shunt capacitor's influence. The steady current is about 16788 A.

The current of traction branch is shown in the Fig. 12.

The current shows a regularly oscillating tendency because of the shunt capacitor's influence. The maximum current is about 1005 A. The current eventually becomes nearly 0 A.

The current of the auxiliary branch is shown in the Fig. 13.

Due to the effect of clamping diode at the inlet of the auxiliary branch, the current will not flow back to the main circuit when the short-circuit fault occurs. The current is small, almost 0 A.



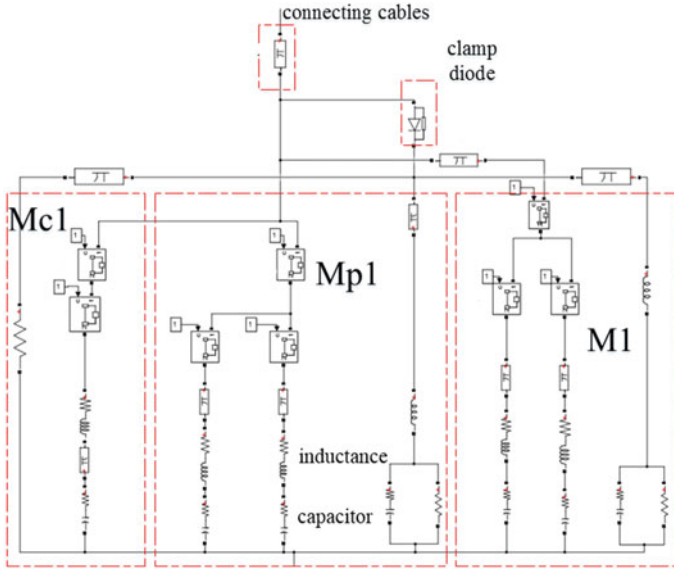


Fig. 9 Simulation schematic diagram of subway train

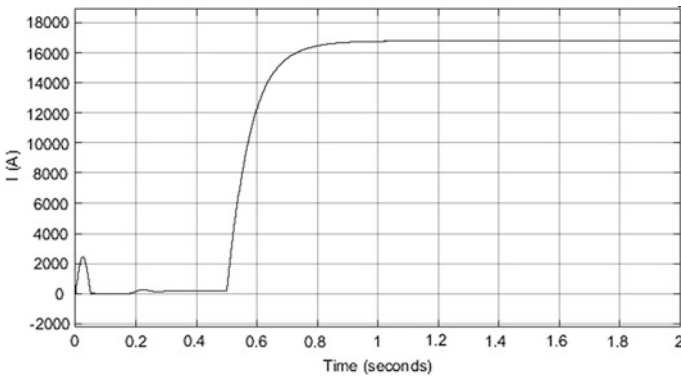


Fig. 10 Current of the feeder line

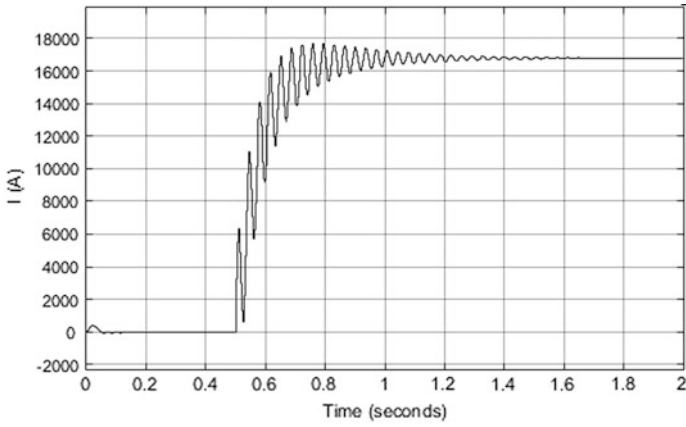


Fig. 11 Current of short-circuit branch

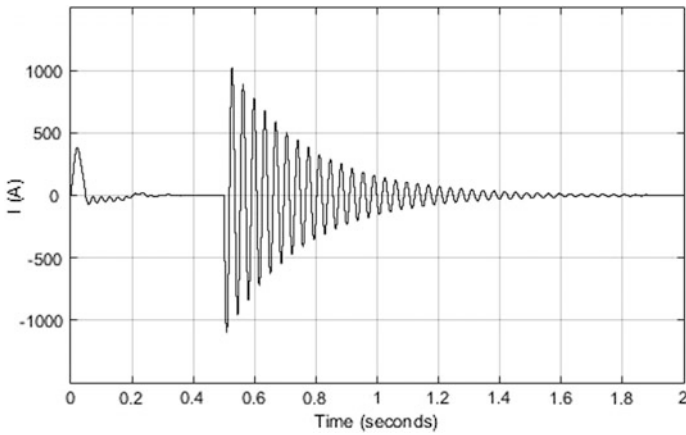


Fig. 12 Current of traction branch

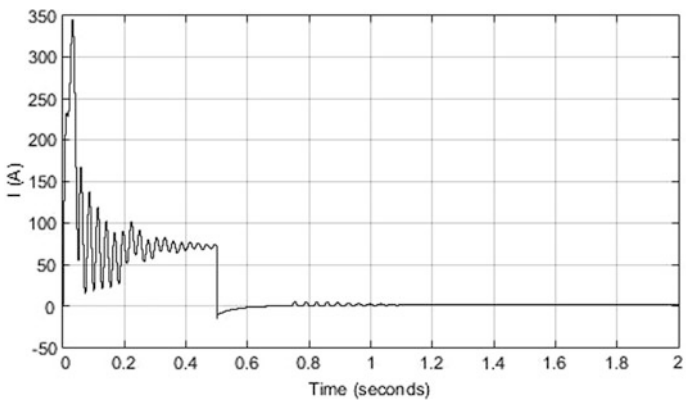


Fig. 13 Current of the auxiliary branch

## 7 Conclusion

The MATLAB/Simulink short-circuit fault test model of DC traction power supply system is built with MATLAB/Simulink platform, which includes rectifier unit model, DC traction network model and subway train model.

When short-circuit fault occurs onboard the subway train, the current can be investigated through this simulation model. The current of branch which has a short-circuit fault can reach to 16788 A. Through the simulation results, the detailed test plan and test equipment can be determined.

## References

1. Xiao T (2012) Analysis of subway DC power supply system model and DC short circuit. South China University of Technology, Guangzhou (in Chinese)
2. Yu L (2012) Research on power supply system and DC feeder protection of DC railway transit system. Beijing Jiaotong University, Beijing (in Chinese)
3. Xie F (2009) Research on the urban rail transit traction power supply rectifier. Southwest Jiaotong University, Chengdu (in Chinese)
4. Li L (2007) Simulation and application of external characteristics curve of 24-pulse rectifier in urban rail transit. *Res Urban Rail Transit* 10(15):52–55 (in Chinese)
5. Gong T (2009) Study on mathematical model and short circuit calculation of DC traction power supply system. Beijing Jiaotong University, Beijing (in Chinese)
6. Brown JC, Allan J, Mellitt B (1992) Calculation and measurement of rail impedances applicable to remote short-circuit fault current. *IEE Proc Electr Power Appl* 2(3):295–302
7. Li X, Wang K (2014) Transient circuit model and parameter analysis of DC traction power supply network. *Trans China Electrotechnical Soc* 29(12):166–172 (in Chinese)
8. Chang CS, Kumar S, Liu B and Khambadkone A (2001) Real time detection using wavelet transform and neural network of short circuit faults within a train in dc transit systems. *IEE Proc-Electr Power Appl* 148(3):251–256
9. Xu C, Wang H, Wang X (2013) Analysis of short-circuit calculation model of DC traction power supply system. *Power Syst Prot Control* 41(22):84–90 (in Chinese)

# Research on Vehicle's Combination Dashboard Diagnostic Protocol Stack

Yanming Li, Feng Gao, Yongliang Ni and Tingting Wu

**Abstract** As the development of Vehicle Electric and Electrical system, Vehicle's digital Combination Dashboard which can be used to learn about the whole vehicle's parameters by driver has made an important role in the reliability of whole vehicle. So it is necessary for us to acquire the whole vehicle's parameters and faults by realizing the on line and off line diagnosis of the combination dashboard. This paper develops a diagnostic design approach for vehicle's digital combination dashboard on the basis of ISO 15765. It has realized the on line and off line diagnosis for vehicle's combination dashboard in order to detect the vehicle's parameters and faults conveniently. The experiment proves that the diagnostic protocol stack is efficient and reliable, it can greatly increase the speed of maintain service for engineers.

**Keywords** Combination dashboard · Diagnostic protocol stack  
Online diagnosis · Multi frame transportation

## 1 Introduction

The development of modern vehicle electronic technology leads to the improvement of vehicle electronization and the increasing of vehicle control unit. Meanwhile, the maintenance and detection of vehicle become more complex, which bring challenges on locating faults and acquiring parameters quickly for basic maintenance staff. In order to solve this problem, self-diagnostic function has been integrated into the design of most of vehicle electronic control units, which can diagnose faults autonomously. By mean of this, the fault codes can be saved in the memory and can be output through the communication port. In virtue of the fault indicator lamps or specialized fault diagnostic devices on the combination dashboard, the operation

---

Y. Li (✉) · F. Gao · Y. Ni · T. Wu  
China North Vehicle Research Institute, Courtyard 4, Huai Shuling,  
FengTai 100072, Beijing, China  
e-mail: lym811016@163.com

© Springer Nature Singapore Pte Ltd. 2018

L. Jia et al. (eds.), *Proceedings of the 3rd International Conference on Electrical and Information Technologies for Rail Transportation (EITRT) 2017*, Lecture Notes in Electrical Engineering 482, [https://doi.org/10.1007/978-981-10-7986-3\\_61](https://doi.org/10.1007/978-981-10-7986-3_61)

597

parameters and fault codes of electronic control units can be easily acquired, and analysis therefore can be conducted conveniently with the assist of professional maintenance handbook. So it can be seen that the diagnostic system is essential in the process of vehicle post maintenance.

As an important digital component of vehicle, combination dashboard is in charge of the display of vehicle system parameters, fault codes from ECU, as well as the formation of alarm logic. So the faults of combination dashboard may bring serious influence for the operation of vehicle. Therefore, it's essential to develop a combination dashboard diagnostic system to real-time display the dash parameters as well as to acquire related faults when the vehicle is stopped.

On line and off line methods are combined for vehicle diagnostic at present. Based on the ECU software and hardware, on line diagnostic can realize the self-diagnostic of each part of real-time monitoring of electronic control system during vehicle operation, in order to detect the faults of electronic control system. The self-diagnostic system can send faults information to driver by certain method (alarm indicator for instance), meanwhile save the faults code and related data into ECU memory, which can be displayed through external diagnostic device. In the other hand, off line diagnostic can operate through diagnostic information acquired from external diagnostic device. The key point to realize the diagnostic is that the communication and service between diagnostic devices and ECU, which is called diagnostic protocol stack.

## 2 Diagnostic Protocol

Conventional diagnostic protocol can be categorized into ISO (International Organization for Standardization) and SAE (Society of Automotive Engineers). The USA adopts SAE standard system, while most of other countries, including China, adopt ISO standard system. Table 1 gives the contrast of the two standard systems [1].

This paper mainly gives the design of combination dashboard diagnostic protocol stack based on the enhancement diagnostic method, and the ISO enhancement diagnostic system is now broadly adopted, so here mainly gives the introduction of ISO 15765 diagnostic system.

**Table 1** Contrast of ISO AND SAE diagnostic standard

OSI reference model	OBD diagnosis		Enhanced diagnosis	
	ISO	SAE	ISO	SAE
Application layer	15031-5	J1939-73	14229/15765-3	J2190
Transport layer	15765-4	J1939-21	15765-2	
Data link layer	11898-1	J1939-21	11898-1	J1939-21
Physical layer	11898-2/3	J1939-11	11898-2/3	J1939-11

ISO 15765 Protocol is suitable for the vehicle diagnostic system based on CAN communication network. This protocol defines the generic specification applied on vehicle diagnostic system based on CAN bus. ISO 15765 is accord with the seven layer model recommended by OSI. According to OSI model, ISO 15765 mainly defines the layers as below (Fig. 1).

- (1) Application layer, established by ISO 15765-3.
- (2) Transport layer, established by ISO 15765-2.

ISO 15765 transport layer is adopted to send and receive message and report the results [2]. Because the longest size of a frame of CAN message is 8 bytes, the transport methods for data shorter and longer than 8 bytes are different. For data shorter than 8 bytes, a frame of CAN message is enough, which is called as single frame transport and is shown in Fig. 2. Data longer than 8 bytes should be divided and send by several CAN messages, and should be reformed when reception is finished, which is called multi frame transport, and is shown in Fig. 3.

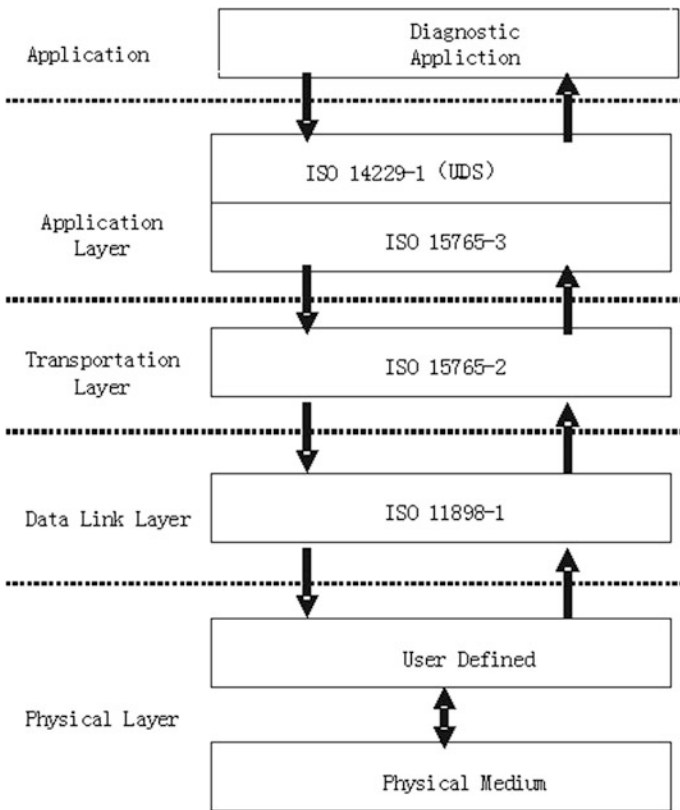


Fig. 1 ISO 15765 system scheme

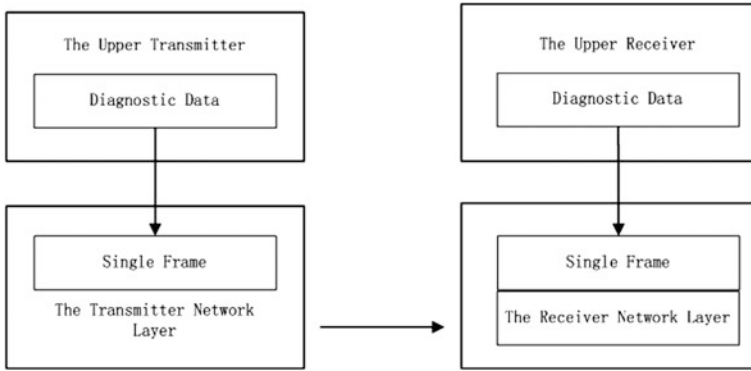
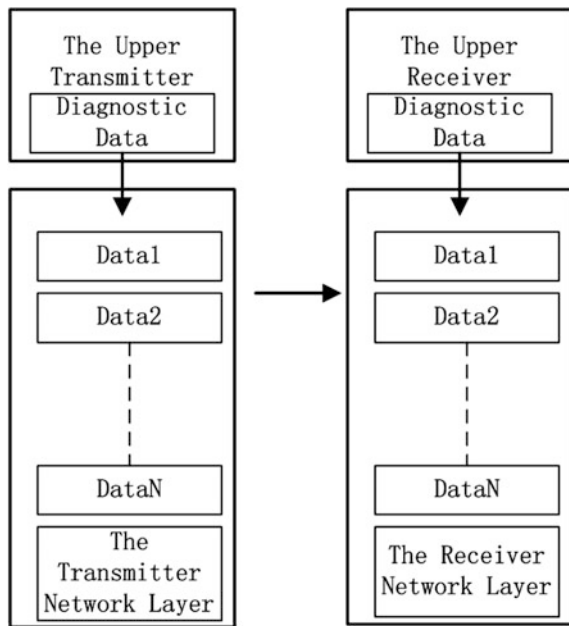


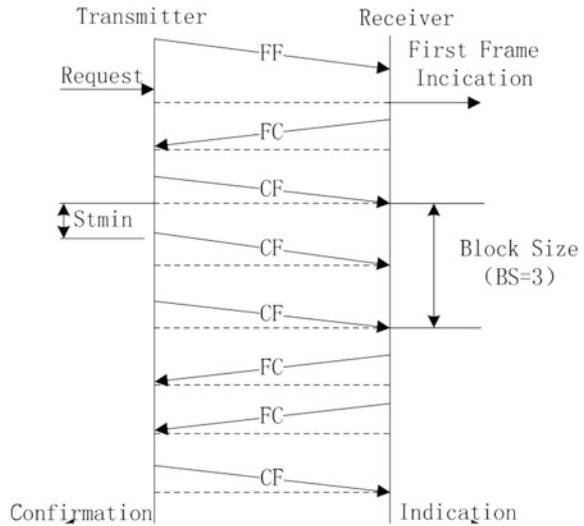
Fig. 2 Single frame transportation

Fig. 3 Multi frame transportation



In the process of multi frame transport, sender and receiver need exchange information constantly. Sender firstly sends a first frame to inform the length of data to be transport; after the related resource distribution and preparation to receive data, receiver returns a flow control frame to set the quantity of data pocket send for once and the time interval, and sender can transport data based on the setting. This kind of transport mechanism is mentioned as flow control mechanism, which is shown in Fig. 4. Through this mechanism, receiver can authorize sender to continue or delay remained continuous frame, or cancel the reception process when data

**Fig. 4** Flow control mechanism process



length exceeds the size of its reception buff. There are two key parameters which can define the receive ability in flow control frame mechanism.

- (1) Block Size (BS), which means the maximum reception quantity of CAN message for once, when CAN frame exceeds BS, more authorization are need to continue the process.
- (2) Shortest Transport Interval (STmin): the minimum interval between two continuous frames.

The application layer ISO 15765-3 follows the ISO 14229 (unified diagnostic service) protocol, designs the transport scheme based on ISO 15765-2. In the communication mode based on ISO 15765, messages execute different requests and response service functions according to the Service ID (SI) included in the first byte of data field. According to the service function, protocol application layer can be divided into six units, including diagnostic and communication management unit, data transport unit, existing data transportation unit, input/output control unit, remote routine activation unit and upload/download unit. The main diagnostic service of each unit are shown in Fig. 5.

### 3 Development of Diagnosis Architecture

The combination dashboard diagnosis architecture is realized mainly by its diagnostic protocol stack and the support of master computer software.

The diagnostics system master computer software is developed based on PC platform, and is connected with CANcaseXL from Vector Co. through USB interface. As the hardware device to support the master computer software,



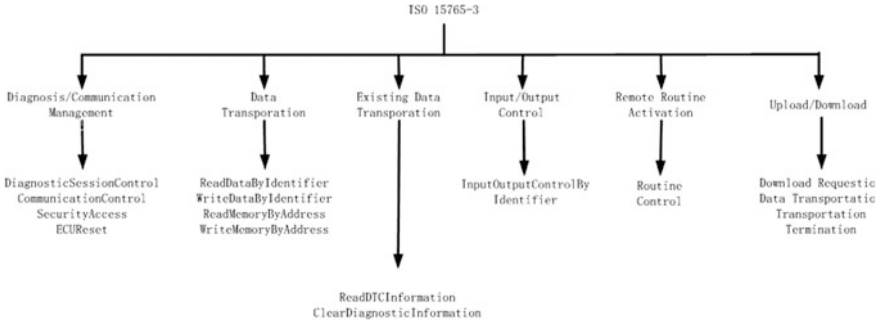


Fig. 5 Diagnostic service

CANcaseXL can transform signals from USB form to CAN form, and realizes the communication between PC and vehicle control unit. Several functions should be developed in master computer software: fault diagnostics (read/clear stored fault code of combination dashboard, real-time display the fault code and information during vehicle operation), real-time data monitoring and curve display of essential parameters. Apart from this, friendly GUI is need, which can improve the perception of operation and display, and can increase the efficiency. Figure 6 is the function architecture of the master computer software.

Apart from master computer software, the development of combination dashboard is essential, which is also the key point of this paper. As shown in Fig. 7, the scheme of combination dashboard mainly contains CAN driver module, transport layer module and diagnostic module.

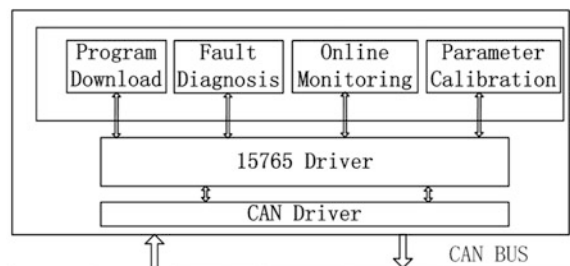
Functions of each module are as below.

(1) CAN driver module

This module is the basic of network communication, and realizes the function of the CAN controller operation, which contains [3].

- CAN Controller Initialization;
- CAN Message Sending;
- CAN Message Reception;
- Bus Off Management;
- Wake Up Management;

Fig. 6 Master computer software functions



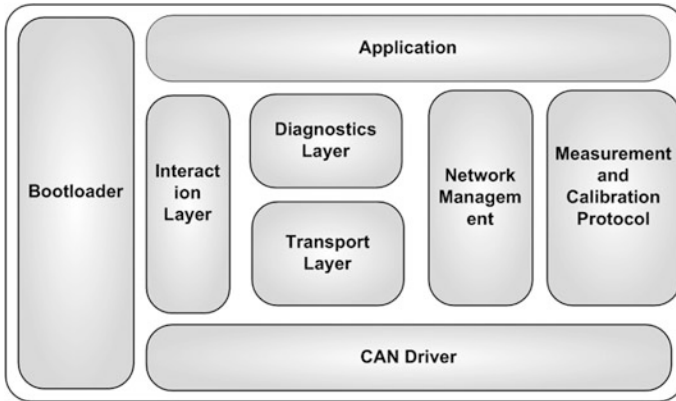


**Fig. 7** Complete related CAN software architecture

Special functions, such as multi-channel CAN supporting, and multi kinds of CAN identifier, etc. [4].

(2) Transport protocol module

This module realizes the transport of diagnostic protocol message based on the ISO 15765-2 standard, which mainly contains [5]:

- Single frame data transport execution;
- Multi frame data transport execution, and pocket operation for application layer diagnostic protocol message longer than 7 bytes (or 6 bytes, depending on the addressing mode)
- Faults detection and over-time monitoring;
- Several addressing modes supporting based on the usage standard: conventional addressing, extend addressing, conventional fixed addressing and hybrid addressing.

(3) Diagnostic layer module

Diagnostic communication is the procession of diagnostic service between diagnostic devices and ECU based on the diagnostic protocol, and is conducted as the form of client-side/server. Diagnostic service mainly realizes fault detection, failure memory access, data acquisition, variate calibration, function monitoring, ECU reprogramming, and identifier reading, etc. The main functions include:

- Diagnostic service and sub-function verifying;
- Diagnostic conversation jump;
- Safe status jump;
- Realization of diagnostics application layer related parameters: P2/P2ext/S3;
- Providing diagnostics service interface related with application program.

## 4 Development of Diagnostic Protocol Stack

### 4.1 Diagnostic Protocol Stack Software Module Division

The design of diagnostic communication can be divided into three modules: CAN Driver (CanDrv) module, CAN Transport (CANTp) module, Diagnostics communication management (Dcm) module [6], which are shown as Fig. 8.

### 4.2 Diagnostic Protocol Stack Module Development

#### 4.2.1 CAN Driver Module (CANDrv)

This module mainly realizes the sendr-receiver function of CAN message.

CANDrv module contains interface functions as below.

- (1) Can\_Transmit(): Service sending function for upper layer (such as CanTp), this function will return the execution result (sending success or failure).
- (2) Can\_RxIndication(): CAN message reception indication function, which is called when receiving CAN Frame (in the CAN receiving interruption function or Can\_MainFunction()).

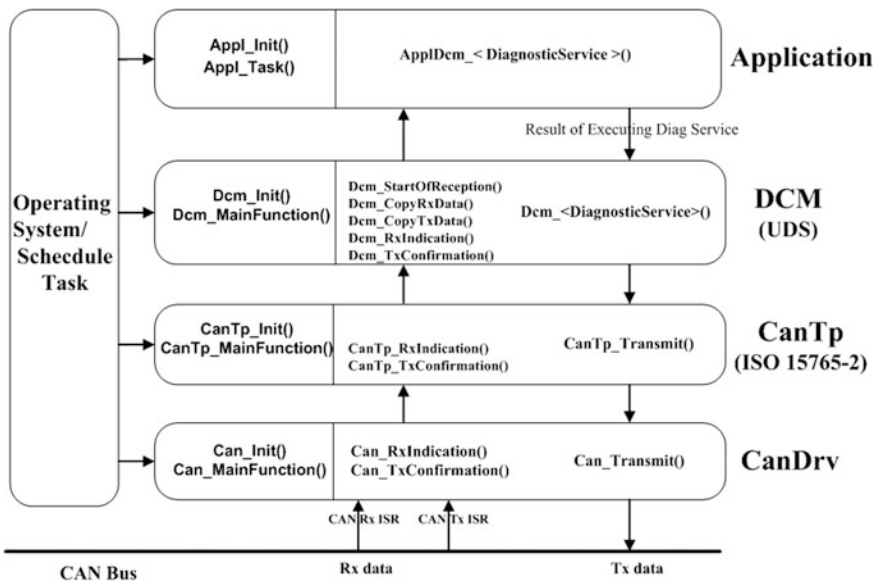


Fig. 8 Diagnostic communication software architecture

- (3) `Can_TxConfirmation()`: CAN message sending confirmation function, which is called when message sending is finished (in the CAN reception interruption function or `Can_MainFunction()`) [7].
- (4) `Can_Init()`: Initialize the CAN controller, called after the power on of system.
- (5) `Can_MainFunction()`: This function should be called by cycles if using inquiry mode to send/receive message.

#### 4.2.2 CAN Transport Layer Module(CANTP)

This module realizes the CAN transport protocol function that accordance to ISO 15765-2 standard, the related time parameters and operation modes can be configured.

CanTp module contains interface functions as below:

- (1) `CanTp_Transmit()`: Sending service function for protocol message provided by upper layer (such as Dcm), and start up the sending procession of diagnosis for protocol message.
- (2) `CanTp_RxIndication()`: Deal with the received transport protocol message (SF, FF, CF, FC) and pocket, this function is called in `Can_RxIndication()`.
- (3) `CanTp_TxConfirmation()`: Confirmation of transport protocol message (SF, FF, CF, FC) sending accomplishment, which is called in `Can_TxConfirmation()`.
- (4) `CanTp_Init()`: Initializing related parameters of transport layer module, called after the power on of system.
- (5) `CanTp_MainFunction()`: The main function of transport layer module, realizing the handling of the over- time and faults, executing the sending and resending of multi frame message, which is called by cycles.

#### 4.2.3 Diagnostic Communication Management (Dcm) Module

This module realizes the diagnostic services defined by USD standard (ISO 15765-3/ISO 14229), and can be configured by the diagnostic services and the sub-services.

The interface functions in Dcm module are as below.

- (1) `Dcm_StartOfReception()`: Sending diagnostic protocol message reception induction to Dcm module, executed in `CanTp_RxIndication` after receiving SF or FF.
- (2) `Dcm_CopyRxData()`: Copying received diagnostic protocol message to the buffer defined by Dcm module. This function is executed in `CanTp_RxIndication()`, called after any frame of transport protocol message reception.
- (3) `Dcm_CopyTxData()`: Copying diagnostic protocol message from buffer defined by Dcm to sending buffer of sending module. This function is called before the sending of any frame of transport protocol message.

- (4) `Dcm_RxIndication()`: Indication to Dcm module of complete diagnostic frame (diagnostic request), this function is executed in `CanTp_RxIndication()`, called after receiving SF or the last frame of CF [8].
- (5) `Dcm_TxConfirmation()`: Confirmation the accomplishment of diagnostic protocol message sending, executed in `TxConfirmation()`, after sending SF or the last frame CF.
- (6) `Dcm()`: Diagnostic service execution function in Dcm module, `ApplDcm()` is called in these functions.
- (7) `Dcm_Init()`: Initialization of Dcm module, called after the power on of system.
- (8) `Dcm_MainFunction()`: Main function of Dcm module, calling the related diagnostic service according to received diagnostic request, sending responding message. This function is executed by cycles.

#### **4.2.4 The Interface Development Between Diagnostic Communication Software and Application Program**

The interface between diagnostic communication software and application include 3 aspects, which first and second only need application (or operation system) to call the related functions.

Interface between diagnostic communication software and application are as below:

- (1) Diagnostic communication software initialization function of each module: called after the initialization of the power on.
- (2) Diagnostic communication software main functions of each module: called on demand by cycles.
- (3) `ApplDcm()`: Interface function between diagnostic communication software and application program, callback function realized by application program according detail contents of diagnostic service, to support functions of diagnostic device.

## **5 Development of Master Computer Software**

### ***5.1 Fault Diagnosis***

Fault diagnosis contains online diagnosis and offline diagnosis. Online diagnosis can display faults codes and information real-time during vehicle operation, and remind driver the corresponding operation through fault indicator lamps. Offline diagnosis contains fault code acquisition and fault code clearance.

### 5.1.1 Online Diagnosis

Online diagnostic function can display combination dashboard's fault code, fault description, fault frequency and corresponding maintenance induction to driver, and classify the severity level through fault indicator lamp, as shown in Fig. 9.

### 5.1.2 Offline Diagnosis

Offline diagnosis can read fault information, which including fault code, code description, fault status and maintenance information saved in combination dashboard when vehicle is stopped. Apart from this, combination dashboard code, software and hardware version number and production serial number can also be read (Fig. 10).

Apart from to be read, fault information can also be loaded to local computer, and be cleared through switch for fault clearance.

## 5.2 On Line Monitoring

In order to analyze some faults more detail, certain data needs to be monitored real-time, sometimes the dynamic curves are also be displayed, which is similar with the calibration of memory parameters. The parameter monitoring GUI is as Fig. 11.

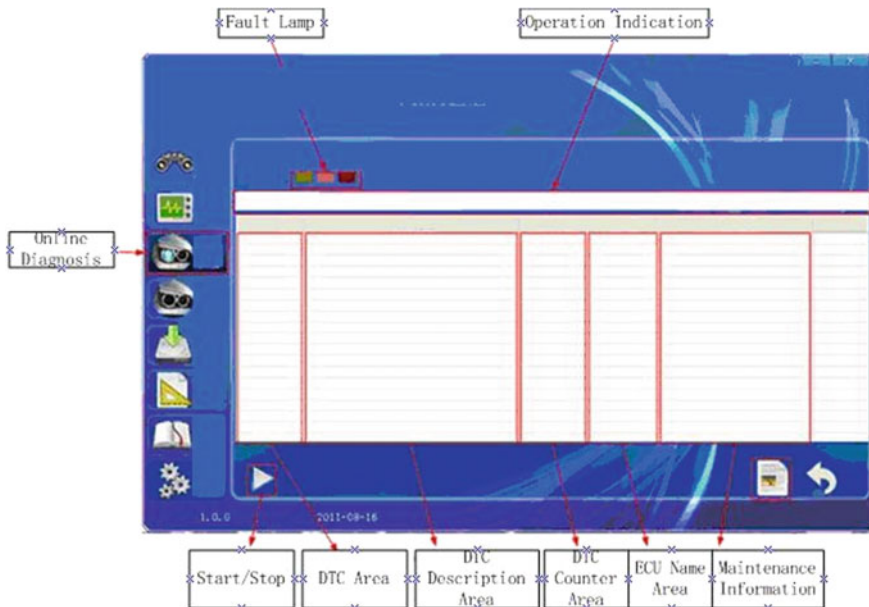


Fig. 9 On line diagnostic interface

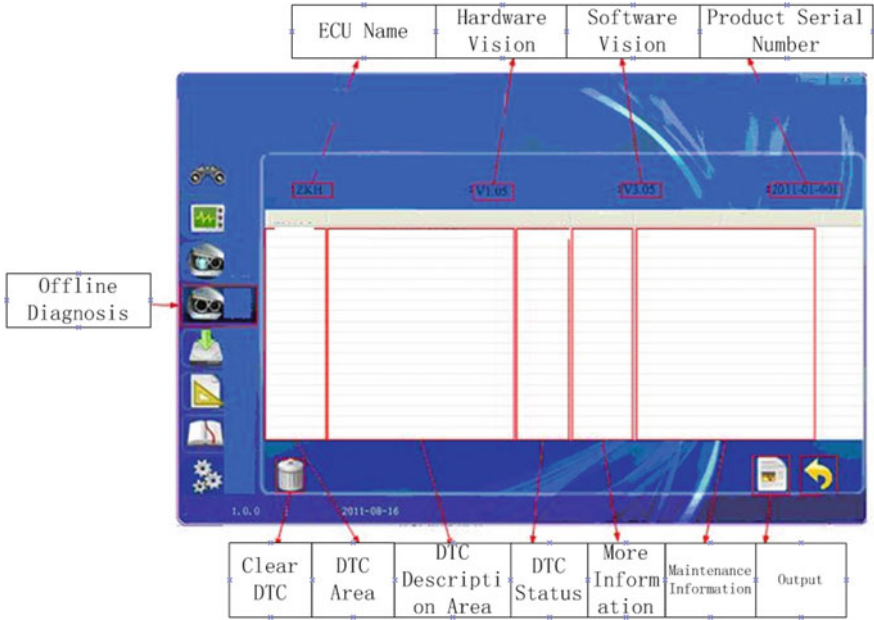


Fig. 10 Off line diagnostic interface

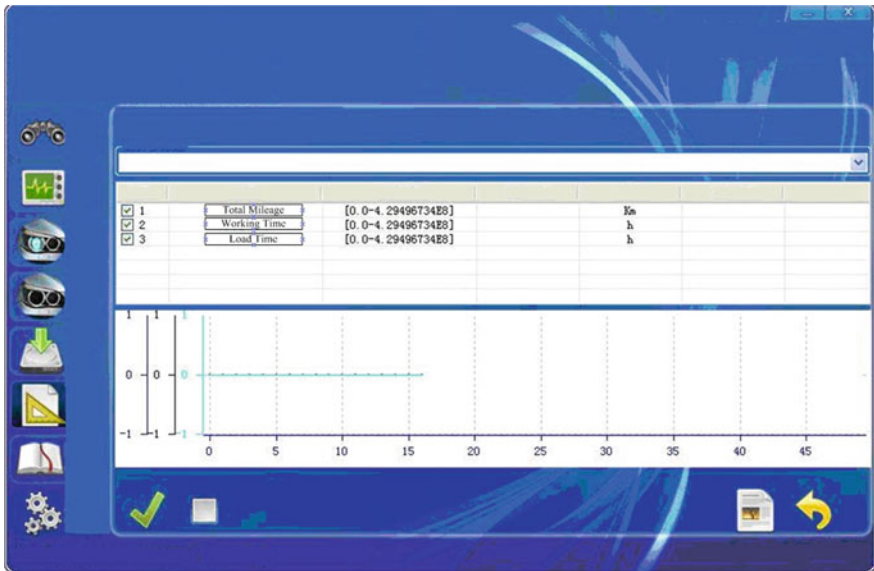


Fig. 11 On line monitoring interface

## 6 Conclusion

Based on the conventional ISO 15765 diagnostic protocol, this paper design the diagnostic protocol stack and master computer software of vehicle combination dashboard, and realizes the online/offline diagnosis and data monitoring of the combination dashboard. This work improves the convenience of getting combination dashboard parameters and fault status real-time for maintenance staff, and save the maintenance time, which makes improvement for practice work.

## References

1. ISO 14229 (2005) Road vehicles—unified diagnostics systems (UDS). International Standard Organization
2. ISO 15765 (2004) Road vehicles—diagnostics on controller area networks (CAN). International Standard Organization
3. AUTOSAR. AUTOSAR\_SWS\_CAN\_Driver[EB/OL]. 2013-06-28
4. AUTOSAR. AUTOSAR\_SWS\_CAN\_Interface[EB/OL]. 2013-06-28
5. AUTOSAR. AUTOSAR\_SWS\_CAN\_Transport[EB/OL]. 2013-06-28
6. Li Z, Liu M (2012) Electric and electrical architecture developing method based on AUTOSAR. *Mechatronics* (11):73–76 (in Chinese)
7. Sun S, Song K, Zhang T (2014) Development and application status of AUTOSAR. *Mechatronics* (11):33–38 (in Chinese)
8. Anyu C, Wang G, Ju L, L H (2013) Design of vehicle instrument communication module based on AUTOSAR architecture. *Autom Instrum* (6):19–23 (in Chinese)



# Optimization and Scheduling Strategy of Energy Storage in Urban Rail Traction Power Supply System

Wei Ma, Wei Wang and Ruonan Hu

**Abstract** In the urban rail traction power supply system, the load power fluctuates greatly, and the regenerated braking energy waste is serious. The fluctuation of load power can be stabilized effectively, and the utilization ratio of renewable energy can be improved when the energy storage system is applied in traction substation. Firstly, based on the load characteristics of traction substation, the minimum operation cost of energy storage investment is taken as the optimization objective, and a hybrid optimization method of traction substation based on ant colony optimization algorithm is proposed. Then, a hybrid energy storage real-time scheduling strategy based on wavelet packet decomposition algorithm is proposed, which can correct the wavelet packet decomposition results according to the real-time SOC state of the storage battery and super capacitor. Finally, the correctness and effectiveness are verified through the simulation results based on the measured data of a traction substation.

**Keywords** Urban rail traction power supply · Energy storage system  
Hybrid energy storage system · Real-time scheduling

## 1 Introduction

At present, the urban rail train mainly adopts traction power supply network to supply power, and the investment cost of traction network construction is high [1, 2]. The uncontrolled rectifier technology is usually used for power supply of traction substation, which makes the train unable to feed the regenerative braking energy to

---

W. Ma (✉) · W. Wang · R. Hu  
National Active Distribution Network Technology Research Center,  
Beijing Jiaotong University, Beijing 100044, China  
e-mail: 16117385@bjtu.edu.cn

W. Ma · W. Wang · R. Hu  
Collaborative Innovation Center of Electric Vehicles in Beijing,  
Beijing 100044, China

the power grid through the traction network, and can only rely on the nearby train or its own resistance to consume energy, causing a great waste of energy [3–5]. Power supply by means of energy storage and the traction network can not only reduce the traction substation power distribution capacity [6], but also can absorb the regenerative braking energy generated by the train. The economy and efficiency of energy utilization can be improved, and the energy loss can be reduced in this way [7].

Some important achievements have been made in the application of energy storage in rail transportation, and the energy storage system capacity allocation technology and energy scheduling strategy has also become a hot topic in recent years [8–12]. The storage capacity and scheduling strategies are complementary, the two must be considered in order to achieve optimal overall effect.

This paper takes the capacity allocation and scheduling strategy of traction substation ground type of energy storage system as the research content, and analyzes the load characteristics of the traction substation. The minimum investment and operation cost of the Hybrid Energy Storage System (HESS) and the traction substation are this papers objective function. Optimization model of HESS is established in, using ant colony optimization the algorithm to solve this model, and to get the optimal configuration of HESS. The wavelet packet decomposition algorithm is used for controlling the charge and discharge of HESS in real-time. In the control process, according to the real-time SOC of battery and super capacitor, dynamic correction methodology is used for the references power instruction of HESS that can ensure the operation of HESS keep safe.

## 2 The Power Characteristic of Traction Substation Load

The Beijing Metro Traction Substation actual load data as the basis for analysis, at the peak time of a day. Up and down train synchronization time is 30s. The departure time interval is 3 min. in the power supply range at the same time, there are 2 trains running. The Typical power characteristic curve of traction substation load is shown in Fig. 1

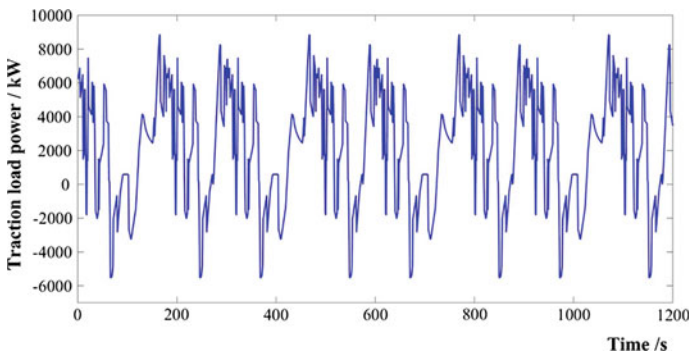


Fig. 1 Typical power characteristic curve of traction substation load

### 3 The Power Characteristic of Traction Substation Load

#### 3.1 The Topology of HESS in Traction Substation

The topology of the HESS in the traction substation is shown in Fig. 2.

The battery and the super capacitor are respectively connected to the DC traction network through a bidirectional DC/DC converter. First of all, HESS can output energy when traction load in peak, reducing the peak load of traction output, so as to reduce the capacity of the traction substation and distribution substation, and reduce investment cost; secondly, HESS, which have the characteristics of power type of storage and energy type of storage, can stabilize the power fluctuation of traction load. When the train in the braking condition, if the regenerative braking energy generated is not absorbed by the adjacent trains, then HESS can absorb the regenerative braking energy, improving the utilization rate of energy regenerative braking.

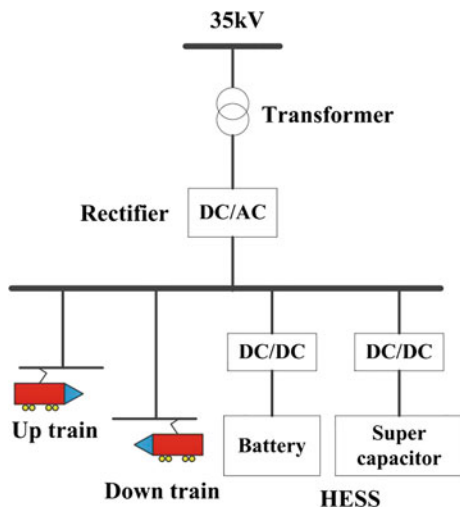
#### 3.2 The Optimization and Configuration Model of HESS

##### 3.2.1 Objective Functions

When the power demand of traction load is satisfied, the minimum investment cost and annual operation cost of traction substation and HESS are taken as objective functions.

$$f_{min} = C_{inv} + C_{om} + C_{kw} + C_{sub} \tag{1}$$

Fig. 2 Topological structure of HESS in traction substation



where,  $C_{inv}$  is the initial investment cost of HESS,  $C_{om}$  is the annual operation and maintenance cost of HESS,  $C_{kw}$  is the investment cost of traction substation, and  $C_{sub}$  is the power consumption of traction substation.

$$C_{inv} = n_{B\_P} \cdot P_{BAT} + n_{B\_E} \cdot E_{BAT} + n_{C\_P} \cdot P_{SC} + n_{C\_E} \cdot E_{SC} \quad (2)$$

where,  $n_{B\_E}$  and  $n_{C\_E}$  are respectively for batteries and super capacitors investment cost per unit capacity.  $n_{B\_P}$  and  $n_{C\_P}$  are the cost of battery and super capacitors DC/DC convert.  $P_{BAT}$ ,  $E_{BAT}$ ,  $P_{SC}$  and  $E_{SC}$  are rated power and capacity of battery and super capacitor.

$$C_{mo} = m_{B\_E} \cdot E_{BAT} + m_{C\_E} \cdot E_{SC} \quad (3)$$

where,  $m_{B\_E}$  is unit capacity of battery maintenance cost, and  $m_{C\_E}$  is unit capacity of super capacitor maintenance cost.

$$C_{kw} = P_{Grid\_max} \cdot \theta \quad (4)$$

where,  $P_{Grid\_max}$  is the maximum output power of the traction substation, and  $\theta$  is the unit investment cost of the traction transformer substation.

$$C_{sub} = \varepsilon E_{sub} = \varepsilon \int_0^T P_{GRID} dt \quad (5)$$

where, the  $T$  represents the running time of the traction substation for one year. The  $E_{sub}$  represents the total energy consumption of the traction substation for one year and the unit is kWh. The  $\varepsilon$  is the electricity price and the unit is kWh.

### 3.2.2 Confinement Conditions

Confinement conditions for the SOC of battery and super capacitor.

$$\begin{cases} P_{BAT,min} < P_{BAT} < P_{BAT,max} \\ P_{SC,min} < P_{SC} < P_{SC,max} \\ 0.2 < SOC_{BAT} < 0.9 \\ 0.15 < SOC_{SC} < 0.95 \end{cases} \quad (6)$$

where,  $P_{BAT}$  is the charge and discharge power of battery,  $P_{SC}$  is charge and discharge power of super capacitor.  $P_{BAT,min}$ ,  $P_{BAT,max}$ ,  $P_{SC,min}$ ,  $P_{SC,max}$  are respectively the upper and lower limitation of battery and super capacitor charging and discharging power.  $SOC_{BAT}$  and  $SOC_{sc}$  are respectively the SOC of battery and super capacitor.

Confinement conditions for traction substation output power.

$$P_{Grid\_min} < P_{Grid}(t) < P_{Grid\_max} - P_{Grid\_R} \tag{7}$$

where,  $P_{Grid\_max}$  and  $P_{Grid\_min}$  are the maximum and minimum values of the output power of the traction substation respectively.  $P_{Grid\_R}$  is the reserve capacity of traction substation.

Confinement conditions for power balance.

$$P_{load}(t) = P_{Grid}(t) + P_{BAT}(t) + P_{SC}(t) \tag{8}$$

Cycle confinement conditions for batteries and super capacitors.

$$\begin{cases} SOC_{BAT}(T) = SOC_{BAT}(T_0) \\ SOC_{SC}(T) = SOC_{SC}(T_0) \end{cases} \tag{9}$$

where,  $T_0$  is the start time of a cyclic scheduling period, and T is the end time.

## 4 The Real-Time Dispatching Algorithms of HESS

### 4.1 Wavelet Packet Decomposition Algorithm

Wavelet analysis is a fixed window size and its shape can be changed, in the process of decomposition of low-frequency signal decomposition, the decomposition is no longer implemented the high frequency signal. The schematic diagram of wavelet packet decomposition algorithm is shown in Fig. 3.

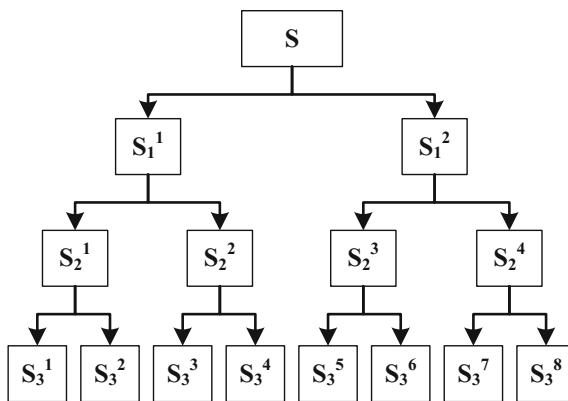


Fig. 3 Schematic diagram of wavelet packet decomposition algorithm

### 4.2 The Power Allocation Strategy of the HESS

Set the traction load is  $P_L(t)$ . In order to smooth the output power fluctuation of the traction substation  $P_{GRID}(t)$ , the fluctuation power of the traction load is stabilized by the HESS, and the charge and discharge power of the HESS  $P_{HESS}(t)$  is expressed as follows.

$$P_L(t) = P_{HESS}(t) + P_{GRID}(t) \tag{10}$$

The three layer wavelet packet decomposition algorithm is used to decompose the power  $P_L$ , and the power decomposition sequence traction load at time of  $t$  is obtained, which is expressed as follows.

$$P_L(t) = S_3^1(t) + S_3^2(t) + S_3^3(t) + \dots + S_3^8(t) \tag{11}$$

where,  $S_3^i$  is the power component after wavelet packet decomposition, in which  $i$  is 1 to 8 positive integers.

The power reference instructions for the battery and super capacitor of the HESS are shown in Fig. 4.

### 4.3 The Correction Methodology of HESS Power Instruction

Objective to modify HESS reference power mainly has two aspects, one is to prevent super capacitor and battery overcharge, over discharge, reduce the battery life, and even cause damage; two is to keep the battery and super capacitor SOC remain in the vicinity of 0.5, running in shallow charge and discharge condition, prolong the service life.

First of all, it is necessary to correct the references power instructions based on the real-time SOC of battery and super capacitor, the first correction of battery is as follows.

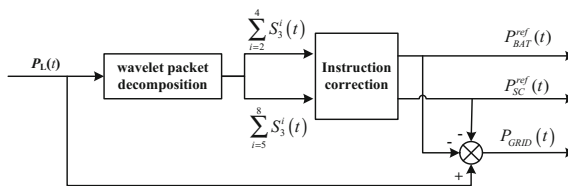


Fig. 4 Power allocation strategies for battery and super capacitor of HESS

$$P_{BAT}^{ref}(t) = \begin{cases} \sum_{i=2}^4 S_3^i(t), & SOC_{BAT}(t) \in [0.35, 0.75] \\ \sum_{i=3}^4 S_3^i(t), & SOC_{BAT}(t) \in [0.2, 0.35] \cup [0.75, 0.9] \end{cases} \tag{12}$$

The first correction of super capacitor is as follows.

$$P_{SC}^{ref}(t) = \begin{cases} \sum_{i=5}^8 S_3^i(t), & SOC_{SC}(t) \in [0.25, 0.85] \\ \sum_{i=6}^8 S_3^i(t), & SOC_{SC}(t) \in [0.15, 0.25] \cup [0.85, 0.95] \end{cases} \tag{13}$$

## 5 Case Studies

### 5.1 The Simulations of HESS Optimization and Configuration

Based on the load curve of the traction substation shown in Fig. 1, the HESS optimization configuration method is simulated in this paper, and the parameters of the battery and super capacitor are shown in Table 1.

The construction cost of traction substation is 280 million yuan/kW, and the cost of power electricity is 1 yuan/kWh. The ant colony optimization algorithm is used to solve the problem; the HESS allocation result and the corresponding operating cost are obtained, as shown in Table 2.

According to the optimization results, the application of HESS system in traction substation, the investment cost of traction substation reduced from the original 252 million yuan to 136.88 million yuan, the traction substation construction investment cost is reduced by 45.68%. Secondly, through braking energy recycling, the annual operating cost of traction substation is reduced by 16.13%. Comprehensive analysis shows that the economic benefits of HESS applied to traction substations are relatively impressive.

**Table 1** The parameters of battery and super capacitor

Battery parameters	Values	Super capacitor parameters	Values
Single cell voltage (V)	2.8	Single cell voltage(V)	2.5
Single cell capacity (Ah)	10	Single cell capacity (F)	7500
Unit price (yuan/kWh)	3000	Unit price (yuan/kWh)	40,000
Unit price of DC/DC (yuan/kWh)	2000	Unit price of DC/DC (yuan/kWh)	2000
Unit price of maintenance (yuan/kWh)	100	Unit price of maintenance (yuan/kWh)	80

**Table 2** The allocation results of HESS(before and after optimization)

	$P_{GRID}/kW$	$E_{BAT}/kWh$	$P_{BAT}/kW$	$E_{SC}/kWh$	$P_{SC}/kW$	Investment cost/ $*10^6$ ¥	Operating cost/ $*10^6$ ¥
Before	9000	0	0	0	0	252.00	47.5657
After	2500	380	4350	40	6700	136.88	39.8936

### 5.2 The Simulation of the Real-Time Dispatching Strategy of the HESS

Based on the load curve of the traction substation shown in Fig. 1, the real-time dispatching strategy of the HESS is simulated, and the output power of the traction substation and HESS are shown in Fig. 5.

As can be seen from Fig. 5, that the traction substation power curve is relatively smooth, the range of power fluctuations is in the [1900, 2300] kW. That indicated that the introduction of HESS can reduce the capacity of distribution substation construction. In addition, the large amplitude power fluctuation of traction load is mainly borne by HESS, the output power range of HESS is [-8000, 6100] kW. According to the optimization results, the maximum output power limitation of HESS is able to meet the actual power requirements. The output power of battery and super capacitor is shown in Fig. 6.

From the simulation results in Fig. 6, the power range of battery is [-4000, 4000] kW, the power range of super capacitor is [-6100, 6000] kW. The optimized

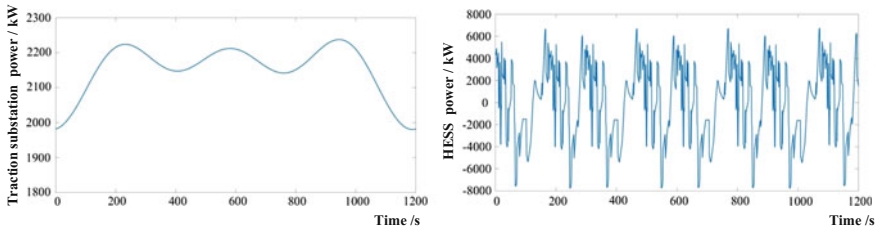


**Fig. 5** The traction substation and HESS power (left: traction substation, right: HESS)

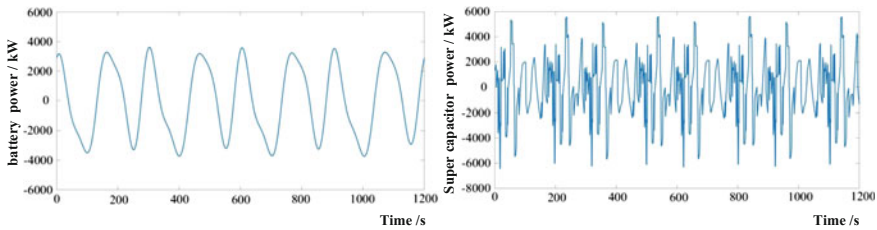


**Fig. 6** The output power of battery and super capacitor (left: battery, right: super capacitor)



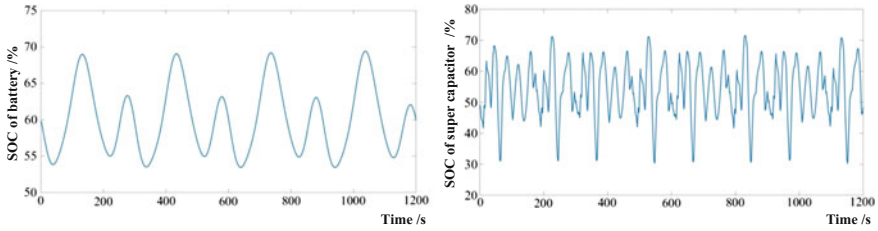


**Fig. 7** The real-time SOC of battery and super capacitor (left: battery, right: super capacitor)

configuration results of HESS can meet the actual output power demand of storage battery and super capacitor. Secondly, the proposed wavelet packet decomposition algorithm can assign HESS instruction power reasonably and effectively. The super capacitor is used for stabilizing power fluctuation components of high amplitude. The battery is used for stabilizing fluctuation of smaller amplitude.

The real-time SOC of battery and super capacitor is shown in Fig. 7.

From the simulation results in Fig. 7, the SOC range of battery is [0.5, 0.7], the SOC range of super capacitor is [0.3, 0.7]. They are always running in the shallow charge and shallow discharge condition. The proposed correction method of HESS references power instruction power, which is based on the real-time SOC of battery and super capacitor, is correct and effective.

## 6 Conclusions

This paper mainly studies the optimal allocation method of HESS in the urban rail traction substation, and the real-time control strategy of the charge and discharge power of the storage battery and the super capacitor in HESS. The main conclusions are:

- a. After applying HESS to the urban rail traction power supply system, it has good economy. First, the power distribution capacity of the traction substation can be reduced, and about 45% of the investment cost of the traction substation will be reduced. Second, the HESS can effectively recover the regenerative braking energy of the train and reduce the operating cost of traction substations by 16% per year.
- b. The proposed optimization and planning model of HESS in traction substation is validated by simulation. The configuration results of HESS, using ant colony optimization algorithm, is correct, that can be obtained to meet the actual demand to stabilize the fluctuation of power of traction load and recovery of regenerative braking energy. In addition, the HESS reference power instruction correction strategy, proposed in this paper, is effective, that can ensure that the storage battery and super capacitor run within the security constraint.

## References

1. Wang J, Jiang P, Yang H (2007) On break-reproduction energy inverter system in UMT. *Urban Railway Syst* 12:23–27 (in Chinese)
2. Zhang Y, Zheng S, Sun C et al (2017) Does subway proximity discourage automobility? Evidence from Beijing. *Transp Res Part D: Transp Environ* 52:506–517
3. Li Y, Sun X, Feng X et al (2012) Study on evacuation in subway transfer station fire by STEPS. *Proc Eng* 45:735–740
4. Xun J, Tang T, Song X et al (2015) Comprehensive model for energy—saving train operation of urban mass transit under regenerative brake. *China Railway Sci* 01:104–110 (in Chinese)
5. Wang Y, Feng H, Xi X (2017) Monitoring and autonomous control of Beijing Subway HVAC system for energy sustainability. *Energy Sustain Dev* 39:1–12
6. Ghaviha N, Campillo J, Bohlin M et al (2017) Review of application of energy storage devices in railway transportation. *Energy Proc* 105:4561–4568
7. Zhang Y, Cheng J, Wu S et al (2016) analysis of regenerating energy utilization based on metro vehicle super capacitor. *Urban Railway Syst* 09:56–60 (in Chinese)
8. Chung C, Hung Y (2014) Energy improvement and performance evaluation of a novel full hybrid electric motorcycle with power split e-CVT. *Energy Convers Manag* 86:216–225
9. Li S, Wang S, Ma Z et al (2017) Using an air cycle heat pump system with a turbocharger to supply heating for full electric vehicles. *Int J Refrig* 77:11–19
10. Lin S, Song W, Feng Z et al (2016) Hybrid energy storage system of Metro and its control method on power dynamic allocation. *Chin J Sci Instrum* 12:2829–2835 (in Chinese)
11. Aiguo X, Shaojun X, Yuan Y et al (2010) Regenerating energy storage system based on ultra-capacitor for urban railway vehicles. *Trans China Electrotech Soc* 3:117–123 (in Chinese)
12. Peng Q, Li W, Wang Y et al (2017) Study on operation strategies for metro trains under regenerative breaking. *J China Railway Soc* (03):7–13 (in Chinese)

# Hierarchical Control Strategy of On-board DC Microgrid

Luming Chen, Zili Liao, Hailiang Xu and Xiaojun Ma

**Abstract** In order to eliminate adverse impacts of instantaneous power loads, configurations, working principle and distributed power characters of on-board DC microgrid were analyzed. To maximize the function of this structure, a hierarchical control strategy was established based on wavelet transform strategy and fuzzy control strategy. And then, examples of application were carried out in MATLAB/Simulink based on a certain driving test cycle and simulation model to verify the effectiveness of the proposed strategy. The final results showed that the proposed strategy had an advantage in meeting demands of power loads. In the meantime, electric energy quality and battery service life could be significantly improved.

**Keywords** DC Microgrid · Fuzzy control · Wavelet transform  
Supercapacitor

## 1 Introduction

In recent years, the topology of traditional grid has made a revolutionary change due to the rapid development of high power semiconductor switching devices, storage technology and power conversion technology. As an important part of smart grid, microgrid technology has drawn great attention around the world. Integrated electric power systems in electric armored vehicles are typically composed of multiple distributed generations, energy storage devices and converters, which may achieve a high degree of autonomy [1]. Thus it can be regarded as on-board DC microgrid system without connecting to large electric power grids.

The performance of on-board DC microgrids is not only depended on topology structures, but also closely related to control strategies [2]. Many efforts on the microgrid control strategies have been made by scholars around the world. A fuzzy

---

L. Chen · Z. Liao (✉) · H. Xu · X. Ma  
Department of Control Engineering, Academy of Army Armored Force,  
No. 21 Du Jia Kan, Feng Tai District, Beijing, China  
e-mail: 18211077415@163.com

© Springer Nature Singapore Pte Ltd. 2018

L. Jia et al. (eds.), *Proceedings of the 3rd International Conference on Electrical and Information Technologies for Rail Transportation (EITRT) 2017*, Lecture Notes in Electrical Engineering 482, [https://doi.org/10.1007/978-981-10-7986-3\\_63](https://doi.org/10.1007/978-981-10-7986-3_63)

621

control strategy was proposed based on a parallel HEV, the simulation result indicated it could improve the performance of HEV fuel economy and emissions [3]. Gheorghe proposed a hybrid algorithm with wavelet decomposition based on the novel configuration with batteries and supercapacitors, which turned out to be effective on the improvement of vehicle performance [4]. Above-mentioned control strategies are best for civilian vehicles when changes of load power demands are relatively stable. However, armored vehicles usually have heavy dead weights and complex working conditions, which lead to a rapid changing of load requirements. Therefore, it is necessary to develop an efficient energy control strategy for the low inertia on-board DC microgrid.

This paper takes the on-board DC microgrid as the research object. Considering its physical characteristics, it is proposed a hierarchical control strategy, combining wavelet transform with fuzzy control, to realize a higher efficient control. To verify the effectiveness of the control strategy, a simulation experiment was carried out based on the Matlab/Simulink model. Finally, it is proved that the proposed control strategy can give full play to different power supplies, extend their life cycles and improve power supply quality of on-board DC microgrid.

## 2 The General Situation of On-board DC Microgrid

### 2.1 On-board DC Microgrid Configurations

On-board DC microgrid consists of distributed generations, energy storage devices and converters [5], and its topology structure is shown in Fig. 1.

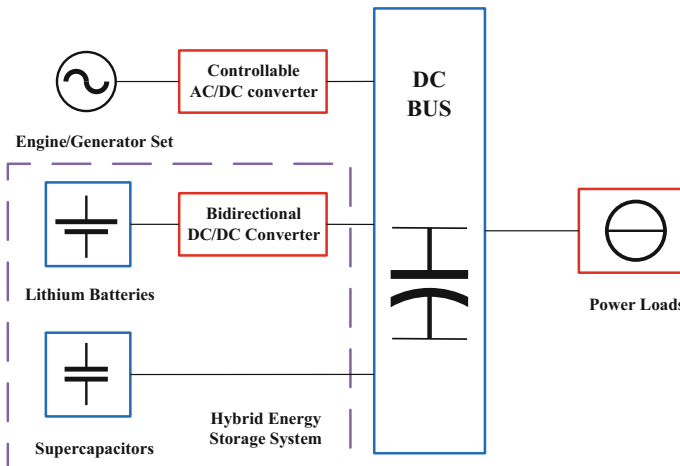


**Fig. 1** Topology structure of on-board DC microgrid

## ***2.2 On-board Microgrid Working Principle***

DC bus is mainly applied to offer stable voltage output for all kinds of electric power loads, whose energy comes from more than one power sources. Firstly, engine/generator set acts as the main power source of on-board DC microgrid, and its AC output can be rectified to DC by controllable AC/DC converter. Secondly, lithium batteries connect to the DC bus through bidirectional DC/DC converter, and play an important role in the recycling of braking energy as well as the provision of silent driving. Finally, supercapacitors and DC bus are connected directly by high-voltage wires, the former is usually used to deal with the situation of load sudden increases or decreases.

## ***2.3 Distributed Power Characteristics***

Engine/generator set: When power loads change dramatically, the operating point of engine/generator set also changes significantly. Nevertheless, the component is a large-lag object, dynamically adjusting may result in severe losses. As a result, the operating efficiency and fuel economy will be a sharper decline.

Lithium batteries: Under a working environment with high power load changes, in-out power changes of lithium batteries will become higher than that of general condition. It leads to a negative influence on lithium battery's life cycle and security.

Supercapacitors: The power density of supercapacitors is 10–100 times more than that of lithium batteries. So it can finish its in-out process within several milliseconds. Its excellent physical characteristics gains an advantage over other power type energy sources.

# **3 Hierarchical Control Strategy**

## ***3.1 Process of Control Strategy***

Since power sources of on-board DC microgrid are in nature of different frequency characteristics, power source efficiency cannot be fully exploited by solely relying on a particular control strategy. To solve this problem, multi-strategy fusion become a key to breaking bottleneck. A hierarchical control strategy is proposed in this paper. For the first step, load power requirements is to be broken up into a high-frequency part and a low-frequency part based on wavelet transform. For the second step, low-frequency power shall be allocated to the engine/generator set and lithium batteries. The process of control strategy is shown in Fig. 2.

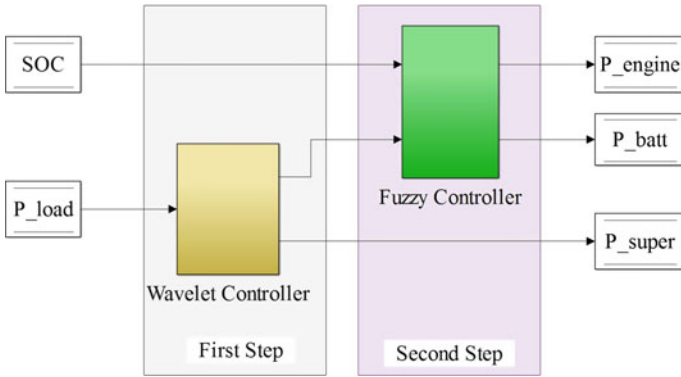


Fig. 2 The process of control strategy

### 3.2 Wavelet Transform Strategy

Wavelet analysis, which is originated in the 1980, is the expansion and extension of Fourier analysis. As a function of wavelet analysis, wavelet transform is mainly used to decompose a given function or time signal into different scales [6].

Wavelet transform will map a 1-D time domain function into a 2-D time-frequency domain function through decomposition process. Wavelet basis function used by wavelet transform is diverse, so how to choose its function becomes the key factor to outcome result [7]. As one of the most popular wavelet basis function, haar wavelet has the shortest length of filtering in the time domain comparing with other wavelets. Therefore, the paper choose the haar wavelet as the wavelet basis function, its expression is shown as below:

$$\psi(t) = \begin{cases} 1 & t \in [0, 1/2] \\ -1 & t \in [1, 2/1] \\ 0 & \text{others} \end{cases} \quad (1)$$

For continuous wavelet transform, the decomposition expression is:

$$L_{\psi}f(a, t) = \frac{1}{\sqrt{c_{\psi}}} \frac{1}{\sqrt{|a|}} \int_{-\infty}^{+\infty} f(u) \overline{\psi\left(\frac{u-t}{a}\right)} du (a \neq 0), (t \in R) \quad (2)$$

For a computer calculation, continuous wavelet transform is not convenient to deal with digital signals. By discrete treatment, Eq. (2) can be changed to

$$L_{\psi}f(a, t) = \frac{1}{\sqrt{c_{\psi}a}} \int_{-\infty}^{+\infty} f(u) \psi\left(\frac{u-t}{a}\right) du \quad (3)$$

$$(a = 2^{-j}, t = k2^{-j}, j, k \in \mathbb{Z})$$

During design process, wavelet decomposition order should be proper to ensure simplicity of calculation and meet demands of the frequency constraints. Hence the paper chooses a third order haar wavelet in decomposition and reconstruction power demand, distribution situation is shown in Fig. 3.

The expression of power supply power allocation is shown as follows:

$$P_{LF} = P_{engine} + P_{batt} = x_0(n) \tag{4}$$

$$P_{HF} = P_{super} = x_1(n) + x_2(n) + x_3(n) \tag{5}$$

### 3.3 Fuzzy Control Strategy

Fuzzy control strategy was published by Prof L.A. Zadech in 1965, then it has got promoted in recent years due to its advantages. Firstly, it does not rely on the accurate object model, which contributes to better adaptability and robustness. Secondly, fuzzy control rules can be expressed by natural languages, so it is easy to implement. Its design flow chart is shown in Fig. 4.

Based on load power demands and lithium batteries SOC, a fuzzy control strategy is designed to execute power distribution between engine/generator set and lithium batteries, which is a typical MIMO design problem [8].

#### (1) Fuzzification

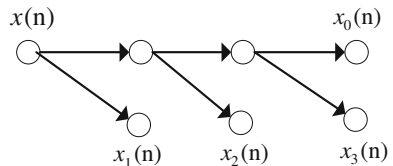
Fuzzification is used to transform input real clarity values into fuzzy input values through domain transformation and relationship mapping. The triangle relationship function is used in the fuzzy controller.

$$f(x, a, b, c) = \begin{cases} 0 & x \leq a \\ \frac{x-a}{b-a} & a \leq x \leq b \\ \frac{c-x}{c-b} & b \leq x \leq c \\ 0 & x \geq c \end{cases} \tag{6}$$

#### (2) Inference Machine

Inference machine is the core of fuzzy control strategy design. A total of 90 fuzzy control rules can be established in the following form:

**Fig. 3** Power dividing sketch map



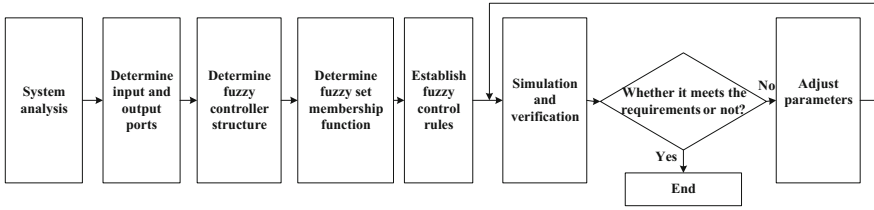


Fig. 4 Fuzzy controller design flow chart

If (conditions which is needed to meet) then (conclusions)

Each fuzzy rule represents a different relationship between fuzzy implications, and its basic form is shown as followings:

$$R_i = (X_i \wedge Y_i) \rightarrow Z_i \tag{7}$$

(3) Defuzzification

In the paper, a area split method is applied to perform defuzzification procedure. First the surrounding area between abscissa and membership function is calculated. When a line parallel to the ordinate bisects the area, its intersection with the horizontal is considered the expected value.

## 4 Examples of Application

### 4.1 Basic Parameters and Design Performance Indicators

In order to calculate load power demands of on-board DC microgrid, basic vehicle parameters and microgrid requirements are listed in Table 1.

### 4.2 Driving Test Cycle

To verify the control strategy, certain driving test cycle should be selected. In view of heavy vehicle characteristics, CYC\_HWFET driving test cycles was adopted [9]. The power spectrum characteristic was shown in Fig. 5.

Table 1 Basic vehicle parameters and microgrid requirements

Vehicle parameters		Microgrid requirements	
Total weight (t)	18	Engine (kW)	330
Windward area (m <sup>2</sup> )	2.2*3	Generator (kW)	350
Motorcycle type	8 × 8	Lithium battery (Ah)	90
Drag coefficient	0.5	Supercapacitors (F)	10



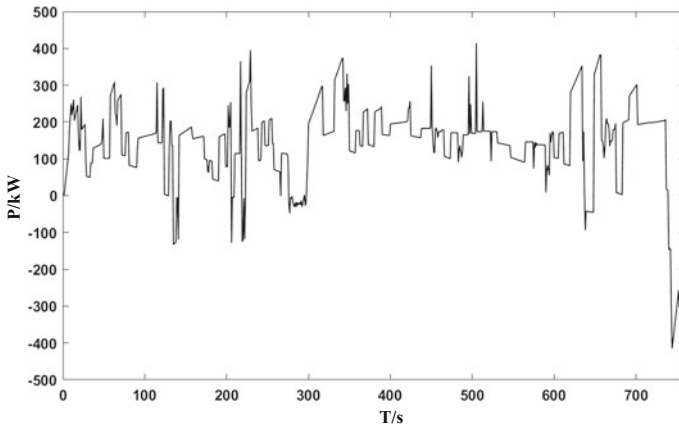


Fig. 5 Power spectrum characteristic of CYC\_HWFET

### 4.3 The Simulation Model

According to the above-mentioned method, the control strategy of on-board DC microgrid was established in MATLAB/Simulink. It is shown in Fig. 6.

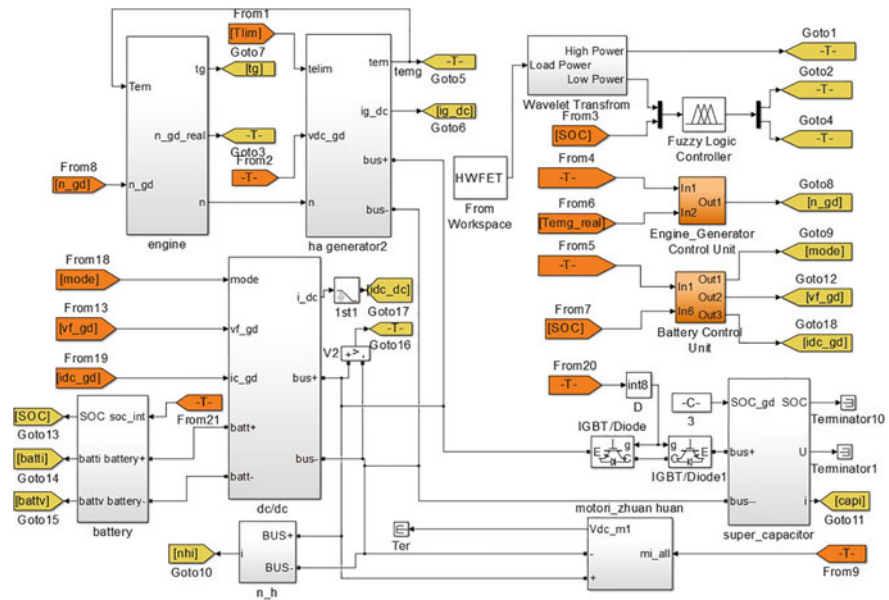


Fig. 6 Control strategy model of on-board DC microgrid

### 4.4 The Simulation Result

Applying the established simulation model of on-board DC microgrid into experiment, the simulation result was shown as the follows:

Figure 7 shows that engine power trends generally keep pace with load power requirements, and its amplitude change frequency gets reduced; Fig. 8 shows that lithium batteries are constantly in the state of charging and discharging process. Although its amplitude change frequency get improved, it is still in a relatively stable working condition; Fig. 9 shows that supercapacitors make full use of its high power density advantages, which can deal with the high frequency component in the system; Fig. 10 shows that the battery SOC stays at a dynamic equilibrium

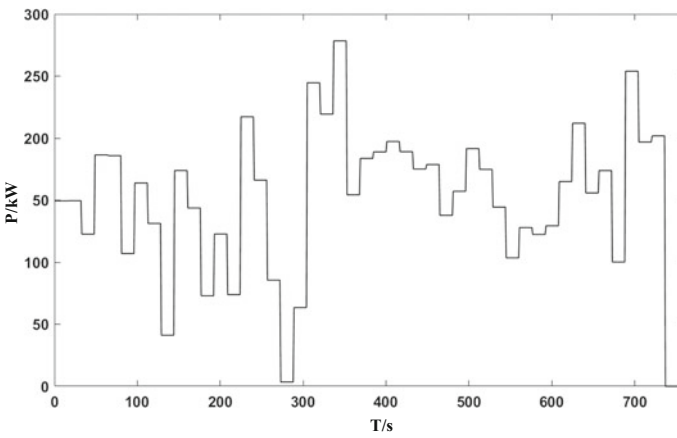


Fig. 7 The power distribution of engine/generator set

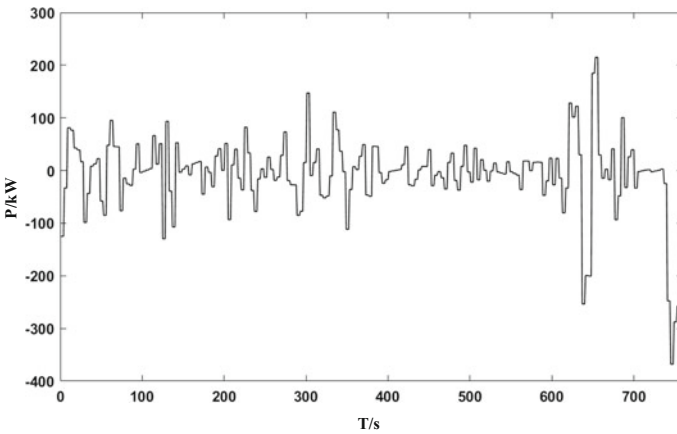


Fig. 8 The power distribution of lithium batteries

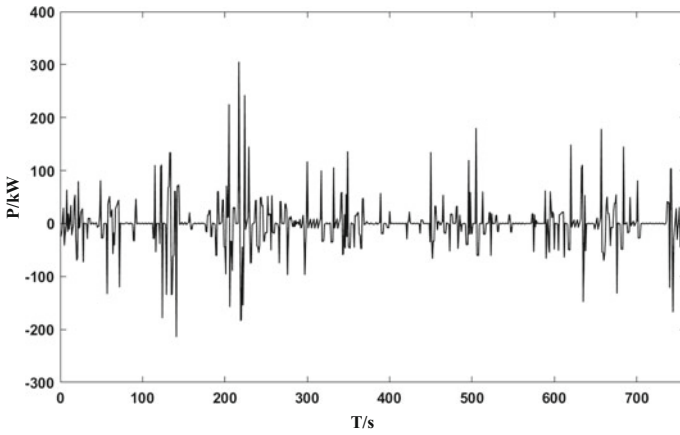


Fig. 9 The power distribution of supercapacitors

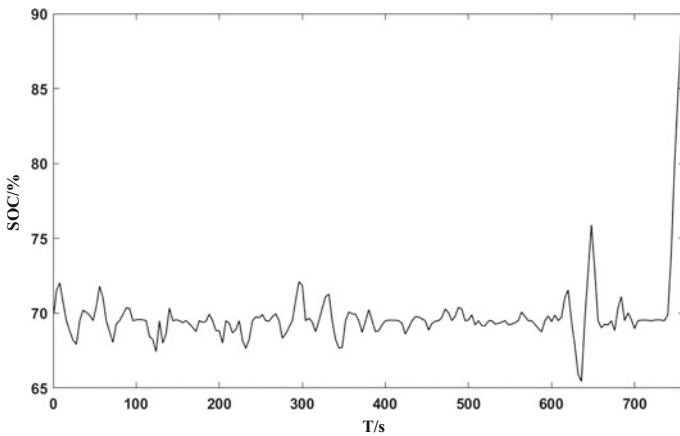


Fig. 10 The dynamic change trend of lithium batteries SOC

state most of the time, it is benefit to exert its high energy density advantages and extend its life cycle.

## 5 Conclusion

The paper established a hierarchical control strategy based on the combination of wavelet transform and fuzzy control, reaching a goal of high frequency power decomposition and low frequency power allocation. These measures tend to result

in an effective reduction of dynamic work losses and a high improvement of power supply quality of on-board DC microgrid.

**Acknowledgements** This work was supported in part by the National Natural Science Foundation of China (No. 51507190) and the China Postdoctoral Science Foundation (No. 2017T100831).

## References

1. Zili L, Xiaojun M, Kemao Z (2008) Research on status quo and key technologies of all-electric combat vehicle. *Fire Control Command Control* 33(5):1–4
2. Meradji M, Cecati C, Gaolin W, Dianguo X (2016) Dynamic modeling and optimal control for hybrid electric vehicle drivetrain. In: 2016 IEEE international conference on industrial technology, pp 1424–1429
3. Ling C, Liang G (2012) A research on the fuzzy control strategy for parallel hybrid electric vehicle. In: 2nd international conference on frontiers of manufacturing and design science, pp 121–126
4. Gheorghe L, Alina-georgiana S (2014) Control strategies for hybrid electric vehicles with two energy sources on board. In: 8th international conference and exposition on electrical and power engineering, pp 142–147
5. Bayrak A (2015) Topology considerations in hybrid electric vehicle powertrain architecture design. The University of Michigan, pp 6–9
6. Kamaraj C (2011) Integer lifting wavelet transform based hybrid active filter for power quality improvement. In: 2011 1st international conference on electrical energy systems, pp 103–107
7. Zhang D (2011) MATLAB wavelet analysis. China Machine Press, Beijing, pp 53–64 (in Chinese)
8. Venkatesh C, Siva DVSS, Sydulu M (2012) Detection of power quality disturbances using phase corrected wavelet transform. *J Inst Eng (India) Ser B*, 37–42
9. Shim BH, Park KS, Koo JM, Jin SH (2014) Work and speed based engine operation condition analysis for new European driving cycle(NEDC). *J Mech Sci Technol* 28(2):755–761

# Design and Simulation of Switched Reluctance Motor Control System

Chengling Lu, Gang Zhang, Chengtao Du, Junhui Cheng  
and Congbing Wu

**Abstract** Based on the analysis of mathematical model of switched reluctance motor and the structure of drive system, position sensor model, power converter model, switched reluctance motor model and other models were established through Simulink module. Through a combination of these models, a system model of APC control was built. The simulation results show the stability of the control system, which provides a reference to physical system designs of such switched reluctance motor.

**Keywords** Switched reluctance motor · Control system · Simulation  
Electromagnetic torque

## 1 Introduction

Switched reluctance machine is divided into switched reluctance motor and switched reluctance generator. Domestic and foreign scholars have applied a wide range of research on the application of switched reluctance motor in rail transit. There are single-phase, two-phase, three-phase, four-phase and multi-phase switched reluctance motor, and in the case of same phase, the number of poles of stator and rotor can have different matches [1, 2]. Switched reluctance motor has the advantages of simple structure, low noise and so on. Currently, three-phase 12/8 switched reluctance motor and four-phase 8/6 switched reluctance motor are most widely used. In this paper, four-phase 8/6 switched reluctance motor is taken as an example and modeling was done on its drive system, which provides theoretical support for physical design.

---

C. Lu (✉) · G. Zhang · C. Du · J. Cheng · C. Wu  
School of Electrical and Photoelectronic Engineering, West Anhui University,  
Yunlu Road, Yuan District, Lu'An 237012, China  
e-mail: luchengling@hotmail.com

## 2 Structure Principle and Mathematical Model

### 2.1 Structure Principle

The operation of switched reluctance motor follows the principle of minimum reluctance, that is to say, The flux is always closed along the minimal path of the magnetoresistance [3, 4]. When the rotor core is rotated to the minimum position of the magnetic resistance, The main axis of the rotor is coincident with the main axis of the electrified phase. The controller sends the control pulse to switch between the stator and the rotor of the switched reluctance motor. The operating principle of four-phase 8/6 switched reluctance motor is shown in Fig. 1.

### 2.2 Mathematical Model

It is assumed that the structure and parameters of the motor are symmetrical and the core loss is ignored, we can derive the mathematical formula for the voltage equation, flux equation, mechanical motion equation and torque equation as follows.

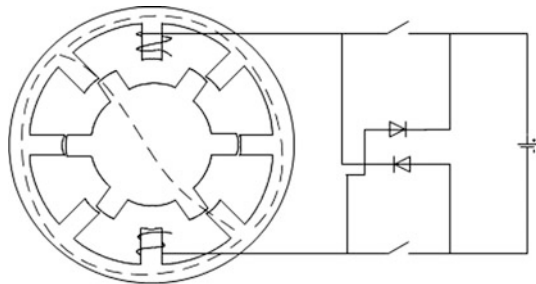
#### 2.2.1 Voltage Equation

According to the analysis of the internal current path of the motor, phase voltage balances equation of switched reluctance motor is derived as follows:

$$u_m = R_m i_m + \frac{d\Psi_m}{dt} \quad (1)$$

Among them,  $u_m$ ,  $i_m$ ,  $R_m$  and  $\Psi_m$  are respectively terminal voltage, current, resistance and flux linkage of m-phase winding.

**Fig. 1** Operating principle of four-phase 8/6 switched reluctance motor



### 2.2.2 Flux Equation

Due to the fact that the phase mutual inductance is very small, it can obtain the function of each phase winding flux and the phase current, the self inductance and the rotor position angle in the case of neglecting the mutual inductance, and the flux equation is simplified as shown in formula (2)

$$\Psi_m = L_m(\theta_m, i_k) i_k \quad (2)$$

The Eq. (2) into Eq. (1), we obtains the following equation.

$$\begin{aligned} u_m &= R_m i_m + \frac{\partial \Psi_m}{\partial t} \frac{di_m}{dt} + \frac{\partial \Psi_m}{\partial \theta} \frac{d\theta}{dt} \\ &= R_m i_m + \left( L_k + \frac{\partial L_m}{\partial i_k} \right) \frac{di_m}{dt} + i_m \frac{\partial L_m}{\partial \theta} \frac{d\theta}{dt} \end{aligned} \quad (3)$$

Equation (3) shows that the supply voltage is equivalent to the plus value of three voltage drops in the circuit. The first item on the left side of the equation denotes the resistance drop in m-phase circuit, the second item denote the electromotive force induced by flux linkage change, which is caused by current variation, the third item denotes the electromotive force induced by flux linkage change in the winding, which is caused by rotor position change.

### 2.2.3 Mechanical Motion Equation

$$T_e = J \frac{d^2\theta}{dt^2} + k_\omega \frac{d\theta}{dt} + T_L \quad (4)$$

Among them,  $T_e$ ,  $J$ ,  $k_\omega$  and  $T_L$  are respectively electromagnetic torque of the motor, rotational inertia of the system, friction coefficient and load torque.

### 2.2.4 Torque Equation

The electromagnetic torque of switched reluctance motor can be obtained by partial derivative of magnetic coenergy  $W'_m$  to rotor position angle  $\theta$ , as shown in Eq. (5)

$$T_e(i, \theta) = \left. \frac{\partial W'_m(i, \theta)}{\partial \theta} \right|_{i=Const} \quad (5)$$

$W'_m(i, \theta) = \int_0^i \Psi(i, \theta) di$  is equation of the magnetic coenergy of the winding.

Equation (1) to (5) constitute the mathematical model of switched reluctance motor. The mathematical model is complete and accurately describes the

electromagnetic and mechanical relations in switched reluctance motor. With the model, switched reluctance motor can be regarded as an electromechanical device with 4 pairs of electrical ports and a pair of mechanical ports, as shown in Fig. 2. However, due to the nonlinearity and switching of circuit and magnetic circuit, it's quite difficult to carry out model calculation, so we construct the Simulink model for simulation and analysis [5].

### 3 Composition of Switched Reluctance Motor Drive System

Switched reluctance motor drive system is mainly composed of four parts: switched reluctance motor, power converter, controller and detecting part [6, 7]. The power converter converts external energy into an energy form suitable for switched reluctance motor, and the controller deals with information from position detection and current detection and accepts the command given by the set value [8]. The detecting part realizes detection of corresponding information through sensor and other components, as shown in Fig. 3.

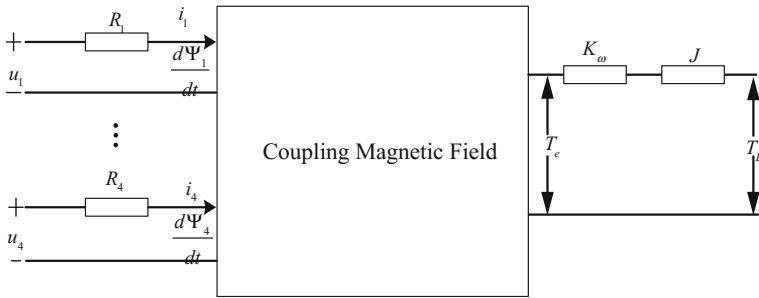


Fig. 2 Four-phase switched reluctance motor system diagram

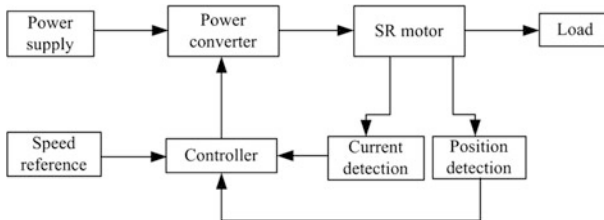


Fig. 3 Switched reluctance motor drive system



## 4 Modeling and Simulation

### 4.1 Modeling of Position Sensor

The signal emission circuit of four-phase 8/6 switched reluctance motor is as shown in the Fig. 4. The rotor angular velocity  $W$  is transformed from rad/s to deg/s through scaling transformation. The relative positions of the four phases are obtained by discrete integrator  $\frac{K T_s}{z-1}$ . There are 15 degrees of difference between the four phases relative to their respective position, so the initial relative positions are 0, 15, 30 and 45, respectively. By changing conduction angle and turn-off angle, corresponding control can be implemented, that is, APC control is used.

### 4.2 Modeling of Power Converter Module

The power converter uses double-switch main circuit. When two main switches IGBT1 and IGBT2 are conducted simultaneously, power will flow into motor winding. when IGBT1 and IGBT2 are turned off simultaneously, phase current continues to flow through fly-wheel diode, thus the magnetic field energy of the motor can be fed back to the power supply quickly in a form of electric energy to realize forced commutation [9, 10]. The simulation model is as shown in Fig. 5.

### 4.3 System Modeling

The system is mainly composed of power supply, power converter, controller, current detection and position detection [11–13]. Based on the previous introduction of core position detection and power conversion, the power supply adopts DC 90 V, and 8/6 switched reluctance motor provided by the system is used. The current detecting part adopts the current hysteresis control module, which is provided by Simulink library through modification of parameters. The module mainly realizes current hysteresis control and provides signals for on-off of the converter. The read-only parameter of switched reluctance motor module was modified,

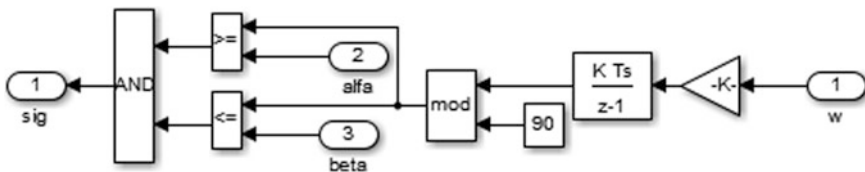


Fig. 4 Model of position sensor

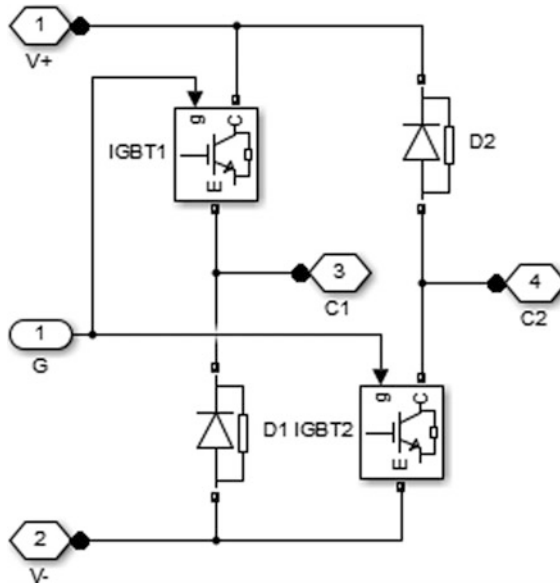


Fig. 5 Model of double-switch power converter

the parameters were altered according to relevant variables in the mathematical model, and the flux linkage, current, electromagnetic torque and rotor speed and waveform of rotor speed were collected in turn. The system modeling is as shown Fig. 6.

## 5 Analysis of Simulation Result

The simulation result shows that the system simulation model is feasible. It can be seen from waveform analysis that, there's a large gap between the four phase flux linkages in the starting moment, along with motor starting, the four phase flux linkages tend to be equivalent, the collected current waveform and electromagnetic torque wave tend to be symmetrical, the rotor speed gradually increases to the rated value, which is in line with the parameter characteristic of the motor. The results are shown in Fig. 7.

Based on the analysis of mathematical Model of switched reluctance motor and drive system, a nonlinear simulation model of switched reluctance motor drive system was built by simulink module, which adopts the APC control method. The nonlinear simulation model provides an effective means for the analysis and design of the switched reluctance motor control system.

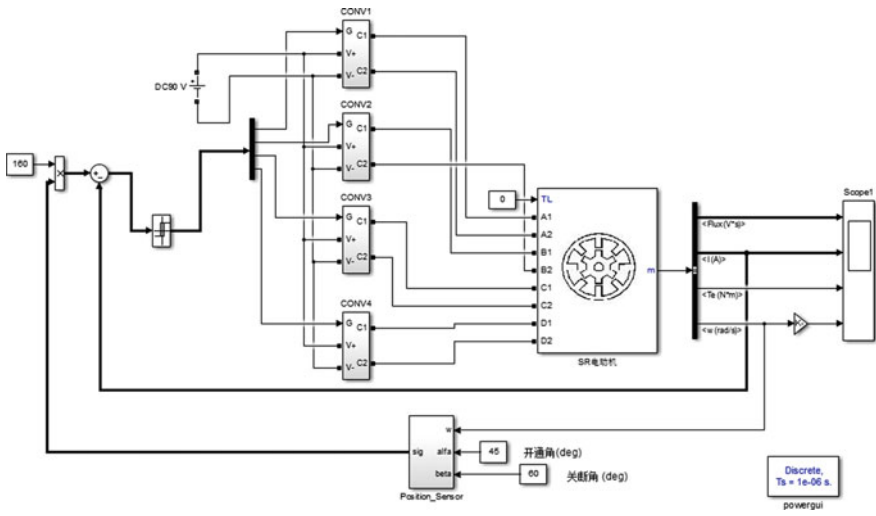


Fig. 6 System modeling

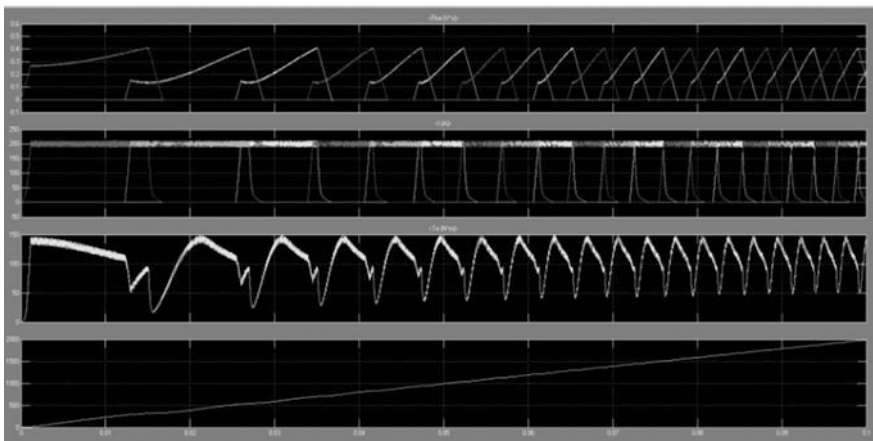


Fig. 7 Simulation result

**Acknowledgements** This work was supported in part by the Talent Project of the Anhui Province for Outstanding Youth under Grant (gxyqZD2016247 & gxyqZD2018CL.Lu) and WXC Foundation under Grant (WXZR201705 & WXZR201725).

## References

1. Lu C, Zhang G, Du C (2015) Design and implementation of low-power SRM control system. *IFAC-PapersOnLine* 48(28):269–272
2. Peng F, Ye J, Emadi A (2016) A digital PWM current controller for switched reluctance motor drives. *IEEE Trans Power Electron* 31(10):7087–7098
3. Huang HN, Hu KW, Wu YW et al (2016) A current control scheme with back EMF cancellation and tracking error adapted commutation shift for switched-reluctance motor drive. *IEEE Trans Industr Electron* 63(12):7381–7392
4. Ye J, Bilgin B, Emadi A (2015) An offline torque sharing function for torque ripple reduction in switched reluctance motor drives. *IEEE Trans Energy Convers* 30(2):726–735
5. Mikail R, Husain I, Islam MS et al (2015) Four-quadrant torque ripple minimization of switched reluctance machine through current profiling with mitigation of rotor eccentricity problem and sensor errors. *IEEE Trans Ind Appl* 51(3):2097–2104
6. Dufour C, Cense S, Bélanger J (2013) FPGA-based switched reluctance motor drive and DC-DC converter models for high-bandwidth HIL real-time simulator. In: 2013 15th IEEE European conference on power electronics and applications, pp 1–8
7. Jakobsen U, Lu K, Rasmussen PO et al (2015) Sensorless control of low-cost single-phase hybrid switched reluctance motor drive. *IEEE Trans Ind Appl* 51(3):2381–2387
8. Ye J, Bilgin B, Emadi A (2015) Elimination of mutual flux effect on rotor position estimation of switched reluctance motor drives considering magnetic saturation. *IEEE Trans Power Electron* 30(2):532–536
9. Chen ZM, Cao GZ, Huang SD et al (2016) Dual-loop control strategy with a robust controller of the planar switched reluctance motor for precise positioning. In: 2016 IEEE 11th conference on industrial electronics and applications, pp 172–177
10. Widmer JD, Martin R, Mecrow BC (2015) Optimization of an 80-kW segmental rotor switched reluctance machine for automotive traction. *IEEE Trans Ind Appl* 51(4):2990–2999
11. Cao X, Yang H, Zhang L et al (2016) Compensation strategy of levitation forces for single-winding bearingless switched reluctance motor with one winding total short circuited. *IEEE Trans Industr Electron* 63(9):5534–5546
12. Guo Y, Ma Q, Ye W (2016) Comparative study on torque ripple suppression method of three-phase 6/4 switched reluctance motor. In: IEEE international conference on aircraft utility systems, pp 356–361
13. Ro HS, Kim DH, Jeong HG et al (2015) Tolerant control for power transistor faults in switched reluctance motor drives. *IEEE Trans Ind Appl* 51(4):3187–3197

# Isolated Transit Signal Priority Control Strategy Based on Lane-by-Lane Vehicle Detection Scheme

Jun Deng and Liang Cui

**Abstract** In contrast to the conventional single-channel detection which uses all the detectors across all the lanes as a single input to a signal phase, the lane-by-lane detection monitors the gaps/headways on a lane-by-lane basis. In the conventional actuated control detection, detectors transmitted information to the signal control machine as long as they were triggered, but signal control machine can not distinguish which lane are they from. In the lane-by-lane detection proposed in this paper, detectors of each lane worked independently and transmitted information of each lane to the signal control machine separately. Based on the probability theory, models were derived for estimating the green extensions with various geometric configurations. Using the proposed models, green extensions for actuated signal controls can be obtained. By comparing the required green extensions of buses and social vehicles to determine whether to give priority to the bus signal. The lane-by-lane control strategy proposed in this paper were simulated by VISSIM. The simulation results showed that the lane-by-lane control strategy has a better control effect in different situations compared with the fixed time control strategy and conventional actuated control strategy.

**Keywords** Lane-by-lane detection • Actuated control • Bus priority  
Green extension • VISSIM

---

J. Deng (✉)  
CCCC Rail Transit Consultants Co., Ltd., No. 18, Pioneering Road,  
Caidian District, Wuhan, China  
e-mail: 81393805@qq.com

L. Cui (✉)  
School of Traffic and Transportation, Lanzhou Jiaotong University,  
No. 88, Anning West Road, Anning District, Lanzhou, China  
e-mail: 1192711588@qq.com

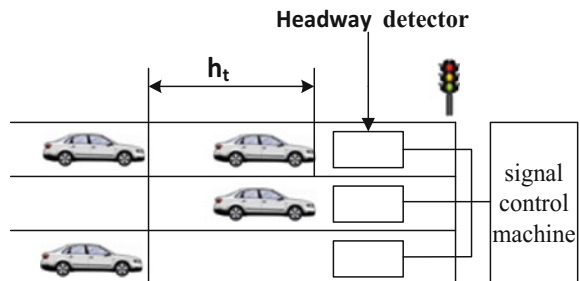
© Springer Nature Singapore Pte Ltd. 2018

L. Jia et al. (eds.), *Proceedings of the 3rd International Conference on Electrical and Information Technologies for Rail Transportation (EITRT) 2017*, Lecture Notes in Electrical Engineering 482, [https://doi.org/10.1007/978-981-10-7986-3\\_65](https://doi.org/10.1007/978-981-10-7986-3_65)

## 1 Introduction

Bus priority is an effective way to improve the efficiency of public transport and improve the level of public transport services. There are two ways to achieve the priority of public transport: the optimization of road space and the optimization of signal timing [1]. The former mainly through the setting of bus lanes or double stop lines and other ways to achieve. However, it is needed to meet various objective conditions, so it is often restricted in practice. The latter is widely used as a result of easy implementation, actuated signal control is one of it. Actuated signal control is a kind of feedback control that adapted signal timing to the changing traffic by detecting the real-time traffic volume of the intersection. Compared with the fixed time control, the actuated control adapted to the fluctuation of traffic better. Vehicle detection is an important part of modern traffic signal control systems [2, 3]. Over the past few decades, research on detector layout and parameter setup has been focused on the size and location of advanced detectors for achieving various operational objectives. Examples of such studies include advanced call detector location and bus signal priority operations [4], and advanced detectors for dilemma zone protection [5]. One of the critical aspects that has not been well studied is regarding detection schemes at typical signalized intersections with multiple lane approaches. At signalized intersections with multilane approaches, current practice is place detectors in each individual lane and as long as detectors were triggered, they transmitted information to the signal control machine, detected headways are less than the actual headways, it is not reflect the actual headways of each lane, as shown in Fig. 1. In the lane-by-lane detection proposed in this paper, detectors of each lane worked independently and transmitted information of each lane to the signal control machine separately, as shown in Fig. 2.

**Fig. 1** Traditional detector operating mode



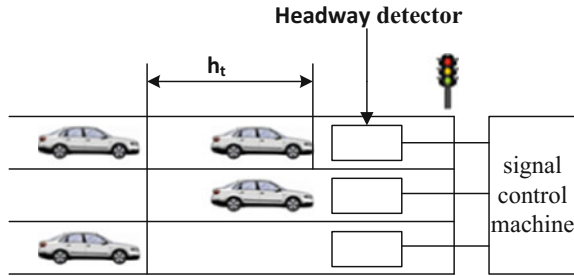


Fig. 2 Improved detector operating mode

## 2 Modeling Green Extension with a Lane-by-Lanevehicle Detection Scheme

For the conventional actuated control detection, Akcelik [6] developed the following formulations.

The green extension (extended green light time) beyond the time to clear queue depends on the maximum allowable headway (MAH),  $h$ . The number of headways that the controller would be expected to hold forms a geometric distribution.

$$P_n = p^n(1 - p) \tag{1}$$

where

$P_n$  = probability of extending  $n$  headways before experiencing a headway greater than  $h$ .

$P$  = probability of having a headway less than or equal to  $h$ .

$n$  = number of headways under consideration.

If the headway distribution function  $f(t)$  is known, we have

$$p = P(t < h) = \int_0^h f(t)dt = F(h) \tag{2}$$

The average number of headways (Expectation of  $n$ ) the controller to hold,  $\bar{N}$ , can be obtained from the characteristics of a geometric distribution:

$$\bar{N} = E(n) = \sum_{n=1}^{\infty} nP_n = \sum_{n=1}^{\infty} np^{n-1}(1 - p)p = p \sum_{n=1}^{\infty} np^{n-1}(1 - p) = \frac{P}{1 - p} \tag{3}$$

The average green extension time would be the product of  $\bar{N}$  and the average length of headway,  $\bar{T}$ .

The average length of the headways that are less than  $h, \bar{T}$ , is

$$\bar{T} = \frac{V \int_0^h t \cdot f(t) dt}{V \int_0^h f(t) dt} = \frac{\int_0^h t \cdot f(t) dt}{\int_0^h f(t) dt} = \frac{\int_0^h t \cdot f(t) dt}{p} \tag{4}$$

where  $V$  is the flow volume under consideration, vph.

The numerator is the total time of those headways less than  $h$  and the denominator is the number of headways that are less than  $h$ . So the expected green extension,  $g_{extent}$ , is

$$g_{extent} = \left[ \sum_{n=1}^{\infty} nP_n \right] \bar{T} = \bar{N} \cdot \bar{T} = \frac{p}{1-p} \frac{\int_0^h t \cdot f(t) dt}{p} = \frac{\int_0^h t \cdot f(t) dt}{1-p} \tag{5}$$

In the original work by Akeclik,  $h$  was added to the green extension, indicating the phase green actually terminates  $h$  after the last gap-out headway. Because the  $h$  portion of the green extension is a constant amount regardless of detection type, eliminating  $h$  from the green extension does not affect the comparison results. If necessary, all the green extensions calculated in this paper can be extended by  $h$ . With different headway distributions,  $g_{extent}$  can be calculated accordingly.

Theoretically, for the lane-by-lane detection, the probability of phase gap-out is the total probability of one lane gaps out while the other lanes have gapped out earlier. The condition of a lane gapping out is when a headway in that lane exceeds  $h$ . If there are three lanes on the road, three possible combinations should be considered in the lane-by-lane detection model:

The probability that Lane 1 gaps out after  $n_1$  detected headways can be obtained from the geometric distribution:

$$P(L_1^{n_1}) = p_1^{n_1} (1 - p_1) \tag{6}$$

Assuming in the same time period there are  $n_2$  gaps detected in Lane 2, the probability that Lane 2 gaps out within the same period is the probability that within the  $n_2$  gaps, at least one gap is larger than  $h$ . This probability can be expressed by the probability equation:

$$P(L_2^{n_2}) = P(\hat{L}_2^{n_2}) = 1 - p_2^{n_2} \tag{7}$$

In the same way:

$$P(L_3^{n_3}) = P(\hat{L}_3^{n_3}) = 1 - p_3^{n_3} \tag{8}$$

Note that  $p_2^{n_2}$  in the equation above is the probability that none of the  $n_2$  headways is greater than  $h$ .  $p_3^{n_3}$  is the probability that none of the  $n_3$  headways is greater than  $h$ .



The probability that Lane 1 gaps out while Lane 2, Lane 3 gaps out earlier is then

$$\begin{aligned}
 & P^{n_1,23} (L_1^{n_1} \cap \hat{L}_2^{n_2} \cap \hat{L}_3^{n_3}) \\
 &= P(L_1^{n_1}) \cdot P(\hat{L}_2^{n_2}) \cdot (\hat{L}_3^{n_3}) = p_1^{n_1} (1 - p_1) (1 - p_2^{n_2}) (1 - p_3^{n_3}) \\
 &= p_1^{n_1} (1 - p_1) (1 - p_2^{n_2} - p_3^{n_3} + p_2^{n_2} p_3^{n_3}) \\
 &= p_1^{n_1} (1 - p_1) - p_1^{n_1} (1 - p_1) p_2^{n_2} - p_1^{n_1} (1 - p_1) p_3^{n_3} + p_1^{n_1} (1 - p_1) p_2^{n_2} p_3^{n_3}
 \end{aligned} \tag{9}$$

Assuming for a given time period the numbers of headways in both lanes are proportional to the traffic flows (this assumption is reasonable because the arrivals are proportional to the flow rates), we have

$$\frac{n_1}{n_2} = \frac{q_1 n_1}{q_2 n_3} = \frac{q_1}{q_3}, \frac{n_2}{n_3} = \frac{q_2}{q_3} \tag{10}$$

where

- $q_1$  = flow rate in lane 1, vph
- $q_2$  = flow rate in lane 2, vph
- $q_3$  = flow rate in lane 3, vph

Thus,

$$\begin{aligned}
 & P^{n_1,23} (L_1^{n_1} \cap \hat{L}_2^{n_2} \cap \hat{L}_3^{n_3}) \\
 &= P(L_1^{n_1}) \cdot P(\hat{L}_2^{n_2}) \cdot (\hat{L}_3^{n_3}) = p_1^{n_1} (1 - p_1) (1 - p_2^{n_2}) (1 - p_3^{n_3}) \\
 &= p_1^{n_1} (1 - p_1) - p_1^{n_1} (1 - p_1) p_2^{n_2} - p_1^{n_1} (1 - p_1) p_3^{n_3} + p_1^{n_1} (1 - p_1) p_2^{n_2} p_3^{n_3} \\
 &= p_1^{n_1} (1 - p_1) - p_1^{n_1} p_2^{\binom{n_2}{n_1 \frac{q_2}{q_1}}} (1 - p_1) \\
 &\quad - p_1^{n_1} p_3^{\binom{n_3}{n_1 \frac{q_3}{q_1}}} (1 - p_1) + p_1^{n_1} p_2^{\binom{n_2}{n_1 \frac{q_2}{q_1}}} p_3^{\binom{n_3}{n_1 \frac{q_3}{q_1}}} (1 - p_1)
 \end{aligned} \tag{11}$$

Note the arrangement of the above equation is for derivation of the following equation based on the characteristics of geometric distributions.

The average number of headways in Lane 1 that keeps the controller to hold,  $\bar{N}_{1,23} = E(n_1, L_1^{n_1} \cap \hat{L}_2^{n_2} \cap \hat{L}_3^{n_3})$ , while both Lane 2 and Lane 3 gaps out earlier can be obtained based on the geometric distribution:

$$\begin{aligned}
 \bar{N}_{1,23} &= E(n_1, L_1^{n_1} \cap \hat{L}_2^{n_2} \cap \hat{L}_3^{n_3}) = \sum n_1 \cdot P^{n_1,23}(L_1^{n_1} \cap \hat{L}_2^{n_2} \cap \hat{L}_3^{n_3}) \\
 &= \sum n_1 \cdot [p_1^{n_1}(1-p_1) - p_1^{n_1}(1-p_1)p_2^{n_2} - p_1^{n_1}(1-p_1)p_3^{n_3} + p_1^{n_1}(1-p_1)p_2^{n_2}p_3^{n_3}] \\
 &= \sum n_1 p_1^{n_1}(1-p_1) - \frac{(1-p_1)}{(1-p_1 p_2^{q_2})} \sum n_1 \left(p_1 p_2^{q_2}\right)^{n_1} (1-p_1 p_2^{q_2}) \\
 &\quad - \frac{(1-p_1)}{(1-p_1 p_3^{q_3})} \sum n_1 \left(p_1 p_3^{q_3}\right)^{n_1} (1-p_1 p_3^{q_3}) \\
 &\quad + \frac{(1-p_1)}{(1-p_1 p_2^{q_2} p_3^{q_3})} \sum n_1 \left(p_1 p_2^{q_2} p_3^{q_3}\right)^{n_1} (1-p_1 p_2^{q_2} p_3^{q_3}) \\
 &= \frac{p_1}{(1-p_1)} - \frac{p_1 p_2^{q_2}}{(1-p_1 p_2^{q_2})^2} (1-p_1) - \frac{p_1 p_3^{q_3}}{(1-p_1 p_3^{q_3})^2} (1-p_1) + \frac{p_1 p_2^{q_2} p_3^{q_3}}{(1-p_1 p_2^{q_2} p_3^{q_3})^2} (1-p_1)
 \end{aligned} \tag{12}$$

The average length of the headways (in Lane 1) that are less than  $h, \bar{T}_1$ , is

$$\bar{T}_1 = \frac{\int_0^h t \cdot f_1(t) dt}{p_1} \tag{13}$$

So the expected green extension of this case,  $g_{3-lane}^{extend}$ , is

$$\begin{aligned}
 g_{3-lane}^{extend}(L_1^{n_1} \cap \hat{L}_2^{n_2} \cap \hat{L}_3^{n_3}) &= \bar{N}_{1,23} \cdot \bar{T}_1 = E(n) \cdot \bar{T}_1 = E(n_1, L_1^{n_1} \cap \hat{L}_2^{n_2} \cap \hat{L}_3^{n_3}) \cdot \bar{T}_1 \\
 &= \left[ \frac{p_1}{(1-p_1)} - \frac{p_1 p_2^{q_2}}{(1-p_1 p_2^{q_2})^2} (1-p_1) - \frac{p_1 p_3^{q_3}}{(1-p_1 p_3^{q_3})^2} (1-p_1) \right. \\
 &\quad \left. + \frac{p_1 p_2^{q_2} p_3^{q_3}}{(1-p_1 p_2^{q_2} p_3^{q_3})^2} (1-p_1) \right] \cdot \frac{\int_0^h t \cdot f_1(t) dt}{p_1}
 \end{aligned} \tag{14}$$

Because of the symmetry, we can get

$$\begin{aligned}
 g_{3-lane}^{extend}(\hat{L}_1^{n_1} \cap L_2^{n_2} \cap \hat{L}_3^{n_3}) &= \left[ \frac{p_2}{(1-p_2)} - \frac{p_2 p_1^{q_1}}{(1-p_2 p_1^{q_1})^2} (1-p_2) - \frac{p_2 p_3^{q_3}}{(1-p_2 p_3^{q_3})^2} (1-p_2) \right. \\
 &\quad \left. + \frac{p_2 p_1^{q_1} p_3^{q_3}}{(1-p_2 p_1^{q_1} p_3^{q_3})^2} (1-p_2) \right] \cdot \frac{\int_0^h t \cdot f_2(t) dt}{p_2}
 \end{aligned} \tag{15}$$

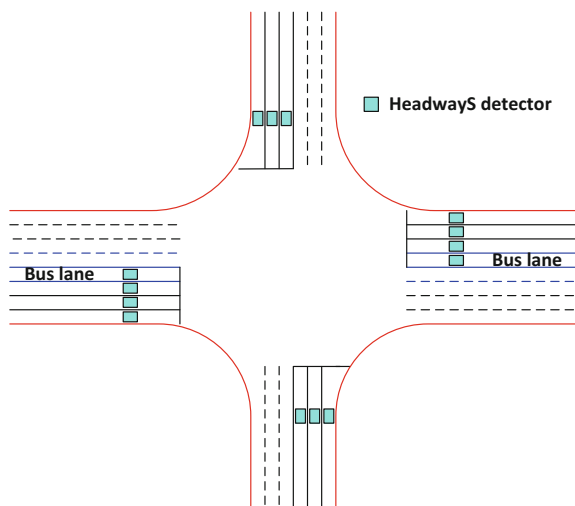
$$\begin{aligned}
 &g_{3-lane}^{extend} (\hat{L}_1^{n_1} \cap \hat{L}_2^{n_2} \cap L_3^{n_3}) \\
 &= \left[ \frac{p_3}{(1-p_3)} - \frac{p_2^{\frac{q_2}{q_3}} p_3}{(1-p_2^{\frac{q_2}{q_3}} p_3)^2} (1-p_3) - \frac{p_3 p_1^{\frac{q_1}{q_3}}}{(1-p_3 p_1^{\frac{q_1}{q_3}})^2} (1-p_3) \right. \\
 &\quad \left. + \frac{p_3 p_1^{\frac{q_1}{q_3}} p_2^{\frac{q_2}{q_3}}}{(1-p_3 p_1^{\frac{q_1}{q_3}} p_2^{\frac{q_2}{q_3}})^2} (1-p_3) \right] \cdot \frac{\int_0^h t \cdot f_3(t) dt}{p_3}
 \end{aligned} \tag{16}$$

### 3 Bus Priority Strategy

The lane-by-lane detection theory changes the traditional working mode of the detector, more realistic response to the traffic conditions of each lane, and we also get the green extension with lane-by-lane vehicle detection scheme. Based on these, we can realize bus priority at actuated traffic signals with a bus lane. The direction of bus lane does not affect the simulation results. The headway detector is located at 50 m from the stop line at the intersection, as shown in Fig. 3.

In this paper, the buses and social vehicles are considered separately, we can get the green extension of buses that meet the extension condition in the bus lane from the Akcelik model. Using  $g_1$  to express the green extension of buses. Applying the lane-by-lane detection method to the detection of social vehicles, we can get the green extension of social vehicles that meet the extension condition. Using  $g_2$  to express the green extension of social vehicles. When the buses and social vehicles in the same direction meet the extension condition, if  $g_1 \leq g_2$ , extending green time  $g_2$ , otherwise extending green time  $g_1$ . When the buses meet the extension

Fig. 3 The position of the headways detector



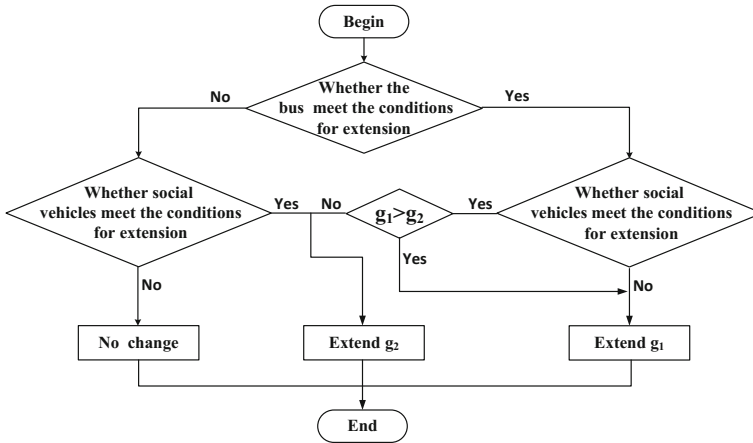


Fig. 4 The logical diagram of the bus priority system

condition, the social vehicles are not satisfied, extending green time  $g_1$ . When the social vehicles meet the extension condition, the buses are not satisfied, extending green time  $g_2$ . When the buses and social vehicles in the same direction not meet the extension condition, operated according to the original phase, as shown in Fig. 4.

### 4 Simulation Results and Analysis

In this paper, the maximum allowable headway (MAH) is 3 s. The headways of buses obey the negative exponential distribution, there are 2 people in each car and 40 people in each bus. Using VISSIM micro simulation software to establish the simulation model, and through the VISVAP module to realize bus priority control strategy based on lane-by-lane detection. Contrast control strategies include: fixed time control strategy, using the Webster formula to calculate the phase control scheme; conventional actuated control strategy, as shown in Fig. 5; lane-by-lane control strategy proposed in this paper. Results of 3 control strategies under different traffic loads, as shown in Tables 1 and 2.

As show in Fig. 6, compared with fixed time control strategy, conventional actuated control strategy, the lane-by-lane control strategy can reduce the average vehicle delay of buses and social vehicles and the average vehicle delay decrease of buses is greater than the average vehicle delay decrease of social vehicles. Similar conclusions can be obtained in the medium and high degree of saturation. As show in Fig. 7, the lane-by-lane control strategy can reduce the delay per person of all vehicles in the intersection.

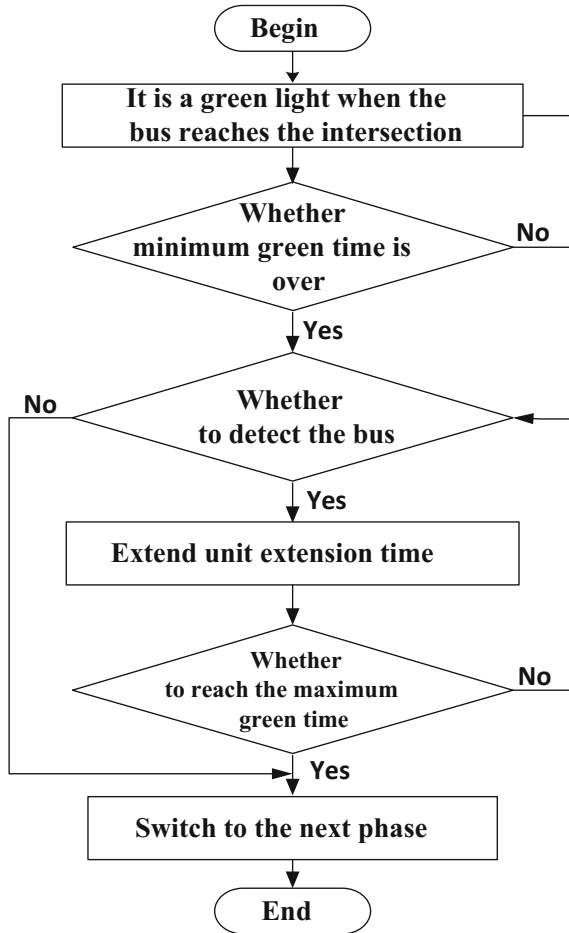


Fig. 5 The logical diagram of conventional actuated control

Table 1 Average vehicle delay of 3 control strategies in different degree of saturation

Average vehicle delay									
	Low saturation			Medium saturation			High saturation		
	All	Vehicles	Buses	All	Vehicles	Buses	All	Vehicles	Buses
FTCSa	25.8	25.7	27.2	34.3	34.2	35.2	44.5	44.3	45.3
CACSB	23.2	23.1	24.3	28.9	28.8	29.1	32.2	32.8	31.9
LLCSc	20.6	21.2	15.1	24.6	25.3	12.0	29.5	30.4	12.8

**Table 2** Per capita delay of 3 control strategies in different degree of saturation

Per capita delay			
	Low saturation	Medium saturation	High saturation
FTCS <sup>a</sup>	26.6	34.8	44.9
CACS <sup>b</sup>	23.8	29.0	32.2
LLCS <sup>c</sup>	14.9	16.9	19.3

<sup>a</sup>The fixed time control strategy

<sup>b</sup>The conventional actuated control strategy

<sup>c</sup>The lane-by-lane control strategy

**Fig. 6** Average vehicle delay of different strategies under low saturation

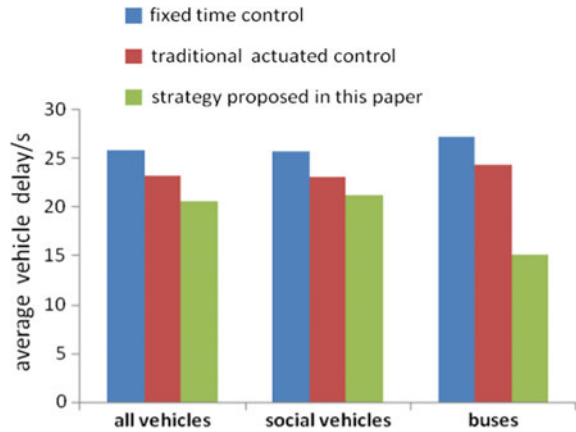


**Fig. 7** The per capita delay of different strategies in different degree of saturation

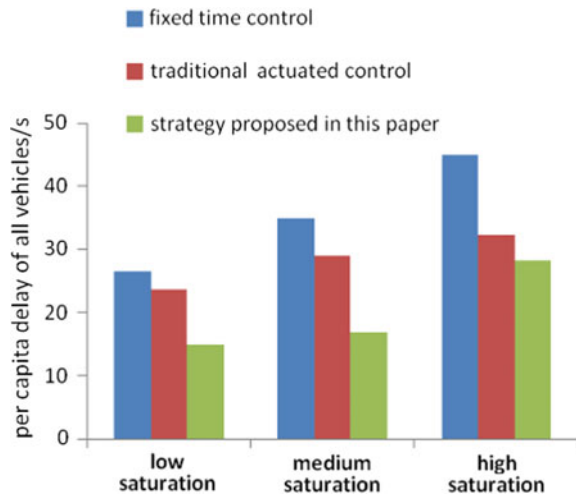
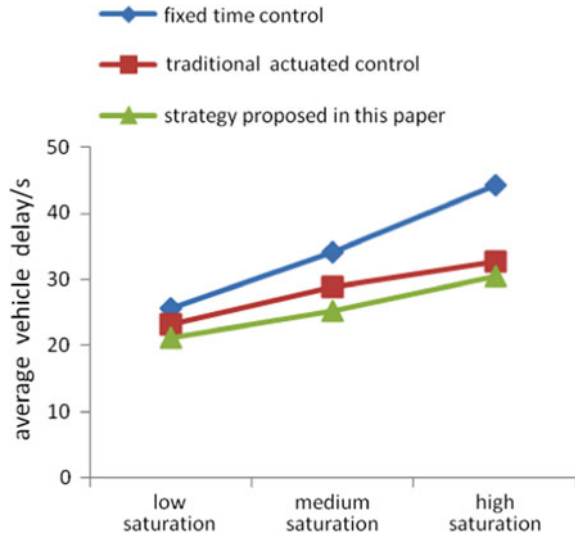
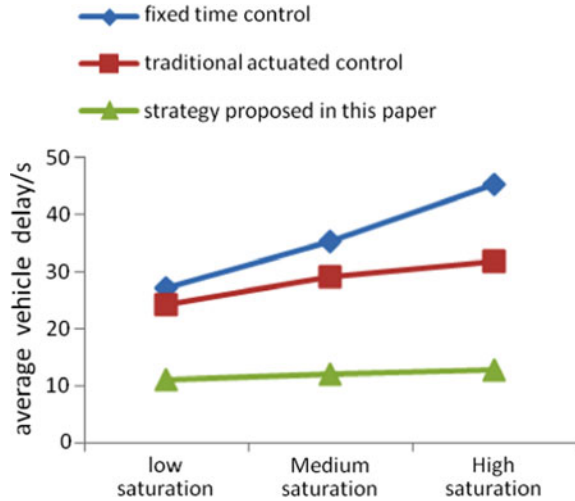


**Fig. 8** Average vehicle delay of social vehicles



As is depicted in Fig. 8, change trends of social vehicles' average vehicle delay of conventional actuated control strategy and lane-by-lane control strategy under the low saturation, medium saturation and high saturation are basically consistent, increase gently. However, for the fixed time control strategy, with the increase of saturation the average vehicle delay of social vehicles increase rapidly. The higher the degree of saturation is, the greater the average vehicle delay reduced amplitude of conventional actuated control and lane-by-lane control strategy is. It shows that the lane-by-lane control strategy can overcome the shortcoming of the fixed time control strategy and the traditional actuated control strategy, so as to reduce the delay of the vehicles. As is depicted in Fig. 9, for the lane-by-lane control strategy, the average vehicle delay of buses increases slowly with the increase of saturation. Compared with the lane-by-lane control strategy and fixed time control strategy, traditional actuated control strategy, the greater the degree of saturation is, the better the control effect is. It is showed that the lane-by-lane control strategy can control and reduce the average vehicle delay of buses.

**Fig. 9** Average vehicle delay of buses



## 5 Conclusion

The simulation test and the analysis results show that compared with the fixed time control strategy and the traditional actuated control strategy, the bus priority strategy based on lane-by-lane vehicle detection scheme proposed in this paper can achieve the bus priority and optimize the whole intersection at the same time. It is not only reduces the average vehicle delay of all vehicles but also reduces the per capita delay of all vehicles, the average vehicle delay and per capita delay reduction of buses is greater than that of social vehicles', which indicates the validity of the bus priority. This paper only selects the typical intersection to establish the simulation model, and carries on the simulation test under certain road traffic condition and signal control condition, the control effect of the actual application in the intersection remains to be tested.

**Acknowledgements** The work described in the paper was supported by Natural Science Foundation of China (No. 61463026, 61463027).

## References

1. Ma W, Yang X (2010) A review of prioritizing signal strategies for bus services. *Urban Transp China* 8(6):70–78 (in Chinese)
2. Bonneson JA, McCoy PT (1993) Methodology for evaluating traffic detector designs. *Transp Res Rec* 1421(2):6–81
3. Bonneson JA, McCoy PT (1995) Average duration and performance of actuated signal phases. *Transp Res Part A Policy Pract* 29(6):429–443



4. Liu H, Skabardonis A, Zhang W, Li M (2004) Optimal detector location for bus signal priority. *Transp Res Rec* 1867(4):144–150
5. Si J, Urbanik T, Han L (2007) Effectiveness of alternative detector configurations for option zone protection on high-speed approaches to traffic signals. *Transp Res Rec* 2035(1):107–113
6. Akcelik R (1994) Estimation of green times and cycle time for vehicle-actuated signals. *Transp Res Rec* 1457(3):63–72

# Analysis of the Effect of a Color Image Encryption Algorithm

Yukun Guo

**Abstract** Because of multimedia information has huge amount of data and high redundancy, traditional encryption technology is not suitable for multimedia information encryption. Multimedia information encryption get great development when chaos appears. Chaos is very suitable for image encryption because of its many advantages. In this paper, I analysed the shortcomings of color image encryption algorithm based on 3D unified chaotic system, then aiming at the algorithm deficiency, I analysed the algorithm which improved by cat map, the security of the algorithm has been greatly improved.

**Keywords** Encryption algorithm · Cat map · 3D unified chaotic system

## 1 Introduction

Today, with the rapid development and popularization of network, it offers many convenience for us. However, lots of data security problem appears, and serious more and more, we must encrypt the important data which transmitted in the network. At present, multimedia is one of the information carriers, it had get great attention for its such abundant data and strong intuition. But, it is difficult to encrypt multimedia information just because its huge amount of data and high redundancy, traditional encryption method can not meet current data security requirements.

Classical science was terminated when chaos appears. Because of chaos sequence has the following advantages: extreme sensitivity of the initial value, pseudo randomness, sequence track unpredictable, etc. [1], it is very suitable for multimedia information encryption, especially for image encryption. Common chaotic systems are the following: Logistic Map, Cat Map, 3D Unified Chaotic System, Hyperchaos, etc. Logistic map is the simplest chaotic system, and it is the

---

Y. Guo (✉)

College of Information Technology and Communication, Hexi University,  
No. 846 Beihuan Road, Zhangye, Gansu Province, China  
e-mail: 284831075@qq.com

© Springer Nature Singapore Pte Ltd. 2018

L. Jia et al. (eds.), *Proceedings of the 3rd International Conference on Electrical and Information Technologies for Rail Transportation (EITRT) 2017*, Lecture Notes in Electrical Engineering 482, [https://doi.org/10.1007/978-981-10-7986-3\\_66](https://doi.org/10.1007/978-981-10-7986-3_66)

653

prototype of chaotic system, its appearance reveals the prelude of the chaotic sequences research. The traditional image encryption algorithms include: gray value substitution, coordinate scrambling, XOR, permutation, etc. These algorithms does not have enough key space, and it is insecurity because key sequence is too simple. Image encryption algorithm based on chaotic sequence has high security because of chaotic sequence has a large key space and it is very complex.

## 2 3D Unified Chaotic System

3D Unified Chaotic System proposed by Liu Jin-hu and others in 2002. It was named unified chaotic system because it is a combination of Lorenz system and Chen system. It is a 3D chaotic system, and has three nonlinear equations and four parameters. The mathematical model of the system is as follows:

$$\begin{cases} x' = (25\alpha + 10)(y - x) \\ y' = (28 - 35\alpha)x - xz + (29\alpha - 1)y \\ z' = xy - (8 + \alpha)z/3 \end{cases} \quad (1)$$

In Eq. (1), the system has the global chaos characteristics when  $\alpha \in [0, 1]$ , and it can be regarded as a generalized Liu system when  $\alpha = 0.8$ ; and it also can be regarded as a generalized Lorenz system when  $\alpha < 0.8$ ; and it can be regarded as a generalized Chen system when  $\alpha > 0.8$ . RGB color image matrix is composed of three matrix R, G, B. 3D system is very suitable for color image encryption because of it can generate three key sequences. There are three sequence:  $f(x)$ ,  $f(y)$ ,  $f(z)$  can be generated by Eq. (1). These three sequences can be used to replace pixel gray value of the three matrix R, G, B.

### 2.1 The Design of Color Image Encryption Algorithm Based on 3D Unified Chaotic System

First of all, take out a primary color matrix RA of the image A to be encrypted, take out three points RA1 (i1, j1, k), RA2 (i2, j2, k), RA3 (i3, j3, k) from the matrix RA' in turn, and set a variable k which value from 1 to 3 cycles.

$$\text{set } \begin{cases} f(x) = (25\alpha + 10)(y - x) \\ f(y) = (28 - 35\alpha)x - xz + (29\alpha - 1)y \\ f(z) = xy - (8 + \alpha)z/3 \end{cases} \quad (2)$$

When  $k = 1$ , do XOR operation to the key sequence that generated by equation  $f(x)$  and the gray value of RA1 ( $i1, i1, k$ ); When  $k = 2$ , do XOR operation to the key sequence that equation  $f(y)$  generated and the gray value of RA1 ( $i2, i2, k$ ); When  $k = 3$ , do XOR operation to the key sequence that equation  $f(z)$  generated and the gray value of RA1 ( $i3, i3, k$ ), Loop until the pixel values of all points in matrix RA is replaced. Then encrypt another two image matrix A two other primary matrix GA and BA in the same way, synthesis of three matrices, get a new matrix A', A' is the ciphertext image. Key construction method is as follows:

Key structure at the first time, setting a variable r, variable r values shown in Eq. (3), Structure  $f(x)$  sequence,  $f(y)$  sequence,  $f(z)$  sequence with Eq. (4), generate three bit decimal number keys  $intkey1, intkey2, intkey3$ .

$$\text{set } r = \begin{cases} f(x)(k = 1) \\ f(y)(k = 2) \\ f(z)(k = 3) \end{cases} \tag{3}$$

$$intkey(1, 2, 3) = \text{fix}((r * 10^4 - \text{fix}(r * 10^4)) * 10^3) \tag{4}$$

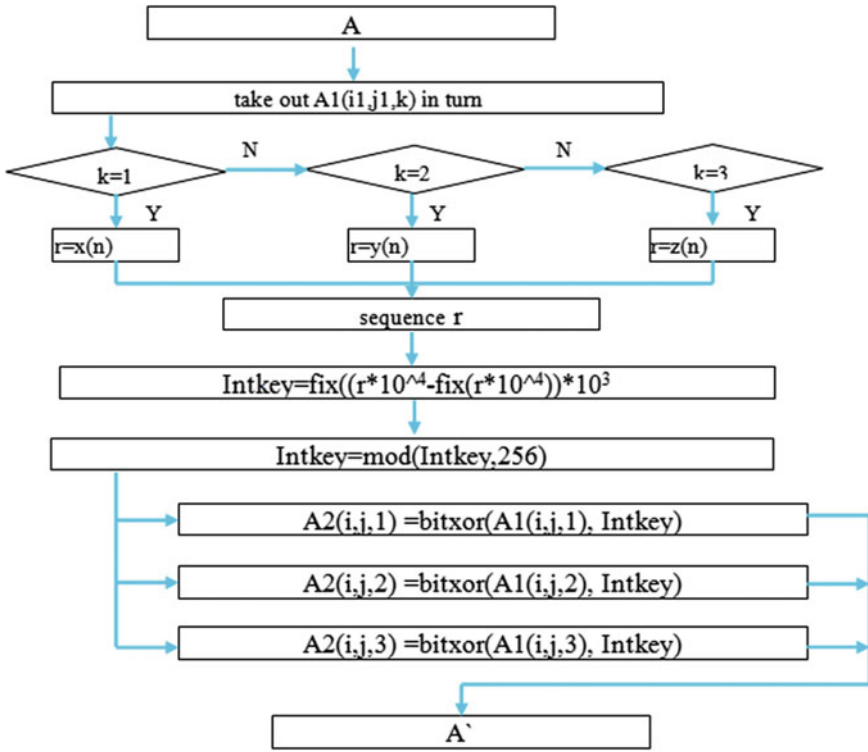
The second structure, to do modulo operation to  $intkey(1, 2, 3)$  and Eq. (5), then get an 8-bit unsigned integer  $intkey$ .

$$intkey = \text{mod}(intkey, 256) \tag{5}$$

The key  $intkey$  complexity is greatly improved after key construction twice, it can be used as the encryption key now. Do XOR operation to the pixel gray value all points of the three matrix with Eq. (6), then get ciphertext matrix RA', GA', BA', and get the ciphertext A' after the synthesis of three matrices. Inverse operation can decrypt.

$$A(i, j, k) = \text{bitxor}(A(i, j, k), intkey) \tag{6}$$

Encryption algorithm flow chart:



## 2.2 The Analysis of Algorithm Security

### 2.2.1 Visual Effects

Select deblur.jpg (256 × 256) and use Matlab7.0 to test this algorithm. Plaintext and ciphertext image as shown in Fig. 1.

The histogram of plaintext and ciphertext image as shown in Fig. 2. Figure 2(1) is the histogram of plaintext image A and Fig. 2(2) is the histogram of ciphertext image A'. The histogram of three primary color image matrix encrypted RA', GA', BA' is also the same as the histogram of the ciphertext of image A'. It can be seen from the histogram of plaintext and ciphertext that the pixel distribution of the plaintext is not uniform before encryption, and it is uniform after encryption, so it can resist known plaintext attack. In addition, using 3D unified chaotic system, it has four system parameters as the initial value, if all of the four parameters is a

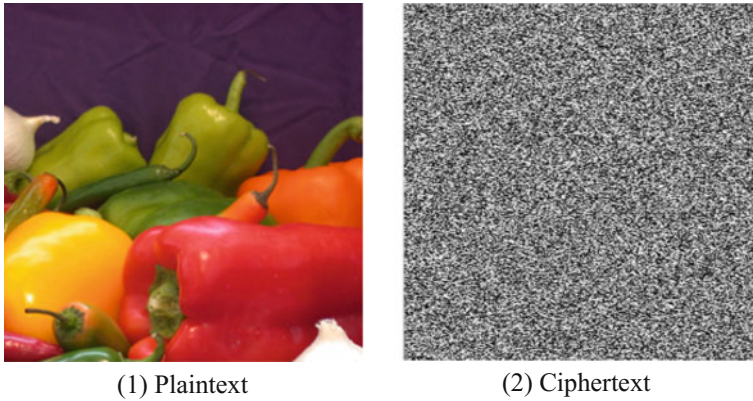


Fig. 1 Plaintext and ciphertext image

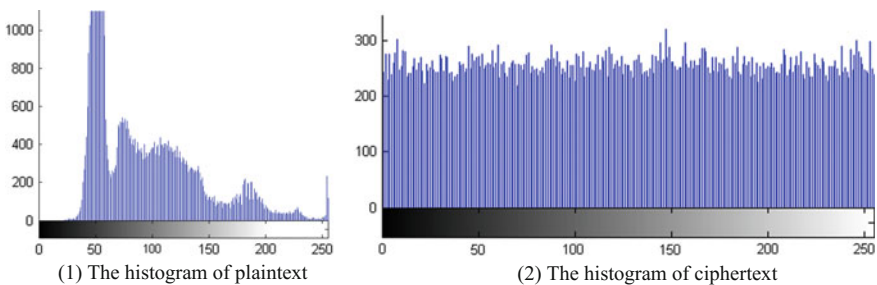


Fig. 2 The histogram of plaintext and ciphertext image

15-bit doubles, the key space can reach  $10^{15+15+15+15} = 10^{60}$ , it has huge key space and enough to resist exhaustive attack.

### 2.2.2 The Effect of Algorithm Decryption

It has extreme initial sensitivity for it is based on 3D unified chaotic system, unable to decrypt if any tiny errors in key appears, the results are shown in Fig. 3. We can see from the histogram of the subtraction of original image and the decrypted image as Fig. 3(2), the 0 matrix is obtained when the key is correct, no error in decryption algorithm.

### 2.2.3 Analysis of the Lack of Algorithm

It has been proved that the algorithm is sensitive to the initial value and has a huge key space, and it is uniform distribution after encryption, so it can resist known

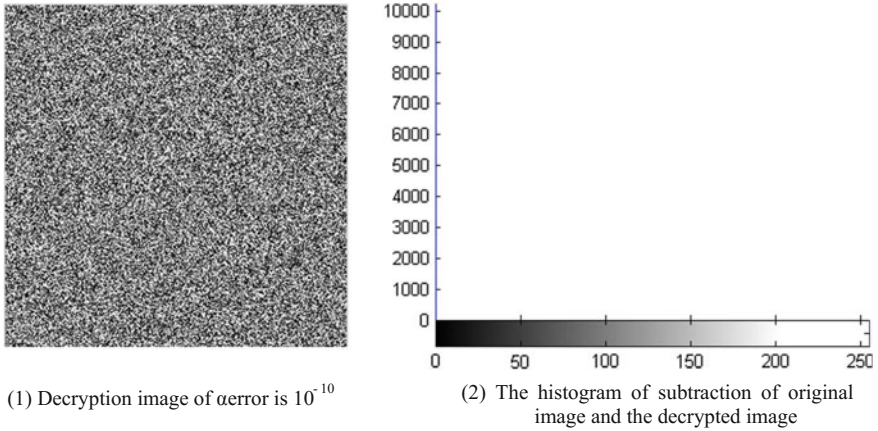


Fig. 3 Decryption effect validation

plaintext attack. But, the algorithm only changes the pixel gray value of plaintext image, no coordinate scrambling, the security of the algorithm can be further improved.

### 3 Improvement of Algorithm by Two Dimensional Cat Map

Arnold is the first person to propose cat map [2], it was named cat map because often use a cat face to show the effect. Its mathematical model is as follows:

$$\begin{cases} x_{n+1} = (x_n + y_n) \bmod 1 \\ y_{n+1} = (x_n + 2y_n) \bmod 1 \end{cases} \tag{7}$$

It can be seen from the mathematical model of cat map, it is only retains decimal part,  $x \bmod 1 = 1 - |x|$ , its phase space in a square of region  $[0, 1]$ . Convert it into matrix model, it becomes a new model as shown in Eq. (8):

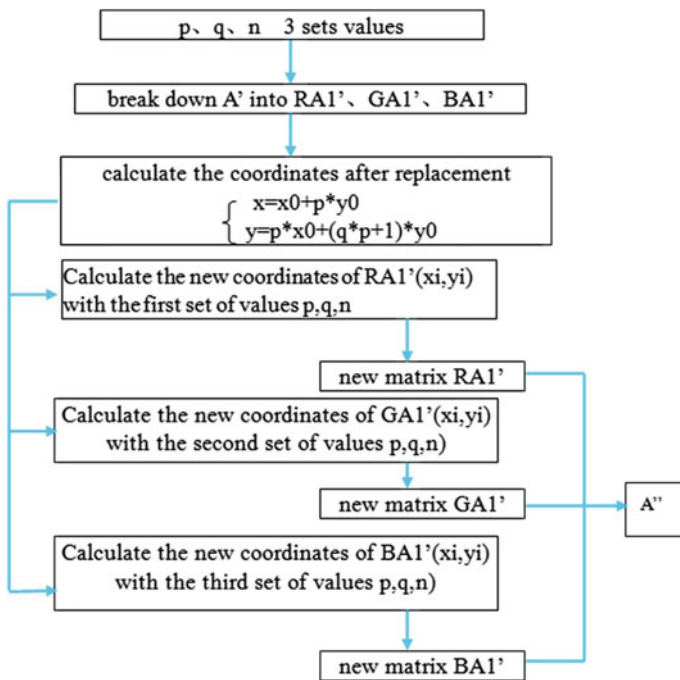
$$\begin{pmatrix} x_{n+1} \\ y_{n+1} \end{pmatrix} = \begin{pmatrix} 1 & 1 \\ 1 & 2 \end{pmatrix} \begin{pmatrix} x_n \\ y_n \end{pmatrix} = C \begin{pmatrix} x_n \\ y_n \end{pmatrix} \bmod 1 \tag{8}$$

After several transformations, cat map can be written as a mathematical model as shown in (9). At this point, it has two independent parameters  $p$  and  $q$ , after do modulo operation to value  $(x_0, y_0)$  and  $N$   $n$  times, and add 1 to the result, then get  $(x_n, y_n)$ , it's very suitable for coordinate scrambling now.

$$\begin{pmatrix} x_n \\ y_n \end{pmatrix} = \begin{pmatrix} 1 & p \\ q & pq + 1 \end{pmatrix}^n \begin{pmatrix} x_0 \\ y_0 \end{pmatrix} \pmod{N + 1} \tag{9}$$

Now, using the sequences generated by Eq. (9), to do coordinate scrambling encrypt to the ciphertext image A' which had encrypted by 3D unified chaotic system. Divide the ciphertext A' into three primary color image matrix RA', GA', BA'. Take one point RA'(xi,yj) from matrix RA', iterate the point (xi,yj) by Eq. (9), and get a new coordinate (xi',yj'), then replace the all coordinates of RA', get a new ciphertext matrix RA''. Using the same method to get matrix GA'' and matrix BA'', synthesis of three matrices, get ciphertext image matrix A''.

Improved Encryption algorithm flow chart:



### 3.1 Security Analysis of the Improved Algorithm

The improved algorithm, for the first time, the pixel gray value of plaintext image A was replaced by the key generated from 3D unified chaotic system, and get ciphertext image A', for the second time, the coordinate of ciphertext image A' was scrambled by the key generated from cat map, and get ciphertext image A''.



Two-dimensional cat map system has three system parameters, 3D unified chaotic system has four system parameters, if all of the seven system parameters using 15-bit doubles, the key space is at least  $10^{15+15+15+15+15+15+15} = 10^{105}$ . The security of the algorithm is improved greatly.

## 4 Concluding Remarks

Although lots of data security work had been done, but data security problem is not completely resolved. We must continue to improve the encryption algorithm, ensure data security

## References

1. Yang H, Lin S (2015) Multi format processing and recognition of image encryption based on Chaos. *J Comput Aided Des Comput Graph* 17(1):105–109 (in Chinese)
2. Gonzalez JA (2010) Absolutely unpredictable chaotic sequences. *Int J Bifurcat Chaos* 10(8): 1867–1874

# Novel Affine Projection Sign Subband Adaptive Filter

Qianqian Liu and Haiquan Zhao

**Abstract** In this paper, we propose a novel affine projection sign subband adaptive filter (NAPSSAF) algorithm which can obtain better performance than the conventional APSSAF. The proposed NAPSSAF is derived by minimizing the  $l_1$ -norm of the subband a posteriori error vector rather than the overall a posteriori error vector, which fully uses the subband adaptive filter's inherent decorrelating property. Simulations in context of the system identification and acoustic echo cancellation (AEC) are carried out to demonstrate the advantages of the proposed algorithms. The results of simulations demonstrate that the proposed NAPSSAF obtains faster convergence rate than the existing algorithms.

**Keywords** Normalized subband adaptive filter · Affine projection algorithm  
Acoustic echo cancellation (AEC)

## 1 Introduction

Since adaptive filter algorithms are widely used in reality practice, it has achieved much attention [1]. Due to its easy implement and low computation complexity, the least mean square (LMS) and normalized LMS (NLMS) algorithms are diffusely applied in practice [1]. However, when the input signals are colored signals, the LMS and NLMS algorithms would obtain the degradation performance. To overcome this drawback, the subband adaptive filter (SAF) was proposed, which partitions the input signals into subband signals that are nearly white [2]. Then, to further improve the performance of SAF, the normalized SAF (NSAF) was developed [3]. Hereafter, to suppress the tradeoff between the convergence rate and

---

Q. Liu · H. Zhao (✉)

The Key Laboratory of Magnetic Suspension Technology and Maglev Vehicle,  
Ministry of Education and the School of Electrical Engineering,  
Southwest Jiaotong University, Chengdu 610031, China  
e-mail: hqzhao\_swjtu@126.com

© Springer Nature Singapore Pte Ltd. 2018

L. Jia et al. (eds.), *Proceedings of the 3rd International Conference on Electrical and Information Technologies for Rail Transportation (EITRT) 2017*, Lecture Notes in Electrical Engineering 482, [https://doi.org/10.1007/978-981-10-7986-3\\_67](https://doi.org/10.1007/978-981-10-7986-3_67)

661

steady state error for fixed step-size, authors proposed several variable step size NSAF algorithms in [4–6].

Unfortunately, the aforementioned algorithms were not robust against impulsive interferences, because they are obtained by solving the optimization problem based on the  $l_2$ -norm. The previous literature has proven that the algorithms obtained by minimizing the  $l_1$ -norm of the error signal are robust against the impulsive interferences [1]. Motivated by this idea, [7] and [8] proposed the sign algorithm (SA) and its variants. However, these algorithms show very slow convergence rate for correlated input, although they can suppress the effect of the impulsive noise. To overcome this drawback, the affine projection sign algorithm (APSA) was proposed by combining the benefits of the affine projection algorithm (APA) and SA [9]. Moreover, a sign subband adaptive filter (SSAF) algorithm was derived by minimizing the  $l_1$ -norm of the subband error vector in [10]. Furthermore, the variable regularization parameter SSAF (VRP-SSAF) algorithm, the variable step-size SSAF algorithms and the affine projection SSAF (AP-SSAF) algorithm were proposed to further enhance the performance of SSAF [10–15]. Besides, the individual weighting factors SSAF (IWF-SSAF) algorithm was derived by assigning an individual weighting factor for each subband [16, 17], which can enhance the performance of SSAF.

In this paper, a novel affine projection sign subband adaptive filter (NAPSSAF) algorithm is proposed to obtain better performance compared with conventional APSSAF. Simulation in context of the system identification and acoustic echo cancellation (AEC) are carried out to demonstrate the advantages of the proposed algorithms. The results of simulation demonstrate that the proposed NAPSSAF obtains faster convergence rate than the existing algorithms.

## 2 Review of APSSAF

Consider the following desired signal  $d(n)$

$$d(n) = \mathbf{u}^T(n)\mathbf{w}_o + \eta(n) \quad (1)$$

where  $\mathbf{w}_o$  is an unknown weight coefficients vector of size  $M$  to be estimated,  $\mathbf{u}(n) = [u(n), u(n-1), \dots, u(n-M+1)]^T$  represents the input vector of size  $M$  and  $\eta(n)$  denotes the measurement noise. The structure of SAF is shown in Fig. 1, where  $N$  is the subband number [4]. The desired signal  $d(n)$  and the input signal  $u(n)$  are divided into  $N$  subband signals by using analysis filters  $\{H_i(z), i = 0, 1, \dots, N-1\}$ , respectively. Then, the subband signals  $y_i(n)$  and  $d_i(n)$  for  $i = 0, 1, \dots, N-1$  are critically decimated to yield  $y_{i,D}(k)$  and  $d_{i,D}(k)$ , respectively, where  $n$  and  $k$  are used to indicate the original sequences and the decimated sequences. The  $i$ th subband output signal is described by  $y_{i,D}(k) = \mathbf{u}_i^T(k)\mathbf{w}(k)$ , where  $\mathbf{w}(k)$  is the tap-weight vector of adaptive filter, and

$\mathbf{u}_i(k) = [u_i(kN), u_i(kN - 1), \dots, u_i(kN - M + 1)]^T$ . The output error of the  $i$ th subband is defined as

$$e_{i,D}(k) = d_{i,D}(k) - y_{i,D}(k) = d_{i,D}(k) - \mathbf{u}_i^T(k)\mathbf{w}(k) \tag{2}$$

where  $d_{i,D}(k) = d_i(kN)$ . Then, we define the  $i$ th subband desired signal vector by collecting the  $P$  most recent desired signals as follows

$$\mathbf{d}_i(k) = [d_{i,D}(k), d_{i,D}(k - 1), \dots, d_{i,D}(k - P + 1)]^T. \tag{3}$$

The  $i$ th subband input signal matrix are defined as

$$\mathbf{U}_i(k) = [\mathbf{u}_i(k), \mathbf{u}_i(k - 1), \dots, \mathbf{u}_i(k - P + 1)]. \tag{4}$$

In the sequel, the desired signal vectors, the input signal matrix, the *a posteriori* error signal vector, and the *a priori* error signal vector are defined as follows

$$\mathbf{d}_A(k) = [\mathbf{d}_0^T(k), \mathbf{d}_1^T(k), \dots, \mathbf{d}_{N-1}^T(k)]^T, \tag{5}$$

$$\mathbf{U}_A(k) = [\mathbf{U}_0(k), \mathbf{U}_1(k), \dots, \mathbf{U}_{N-1}(k)], \tag{6}$$

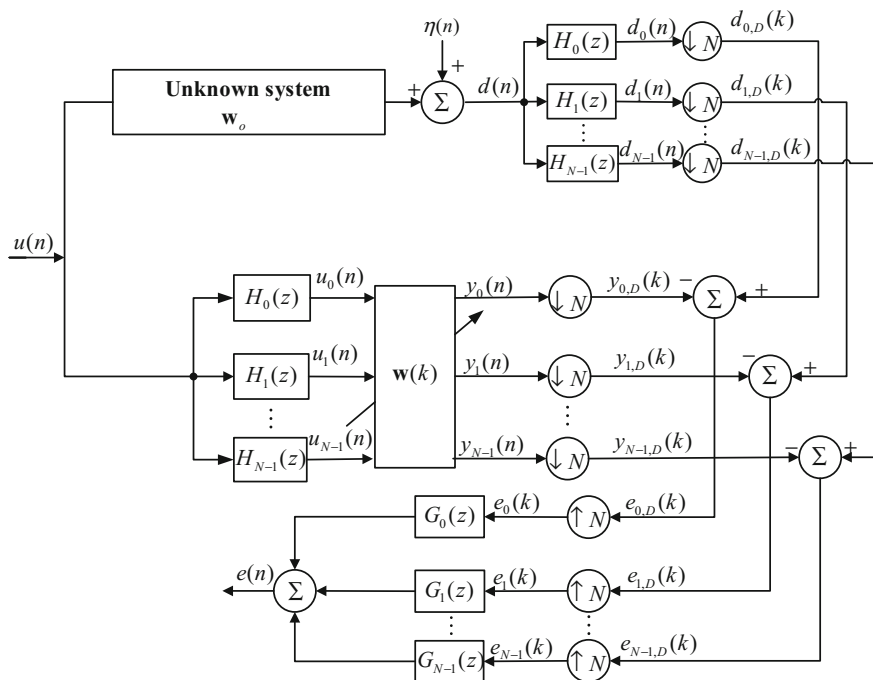


Fig. 1 Multiband structure of subband adaptive filter

$$\boldsymbol{\xi}_A(k) = \mathbf{d}_A(k) - \mathbf{U}_A^T(k)\mathbf{w}(k+1) = \left[ \boldsymbol{\xi}_{0,A}^T(k), \boldsymbol{\xi}_{1,A}^T(k), \dots, \boldsymbol{\xi}_{N-1,A}^T(k) \right], \quad (7)$$

$$\mathbf{e}_A(k) = \mathbf{d}_A(k) - \mathbf{U}_A^T(k)\mathbf{w}(k) = \left[ \mathbf{e}_{0,A}^T(k), \mathbf{e}_{1,A}^T(k), \dots, \mathbf{e}_{N-1,A}^T(k) \right], \quad (8)$$

where

$$\mathbf{e}_{i,A}(k) = \mathbf{d}_i(k) - \mathbf{U}_i^T(k)\mathbf{w}(k) = [e_{i,D}(k), e_{i,D}(k-1), \dots, e_{i,D}(k-P+1)]^T, \quad (9)$$

$$\boldsymbol{\xi}_{i,A}(k) = \mathbf{d}_i(k) - \mathbf{U}_i^T(k)\mathbf{w}(k+1). \quad (10)$$

The APSSAF algorithm is obtained by solving the following optimization problem

$$\min_{\mathbf{w}(k+1)} \|\mathbf{d}_A(k) - \mathbf{U}_A^T(k)\mathbf{w}(k+1)\|_1 \quad (11)$$

$$\text{subject to } \|\mathbf{w}(k+1) - \mathbf{w}(k)\|_2^2 \leq \mu^2 \quad (12)$$

Using the method of Lagrange multipliers, the updating the weight vector of the APSSAF algorithm is described as

$$\begin{aligned} \mathbf{w}(k+1) = & \mathbf{w}(k) \\ & + \mu \frac{\mathbf{U}_A(k) \text{sgn}[\mathbf{d}_A(k) - \mathbf{U}_A^T(k)\mathbf{w}(k)]}{\sqrt{\delta + \{\mathbf{U}_A(k) \text{sgn}[\mathbf{d}_A(k) - \mathbf{U}_A^T(k)\mathbf{w}(k)]\}^T \{\mathbf{U}_A(k) \text{sgn}[\mathbf{d}_A(k) - \mathbf{U}_A^T(k)\mathbf{w}(k)]\}}} \end{aligned} \quad (13)$$

where  $\mu$  ( $0 < \mu < 1$ ) is the step size,  $\delta$  is a small positive number to avoid division by zero.

### 3 Proposed NAPSSAF Algorithm

According to [16], to make full use of the advantages of subband adaptive filtering, signal vector or matrix of each subband (i.e.,  $\mathbf{d}_i(k)$  and  $\mathbf{U}_i^T(k)$ ) should make an irreplaceable contribution on the overall performance of the subband adaptive filter. Unfortunately, from (11) and (12), it is easy to find the APSSAF algorithm is derived by minimizing the  $l_1$ -norm of the overall a posteriori error vector with a constraint on the filter coefficients, which doesn't consider effect of signal vector or matrix of each subband. Thus, to improve the performance of APSSAF algorithm, we derive the NAPSSAF algorithm by minimizing the  $l_1$ -norm of the subband a posteriori error vector. Specifically, the NAPSSAF is obtained by the following  $N$  optimization problems

$$\min_{\mathbf{w}(k+1)} \|\mathbf{d}_i(k) - \mathbf{U}_i^T(k)\mathbf{w}(k+1)\|_1, i = 0, 1, \dots, N - 1 \tag{14}$$

$$\text{subject to } \|\mathbf{w}(k+1) - \mathbf{w}(k)\|_2^2 \leq \rho^2 \tag{15}$$

According to the method of Lagrange multiplier, the cost functions are given by

$$J_i(k) = \|\mathbf{d}_i(k) - \mathbf{U}_i^T(k)\mathbf{w}(k+1)\|_1 + \lambda_i \left[ \|\mathbf{w}(k+1) - \mathbf{w}(k)\|_2^2 - \rho^2 \right], \tag{16}$$

$$i = 0, 1, \dots, N - 1$$

where  $\lambda_i$  is the Lagrange multiplier. Then, setting the derivative of (16) with respect to  $\mathbf{w}(k+1)$  to zero, we have

$$\mathbf{w}(k+1) = \mathbf{w}(k) + \frac{1}{2\lambda} \mathbf{U}_i(k) \text{sgn}[\mathbf{d}_i(k) - \mathbf{U}_i^T(k)\mathbf{w}(k+1)], i = 0, 1, \dots, N - 1. \tag{17}$$

Substituting (17) into the constraint (15) yields

$$\frac{1}{2\lambda_i} = \frac{\rho}{\|\mathbf{U}_i^T(k) \text{sgn}[\mathbf{d}_i(k) - \mathbf{U}_i^T(k)\mathbf{w}(k+1)]\|_2},, i = 0, 1, \dots, N - 1. \tag{18}$$

Substituting (18) into (17) yields

$$\mathbf{w}(k+1) = \mathbf{w}(k) + \rho \frac{\mathbf{U}_i(k) \text{sgn}[\mathbf{d}_i(k) - \mathbf{U}_i^T(k)\mathbf{w}(k)]}{\|\mathbf{U}_i(k) \text{sgn}[\mathbf{d}_i(k) - \mathbf{U}_i^T(k)\mathbf{w}(k)]\|_2},, i = 0, 1, \dots, N - 1. \tag{19}$$

Introducing the parameters  $\delta$  into (19), we have

$$\mathbf{w}(k+1) = \mathbf{w}(k) + \rho \frac{\mathbf{U}_i(k) \text{sgn}[\mathbf{d}_i(k) - \mathbf{U}_i^T(k)\mathbf{w}(k)]}{\sqrt{\delta + \{\mathbf{U}_i(k) \text{sgn}[\mathbf{d}_i(k) - \mathbf{U}_i^T(k)\mathbf{w}(k)]\}^T \{\mathbf{U}_i(k) \text{sgn}[\mathbf{d}_i(k) - \mathbf{U}_i^T(k)\mathbf{w}(k)]\}}},$$

$$i = 0, 1, \dots, N - 1 \tag{20}$$

Obviously, it is difficult to find a solution to satisfy all optimization problems in (14) and (15). Thus, we get the solution which approaching all solutions of  $N$  optimization problems in (14) as follows

$$\begin{aligned} \mathbf{w}(k+1) &= \mathbf{w}(k) \\ &+ \mu \sum_{i=0}^{N-1} \frac{\mathbf{U}_i(k) \text{sgn}[\mathbf{d}_i(k) - \mathbf{U}_i^T(k) \mathbf{w}(k)]}{\sqrt{\delta + \{\mathbf{U}_i(k) \text{sgn}[\mathbf{d}_i(k) - \mathbf{U}_i^T(k) \mathbf{w}(k)]\}^T \{\mathbf{U}_i(k) \text{sgn}[\mathbf{d}_i(k) - \mathbf{U}_i^T(k) \mathbf{w}(k)]\}}} \end{aligned} \quad (21)$$

where  $\mu = \rho/N$ .

From (21), we get that each subband input vector in NAPSSAF algorithm is normalized by its own variance. Equivalently, the subband with smaller (larger) input signal power achieves larger (smaller) weight, which is different from APSSAF where all subbands have the same weight. Therefore, the proposed NAPSSAF algorithm can obtain a significant improvement in the convergence rate as comparison with the APSSAF algorithm.

## 4 Simulation Results

The performance of the proposed algorithms is examined by simulations in the context of system identification and echo cancellation scenarios. The unknown vector to be estimated is an echo path with length  $M = 512$ . The length of the adaptive filters is also equal to 512. The background noise is the white Gaussian process with signal-to-noise rate (SNR) of 30 dB. The variance of background noise is  $\sigma_v^2$ . The impulsive noise is expressed as,  $v'(n) = z(n)A(n)$ , where  $z(n)$  is a Bernoulli process with occurrence probability  $p\{z(n) = 1\} = P_r$ , and  $A(n)$  is white Gaussian with zero-mean and variance  $\sigma_A^2 = 100E[(\mathbf{u}^T(n)\mathbf{w}_o)^2]$ . The measure of performance is normalized mean square deviation (NMSD), which is defined as  $10 \log_{10}(\|\mathbf{w}_o - \mathbf{w}(k)\|_2^2 / \|\mathbf{w}_o\|_2^2)$ .

### 4.1 System Identification with AR(1)

In this subsection, the input signal is generated by filtering white Gaussian noise through the following first-order autoregressive (AR(1)) system

$$G(z) = \frac{1}{1 - 0.9z^{-1}}.$$

In addition, to evaluate the tracking ability of proposed algorithm, an abrupt change occurs in the middle of iterations. The detailed parameter settings are provided in the caption of corresponding figure.

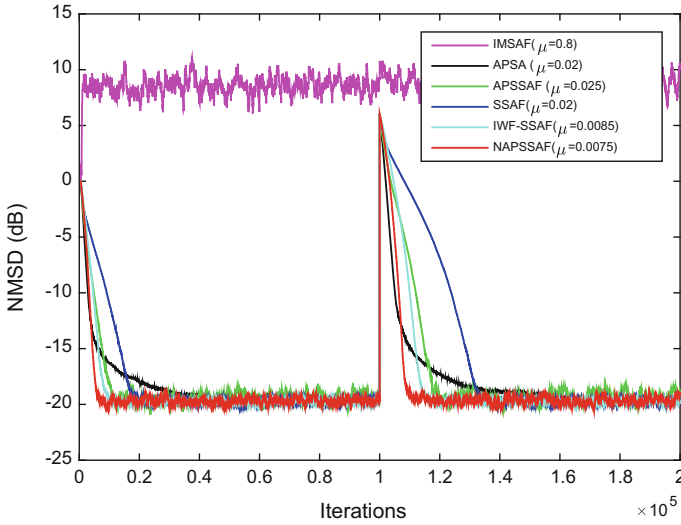


**Fig. 2** The NMSD results of APSSAF, IMSAF, SSAF, IWF-SSAF, APSSAF and NAPSSAF algorithms for AR(1) inputs. ( $P_r = 0.01$ )

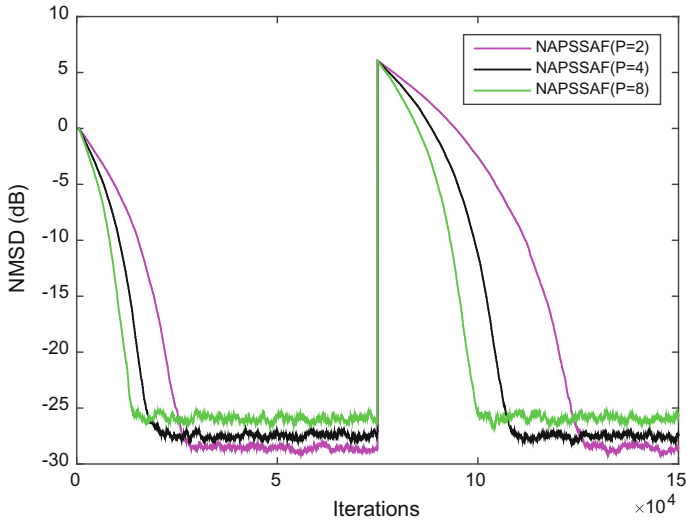
Figure 2 compares the transient NMSDs of the APSSAF, IMSAF, SSAF, IWF-SSAF, APSSAF and NAPSSAF algorithms for AR(1) input. In order to get the fair comparison, we select the parameters of all algorithms have the same steady-state NMSD. As can be seen, all algorithms are robust against the impulsive noise. In addition, the proposed NAPSSAF algorithm can obtain the fastest convergence rate and the best tracking capability compared with the other algorithms. Interestingly, it is also found that the conventional APSSAF is even inferior to the APSSAF for AR(1) input.

Figure 3 shows the transient NMSDs of NAPSSAF algorithm with different projection order  $P$ . It is found that NAPSSAF with smaller  $P$  has slower convergence and lower steady-state error, and vice versa.

### 4.2 Acoustic Echo Cancellation

In this subsection, the performance of proposed NAPSSAF algorithm is verified in acoustic echo cancellation application. The basic goal of echo cancellation is also to identify the echo path  $\mathbf{w}_o$ . The input signals are the true speech signals. Figure 4 depicts the transient NMSDs of the APSSAF, IWF-SSAF, APSSAF and NAPSSAF algorithms. It is found that the proposed NAPSSAF also outperforms the IWF-SSAF and APSSAF for speech input signals.





**Fig. 3** The NMSD results of NAPSSAF algorithm with  $P = 8, 4$  and  $2$  for AR(2) inputs ( $P_r = 0.01, \mu = 0.002$ )

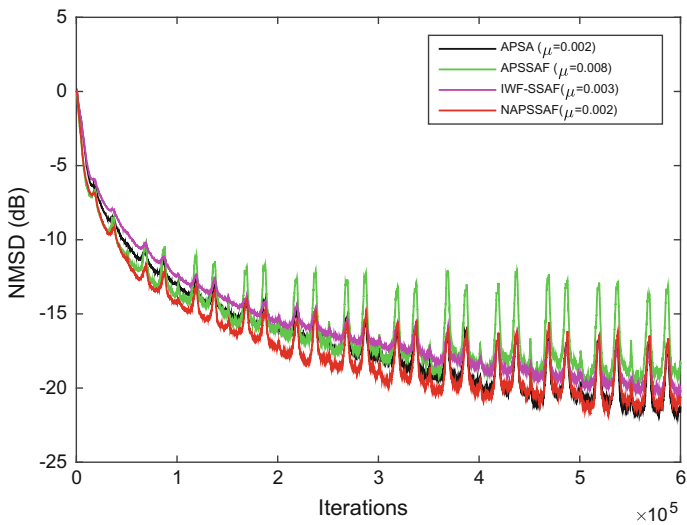


**Fig. 4** The NMSD results of APSSAF, IWF-SSAF, APSSAF and NAPSSAF algorithms for speech inputs ( $P_r = 0.01$ )

## 5 Conclusions

In this paper, a novel affine projection sign subband adaptive filter (NAPSSAF) algorithm is proposed, which is derived by minimizing the  $l_1$ -norm of the subband a posteriori error vector rather than the overall a posteriori error vector. Since the proposed NAPSSAF fully uses the of subband adaptive filter's inherent decorrelating property, it can obtain better performance than the conventional APSSAF. Simulations are carried out to demonstrate the advantages of the proposed algorithms. The results of simulation illustrate that the proposed NAPSSAF obtain faster convergence rate than the existing algorithms.

**Acknowledgements** This work was partially supported by National Science Foundation of P.R. China (Grant: 61571374, 61271340 and 61433011).

## References

1. Haykin S (2002) Adaptive filter theory. Prentice-Hall, Englewood Cliffs, NJ
2. Lee KA, Gan WS, Kuo SM (2009) Subband adaptive filter: theory and implementation. Wiley, Chichester, UK
3. Lee KA, Gan WS (2004) Improving convergence of the NLMS algorithm using constrained subband updates. *IEEE Signal Process Lett* 11(9):736–739
4. Seo JH, Park PG (2014) Variable individual step-size subband adaptive filtering algorithm. *Electron Lett* 50(3):177–178
5. Yu Y, Zhao H, Chen B (2016) A new normalized subband adaptive filter algorithm with individual variable step sizes. *Circ Syst Signal Process* 35(4):1407–1418
6. Ni J, Li F (2010) A variable step-size matrix normalized subband adaptive filter. *IEEE Trans Audio Speech Lang Process* 18(6):1290–1299
7. Mathews VJ, Cho SH (1987) Improved convergence analysis of stochastic gradient adaptive filters using the sign algorithm. *IEEE Trans Acoust Speech Signal Process* 35(4):450–454
8. Cho SH, Kim SD, Kim SS (1997) A modified adaptive sign algorithm used on the hybrid norm error criterion. In: *Proceedings of the 40th Midwest symposium on circuits and systems*, vol 2. Issue 2, pp 1346–1349
9. Shao T, Zheng YR, Benesty J (2010) An affine projection sign algorithm robust against impulsive interferences. *IEEE Signal Process Lett* 17(4):327–330
10. Ni J, Li F (2010) Variable regularisation parameter sign subband adaptive filter. *Electron Lett* 46(24):1605–1607
11. Kim JH, Chang JH, Nam SW (2013) Sign subband adaptive filter with  $l_1$ -norm minimisation-based variable step-size. *Electron Lett* 49(21):1325–1326
12. Shin JW, Yoo JW, Park PG (2013) Variable step-size sign subband adaptive filter. *IEEE Signal Process Lett* 20(2):173–176
13. Yoo JW, Shin JW, Park PG (2014) A band-dependent variable step-size sign subband adaptive filter. *Signal Process* 104:407–411
14. Ni J, Chen X, Yang J (2014) Two variants of the sign subband adaptive filter with improved convergence rate. *Signal Process* 96:325–331

15. Zhao H, Zheng Z Wang Z, Chen B (2017) Improved affine projection subband adaptive filter for high background noise environments. *Signal Process* 137:356–362
16. Yu Y, Zhao H (2016) Novel sign subband adaptive filter algorithms with individual weighting factors. *Sig Process* 122:14–23
17. Yu Y, Zhao H (2017) Novel combination schemes of individual weighting factors sign subband adaptive filter algorithm. *Int J Adapt Control Signal Process*. <https://doi.org/10.1002/acs.2755>

# Research on Redundancy and Fault-Tolerant Control Technology of Levitation Join-Structure in High Speed Maglev Train

Mingda Zhai, Xiaolong Li and Zhiqiang Long

**Abstract** The phenomenon occasionally occurs during the running of the high-speed maglev train that the suspension control unit fail to work. However, whether the suspension system is normal is directly related to the safety of the train. Therefore, the particular levitation join-structure is adopted in the high speed maglev train. This study is conducted to obtain redundancy and fault-tolerant control technology of levitation join-structure. The mathematical model of levitation join-structure is established and the suspension controllers are designed, so as to solve the failure problem of one suspension control unit and improve the reliability of the entire suspension system

**Keywords** Levitation join-structure · Redundant and fault-tolerant control  
High speed maglev train · Reliability

## 1 Introduction

Maglev train is through the electromagnetic force to levitate the vehicle upon the track contactless and run the train by the linear motor. Compared with the conventional high-speed rail, it is generally believed that the maglev train have not only less resistance, less noise, lower cost, but also higher speed [1]. Suspension system is the most unique and critical system of maglev train. Whether the suspension system is normal is directly related to the safety of the train. Therefore, the particular levitation join-structure is adopted in the high speed maglev train. Each join-structure has two suspension control unit. One of the suspension control unit turn off due to failure, and the other can still levitate the whole join-structure. This study is conducted to obtain redundancy and fault-tolerant control technology of levitation join-structure. The mathematical model of levitation join-structure is established and the suspension controllers are designed, so as to solve the failure

---

M. Zhai · X. Li · Z. Long (✉)  
National University of Defense Technology, Changsha, China  
e-mail: lzq@maglev.cn

problem of one suspension control unit, improve the reliability of the entire suspension system and even enhance the safety of the high speed maglev train.

## 2 Model and Control of Levitation Join-Structure

Figure 1 is the illustration of the levitation join-structure of high-speed maglev train. In the figure, the levitation electromagnets on the left and right sides support the corbel respectively with a metal rubber spring which can be equivalent to a spring damping system.

The gap of the left electromagnet is  $\vec{c}_{xl}$ , and the gap of the right electromagnet is  $\vec{c}_{xr}$ ; the external interference force acting on the left electromagnet is  $\vec{F}_{xdl}$ , and the external interference force acting on the right electromagnet is  $\vec{F}_{xdr}$ ; the height and mass of the left electromagnet is  $h_{xl}$  and  $m_{xl}$  respectively; the height and mass of the right electromagnet is  $h_{xr}$  and  $m_{xr}$  respectively; the natural length, stiffness and equivalent damping of the left laminated spring is  $l_{xl0}$ ,  $k_{xl}$  and  $\eta_{xl}$  respectively; the natural length, stiffness and equivalent damping of the right laminated spring is  $l_{xr0}$ ,  $k_{xr}$  and  $\eta_{xr}$  respectively; the voltage and current at the two ends of the left electromagnet is  $u_{xcl}$  and  $i_{xl}$ , the electromagnetic force is  $\vec{F}_{xeml}$  and the restoring force of the laminated spring acting upon the corbel be  $\vec{F}_{xsl}$ ; the voltage and current at the two ends of the right electromagnet is  $u_{xcr}$  and  $i_{xr}$ , the electromagnetic force is  $\vec{F}_{xemr}$  and the restoring force of the laminated spring acting upon the corbel is  $\vec{F}_{xsr}$ ; the equivalent mass of the upper bogie is  $m_{xb}$  and the interference force suffered be  $\vec{F}_{xdb}$ ; the displacement of the lower edge of the corbel to the lower surface of the guideway be  $\vec{H}$ . Thus, the system equations can be obtained as follows [2, 3]:

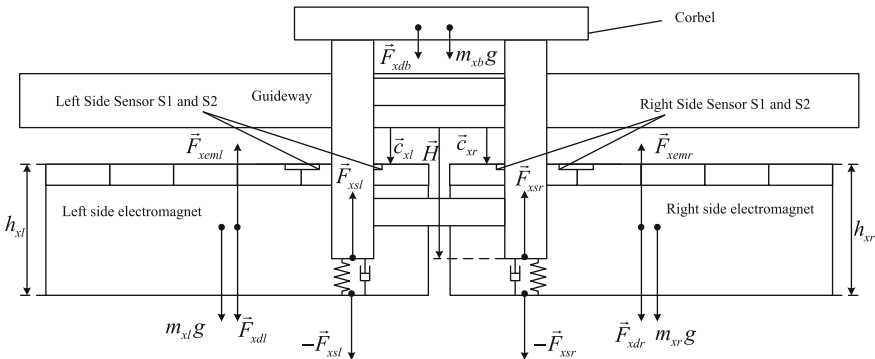


Fig. 1 Illustration of levitation join-structure

$$u_{xcl}(t) = R_x i_{xl}(t) + \frac{d}{dt} \left( \frac{N_x^2 i_{xl}(t)}{2c_{xl}(t)/\mu_0 A_x} \right) \tag{1}$$

$$u_{xcr}(t) = R_x i_{xr}(t) + \frac{d}{dt} \left( \frac{N_x^2 i_{xr}(t)}{2c_{xr}(t)/\mu_0 A_x} \right) \tag{2}$$

$$F_{xemi}(i_{xl}, c_{xl}) = \frac{\mu_0 N_x^2 A_x}{4} \left[ \frac{i_{xl}}{c_{xl}} \right]^2 \tag{3}$$

$$F_{xemr}(i_{xr}, c_{xr}) = \frac{\mu_0 N_x^2 A_x}{4} \left[ \frac{i_{xr}}{c_{xr}} \right]^2 \tag{4}$$

$$F_{xsl} = k_{xl}[l_{xl0} - (c_{xl} + h_{xl} - H)] - \eta_{xl}[\dot{c}_{xl}(t) - \dot{H}(t)] \tag{5}$$

$$F_{xsr} = k_{xr}[l_{xr0} - (c_{xr} + h_{xr} - H)] - \eta_{xr}[\dot{c}_{xr}(t) - \dot{H}(t)] \tag{6}$$

$$m_{xl}\ddot{c}_{xl} = m_{xl}g + F_{xsl} + F_{xdl} - F_{xemi} \tag{7}$$

$$m_{xr}\ddot{c}_{xr} = m_{xr}g + F_{xsr} + F_{xdr} - F_{xemr} \tag{8}$$

$$m_{xb}\ddot{H} = m_{xb}g + F_{xdb} - F_{xsl} - F_{xsr} \tag{9}$$

For the convenience of controller design, the above equations can be linearized near the working point. After linearization, the state equation of the system can be rewritten as:

$$\left\{ \begin{array}{l} \begin{pmatrix} \dot{\mathbf{x}}_{xl} \\ \dot{\mathbf{x}}_{xr} \\ \dot{\mathbf{x}}_{xb} \end{pmatrix} = \begin{pmatrix} \mathbf{A}_{xl} & \mathbf{0} & \mathbf{A}_{xlb} \\ \mathbf{0} & \mathbf{A}_{xr} & \mathbf{A}_{xrb} \\ \mathbf{A}_{xbl} & \mathbf{A}_{xbr} & \mathbf{A}_{xb} \end{pmatrix} \begin{pmatrix} \mathbf{x}_{xl} \\ \mathbf{x}_{xr} \\ \mathbf{x}_{xb} \end{pmatrix} \\ \quad + \begin{pmatrix} \mathbf{B}_{xl} & & \\ & \mathbf{B}_{xr} & \\ & & \mathbf{B}_{xb} \end{pmatrix} \begin{pmatrix} \mathbf{u}_{xl} \\ \mathbf{u}_{xr} \\ \mathbf{u}_{xb} \end{pmatrix} \\ \begin{pmatrix} \mathbf{y}_{xl} \\ \mathbf{y}_{xr} \\ \mathbf{y}_{xb} \end{pmatrix} = \begin{pmatrix} \mathbf{C}_{xs} & & \\ & \mathbf{C}_{xs} & \\ & & \mathbf{C}_{xb} \end{pmatrix} \begin{pmatrix} \mathbf{x}_{xl} \\ \mathbf{x}_{xr} \\ \mathbf{x}_{xb} \end{pmatrix} \end{array} \right. \tag{10}$$

where  $\mathbf{x}_{xl} = (c_{xl} \ \dot{c}_{xl} \ i_{xl})^T$ ,  $\mathbf{x}_{xr} = (c_{xr} \ \dot{c}_{xr} \ i_{xr})^T$ ,  $\mathbf{u}_{xl} = (u_{xcl} \ F_{xdl})^T$ ,  $\mathbf{u}_{xr} = (u_{xcr} \ F_{xdr})^T$ ,  $\mathbf{u}_{xb} = F_{xdb}$ ,  $\mathbf{y}_{xl} = c_{xl}$ ,  $\mathbf{y}_{xr} = c_{xr}$ ,  $\mathbf{y}_{xb} = H$

$$\begin{aligned}
\mathbf{A}_{xl} &= \begin{pmatrix} 0 & 1 & 0 \\ \frac{k_{xzl}-k_{xl}}{m_{xl}} & -\frac{\eta_{xl}}{m_{xl}} & -\frac{k_{xil}}{m_{xl}} \\ 0 & \frac{k_{xil}}{L_{xl0}} & -\frac{R_x}{L_{xl0}} \end{pmatrix}, \quad \mathbf{A}_{xr} = \begin{pmatrix} 0 & 1 & 0 \\ \frac{k_{xer}-k_{xr}}{m_{xr}} & -\frac{\eta_{xr}}{m_{xr}} & -\frac{k_{xir}}{m_{xr}} \\ 0 & \frac{k_{xir}}{L_{xr0}} & -\frac{R_x}{L_{xr0}} \end{pmatrix} \\
\mathbf{A}_{xb} &= \begin{pmatrix} 0 & 1 \\ -\frac{k_{xl}+k_{xr}}{m_{xb}} & -\frac{\eta_{xl}+\eta_{xr}}{m_{xb}} \end{pmatrix} \\
\mathbf{A}_{xlb} &= \begin{pmatrix} 0 & 0 \\ \frac{k_{xl}}{m_{xl}} & \frac{\eta_{xl}}{m_{xl}} \\ 0 & 0 \end{pmatrix}, \quad \mathbf{A}_{xrb} = \begin{pmatrix} 0 & 0 \\ \frac{k_{xr}}{m_{xr}} & \frac{\eta_{xr}}{m_{xr}} \\ 0 & 0 \end{pmatrix}, \quad \mathbf{A}_{xbl} = \begin{pmatrix} 0 & 0 & 0 \\ \frac{k_{xl}}{m_{xb}} & \frac{\eta_{xl}}{m_{xb}} & 0 \end{pmatrix} \\
\mathbf{A}_{xbr} &= \begin{pmatrix} 0 & 0 & 0 \\ \frac{k_{xr}}{m_{xb}} & \frac{\eta_{xr}}{m_{xb}} & 0 \end{pmatrix}, \\
\mathbf{B}_{xl} &= \begin{pmatrix} 0 & 0 \\ 0 & \frac{1}{m_{xl}} \end{pmatrix}, \quad \mathbf{B}_{xr} = \begin{pmatrix} 0 & 0 \\ 0 & \frac{1}{m_{xr}} \end{pmatrix}, \quad \mathbf{B}_{xb} = \frac{1}{m_{xb}} \\
\mathbf{C}_{xs} &= \begin{pmatrix} 1 & \frac{1}{L_{xl0}} & 0 \\ 0 & 0 & 0 \end{pmatrix}, \quad \mathbf{C}_{xb} = \begin{pmatrix} 1 & \frac{1}{L_{xr0}} & 0 \\ 0 & 0 & 0 \end{pmatrix}
\end{aligned}$$

It can be observed that the levitation joint system is formed by the coupling of the two electromagnets on the left and right sides and the corbel system. The respective state equations of the two electromagnets are:

$$\begin{cases} \dot{\mathbf{x}}_{xl} = \mathbf{A}_{xl}\mathbf{x}_{xl} + \mathbf{B}_{xl}\mathbf{u}_{xl} \\ \mathbf{y}_{xl} = \mathbf{C}_{xs}\mathbf{x}_{xl} \end{cases} \quad (11)$$

$$\begin{cases} \dot{\mathbf{x}}_{xr} = \mathbf{A}_{xr}\mathbf{x}_{xr} + \mathbf{B}_{xr}\mathbf{u}_{xr} \\ \mathbf{y}_{xr} = \mathbf{C}_{xs}\mathbf{x}_{xr} \end{cases} \quad (12)$$

The state equation of the corbel system is:

$$\begin{cases} \dot{\mathbf{x}}_{xb} = \mathbf{A}_{xb}\mathbf{x}_{xb} + \mathbf{B}_{xb}\mathbf{u}_{xb} \\ \mathbf{y}_{xb} = \mathbf{C}_{xb}\mathbf{x}_{xb} \end{cases} \quad (13)$$

The current feedback method commonly used in levitation control is adopted to reduce the order of the model [4]. Bring parameters into the above equations, and the state equation of the system after order-reduction is obtained:

$$\left\{ \begin{array}{l}
 \dot{\mathbf{x}} = \begin{pmatrix} 0 & 1 & 0 & 0 & 0 & 0 \\
 \frac{171000}{3} & 0 & 0 & 0 & \frac{200000}{3} & 0 \\
 0 & 0 & 0 & 1 & 0 & 0 \\
 0 & 0 & \frac{171000}{3} & 0 & \frac{200000}{3} & 0 \\
 0 & 0 & 0 & 0 & 0 & 1 \\
 \frac{2000000}{45} & 0 & \frac{2000000}{45} & 0 & -\frac{4000000}{45} & 0 \end{pmatrix} \mathbf{x} \\
 + \begin{pmatrix} 0 & 0 \\
 -4.13 & 0 \\
 0 & 0 \\
 0 & -4.13 \\
 0 & 0 \\
 0 & 0 \end{pmatrix} \mathbf{u} \\
 \mathbf{y} = \begin{pmatrix} 1 & 0 & 0 & 0 & 0 & 0 \\
 0 & 0 & 1 & 0 & 0 & 0 \end{pmatrix} \mathbf{x}
 \end{array} \right. \quad (14)$$

It can be seen from Eq. (14) that the system is not stable, but it can be completely controllable and observable. Consequently, a full-state feedback controller can be designed for arbitrary pole assignment. When the design method of linear quadratic optimal controller is adopted, a group of controller feedback parameters can be obtained [5, 6]:

$$\mathbf{K} = \begin{pmatrix} -6130 & -1001 & -5771 & -1.4 & 1470 & -2.2 \\
 -5771 & -1.4 & -6130 & -1001 & 1470 & -2.2 \end{pmatrix} \quad (15)$$

### 3 Redundancy and Fault-Tolerant Control of Join-Structure

The levitation system is to high-speed maglev train is equivalent to what the wheel is to rail vehicle. A failure occurring in the “wheels” will exert devastating consequences on the train in high speed operation. As system failures are unavoidable, the ideal approach to improving reliability is to have redundancy. In the levitation join-structure, two electromagnets jointly support the corbel, which provides redundancy design for the levitation system in terms of structure. Nevertheless, the realization of the redundant function for the join-structure will, eventually, depend on the Adaptive controller [7, 8].

When one levitation unit fails, for the join-structure, only one electromagnet supports the entire levitation point involved. Accordingly, the system is simplified to a system with one single electromagnet. For the sake of generality, the left levitation unit is assumed to fail, taking no account of the effect of the corbel system



on the right electromagnet, and regarding it as an interference force. Then the state equation of the system can be simplified as:

$$\begin{cases} \begin{pmatrix} \dot{c}_{xr} \\ \ddot{c}_{xr} \end{pmatrix} = \begin{pmatrix} 0 & 1 \\ \frac{171000}{3} & 0 \end{pmatrix} \begin{pmatrix} c_{xr} \\ \dot{c}_{xr} \end{pmatrix} + \begin{pmatrix} 0 \\ -4.13 \end{pmatrix} u_{xcr} \\ \mathbf{y} = (1 \quad 0) \begin{pmatrix} c_{xr} \\ \dot{c}_{xr} \end{pmatrix} \end{cases} \quad (16)$$

This is a two-order system which is completely controllable through verification. For a two-order system, the controller design is relatively simple. Here the linear optimal quadratic controller design method is still adopted to design the controller, and a group of controller feedback parameters can be obtained.

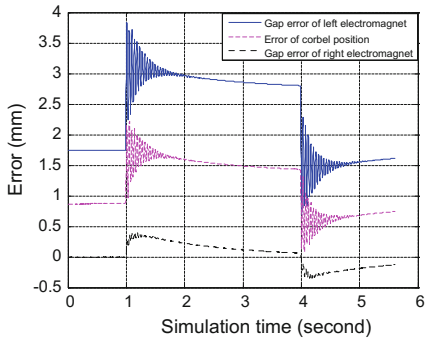
$$u_{xcr} = -\mathbf{k}(c_{xr} \quad \dot{c}_{xr})^T \quad (17)$$

$$\mathbf{k} = (-20706 \quad -1005) \quad (18)$$

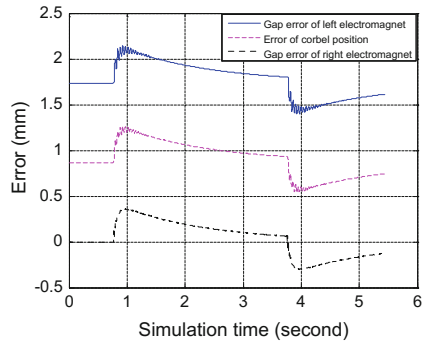
The nonlinear simulation model is adopted to conduct simulation analysis for the controller for the purpose of checking whether the controller meets the performance requirement, the simulation conditions being the same as the previous section. The responses of the system in the three cases are illustrated in below Fig. 2.

From the figure, it can be seen that the gap error of the left electromagnet approximates 2 mm, for the left electromagnet is unable to output electromagnetic force. The error is caused by the deformation of the rubber spring: the right rubber spring bears pressure since it needs to support the corbel system and the left electromagnet is compressed, while the left rubber spring is stretched by the gravity of the left electromagnet. At the same time, as the corbel system is supported only by the right rubber spring, the compression degree of the right rubber spring is greater than that when the corbel system is jointly supported by two rubber springs. Furthermore, the position of the corbel is lower than that under normal condition, as shown in Fig. 2, in which the position of the corbel is about 1 mm lower than that under normal condition.

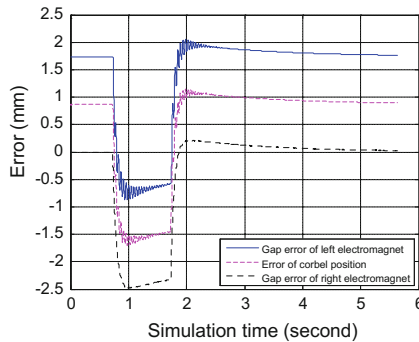
When the step interference force is applied to the left electromagnet, the vibration amplitude of the left electromagnet and the corbel is larger and their convergence speed is slow. The left electromagnet is uncontrollable and the equivalent damping of the metal rubber spring is quite small. Meanwhile, the vibration abatement of the left electromagnet totally rely on the right electromagnet.



(a) A step interference force of 10kN on the left electromagnet



(b) A step interference force of 10kN on the right electromagnet



(c) A step interference of 2mm on the gap sensor

**Fig. 2** The responses of join-structure. **a** A step interference force of 10 kN on the left electromagnet, **b** A step interference force of 10 kN on the right electromagnet, **c** A step interference of 2 mm on the gap sensor

### 4 Conclusion

The study shows that one suspension control unit is able to levitate the whole join-structure when the other shut down due to failure. The established mathematical model of levitation join-structure is adopted to design suspension controllers and obtain redundancy and fault-tolerant control strategy. Significantly, the redundant and fault-tolerant control strategy solve the failure problem of one suspension control unit of levitation join-structure, improve the reliability of the entire suspension system and even enhance the safety of the high speed maglev train..

**Acknowledgements** This work was supported by “National Key R & D Program of China” under Grant 2016YFB1200602.

## References

1. Yan LG (2002) Progress of high-speed Maglev in China. *IEEE Trans Appl Supercond* 12: 944–947
2. Chang W (2003) Maglev technology development and automatic control. In: The 22th Chinese control conference, vol 8, pp 27–30
3. Liu H (2005) Research on suspension control problems of EMS high-speed Maglev train double bogies join-structure. National University of Defense Technology (in Chinese)
4. Yungang Li (1999) Cascade control of an EMS Maglev vehicle's levitation control system. *Acta Automatica Sinica* 25(2):247–251 (in Chinese)
5. Long Z, Chen H, Chang W (2007) Fault tolerant control on single suspension module of maglev train with electromagnet failure. *IET Control Theor Appl* 24(6):1033–1037
6. Wang Y, Zhou D, Gao F (2007) Robust fault-tolerant control of a class of non-minimum phase nonlinear processes. *J Process Control* 17(6):523–537
7. Guo T, Chen W (2016) Adaptive fuzzy decentralised fault-tolerant control for uncertain non-linear large-scale systems with unknown time-delay. *IET Control Theor Appl* 10 (18):2437–2446
8. Yin S, Luo H, Ding SX (2013) Real-time implementation of fault-tolerant control systems with performance optimization. *IEEE Trans Industr Electron* 61(5):2402–2411

# Short-term Passenger Flow Forecasting Based on Phase Space Reconstruction and LSTM

Yong Zhang, Jiansheng Zhu and Junfeng Zhang

**Abstract** In this paper, the chaotic characteristics of the railway passenger flow are considered, and the PSR-LSTM (Phase Space Reconstruction-Long Short Term Memory) model is proposed by the phase space reconstruction method to recover the hidden trajectory in the passenger flow. First, this model uses C-C method to calculate the time delay and embedding dimension, and carry out phase space reconstruction. Afterwards, the LSTM neural network is used to predict short-term passenger flow. In the experimental part, it is proved that the passenger flow data with chaotic characteristics are reconstructed by phase space processing can get more accurate predictions. Then, in order to further verify the accuracy of the model, this model is compared with the BP neural network model and the SVR model, which is also subjected to phase space reconstruction processing. The experimental results show that the model has high accuracy.

**Keywords** Chaotic characteristics · Phase space reconstruction  
C-C method · LSTM

## 1 Introduction

Short-term passenger flow forecasting has always been the focus and difficulty of railway passenger flow forecast. In the past studies, there are linear prediction and nonlinear prediction methods: linear methods include: Grey System Theory [1] and ARIMA [2] and other methods; nonlinear mainly BP neural network [3] and SVR algorithm [4] and so on.

In fact, the railway passenger flow has nonlinear, uncertain and random and other chaotic characteristics to a certain extent, affecting the passenger flow forecast. At the same time, passenger flow is affected by many factors (such as weather,

---

Y. Zhang · J. Zhu (✉) · J. Zhang  
China Academy of Railway Sciences, No. 2, Daliushu Road, Haidian District, Beijing,  
People's Republic of China  
e-mail: zhujiansheng@sina.com

major events, etc.), but in actual work, these data are difficult to collect and use. In order to solve the above problems, firstly, this paper takes use of the existing data of the passenger in the China railway system, and only describes the factors of time. Secondly, this paper presents the PSR-LSTM model. The method of phase space reconstruction (PSR) is used to extract and restore the chaotic time series. Based on Takens' embedding theorem [5], it is proved that a suitable embedding dimension can be found, that is, if the embedding dimension  $m \geq 2d + 1$  (where  $d$  is the dimension of the dynamical system), the embedded dimension space makes a regular track recover. In paper [6], it is proved that the time delay and the embedded dimension are closely related. Therefore, the time delay and embedding dimension are calculated by C-C method. LSTM (Long short term memory algorithm) depth learning neural network is used to predict short-term passenger flow, which overcomes the long-term dependence of traditional neural network.

## 2 C-C Method

In 1996, Kugiumtzis [7] thought that the selection of time delay windows  $\tau_w$  should not be independent of the embedded dimension  $m$ , so they proposed the concept of time delay window  $\tau_w = (m - 1)\tau_d$  ( $\tau_d$  is time delay), which represents the total time span of each embedding point. D. Kugiumtzis et al. believe that there is a chaotic time series  $x = \{x_i | i = 1, 2, \dots, N\}$ , the time delay  $\tau_d$  ensures that the time series of time points  $x_i$  are interdependent but do not depend on the embedded dimension  $m$ ; and the time delay window  $\tau_w$  depends on  $m$ , and  $\tau_d$  varies with  $m$ .

In 1999, Kim [8] proposed the use of C-C method to estimate  $\tau_w$  and  $\tau_d$ . This method as Eq. (2) is an improvement in the statistical method, which is used to calculate the nonlinear time based on paper [9] accord to Eq. (1).

$$S(m, N, r) = C(m, N, r) - C^m(1, N, r) \tag{1}$$

$$S(m, N, r, t) = C(m, N, r, t) - C^m(1, N, r, t) \tag{2}$$

$C(m, N, r)$  is the correlation integral, which is the cumulative distribution function, calculate the distance of any two points in the phase space within the range of  $r$ , where  $r > 0$ , as follow:

$$C(m, N, r, t) = \frac{2}{M(M - 1)} \sum_{1 \leq i < j \leq M} \theta(r - d_{ij}), \quad r > 0 \tag{3}$$

In the above formula,  $d_{ij} = \|X_i - X_j\|_\infty$ ,  $\theta$  is the Heaviside function:  
 if  $(r - d_{ij}) < 0$ ,  $\theta(x) = 0$ ; if  $(r - d_{ij}) \geq 0$ ,  $\theta(x) = 1$ .  $M = N - (m - 1)\tau$ ,  $\tau$  is the time delay.

The basic steps of the algorithm are as follows:

1. According to the empirical method to set the time delay  $t$ , set  $t$  [1, 4].
2. The discrete time series  $\{x_i\}$  ( $i = 1, 2, 3, 4, \dots, N$ ) are divided into  $t$  disjoint time blocks, i.e.  $\{x_1, x_{t+1} \dots x_{N-t-1}\}, \{x_2, x_{t+2} \dots x_{N-t-1}\} \dots \{x_t, x_{2t} \dots x_N\}$  where  $N$  is an integer multiple of  $t$ .
3. It uses the block average strategy to calculate the statistics:

$$S_2(m, N, r, t) = \frac{1}{t} \sum_{s=1}^t [C_s(m, N/t, r, t) - C_s^m(1, N/t, r, t)] \quad (4)$$

When  $N \rightarrow \infty$ :

$$S_2 = \frac{1}{t} \sum_{s=1}^t [C_s(m, r, t) - C_s^m(1, r, t)] \quad (5)$$

Since the time series is finite and there is a correlation, if we measure the maximum deviation of the radius  $r$ , then the optimal time delay is the first zero point of  $S_2(m, r, t)$ , or for the pair. The radius  $r$  is the smallest difference between the time points. In this case, the points in the reconstructed phase space are closest to the uniform distribution, so we are the points of the maximum and minimum radii, and the difference is defined:

$$\Delta S_2(m, t) = \max\{S_2(m, r_j, t)\} - \min\{S_2(m, r_j, t)\} \quad (6)$$

According to the conclusion of BDS statistics, we can get embedded dimension  $m \in [2, 5]$ ,  $r = i * \sigma/2$ , where  $\sigma$  is the standard deviation of time series, Then it is calculated as Eq. (7-9):

$$\bar{S}_2 = \frac{1}{16} \sum_{m=2}^5 \sum_{i=1}^4 S_2(m, r_j, t) \quad (7)$$

$$\Delta \bar{S}_2 = \frac{1}{4} \sum_{m=2}^5 \Delta S_2(m, t) \quad (8)$$

$$S_{2cor}(t) = \Delta \bar{S}_2(t) + |\bar{S}(t)| \quad (9)$$

The first zero point of  $\bar{S}_2(t)$  or the first partial minimum point  $\Delta \bar{S}_2(t)$  is optimal  $\tau_d$ , the global minimum point of  $S_{2cor}(t)$  is the optimal embedding window  $\tau_w$ , which is optimal estimation of average orbital period.

### 3 Phase Space Reconstruction

The above C-C method calculates the optimal time delay and embedding dimension. In other words, we find the regular factors hidden in the chaotic time series data, based on these factors can be reconstructed phase space.

$N$  is the length of time series  $(x_1, x_2 \dots x_N)$ , and time delay is  $\tau$ , embedded dimension  $m$ , so the result of phase space reconstruction:

$$\begin{aligned}
 & (X(1), X(2) \dots X(N - (m - 1)\tau))^{-1} \\
 = & \begin{bmatrix} x(1) & x(1 + \tau) & \dots & x(1 + (m - 1)\tau) \\ x(2) & x(2 + \tau) & \dots & x(2 + (m - 1)\tau) \\ \vdots & \vdots & \dots & \vdots \\ x(N - (m - 1)\tau) & x(N - (m - 2)\tau) & \dots & x(t_n) \end{bmatrix} \quad (10)
 \end{aligned}$$

From the above phase space reconstruction sequence, we can see that for the initial chaotic time series, the reconstructed phase space extracts and restores the chaotic sequence rule, which is a regular trajectory under high dimensional space.

### 4 LSTM Neural Network

In this paper, the LSTM algorithm is proposed by Hochreiter and Schmidhuber [10] on the basis of RNN (Recurrent Neural Network) in 1997. In order to solve the problem that traditional neural networks can not deal with continuous events. The RNN can be connected as well as the traditional neural network, and its hidden layer is directly connected to each other. The input of the hidden layer includes not only the output of the input layer but also the output of the hidden layer at the last time. As shown in Fig. 1.

The Fig. 2 is a hidden view of the three layers from the hidden layer.  $x_t$ ,  $h_t$  and  $o_t$  are input, hidden and output state at time  $t$ .  $W_{ih}$  is the weight matrix of the input layer to the hidden layer;  $W_{hh}$  is the weight matrix of the hidden layer into the itself and between the other layers, which is responsible for “memory” the results of each update; Finally,  $W_{ho}$  is the weight matrix of the hidden layer to the output layer. The weight update of the RNN neural network is still using the gradient descent method.

However, RNN still has a “long-term dependence” problem, that is, for the sample between the predicted point and the actual training label interval larger, RNN will lose the ability to learn to connect distant information. The LSTM network chooses to memorize information that is beneficial to the target by adding “forgetting the gate” in the hidden layer to control forgetting some of the useless information. The following two figures can be seen more clearly LSTM made improvements.

**Fig. 1** Construction of RNN

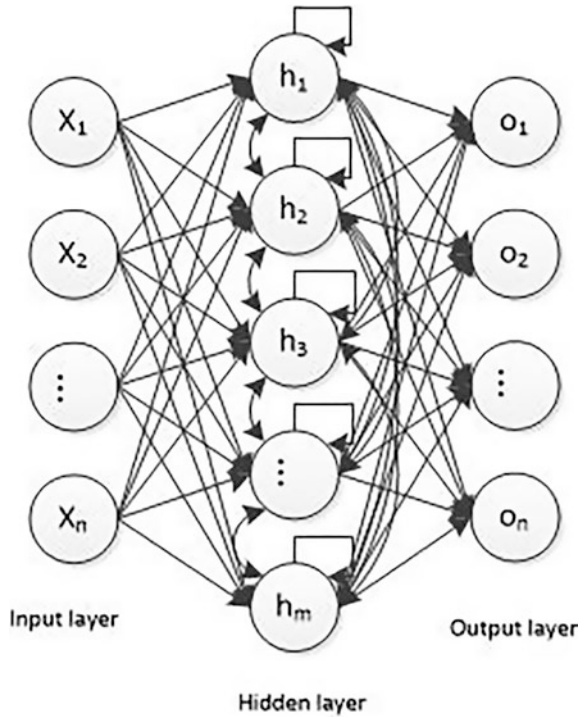
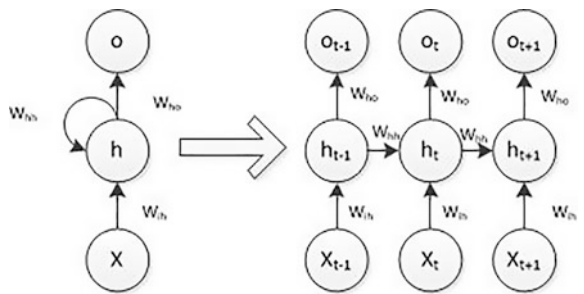


**Fig. 2** RNN neural network hidden layer contains the cycle



It can be seen from Fig. 3 that the RNN neurons are relatively simple. Neurons give predictions  $h_t$  and output states  $C_t$  for the next neuron from the same bipolar (tanh) layer. Figure 4 shows the structure of the LSTM neurons is more complex, there are three segments. Segment 1 is the “forgotten gate layer”, input  $h_{t-1}$  and  $x_t$  passed through the Sigmoid layer, which give an interval in the number of  $[0,1]$ , where 1 represents the complete hold, 0 stands for completely forgotten. As shown in Eq. 11:



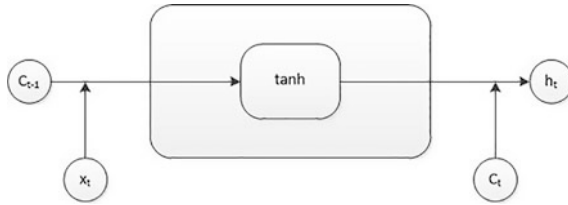


Fig. 3 A neuron from RNN

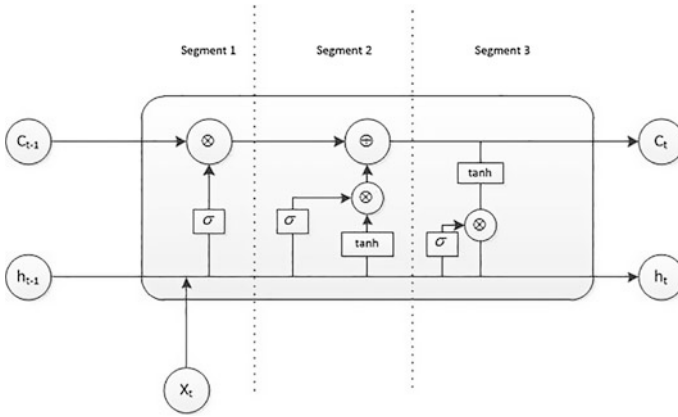


Fig. 4 A neuron from LSTM

$$f_t = \sigma(W_f \cdot [h_{t-1}, x_t] + b_f) \quad (b_f \text{ is offset variable}) \tag{11}$$

In the segment 2, this is the same as the first segment is still using the Sigmoid layer to update the input value. At the same time, the input value to go through a bipolar layer (tanh) to generate a post-election state. As shown in Eq. 12:

$$\tilde{C}_t = \tanh(W_C \cdot [h_{t-1}, x_t] + b_C) \tag{12}$$

At this point, we based on the results of the previous two parts, you can calculate the output status:

$$C_t = f_t * C_{t-1} + i_t * \tilde{C}_t \tag{13}$$

In the segment 3, for getting the result of hidden layer  $h_t$ . Firstly,  $h_{t-1}$  and  $x_t$  pass through Sigmoid layer, which determines which part of the neuronal state is output. Apart from this, the state of the neuron passes through the bipolar layer and multiplies the output of the Sigmoid layer:

$$o_t = \sigma(W_o[h_{t-1}, x_t] + b_o), h_t = o_t * \tanh(C_t) \quad (14)$$

In the case of using LSTM to predict, this paper takes the phase space  $m - 1$  dimension data  $\{x(i), x(i + \tau), \dots, x(i - 1 + (m - 1)\tau)\}$  as the factor input and the last one dimension of the next time data as input. At the same time, as in the later part of the experiment, this paper will forecast short-term holiday passenger flow and short-term regular date passenger flow, so the training set will mark the ordinary date, three days of small holiday and seven days of holiday, and mark as a dimension of input factors.

In order to eliminate the influence of the original data form, the feedback speed and the convergence speed of the algorithm are improved. Before the training set enters the model, the data needs to be normalized.

## 5 Experiment

This paper regards the China railway daily passenger flow on the March 6 to March 12 a week of the ordinary date in 2017 and 2016 Labor Day, 2016 Dragon Boat Festival, 2016 Mid-Autumn Festival, 2016 National Day, 2017 New Year's Day, 2017 Spring Festival and 2017 Ching Ming these holidays as the object to be predicted. The data for the three years to be predicted is selected as the training set for phase space reconstruction. It verifies whether the training set has chaos in the below Table 1 and the time delay and embedding dimension calculated using the C-C method.

It can be seen from the above Table 1 that the Lyapunov exponents [11] of the training set data are all greater than 0, so they are all chaotic time series. Then, in order to verify that the phase space reconstruction can recover the chaotic time series data and improve the prediction accuracy, we compare the model with the

**Table 1** Training set chaos judgment and result of time delay, embedded dimension

Forecast target date	Lyapunov exponents	Time delay (days)	Embedded dimension
2017.3.6–2017.3.12	3.20	1	4
2016 Labor Day	0.65	3	2
2016 Dragon Boat Festival	0.36	1	2
2016 Mid-Autumn Festival	0.47	6	2
2016 National Day	1.32	2	5
2017 New Year's Day	4.8	3	4
2017 Spring Festival	0.77	2	4
2017 Ching Ming	0.69	6	2

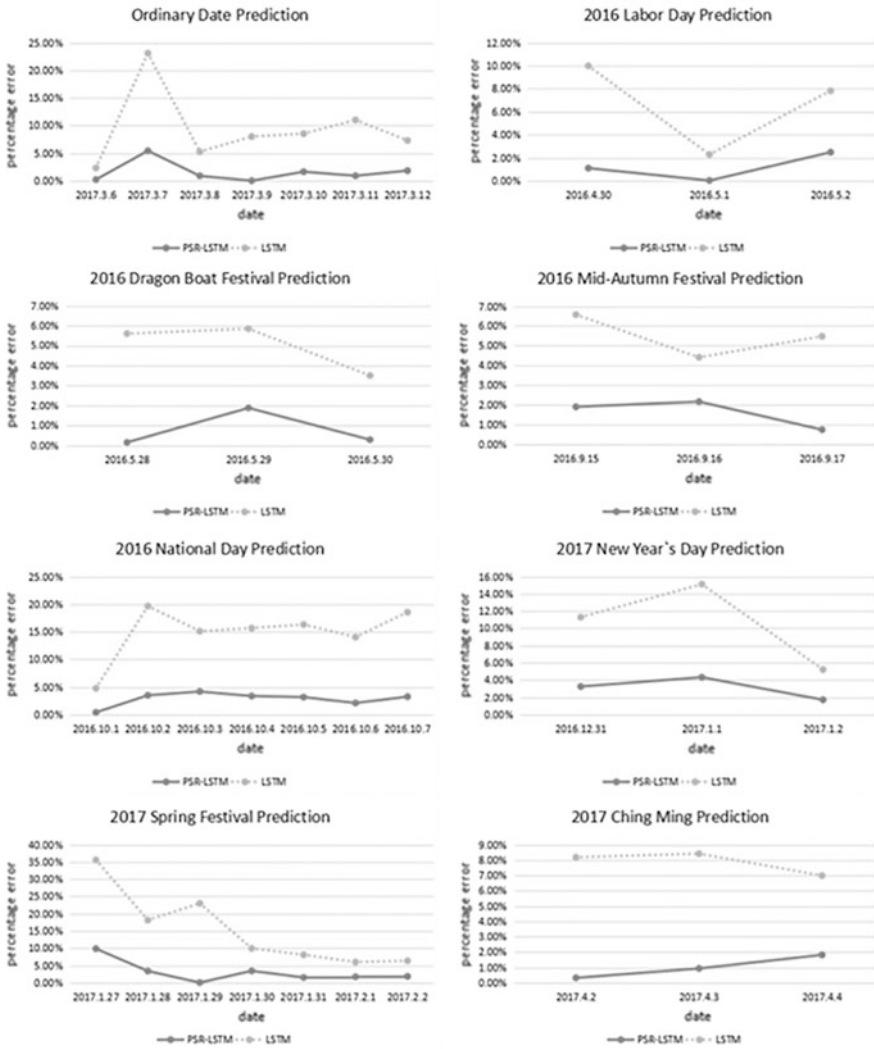


Fig. 5 Comparison of PSR-LSTM and LSTM predictive results

prediction accuracy of the LSTM model without phase space reconstruction. In this paper, the percentage error between the predicted value and the actual value is taken as the evaluation criterion, and then the closer to 0% the higher the accuracy.

As can be seen from the above Fig. 5, the solid line represents the prediction accuracy of the PSR-LSTM, which has a higher accuracy than the untreated obviously for different days of passenger flow.

Furthermore, in order to verify whether the LSTM neural network used in this model is reasonable, we will use the BP neural network (PSR-BPNN) with phase

space reconstruction and the SVR model with RBF (Radial Basis Function) kernel function under the same training set PSR-SVR), and the accuracy is verified by the percentage error.

Accordingly, as can be seen from the Fig. 6, it can be seen from the above experimental results that the LSTM neural network used in this paper has higher prediction accuracy than other models for different days of passenger flow.

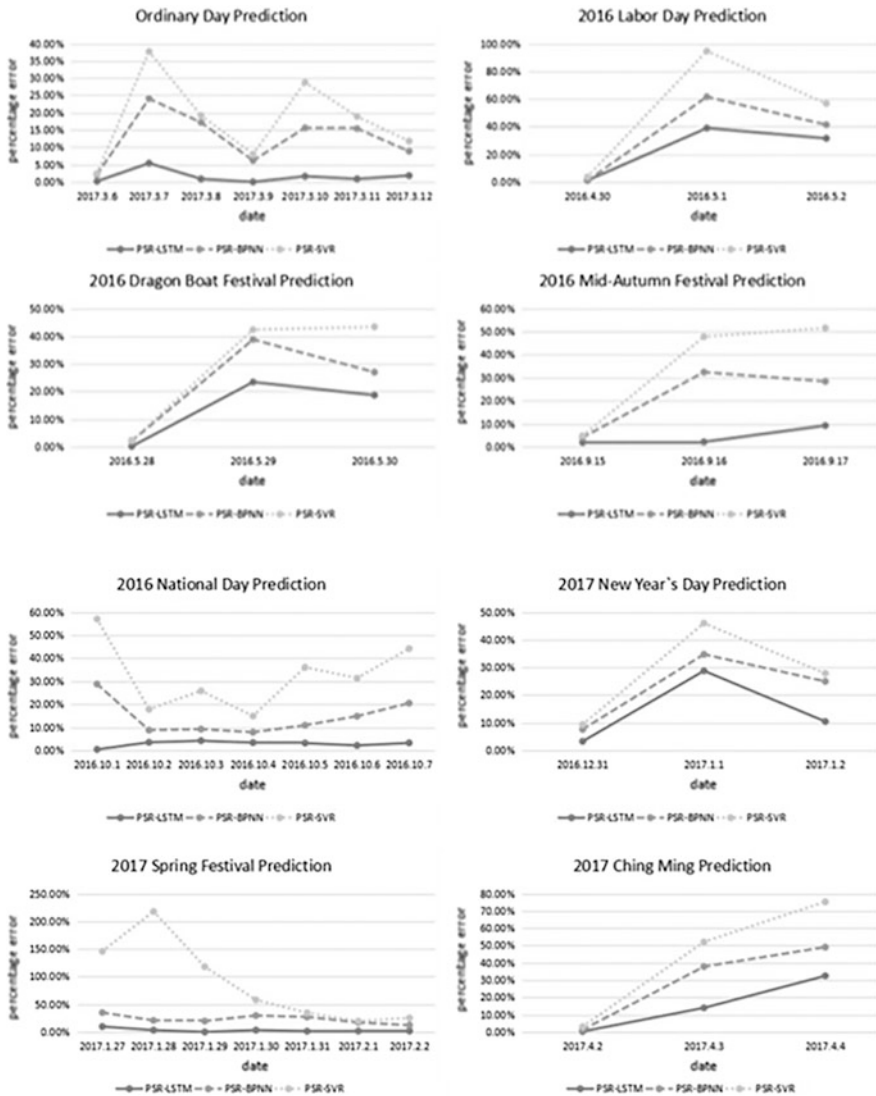


Fig. 6 Comparison of PSR-LSTM and PSR-BPNN, PSR-SVR predictive results

## 6 Conclusion

In this paper, the theory of phase space reconstruction is used to recover the regular orbit of railway passenger flow, and the short term passenger flow is predicted by LSTM neural network. From the experimental results of two parts, it can be seen that the passenger flow data with chaotic characteristics can improve the prediction accuracy of short-term passenger flow if the regularity factor can be found by phase space reconstruction. At the same time, LSTM neural network compared with other algorithms, can significantly improve the nonlinear short-term passenger flow prediction accuracy.

**Acknowledgements** This work is supported by Railway Corporation Research Project (NO. 2016X005-B). Jiansheng Zhu is the corresponding author.

## References

1. Huang Z, Feng S (2014) Grey forecasting model in the application of railway passenger flow prediction research. *Technol Econ Areas Commun* 16(1):57–60 (in Chinese)
2. Zhang B (2014) Study on short-term forecast of Shanghai-Nanjing intercity railway passenger flow. *Chin Railways* 2014(9):29–33 (in Chinese)
3. Dong S (2013) The research of short-time passenger flow forecasting based on improved BP neural network in urban rail transit. Beijing Jiaotong University (in Chinese)
4. Deng J, Kong F, Chen X (2008) Passenger flow forecast of urban rail transit based on support vector regression. *J Chongqing Univ Sci Technol (Nat Sci Edn)* 10(3):147–149 (in Chinese)
5. Takens F (2006) Determining strange attractors in turbulence. *Lecture Notes Math* 2006: 366–381
6. Ma H, Li X, Wang G, Han C et al (2004) Selection of embedding dimension and delay time in phase space reconstruction. *J Xi'an Jiaotong Univ* 38(4):335–338 (in Chinese)
7. Kugiumtzis D (1998) State space reconstruction parameters in the analysis of chaotic time series—the role of the time window length. *Physica D-Nonlinear Phenomena* 95(1):13–28
8. Kim H, Eykholt R, Salas J (1999) Nonlinear dynamics, delay times, and embedding windows. Elsevier Science Publishers B. V
9. Broock W, Scheinkman J, Dechert W et al (1996) A test for independence based on the correlation dimension. *Econometric Rev* 15(3):197–235
10. Hochreiter S, Schmidhuber J (2012) Long short-term memory. *Neural Comput* 9(8): 1735–1780
11. Rosenstein M, Collins J, Luca C (1993) A practical method for calculating largest Lyapunov exponents from small data sets. *Physica D-Nonlinear Phenomena* 65(1–2):117–134

# Application of Improved Gaussian-Hermite Moments in Intelligent Parking System

Xing He, Lin Wang and Zhongyou Zuo

**Abstract** The Gaussain-Hermite moments theory is applied to license plate recognition system in this paper. At the same time, the order of Gaussian-Hermite moments are improved by two-dimensional simulated annealing algorithm, the image reconstruction is achieved by obtaining characteristic moments. Experimental results show that the algorithm has high research value and application value.

**Keywords** Gaussian-Hermite moments · Simulated annealing algorithm  
Feature extraction · Image reconstruction · Character recognition

## 1 Introduction

The image feature extraction technology is a core component of intelligent identification system. Accuracy and reliability of feature extraction determines the recognition rate of the Intelligence system, Therefore, it's need to propose an image feature extraction algorithm with high accuracy and robustness. The image feature extraction can be divided into common feature extraction algorithm based on color image and texture feature extraction algorithm etc., there are some classic foreign image feature extraction algorithms. J. Shen first proposed the orthogonal Gaussian-Hermite moments analysis image features [1], the author combines Gaussain function and Hermite polynomial, in order to the convergence of the Hermite polynomial in the edge of the window function, and put forward the 2D orthogonal polynomial Gaussian-Hermite separation algorithm and recursive algorithm. W. Shen proposed comparison algorithm of geometric moments and orthogonal moments [2], the author presents a comparison of Gaussain-Hermite orthogonal polynomial and geometric moment polynomial, Legendre polynomial,

---

X. He (✉) · L. Wang · Z. Zuo  
Guizhou University for Nationalities, Huaxi, Guiyang, China  
e-mail: 1031869687@qq.com

Hermite polynomial between time domain and frequency domain. R. Mukundan on the basis of previous studies, they search for the orthogonal polynomials and put forward the image features of based on the Tchebichef moment analysis algorithm [3]. The algorithm finds the orthogonal polynomials, and then extract and analyze the characteristics of image. Bo Yang proposed the research of J. Shen analysis of Gaussian-Hermite moments parameter [4]. The algorithm to obtain the very good results. On the basis of the above methods, there are some classic image feature extraction algorithms in China: Wang Lin proposed a feature extraction algorithm based on Gaussian-Hermite moments in the fingerprint recognition application [5], the experiment proved that the algorithm has better recognition effect in the fingerprint recognition system. Wu Youfu proposed the vehicle identification algorithm based on Gaussian-Hermite moment [6], the experimental results show that the improved algorithm has important research significance and practical application values.

This paper presents a Gaussian-Hermite based on moment parameter analysis algorithm, combined with the improved 2D simulated annealing algorithm to search the optimal parameters of image reconstruction rate.

## 2 Gaussian-Hermite Moments and Orthogonal Calculation

### 2.1 1D Hermite Polynomial and Orthogonal Algorithm

The 1D continuous n-order Hermite polynomial is defined as follows

$$H_n(x) = (-1)^n \exp(x^2) \frac{d^n}{dx^n} \exp(-x^2) x \in (-\infty, \infty) \quad (1)$$

therefore,  $H_0(x) = 1$ ,  $H_1(x) = 2x$ ,  $H_{n+1}(x) = 2xH_n(x) - 2nH_{n-1}(x)$ . Because the  $H_n(x)$  polynomial is not orthogonal function, therefore, the weight function is introduced.

$$\rho(x) = \exp(-x^2) x \in (-\infty, \infty) \quad (2)$$

Therefore

$$\int_{-\infty}^{\infty} \exp(-x^2) H_n(x) H_m(x) dx = 2^n n! \sqrt{\pi} \delta_{mn} \quad (3)$$

Among  $\delta_{mn}$  is the Kronecker function. therefore, Hermite standard orthogonal polynomial can be written as

$$\widehat{H}_n(x) = \frac{1}{\sqrt{2^n n!} \sqrt{\pi}} \exp\left(-\frac{x^2}{2}\right) H_n(x) \tag{4}$$

At the same time, 1D continuous Hermite polynomial normalized be written as

$$\int_{-\infty}^{\infty} \widehat{H}_m(x) \widehat{H}_n(x) dx = \delta_{mn} \tag{5}$$

For the 1D continuous signal  $I(s)$ , the moment of n-order Hermite is defined as follows

$$M_n(x, I(s)) = \int_{-\infty}^{\infty} \widehat{H}_m(x) I(x+s) ds \tag{6}$$

In order to give the Eq. (4) schematic diagram of 1D continuous, and give  $\widehat{H}_p(x)$  dimensional display function transformation function

$$\varphi(\widehat{H}_p(x)) = \text{sign}(\widehat{H}_p(x)) \left(1 + \log|\widehat{H}_p(x)|\right) \tag{7}$$

Figure 1 gives to the 1D orthogonal Hermite polynomial basis function in the window size is  $[-5, 5]$ . It is easy to see on the boundary of the windows at the orthogonal basis is not convergence to 0. This property will affect the image at the edge of the reconstruction results.

### 2.2 2D Hermite Polynomial Orthogonal Separation Algorithm

By the 2D Hermite polynomial separability

$$H_{mn}(x, y) = H_m(x)H_n(y) \tag{8}$$

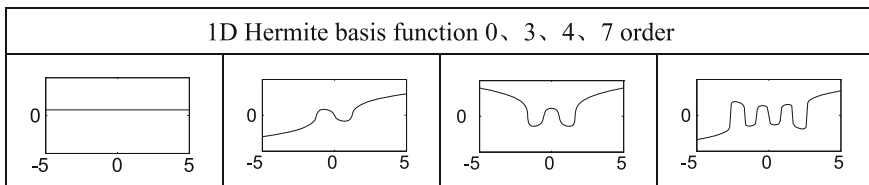


Fig. 1 The basis function sketch map of Hermite polynomial



The orthogonal separable equations for 2D Hermite Polynomials

$$\widehat{H}_{mn}(x, y) = \widehat{H}_m(x)\widehat{H}_n(y) \tag{9}$$

The 2D continuous signal  $I(s, t)$ , the  $(m, n)$  order Hermite moments can be defined as follows

$$M_{mn}(x, I(s, t)) = \int_{-\infty}^{\infty} \int_{-\infty}^{\infty} I(s, t)\widehat{H}_m(s)\widehat{H}_n(t)dsdt \tag{10}$$

Figure 2 2D orthogonal Hermite polynomial basis function in the window size  $s, t \in [-5, 5]$ . In the window edge image, here is still a divergence of this property, the Hermite polynomial basis function in window edge converges to 0. We will make a detailed demonstration of the nature of the Gaussian function in the next section.

### 2.3 Gaussian-Hermite Polynomial and Orthogonal Separation Algorithm

The Gauss function is a kind of low pass filter fuzzy of image, the normal distribution is calculated for each pixel in the image transform, fuzzy Gauss have very good characteristics, the function has no obvious boundary and not the formation of turbulence in the filtered image, so Gaussian function is introduced to the Hermite orthogonal polynomial. Not only make the image in the edge of the window the convergence, but also has a good smoothing effect for images with high noise. The 1D Gauss functions is defined as follows

$$G(x, \sigma) = (2\pi\sigma^2)^{-1/2} \exp\left(\frac{-x^2}{2\sigma^2}\right) \tag{11}$$

among  $\sigma^2$  for standard deviation, we can define a 1D signal sequence of  $I(x)$  Gaussian-Hermite moments (Fig. 3).

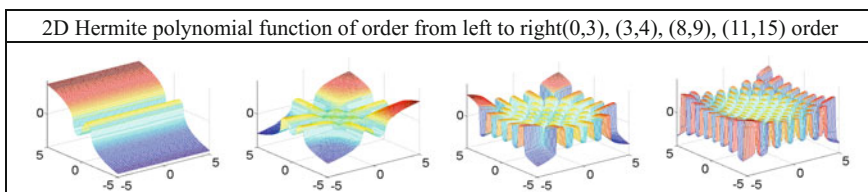


Fig. 2 The basis function sketch Map of 2D standard orthogonal Hermite polynomials

$$B_n(x) = G(x, \sigma)H_n\left(\frac{x}{\sigma}\right) \tag{12}$$

$$M_n(x, I(s)) = \int_{-\infty}^{\infty} B_n(x)I(x + s)ds \tag{13}$$

so the orthogonal basis function polynomial Gaussian-Hermite increase the scale parameters  $\sigma$  of the Eq. (4) can be rewritten as

$$\check{H}_n(x) = \frac{1}{2^n n! \sqrt{\pi}} \exp\left(-\frac{x^2}{2\sigma^2}\right) H_n\left(\frac{x}{\sigma}\right) \tag{14}$$

The window size is in  $[-1,1]$ ,  $\sigma = 0.12$ , according to the Gaussian function and Hermite polynomial separability, Eq. (12) can be rewritten as

$$\check{H}_{mn}(x, y) = \check{H}_m(x)\check{H}_n(y) \tag{15}$$

The 2D continuous signal  $I(s, t)$ ,  $(m, n)$  order Gaussian-Hermite moment are defined as follows

$$M_{mn}(x, I(s, t)) = \int_{-\infty}^{\infty} \int_{-\infty}^{\infty} I(s, t)\check{H}_m(s)\check{H}_n(t)dsdt \tag{16}$$

Figure 4 2D orthogonal Gaussian-Hermite polynomial basis functions in the window size  $s, t \in [-1, 1]$ ,  $\sigma = 0.12$ . The discrete gray-scale image  $I(i, j)$ , The coordinate domain of an image in the  $[0, T - 1]$ , if the use of Gaussian-Hermite polynomial basis function to extract the image local feature, we require the image coordinate transform to  $u, v \in [0, T]$ , by transformation  $s = \frac{2}{T-1}i - 1, t = \frac{2}{T-1}j - 1$ . Through the above coordinate transformation, the Eq. (14)increase the transform coefficients the discrete Gaussian-Hermite polynomials can be written as

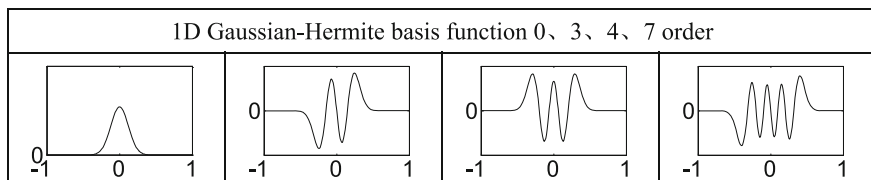
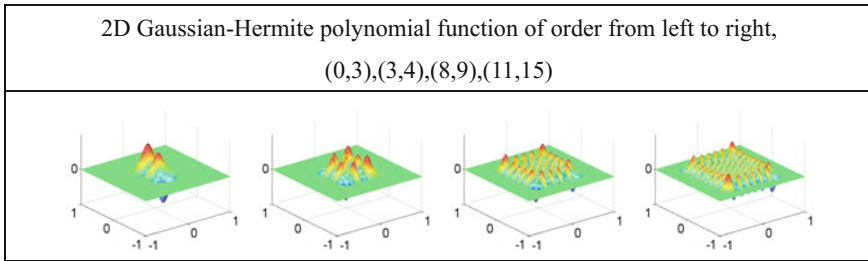


Fig. 3 The basis function sketch map of Gaussian-Hermite polynomial



**Fig. 4** 2D standard orthogonal Gaussian-Hermite polynomials

$$\begin{aligned} \check{H}_m(i) &= \frac{1}{\sqrt{2^{m-1}m!\sigma T\sqrt{\pi}}} \exp\left(-\frac{s^2}{2\sigma^2}\right) M_m\left(\frac{s}{\sigma}\right) \\ \check{H}_n(j) &= \frac{1}{\sqrt{2^{n-1}n!\sigma T\sqrt{\pi}}} \exp\left(-\frac{t^2}{2\sigma^2}\right) M_n\left(\frac{t}{\sigma}\right) \end{aligned} \tag{17}$$

By Eq. (17) can be get Gaussian-Hermite moments of discrete images, we can be defined as follows

$$M_{m,n} = \sum_{i=0}^{T-1} \sum_{j=0}^{T-1} I(i,j)\check{H}_m(i)\check{H}_n(j) \tag{18}$$

The reconstructed image is  $\hat{I}(i,j)$ , then the calculation formula is as follows

$$\hat{I}(i,j) = \sum_{m=0}^P \sum_{n=0}^{P-m} M_{m,n}\check{H}_m(i)\check{H}_n(j) \tag{19}$$

For 2D discrete gray image, the length and width ratio of 1:1, Fig. 5 the Gaussian-Hermite moments of image reconstruction, the first act of the original image and the second fixed size parameter  $\sigma = 0.1$ , the order of moments where  $n = 0, 5, 10, 20, 40, 60, 80$ . When  $\sigma$  fixed time with the increase of the order parameter accuracy of image reconstruction and rising trend. Third fixed order parameter  $n = 50$ , the size parameter  $\sigma = 0.05, 0.1, 0.2, 0.4, 0.6, 0.8, 1$ . There are



**Fig. 5** 2D Gaussian-Hermite moment image reconstruction

also increase of the order parameter accuracy of image reconstruction is decreased gradually after the rising trend. In the next section we will analyze the detailed image reconstruction parameters *order* and  $\sigma$ , and the relationship between the size of the image of *T* three and value.

### 3 Gaussian-Hermite Analysis of Moment Parameters

For the relationship between the reconstruction parameters  $n$ ,  $\sigma$  and image size  $T$ , make  $I(i, j)$  for the original discrete gray image, gray level in  $[0, 255]$ , the image coordinate domain  $[0 \leq i, j \leq T - 1]$ , in the sigma is  $\sigma = 0.12$ , the image reconstruction rate  $P$  is defined as follows  $P = \frac{S}{T^n}$ , where  $S$  is the same number, The Fig. 6 (left) is  $n$  when the parameter  $\sigma = 0.12$ , the relationship between  $P$  and  $n$ , the increased rate of image reconstruction with the order of moments of the increase of the figure shows, the overall upward trend, when the order reaches a certain value,  $P$  remain the same. The Fig. 7 (right) is  $n$  when the parameter *order* = 50, the relationship between  $P$  and  $\sigma$ . The figure shows with increasing parameter,  $\sigma$  the  $p$  fluctuations increased first and then decreased. However, in the actual application, at the same time to consider the problem of real-time and accuracy of both compatible.

We proposed an improved simulated annealing algorithm to search the optimal solution of the rate of  $P$  image reconstruction.

The based on the 2D discrete simulated annealing algorithm for image reconstruction rate  $P(\sigma, n)$  between a Gaussian-Hermite moments parameter  $\sigma$  and  $n$  value relationship, the design steps are as follows:

- (1) Random initialization  $\sigma = 0.1, n = 1, T = 0.2$ .
- (2)  $Variable\_Point = Start\_Point + \Delta Point$  among  $Start\_Point$  for initialization  $\Delta Point$  as a parameter  $\sigma$  and  $n$  of random increment.  
 $Variable\_Point$  to search for the current variable value. To the calculation  $\Delta P = P(Variable\_Point) - P(Start\_Point)$ .

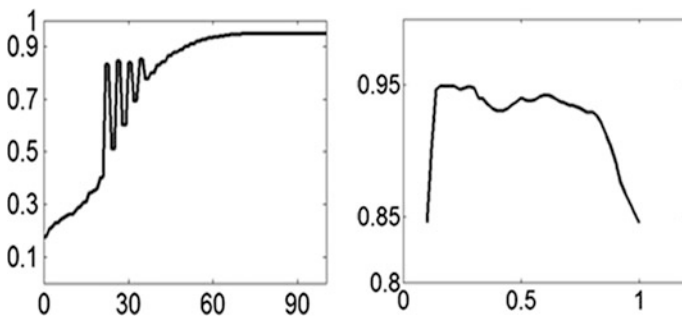
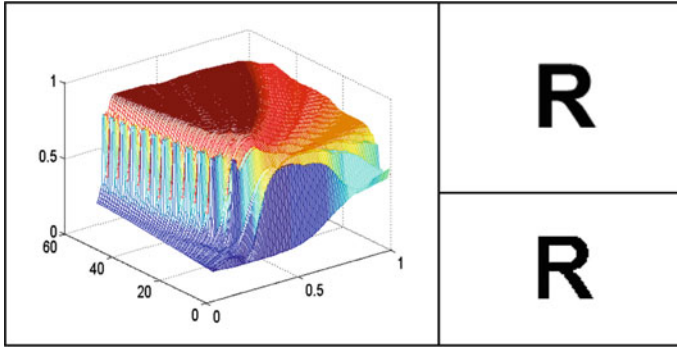


Fig. 6 The relationship between  $P$  and  $\sigma, n$



**Fig. 7** Image reconstruction

- (3) If the  $\Delta P < 0$ , they will be allowed to take  $\text{Variable\_Point}_{\sigma, \text{order}}$  value for the new state, otherwise  $P = \exp\left(-\frac{\Delta P}{KT}\right)$  accept  $\text{Variable\_Point}$ , the  $K$  is the Boltzmann constant.
- (4) Repeat step second and third, until  $P$  equilibrium, until  $T$  approach to 0.

In Fig. 7, the relationship between  $P$  and Gaussian-Hermite moments parameter  $n$  and  $\sigma$ , we used the improved two-Dimensional simulated annealing algorithm is used to search the global optimal solution, final search results for  $\text{order} = 50$ ,  $\sigma = 1$ , the fixed image size  $T = 85$ . Right image for the original image, the right image for the search of the global threshold of the reconstruction image, which the image reconstruction rate  $P = 0.9349$ .

## 4 The Application of Gaussian-Hermite Moments

### 4.1 Gaussian-Hermite Moment Feature Conversion

In this paper, we will introduce the Gaussian-Hermite moments as the input basis of the vehicle license plate character recognition. The expression is defined are as follows.

$$GHM_{mn} = \begin{matrix} M_{00} & M_{01} & \cdots & M_{0n} \\ M_{10} & M_{11} & \cdots & M_{1n} \\ \vdots & \vdots & \ddots & \vdots \\ M_{m0} & M_{m1} & \cdots & M_{mn} \end{matrix} \tag{20}$$

The extracted  $GHM_{mn}$  moment vectors are converted into BP neural networks with input features as

$$GHM_{mn} = (M_{00}, \dots, M_{0n}, \dots, M_{m0}, \dots, M_{mn}) \tag{21}$$

### 4.2 Experimental Results and Analysis

In this paper, the video based automatic toll collection management system is implemented in the software development platform of C++ Visual and Opencv, the BP neural network is used for identification.

#### 4.2.1 Experimental Result

The system interface of this paper is shown in Fig. 8.

#### 4.2.2 Systems Analysis

The system after several tests. The results showed that the stability of the system is relatively high, results achieved very good results, due to phase identification and license plate location, license plate character segmentation, character feature extraction is closely related to, so the system to input the actual city field needs further improvement:

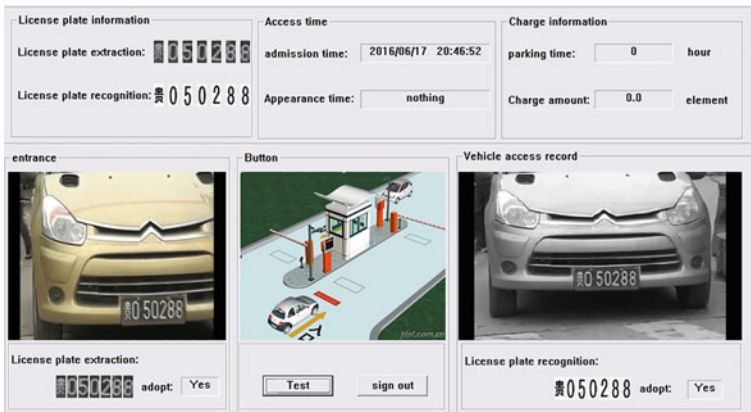


Fig. 8 The system operation interface

**Table 1** Real-time license plate recognition rate results

Chinese character recognition	Letter recognition	Number
92.3%	98.67%	100%

- (1) How to obtain the real-time video data speed to be improved, this process is one of the reasons that affect the real-time performance of the system.
- (2) Moving target detection algorithm needs to be fully improved, inter frame difference algorithm although can reduce the light, such as the weather, but prone to moving target empty phenomenon. Secondly, the value of time and target motion threshold selection is the key; background subtraction algorithm can extract the moving object is, however, background update is very difficult to accurately extract; optical flow method can improved inter frame difference algorithm and background difference problems, but require many iterations, unable to meet the requirements of real-time system. In this paper, the improved multi Gauss background modeling is needed to be improved in the running times.
- (3) In this paper, the location of the license plate in the complex environment can also be a good effect; the character of the same will be satisfied with the results.
- (4) For feature extraction of license plate characters, the value of the Gaussian-Hermite moments feature extraction, the algorithm in the image reconstruction process obviously obtained satisfactory results, however, in the process of recognition has increased the dimensionality of the feature, the better algorithm needs further study.

In the 32,000 frame video image sequence acquisition, a total of vehicles more than 100 vehicles, including cars, trucks, cars, the recognition P is shown in the Table 1.

## 5 Conclusion

In this paper, an improved simulated annealing algorithm for two-dimensional Gaussian-Hermite moment parameter  $n$  and  $\sigma$  is given, the algorithm is based on the invariant size of the image, the problem of global optimal solution of P is discussed. Consider the complexity and accuracy of the algorithm in the practical application research, depending on the size of the image, through the above search algorithm, the best moment parameters  $n$  and  $\sigma$  can be obtained.

Because the actual scene is more complex, the license plate location need to consider all the circumstances, the key lies in the accurate positioning of the license plate, license plate character segmentation and character feature extraction three steps were studied. The future research is mainly to build parking lot vehicle intelligent scenario can monitor system model and application system in the actual scene.

**Acknowledgements** **Foundation item:** Science and technology fund of Guizhou province (LH [2014]7390).

**Foundation item:** Research foundation of Guizhou Minzu University for Nationalities (16jsxm026).

## References

1. Shen J (1997) Orthogonal Gaussian-Hermite moments for image characterization. In: Proceedings of the SPIE intelligent robots computer vision XVI. Pittsburgh, pp 224–233
2. Shen J, Shen W, Shen DF (2000) On geometric and orthogonal moments. *Int J Pattern Recogn Artif Intell* 14(7):875894
3. Mukundan R, Ong SH, Lee PA (2001) Image analysis by Tchebichef moments. *IEEE Trans Image Process* 10(9):1357–1364
4. Yang B (2012) Image reconstruction from continuous Gaussian-Hermite moments implemented by discrete algorithm. *Pattern Recogn* 45:1602–1616
5. Wang L (2007) Some aspects of Gaussian-Hermite moments in image analysis. *Nat Comput, ICNC 2007*
6. Wu Y (2007) Discrete Gaussian-Hermite moments and its applications. *Networking Mobile Comput* 29:12044–12463 (China 12–17 October 2008)



# Research on Optimization of Passenger Volume Flow Monitoring Through the Metro Network Video Surveillance Technology

Yuekun Zhang, Feng Xu, Tianxiang Mao and Bing Han

**Abstract** In order to manage the constantly increasing flow of metro passengers and speed up the response to passenger congestion arising from various emergencies in the metro system, the Beijing Metro Network Administration Co., Ltd. (hereinafter referred to as the “BMNA”) will begin construction of the Metro Network Video Surveillance Center (hereinafter referred to as the “Surveillance Center”). This essay analyzes the characteristics of passenger flow congestion in the metro system and the traditional method of passenger flow density monitoring. Based on the system requirements and initial design of the Metro Network Video Surveillance Center, this essay applies scientific principles and methods to make suggestions to improve the supervisory of passenger flow congestion, by proposing a systematic congestion pre-warning mechanism using refined Video Analytics technology. Its aim is to provide references and support for the establishment of the Surveillance Center in future.

**Keywords** Passenger flow congestion pre-warning · Video surveillance  
Refined video analytics · Machine learning · Passenger flow density alert threshold setting

## 1 Preface

### 1.1 Research Background

As an essential urban transport carrier, metro transportation faces the constant challenge of rapid route expansion and maintaining secure operations with ever increasing passenger densities.

---

Y. Zhang (✉) · F. Xu · T. Mao · B. Han  
Beijing Metro Network Administration Co., Ltd., No. 6 Xiaoying North Road,  
Chaoyang District, Jingtou Mansion, Beijing, China  
e-mail: Yuekun\_zhang@126.com

© Springer Nature Singapore Pte Ltd. 2018  
L. Jia et al. (eds.), *Proceedings of the 3rd International Conference on Electrical and Information Technologies for Rail Transportation (EITRT) 2017*, Lecture Notes in Electrical Engineering 482, [https://doi.org/10.1007/978-981-10-7986-3\\_71](https://doi.org/10.1007/978-981-10-7986-3_71)

The Beijing CPC Municipal Committee and the Beijing Municipal Authority highly value the informatization of Beijing's metro system, and safe travel is one of the top priorities in daily passenger routines. Surveys and statistics show that many accidents are caused by overcrowding and disorder. Extremely high passenger flow density in a short period of time causes passenger congestion, and can even lead to stampedes or other serious accidents, resulting in injuries and deaths. It is therefore necessary to conduct real-time monitoring on passenger flow density and congestion levels, so that metro stations can give early alerts and intervene in advance.

How to effectively monitor passenger flow congestion and give timely alerts while taking effective intervention actions is an urgent and essential question in the development of the metro system.

## ***1.2 The Metro Network Video Surveillance Center***

The "Notice of the General Office of the People's Municipality of Beijing Issuing a Working Plan to Further Improve the Security of Metro Operations" (Publication no. [2013] 59 of the General Office) was released in November 2013. Its stipulations include:

"(15) Improving the Establishment of a Support System for Emergency Command. Increase the quantity of video and image data from each metro line that is sent to the BMNA; upgrade and rebuild the connections between the BMNA, and the broadcast system, passenger information, and closed circuit television (CCTV) system; build service platforms for emergency scheduling, passenger guidance, and information release."

In order to implement this notice, the BMNA analyzed the current capabilities of the command system for emergency network scheduling, and carefully considered the problems in each relevant system. It then decided to establish the Surveillance Center, in order to conduct video surveillance and replay, and other related business and management tasks at network level.

## **2 Analysis of the Current Situation and Main Problems**

The Beijing metro network is developing rapidly, and it now has over 300 stations completed and operational. In newly built stations, the number of cameras and the scope of video surveillance have significantly increased. Traditional methods of passenger flow monitoring are based on manual checking of CCTV, which is no longer suitable for the huge number of monitoring points which now have to be covered. One of the main purposes of building the Surveillance Center is to research methods for automatic monitoring of passenger flow density and early alerts, which is one of its core functions.

In the early stage of feasibility research and preliminary design, the authors found that two major obstacles must be overcome before automatic monitoring and early alerts for passenger flow density can be implemented.

### ***2.1 Accuracy of Automatic Passenger Flow Density Monitoring***

The current automatic passenger flow density monitoring technology, based on video analysis, does not always provide accurate results in congested scenes. That is because traditional monitoring may be affected by lighting, moving targets, building facilities, views blocked by crowds, the angle of the surveillance cameras, etc., which can lead to inaccuracy.

Due to limited space in metro stations, surveillance cameras are often installed in lower positions, resulting in a limited angle of view. When passenger flow density is low, monitoring is more effective; but when passenger flow density is high, the view of the cameras can be significantly blocked by crowds, causing greater errors in automatic monitoring, which means the system often releases incorrect alerts.

### ***2.2 Standards for Setting the Passenger Flow Alert Threshold***

Setting the right threshold for the automatic alert system is a complex and challenging question for the metro monitoring and alert system design. Due to a lack of theoretical understanding and industrial standards, this problem has not been resolved. If the threshold is set too high, the system frequently issues incorrect alerts, not merited by the situation on the ground; if it is set too low, the system may ignore or miss situations where there is a crush risk. Therefore, even if the accuracy of automatic passenger flow density monitoring can be significantly improved, without effective rules for passenger flow density alerts, the alert effectiveness will be considerably weakened, and the operational management requirements will not be met.

## **3 Research and Testing of Solutions**

In order to find solutions to the two issues mentioned above, the authors have conducted specific research and testing, and they propose the following solutions.

### 3.1 *Improving Monitoring Accuracy of Passenger Flow Density When Stations Are Crowded*

The traditional pedestrian density monitoring algorithm is based on analysis of target areas on video to compute the current level of pedestrian density (percentage) in each area. When the density level reaches the pre-set threshold, the alert is triggered and staff can handle the situation accordingly. (As shown in the Fig. 1.)

Traditional flow density estimates are conducted through holistic or partial (head/shoulder) pedestrian detection. The system usually takes a large amount of sample pictures of pedestrians as detection training materials for feature extraction. Common features include Edgelet features (describing outlines of parts of the human body, including straight lines, curves and other shapes. The detection training categorizes human body sections into the whole body, head and shoulders, legs, and torso); Shapelet features (mainly uses machine learning to automatically generate adaptive local features and describe shape features based on the gradient of localized portions of an image); HOG (the Histogram of Oriented Gradients is a feature descriptor used in computer vision and image processing for the purpose of object detection. It produces a histogram of gradient orientation in localized portions of an image) etc. The types of classifiers will greatly affect the detection rate and speed, so an accurate classifier needs to strike a balance between these two factors [2].

There are currently many types of classifiers. Even with a high detection rate, some of them cannot be widely applied because of their high time complexity. Linear classifiers (e.g. Boosting, Linear SVM and Random Forest) have been



**Fig. 1** Traditional passenger flow density analysis [1]

widely applied due to their simple algorithms and fast detection speed; but linear classifiers have a relatively low detection rate. Their passenger flow density statistics can be subject to the influence of image blocking or complex backgrounds, resulting in low accuracy and performance of the individual-based passenger flow density estimation algorithm in crowded scenes. Although pedestrian detection and tracking technologies have improved dramatically in recent years, tracking in crowded scenes is still an unsolved problem [3].

Regression Analysis is a widely applied method of statistical analysis to determine the quantitative relationship between two or more dependent or independent variables. The regression-model crowd-density estimation method avoids tracking single individuals. It takes the crowd in the video as a continuum and uses the mature regression model or classification technology to estimate the pedestrian density. As the regression-model method does not require explicit foreground segmentation and pedestrian tracking, this could be a feasible way to estimate pedestrian density against a complex background.

The working process of the regression-model crowd-density estimation algorithm is shown in the Fig. 2. The foreground is first extracted from the video sequence, then multiple features are extracted from the foreground. The algorithm is trained with the correct regression model and finally, it estimates the pedestrian density based on test samples.

The regression model needs to extract various features, including foreground pixel features and texture features. Research findings show an approximately linear correlation between pedestrian density and the area of foreground pixels, so the regression fitting method can be employed to calculate the number of pedestrians in the video. Calculations using this method are more accurate in scenes of low pedestrian density; however, the crowds monitored in metro stations are usually of high density, which can easily lead to camera views being blocked. In addition, because of the perspective in the video image, the size of individuals in the video changes with their distance from the camera. The further they are from the camera, the smaller they are, and vice versa. This means that when estimating pedestrian density, the perspective correction method should be applied to each pixel in the scene. There are differences in texture between high and low density images. With low pedestrian density, the image texture is rougher than with high pedestrian density. For this reason, texture feature extraction methods such as LBP are more scientific and effective ways to obtain crowd information [4].

LBP (Local Binary Pattern) is a type of descriptor used to describe the texture of different parts of an image. The initial computing unit is a  $3 \times 3$  pixel window. The value of the center pixel is treated as the threshold for the 8 neighboring pixels. Where a neighboring pixel's value is greater than the center pixel's value, this is

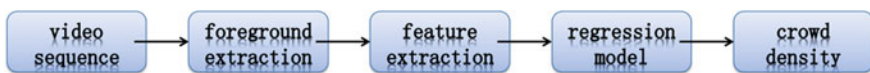


Fig. 2 Estimation of pedestrian density based on the regression model

recorded as “1”. Otherwise, it is recorded as “0”. This gives a binary image. Following the pixels clockwise in a circle from the first pixel at the top-left corner of the image, this produces a binary string, 00001111, which is equal to 15 when converted to a decimal number.

Apart from the center pixel, the remaining pixels in the  $3 \times 3$  window can output 8 bits of unsigned numbers, which constitute the LBP value of the window. This LBP value can be used to express the texture information of a certain area of an image, based on the following process:

This LBP algorithm is modified and optimized over time, producing the circular LBP descriptor, the rotation invariant pattern, the LBP uniform pattern, etc.

The original LBP descriptor covers only a small and fixed area and with limited descriptive power, so in order to be suitable for textures of various scales and frequencies, the original LBP descriptor is modified by replacing the previous rectangular area with a circular area and allowing the  $3 \times 3$  window to expand into any area. As a result, the circular area with  $P$  as the center and  $R$  as the radius allows multiple pixels.

The LBP value of the area around point  $P$  with  $R$  as the radius,  $g_c$  as the center pixel and  $g_p$  as the neighboring pixels is as follows:

$$LBP_{R,P} = \sum_{p=0}^{P-1} s(g_p - g_c)2^p \tag{1}$$

$$s(x) = \begin{cases} 1, & x \geq 0 \\ 0, & x < 0 \end{cases} \tag{2}$$

The righthand picture in Fig. 3 represents a circle with a radius of 1 and 8 neighboring pixels.

The pedestrian density indicator in metro stations is calculated based on the regression function model, which maps the features of a surveillance video scene to the number of people in a crowd. The regression function is widely used and there are many ways to construct a regression function model, such as linear regression, block-based linear regression or neural networks. The comparison of algorithms and the study results show that the algorithm of the partial least squares regression

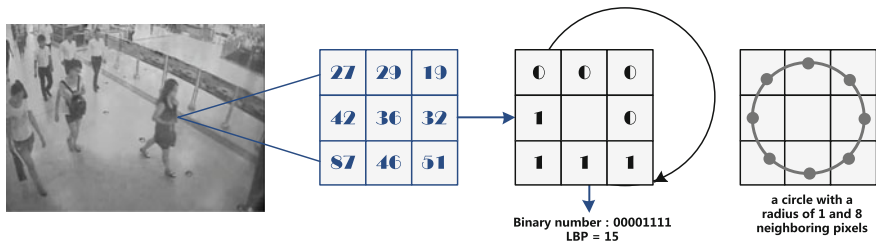


Fig. 3 Extraction of the LBP descriptor

(PLSR) model, containing concepts from many other regression models and dimension reduction algorithms, is better able to solve the multi-collinearity problem, when there exist multiple correlations and a limited amount of information has been obtained. PLSR is therefore often applied to the analysis and study of crowds in high density videos, whose distribution is affected by the surrounding environment.

To calculate the number of pedestrians in the video scene, two parameters, namely the number of pixels and the number of pedestrians, are extracted from the training samples, and a curve and function are constructed to approximately fit the data of these parameters based on the least squares method. The number of pixels per frame is then input to the function to calculate the number of pedestrians in the scene.

The specific calculation procedure, based on PLS, is given below. If  $n$  training samples  $\{(x_i, y_i)\}_{i=1}^n \in R^p \times R^q$  are mean-centered, PLSR is applied to calculate the values of projected unit vectors  $\alpha$  and  $\beta$ . If the projected vectors  $x^* = X\alpha$  and  $y^* = Y\beta$  cover variability of the variables, and the correlation degree between  $x^*$  and  $y^*$  reaches the highest value, then it calculates when the covariance between  $x^*$  and  $y^*$  is at its highest:

$$Cov(x^*, y^*) = \alpha^T E(x^T Y) \beta = \alpha^T G_{x,y} \beta \rightarrow m \tag{3}$$

$$J_{PLS}(\alpha, \beta) = \alpha^T G_{xy} \beta = \frac{\alpha^T G_{xy} \beta}{(\alpha^T \alpha \cdot \beta^T \beta)^{\frac{1}{2}}} \tag{4}$$

This includes  $\alpha^T \alpha = \beta^T \beta = 1$ .

The vectors  $\alpha$  and  $\beta$  which output the largest criterion function are named correlated projected vectors of PLS. When the original samples are projected to these correlated projected vectors, the covariance value is the largest between  $x^*, y^*$ .

### 3.2 Improving the Customization and Accuracy of the Passenger Flow Alert Threshold

Based on research outcomes, the US Transit Capacity and Quality of Service Manual recommends that the areas inside public transportation stations should be clearly divided into pedestrian areas and service areas [5].

In pedestrian areas, walking speed is the key factor that affects passenger flow density. Pedestrians need sufficient space to walk with free movement at average speed, in order to pay attention to possible obstacles within their sight. Increased passenger flow density reduces the available walking space and increases the possibility of collision.

In service areas, the average space taken up by each person is the key factor that affects passenger flow density. The average space used by each person has a direct

impact on their flexibility of movement as well as their sense of comfort. In dense passenger flows, almost no space is available for free movement, and as the average space consumed by passengers increases, they can only move freely within limited areas.

Metro stations can be divided into pedestrian areas and service areas based on different functions. The pedestrian density in these areas can be monitored separately, with a different threshold value designed for them, so that alerts are more accurately triggered.

Table 1 gives the relationship between walking speed and the average space consumed by pedestrians. It shows that pedestrians can walk at normal speed when the average space available for each person is 3.3 m<sup>2</sup> or over. As the average space drops below 3.3 m<sup>2</sup>, the walking speed drops quickly. When the average space available for each pedestrian drops to 0.5 m<sup>2</sup> or below, the walking speed becomes very slow, about 46 m per minute. In such conditions, crushes and stampedes are likely to occur and close monitoring and early warnings are required.

According to the following figure, when the service level reaches D in a walking area, the Surveillance Center video monitoring system should issue an alert to remind the transportation or service staff of the risk of a crush, so that they can reduce traffic pressure in advance (Fig. 4).

The following table shows different service levels in pedestrian areas. The table shows that when the average area occupied by pedestrians is 1.2 m<sup>2</sup> or more, the average distance between people is over 1.2 m. Below this point, the average distance between people falls rapidly. When the average area occupied by pedestrians is less than 0.2 m<sup>2</sup>, the average space between them falls to below 0.6 m. Generally speaking, as waiting times get longer, pedestrians need more space. Their tolerance of crowdedness changes over time. In such conditions, measures should be taken to prevent accidents caused by jostling and fighting, including emergency scheduling of trains, crowd dispersal, close monitoring, etc. (Table 2).

According to the following figure, when the service level reaches E in a service area, the Surveillance Center video monitoring system should issue an alert to remind the transportation or service staff of the risk of accidents, so that they can evacuate pedestrians in advance if required (Fig. 5).

**Table 1** Service levels in pedestrian areas

Service levels	Space available for each pedestrian (m <sup>2</sup> /pedestrian)	Expected passenger flow and walking speed	
		Average walking speed S (m/min)	Saturation level
A	≥ 3.3	79	0.0–0.3
B	2.3–3.3	76	0.3–0.4
C	1.4–2.3	73	0.4–0.6
D	0.9–1.4	69	0.6–0.8
E	0.5–0.9	46	0.8–1.0
F	<0.5	<46	N.A.



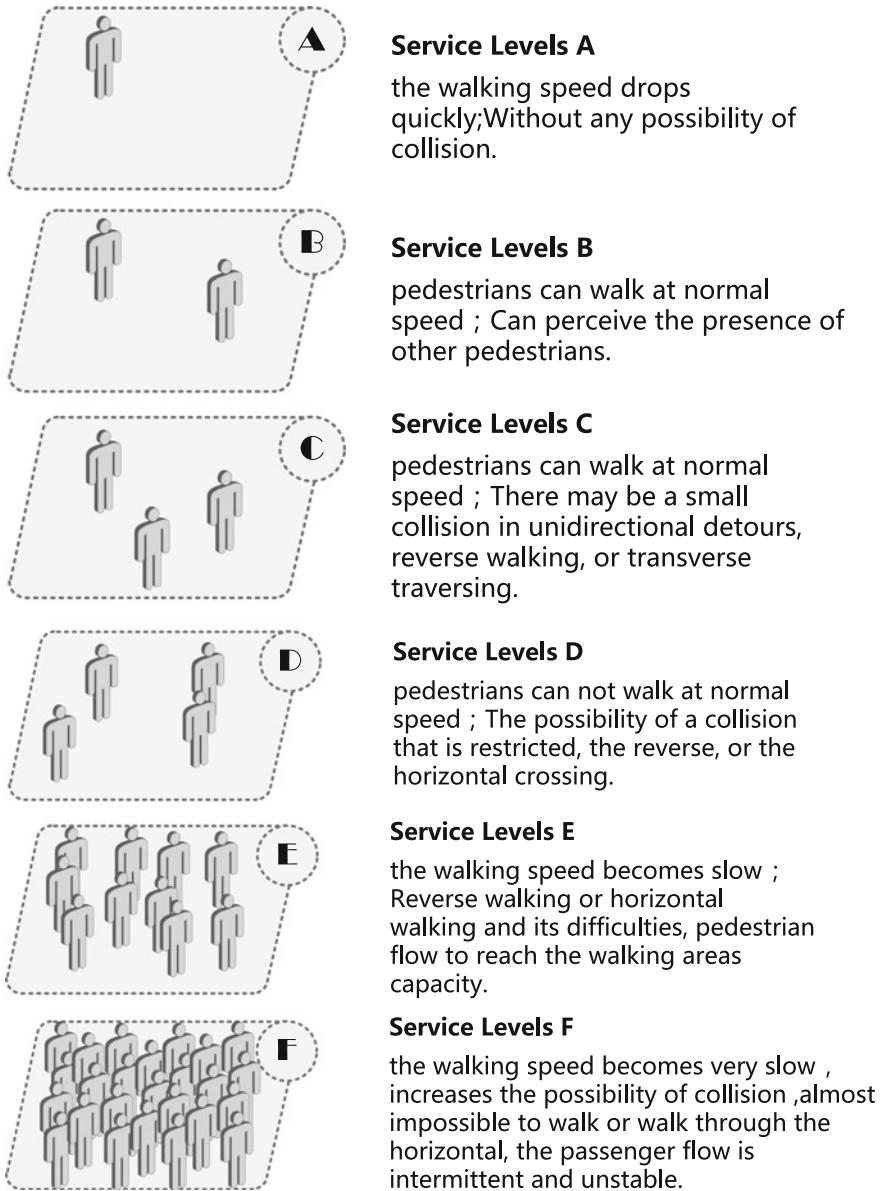


Fig. 4 Service levels in pedestrian areas

Based on the above analysis, the video surveillance area in a metro station can be divided into service areas and pedestrian areas. The service areas include train stopping points along platforms, fenced areas outside metro stations, ticket offices, etc. The pedestrian areas include stairs and escalators, entrances and exits and

**Table 2** Service levels in service areas

Service Levels	Average area occupied by pedestrians (m <sup>2</sup> /pedestrian)	Average space between people (m)
A	≥ 1.2	≥ 1.2
H	0.9–1.2	1.1–1.2
C	0.7–0.9	0.9–1.1
D	0.3–0.7	0.6–0.9
E	0.2–0.3	<0.6
F	<0.2	N.A.



**Service Levels A**

free to stand or free to cross the team, the behavior will not affect others.



**Service Levels B**

Can be standing in the service areas, the activities will be due to avoid others and part of the restrictions.



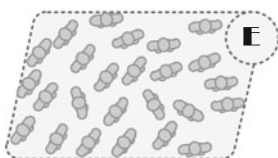
**Service Levels C**

Can stand in the service areas, can also be activities, but will affect other people; passenger flow density within the personal comfort range.



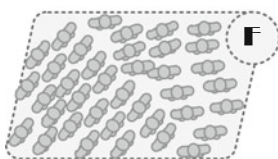
**Service Levels D**

Standing contact with others is inevitable. In the ranks of the walk is subject to great restrictions, only as a team to move forward, in the level of traffic density for a long time waiting is not comfortable.



**Service Levels E**

Standing contact with others is inevitable. Walking in the ranks is impossible. In such circumstances, queuing up in most of the time will have a serious feeling of discomfort.



**Service Levels F**

All the people in the service areas are actually in contact with others, at the level of pedestrian density pedestrians and their uncomfortable. Moving in the service areas is impossible, and there may be pushing and generating collective panic.

**Fig. 5** Service levels in service areas

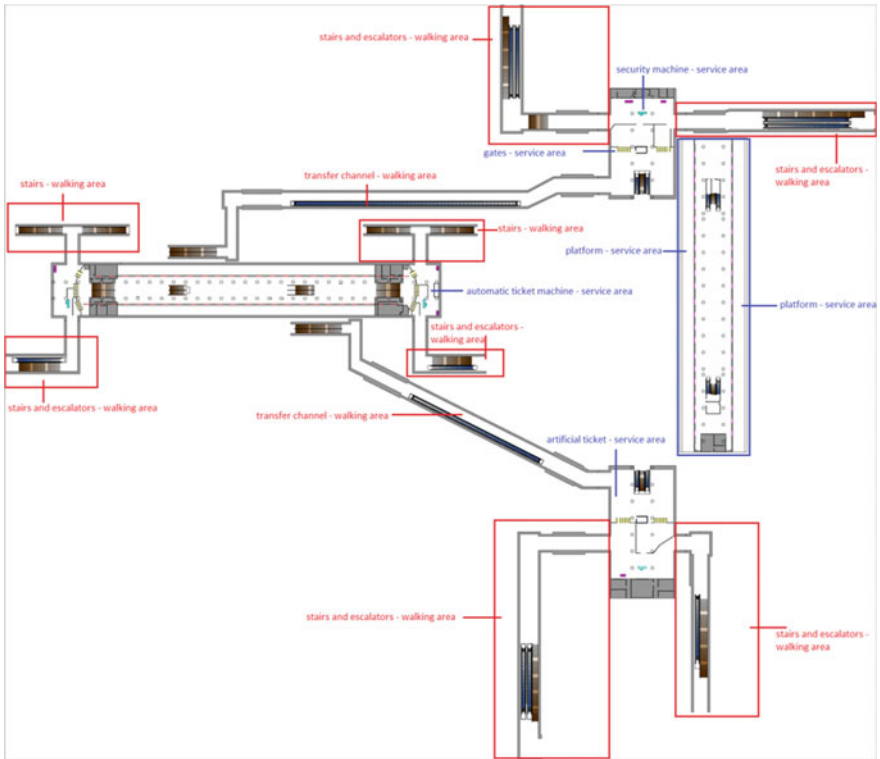


Fig. 6 Space division in metro stations [6]

transfer channels. Different parameters and passenger flow alert thresholds can be set for different surveillance areas.

The following figure shows the space division in one of Beijing’s metro stations. The service areas are indicated by blue rectangles and the pedestrian areas by red rectangles (Fig. 6).

### 3.3 Testing Process and Results

Three pedestrian areas and three service areas with heavy passenger flow during the morning and evening rush hours and light passenger flow in off-peak times were selected as samples from videos of a Beijing metro station to test the solution. The Research Department of ST Electronics Info-Software Systems was commissioned to calculate passenger flow densities, using both the traditional method and the new method based on the regression model (Fig. 7).

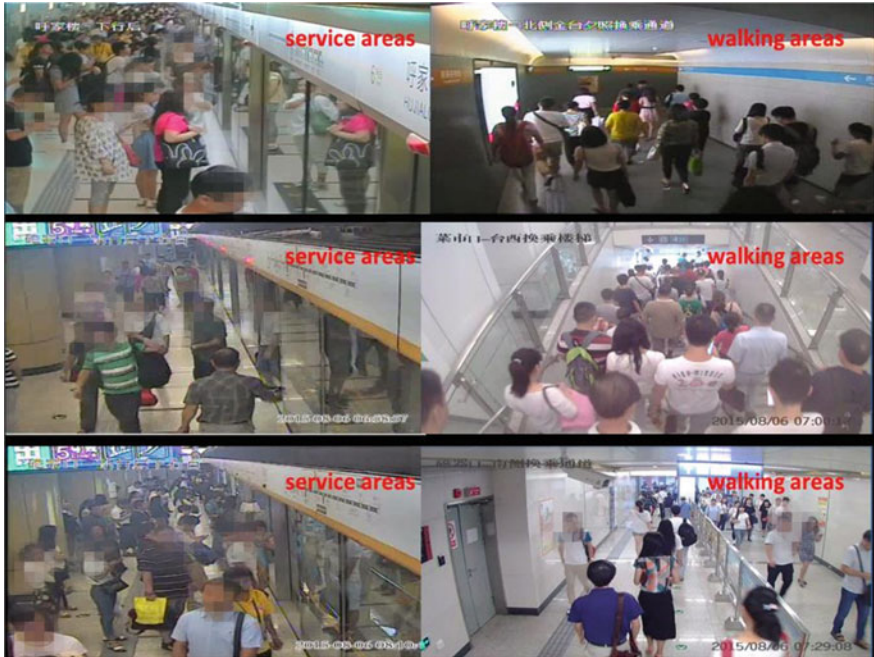


Fig. 7 Testing each method at a metro station [7]

The test results are shown in the Table 3.

These test results indicate that during low-density passenger flow, both the traditional and the new monitoring methods show a high level of accuracy. However, during high-density passenger flow, the traditional method does not calculate the passenger flow densities accurately due to the impact of light, blocked cameras and other factors, while the passenger flow densities calculated using the pedestrian density estimation method, based on the regression model, are closer to the actual value. Applying the LBP texture feature extraction method, the new

Table 3 Implementation results of the passenger flow density analysis solution

Sample areas for passenger flow density analysis	Actual situation	Traditional method	New method
	Density (pedestrians/m <sup>2</sup> )	Density (pedestrians/m <sup>2</sup> )	Density (pedestrians/m <sup>2</sup> )
Service area 1—platform	6	4	5.5
Service area 2—platform	3	3	3
Service area 3—platform	4.5	3	4
Walking area 1—transfer channel	1	1	1
Walking area 2—stairway	2.5	2.5	2.5
Walking area 3—transfer channel	0.5	0.5	0.5

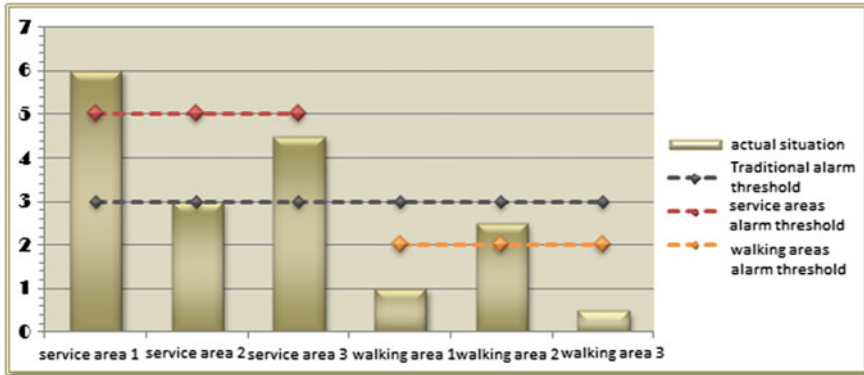


Fig. 8 Comparison of passenger flow alert thresholds and actual passenger flow density

solution shows a higher level of accuracy and performance in identifying dynamic patterns. Together with the PLSR model, it can calculate high-density passenger flow more accurately.

Based on actual passenger flow congestion, the traditional and new passenger flow alert systems issue alerts in different situations, based on the standard alert threshold and special alert thresholds for different areas. The details are shown in the Fig. 8.

The traditional passenger flow monitoring method does not differentiate between service areas and pedestrian areas, with the system releasing alerts for high passenger flow density when it exceeds 3 pedestrians/m<sup>2</sup>. However, pedestrians in service areas who are standing in queues do not need as much space as those who are walking. So even if passenger flow density exceeds 3 pedestrians/m<sup>2</sup>, service areas will not be overcrowded and the system does not need to release an alert. However, once passenger flow density exceeds 2 pedestrians/m<sup>2</sup>, the pedestrian areas will seem crowded and the system needs to release an alert.

The new passenger flow monitoring method clearly divides the metro station into service and pedestrian areas and sets different passenger flow alert thresholds for each area. The passenger flow alert threshold of the service areas is 5 pedestrians/m<sup>2</sup> and for pedestrian areas it is 2 pedestrians/m<sup>2</sup>. When the passenger flow density calculated by the video surveillance system exceeds the alert threshold, the system issues an alert.

With the traditional alert threshold, an alert is issued for service areas 1, 2 and 3. However, based on differential alert thresholds for service areas and pedestrian areas, alerts are issued for service area 1 and walking area 2 only. The new method, setting different alert thresholds for different areas is a better reflection of the situation on the ground and its passenger flow congestion alerts are more accurate.

## 4 Conclusion

The authors conducted a study of the Beijing metro system, and explored an IT-based solution for automatic passenger flow density supervisory. They concluded that the two main challenges to this solution are the accuracy of the technology for automatic passenger flow density monitoring, and uniform passenger flow alert thresholds.

Analysis of the methods used to measure passenger flow density found that traditional video analytics methods often fail to provide accurate measurements when metro stations are crowded, and that a refined video analytics method based on the regression model may be feasible to measure passenger flow density in diverse situations. Based on these findings, the authors have developed a measurement method that deploys LBP descriptors for texture feature description and the PLS method to achieve more accurate monitoring in high passenger flow scenarios. As the regression model-based method for measuring passenger flow density is still in trial and has not been widely applied in actual scenarios, the method calls for further study, communication with major video surveillance manufacturers, and a feasibility study before it can be applied for the purpose of passenger flow density monitoring at the Beijing Metro Network Video Surveillance Center, with a regression model customized to the characteristics of passenger flow in Beijing metro stations.

In addition, based on the results of research into crowd behavior analysis from China and beyond, and taking into consideration the user requirement of the metro system, the authors propose setting different passenger flow alert thresholds for different areas. In metro stations, different areas can be categorized as pedestrian areas or service areas, and two different thresholds should be set based on peoples' need for space in each area. Given that space requirements are different in service and pedestrian areas, it is more effective to monitor and analyze passenger flow density and set passenger flow thresholds as proposed.

In short, passenger flow density can be monitored efficiently and overcrowding alerts issued appropriately by developing a more accurate method of automatic passenger flow density monitoring and setting different passenger flow alert thresholds for pedestrian areas and service areas.

In order to achieve comprehensive tracking and effective management of passenger activity, the design of a metro network video surveillance center should include the categorization of the areas under video surveillance proposed in this paper, introduce more comprehensive tools for metro network video monitoring and take into full consideration the advanced smart technologies for surveillance video analysis. The design should also take advantage of the abundant existing passenger transport statistics and methods of analysis and assessment to establish an alert procedure that includes video analysis for appropriate overcrowding alerts, ensuring a safe journey for every passenger and the smooth operation and rapid development of the Beijing metro system.

## References

1. This is the CCTV video data of the BMNA TCC system, the picture is nine line QiLiZhuang station up direction August 2, 2015 video screenshot
2. Pei GJ (2011) Density estimation and activity analysis of crowds in surveillance videos (in Chinese)
3. He K, Liu Z, Qi LN, Yang H, Zhu T, Liu YW, Zhou JM (2014) The panoramic density estimation method in complex scenes (in Chinese)
4. Lin Q (2014) Pedestrian density and abnormal behavior analysis on video (in Chinese)
5. Yang XG, Teng JY (2010) Transit capacity and quality of service manual, 2nd edn. (in Chinese)
6. This is the spatial structure diagram of ChongWenMen station in TCC simulation system
7. This is the CCTV video data of the BMNA TCC system. The left one is line six HuJiaLou Station down direction video screenshot. The left two is the line five CiQiKou station down direction video screenshot. The left three is the line five CiQiKou station down direction video screenshot. The right one is line six HuJiaLou Station on the north side of JinTaiXiZhao station transfer channel video screenshot. The right two is line four CaiShiKou station on the west side of the stairs right transfer video screenshot. The right three is line five Ciqikou station on the south side of the transfer channel video screenshot. All the above video is August 2, 2015

# Adaptive Locomotive Headlamp System Based on Monocular Vision

Juan Gong

**Abstract** How to ensure the safety of a locomotive is a crucial problem, when it moves in a curved railway at night. For solving this problem, a new adaptive locomotive headlamp system based on monocular vision is proposed in this paper. The method consists of two key steps. First, a single-camera is provided to capture the tracks in front of the locomotive, and an image processing algorithm is proposed to obtain the key related parameters. Next, combined with the position feedback signal of the headlamps and the parameters obtained in the previous step, an adaptive control method is proposed to rotate the headlamps. By this way, the light emitted from the headlamps will always be on the axis of the railway, thus ensuring the safety of the locomotive.

**Keywords** Tracks detection · Machine vision · PID control · Adaptive headlamp system

## 1 Introduction

The traditional headlamps fixed in front of a locomotive cannot be rotated. The light emitted from these headlamps always parallels to the central axis of the locomotive, such that a sufficient view can be provided for drivers. However, when the locomotive moves in a curved railway, the light will deviate from the axis of the railway, or even completely be out of the railway. It forms a dangerous and extreme environment due to losing drivers 'sight.

In order to solve this problem, the importance of using flexible rotatory headlamps has been proposed by the technologists in Soviet in 1989 [1]. However, subjected to the technical conditions at that time, it was very difficult to propose an effective and adaptive control for rotatory headlamps. In 1996, Hengjun Zhu [2]

---

J. Gong (✉)

Department of Railway Traction and Motivation, Hunan Railway Professional Technology College, No. 98, Tiandong Road, Zhuzhou City, Hunan Province, China  
e-mail: Juan9615061@163.com



proposed a headlamp control method for the first time in domestic. This paper pointed out that combining with camera systems and image processing algorithms may monitor the curvature of the curved railway in real time. However, limited by the technical conditions, the paper just used the pre-known railway data and high-precision measuring sensors to detect the curvature of the railway. The accuracy of this open-loop control extremely depends on the accuracy of measurement. In 2005, GPS technology was first used to measure the curvature of the railway in the literature [3]. On the one hand, this method requires building a GIS map for all railway lines, which is time-consuming and laborious. On the other hand, when locomotives are running in mountainous areas and tunnels, the GPS signal may be often lost, such that the method becomes invalid. In 2009, the literature [4] used a dedicated sensor to record relative angular displacements between the locomotive and the bogie when the locomotive was running into a curved railway. Then the features were extracted from these angular displacements. However, it is often difficult to eliminate the measurement errors caused by the locomotive traction weight, running speed, railway line slope and railway smoothness, etc. Moreover, because the sensor starts to work until the locomotive has been in the curved railway, the control will be lagged. In the literatures [5, 6], the LKJ-2000 system was used to measure the curvature of the curved railway. The method inherited the main purpose of the literature [2]. The accuracy of the measurement is particularly important for this open-loop control. However, the LKJ-2000 system calculates the speed of a locomotive according to the pulse speed of the photoelectric sensor mounted on the wheel-to-axle shaft. Due to the problems such as idling, roller skating and so on, the LKJ-2000 system may introduce a lot of measurement errors. In addition, the method establishes the mathematical model based on the railway design specification. It is not a flexible and scientific method since the railway is varied.

The adaptive front-lighting system (AFS) technology has been developed rapidly in automotive in recent years [7, 8]. The system commonly used the machine vision technology to detect the lane line [9–13], pedestrian, and obstacles. The measurement results are used for the adaptive control of headlamps. In fact, tracks detection is very similar to lane line detection, so the AFS technology in automotive can be a good extension to the locomotive. This paper presents an adaptive locomotive headlamp system based on monocular vision. The method firstly uses the image processing technology to measure the parameters of the curved railway. Next, a closed-loop PID control is realized by combining with the position feedback signal provided by the headlamp sensor and the curvature of the railway. Monitoring the curvature of the railway without any pre-known railway data is one of advantages of this method. Moreover, since the specialized DSP chip provides strong abilities of parallel computing, the tracks detection is effective and in real-time. Based on these advantages, it ensures that the light emitted from locomotive headlamps can follow the changes of the railway, which provides a guarantee for locomotive running safety at night.

## 2 Adaptive Locomotive Headlamp System

As shown in Fig. 1, the adaptive locomotive headlamp system is composed of three parts. The image recognition module first captures the images of tracks in real time by using an industrial camera. Then it sends the images into the embedded image processing chip through LVDS. Finally it executes the tracks detection algorithm to extract the deflection angle. The PID controller in decision control module combines with the calculated deflection angle and the current position of headlamps to output PWM waves for driving stepping motor. The last module rotates the headlamps by using the stepping motor. It also provides position feedback signal of the headlamps obtained from the specialized sensor. It forms a closed-loop control of the headlamps.

### 2.1 Tracks Detection Algorithm Based on Monocular Vision

The image recognition module is responsible for detecting the parameters of the railway. The tracks identification algorithm is the key component. The algorithm is composed of three parts, including the feature extraction, the tracks tracing and the camera calibration.

#### 2.1.1 The Feature Extraction of Tracks

The feature extraction of tracks includes a series of image preprocessing algorithms as follows:

**Step1:** The non-linear gray-scale transformation method is used to achieve gray images of tracks. It will reduce the complexity and improve the overall contrast of images in comparison with the original images.

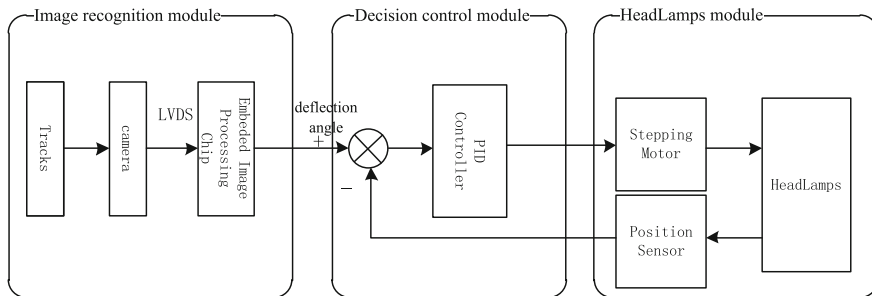


Fig. 1 Adaptive locomotive headlamp system

**Step2:** Setting an interest area (ROI) for images can exclude the invalid background and reduce the complexity of the algorithm. In this paper, a specified ROI is initialized at the first frame. Next, the left and right tracks in current frame are detected by algorithm, such that the ROI in next frame can be dynamically set by taking account into the small rectangles of these detected tracks.

**Step3:** The median filter method [12] is used to smooth the image. It can effectively reduce the noise caused by the railway environment, and enhance the edges of the tracks. The principle is to sort the pixel values in the selected kernel window and obtain the median value. Then all gray values in the window are substituted by this median value so as to achieve the effect of smoothing noise.

**Step4:** In order to extract and identify the tracks quickly and accurately, the edges of the image are required. The edges of the tracks can be reflected by the discontinuity of the gray value of the image. The Sobel operator [13] is an available method to obtain the edges of the tracks. The gradients of gray values are calculated by using a 3 \* 3 kernel window to avoid the unnecessary interpolation between adjacent pixels. The formula is as follows:

$$G_x = \begin{vmatrix} f(x+2, y) + f(x+2, y+1) + f(x+2, y+2) \\ -f(x, y) - f(x, y+1) - f(x, y+2) \end{vmatrix} \quad (1)$$

$$G_y = \begin{vmatrix} f(x, y) + f(x+1, y) + f(x+2, y) - f(x, y+2) \\ -f(x+1, y+2) - f(x+2, y+2) \end{vmatrix} \quad (2)$$

The gradient magnitude of edges in the image is:

$$\nabla F(i, j) = \sqrt{G_x^2 + G_y^2} \quad (3)$$

**Step5:** The maximum variance threshold segmentation method (Otsu) is used to segment the image. Hence an image is transformed into a binary image. At this time, the features of the tracks can be easily extracted. The method can split the original image into foreground and background by automatically determining the threshold. The threshold should maximize difference of the average gray values between the foreground, the background and the whole image. This difference is represented by the variance of the region. The algorithm has been illustrated in literature [12].

### 2.1.2 Tracks Tracing

Hough transform [11], least squares and spline interpolation are common ways to fit the tracks. Hough transform is a parameter estimation method based on voting principle. It is robust and often used for linear tracks monitoring. However, the

algorithm has high complexity and consumes large memory, such that it is not suitable for embedded systems. The least squares method is an approximating method of fitting curves. In some particular cases, it performs good effect. However, the fitting curves may no longer maintain the main features of tracks and lose the key information. The spline interpolation curves are fitted by using the key points in tracks. These curves are controlled by these specified points. Generally, the first and second derivatives are continuous in these points. The advantages of continuous and uniform curvature make it very suitable for fitting tracks. In order to improve the accuracy of the spline function, the B-spline [11] is used in this paper. The kernel function is as follows:

$$G_{i,3}(t) = \frac{1}{3!} \sum_{j=0}^{3-i} (-1)^j C_4^j (t+3-i-j)^3, t \in [0, 1], i = 0, 1, 2, 3 \quad (4)$$

Tracks tracing can use the database to match the detected tracks. It is especially useful when the tracks in current frame are not detected. The matching rules between the two tracks in different frames are according to their correlation. If the degree of correlation is less than a specified threshold, two tracks have been matched. The track  $\alpha_i$  is an element of the array  $H = \{\alpha_1, \alpha_2, \dots, \alpha_n\}$ . When a new detected track  $\alpha$  matches with the track  $\alpha_i$  in the array, the old track is substituted, i.e.  $\alpha_i = \alpha$ . At this time, the matching degree  $h(i)$  plus 1, and the matching degree of other tracks subtract 1, i.e.  $h(j) - 1, \forall j \neq i$ . When one of matching degrees is greater than the specified threshold, i.e.  $h(i) > T$ , the track  $\alpha_i$  is treated as a valid track. When the new detected track  $\alpha$  does not match any tracks in database, the track  $\alpha_i$  with  $h(i) = 0$  will be substituted.

### 2.1.3 Camera Calibration

In order to calculate the parameters of tracks in the world coordinates, it is necessary to transform the image coordinates to world coordinates. To complete the camera calibration, the camera model should be established and solved. The camera model can be found in the literature [13]. The conversion formula is as follows.

$$\begin{bmatrix} u \\ v \\ 1 \end{bmatrix} = \frac{1}{z_c} \begin{bmatrix} \frac{f}{k} & -\frac{f}{k} \cot \theta & u_0 & 0 \\ 0 & \frac{f}{l \sin \theta} & v_0 & 0 \\ 0 & 0 & 1 & 0 \end{bmatrix} \begin{bmatrix} R & T \\ 0^T & 1 \end{bmatrix} \begin{bmatrix} x^w \\ y^w \\ z^w \\ 1 \end{bmatrix} \quad (5)$$

where  $(u, v)$  represent the image point.  $f$  represents the focal length. The skewed angle between image coordinates and camera coordinates is denoted as  $\theta$ , which caused by the camera manufacturing error.  $k, l, u_0, v_0$  represent the converted coefficients between image physical coordinates and image pixel coordinates. The point in the world coordinates system is denoted as  $(x^w, y^w, z^w)$ .

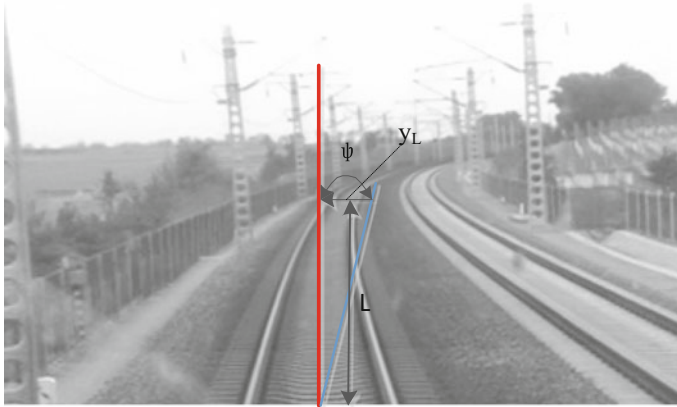


**Fig. 2** Schematic of tracks

The steps to solve the camera model are as follows.

**Step1:** Calculate the rotation matrix  $R$  and the translation matrix  $T$  based on the relationship between world coordinates and camera coordinates.

**Step2:** Solve the  $f, \theta$  based on the perspective transformation of the pinhole model.

**Step3:** Get the parameters  $k, l, u_0, v_0$  by converting image physical coordinates to image pixels coordinates.

Varieties of combinations of parameters can be used to control the headlamps. For the sake of simplicity, as shown in Fig. 2, the deviation distance between the specified aiming point and the track, i.e.  $y_L$ , the deviation angle of the track, i.e.  $\varphi$  and the curvature of the track are extracted. They can be used for locomotive headlamp control. Using the aiming point can reduce the influence of the position change of the locomotive. These changes are caused by the high speed movement of the locomotive during the execution period of headlamp control.

## 2.2 Adaptive Headlamp System Based on PID Control

The deviated angle of the track  $\varphi_1(k)$  is obtained by the camera module. The position of the headlamp  $\varphi_2(k)$  is fed back by the position sensor. The input position  $e(k)$  is calculated according to these two parameters. The incremental PID control algorithm is used to drive the stepping motor of the headlamp. The discrete PID control formula is as follows:

$$\Delta u(k) = K_C[e(k) - e(k-1)] + K_I e(k) + K_D[e(k) - 2e(k-1) + e(k-2)] \quad (6)$$

where  $K_C, K_I, K_D$  represent proportional, integral and differential coefficients respectively. The output signal of the incremental PID control is used to generate

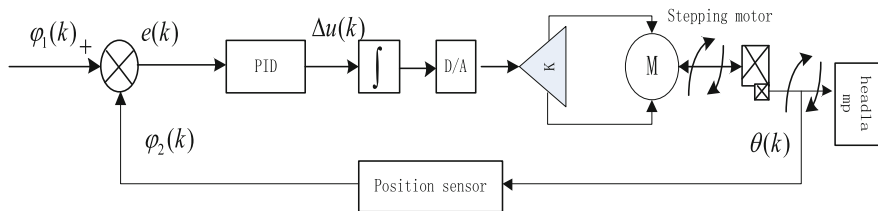


Fig. 3 Schematic of PID control

PWM wave. Depending on it, the stepping motor will rotate  $\theta(k)$ . The control process can be represented by function  $f(\cdot)$ , i.e.

$$\theta(k) = f(u(k)) \tag{7}$$

The feedback signal is generated by the position sensor. This is a typical Hall feedback process. The angle is first converted to a voltage and then converted to an angle  $\varphi_2(k)$  in the controller (Fig. 3). In a PID control, the motor control function can be unknown. The parameters of the PID control can be tested by the Ziegler-Nichols method. The principle is to increase the differential gain until the control system reaches the boundary of stability and produce continuous oscillation. The oscillation period and the gains are taken into the Ziegler-Nichols equation to obtain the PID control parameters [7]. With this PID closed-loop control, the controller can quickly drive the motor to respond to the deviations between locomotive and tracks.

### 3 Experiment

#### 3.1 Simulations of Tracking Detection

As shown in Fig. 4a, a ROI is added to the original image captured by the camera on the locomotive. It reduces the impact of environmental noise on the algorithm. The processed image using the tracks detection algorithm is shown in Fig. 4b. The edges of the tracks are obviously detected by using Sobel operator. In addition, the required control parameters can be easily obtained from these edges in Fig. 4b.

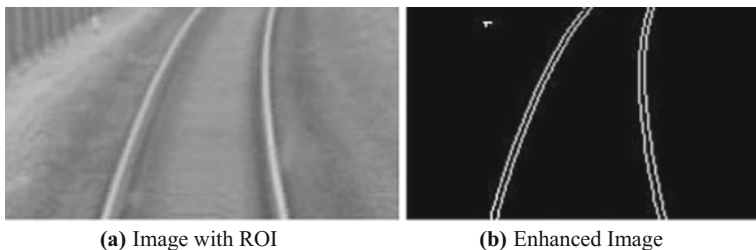


Fig. 4 a Image with ROI b Enhanced Image

### 3.2 Simulations of Adaptive Headlamp System

An adaptive headlight system cooperating with Xingyu Co. is shown in Fig. 5. Due to the huge cost of building a mold for experimental locomotive rotatory headlamps, the rotatory headlamps of the automotive by Xingyu is used to build the experiments. Their principle is exactly as same as the locomotive headlamps.

The image recognition module is shown in Fig. 6. The key parameters of used industrial camera are shown in Table 1. A Texas Instruments TDA2X series chip is used for image processing. The chip includes a heterogeneous and extensible architecture. This architecture includes a TMS320C66x digital signal processor (DSP) that supports fixed-point and floating-point operations, a dedicated visual acceleration hardware named Vision AccelerationPac and an ARM Cortex-A15 MPCore. In these parts, ARM processor is used for the common system control and

**Fig. 5** Rotatory headlamps of the automotive



**Fig. 6** Image recognition device



**Table 1** Parameters of the camera

No.	Item	Value
1	Sensor	CMOS
2	Resolution	1024*512
3	Color	Mono
4	Dynamic range	>150 db
5	Frame rate	30 fps
6	FOV (horizontal)	52°
7	FOV (vertical)	30°

the optimized DSP processor is used for processing object detection and other image processing. Vision AccelerationPac hardware is designed to reduce computing pressure of the DPS and ARM core. It can also reduce the consumption of the system energy. Using this chip can guarantee that the frame rate of video processing is more than 25 frames per second.

As shown in Fig. 5, A tracks video is played in front of the image processing module. The camera captures the video images and obtains the deflection angles. The experimental results show that the headlamps can rotate adaptively by following the curved tracks.

## 4 Conclusions

In order to address the safety problem of the locomotive running in a curved railway at night, an adaptive locomotive headlamp system based on monocular vision is proposed in this paper. The system first captures video frames of the tracks in real-time. Then gray-scale conversion, noise smoothing, edge enhancement and other image preprocessing technologies are used to extract effective features. Meanwhile, coordinate transformation and B-spline interpolation are used to extract the control parameters from these features. Finally, combined with these parameters and position feedback signal of headlamps, PWM wave is generated by a PID controller to drive the stepping motor of the headlamps. The method can ensure that the light emitted from locomotive headlamps focuses on the axis of the railway. It extremely extends the drivers 'view.

The tracks detection based on the monocular vision can also be used for adaptive locomotive fuel injection control. This technology can effectively improve the accuracy of fuel injection and reduce the cost. It could be the future research direction.

**Acknowledgements** 2017 Hunan Provincial Department of Education Scientific Research Project—Research on Intelligent Follower Track Control of Train Front Light Based on Monocular Vision, issue number: 17C1041.



## References

1. Баяабин ВН, Dongyun Z (1990) Locomotive should be equipped with rotary headlamps. *Foreign Diesel Locomotives* (8):13–17 (in Chinese)
2. Hengjun Z, Yanxin X (1996) Study on control method of rotating locomotive headlamp. *J Beijing Jiaotong Univ* (4):489–494 (in Chinese)
3. Hua Y (2005) Design and implementation of automatic tracking system for embedded locomotive headlight. *J Univ Electron Sci Technol China* (in Chinese)
4. Geng W (2009) Design and realization of automatic steering device for locomotive headlamp. *University of Electronic Science and Technology of China* (in Chinese)
5. Qingsuo S (2010) Research and implementation of intelligent locomotive headlamp control system. *Lanzhou University of Technology* (in Chinese)
6. Shihua D (2015) Design and implementation of locomotive headlamp control system based on LKJ2000. *J Comput Appl Softw* (6):220–223 (in Chinese)
7. Liang D, Bao xue C, Jian bin Z (2011) Calculation model of AFS headlamps rotation. *Mech Eng China* (7):864–869 (in Chinese)
8. Weifeng W, Qing W, Zhanyong L (2009) Modeling and simulation of adaptive headlamp control. *J Wuhan Univ Technol* (9):70–74 (in Chinese)
9. Weiwei Z, (2015) Vehicle detection and tracing for driving assistance system. *Hunan University* (in Chinese)
10. Tianhong Y (2006) Lane departure warning system based on machine vision. *Jilin University* (in Chinese)
11. Jingjing G (2007) Lane line detection and recognition based on monocular vision. *Harbin Institute of Technology* (in Chinese)
12. Maliang S (2013) Traffic warning based on monocular vision. *Kunming University of Science and Technology* (in Chinese)
13. Hongfeng M (2014) Distributed intelligent technology for monitoring obstacles in railways based on machine vision. *Lanzhou Jiaotong University* (in Chinese)

# Influence Analysis of the Grounding Grid of Communication Tower Base on Lightning Signal

Jin Yang and Zhiyu Li

**Abstract** Communication tower is often close to machine room. When the lightning strikes the communication tower, it raises electrical potential of grounding grid and transient ground potential raise could damage weak electrical equipment in machine room. In order to solve this problem, in this paper, a response calculation model under the condition of the lightning transient was established, which was based on the construction drawing of a communication tower and machine room grounding grid in Bao-Lan PDL (Passenger Dedicated Line). This model analyzed potential changes under the conditions of various factors when the lightning current injected grounding grid, including two grounding grid is equipotential connected or not, different distances and soil resistivity between two grounding grid, etc. Computational results show that transient ground potential of the machine room can reduce by 70% when the distance of two grounding grid increased from 5 to 20 m, and transient ground potential can be 10 times higher when two grounding grid is equipotential connected. Finally, the propose suggestions related to requirements engineering based on these analysis.

**Keywords** Communication tower · Lightning · Grounding grid  
Machine room

## 1 Introduction

Communication towers erected along the line are critical equipment of high speed railway wireless communication and the towers' height is usually about 30–50 m. Communication equipment and signal control equipment are placed in the machine room which is set up along the high speed railway. In the process of high-speed railway construction, if the investment is considered, the distance between machine

---

J. Yang (✉) · Z. Li

Beijing National Railway Research & Design Institute of Signal & Communication Co., Ltd., No. 1 Qi Che Bo Wu Guan Nanlu, Feng Tai District, Beijing, China  
e-mail: yangjin@crsdc.com.cn

© Springer Nature Singapore Pte Ltd. 2018

L. Jia et al. (eds.), *Proceedings of the 3rd International Conference on Electrical and Information Technologies for Rail Transportation (EITRT) 2017*, Lecture Notes in Electrical Engineering 482, [https://doi.org/10.1007/978-981-10-7986-3\\_73](https://doi.org/10.1007/978-981-10-7986-3_73)

727

room and communication tower grounding grids is often less than 15 m or even 5 m. When communication tower is struck by lightning, the current can make the two grounding grids potential rise rapidly. The track circuit controls the remote units which are installed along the rail-side by the cables which length are always 10 km. When machine room grounding grid potential rises, the cables remote grounding potential is lower and high potential difference caused by “ground counterattack” can damage communication and signal equipment in machine room as shown in Fig. 1.

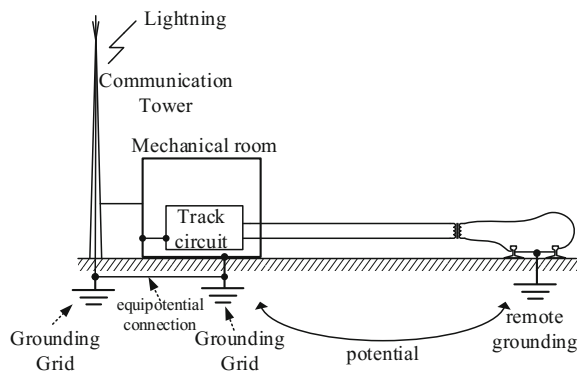
## 2 The Modeling Method and Mode of Two Grounding Grid Lightning Transient

In the construction drawing of communication tower and machine room, Baoji-Lanzhou passenger dedicated line, the construction and connection of grounding grids are shown in Fig. 2. Foundation reinforcement were welded into foundation grounding grid and finally became grounding grid of communication tower and machine room by using hot dip galvanized flat steel to weld crosswise, grid around is formed like rectangle shaped. Two grounding grid were connected at different position by two hot dip galvanized flat steel to implement electrical connection.

### 2.1 Modeling Method

The foundation structure of communication tower and machine room looks like rectangle shaped unit. To build the circuit model of this grounding grid, using self and mutual inductance to describe magnetic field effects around conductors, and using impedance to describe the loss of frequency changing and using inductance to describe electric field effects caused by conductor charge [1].

**Fig. 1** Ground counterattack in Machine room



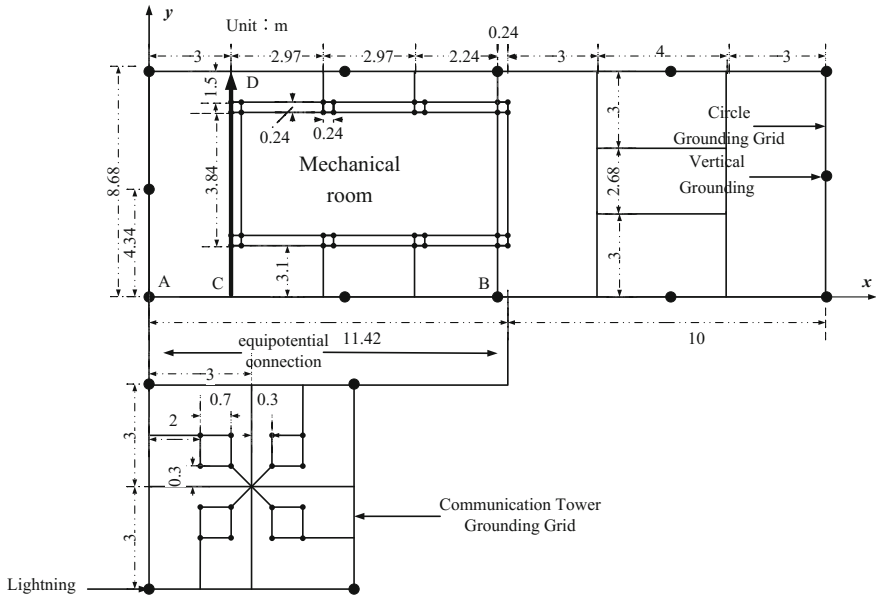


Fig. 2 The structure diagram of grounding grid

Assumptions are made as follows: the conductor cross-section of grounding grid is circular and non-circular cross-section can be equivalent to the same circumference circular cross section; the length of each conductor is much longer than the conductor's diameter and each section can be thought of a line which can ignore its diameter; when calculate the self and mutual of resistance to ground, leakage current is thought to be release equably from cylinder's central axis to soil; the leakage current of each section in conductor all leaks at the center of conductor [2, 3].

The equivalent circuit model of conductor's self-impedance and magnetic field effects around conductors display in Fig. 3 based on above assumptions. M1.M2... M8 represents module containing resistance and inductance effect of metal mesh. Self-impedance in conductors have frequency varying feature, it can't be described by simply connecting a resistance and inductance in series and its equivalent model display in Fig. 4. L11, L22 and L88 represent external self-inductance of each conductor. L12, L28 and L18 represent mutual inductance of each conductor. P1, P2 and P8 represent internal self-impedance of equivalent circuit. The parameters of this model acquired based on the calculation of electromagnetic field, so it's called the electromagnetic field model [4, 5].

Combining equivalent circuit model and electromagnetic field equivalent circuit model can acquire a synthesis circuit model. This model neglected the soil discharge and effects of ferromagnetic materials in soil.

**Fig. 3** Equivalent circuit model of rectangle shaped grounding grid

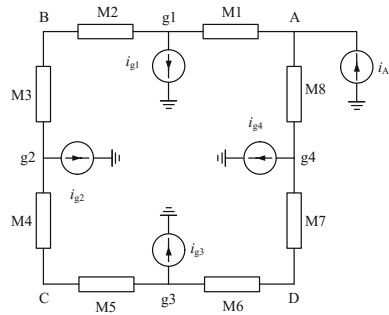
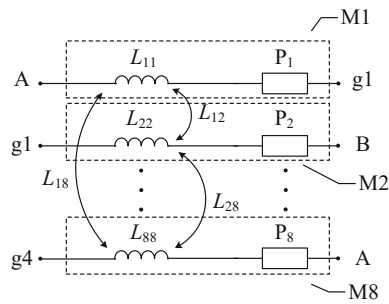


**Fig. 4** Equivalent circuit of metal network



## 2.2 Parameter Calculation

According to electromagnetic theory, we can calculate the grounding resistances and parts of capacitance parameters.

### 2.2.1 Inductance and Mutual Inductance

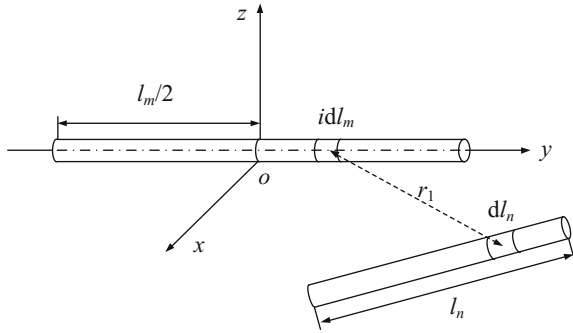
Considering the condition that the permeability of soil is approximately equal to that of air, the problem of calculating the mutual inductance of two conductors is: calculate mutual inductance between two conductors in the infinite homogeneous medium. Conductor m and conductor n display in Fig. 5.

Mutual inductance between two conductors [6]:

$$L_{mn} = \frac{\mu_0}{4\pi} \int_{l_n} \int_{l_m} \frac{1}{r_1} dI_m dI_n \tag{1}$$

Given that the conductor cross-section radius is a, analytical expression of external self-inductance is:

**Fig. 5** Schematic diagram of calculation of mutual inductance between two conductors



$$L_{mm} \approx \frac{\mu_0 l_m}{2\pi} \left( \ln \frac{2l_m}{a} \right) \tag{2}$$

**2.2.2 Self-Impedance in Conductor**

Radius of cylindrical conductor is  $a$ , conductivity is  $\sigma_c$ , permeability is  $\mu_c$ , when angular  $\omega = 2\pi f$ , its admittance form of internal self-impedance is:

$$y_{in} = \frac{2\pi a I_1(a\sqrt{j\omega\sigma_c\mu_c})}{j\omega\mu_c I_0(a\sqrt{j\omega\sigma_c\mu_c})} \tag{3}$$

Thereinto,  $I_0$  is the first class of 0-order modified Bessel function,  $I_1$  is the first class of 1-order modified Bessel function [7].

Apparently, formula (3) is hard to be described by one simple component, so using vector fitting method to fit  $y_{in}$ :

$$y_{in} = \sum_{n=1}^N \frac{C_n}{j\omega - a_n} + d \tag{4}$$

$N$  is called order. In this article,  $N = 3$ . Circuit form to formula (4) as shown in Fig. 8.

Thereinto,

$$\begin{cases} r_n = -\frac{a_n}{C_n}, & L_n = \frac{1}{C_n} \quad (n = 1, 2, 3) \\ r_4 = \frac{1}{d} \end{cases} \tag{5}$$

**2.3 Example of Verification**

This section compared the example of reference [8] to test the rationality and validity of the above modeling method.

### 2.3.1 Example 1

The length of grounding conductor is 15 m and its radius is 0.012 m. Soil parameters: electrical resistivity  $\rho = 70 \Omega\text{m}$ , relative dielectric constant  $\epsilon_r = 15$  and relative permeability  $\mu_r = 1$ . Injection current uses fitting  $0.8 \mu\text{s}/12 \mu\text{s}$  double exponential current  $I(t) = 36.5(e^{-60000t} - e^{-600000t})$ .

The endpoint potential of  $x = 0$ ,  $x = 3.5 \text{ m}$  and  $x = 7.0 \text{ m}$  in current injected conductor rod display in Fig. 6. At the endpoint of  $x = 3.5 \text{ m}$  and  $x = 7.0 \text{ m}$ , transmission line method is in good agreement with the method proposed in this paper. Results are different at the endpoint of  $x = 0$ , the peak of transmission line method is 599.17 V, peak time is 0.158  $\mu\text{s}$ . The peak relative deviation is 12.3%.

### 2.3.2 Example 2

The length of rectangle shaped grid is 10 m, cross-section radius of conductor is 7 mm, burial depth is 0.5 m. Soil parameters: electrical resistivity  $\rho = 1000 \Omega\text{m}$ , relative dielectric constant  $\epsilon_r = 9$  and relative permeability  $\mu_r = 1$ . Injection current from the corner  $I(t) = I_0(e^{-\alpha t} - e^{-\beta t})$ ,  $I_0 = 1\text{A}$ ,  $\alpha = 2.7 \times 10^4 \text{ s}^{-1}$ ,  $\beta = 2.7 \times 10^4 \text{ s}^{-1}$ .

The results of method proposed in the paper basically agree with reference [8] at the point potential of corner injection current as shown in Fig. 7. The two examples show the rationality and validity of modeling method in this paper.

## 2.4 Transient Model of Two Grounding Girds

In the construction drawing of communication tower and machine room, Baoji-Lanzhou passenger dedicated line, the grounding situation: foundation

**Fig. 6** Results of 15 m horizontal buried conductor

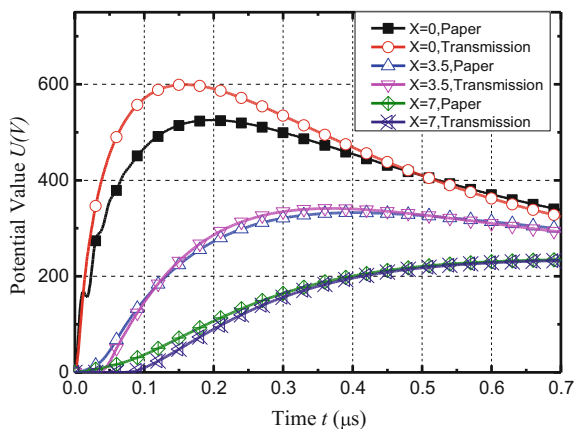
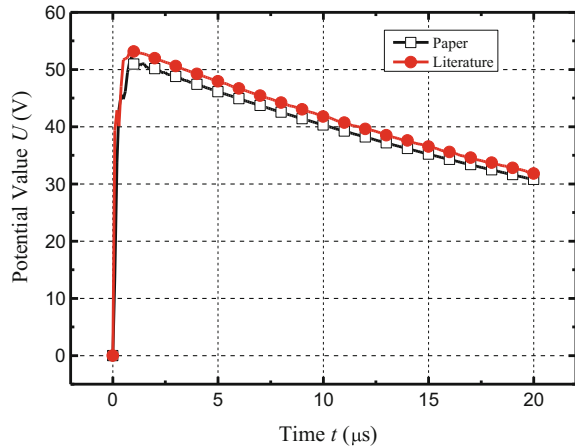


**Fig. 7** Results of rectangle shaped grounding grid



reinforcement of building structure is welded to the foundation of grounding grid, welded crosswise to grid by  $40 \times 4$  hot dip galvanized flat steel, the width of grid should be no greater than  $3 \text{ m} \times 3 \text{ m}$ , a closed loop is formed around the grid. The surrounding area is supported by artificial annular grounding device, which can be welded reliably to ensure the complete electric channel. Horizontal grounding body of grounding grid was made by  $40 \times 4 \text{ mm}$  hot dip galvanized flat steel, and set up vertical grounding body around grounding grid, vertical grounding body was made by  $50 \text{ mm} \times 50 \text{ mm} \times 5 \text{ mm}$ ,  $l = 2.5 \text{ m}$  hot dip galvanized angle steel, burial depth of horizontal grounding body is  $1.0 \text{ m}$ . The distance of two vertical grounding electrodes is  $5 \text{ m}$ .

According to the above actual situation of grounding grid, this paper established an equivalent circuit and used EMTP (Electro-Magnetic Transient Program) to build lightning simulation model: Three-dimensional coordinates of lightning transient simulation mode of communication tower and machine room as shown in Fig. 2.

### 3 Analysis on the Key Factors of the Interaction Between Communication Tower and Machine Room

#### 3.1 Model Parameter

Lightning current is double exponential wave, and its waveform is  $2.6/50 \mu\text{s}$  and amplitude is  $10 \text{ kA}$ . The point of lightning current is injected at the bottom left corner of the tower as shown in Fig. 2.

The radius of horizontal grounding conductor  $r = 0.014 \text{ m}$ , electric conductivity of grounding grid conductor  $\sigma_c = 7 \times 10^6 \text{ S/m}$ , relative permeability of grounding



grid conductor is 1, burial depth  $d = 1$  m, soil conductivity  $\sigma_1 = 1/100$  S/m, relative dielectric constant  $\epsilon_r = 10$  and relative permeability  $\mu_r = 1$ . The radius of vertical foundation reinforcement is 8 mm.

### 3.2 The Influence of with or Without Equipotential Connection Between Two Grounding Grids

When calculating the lightning current injects into grounding grid from the communication tower, there are two kinds of situations: with/without equipotential connection between the two grounding grids, lightning response of points A and B in machine room as shown in Fig. 2. The results of transient response are shown in Fig. 8a, b. When there are equipotential connection, transient potential of machine room grounding grid increases a lot.

Table 1 displayed that when there aren't equipotential connection, the maximal lightning response and relative value added of points A and B in machine room grounding grid. The Table 1 also shows that the transient potential of the machine room grounding grid increases 1–10 times when there are equipotential connections.

### 3.3 The Influence of the Distance Between Two Grounding Grids

When the distance between the two grounding grids of communication tower and machine room is 5, 10, 15 and 20 m, the lightning response of point A is shown in

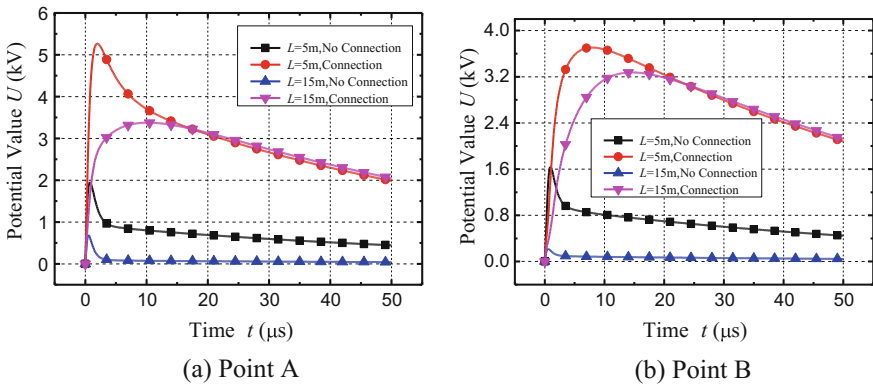


Fig. 8 The lightning response of point A and point B in machine room grounding grid when there are or aren't equipotential connection

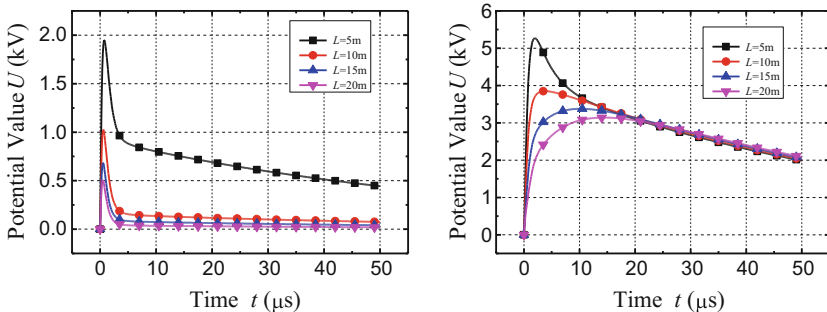
**Table 1** Maximal lightning response of point A and B in machine room grounding grid

Distance (m)		Maximal potential (V)		Increase proportion (%)
		With	Without	
5	Point A	5271.28	1950.36	170.27
	Point B	3706.10	1640.44	125.92
15	Point A	3376.24	685.08	392.82
	Point B	3274.61	220.19	1387.19

Fig. 9a, b. The results show that the potential of machine room grounding grid is inversely proportional to the distance between the two grounding grids.

### 3.4 The Influence of Soil Resistivity

Given the distance from communication tower to machine room grounding grid is 5 m, calculating the lightning response of point A when the soil resistivity is 10, 20, 40, 60, 80, 100 Ω m with or without equipotential connection. The results are shown in Fig. 10a, b and shown that lightning transient potential of machine room grounding grid is directly linear proportional to soil resistivity. When the soil resistivity increases, the lightning response of machine room grounding grid and potential rise will increase.



(a) Without equipotential connection (b) With equipotential connection

**Fig. 9** The lightning response of point A in machine room grounding grid

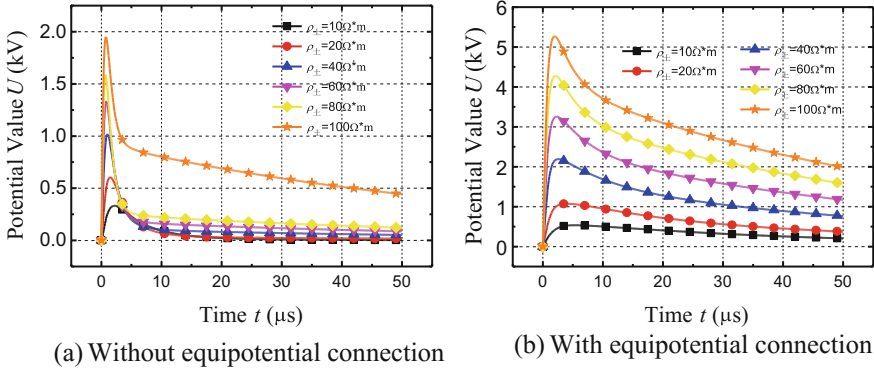


**Fig. 10** Lightning response of point A in machine room grounding grid under condition of different soil resistivity when there are or are not equipotential

## 4 Conclusion

### 4.1 Summing-up

- (1) No matter how long the distance between two grounding grids is, if there is equipotential connection, machine room grounding grid will increase, the maximal transient potential is 10 times higher than without it.
- (2) With the increase of distance between the two grounding grids, lightning response will decrease whatever there is equipotential connection. When the distance between the two grounding grids adds from 5 to 20 m, peak value of lightning response in machine room grounding grid can lower 70% at 20 m.
- (3) With the increase of soil resistivity, the lightning response of machine room grounding grid will increase. Especially when there is equipotential connection, it changes more dramatically.

### 4.2 Engineering Proposal

- (1) For the new lines, the distance between the two grounding grids should be not less than 15 m without equipotential connection.
- (2) For lines which have been built, if the distance between the two grounding grids is less than 15 m, we could cancel the equipotential connection and reduce the grounding resistance of the grids.

## References

1. Ruan W, Ma J, Liu J et al (2002) Performance of HVDC ground electrode in various soil structures. In: Proceedings of IEEE 2002 international conference on power system technology, vol 2. IEEE, New York, pp 962–968
2. Zhang L, Yuan J (2000) Numerical calculation of substation grounding grid with unequal potential model. In: Proceedings of the Chinese society for electrical engineering, vol 20, issue (1), pp 1–3 (in Chinese)
3. Du Z, Wang J, Liu X (2007) Analysis of the performance of the grounding UHVDC ring. High Voltage Eng 32(12):146–149 (in Chinese)
4. Ge W, Ruan B (1990) Recursion formula of the electric field of the ground point source in the vertical multi-layer dielectric. J Guilin Coll Metall Geol 10(2):173–181 (in Chinese)
5. Ge W (1994) Analysis of point source electric field in layered medium and its application. Chin J Geophys 37(II):534–541 (in Chinese)
6. Dawalibi FP, Ma J, Southey RD (1994) Behaviour of grounding systems in multilayer soils: a parametric analysis. IEEE Trans Power Deliv 9(1):334–342
7. Guo W, Wen X, Tan J (2013) Calculation method of grounding parameters of grounding grids using fast multipole method. Power Syst Technol 37(3):753–758 (in Chinese)
8. Liu Y, Zitnik M, Thottappillil R (2001) An improved transmission-line model of grounding system. IEEE Trans Electromagn Compat 43(3):348–355

# Simulation Model of Direct Power Supply System with Return Wire in Tunnel Section

Zhiming Liu, Jiangjian Xie, Zhixin Wang and Jin Yang

**Abstract** Traction power system simulation is needed, not only before system construction or reformation, but also the sensitivity analysis for the parameters of existing line. Due to the special landscapes for tunnel section, parameter calculation method of wires in traction power supply system should be different from the other kinds of section. Take Wushaoling super long tunnel section as example, the simulation model of direct power supply system with return wire was built based on the multiconductor transmission line (MTL) theory. The characteristic impedance was used to dispose the end effect of the return current network, the impedance parameters of traction network were calculated through Tylavsky formulas. At last, Field tests were performed to validate the correctness of the simulation model, this modeling method could be promoted to the simulation of other tunnel sections.

**Keywords** Electrified railway · Power supply system · Tunnel section  
Simulation model

## 1 Introduction

There are many advantages of electrified railway, such as high transport capacity, low pollution, and so on. 64.8% of railways have been electrified in china by 2016. Rail is used as the return conductor for traction current, rail potential may largely go beyond safety criterion when traction current increased, it is a big threat to the safety of the passengers and equipment along railway. So, the calculation or

---

Z. Liu (✉) · Z. Wang · J. Yang  
Beijing National Railway Research & Design Institute of Signal & Communication Co., Ltd., Auto Museum East Road, Feng Tai District, Beijing, China  
e-mail: liuzhiming@crscd.com.cn

J. Xie  
School of Technology, Beijing Forestry University, NO. 35 Qinghua East Road, Hai Dian District, Beijing, China

© Springer Nature Singapore Pte Ltd. 2018  
L. Jia et al. (eds.), *Proceedings of the 3rd International Conference on Electrical and Information Technologies for Rail Transportation (EITRT) 2017*, Lecture Notes in Electrical Engineering 482, [https://doi.org/10.1007/978-981-10-7986-3\\_74](https://doi.org/10.1007/978-981-10-7986-3_74)

simulation of rail potential is required, it's necessary to build suitable simulation model for traction power supply system.

There are many researches on the simulation model to study the rail potential of electrified railway, a distributed parameter model of direct feeding system was established in [1]. Wu [2] deduced the numerical formulas to analyze the relationships between rail potential and integrated grounding line (IGL) parameters. By using a simplified parallel circuit, the optimum transverse connection interval of return current network was decided to limit the rail potential [3]. Bodnar [4] used an auxiliary program package LINEP to calculate the transmission line parameters of the multi-conductor system, and the MULTC software package was used to study the rail potential change due to the different intervals between the bonds of overhead contact line and reinforcing wire. Mi [5] proposed a chain network model based on multi-conductor transmission lines to model a AT-fed traction power system, the impact of changing the traction network structures and parameters to rail potential has been studied.

Super long tunnel section of railway is very common in mountain area, due to the different structure from other kinds of section, the simulation model and the calculation of electrical parameters in tunnel should be researched especially. We proposed a simulation model of the traction system in tunnel, and related field tests had been carried out on Wushaoling super long tunnel section of Lanzhou-Wuwei second line, to validate the correctness of the simulation model.

## 2 Traction Power System of the Wushaoling Super Long Tunnel Line

Wushaoling super long tunnel locates in the second line of Lanzhou-Wuwei second line between Dacagou station and Longgou station, the length of which is 20.05 km (upstream line from K159+327 to K179+915, downstream from K159+294 to K179+521). Lanzhou-Wuwei second line is powered by AC  $1 \times 27.5$  kV direct power supply system with return wire (as shown in Fig. 1).

The required traction power is taken from the three-phase public grid. Traction current flows to the locomotive along the catenary, then comes back to the station through the return current system, which contains rail, return wire, and ground wire. Rail and return wire are connected to the ground wire by transverse connecting line through the neutral points of retardation coils. The average interval between the transverse connecting lines is about 1500 m. The distance between upstream and downstream lines is 20 m, both lines are powered by the same feeding section of ShenGou traction substation. These two lines are linked by transverse connection lines at two ends of the tunnel.

The arrangement of these wires is shown in Fig. 2, and Table 1 lists the materials and electrical parameters of wires. Rigid suspension composes of two parts: aluminum bus line and silver copper alloy wire.

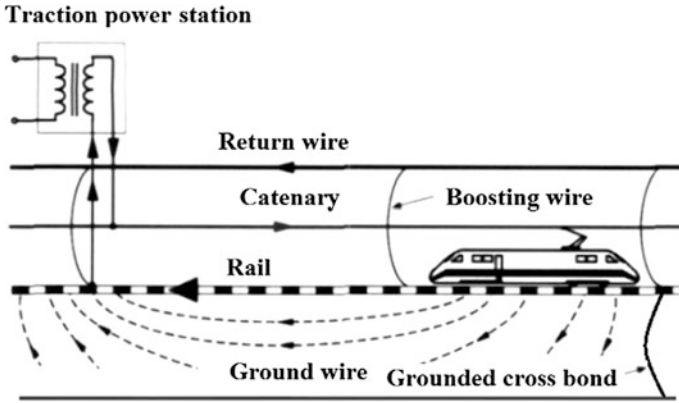


Fig. 1 Structure of direct power supply system with return wire

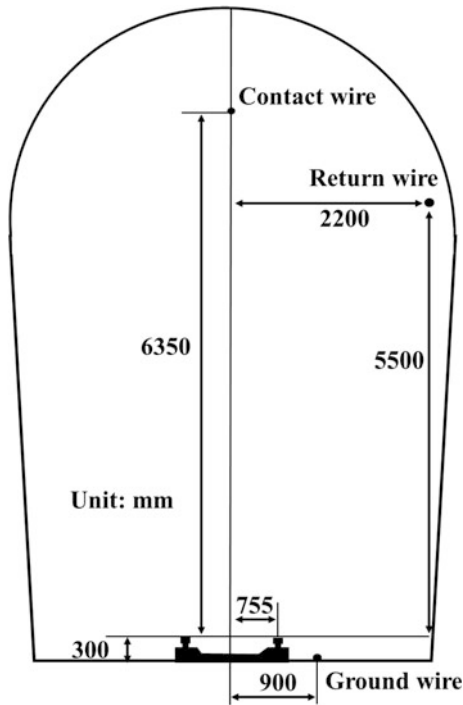


Fig. 2 The arrangement of the wires in tunnel

**Table 1** Materials and electrical parameters of wires

	Material	Resistance ( $\Omega/\text{km}$ )	Radius (mm)
Contact wire (CW)	CTHA120 silver copper alloy	0.147	6.45
Aluminum bus line	110 mm <sup>2</sup> aluminum	0.0117	57.26
Rail (R)	P60	0.135	12.8
Ground wire (GW)	35 mm <sup>2</sup> Copper stranded wire	0.478	3.34
Return wire (RW)	LBGLJ150 Aluminum clad steel	0.211	8.03

### 3 Impedance Parameter Calculation Method

#### 3.1 Ground Wire

Ground wire is a kind of bare conductor which is buried in cable groove or underground, calculation of the impedance parameter of ground wire was deduced by CCITT and UIC [6]. The self-impedance and self-admittance of buried bare conductor are derived by:

$$Z(\Gamma) = R_{\text{int}} + j \frac{\omega\mu_0}{2\pi} \ln \frac{1.851}{\sqrt{r_i^2 + 4x_i^2} \sqrt{j\omega\mu_0(\frac{1}{\rho} + j\omega\epsilon_0) + \Gamma^2}} \tag{1}$$

$$Y(\Gamma) = \left( \frac{\rho}{\pi} \ln \frac{1.123}{\Gamma \sqrt{2r_i|x_i|}} \right)^{-1} \tag{2}$$

$$\Gamma = \sqrt{ZY} \tag{3}$$

where  $\Gamma$  is propagation coefficient (1/m),  $R_{\text{int}}$  is the dc resistance of conductor  $i$ ,  $\omega$  is angular frequency (rad/s),  $\mu_0$  is permeability of vacuum (H/m),  $r_i$  is the equivalent radius of conductor  $i$  (m),  $x_i$  is the height of conductor  $i$  below ground (m),  $\rho$  is earth resistivity ( $\Omega\text{m}$ ),  $\epsilon_0$  is dielectric constant of vacuum (F/m).

Mutual-impedance between aerial wire and buried bare conductor is given by:

$$Z_{ik} = j \frac{\omega\mu_0}{2\pi} \left[ \ln \frac{1.851}{d_{ik} \sqrt{j\omega\mu_0(\frac{1}{\rho} + j\omega\epsilon_0) + \Gamma^2}} + \frac{2}{3} (x_i + x_k) \sqrt{j\omega\mu_0(\frac{1}{\rho} + j\omega\epsilon_0)} \right] \tag{4}$$

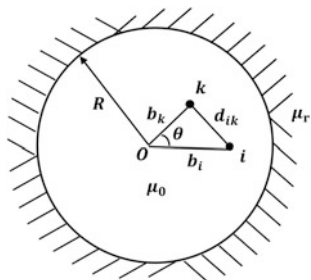
where  $d_{ik}$  is the distance between conductor  $i$  and conductor  $k$  (m).

#### 3.2 Conductor in Tunnel

The semi-infinite earth model is no longer suitable for long and large tunnel, which should be replaced with the peripheral infinite earth model (as shown in Fig. 3).



**Fig. 3** Conductors in a circular tunnel with peripheral infinite earth



Wu [7] studied that Tylavsky formulas were more suitable for conductors in long and large tunnel, by comparing the results of Tylavsky formulas and Carson formulas. Supposed that the tunnel is surrounded by homogeneous earth with same resistivity and same permeability, and extends to infinity. Ignoring the displacement current, only axial electric field was considered, Tylavsky deduced the formulas for calculating the impedance of conductor-earth circuits:

$$Z_s = R_{int} + \frac{j\omega\mu_0}{2\pi} \ln \frac{R}{r_i} + \frac{j^{1/2}m\rho}{2\pi R} \frac{K_0(j^{1/2}mR)}{K_1(j^{1/2}mR)} + \frac{j^{1/2}m\rho}{2\pi R} \sum_{n=1}^{\infty} \frac{1}{n} \left[ \frac{b_i(b_i + r_i)}{R^2} \right]^n \left[ \frac{\frac{j^{1/2}mR}{\mu_r} K'_n(j^{1/2}mR) + nK_n(j^{1/2}mR)}{\frac{\mu_r n}{j^{1/2}mR} K_n(j^{1/2}mR) - K'_n(j^{1/2}mR)} \right] \tag{5}$$

$$Z_m = \frac{j\omega\mu_0}{2\pi} \ln \frac{R}{d_{ik}} + \frac{j^{1/2}m\rho}{2\pi R} \frac{K_0(j^{1/2}mR)}{K_1(j^{1/2}mR)} + \frac{j^{1/2}m\rho}{2\pi R} \sum_{n=1}^{\infty} \frac{\cos(n\theta)}{n} \left[ \frac{b_i b_k}{R^2} \right]^n \left[ \frac{\frac{j^{1/2}mR}{\mu_r} K'_n(j^{1/2}mR) + nK_n(j^{1/2}mR)}{\frac{\mu_r n}{j^{1/2}mR} K_n(j^{1/2}mR) - K'_n(j^{1/2}mR)} \right] \tag{6}$$

where  $Z_s$  and  $Z_m$  is self-impedance and mutual-impedance of conductor respectively,  $R$  is the equivalent radius of tunnel cross section (m), for non-circular cross section, the equivalent circle can be formed under the rules that perimeters of these two cross sections are equal and two cross sections are tangent on top of the tunnel,  $m = \sqrt{\frac{\omega\mu}{\rho}}$ ,  $b_i$  and  $b_k$  is the distance from the center of the equivalent circle to conductor  $i$  and  $k$  respectively (m),  $d_{ik}$  the distance between conductor  $i$  and conductor  $k$  (m),  $\theta$  is the angle between conductor  $i$  and conductor  $k$  referring to the center of the equivalent circle,  $K_n(z)$  is the  $n$ th order of modified Bessel functions of the second kind. When  $\mu_r = 1$ , these formulas can be simplified:

$$Z_s = R_{int} + j \frac{\omega\mu_0}{2\pi} \ln \left( \frac{R+p}{r_i} \right) \quad (\Omega/m) \tag{7}$$

$$Z_m = j \frac{\omega \mu_0}{2\pi} \ln \left( \frac{R+p}{d_{ik}} \right) \quad (\Omega/\text{m}) \tag{8}$$

where  $p$  is complex depth,  $p = \sqrt{\frac{\rho}{j\omega\mu_0}}$  (m).

## 4 Simulation Model of the Wushaoling Super Long Tunnel Line

### 4.1 The Equivalent Circuit Model of System

The equivalent circuit model of direct power supply with return wire is shown in Fig. 4. Traction power system is simplified as 27.5 kV AC source. The aluminum bus line and silver copper alloy wire can be equivalent to one line (T). The contact of rail and ballast is poor insulation contact, there is leakage current between them, so the rail impedance consists of two parts. The first part is the inherent impedance of rail, the other part is the impedance between rail and earth [8]. The impedance of ground wire is the same as rail.

### 4.2 Line Model

Multiconductor transmission line (MTL) theory is adopted to model the lines of traction network. Mutual Inductance block in SimPowerSystem toolbox is used to simulate the lines, and the per-unit-length impedances of these lines are calculated

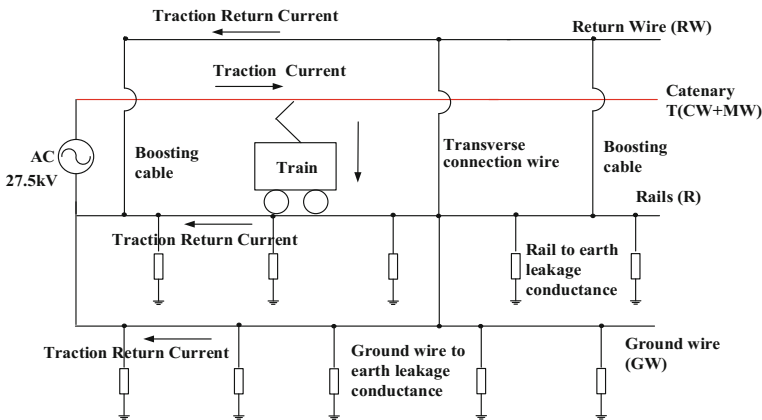


Fig. 4 Circuit mode of direct power supply system with return wire

by Tylavsky formulas. The rail to earth conductance and ground wire earth conductance were both modeled by series RLC branch block. There are five lines: return wire (RW), T, two rails (R1, R2) and ground wire (GW), for downstream and upstream lines, there are ten lines totally, the model of per-unit-length is shown in Fig. 5.

### 4.3 Disposal of End Effect of Return Current Network

Return current network goes along the whole railway, which may spread thousands of kilometers without interruption, can be considered as infinitely stretching transmission lines. When analyses the current distribution of traction power system, only the traction network of study range is researched, so the equivalent conductor with the same value of characteristic impedance should be shunted to the end of traction network to dispose the end effect [9]. The characteristic impedance matrix can be described by:

$$Z_c = Y^{-1} \sqrt{ZY} \tag{9}$$

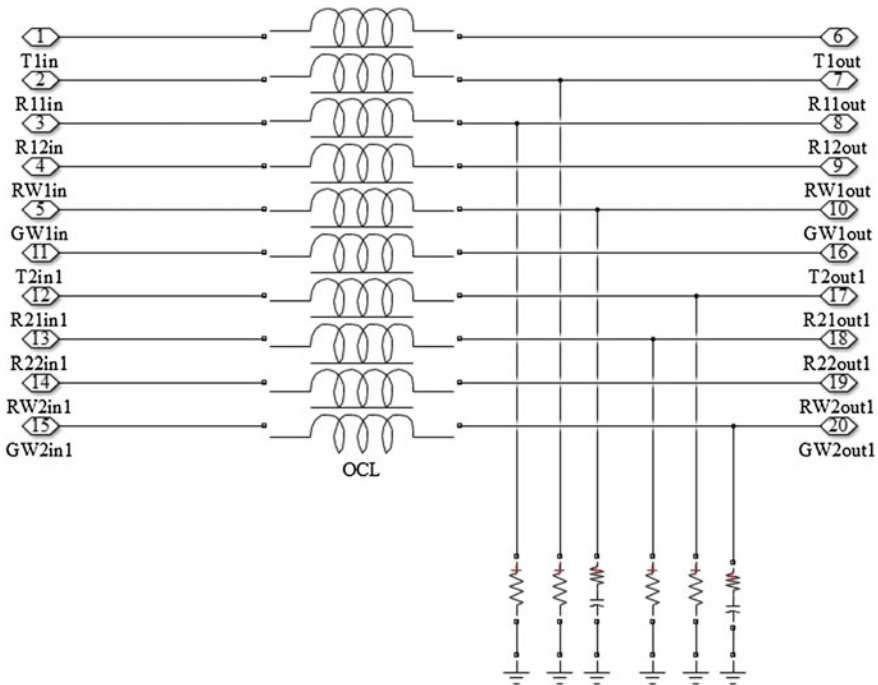


Fig. 5 Model of traction network

where  $Z, Y$  is the impedance matrix and conductance matrix of the return current network respectively.

### 4.4 Simulation Model

The traction power system model of Wushaoling super long tunnel section was shown in Fig. 6. And the locomotive was simplified as a current source with the given value. By the field tests, we set the value of other parameters, such as: Earth resistivity is  $900 \Omega\text{m}$ , ground wire-earth leakage resistance is  $30 \Omega\text{km}$ , rail-earth leakage resistance is  $250 \Omega\text{km}$ .

## 5 Field Test

### 5.1 Test Content

To validate the correctness of the model, the tests had been performed at March 22nd and 24th. There were three test point along the trackside, the points were shown in Fig. 7. The potential difference between rail with ground wire ( $U_{rg}$ ) and the current of ground wire ( $I_g$ ) were monitored in all test points, the current of boosting cable ( $I_{bc}$ ) was monitored only in test point 2. Track circuit fault analysis system ME2000P (Micsig) was used for data acquisition.

The railway traffic situation which contains the number and the currents of locomotive in test section during the test period, which were concluded by checking the running schedule, feeder current and rail-earth return current of the main transformer.

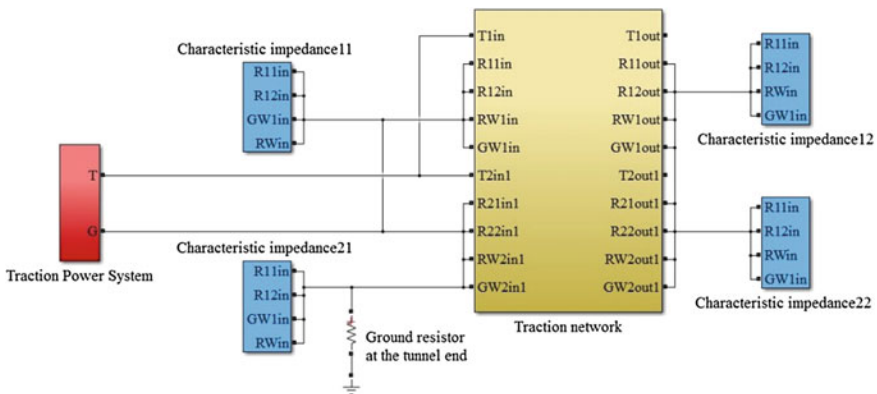


Fig. 6 System simulation model

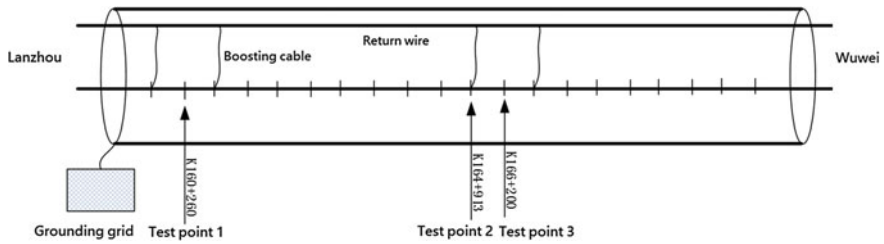


Fig. 7 Position of test point

### 5.2 Validate of Simulation Model

By checking running schedule and feeder current, the detail situations of locomotive passing through the tunnel section are listed in Table 2.

Then the corresponding situations were simulated in MATLAB/SIMULINK by using above model which was proposed in chapter 4. The results are shown in Tables 3 and 4.

From above tables, we can see that the  $I_g$  of simulation result are higher than of test result, the corresponding  $U_{rg}$  and  $I_{bc}$  is lower, which due to the reason that the distributed stray current was simulated by the current of many lumped leakage

Table 2 Detail situations of locomotive passing through the tunnel section

Time	Test point	Position of locomotive	Current of locomotive (A)
22nd 2:45	1 and 3	K178+395 (upstream)	563
24th 2:55	2	K178+165 (upstream) & K173+989 (downstream)	234 & 285

Table 3 The comparison between test results and simulation results at 22nd 2:45

Test point	Item	Test result	Simulation result	Relative error (%)
1	$U_{rg}$ (V)	27.8	27.2	-2.2
	$I_g$ (A)	2.8	3.0	7.1
3	$U_{rg}$ (V)	36.4	35.6	-2.2
	$I_g$ (A)	10.7	11.5	7.5

Table 4 The comparison between test results and simulation results at 24th 2:55

Test point	Item	Test result	Simulation result	Relative error (%)
2	$U_{rg}$ (V)	32.3	31.6	-2.2
	$I_g$ (A)	11.8	12.1	2.5
	$I_{bc}$ (A)	3.8	3.7	-2.6

resistances in the simulation model. But the differences between simulation results and test results are relatively small, the biggest relative error is only 8.0%, so the correctness of the simulation model is validated.

## 6 Conclusion

The modeling method of direct power supply system with return wire in tunnel section was studied based on the MTL theory, Tylavsky formulas were used to calculate the impedance parameters of the traction network. To validate the correctness of model, the field tests were performed. Compared with the test and simulation results, the differences between them are relatively small. Also, the modeling method can be used for other line to simulate the distribution of traction current, return current and rail-earth potential, which can provide theoretical basis for design and reformation of traction power supply system.

**Acknowledgements** This work was supported by “the Fundamental Research Funds for the Central Universities (NO. 2017JC14)”.

## References

1. Yang G, Liu MG, Li N (2010) Research on model of rail potential distribution and its simulation. *J Beijing Jiaotong Univ* 34(2):137–141 (in Chinese)
2. Wu G, Gao G, Dong A et al (2011) Study on the performance of integrated grounding line in high-speed railway. *IEEE Trans Power Delivery* 26(3):1803–1810
3. Huang W, He Z, He Z et al (2013) Study on distribution coefficient of traction return current in high-speed railway. *Energy Power Eng* 5(4):1253–1258
4. Bodnar I, Varju G (2013) Effect of the intervals between the bonds of overhead line and reinforcing feeder wire in the case of 25 kV traction feeding at 50 Hz. In: International youth conference on energy. *IEEE*, pp 1–6
5. Mi Z, Li Q, Ma Q et al (2013) Sensitivity analysis of rail potential for AT-fed traction power system. *Electr Eng* 14(9):24–28 (in Chinese)
6. Yang B (2009) Comprehensive simulation of AT traction power supply and integrated grounding system. MSc, Beijing Jiaotong University, Beijing, China (in Chinese)
7. Wu ML, Yu F, Xin CS (2006) Impedance of conductor-earth circuits in electric railway tunnel. *Proc CSEE* 26(5):176–181 (in Chinese)
8. Deng ML (2009) The study on the rail traction return current and rail potential rule of high-speed heavy railway. MSc, Southwest Jiaotong University, Chengdu, China (in Chinese)
9. Ma QA, Liu W, Xu YL et al (2013) Determination of characteristic impedance matrix of earth return circuit for autotransformer-fed traction power network. *Power Syst Technol* 37(6):1764–1768 (in Chinese)

# Application of Moving Average Filter to Train's Active Control System

Xu Wang, Jiaxin Ji and Peida Hu

**Abstract** Based on the integrator drift problem of acceleration in active control system, a method using the moving average filter on the original acceleration signal was adopted, which filtered out the DC component of curve passing to ensure the active control system work properly. The principle of the moving average filter was illustrated, and some influencing factors of real-time filter were analyzed. Compensating the static error caused by the ramp function to the low frequency component, a high-pass filter with 0.2 Hz cut-off frequency was designed. Using the active control model of vehicle system, the designed filter was simulation analyzed. In addition, the filter was used to process the acceleration information measured on the actual line. The simulation and experimental results indicated that the moving average filter can effectively filter out the centrifugal acceleration of curve passing, and inhibit integral drift, without significant influence on the performance of the active control system.

**Keywords** Moving average filter · Active control · Integrator drift  
High-speed train · DC component

---

X. Wang (✉)

R&D Center, CRRC Qingdao Sifang Co., LTD, No. 88 Jinhongdong Road,  
Chengyang District, Qingdao, China  
e-mail: wx861011@163.com

J. Ji

College of Mechanical and Electronic Engineering, China University of Petroleum,  
Qingdao 266580, People's Republic of China  
e-mail: jijiaxin0226@163.com

P. Hu

Department of Precision Instruments, Tsinghua University, Haidian District, Beijing, China  
e-mail: hpd07@mails.tsinghua.edu.cn

© Springer Nature Singapore Pte Ltd. 2018

L. Jia et al. (eds.), *Proceedings of the 3rd International Conference on Electrical and Information Technologies for Rail Transportation (EITRT) 2017*, Lecture Notes in Electrical Engineering 482, [https://doi.org/10.1007/978-981-10-7986-3\\_75](https://doi.org/10.1007/978-981-10-7986-3_75)

749

## 1 Introduction

Intelligent train is a direction of the development of high-speed train in the future. Intelligent mainly means self-testing, self-control, self-adaptive, etc. Active control suspension system can detect the vibration of the train in real time, and adjust the movement of the actuator according to the actual conditions of the line, to minimize the transmission of vibration of the vehicle suspension system and improve the ride comfort.

At present, the most commonly used active control strategy is the sky-hook control system [1], which needs to use the absolute lateral vibration velocity of the car body. However, in practical engineering applications, the absolute velocity is not easy to measure directly. Venhovens [2] proposed two methods to obtain this state. One is direct integration or filtering of the acceleration signal. Another is to establish the state-space equation, estimating the absolute velocity of the car body according to real time track state model and vehicle information. The first method has a major disadvantage: integrator draft, while the second method needs to establish the accurate state-space equation of the real vehicle system. In Kim's work [3], two acceleration sensors and four relative displacement sensors were used to modify the skyhook control. The estimates of the velocities were obtained by integrating and passing through a high pass filter of 0.2 Hz cut-off frequency.

It is well know that when the train passes through a curve, a low-frequency DC component will be introduced into the vibration acceleration signal due to the centrifugal force. If the acceleration is directly integrated, there must be a large integrator drift. Therefore, a reasonable real-time filter must be designed to preprocess the original acceleration signal. Kalman filter is the most commonly used real-time filtering method, but the parameter identification is complicated. Many researchers have done a lot of work [4–7], mainly to improve the accuracy of the filter. Venhovens [2] designed a second-order high-pass filter with a cut-off frequency of 0.1 Hz and analyzed its amplitude and phase frequency characteristics. The results show that the phase error at the natural frequency of 1.0 Hz is 11.4°. Margolis [8] pointed out that using the high-pass filter and integrator directly will reduce the performance of the active control system in the low-frequency region significantly.

In this paper, the moving average filtering method is applied to preprocess the original acceleration signal of the active control system. The principle of moving average filter (MAF) is introduced, and its advantages in real-time are analyzed. Combined with the characteristics of the vibration signal of the vehicle system, a high-pass filter with 0.2 Hz cut-off frequency is designed. The simulation analysis and the actual line test are carried out by using this filter, and the results verify its feasibility in the active control system.

## 2 Design of the Moving Average Filter

The general purpose of the moving average filter is to smooth and filter the dynamic test signal, so as to suppress the random error or eliminate the measurement noise. For test signals  $y(t)$ , it is often composed of deterministic components



$f(t)$  and random components  $e(t)$ , while the former is a valid signal. The moving average filtering method considers the nonstationary signal  $y(t)$  to be smooth in the appropriate interval, and averages the data in each cell as the latest test result of the endpoint, as shown in Eq. (1).

$$\bar{y}(t) = \frac{1}{T_w} \int_{t-T_w}^t y(\tau) d\tau \quad (1)$$

where  $T_w$  is the duration of each cell, whose choice has an important influence on the performance of filter. Assuming that the cut-off frequency of the filter is  $f_d$ , then  $T_w$  can be determined by Eq. (2) [9].

$$T_w = \frac{1}{f_d} \quad (2)$$

If the sampling frequency of the original data is  $f_0$ , then the number of data participated in the mean calculation in each cell can be expressed as

$$N = T_w \cdot f_0 \quad (3)$$

In actual calculation, we usually take  $N$  sample data as a sequence. The newly sampled data is placed at the end of the sequence, while removing a data from the sequence header. According to the principle of first-in first-out, the length of the queue is fixed to  $N$ , and the data output by the filter is always the arithmetic mean of these  $N$  data in the current queue. It can be seen that the moving average filter needs to collect  $N$  original data in time  $T_w$  before starting to calculate. This problem should be paid attention to in practical use. In order to avoid this problem, the filter should start working in advance. Once the filter has accumulated  $N$  raw data, it can output the results of the smooth filtering in real time.

In addition, Robles's research results [10] showed that: if the slope of the original signal  $y(t)$  is constant  $k$ , it is necessary to add a delay error compensation  $d = kT_w/2$  to the output signal  $y_0(t)$  on the basis of  $\bar{y}(t)$ . In this paper, based on the literature [9] and [10], the average value is solved by the moving average method, and the slope  $\hat{k}$  is estimated by the one-time curve fitting method. It can be obtained that

$$y_0(t) = \bar{y}(t) + \hat{k}T_w/2 \quad (4)$$

In the active control system, given the cut-off frequency of the sliding filter, the low-frequency component of the original signal can be estimated by the Eq. (4), which contains the DC component of the centrifugal acceleration. By subtracting the low frequency component from the original signal, the useful acceleration information needed in the control strategy can be obtained, as shown in Eq. (5).

$$\widehat{y(t)} = y(t) - y_0(t) \tag{5}$$

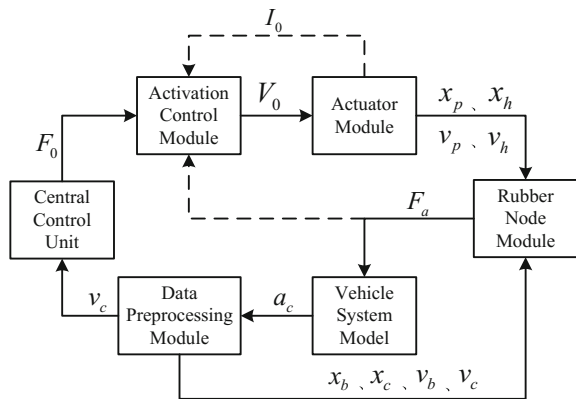
### 3 Simulation Analysis

The SIMPACK and MATLAB software were used to establish a co-simulation model, as shown in Fig. 1.

The vehicle dynamics model is established based on a trailer of high speed EMU, which consists of 1 car body, 2 bogies, 4 wheelsets, and 8 axle arms. The dynamics of the car body, bogie and wheelset are characterized by the lateral ( $Y$ ), bounce ( $Z$ ), longitudinal ( $X$ ), roll ( $\phi$ ), yaw ( $\psi$ ) and pitch ( $\beta$ ), while the axle arm just consider the pitch movement. The whole system has a total of  $50^\circ$  of freedom. In the process of modeling, the nonlinear wheel/rail contact relationship and the nonlinear suspension parameters are fully considered. The moving average filter is integrated in the data preprocessing module. The length of the curve track is 500 m, the radius of curve is 5000 m, the superelevation is 150 mm, and the train speed is 360 km/h. Here, the cut-off frequency of the high-pass filter is set to 0.2 Hz, which can filter out the low-frequency components caused by the centrifugal acceleration without distorting the sensitive frequency components that affect the running stability of the vehicle.

In order to analyze the influence of the filter on the active control system, the curves of the actual output force of the actuator before and after adopting the filter are shown in Fig. 2. The red dashed line represents the actual output force without filter, while the black solid line represents the case with filter. The green dashed line represents the curve radius of the track. It can be seen from the figure that between 0 and 5 s the vehicle is in a straight line and the output force is basically the same with each other in these two cases. Between 5 and 10 s, the vehicle is in a curve and the lateral velocity of the car body caused by centrifugal acceleration severely drift, causing the actuator force calculated by the lateral vibration velocity of the car body to drift along with it. However, due to the self-protection function of the actuator itself, the actual force can only reach the maximum output force of the actuator.

**Fig. 1** Diagram of the co-simulation model



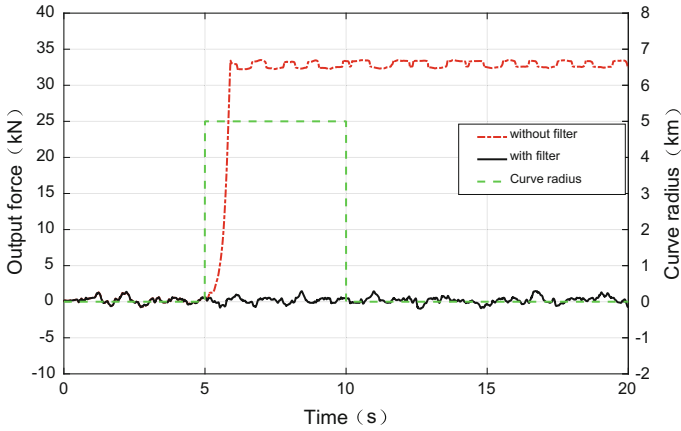


**Fig. 2** Time history of the actuator output force and radius of the track

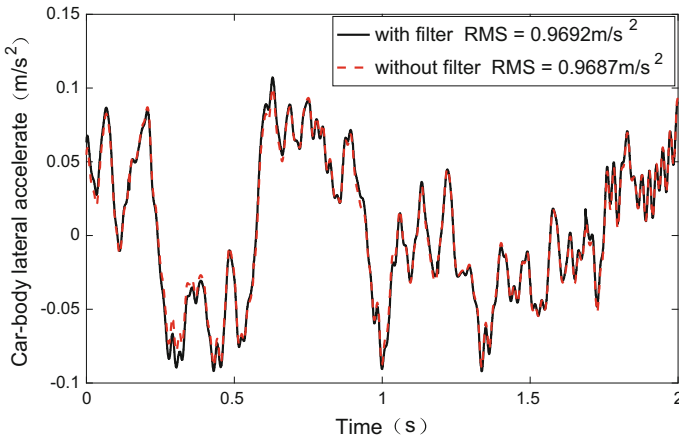


**Fig. 3** Time history of the lateral car body acceleration

After 10 s, even if the vehicle enters the straight line, the control system will still use the drifting velocity to calculate the force, which is extremely unfavorable for the running safety of the vehicle. After the high pass filter is adopted, the centrifugal acceleration of the curve segment is filtered out, and the output force of the actuator is fluctuating near the zero-mean.

In order to more comprehensively evaluate the influence of the designed filter on the active control system, the RMS value of the lateral acceleration of the car body and the bogie on a part of straight line is calculated, as shown in Figs. 3 and 4. Similarly, the red dashed line represents the case without filter, while the black solid line represents the case with filter.

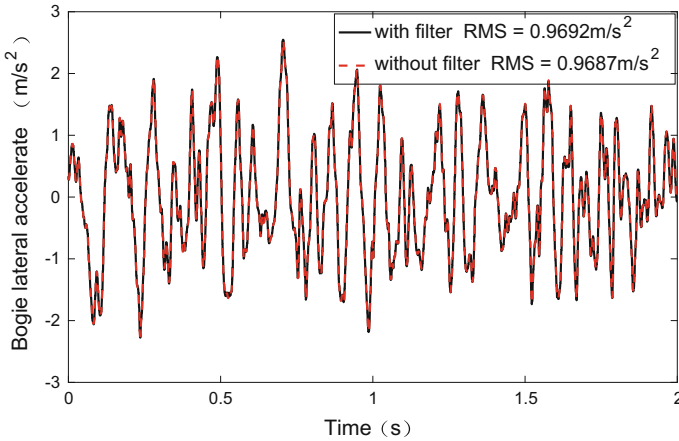


**Fig. 4** Time history of the lateral bogie frame acceleration

It can be found that before and after adopting the moving average filter, the lateral vibration acceleration of the car body only has some differences at the peak value, and the lateral vibration acceleration curve of the bogie is almost coincident. Without the filter, the RMS of the lateral acceleration of the car body and the bogie are  $0.0479 \text{ m/s}^2$  and  $0.09687 \text{ m/s}^2$ , respectively. After adopting the filter, the RMS of the lateral acceleration of the car body and the bogie are  $0.0498 \text{ m/s}^2$  and  $0.09692 \text{ m/s}^2$ , respectively. The usage of the filter has little effect on the performance of the active control system, whether it is the car body or the bogie.

## 4 Actual Line Test

The designed moving average filter is used to process the actual measured lateral acceleration of the vehicle. The sampling frequency of the original data is 500 Hz. Since the cut-off frequency of the high-pass filter is 0.2 Hz, so  $T_w = 5 \text{ s}$ , and each sequence is calculated using 2500 data. The filtering result of a typical curve line is intercepted, as shown in Fig. 5. In the figure, at the beginning of the 5 s, the filter needs to accumulate data. During this time period, the moving average filter uses the original signal instead of the low frequency component. After 5 s, the filter begins to use the collected 2500 data to estimate the low frequency components and gradually slip. It can be clearly seen that the curve centrifugal acceleration of the car body between 27 s and 52 s is well recognized.

Subsequently, the desired signal  $\widehat{y}(t)$  can be obtained by removing the low frequency component from the original signal. In order to more intuitively evaluate the filtering effect of the filter on the DC component, the frequency domain analysis of the signal before and after filtering are carried out, as shown in Fig. 6. The frequency of the curve centrifugal acceleration  $f_L$  depends on the running speed of

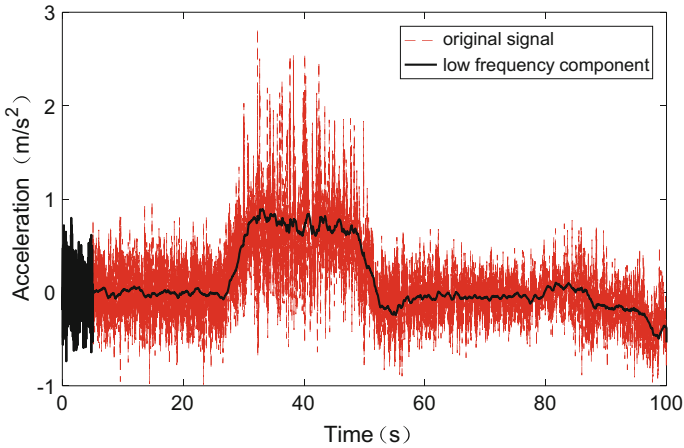


**Fig. 5** Time history of the original acceleration of car body and its low frequency component

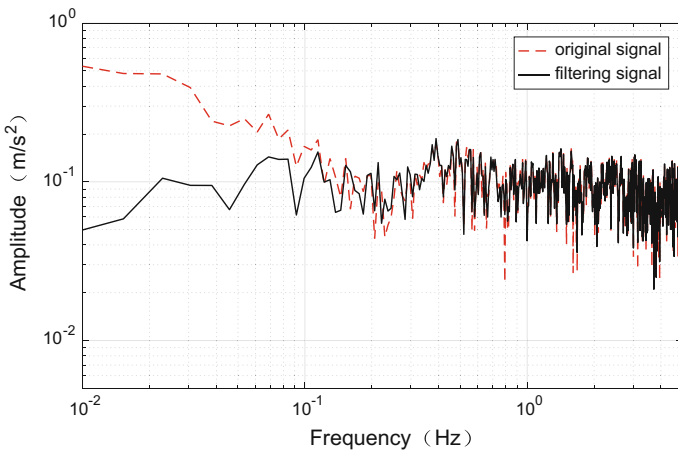


**Fig. 6** Power spectrum densities of the car body accelerations before and after filtering

the vehicle and the radius of the curve. In general, the frequency  $f_L$  is less than 0.03 Hz. As can be seen from the figure, the low frequency component of the original acceleration signal is mainly concentrated below 0.1 Hz, especially below 0.03 Hz. The moving average filter designed in this paper is capable of attenuating the amplitude of the frequency component below 0.03 Hz to a very low level, about 10 dB at 0.01 Hz, and 6 dB at 0.03 Hz. And for the frequency component above the cut-off frequency 0.2 Hz, the filter has little effect on its amplitude.

As mentioned above, the sky-hook control system needs to use the absolute lateral vibration velocity of the car body to calculate the actuator force. In this paper, the vibration acceleration before and after filtering are integrated to obtain

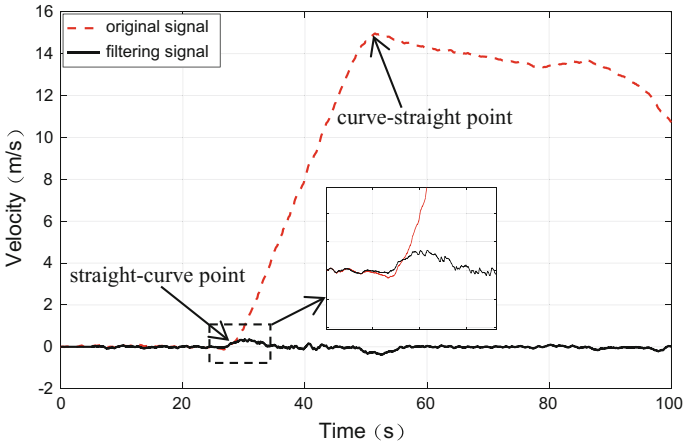


**Fig. 7** Time history of the car body vibration velocity before and after filtering

the vibration velocity, as shown in Fig. 7. It can be seen from the figure that the velocity signal obtained by integrating the original acceleration signal directly begins to drift at the position where the straight line is just entering the curve. When the vehicle just enters the straight line from the curve, the vibration velocity reaches the maximum value. Subsequently, the vehicle enters a reverse curve line, and the vibration velocity starts to decrease. As already mentioned in the previous analysis, this will make the active control system unable to work. After the designed high-pass filter is adopted, the integral lateral vibration acceleration of the car body fluctuates near the zero-mean. Obviously, the integral drift of the DC component of the acceleration is suppressed which ensures the normal operation of the active control system. It can be seen clearly from the details of the figure that the vibration velocity of the car body is very significant difference before and after adopting the filter at the position where the straight line is just entering the curve.

## 5 Conclusion

In this paper, a real-time high-pass filter was designed by moving average method and applied to the active control system of high-speed train. The theoretical analysis showed the real-time advantage of the moving average filter in the active control system. The simulation and actual line test results showed that: the moving average filter has a certain delay at the beginning of the calculation, but once the sufficient data has been accumulated, the filter is able to filter the raw data in real time. The real-time performance of the filter ensured that the lateral acceleration of the car body and the bogie in the active control system were not affected by phase lag. The designed high pass filter with the cut-off frequency 0.2 Hz can filter out the DC

component and restrain the integral drift of the vibration velocity commendably. In addition, adjusting the cut-off frequency of the moving average filter and combining low-pass and high-pass filters, the signal components in any frequency band can be obtained, which is very meaningful in the active control system.

**Acknowledgements** This work is partially supported by the National Key Technology Research and Development Program of the Ministry of Science and Technology of China (No. 2015BAG12B01).

## References

1. Karnopp D, Crosby MJ, Harwood RA (1974) Vibration control using semi-active force generators. *J Eng Ind* 96(2):619–626
2. Venhovens PJT (1994) The development and implementation of adaptive semi-active suspension control. *Veh Syst Dyn* 23(1):211–235
3. Kim RK, Hong KS (2007) Skyhook control using a full-vehicle model and four Relative Displacement Sensors. In: International conference on control, automation and systems. IEEE pp 268–272
4. Cui P, Zhang H, Lam J et al (2013) Real-time Kalman filtering based on distributed measurements. *Int J Robust Nonlinear Control* 23(14):1597–1608
5. Schenkendorf R, Mangold M (2013) Online model selection approach based on Unscented Kalman Filtering. *J Process Control* 23(1):44–57
6. Hoshiya M, Saito E (1984) Structural identification by extended Kalman Filter. *J Eng Mech* 110(12):1757–1770
7. Ding F (2014) Combined state and least squares parameter estimation algorithms for dynamic systems. *Appl Math Model* 38(1):403–412
8. Donald LMARGOLLS (1982) The response of active and semi-active suspensions to realistic feedback signals. *Veh Syst Dyn* 11(11):267–282
9. Gabriel F, Belie FD, Neyt X et al (2013) High-frequency issues using rotating voltage injections intended for position self-sensing. *IEEE Trans Industr Electron* 60(12):5447–5457
10. Robles E, Pou J, Ceballos S et al (2011) Frequency-adaptive stationary-reference-frame grid voltage sequence detector for distributed generation systems. *IEEE Trans Ind Electron* 58(9):4275–4287

# The Simulation of the Longitudinal Force of Heavy Haul Trains

Shize Huang, Qiyi Guo, Liangliang Yu, Yue Liu and Fan Zhang

**Abstract** To improve the transportation capacity of the train, 10,000 tons level train is getting wide application and further research is required. Considering the significance of the longitudinal force and the synchronous control performance to the safe operation of the train, a simulation model on the longitudinal force of the heavy haul train is set up in this paper and theoretical calculations on longitudinal traction force, braking force, running resistance and coupler buffer force are conducted and then the whole process of the train starting to the train braking is simulated. Finally, the simulation test about the emergency brake of the heavy haul train is made to prove the feasibility of the simulation model.

**Keywords** Heavy haul train · Longitudinal dynamics · Synchronous control Simulation model

## 1 Introduction

In recent years, the world economy and relative logistics are getting a sharp boom. Train is the main form of current transport. It has many advantages in aspects like capacity, energy consumption and commercial benefits. It is train's capacity that determines whether the high haul railway dominates other modes of transport in today's society. Thereby, more breakthrough is expected [1, 2].

In today's China, prosperity in the economic urges a high level transport system. Relevant departments give high priority to the heavy haul railway. There is no doubt that there are still a lot of problems to be solved. Today, pioneers have got

---

S. Huang (✉) · F. Zhang

Key Laboratory of Road and Traffic Engineering of Ministry of Education,  
Tongji University, 4800 Caoan Road, Shanghai, People's Republic of China  
e-mail: hsz@tongji.edu.cn

Q. Guo · L. Yu · Y. Liu

College of Electronics and Information Engineering, Tongji University,  
4800 Caoan Road, Shanghai, People's Republic of China

© Springer Nature Singapore Pte Ltd. 2018

L. Jia et al. (eds.), *Proceedings of the 3rd International Conference on Electrical and Information Technologies for Rail Transportation (EITRT) 2017*, Lecture Notes in Electrical Engineering 482, [https://doi.org/10.1007/978-981-10-7986-3\\_76](https://doi.org/10.1007/978-981-10-7986-3_76)

759



some remarkable achievements in the research of the high haul trains. Ding et al. [3]. established an integrated model of train longitudinal dynamics which was validated by using measured longitudinal force time histories and a serial of tests were performed to discuss the change and delivery law of the longitudinal forces when the 5000 t-marshalling train was running under the cases of braking and starting. To solve the problem of modeling difficulty and the long calculation time of the heavy haul train, a new method named Circular-Variable Modeling and Calculation Method was introduced by Jiang et al. [4]. Ma et al. [5] developed a train dynamic model to study the dynamic performance of heavy haul locomotives, taking into account the use of different buffer systems under conditions of severe longitudinal forces. Geng et al. [6] put forward an idea that we can solve the nonlinearity equation by Newmark integral method, which simplifies the process a lot. So it gives possibility to get further data of the longitudinal force. Wang et al. [7] combined with LOCOTROL Locomotive Wireless Control Technology Application in Daqin line, pointed out that the overloading of Locotrol system 2 million tons of combination trains in normal circumstances can effectively improve the train longitudinal force and longitudinal trend. The data points out that master-slave control effect of communication delay between cars on the train longitudinal force. Ma et al. [8] studied on busy trunk feasibility of 5000 t heavy haul train to test the emergency braking distance and time. After comparing the longitudinal force of different state of emergency braking, they draw the conclusion that 5000 t heavy haul train is feasible and can improve the railway transport capacity.

From the current domestic and foreign research, the existing research mostly stays on the macro research of the heavy haul train; it has not carried out the thorough research on the heavy haul train's longitudinal traction. And the modeling and Simulation of the longitudinal force is very important for the safety of heavy haul trains.

A simulation model on the longitudinal force of the heavy haul train is set up in this paper and theoretical calculations on longitudinal traction force, braking force, running resistance and coupler buffer force are conducted and then the whole process of the train from starting to braking is simulated. Finally, the simulation test about the emergency brake of the heavy haul train is made to prove the feasibility of the simulation model.

## **2 Longitudinal Force Analysis and Simulation Model of Heavy Haul Train**

The heavy haul train has three important mechanical processes including starting up, braking and releasing. In the above process, the train is working in the cycle of stretching vibration all the time, which includes a complicated force. The main part of this force analysis is the research of the longitudinal force, which is caused by the

stretching and compression between joint couplers during the process between starting and braking. Traction force, running resistance, braking force and coupler buffer force comprise the longitudinal force. And theoretical calculation gives the basic reference to the establishment of simulation model. Thereby, we can get the formula of the force analysis in the above model to complete the simulation model of the longitudinal force.

### 2.1 The Simulation Model of the Longitudinal Force in the Heavy Haul Train

The calculation model of the longitudinal force in the heavy haul train can be seen in Fig. 1.

In this paper, the longitudinal force of the adjacent vehicles is shown by formula (1).

$$M_i \ddot{x}_i = F_1 + f_i - f_{i+1} - B_i - F_2 \tag{1}$$

$F_1$  is the traction force of the locomotive and  $F_2$  is the running resistance of the locomotive and  $B_i$  is the braking force and  $f$  is the buffering force of the coupler.

The longitudinal force equations of the whole train are shown in formula (2).

$$\begin{cases} M_1 \ddot{x}_1 = F_1 + f_1 - f_2 - B_1 - F_2 \\ \vdots \\ M_i \ddot{x}_i = F_1 + f_i - f_{i+1} - B_i - F_2 \end{cases} \tag{2}$$

$F_1, F_2, B_i$  and  $f$  are defined just as above.

The system has  $n$  equations in all. The acceleration of each carriage can be determined by solving it. Then the motion parameters in the longitudinal motion

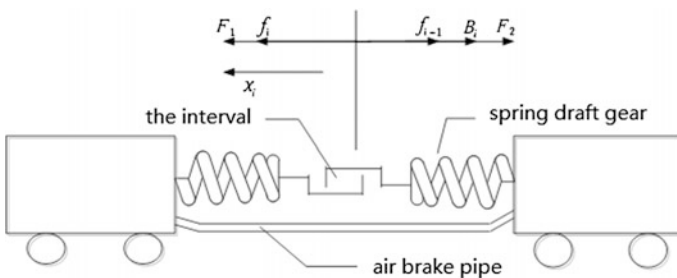


Fig. 1 The model of the longitudinal movement of the heavy haul train

process of each carriage and its specific movement process and trend can be got from the relationship between acceleration and velocity.

When solving the Eqs. 1 and 2, we need to solve each section of the carriage by each component, these components are given below the theoretical calculation method.

## 2.2 The Calculation of the Longitudinal Force

### 2.2.1 The Calculation of the Traction Force

The external force, which is caused by the power transmission device, is the same as the direction of the train running direction and it is called the traction force. In general, the adhesion force is studied, and the adhesion traction force is limited by the adhesion between the wheel and rail. The calculating formula is as shown in formula (3).

$$F_{\mu} = 1000 \times p_f \cdot \mu_j = 1000 \times (p_{\mu} \cdot g) \cdot \mu_j \quad (3)$$

$P_f$  is the adhesive gravity of the locomotive (KN) and  $P_{\mu}$  is the quality of locomotive adhesion (t) and  $g$  is Gravity ( $m/s^2$ ) and  $\mu_j$  is the calculation adhesive index.

Calculation adhesion index is affected by climatic environment, running speed, engine structure, the quality of a line, and the rail surface shape and other factors. Theory analysis method is hardly used to calculate and determine calculation adhesion index. Calculation adhesion index is on the basis of a large number of experiments, combined with the use of experience. The calculation adhesion index formula of electric locomotive is as follows.

$$\mu_j = 0.24 + \frac{12}{100 + 8V} \quad (4)$$

$V$  is running speed (km/h).

### 2.2.2 The Calculation of the Running Resistance

Running resistance is the external force which blocks the running of the train. Typically, it's divided to basic resistance and additional resistance. 90% above of the resistance force is proportional to the mass of the train.

Basic resistance is an inherent resistance coming from mechanical friction, air friction and etc. A lot of test finally get a quadratic function:  $av^2 + bv + c$ , and a, b, c are in correlation with the model of the train.

Additional resistance is caused by the line, slope changes, tunnel and other factors and it can always be divided into the ramp of the additional resistance, the curve additional resistance and the tunnel additional resistance.

### 2.2.3 The Calculation of the Brake Force

Currently, most of Chinese trains adopt traditional braking show which is powered by compressed air. It produces the braking force comes from the mechanical friction between the wheel and the braking shoe to apply the brake. Moreover, it transfers train's kinetic energy into heat which dissipated into air finally.

The calculation formula of brake force is shown by formula (5).

$$F_{B_i} = K_i \varphi_{k_i} \quad (5)$$

$K_i$  is the brake shoe's pressure on the NO.i train and  $\varphi_{k_i}$  is the friction index between wheel and brake shoe on the NO.1 train.

The calculation formula of each carriage brake pressure is shown as formula (6).

$$K_i = \frac{\pi \cdot d_Z^2 \cdot p_{Z_i} \cdot \eta_Z \cdot \gamma_Z \cdot n_Z}{n_K \cdot 10^6} \quad (6)$$

$\pi$  is circumference ratio, adopt 3.1416 and  $d_Z$  is the diameter of the brake cylinder (mm) and  $p_{Z_i}$  is the air pressure of brake cylinder on the NO.1 train and  $\eta_Z$  is the calculated rigging efficiency of basic brake device and  $\gamma_Z$  is leverage ratio of the brake and  $n_Z$  is the number of the brake cylinder and  $n_K$  is the number of the brake shoe.

The friction index between wheel and brake shoe is decided by the model.

### 2.2.4 Calculation in the Buffer Force of the Draft Gear

The coupler and draft gear functions to connect the train's carriage and keep a given distance and transfer the longitudinal force and release the impact force.

In the analysis of the longitudinal force, we always serve an adjacent coupler draft gear as a whole to do further research. Given the interval between couplers and impedance features of the adjacent draft gear, we could calculate the relative displacement and the relative speed by integral calculation. So we could figure out the force of the coupler.

### 2.3 Calculation on the Longitudinal Force in the Simulation Model

Based on theoretical formula of the component of the longitudinal force, we calculate them in the simulation model. The formula of each variable is shown as formula (7).

$$\begin{cases} M_i = 80 \text{ t} \\ F_1 = A \left( 0.24 + \frac{12}{100+8} V \right) \\ B_i = 2000 \text{ N} \\ F_2 = 0.2 M_i (1.02 + 0.0035 V + 0.000426 V^2) \\ f_i = k_i \Delta x \quad (i = 1, 2, 3, 4) \\ f_{i+1}(t) = f_i(t + \Delta t) \end{cases} \quad (7)$$

A is traction ratio and  $k_1$  is stretching elastic ratio when loaded and  $k_2$  is stretching elastic ratio when unloaded and  $k_3$  is compressing elastic ratio when loaded and  $k_4$  is compressing elastic ratio when unloaded and  $\Delta x$  is coupling displacement and  $V$  is the speed of the train (km/h).

### 3 The Simulation of Synchronism Control of the Heavy Haul Train

On the last part, we establish a basil simulation model about two joint carriages. Now we try to combine the carriages in the form of ‘1 + 1 + 1’, specifically, 1 locomotive + 100 carriages + 1 locomotive + 1 locomotive + 100 carriages. Each carriage is featured by that axle load is 25 t and mass is 80 t. The model of the locomotive is SS4B. The total quantity of the train is 18,160 t. Each carriage has a length of 20 m, while the locomotive is 18 m long. The total length of the train is 4054 m. The interval of the adjacent is 10 mm. The limited displacement of the draft gear is 15 mm. the scheme of the combination of the haul heavy train is shown as Fig. 2.

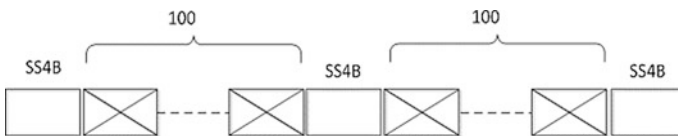


Fig. 2 The scheme of the combination of the heavy haul train

The haul heavy carriage combined, we try to simulate the longitudinal force through simulation software-MATLAB. The key procedure of the simulation is shown by Fig. 3.

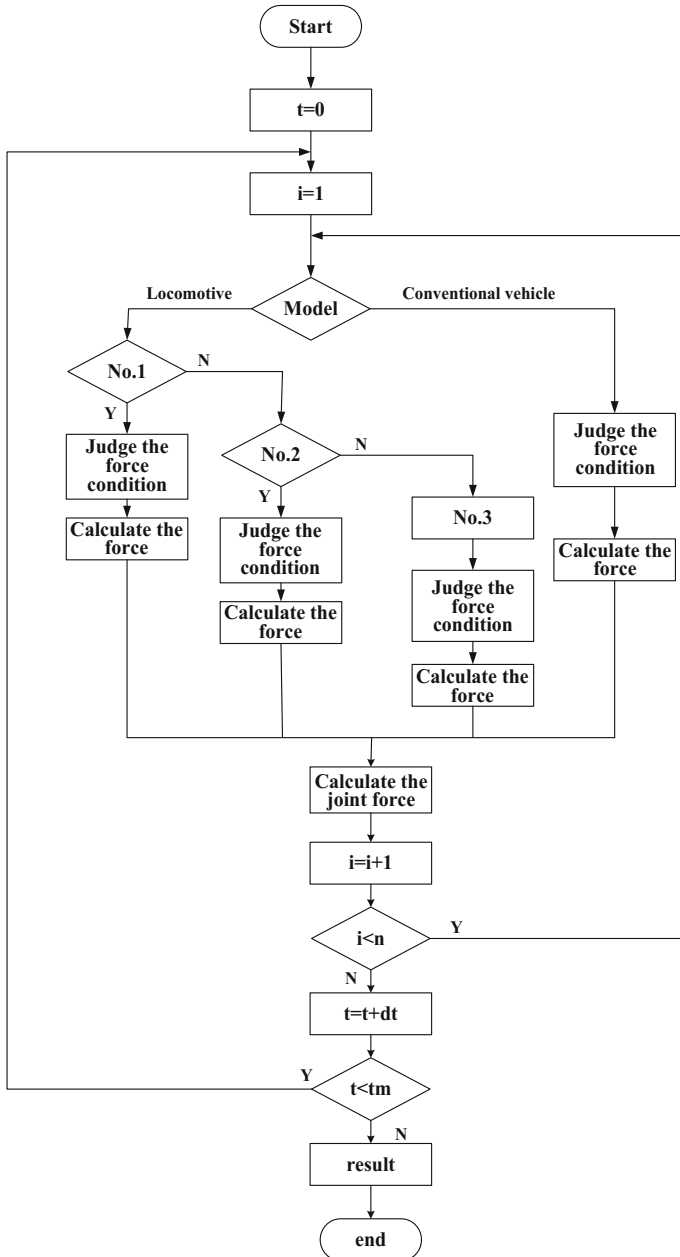


Fig. 3 The flow chart of the force analyzing

We try to conduct the simulation based on that the stress state can be ensured through the judgment on the state of each carriage from the starting-up to braking. Firstly, the program tries to analysis the state of three synchronism-controlled locomotives, next is carriage. Finally, the program conducts the stress state of each carriage, so we could solve the join forces. Then the curve shows the relationship between speed and the displacement is available.

## 4 The Analysis and Discussion on the Result of the Simulation

### 4.1 The Working Process of the Train on Level and Straight Track

Assuming that the train is running on a level and straight track, we get the simulation result of above train combination are shown in Figs. 4, 5, 6 and 7.

The conclusions of the simulation can be draw as follows.

- (1) In the starting-up, all the carriages are started up in proper order, which is accelerated from 0 to 19 m/s, then keeps a uniform motion. The closer the carriage is to the first locomotive, the earlier the carriage starts to move. The carriage which is close to the middle locomotive didn't move instantly, but they conduct a motion along the driving direction. This motion caused by the traction of the middle locomotive lead to a vibration among the middle-position carriages. The vibration ends up when the train is definitely starting up.
- (2) In the braking process, the force working on the carriage offsets or overlaps. Thereby, some carriages will suffer a biggest force-the maximum coupler force-caused by the above interaction force. The braking process is also a vibration process. All the carriages are not stopped in the same instant; instead, the speed of each carriage fades by the vibration.

**Fig. 4** The starting-up curve of the 20th, 50th and 80th carriage

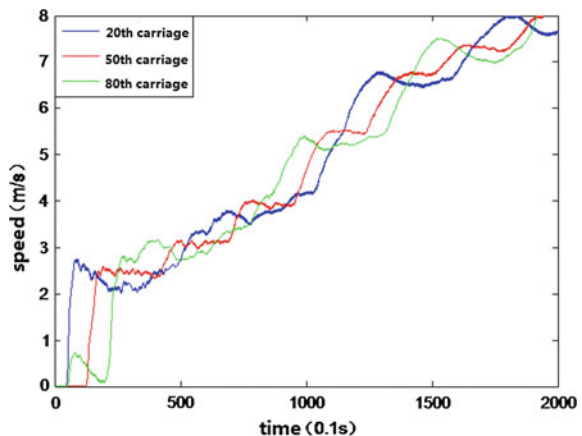


**Fig. 5** The braking curve of the 20th, 50th and 80th carriage

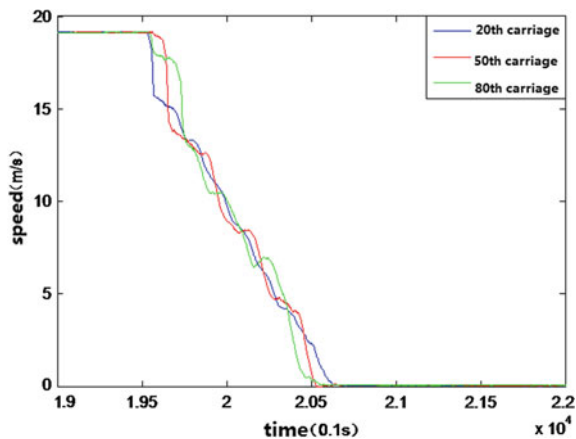


**Fig. 6** The starting-up curve of the 120th, 150th and 180th carriage

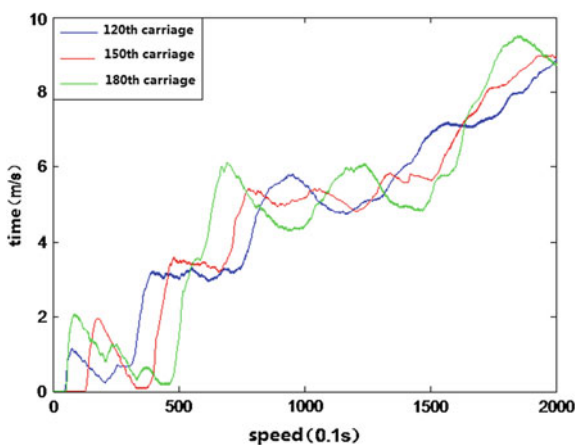


**Fig. 7** The braking curve of the 120th, 150th and 180th carriage

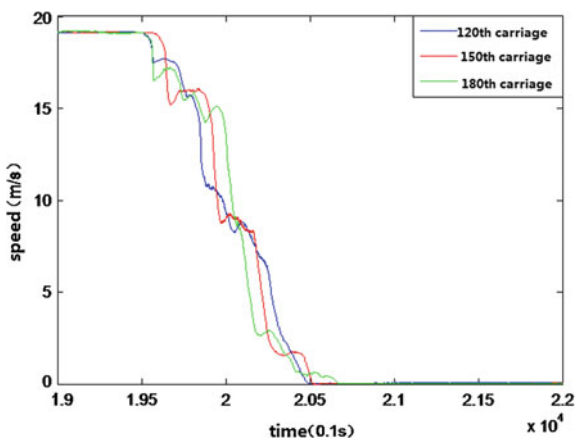




**Table 1** The simulation result of the equivalent time-delay state

Time-delay (s)	Maximum thrust (*10 <sup>5</sup> (N))	Carriage (th)	Maximum stress (*10 <sup>6</sup> (N))	Carriage
T12 = T23 = 1	7.5489	88	-1.1327	185
T12 = T23 = 2	7.5111	70	-1.1655	181
T12 = T23 = 3	7.6404	82	-1.1530	180
T12 = T23 = 4	7.9940	80	-1.1567	183
T12 = T23 = 5	8.6840	78	-1.1695	183
T12 = T23 = 6	9.3645	72	-1.1679	183
T12 = T23 = 7	9.4151	70	-1.1700	181
T12 = T23 = 8	10.0334	68	-1.1751	185

#### ***4.2 The Simulation of the Equivalent Time-Delay State Under the Emergency Brake***

The emergency brake is endowed with the top priority in the research of all working states, for that the interaction force is very complicated in this case. It deserves our effort to do further research on the brake method to stop the train quickly. This paper explains the simulation on a train has an equal time-delay state-the time-delay between the 1st and the 2nd locomotive equals that between 2nd and 3rd locomotive-whose initial speed is 70 km/h. The results are shown as Table 1.

Analyzing the data in Table 1, the maximum coupler force rises with the increase in delayed interval. Mostly, the percentage increase is in ascending order. From the '4 s' in chart, each 1 s increased, the faster the maximum the coupler thrust increased. The peak of the coupler thrust is between the 70th and 80th carriages which located in front of the second locomotive. With the increase in delay interval, the maximum stress increases with a smaller range. The maximum coupler stress is around the 180th carriage which is located around the third locomotive.

## **5 Conclusion**

Heavy haul train has the history of half a century; in China and other countries in the world investment is increasing in scientific research and funding. Million tons of heavy haul train research has become the consensus of today's railway sector and academia. The simulation and research of the longitudinal dynamics of heavy haul train is of great significance to the safe operation of the train operation.

This paper mainly carries on the detailed simulation, analysis and experimental verification of the heavy haul train's movement process and the emergency braking process. Through the theoretical analysis, the simulation model is established, and the simulation results are analyzed by simulation software-MATLAB. In the end,

a simple simulation experiment is carried out to improve the longitudinal impact of the train. Simulation and experiment proved that the can through the establishment of the particle model to simulate the train's start-up and braking process. We study the main influence the maximum coupler force variables and factors. Study and analysis of the maximum coupler force give us a wonderful guidance on how to optimize performance of synchronous control.

**Acknowledgements** This work is supported by National Key R&D Program of China (2016YFB1200402 and 2015BAG19B02). The authors are grateful for the reviewer of initial drafts for their helpful comments and suggestions.

## References

1. Li W (2012). The study and application on the control of the wireless control of the heavy haul locomotive. ZhongNan University. (in Chinese)
2. Cheng L (2016) Study on operation strategies for heavy-haul train based on genetic algorithm. Jiaotong University, Beijing. (in Chinese)
3. Lifen D, Jilong X (2010) Test and simulation study on the longitudinal impact of heavy-haul train. In: Third international conference on information and computing
4. Jiang Y, Chi M (2015) Dynamic simulation of heavy haul train based on circular-variable modeling and calculation method. In: International conference on mechanics and control engineering (MCE)
5. Ma W, Luo S, Song R (2012) Coupler dynamic performance analysis of heavy haul locomotives. *Carriage Syst Dyn* 50(9):1435–1452. (in Chinese)
6. Geng Z (2009) Heavy load transportation technology on Daqin Railway. China Railway Publishing House, Beijing. (in Chinese)
7. Zhao X, Kang X, Wang C, Ma D (2009) Research and verification on longitudinal dynamics simulation and calculation of Datong-Qinhuangdao line 20,000 tons heavy haul train. In: 9th International heavy haul conference. Shanghai, China, China Railway-Publishing House, pp 775–782
8. Wang K, Feng Q, Zhai Q et al (2009) Effect of the coupler free angle on wheel/rail dynamic safety performance of heavy haul locomotive. *China Railway Sci* 30(6):72–76 (in Chinese)

# Nash Bargaining Game of Cloud Resource Provision in Cooperative Market

Xiaoqing Zhang

**Abstract** Market economics can achieve optimal allocation of resource by the equilibrium theory, cloud resource provision mechanism based on market economics is studied. For increasing collective revenue further and improving the efficiency and fairness of resource allocation, a resource provision algorithm RPABG is proposed in bargaining market of cloud computing. RPABG builds the model with bargaining game and its objective is to find Nash bargaining solution (NBS). NBS is solved respectively in two different conditions by our proposed iteration algorithm. Simulation experimental results show that RPABG not only has a faster convergence speed, compared with our earlier work based on non-cooperative game, but can improve the overall utility of resource providers and realize Pareto efficiency, which can lead to an optimal allocation of cloud resource with fairness, rationality and equilibrium.

**Keyword** Cloud computing · Resource provision · Nash bargaining

## 1 Introduction

Cloud computing has been emerged to be the promising solution saving cost and generating more revenue for IT firms [1]. Cloud resources are provided dynamically and scalably as the accessible and reliable services to users in Internet on demand [2]. Therefore, resource provision is a key issue of cloud [3, 4], which not only requires collaborative resource sharing and allocation, but has to satisfy all demands of cloud users and providers.

In cloud, providers can form the cooperation to share the available resource for reducing the cost. This paper will focus on the resource provision in this market. Note that this paper extends our work [5] where the non-cooperative game [6] is used to

---

X. Zhang (✉)  
School of Mathematics and Computer Science,  
Wuhan Polytechnic University, Wuhan, China  
e-mail: zxqtzy@126.com

analyze the resource provision and revenue sharing. RPANCG [5] can get mutual optimal profit of providers that is not a maximum profit. All providers can cooperate to improve their profits, which will get more collective profit further. In general, the profit of resource provider in cooperative and bargaining market is not less than that in non-cooperative and competitive market. However, the bargaining solution strategy of the cooperative resource providers may not be the best response of other resource provider. So, if the game is played only one, some resource providers can deviate from bargaining solution to the best response. And, if game is played repeatedly, the deviation of resource provider will depend on the future profit.

In bargaining market, all providers can improve their profits through bargaining. This cooperative market can be modeled using the bargaining game in which the providers can negotiate with each other to reach efficient and fair solution. The efficiency demand contains two hierarchical demands, Pareto efficiency and maximal total profit. The total profit maximization may be inconsistent with individual rationality, so it is not necessarily accepted by both bargaining sides. Therefore, Pareto efficiency that is consistent with individual rationality is the basic efficiency demand that must be satisfied. In this condition, providers are group rational, whose objective is to maximize total profits, and at the same time individual profit allocation of each provider is fair. We will present a new algorithm RPABG (Resource Provision Algorithm Based on Bargaining Game) to solve this optimization in this cooperative market.

## 2 Market Model in Cloud Resource Provision

Figure 1 shows the market model of cloud resource provision, including users, private clouds, public clouds and resource market [8]. When private clouds can not meet the users' requirements, they purchase resources from public clouds in market. The cloud resource market is established for the VM selling and buying between private clouds and service providers in public clouds [8]. In this market, private clouds as a buyer determines the willingness to pay given the supplied VMs from all service providers. Given the willingness to pay, service provider as a seller determines the supply strategy to the market. In this case, the supply strategy will affect capacity planning and consequently profit of service providers. The VMs from all providers are assumed to be identical, i.e., offering identical CPU speed, memory capacity, and bandwidth.

## 3 Nash Bargaining Game Model of Resource Provision-RPABG

**Definition 1** All resource providers in cloud market are defined as game players, marked as  $RP_o$ ,  $o = \{1, 2, \dots, O\}$ .

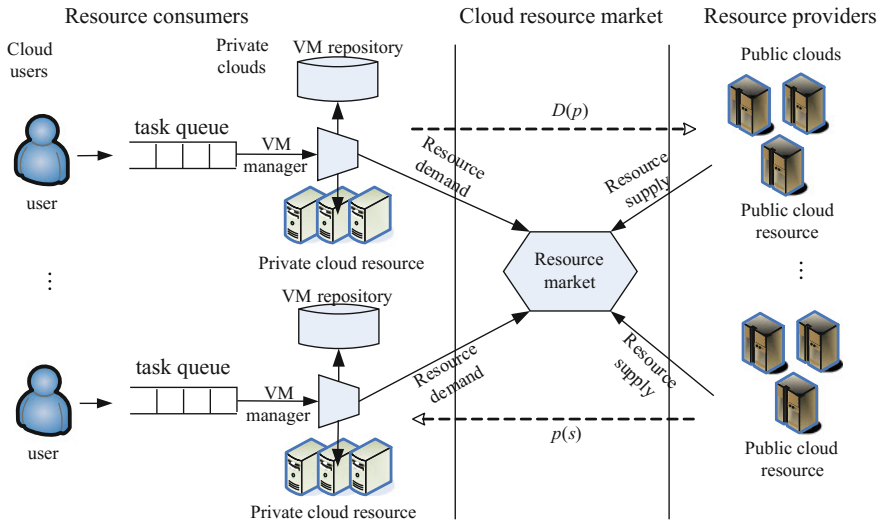


Fig. 1 Model of resource provision in economic market

**Definition 2**  $B$  denotes bargaining problem set of VMs,  $F \in \mathbf{R}^O$  is the feasible revenue set space of resource providers, defined by the utility of non-cooperative game,  $\bullet$  is the disagreement point or minimum revenue expectations, which denotes the revenue of resource provider when there is no agreement negotiations.  $\bullet = (R(I) * NE, \dots, R(o) * NE, \dots, R(O) * NE)$ ,  $R(o) * NE$  is the minimum revenue of provider  $o$ . Nash equilibrium solution of non-cooperative game is selected as initial point of bargaining problem, which means if negotiation fails, the non-cooperative game solution will be the final result.

**Definition 3** If  $\{R(O) \text{ bar} \in F | R(O) \text{ bar} \geq R(O) * NE\}$  is a non-empty bounded set,  $(F, \bullet) \in B$  is a bargaining game problem of  $o$  providers.

The solution of a bargaining problem is a function  $\psi: B \rightarrow \mathbf{R}^O$ , which can relate each bargaining problem  $(F, \bullet) \in B$  and a special result  $R^* \text{ bar} = \psi(F, \bullet)$ . Different axiom systems will lead to different bargaining solutions. There exist the following Nash axioms [7]:

**Axiom 1** Feasibility axiom

$$R^*_{\text{bar}} \in F \tag{1}$$

**Axiom 2** Individual rationality axiom

$$R^*_{\text{bar}} \geq R^*_{NE}, \forall o \tag{2}$$

**Axiom 3** Pareto efficiency axiom

$$R_{bar} \geq R_{bar}^* = \psi(F, \Gamma) \Rightarrow R_{bar} = R_{bar}^* = \psi(F, \Gamma) \quad (3)$$

**Axiom 4** Invariance of linear transformation

For any linear transformation  $\varphi$ ,  $R^* \text{ bar} \in F$  means

$$\varphi(\psi(F, \Gamma)) = \psi(\varphi(F), \varphi(\Gamma)) \quad (4)$$

**Axiom 5** Independent of independent choice

For any subset  $E$  of  $F$ , convex intensive set  $E$

$$R_{bar}^* \in E \subseteq F \Rightarrow \psi(E, \Gamma) = \psi(F, \Gamma) \quad (5)$$

**Axiom 6** Symmetry axiom

If  $(F, \bullet)$  exist:  $R(i)^* NE = R(j)^* NE$ ,  $R(i)^* \text{ bar}$ ,  $(R(i) \text{ bar}, R(j) \text{ bar}) \in F$ , means  $(R(j) \text{ bar}, R(i) \text{ bar}) \in F$ , then  $(R(i)^* \text{ bar}, R(j)^* \text{ bar}) \in \psi(F, \bullet)$  has to satisfy  $R(i)^* \text{ bar} = R(j)^* \text{ bar}$ .

**Corollary 1** If axiom 1–6 are satisfied, the only solution of Nash bargain solution is a utility vector that maximizes Nash product, which satisfies the solution of the following constraint optimization problem:

$$\begin{aligned} \psi(F, \Gamma) \in \arg \max \prod_{o=1}^O (R_{bar}^{(o)*} - R_{NE}^{(o)*}) \\ \text{s.t. } R_{bar}^* \in F, R_{bar}^{(o)*} \geq R_{NE}^{(o)*} \end{aligned} \quad (6)$$

This solution is Nash bargaining solution (NBS).

Generally, the Nash product is a concave function and the utility configuration set is a convex and compact set. The above optimization problem usually exists only one solution. We can get the corresponding strategy  $s + o$  from Nash bargaining solution of profit allocation in Eq. (6).

Considering the limitation of VM number  $s^{max}$  provided by each resource providers and the minimum profit  $\bullet$  of resource providers in non-cooperative game, the optimization goal of bargaining between resource providers is to achieve utility optimization through controlling effectively the VMs number. Utility function  $U$  is

$$\begin{aligned} \text{NBS : } U = \prod_{o=1}^O (R_{bar}^{(o)*} - R_{NE}^{(o)*}) \\ \text{s.t. } R_{bar}^* \in F, R_{bar}^{(o)*} \geq R_{NE}^{(o)*}, s_o \leq s^{max} \end{aligned} \quad (7)$$

## 4 Solution to Bargaining Game of RPABG

### 4.1 Nash Bargain Solution of Two Persons Game

When  $O = 2$ , Eq. (7) can be expressed as the Nash standard solution of the following equation.

$$\begin{aligned}
 (R_{bar}^{(i)*}, R_{bar}^{(j)*}) &= \psi(F, \Gamma) \\
 &= \arg \max_{R_{bar}^{(i)*} \in F, R_{bar}^{(j)*} \geq R_{NE}^{(o)*}, o=i,j} (R_{bar}^{(i)} - R_{NE}^{(i)*}) \times (R_{bar}^{(j)} - R_{NE}^{(j)*}) \quad (8)
 \end{aligned}$$

The steps of resource provision in Nash bargain of two persons are:

**Step 1** Get the resource demand of consumers and the parameters of resource providers, initialize the VMs provision strategy  $s_i = sinit\ i$ ,  $s_j = sinit\ j$ .

**Step 2** Select step size  $\epsilon$  of provided VMs,

$$\begin{cases} s_i^{(k+1)} = s_i^{(k)} + \epsilon \\ s_j^{(k+1)} = s_j^{(k)} + \epsilon \end{cases} \quad (9)$$

Search step by step in  $[0, smax\ i]$  and  $[0, smax\ j]$  and compute Pareto point as showed in Fig. 2.

**Step 3** Compute the strategy  $s_i$  and  $s_j$  according to the Eq. (10),

$$(R_{bar}^{(i)} - R_{NE}^{(i)*}) \times (R_{bar}^{(j)} - R_{NE}^{(j)*}) = C \quad (10)$$

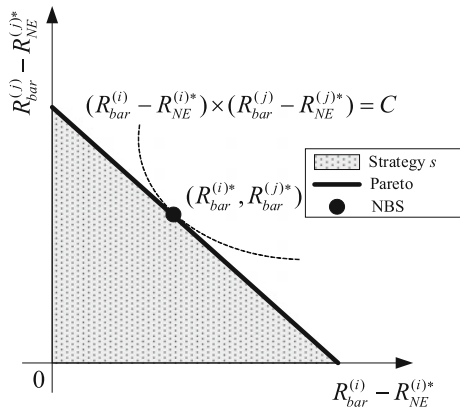
and compute the profit of resource providers in NBS; turn to Step 2, if  $s_i$  and  $s_j$  can reach convergence,  $s_i$  and  $s_j$  are the optimal solution  $s + i, s + j$ . Otherwise, turn to Step 2, record all convergence values and compute the convergence points that satisfy  $\pi$ ,

$$\pi = \arg \max_s \left[ \frac{(R_{bar}^{(i)} + R_{bar}^{(j)})}{(s_i + s_j) \cdot |R_{bar}^{(i)} - R_{bar}^{(j)}|} \right] \quad (11)$$

Then, return the corresponding  $s + i, s + j$ .

**Step 4** Compute  $R(i)*\ bar$  and  $R(j)*\ bar$  through  $s + i$  and  $s + j$ .

**Fig. 2** NBS of two persons bargain



### 4.2 Nash Bargain Solution of $O$ Persons Game

There are two cases when  $O > 2$ . First,  $O$  is an even number. We can achieve two bargaining through assigned groups. Second,  $O$  is an odd number. We can get  $O + 1$  resource providers through filling zero, while any resource provider can not bargain with resource provider  $O + 1$ . Then, Nash bargain of  $O$  persons can be transferred into bargain problem of two persons. How to assign two-two bargain group to ensure optimal system performance of resource provision? Generally, there are two methods to solve this assignment optimization problem, Hungarian method and branch and bound method, while the former is a better choice due to better efficiency. We choose Hungarian method to achieve two-two group bargain of  $O$  resource providers.

**Definition 4** The value matrix of Hungarian method is expressed as the difference value of the profit between two bargaining,

$$H = \begin{bmatrix} 0 & \Omega_{12} & \Omega_{13} & \dots & \Omega_{1n} \\ \Omega_{21} & \Omega_{22} & \Omega_{23} & \dots & \Omega_{2n} \\ \dots & \dots & \dots & \dots & \dots \\ \Omega_{n1} & \Omega_{n2} & \Omega_{n3} & \dots & 0 \end{bmatrix} \tag{12}$$

Where  $\Omega_{ij} = \max \left\{ (U(\widetilde{R}_{bar}^{(i)} - \widetilde{R}_{bar}^{(j)}) - U(\widetilde{R}_{bar}^{(i)} - \widetilde{R}_{bar}^{(j)})), 0 \right\}$  is the bargain profit of provider  $i$  and  $j$ ,  $R(i)$  bar and  $R(j)$  bar respectively denotes the profit of  $i$  before bargaining with  $j$  and after bargaining with  $j$ . If  $\Omega_{ij} = 0$ , the bargain ends.

Nash bargain of  $O$  persons can be translated into the bargain problem of two persons through Hungarian method and the value matrix  $H$ . The steps of the resource provision algorithm of Nash bargain of  $O$  ( $O > 2$ ) persons is:

**Step 1** Get the parameters of supply and demand sides in cloud market;

**Step 2** If the number  $O$  of providers is an even number, turn to Step 3 to group and select two persons bargaining combination; if  $O$  is an odd number, generate a null provider, then the number of resource providers is an even number, any resource provider can not bargain with resource provider  $O + 1$ , turn to Step 3 to group and select two persons bargaining combination;

**Step 3** Achieve two-two grouping of resource providers through Hungarian method to guarantee an optimal resource provision performance;

**Step 4** Return Nash solution of two persons bargaining  $s_i, s_j, R(i)$  bar,  $R(j)$  bar through two persons bargaining method;

**Step 5** Return Step 3 and Step 4 until NBS defined by Eqs. (6) and (7) can not improve, return  $s^+, R^*$  bar, e.g., final bargaining equilibrium solution.



### 5 Experimental Results

Simulation experiments are conducted in CloudSim for evaluating the performance of RPABG. Experimental parameters are first set: the number of resource consumers is 3, the number of hosts in private clouds is 2, the average task processing time is 30 s, the number of sub-tasks running on one VM is 1, the cost of purchasing VMs from resource market is 2.

Figure 3 shows that the market size impacts on RPABG’s convergence under different numbers of providers. It shows that RPABG needs more iterations to reach Nash bargaining equilibrium when increasing resource providers. It shows that from the change of utility, no providers can improve its utility by changing provision strategy while the other providers keep their strategies unchanged or non decreased. That means the Nash bargaining solution locates at Pareto optimal point, which can guarantee maximized utility product. The convergence state of utility means that Pareto optimal has reached the border part of bargaining strategy set in which the corresponding bargaining strategy and the corresponding utility are fair for all providers.

Figure 4 shows the average utility of providers. It shows the average utility increases with the increasing of consumers due to the increasing of resource requests. In addition, for the same number of consumers, the utility is the highest when  $O = 1$  in which there is only one provider that occupies the market

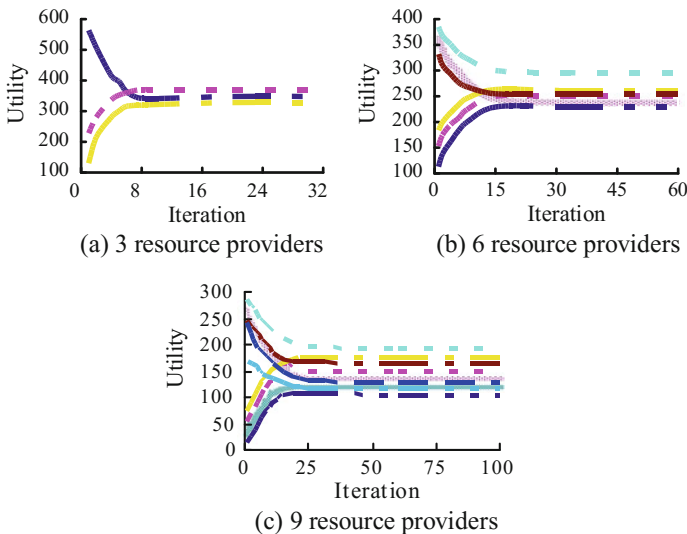
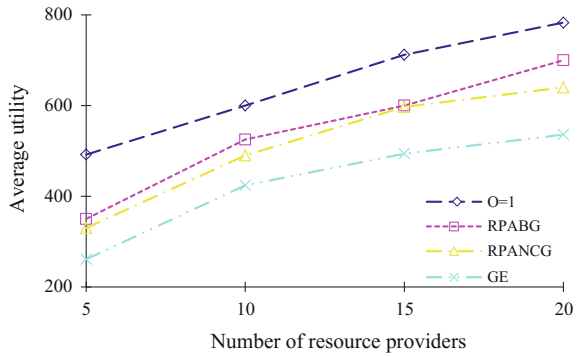


Fig. 3 Convergence of RPABG

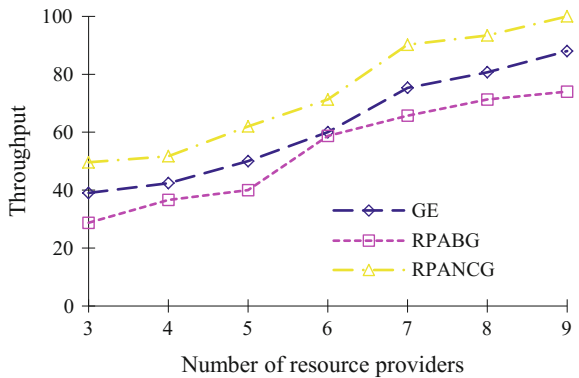
**Fig. 4** Number of consumers impacts on average utility



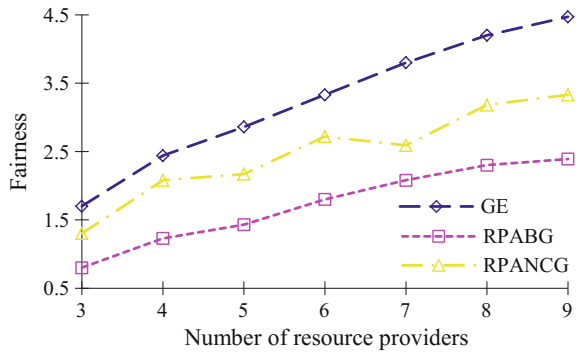
(monopoly market). But, the monopoly is much disadvantageous for the development of market though highest utility. Other 3 cases show the average utility of RPANCG, RPABG and GE (General Equilibrium algorithm) when  $O = 3$ . Obviously, RPABG's utility is always higher than or equal to that of RPANCG. This is because the negotiation between providers can reduce the provision number of VMs in the bargaining market, which leads to higher resource price and utility. In non-cooperative market of competitive relation, providers compete with each other by providing more VMs to gain more market share. Negatively, the resource price is low, hence the total utility is not maximized and is mutual optimal. GE does not consider the relationship of competition and cooperation between providers and merely adjusts adaptively the resource price according to the consumers demand, which is bound to affect the individual benefit. As a result, GE's average utility is the lowest.

Figure 5 shows the changes of throughput. It can be seen that with the increasing of providers, due to the increasing of processed tasks per unit time, the system throughput increases continuously. RPANCG has maximal throughput because it

**Fig. 5** System throughput



**Fig. 6** Fairness of resource provision



provides more VMs through reducing resource price. RPABG sacrifices some throughput but increases total utility. GE is about 19.4% lower than RPANCG and about 23.2% higher than RPABG.

Figure 6 shows the fairness of three algorithms. In RPABG, the performance parameter  $\pi$  gives consideration to both fairness and the throughput of unit resource. In the figure, the changes trend of GE and RPAGCG are significantly greater than RPABG with the increasing of resource providers. GE ignores the mutual influence among resource providers whose allocation results lack of fairness. RPABG’s NBS pays same attention to the welfare of both bargaining sides, which does not encourage blindly to pursue their utility and ignore the utility of opposite side. On the contrary, Nash equilibrium of RPANCG is a kind of mutual optimal utility, the fairness of which is not stable.

## 6 Conclusions

The bargaining solution in cooperative oligopoly market and the resource provision game problem are researched in bargaining market, and a resource provision algorithm RPABG based on bargaining game is proposed. Nash bargaining solution of RPABG is solved. Experimental results shows that RPABG not only can increase overall system utility, but can further improve the fairness and efficiency of resource provision in cloud.

**Acknowledgements** The work is supported by Youth Scientific Research Project of Education Department in Hubei Province (Q20171708).

## References

1. Laili Y, Tao F, Zhang L et al (2012) A study of optimal allocation of computing resources in cloud manufacturing systems. *Int J Adv Manuf Technol* 63(5):671–690
2. Arroba P, Risco-Mart JL, Zapater M et al (2014) Server power modeling for run-time energy optimization of cloud computing facilities. *Energy Procedia* 62(1):401–410
3. Chaisiri S, Lee B-S, Niyato D (2012) Optimization of resource provisioning cost in cloud computing. *IEEE Trans Serv Comput* 5(2):164–177
4. Papagianni C, Leivadreas A, Papavassiliou S et al (2013) On the optimal allocation of virtual resources in cloud computing networks. *IEEE Trans Comput* 62(6):1060–1071
5. Xiaoqing Zh, Fenglin G (2015) Non-cooperative game cloud resource provision in market economy environment. *J Comput Info Syst* 11(5):1665–1672
6. Smelser NJ, Baltus PB (2001) Game theory: noncooperative games. In: *International encyclopedia of the social and behavioral sciences*, pp 5873–5880
7. Niyato D (2011) Optimization-based virtual machine manager for private cloud computing. In: *Proceedings of the 2011 IEEE third international conference on cloud computing technology and Science*, pp 99–106
8. Weinhardt C, Anandasivam A, Blau B et al (2009) Business models in the service world. *IT Professional* 11(2):28–33

# Research on the Method of Calculating Train Congestion Index Based on the Automatic Fare Collection Data

Wenxuan Zhang and Jinjin Tang

**Abstract** With the increasing operating mileage of the urban railway transit, the traffic volume of the urban railway network has risen sharply. In order to enhance the performance and safety of the urban railway transit, the research on the train congestion index is imminent. In this paper, firstly, the definition of congestion index is proposed, and the congestion degree model is formulated. Secondly, the real-time congestion degree of train lines is obtained by using the algorithm based on the spatial and temporal K-shortest path. Finally, the train congestion of Xi'an subway is analyzed and calculated by the model based on the data of passengers' transportation cards and the process consumes just 3 min. Comparing with the actual results, we come to the conclusion that the train congestion model and space-time K-shortest path algorithm are correct and feasible, which can provide constructive suggestions on the operation and management of the urban railway network and the flow limitation of the station.

**Keyword** Passenger card data · Train congestion index · K-shortest path algorithm · Urban rail transit

## 1 Introduction

With the increase in the size of city population in recent years, nowadays, the major problem we faced with is how to reduce the pressure of the urban railway transit. At present, the Urban Rail Transit has developed rapidly. For example, both Beijing and Shanghai have formed a complex rail network in the shape of ring and radiation, while Tianjin, Nanjing, Xi'an, Dalian and other cities are also accelerating the construction of urban rail transit network [1]. However, the calculation of the real-time traffic flow manually is not only time-consuming but also inaccurate, due to we can't get access to the real-time traffic flow of the train in the stations and

---

W. Zhang · J. Tang (✉)

School of Traffic and Transportation, Beijing Jiaotong University, Beijing, China  
e-mail: 16120933@bjtu.edu.cn

© Springer Nature Singapore Pte Ltd. 2018

L. Jia et al. (eds.), *Proceedings of the 3rd International Conference on Electrical and Information Technologies for Rail Transportation (EITRT) 2017*, Lecture Notes in Electrical Engineering 482, [https://doi.org/10.1007/978-981-10-7986-3\\_78](https://doi.org/10.1007/978-981-10-7986-3_78)

781

trains by cars, station monitors and other equipment timely and accurately. As a result, it may cause overcrowding and accidents. Therefore, the calculation of real-time train congestion based on passengers' transportation card data is proposed in this paper, and the result has reference value because of the few time-consuming.

Although the widely used of AFCs has realized a new transfer mode called "one ticket for whole journey" [2], there are still few researches focused on the congestion of urban rail transit in China. For example, K shortest path search algorithm is proposed by Zhou [3] and Hoffman [4]. But the time factor is not considered in it, which makes it too simple to accurately reflect the actual situation of passengers' travel. Liu has referred to the term Train Congestion but the definition of it is not given. And the results are not accurate [5].

The determination of the train congestion index can improve the operating level of Urban Rail Transit, reduce traffic safety risks and achieve a better internal operation and management of rail network. Moreover, it can be an important reference for the station to dynamically limitation the traffic flow.

## 2 Modelling of the Train Congestion Degree

### 2.1 The Definition and Calculation of the Index

In order to describe whether the transportation capacity can meet the demand or not, in the paper, the concept of the train congestion degree is proposed. The train congestion is closely related to the train load factor in practice. The train congestion index refers to the mean value of the train load rate in a certain period of time:

$$\varphi = \frac{\sum_n C_i \times a_{load}}{n} \quad (1)$$

where  $a_{load}$  is the penalty for section full load factor. Note that if the load factor is less than 30%,  $a_{load} = 1$ . If the load factor is between 31 and 50%,  $a_{load} = 1.1$ . If the load factor is more than 50%,  $a_{load} = 1.2$ .

$C_i$  refers to the load factor in the section  $i$ .

$n$  refers to the number of operating trains in this period of time.

### 2.2 Process of Modelling

#### 2.2.1 Assumptions

We assume that the AFC data sources are real, complete and effective. In the process of obtaining the Origin-Destination (OD) data, we cannot get the precise



We suppose trains are running on schedule and there are no emergencies like delay.

We suppose there are no exceptional cases occur to passengers. That is to say, no one will stay at the station for long or take the wrong train.

### 2.2.2 Definition on Model Symbols

(Table 2).

### 2.2.3 Decision Variables

According to k shortest path algorithm, path set and costs  $X_1 = \{x_1^{od}, x_2^{od}, \dots, x_k^{od}\}$ .

### 2.2.4 Constraints

Impediment constraint ( $\Omega$ ): we use it to describe the satisfaction of passengers on this route. When the constraint bigger, this path is more unreasonable. Its calculate method is as follows:

$$\Omega_w^n = \langle a_{transfer} E_w^n + T_w^n \rangle \langle 1 + Y(x) \rangle \tag{4}$$

**Table 2** Symbol definition

Symbol	Definition
$\Omega_w^n$	The index of the pairs of OD at the $w$ route comprehensive impedance [8]
$T_w^n$	The index of the pairs of OD at the $w$ route travelling time, stopping time at the non-transfer station and walking time in the station
$E_w^n$	The transferring time of the pairs of OD at the $w$ route's index(include transferring waiting time and walking time in the station) [9]
$a_{transfer}$	The penalty coefficient of transfer time ( $a_{transfer} > 1$ )
$Y(x)$	Congestion degree of carriage
$x$	The average of passenger flow in this section
$z$	The seating capacity of this train in this section
$c$	Maximum number of passengers of this train
$A, B$	The coefficient of extra time at the crowded time. $A = 1.2, B = 1.5$
$\partial_n^{ij}$	The probability of effective path from $i$ to $j$
$\Theta$	Familiarity with passenger network
$Q^{ij}$	The passenger flow from $i$ to $j$
$\rho_n^{ij}$	The passenger flow in the effective path from $i$ to $j$
$p_\sigma$	The probability of passengers picking-up with the full load proportion about $\sigma$



$Y(x)$  formulation is as follows:

$$Y(x) = \begin{cases} \frac{x-z}{z}A + \frac{x-1.3*z}{z}B, & |x \geq 1.3 * z \\ \frac{x-z}{z}A + \frac{x-1.3*z}{z}B, & |x \geq 1.3 * z \\ 0 & |x < z \end{cases} \tag{5}$$

Then we can calculate resistance  $\Omega_1 = [\Omega_1, \Omega_2, \Omega_3, \dots, \Omega_n]$  of paths in the feasible sets  $X_1$ . Among those paths, the shortest path's resistance is  $\Omega_{min}$ .

Practical rational path constraint  $\theta = \frac{\Omega_n}{\Omega_{min}} < 2.2$ , if  $\theta < 2.2$ , it belongs to reasonable path [8]. Finally, we get a reasonable path from  $i$  to  $j$ .  $X_1^{ij} = [x_1^{ij}, x_2^{ij}, \dots]$ , and obtain their resistances  $\Omega_1^{ij} = [\Omega_1^{ij}, \Omega_2^{ij}, \dots]$ .

The average of full load rate of interval section constraint:

$$C_i = Q^{ij} * \frac{\exp(-\theta \Omega_n^{ij} / c_{min}^{ij})}{\sum_m \exp(-\theta \Omega_n^{ij} / c_{min}^{ij})} / z \tag{6}$$

We use maximum likelihood estimation method to actual survey data. Then, we get the value of  $\vartheta$  and  $\theta$  according to different traveling grade [9] (Table 3).

### 3 Train Congestion Algorithm Based on the Space-Time K Short Algorithm

After we build up the congestion degree model, we need to search for the space-time K-shortest path according to decision variables of the model. Compared with urban public transportation system, the operation of metro trains won't be influenced by various external factors such as road traffic. So the train schedule is more suitable for the actual situation. That is to say, it is better to optimize the K-shortest path algorithm based on the train schedules [10]. When the ordinary physical K-shortest path becomes the space-time K-shortest path, passengers will choose different paths. This paper will use the space-time K-shortest path algorithm to analyse the actual situation which passengers choose.

**Table 3** The value of  $\vartheta$  and  $\theta$  according to different traveling grade

Grade	Short	Medium	Long
time	<20	21-40	>40
$\alpha$	2.7	2.0	1.8
$\theta$	7.03	15.21	19.83

### 3.1 The Space-Time K-Shortest Path Algorithm

The calculation of k shortest path searching algorithm is large, especially complex network [2]. Based on the above situation, we optimize and improve the k shortest path algorithm, and we propose the K-shortest path separation algorithm.

- Step 1 Giving a cost matrix, we should use Dijkstra algorithm to obtain the shortest path  $T_1^{od}$  from O to D. Then put this path into the dataset  $X_1$  [8] ( $X_1$  refers to the set of the K-shortest path).
- Step 2 Delete one of the edge  $T_1^{od}$  in the shortest path. Then, we continue to use Dijkstra algorithm from separation point I to terminal station. Next, adding the length  $T_2^{oi}$  from starting station to separation point. Finally, we get a whole path  $T_2^{od}$ .
- Step 3 Delete one edge of the shortest path in sequence, and circle method 2 getting  $n_1$  paths  $\{T_3^{od}, T_4^{od} \dots T_{n+1}^{od}\}$ . Then we put the path into  $X_2$  data set ( $X_2$  refers to alternative k short algorithm set). Then, we search the second shortest path in  $X_2$  data set.
- Step 4 Delete one of the edge of the second shortest path successively, repeating step 3, then obtain the third shortest path, the fourth shortest path and so on. Finally, we get the K-shortest path set  $X_1 = \{x_1^{od}, x_2^{od}, \dots, x_k^{od}\}$ .

Note that in order to avoid search path where ever selected. When we delete the nodes from  $k_i$  to  $k_{i+1}$ .in the kth. Path. We need to judge whether there is a path that we ever searched and the nodes from 0 to  $k_i$ . is same to that path. If this situation occurs, we need to find the index of the node j. When we disconnected the j node, we should also search all the paths in the  $X_1$  set. If  $x_n^{od}$  contains O-j, we also need to disconnect the edge from the index of j.

- Step 5 Based on the physical network, we can consider the train diagram factor. And then it becomes a complex network. To build up a urban subway operation space expansion network based on the train diagram. We add train diagram to urban rail transit network, then add time axis in the two-dimensional spatial network [5]. Finally, we obtain the space time k short algorithm  $X_{\text{space-time}} = \{x_1^{od}, x_2^{od}, \dots, x_k^{od}\}$ .

According to above method, we use K short circuit separation algorithm to ensure every OD pairs among all paths. It has lots of advantages, such as efficient, high-speed. It lays a good foundation for the following work.

### 3.2 Determine the Reasonable Path

We need to consider the time of passengers walking and waiting in the station when passengers transfer because the transfer stations of different lines locate in different places. So we need to process the fundamental matrix of urban rail network in order to make the consequence of the algorithm closer to the actual travel path.

- (1) Processing method: First, we should transform one transfer station node into several virtual nodes that represent this transfer station of different lines. Next, connect these virtual nodes in dotted lines [9], which refer to the time of passengers walking in the station. If the transfer station is structured like “T”, the transform method is shown in Fig. 1. If the transfer station is structured like a cross, the method is shown in Fig. 1.

We transform the matrix of cost as above. Then, we obtain each K-shortest path between nodes by using K-shortest path search algorithm. Finally, we merge the nodes and keep the cost of the matrix unchanged. Now, the result includes paths and costs between pre-calculated position and virtual point. And choose the path with the lower cost as the passenger’s actual path [11]. That is to say, passengers will get out of the station as soon as arriving at the destination station.

- (2) The path passengers transfer from line A to line B and then transfer to line A again is invalid.
- (3) A path of which the cost is more than 60% is invalid.
- (4) If a transfer station has three lines, we must avoid the loop.
- (5) If the origin station and the destination station belong to the same line, we don’t need to calculate the K-shortest path. That is to say, the probability of selecting this direct path is 1 and others 0.

## 4 Case Analysis

The Xi’an urban railway network currently has 3 lines and 66 stations shown in Fig. 2, whose the operating mileage has reached 91.35 km. The average daily passengers flow is about 1,270,000. There are 738,000 getting in the station and 532,000 of transfer flows.

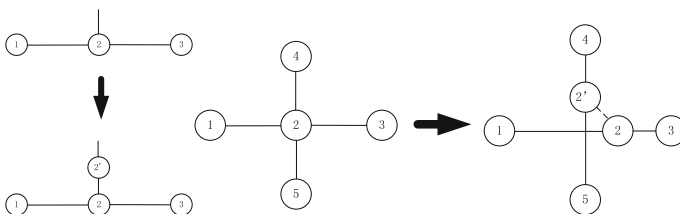
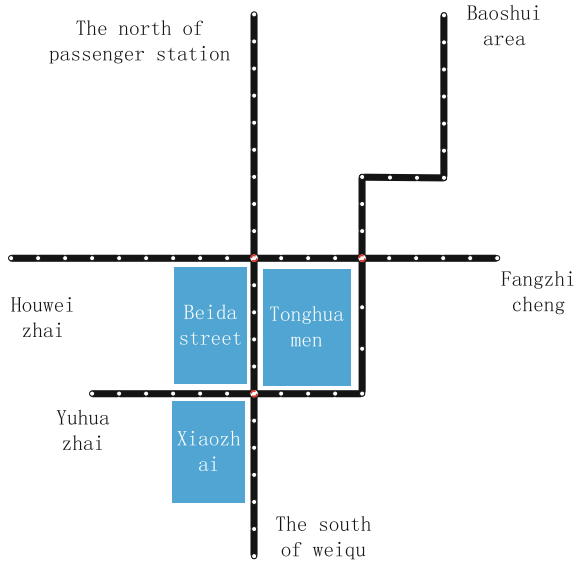


Fig. 1 The transform method of T and cross shaped lines

**Fig. 2** The urban railway network of Xi'an



**4.1 Basic Data**

Xi'an metro station and line profile are shown in Table 4.

**4.2 Results and Evaluation**

According to the model, the algorithm based on the spatial and temporal K-shortest path congestion described above, the results are shown in Tables 5 and 6.

According to load factor in the section, line transfer capacity and train congestion index which are calculated in 3 min, we finally propose the following measures (only train congestion index is shown in the table order by size).

According to load factor in the section. The largest passengers flow section is “Longshouyuan-nanshaomen” at morning peak and evening peak in line 2. The train congestion in morning peak is 116.42% in section “beidajie-zhonglou” at 8:00–9:00. The train congestion in evening peak is 80.14% in section “beidajie-zhonglou” at 18:00–19:00. So, we draw a conclusion that we need to limit

**Table 4** Summary of AFC data in Xi'an metro (partly)

No	Station count	Medium	Long
Line 1	19	2	526,681
Line 2	21	2	846,122
Line 3	26	2	472,518

**Table 5** Data source

Starting station	Destination station	Path	K-shortest path	Transfer count	Select probability (%)	Line impedance	Passenger flow	Passenger flow in specific path
Tonghuamen	Xiaozhai	Tonghuamen-zhonglou-xiaozhai	1-2	1	40.18	32.78	695	279.3
Tonghuamen	Xiaozhai	Tonghuamen-qinglongsi-xiaozhai	3	0	59.82	26.4	695	415.7
Tonghuamen	Beidajie	Tonghuamen-wulukou-beidajie	1	0	99.92	15.4	1044	1043.2
Tonghuamen	Beidajie	Tonghuamen-xiaozhai-beidajie	3-2	1	0.08	46.2	1044	0.8
The city Library	Shijia street	The city Library-wulukou-shijia street	2-1-3	2	95.44	51.7	75	71.6
The city Library	Shijia street	The city Library-xiaozhai-shijia street	2-3	1	4.56	62.92	75	3.4

Description 1 The unit of passenger flow is: million/person. 2 Select time is working day

**Table 6** Train congestion (per hour)

Line number and direction	Time	Section	Train congestion (%)
Line1 down	7:00–8:00	Sanqiao-houweizhai	17.23
Line1 up	9:00–10:00	Beida street-wulukou	62.3
Line2 up	10:00–11:00	The city Library - daminggongxi	2.62
Line2 up	13:00–14:00	The city Library - daminggongxi	37.43
Line3 down	18:00–19:00	Taohuatan-guangtaimen	10.7
Line3 down	18:00–19:00	Shijia street-hujiamiao	20.02

the passengers flow at longshouyuan station and daminggongxi station at morning peak.

Compared with the actual situation, we verify the accuracy of the model and algorithm.

## 5 Summary

In the paper, the model of train congestion is proposed and established. Then, determine the OD paths and constraints based on the model of train congestion. Next, we use the improved logit multi-probability selection model to obtain the index of the real-time train congestion. The algorithm of train congestion degree based on the Space-time K-shortest path has a lot of advantages, such as efficient and few time-consuming. It lays a good foundation for the following research. The study on passenger travel distribution in theory plays a guiding role for rail operators in dispatching the trains, determining the reasonable interval, planning the construction of new lines, limiting the passenger flow in the station, handling the emergencies, even monitoring the route of suspects for police and so on.

## References

1. Han B (2011) Discussion on development tendency of urban light rail transit under the new situation. 30(36):49–49. (in Chinese)
2. Niu X, Pan Y (2005) Research on the allocating algorithm in rail systems. The time of computer. 2:17–18. (in Chinese)
3. Zhou W (2013) Research on urban rail transit ticket clearing under the accessibility ride. (in Chinese)

4. Hoffman W, Pavley R (1959) A method for the solution of the best path problem. *J ACM* 6 (4):506–514
5. Liu J (2012) Transfer-based modeling flow assignment with empirical analysis for urban rail transit network. Beijing jiaotong University. (in Chinese)
6. Zhou Q, Li S (2013) Discussion on statistical problems of several operational indexes of Urban Rail Transit. *Urban rail transit research*. 16(7):1–3. (in Chinese)
7. Zhou C (2007) Metro OD information processing based on IC card data. *Modern urban rail transit*. 47–49. (in Chinese)
8. Jia N(2008) Research on the problems of city rail traffic ticket income distribution. Beijing jiaotong University. (in Chinese)
9. Qin Z (2011) Study on passenger route choice of Urban Rail Transit under network condition. Beijing jiaotong University. (in Chinese)
10. Liu X (2013) Study on subway dynamic assignment model based on Timetable. Chang'an University. (in Chinese)
11. Lai S (2008) Study on the method of city rail traffic ticket income distribution. Beijing jiaotong University. (in Chinese)
12. Li W (2004) Research on delay constrained minimum cost multicast routing algorithm. Chinese Science and Technology University. (in Chinese)

# Research on Shortest Paths-Based Entropy of Weighted Complex Networks

Zundong Zhang, Zhaoran Zhang, Weixin Ma and Huijuan Zhou

**Abstract** In order to provide a new measure for the structural characteristics of complex networks, a new shortest paths-based entropy (SPE) is proposed to describe the influence of degree and shortest path on network characteristics in this paper. The novel measurement based on shortest paths of node pairs and weights of edges. Many different approaches to measuring the complexity of networks have been developed. Most existing measurements unable to apply in weighted network that consider only one characteristic of complex networks such as degree or betweenness centrality. To some extent, the shortest paths-based entropy overcome the inadequacies of other network entropy descriptors. The method combines node degrees with shortest paths. For the purpose of proving the reasonableness of this method, we carry on a contrast analysis of the SPEs of different type networks, including: ER random network, BA scale-free network, WS small-world network and grid network. The results show that shortest paths-based entropy of complex networks is meaningful to evaluation of networks.

**Keywords** Complex networks · Contrast analysis · Shortest Paths-based entropy (SPE)

## 1 Introduction

Complex systems widely exist in nature and human society, and it can be described by a variety of complex networks. Network science is an emerging subject which many fields are widely interdependent. Research on complex networks has greatly promoted the development of complex systems, it has become one of the most important frontier scientific in complex system and complex scientific research.

---

Z. Zhang (✉) · Z. Zhang · W. Ma · H. Zhou  
Beijing Key Lab of Urban Road Transportation Intelligent Control Technology,  
North China University of Technology, Beijing, People's Republic of China  
e-mail: zdzhang@ncut.edu.cn

© Springer Nature Singapore Pte Ltd. 2018  
L. Jia et al. (eds.), *Proceedings of the 3rd International Conference on Electrical and Information Technologies for Rail Transportation (EITRT) 2017*, Lecture Notes in Electrical Engineering 482, [https://doi.org/10.1007/978-981-10-7986-3\\_79](https://doi.org/10.1007/978-981-10-7986-3_79)

793



In this information age, complex networks have become an integral part and play an important role [1].

Complex networks refer to networks with some or all characteristics of self-organization, self-similar, attractors, small world or scale-free. Complexity of networks mainly manifested in the diversity of structure and nodes, evolution of network, complexity of dynamics, and the interplay between the above-mentioned [2]. In the last two decades, there has been an explosion in complex networks research, and the research cover life sciences networks, Internet networks, social networks and industrial networks. In the field of natural sciences, the basic characteristics of the network are node degree and degree distribution, betweenness centrality, the shortest path length, clustering coefficient etc., among them, entropy is a very important statistical descriptor [3].

Initially, entropy was introduced as a thermodynamic concept which used to measure the disorder of system. Recently, entropy is a measurement of the uniformity of energy distribution, which can represent the state and the trend of the system. The less uniform the distribution, the smaller the regularity and the higher the entropy [4]. The research on complex networks entropy can be used to analyze the structural characteristics of networks, and can further research the reliability of complex networks, efficiency of organizational structure, evolution of networks and so on [5].

Entropy reflects the overall structure characteristics of networks, but previous studies are not comprehensive. This paper combines the strength of vertices and the shortest paths, which can reflect the characteristics of the network structure. The strength of vertex not only takes into account the node degree, but also considers the weights between node and its neighbors, which is a comprehensive reflection of local information. The shortest path is the global characteristic of networks, the combination of strength of vertex and shortest path can more accurately reflects the characteristics of complex networks [6].

## 2 Network Entropy

Entropy is a very important physical quantity in thermodynamics, which can characterize material state and measures the system's efficiency. The concept was proposed by the German physicist Clausius in 1854. In 1877, Boltzmann used the probabilistic approach to demonstrate the relationship between entropy and the probability of thermodynamic states. From the beginning of Boltzmann's description of entropy, the concepts of entropy in many fields are described quantitatively, which lead to the extensive application of generalized entropy in today's natural and social sciences. The founder of the information theory, Shannon, put forward the information measure based on the probability statistics model. He defined the information as "the thing used to eliminate the uncertainty". In 1948, Shannon borrowed the concept from thermodynamics and put forward the mathematical expression of information entropy as below:

$$H(X) = - \sum_{i=1}^m p_i \log_2(p_i) \quad (1)$$

where  $m$  is the subset number of system  $X$  and  $p_i$  is the proportion of element in the  $i$ th subset. Information entropy can be regarded as a method of evaluating system. The higher the entropy of system, the greater the amount of information it contains, and the smaller the uncertainty of the system [7].

## 2.1 Research Progress of Network Entropy

Entropy has great significance in the research on complex networks, and it is also defined as entropy of degree distribution, target entropy, structure entropy, search information entropy, road entropy, etc. In recent years, the research of networks entropy has attracted attention and made great progress. Several static geometric features such as node degree, degree distribution, eigenvalues, betweenness and centrality, have been used in many methods of computing entropy [8]. Safara and Sorkhoh investigated which topologies of complex networks will cause the maximum degree entropy. They used genetic algorithm to prove that networks with a uniform distribution topology has the maximum degree entropy [9]. Rajaram and Castellani considered the question of measuring the complexity in a system, and propose an entropy based Shannon entropy and von Neumann entropy to quantify the network complexity [10]. Zhang and Li proposed a local structure entropy to identifying the influential nodes in the complex network which is based on the degree centrality and the statistical mechanics. They used the Susceptible-Infective model to evaluate the performance of the influential nodes and prove the rationality of the new method by simulation on real networks [11]. Xu and Hu constructed the degree dependence matrices and extracted a new degree dependence entropy (DDE) descriptor to describe the degree dependence relationship and corresponding characteristic of complex networks. The simulation experiments prove that the DDE can reflect the complexity and other characteristic of complex networks [12]. Zhang and Li proposed a new structure entropy of complex networks which based on nonextensive statistical mechanics, and they proved that it is reasonable to use the betweenness of each node as the entropic index of each subsystem to describe the nonextensive additivity between the subsystem and the whole network [13].

## 2.2 The Innovation of This Method

In the proposed method, we quantified the structure complexity of complex networks by node degree and shortest path length. In this paper, the influences of degree and shortest path on network structure are fused in the new proposed

entropy. In the existing methods, most network models are unweighted. However, networks are basically weighted in the real world. In order to be suitable to actual circumstances, we need to consider the impact of strength of vertex and shortest path on the network characteristics. The strength of vertex defined as:

$$S_i = \sum_{j \in N_i} w_{ij} \tag{2}$$

where  $N_i$  is the neighbor set of node  $i$ . The weight of the edge from node  $i$  to node  $j$  is denoted by  $w_{ij}$ . In this paper, we calculated the shortest path length and the average weight of the shortest path. Then, we constructed the average weight matrices based on the shortest paths between node pairs and extracted the entropy from the average weight matrices.

### 3 Shortest Paths-Based Network Entropy

For a weighted network, the following should be done before defining the shortest paths-based entropy (SPE): First, we constructed a directed weighted network  $G = (V, E)$ , assuming that there are  $n$  vertices  $V = (V_1, V_2, \dots, V_n)$  in the network and  $E$  is a set of weighted edges.  $E_{ij}$  is the edge from node  $i$  to node  $j$ . Second, removed the weights of the network, and calculated the shortest path length  $d_{ij}$  between all node pairs by Dijkstra algorithm. If there is no path between two nodes, we set the shortest path length equal to 0. Third, loaded the weights into edges, the sum of weights of the shortest path divided by  $d_{ij}$  is recorded as  $AW_{ij}$ .  $AW_{ij}$  is the average weight of the shortest path of node  $i$  to node  $j$ . Fourth, there are corresponding matrix  $A$  for different path length,  $A^d$  represents the average weight on the shortest path of all node pairs with the shortest path length  $d$ .

**Definition 1** Let  $A_{mn}^d$  is the average weight of all shortest paths with the shortest path length  $d$ .

$$A_{mn}^d = \{AW_{mn} | (V_m, V_n), d_{mn} = d\} \tag{3}$$

**Definition 2** The shortest paths-based entropy (SPE) with shortest path length  $d$  is computed as

$$SPE(A^d) = - \sum_{m=1}^N \sum_{n=1}^N (A_{mn}^d / \sum A) \cdot \log(A_{mn}^d / \sum A) \tag{4}$$

where  $\sum A$  is the sum of all elements in matrix  $A$ .

The following steps are the specific calculation process of SPE. Step 1: Set the weights of the edges equal to 1, and calculate the shortest path length of each node pairs with Dijkstra algorithm and record all edges of the shortest paths. Step 2: Load the weight of the weighted graph into the edges of the shortest paths obtained in the

first step, and calculate the sum of weights between each node pairs. Step 3: Obtain the average weight of the shortest paths by using the sum of weights divided by the shortest path length. Step 4: Classify the nodes according to the shortest path length. Then, extract the average weight matrices under different path lengths and calculate the proportion of each element in the matrices. Step 5: Calculate the SPEs under different shortest path length by Eq. (4).

## 4 Simulation Experiments and Result Analysis

In order to prove the reasonability of the novel method, we generated different type networks, including: ER random network (vertices number:  $N = 100$ , connection probability of node pairs:  $p = 0.05$ ), BA scale-free network (vertices number of initial network = 5, generates a scale-free network of 100 nodes from the initial network), Watts Strogatz network ( $N = 100$ , average degree = 4, replacement probability  $p = 0.05$ ), grid network ( $N = 100$ ).

### 4.1 Experimental Results

In the first experiment, we find differences in SPE values with different network structure. The results are shown in Fig. 1. In the second experiment, we generate four new weighted networks, we sort weights according to the degrees of nodes and load them into the edges. The results are shown in Fig. 2. At last, we compare the SPE values of WS small-world networks with different replacement probability as shown in Fig. 3.

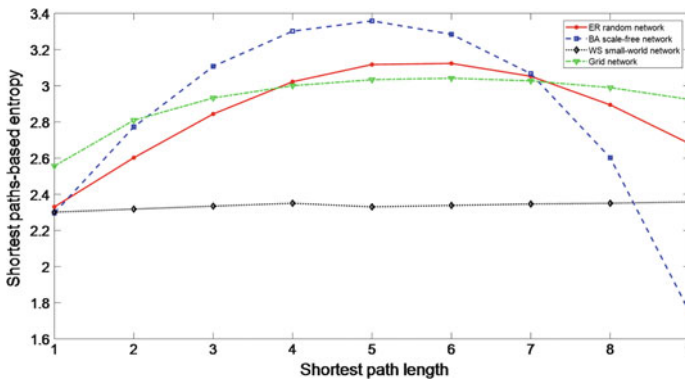


Fig. 1 SPEs of four network types

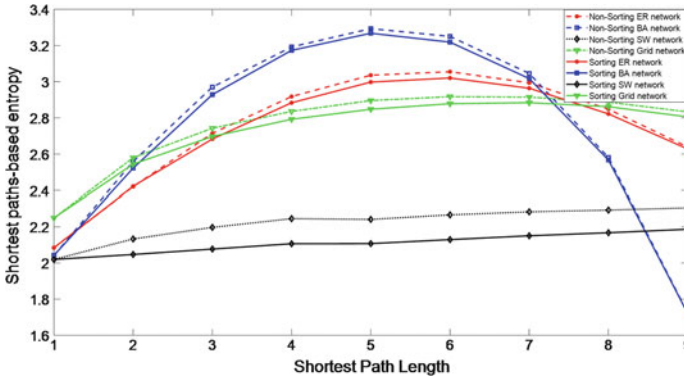


Fig. 2 SPEs with sorting and non-sorting

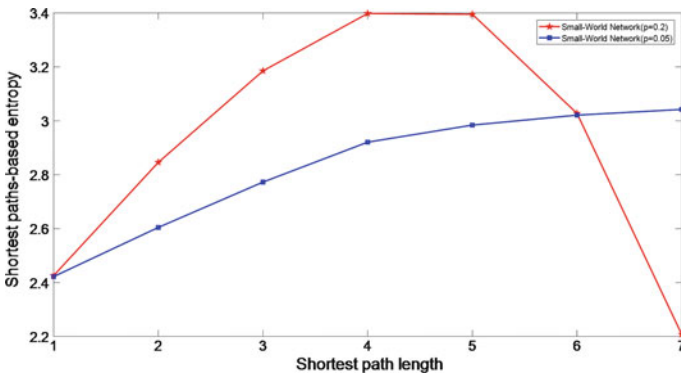


Fig. 3 SPEs with different replacement probability  $p$

### 4.2 Results Analysis

From Fig. 2, the complexity of the network composed of these shortest paths are increasing first and decreasing afterwards with the increasing of shortest path length, so the SPEs are present the same trend.

Taken as a whole, BA network has the highest SPE values with the same shortest path length. In the theory of complex networks, BA scale-free network model has two characteristics which are growth and preferential attachment. Initially, this model only has a few nodes, and then new nodes are added. The connect probability of the selected nodes and new nodes are directly proportional to the degree of the selected nodes. The average path length and the clustering coefficient of BA network model are very small. However, due to the large degree of “critical nodes” and the small degree of “tip nodes”, the scale-free network is obviously not uniform, so the SPE values are the highest. Each node pair has the same connect

probability in ER random network model and the average path length and clustering coefficient are small. For the small-world network, each node is connected with  $2 * m$  edges. Then, each edge is randomly reconnected with the probability  $p$ . The small world network model has small average path length and high clustering coefficient.

From Fig. 3, it can be seen that the non-sorting networks have higher SPE values. Therefore, these non-sorting networks have less regularity and higher disorder than the sorting networks.

From Fig. 4, the SPE values with  $p = 0.2$  are higher than that when  $p = 0.05$ , which indicates that high SPE values mean less regularity and more complexity.

## 5 Conclusions

In this paper, we introduced the research status of complex networks entropy. According to the previous research methods, the SPE is proposed. The experiment results show that the higher disorder and the less regularity of network, the higher the SPE values, which reflect the structural characteristics of complex network. The SPE values of three networks followed the order of BA scale-free network > ER random network > WS small-world network, and the disorder of networks is the same.

According to the simulation on four networks, we proved this new method of calculating the SPEs of weighted networks is efficacious and logical to measure the heterogeneity of complex networks. The method can be helpful to understand the structural characteristics of complex network, and it can supply meaningful quantitative statistical characteristic for complex networks research.

**Acknowledgements** This paper is supported by The Chinese the State 13 Five-year Scientific and Technological Support Project (2016YFB1200402), The Big-Data Based Beijing Road Traffic Congestion Reduction Decision Support Project (PXM2016014212000036) and The Project of The Innovation and Collaboration Capital Center for World Urban Transport Improvement (PXM2016014212000030).

## References

1. Lu GX, Li BQ, Wang LJ (2015) Some new properties for degree-based graph entropies. *Entropy* 17(12):8217–8227
2. Mowshowitz A, Dehmer M (2012) Entropy and the complexity of graphs revisited. *Entropy* 14(3):559–570
3. Cao SJ, Dehmer M, Shi YT (2014) Extremality of degree-based graph entropies. *Inf Sci* 278:22–33
4. Bianconi G (2013) Statistical mechanics of multiplex networks: entropy and overlap. *Phys Rev E Stat Nonlin Soft Matter Phys* 87(6):062806
5. Rajaram R, Castellani B (2016) An entropy based measure for comparing distributions of complexity. *Phys A* 453:35–43

6. Chen ZQ, Dehmer M, Shi YT (2014) A note on distance-based graph entropies. *Entropy* 16 (10):5416–5427
7. Chakrabarti CG, Chakrabarty I (2005) Shannon entropy: axiomatic characterization and application. *Int J Math Math Sci* 17:2847–2854
8. Chen ZQ, Dehmer M, Shi YT (2015) Bounds for degree-based network entropies. *Appl Math Comput* 265:983–993
9. Safara MH, Sorkhoh IY, Farahat HM, Mahdi KA (2011) On maximizing the entropy of complex networks. *Procedia Computer Science* 5:480–488
10. Anand K, Bianconi G (2009) Entropy measures for networks: toward an information theory of complex topologies. *Phys Rev E* 80(4 Pt 2):045102
11. Zhang Q, Li MZ, Du YX, Deng Y (2014) Local structure entropy of complex networks. *Comput Sci*
12. Xu XL, Hu XF, He XY (2013) Degree dependence entropy descriptor for complex networks. *Adv Manufact* 1(3):284–287
13. Zhang Q, Li MZ, Deng Y (2016) A new structure entropy of complex networks based on nonextensive statistical mechanics. *Int J Mod Phys C* 27(10):440–452

# Train-Mounted Head-up Display System Based on Digital Light Processing Technology

Ai-jun Su

**Abstract** Rail transit has been playing an important role in public transportation. Ensuring its safety is a key issue in the field of rail transportation. HUD (Head-Up Display), an auxiliary system to improve drive safety, has been successfully applied in the automotive industry. In this paper, a study of HUD applied in the field of rail transit is presented, followed by the structure and the working principle of train mounted HUD based on DLP (digital light processing) projection display technology. In addition, the feasibility of HUD used in the field of rail transportation is verified by experiments.

**Keywords** Rail transit · Head-up display system · Safe driving

## 1 Introduction

HUD [1], namely Head-Up Display, is a visual auxiliary safety system. A typical HUD is composed of a specially handled head-up mirror, an overhead projector, a computer and a display panel. The display panel shows some relevant graphics and text information on the front windshield before the driver, and presents the driving information from the head-up angle. So, the driver can get relevant information immediately in large view on the eye-level platform. In this way, driving safety is improved. HUD system was originally used in the field of aviation as a flight auxiliary instrument. After years of technology improvements, it has now been used on automobiles widely [2, 3].

Locomotive drivers, train drivers and metro drivers are obliged to retrieve much information during driving. The loss of drivers' focus on the front orbit can cause the longer reaction time when the train is under emergency situations. This risk is amplified when the velocity increases. HUD can be a proper solution to reduce the risk by showing the driving information on the front windshield, which helps

---

A. Su (✉)

CRRC ZHUSHOU Institute Co., Ltd, Zhu Zhou, Hu Nan, China

e-mail: suaj@csrzc.com

© Springer Nature Singapore Pte Ltd. 2018

L. Jia et al. (eds.), *Proceedings of the 3rd International Conference on Electrical and Information Technologies for Rail Transportation (EITRT) 2017*, Lecture Notes in Electrical Engineering 482, [https://doi.org/10.1007/978-981-10-7986-3\\_80](https://doi.org/10.1007/978-981-10-7986-3_80)

801



drivers to get information faster and safer, and is of great significance to improve the safety performance of vehicles [4]. In order to change the presenting method of information and improve the safety of driving, an information combination and a representation on the drivers' eye-level platform are required. This article focuses on the research of train mounted head-up display system and introduces the overall structure of HUD and the composition of DLP display system. Finally, this paper gives the experiments results of train mounted HUD to justify the design and the feasibility of the system.

## 2 Train Mounted Head-up Display System

### Head-up Display Structure

The train mounted head-up display system is a platform for interactive information exchange between a driver and a vehicle. The system involves the interaction between human being and equipments. The relationship between human—machine—environment in the cab should be taken into full consideration in designing the HUD, so as to achieve the integrity of the three major factors. Consequently, the train mounted HUD is designed as shown in Fig. 1. The display installed below the driver's console can project the received data onto the front windshield.

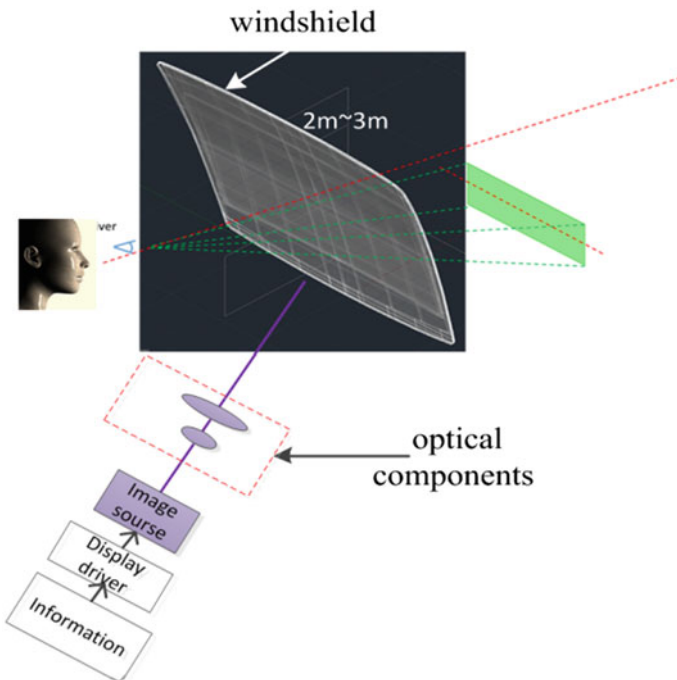


Fig. 1 HUP structure

As shown in Fig. 1, the train mounted HUD consists of four parts: optical components, image source components, display driver components and forward windshield. The HUD projects a colorful image in about  $400 \times 200$  mm onto the windshield that is 2–3 m ahead of the driver. The optical components make the information from the image source form an image in front of the observers, and the display driver transforms vehicle information and video signals into images, which is the video source of head-up display system.

### 3 HUD Based on DLP Display Technology

*Hardware Design* As one of the three representative products of MEMS (Micro Electro Mechanical Systems), the DMD (Digital Micro-mirror Devices) shows unique advantages in DLP [5–7]. The HUD system adopts DLP display technology, whose internal projection devices includes three parts such as projection light source, display chips and optical devices, is primarily used to light source display chips with high brightness, and projects the images in display chips onto the screen using the optical system. Hardware design of DLP includes overall frame, principle of DLP core chipset, power supply and circuits. There are four key parts in the DLP inner functional module, namely DMD controller, DMD driver, DMD digital micro-mirror and an independent power module. The independent power module is added for projection part as a stable power supply of the light source. Figure 2 shows the hardware structure of DLP.

#### DMD Controller

The micro-mirror controller is designed to convert the image format and optimize the image. It is used to adjust color space, reduce signal noise and unify the signals into the same frame rate. Subsequently, image color quality and resolution are adjusting.

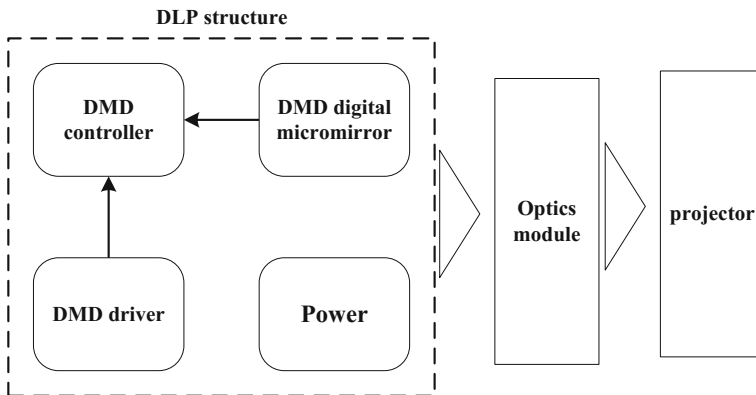


Fig. 2 Hardware structure of DLP

### DMD Driver

The DMD driver, whose function is converting the video signals, transforms multimedia data into binary format. Different bits in this data express different meanings, including time information mostly, initialization, refreshing and stop as well. The DMD devices are used for optical processing when the system is working. The micro-mirror wafer keeps on starting and the original position restoring process until the end of the addressing of all of the binary format data.

### DMD Micro-mirror

On the basis of the received video image signals, micro-mirror wafer transforms between the positive angle and negative angle. When wafer turns to the positive angle, the reflected light beam of the micro-mirror builds bright spots on the projection screen through the light hole; otherwise, the reflected light beam is blocked on the outside of the light hole by the micro-mirror wafer, and the screen will display dark spots instead. After constantly updating operations, the micro-mirror wafer displays the input signals on the projection screen.

### Power Module

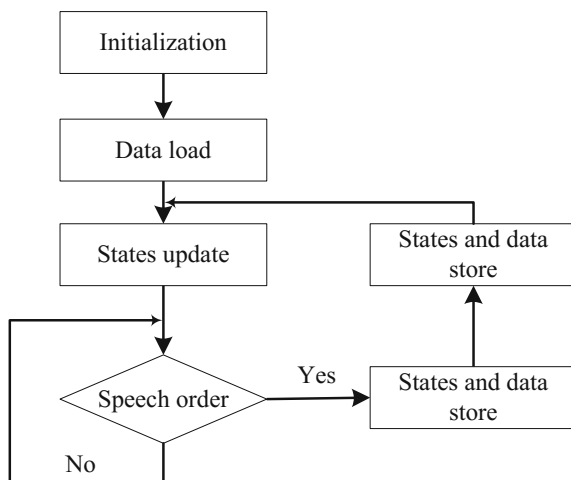
The main reference factors for the employment of DLP power supply are proved to be energy consumption optimization and the stability of power supply. Selections can be different depend on the corresponding light sources.

### Optical Components

The design of optical system mirror group structure should be optimized based on the installation angle in order to display clear images on the front windshield.

*Software Design* The software system of DLP is the main component of the whole system design, which realizes the control and management of each function unit module. Figure 5 shows the flow chart of the main program of the system software (Fig. 3).

**Fig. 3** Flow chart of the main program of system software



In the main program of the system, the initialization is completed first, which includes the initialization of system memories, ports, chips and circuits. The data loading of the initial state of the system and working parameters are finished afterwards. After that, it updates the system displays and states according to the data loaded. These three steps consists the work of initial stage of the system. Following that the state machine steps into the main loop, in which the system recognizes the received speech orders via the sound-pickup, and finishes the related functional operations. After performing the corresponding functions, the state machine reenters the next loop and checks if there are standing requests.

*Head-up Display Driver* Digital and analog signals can be received, and transformed into red, green and blue (RGB) data by DLP chipset through the inner video processing [8, 9]. Thus, the video sources of the HUD system can be from the display content of original monitor of the train. The hardware interface connects the monitor and DLP system via Ethernet to provide video sources for HUD. However, HUD is a better choice than the original monitor, which means an additional display driver in the DLP should be employed to provide video sources. The DLP hardware is based on the ARM system and is mounted to the embedded system via the I2C interface, and the display driver system is constructed by the Ethernet, serial ports and network transmission software.

*Experimental Verification* In order to verify the performances of HUD based on DLP display technology, we carried out the comparison by projecting images onto specific demonstration glass and real train windshield respectively. Figures 4a, b are the effects when images are projected onto a demonstration glass, the contents show the relevant information of vehicle. Clear and colorful images are presented and the brightness can be adjusted according to the outside light intensity.

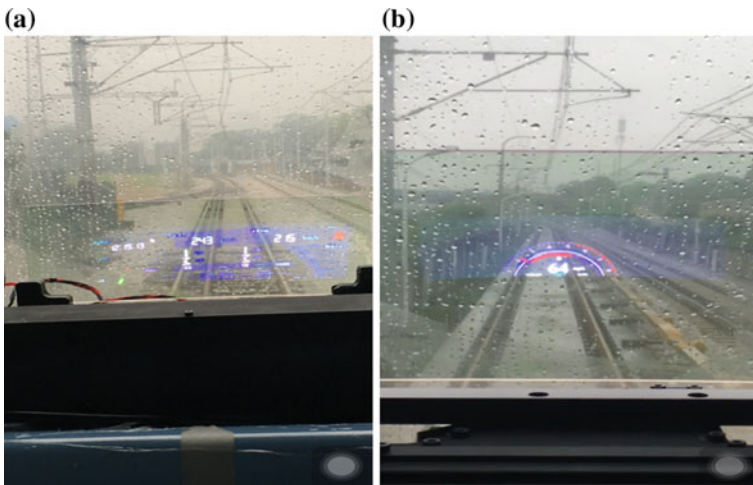


Fig. 4 DLP projected on the demonstration glass

**Fig. 5** DLP projected on the windshield of the train



The driver can simultaneously observe the external environment as well. Figure 5 is the projection effect of a real train windshield, since the projection device has not used any specific optical adjustment for the train windshield, we can find double images in the projection result, and the image size has distorted, nevertheless, the color and the brightness is still ideal.

From the experimental results, the key factors determining the performance of HUD involve the installation location of display, specific parameter of the front windshield including curvature, inclination and so on. The mentioned aspects should be concerned when we adjust the DLP display system and the optical mirror group for the ideal display performances.

## 4 Conclusion

This paper introduces a train mounted HUD system based on DLP display technology, and elaborates the design of the system, including hardware, software and display driver. By analyzing the projection effects of the system on the demonstration glass and on the train windshield, the experiment shows that the decisive factors affecting the display performances lie in meeting the installation angle of the windshield by adjusting the optical mirror. Simultaneously, we can find out the fact from demonstration that HUD can acquire vehicle information in the projection

display without influencing the driver to observe the front road conditions. Therefore, HUD system can improve traffic safety, and provide a better man-machine interactive experience for the driver, which is an ideal train auxiliary visual system.

## References

1. Liu X (2014) The HUD technology in the field of aviation. *Sci Technol Info* 13. (in Chinese)
2. Zhu F (2014) The HUD technology and application. *Sci Wind* (14):73–73. (in Chinese)
3. Zhang J (2014) Design of train-mounted HUD interface and vision. *J Shan Dong Industrial art Inst* (2):41–46. (in Chinese)
4. Wang X, Qi Q (2014) The HUD technology. *Light Control* 21(1):55–58 (in Chinese)
5. Michael R (2003) Douglass DMD reliability: a MEMS success story. *Proc SPIE* 4980:1–11
6. Migl TW (2001) Interfacing to the digital micro-mirror device for home entertainment applications. In: *Proceedings of IPACK'01, Kauai, Hawaii, USA, 2001*, pp 1–81
7. Tian W (2003) Calculation between shrapnel and foundation. *J Instruments* 24(S):528–530. (in Chinese)
8. Tewetai C (1994) Electronic control of a digital micromirror device for projection displays. *IEEE Solid-state Circuits Dig Technical Pap* 37:130–131
9. Mo Z (2009) The driver circuit based on the TI DLP technology. *Optics Instruments* (12):48–51

# An Effective Detection Algorithm of Zebra-Crossing

Zu Sheng Chen and Dao Fang Zhang

**Abstract** In order to improve the function of driver-assistance system, this paper proposes a real-time detection method of zebra crossing based on the on-board monocular camera, it doesn't only detect the zebra crossings we can see from the road, but also detect some zebra crossings obscured by other objects. Firstly, integral method based on horizontal projection is used to separate possible zebra crossings from lane. However, the integral of other road traffic signs may be similar to a zebra crossing, in order to overcome this problem, the number of identifier are calculated respectively for each effective projection region, it is obvious that the number of zebra crossing are more than others, experimental results show that our method proposed in this paper is effective.

**Keywords** Traffic · Signs zebra · Crossings projection · Integral detection

## 1 Introduction

With the development of urbanization and the popularization of automobiles, the number of cars are increasing, urban traffic congestion, traffic accident frequency has become a serious social problem. The driver-assistance system based on computer vision is one of the important measures to solve traffic safety and transportation efficiency. It mainly includes three aspects: road recognition, collision detection and traffic sign recognition. In the field of road recognition and collision detection, it has achieved many good results. However, there are few studies on recognition of road traffic sign, especially detection of zebra crossing [1–4]. Zebra crossings are found by detecting a groups of parallel lines, then, edges are segmented using gray intensity variation [5]. This method is to estimate the pose of zebra-crossings using homography search approach and a priori model. But the algorithm is working slowly, so it is hard to meet real-time requirement. A robust

---

Z. S. Chen · D. F. Zhang (✉)  
Guizhou University for Nationalities, Guiyang, China  
e-mail: 1042542950@qq.com

© Springer Nature Singapore Pte Ltd. 2018

L. Jia et al. (eds.), *Proceedings of the 3rd International Conference on Electrical and Information Technologies for Rail Transportation (EITRT) 2017*, Lecture Notes in Electrical Engineering 482, [https://doi.org/10.1007/978-981-10-7986-3\\_81](https://doi.org/10.1007/978-981-10-7986-3_81)

809

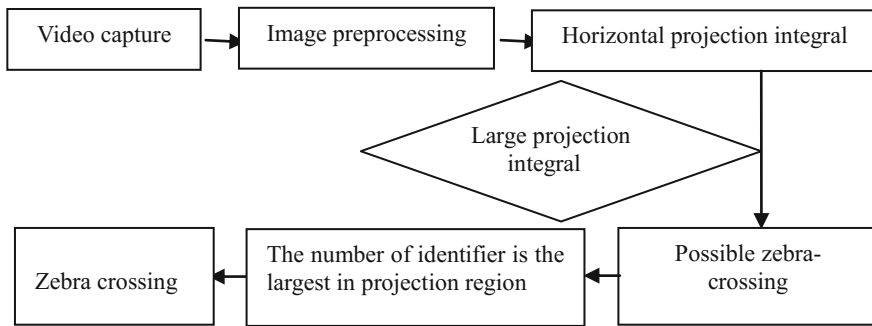


**Fig. 1** Flow chart of zebra-crossing detection algorithm

autonomous detection method of zebra-crossings based on driving assistance system was proposed [6]. Firstly, an aerial view of road image is obtained by inverse perspective map, then, zebra-crossing are recognized by features of shape and appearance. However, distinguishing mistakes are still hard to avoid owing to far distance. A robust detection method of zebra crossings is proposed [7]. Firstly, in order to make image coming from video camera become a top image, the inverse perspective mapping is done; Then, interest area is delineated in top image and segmented using a local threshold; Secondly, each band is extracted from interest region, every length and direction from each region is analysed. Finally, all bands from a zebra crossing are extracted. However, the recognition rate of the method is not high enough. Paper [8] provides a method to detect vehicle that parks in zebra crossing. If the vehicle parked on the zebra crossing is detected, obviously, the car violates the traffic rule. This method is carried out under a fixed camera, and the detection rate is only 90%.

In order to settle above problems, a real-time detection method on zebra crossing based on an on-board monocular camera is proposed in this paper. Firstly, horizontal projection integral is used to distinguish possible zebra crossing from lane. Then, areas with large projection integral are found. Finally, the number of identifier is calculated respectively in the effective projection region. Obviously, there is a zebra crossing in effective projection region that contains most identifier. A flow chart of the detection algorithm is shown in Fig. 1.

## 2 Image Preprocessing

### 2.1 Image Segmentation

In order to segment zebra crossing, a segmentation method based on average gray approximating the optimal threshold is applied in this paper [9].



Given an image  $I_1$ ,  $N_1$  represents the pixel gray sum of  $I_1$ ,  $n_1$  represents the number of pixel in  $I_1$ ,  $G_1 = N_1/n_1$  represents average gray of  $I_1$ . If the gray value less than  $G_1$ , let it become 0, otherwise, gray value maintain unchanged. Then, let the image is  $I_2$ . In this way, let  $N_2$  represents the pixel gray sum, which is more than 0,  $n_2$  represents the number of pixel that gray value is more than 0 in  $I_2$ ,  $G_2 = N_2/n_2$  represents average gray in  $I_2$ , so it went on, until  $G_k = 255$ . Let  $G = \{G_1, G_2, \dots, G_k\}$  make up a set, where  $G_i$  represents the average gray of  $I_i$ . So, an optimal segmentation threshold can be approximated by combination of  $G_i$  and  $G_{i+1}$  or  $G_i$  and  $G_{i-1}$ .

Let

$$L_i = G_{i+1} - G_i, i = 1, 2, \dots, k - 1 \tag{1}$$

$$H_i = L_i/L_{i+1}, i = 1, 2, \dots, k - 1 \tag{2}$$

If  $H_r, r = 1, 2, \dots, k - 1$  is smallest, so, increment of  $G_r$  ( $r$  is corresponding index of  $H_r, r = 1, 2, \dots, k - 1$ ) is slowest. So an optimal threshold (th) can be obtained from Eqs. (3)–(5).

When  $r = 1$

$$\text{th} = \begin{cases} G_{r+1} - G_r, & \text{if } (G_{r+1} - G_r > G_r) \\ G_{r+1}, & \text{if } (G_{r+1} - G_r \leq G_r) \end{cases} \tag{3}$$

When  $r \geq 1$

(1) if  $H_{r+1} - H_r \leq 1$ , the th is

$$\text{th} = \begin{cases} G_{r+1} - G_r, & \text{if } (G_{r+1} - G_r > G_r) \\ G_{r+1}, & \text{if } (G_{r+1} - G_r \leq G_r) \end{cases} \tag{4}$$

where  $r$  is index of the smallest value  $H_r, r = 1, 2, \dots, k - 1$ .

(2) if  $H_{r+1} - H_r > 1$ , the th is

$$\text{th} = \begin{cases} G_r - G_{r-1}, & \text{if } (G_r - G_{r-1} > G_{r-1}) \\ G_r, & \text{if } (G_r - G_{r-1} \leq G_{r-1}) \end{cases} \tag{5}$$

where  $r$  is index of the smallest value  $H_r, r = 1, 2, \dots, k - 1$ .

The segmentation result of an image is shown in Fig. 2.

## 2.2 Image Filtering

In order to decrease noise interference, binary image is firstly filtered. The purpose is to filter larger area and smaller area, including isolated noise points. The region

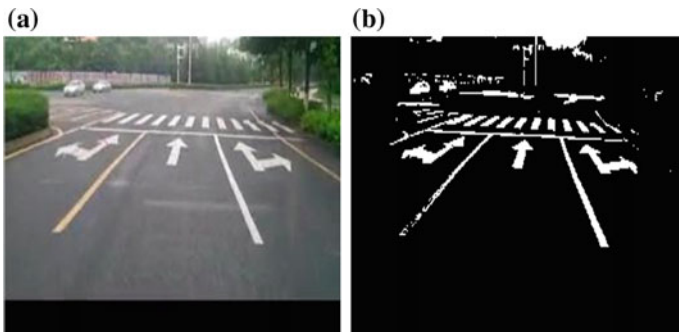


Fig. 2 a Original image, b Segment image

Fig. 3 Filtering image



mark is to obtain the square and coordinate of each region so that the image can be processed further. For a given binary image  $I$ ,  $N$  is defined as tagged region number,  $s(i)$  is the square of  $i$ th mark area and  $x_{\min(i)}$ ,  $x_{\max(i)}$ ,  $y_{\min(i)}$ ,  $y_{\max(i)}$  are defined as position coordinates of region  $i$ . Then larger area region and smaller area region are removed, which are more than or less than zebra crossing. The threshold value of removing larger area region is  $T_1$  and the threshold of removing smaller area region is  $T_2$ . The result of filtering image is shown in Fig. 3.

### 3 Zebra Crossing Detection

#### 3.1 The Basic Principle of Zebra Crossing Detection

The zebra crossing on the road has a distinct feature, it is made up of many rectangular areas in the middle of the road. The simplified diagram of zebra crossing is shown in Fig. 4. Horizontal projection integral is shown in Fig. 5. It is obvious that the horizontal projection product is greater at the zebra crossing.

**Fig. 4** A simplified diagram of zebra crossing

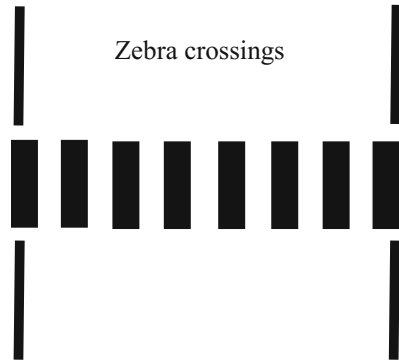
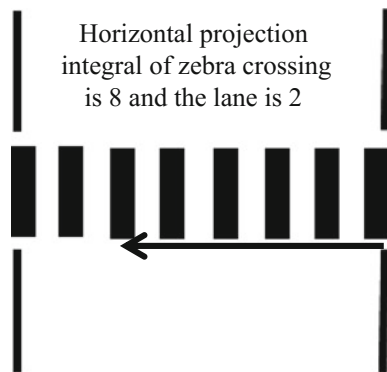


**Fig. 5** Horizontal of projection integral zebra crossing



### 3.2 Image Integral Projection

The projection method is based on the projection distribution feature of an image in some direction, this method is actually a statistical method. Horizontal projection integration of an image is considered in this paper, because of the horizontal projection integration of a zebra crossing is larger than other signs.

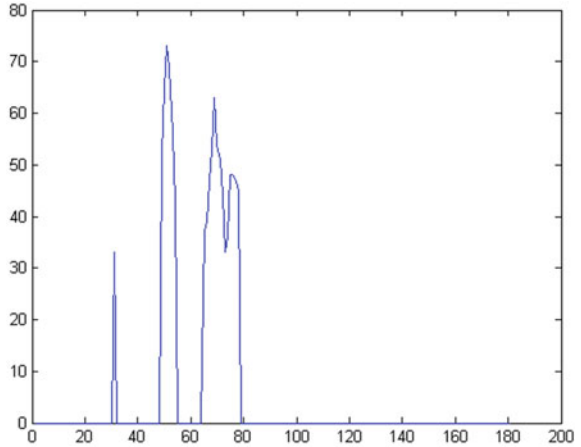
Horizontal projection integral of pixel value from each row in an image is calculated, that is, the statistical value  $h(i)$  of line  $i$  is calculated by Eq. (6)

$$h(i) = \sum_j I(i, j) \tag{6}$$

Statistical results are normalized by Eq. (7)

$$H(i) = \begin{cases} \frac{h(i)}{255} & \text{if } (h(i) > T_3) \\ 0 & \text{otherwise} \end{cases} \tag{7}$$

**Fig. 6** Result of horizontal integral projection



An experimental result of Fig. 3 is shown in Fig. 6, where, the ordinate represents the height of the projection image, and the abscissa represents the position of the target.

### 3.3 Zebra Crossing Detection and Location

We can see from Fig. 4, there are three effective projection areas, therefore, the number of identifier is respectively counted in each effective projection area. If the number of identifier is maximal, it indicates that there is a zebra crossing sign in this area. The detection results of some zebra crossings are shown in Fig. 7.

## 4 Experimental Results and Parameter Analysis

### 4.1 Experimental Results

This algorithm is completed using MATLAB language in win7 operating environment, core i5-7200 CPU, 4 GB. In order to test the validity of this method, 5 video with 50 zebra crossings from different environment are tested, 10 zebra crossings come from the case obscured by other objects, 20 come from the case with good illumination, 10 come from the case with weak light, 8 come from the case with intense light and 2 come from the case with damage. The experiment results are shown in following Table 1.



**Fig. 7** Some experimental results of zebra detection

**Table 1** Data statistics of zebra crossings detection

Different conditions	Number of zebra crossing	Successful detection
Obscured	10	8
Good light	20	20
Weak light	10	10
Intense light	8	8
Damage badly	2	0
Total	50	46
Accuracy rate	92%	

### 4.2 Parameter Analysis

There are three parameters in our system, which are respectively  $T_1, T_2, T_3$ . Here,  $T_1, T_2, T_3$  are assigned by 80,2500,45 in our experiment, they play a crucial role in the detection of zebra crossing. However, these parameters are obtained based on the actual situation, and the future work is to find new methods to make these parameters become adaptive values, and they can adapt to a variety of complex road scenes.

## 5 Conclusion

The method presented in this paper is not only simple but also easy to implement. In addition, less time is consumed, it is only 0.083 s, so, it can meet real-time requirement. Of course, this paper also has some problems. Firstly, the zebra crossings are severely blocked, this method will fail. What’s more, when the zebra crossings are severely damaged, our method is also not enough to solve these problems.

**Acknowledgements** This work was supported by Science Technique Department of Guizhou Province of China ([2014]2096).

## References

1. Kheyrollahi A, Breckon TP (2012) Automatic real-time road marking recognition using a feature driven approach. *Mach Vis Appl* 23(1):123–133
2. Sampathkumar J, Rajamani K (2013) Automatic detection of zebra crossing violation. In: *Proceedings of the fourth international conference on signal and image processing 2012 (ICSIP 2012)*, India, pp 499–509
3. Ng HF (2004) Automatic thresholding for defect detection. *Pattern Recogn Lett* 27(14):1644–1649
4. Zhou ZZ, Yu HY, Zhao ZF, Qiao XL. (2010) SS-based sketch recognition for graphics of traffic accident. In: *Proceedings of seventh international conference on fuzzy systems and knowledge discovery Yantai, China*, pp 2558–2562
5. Se S (2000) Zebra-crossing detection for the partially sighted. In: *2013 IEEE conference on computer vision and pattern recognition vol (2)*, pp 2211–2211
6. Wang C, Zhao C, Wang H (2014) Robust zebra-crossing detection for autonomous land vehicles and driving assistance systems. *Appl Mech Mater* 556–562:2732–2739
7. Li H, Feng MY, Wang X (2012) A zebra-crossing detection algorithm for intelligent vehicles. *Appl Mech Mater* 236–237:390–395
8. Ahmetovic D, Bernareggi C, Gerino A, Mascetti S (2014) Zebra recognizer: efficient and precise localization of pedestrian crossings. In: *Proceedings of international conference on pattern recognition*, pp 2566–2571
9. Chen ZS, Wu YF (2014) A segmentation method of traffic marking based on Average gray approximating the optimal threshold. In: *Proceedings of conference on 2nd international conference on signal processing, image processing and pattern recognition Guilin, China*, pp 3510–3513

# A Node Pair Entropy Based Similarity Method for Link Prediction in Transportation Networks

Zundong Zhang, Weixin Ma, Zhaoran Zhang and Huijuan Zhou

**Abstract** Link prediction is a challenging problem. It is an approach to determine the possibility of potential or missing link between node pairs in a network. Researches on transportation network's link prediction are mainly about travel time prediction, path prediction, traffic flow prediction, congestion prediction and so on. However, current studies are restrained by direction of the link or a new route. To solve this problem, a node pair entropy based similarity method for link prediction is proposed. Firstly, the initial state of all nodes in the node pair are initialized. Then, the influence weights of upstream node to lower nodes and the feedback state are determined. So the uncertainty degree of a path is obtained. Finally, the link prediction of the unconnected node pair is measured by node pair entropy. This method differentiates the roles of different nodes, and the connection between the common points is considered. It becomes a good solution for transportation network's link prediction.

**Keywords** Transportation networks · Link prediction · Node pair entropy  
Similarity-based method

## 1 Introduction

Link is the connection of nodes in networks. Link prediction plays an important role in measuring the complexity of networks, which draw great interests among different subjects. Finding the missing and the potential links between two unconnected nodes by estimating the existence likelihood of interacted nodes is the chief target of this work. Any domain where entities interact in a structured way can potentially benefit from link prediction.

---

Z. Zhang (✉) · W. Ma · Z. Zhang · H. Zhou  
Beijing Key Lab of Urban Road Transportation Intelligent Control Technology,  
North China University of Technology, Beijing, People's Republic of China  
e-mail: zdzhang@ncut.edu.cn

© Springer Nature Singapore Pte Ltd. 2018  
L. Jia et al. (eds.), *Proceedings of the 3rd International Conference on Electrical and Information Technologies for Rail Transportation (EITRT) 2017*, Lecture Notes in Electrical Engineering 482, [https://doi.org/10.1007/978-981-10-7986-3\\_82](https://doi.org/10.1007/978-981-10-7986-3_82)

A large numbers of link predictions approaches have been proposed, including similarity-based methods, probabilistic and statistical methods, algorithmic method, preprocessing methods, etc. Specifically, similarity-based methods can be classified into three types: Local methods are usually defined by using node neighborhood-related structural information, global methods are defined based on the whole network topological information, and Quasi-local methods are defined between global and local network topological information. Generally, the prediction accuracy of local indices is the lowest among the three groups of indices. However, the computational cost of local indices is the smallest among three. Global indices are the opposite of local indices, while quasi-local indices fall in between them. Most of the local index (such as HPI [1], HDI [1], PA [2], etc.) based on the assumptions: for predicting node pairs, the contribution of each element in the set of common neighbor nodes is same. So it is not conducive to distinguish the contribution of each common neighbor. In order to solve this problem, the contribution of different common neighbor nodes is given by assigning the weights of each node (e.g. (AA) [3–5] (RA) [6] (LNB) [7]). However, these method ignored the influence of the connection among adjacent nodes. The core of these algorithms is the clustering coefficient of the common nodes. Katz index will be more comprehensive consideration of the factors of network structure, and further improve the calculation accuracy, This algorithm takes into account the four level path, the five level path, and even the  $n$  level path, and has lower time complexity with the increase of the path level [8]. The global Leicht-Holme-Newman index (GLHN) is based on the same fundamentals that the Katz index used [9].

In this paper, we proposed a new node pair entropy method to illustrate the association between two nodes, networks with directional weights, the process of transferring the weight to the downstream node can be equal to the process that the node exerts influence on the downstream node. In order to quantify the influence of this transfer, the concept of entropy is proposed to describe the uncertainty of the transfer process between nodes. For any node pair, the greater their node pair entropy is, the greater the uncertainty between them. It means the transmission of information is more likely to happen between them. Furthermore, the smaller value of entropy is, the more crowded of path between two nodes will be. This method is not affected by the direction and the new route.

## 2 Link Prediction

Previous research on link prediction in transportation network, which is the variable type of Probability or opportunity cost of route choice for drivers, usually based on historical data to build probabilistic model. According to the prediction distance, which is divided into two kinds, short distance prediction method and long distance prediction method. Short distance prediction method, which included Markoff prediction [10]. Shortest path, method, Dijkstra's algorithm, etc., was defined with local observation data. However, the direction of the road (for instance a single



lane) interfered with these methods. The Long distance prediction method was based on the global observation data., then matching the current travel route with the historical route mode to achieve the prediction of the future route. But these methods will be out of action for new routes.

Entropy-Based Method has been a tool for qualifying the complexity of networks structure, classified into probabilistic and statistical methods [11]. Furthermore, Due to the connection between node pairs can be translated into information entropy, and link can represent for the strength of these connection, so information entropy is closely connected with link prediction. Xu. studied the contributions of paths in link prediction based on node pair entropy, and finally provided a node pair entropy based similarity index [12]–[13]. However, the above Entropy-Based Method are only valid in undirected networks.

The Node Pair Entropy link prediction method, which prototype is Shannon entropy, is used for quantify the uncertainty of information transfer between two nodes in a network. And this method satisfies three basic requirements of information measurement: the total weight propagation from independent paths is the sum of the uncertainties of each receiver; the uncertainties of remover is monotone correlation with the weight propagation from independent paths; the whole process is computable.

### 3 The Node Pair Entropy Based Similarity Method

In the information theory, the uncertainty of the event depends on the probability of its occurrence. The probability space must suit such requirement: The events in the probability space are not compatible with each other. Among the probability space the probability of all events must be nonnegative.

So, It is therefore possible to formulate the node pair entropy  $H(v_i v_j)$  between any two nodes (i, j) as follows

$$H(v_i v_j) = - \sum P_l \ln P_l \quad (1)$$

$P_l$  represent the probability of transmitting the corresponding weight on a path in the propagation process, then The problem of calculating the node pair entropy between any two nodes translate into the problem of computing the probability of the corresponding weight of any path between nodes.

For a non-adjacent node pair (Va, Vb),  $M_i(v)$  represents the state of the V in layer i. The value of the initial node M (Va) is the sum of its downstream edge weight  $w(e)$ , and for the other nodes the value of M (V) assigned with 0.

$$\begin{aligned}
 M_0(V_a) &= \sum w(e); \\
 M_0(V_1) &= M_0(V_2) = M_0(V_3) = \dots = M_0(V_b) = 0
 \end{aligned}
 \tag{2}$$

From the initial node  $V_a$  pass the value of  $N_i(e)$  to its downstream nodes layer by layer. The value of  $N_i(e)$  can be computed as:

Sort the weight of the downstream edge in ascending order. When the sum of downstream weights is less than the state value of upstream node, then

$$\begin{aligned}
 \sum w(e) &\leq M_{i-1}(V) \\
 N_i(e) &= w(e)
 \end{aligned}$$

While

$$\sum w(e) > M_{i-1}(V)$$

For

$$\sum w(e) - w(e)_{\max}$$

Until

$$\begin{aligned}
 \sum w(e) &\leq M_{i-1}(V_a) \\
 N_i(e) &= w(e)
 \end{aligned}
 \tag{3}$$

Priority principle:

we give prioritizing distribution to the edges, which downstream node is the upstream node on the other edges.

If not, selecting any edge of the smallest value randomly, and the value of  $N_i(e)$  to this edge can be described as

$$N_i(e) = M_{i-1}(V) - \sum w(e)
 \tag{4}$$

Each pass, the state value of the upstream node corresponding to reduce the weight of its downstream edge, the state value of the downstream node corresponding to add this value.

The transmission method is parallel transmission.

$$\begin{aligned}
 M_i(v_{\text{up}}) &= M_{i-1}(v_{\text{up}}) - N_i(e) \\
 M_i(v_{\text{down}}) &= M_{i-1}(v_{\text{down}}) + N_i(e)
 \end{aligned}$$

Other nodes

$$M_i(v) = M_{i-1}(v) \quad (5)$$

The information transmission probability from upstream node to downstream node can be computed with follow formula:

$$P_i(v_{\text{up}}v_{\text{down}}) = \frac{N_i(e)}{M_{i-1}(v_{\text{up}})} \quad (6)$$

The contribution probability of a node can be expressed as:

$$P_i(v) = \sum_{i=1}^i P_i(v) \quad (7)$$

$$P_l = \prod (P_i(v)) = \prod \left( \sum_{i=1}^i P_i(v) \right) \quad (8)$$

Thus, the node pair entropy can be expressed as:

$$H(v_i v_j) = - \sum P_l \ln P_l = - \sum \left( \left( \prod \left( \sum_{i=1}^i P_i(v) \right) \right) \ln \left( \prod \left( \sum_{i=1}^i P_i(v) \right) \right) \right) \quad (9)$$

## 4 A Simple Example

Here a simple example is given to illustrate the entropy between  $V_0 V_t$

### 4.1 Original Data

See (Fig. 1).

The following table represent the edges between nodes and their corresponding weights (Tables 1 and 2).

Fig. 1 Example network

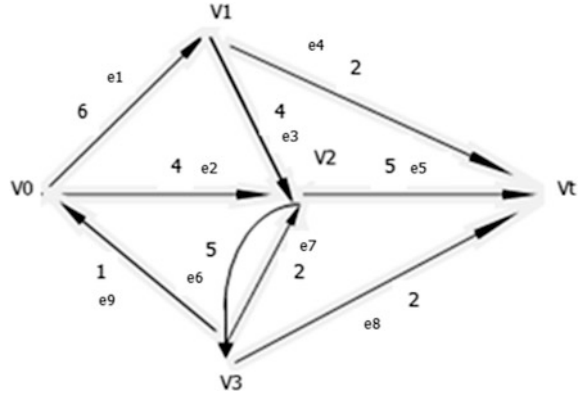


Table 1 Edges between nodes

	V0	V1	V2	V3	Vt
V0		e1	e2		
V1			e3		e4
V2				e6	e5
V3	e9		e7		e8
Vt					

Table 2 Weights of edges in Table 1

	V0	V1	V2	V3	Vt
V0		6	4		
V1			4		2
V2				5	5
V3	1		2		2
Vt					

### 4.2 Calculation Process

Firstly, the initial state of all nodes in the node pair are initialized:

$$M_0(V_0) = \sum w(e) = 6 + 4 = 10;$$

$$M_0(V_1) = M_0(V_2) = M_0(V_3) = M_0(V_t) = 0$$

Then, the influence weights of upstream node to lower nodes and the feedback state are determined:

$$\begin{aligned}
N_1(e_2) &= w(e_2) = 4; N_1(e_1) = w(e_1) = 6 \\
M_1(V_2) &= M_0(V_2) + N_1(e_2) = 0 + 4 = 4 \\
M_1(V_1) &= M_0(V_1) + N_1(e_1) = 0 + 6 = 6 \\
M_1(V_0) &= M_0(V_0) - N_1(e_1) - N_1(e_2) = 10 - 6 - 4 = 0 \\
M_1(V_3) &= M_0(V_3) = 0 \\
M_1(V_i) &= M_0(V_i) = 0
\end{aligned}$$

The uncertainty degree of a short road:

$$\begin{aligned}
P(V_0V_2) &= N_1(e_2)/M_0(V_0) = \frac{4}{10} = \frac{2}{5} \\
P(V_0V_1) &= N_1(e_1)/M_0(V_0) = \frac{6}{10} = \frac{3}{5}
\end{aligned}$$

The processing of downstream nodes is the same as above, until the endpoint or initial node is found:

$$\begin{aligned}
N_2(e_3) &= w(e_3) = 4; N_2(e_4) = w(e_4) = 2 \\
M_2(V_2) &= M_1(V_2) + N_2(e_3) = 4 + 4 = 8 \\
M_2(V_i) &= M_1(V_i) + N_2(e_4) = 0 + 2 = 2 \\
M_2(V_1) &= M_1(V_1) - N_2(e_3) - N_2(e_4) = 6 - 4 - 2 = 0 \\
M_2(V_3) &= M_1(V_3) = 0 \\
M_2(V_0) &= M_1(V_0) = 0 \\
P(V_1V_2) &= N_2(e_3)/M_1(V_1) = \frac{4}{6} = \frac{2}{3} \\
P(V_1V_i) &= N_2(e_4)/M_1(V_1) = \frac{2}{6} = \frac{1}{3}
\end{aligned}$$

Then, we find a path  $(V_0V_1V_i)$ , and calculate the uncertainty degree of it:

$$\begin{aligned}
P(V_0V_1V_i) &= P(V_0V_1) \times P(V_1V_i) = \frac{3}{5} \times \frac{1}{3} = \frac{1}{5} \\
P(V_0V_1V_2) &= P(V_0V_1) \times P(V_1V_2) = \frac{3}{5} \times \frac{2}{3} = \frac{2}{5}
\end{aligned}$$

At the same time, we obtain the uncertainty of the downstream nodes:

$$P(V_2) = P(V_0V_2) + P(V_0V_1V_2) = \frac{2}{5} + \frac{2}{5} = \frac{4}{5}$$

The next points and paths are calculated as above:

$$\begin{aligned}
 P(V_0V_1V_2V_t) &= P(V_2) \times P(V_2V_t) = \frac{4}{5} \times \frac{3}{8} = \frac{3}{10} \\
 P(V_3) &= P(V_0V_1V_2V_3) = P(V_2) \times P(V_2V_3) = \frac{4}{5} \times \frac{5}{8} = \frac{1}{2} \\
 P(V_0V_1V_2V_3V_0) &= P(V_3) \times P(V_3V_0) = \frac{1}{2} \times \frac{1}{5} = \frac{1}{10} \\
 P(V_0V_1V_2V_3V_t) &= P(V_3) \times P(V_3V_t) = \frac{1}{2} \times \frac{2}{5} = \frac{1}{5} \\
 P(V_2) &= P(V_0V_1V_2V_3V_2) = P(V_3) \times P(V_3V_2) = \frac{1}{2} \times \frac{2}{5} = \frac{1}{5} \\
 P(V_0V_1V_2V_3V_2V_t) &= P(V_2) \times P(V_2V_t) = \frac{1}{5} \times 1 = \frac{1}{5}
 \end{aligned}$$

In this way, we get uncertainty degree of five paths. So the entropy will be Confirm by following formula:

$$\begin{aligned}
 H(v_0v_t) &= - \sum P_l \ln P_l = - \left( \frac{1}{5} \ln \frac{1}{5} + \frac{3}{10} \ln \frac{3}{10} + \frac{1}{10} \ln \frac{1}{10} + \frac{1}{5} \ln \frac{1}{5} + \frac{1}{5} \ln \frac{1}{5} \right) \\
 &= 1.56
 \end{aligned}$$

$H(v_0v_t) = H(v_tv_0)$  It shows that the node entropy is independent of the initial node, and further explained that the node pair entropy can explain the interaction strength between the two nodes.

The node pair entropy between  $v_0$  and the other nodes is zero. This shows that the path between  $v_0$  and these nodes is very smooth. Therefore, this value is practical. The highest path level between  $(v_0v_t)$  is 5. The higher the number of layers considered, the greater value of node pair entropy we will get. When this theory is applied to the transportation network, it is obvious that the greater value of node pair entropy is, the more crowded the area is. The number of layers can be adjusted for different requirements. If we want to get this value of the whole network, we must take into account all the layers.

## 5 Conclusion

In this paper, we proposed node pair entropy based similarity method for link prediction in transportation network in which the contributions from nodes and their connection can be measured and combined in terms of their values of information. By introducing the recent study on similarity for link prediction, we designed the node pair entropy which prototype is Shannon entropy, based on entropy to quantify the uncertainty of information transfer between two nodes in a network.

Compared to other methods, this method takes into account the four level search path, the five level search path, and even the n level search path, and not affected by the direction and the new route. Our next step will be to do experiments to verify the importance of this method.

**Acknowledgements** This paper is supported by The Chinese the State 13 Five-year Scientific and Technological Support Project (2016YFB1200402), The Big-Data Based Beijing Road Traffic Congestion Reduction Decision Support Project (PXM2016014212000036) and The Project of The Innovation and Collaboration Capital Center for World Urban Transport Improvement (PXM2016014212000030).

## References

1. Ravasz E, Somera AL, Mongru DA et al (2002) Hierarchical organization of modularity in metabolic networks. *Science* 297(5586):1551
2. Mitzenmacher Michael (2003) A brief history of generative models for power law and lognormal distributions. *Internet Mathe* 1(2):226–251
3. Liben-Nowell D, Kleinberg J (2007) The link-prediction problem for social networks. *J Assoc Info Sci Technol* 58(7):1019–1031
4. Adamic LA, Adar E (2003) Friends and neighbors on the Web. *Soc Netw* 25(3):211–230
5. Martínez V, Berzal F, Cubero JC (2016) Adaptive degree penalization for link prediction. *J Comput Sci* 13:1–9
6. Lü L, Jin CH, Zhou T (2009) Similarity index based on local paths for link prediction of complex networks. *Phys Rev E Stat Nonlin Soft Matter Phys* 80(4 Pt 2):046122
7. Li RH, Yu JX, Liu J (2011) Link prediction: the power of maximal entropy random walk. In: *ACM International conference on information and knowledge management, ACM*, pp 1147–1156
8. Katz L (1953) A new status index derived from sociometric analysis. *Psychometrika* 18 (1):39–43
9. Leicht EA, Holme P, Newman ME (2006) Vertex similarity in networks. *Phys Rev E Stat Nonlin Soft Matter Phys* 73(2 Pt 2):026120
10. Simmons R, Browning B, Zhang Y et al (2006) Learning to predict driver route and destination intent. In: *IEEE intelligent transportation systems conference, IEEE*, pp 127–132
11. Mowshowitz A (1967) Entropy and the complexity of graphs. University of Michigan, pp 225–240
12. Xu Z, Pu C, Yang J (2016) Link prediction based on node pair entropy. *Physica A Stat Mech Appl* 456(5):294–301
13. Xu Z, Pu C, Sharafat RR et al (2016) Entropy-based link prediction in weighted networks. *Chinese Physic b English* 1:588–594

# Transfer Domain Class Clustering for Unsupervised Domain Adaptation

Yunxin Fan, Gang Yan, Shuang Li, Shiji Song, Wei Wang and Xiping Peng

**Abstract** In this paper, we propose a transfer domain class clustering (TDCC) algorithm to address the unsupervised domain adaptation problem, in which the training data (*source domain*) and the test data (*target domain*) follow different distributions. TDCC aims to derive new feature representations for source and target in a latent subspace to simultaneously reduce the distribution distance between two domains, which helps transfer the source knowledge to the target domain effectively, and enhance the class discriminativeness of data as much as possible by minimizing the intra-class variations, which can benefit the final classification a lot. The effectiveness of TDCC is verified by comprehensive experiments on several cross-domain datasets, and the results demonstrate that TDCC is superior to the competitive algorithms.

**Keywords** Feature learning · Distribution adaptation · Domain adaptation  
Transfer learning

## 1 Introduction

Traditional machine learning algorithms assume that the labeled training data (*source domain*) and unlabeled test data (*target domain*) are sampled from the identical distribution. However, in the real-world applications, the training and test samples often follow different distributions due to various factors, and the conventional algorithms cannot perform well in these scenarios. Domain adaptation approaches aim to transfer knowledge from the source domain to construct an

---

Y. Fan · G. Yan (✉) · W. Wang · X. Peng  
The State Key Laboratory of Heavy Duty AC Drive Electric Locomotive  
Systems Integration, Hunan, China  
e-mail: yan.x.gang@163.com

S. Li · S. Song  
Tsinghua University, Beijing, China



effective model for the target domain, under the situation that both source and target data are from different but related distributions [1].

Domain adaptation methods can be roughly divided into two subcategories. The first one is to solve semi-supervised domain adaptation problem, in which labeled source samples, a small part of labeled target samples and numerous unlabeled target data are accessible. The second category focuses on addressing unsupervised domain adaptation problem, where only unlabeled data are available for the target domain. In this paper, we mainly target at solving unsupervised domain adaptation problem, which is a more challenging task.

In the recent decades, domain adaptation has been extensively studied and widely used in many real-world applications, such as computer vision [2, 3] and text classification [4]. Since the distributions of source and target are different, it is of vital importance to discover a good feature representation in the latent subspace. In this subspace, data of both domains could be draw closer and become similar, then the traditional classification methods can be applied to the unlabeled target domain by learning the labeled data in the source domain. Pan et al. [5] propose a feature extraction algorithm called transfer component analysis (TCA) to decrease the distance of marginal distributions of source and target data by minimizing a maximum mean discrepancy (MMD) metric. Based on TCA, [3] proposes a joint distribution adaptation (JDA) method to minimize the distance of both marginal and conditional distributions across two domains.

In this paper, we propose a transfer domain class clustering (TDCC) algorithm to address several crucial issues in unsupervised domain adaptation problems. First, to effectively mitigate the domain shift across two domains, TDCC aims to learn new feature representations in a latent subspace for source and target by minimizing the distance between both marginal and conditional distributions of the source and target domains. Second, to benefit the final classification for unlabeled target data, TDCC will enhance the discriminative ability of both domains by minimizing the intra-class variations. TDCC enforces the summation of distance between each sample and the class center in each class to be minimized. Third, the conventional classification methods, i.e. Support Vector Machine (SVM) [6] and  $k$ -Nearest Neighbor ( $k$ -NN) [7], can be learned using labeled source data, and be applied to the unlabeled target data. Figure 1 has shown the motivation of TDCC. Comprehensive experimental results on several domain adaptation data sets verify the superiority of TDCC to the existing domain adaptation approaches.

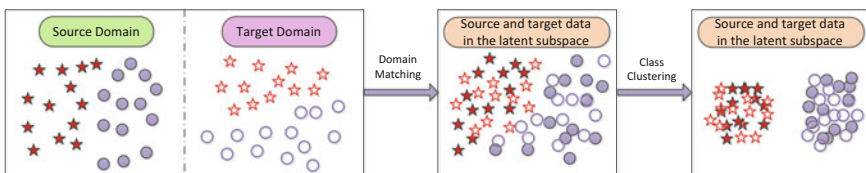


**Fig. 1** The motivation of TDCC. Source and target data follow different distributions. After domain matching and class clustering procedures, samples in both domains become more similar in the latent subspace, and are easier to classify

## 2 Transfer Domain Class Clustering Algorithm

In this section, we will first introduce the problem formulation of unsupervised domain adaptation and the maximum mean discrepancy (MMD) criterion that we use. Then our proposed transfer domain class clustering approach will be presented.

### 2.1 Problem Formulation

In unsupervised domain adaptation problem, we can access a large amount of labeled source data, i.e.  $D_S = \{\mathbf{x}_{S_i}, y_{S_i}\}_{i=1}^{n_S} = \{\mathbf{X}_S, \mathbf{y}_S\}$ , and numerous unlabeled target data, i.e.  $D_T = \{\mathbf{x}_{T_j}\}_{j=1}^{n_T} = \{\mathbf{X}_T\}$ , where  $y_{S_i}$  is the corresponding label of source sample  $\mathbf{x}_{S_i}$ , and  $n_S, n_T$  are the numbers of the source and target data, respectively.

We denote  $P_S(X_S, Y)$  and  $P_T(X_T, Y)$  as the joint distributions of the sample and label in the source and target domains. Since the source domain  $D_S$  and the target domain  $D_T$  follow different probability distributions, i.e.  $P_S(X_S, Y) \neq P_T(X_T, Y)$ , we aim to find a transformation function  $\pi(x)$  which satisfies  $P_S(\pi(X_S), Y) \approx P_T(\pi(X_T), Y)$ . Thus, we propose to match both marginal and conditional distributions of involved domains utilizing maximum mean discrepancy criterion to achieve this goal.

### 2.2 Maximum Mean Discrepancy

Maximum mean discrepancy (MMD) [8] is an effective non-parametric criterion to measure the distance between two different distributions, and MMD has been widely applied to the domain adaptation field. MMD could statistically test whether two probability distributions  $p_1$  and  $p_2$  are identical by measuring the maximum difference between the values of their mean function:

$$\text{MMD}^2(\mathcal{F}, p_1, p_2) = \sup_{f \in \mathcal{F}} \left\| \mathbb{E}_{x_1 \sim p_1} [f(x_1)] - \mathbb{E}_{x_2 \sim p_2} [f(x_2)] \right\|^2. \quad (1)$$

where  $\mathcal{F}$  is a given function class.

A large number of domain adaptation methods use MMD metric to measure the distance between source and target. To compute MMD more effectively, we could utilize the empirical MMD formulation in a reproducing kernel Hilbert space as [3]:

$$\text{MMD}^2(D_S, D_T) = \left\| \frac{1}{n_S} \sum_{i=1}^{n_S} \pi(\mathbf{x}_{S_i}) - \frac{1}{n_T} \sum_{j=1}^{n_T} \pi(\mathbf{x}_{T_j}) \right\|_{\mathcal{K}}^2. \quad (2)$$

Thus, we could reduce the MMD distance between the marginal and conditional distributions of two domains to effectively match the source and target data in the latent subspace.

### 2.3 TDCC Approach

Our proposed transfer domain class clustering approach consists of two parts: domain matching and class clustering. We will introduce them in detail.

#### 2.3.1 Domain Matching of TDCC

Since the distributions of source and target are diverse but related, it is of vital importance to derive domain invariant features across two domains. Then the target data can be predicted correctly by the corresponding source classifier. Specifically, we aim to learn a transformation  $\pi$  to match both marginal and conditional distributions for cross-domain data effectively, which means  $P_S(\pi(X_S)) \approx P_T(\pi(X_T))$  and  $P_S(\pi(X_S)|Y) \approx P_T(\pi(X_T)|Y)$ .

For simplicity, we assume  $\pi(X) = W^T X$  is a linear projection, and MMD metric is applied to measure the distribution distance. To be more precise, we want to minimize:

$$\begin{aligned} \text{MMD}^2(D_S, D_T) = & \left\| \frac{1}{n_S} \sum_{i=1}^{n_S} W^T \mathbf{x}_{S_i} - \frac{1}{n_T} \sum_{j=1}^{n_T} W^T \mathbf{x}_{T_j} \right\|^2 \\ & + \left\| \frac{1}{n_S^c} \sum_{\mathbf{x}_{S_i} \in D_S^c} W^T \mathbf{x}_{S_i} - \frac{1}{\hat{n}_T^c} \sum_{\mathbf{x}_{T_j} \in \hat{D}_T^c} W^T \mathbf{x}_{T_j} \right\|^2, \end{aligned} \quad (3)$$

where  $D_S^c = \{\mathbf{x}_{S_i} : y_{S_i} = c\}$ , and  $c$  is the belonging class of  $\mathbf{x}_{S_i}$ .  $n_S^c$  is the number of samples of source data in class  $c$ . The same rule is also applied for the target data. Because we cannot access the labels of target data, we propose to utilize the pseudo labels of target data, which are predicted by the source classifier. We can also refine the pseudo labels of target data by using the iterative source classifier trained on the learned source features.

If we denote  $\mathbf{X} = [\mathbf{X}_S, \mathbf{X}_T]$ , the MMD distance can be rewrote as:

$$\text{MMD}^2(D_S, D_T) = \sum_{c=0}^C \text{tr}(W^T \mathbf{X} H_c \mathbf{X}^T W), \quad (4)$$

where

$$(H_0)_{ij} = \begin{cases} \frac{1}{n_S^c}, & \mathbf{x}_i, \mathbf{x}_j \in D_S \\ \frac{1}{n_T^c}, & \mathbf{x}_i, \mathbf{x}_j \in D_T \\ -\frac{1}{n_S n_T}, & \text{otherwise,} \end{cases} \quad (5)$$

and

$$(H_c)_{ij} = \begin{cases} \frac{1}{(n_S^c)^2}, & \mathbf{x}_i, \mathbf{x}_j \in D_S^c \\ \frac{1}{(\widehat{n}_T^c)^2}, & \mathbf{x}_i, \mathbf{x}_j \in \widehat{D}_T^c \\ -\frac{1}{n_S^c \widehat{n}_T^c}, & \begin{cases} \mathbf{x}_i \in D_S^c, \mathbf{x}_j \in \widehat{D}_T^c \\ \mathbf{x}_i \in \widehat{D}_T^c, \mathbf{x}_j \in D_S^c \end{cases} \\ 0, & \text{otherwise.} \end{cases} \quad (6)$$

TDCC targets at reducing the distance between source and target in a learned latent subspace by minimizing Eq. (4). However, we believe the class discriminative information is also crucial to improve the classification ability of target data.

### 2.3.2 Class Clustering of TDCC

To explore the underground discriminative information of data in both domains, we want the projection of both data not only to be domain invariant, but also to be class discriminative. This intuition will yield good classification performance for target samples. To be specific, TDCC also minimizes the distance between every sample to their projected class center for each class, which will encourage each class to form a compact cluster. Here, we take the source data as an example to introduce the second loss term of TDCC:

$$\mathcal{L}_{center}^S = \sum_{c=1}^C \sum_{\mathbf{x}_{S_i} \in D_S^c} \left\| W^T \mathbf{x}_{S_i} - \frac{1}{n_S^c} \sum_{\mathbf{x}_{S_i} \in D_S^c} W^T \mathbf{x}_{S_i} \right\|^2. \quad (7)$$

For target data, by using pseudo labels, we can obtain:

$$\mathcal{L}_{center}^T = \sum_{c=1}^C \sum_{\mathbf{x}_{T_j} \in \widehat{D}_T^c} \left\| W^T \mathbf{x}_{T_j} - \frac{1}{\widehat{n}_T^c} \sum_{\mathbf{x}_{T_j} \in \widehat{D}_T^c} W^T \mathbf{x}_{T_j} \right\|^2. \quad (8)$$

If we integrate Eqs. (7) and (8) into one formulation, which can be wrote as:

$$\mathcal{L}_{center} = \mathcal{L}_{center}^S + \mathcal{L}_{center}^T = \text{tr}(W^T X G X^T W). \quad (9)$$

Then, we can yield the optimization problem:

$$\begin{aligned} \min_W \quad & \text{MMD}^2(D_S, D_T) + \rho \mathcal{L}_{center} + \theta \|W\|_F^2 \\ \text{s.t.} \quad & W^T X K X^T W = I, \end{aligned} \quad (10)$$

where  $\rho$  and  $\theta$  are two tradeoff parameters. The constraints in (10) is derived from the famous principal component analysis (PCA) [9], which can preserve the important properties of data.  $K$  is the centering matrix, and  $I$  is an identity matrix.

### 2.3.3 Optimization of TDCC

Obviously, (10) is a constrained nonlinear optimization problem, we can apply Lagrange techniques to get the Lagrangian function for (10):

$$L(W, \Psi) = \text{tr} \left( W^T \left( X \left( \sum_{c=0}^C H_c + \rho G \right) X^T + \theta I \right) W \right) + \text{tr}((I - W^T X K X^T W) \Psi), \quad (11)$$

where  $\Psi = \text{diag}(\varphi_1, \varphi_2, \dots, \varphi_d)$  is a diagonal matrix with Lagrange Multipliers. If we set the gradient of  $L(W, \Psi)$  with respect to  $W$  and  $\Psi$  equal to 0, we can obtain

$$\left( X \left( \sum_{c=0}^C H_c + \rho G \right) X^T + \theta I \right) W = X K X^T W \Psi. \quad (12)$$

By observing Eq. (12), it is a typical generalised eigen-decomposition problem, which can be effectively and efficiently solved by calculating the eigenvectors of (22) corresponding to the  $d$ -smallest eigenvalues.

Here, we take the linear projection as an example for TDCC, and TDCC also can be extended to the nonlinear case (kernelization) by empirical kernel map techniques [10].

## 3 Data Sets Description

To extensively evaluate our proposed TDCC approach, we have tested TDCC and some related domain adaptation methods on several widely used data sets, such as Office, Caltech 256, COIL 20, MNIST and USPS [2, 3]. The samples and description of these data sets are listed as follow (Fig. 2 and Table 1).

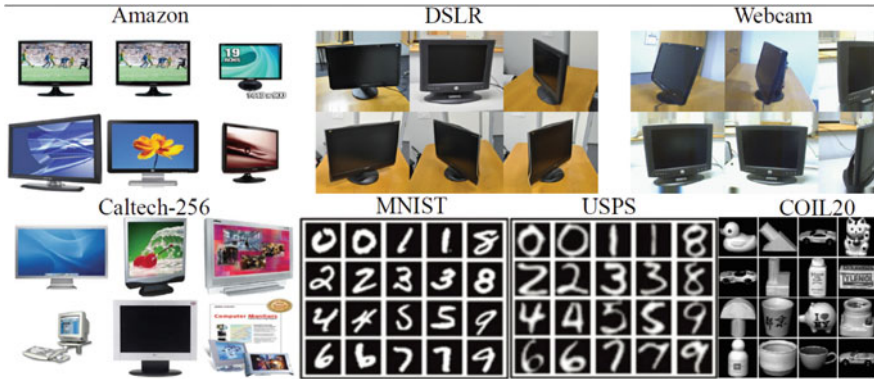


**Fig. 2** Image samples from office (Amazon, DSLR, Webcam), Caltech-256, MNIST, USPS and COIL20 data sets

**Table 1** Description of data sets used in our experiments

Data set	Type	#Classes	#Samples	#Features
AMAZON (A)	Object	10	958	800
CALTECH (C)	Object	10	1123	800
DSLRL (D)	Object	10	157	800
WEBCAM (W)	Object	10	295	800
COIL20 (COIL1 and COIL2)	Object	20	1440	1024
MNIST	Digit	10	2000	256
USPS	Digit	10	1800	256

## 4 Experiments and Results

We select several state-of-the-art domain adaptation methods as our baselines to justify the effectiveness of TDCC. Specifically, we compare two conventional machine learning methods: 1-NN and PCA, and five domain adaptation methods: GFK [11], TCA [5], JDA [3], TJM [2] and CDML [12].

For unsupervised domain adaptation problem, only unlabeled target data are available, so we couldn't select the best parameters for all the baselines by cross-validation procedure. We just evaluate all the baselines by grid-searching the trade-off parameters, and their best results are reported. In TDCC, there are two trade-off parameters  $\rho$  and  $\theta$  to decide. In practice, we find that TDCC is not sensitive to the choice of  $\rho$  and  $\theta$ , thus we empirically set  $\rho$  and  $\theta$  all equal to 0.1. Moreover, we choose 1-NN as our basic classifier, which has no parameters to tune and is easy to implement.

Finally, we have tested all the methods on the cross-domain data sets under the same experiment settings, and the results are shown as Table 2.

**Table 2** Average Classification Accuracy (%) of AMAZON (A), CALTECH (C), DSLR (D), WEBCAM (W), COIL1, COIL2, MNIST and USPS from “Source Domain  $\rightarrow$  Target Domain”

Task \ methods	1-NN	PCA	GFK	TCA	JDA	TJM	CDML	TDCC
C $\rightarrow$ A	23.70	36.95	41.02	38.20	44.78	46.76	<b>47.82</b>	47.18
C $\rightarrow$ W	25.76	32.54	40.68	38.64	41.69	38.98	36.91	<b>48.47</b>
C $\rightarrow$ D	25.48	38.22	38.85	41.40	45.22	44.59	43.93	<b>47.13</b>
A $\rightarrow$ C	26.00	34.73	40.25	37.76	39.36	39.45	41.72	<b>42.03</b>
A $\rightarrow$ W	29.83	35.59	38.98	37.63	37.97	42.03	38.25	<b>43.05</b>
A $\rightarrow$ D	25.48	27.39	36.31	33.12	39.49	<b>45.22</b>	35.92	38.85
W $\rightarrow$ C	19.86	26.36	30.72	29.30	31.17	30.19	31.14	<b>32.06</b>
W $\rightarrow$ A	22.96	31.00	29.75	30.06	32.78	29.96	32.26	<b>33.19</b>
W $\rightarrow$ D	59.24	77.07	80.89	87.26	<b>89.17</b>	89.17	84.84	88.54
D $\rightarrow$ C	26.27	29.65	30.28	31.70	31.52	31.43	32.63	<b>33.13</b>
D $\rightarrow$ A	28.50	32.05	32.05	32.15	33.09	32.78	29.87	<b>33.51</b>
D $\rightarrow$ W	63.39	75.93	75.59	86.10	89.49	85.42	82.34	<b>90.85</b>
USPS $\rightarrow$ MNIST	44.70	44.95	46.45	51.05	59.65	52.25	52.25	<b>60.45</b>
MNIST $\rightarrow$ USPS	65.94	66.22	67.22	56.28	67.28	63.28	63.28	<b>67.89</b>
COIL1 $\rightarrow$ COIL2	83.61	84.72	72.50	88.47	89.31	91.53	88.93	<b>95.00</b>
COIL2 $\rightarrow$ COIL1	82.78	84.03	74.17	85.83	88.47	91.81	87.32	<b>92.64</b>
Average	40.84	47.34	48.48	50.31	53.78	53.43	51.84	<b>55.87</b>

From Table 2, we can see that TDCC achieves the best performance compared with other baselines. TDCC have performed the best in 12 out of 14 tasks, and achieves 55.87% average classification accuracy. The comprehensive experiments have verified that TDCC is superior to other baselines.

We can also observe that all the domain adaptation methods are better than conventional machine learning approaches, because the traditional methods don't consider to reduce the difference between the training and test data. Therefore, the trained source classifier will perform poorly on the unlabeled target data.

## 5 Conclusion

This paper has introduced a transfer domain class clustering (TDCC) algorithm to solve unsupervised domain adaptation problems. TDCC focuses on deriving both domain invariant and class discriminative features, which simultaneously minimizes the MMD distance between two domains, and minimizes the intra-class variations for source and target. TDCC could make both domains become similar in

the latent subspace, and preserve the class discriminative ability. The optimal solution of TDCC can be effectively obtained, and comprehensive experimental results on cross-domain data sets have demonstrated the effectiveness of our proposed TDCC.

**Acknowledgements** This research is supported by the CRRC Major Scientific Projects under Grant No. 2106CKZ206-1 and National Key R&D Program under Grant No. 2016YFB1200203.

## References

1. Pan SJ, Yang Q (2010) A survey on transfer learning. *IEEE Trans Knowl Data Eng* 22 (10):1345–1359
2. Long M, Wang J, Ding G et al (2014) Transfer joint matching for unsupervised domain adaptation. In: *Proceedings of the IEEE conference on computer vision and pattern recognition*, pp 1410–1417
3. Long M, Wang J, Ding G et al (2013) Transfer feature learning with joint distribution adaptation. In: *Proceedings of the IEEE international conference on computer vision*, pp 2200–2207
4. Li S, Song S, Huang G (2016) Prediction reweighting for domain adaptation. *IEEE Trans Neural Netw Learn Syst*
5. Pan SJ, Tsang IW, Kwok JT et al (2011) Domain adaptation via transfer component analysis. *IEEE Trans Neural Netw* 22(2):199–210
6. Suykens JAK, Vandewalle J (1999) Least squares support vector machine classifiers. *Neural Process Lett* 9(3):293–300
7. Fukunaga K, Narendra PM (1975) A branch and bound algorithm for computing k-nearest neighbors. *IEEE Trans Comput* 100(7):750–753
8. Gretton A, Borgwardt KM, Rasch MJ et al (2013) A kernel two-sample test. *J Mach Learn Res* 13:723–773
9. Jolliffe I (2002) *Principal component analysis*. Wiley
10. Schölkopf B, Smola A, Müller KR (1998) Nonlinear component analysis as a kernel eigenvalue problem. *Neural Comput* 10(5):1299–1319
11. Gong B, Shi Y, Sha F et al (2012) Geodesic flow kernel for unsupervised domain adaptation. In: *Computer vision and pattern recognition (CVPR), 2012 IEEE Conference on IEEE*, pp 2066–2073
12. Wang H, Wang W, Zhang C et al (2014) Cross-domain metric learning based on information theory. *AAAI*, pp 2099–2105



# Nodes Deployment of Wireless Sensor Networks for Underground Tunnel Environments

Cuiran Li, Jianli Xie, Wei Wu, Yuhong Liu and Anqi Lv

**Abstract** Wireless nodes deployment is a key point for monitoring and localization of the trains in railway underground tunnels, which is critical to guarantee high-efficiency and safe operation of railway traffic. In this paper, based on the surface mapping and expansion theory, the mapping of 3D tunnel surface onto 2D domain is firstly investigated. Reliable communication links among the wireless nodes in localization are vital for successful data transmission. Then, the propagation pathloss, as well as the fading of radio signals transmitting in tunnel environments is analyzed. Also, the maximum transmission range of wireless nodes under the constraint of network connectivity is estimated according to the wireless link budget. The three grid-division (nodes deployment) in wireless sensor network (WSN), i.e., triangular-grid, square-grid, and rhombus-grid are obtained in the mapped 2D domain of actual tunnel.

**Keywords** Wireless nodes · Railway tunnel · Surface mapping  
Network connectivity · Wireless link budget

## 1 Introduction

In the recent decades, various location-dependent services and potential applications has attracted many attention in railway communication system. Railway vehicles localization plays an important role in ensuring the safe and efficient operation of trains. Onboard localization has widely used the Global navigation satellite systems, common named GPS. However, GPS is energy-hungry [1], and furthermore, the GPS localization will fail when the train is running in high

---

C. Li · W. Wu · Y. Liu · A. Lv  
School of Electronics & Information Engineering,  
Lanzhou Jiaotong University, Lanzhou, China

J. Xie (✉)  
Key Laboratory of Opto-Technology and Intelligent Control Ministry of Education,  
Lanzhou Jiaotong University, Lanzhou, China  
e-mail: xiejl@mail.lzjtu.cn

mountains or under tunnels. In [2, 3], it has revealed that the train localization based on GPS cannot meet the demand of safe operation of railway trains in under tunnel environments. And, it is suggested that a certain number of sensors be put on the train to improve the safety. Placing additional infrastructures, such as European train control system level 2 (ETCS-2) for the high-speed railway, can improve the positioning accuracy of vehicle trains, but it also brings high maintenance cost.

In order to reduce the cost of construction and maintenance, a distributed localization algorithm based on the radio frequency time-of-flight (RF-TOF) range has been proposed in [4]. In the algorithm, the Newton iteration operation is used to estimate the location of a blind node, meanwhile, the linear least square method is adopted to provide the initial location estimation and improving the convergence of iterative operation. A dynamic WSN localization algorithm operating in underground tunnel is presented in [5], which is based on the received signal strength (RSS). In the algorithm, in addition to the Euclidean distance, RSS between neighboring anchor nodes is considered to establish more accurate path loss model.

However, the WSN node deployment in underground tunnel is seldom well-considered in the location of vehicle trains. And, especially, when fast moving trains are taken into account, unreasonable deployment of wireless nodes may bring location bias and seriously affect the positioning accuracy.

In this paper, we propose a nodes deployment strategy in WSN for underground tunnel environments. Based on the surface mapping and expansion theory, the mapping of 3D tunnel surface onto 2D domain is investigated. The propagation pathloss model, in addition to the fading of radio signals transmitting in tunnel environments is analyzed. Also, the maximum transmission range of wireless nodes under the constraint of network connectivity is estimated according to the wireless link budget. The three grid-division (nodes deployment) in wireless sensor WSN, i.e., triangular-grid, square-grid, and rhombus-grid are obtained in the mapped 2D domain of actual tunnel.

## 2 Mapping of 3D Tunnel Surface onto 2D Domain

In general, the actual tunnel can be approximately cylindrical in which the WSN node is to be deployed, shown in Fig. 1a [6]. The cylinder is a curved surface formed by the straight generatrix according to certain rules, also named ruled surface [7]. Figure 1b gives the general form of the ruled surface, in which the curve  $c: \mathbf{a} = \mathbf{a}(u)$  is the conductor. At each point of the wire there is a generatrix (any position of the straight generatrix), and  $\mathbf{b}(u)$  is the unit vector in the direction of  $\mathbf{a}(u)$  straight generatrix on the wire. At any point of straight generatrix,  $P(u, v)$ , the radius vector of  $P(u, v)$  is

$$\mathbf{r} = \mathbf{a}(u) + v\mathbf{b}(u) \quad (1)$$

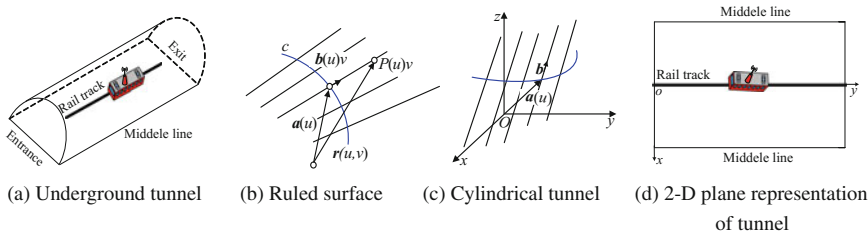


**Fig. 1** Underground railway tunnel and 2-D representation **a** Underground tunnel **b** Ruled surface **c** Cylindrical tunnel **d** 2-D plane representation of tunnel

Equation (1) is the vector equation of ruled surface. If the normal direction of the ruled surface does not change along the same straight generatrix, that is, there is a common tangent plane along the same straight line surface, which is called developable surface. The cylinder is a developable surface, and it can be completely fit with the plane through continuous bending. The underground railway tunnel, can be approximately cylindrical in shape, therefore, there is isometric mapping between tunnel surface and 2-D plane.

In Fig. 1c, the directrix of cylindrical tunnel surface is  $\mathbf{a}(u) = (f(u), g(u), h(u))$  in  $xyz$  rectangular coordinates, the unit vector  $\mathbf{b} = (l, m, n)$  in the direction of generatrix. The underground tunnel can be imagined to be cut horizontally and unrolled. Then, the upper half of the underground tunnel can be seen as a 2-D square, which facilitate the deployment of WSN nodes, shown in Fig. 1d.

The parameter equation of cylinder tunnel is [7].

$$\begin{cases} x = f(u) + lv \\ y = g(u) + mv \\ z = h(u) + nv \end{cases} \quad \left( \begin{array}{l} a \leq u \leq b \\ -\infty < v < +\infty \end{array} \right) \quad (2)$$

The vector equation is

$$\mathbf{r}(u, v) = \mathbf{a}(u) + \mathbf{b}v \quad (3)$$

To solve a curve  $\mathbf{c}(u)$  on the cylinder, which is perpendicular to the generatrix, over the point  $M_0 (f(u_0), g(u_0), h(u_0))$ , the corresponding parameter  $u = u_0, v = 0$ . The plane equation of the point  $M_0$  perpendicular to the generatrix is

$$l[x - f(u_0)] + m[y - g(u_0)] + n[z - h(u_0)] = 0 \quad (4)$$

Substitution Eq. (2) into Eq. (4), then the equation of  $\mathbf{c}(u)$  is

$$l[f(u) + lv - f(u_0)] + m[g(u) + mv - g(u_0)] + n[h(u) + nv - h(u_0)] = 0 \quad (5)$$

and

$$v = l[f(u_0) - f(u)] + m[g(u_0) - g(u)] + n[h(u_0) - h(u)] \tag{6}$$

Furthermore, substitution Eq. (6) into Eq. (2), then the parameter equation of tunnel cylinder can be written as

$$\begin{cases} x = f(u) + l\{l[f(u_0) - f(u)] + m[g(u_0) - g(u)] + n[h(u_0) - h(u)]\} \\ y = g(u) + m\{l[f(u_0) - f(u)] + m[g(u_0) - g(u)] + n[h(u_0) - h(u)]\} \\ z = h(u) + n\{l[f(u_0) - f(u)] + m[g(u_0) - g(u)] + n[h(u_0) - h(u)]\} \end{cases} \tag{7}$$

The deviation of Eq. (7) is

$$\begin{cases} x' = f'(u) - l^2f'(u) - lmg'(u) - lnh'(u) \\ y' = g'(u) - mlf'(u) - m^2g'(u) - mnh'(u) \\ z' = h'(u) - nlf'(u) - nmg'(u) - n^2h'(u) \end{cases} \tag{8}$$

The cylinder surface is flattened with curve  $c(u)$  as the basis, and the flattening direction is  $y$  axis. Its length is

$$\begin{aligned} s &= \int_a^u \sqrt{x'^2 + y'^2 + z'^2} du \\ &= \int_a^u \sqrt{[mf'(u) - lg'(u)]^2 + [nf'(u) - lh'(u)]^2 + [ng'(u) - mh'(u)]^2} du \end{aligned} \tag{9}$$

Coordinate  $x$  of any point in generatrix can be obtained as

$$x = v + \mathbf{a}(u)\mathbf{b} \tag{10}$$

where  $\mathbf{a}(u)\mathbf{b}$  is the projection length of vector  $\mathbf{a}(u)$  a in vector  $\mathbf{b}$ ,  $\mathbf{a}(u)\mathbf{b} = lf(u) + mg(u) + nh(u)$ . Then, the equation of the cylinder tunnel is

$$\begin{cases} x = v + lf(u) + mg(u) + nh(u) \\ y = \int_a^u \sqrt{[mf'(u) - lg'(u)]^2 + [nf'(u) - lh'(u)]^2 + [ng'(u) - mh'(u)]^2} du \end{cases} \tag{11}$$

Equation (11) is the isometric mapping relation between the cylinder tunnel  $\mathbf{r}(u, v) = \mathbf{a}(u) + \mathbf{b}v$  and the  $xOy$  plane.

When the directrix  $\mathbf{a}(u)$  is located in the  $xOy$  plane and perpendicular to the generatrix, we have  $\mathbf{b} = (0, 0, 1)$ , i.e.,  $l = m=0, n = 1, \mathbf{a}(u) \cdot \mathbf{b} = 0$ , and  $\mathbf{a}'(u) \cdot \mathbf{b} = 0$ . Therefore, the parameter equation of tunnel cylinder can be obtained as

$$\begin{cases} x = f(u) \\ y = g(u), \quad a \leq u \leq b, -\infty < v < +\infty \\ z = v \end{cases} \tag{12}$$

And, the isometric mapping of 3D tunnel surface onto 2D domain is

$$\begin{cases} x = v \\ y = \int_a^u \sqrt{f'^2(u) + g'^2(u)} du \end{cases} \quad (13)$$

### 3 Channel Characteristics in Tunnel Environments

Reliable communication links among WSN nodes are vital for successful data gathering and transmission. It is assumed that the propagation of radio signals in underground tunnel obeys a two-slope regression piecewise linear model. The two-slope pathloss model has been proved in [6] to provide the lower mean squared error than does a single regression pathloss model. There is few appropriate empirical propagation model in underground tunnel. In [8, 9], the transmission characteristic of radio signals in tunnel is analyzed, and valid pathloss and fading distribution models are developed. The path loss expression given in (14) is determined by fitting the two-slope regression line to the measured data [6, 8, 9].

$$PL(r) = \begin{cases} (10n_1) \log_{10}(r) + PL_{ref} & \text{if } 1 < r < r_b \\ (10n_2) \log_{10}(r/r_b) \\ + (10n_1) \log_{10}(r_b) + PL_{ref} & \text{if } r > r_b \end{cases} \quad (14)$$

where  $r$  is the range,  $n_1$  and  $n_2$  are two power law exponents,  $r_b$  is the break point distance and  $PL_{ref}$  is the path loss in dB at the reference distance of 1 m. There are two cases of node antenna positions, side-to-same-side (SSS) or side-to-opposite-side (SOS) in underground tunnel. The four parameters in (14) have been determined in underground tunnels in order to yield appropriate pathloss model, see Table 1.

In addition to pathloss, the radio signal will undergo the fading in wireless environment. The Ricean distribution has been found to be well describe the fading characteristic of radio signals in underground tunnel [9]. The Ricean probability density function (PDF) is written as [10].

$$P_r = \frac{r}{\sigma^2} e^{-r^2/(2\sigma^2)} e^{-k} I_0 \left( \frac{r\sqrt{2k}}{\sigma} \right). \quad (15)$$

where  $r$  is the fading amplitude,  $\sigma^2$  is the variance of the multipath components,  $s$  is the magnitude of the line-of-sight (LOS) component,  $I_0$  is the zero-order Bessel function of the first kind and  $k$  is the Ricean factor, expressed by

**Table 1** Estimated parameters for path loss model and Ricean fading [6]

Node position	$n_1$	$n_2$	$r_b$	$PL_{ref}$
SSS	1.5	5.4	76	51
SOS	1.6	2.4	23	48

$$k = \frac{s^2}{2\sigma^2}. \tag{16}$$

The fading margin  $L_{FM}$  is given by Table 2, in underground tunnels for specified levels of data packet outage probability.

### 4 Nodes Deployment of WSN in Tunnels

In the mapped 2D domain of actual tunnel, the monitoring area is divided into a plurality of grids based on the geometric lattice. Three typical types of grid are triangular-grid [11], square-grid [12], and rhombus-grid [13] as shown in Fig. 2a, b and c. The three types of grid-division can achieve seamless coverage.

The spacing between WSN nodes in different grid-division should be determined carefully for reliable communication links among the nodes. The spacing is initially defined according to the wireless link budget [14], which is widely used for determination of the connectivity between wireless nodes in wireless communication. The wireless link budget is defined as

$$P_r = P_t + G_T - PL(r) - L_{FM} + G_R. \tag{17}$$

**Table 2** Fade Margin (dB) [6]

Outage probability %	$k = 0$ (SSS)	$k = 0.33$ (SOS)
10	8.22	8.12
5	11.39	11.27
1	18.65	18.51
0.8	19.66	19.53
0.5	21.81	21.68
0.1	29.32	29.22

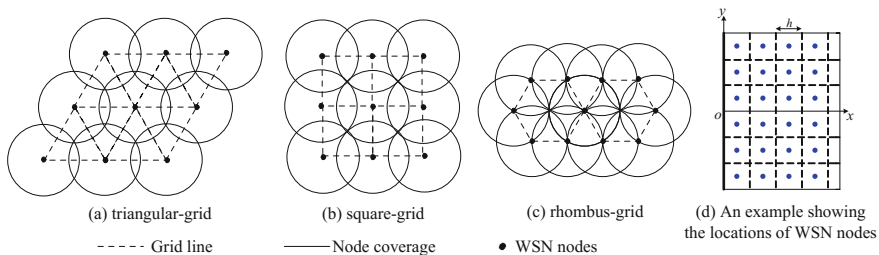


**Fig. 2** Three types of grid-division and example of location of WSN nodes

where  $P_r$  is the node received power in dBm,  $P_t$  is the transmitter output power in dBm,  $G_T$  is the transmitter antenna gain in dBi,  $PL(r)$  is the path loss in dB at distance  $r$  between transmitter and receiver in the tunnel environments,  $L_{FM}$  is the fading margin in dB and  $G_R$  is the receiver antenna gain in dBi.

The network connectivity is well guaranteed on the condition that the estimated received power  $P_r$  greater than or equal to the receiver sensitivity.  $P_t$ ,  $G_T$  and  $G_R$  are set by designers, but  $PL(r)$  and  $L_{FM}$  are determined by the wireless transmission environments in which WSN is deployed. Tables 1 and 2 enable the appropriate parameters to be input to the path loss model and Ricean fading model respectively when we deploy in a curved concrete underground tunnel. To ensure a communication range that extends over a distance of e.g., at least two spacing, the spacing should be set to about half of the estimated maximum transmission range.

The spacing for near region transmission is established using the worst case in underground tunnels, i.e., with a cast iron lining, a curved shape, SOS node positions and outage probability of 0.1%. With the aid of Eqs. (14) and (17), and Tables 1 and 2, we have

$$\begin{aligned} P_r &= P_t + G_T - (10n_1) \log_{10}(r) - PL_{ref} - L_{FM} + G_R \\ &= P_t + G_T - 16 \log_{10}(r) - 77.22 + G_R \end{aligned} \quad (18)$$

Then, the estimated maximum transmission range under the constraint of network connectivity is

$$r = 10^{0.0625(P_t + G_T + G_R - \beta) - 4.82625}. \quad (19)$$

where  $\beta$  is the receiver sensitivity in dBm. And, the sensing radius is

$$r_s \doteq \frac{1}{2}r = 10^{0.03125(P_t + G_T + G_R - \beta) - 2.413}. \quad (20)$$

The spacing between nodes in triangular-grid, square-grid, and rhombus-grid in Fig. 2 can be determined as

$$h \doteq \begin{cases} \sqrt{3}r_s = \sqrt{3} \cdot 10^{0.03125(P_t + G_T + G_R - \beta) - 2.413} & \text{triangular - grid} \\ \sqrt{2}r_s = \sqrt{2} \cdot 10^{0.03125(P_t + G_T + G_R - \beta) - 2.413} & \text{square - grid} \\ \sqrt{3}r_s = \sqrt{3} \cdot 10^{0.03125(P_t + G_T + G_R - \beta) - 2.413} & \text{rhombus - grid} \end{cases} \quad (21)$$

For example, considering a 2-D plane shown in Fig. 1d, in order to place the nodes, the area where the WSN is to be deployed is divided into squares, as illustrated in Fig. 2d. In the figure, WSN node is represented as the solid dot. As shown in the figure, in each square there is a node seating at the centre. The side length of the squares is exactly the spacing between nodes in square-grid, expressed by Eq. (21).

## 5 Conclusions

In this paper, we have investigated the node deployment strategy in WSN for underground tunnel environments when a near-field path loss model and Ricean fading model are considered for radio signal propagation in tunnels. The maximum transmission range under the constraint of network connectivity is estimated. Three grid-division (nodes deployment) in WSN, i.e., triangular-grid, square-grid, and rhombus-grid are obtained in the mapped 2D domain of actual tunnel. In addition, an example of square-grid deployment of WSN nodes is discussed.

**Acknowledgements** This work was supported in part by the National Natural Science Foundation of China (61661025, 61661026), Key Laboratory of Opto-Technology and Intelligent Control Ministry of Education (KFKT2016-2), and Foundation of A hundred Youth Talents Training Program of Lanzhou Jiaotong University.

## References

1. Aly H, Youssef M (2013) Dejavu: an accurate energy-efficient outdoor localization system. In: 21st ACM SIGSPATIAL international conference on advances in geographic information systems, Florida, USA, November 5–8, pp 154–163
2. Filip A, Bazant L, Mocek H, Cach J (2000) GPS/GNSS based train position locator for railway signaling. In: VII of international conference on computers in railway, pp 1227–1242
3. Beugin J, Marais J (2012) Simulation-based evaluation of dependability and safety properties of satellite technologies for railway localization. *Trans Res Part C Emerg Technol* 22:42–57
4. Qin YQ, Zhou C, Yang SH, Wang F (2012) A distributed newton iteration based localization scheme in underground tunnels. In: UKACC international conference on control, Cardiff, UK, September 3–5, pp 851–856
5. Qiao GZ, Zeng JC (2010) Localization algorithm of beacon nodes chain deployment based on coal mine underground wireless sensor networks. *J China Coal Soc* 35(7):1229–1233
6. Liu RS, Wassell IJ, Soga K (2010) Relay node placement for wireless sensor networks deployed in tunnels. In: 2010 IEEE 6th international conference on wireless and mobile computing, networking and communications, pp 144–150
7. Mao X, Ma M (2013) Surface mapping and geometric analysis of expansion. Tsinghua University Press. (in Chinese)
8. Wu Y, Lin M, Wassell IG (2009) Modified 2D finite-difference time-domain based tunnel path loss prediction for wireless sensor network applications. *J Commun* 4(4):214
9. Lin M (2009) Channel modelling for wireless sensor networks. Ph.D. dissertation, University of Cambridge
10. Saunders S (1999) Antennas and propagation for wireless communication systems. Wiley
11. Xue-qing W, Yong-tian Y, Sun T, Zhong-lin Z (2006) Research on the grid-based coverage problem in wireless sensor networks. *Comput Sci* 33(11):38–39 (in Chinese)
12. Li Z, Yun L (2007) Grid movement based deployment algorithm of wireless mobile sensor networks. *J Beijing Jiaotong Uni* 31(5):6–10 (in Chinese)
13. Wang X, Yang Y (2006) Sensor deployment algorithm based on virtual rhomb grid. *Comput Appl* 26(7):1554–1556. (in Chinese)
14. Qi XG, Qiu CX (2009) An improvement of gaf for lifetime elongation in wireless sensor networks. *Proc IEEE WiCom Beijing, China*, IEEE Press, pp 1–4



# Application of DBN for Assessment of Railway Intelligent Signal System Reliability

Zhengjiao Li, Bai-gen Cai, Shaobin Li, Jiang Liu and Debiao Lu

**Abstract** According to the variable structure characteristics of railway intelligent signal system (RISS) with different railway station scale, a new reliability assessment method based on Dynamic Bayesian Networks (DBN) is studied. A comparison between DBN model and probabilistic model is studied to verify the accuracy and correctness of DBN model. Based on DBN model, the static gates analyzing results deliver a calculation with no error, while the spare gate analyzing results deliver a calculation with a tolerable error that leads to more strictly and credible calculations. Meanwhile, this paper analyzes reliability indexes of RISS with four different railway station scale. The results show that: when the railway station scale increases, the reliability of RISS decreases, which has little impact on the ranking of the components' Birnbaum importance factor and diagnostic importance factor.

**Keywords** Railway intelligent signal system · Dynamic bayesian networks  
Reliability assessment

## 1 Introduction

A new railway intelligent signal system (RISS), which achieves distributed control through secure communication system, has the advantages of saving cable, reducing cost, thus reducing break or mixed cable fault and security risks [1, 2]. Quantitative evaluation of the reliability of RISS, enables identification of the most important elements in RISS. The assessment results can offer some suggestions to the design and maintenance of RISS.

The establishment of reliability model and solving is the key to quantitative evaluation of the reliability of RISS. There are many reliability modeling methods

---

Z. Li (✉) · B. Cai · S. Li · J. Liu · D. Lu  
School of Electronic and Information Engineering, Beijing Jiaotong University,  
Beijing, China  
e-mail: lizhj@bjtu.edu.cn

that are applied to reliability assessment of railway system in the state-of-the-art, such as Reliability block diagram (RBD) [3], Fault tree (FT) [4–6], Bayesian networks (BN) [5, 6], Dynamic fault tree (DFT) [7, 8] and so on. FT is one of the most prominent techniques here and is widely used in railway system reliability assessment. FT is a graphical method that model how component failures lead to system failures, as well as qualitative analysis and quantitative analysis can be performed. DFT analysis is an extension of FT analysis that allows the modeling of dynamic behavior (sequence of events and functional dependence between events). DFT can be more perfect to describe system reliability model, to achieve more accurate logic processing [9]. BN analysis, which has the ability of disposing common cause factor (CCF), system polymorphisms and uncertain logical relationships [10, 11], can compute system failure probability, sensitivity index and diagnostic importance factor through forward and backward inference.

The remainder of the paper is divided as follows. In Sect. 2 we present RISS introductions and its corresponding DFT model. In Sect. 3 DBN model and probabilistic model are used to analyze the static gates and spare gate of DFT, and the analysis results are given to verify the accuracy and correctness of DBN model. In Sect. 4 the reliability indexes of four types of RISS with different railway station scale are compared and analyzed. Finally, the main conclusions are presented.

## 2 RISS and Dynamic Fault Tree Model

Without changing the structure of traditional interlocking system of railway station, RISS moves signal controller to the outdoor next to the Signal Lamp, which helps to reduce cable length, simplify the structure, convenient to maintain. Structure diagram of the connection between RISS and interlocking system is shown in Fig. 1.

Seen from the structure, the core function of RISS is to replace the outdoor signal and lighting circuit of traditional interlocking system. When we establish dynamic fault tree of RISS, some executable indices, such as the input and output wiring interface that connect to the I/O circuit of interlocking system, are not considered. Because they have nothing to do with the core function, likewise, the

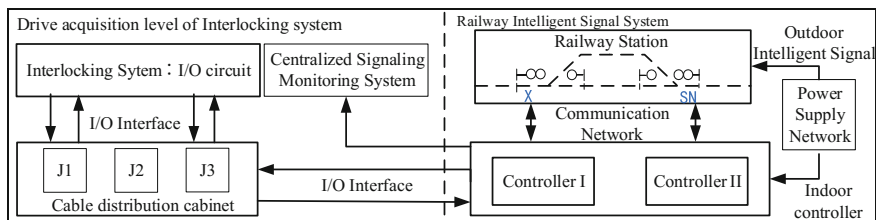
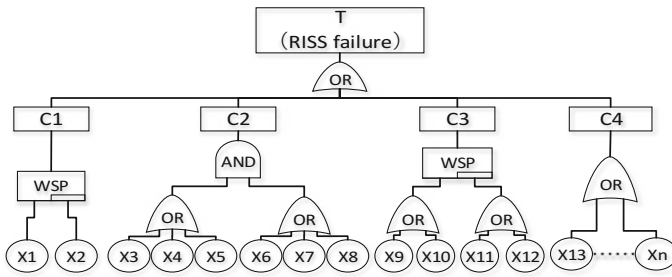


Fig. 1 Structure diagram of the connection between RISS and interlocking system



**Fig. 2** Dynamic Fault Tree of RISS

railway centralized signalling monitoring system (CSM) also is not considered. Assuming that there is no online maintenance during operation. Only the key devices of RISS, such as double 2-vote-2 secure control system (DSCS), outdoor intelligent signal (IS), communication network (CN) and power supply network (PSN), are considered.

In accordance with the basic steps of the DFT model [12], RISS failure is selected as the top event, firstly, and then the whole DFT is shown in Fig. 2.

In Fig. 2, the middle events C1, C2, C3, C4 represent PSN failures, CN failures, DSCS failures and IS system failures, respectively. The quantity of the bottom events of the DFT of RISS is  $n$ , where the events X1, X2, ..., X12 are invariant events, and the events X13, X14, ..., Xn are variant events whose quantity depending on the different railway station scale. All the bottom events follow the exponential distribution. Table 1 shows the list of the event, codes, names, and their prior probabilities in DFT of RISS, the data come from the references [13–15], where 365 days as a year, and 24 h as a day.

### 3 DFT Analysis Using DBN Model and Probabilistic Model

When the graph structure and the parameters of a DFT are given, there are many inference approach, such as Junction Tree algorithm, Variable Elimination Algorithm, Global inference methods and etc. and corresponding software packages [16, 17] can be used to quantitative analyze DFT. It will be a simple matter to compute the system failure probability by the forward inference DBN. Also, it is more suitable to apply DBN to compute the reliability index of the components' Birnbaum importance factor and diagnostic importance factor because the bidirectional inference can be done with it.

A comparison analysis of DBN model and probabilistic model is given to verify the accuracy and correctness of DBN model. Considering the DFT structure of RISS, this section mainly discusses and analyse three types of logic gate of DFT: static gates (AND gate, OR gate), spare gate (WSP gate). The basic assumptions of

**Table 1** The event, codes, names and their prior probabilities in DFT of RISS

Event code	Event name	Failure rate (/h)	Event code	Event name	Failure rate (/h)
X1	Power supply 1 fault	3.5e-5	X9	RISS Controller I unit 1 fault	1.7e-5
X2	Power supply 2 fault	3.5e-5	X10	RISS Controller I unit 2 fault	1.7e-5
X3	CAN bus I transceiver 1 fault	5e-5	X11	RISS Controller II unit 1 fault	1.7e-5
X4	CAN bus I cable fault	5e-5	X12	RISS Controller II unit 2 fault	1.7e-5
X5	CAN bus I transceiver 2 fault	5e-5	X13	Intelligent signal 1	8.5e-7
X6	CAN bus II transceiver 1 fault	5e-5	...	Other intelligent signals	8.5e-7
X7	CAN bus II cable fault	5e-5	Xn	Intelligent signal n	8.5e-7
X8	CAN bus II transceiver 2 fault	5e-5			

the standard DFT methodology are recalled as: (1) events are binary events (0 = working, 1 = failure); (2) events are statistically independent.

### 3.1 Probabilistic Model Analysis of Logic Gates

The AND gate, which is used to show the output event occurs only if all the input events occur, is equal to the reliability block diagram (RBD) of series system.

The output probability of the AND gate can be calculated as:

$$P_{AND}(t) = \prod_{i=1}^n P_i(t)$$

where the term “ $P_i(t)$ ” denotes the probability of event  $A_i$  failure occurs.

The OR gate, which is used to show that the output event occurs only if one or more of the input events occur, is equal to the RBD of parallel system.

The output probability of the OR gate can be calculated as:

$$P_{OR}(t) = 1 - \prod_{i=1}^n [1 - P_i(t)]$$

WSP gate has one primary input and one or more spare inputs. If every component (either principal or spare) is failed, the gate produces a fault. If we assume the failure rate of a powered spare is equal to  $\lambda$ , then the failure rate of an

unpowered spare is equal to  $\alpha\lambda$ , with  $0 \leq \alpha \leq 1$  called the dormancy factor. Spares are more properly called “hot” if  $\alpha = 1$  and “cold” if  $\alpha = 0$  [11, 12].

Here, we take a WSP gate where a single component A can be substituted by a spare B as an example. We assume that all the input events follow the exponential distribution.  $\lambda_p$ ,  $\lambda_d$  and  $\lambda_a$  are the failure rate of the primary input in the working state, the spare input in the dormant mode and the spare input in the active mode, respectively. Then the reliability of the WSP gate can be calculated as below [18]:

$$R_{ws}(t) = \frac{\lambda_p e^{-\lambda_a t}}{\lambda_a - \lambda_d - \lambda_p} (e^{(\lambda_a - \lambda_d - \lambda_p)r} - 1) + e^{-\lambda_p r}$$

### 3.2 DBN Model Analysis of Logic Gates

To define a DBN, we must specify the graph structure and then the parameters. Here, we take the system that have dual components as an example, the AND gate represent the system failure only if all of the component failure, and the OR gate represent the system failure if one or more components are failure. Due to the structure diagram of the two static logic gates have the same structure, the DBN for the AND gate and the OR gate can be drawn in Fig. 3a.

In Fig. 3a, the above DBN model is usually called two time-slice Temporal Bayesian Network (2TBN) [10, 11]. In particular, nodes  $A(T + \Delta t)$  and  $B(T + \Delta t)$  at time  $T + \Delta t$  depend on their “historical” copy (i.e. on the same variable at time  $T$ ). Take the AND gate as an example, Nodes  $A(T)$ ,  $B(T)$ ,  $A(T + \Delta t)$  and  $B(T + \Delta t)$  have 2 different values namely 0 = working, 1 = failure. Node AND is a deterministic node with the following functional rules:

$$P(\text{AND} = 1 | A(T + \Delta t) = 1, B(T + \Delta t) = 1) = 1, P(\text{AND} = 1 | \text{else}) = 0$$

Then we can also calculate the conditional probabilities for the faulty values of Nodes  $A(T + \Delta t)$  and  $B(T + \Delta t)$  of the AND gate as below:

$$P(A(T + \Delta t) = 1 | A(T) = 0) = \int_T^{T + \Delta t} f_B(t) dt, P(A(T + \Delta t) = 1 | A(T) = 1) = 1$$

$$P(B(T + \Delta t) = 1 | B(T) = 0) = \int_T^{T + \Delta t} f_B(t) dt, P(B(T + \Delta t) = 1 | B(T) = 1) = 1$$

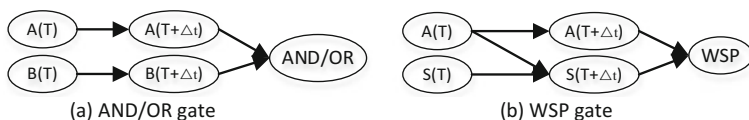


Fig. 3 DBN for logic gates of dual components

Here,  $f_i(t)$  denote the probability density function for the  $i$  component in the time  $t$ .

From Fig. 3a, we can find that the conditional probabilities for the faulty values of Nodes  $A(T + \Delta t)$  and  $B(T + \Delta t)$  of the OR gate are the same as the AND gate, so we only need to calculate the conditional probabilities for the faulty values of the OR gate which are assigned as below (in all the cases not reported, the probability of failure is 0).

$$\begin{aligned} P(\text{OR} = 1 | A(T + \Delta t) = 1, B(T + \Delta t) = 0) &= 1 \\ P(\text{OR} = 1 | A(T + \Delta t) = 0, B(T + \Delta t) = 1) &= 1 \\ P(\text{OR} = 1 | A(T + \Delta t) = 1, B(T + \Delta t) = 1) &= 1 \end{aligned}$$

Here, we take the WSP system that have dual components as an example. If the primary component  $A$  fails, it can be substituted by a spare component  $S$ , if every component (either principal or spare) is failed, the gate produces a fault. We can take  $f_i(t)$  as the probability density function for the component  $i$  in the working time  $t$ , and  $f_{\alpha s}(t)$  denotes the probability density function for the spare component  $S$  in the dormancy time  $t$ . Then the DBN for the WSP gate can be drawn in Fig. 3b.

From Fig. 3b, we can find that node  $S(T + \Delta t)$  at time  $T + \Delta t$  may depend not only on its “historical” copy (i.e. on the same variable at time  $T$ ), but also on the values of node  $A(T)$  in the previous time slice. If the primary component  $A$  is working in the time  $T$ , the probability density function for the spare component  $S$  at time  $T + \Delta t$  will be  $f_{\alpha s}(t)$ . On the contrary, If the primary component  $A$  is failure in the time  $T$ , the probability density function for the spare component  $S$  at time  $T + \Delta t$  will be  $f_s(t)$ . According to the above analysis, the conditional probabilities for the faulty values of all the Nodes in Fig. 3b can be calculate as below:

$$\begin{aligned} P(A(T + \Delta t) = 1 | A(T) = 0) &= \int_T^{T+\Delta t} f_A(t)dt, P(A(T + \Delta t) = 1 | A(T) = 1) = 1 \\ P(S(T + \Delta t) = 1 | S(T) = 1) &= 1 \\ P(S(T + \Delta t) = 1 | S(T) = 0, A(T) = 0) &= \int_T^{T+\Delta t} f_{\alpha s}(t)dt \\ P(S(T + \Delta t) = 1 | S(T) = 0, A(T) = 1) &= \int_T^{T+\Delta t} f_s(t)dt \\ P(\text{WSP} = 1 | S(T + \Delta t) = 1, A(T + \Delta t) = 1) &= 1 \end{aligned}$$

### 3.3 Comparison Analysis of DBN Model and Probabilistic Model

For verifying the accuracy of DBN model, the reliability analysis on the logic gates are given by DBN model and probabilistic model by using the Bayes Net Toolbox

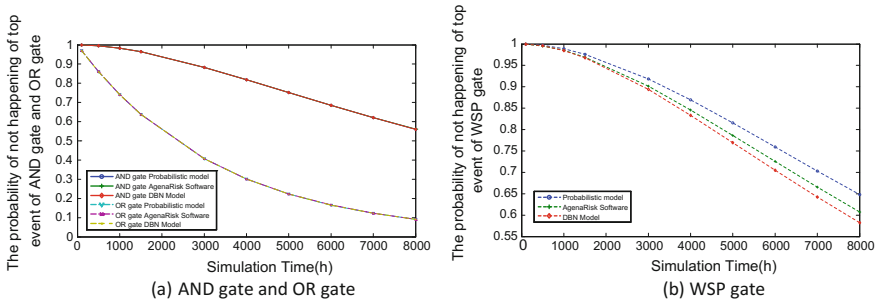


Fig. 4 The comparison results of logic gate

for Matlab R2010b [16, 17]. Meanwhile, we also use the business analysis software AgenaRisk [19, 20] to verify the correctness of DBN model in Matlab.

According to the dual component system of logic gate, the simulation conditions are set as follows: the simulation time  $t$  is equal to 8000 h, the interval of the simulation time  $\Delta t$  is equal to 0.5 h, component A and component B follow the exponential distribution, the failure rate  $\lambda_A = \lambda_B = 0.0000006 \text{ Fits}$  in Fig. 4(a), while  $\lambda_A = 0.0001 \text{ Fits}$ ,  $\lambda_B = 0.002 \text{ Fits}$  in Fig. 4b, the comparison results are shown in Fig. 4.

From Fig. 4, we can find that compared with the traditional DFT probabilistic model analysis method, DBN model is used to analyze the standard fault tree (include only AND gate and OR gate) with no calculation error. However, for the analysis of the spare gate commonly used in the railway system, DBN model have an error due to the use of the principle of time discretization, but the error is tolerable and leads to more strictly calculations. Therefore, the use of DBN calculated by the reliability of such systems is credible.

## 4 Reliability Analysis of RISS

As different railway station has different station scale, the quantity of intelligent signal in RISS are also different. Take a railway station with three tracks in Cheng-Kun railway for example, the structure diagram of RISS is shown in Fig. 5.

According to the DFT shown in Fig. 2 and the structure diagram of RISS with three tracks shown in Fig. 5, we can convert the DFT of RISS with three tracks into the corresponding DBN, by using DBN models of the logic gates in the previous section. The conversion results are shown in Fig. 6.

To analyze the reliability indexes of RISS with different railway station scale, we choose four types of RISS with 2 signals, 4 signals, 7 signals and 14 signals to discuss. Considering the communication network and the power supply network are

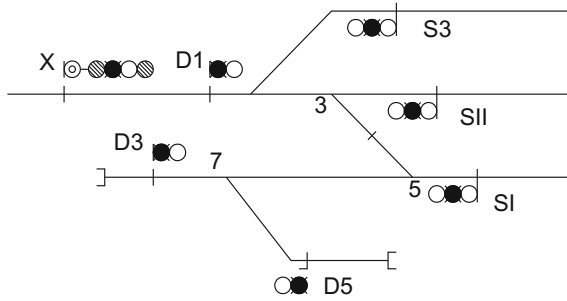


Fig. 5 Structure diagram of RISS with three tracks

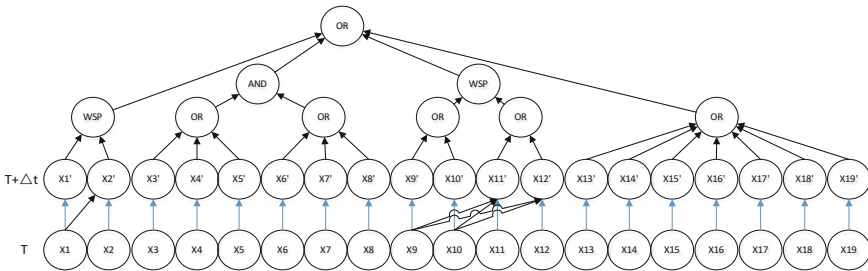


Fig. 6 DBN model of RISS with three tracks

dual redundancy system, we can set up the dormancy factor  $\alpha$  of the spare gate is equal to 1, it means that the logic gate of DFT of these system is a HSP gate.

### 4.1 Computing Reliability

According to the DBN model of RISS with three tracks shown in Fig. 6 and the basic failure data shown in Table 1, we can compute the failure probability of RISS with 7 signals using the inference algorithm. Meanwhile, the failure probability of RISS with 2 signals, 4 signals and 14 signals can also be computed by their DBN model and the basic failure data. The main different between these DBN model is the quantity of the input event of the OR gate. Here, we use the Junction Tree algorithm to calculate the reliability index of RISS. Figure 7 shows the reliability comparison results of RISS with different signals.

The simulation conditions of Fig. 7 are set as follows: the simulation time  $t$  is equal to 3000 h, the interval of the simulation time  $\Delta t$  is equal to 0.5 h. As we can see in Fig. 7, the reliability of RISS decreases linearly with the increase of the quantity of intelligent signal in RISS.



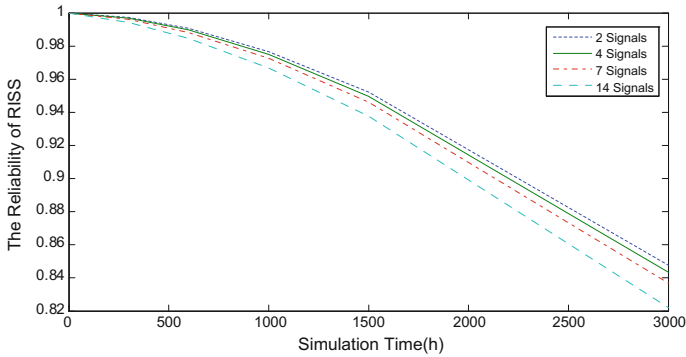


Fig. 7 The reliability comparison results of RISS with different signals

### 4.2 Sensitivity Analysis

Sensitivity analysis can help designers find design flaws or important components that have a significant impact on the normal operation of the system, and the impact the improvement of important component reliability will have on the overall system reliability. Here, we show how one can perform sensitivity through the usage of the Birnbaum importance factor (BIF) [21].

The BIF of basic event  $j$ ,  $BIF_j$ , is defined as

$$BIF_j = P(\text{System} = 1 | j = 1) - P(\text{System} = 1 | j = 0)$$

where  $P(\text{System} = 1 | j = 1)$  is the probability of the system failure when basic event  $j$  happens, and  $P(\text{System} = 1 | j = 0)$  is the probability of system failure when basic event  $j$  cannot happen. System and basic event failure or working are indicated by 1 or 0, respectively.

Table 2 shows the BIF of all components for RISS with different signals, and the simulation time  $t$  is equal to 1000 h. According to Table 2, we know that the intelligent signal has the maximum BIF, followed by CAN bus system, and the impact of variable structure of RISS has little effect on the order of BIF ranking of each component of RISS. So, we should improve the reliability of the intelligent signal and CAN bus system at the stage of product design in order to decrease the failure probability of RISS by several approaches.

### 4.3 Performing Diagnosis

Diagnostic importance, which can be calculated by the minimum cut sets method, is mainly used to analyze the fault diagnosis order of system components [22]. We can conveniently calculate diagnostic importance factor (DIF) by DBN and

**Table 2** The BIF and DIF of all components for RISS at the given time of 1000 h

Components	Birbaum importance factor				Diagnostic importance factor			
	2 signals	4 signals	7 signals	14 signals	2 signals	4 signals	7 signals	14 signals
X1, X2	0.033049	0.032993	0.032909	0.032714	0.041508	0.0398655	0.037777	0.034130
X3-X8	0.122434	0.122226	0.121915	0.121191	0.151124	0.1425265	0.131598	0.112513
X9-X12	0.031863	0.031808	0.031727	0.031539	0.019931	0.0191515	0.018160	0.016429
X13-Xn	0.977096	0.975438	0.972953	0.967181	0.018222	0.0170116	0.015473	0.012787

perform diagnosis to locate the system failure. DIF is defined conceptually as the probability that an event has occurred given that the top event has also occurred.

The DIF of basic event  $j$ ,  $DIF_j$ , is defined as

$$DIF_j = P(j | \text{System} = 1)$$

where  $P(j | \text{System} = 1)$  is the probability of basic event  $j$  failure when the top event happens, and  $j$  is a component in the system.

Table 2 shows the DIF of all components for RISS with different signals, and the simulation time  $t$  is equal to 1000 h. According to Table 2, we know that the CAN bus system has the maximum DIF, and the impact of variable structure of RISS has little effect on the order of DIF ranking of each component of RISS. So, we should give priority to the CAN bus system fault check, followed by the power supply network, indoor double 2-vote-2 secure control system, and finally the outdoor intelligent signal when the system fails.

## 5 Conclusion

The compositional approach of DFT analysis and DBN analysis has been described in detail. From the simulation results, we can get an approximation of railway signal system reliability by using DBN model, but the results will be more strictly and credible. Based on the forward and backward inference of DBN, the reliability indexes of RISS, such as the system reliability, BIF and DIF, can be easily calculated. From the calculation results, we can see that the intelligent signal and CAN bus system have the most contribution to the top event probability. So, we should improve their reliability at the stage of product design in order to decrease the failure probability of RISS by several approaches.

**Acknowledgements** This work was supported by National Natural Science Foundation of China under Grant No. 61490705, National Natural Science Foundation of China under Grant No. 61603027 and the Fundamental Research Funds for the Central Universities under Grant 2015JBM012.

## References

1. Kuang W (2012) Distributed computer interlocking system of railway station. *China Railway Sci* 33(5):139–143
2. Li S, Li W (2015) Design and implementation of a novel intelligent signal control system for railway. *Modern Electron Tech* 38(14):156–159
3. Liu J, Guo H et al (2015) Research on reliability of auxiliary power system of CRH3 electric multiple units. *J China Railway Soc* 37(11):44–51
4. Shang G, Yuan M et al (2016) Design of and performance evaluation methods for GNSS-based train positioning unit. *J China Railway Soc* 38(2):64–73

5. Wang H, Lu Z, Zhang B (2012) Analysis method for the operational reliability of emu running gear based on Fault tree and Bayesian network. *China Railway Sci* 33(8):60–64
6. Su H, Che Y, Zhang Y (2014) Dependability assessment of CTCSS-3 on-board subsystem based on bayesian network. *China Railway Sci* 35(5):96–104
7. Xue Feng, Wang X (2011) Analysis on reliability and performance of computer-based interlocking system with the dynamic fault tree method. *J China Railway Soc* 33(12):78–82
8. Tan X, He Z et al (2011) Analysis on reliability of the subway station-level integrated supervisory and control system based on dynamic fault tree analysis. *J China Railway Soc* 33(7):52–60
9. Ruijters E, Stoelinga M (2015) Fault tree analysis: a survey of the state-of-the-art in modeling, analysis and tools. *Comput Sci Rev* 15:29–62
10. Montani S, Portinale L, Bobbio A (2005) Dynamic Bayesian networks for modeling advanced fault tree features in dependability analysis. In: *Proceedings of the 16th european conference on safety and reliability, Leiden, The Netherlands, AA Balkema*, pp 1415–1422
11. Zhuo Z, Ma Z et al (2008) Dynamic fault tree analysis based on dynamic Bayesian networks. *Syst Eng-Theory Pract* 28(2):35–42
12. Liu D, Zhang H et al (2013) *Methodologies of dynamic fault trees analysis*. National Defense Industry Press, Beijing
13. Duan R, Fan J (2014) Reliability evaluation of data communication system based on dynamic fault tree under epistemic uncertainty. *Math Problems Eng*
14. Su H (2013) Reliability and security analysis on two-cell dynamic redundant system. *Indonesian J Electr Eng Comput Sci* 11(5):2594–2604
15. Xia J, Zhang C, Bai R et al (2013) Real-time and reliability analysis of time-triggered CAN-bus. *Chin J Aeronaut* 26(1):171–178
16. Zhou D (2014) *The application of bayesian networks in system reliability*. Arizona State University
17. Murphy K (2001) The bayes net toolbox for matlab. *Comput Sci Statistics* 33(2):1024–1034
18. Cheshmikhani E, Zarandi HR (2015) Probabilistic analysis of dynamic and temporal fault trees using accurate stochastic logic gates. *Microelectron Reliab* 55(11):2468–2480
19. Marquez D, Neil M, Fenton N (2010) Improved reliability modeling using Bayesian networks and dynamic discretization. *Reliability Eng Syst Safety* 95(4):412–425
20. Agena Ltd (2016) AgenaRisk software package, [www.AgenaRisk.com](http://www.AgenaRisk.com)
21. ELSAYED A (2013). *Reliability engineering (Second Edition)*. (trans: Zhou Y). Electronic Industry Press, Beijing, pp 98–106
22. Tao Y, Dong D, Ren P (2010) An improved method for system fault diagnosis using fault tree analysis. *J Harbin Institute Technol* 1:143–147

# Key-Point Feature Detection Method for Surrounding-Field-of-View Image Applications

Mai Jiang, Qi cheng Yan and Cheng tao Cai

**Abstract** This paper describes a robust feature detection method for omni-directional image which used for target and region-of-interest (ROI) detection. The omni-directional system can provide much larger FOV (field of view) which can support 360° of the whole environment. Firstly, we briefly introduce the back-transformation model of the omni-directional system. Then, the Harris and SIFT (scale invariant feature transform) is applied to find the key-point features of the around area. Finally, we compared the above feature detection methods (Harris and SIFT) for the omni-directional image and its corresponding unwrapping panoramic-cylindrical and solve this matching problem with some experiment and discussion.

**Keywords** Omni-directional image · Back-transformation model  
Feature detection · SIFT

## 1 Introduction

Generally, conventional cameras only present a limited field of view. For automotive applications, a surrounding view of the circumstance brings significant advantages and a 3D perception of the surroundings is crucial and helpful. In surveillance, wide angle can provide significant information in one video-stream [1], the global view is very suitable for highly dynamic environments in fully automation soccer player robot application [2], because for robot navigation and

---

M. Jiang (✉)

Criminal Investigation Department, National Police University of China, Shenyang, China  
e-mail: jiangmai@npcu.edu.cn

Q. Yan

Crime Investigation Department, Public Security Bureau of Xuhui, Shanghai, china

C. Cai

College of Automation, Harbin Engineering University, Harbin, China

© Springer Nature Singapore Pte Ltd. 2018

L. Jia et al. (eds.), *Proceedings of the 3rd International Conference on Electrical and Information Technologies for Rail Transportation (EITRT) 2017*, Lecture Notes in Electrical Engineering 482, [https://doi.org/10.1007/978-981-10-7986-3\\_86](https://doi.org/10.1007/978-981-10-7986-3_86)

857

map building the surrounding field of view solve the robot to look around using moving equipment [3].

There lots of ways have a large field of view, such as multi-part mirror or multiple cameras construction(stereo vision), omni-directional cameras, fisheye cameras, and single camera on a pan-tilt unit, etc. [4, 5]. But limitations still exist, such as multi-part mirror or multiple cameras which structure need more time consume because need to stitch the images together into a panoramic image, omni-directional cameras with lower resolution compare with the conventional camera, single camera existing frame loss condition and must be calibrated in addition.

The global surrounding view output by the omni-directional vision system especially suitable for highly dynamic large environments and it is also very useful take the omni-directional cameras to enlarge the viewer range and through the wide field of view of the 3D information we can perceive accurate geographical situation. The algorithms relative stability in omni-directional image despite there exist lower resolution and poor in peripheral area [6].

Many surveillance systems need to adding intelligent functions into the software, basically, image analysis may process straight onto the omni-directional images or we transform those into traditional images in advance, and most of the above methods do not concern the circle image feature points extracting technology, but it is necessary to extract more information from a captured image in order to process it for the next step (e.g. object detection, obstacle avoidance and target tracking, etc.). In this paper, we investigate omni-directional based feature point detection method.

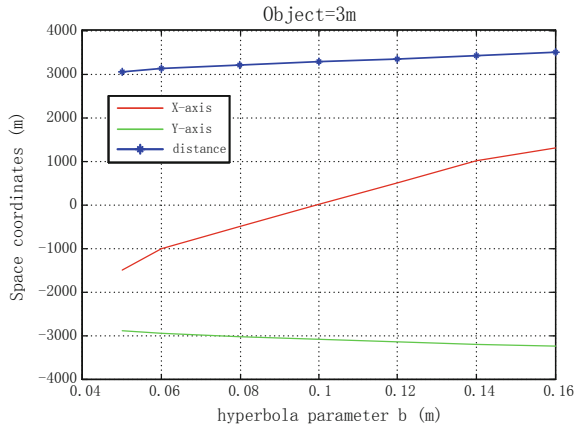
In the remainder of this paper, in Sect. 2 we present a briefly introduced the omni-directional vision system composition and some resolution analysis under different circumstances. Then in Sect. 3 we present the SIFT algorithm for the image feature point detection based on omni-directional system and gives an overview about the back-transformation model. Some experimental results and conclusions are presented in Sect. 4.

## 2 Omni-Directional Vision System

The omni-directional vision system generally consists of a convex mirror and digital camera which used to refracting and reflecting the light, respectively: the convex mirror commonly conical, cylindrical, ellipsoidal, spherical, parabolic or hyperbolic which can reflect the whole space around the vision system into the camera. For obtain acquire a single image which including the whole scenario information the mirror and the camera must be arranged in the vertical alignment way to guarantee the single effective viewpoint. Paper [7] has introduces the use of convex mirrors in details with different mirror shapes and their differences.

The goal of this work is to find a method which covers a large field of view. Our omni-directional vision system, which includes a traditional perspective CCD or CMOS camera and a hyperbolic-shaped mirror, the hyperbolic mirror is set above the camera and normal toward to the camera lens and their axis center remain stay

**Fig. 1** The vertical space resolution ability with the object = 3 m



same. This component can provide 360° (omnidirectional vision). The output image is very reliable and accurate because this system accord with single-viewpoint constraint criterion.

The resolution characteristic of the hyperbolic mirror can be performed by computer simulation mathematically or by trial and error, for achieve the best resolution result from the computer vision system, we experiment beforehand and the simulation is divided into two parts: we first deduced the refraction and reflection function among the object, the fixed shape hyperbolic mirror and the camera sensor in different distance, this calculation is based on the kind of resolution which we want, next, we computed the resolution result of different shape hyperbolic mirror with fixed location for our expected in future.

For instance, Fig. 1 displayed the minimum resolution distance curve with object’s vertical length of 3 m, where  $b$  is the minor axis parameter,  $X$ -axis,  $Y$ -axis and distance is the space distance separately, after we have simulation our expect omni-directional resolution algorithm with software in advance, and fabricate the mirror at the special manufacture to meet our needing. The mirrors are shape of convex quadric surface and coated with nickel alloy for the best reflection.

### 3 Omni-Directional Image Processing

#### 3.1 Back-Transformation Model

In this section we show the transform method from omni image into cylindrical panoramic image, because the original omni-directional image with circle shape, to process the gathered images in regular algorithm we should transform the omni-directional image into an image without distortion through pinhole transformation ideally. We know each incident light ray strikes the mirror surface must pass the mirror focus and reflected to the second focus (the camera focus), so it is

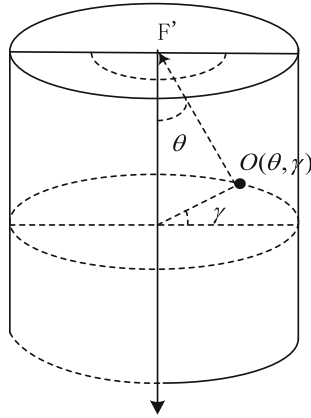


Fig. 2 Transforms between hyperbolic and cylindrical cameras system

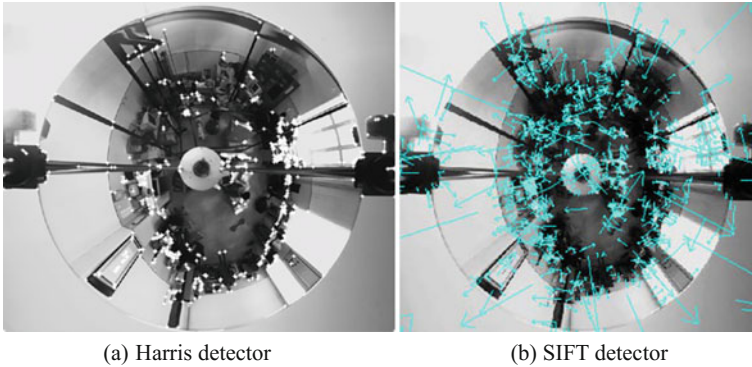


Fig. 3 Feature points detection results with the original image

possible to compute the relationship between the each pixel and light after we have the system geometry (Fig. 2). Figure 3 illustrates mapping of a hyperbolic image into cylindrical camera system.

Where  $O(\theta, \gamma)$  is the polar coordinates presentation of  $(u, v)$   $F'$  indicates the hyperbolic mirror's focus, and  $\theta, \gamma$  is the roll and pitch angles, respectively. According to [8], the relation between a space point  $(X, Y, Z)$  in the camera coordinates and the corresponding image coordinates  $(u, v)$  can be described by the following equations in this geometric configuration:

$$u = \frac{Xf(b^2 - c^2)}{(b^2 + c^2)(Z - c) - 2bc\sqrt{(Z - c)^2 + X^2 + Y^2}} \tag{1}$$



$$v = \frac{Yf(b^2 - c^2)}{(b^2 + c^2)(Z - c) - 2bc\sqrt{(Z - c)^2 + X^2 + Y^2}} \quad (2)$$

### 3.2 SIFT Feature Point Descriptors

The feature point detection is the most critical and the first step of many vision sense technologies, such as object recognition and tracking, SLAM, self-location, image matching and 3D reconstruction. Because we have interest in object recognition applications and especially demands more accuracy, so we employed the SIFT algorithm for a relative fast and quality feature extraction method in the omni-directional image. Through Eq. (3) the key-point location can be achieved, which  $L(x, y)$  represents the Gaussian smooth image and  $k$  is the constant multiplicative factor and  $\sigma$  denotes scope value. The SIFT key-point orientation assignment method can be adopted as the two Eqs. (4) and (5) which describe the magnitude  $o(x, y)$  and orientation  $\alpha(x, y)$  separately.

$$D(x, y, \sigma) = L(x, y, \sigma)L(x, y, k\sigma) - L(x, y, \sigma) \quad (3)$$

$$o(x, y) = \sqrt{(L(x+1, y) - L(x-1, y))^2 + (L(x, y+1) - L(x, y-1))^2} \quad (4)$$

$$\alpha(x, y) = (L(x, y+1) - L(x, y-1)) / (L(x+1, y) - L(x-1, y)) \quad (5)$$

After assigned the image position, scale, and key-point orientation which introduced above, the local image descriptor with 128 dimensions is computed.

Figure 3a, b shows the key-point detection results with Harris and SIFT detections in the original images, respectively [9].

In Fig. 4 from top to bottom, displays the key-point detection results with Harris and SIFT detections in the unwrapping panoramic-cylindrical images separately. From the implementation of Harris, approximately 600 and 900 points were generated on the original image and the unwrapping image, respectively. Similarly, approximately 1000 and 1500 points were found on the original image and the unwrapping image when we adopt the SIFT method. Compared with the Harris feature detectors the SIFT detector is more robust to the noise and find more object details in the same scenario.

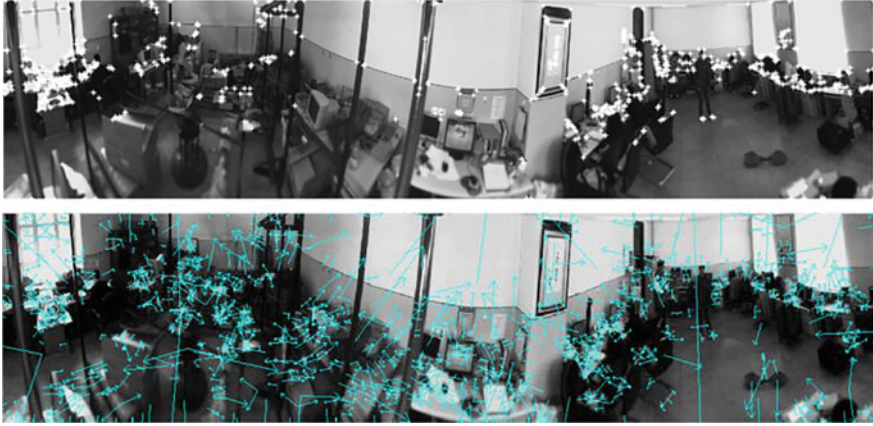


**Fig. 4** Feature points detection results with the unwrapping image (top: Harris, bottom: SIFT)

## 4 Experiment Results and Conclusions

The goal of this paper is to find a robust feature detection method for the omni-directional image. In this section we will mainly discuss the feature detection result of the omni-directional image and its unwrapping image. Dimensions of the original images are set to  $486 \times 486$  and cylindrical panoramic image  $1018 \times 486$ , respectively. We choose two human targets and the dimensions of the image are set to  $122 \times 344$ . The target detection results in the original omni-image and the cylindrical panoramic image displayed in Figs. 5 and 6, respectively.

With a large number of experiments we evaluate the repeatability of the Harris and SIFT detection method, the SIFT detection is obviously robust to the presence of disturbance (e.g. noise), relative to Harris detector more feature points can be detected in both original image and its unwrapping image, it is noteworthy that mistaken detection occurred in the unwrapping at times, it can be expected: since the SIFT convolution is linear and the panoramic image unwrapping algorithm is nonlinear and image distortion cause the error and we will explore the high precision omni-directional image recovery algorithm in the future work. The omni-directional vision system provides a  $360^\circ$  surrounding-field-of-view for saving the security of human and machine, meanwhile, and the SIFT feature detector yield a higher recognition and matching rates for the omni-directional image, it is very helpful for suspect monitoring and detection of the criminal cases, the next step in this work will be the test of the vision system in dynamic environment.

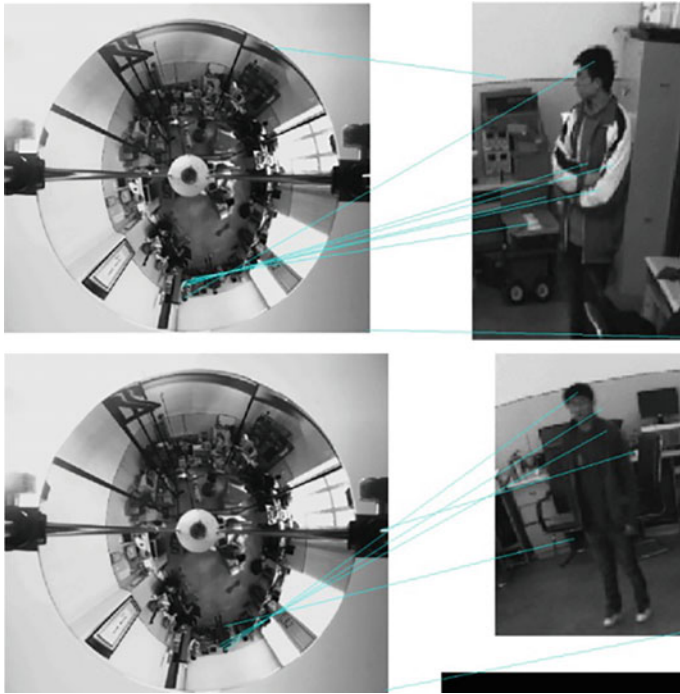


Fig. 5 Matching between the original omni-image and the targets (top: target 1, bottom: target 2)

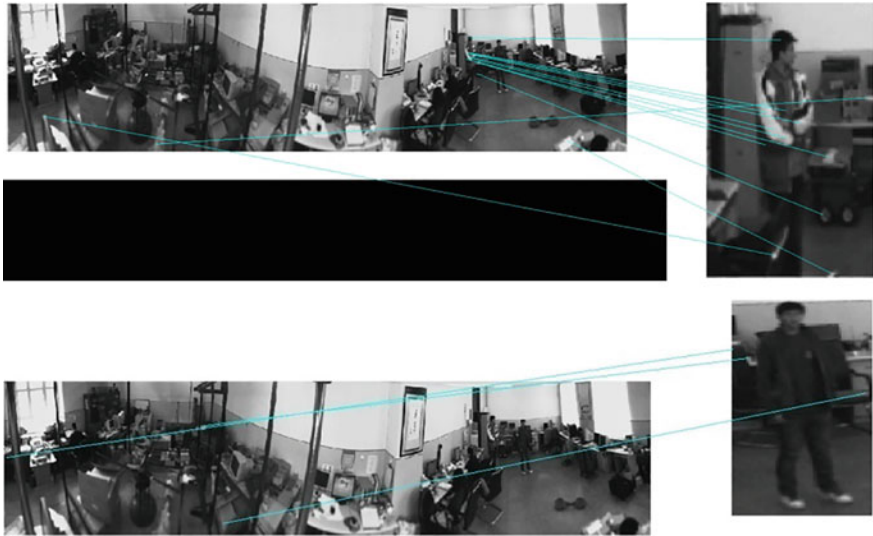


Fig. 6 Matching between the cylindrical panoramic image and the targets (top: target 1, bottom: target 2)

## References

1. Bistry H, Zhang J (2014) Development of an Intelligent Omnivision Surveillance System, vol 215(1). Springer Berlin Heidelberg, pp 783-794
2. Mohades Kasaei Sh, Mohades Kasaei SM, Mohades Kasaei SA, Taheri M (2009) Design and implementation a fully autonomous soccer player robot, vol 3. World Academy of Science, Engineering and Technology, pp 03-28
3. Mohades Kasaei SMR, Mohades Kasaei SHR (2010) Effective mechatronic models and methods for implementation an autonomous soccer robot. *Int J Industrial Eng Prod Res* 163-171
4. Onoe Y, Yamazawa K, Takemura H, Yokoya N (1998) Telepresence by real-time view-dependent image generation from omnidirectional video streams. *Comput Vis Image Underst* 71(2):154-165
5. Ukida H, Yamato N, Tanimoto Y, Sano T, Yamamoto H (2008) Omni-directional 3D measurement by hyperbolic mirror cameras and pattern projection. In: *Proceedings 2008 IEEE conference on instrumentation and measurement technology Victoria, BC, Canada, May 2008*, pp 365-370
6. Salinas C, Armada M., Gonzalez de Santos P (2008) A new approach for terrain description in mobile robots for humanitarian demining missions. *All Publications*
7. Lopes G, Ribeiro F (2012) Catadioptric system optimization for omnidirectional Robocup MSL robots, vol 7416. Springer-Verlag, pp 318-328
8. Yagi Y (1999) Omnidirectional sensing and its applications. *Survey on image processing technologies-algorithms. Sensors and applications*. E82
9. Lowe D (2005) SIFT demo program (Version 4, July 2005): <http://www.cs.ubc.ca/~lowe/keypoints/>

# The Analysis of the Communication Distance in Wireless Optical Communications for Trains

Tairan Zhang, Jianghua Feng, Jiabo Xiao and Jun Tang

**Abstract** Wireless optical communications is considered as a good way to provide big bandwidth for wireless communications. Therefore, the ground-to-train wireless optical communication can supply fast wireless communication service for running trains. In this paper, we demonstrate a system model to analyze and evaluate the communication distance in wireless optical communications for trains. After that, the simulation performance fully prove that the divergence angle and weather condition are two key factors that influence the communication distance. Moreover, the proper distance between two consecutive ground transceivers and the reasonable divergence angle are also displayed which have a significant meaning for guiding the deployment of ground transceivers.

**Keywords** Wireless optical communication · Divergence angle  
Weather condition · Train

## 1 Introduction

Because wireless communications play a important role for constructing intelligent trains, many technologies have been employed, such as radio frequency (RF) wireless technologies, wireless fidelity (WiFi), worldwide interoperability for microwave access (WiMAX) and leaky coaxial cables. However, their bandwidths are limited [1–3]. For example, WiFi can deliver data rates up to 75 Mbps in theory, but its actual data rates are always lower than 10 Mbps.

Recently, wireless optical communications (WOC) is considered as a good way to provide big bandwidth for wireless communications. In WOC, a laser diode emits modulated optical beam whose data rate is in the range of gigabit per second. After the light going through air and finally arriving at the photo-detector (PD), the

---

T. Zhang (✉) · J. Feng · J. Xiao · J. Tang  
CRRC Zhuzhou Institute Co. Ltd., No. 169, Shi Dai Road, Shifeng District,  
Zhuzhou, Hunan, China  
e-mail: zhangtr@csrzc.com

© Springer Nature Singapore Pte Ltd. 2018

L. Jia et al. (eds.), *Proceedings of the 3rd International Conference on Electrical and Information Technologies for Rail Transportation (EITRT) 2017*, Lecture Notes in Electrical Engineering 482, [https://doi.org/10.1007/978-981-10-7986-3\\_87](https://doi.org/10.1007/978-981-10-7986-3_87)

865

optical information can be converted into electronic digital data [4]. The wavelengths of WOC always exist between 780 and 1600 nm since their losses are lower than other wavelengths while traveling over long distances in space. Compared with other wireless technologies mentioned above, the advantages of WOC can be concluded as follows: (1) WOC can easily realize gigabit data transmission [5]; (2) WOC is transparent to any protocol; (3) WOC has no need to apply for frequency permission; (4) WOC is immune to electromagnetic interference; (5) the safety and security of WOC are much better due to its directed light. As a result, WOC is regarded as an alternative technology to supply ideal wireless communications for trains. In WOC, the transmitter emits laser beam with micro divergence angle to the air, and no matter how far away, the receiver is able to performing signal detection as long as it stands in the range of beam. The reason to adopt micro divergence angle is to avoid the risk of making light disperse too much if the communication distance is more than 100 m, which is difficult for a PD to receive enough optical power. Moreover, since WOC is susceptible to weather conditions such as fog, haze, rain, snow, or their combinations [6], the distance is also limited by weather condition.

The remainder of this paper is organized as follows. Section 2 presents system model for communication distance problem. Section 3 display the different simulation results to show how long the acceptable distance is while using WOC for trains. Finally, we conclude this paper in Sect. 4.

## 2 System Model

In a typical ground-to-train WOC, a transceiver is mounted on the train and many base stations (BS), each one has a transceiver, stand along the railway track. There is a distance between a pair of BSes. We use a system model to analyze and evaluate the communication distance of WOC for trains. As shown in Fig. 1, we assume a train travels from point D to point B and a BS stands at point A.  $L1$  is the length of gap between the BS and the track. Suppose the transceiver's divergence angle of BS is  $2\theta$ , and the coverage range of its beam and line DB are point E and point B, respectively.  $L2$  denotes the horizontal distance of  $|DE|$  and  $L3$  represents the coverage range of  $|EB|$ . The value of  $\theta$  will impact the beam radius  $R$  and the  $L3$  along the track [7, 8].

From Fig. 1, we can see  $X^2 = L1^2 + L2^2$ ,  $\tan\beta = L1/L2$ ,  $\tan\delta = L1/(L2 + L3)$  and  $2\theta = \beta - \delta$ . Hence,  $L3$  can be calculated as

$$L3 = \frac{X^2 \tan 2\theta}{L1 - L2 \tan 2\theta} \quad (1)$$

The dotted line AO is the optical axis, and Z is the achievable distance from light source A along the optical axis. It is easy to know that Z is

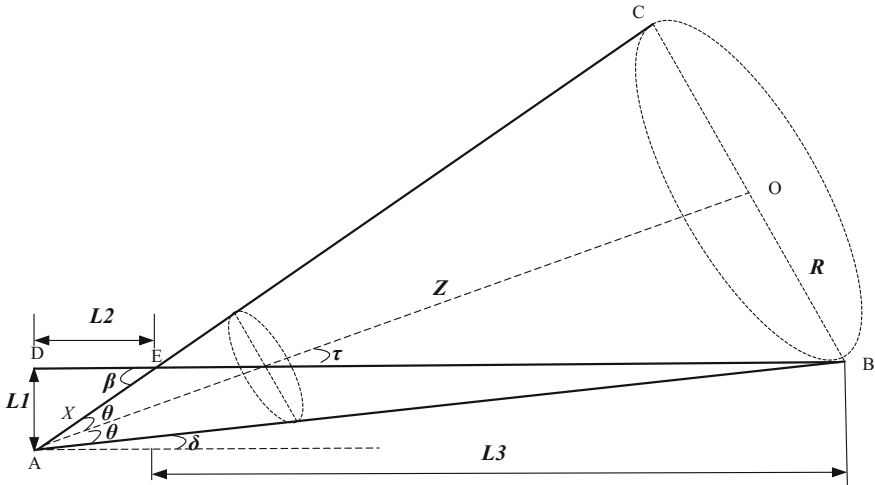


Fig. 1 The top view of ground-to-train WOC

$$Z = L3 \cos \tau + X \cos \theta \tag{2}$$

where  $\tau = \theta + \delta$ . The beam radius corresponds to Z is R, which equals  $Z * \tan \theta$ .

The power obtained by remote receiver at distance Z for the beam is

$$P_r = \frac{P_t A_r}{\pi R^2} e^{-\alpha Z} \tag{3}$$

where  $P_t$  is transmission power out of the transmitter,  $A_r$  is the effective light collection area, and  $\alpha$  is the loss index decided by air condition, respectively.

$A_r$  can be obtained by [9]

$$A_r = \frac{n^2 A_d}{\sin^2 \mu} \tag{4}$$

where  $n$  is refractive index of an optical concentrator that is in charge of focusing light on PD,  $A_d$  is the photosensitive area of PD and  $\mu$  is the half angle field-of-view of the receiver. We set  $n = 1.5$ ,  $A_d = 7 \times 10^{-6} \text{ m}^2$ ,  $\mu = 100 \text{ mrad}$  ( $1 \text{ mrad } 0.057^\circ$ ) [10].

$\alpha$  is the loss index decided by weather condition. It can be calculated as [11].

$$\alpha = \frac{3.91}{V} \left( \frac{550}{\lambda} \right)^q \tag{5}$$

where  $\lambda$  is the wavelength,  $V$  is the visibility and  $q$  is decided by

$$\begin{aligned}
 V \geq 50 \text{ km} & \quad q = 1.6 \\
 50 \text{ km} > V \geq 6 \text{ km} & \quad q = 1.3 \\
 6 \text{ km} > V & \quad q = 0.585\sqrt[3]{V}
 \end{aligned} \tag{6}$$

### 3 Simulation Results

In this section, we use Matlab to perform numerical evaluations of the model described from (1) to (7). The analysis mainly focuses on the impact of the divergence angle of a laser beam and weather condition on the maximum achievable distance and coverage length. The corresponding parameters to our WOC system are listed in Table 1. We choose 850 nm as the value of  $\lambda$  in terms of its reliability, high-performance capabilities, and lower cost of laser diodes and PD.

Based on Fig. 1 and all functions mentioned above, we can understand that the longer the  $Z$  is, the less power the receiver can get. Therefore, the maximum achievable distance,  $Z_{max}$ , for a divergence angle  $\theta$  can be calculated according to the receiver sensitivity threshold, which is  $-36$  dBm at 1 Gbps (corresponding to  $10^{-3.6}$  mW  $\approx$  251 nW) by using an 850 nm vertical cavity surface emitting laser (VCSEL).

Figure 2 shows different values of  $Z_{max}$  and  $L3$  if  $\theta$  varies from 0.05 mrad to 2.3 mrad in 0.25 mrad steps when  $V$  is 5 km (not a good weather). It is obvious that  $Z_{max}$  can reach up to 6932 m from the BS when  $\theta$  is 0.05 mrad. However,  $Z_{max}$  decreases sharply with the increase of  $\theta$ . This result is reasonable since the highly collimated narrow laser beam will lead to a high light intensity at the receiver for a given transmitted power, which in turn results in a bigger  $Z_{max}$  than that of a wide

**Table 1** System model parameters

Parameter	Description	Value	Unit
$\lambda$	Laser wavelength	850	nm
$\theta$	Half of beam divergence angle	Variable	mrad
$L1$	Vertical distance of the BS from the track	1	m
$L2$	Horizontal distance of the BS from the track	Variable	m
$L3$	Coverage range	Variable	m
$Z$	Achievable distance from light source A along the optical axis	Variable	m
$R$	beam radius	Variable	m
$P_t$	Transmission power out of the transmitter	2	mW
$S$	Receiver sensitivity at 1Gbps	-36	dBm
$n$	Refractive index of the telescope	1.5	
$\mu$	Receiver half angle field-of-view	100	mrad
$A_d$	PD area	$7 \times 10^{-6}$	m <sup>2</sup>
$V$	Visibility	Variable	km



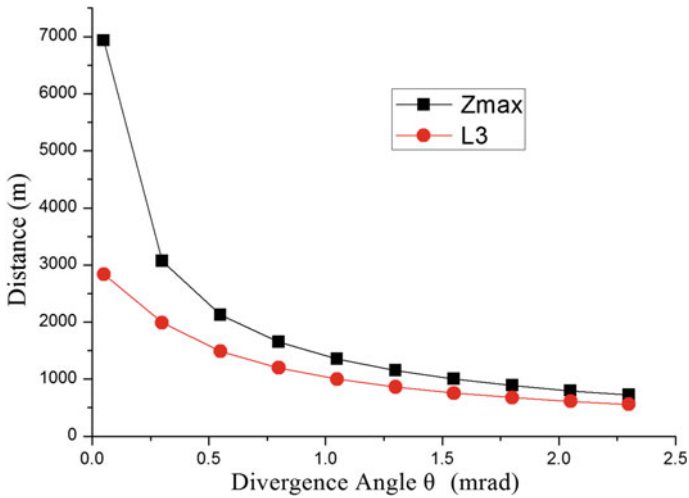


Fig. 2  $Z_{max}$  and  $L3$  for  $\theta$  varying from 0.05 to 2.3 mrad when  $V$  is 5 km

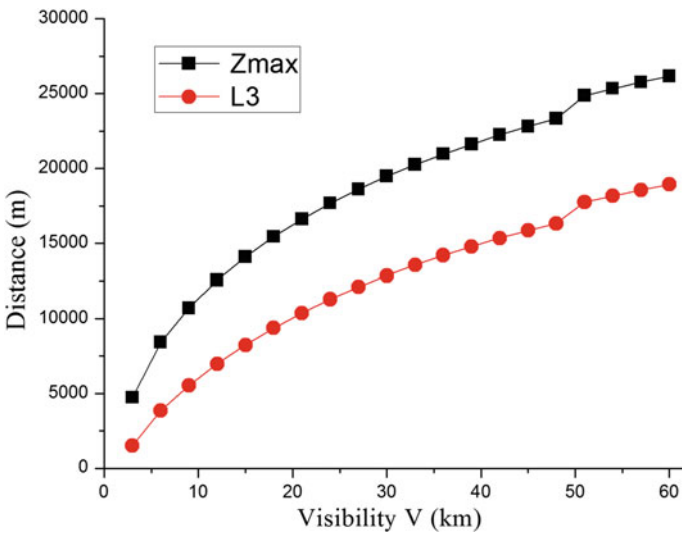


Fig. 3  $Z_{max}$  and  $L3$  for  $V$  varying from 3 to 60 km when  $\theta$  is 0.05 mrad

beam. Due to the limits of  $\theta$  and  $Z_{max}$ ,  $L3$  has the same change trend as  $Z_{max}$ . The significance of  $L3$  is to guide us how to set proper distance between two consecutive BSes.

Figure 3 presents the variation of  $Z_{max}$  and  $L3$  with the change of weather condition when  $\theta$  is 0.05 mrad, respectively. Obviously, the better the visibility is, the longer the  $Z_{max}$  and  $L3$  can be.

## 4 Conclusion

In this paper, we have proposed a model to analyze the communication distance in WOC for trains. The model shows divergence angle and weather condition are two very important factors that decide the communication distance of WOC. Afterwards, the simulation results from Matlab prove that point well, and we are aware of how to set the reasonable distance between two consecutive BSes according to the simulation and analysis.

**Acknowledgements** This work was supported by the China National Science and Technology Support Program under Grant (2015BAG14B00).

## References

1. Yuge T, Sasaki S (1984) Train radio system using leaky coaxial cable. In: Vehicular technology conference 1984, 34th IEEE. vol 34, pp 43–48
2. Aguado M, Onandi O, Agustin P, Higuero M, Taquet E (2008) Wimax on rails. *IEEE Trans Veh Technol* 3(3):47–56
3. Fokum DT, Frost VS (2010) A survey on methods for broadband internet access on trains. *Commun Surv Tutoriels IEEE* 12(2):171–185
4. Alkholidi AG, Altowij KS (2014) Free space optical communications—theory and practices
5. Urabe H, Haruyama S, Shogenji T, Ishikawa S, Hiruta M, Teraoka F, Arita T, Matsubara H, Nakagawa S (2012) High data rate ground-to-train free-space optical communication system. *Optical Eng* 51(3):031204-1–031204-9
6. Bloom S, Korevaar E, Schuster J, Willebrand H (2003) Understanding the performance of free-space optics [invited]. *J Optical Netw* 2(6):178–200
7. Kaymak Y, Rojas-Cessa R, Feng J, Ansari N, Zhou M (2017) On divergence-angle efficiency of a laser beam in free-space optical communications for high-speed trains. *IEEE Trans Vehicular Technol* 99. (Online)
8. Fathi-Kazerooni S, Kaymak Y, Rojas-Cessa R, Feng J, Ansari N, Zhou M, Zhang T (2017) Optimal positioning of ground base stations in free-space optical communications for high-speed trains. [arXiv:1706.XXXXX](https://arxiv.org/abs/1706.XXXXX). [cs.NI]
9. Brien DC, Faulkner G, Le Minh H, Bouchet O, El Tabach M, Wolf M, Walewski JW, Randel S, Nerreter S, Franke M et al (2009) Gigabit optical wireless for a home access network. In: Personal, indoor and mobile radio communications, 2009 IEEE 20th international symposium on. IEEE, pp 1–5
10. Paudel R, Ghassemlooy Z, Le-Minh H, Rajbhandari S (2013) Modeling of free space optical link for ground-to-train communications using a gaussian source. *IET Optoelectron* 7(1):1–8
11. Ji Y (2013) The research on the beacon light and signal optical transmitter module for vehicle wireless optical communication. University of Electronic Science and Technology of China

# The Research on Route Search Based on Heuristic Strategy

Cheng Wang, Shaobin Li, Yan Li, Ziwei Liu and Huiyong Liu

**Abstract** Route search, actually in rail transit, is finding an accessible and safe route for train dispatching. Route search is the basic function of computer based interlocking system. The efficiency of route search and the correctness of the target route searched are of great significance to ensure the traffic safety. In view of the similarity between the railway yard and the directed graph, the railway yard will be modeled as a directed graph. In this paper, a new route search method, combining the depth-first traversal and heuristic strategy, has been proposed. Test results based on real yard show this method can quickly and accurately search target route. And it has high practical application value.

**Keywords** Route search · Depth-first traversal · Heuristic search  
The directed graph

## 1 Introduction

With the rapid development of railway transportation, computer based interlocking system (CBI) has been widely used in signal control field. It mainly deals with the interlocking relationship between switch, signal and track circuit, and improves the efficiency of transportation on the premise of ensuring safety [1]. A basic function of computer based interlocking system is to find strictly correct and available route for train dispatch, to avoid train collisions and derailments [2]. Route search, literally, is searching the target route according to the start signal and the end signal given [3]. Recent interlocking systems mainly adopt one of the implementation styles: called as route-list based style and route-search based style. The former one contains a set of static data consisted by all possible routes which are generated

---

C. Wang (✉) · S. Li · Y. Li · Z. Liu · H. Liu  
School of Electronic and Information Engineering, Beijing Jiaotong University,  
Beijing, China  
e-mail: 15120277@bjtu.edu.com

© Springer Nature Singapore Pte Ltd. 2018  
L. Jia et al. (eds.), *Proceedings of the 3rd International Conference on Electrical and Information Technologies for Rail Transportation (EITRT) 2017*, Lecture Notes in Electrical Engineering 482, [https://doi.org/10.1007/978-981-10-7986-3\\_88](https://doi.org/10.1007/978-981-10-7986-3_88)

previously. The latter one, contrarily, is embedded by real-time route-search process other than data copies [2]. In this paper, we mainly discuss the latter one.

In view of the similarity between the railway yard and the directed graph, the railway network will be modeled as a directed graph for route search. And in order to improve efficiency, the artificial intelligence theory is applied in the computer interlocking system. A method combining the idea of heuristic search and depth-first traversal has been put forward, to improve the existing route search method.

## 2 Railway Yard Model

### 2.1 Layout of Railway Yard

In a railway yard, signal equipment mainly includes signal, switch, track circuit and so on. Each equipt has a circuit to output its real-time status (busy or idle) and acts according to the operation command. A typical railway yard is shown in Fig. 1. This is a throat area in down direction.

According to the physical connect among signal equipment, whole station network can be abstracted as a directed weighted Graph  $G(V,E)$ .  $V$  is the set of nodes,  $V = \{ v_1, v_2, v_3, v_4, \dots, v_i \}$ .  $E$  is the set of connections between two nodes,  $E = \{ e_1, e_2, e_3, e_4, \dots, e_i \}$  [4].

### 2.2 The Directed Graph Model of Railway Yard

The signal equipments, signal, switch, track circuit without switch (NoSwitch for short), and intruded-limit insulated joints (CX for short), have been chose as nodes

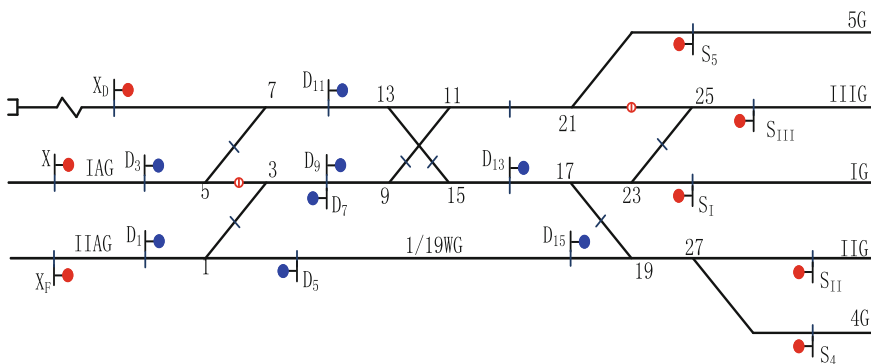


Fig. 1 Layout of railway yard

in the railway-yard directed graph. The physical connects among these signal equipments are regarded as edges. The railway-yard directed graph can generated automatically according to the coordinates of signal equipment in the layout of railway yard. The railway-yard directed graph for testing is shown in Fig. 2.

### 2.3 Data Storage Structure

There are two data storage structures for directed graph, adjacency list and adjacency matrix. The adjacency list is a popular choice because its structure is very compact in the representation of a sparse graph. Hence adjacency list is chose to storage railway-yard directed graph.

For a directed graph, a inverse adjacency list is necessary. The adjacency is used to record the out-degree of node, while the inverse adjacency list is used to record the in-degree of node. The storage structure of adjacency list is defined in Fig. 3. And the additional node information of node is shown in Table 1. Note that if one node don't have subsequent node, it's a dead node [5]. It is important in programming.

## 3 Route Search Algorithm on Heuristic Strategy

For a directed acyclic graph, there are generally two ways for traversal: depth-first search (DFS) and breadth-first search (BFS) [6]. Depth-first traversal is similar to DLR in binary tree [7]. It is the common choice in railway-yard route search. The process of DFS is stated as follows:

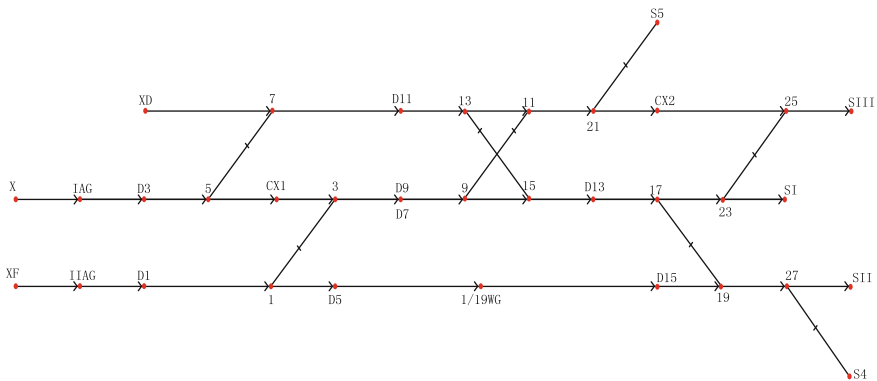


Fig. 2 Railway-yard directed graph

```
#define MAXV the largest number of vertices
#define MAXL the largest number of data information
typedef struct ANode {
    int adjvex;
    struct ANode *nextarc;
}ArcNode;
typedef struct VNode {
    char data[MAXL];
    ArcNode *firstarc;
    ArcNode *vfirstarc;
}VNode
typedef struct AdjList[MAXV];
typedef struct{
    AdjList adjlist;
    int n,e;
}ALGraph;
```

**Fig. 3** Storage structure of adjacency list

**Table 1** Additional node information

Field	Explanation
No	The natural number
Type	Type of the signal equipment
Direct	Open direction of the frog or direction of paratactic shunting signal
Xp	X-coordinate in the directed graph
Yp	Y-coordinate in the directed graph
Remark	No of the linkage switch or of the paratactic shunting signal

- Visit the starting point *u*, and set visited flag.
- Then visit every adjacent node *v* of *u*, if *v* is not visited, *v* will be the new starting point *u*, and turn to step 1(This is a recursion process). If not, backtrack.

In brief, DFS visits nodes as deep as possible. The pseudo code is described in Fig. 4.

**Fig. 4** Pseudo code of DFS

```
void DFS(Vetex v)
{
    Visited[v] = true;
    for each w adjacent to v
        if (!Visited[w])
            DFS(w);
}
```

However, DFS is a blind algorithm. In order to improve efficiency, a new search method combining the depth-first traversal with heuristic strategy has been put forward.

Heuristic search uses the characteristics of the problem itself to control search direction. It gives priority to visit the most promising node which is in the optimal route, making it close to the optimal solution, and getting high search efficiency. In fact, when switch node is visited in search process and its frog open direction is in accordance with the search direction, judge the two adjacency node which is more promising to get the target node by the calculation of evaluation function. Evaluation function is a real function used to estimate the node importance. It is got according to the practical experience and experiment optimization. Considering that the effects of longitudinal linear distance change is more than that of horizontal linear distance change, hence weighted Manhattan Distance has been chosen as the evaluation function  $h(v)$ . The function is stated as following. Note that  $V_i$  is the arbitrary node in the search process. Its coordinates are  $(x_i, y_i)$ . The  $V_j$  is the target node. The coordinates are  $(x_j, y_j)$ .

$$h(v_i) = |x_i - x_j| + 2 * |y_i - y_j| \quad (1)$$

In addition, railway-yard route search is an actual problem. Therefore there are some constraints according to the relevant regulation, stated as bellow:

- In order to avoid detour route, only search along the same direction of siding is allowed. In this way, we won't find a detour route. This principle isn't used in spared route search.
- The change point must be specified in spared route search.

The entire route search process has been described in detail in the flowchart in Fig. 5.

## 4 Experiment and Analysis

Before testing, the first step is to generate the table of route node pair [8]. All possible route node pair is ruled in Table 2.

This method is used before train dispatch. Hence it will give CBI all involved signal equipment in the target route. If the route searched satisfies the interlocking relationship, it will display in the form of white light band. We choose X as the start signal and SIII as the terminal signal. Search the incoming route to IIIG. Test result is shown in Fig. 6. We choose D11 as the start signal and D13 as the terminal signal. Shunting route test result is shown in (Fig. 7).

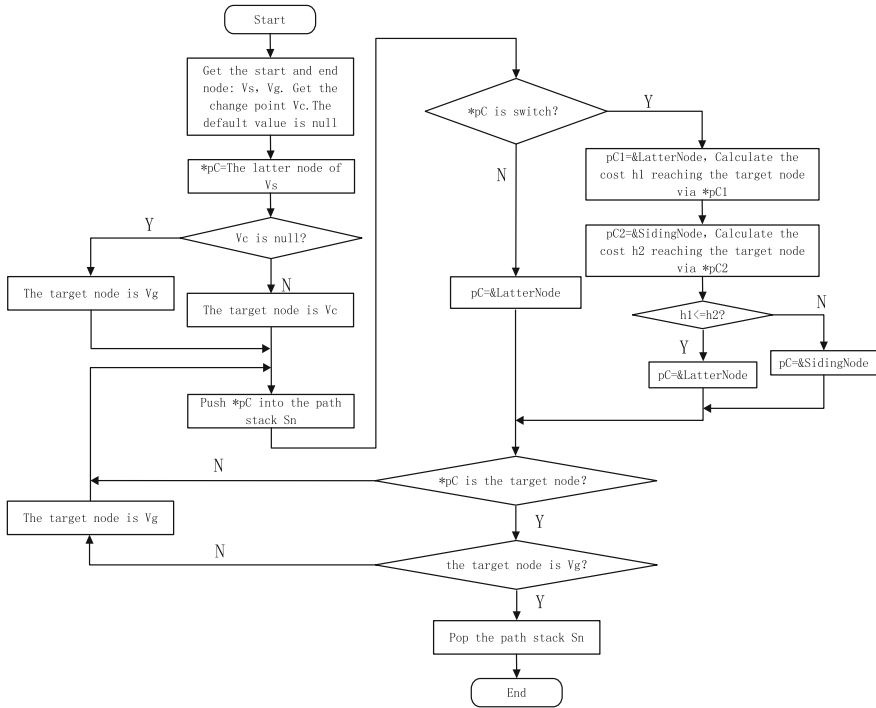


Fig. 5 Flowchart of route search algorithm

Table 2 Route node pair

Start node	Terminal node	Route type
Inbound train signal	Outbound train signal in the same throat area	Incoming route
Outbound train signal	Inbound train signal in the same throat area	Outgoing route
Inbound train signal	Inbound train signal in different throat area	Through route
Shunting signal	Single shunting signal in the same direct and same throat area	Shunting route
Shunting signal	Reverse paratactic shunting signal in the same throat area	Shunting route
Shunting signal	Reverse staggered shunting signal in the same throat area	Shunting route
Shunting signal	Reverse outbound-shunting signal in the same throat area	Shunting route
Shunting signal	Reverse signal shunting signal. The outside is an outbound signal	Shunting route



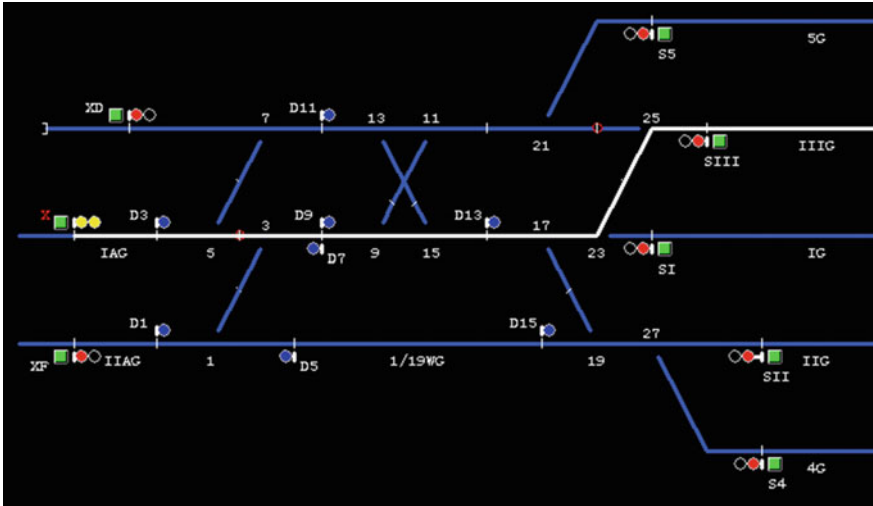


Fig. 6 Test result of incoming route

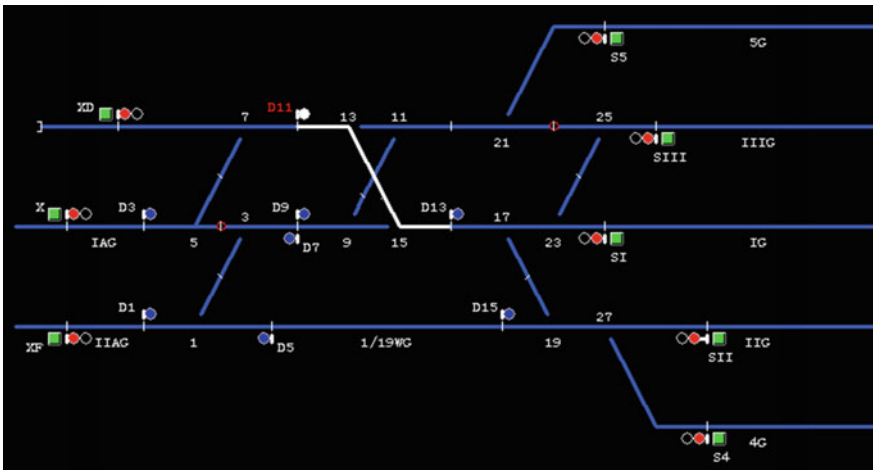


Fig. 7 Test result of shunting route

## 5 Conclusion

Because of the heuristic information, it makes more intelligent in judging the search direct. Effectively reduces the number of search times. Meanwhile, the application of evaluation function only in switch node improves the search efficiency. Hence, the Route search algorithm based on heuristic strategy has a great advantage in the simplicity of time redundancy and programming.

## References

1. Xie L, Yang Y (2015) Two-dimensional coordinate information based route searching algorithm. *Railway Comput Appl* 08:16–19 (in Chinese)
2. She X, Sha Y, Chen Q, Yang J (2007) The application of graphic theory on railway yard interlocking control system. In: *IEEE intelligent vehicles symposium*, 883–887. Istanbul, Turkey
3. Song Y (2014) The Research on route searching based on a-star algorithm. *Southwest Jiaotong University*: 5 (in Chinese)
4. Xiao M, Ning H, Zhao Z (2012) Directed graph based route searching research and design. *Autom Instrum* 06:69–73 (in Chinese)
5. Wen W, Wang X (2008) Analysis of data structure and route search in computer interlocking system. *J Chongqing Univ (Nature Science Edition)*, (06):51–53. (in Chinese)
6. Geng J, Cai B, Wang J, Shang G (2012) Traversing algorithm of railway yard based on DFS. *J China Railway Soc* 04:51–56 (in Chinese)
7. Xu X, Chen G (2011) Research and application of designing computerized interlocking software and route searching algorithm. *Railway Comput Appl* 01:49–52 (in Chinese)
8. Peng J, Yin R (2006) Algorithm of route searching based on adjacency list. *Comput Eng Des* 18:3400–3402 (in Chinese)

# Active Compensation Method for Long Time Delay and Packet Loss in Networked Control System

Wei Fu, Xianyi Yang and Ning Li

**Abstract** To achieve required performance of networked control system, this paper proposes an active compensation method for long time delay and packet loss. The controller predicts multi-step future control inputs based on optimization algorithm. This strategy has less conservativeness than others because that the state feedback gain is not fixed, but a variable value depending on feedback delay. The compensator located in actuator side actively compensates the time delay and data packet loss. According the strategy, the rule is established for the selection of data packet and control input, the closed-loop system is modeled as a switched system. The simulated results confirm the analytical results given in this paper.

**Keywords** Networked control systems · Time delay · Predictive control

## 1 Introduction

Because of time delay, packet disorder and loss, system analysis and synthesis be faced with great challenge in networked control systems (NCS) [1, 2]. In order to ensure system performance and stability, a large number of literature present many approaches. In [3], the network random delay of the Wide-area damping controller for power system is compensated by using generalized predictive control (GPC). Zhang et al. [4] propose a new observer for the delay problem of the feedback channel, and then compensate the time delay by predictive control. In [5–7], the model predictive control algorithm is used to compensate the delay and packet loss. The system performance is improved with the stability of the closed-loop system. In [8, 9], a data-based predictive control algorithm is proposed by using the

---

W. Fu (✉) · X. Yang  
College of Automation, Chongqing University, No. 174, Sha Zheng Street,  
Sha Ping Ba District, Chongqing, China  
e-mail: linefw@163.com

N. Li  
CRRC Qingdao Sifang Locomotive and Rolling Stock Co., Ltd, Qingdao, China

time-stamped packet transmission mechanism, which effectively compensates the dual-channel data packet loss. In most of articles, the ZOH method is mostly used for packet loss, that is, the old control input is continuously used if the packet is lost continuously. This method does not guarantee system stability.

Different from traditional methods, the method developed in this paper can actively compensate time delay and packet loss. With less conservativeness, the feedback gain is not fixed, but a variable value according to different feedback delay. The compensator on actuator side selects the packet with smallest delay, and picks out appropriate control signal from it to act on object. When packet is lost, the next control input in buffer will be selected. According to this feature, the closed-loop system is modeled as a switched system with finite subsystems.

## 2 Problem Statement

The NCS is shown in Fig. 1. Time delay, packet disorder and loss also exist in feedback channel (sensor-to-controller) and forward channel (controller-to-actuator). Consider the linear discrete controlled object as follows.

$$\begin{cases} x(k+1) = Ax(k) + Bu(k) \\ y(k) = Cx(k) \end{cases} \tag{1}$$

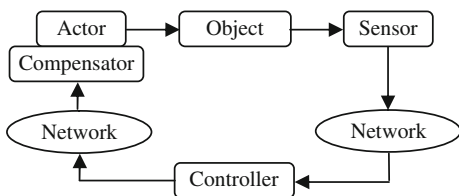
where  $x(k) \in \mathbb{R}^n$  is system state vector,  $u(k) \in \mathbb{R}^m$  is control input vector,  $y(k) \in \mathbb{R}^p$  is measured output vector.  $A \in \mathbb{R}^{n \times n}$ ,  $B \in \mathbb{R}^{n \times m}$  and  $C \in \mathbb{R}^{p \times n}$  are system matrixes. For the sake of convenience, the following assumptions are made.

**Assumption 1** The system is controllable and detectable, respectively.

**Assumption 2** The sensors and actuators run in time-driven mode with time synchronization. The controller runs in event-driven mode.

The single packet that contains multi-step future control signals will be transmitted in network with time-stamp. At time  $k$ , the feedback delay is  $\tau_k^{sc}$ , the forward delay is  $\tau_k^{ca}$ ,  $0 \leq \tau_k^{sc} + \tau_k^{ca} \leq d_m T$ , where  $T$  is sampling period, and  $d_m$  is a positive integer. In subsequent description,  $T$  is normalized to one. Denote the maximum number of consecutive packet loss by  $\bar{d}$ . When the sampling data sent by sensor at time  $k-i$  arrives at controller side after delay  $\tau_{k-i}^{sc}$ , the controller predicts the multi-step future control inputs base on the below equations.

**Fig. 1** The structure of predictive control for NCS



$$\hat{x}(l+1|k-i) = A\hat{x}(l|k-i) + B\hat{u}(l|k-i) \tag{2}$$

$$\hat{u}(l+1|k-i) = K\hat{x}(l+1|k-i) \tag{3}$$

where, the feedback gain  $K$  is to be designed, and  $l = k - i, k - i + 1, \dots, k - i + d_m + \bar{d}$ .

### 3 Predictive Control Design

The predictive controller predicts multi-step system state according to Eq. (2). Define the predictive output vector and control input vector as follows.

$$Y(k-i+1|k-i) = \begin{bmatrix} \hat{y}(k-i+1|k-i) \\ \hat{y}(k-i+2|k-i) \\ \vdots \\ \hat{y}(k-i+d_m+\bar{d}|k-i) \end{bmatrix}, \tag{4}$$

$$U(k-i) = \begin{bmatrix} \hat{u}(k-i) \\ \hat{u}(k-i+1) \\ \vdots \\ \hat{u}(k-i+d_m+\bar{d}-1) \end{bmatrix}$$

The future output can be calculated base on the equation as follows.

$$Y(k-i+1|k-i) = S_x x(k-i) + S_u U(k-i) \tag{5}$$

$$S_x = \begin{bmatrix} CA \\ CA^2 \\ \vdots \\ CA^{d_m} \\ \vdots \\ CA^{d_m+\bar{d}} \end{bmatrix}, S_u = \begin{bmatrix} CB & 0 & \dots & 0 & \dots & 0 \\ CAB & CB & \dots & 0 & \dots & 0 \\ \vdots & \dots & \ddots & \vdots & \vdots & \vdots \\ CA^{d_m}B & CA^{d_m-1}B & \dots & CB & \dots & 0 \\ \vdots & \vdots & \ddots & \vdots & \ddots & \vdots \\ CA^{d_m+\bar{d}-1}B & CA^{d_m+\bar{d}-2}B & \dots & \dots & CAB & CB \end{bmatrix}$$

Consider the below objective function,

$$J = \sum_{j=1}^{d_m+\bar{d}} \|q_j \hat{y}(k-i+j|k-i)\|^2 + \sum_{l=0}^{d_m+\bar{d}-1} \|r_l \hat{u}(k-i+l|k-i)\|^2 \tag{6}$$

where  $q_j$  and  $r_j$  are weight factors. Write above formula as a matrix vector form,

$$J = \|QY(k - i + 1|k - i)\|^2 + \|RU(k - i)\|^2 \tag{7}$$

The weight matrix  $Q$  and  $R$  are diagonal matrixes. By solving partial differential equation  $\partial J/\partial U = 0$ , the optimal solution is obtained.

$$U(k - i) = -(S_u^T Q^T Q S_u + R^T R)^{-1} S_u^T Q^T Q S_x x(k - i) \tag{8}$$

Define the state feedback gain which depends on the feedback delay as follows,

$$K = - \left[ \underbrace{\begin{matrix} \tau_{k-i}^{sc} \\ 0 & \dots & 0 & I & \dots & 0 \end{matrix}}_{d_m + \bar{d}} \right] \times (S_u^T Q^T Q S_u + R^T R)^{-1} S_u^T Q^T Q S_x \tag{9}$$

### 4 Stability Analysis

Base on Eq. (2) the predictive control input sequence will be obtained, such as

$$\begin{aligned} K\hat{x}(k - i + 1|k - i) &= K(A + BK)x(k - i) \\ &\vdots \\ K\hat{x}(k - i + \tau_{k-i}^{sc}|k - i) &= K(A + BK)^{\tau_{k-i}^{sc}}x(k - i) \\ &\vdots \\ K\hat{x}(k - i + d_m + \bar{d}|k - i) &= K(A + BK)^{d_m + \bar{d}}x(k - i) \end{aligned}$$

The sequence will be packed into one packet, denoted as  $U(k-i)$ , with time-stamp. The packet will reach actuator side at time  $k - i + \tau_{k-i}^{sc} + \tau_{k-i}^{ca}$ . There are more than one packet will arrive in the period  $[k - 1, k]$ . The packet  $U(k - i)$  can be selected only if it arrive before time  $k$ , i.e.,  $k - i + \tau_{k-i}^{sc} + \tau_{k-i}^{ca} \leq k$ . Define  $\tau_{k-i} = \tau_{k-i}^{sc} + \tau_{k-i}^{ca}$ , then  $\tau_{k-i} - i \leq 0$ . The delay  $\tau_{k-i}$  of packet  $U(k-i)$  is the minimum one, that is, the variable  $i$  satisfies the rule  $\min\{i|\tau_{k-i} - i \leq 0\}, i = 0, 1, \dots, d_m$ .

Assuming packet is continuously lost during  $n$  sampling period before time  $k$ ,  $0 < n < \bar{d}$ . Because the packet reserved in compensator buffer is the one with minimum time delay between all packets which arrived before time  $k-n$ . So, the times  $n$  satisfies the rule  $\min\{i + n|k-i - n \leq 0\}$ . Define the switching rule as follows,

$$\sigma(k) = \min\{i + n|\tau_{k-(i+n)} - (i + n) \leq 0\} \tag{10}$$

At time  $k$ , the control input is selected to act on object as follows,

$$\hat{u}(k|k-i-n) = \Gamma_{(i+n)\sigma(k)}K(A+BK)^{i+n}x(k-i-n) \tag{11}$$

$$\Gamma_{(i+n)\sigma(k)} = \begin{cases} I & i+n = \sigma(k) \\ 0 & i+n \neq \sigma(k) \end{cases}, n = 0, 1, \dots, \bar{d}, i = 0, 1, \dots, d_m$$

The value of  $\Gamma_{(i+n)\sigma(k)}$  depends on the delay  $\tau_{k-i}$  and the number of consecutive packet loss  $n$ . Define  $\bar{B}_{(i+n)\sigma(k)} = \Gamma_{(i+n)\sigma(k)}BK(A+BK)^{i+n}$ ,  $\bar{A} = A + \bar{B}_{0\sigma(k)}$ . The closed-loop system can be expressed as follows,

$$x(k+1) = \bar{A}x(k) + \bar{B}_{(i+n)\sigma(k)}x(k-i-n) \tag{12}$$

Although the variables  $i$  and  $n$  may take different values, the control input applied to object is the same as long as the value of  $i+n$  is the same. Denote  $\theta = i+n$ . The Eq. (12) can be rewritten as follows,

$$x(k+1) = \bar{A}x(k) + \sum_{\theta=1}^{d_m+\bar{d}} \bar{B}_{\theta\sigma(k)}x(k-\theta) \tag{13}$$

Define the vector  $\xi(k) = [x^T(k)x^T(k-1)\dots x^T(k-d_m)\dots x^T(k-d_m-\bar{d})]^T$ . The closed-loop system (12) can be expressed as follows,

$$\xi(k+1) = \Phi_{\sigma(k)}\xi(k) \tag{14}$$

$$\Phi_{\sigma(k)} = \begin{bmatrix} \bar{A} & \bar{B}_{1\sigma(k)} & \dots & \bar{B}_{(d_m+\bar{d}-1)\sigma(k)} & \bar{B}_{(d_m+\bar{d})\sigma(k)} \\ I & 0 & \dots & 0 & 0 \\ 0 & \ddots & \dots & 0 & 0 \\ \vdots & \vdots & \ddots & \vdots & \vdots \\ 0 & 0 & \dots & I & 0 \end{bmatrix}$$

**Definition 1** The closed-loop system (14) is exponentially stable with exponential delay rate  $\lambda$ , if there exist constants  $c > 0$  and  $0 < \lambda < 1$  such that the solution of system (14) satisfies  $\|\eta(k)\| \leq c\lambda^k\|\eta_0\|$  for any initial state  $\eta_0 = \eta(0) \in \mathfrak{R}^{(d_m+\bar{d}+1)n}$ , where  $\eta_0 = [x^T(0)x^T(-1)\dots x^T(-d_m-\bar{d})]^T$ .

**Definition 2** For any switching signal  $\sigma(k)$  and  $k \geq 1$ , let  $N_\delta[0, k]$  is the number of switching times in the interval  $[0, k]$ . If  $N_\delta[0, k] \leq N_0 + k/T_\alpha$  holds for  $N_0 \geq 0$  and  $T_\alpha \geq 0$ , then  $T_\alpha$  is called the average dwell time and  $N_0$  is the chatter bound.

For simplicity, but without loss of generality, the number of  $N_0$  is zero in the below development. Let  $S_j$  denote the subsystem, and  $M$  is the upper bound of the number of subsystems, where  $M = d_m + \bar{d} + 1$ . So,  $\sigma(k) \in \Omega_M = \{1, \dots, M\}$ .  $N_j$  represents the active times of the subsystem  $S_j$  in the period  $[0, k]$ . Where  $J \in \Omega_M$ .

**Theorem** Given positive scalars  $\lambda_j, \lambda < 1$  and  $\mu > 1$ , if there exist matrices  $P_j > 0$  with appropriate dimensions such that the below inequalities hold

$$\Phi_j^T P_j \Phi_j - \lambda_j^2 P_j < 0 \tag{15}$$

$$P_\alpha \leq \mu P_\beta, \forall \alpha, \beta \in \Omega_M \tag{16}$$

$$\sum_{j=1}^M n_j (\ln \lambda_j - \ln \lambda) \leq 0 \tag{17}$$

$$T_\alpha > T_\alpha^* \stackrel{def}{=} \ln \mu / (2 \ln(1/\lambda)) \tag{18}$$

Then the closed-loop NCS (14) is exponentially stable with decay rate  $\lambda^\theta$ , where  $\theta = 1 + \ln \mu / (2 T_\alpha \ln \lambda)$ .

*Proof* The subsystem of the switched system (14) is

$$S_j : \eta(k+1) = \Phi_j \eta(k), \quad j \in \Omega_M \tag{19}$$

Choose Lyapunov function as  $V_j(k) = \eta^T(k) P_j \eta(k)$ . Where  $P_j > 0, j \in \Omega_M$ . According to inequality (15), the below inequality holds

$$V_j(k+1) - \lambda_j^2 V_j(k) = \eta^T(k) (\Phi_j^T P_j \Phi_j - \lambda_j^2 P_j) \eta(k) \leq 0$$

It means  $V_j(k+1) < \lambda_j^2 V_j(k)$ . So, every subsystem is exponentially decayed. Choose Lyapunov function as  $V_{\sigma(k)}(k) = \eta^T(k) P_{\sigma(k)} \eta(k)$  for NCS (14). Let  $0 < k_1 < \dots < k_i < k, i \in \Omega_M$  denote the switching point of  $\sigma(k)$  during the interval  $[0, k)$ . Then, the equations as follows hold.

$$V_{\sigma(k)}(k) = V_{\sigma(k_i)}(k), V_{\sigma(k_j-1)}(k_j) = V_{\sigma(k_{j-1})}(k_j) \tag{20}$$

where  $j = 1, 2, \dots, i$ . According to Eq. (20), the below inequalities hold

$$\begin{cases} V_{\sigma(k_i)}(k) = V_{\sigma(k)}(k) \leq \lambda_{k_i}^{2(k-k_i)} V_{\sigma(k_i)}(k_i) \\ V_{\sigma(k_j-1)}(k_j) = V_{\sigma(k_{j-1})}(k_j) \leq \lambda_{\sigma(k_{j-1})}^{2(k_j-k_{j-1})} V_{\sigma(k_{j-1})}(k_{j-1}) \end{cases} \tag{21}$$

Since the state of system (14) does not jump at the switching points, the below expression will be got by inequality (16).

$$V_{\sigma(k_i)}(k_i) = \eta^T(k_i) P_{\sigma(k_i)} \eta(k_i) \leq \mu \eta^T(k_i) P_{\sigma(k_{i-1})} \eta(k_i) = \mu V_{\sigma(k_{i-1})}(k_i) \tag{22}$$

Rewrite inequality (17) as follows,



$$\sum_{j=1}^M n_j (\ln \lambda_j - \ln \lambda) = \ln(\lambda_1^{n_1} \lambda_2^{n_2} \dots \lambda_M^{n_M}) - \ln \lambda^{n_1 + n_2 + \dots + n_M} = \ln \frac{\lambda_1^{n_1} \lambda_2^{n_2} \dots \lambda_M^{n_M}}{\lambda^{n_1 + n_2 + \dots + n_M}} \leq 0$$

Then  $\lambda_1^{n_1} \lambda_2^{n_2} \dots \lambda_M^{n_M} \leq \lambda^{n_1 + n_2 + \dots + n_M} = \lambda^k, \prod_{j=1}^M \lambda_j^{2n_j} \leq \lambda^{2k}$

(23)

According to expression (21), (22), (23) and the definition of  $T_\alpha$ , the below expression can be got.

$$\begin{aligned} V_{\sigma(k)}(k) &\leq \lambda_{\sigma(k_i)}^{2(k-k_i)} V_{\sigma(k_i)}(k_i) \leq \mu \lambda_{\sigma(k_i)}^{2(k-k_i)} V_{\sigma(k_{i-1})}(k_i) \leq \mu \lambda_{\sigma(k_i)}^{2(k-k_i)} \lambda_{\sigma(k_{i-1})}^{2(k_i-k_{i-1})} V_{\sigma(k_{i-1})}(k_{i-1}) \\ &\vdots \\ &\leq \mu^{N_\sigma[0,k]} \lambda_{\sigma(k_i)}^{2(k-k_i)} \lambda_{\sigma(k_{i-1})}^{2(k_i-k_{i-1})} \dots \lambda_{\sigma(0)}^{2k_1} V_{\sigma(0)}(0) = \mu^{N_\sigma[0,k]} \prod_{j=1}^M \lambda_j^{2n_j} V_{\sigma(0)}(0) \\ &\leq \mu^{\frac{k}{T_\alpha}} \lambda^{2k} V_{\sigma(0)}(0) = (\lambda \mu^{\frac{1}{2T_\alpha}})^{2k} V_{\sigma(0)}(0) = (\lambda \times \lambda^{\frac{1}{2T_\alpha \log_\lambda \mu}})^{2k} V_{\sigma(0)}(0) \\ &= (\lambda \times \lambda^{\frac{\ln \mu}{2T_\alpha \ln \lambda}})^{2k} V_{\sigma(0)}(0) = (\lambda^\theta)^{2k} V_{\sigma(0)}(0) \end{aligned}$$

(24)

where,  $\lambda < 1, \ln \lambda < 0, \theta = 1 + \ln \mu / (2T_\alpha \ln \lambda)$ . According to inequality (18),  $\theta \geq 0$  holds. Then NCS (14) is exponentially stable with decay rate  $\lambda^\theta$ .

### 5 Numerical Example

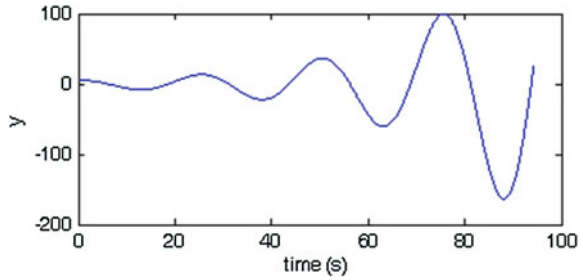
In this section, a simulation example is given to demonstrate the effectiveness of developed method. Consider a third-order system as follows.

$$A = \begin{bmatrix} 1.12 & 0.213 & -0.333 \\ 1 & 0 & 0 \\ 0 & 1 & 0 \end{bmatrix}, B = \begin{bmatrix} 1 \\ 0 \\ 0 \end{bmatrix}, C = [0.0541 \quad 0.0050 \quad 0.0001]$$

Let the initial state is  $[83.879 \quad 68.752 \quad 72.336]^T$ , the sampling period  $T = 0.04$  s, the upper bound of time delay is  $3T$ , the maximum number of consecutive packet loss is 4, and the packet loss rate is 20%. If the LQR control method without delay compensation is used, the feedback gain can be calculated as  $K = [0.9209 \quad 0.1118 \quad -0.2681]$ . It can be seen form the output response in Fig. 2 that the method without compensation can not ensures system performance and stability.

Consider the method proposed in this paper, let the weight matrix  $Q = I, R = I$ . The state feedback gain can be gotten by optimization method as follows,

**Fig. 2** The effect of LQR control method without compensation



$$K_1 = [0.0501 \quad -0.0034 \quad -0.0156], K_2 = [0.0426 \quad -0.0038 \quad -0.0134],$$

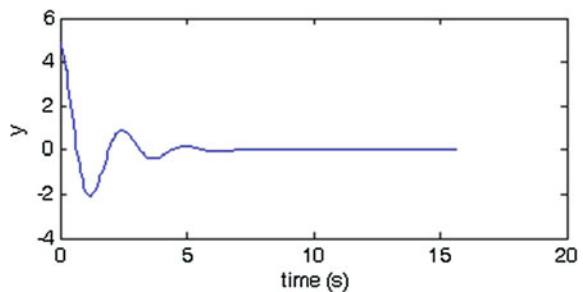
$$K_3 = [0.0342 \quad -0.0033 \quad -0.0110]$$

where  $K_1, K_2, K_3$  correspond to the delay  $\tau_{sc}$  which equals to  $T, 2T$  or  $3T$ , respectively. The system output response is shown in Fig. 3.

## 6 Conclusion

The control strategy proposed in this paper can actively compensate the effect of the time delay and packet loss in NCS which can deteriorate system performance even lead to be unstable. Based on the time-stamp and packet that contains multi-step future control signals, the compensator is set at actuator side to select the minimum delay packet and pick up appropriate control signal to act on object according to time-stamp. Compared with the traditional method in other articles, this method has better effect and less conservativeness because that the control gain is a variable that takes different values according to the feedback delay. The numerical example results illustrated the effectiveness.

**Fig. 3** The output response with compensation for time delay and packet loss



## References

1. Yong C, Meng L (2016) Overview and research trends of predictive control method for network control systems. *J Univ Electron Sci Technol China* 45(4):564–572 (in chinese)
2. Jian-bin Q, Hui-jun G, Steven XD (2016) Recent advances on fuzzy-model-based nonlinear networked control systems: a survey. *IEEE Trans Industr Electron* 63(2):1207–1217
3. Yao W, Jiang L, Wen J, Wu Q (2015) Wide-area damping controller for power system interarea oscillations: a networked predictive control approach. *IEEE Trans Control Syst Technol* 23(1):27–36
4. Zhang J, Lin Y, Shi P (2015) Output tracking control of networked control systems via delay compensation controllers. *Automatica* 57:85–92
5. Franze G, Tedesco F, Famularo D (2015) Model Predictive control for constrained networked systems subject to data losses. *Automatica* 54:272–278
6. Pang Z, Liu G, Zhou D et al (2014) Output tracking control for networked systems: a model-based prediction approach. *IEEE Trans Industr Electron* 61(9):4867–4877
7. Renquan L, Yong X, Zhang R (2016) A new design of model predictive tracking control for networked control system under random packet loss and uncertainties. *IEEE Trans Industr Electron* 63(11):6999–7007
8. Pang Z, Liu G, Zhou D et al (2015) Data-based predictive control for networked non-linear systems with two-channel packet dropouts. *IET Control Theory Appl* 9(7):1154–1161
9. Pang Z, Liu G, Zhou D et al (2016) Data-based predictive control for networked nonlinear systems with network-induced delay and packet dropout. *IEEE Trans Industr Electron* 63(2):1249–1257

# Urban Rail Transit Platform Passenger Alighting and Boarding Movement and Experiment Research

Yang Li and Yanhui Wang

**Abstract** With the improvement of the urban rail transit network and the rights of passengers demand, passenger traffic continuously raised, the operation of urban rail transit with the rights to add pressure. For urban rail transit system, the station for line capacity plays a decisive role, while getting in motion in the station is a key part of the passenger flow in the platform. So, in this paper, we study focuses on the junction between the train and the platform of passengers getting on or off motion and its influencing factors. This paper uses orthogonal experimental method to design experiment. Using the simulation experiment platform and the simulation experiment of the simulation software, two methods are used to study the passengers' on and off motion. The time of getting on and off is used as experimental index to evaluate the result of experiment. As a result, it is important to cut down the time of train stop, reduce platform congestion and reinforce the operation and management level of urban rail transportation.

**Keywords** Urban rail transit · Station platform · Passenger alighting and boarding movement · Orthogonal experiment design method · Alighting and boarding movement experiment

---

Y. Li · Y. Wang (✉)

State Key Laboratory of Rail Traffic Control and Safety,  
Beijing Jiaotong University, Beijing 100044, China  
e-mail: wangyanhui@bjtu.edu.cn

Y. Li · Y. Wang

School of Traffic and Transportation, Beijing Jiaotong University,  
Beijing 100044, China

Y. Li · Y. Wang

Beijing Jiaotong University, No. 3 Shangyuancun Haidian District,  
Beijing 100044, People's Republic of China

© Springer Nature Singapore Pte Ltd. 2018

L. Jia et al. (eds.), *Proceedings of the 3rd International Conference on Electrical and Information Technologies for Rail Transportation (EITRT) 2017*, Lecture Notes in Electrical Engineering 482, [https://doi.org/10.1007/978-981-10-7986-3\\_90](https://doi.org/10.1007/978-981-10-7986-3_90)

## 1 Introduction

The movement of passengers on and off occurs at the junction of platform and train, and has potential relation with platform, train and passenger. It is of great significance to study the relationship between passengers' on board and off train and these factors in order to improve the operation and management of urban rail transit.

Passengers on and off time is an important part of the train stop time. It is of great significance to improve the efficiency of moving up and down, shorten the stop time, reduce the congestion of the platform and strengthen the operation and management level of the urban rail traffic. The research on the relationship between factors of pedestrian traffic and pedestrian behavior influence between the main, Frank and Dorso [1] statements will be arranged in the vertical armrest width of L off the mouth before the 1.1 L, can reach a maximum speed of passenger evacuation. Furthermore, Alonso-Marroquin [2] confirmed that when the vertical handrail was installed in this way, the flow rate increased by 16%, and the maximum value of the flow was found in the distance between the vertical armrest and the bottleneck. Harris and Anderson [3] analyzes the estimation model of the train stopping time, and analyzes the various time periods. Zhang et al. [4] studied the timing of passengers on and off the Beijing subway station, and the impact of different characteristics, number of off and off passengers on the time of getting on and off. Harris [5] take into account the physical characteristics of the width of the car, passenger volume and other factors, the speed of passengers on and off the vehicle were analyzed. Daamen et al. [6] consider car mouth width, get in the car rate, the horizontal and vertical distance between the mouth and the platform, through the age of 25 simulation experiments on the number of passengers getting on or off motion and time were studied. Harris et al. [7] through the analysis of passengers getting on or off motion, get the influence of 17 on the independent variables, and studied the relationship between them. Zhang [8] by analyzing the process of urban rail transit passengers to get off, get off time piecewise mathematical model was established based on the measured data. Wiggeraad [9] explain the difference between getting in and out of the crowd, and explaining that the passengers who eventually ran on the bus should not be part of the main passenger train.

This paper, taking the train station dwell time to select the appropriate factors as the experimental factors, design of passengers getting on or off motion orthogonal experiment plan, using simulation experiments of laboratory experiment platform and the simulation software of simulation experiment, the two methods to determine the influence factors of primary and secondary order and getting movement combination optimal level, on the basis of analyzing the passengers boarding time, put forward the measures of business passengers boarding efficiency, namely the optimal level combination, platform to ease traffic congestion, to ensure the safety of passengers, to enhance the efficiency of the urban rail transit operation.

## 2 Simulation Experiment of Passengers' Alighting and Boarding Movement Based on Experiment Platform

### 2.1 Brief Introduction of Simulation Platform

The simulation carriage adopts all aluminum alloy material, foldable and movable, for mobile TV unit, car radio unit provides the data interface, the size of the car 3600 \* 1200 \* 2800 mm (length \* width \* height), the door size is 1400 \* 2800 mm (width \* height), the switch port for 3.5 s. The simulation platform for 3600 mm \* 1800 mm size (length \* width); simulation platform using the platform off the mark, simulation and simulation platform can simulate the car off for realizing the motion of passengers. As shown in Fig. 1.

### 2.2 Factor Selection and Level Determination of Simulation Experiment

The factors and levels of the simulated experiment are as follows:

1. Number of Passengers on Board/Alight Passengers (A)  
Combined with Daamen et al. [6] and Zhang et al. [4] the number of passengers getting on or off to boarding sports study, the influence of count/get off passengers get on the bus passengers in laboratory simulation experiment 3, 1, 1/3.
2. Door Width (B)  
Given the Daamen et al. [6] on the impact of the train mouth width on getting research, combines the actual conditions of laboratory simulation train car mouth width is 1.4 m, so the simulation experiment of car mouth width values of 1.4, 1.2, 1 m.

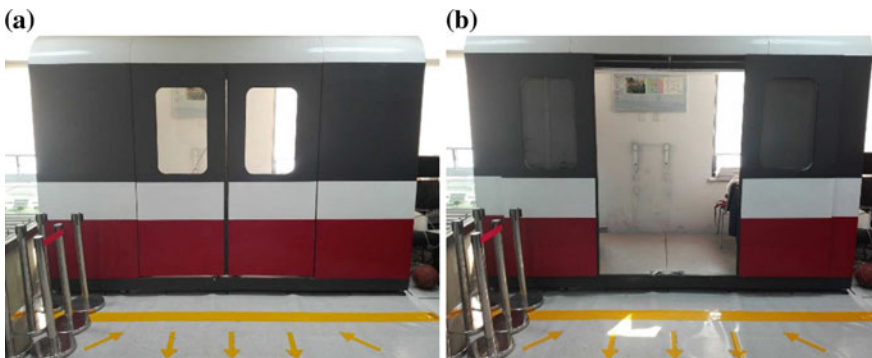


**Fig. 1** Entity figure of simulation car and simulation platform

3. Forbidden Area Size (C)

This section identifies the laboratory simulation experiment in the size of the forbidden area, it is expressed in the form of “length \* width”, suppose the width of the simulation platform is D. Specific values were 1.6 \* 0.5 D, 1.6 \* 0.75 D, 1.6 \* D, D = 1.8 m in the lab, so the size of the off-limits areas were 1.44, 2.16 and 2.88 m<sup>2</sup>.

4. The Position of the Vertical Armrest (D)

Combination with Frank and Dorso [1] research on vertical arm position, using vertical rails to the door of the distance of the center line of characterization of the location of the vertical arm, assuming the breadth of the carriage is L, the simulation experiment of the location of the vertical rails in 0, 0.25 and 0.5 L, in this paper L = 1.2 m, simulation experiments in this paper the simulation experiments of vertical arm position values of 0, 0.3, 0.6 m.

Details are shown in Table 1.

### 2.3 Orthogonal Experimental Scheme

According to the simulation experiment and the level of factors that passengers motion simulation of 4 factors and 3 levels experiment, the 4 factors of the experimental arrangement to the columns of the table on the orthogonal table header, then the orthogonal table in each level figure into the actual level of the corresponding values of the factors are orthogonal the experimental scheme of simulation experiment, as shown in Table 2.

### 2.4 Simulation Experiment Conclusion

Based on the aforementioned experimental scheme, experiments were conducted and the results were as follows:

1. For on and off time, the influence factors of the primary and secondary order are the door width, vertical armrest position, the size of the area, banned passengers on the train number/the number of passengers get off.

**Table 1** Factors and levels of passenger alighting and boarding movement model experiment

Rank	Experimental factors			
	A	B (m)	C (m <sup>2</sup> )	D (m)
1	3	1.4	1.44 (1.6 * 0.5 D)	0 (0)
2	1	1.2	2.16 (1.6 * 0.75 D)	0.3 (0.25 L)
3	1/3	1	2.88 (1.6 * D)	0.6 (0.5 L)

**Table 2** Experimental program of passenger alighting and boarding

Experimental serial number	Experimental factors			
	A	B (m)	C (m <sup>2</sup> )	D (m)
1	3	1.4	1.44	0
2	3	1.2	2.16	0.3
3	3	1	2.88	0.6
4	1	1.4	2.16	0.6
5	1	1.2	2.88	0
6	1	1	1.44	0.3
7	1/3	1.4	2.88	0.3
8	1/3	1.2	1.44	0.6
9	1/3	1	2.16	0

2. To get off the average time, the order of main factors is the size of the area, no passengers on the train number/off passengers, perpendicular position, door width, the influence of off limits in the first row, the car and the passengers are not allowed to wait in front of the car, more convenient for passengers to get off is inseparable. The door width at the last one, and simulation experiments both door width in which passengers are two level off a relationship.
3. The average time for the car, the order of main factors is perpendicular position, the number of passengers get off the car/passenger number, door width, the size of the forbidden area.
4. Analyze the average speed of passengers on and off. Calculate the total number of passengers on the train, the average speed V, the average speed of passengers on board V1, and the average speed of passengers on board V2. See Table 3.

According to the data in Table 3 and plot the image of change trend of average speed which is shown in Fig. 2.

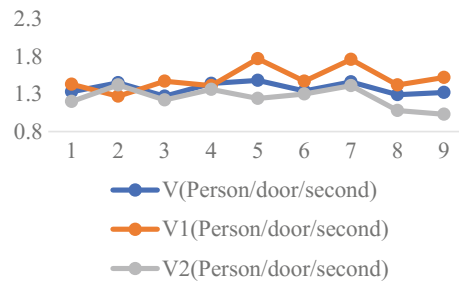
For passengers to get off the motion simulation experiment, the total number of simulation experiments in equal, therefore, the change trend of average speed of passengers on or off the train is contrary to the trend of the total time of getting on and off, the changing trend of average speed of passengers on board and off passengers is opposite to the change trend of up and down time.

**Table 3** Alighting and boarding average rate of each experiment

Experiment number	1	2	3	4	5	6	7	8	9
V (person/door/second)	1.33	1.45	1.27	1.44	1.48	1.34	1.46	1.29	1.32
V1 (person/door/second)	1.43	1.27	1.47	1.41	1.77	1.47	1.76	1.42	1.52
V2 (person/door/second)	1.2	1.42	1.22	1.36	1.24	1.3	1.41	1.08	1.03



**Fig. 2** Change trend of alighting and boarding average rate of each experiment



### 3 Simulation Experiment of Passenger Alighting and Boarding Movement Based on Simulation Experiment

Through simulation experiments, the second chapter passenger movement, this paper obtained the data simulation experiment, analysis of the simulation results, in order to further demonstrate effects of factors on the passenger movement, based on simulation test, this chapter is modeled and simulated with simulation software of environmental factors and the influence of simulation experiment using the method of orthogonal experiment, the arrangement of the simulation experiment, and the simulation results are analyzed.

Each simulation experiment and the simulation experiment of two different experiments, the experimental results are consistent, the simulation conclusion is to simulate the experimental results verify the correctness of the simulation, in turn, the conclusion of the experiment is to verify the accuracy of the simulation results.

#### 3.1 Design of Simulation Experiment for Passengers' Alighting and Boarding Movement

Considering the door width, area size, cut into the vertical armrest position of 3 factors on the total time of passengers, and the possible errors in the simulation experiment, the total exercise time for passengers to get off the experiment index, for passengers to get off the movement simulation experiment, experimental scheme to design the simulation experiment by orthogonal design method the simulation experiments for 3 factors and 3 levels orthogonal experiment, simulation experiment factors and levels are shown in Table 4. The scheme of simulation experiment is shown in Table 5.

**Table 4** Factors and levels of simulation experiment

Levels	Factors of simulation experiment		
	B (m)	C (m <sup>2</sup> )	D (m)
1	1.4	1.44 (1.6 * 0.5 D <sub>p</sub> )	0 (0)
2	1.2	2.16 (1.6 * 0.75 D <sub>p</sub> )	0.3 (0.25 L <sub>c</sub> )
3	1	2.88 (1.6 * D <sub>p</sub> )	0.6 (0.5 L <sub>c</sub> )

**Table 5** Experimental program of passenger alighting and boarding simulation experiment

Experimental serial number	Factors of simulation experiment		
	B (m)	C (m <sup>2</sup> )	D (m)
1	1 (1.4)	1 (1.44)	1 (0)
2	2 (1.2)	2 (2.16)	2 (0.3)
3	3 (1)	3 (2.88)	3 (0.6)
4	1.4	2.16	0.6
5	1.2	2.88	0
6	1	1.44	0.3
7	1.4	2.88	0.3
8	1.2	1.44	0.6
9	1	2.16	0

### 3.2 Behavior of Passengers Alighting and Boarding Movement

This section carries on the AnyLogic modeling simulation for the 9 sets of simulation experiments in Table 5 Through the analysis and analysis of the movement of passengers get off, passengers get pressure proper behavior mainly includes the following steps:

1. The generation of passengers alighting and boarding;
2. On the train passengers walking to the station is designated location, waiting on the train; passengers get off in the car waiting pressure;
3. A car motion command on the bus and the passengers to get off pressure;
4. Get off the passengers to get off the end and the movement of passengers on the train to start the car pressure;
5. Passengers leave the simulation platform, the car passengers on the train after exercise, and reached the passenger compartment pressure;
6. The statistical record of passengers' on board and off time, mainly recording the total time of passengers' on board and off. Pressure

According to the above analysis, this section uses the AnyLogic pedestrian library to build up and down passenger behavior model.

### 3.3 Modeling and Simulation of Passengers' Alighting and Boarding Movement

The modeling and Simulation of the AnyLogic pedestrian Library in this section is based on the simulation experiments in the previous chapter. Therefore, the scene design of the simulation experiment is set up according to the simulation platform, the simulation carriage and the simulation platform. The main interface of modeling and simulation is shown in Fig. 3.

The source of the passenger can be divided into two parts, passengers alighting and passengers boarding. Passengers boarding come from the platform, Passengers arrive at the forbidden area on both sides of the car to wait; passengers alighting are simulated from inside the car, passengers are waiting near the door to get off, they got off the bus when they got the order to get off, after getting off, judge the path and leave the platform; follow the principle of "After first under on". The process of getting on and off passengers is shown in Fig. 4.

Fig. 3 Simulation environment

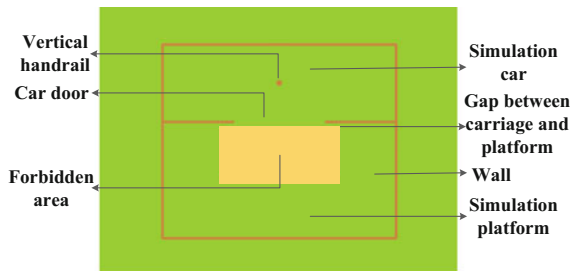
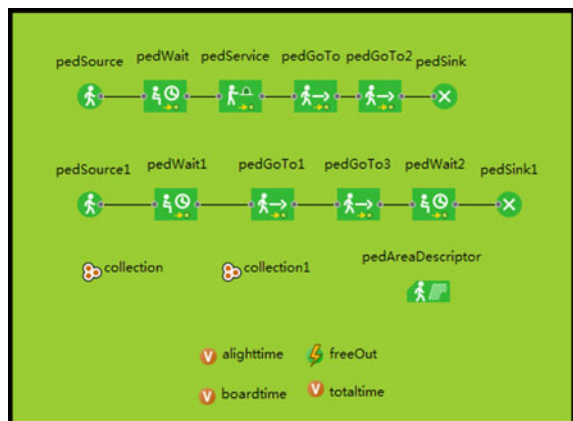


Fig. 4 Flow chart of alighting and boarding behavior modeling



**Table 6** The results of simulation experiment

Experimental serial number	Experimental factors			Experiment index
	B (m)	C (m <sup>2</sup> )	D (m)	$T_{total}$
1	1 (1.4)	1 (1.44)	1 (0)	14.831
2	2 (1.2)	2 (2.16)	2 (0.3)	14.764
3	3 (1)	3 (2.88)	3 (0.6)	15.325
4	1.4	2.16	0.6	14.653
5	1.2	2.88	0	14.676
6	1	1.44	0.3	15.509
7	1.4	2.88	0.3	14.098
8	1.2	1.44	0.6	14.202
9	1	2.16	0	16.325

### 3.4 Data Analysis of Simulation Experiment Results

AnyLogic simulation software is used to simulate and simulate the 9 groups of simulation experiments, and get the simulation results of the 9 sets of simulation experiments, as shown in Table 6.

The experiment proved that 3 factors affect the car width, forbidden zone size and the vertical position of the handrail passengers movement significantly, influencing factors of the sequence is the car width, perpendicular position, forbidden area size, simulation experiment and simulation analysis results. So these factors in passengers role can not be ignored, as the operation of city rail transportation and management, should be the rational use of these factors, by improving the design of metro train design, to get off the passengers on the high efficiency.

## 4 Conclusion

In this paper, simulation experiments and simulation experiments are conducted to verify the influence of passengers' on and off motion on the up and down, the number of passengers on the train/off passengers, doors width, vertical handrails and forbidden area size was used as experimental factors, the total time for passengers to get on and off is used as an indicator of the experiment, the experiment was arranged by orthogonal experimental design, the simulation experiment environment and passenger behavior are modeled and simulated by using AnyLogic simulation software, the experimental results are analyzed, influence of passengers of the total time factors is the door width, vertical armrest position, cut into the size of the area. This paper studies the influence factors of passengers' on and off motion on the up and down, to a certain extent, it provides a reference for improving the efficiency of passengers on and off.

**Acknowledgements** The authors gratefully acknowledge the support from “Key Research Project of Safety Assurance Technology of Urban Rail System” under China National “13th Five-Year Plan” (Grant No. 2016YFB1200402-002).

## References

1. Frank GA, Dorso CO (2011) Room evacuation in the presence of an obstacle. *Phys Stat Mech Appl* 390(11):2135–2145
2. Alonso-Marroquin F, Azeezullah SI, Galindo-Torres SA et al (2012) Bottlenecks in granular flow: when does an obstacle increase the flow rate in an hourglass? *Phys Rev E* 85(2):020301
3. Harris NG, Anderson RJ (2007) An international comparison of urban rail boarding and alighting rates. *Proc Inst Mech Eng Part F: J Rail Rapid Transit* 221(4):521–526
4. Zhang Q, Han B, Li D (2008) Modeling and simulation of passenger alighting and boarding movement in Beijing metro stations. *Transp Res Part C: Emerg Technol* 16(5):635–649
5. Harris NG (2006) Train boarding and alighting rates at high passenger loads. *J Adv Transp* 40(3):249–263
6. Daamen W, Lee Y, Wiggendaad P (2008) Boarding and alighting experiments: overview of setup and performance and some preliminary results. *Transp Res Rec J Transp Res Board* 2042:71–81
7. Harris NG, Graham DJ, Anderson RJ et al (2014) The impact of urban rail boarding and alighting factors. In: TRB 9nd3 2014 annual meeting
8. Zhang P, Zhang GW (2011) Characteristics analysis and modeling for passengers getting off time in urban rail transit. *Urban Mass Transit* 14(11):80–82 (In Chinese)
9. Wiggendaad PBL (2001) Alighting and boarding times of passengers at Dutch railway stations. TRAIL Research School, Delft

# Research on Running Curve Optimization of Automatic Train Operation System Based on Genetic Algorithm

Hao Liu, Cunyuan Qian, Zhengmin Ren and Guanlei Wang

**Abstract** The running curve optimization of automatic train operation (ATO) system usually takes into account running time, energy consumption and passenger comfort. In this paper, in order to provide more comprehensive optimization and accurate reference of running curve for ATO system, we adopted the multi-objective optimization strategy of genetic algorithm (GA) to optimize from five aspects: speeding (safety), parking accuracy, punctuality, energy consumption and comfort. The GA optimization program is written by M language in MATLAB, and combined with a graphical user interface (GUI) tool to design the optimization system of running curve of ATO based on genetic algorithm. Its validity is verified by comparison between the tests based on three different interstation of Shanghai Metro Line 11. The results show that it is effective and practicability to use the designed system to optimize the running curve of ATO system.

**Keywords** ATO (Automatic train operation) · GA (Genetic algorithm) · Multi-objective optimization · Running curve · Urban rail transit

## 1 Introduction

As one of the key subsystems of the ATC (Automatic Train Control) system, the Automatic Train Operation (ATO) system is the foundation for achieving automatic driving, reducing energy efficiency, improving driving efficiency and safety of urban rail transit. Train equips with ATO system is to guarantee its safety and improve its efficiency through automatic control. The main function of ATO system need to generate the target speed curve based on various requirements both of the train and line condition, then relative speed control command will send to the

---

H. Liu · C. Qian (✉) · Z. Ren · G. Wang

Department of Electrical Traction & Control, Institute of Rail Transit, Tongji University, Building H112, No. 4800 Cao'an Road, Jiading District, Shanghai, China  
e-mail: cy\_qian@tongji.edu.cn

© Springer Nature Singapore Pte Ltd. 2018

L. Jia et al. (eds.), *Proceedings of the 3rd International Conference on Electrical and Information Technologies for Rail Transportation (EITRT) 2017*, Lecture Notes in Electrical Engineering 482, [https://doi.org/10.1007/978-981-10-7986-3\\_91](https://doi.org/10.1007/978-981-10-7986-3_91)

899

control center from ATO system to control train to track the target speed curve. This is the whole process of automatic driving of ATO system.

This paper is focusing on the running curve optimization, mainly to achieve the intelligence and effectiveness of ATO system during the optimization process of running curve. We chose the multi-objective optimization of GA as the optimization engine, many researchers had been working on this area with lots of achievements. The study in reference [1, 2] suggested that GA was successfully applied in railway operation; The attempt of applying GA to optimize coasting control in a dynamic way by Wang and Ho has shown promising results [3, 4] proposed an integrated algorithm to generate the global optimal operation scheme, which can simultaneously obtain the optimal timetable and better energy-saving performance; GA was used to generate an optimum coast control table preliminarily, which would be referenced by the train at running time for deciding when to initiate coasting or resume motoring control, based on evaluation of the punctuality, riding comfort and energy consumption [5]. In this paper, we concentrated on providing more comprehensive optimization and accurate reference of running curve for ATO system.

## 2 Performance Evaluation Index

We adopted GA to optimize the running curve based on five performance evaluation indexes, which include speeding, punctuality, parking accuracy, energy consumption, comfort. The performance evaluation function is defined as speeding ( $K_c$ ), punctuality ( $K_t$ ), parking accuracy ( $K_s$ ), comfort ( $K_a$ ) and energy consumption ( $K_e$ ) as follows equations.

### 2.1 Speeding Evaluation Function

The following shows the evaluation function is used to compute the speeding index of the train running between interstation. When the value of  $K_c$  is 0, means there is no speeding situation, which could guarantee the safety of train, otherwise, it is unsafety for train running. The greater  $K_c$  is, the more insecure of a train.

$$K_c = \begin{cases} 0 & V_i < V_{limit} \\ \sum_{i=1}^n (V_i - V_{limit}) & V_i > V_{limit} \end{cases} \quad (1)$$

where  $V_i$  is train speed of the position of key condition;  $V_{limit}$  is the limit speed during the line.

### 2.2 Punctuality Evaluation Function

When  $K_t$  is positive value, represents train delays  $|K_t|$  seconds; when the value of  $K_t$  is 0, means train arrives on time; otherwise, it means train arrives ahead of the scheduled time  $|K_t|$  seconds.

$$K_t = T - T_0 = \sum_{i=1}^{n+1} T_i - T_0 \tag{2}$$

where  $T$  is the actual running time in seconds;  $T_0$  is the scheduled time in seconds;  $T_i$  is the running time between two positions of key condition.

### 2.3 Parking Accuracy Evaluation Function

$K_s$  represents parking accuracy of train, when  $K_s$  is positive value, represents train exceed the scheduled parking position  $K_s$  meters; while the value of  $K_s$  is 0, means train arrives exactly on the right position; otherwise, it means train arrives ahead of the parking position  $|K_s|$  meters.

$$K_s = S - S_0 = \sum_{i=1}^{n+1} S_i - S_0 \tag{3}$$

where  $S$  is the actual running distance in meters between stations;  $S_0$  is the scheduled distance in meters between stations;  $S_i$  is the running distance between two positions of key condition.

### 2.4 Comfort Evaluation Function

The following shows the evaluation function is used to compute the comfort which measured by the absolute value of the acceleration difference between two positions of key condition. In order to measure the comfort evaluation index, we divided the index into level 1–6.

$$K_a = \sum_{i=1}^n |a_i - a_{i-1}| \tag{4}$$

where  $a_i$  is the acceleration between two positions of key condition.



## 2.5 Energy Consumption Evaluation Function

We simplified train energy consumption as the power produced by overcoming the resistance during the whole running process. Computing method as below:

$$K_e = \sum_{i=1}^{n+1} ma_i(S_i - S_{i-1}) \quad (5)$$

The regenerative energy feedback is added when calculating energy consumption of train and energy feedback efficiency of Shanghai Metro Line 11 is 40% [6].

## 3 Optimization Approach

GA was originated from the computer simulation of biological systems. In recent years, with the rise of artificial intelligence, GA has been developed very rapidly, especially in the multi-objective optimization field, so we chose GA to optimize running curve of train. GA simulates the process of gene recombination and evolution, encodes the relevant variables that need to be solved to constitute a chromosome, which will evolve based on the fitness objective function through genetic operators, those operators include natural selection, crossover, mutation, reinsertion. In the end of evolution, the fittest chromosome is obtained. The procedure of the GA is shown in Fig. 1.

### 3.1 Encoding and Decoding Method of Key Condition's Position

#### 3.1.1 Key Condition Encoding Method

The positions of key condition are shown in Fig. 2. Each position of key condition contains four variables: position ( $S$ ), velocity ( $V$ ), time ( $t$ ), acceleration ( $a$ ). Encoding position and gear of each position of key condition by binary digits as one gene of the chromosome (individual) as shown in Fig. 2, we can compute train speed and running time with decoded information of position and gear in each section. Position gene has a length of 10 bits given the distance between two stations is 1000 m, gear gene has a length of 3 bits given there are total 8 gears, gear encoding profile is shown in Table 1. Each chromosome includes all genes of the line and therefore it has a length of 130 bits.

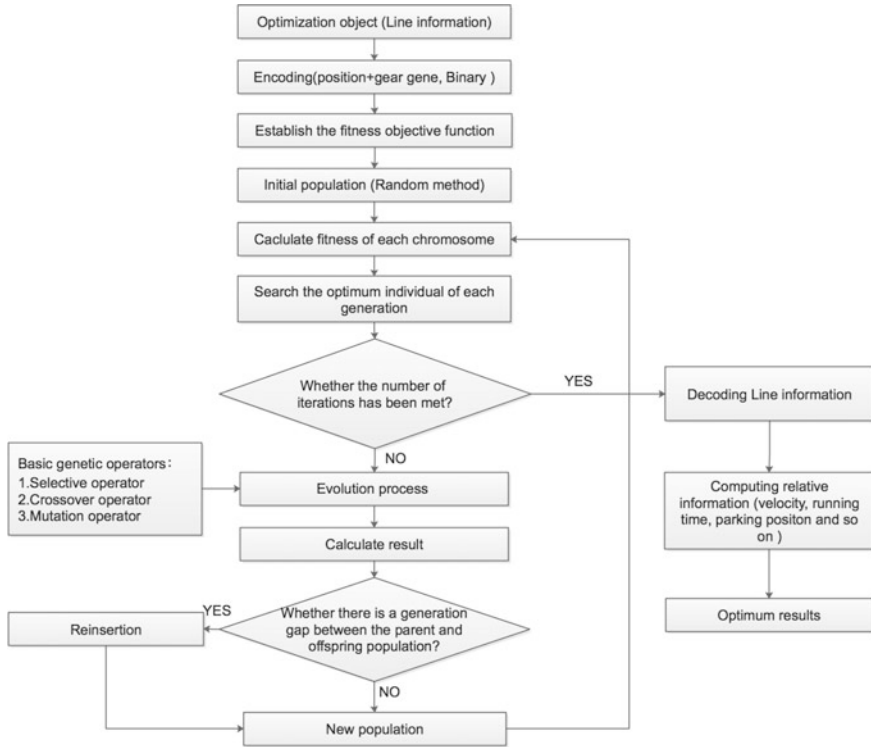


Fig. 1 Process of genetic algorithm

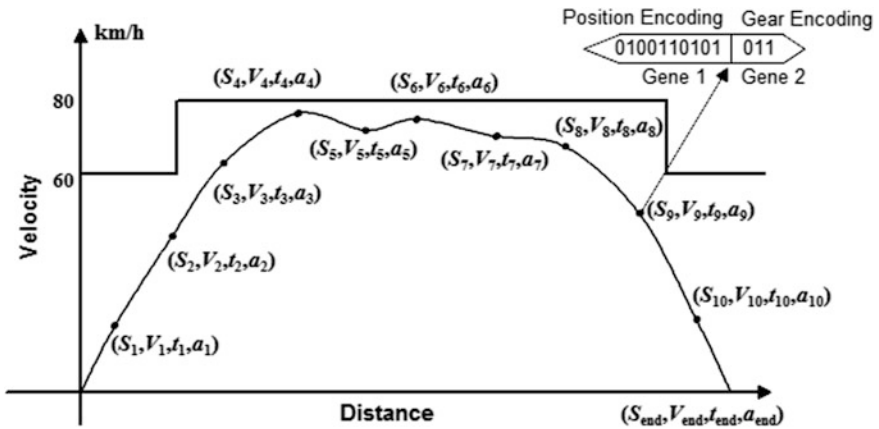


Fig. 2 Encoding method of key condition

**Table 1** Encoding method of gear

Gear	Acceleration/deceleration (m/s <sup>2</sup> )	Binary encoding
Coasting acceleration	0	000
Traction acceleration level 1	0.2	001
Traction acceleration level 2	0.4	010
Traction acceleration level 3	0.6	011
Traction acceleration level 4	0.8	100
Brake deceleration level 1	-0.2	101
Brake deceleration level 2	-0.5	110
Brake deceleration level 3	-0.8	111

### 3.1.2 Decoding Method

The decoding method for the distance gene as below:

$$x = a + decimal(string) \times \frac{b - a}{2^m - \delta} \tag{6}$$

where,  $x \in [a, b]$ ,  $decimal(string)$  represents the decimal value of  $x$ ;  $m$  is length of the binary string;  $\delta$  is a random number between 0 and 1, to ensure the randomness of the decoded position.

### 3.2 Fitness Objective Function

Each chromosome represents information of key conditions of train which running on the specific road and the fitness of the chromosomes is the result respond to five performance evaluation indexes, include speeding (safety), parking accuracy, punctuality, energy saving and comfort. The purpose is to find the fittest chromosome which represent the best optimum running curve based on the current situation through tests using a fitness objective function as a gauge of performance. The fittest chromosome is the one with the highest fitness.

$$K_{fitness} = \frac{1}{w_c \cdot K_c + w_t \cdot K_t + w_s \cdot K_s + w_a \cdot K_a + w_e \cdot K_e} \tag{7}$$

where  $w$  is the weight of relative performance evaluation index; GA maximize the fitness value  $K_{fitness}$ , that means minimize each performance evaluation index in an optimum way according to this fitness objective function.

### 3.3 Evolution Process

In order to guarantee the genetic diversity during the evolution process, a number of genetic operators are available to use in this process. Genetic operators as follows:

- **Selector operator** chooses chromosomes according to their fitness for mating to produce offspring. More fitter individuals get higher probability to mate. We choose the roulette-wheel selector operator to reproduce offspring [7].
- **Crossover operator** is used to exchange genes between the parent chromosomes. This reordering or recombination includes the effects of both exploration and exploitation. We choose two-point crossover to generate new individual [8]. The two-point crossover method is shown in Fig. 3.
- **Mutation operator** introduces a new gene by random changes in the chromosome. As one of the important way to increase the diversity of the population, mutation operator also decides the local search ability of GA, improves the global and local search ability combined with the crossover operator.

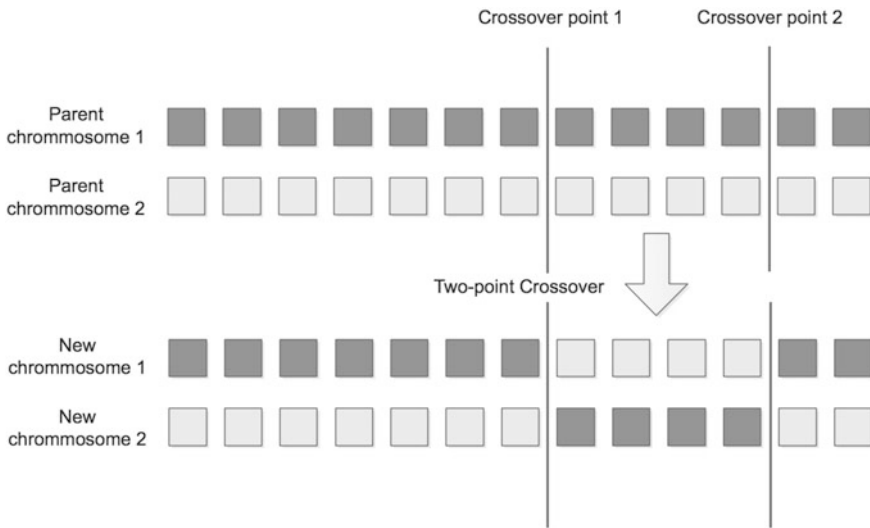


Fig. 3 Two-point crossover

### 4 Optimization System of Running Curve of ATO

The algorithm was programed in MATLAB by M language based on the performance evaluation functions and traction transform rules, then used a GUI tool to design the optimization system of running curve of ATO. The interactive interface of this system is shown in Fig. 4, includes following parts: (1) Line parameter setting; (2) Acceleration setting; (3) Marshalling mode setting; (4) Load mode setting (include average weight of passengers setting and load state setting); (5) Regenerative energy feedback efficiency setting; (6) Weight of performance evaluation index setting; (7) Genetic parameter setting; (8) Display of key condition's parameters; (9) Display of running curve; (10) Display of optimum value.

### 5 Verification and Analysis of GA's Effectiveness

In this paper, we chose Shanghai Metro Line 11 for the case studies. The parameter of the train and interstation is shown in Tables 2 and 3 respectively.

In order to verify the effectiveness and optimized ability of GA, we designed three different experiments based on different genetic parameters, it is shown in Table 4.

Figure 5 illustrates the convergence of the GA based on three different experiments, experiment 3 with the highest fitness is shown on the graph; Fig. 6 represents the target speed profile of the train of each experiment; Fig. 7 shows the

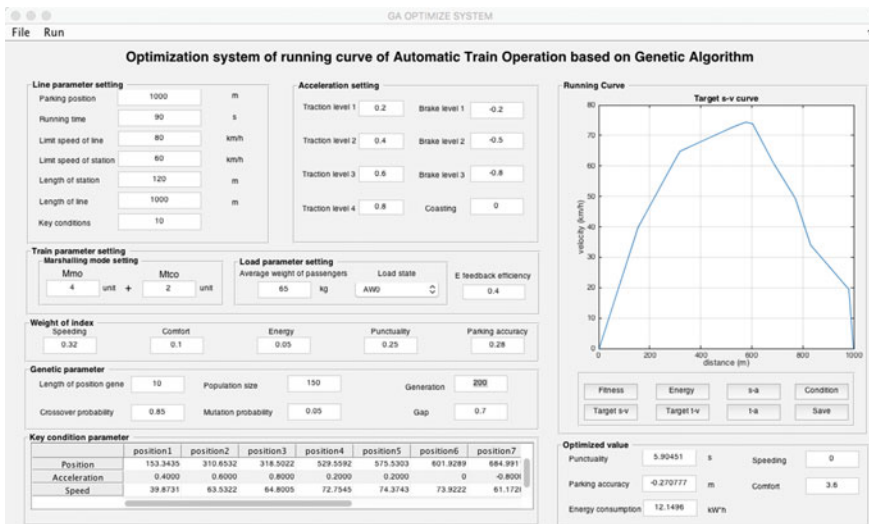


Fig. 4 Optimization system of running curve of ATO based on algorithm

**Table 2** Parameter of Shanghai Metro Line 11

Items	Value
Marshalling mode	4 M + 2T
Weight of the train	224t (Mmo: 38t/unit, Mtco: 36t/unit)
AW0	0
AW1	17.29t (passengers: 266 * 65 kg)
AW2	120.9t (passengers: 1860 * 65 kg)
AW3	159.9t (passengers: 2460 * 65 kg)
Maximum speed	100 km/h

**Table 3** Parameter of interstation of Shanghai Metro Line 11

Cao Yang Road—Long De Road	Value
Length of interstation	1000 m
Scheduled running time	90 s
Length of station	120 m
Limit speed of station	60 km/h (16.67 m/s)
Limit speed of line	80 km/h (22.22 m/s)

**Table 4** Genetic parameter settings of different experiments

	Load state	Population size	Generations	Crossover probability	Mutation probability	Gap
Experiment 1	AW2	50	100	0.85	0.05	0.7
Experiment 2	AW2	100	200	0.85	0.05	0.7
Experiment 3	AW2	200	1000	0.85	0.05	0.7

**Fig. 5** Fitness evolution trend

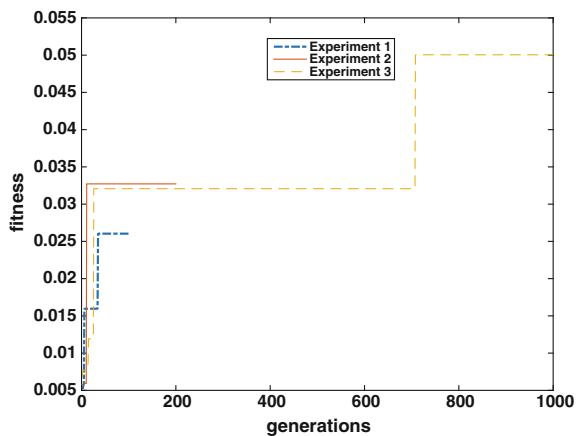


**Fig. 6** Target distance-speed curve

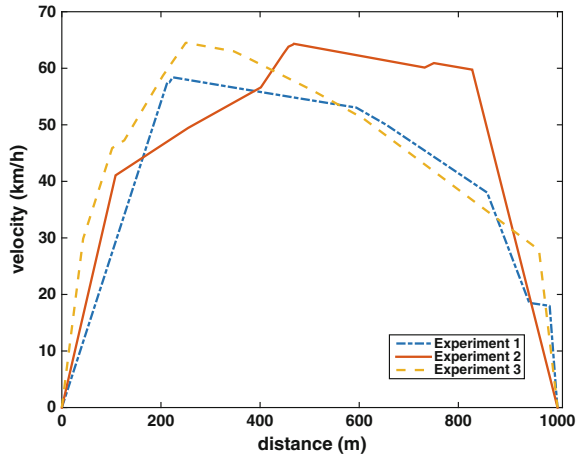
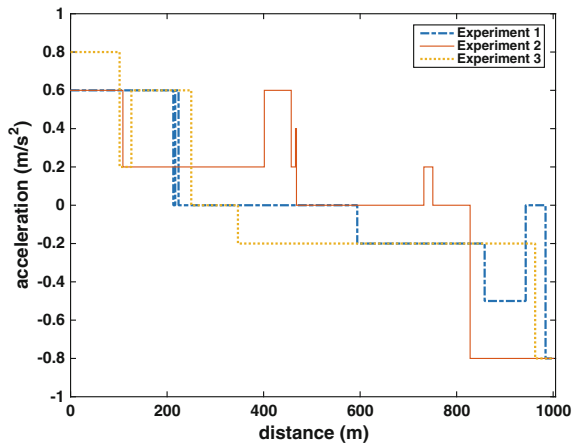


**Fig. 7** Acceleration profile



acceleration profile of the train of each experiment. Figure 8 shows the energy consumption of the train of each experiment.

Table 5 shows the comparison of optimum value of performance evaluation index between three different experiments. Experiment 3 achieved significant improvements over the other two Experiments in all performance evaluation indexes and also with the highest fitness.

Table 6 shows the evolution trend of performance evaluation index and fitness of experiment 3. The analysis of the results as follows:

1. Speeding: the optimum value of speeding through 1000 generations is 0, which means there is no speeding condition, and it is ensuring the safety of the train.

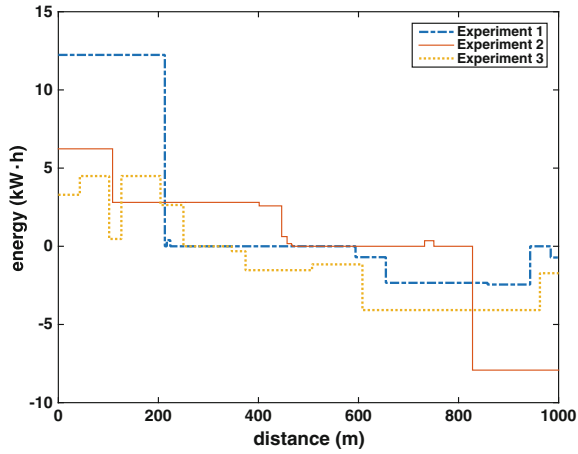


Fig. 8 Energy consumption

Table 5 Comparison of optimum value of performance evaluation index

	Speeding	Punctuality (s)	Parking accuracy (m)	Energy consumption (kW h)	Comfort	Fitness value
Experiment 1	0	7.3261	-0.1739	18.8305	3.6	0.0260
Experiment 2	0	-3.7066	-0.1541	19.0741	3	0.0327
Experiment 3	0	-0.2493	-0.1302	16.9882	2.4	0.0501

Table 6 The evolution trend of performance evaluation index and fitness of the experiment 3

Generations	Speeding	Punctuality (s)	Parking accuracy (m)	Energy consumption (kW h)	Comfort	Fitness
1	0	-56.5313	0.0635	18.0261	3.4	0.0068
3	18.5929	-31.2457	-1.3509	36.0382	3.2	0.0077
14	0	-39.6462	-2.8495	-7.1948	1.4	0.0090
19	0	-37.2751	0.0358	-2.7528	3	0.0122
26	0	0.8907	0.9742	17.9042	3.4	0.0321
707	0	0.8907	0.9742	17.9042	3.4	0.0321
708	0	-0.2493	0.1302	16.9882	2.4	0.0501
1000	0	-0.2493	0.1302	16.9882	2.4	0.0501



2. Punctuality: the value optimized from  $-56.5313$  s to  $-0.2493$  s, which means the train arrives  $0.2493$  s earlier in the end through the optimization. Punctuality is tremendously improved.
3. Parking accuracy: the optimum value is  $0.1302$  m, which totally within the criterion of  $\pm 30$  cm, although with fluctuation during the evolution of parking accuracy.
4. Energy consumption: the optimum value is  $16.9882$  kW h, which was calculated under the AW2 load state. It is within a reasonable range compare to the  $15.76$  kW h ( $3.94$  kW h  $\times 4$ ) which was calculated under the AW0 load state by Chen with cRIO acquisition system for one power car [9].
5. Comfort: the optimum value is  $2.4$ , which means comfort level is 3 (slight comfortable) according to the comfort level evaluation rules.
6. Fitness: as shown in Table 6, the fitness is evolved from  $0.0068$  to  $0.0501$ , which means the adaptability of individual is getting more and more higher during the evolution process. It also with the highest fitness compares to the other experiments.

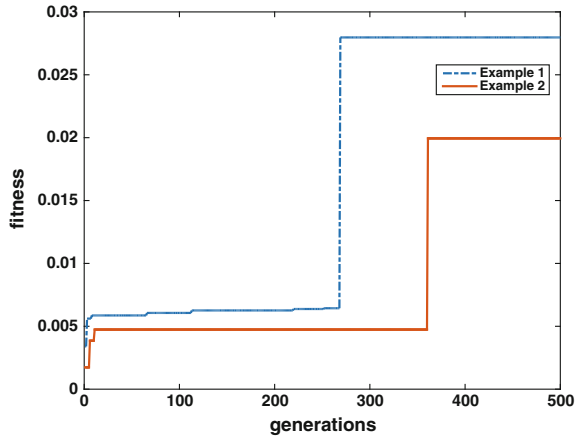
As analysis of the optimized results above, we can conclude that application of GA on running curve of ATO is successful and effective.

## 6 Verification of the Integrated Optimization System

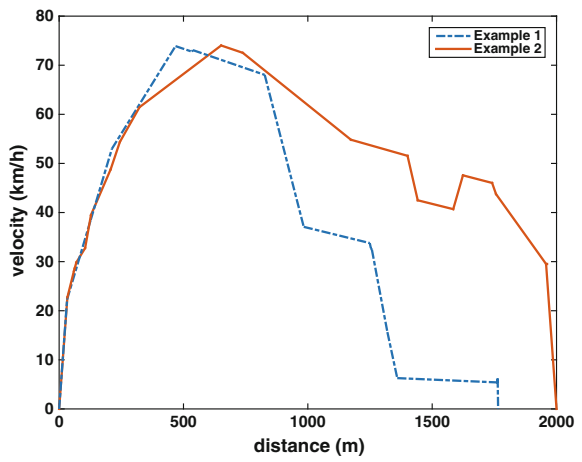
The verification of the integrated optimization system needs to be implemented after we already verified of the effectiveness of GA in the last step, so we applied optimization system to two more interstation. The first interstation example is  $1765$  m between Shanghai Swimming Center and Xujiahui station, the normal schedule time of train to cover the distance is  $140$  s; The second interstation example is  $2000$  m between Shanghai Automobile City and East Changji Road station, the scheduled time is  $160$  s. Other parameters of the two tracks are same as the interstation between Caoyang Road and Longde Road station. The optimum running curves are shown as follows (Figs. 9, 10, 11 and 12).

Table 7 shows the optimum results of the performance evaluation index of the train under the two interstation examples. With designed optimized system based on GA, the results of both examples achieved a good performance in Speeding, Punctuality, Parking accuracy, Energy consumption. Although the Comfort value of the train is slightly higher, it is still within the acceptable limit. The simulation results as the further evidence verified the effectiveness of the integrated optimization system.

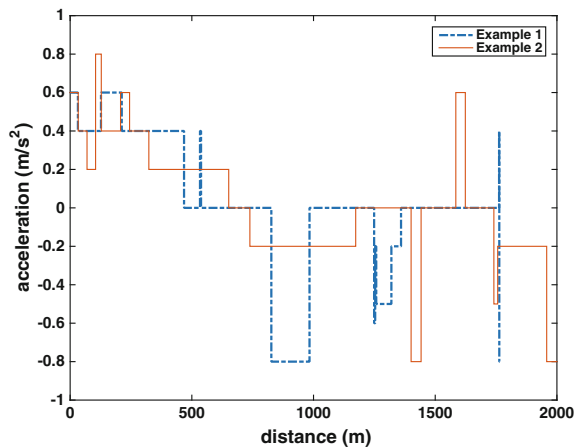
**Fig. 9** Fitness evolution trend



**Fig. 10** Target distance-speed curve



**Fig. 11** Acceleration profile



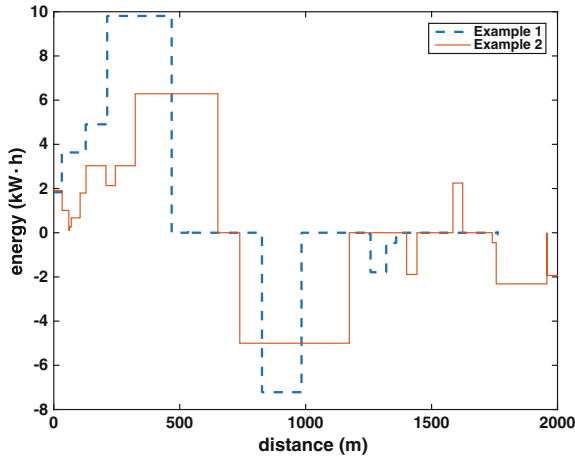


Fig. 12 Energy consumption

Table 7 Comparison of optimum value of performance evaluation index

	Speeding	Punctuality (s)	Parking accuracy (m)	Energy consumption (kW h)	Comfort
Example 1 (Shanghai Swimming Center-Xujiahui)	0	3.0796	0.1005	25.6247	6.8
Example 2 (Shanghai Automobile City-East Changji Road)	0	-3.4972	0.0041	29.584	6.8

## 7 Conclusions

This paper discussed how to optimize the running curve of ATO system. We used GA to solve the optimization problem which needs to find a global optimal solution of the objective fitness function based on five performance evaluation indexes. An optimization system of running curve of ATO based on GA has been designed and it performs very well when we applied it on the interstation of Shanghai metro Line 11 between Caoyang Road and Longde Road. We also used other two interstation of Shanghai metro Line 11 for the case studies. As the result of tests, we verified that it is effective to use this optimization system to optimize the running curve for ATO system. Although the integrated optimization system with good optimization ability and practicability, it is still needed to improve furtherly, such as more accurate functions of each performance evaluation indices and objective fitness require further research. The future work will focus on the performance evaluation indices research and we are also going to implement neural networks to this

optimization problem to examine which one is best for the running curve optimization of ATO system between neural networks and GA.

**Acknowledgements** This work is supported by the National “Twelfth Five-Year” Pillar program for Science & Technology – the Interoperability Comprehensive Evaluation Integrative Platform and Demonstration for Urban Rail Transit (No.2015BAG19B02).

## References

1. Chang CS, Du D (1998) Improved optimization method using genetic algorithm for mass transit signaling block-layout design. *IEE Proc Electr Appl* 145(3):266–272
2. Ho TK, Yeung TH (2000) Railway junction conflict resolution by genetic algorithm. *Electron Lett* 36(8):771–772
3. Wang KK, Ho TK (2004) Dynamic coast control of train movement with genetic algorithm. *Int J Syst Sci* 35(13–14):835–846
4. Su S, Tang T, Li X, Gao ZY (2014) Optimization of multitrain operations in a subway system. *IEEE Trans Intell Transp Syst* 15(2):673–683
5. Chang CS, Sim SS (1997) Optimizing train movements through coast control using genetic algorithms. *IEE Proc Electr Power Appl* 144(1):65–73
6. Li JQ (2013) Analysis of the train’s traction energy consumption of Shanghai Metro Line 11. *Mechatronics* 19(6):32–35 (in Chinese)
7. Kumar Rakesh (2012) Blending roulette wheel selectin & rank selection in genetic algorithms. *Int J Mach Learn Comput* 2(4):365–370
8. Kaya M (2011) The effects of two new crossover operators on genetic algorithm performance. *Appl Soft Comput* 11(1):881–890
9. Chen Y, Qian CY, Xi XD (2016) Traction energy consumption test and analysis for Shanghai Metro AC 16 electromotive train. *Urban Mass Transit* 19(9):34–38 (in Chinese)

# Research on Tram Detector Location Based on Vehicle–Infrastructure Communication

Huang Yan, Dongxiu Ou, Ziyang Chen and Yang Yang

**Abstract** Modern tram vehicle infrastructure system mainly relies on tram detectors to communicate with the trams, providing the basis for optimal control of the tram operation. This paper presents a calculation method to find the optimal locations of announcement detectors and request detectors based on characteristics such as system operation instructions, tram speed, signal priority strategy and manual operation habits. The critical location for detectors is proposed considering the intersecting-road hierarchy and the signal priority parameters. A sample model application and simulation experiments on a real-life intersection are included. Compared with the tram delay of different request detector locations, the outcome indicates that the most effective tram priority is determined when the detectors are placed according to the method proposed in this paper.

**Keywords** Tram detector location · Vehicle–infrastructure communication  
Tram signal priority · VISSIM

## 1 Introduction

Modern tram system is vigorously promoted at home and abroad due to the advantages of large capacity, low cost and energy saving. At present, many cities have begun many modern tram applications, and the semi-independent way is the most common form of modern tram in China. Although trams can operate on exclusive rail tracks, conflicts between trams and other traffic at intersections are inevitable [1]. Meanwhile, tram operation in most Chinese cities uses driver manual control mode, so reliable and personalized operation instructions can help the driver

---

H. Yan · D. Ou (✉) · Z. Chen  
Key Laboratory of Road and Traffic Engineering of the Ministry  
of Education, Tongji University, Shanghai, China  
e-mail: ou.dongxiu@tongji.edu.cn

Y. Yang  
Casco Signal Ltd., Shanghai, China

achieve better vehicle control [2]. Therefore, to ensure the operation efficiency and safety of trams, a modern tram vehicle infrastructure system is often used to guide the operation of modern trams.

In V2I communication, tram detectors placed upstream of the intersection send information to the intersection signal controller by detecting the arrival of a tram. The system informs the tram of the operation interaction or priority feedback (such as a strategy of green extension or green advance) [3, 4] according to the tram information. Due to the limitation of intermittent communication, the tram detector location affects the implementation of the priority strategy and the driver operation [5, 6]. Therefore, this paper reports an optimization mechanism for safety interaction information and a tram signal priority strategy based on V2I communication, providing a method for optimizing the location of tram detectors.

## 2 Modern Tram Vehicle Infrastructure Communication

### 2.1 System Structure

Modern tram vehicle infrastructure (V2I) communication system mainly includes tram detector, intersection signal control subsystem, traffic signal controller and road traffic control center, as shown in Fig. 1. They can record the tram speed and location and other operating data and transmit the interaction information to the tram, providing the basis for optimal control of the tram operation.

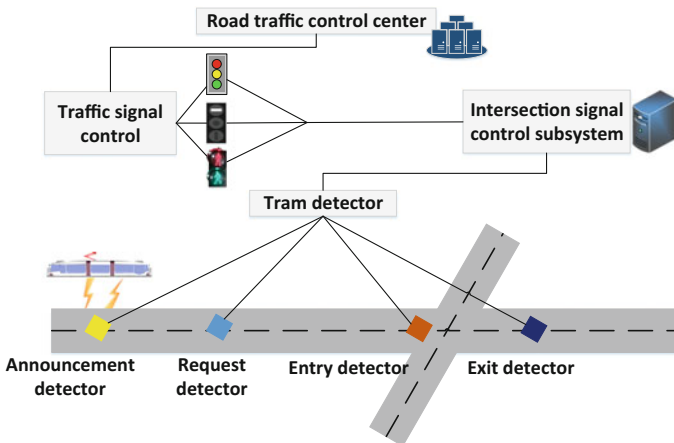


Fig. 1 Tram V2I intermittent communication structure

### 1. Tram detector

The tram detector is deployed around the tram track and connects with the intersection signal control subsystem. It can detect the tram arrival, record the vehicle speed and so on. Some detectors can achieve data communication with vehicles. Tram detectors mainly include four kinds of detectors: the announcement detector, the request detector, the entry detector and the exit detector, each used for different steps of tram priority control [7, 8].

### 2. Intersection signal control subsystem

The intersection signal control subsystem can receive and parse the data from the tram detector and estimate the arrival time of the tram. It is connected with the traffic signal controller and informs the tram of interaction information.

### 3. Traffic signal controller

The traffic signal controller is the signal controller of an intersection, with the function of a traffic light control, signal timing program configuration, local intersection off-line control, road traffic control center communication, etc. It consists of tram, road and pedestrian signal equipment.

### 4. Road traffic control center

The road traffic control center is connected with urban intelligent traffic control equipment and has the highest decision-making power. It can achieve the central control of urban traffic, consider the city's regional traffic conditions and achieve interconnection with the signal controller of an intersection.

## 2.2 *Interface Scheme*

Under the semi-independent right of way, conflicts between trams and other traffic at intersections are inevitable. It is necessary to consider the operation efficiency of the tram to achieve priority control. In addition, the operation safety of trams at intersections must be ensured to prevent collisions with vehicles travelling in different directions. Therefore, when a tram arrives at the detector, the V2I communication in intermittent mode can be divided into four stages according to detector placement: announcement, request, check-in and check-out.

#### 1. Announcement stage

When a tram passes through the announcement detector, the tram and the detector will establish a communication data link. The tram sends information such as vehicle speed and real-time clock to the detector. The detector then sends a recommended speed to the tram according to the tram arrival time and current phase status. The driver begins to adjust the speed according to the speed information to increase the chance of passing through the intersection without stopping.

## 2. Request stage

When the tram arrives at the request detector, the tram will send information including the priority parameter, real-time clock and vehicle speed to the detector. The detector then sends the tram information to the intersection signal control subsystem, which calculates the time when the tram is expected to reach the stop line. The traffic signal control system will decide whether to execute the priority command based on the system limitation and send it back to the vehicle. The driver will decide whether to stop the tram according to the feedback.

## 3. Check-in stage

When the entry detector is activated, the traffic signal control system receives the information that the intersection is occupied and locks the intersection signal to prevent a conflicting signal, which would ensure that the stage including the tram movement would not lose right of way.

## 4. Check-out stage

When the tram passes through the exit detector, the signal is sent to the traffic signal control system, indicating that the tram has departed from the intersection. The signal including the tram movement is unlocked, and the signal switches to the next phase. If the exit detector is not activated after a defined time, it will be assumed that the tram is not detected for an unknown reason. In this case, the signal stage will change according to the signal program.

# 3 Research on the Location of the Tram Detector

There are no regulations or standards for the tram detector location. The design of the detector location has a significant effect on realizing the signal control strategy and driving information effectively, but the methodology to determine the detector location has not been sufficiently addressed.

Considering the function of the entry detector and the exit detector, the entry detector is placed at the nearest location before the intersection stop line, and the exit detector is placed downstream from the intersection with the distance of the length of a tram. However, the locations of the announcement detector and the request detector are calculated according to the signal strategy and tram parameters. In the design of practical projects, the announcement detector is generally recommended to be placed in front of the request detector at a remote distance, and the request detector is placed at a safe braking distance under the maximum speed limit. However, this detector location is not proper for signal priority.

Because of the lower speed and longer size of trams, the green truncation design in the stage including the tram movement is designed and implemented with the goal of achieving tram safety. A tram that enters the intersection at the end of the phase can cross the intersection safely. For a given cycle, an example of a tram green truncation design by two different priority strategies is shown in Fig. 2.



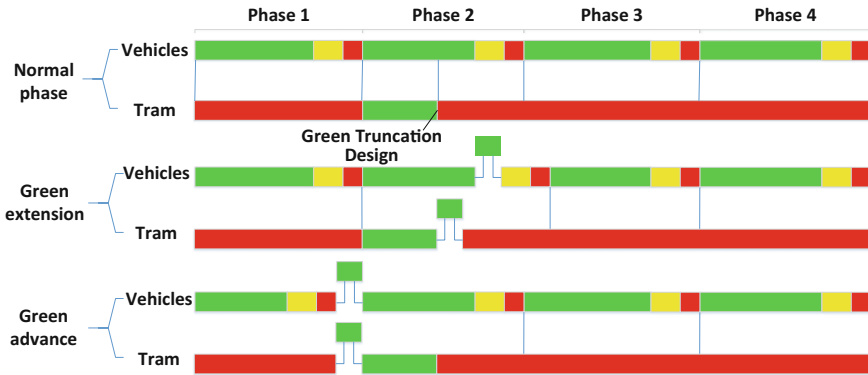


Fig. 2 Signal priority based on tram green truncation design

### 3.1 Announcement Detector Location Analysis

Assuming that there is no station near the intersection entrance, only a green extension and green advance are used to provide signal priority for trams. As shown in Fig. 3, the announcement detector is placed at  $p1$ , and  $S$  is the distance between the stop line and detector.  $t_1$  is the start time of green in the tram phase, and  $t_2$  is the end time of green in the tram phase.  $T$  is the cycle time.  $\Delta t$  is the maximum green extension time, and  $\Delta t'$  is the maximum green advance time for priority. The speed limits are marked with dashed lines. The maximum speed line illustrates that a tram following the maximum speed  $V_{max}$  arrives at the stop line just at the latest end time  $t_2 + \Delta t$ , and  $t_1'$  is the moment at which this tram passes the announcement detector. However, the minimum speed line represents a tram following the minimum speed  $V_{min}$  and arriving at the stop line just at the earliest start time  $t_1 - \Delta t' + T$ , and  $t_2'$  is the moment at which this tram passes the announcement detector. We assume that the tram enters the intersection at a constant speed after passing the detector.

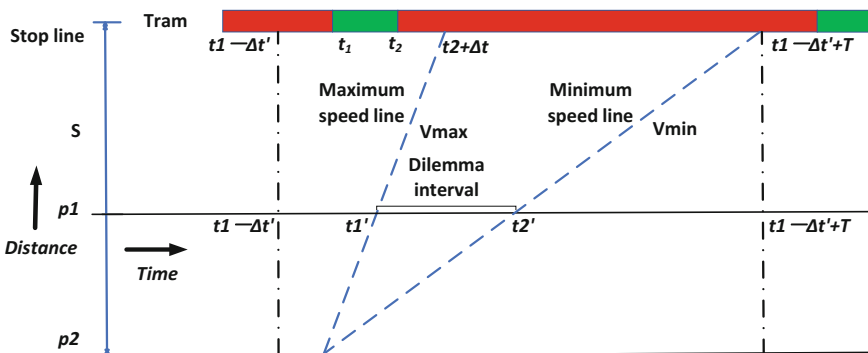


Fig. 3 Announcement detector location analysis

The system will provide a recommended speed to the tram terminal to increase the chance of passing the intersection without stopping when the tram passes the detector. Because of the speed limitation, the recommended speed must be on the interval  $[V_{\min}, V_{\max}]$ . When the announcement detector is at  $p1$ , the tram arrival time  $t_{\text{arr}}$  has the following three situations:

$t_{\text{arr}} \in [t_1 - \Delta t', t_1']$ : The tram can reach the recommended speed, which is no more than  $V_{\max}$ , by appropriate acceleration so that it can arrive at the stop line before the maximum green extension time;

$t_{\text{arr}} \in [t_2', t_1 - \Delta t' + T]$ : The tram can reach the recommended speed, which is no less than  $V_{\min}$ , by appropriate deceleration so that it can arrive at the stop line during the green advance interval or the green time of the next cycle;

$t_{\text{arr}} \in [t_1', t_2']$ : The tram arriving at the announcement detector in this interval cannot attain a reasonable recommended speed within  $[V_{\min}, V_{\max}]$  to pass through the intersection in this or the next cycle due to system speed limitation.

It can be seen from the analysis above that the announcement detector located at  $p1$  will cause a dilemma time interval, which prevents the system from providing a recommended speed to the tram. However, the dilemma time interval is eliminated with the distance between the detector and stop line in Fig. 3. We can easily find the optimal location for the announcement detector as

$$S = \frac{V_{\max} \times V_{\min}}{V_{\max} - V_{\min}} \times (T - \Delta t - \Delta t' - g) \tag{1}$$

where  $g$  is the green time of the tram phase.

At present, the speed limitation in many Chinese tram lines is between 30 and 70 km/h and less than 30 km/h at the intersection. Considering the safety of tram operation, the recommended speed ranges from 20 to 60 km/h. When the cycle is 120 s and the green time is 20 s, the distance between the announcement detector and stop line is listed in Table 1.

In actual projects, the length of the upstream section of the intersection may not be sufficient to meet the location of the detector. Therefore, it is usually advisable to place the announcement detector at the downstream section of the front intersection and share the same location as the exit detector.

**Table 1** The comparison of announcement detector locations

Degree of tram	Maximum green extension time (s)	Maximum green advance time (s)	Distance from detector to stop line (m)
No priority	–	–	–
Semi-priority	10	10	660
Top priority	15	15	580

### 3.2 Request Detector Location Analysis

#### 3.2.1 Request Detector Location Analysis Based on Green Extension Judgment Interval

When a tram arrives at the request detector, it sends a message to the signal controller, which will or will not allow priority to the tram. The request detector location analysis based on the green extension strategy is presented as an example. As shown in Fig. 4, the distance between the request detector and the stop line is  $L$ , and we assume that the tram enters the intersection at a constant speed  $V$  after passing the detector.

A tram arriving at the request detector at time interval  $[t_1', t_2']$  can cross the intersection without priority application. However, after  $t_2'$ , a priority application is needed to cross the intersection without stopping, so  $t_2'$  is the beginning of the green extension judgment interval. According to the constraint of the maximum green extension time, the tram arriving at the request detector after  $t_2' + \Delta t$  will be unable to request the green extension. It must wait for the next green time to cross the intersection.  $t_2' + \Delta t$  is the end of the green extension judgment interval. Once the tram passes the request detector in the green extension judgment interval, the tram phase will remain green until the tram enters the intersection, and then the green time ends.

According to the green truncation design in the stage including the tram movement, the tram signal will turn to red when it reaches  $t_2$ . The green extension judgment is then invalid. Therefore, the priority request of a tram arriving at the detector during the judgment interval  $[t_2, t_2' + \Delta t]$  will be invalidated if the end of the green extension judgment interval is after the tram green truncation time. Thus, the distance between the request detector and stop line should meet the following condition:

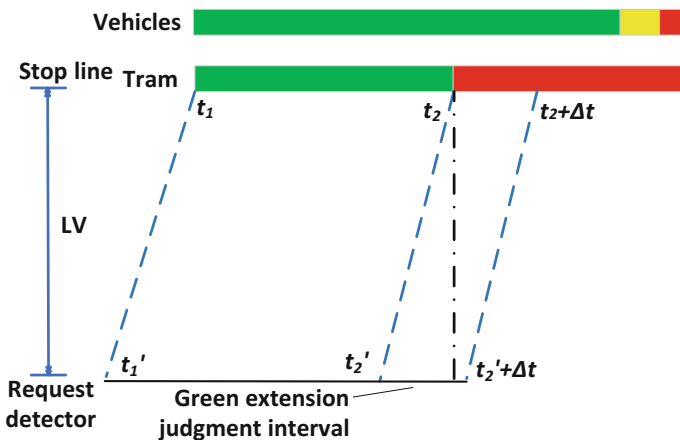


Fig. 4 Analysis of the detector location based on green extension decision interval

$$\frac{L}{V} \geq \Delta t \tag{2}$$

### 3.2.2 Request Detector Location Analysis Based on Manual Driving Habit

At present, most Chinese tram lines use driver manual control mode rather than automatic driving mode, so reliable and personalized operation instructions can help the driver achieve better vehicle control. When a tram arrives at the detector, the interaction information on whether the tram can pass the intersection directly during this cycle is displayed on the screen. According to the interacting information and the signal state of the intersection, the driver will decide whether to stop the tram. Therefore, accurate and reliable information on the operation of the tram plays an important role.

As shown in Fig. 5, when the judgment interval is before the tram green truncation time and the tram arrives at the request detector during the interval  $[t_2' + \Delta t, t_2]$ , the driver is informed that it is unable to pass in this cycle, but the state of the signal light is green until  $t_2$ . This will lead to hesitation in the driver's decision because of the conflict of the interaction information and the signal state. Therefore, the existence of the decision dilemma zone ought to be avoided. Meanwhile, to maintain a stable vehicle speed under artificial driving, the detector should not be too far from the intersection. Thus, the distance between the request detector and the stop line should meet the following condition:

$$\frac{L}{V} \leq \Delta t \tag{3}$$

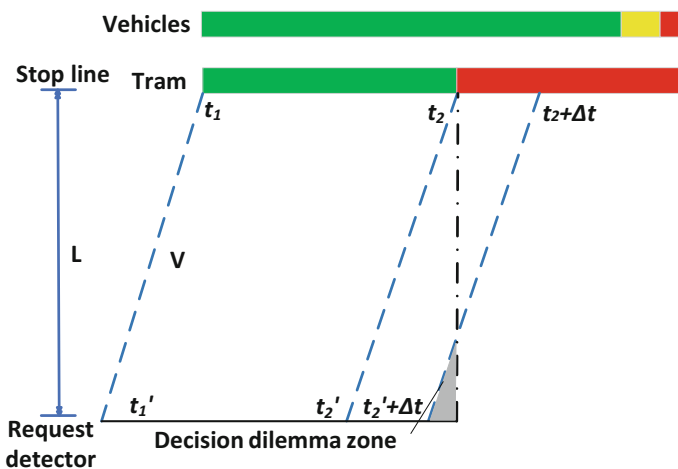


Fig. 5 Analysis of the detector location based on manual driving

**Table 2** The comparison of request detector location

The intersecting-road hierarchy	Degree of tram	Maximum green extension time (s)	Distance from detector to stop line (m)
High	No priority	–	–
Medium	Semi-priority	10	125
Low	Top priority	15	188

Judging from the analysis of the tram system based on V2I communication, under the condition of intermittent communication and considering the priority judgment mechanism of the green extension priority strategy and manual driving, the optimal location of the request detector should satisfy the equation below:

$$L = V \times \Delta t \tag{4}$$

The location of the request detector is related to not only the tram speed but also the priority parameters used in the intersection, which are more important. The priority parameters of the tram are different among the different intersections in actual lines. The operating speed of 45 km/h is used as an example, which is shown in Table 2.

## 4 Case Study

An intersection in Shenzhen City, China, was selected to evaluate the performance of the proposed model for the request detector. The intersection, as shown in Fig. 6, sets a semi-independent way in the middle. The simulation of this intersection is realized by VISSIM and VisVAP. The maximum green extension time is 10 s, and the headway of the tram is 300 s. The average delay of the tram is used as the measure of effectiveness. To highlight the performance of the proposed model, four cases are applied to the simulation. Except for the fixed-time control simulation, the distances from the request detector to the stop line are 80, 125 m (proposed model), and 200 m.

Figure 7 presents the result based on a 2-h simulation in VISSIM and indicates the tram average delay for all cases. The model with signal priority shows a significant improvement over the fixed-time model, and the proposed model works best. In addition, compared with the proposed model, the tram speed upon arriving at the request detector is unstable at a distance of 200 m, which reduces the chance of tram signal priority and causes a decision dilemma zone.

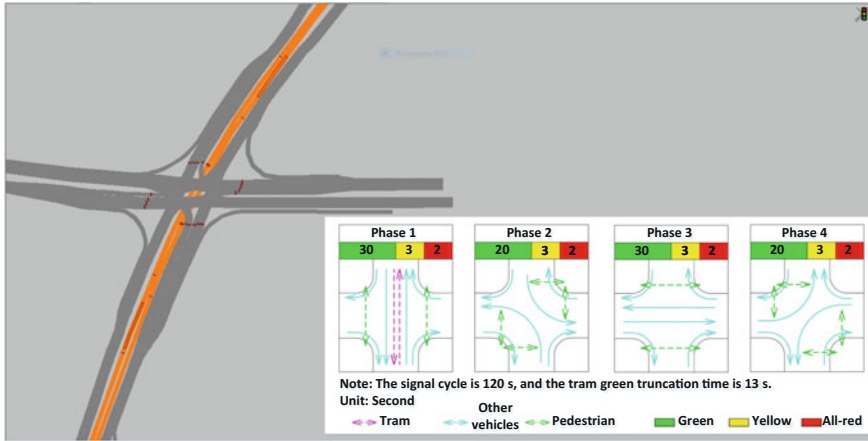
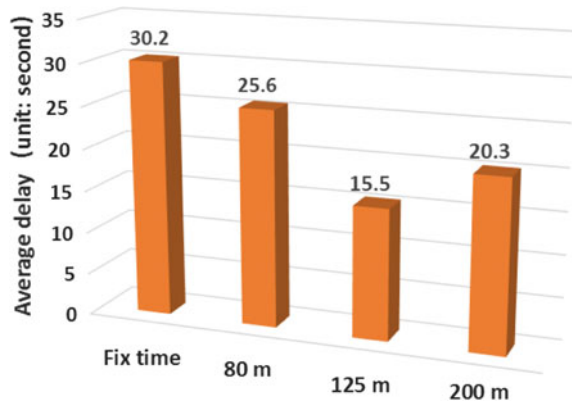


Fig. 6 Intersection simulation model

Fig. 7 The comparison of average delay



## 5 Conclusion

This paper introduced the process of the information interaction between a tram and detector and analyzed the application of tram signal priority in detail. This paper analyzed the most general green extension and green advance for the priority strategy and proposed a calculation method for the announcement detector and request detector.

The location calculation model for resolving the dilemma of recommended speed was developed in this study based on the interactive process of the announcement detector. To improve the tram signal priority and avoid decision dilemma zones, the request detector location was determined with the tram speed and signal parameters. The simulation results proved the effectiveness of the model

for the request detector. The results of a micro-simulation using VISSIM and VisVAP showed that the optimal location of the request detector for minimal signal delay is based on the proposed model.

**Acknowledgements** This work is supported by the National Key R&D Program of China (2016YFB1200402) and Research Program of Shanghai Science and Technology Committee (16511104902).

## References

1. Luo M, He W, Chen Y, et al (2016) Research on control strategies of modern streetcar at intersection under semi-independent way condition. In: Vehicle power and propulsion conference (VPPC), 2016 IEEE. IEEE, pp 1–6
2. Sun Z, Dai L, He G (2015) Signal priority control methods of modern tram at intersections. In: ICTE 2015, pp 520–527
3. Zhao B, Zhang Y, Zhang Z et al (2013) Study on signal priority implement technology of tram system. *Procedia-Soc Behav Sci* 96:905–913
4. Sermpis D, Papadakos P, Fousekis K (2012) Tram priority at signal-controlled junctions. In: *Proceedings of the institution of civil engineers-transport*. Thomas Telford Ltd., vol 165, No 2, pp 87–96
5. Zhou Y, Jia S, Zhang S, et al (2016) Study on detecting location for bus rapid transit with signal priority. In: *International conference on computer and information technology applications*
6. Yan F, Li K, Sun J (2009) Detector location for transit signal priority at intersection with countdown signals. *J Transp Inf Saf* 06:79–83 (in Chinese)
7. Chen F, Tan X (2016) Research on the crossing priority parameters of modern trams. *J Railway Eng Soc* 33(8):116–120 (in Chinese)
8. Naznin F, Currie G, Sarvi M et al (2016) An empirical Bayes safety evaluation of tram/streetcar signal and lane priority measures in Melbourne. *Traffic Inj Prev* 17(1):91–97

# Research on Real-Time Performance of Train Communication Network Based on HaRTES

Luyao Bai, Lide Wang, Jie Jian, Ping Shen, Chuan Yue  
and Xingyuan Wei

**Abstract** With the development of rail transportation technology, the integration of train control multimedia information into a network has become the trend of the future. Ethernet can meet this demand because of its high speed, large bandwidth and so on. In this paper, the Hard Real-Time Switching architecture is introduced into the train communication network. The data communication of train communication network depends on many switches, so a multi hop scheduling algorithm based on hard-real-time switch is proposed in this paper to ensure the real-time performance of train communication network data transmission. Finally, according to the actual communication process, this paper built the train communication network topology. The OPNET simulation results show that the proposed scheme can satisfy the real-time requirements of train communication network.

**Keywords** HaRTES · Train communication network · Multi-hop

## 1 Introduction

Train communication network is a network technology which integrates train communication and control [1]. With the increase of train network related control data, the current train communication network, such as TCN, can not meet the demand of data transmission in the future. Switched Ethernet adopts full duplex and micro segment technology, which can improve the real-time performance of the network to a certain extent.

With the extensive application of Ethernet, numerous Ethernet Real-time protocols RTE (Real-Time, Ethernet) have emerged, such as TTEthernet, PROFINET, IRT, POWERLINK and so on. The existing RTE protocols mainly include Time Triggered (TT) and Event Triggered (ET), the flexibility of Time Triggered mode is relatively poor, and the Event Triggered mode and can not guarantee the real-time

---

L. Bai (✉) · L. Wang · J. Jian · P. Shen · C. Yue · X. Wei  
School of Electrical Engineering, Beijing Jiaotong University, Beijing, China  
e-mail: lybai1103@163.com



requirement [2]. Flexible Time-Triggered Switched Ethernet uses master-slave operation mode, and it supports TT and ET as well as the dynamic adjustment, but the specific main node is responsible for communication scheduling, which has a great dependence on the terminal node, the node failure will cause noticeable loss of communication process. In this paper, [3] a hard real-time switch with main node function is introduced into the train communication network, whose main module is responsible for communication scheduling which solves the dependence of the terminal node. In addition, hard real-time switches can dynamically adjust the reserved bandwidth according to the link conditions to meet the requirements of the network bandwidth of the multimedia streaming data proposed by IEC61375-3-4 [4].

The network architecture of a single switch can't meet the requirements of train communication network in which data transmission usually across multiple vehicles. The research of single switch scheduling method in small networks is relatively mature [5], and the scheduling strategy of large and medium-sized networks with multiple switches is becoming the focus of research.

## **2 Multi-hop Scheduling Mechanism of Train Communication Network Based on HaRTES**

### ***2.1 Architecture of Train Communication Network Based on HaRTES***

The IEC announced standard IEC61375-2-5 (ETB, Ethernet Train Backbone) and IEC61375-3-4 (ECN, Ethernet Consist Network).

Referring to a subway network topology, the train network topology is divided into six sections, consisting of two trailers (TC1/TC2) and four motor trains (M1/M2/M3/M4). According to the two level architecture, the upper layer is ETB, and the lower layer is ECN, wherein TC1 and M1 and M2 form a ring network through the interconnection of the Consist Switch (CS) [6]. ETB and ECN communicate with each other through Ethernet Train Backbone Node (ETBN).

In order to meet the needs of real-time scheduling, both the CSs and ETBNs use HaRTES, which integrate the main scheduling module. Figure 1 is a multi-switch network, ending nodes (ED) connecting with the switch can be used as not only the source to generate data, but also the destination to receive the data. Each ED interacts with each other through a multi-switch network.

Each consist network is connected to at least one ETBN through CS. Each switch acts as a scheduler master node. This paper defines a backbone switch as the root master node. When the two nodes are connected directly, the superior master node is the parent node of the subordinate main node, and the subordinate master node is the child node of the higher master node.

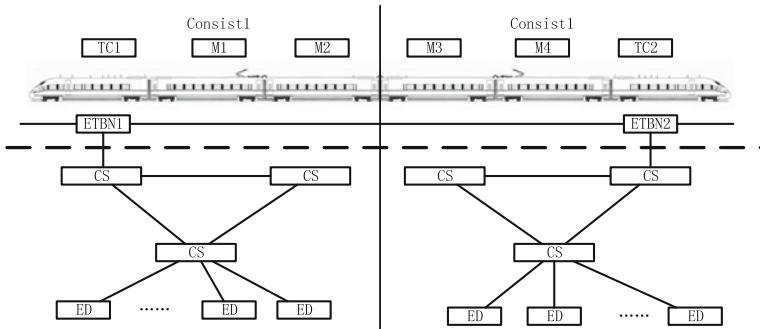


Fig. 1 Train communication network topology

### 2.2 Data Type and Time Delay Requirement

IEC61375-3-4 stipulates that the data transmitted by the train communication network can be divided into five kinds: Monitoring Data, Process Data, Message Data, Streaming data and the Best-effort data. The typical parameters of the five data types are shown in Table 1.

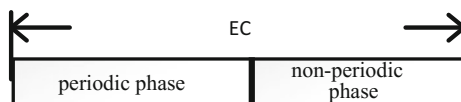
Classify the above five data into three kinds: Real-time Cycle Data, including Monitoring Data and Process Data; Real-time Aperiodic Data, including Message Data and Streaming data; Non-real-time Data, including Best-effort Data.

Referring to the MVB data transmission mechanism, as shown in Fig. 2 the data transmission is divided into fixed time slots, i.e., the Elementary Cycle (EC). Each EC is divided into two windows, the periodic phase in which the Real-time Cycle Data is transmitted and the non-periodic phase in which the Real-time Aperiodic Data and the Non-real-time Data are transmitted.

Table 1 Data class service parameters

Data type	Cycle time (max)	Latency (max)
Monitoring data	10 ms	10 ms
Process data	20 ms	10 ms
Message data	Aperiodic	100 ms
Streaming data	Aperiodic	100 ms
Best-effort Data	Aperiodic	125 ms

Fig. 2 Elementary cycle



### 2.3 Multi Hop Scheduling Algorithm

A switch directly connected with the source node is responsible for scheduling the entire transmission flow of Real-time Cycle Data. At the beginning of each EC, the master scheduling module inside the switch generates a schedule for the current EC. The switch sends the schedule to the ED via broadcasting notification message (NM), and the nodes send the data in an orderly manner according to the schedule. The Multi hop scheduling algorithm for Real-time Cycle Data is shown in Fig. 3.

Data is placed in the queue of the corresponding port in conjunction with the priority of the data. When the flowing data comes, the process repeats until the end of the current phase of the EC, at this point, the data is cached to the switch, waiting for the arrival of the next periodic phase window. Clock synchronization is achieved between the switches via the IEEE1588 [7].

In the output port of the switch, priority scheduling is adopted, and each output port has three queues, which are responsible for the transmission of the Real-time Cycle Data, the Real-time Aperiodic Data and the Non-real-time Data. The scheduler is responsible for choosing the output port and placing data in the

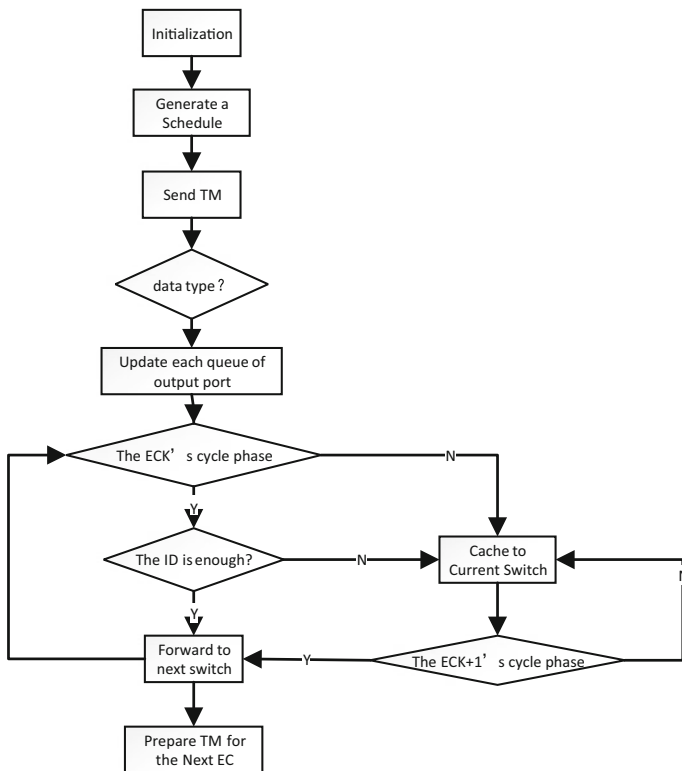
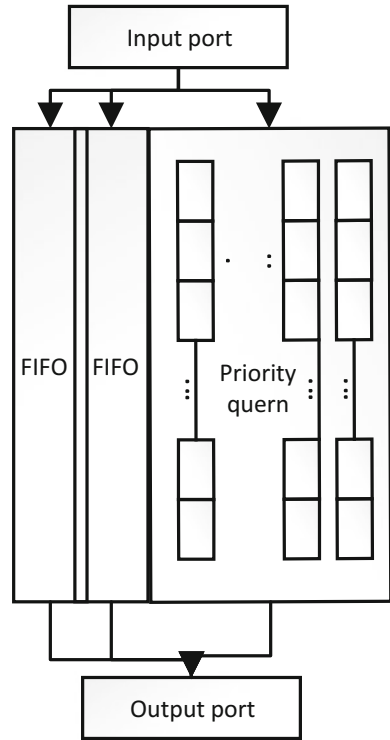


Fig. 3 Multi hop scheduling algorithm for real-time cycle data

**Fig. 4** HaRTES scheduling algorithm model



corresponding queue on the basis of the data type. For Real-time Cycle data, different priority queues are divided according to the data priority.

In periodic phase, aperiodic data is cached in the switch and forwarded in the FIFO mode until the aperiodic phase arrives. HaRTES scheduling algorithm model is shown in Fig. 4.

### 3 Experimental Verification

A simulation model of train communication network is constructed by using the OPNET Modeler simulation platform [8], as shown in Fig. 5, where each communication node represents a vehicle, and the internal model of the vehicle is shown in Fig. 6.

In order to verify the effectiveness of the multi hop scheduling method, the communication test of large amount of data is carried out in three nodes, taking TC1, M1 and M2 as examples. This test examines 15 sets of real-time cycle data streams among vehicle control unit (VCU1) and brake control unit (BCU1) in TC1, and BCU2 in M1, while the maximum frame length of the data is 1500 Byte, the

**Fig. 5** Simulation model of train communication network

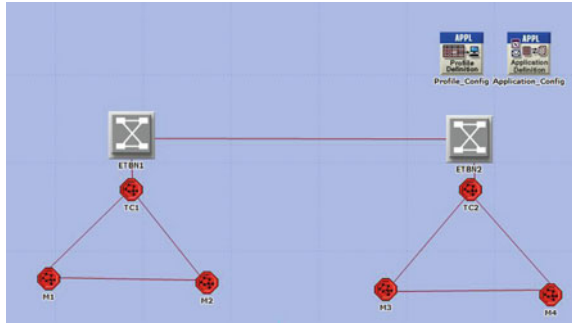
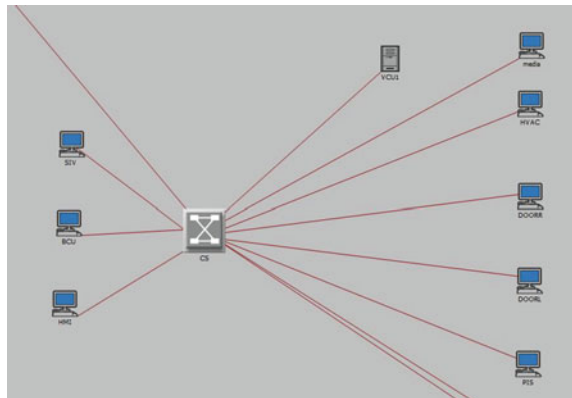


**Fig. 6** Internal model of the vehicle



transmission time is 123  $\mu$ s, and the period of real-time cycle data is [10,25] EC. The data flow configuration is shown in Table 2.

In this paper, the simulation time is set to 1 min, the response time of each data stream is recorded, and the maximum, minimum and average values are extracted, which are expressed by the number of the basic period EC.

The network bandwidth is 100 M, the input and output port speed is 100 Mbit/s. The EC is 1 ms. In order to facilitate the calculation, the size of the phase window is fixed to 700  $\mu$ s. The simulation results are shown in Fig. 7.

As can be seen from the diagram, when the amount of data between nodes is large, the response time of real-time cycle data is less than 5EC, that is, 5 ms, which meets the delay requirements of IEC61375-3-4 for the real-time cycle data such as process, data, monitoring data and so on.

In addition, the response time of the data is related to the priority of the data and the number of switches that passed during the transmission. For example, the data response times with priority levels of 1 and 2 are at most one EC, whereas data with a priority of 6 or 7 is 2–5 ECs.

**Table 2** Data flow configuration

Data	Cycle time (ms)	Priority	Source	Destination
m1	10	1	VCU1	BCU2
m2	12	2	BCU2	BCU1
m3	12	2	BCU1	BCU2
m4	12	2	VCU1	BCU2
m5	15	3	BCU1	VCU1
m6	16	4	VCU1	BCU1
m7	16	4	BCU1	BCU2
m8	16	4	BCU1	VCU1
m9	18	5	VCU1	BCU1
m10	18	5	BCU2	BCU1
m11	20	6	VCU1	BCU2
m12	20	6	BCU2	VCU1
m13	20	6	VCU1	BCU1
m14	25	7	VCU1	BCU2
m15	25	7	VCU1	BCU1

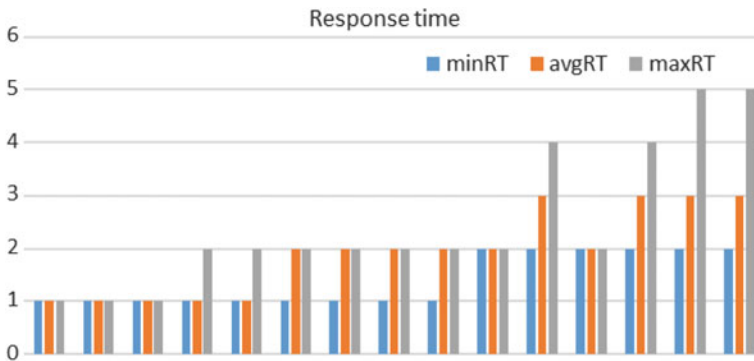


**Fig. 7** Simulation results of response time

## 4 Conclusion

This paper proposes a train communication network scheme based on hard real time switch, which uses the multi-hop scheduling mechanism to meet the real-time requirement of train communication network and the bandwidth requirement of multimedia data transmission. Finally, the architecture of train communication network is built in OPNET to verify the effectiveness of the proposed scheme.

**Acknowledgements** This work is supported by the Fundamental Research Funds for the Central Universities (2017JBM058) and the Fundamental Research Funds for the Central Universities (2017YJS181).

## References

1. Zhou J (2014) Real-time communication techniques of train communication network based on switched ethernet. Beijing Jiaotong University, Beijing (in Chinese)
2. Mifdaoui A, Frances F (2010) Performance analysis of a master/slave switched ethernet for military embedded applications. *IEEE Trans Ind Inf* 6:534–547
3. Álvarez I, Almeida L (2016) A first qualitative comparison of the admission control in FTT-SE, HaRTES and AVB. In: *IEEE world conference on factory communication systems (WFCS)*
4. IEC (2014) IEC 61375-3-4 Electronic railway equipment—train communication network (TCN)—Part 3–4: Ethernet Consist Network (ECN)
5. Ashjaei M, Behnam M (2012) A compact approach to clustered master-slave ethernet networks. In: *IEEE world conference on factory communication systems (WFCS)*
6. Qian Z (2015) Research on real-time and reliability of train communication network based on ethernet. Beijing Jiaotong University, Beijing (in Chinese)
7. Ashjaei M, Silva L (2016) Improved message forwarding for multi-hop HaRTES real-time ethernet networks. *J Sig Process Syst Sig Image Video Technol* 84(1):47–67
8. Wang T, Wang L (2015) Research on real-time performance of train communication network based on the switched ethernet technology. *J China Railway Soc* 37(4):39–45

# Data Cache in Mobile Environment Based on Extensible Markup Language

Jiusheng Du, Luyao Ma and Zheng Hou

**Abstract** Based on the research of data caching mechanism, this paper aims at the method that uses extensible markup language (XML) to cache the mobile terminals data. Taking an open-pit mine truck dispatching system as an example, wireless LAN following the 802.11 protocol is used as the study background, and mobile terminals with data acquisition function is the study object. Against the phenomenon that the mobile terminal in no signal or weak signal area cannot properly connect to the network, XML is proposed to cache data. The cached data can be send to the server in time through real-time monitoring network connectivity status of the mobile terminal and ensure the timeliness of data transmission. Field test proved that the method has certain reference significance for similar work.

**Keywords** XML · Mobile data transmission · Cache

## 1 Introduction

Wireless fidelity (Wi-Fi) wireless communication technology is made up of wireless communication technology, wireless location technology and computer technology and enables low-power, low-cost, secure, open-pit wireless communications. The currently available Wi-Fi standards are IEEE802.11a, IEEE802.11b and IEEE802.11g, and cover many aspects including effective long distance, transmission speed, high reliability, and high efficiency. In this paper, an open-pit with built Wi-Fi network is used as the research background.

In recent years, mobile devices such as smart phones, PDA, etc. have developed very quickly, and mobile data transmission has been widely used in urban transport, railways, oil, land and resource management, mining and other industries [1–3].

---

J. Du (✉) · L. Ma · Z. Hou  
Department of GIS, School of Surveying and Land Information Engineering,  
Henan Polytechnic University, 2001 Shiji Road, Jiaozuo, Henan 454000,  
People's Republic of China  
e-mail: rosepig.djs@gmail.com



Therefore, real-time data collection and real-time data transmission to the data centre using mobile devices have great practical significance [4].

Based on the depth analysis of data caching mechanisms, extensible markup language (XML) can be used to cache temporarily unsendable mobile terminal data and establish effective mechanisms to ensure data integrity and timeliness.

## 2 System Structure

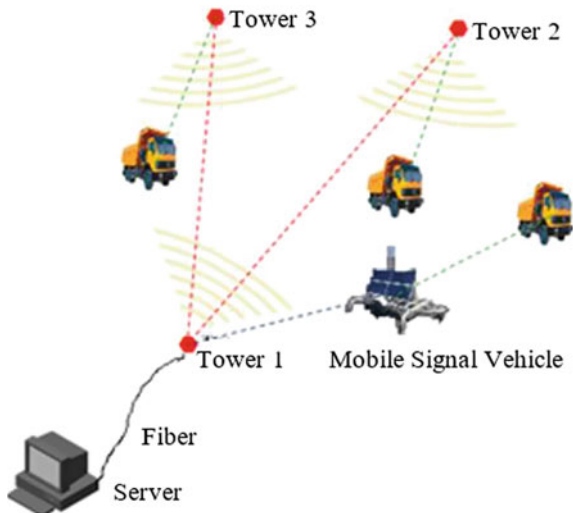
### 2.1 Network Architecture

Taking an open-pit mine truck dispatching system as an example, the wireless signal tower in the mining area is equipped with a 5.8 GHz antenna for directional transmission of signals between towers and a 2.4 GHz antenna for signal coverage. The server in the control room connects with the No. 1 tower via optical fibre to achieve wired and wireless networking. The vehicle terminal has a Wi-Fi function and can connect to the mine’s wireless LAN through the signal tower.

To avoid signal dead zone, vehicles equipped with wireless signals are provided as movable signal towers. These vehicles could be moved according to the actual situation of mining progress and are cost-effective.

Figure 1 shows the network deployment of an open pit, where the red dots indicate the wireless signal tower, red dotted lines show the directional transmission of signals between the signal towers, green dashed lines indicate that vehicles connect to the signal towers with stronger signal strength, blue colour dotted lines show the directional transmission of signals between the signal towers and the mobile signal vehicle and black solid line represents the optical fibre.

Fig. 1 Network architecture



## ***2.2 Data Acquisition Terminal***

The data acquisition terminal is placed in the mining vehicle and has the following characteristics: (1) Its position changes with the vehicle running; (2) It can collect real-time status information of vehicles; (3) Its collected information needs to be completely transferred to the server; (4) It needs to connect to the network through different AP during operation; (5) It has signal dead angles.

## **3 Data Cache Method**

### ***3.1 Necessity***

The stability of data transmission is affected by the wireless network condition. No matter how to lay wireless access point (such as signal towers, mobile signal vehicles), it cannot guarantee no signal dead angles. Therefore, effective measures should be taken to make sure that in no signal or weak signal areas, the wireless device could collect the data, store them in good conditions, and send them in a timely manner to the data center once the network connectivity resumes.

### ***3.2 Cache Mechanism***

Traditionally, the data cache means to cache frequently accessed data to the mobile nodes. Mobile terminal stores a copy of a subset of the overall database [5]. In the mobile computing environment, client caching is an important mobile computing technology, which not only improves system performance, but also enables users to access the data connection in the disconnect or weak state [6]. In recent years, many researchers have explored data cache and divide data cache management into file system and database system layers.

In this paper, data cache refers to data processing according to the network state. When the network is disconnected, mobile terminal data that unable to send to the server in real time should be temporarily stored in the machine. Once the network is connected, data will be sent to the server timely.

### ***3.3 XML***

XML formulated by the W3C (World Wide Web Consortium) organization is a drastically simplified subset of the W3C's Structured General Markup Language (SGML) designed to transfer and carry data [7]. Converting the data to XML can greatly reduce their complexity and make them readable by many different types of applications.

### 3.3.1 Features

1. Extensible: XML supports user-defined tags that contain rich semantic information. For example, <book> </book> indicates a book information.
2. Semi-structured: Unlike plain-text data, XML data are hierarchical data and can be regulated by the DTD.
3. Independent on Platform and Application: XML document content is based on the UNICODE text, and applies to network transmission.
4. Machine Processable: Relative to the completely random text, XML documents are easy to handle; relative to HTML documents with unclear semantics, XML documents are easy to understand by computers and readable to human.

### 3.3.2 Main Function

1. XML uses extensible markup to describe the information.
2. XML links information uses the XML linking language (XLink), which is a language for describing links between resources by means of XML attributes and a special namespace and offers two types of links: simple links and extended links.
3. XML sets the document display format using extensible style language (XSL), which specifies the XML document display format.

### 3.3.3 XML and Mobile Applications

XML is an open data standard. Because of its simple structure, good self-description, scalability and operational efficiency, XML data is suitable for mass data storage and exchange in mobile computing systems [8]. XML has been proposed for mobile data broadcasting [8]. According to its characteristics, XML also can be used for the data cache and an XML-based mobile application has been designed and developed [9].

1. Mobile applications should understand the contents of an XML document.
  - To understand XML syntax, the mobile application should be capable of handling XML.
2. Application of XML can promote the development of mobile applications.
  - Mobile applications could use XML documents for data exchange.
  - A device or server configuration file can be encapsulated in an XML file.

## **4 Cache Implementation**

### **4.1 Cache Requirements**

When the mobile terminal is running, only part of the data needs to be cached.

#### **4.1.1 Mobile Terminal Login**

When login to mobile terminal in no signal or weak signal area, one normally cannot access. To ensure accurate recording of the terminal operation, the resultant data should be cached.

#### **4.1.2 System Running**

1. Cannot be Networked
  - After mobile terminal has been logged in normally, if it runs to no signal or weak signal area, one cannot access the wireless LAN. Thus, the collected data are unable to be sent to the server, and should be stored in the local host.
2. Network Recovery
  - After the network is connected, the local cached data should be promptly sent to the server.
3. Network Disconnected Again
  - After the network is connected, the local cached data will be timely sent to the server. During this process, if the network is disconnected again, mobile terminal program should carry out the following operations:
    - Record the cached data that are not transmitted.
    - Cache new generated data.
4. Abnormal Shutdown
  - If the mobile terminal machine suddenly loses power, after reboot, the cached data should be able to send to the server, and this operation should not be performed repeatedly.

## 4.2 Data Structure

### 4.2.1 Real-Time Recording the Cached Data Transmission State

The data cache situation can be expressed using the XML file name in the format as ‘Table name + Storage state + Storage record number’. The meanings of the various components are as follows.

1. Table name
  - When the data has been sent to the server, it should be stored in a data table in database with the table name being the name of the data table.
2. Storage state
  - To indicate whether the contents of the XML file have been sent to the server, the file name can be sa for all data are stored, npN for N records have been transferred and ns for all data are not stored.
3. Storage record number
  - Only when the storage state is npN (partial storage), the number is valid.

### 4.2.2 Access the Cached Data that Need to Be Send by Scanning

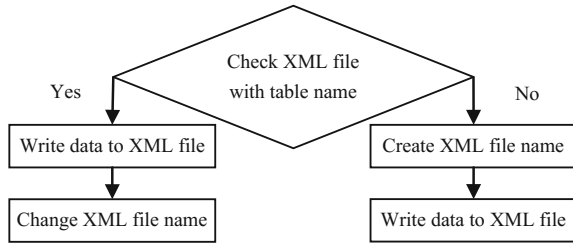
Establish a number of XML files to record the cached data and build structure XmlFileMessage to store the XML file information. As shown below, the struct XmlFileMessage we can be defined using the C# language:

```
public struct XmlFileMessage
{
    public String filename;
    public String tablename;
    public String savestate;
    public int savenum;
};
```

## 4.3 Write to XML File

When the network is disconnected, the data collected by the mobile terminals should be stored in local XML files (Fig. 2).

**Fig. 2** Write data to XML file



## 4.4 Transfer the XML Files

### 4.4.1 Scanning the XML Files

Scan XML files in the program folder and determine whether the document records need to be transmitted based on the file name and obtain the number of records need to be transferred.

### 4.4.2 Storing to Dynamic Array

Store the scanned information in struct XmlFileMessage variable and add the variable to XML file array.

### 4.4.3 Traversing XML File Array

Traverse XML file array by sending data that needs to be transmitted to the server and change the name of XML files.

## 5 Conclusion

Using XML to cache the mobile terminal data that cannot be send temporarily is a convenient and practical data caching method. The cached data can be send to the server in time through real-time monitoring network connectivity status of the mobile terminal and ensure the timeliness of data transmission. Accurate grasping data transmission status can be achieved by combining the characteristics of XML files, thus ensuring the integrity of data storage.

**Acknowledgements** This study was funded by the key scientific and technological project of Henan province (Grant no. 172102210277), the key scientific research project of department of education of Henan province (Grant no. 16A420002), and Guiding program for national coal association science and technology research (Grant no. MTKJ2016-212)

## References

1. Deng H, Hou IH (2017) On the capacity-performance trade-off of online policy in delayed mobile offloading. *IEEE Trans Wirel Commun* 16(1):526–537
2. Zhang Y, Li Q (2014) Exploiting ZigBee in reducing WiFi power consumption for mobile devices. *IEEE Trans Mob Comput* 13(12):2806–2819
3. Kang X, Chia YK, Sun S et al (2014) Mobile data offloading through a third-party WiFi access point: an operator’s perspective. *IEEE Trans Wirel Commun* 13(10):5340–5351
4. Du J, Chen Y (2011) The technical research of mobile data transmission security. *Comput Eng Appl* 47:11–14 (in Chinese)
5. Meng X, Ding Z (2009) Mobile data management concepts and techniques new catalytic materials. Tsinghua University Press, Beijing (in Chinese)
6. Li Z (2006) Research of key technologies on mobile computing. Tianjin University, Tianjin (in Chinese)
7. Horst KN (2010) Standard generalized markup language. Betascript Publishing. [https://en.wikipedia.org/wiki/Standard\\_Generalized\\_Markup\\_Language](https://en.wikipedia.org/wiki/Standard_Generalized_Markup_Language). Cited 15 Jan 2017
8. Gong S (2009) An adaptive xml data broadcast scheme in mobile computing environment. Huazhong Normal University, Wuhan (in Chinese)
9. B’far Reza (2006). Mobile computing principles-designing and developing mobile applications with UML and XML (tran: Gu G, T. Li) Publishing House of Electronics Industry, Beijing (in Chinese)

# Fully Automatic Operation System in Urban Rail Transit Is Applying in China

Fei Yan, Bo Liu, Yao Zhou, Chunhai Gao and Tao Tang

**Abstract** Fully Automatic Operation (FAO) is the highest level in the automation level of urban rail transit train operation and can reduce the security risk caused by human behavioral mistakes so as to provide more secure and efficient technical support for the urban rail transit operation. The FAO system is a complicated system and covers the whole lines and each station and train. This paper emphatically introduces development of the FAO system in domestic. FAO system will be applied to Beijing Metro Yan Fang line. Its application not only improves the automation level of technical equipment, but also comprehensively improves the technical level, the operation mode of rail transportation and the RAMS (Reliability, Availability, Maintainability and Safety) level of the whole rail transportation control equipment so as to ensure high-security, high-reliability and high automation operation under the unattended supervision situation. FAO system will be applied in several cities of the country in the near future, and it has a wide prospect of application in China.

**Keywords** FAO · Yanfang line · Technical support · Prospect

FAO is the highest level in the automation level of urban rail transit operation and has been widely applied in many countries such as France, Germany and Singapore, so the fully automatic operation system developed in China will go into operation in Yanfang Line in 2017. This paper has made a brief introduction for the definition, characteristics and development of the FAO system in China

---

F. Yan (✉) · B. Liu · Y. Zhou · C. Gao · T. Tang  
National Engineering Research Center for Rail Traffic Operation and Control,  
No. 3, Shang Yuan Cun, 100044 Hai Dian District, Beijing, China  
e-mail: fyan@bjtu.edu.cn

© Springer Nature Singapore Pte Ltd. 2018  
L. Jia et al. (eds.), *Proceedings of the 3rd International Conference on Electrical and Information Technologies for Rail Transportation (EITRT) 2017*, Lecture Notes in Electrical Engineering 482, [https://doi.org/10.1007/978-981-10-7986-3\\_95](https://doi.org/10.1007/978-981-10-7986-3_95)



# 1 Introduction of Urban Rail FAO System

## 1.1 Concept of Urban Rail FAO System

The International Association of Public Transport (UITP) divides the grade of automation (GoA for short) of train operation into 5 grades [1, 2], Including (Fig. 1).

The fully automatic operation (FAO) system is collectively called GoA3 and GoA4 above, which is a new generation of urban rail transit system which realizes automation during the whole train operation based on technologies such as the modern computer, communication, control and system integration. The FAO rail transportation can realize automatic awaking, driving out of the rail yard, operation in the main track according to the timetable, driving among stations, precisely train stopping, door opening and closing, departing from station, train turn-back operation, clearing of passengers after operation, train depot returning and sleep..., no intervention of driver and crew members is needed for the whole process.

## 1.2 Advantages of Urban Rail FAO System

Compared with the existing manned operation system widely applied, FAO can reduce the security risk caused by human behavioral mistakes. Manned operation of traditional train relies heavily on the personal response of driver, so it is hard to precisely control the human factors. However, for the metro cars with fully automatic operation, the computer program can automatically respond and make a decision at the first time during operation according to the situation happens immediately. Moreover, the train with fully automatic UTO will not be influenced due to fatigue and sudden disease of driver or other situations.

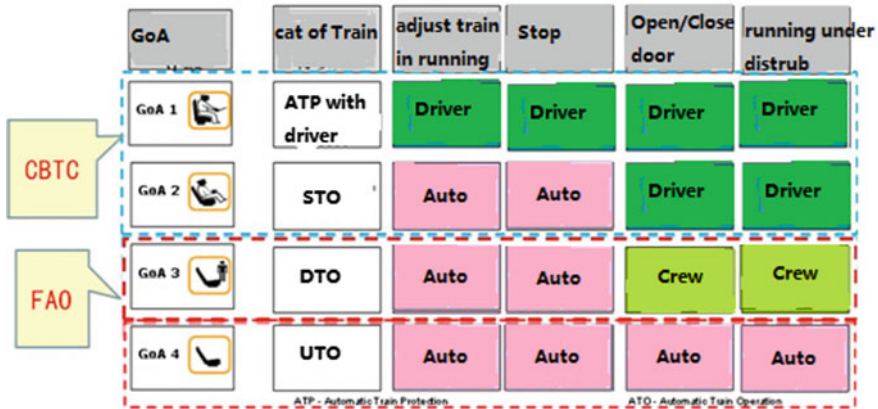


Fig. 1 5 grades of automation



Fig. 2 Video monitor and emergency talking devices in FAO

The FAO system can free the driver from repetitive operation, configure crew members on the train, improve the service level for passengers and can monitor the train operation state simultaneously [3].

In addition, the FAO system can enhance the functions of video monitoring and emergency talkback on the train so as to improve the capabilities of emergency disposal and counter terrorism (Fig. 2).

## 2 Components and Technical Features of FAO System

### 2.1 FAO System Components

The FAO system is a complicated system which is composed of the central monitoring system, the station subsystem, the on-board controller and the train-ground communication network and covers the whole line and each station and trains [4–6]. In addition, it is also a system with high reliability, high safety and high automation and can operate continuously for the whole day. The system structure is shown as the following figure.

The strengthened central monitoring system is in charge of monitoring, controlling and maintaining the whole line equipment such as driving, trains, electromechanical device and power supply units and conducting emergency disposal under emergency or accidental situations; the station subsystem is in charge of train management within the area, access handling, station monitoring, track-side location layout, zone occupation, turnouts and annunciator; the on-board controller realizes the functions such as train safety protection, automatic operation, passenger response and train monitoring; and the train-ground communication network realizes the two-way wireless train-ground communication with high-capacity and comprehensive load bearing [7].

## 2.2 Technical Features of FAO System

The FAO system not only improves the automation level of technical equipment, but also comprehensively improves technical level and the operation mode of rail transportation. Meanwhile, it improves the RAMS grade of the whole rail transportation control equipment so as to ensure high-safety, high-reliability and high-automation operation under the unattended supervision [8]. However, the FAO system shall solve the following technical problems:

1. Improve the whole automation level through multi-discipline deep integration.

Take the train traffic control as the core, deeply integrate signals with multiple systems such as trains, electric power, electromechanical and communication, realize multi-discipline automatic linkage under normal and fault conditions and improve the whole automation level of the rail transportation operation system. The Integrated supervision and control platform is shown as the following Fig. 3.

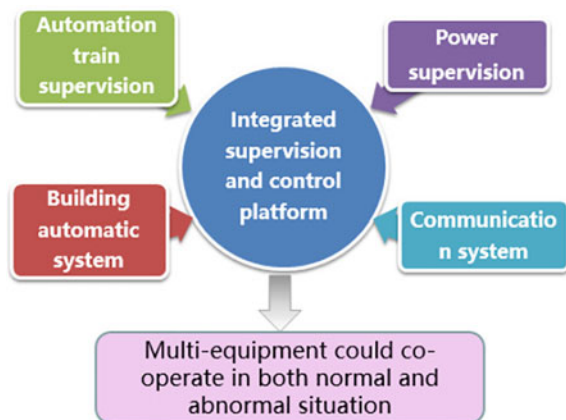
2. Improve the reliability of system through the comprehensive and sufficient redundancy configuration.

Signals enhance the redundancy configuration based on the existing equipment redundancy. For example, the train enhances dual-network redundancy control and increase interface redundancy configuration with signals and PIS (Passenger Information System).

3. Improve the overall security through enhancing the protection of passengers and operation staff.

Enhance the protection function for passengers, protect the train on-off and interior safety of passengers, enhance the protection function of operation staff and increase each system linkage function under the emergency situation, such as the linkage of ventilation, driving, power supply, videos and broadcast under the fire situation.

**Fig. 3** Multi-equipment multi-domain deep integration and cooperation in FAO



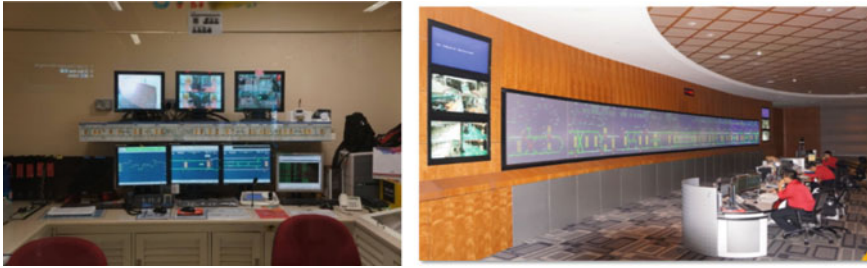


**Fig. 4** FAO use enhanced control center functions

4. Improve the emergency treatment capability through rich central control functions.

The FAO system will weaken the station functions, enhance the control function of center, realize comprehensive monitoring of the train FAO, conduct detailed monitoring and maintenance dispatching of each equipment system and provide the remote service facing passengers. The control center newly increases the functions of train dispatching and passenger dispatching so as to realize the functions of train remote control, state monitoring and passenger service [9] (Fig. 4).

5. Reduce the maintenance cost of system equipment through the maintenance comprehensive dispatching system based on big data.

According to the modern operation demands, set up a metro operation maintenance dispatching command platform based on big data by adoption of the thought “Network+”, taking the user as the core, with co-construction of all disciplines and based on the data method. Therefore, the system fault rate and the maintenance cost can be reduced [10].

### 3 Application of FAO System in China

China’s construction on the FAO rail transportation system has just begun. Currently, there are only 2 FAO lines which are respectively Beijing Airport Express and Shanghai Metro Line 10. Beijing Airport Express went into operation in July 2008 and had the UTO function in March 2012, the total length is 28.1 km, with the maximum running speed of 100 km/h, and the control system adopts the Urbalis CBTC UTO system of ALSTHOM LTD. Shanghai Metro Line 10 (Phase I), the first large-volume rail transportation line by adoption of UTO level in domestic, went into operation in November 2010, the total length is 36.2 km, with the maximum running speed of 80 km/h, and the control system adopts Urbalis CBTC UTO system of CASCO Signal Ltd. In order to ensure the traffic safety, one steward is respectively configured on both lines during actual operation,



**Fig. 5** FAO lines in China

when the UTO system operates normally, the steward is responsible for monitoring the operation state of train; and when a fault occurs, the steward can conduct emergency treatment in time and manipulate the train to run. At present, this kind of system is continuously planned and adopted by various cities such as Beijing, Shanghai, Chongqing, Shenzhen and Qingdao (Fig. 5).

China have completed the development, equipment development and test procedure of the FAO system, and the engineering implementation of Beijing Metro Yanfang Line is being carried out at present.

Operation analysis and design of Beijing Subway Yanfang Line is jointly completed by the construction unit and Beijing Jiaotong University. The whole operation process of ATO system were analyzed from the angle of system, and the Operation Scenario of ATO system is compiled. In combination with the Operation Scenario of ATO system, the personnel organization structure and post responsibilities of ATO system control center, rail yard and station were analyzed, and the management rules and emergency disposal rules under GOA3 and GOA4 were formulated. The control center dispatching responsibilities were combed according to the operation scenario of Yanfang Line. Based on the analysis results of dispatching load, the configuration scheme of control center dispatchers and professional equipment of the dispatching console is designed, and the site layout plan and console design scheme were designed.

Operation control equipment of Beijing Subway Yanfang Line is developed by Beijing TCT. The system realizes automatic execution or center manual execution of remote sleep awake through the sleep awake module. Realize the LTE-based large-capacity vehicle-ground communication technology, realize CBTC signal system, PIS, CCTV, emergency text and train real-time status by setting different priorities. Realize highly reliable on-board automatic train operation control, and improve reliability through head and tail BTM redundancy, head and tail speed measurement redundancy and red-blue dual net vehicle-ground communication redundancy; improve fault tolerance through contraposition isolation of the car door and platform door and platform jumping benchmarking; improve recoverability thorough remote fault isolation and remote fault reset. The system can realize unmanned automatic turn-back after the train arrives at the turn-back station, and the accuracy rate of automatic turn-back is over 99.99%; the probability for the train

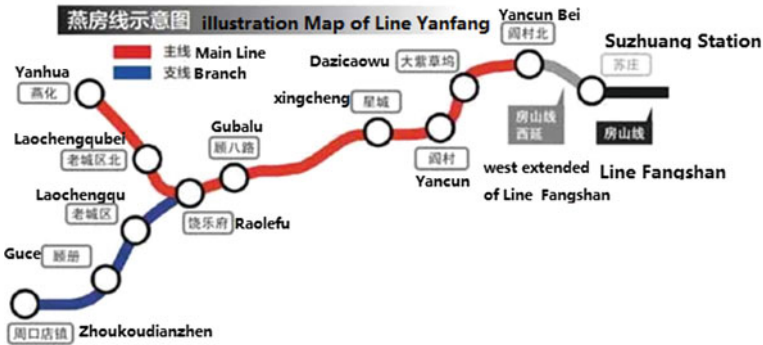


Fig. 6 Illustration map of line Yanfang

to park within  $\pm 0.3$  m parking accuracy range is over 99.99%; the probability for the train to park within  $\pm 0.5$  m parking accuracy range is over 99.9998%.

The Beijing Metro Yanfang Line with FAO will go into operation in 2017 (Fig. 6).

#### 4 Conclusion

FAO is the highest level in the automation level of urban rail transit train operation and can reduce the security risk caused by human behavioral mistakes so as to provide more secure and efficient technical support for the urban rail transit operation. It not only improves the automation level of technical equipment, but also comprehensively improves the technical level, the operation mode of rail transportation and the RAMS level of the whole rail transportation control equipment so as to ensure high-security, high-reliability and high automation operation under the unattended supervision situation.

Although FAO system has been widely applied in the world urban rail transit, its construction in China has just begun. The FAO system developed in China will go into operation, and FAO system will be applied in several cities of the country in the near future. It is obvious that the FAO system has a wide prospect of application in China.

#### References

1. Belgium (2007) A global bid for automation: UITP Observatory of Automated Metros confirms sustained growth rates for the coming years. <http://www.uitp.org/metro-automation-facts-figures-and-trends>. Accessed 24 Feb 2012

2. Fischer E (2011) Justifying automation. <http://www.railway-technology.com/features/feature127703/>. Accessed 23 Aug 2011
3. Cappaert-Blondelle S (2012) Media backgrounder metro automation facts, figures and trends—a global bid for automation. Director Communications & Publications, UITP 2012
4. Wang Y (2006) Fully automatic driverless operation system—a new concept of urban rail transport mode. *Urban Mass Transit* 9(8):1–5 (in Chinese)
5. Xiao Yan, et al (2014) The signaling functional requirements analysis of fully automatic operation system. *Railway Signaling and Communication* 2014(12). (in Chinese)
6. Zhang Y et al (2015) Reflections on the development of fully automatic operation in urban rail transit. *Railway Transp Econ* 9 (in Chinese)
7. Malla R (2014) Automation sets a new background. *Metro Report Int* 3
8. Xun J et al (2013) Coordinated train control in a fully automatic operation system for reducing energy consumption. *Computers in Railways XIII: Comput Syst Des Oper Railway Transit Syst* 127(3) (in Chinese)
9. Turner C et al (2015) A review of key planning and scheduling in the rail industry in Europe and UK. *Proc Inst Mech Eng Part F: J Rail Rapid Transit* 230(3):984–998
10. Domínguez M et al (2011) Optimal design of metro automatic train operation speed profiles for reducing energy consumption. *Proc Inst Mech Eng Part F: J Rail Rapid Transit* 225 (5):463–474

# Discrete Fuzzy Model Optimal Identification Based Approach for High Speed Train Operation

Kunpeng Zhang and Chunlan An

**Abstract** This paper investigates the problem of high speed train operation with special attention to minimizing the discrete constraint conditions between on-board traction network and group signaling equipment. A new discrete fuzzy model for train operation is developed, and its novelty lies in the fact that it optimizes the discrete model using relative degree criterion, which contains two processes of model order identification and model parameters local optimization. Then, we utilize a fuzzy weighted least square method to solve the global optimization problem of model parameters. In the end, simulation experiments have been implemented on the CRH2C-type high speed train, which validates the correctness of the proposed model.

**Keywords** High speed train · Discrete fuzzy model · Relative degree criterion  
Optimal identification

## 1 Introduction

A high speed train (HST) signal system consists of several discrete interacting units with a safe and reliable operation mode. From system identification point of view, it can be regarded as a class of uncertain discrete systems in relation to the interlocking arrangement of computer interlocking and temporary speed restriction [1, 2]. With along the speed increases, the uncertain discrete features subject to fail-safe scheme become remarkable. Thus, it is critical to study the effective identification model to support HST safe operation.

For HST traditional modeling approach, it has complex computational burden and can be only applied to the dynamics around the equilibrium points [3]. To better balance the modeling complexity and availability, a data-driven RBF neural

---

K. Zhang (✉) · C. An  
School of Electrical and Automation Engineering,  
East China Jiaotong University, Nanchang, China  
e-mail: ecjtu.zhangkunpeng@163.com



network is used to identify the nonlinear characteristics of HST operation in [4], it still suffers from slow training and local minima. Considering the global optimal solution, [5] proposed a fast learning algorithm with extreme learning machine. Since the single model structure is usually sensitive to the model identification accuracy, [6] adopted multi-model theory to describe the complex characteristics of HST operation. Unfortunately, the hard index may cause model estimation deterioration at the transition stage. In contrast to the above methods, [7] turned to apply a fuzzy model identification scheme. Nevertheless, the effects of modeling discretization and model order have also been ignored. In fact, the model relative degree estimation plays a significant role in determining HST optimal operation [8, 9].

Aiming at the uncertain discrete nonlinear dynamics of HST, a discrete fuzzy model optimization identification based approach has been presented in the paper. Firstly, a model relative degree index is used to calculate the optimal model order. Then, the discrete model parameters are identified with a fuzzy weighted bilinear least square method.

## 2 The High Speed Train Operation Analysis

The typical operation modes of HST consists of starting, traction, cruise, coasting and braking. And during the long distance steady-state operation, the relative displacement between adjacent cars is usually approximately zero, and thus the speed of each vehicle can be assumed equal [2, 3]. Under this condition, a HST consisting  $N$  passenger cars can be described as:

$$\begin{aligned}
 m_1 \dot{v} &= f(u_1 \otimes v) + u_1 - (m_1 c_{12} v^2 + m_1 c_{11} v) \\
 m_2 \dot{v} &= f(u_2 \otimes v) + u_2 - (m_2 c_{22} v^2 + m_2 c_{21} v) \\
 &\vdots \\
 m_N \dot{v} &= f(u_N \otimes v) + u_N - (m_N c_{N2} v^2 + m_N c_{N1} v)
 \end{aligned} \tag{1}$$

To add each items in (1), one can further obtain

$$M \dot{v} = F(U \otimes v) + U - (C_2 v^2 + C_1 v) \tag{2}$$

where, the system input is control force  $U$ , and the corresponding output is speed  $v$ . In the model, the Kronecker operator  $F(U \otimes v)$  means the control and speed variables satisfying the nonlinear multiplication relations. In addition,  $M$  denotes the HST's mass,  $C_1$  and  $C_2$  are the uncertain coefficient of air resistance and mechanical resistance, respectively.

### 3 Discrete T-S Fuzzy Model for High Speed Train

For the continuous-time nonlinear (2) with millisecond sampling, it is known that the infinite zero structure of the linearized discrete-time model is invariant [9]. Focus on the discrete-event descriptions, T-S bilinear discrete fuzzy model approximates HST dynamics with a high accuracy, the  $i$ th fuzzy rule of the model with an available operation point:

$$\begin{aligned}
 R_i : & \text{ If } v(k-1) \text{ is } \alpha_{i1} \dots \text{ and } v(k-p) \text{ is } \alpha_{ip} \text{ and} \\
 & U(k-1) \text{ is } \beta_{i1} \dots \text{ and } U(k-p) \text{ is } \beta_{ip} \\
 \text{Then } & A_i(z^{-1})v(k) = B_i(z^{-1})U(k-1)v(k-1) \\
 & + C_i(z^{-1})U(k-1) + \xi(k)
 \end{aligned} \tag{3}$$

where,  $i = 1, 2, \dots, n, j = 1, 2, \dots, q, n$  and  $q$  are the number of fuzzy rules and model order, respectively.  $\xi(k)$  refers to the stochastic noise sequence,  $A_i(z^{-1}), B_i(z^{-1}), C_i(z^{-1})$  are the discrete domain model parameters to be identified.  $\alpha_i$  and  $\beta_i$  are Gauss type membership functions in the input domain.

According to the above analysis, the discrete model outputs is obtained using the following defuzzification

$$\begin{aligned}
 v(k) &= \sum_{i=1}^n \bar{\mu}_i \{ (1 - A_i(z^{-1}))v(k) + B_i(z^{-1})U(k-1)v(k-1) + \\
 & C_i(z^{-1})U(k-1) + \xi(k) \} \\
 \bar{\mu}_i &= \mu_i / \sum_{i=1}^n \mu_i
 \end{aligned} \tag{4}$$

where  $\mu_i = \prod_{j=1}^q \alpha_{ij} \wedge \prod_{j=1}^q \beta_{ij}$  is the matching degree that the input variables match the  $i$ th fuzzy rule subject to the relative degree.

#### 3.1 Identification of Relative Degree

In high speed train commercial operation, the control characteristics between control and output variables usually follow the TCU (traction control unit) query commands tables. And it is possible to identify model parameters with prior data knowledge. However, current parameter identification methods often assume that the model order is known, which is not suitable for the high speed train with time-varying relative degrees. Consequently, the super order estimation is likely to

cause a large amount of calculation, and less order identification may not meet the safety requirements under different operation conditions. Therefore, considering the sample data capacity  $N$ , the variance of model estimation error  $\sigma_e^2$  and model estimation parameters  $\theta = [A_i; B_i; C_i]^T$ , the model order can be determined by the relative degree criterion  $J(q, \sigma_e^2, \theta)$ , as:

$$J(q, \sigma_e^2, \theta) = \frac{1}{2w} \theta^T \sigma_e^2 \theta + \frac{1}{2} q \log N + \frac{N}{2} \log w \tag{5}$$

To optimize the structure of discrete T-S fuzzy model, a reasonable relative degree is crucial for the model identification speed and accuracy. Commonly used relative degree estimation criterion includes clustering algorithm. For the  $l$  operation data  $X_\eta(U_\eta, v_\eta)$ , the number of optimal fuzzy rules  $P^*$  is obtained by subtractive clustering, as shown in [6].

### 3.2 Identification of Discrete Model Parameters

For ease of analysis, (4) can be transformed into the following discrete form

$$v(k) = \sum_{i=1}^{P^*} \Phi^T \theta_{ik} + \zeta(k) \tag{6}$$

where, the observable vector

$$\Phi(k) = \begin{bmatrix} (v(k-1), \Delta v(k-1)U(k-1), U(k-1)), \dots \\ (v(k-p), \Delta v(k-p)U(k-p), U(k-p)) \end{bmatrix}^T, \Delta v$$

is speed increment,  $\theta_{ik} = [a_{i1}, \dots, a_{iq}, b_{i0}, \dots, b_{iq}, c_{i0}, \dots, c_{iq}]^T$  is discrete parameters to be identified, which is a typical least squares estimation problem. However, it is known that its objective function is global optimization, and it can not accurately describe the dynamic characteristics of each local rule.

To optimize the comprehensive perceive capability of high-speed train passing the ground signal, a fuzzy weighted bilinear least square algorithm is used to iteratively optimize the model parameters, as shown in [2].

### 4 Simulation Verification

In order to illustrate the modeling effectiveness of the proposed method, the simulation of the new generation CRH2C high-speed train has been carried out. And the operation parameters are shown in [2]. When high speed train runs safely, the operation speed will not change dramatically, and the relative degree between the input and output variables will not be too large. Hence, the upper order of the discrete model can be set as 3. As shown in Table 1, the minimum description length criterion under various model orders can be described.

To analyze the key influencing factors in Table 1 with (5), it shows that when the model order becomes larger, the model error variance is smaller, yet the number of model parameters grows in proportion and the computation increases exponentially. As the model order closes 2, the relative degree criterion is minimum. As a result, the optimal relative degree is 2.

According to the traction characteristic curve of CRH2C high speed train, 2000 data sets vary in [0 350 km/h] range are simulated. Similarly, 1000 data sets [350 km/h 300 km/h] of the coasting resistance characteristic and 3000 data sets [350 km/h 0] of the braking dynamic are also simulated. To analyze these data with the relative degree criterion in [6], we can get the optimal six fuzzy rules.

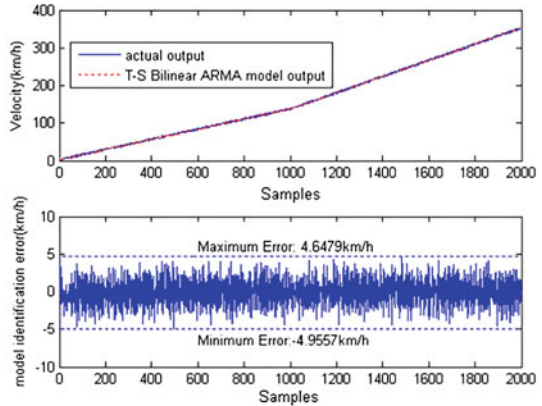
On the basis of the above analysis, Fig. 1 shows the model output and the corresponding error curves in terms of traction, coasting and braking conditions. Consider the invariance properties of discrete system infinite zero structure, the dynamics and convergence of the six parameters are shown in Fig. 2.

It can be seen from Fig. 1 that T-S discrete fuzzy model fits the actual output with higher accuracy. Namely, the maximum positive and negative errors are no more than 7 km/h, satisfying the safety error requirement of the CTCS-3 train control system [2]. As can be seen from Fig. 2, the model parameters have faster convergence and better adaptability under different conditions. Especially, in Fig. 2a, though great changes occur in traction stage (1000 th data samples), the convergence of model parameters still has good adaptability, satisfying the robustness and rapidity requirements.

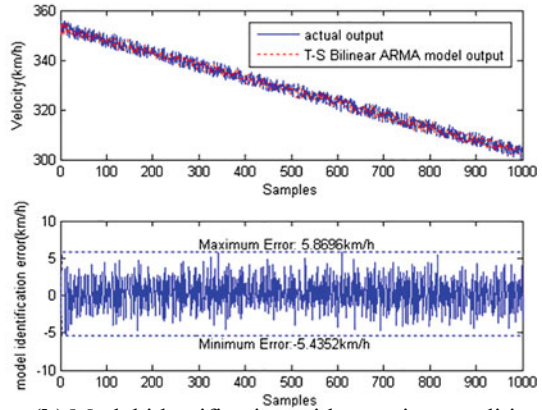
**Table 1** Performance indexes with various relative degree

Model relative degree	First-order model	Second-order model	Three-order model
Sample capacity	2000	2000	2000
Variance of model estimation error	3.8632	2.9538	2.6271
Numbers of model parameters	3	6	9
Model order index	2.5659	2.0732	2.468

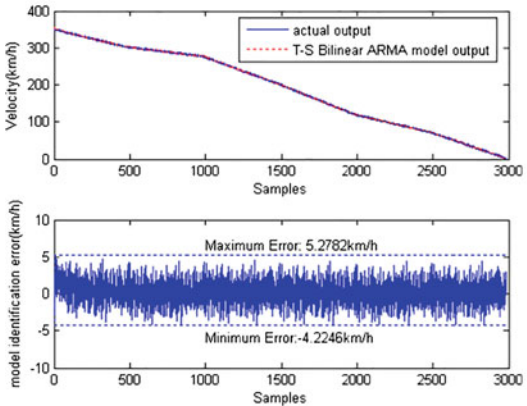
**Fig. 1** **a** Model identification with traction conditions. **b** Model identification with coasting condition. **c** Model identification with braking condition



**(a)** Model identification with traction conditions

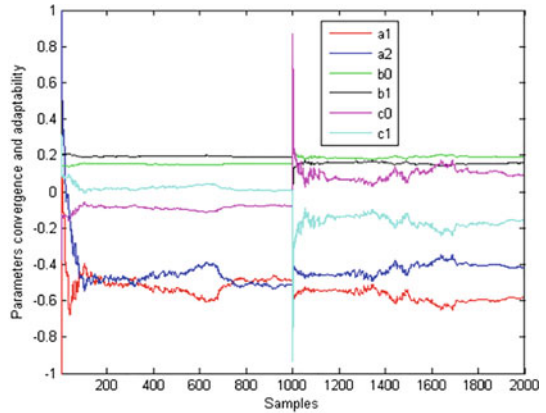


**(b)** Model identification with coasting condition

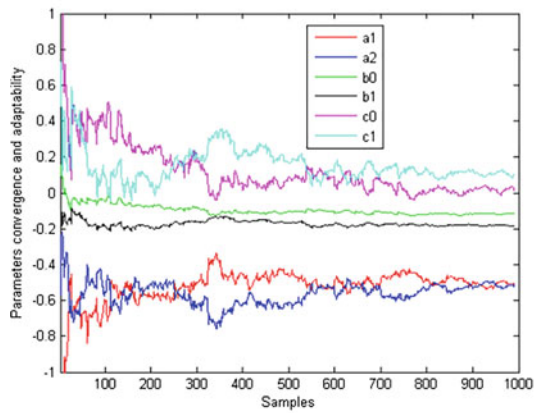


**(c)** Model identification with braking condition

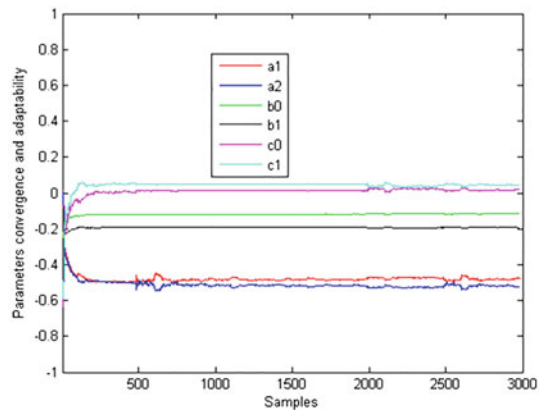
**Fig. 2 a** Model parameters under traction. **b** Model parameters under coasting. **c** Model parameters under braking



**(a)** Model parameters under traction



**(b)** Model parameters under coasting



**(c)** Model parameters under braking

## 5 Conclusion

In this paper, discrete dynamics identification problem has been investigated for high speed train operation process with traction/braking characteristic curves. To ensure the uncertain system reliability, a discrete fuzzy model optimization identification based approach has been proposed. It is verified that the optimal model has a good robustness and predictive precision.

**Acknowledgements** This work is partly supported by the Natural Science Foundation of Jiangxi Province, China under Grant 20132BAB201042, and in part by the research fund of East China Jiaotong University under Grant 12DQ04.

## References

1. Liu AH, Yang Q, Zhang X, Deng WB (2017) Collision avoidance radar system for the bullet train: implementation and first results. *IEEE Aero Electron Syst Mag* 32(5):4–17
2. Yang H, Zhang KP, Liu HE (2016) Online regulation of high speed train trajectory control based on T-S fuzzy bilinear model. *IEEE Trans Intell Trans Syst* 17(6):1496–1508
3. Dong HR, Ning B, Cai BG, Hou ZS (2011) Automatic train control system development and simulation for high-speed railways. *IEEE Circuits Syst Mag* 10(2):6–18
4. Song Q, Song YD (2012) Data-based fault-tolerant control of high-speed trains with traction/braking notch nonlinearities and actuator failures. *IEEE Trans Neural Netw* 22(12):2250–2261
5. Zeng YJ, Xu X, Shen DY, Fang YQ, Xiao ZP (2017) Traffic sign recognition using kernel extreme learning machines with deep perceptual features. *IEEE Trans Intell Trans Syst* 18(6):1647–1653
6. Yang H, Fu YT, Wang DH (2017) Multi-ANFIS model based synchronous tracking control of high-speed electric multiple unit. *IEEE Trans Fuzzy Syst* 99:1–14
7. Guo XG, Wang JL, Fang Liao (2017) Adaptive fuzzy fault-tolerant control for multiple high-speed trains with proportional and integral-based sliding mode. *IET Control Theor A* 11(8):1234–1244
8. Cassar T, Camilleri KP, Fabri SG (2010) Order estimation of multivariate ARMA models. *J Sel Top Sig Process* 4(3):494–503
9. Guo JX, Gang Tao (2015) A discrete-time multivariable MRAC scheme applied to a nonlinear aircraft model with structural damage. *Automatica* 53:43–52

# Research on GIS Database Construction and Application for UGV in the Campus Traffic Environment

Mingtao Wu, Yanhui Wang and Xiaofeng Li

**Abstract** As the research hotspot of intelligent transportation system (ITS), unmanned ground vehicle (UGV) with high intelligence is able to reduce the probability of traffic accidents and traffic congestion, and improve the efficiency of urban transportation system. Environmental perception is one of the key research topics in the research of key technologies of UGV. The campus transportation environment, as a simple version of the urban transportation environment, needs to perceive as much traffic information as the urban traffic environment. At the same time, the geographic information system (GIS) has capabilities of strong geographical information storage and management, which can play a critical role in the environmental perception of UGV. In this paper, we study the autonomous driving of unmanned ground vehicle in the campus traffic environment, and the construction method of GIS database is proposed for the perception demand of UGV in the traffic environment of campus. Then, according to the GIS database, autonomous navigation control of UGV is carried out to verify its applicability and effectiveness. After testing, the GIS database proposed in this paper can assist the autonomous driving of UGV well and complete the driving tasks in the campus environment.

**Keywords** Geographic information system (GIS) · Unmanned ground vehicle (UGV) · Navigation

---

M. Wu · Y. Wang · X. Li

State Key Laboratory of Rail Traffic Control and Safety, Beijing Jiaotong University, Beijing 100044, China

M. Wu (✉) · Y. Wang · X. Li

School of Traffic and Transportation, Beijing Jiaotong University, Beijing 100044, China  
e-mail: 13251081@bjtu.edu.cn

© Springer Nature Singapore Pte Ltd. 2018

L. Jia et al. (eds.), *Proceedings of the 3rd International Conference on Electrical and Information Technologies for Rail Transportation (EITRT) 2017*, Lecture Notes in Electrical Engineering 482, [https://doi.org/10.1007/978-981-10-7986-3\\_97](https://doi.org/10.1007/978-981-10-7986-3_97)

959



## 1 Introduction

Unmanned ground vehicle (UGV) with high intelligence is able to reduce the probability of traffic accidents and traffic congestion, and improve the efficiency of urban transportation system. Besides, UGV can also take the place of human in harsh environments, so that we can explore those areas where human is currently unable to access. Therefore, UGV is a research hotspot in the field of intelligent transportation system and automobile control. While the research on the application of GIS to UGV mainly focuses on the positioning of UGV, map construction and path planning at present, the research of GIS database construction method for UGV is less developed [1]. This paper studies the application demand of autonomous driving in campus traffic environment. On the one hand, the complexity of campus traffic environment is not as high as urban traffic environment, but campus traffic environment which needs to perceive many traffic information can be seen as a simple urban traffic environment because of their similarity of road topologies. On the other hand, geographic information systems (GIS) have a powerful capacity of geographical information store management. In this paper, firstly we understand the traffic information that UGV needs to sense by analysing the perceived demand for autonomous driving in the campus traffic environment; secondly, the construction of GIS database is completed with the environment perception and the features of campus traffic environment; finally, the GIS database we proposed is used to achieve the autonomous navigation of UGV in order to verify the applicability of GIS database.

## 2 Construction of GIS Database

### 2.1 UGV Experiment Platform

With the ability to drive autonomously in the campus traffic environment, the UGV used in this paper is a small vehicle designed according to automotive chassis design principles, as is shown in Fig. 1. The chassis of the vehicle takes the way that its front wheel steer and its rear wheel drive, and its structure is the original “Double Ackerman” structure. The vehicle has three information transmission network: CAN bus for vehicle electronic control; Ethernet used for environment perception such as video, radar, navigation system, etc.; 4G and Wifi for vehicle-ground communication.



**Fig. 1** UGV experiment platform

## ***2.2 Demand Analysis for the Perception of UGV***

The perception of the structured road environment in the city is easier than that of the unstructured road environment in the wild. As a simplified urban traffic environment, campus traffic environment can ignore complicated traffic rules in the demand analysis to reduce the difficulty in the perception of traffic environment information used by UGV. Therefore, when the vehicle is driving in the campus traffic environment, the basic environmental information that the vehicle needs to perceive is as follows: road attribute information. It mainly includes the road length and width, the direction of the road. Among them, the direction of the road is the Angle between the radiation from the beginning and end of the road and the geographic North Pole; real-time driving information. In real-time driving, the vehicle needs to obtain its own position, speed and course information through the differential GPS system. The road attribute information in the above environment information is static, and we can know in advance and store it in a GIS database.

## **2.3 The Construction of GIS Database**

### **2.3.1 Introduction of GIS**

Geographic information system (GIS) is a highly integrated discipline with multiple disciplines, involved in mathematics and statistics, cartography and cartography, photogrammetry, remote sensing and computer science, etc. It is the carrier of geographic information, which is the control information system for acquiring, storing, editing, processing, analyzing and displaying GIS data including spatial data and attribute data. Spatial data describes the spatial location and spatial topology of terrain objects, such as the coordinate points of the road [2]. Attribute data describes the property information of terrain property, such as the length, width and direction of the road. Spatial data and attribute data are one-to-one correspondence.

### **2.3.2 The Construct Process of GIS Database**

This paper uses the ArcGIS software designed by ESRI to complete the GIS database construction. Firstly, we should obtain a high-resolution map as a map of geographical data. In this paper, Google Earth is used to obtain a satellite map with accuracy of 1 m, which is used as a base map to build a GIS database for a university campus in Beijing. And then we import the base map in ArcGIS. Since there is no coordinate information on the base map, the coordinate system is set to the WGS84 coordinate system consistent with the base map. The base map, a raster image, has no spatial location information. Therefore, it needs to be matched, and the base map is calibrated with coordinates and projections. Next, we need to complete the input for the GIS data. In this paper, we store the spatial data first and then build its attribute information for each spatial data. Firstly, the map layer is established in ArcGIS to draw every road in the campus. In order to show the direction of the road, the two-way road is represented by two line objects, and the direction of the two line objects is set respectively. Besides, a one-way road is represented by a line object. Secondly, we create a point layer to draw every node in the campus. Once the spatial data is stored, the properties information can be set.

### **2.3.3 Settings for Attribute Information**

Attribute data exists as a property sheet. Each spatial data corresponds to a property sheet, while a property sheet carries multiple attribute fields such as FID, name, topology information, and so on. The property sheet established for the Intersection node is shown in Table 1. The property sheet that is built for the section is shown in Table 2.

**Table 1** Intersection node property sheet

Serial number	Name	Alias	Field type
1	FID	Object number	Object ID
2	Shape	Object graphics	Geometry
3	Name	Node name	String
4	x	Longitude	Double precision
5	y	Latitude	Double precision
6	Intersection		Long integer

**Table 2** Section data property sheet

Serial number	Name	Alias	Field type
1	FID	Object number	Object ID
2	Shape	Object graphics	Geometry
3	StartNode	Road start ID	Long integer
4	EndNode	Road end ID	Long integer
5	LaneNum	Number of lanes	Long integer
6	Length	Section length	Double precision
7	ResistS2E	Positive resistance	Double precision
8	ResistE2S	Reverse resistance	Double precision
9	Direction	Road direction	Double precision

Among them, ResistS2E of table refers to the positive resistance which is a weight value indicating whether the road can pass. If ResistS2E equal one, cars can pass the road. If ResistS2E equal zero, car can't pass the road. This field is used to prevent bi-directional routes from being serialized. The function of ResistE2S is consistent with the for Positive resistance, but the direction of the constraint is opposite to the Positive resistance.

### 3 Automatic Navigation Control Method of UGV Based on GIS Database

UGV's automatic navigation control method is one of the necessary conditions to ensure that it can travel reliably [2]. The perception information required for unmanned driving is provided by the GIS database we proposed. In the GIS database, we can get the intersection node data and road data that UGV requires so that it is easy to plan the path of the vehicle to obtain the minimum cost of path for unmanned driving. First of all, we need to access to the road where the vehicle is according to the vehicle's location information and the vehicle may not be right on

the lane, but on the side of the road between the two intersections. When it is not on the lane, the vehicle should be driven to the right lane. Finally, the vehicle must not deviate from the lane and must complete the mission that it travels follow the planned route.

### 3.1 Automatic Matching and Control Method for Vehicle Position

The control of UGV is mainly to control the direction of UGV, and we set the speed of the unmanned car to a constant value. First of all, we need to tell the unmanned car is on which lane, as shown in Fig. 2 [6]. Next, the vehicle on the side of the road should be driven to the right lane, which is shown in Fig. 3.

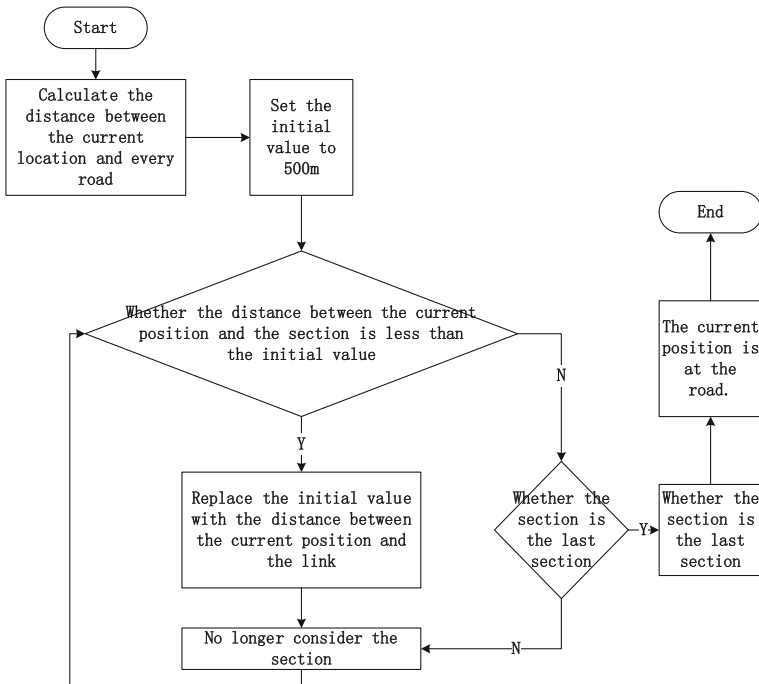


Fig. 2 Vehicle position matching process

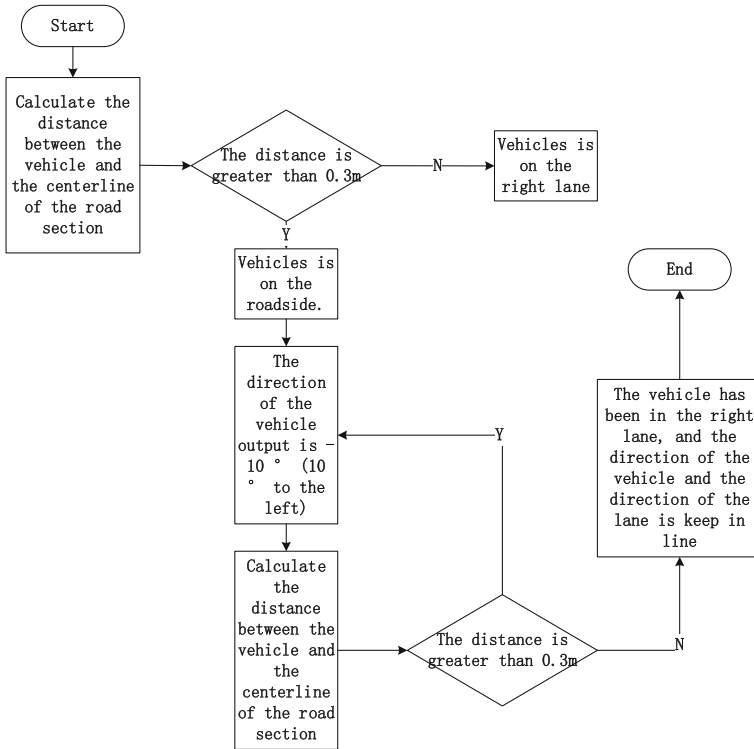


Fig. 3 The vehicle on the side of the road should be driven to the right lane

### 3.2 Method of Unmanned Vehicle Path Planning

In this paper, the starting point of the shortest path is the end of the road where the starting point of the vehicle is, and the end of the shortest path is the starting point for the end of the road where the destination is. The shortest path solution is a common Dijkstra algorithm. The route that UGV may travel starts at the starting point of the vehicle, go through the starting point of the shortest path and the end point of shortest path, and ends up the destination [3].

### 3.3 Target—Oriented Vehicle Automatic Matching and Control

After the route is obtained, UGV will in turn navigate to the node in the path, and each node is the target point. Whenever the vehicle reaches a target, it switches the

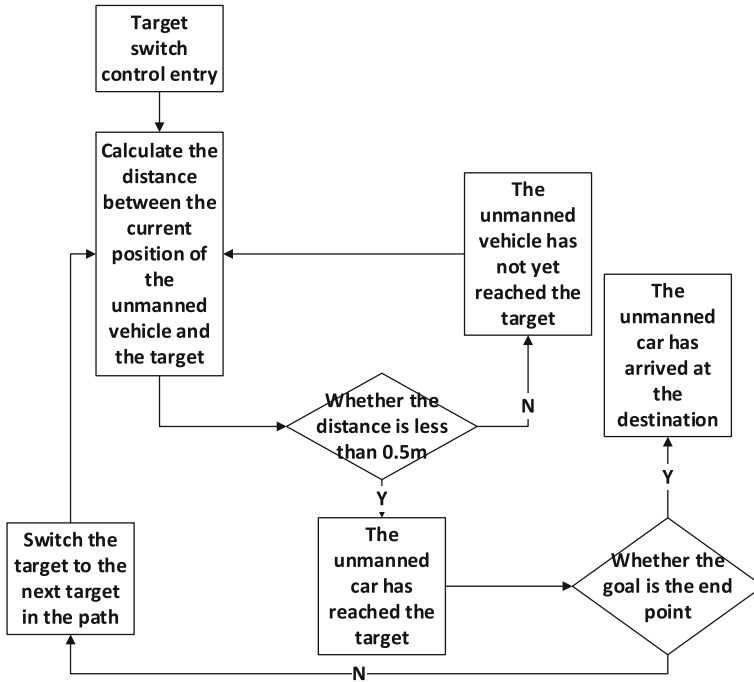
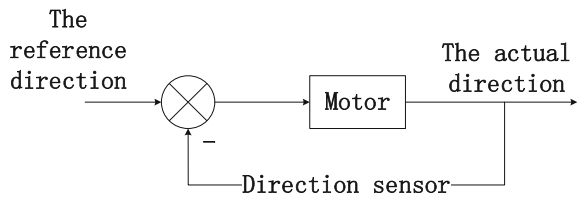


Fig. 4 The method of target switching

Fig. 5 Direction control block diagram



target to the next target in the path until it reaches the last node in the path. The method of target switching is shown in Fig. 4 [4, 5].

The vehicle is running at a constant speed while the vehicle is running towards the target point. We need to control the direction of the vehicle when driving, so that the vehicle may not deviate from the direction of the lane. Depending on the difference between the actual direction of the vehicle and the given reference direction, the motor of the vehicle is output in the direction we need, as Fig. 5 shown.

Depending on the target category, we have different direction control methods. The first case: the vehicle in a straight lane is driving towards the end of the lane, and the target point is the lane of the end. The reference direction of the vehicle direction control is the direction of the lane. The second case: the vehicle drives into

the intersection, then the vehicle may move forward, turn right or turn left to leave the intersection. First of all, we calculate the difference between the direction of the vehicle and the direction of the lane in which the target is located. That is, the direction angle of the lane where the target point is located is subtracted from the direction angle of the vehicle [6, 7]. If the difference is between  $-45^\circ$  and  $45^\circ$ , then the vehicle can be considered to pass straight. In this case, the reference direction may be the direction in which the vehicle is located as the starting point and the target point as the end point. If the difference is greater than  $45^\circ$ , then the vehicle needs to turn left, and the steering of the vehicle is set to  $-10^\circ$  ( $10^\circ$  to the left) until the target is reached. If the difference is less than  $-45^\circ$ , then the vehicle needs to turn right, and the steering of the vehicle is set to  $15^\circ$  ( $15^\circ$  to the right) until the target point is reached. The third case, the target point of the vehicle is the end point, and the vehicle needs to travel straight along the driveway. When the distance between the vehicle and target point is 3 m, set the direction of the vehicle to  $10^\circ$  until the vehicle reaches the finish line.

## 4 Experimental Verification

### 4.1 *Establish Differential GPS Positioning System*

First, we need to establish a differential GPS system to meet the high-precision positioning needs of unmanned vehicles. We take two GPS receiver at the same time work to receive GPS satellite signals. One of the GPS receiver is as a precise location of the base station, which is the GPS base station. It is placed on the rooftop of the tallest building near the test route, with no obstructions such as trees and buildings to block GPS satellite signals. Another GPS receiver is installed on the roof of UGV as a rover (mobile station) [8].

### 4.2 *Unmanned Vehicle Navigation*

Our test place is a university campus in Beijing, and the test route as shown in Fig. 6. Test results are unmanned vehicles can output the right direction. Although slightly offset from the center line of the road, but the direction of the vehicle can be consistent with the direction of the lane. The vehicle can eventually reach the destination.



**Fig. 6** The test route



## 5 Conclusion

Based on the ArcGIS Desktop platform developed by Esri, this paper constructs a GIS database suitable for auxiliary cruise control. By setting the given path for UGV, the cruise control strategy of the unmanned aerial vehicle is assisted by the GIS database. After testing, the GIS database proposed in this paper can assist the autonomous driving of UGV well and complete the driving tasks in the campus environment.

**Acknowledgements** The authors gratefully acknowledge the support from “Key Research Project of Safety Assurance Technology of Urban Rail System” under China National “13th Five-Year Plan” (Grant No. 2016YFB1200402-002).

## References

1. Yang Q, Wang M, Kwan MP et al (2015) A novel GIS platform for UGV application in the unknown environment. In: International conference on geoinformatics IEEE, pp 1–6
2. Park WI, Kim DJ, Lee HJ (2013) Terrain trafficability analysis for autonomous navigation: a GIS-based approach. *Int J Control Autom Syst* 11(2):354–361
3. Pan YH (2016) Research on unmanned ground vehicle routing based on. Beijing Institute of Technology (in Chinese)
4. He Y (2015) Research on GPS navigation method based on high fine map. Shanghai Jiaotong University (in Chinese)
5. Wang XP (2015) Construction and application of GIS database for unmanned vehicles in urban traffic environment. Beijing Institute of Technology (in Chinese)
6. Fang YJ, Zhou TT, Fang Y (2012) Research on the method of unmanned vehicle location based on GIS and environment perception. *Autom Instrum* 5:1–4 (in Chinese)
7. Bo BH (2009) An example of geographic information system development based on MapX technology. Tsinghua University Press (in Chinese)
8. Liu J Research on path planning technology of small unmanned ground maneuvering platform. Beijing Institute of Technology (in Chinese)

# Research on Algorithm of Correlation Denoising Based on Wavelet Transform

Lei Yang, Feng Xue, Hong hai Wang and Hua wei Cheng

**Abstract** Aiming at the problem of noise in the traffic monitoring, especially at night, an image denoising algorithm is proposed. Application of correlation denoising algorithm based on wavelet transform in traffic monitoring. Firstly, Haar wavelet is used as the transform matrix, then image data are denoised. And The similarity of the image is evaluated by the peak signal to noise ratio. Finally, the obtained data is compared with the algorithm of existing adaptive threshold. It is found that the improved algorithm of correlation denoising achieved the expected effect and can denoise the monitoring image of nighttime very well.

**Keywords** Correlation denoising · Wavelet transform · Traffic monitoring

## 1 Introduction

In the current traffic image monitoring there are many problems, including the image monitoring and processing capacity of the lack of increasingly prominent. Wavelet transform is becoming more and more important in image processing. Its effect is superior to Fourier transform. It is mainly due to the decomposition effect of wavelet in time and frequency domain. It can decompose the signal into wavelet signal and analyze it one by one [1].

The research focus of this paper is mainly based on the wavelet transform of the correlation image denoising algorithm in traffic monitoring application and research, through wavelet transform the image data of the monitoring, and then correlation denoising, to achieve the purpose of noise removal [2]. There are three main classes in the method of wavelet denoising, including modulus maxima denoising, threshold denoising and correlation denoising. Among them, the modulus maxima denoising algorithm is less used, because the algorithm is more complicated. In this paper, we improve the correlation denoising method and

---

L. Yang (✉) · F. Xue · H. h. Wang · H. w. Cheng  
An Hui San Lian University, Hefei 230601, China  
e-mail: 739849206@qq.com

compare the adaptive threshold denoising algorithm [3]. Observe the superiority of both algorithm and the actual use of the effect.

## 2 Correlation Denoising Algorithm Based on Haar Wavelet Transform

The typical orthogonal wavelet—Haar wavelet, Haar basic wavelet function is defined in the interval [0,1].

The formula is:

$$h(t) = \begin{cases} 1 & 0 \leq t < \frac{1}{2} \\ -1 & \frac{1}{2} < t \leq 1 \\ 0 & \text{other} \end{cases} \tag{1}$$

The time domain and frequency domain of Haar wavelet are shown as Figs. 1 and 2.

Fig. 1 Time domain

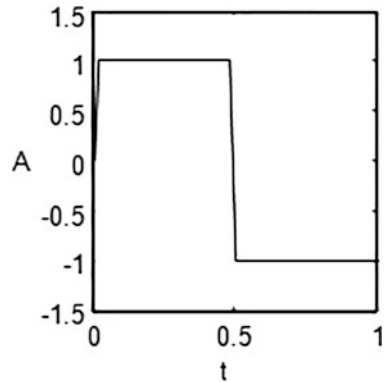
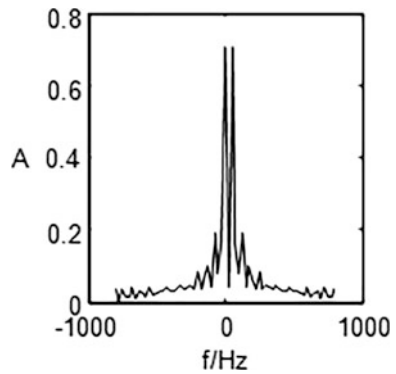


Fig. 2 Frequency domain



There is a strong correlation between the upper and lower layers of the wavelet coefficients of the signal, and the noise does not have such a correlation, which makes it possible to use correlation denoising when performing image denoising [4].

Discrete signal:

$$f(n) = x(n) + s(n), \quad n = 0, 1, \dots, N - 1, s(n) \in N(0, \sigma^2) \tag{2}$$

$f(n)$  is transformed by wavelet:

$$Wf(j, k) = 2^{-j/2} \sum_{n=0}^{N-1} f(n) \varphi(2^{-j}n - k) \tag{3}$$

In the formula  $Wf(j, k)$  is a wavelet coefficient, Referred to as  $W_{j,k}$ .

The linear properties of the wavelet transform can be known,  $W_{j,k}$  is made up of two aspects, One aspect is the  $x(n)$  corresponding coefficient  $u_{jk}$ ; The second aspect is  $s(n)$  corresponding coefficient  $v_{jk}$ .

The formula for the correlation coefficient is:

$$CW_{j,k} = W_{j,k}W_{j+1,k} \tag{4}$$

The correlation coefficient of the wavelet coefficients at this scale of  $j$  is  $CW_{j,k}$ , also the correlation coefficient.

Then how to correlate the correlation coefficient to help determine whether the correlation of the adjacent coefficients is strongly correlated or weakly correlated, but also integrated the correlation coefficient;

$$\overline{W_{j,k}} = CW_{j,k} \sqrt{\frac{PW_j}{PCW_j}} \tag{5}$$

$\overline{W_{j,k}}$  is the normalized correlation. Where  $PW_j$  represents the energy of the  $j$ th layer coefficient and  $PCW_j$  represents the correlation coefficient energy at the  $j$ -scale.

$$PCW_j = \sum_k CW_{j,k}^2, \quad PW_j = \sum_k W_{j,k}^2 \tag{6}$$

The correlation denoising principle is to compare the normalized correlation coefficients for each location and determine the point of the signal or the noise control from the correlation size [5].

The specific steps are:

1. Given the number of decomposition layers,  $M$ , select the wavelet function, calculate the wavelet coefficients ( $W_{j,k}$ ) of each layer with noise signal;
2. Compare  $\overline{W_{j,k}}$  and  $W_{j,k}$ , and judge:

If  $\overline{W_{j,k}} \geq W_{j,k}$ , it is considered that the large correlation quantity corresponds to the characteristic of the signal, let  $\overline{W_{j,k}} = W_{j,k}$ , set  $W_{j,k} = 0$ ;

If  $\overline{W_{j,k}} \leq W_{j,k}$ , it is assumed that the wavelet coefficients at point  $k$  are controlled by noise, leaving  $W_{j,k}$ , and set  $\overline{W_{j,k}} = 0$ ;

3. Recalculate  $\overline{W_{j,k}}$  on each scale;
4. Repeat the above procedure;
5. Each of the  $\overline{W_{j,k}}$ 's points is controlled by the signal, and the points in the  $W_{j,k}$  all correspond to the noise.

Region correlation coefficient:  $CN_{j,k} = N_{j,k}N_{j+1,k}$  is the regional correlation coefficient at  $k$  on scale  $j$ . And  $N_{j,k} = \sum_{l=k-m}^{k+m} W_{j,l}$ .

The normalized correlation of the region gives  $\overline{N_{j,k}} = CN_{j,k} \sqrt{\frac{PN_j}{PCN_j}}$  as the normalized correlation, and  $PN_j = \sum_k N_{j,k}^2$ ,  $PCN_j = \sum_k CN_{j,k}^2$ .

### 3 Experiments and Results

1. Experimental steps:

- (A) Read the image, divided into three color channels [6];
- (B) Select the wavelet base, "haar" decomposition layer is 2;
- (C) Add noise, select "Gaussian" noise;
- (D) Correlation method denoising, to obtain the denoising results;
- (E) Get the values of PSNR, MSE, NC.

2. Simulation and analysis of results.

In the simulation experiment, the night image of traffic monitoring is used as the simulation image data, and the "haar" wavelet is used as the wavelet base to transform and decompose. As shown in the following Figs. 3, 4, 5 and 6, the image pixels are 2048 \* 1257. Using the correlation denoising method, the original image with noise is denoised and compared with the algorithm of adaptive acquisition threshold, as shown in Figs. 5 and 6.

From Figs. 4, 5 and 6 can be seen: traffic monitoring image processing, the two methods to denoise the image visual effects, have reached the expected results of denoising, visual contrast results are not very obvious.

It can be concluded from Table 1 that the correlation denoising algorithm is compared with the adaptive threshold denoising algorithm, the peak signal to noise

**Fig. 3** Original image**Fig. 4** Noise image**Fig. 5** Threshold de-noising image

ratio is larger, the mean square error value is smaller and the normalization correlation is slightly larger. This three point highlights the superiority of the improved correlation denoising algorithm, but the computation time of the algorithm is longer. This is also due to the complexity of the algorithm itself.

The simulation results show that correlation denoising method can be used to denoise the traffic monitoring image data.

**Fig. 6** Correlation denoising image



**Table 1** Simulation data comparison

Denoising method	PSNR	MSE	NC	Time
Adaptive threshold denoising	66.378	85.149	0.974	9.419
Relevant denoising	72.978	44.023	0.995	19.181

## 4 Summary

In this paper, the correlation denoising algorithm of wavelet transform is used to deal with the image data of night traffic monitoring, and the effect is achieved. For the actual night image to make a certain effort to denoise.

But in the de-noising algorithm in the consumption of more time, the latter should be in-depth study in this area.

### Acknowledgements

Project fund:

1. Natural Science Research Project of Anhui Province. Item Number: KJ2017A522;
2. Anhui Sanlian university research fund. Item Number: Yjt16002;
3. Anhui Sanlian university research fund. Item Number: kjzd2016002;
4. Anhui Sanlian university research fund. Item Number: PTZD2017001;
5. Anhui Sanlian university research fund. Item Number: 14zlgc045;
6. Anhui Sanlian university research fund. Item Number: kzyb2016002.

## References

1. Zhang L, Bao P (2003) Denoising by spatial correlation thresholding. *IEEE Trans Circuits Syst Video Technol* 13(6):535–538
2. Portilla J, Simoncelli EP (2000) Image denoising via adjustment of wavelet coefficient magnitude correlation. In: *Proceedings of international conference on image processing*. IEEE, vol 3, pp 277–280
3. Zhan DQ, Sun SQ, Zhou Q et al (2004) Wavelet denoising and optimization of two-dimensional correlation IR spectroscopy. *Spectrosc Spectral Anal* 24(12):1549

4. Portilla J, Strela V, Wainwright MJ et al (2003) Image denoising using scale mixtures of Gaussians in the wavelet domain. *IEEE Trans Image Process Publ IEEE Sig Process Soc* 12 (11):1338
5. Sardy S (2000) Minimax threshold for denoising complex signals with waveshrink. *IEEE Trans Sig Process* 48(4):1023–1028
6. Buades T, Lou Y, Morel JM et al (2015) A note on multi-image denoising. In: *International workshop on local and non-local approximation in image processing*. IEEE, pp 1–15



# Distributed Simulation Modeling and System Construction for the Networked Operation of Urban Railway System

Jiaping Feng, Xi Jiang, Feifan Jia and Chi Zhang

**Abstract** Facing the situation of the large-scale network, we conducted the research and construction on simulation and system modeling towards the problem of how to economically and efficiently conduct the operation and simulation of urban rail transit network. We built a core simulation model mainly formed of topology infrastructure model of the network, simulation model for the process of train operation and the simulation model for the process of passengers' travel in order to meet the need of the train operation and passengers' travel. Having constructed the distributed simulation structure for the networked operation based on fixed distributed strategy, we proposed a simulation clock coordination mechanism based on key synchronous events, and developed a distributed simulation system for the networked operation of urban rail transit system. Taking the congestion situation for the passenger flow of Beijing's subway and the confirmation for the passenger flow limitation scheme of the network coordination as the backgrounds, two conducted the applied research on the distributed simulation system for the operation of urban rail transit system.

**Keywords** Urban railway system · Distributed simulation · Congestion of the passenger flow · Passenger flow limitation scheme

## 1 Instruction

In recent years, the network operation of urban rail transit in China has become the main feature. The network operation mode provides more convenient transportation service for passengers, at the same time, it also increases the difficulty of urban rail transit operation decision. Computer simulation technology, because of its advantages in solving complex problems, began to be used more often in urban rail transit

---

J. Feng · X. Jiang (✉) · F. Jia · C. Zhang  
State Key Lab of Rail Traffic Control and Safety, School of Traffic  
and Transportation, Beijing Jiaotong University, Beijing, China  
e-mail: xjiang@bjtu.edu.cn

system analysis and operational decision-making. For example, through simulation station passenger behavior analysis to evaluate subway station operation states [1–3], in the station passenger simulation modeling method, some research results [4–6]. There are some mature pedestrian micro simulation software, such as MicroPedSim, SimPed, Nomad, Legion, STEPS, Anylogic, VISSIM [7, 8], and train operation simulation software such as RAILS, TrainSTAR, UTRAS, OpenTrack, Railsys [9–11]. At the network level, the simulation modeling study of train flow, passenger flow and their dynamic interaction has just started in the literature [12], the author studies the multi-granularity simulation modeling method of urban rail transit network under the stand-alone operation environment for the goal of network planning.

However, the operation simulation of urban rail transit network faces the problem of complex system and huge simulation scale. In the case of available simulation resources and single machine computing capacity constraints, using distributed technology to build simulation system becomes an effective way to realize the whole network operation simulation efficiently and economically. But in the field of urban rail transit simulation, there are few reports on the distribution simulation of large-scale network operation. This paper focuses on the construction of simulation model, simulation system and the application of simulation system for the construction of network operation simulation system under distributed environment.

## 2 Distributed Simulation Architecture

In order to build a distributed simulation system, the simulation architecture of the system should be established firstly, which depends on the choice of the distribution mode of the system nucleus simulation model. In general, large-scale distributed simulation systems are mainly divided into two main types: function-based distribution and region-based distribution. In the conditions of network operation, urban rail transit system is composed by multiple subsystems, including road network infrastructure, trains, passengers and transportation organizations, etc. Each subsystem is relatively independent and interact, therefore, function-based distribution is preferred. In addition, the urban rail transit system can be divided into several station subsystems connected by the metro line in space, thus a distributed system can be built naturally using region-based distribution. Therefore, in this paper, a hybrid distribution strategy is adopted to realize the distributed simulation system of urban rail transit network operation, so as to realize the expansion of simulation function and scale.

In this paper, a distributed architecture of urban rail transit network operation simulation system based on hybrid distribution strategy is constructed. At the top of the simulation system, the function-based distribution method can be used to divide the system running online into the subway system simulation, train operation simulation, simulation data processing and index calculation, simulation process

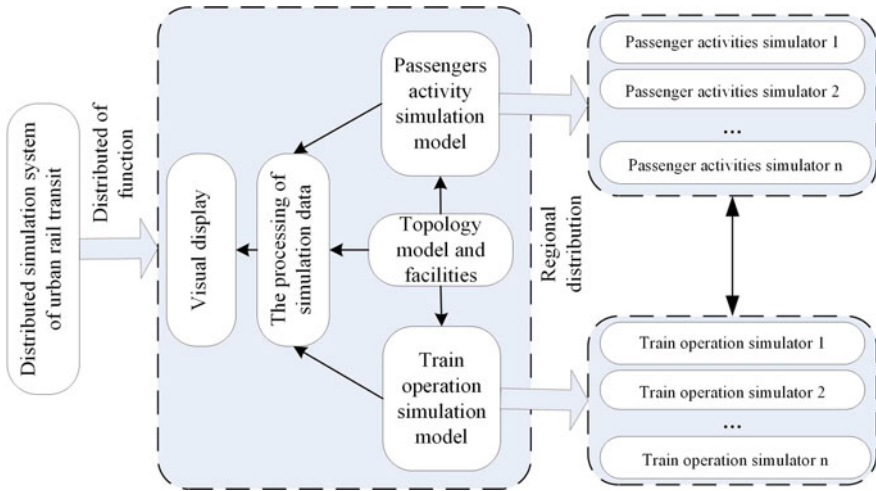


**Fig. 1** A distributed simulation framework based on hybrid distribution strategy

and result display. Further, the system can be divided into second layers based on region-based distribution according to the system size and computing power. Among them, based on the location of the passengers, passenger activities of some stations with large computational complexity are distributed by the simulation of passenger movement in road network to a number of station passenger simulators. The train operation can be directly distributed to a number of nodes according to the route, which is focused on a number of lines, as shown in Fig. 1.

### 3 Simulation Modeling

#### 3.1 Topology Model

The urban rail transit network model is a general description of the road network topology, and the construction of the urban rail transit network topology model can be divided into the following way.

1. Consisting of node and arc, which represents the station and the section;
2. Consisting of node and arc, which represents the intersection of arcs and the transfer between stations;
3. Net topology of node and arch, which represents the connection direction and interval of transfer station and station room.

These urban rail transit network topology modeling methods are different in network size and sophistication. However, the problem of insufficient description ability is common in the process of supporting passenger travel and train operation

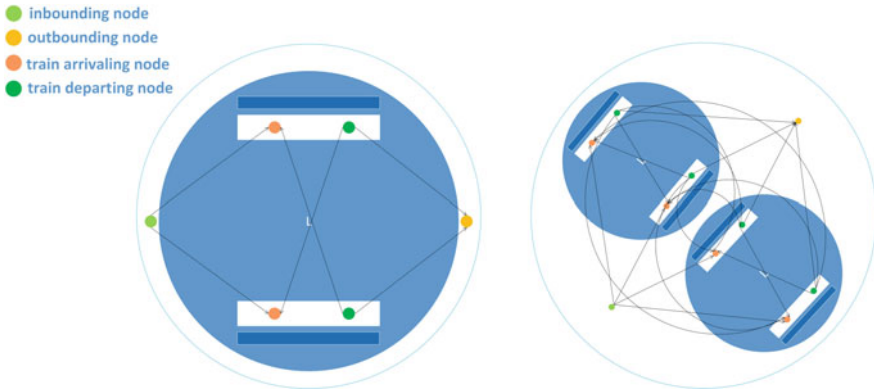


Fig. 2 The urban rail transit network topology model based on multiple nodes and arcs

simulation. In order to describe the spatial relationship between train activities and passenger activities accurately and efficiently, this paper builds a network model composed of multi-class nodes and arcs, which provided a unified network topology description for train operation and passenger activity simulation as shown in Fig. 2. The nodes include the inbound point, the outbound point, the train arriving point, the train departing point, the arcs include the inbound arc, the outbound arc, the stop arc, the line transfer arc, the adjacent line transfer arc, the section running arc.

In the distributed conditions, with the positive line access, access point as a demarcation point, the entire network can be divided into multiple subnet stop support for distributed simulation, as shown in Fig. 2.

### 3.2 System State Deduction Model

In the simulation system, the trains and passengers are the dominant entities that determine the state of system. In the respective life cycle, the train and passengers perform a series of activities in accordance with certain rules of behavior and interact with other entities, thus forming a state change of the system. Urban rail network operation decision-making is concerned about the dynamic changes in the activities of the train during the operation and passenger travel, such as train getting in and out of the section, passing in and out station, stopping, turning-back, train running in section and other activities, as well as passengers arriving at the station, waiting, transferring, boarding on the train and so on, but ignoring the precise position, speed, acceleration, etc. of a train or passenger at a given moment.

Thus, in this paper, each train operation and passenger travel process on the road network is considered as a series of activity sequences determined by train timetable, train routing, passenger od and path, station streamline and other factors, so

**Table 1** Train and passenger activity sheet

Attribute	Meaning	Value
Type	Type of train or passenger activity	Train :{Running,Dwelling,TurnAround,Storage,maintenance} Passenger :{EnterSta,ExitSta,WaitingTrain,TravelOnTrain,Transfer}
Place	The node or arc occupied by the activity	$Nodej \in odejode, Arkj \in NetArk$
StartTime	The beginning of the activity	$initial\ time < = StartTime < = end\ time$
SetupTime	Prepare the time before the activity begin	$0 < = StartTime < = Simulation\ run\ time$
DurTime	The amount of time the activity need	$0 < = DurTime < = Simulation\ run\ time$
State	Active status	{Pending, Doing, Done}
PreOperation	Proactive activities of this activity	$Pr\ eOperation \in O, begin\ of\ activity\ is\ \phi$
Nextoperation	Follow-up to this activity	$Nextoperation \in on \in O, of\ activity\ is\ \phi$

the train operation process and the passenger travel process can be described as sequence  $O = \langle O1, O2, \dots On \rangle$ , and the  $O_i, i \in N$  is the active link, which is an activity of a train or passenger in an interval or station, these activities can be expressed in eight tuples, {Type, Place, StartTime, SetupTime, DurTime, State, preOperation, NextOperation}, and the attributes describing train and passenger activity are shown in Table 1.

According to train basic operation chart or operation adjustment diagram, with the simulation clock advance, the trains carry out each activity in sequence, such as getting on line, getting off line, setting up operation, executing operation and so on. It provides the necessary conditions for passengers to get on and get off the train, as shown in Fig. 3.

Passengers are generated according to the travel time and place rules in the network (arrive state), to achieve the state transfer model of the passengers travel, including getting into the station, walking in station arc, waiting train on platform and so on, and the passengers state transfer model as shown in Fig. 4.

## 4 Coordination of Distributed Simulation Clock

### 4.1 The Simulation Clock Coordination Mechanism Based on Key Events

Because of distributed simulation system components of the computing nodes running on computer network, a certain simulation clock propulsion mechanism is

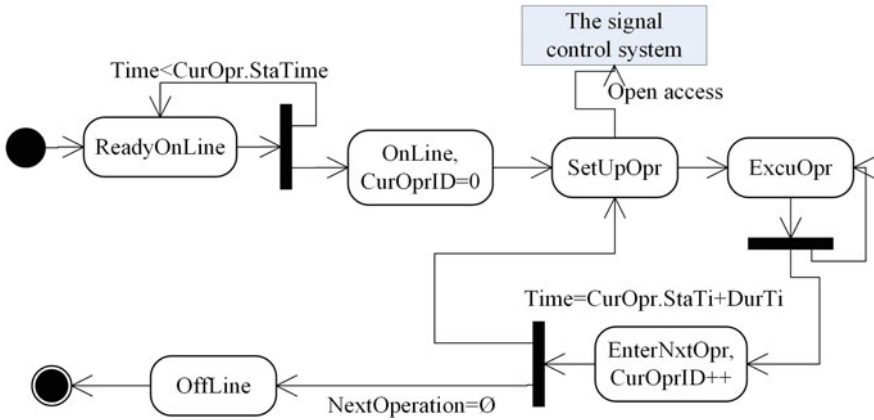


Fig. 3 The state transfer model in the process of train running

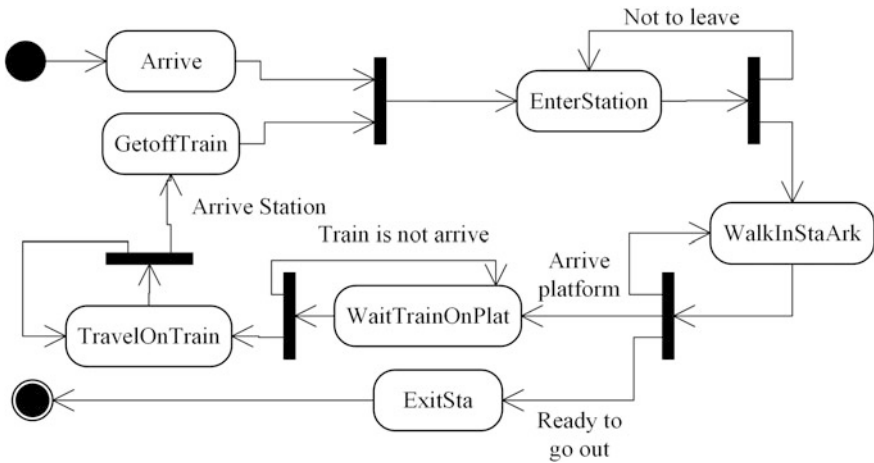


Fig. 4 The state transfer model of the passengers travel

needed to maintain the temporal and spatial consistency of the system. The classic clock propulsion mode has two basic types: time step and event step, the former easily keeps the ratio between the simulation clock and the actual clock, which is more suitable for visual display and human-computer interaction; the latter has higher simulation operation efficiency and less simulation error. According to the above system distribution strategy, the urban rail transit network operation simulation system can be distributed as a number of line train running simulator and station simulator, together with passenger activity simulator, simulation operation process and dynamic display of multiple subsystems, these distributed simulation subsystems have different requirements for clock advance.

1. The train operation process is closely related to the signal system, and the simulation error control requirements are strict, therefore, the line train operation simulator is appropriate to advance the clock in accordance with the event step.
2. Each station simulator needs to deal with a large number of individual activities with independent behavior and its dynamic relationship with the facilities, most time steps are adopted to advance the clock, and select the step size is shorter to maintain high simulation accuracy.
3. According to the event step method to deal with higher accuracy, passenger activity simulator need to consider both the station passenger activities and train activities and follow the time of the train arrived, leaving the station.
4. From the perspective of visual display, the simulation operation process and the result dynamic display subsystem are suitable for the time step method. To show the effect is more smooth and realistic, the simulation step should be as small as possible.

It can be seen that the time step and the event step may exist in the system at the same time, and the simulation subsystem using the time step method may adopt the step interval of length, so the simulation clock needs to meet the hybrid clock in advance. The hybrid clock propulsion facilitates the simulation model and increases the difficulty of the coordinated operation of the distributed simulation system.

Classic simulation clock synchronization is divided into conservative strategy and optimistic strategy. In view of these two strategies, some mature synchronization algorithms have been formed. In this paper, based on the conservative strategy, combined with the distribution policy of urban rail transit network operation simulation system, and the characteristics of information interaction between simulation models, we designed a coordination mechanism based on the key events of master-slave simulation clock, in a simple way to achieve efficient clock synchronization.

In the simulation system of urban rail transit network, each distributed simulation node does not need to be kept in sync with other nodes in specific situations. As the train is running in accordance with the timetable, at the same time, the train attendant and leave decision to change the passengers on the platform, so the event of the train arriving and departure has become the key process of contact different simulators propulsion system. The events of train arriving and departure occurred, not only is one of the basis of train operation simulation subsystem clock forward, is also the reference time of the whole system simulation to synchronize, known as the key synchronization event in the system.

In that case, this paper proposes a simulation based clock coordination mechanism based on critical events, analysis of the situation and timing need to be synchronized, extract events that trigger synchronization for critical synchronization events, and to produce the event simulation node as the leading, to achieve the coordination of the simulation logic clock. According to the logical control relationship among the core simulation objects of each subsystem in the simulation system, the simulation subsystem is divided into three types, and the simulation clock is promoted by the clock coordination mechanism.

1. Leader emulator, including the train running simulator of each line, which generates key synchronization events in the system. When the leader emulator performs a critical synchronization event, the system initiates a synchronization process.
2. Semi-dominant simulator, including the passenger activities simulator of the station, the simulation clock is not only independent but also controlled by critical synchronization events. During a synchronization process, the logical clock will be calibrated with the time of the key synchronization event.
3. Following simulator, it mainly refers to the dynamic display subsystem and the simulation index analysis subsystem, the simulation time is definitely followed by the provider of dynamic simulation data, which cannot influence the simulation time of the system.

## ***4.2 The Implementation of the Simulation Clock Coordination***

According to the coordination mechanism, the key of the clock coordination is to set the clock coordinator to be centered by the Synchronization Event Manager, the primary function is to build and maintain critical synchronization event pools, and manages the future synchronization event information generated by the pilot simulator, and sent update message to the other emulators in sync. When the leader simulator is going to perform a critical synchronization event, the coordinator sends a synchronization message to the other emulators and sends a synchronized feedback message by semi-pilot simulator to the master emulator to indicate that the synchronization is complete.

The clock coordinator's workflow is as follows:

1. Receive the Generate Synchronization Event message sent by each leader emulator.
2. Updates events in critical synchronization event pools based on received messages.
3. According to the scope of the synchronization event, generate a "synchronous event update" message and sent to the corresponding semi-master emulator and following emulator.
4. When receiving the leader simulator "starting a synchronous" message, according to the scope of synchronous event, produce "synchronous message", and sent it to the corresponding Semi-dominant simulator.
5. When a semi-dominant simulator associated with a synchronization event sends a "sync confirmation" message, it returns a "synchronization completion" message to the corresponding master emulator.



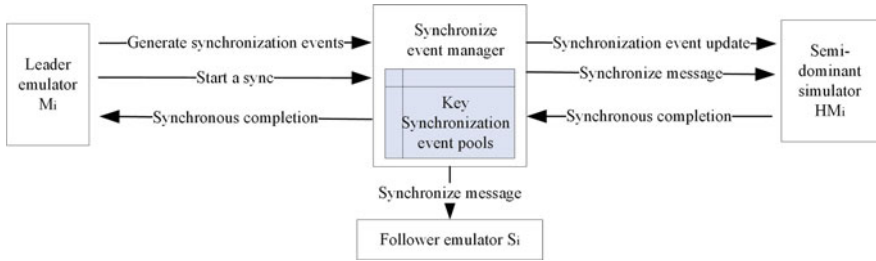


Fig. 5 The simulation clock information interaction in the process of coordination

In the urban rail transit network operation simulation system, the main information exchange related to the clock coordination of the simulation system is shown in Fig. 5.

The  $i$ th initiator emulator  $M_i$  in the system has its logical clock  $LV_i$  value at the current time  $t$ . Before the end of the simulation, follow the steps and rules to advance the clock:

1. The simulator  $M_i$  simulates at  $LV_i$  and predicts the future event sequence  $FEventList$ .
2. Extracts a key synchronization event in the  $FEventList$ , forms the data packet, sends the “Generate Synchronization Event” message to the clock synchronization mechanism.
3. Scan  $FEventList$ , get the next event  $MEvent$ .
4. If  $MEvent$  is a non-critical synchronization event, then convert  $LV_i$  to the time of occurrence of  $MEvent$ . Go to step 1.
5. Otherwise send the start a synchronization message, enter the synchronization operation, and then block it.
6. It will be activated if the “synchronization completion” message from the clock coordinating unit is received, then convert  $LV_i$  to the time of occurrence of  $sMEvent$ . Go to step 1.

The  $i$ th semi-dominant simulator  $HM_i$  in the system uses the time step method. Assuming that the step size is  $\Delta T_i$ , the value of the logical clock  $LV_i$  is the current time  $t$ . Before the end of the simulation, follow the steps and rules to proceed the clock:

1. Simulator  $HM_i$  is operated in the  $LV_i$  moment.
2. Receiving the “synchronization event update” message from the clock synchronization mechanism, updating its synchronization event sequence, and rescan the nearest critical synchronization event at the extraction point, setting the time as  $T$ .

3. If  $LV_i + \Delta T_j < T$ , then, proceed  $LV_i$  to  $LV_i + \Delta$ .
4. Otherwise, the emulator  $HMi$  is blocked to wait for the synchronization message.
5. When a synchronization message is received, the  $LV_i$  is proceed to  $T$  and the synchronization confirmation message for the  $MCEvent$  is sent by the emulator. Go to step 1.

In the system, the  $i$ th follower simulator  $S_i$  is driven with time stamped simulation data, and the simulation data containing the timestamp is continuously received to form the simulation data list *SimuDataList*. Set the logic simulation clock  $LV_i$  initial value of  $t_0$ , when receiving the synchronization message, and then set the logic simulation clock  $LV_i$ . The clock advance rules are as follows:

1.  $LV_i = t_0$ .
2. When the synchronization message is received, extracted the occurrence time  $T$  of the key synchronization event in the message.
3. Take out all the simulation data in the  $[LV_i, T]$  of the *SimuDataList*. Let  $n$  be the number of data, and sort it by timestamp. Then, read the timestamp  $T_j (0 < j < n)$  in the simulation data, and convert  $s LV_i$  to  $T_i$ .
4. After looping for  $n$  times, go to step 2.

## 5 Simulation Case

Based on the distributed simulation method proposed in this paper, the distributed simulation system of urban rail transit network operation is developed in C# development environment, and the urban rail transit system of Beijing is taken as an example. The system is deployed to six computers on the network for distributed operate. One of the computers running simulation process dynamic display subsystem, simulation index calculation and display subsystem, simulation experiment management and operation control subsystem. 3 computers running station passenger activity simulation subsystem. One of the three computers running train running simulation subsystem, One of the three computers running road network passenger simulation subsystem and simulation data acquisition and distribution subsystem. Despite the two subsystems with interactive functions, the other subsystems run on the background server. The running interface of dynamic display subsystem of simulation running process is shown in Fig. 6.

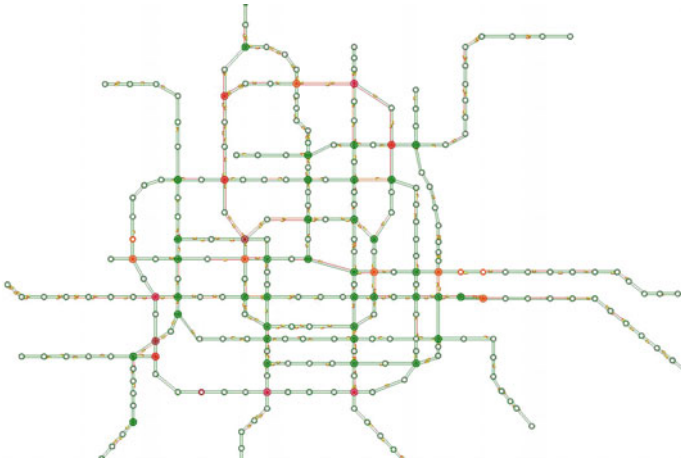


**Fig. 6** Running interface—visualization of the running process

## 6 Conclusion

With the rapid development of urban rail transit and the trend of network operation, this paper studied the network operation simulation model and system construction of urban rail transit from the following aspects.

1. The structure of the core simulation model was studied, the network topology and facility model, the train operation process simulation model and the passenger travel process simulation model are constructed, and the system state simulation deduction of train flow and passenger flow coordination was realized.
2. The distributed architecture of urban rail transit network operation simulation system based on hybrid distribution strategy is studied, and the efficient clock synchronization was realized by using the simulation clock coordination mechanism based on key synchronization events.
3. On the basis of the simulation model and distributed simulation method, the urban rail transit network operation simulation system is constructed.

**Acknowledgements** The authors gratefully acknowledge the support provided by the national key research project “Safety assurance technology of urban rail system” (Grant No. 2016YFB1200402) in China.

## References

1. Song W (2011) Simulation of subway station emergency evaluation. Southwest Jiaotong University, Chengdu (in Chinese)
2. Li D (2007) Modeling and simulation of microscopic pedestrian flow in MTR hubs. Beijing Jiaotong University, Beijing (in Chinese)
3. Hoogendoorn SP (2003) Microscopic simulation of pedestrian flows [DB/CD]. Transportation Research Board, USA
4. Victor J, Blue JLA (2001) Cellular automata microsimulation of bi-directional pedestrian flows. *Transp Res Part B: Methodol* 3:293–312
5. Antonini G, Bierlaire M, Weber M (2006) Discrete choice models of pedestrian walking behavior. *Transp Res Part B* 40:667–687
6. Hoogendoorn SP, Bovy PHL (2004) Pedestrian route-choice and activity scheduling theory and models. *Transp Res Part B* 38:169–190
7. Dong H, Rui Z (2008) Movement vs. behavioral models in pedestrian micro-simulation: a comparison between STEPS and NOMAD. *Urban Transp China* 6(6):33–40 (in Chinese)
8. Qixin HMS (2009) Comparative study of pedestrian simulation model and related software. *J Transp Inf Saf* 4(27):122–127 (in Chinese)
9. Gui X (2008) Research and development of urban rail transit traction calculation system. Beijing Jiaotong University, Beijing (in Chinese)
10. Yalçınkaya Ö, Bayhan GM (2009) Modelling and optimization of average travel time for a metro line by simulation and response surface methodology. *Eur J Oper Res* 196:225–233
11. Yang Z, Mao B, Ho T (2002) Situation and development of railway transportation system simulators. *J Northern Jiaotong Univ* 26(5):1–8 (in Chinese)
12. Jiang X, Miao J, Liu J (2014), Multi-resolution modeling and simulation for urban rail transit network planning and analysis. *J Railway Eng Soc* 31(192):115–120 (in Chinese)

# Automatic Train Control with Actuator Saturation Using Contraction Theory

Yue Li

**Abstract** Application of contraction theory provides a platform to analyze the exponential stability of nonlinear system. To effectively compensate the time-varying parametric uncertainties exist in the longitudinal dynamics of the train, this paper proposes a contraction based saturated adaptive robust control for automatic train operation, which is subject to input limit of actuator. With consideration of actuator saturation, a recently developed robust modification is used to saturate the control input in each step, while the global stability is preserved. The resulting saturated adaptive robust control renders the transformed error enter the predefined region, furthermore, inside the predefined region, the contracting behaviour of closed-loop dynamics is regained and the tracking error exponentially converges to a residual set subsequently. The results of comparative experiments under different control strategies also verify the effectiveness of the proposed saturated adaptive robust control.

**Keywords** Automatic train operation Actuator saturation Contraction theory Adaptive robust control

## 1 Introduction

Railway transportation has been widely constructed and utilized all over the world, especially the high-speed railway in recent decades. To meet the high safety and efficiency requirements of high-speed train, the automaticity in train control is continuously raising. As an essential part of automatic train control (ATC), automatic train operation (ATO) is an on-board equipment whose main function is speed regulation to render the train tracking with the desired trajectory [1].

The desired trajectory is generated by certain optimal algorithm in accordance with prescribed operating criteria, which mainly includes safety, ride-comfort,

---

Y. Li (✉)  
Beijing, China  
e-mail: liyue\_cto@boe.com.cn

timetable, energy-efficiency, etc. The discussion of optimal algorithm can be found in [2–4], and this paper focus on improving the tracking performance of ATO. As travelling speed increases, the effect caused by the inherent time-varying uncertainties in the longitudinal dynamics of the train keeps growing, so excellent tracking performance is not easy to achieve. There are much research had been done to reduce the dependence on inaccurate modeling process, including [5–9].

In this paper, based on the treatment of actuator saturation is motivated by [11], we further improved in [10], where the actual state is replaced by desired velocity in both model compensation and parameter adaptation. The overall saturated adaptive robust control is designed to preserve the contracting behaviour of closed-loop dynamics during normal working range while guarantee global stability for large magnitude of modeling uncertainties.

## 2 Saturated Adaptive Robust Control

With consideration of actuator saturation, the control law should to be synthesized to satisfy input constraint. By using the same structure of contraction adaptive control developed in [10], the saturated adaptive robust control is developed as follows.

Step 1.

By considering the saturation problem, the control law  $\alpha_1$  is re-designed as

$$\begin{cases} \alpha_1 = \alpha_{1a} + \alpha_{1s} \\ \alpha_{1a} = \dot{x}_d \\ \alpha_{1s} = -\sigma_1(z_1) \end{cases} \tag{1}$$

where  $\sigma_1(z_1)$  is a smooth saturation function with respect to  $z_1$ , and it is designed to have the following properties:

- (i)  $|\sigma_1(z_1)| = M_1$ , if  $|z_1| \geq L_{12}$ ;
- (ii)  $z_1 \sigma_1(z_1) > 0$ , for all  $z_1 \neq 0$ ;
- (iii)  $\begin{cases} \frac{\partial \sigma_1}{\partial z_1}(z_1) = \iota_1, & \text{if } |z_1| < L_{11}, \\ \frac{\partial \sigma_1}{\partial z_1}(z_1) \leq \iota_1, & \text{if } L_{11} \leq |z_1| < L_{12}, \\ \frac{\partial \sigma_1}{\partial z_1}(z_1) = 0, & \text{if } |z_1| \geq L_{12}. \end{cases}$

Since  $\alpha_{1a}$  is bounded, the overall  $\alpha_1$  can be bounded. By applying Eq. (1), we obtain

$$\dot{z}_1 = -\sigma_1(z_1) + z_2, \tag{2}$$

$$\dot{z}_2 = \frac{1}{m}u - \theta^T \phi - \ddot{x}_d + \frac{\partial \sigma_1}{\partial z_1}(-\sigma_1 + z_2), \tag{3}$$

In *Step 1*,  $\iota_1, L_{11}, L_{12}, M_1$ , are controller parameters.

Step 2.

For the control law given by [11], both  $u_a$  and  $u_s$  should to be bounded to satisfy the actual input constraints. Due to the difference introduced by  $\sigma_1$ , we re-expressed Eq. (3) as

$$3. \quad \dot{z}_2 = \frac{1}{m} \left[ u_a - \theta^T \phi - m \left( \ddot{x}_d + \frac{\partial \sigma_1}{\partial z_1} \sigma_1 \right) \right] + \frac{\partial \sigma_1}{\partial z_1} z_2 + \frac{1}{m} u_s. \quad (4)$$

Intuitively,  $u_a$  should to be designed to cancel the model dynamics  $-\hat{\theta}^T \phi - \hat{m} \left( \ddot{x}_d + \frac{\partial \sigma_1}{\partial z_1} \sigma_1 \right)$ , however, since  $\phi(x)$  depends on  $x_2$ , it is impossible to put a bound on  $u_a$ . Motivated by [11], we re-formulate the regressor as a function of the desired trajectory only and re-design  $u_a$  as

$$u_a = \hat{\theta}^T \phi_d + \hat{m} \left( \ddot{x}_d + \frac{\partial \sigma_1}{\partial z_1} \sigma_1 \right), \quad (5)$$

where  $\phi_d = \phi(\dot{x}_d) = [1, \dot{x}_d, \dot{x}_d^2]^T$ . Automatically, the adaptive law is modified as

$$\begin{cases} \dot{\hat{\theta}} = \text{Pr}[-\Gamma \phi_d z_2], \\ \dot{\hat{m}} = \text{Pr}[-\gamma \left( \ddot{x}_d + \frac{\partial \sigma_1}{\partial z_1} \sigma_1 \right) z_2], \end{cases} \quad (6)$$

where  $\Gamma = \Gamma^T > 0$ ,  $\gamma > 0$  are adaptive gain. Due to the property of  $\text{Pr}(\bullet)$ , the lower bound  $\underline{u}_a$  and upper bound  $\bar{u}_a$  of  $u_a$  can be easily determined. Furthermore, the desired compensation control Eqs. (5) and (6) also enhance the capacity of noise-rejection in implementation, and large adaptation gain can be used to improve train tracking performance, as discussed in [11].

By applying Eq. (5), we obtain

$$\dot{z}_2 = \frac{1}{m} \left[ \hat{\theta}^T \phi_d - \theta^T \phi + \tilde{m} \left( \ddot{x}_d + \frac{\partial \sigma_1}{\partial z_1} \sigma_1 \right) \right] + \frac{\partial \sigma_1}{\partial z_1} z_2 + \frac{1}{m} u_s. \quad (7)$$

Noting that  $\hat{\theta}^T \phi_d - \theta^T \phi$  can be re-written as  $\tilde{\theta}^T \phi_d + \theta^T (\phi_d - \phi)$ . So Eq. (7) can be forward expressed as

$$\dot{z}_2 = \frac{1}{m} \left[ \tilde{\theta}^T \phi_d + \tilde{m} \left( \ddot{x}_d + \frac{\partial \sigma_1}{\partial z_1} \sigma_1 \right) + \theta^T (\phi_d - \phi) \right] + \frac{\partial \sigma_1}{\partial z_1} z_2 + \frac{1}{m} u_s. \quad (8)$$

Equations (1) and (2), we have

$$\begin{aligned} \theta^T (\phi_d - \phi) &= \theta^T [0, \sigma_1 - z_2, (\sigma_1 - z_2)(\dot{x}_d + x_2)]^T \\ &= -[c_b + c_a(\dot{x}_d + x_2)]z_2 + c_a \sigma_1 z_2 + c_b \sigma_1 + c_a \sigma_1 (2\dot{x}_d - \sigma_1). \end{aligned} \quad (9)$$

Substituting Eq. (9) into Eq.(8), we have

$$\begin{aligned} \dot{z}_2 = & \frac{1}{m} \left[ \tilde{\theta}^T \phi_d + \tilde{m} \left( \ddot{x}_d + \frac{\partial \sigma_1}{\partial z_1} \sigma_1 \right) + c_v \sigma_1 + c_a \sigma_1 (2\dot{x}_d - \sigma_1) \right] \\ & - \frac{1}{m} [c_v - c_a \sigma_1 + c_a (\dot{x}_d + x_2)] z_2 + \frac{\partial \sigma_1}{\partial z_1} z_2 + \frac{1}{m} u_s. \end{aligned}$$

Since  $M_1 \geq |\sigma_1|$  can be designed, if we choose  $M_1 \leq (\underline{c}_v / \bar{c}_a)$ , then the term  $-c_a \sigma_1$  can be dominated by  $c_v$ , i.e.,  $c_v - c_a \sigma_1 \geq 0$ . Letting  $\varepsilon_2 \triangleq c_v - c_a \sigma_1 + c_a (\dot{x}_d + x_2)$ , because parameter  $c_a$ , and desired and actual train speed  $\dot{x}_d, x_2$  are all positive-definite,  $\varepsilon_2$  is positive-definite. Then, the derivative  $\dot{z}_2$  can be forward expressed as

$$\begin{aligned} \dot{z}_2 = & \frac{1}{m} \left[ \tilde{\theta}^T \phi_d + \tilde{m} \left( \ddot{x}_d + \frac{\partial \sigma_1}{\partial z_1} \sigma_1 \right) + c_v \sigma_1 + c_a \sigma_1 (2\dot{x}_d - \sigma_1) \right] \\ & - \varepsilon_2 z_2 + \frac{\partial \sigma_1}{\partial z_1} z_2 + \frac{1}{m} u_s. \end{aligned} \tag{10}$$

The residual term  $-\varepsilon_2 z_2$  acts as a damping term to help stabilizing the dynamic  $\dot{z}_2$ , so the robust control  $u_s$  needs to suppress  $\frac{\partial \sigma_1}{\partial z_1} z_2$  and model mismatch to render  $z_2$  converge or at least, bounded. By considering the saturation problem, the robust control is designed as sign

$$u_s = -\sigma_2(z_2), \tag{11}$$

$$-\sigma_2(z_2) = \begin{cases} \iota_2 z_2, & \text{if } |z_2| < L_2 \\ \text{sign}(z_2) M_2 & |z_2| \geq L_2 \end{cases} \tag{12}$$

Noting this is the last step, thus  $\sigma_2(z_2)$  only needs to be continuous. Thus, the overall of the control input is given by

$$\begin{cases} u = u_a + u_s, \\ u_a = \tilde{\theta}^T \phi_d + \tilde{m} \left( \ddot{x}_d + \frac{\partial \sigma_1}{\partial z_1} \sigma_1 \right), \\ u_s = -\sigma_2(z_2). \end{cases} \tag{13}$$

In Step 2,  $\iota_2, L_2, M_2$ , are controller parameters.

**Theorem 1** *If the saturated adaptive robust control Eqs. (13) and (6) is applied to train model, while the selection of design parameters satisfying (a)  $\iota_2 > \bar{m} \iota_1$ , (b)  $\iota_1 L_{11} > L_{22}$ , (c)  $M_1 \leq (\underline{c}_v / \bar{c}_a)$ , (d)  $M_2 > \bar{m} (h + k_1 M_1)$ , (e)  $-\bar{B} - \underline{u}_a \leq M_2 \leq \bar{F} - \bar{u}_a$ , then the following results can be guaranteed:*

- i) The closed-loop system is global stable.
- ii) At steady-state, the location and velocity tracking errors of the train converge to the following residual set



$$\Omega'_d = \left\{ e(t) \in \mathbb{R}^2 \mid |e| \leq \frac{h}{k_2} \right\},$$

where,  $h, k_2$  are positive constants, which will be specified in the proof analysis.

### 3 Comparative Experiments

#### 3.1 System Setup and Implementation

Comparative experiments are constructed in the form of numerical simulation to demonstrate the effectiveness of the proposed saturated adaptive robust control. The train dynamics under study is stemmed from *CRH3* series high-speed trains, which have been operating in *Beijing-Tianjin Intercity Railway* for more than five years, and the nominal values of their primary parameters are listed in Table 1, where,  $\omega$  denotes the running resistance of mass per unit quality,  $\bar{F}$  denotes the traction capacity of actual motors,  $\bar{B}_1$  denotes the capacity limit of regenerating braking,  $\bar{B}_2$  denotes the capacity limit of electropneumatic braking. The force of traction and regenerating braking that train traction motors can supply are correlated with travelling velocity, as shown in paper [11]. The electropneumatic braking is a reserve equipment, which is enabled in the situation of regenerating braking is deficiency (usually in low travelling velocity range), so the total braking force can be calculated from  $\bar{B} = \bar{B}_1 + \bar{B}_2$ .

From design and empirical record, the prior region of train dynamics is defined as

$$\Theta \in [[450, 1, 0.02, 0.0005]^T, [500, 20, 0.2, 0.005]^T].$$

The controller parameters are selected as follows,  $\iota_1 = 0.5$ ,  $L_{11} = 2m$  ( $m$ : denotes distance unit meter),  $L_{12} = 3 \text{ m}$ ,  $M_1 = 1.25$ ,  $\iota_2 = 0.6 \text{ m}$ ,  $L_2 = 0.3 \text{ m/s}$ ,

**Table 1** Parameters of *CRH-300*

Category	Value	Condition	Unit
$m$	475		t
$\omega$	$7.75 + 0.06327v + 0.00128v^2$		N/t
$\bar{F}$	$-0.285v + 300$	$v < 119 \text{ km/h}$	kN
	$\frac{31500}{v}$	$v \geq 119 \text{ km/h}$	
$\bar{B}_1$	$59.8v$	$v < 5 \text{ km/h}$	kN
	$-0.285v + 300$	$5 \text{ km/h} \leq v < 106.7 \text{ km/h}$	
	$\frac{28800}{v}$	$v \geq 106.7 \text{ km/h}$	
$\bar{B}_2$	450		kN

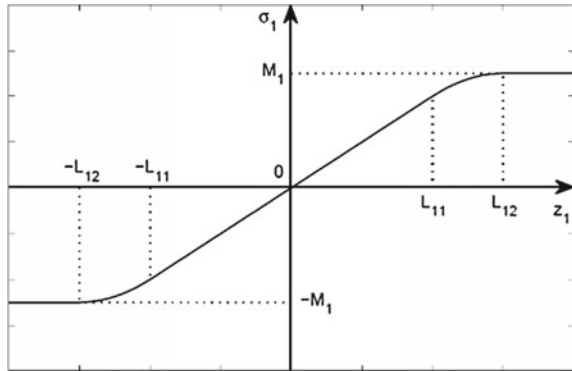
$$M_2 = \begin{cases} \bar{F} - u_a, & \text{if } u > 0 \\ -B - u_a, & \text{if } u < 0 \end{cases}$$

where  $u_a$  can be easily calculated on-line from Eq. (5). It can be verified that these parameters satisfy the selection guidance of Theorem 1. Apparently, the saturation function  $\sigma_1, \sigma_2$  are also determined, as shown in Fig. 1.

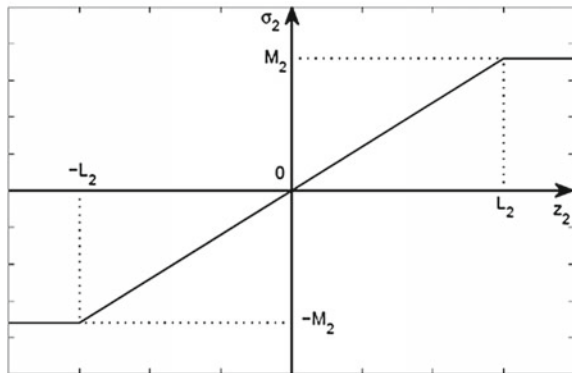
### 3.2 Comparable Results

The experiment is constructed to operate the train travelling through a distance of 28.565 km, and the whole process is design to consist of three typical mode: acceleration, cruising and braking in turn. The desired location and velocity are given in Fig. 2. Some *Gaussian white noises* are added to the nominal values of resistance coefficients to obtain time-varying parameters, and abrupt changes are

**Fig. 1** Saturation function designed for  $z_1, z_2$

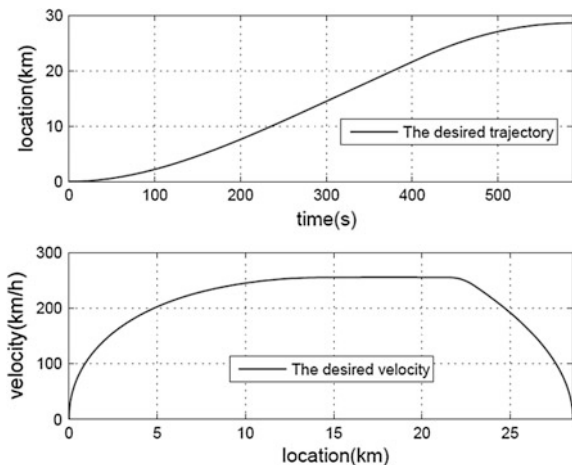


(a) Saturation function  $\sigma_1$



(b) Saturation function  $\sigma_2$

**Fig. 2** Desired location and velocity trajectory

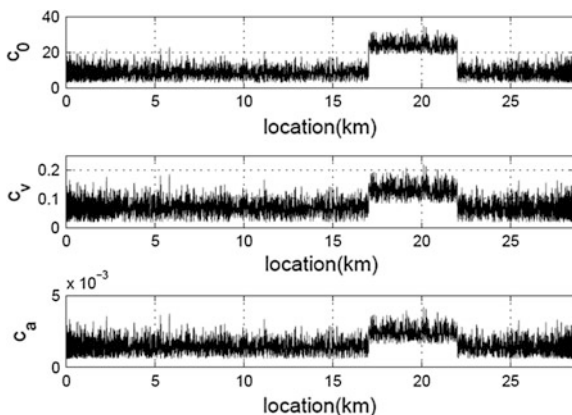


imposed at  $s = 17$  km,  $s = 22$  km to simulate the train travelling through a tunnel, as shown in Fig. 3. To give a comparison, we construct the following two cases:

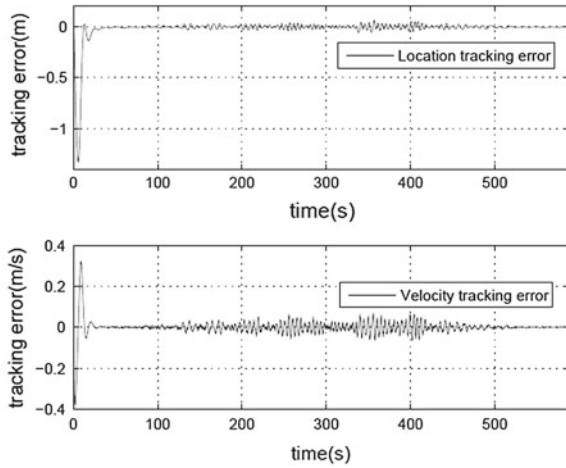
- (i) The contraction adaptive control given in [11] is used, but the input is truncated when the control effort reaches the actuator limit.
- (ii) The saturated adaptive robust control given in Theorem 1 is used.

Both the cases are running with the same configurations. The tracking errors and control input under Case i and Case ii are given in Figs. 4 and 5, and the comparison of transient response and steady-state tracking performance is given in Fig. 6. Under Case (i), the control input is truncated at the place marked by ellipse as shown in Fig. 4b, and the tracking error is enlarged consequently as shown in

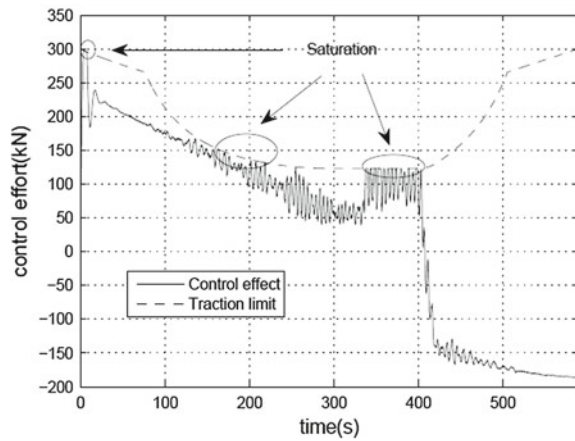
**Fig. 3** Time-varying resistance coefficients



**Fig. 4** Tracking errors and control input under Case (i)



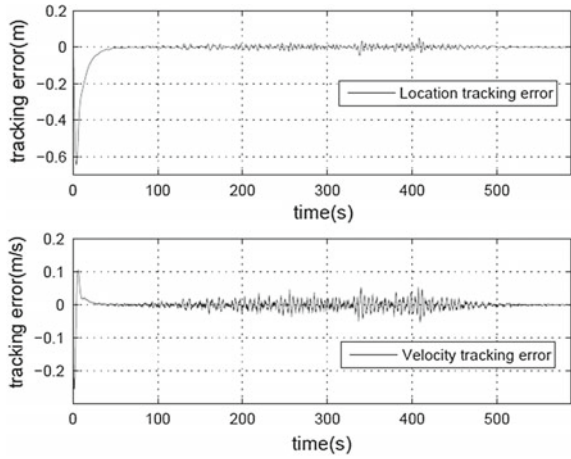
(a) Tracking errors under Case i)



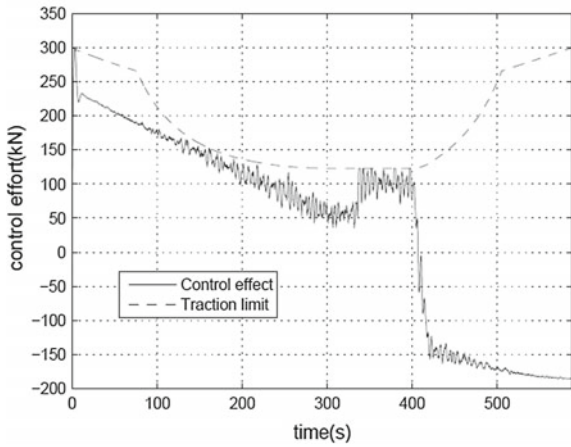
(b) Control input under Case i)

Fig. 6. Under Case (ii), the control input generated by the proposed saturated adaptive robust control are always within the capacity limit of actuator as shown in Fig. 5b, and compensates the model dynamics effectively, so the closed-loop dynamics is working within the normal region  $\Omega_C$  for almost all the time as shown in Fig. 5a, and superior transient and steady-state tracking performance is achieved as shown in Fig. 6.

**Fig. 5** Tracking errors and control input under Case (ii)

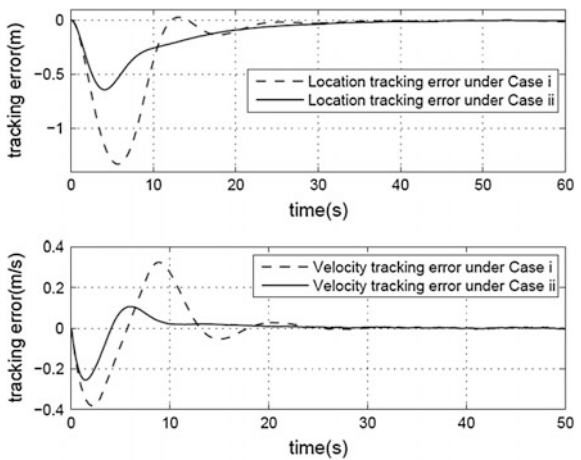


(a) Tracking errors under Case ii)



(b) Control input under Case ii)

**Fig. 6** Transient response comparison



## 4 Conclusion

A Bead on contraction theory, a saturated adaptive robust control strategy is proposed to improve the tracking performance of ATO which is subject to the capacity limit of practical actuator. By using contraction analysis, the selection of Lyapunov-like energy function is not needed, and this dramatically facilitate the controller design of nonlinear systems, furthermore, it provides a platform to analyze the exponential stability of the closed-loop dynamics. With consideration of actuator saturation, a robust modification of saturation is developed, which preserves the global stability of the closed-loop system and renders the transformed output error with any initial state converging to the prescribed normal region. When the transformed error enters the normal region, the contraction behaviour of the closed-loop dynamics is regain, and train tracking errors exponential converge to a residual set subsequently. Comparative experiments under different control strategies are constructed, and the results con.rm the superiority of the proposed saturated adaptive robust control.

## References

1. IEEE Standard for Communications-Based Train Control (CBTC) Performance and Functional Requirements, IEEE Standard 1474.1-2004, 2004
2. Howlett PG, Milroy IP, Pudney PJ (1994) Energy-efficient train control. *Control Eng Pract* 2(2):193–200
3. Howlett PG (2000) The optimal control of a train. *Ann Oper Res* 98(1–4):65–87
4. Khmelnitsky E (2000) On an optimal control problem of train operation. *IEEE Trans Autom Control*, 45(7):1257–1266
5. Yasunobu S, Miyamoto S, Ihara H (2002) A fuzzy control for train automatic stop control. *Trans Soc Instrum Control Eng*, E-2(1):1–9
6. Yang CD, Sun YP (2001) Mixed  $H_2/H_\infty$  cruise controller design for high speed train. *Int J Control* 74(9):905–920
7. Chou M, Xia X (2007) Optimal cruise control of heavy-haul trains equipped with electronically controlled pneumatic brake systmes. *Control Eng Pract* 15(5):511–519
8. Song Qi, Song Yong-duan, Tang Tao, Ning Bin (2011) Computationally inexpensive tracking control of high-speed trains with traction/braking saturation. *IEEE Trans Intell Transp Syst* 12(4):1116–1125
9. Ioannou PA, Sun J (1996) *Robust adaptive control*. Prentice Hall, Englewood Cliffs
10. Hong Y, Yao B (2007) A globally stable saturated desired compensation adaptive robust control for linear motor systems with comparative experiments. *Automatic* 43(10):1840–1848
11. Wang L, Xu H, Luo H (2016) Contraction-based adaptive control for automatic train operation. *Control Intell Syst* 44(1)

# Linear Quadratic Optimal Control of Passenger Flow in Urban Rail Transfer Stations

Huijuan Zhou, Qiang Zhang, Yanwei Feng, Yu Liu  
and Guorong Zheng

**Abstract** In order to solve the problem of overload passenger flowing in urban rail transfer stations at peak hour, this paper proposes a passenger flow control model for transfer stations. To minimize the passenger density on platform, the passenger flow control model is built based on linear quadratic optimal control theory. And the optimal control passenger sequence flowing into platform is calculated during the control periods. Finally, taking Huixinxijienankou Station on lines 5 and 10 in Beijing subway as an example, the station simulation model using Anylogic software is established and used to verify the passenger flow control model. The simulation results show that the control model can reduce the passenger flow effectively on platform at peak hour and provides guidelines for boarding limit.

**Keywords** Urban rail traffic · Passenger flow control · Linear quadratic optimal control · Anylogic simulation

## 1 Introduction

With the contradiction between urban rail transit and passenger capacity demand, the supply imbalance is increasingly prominent. Overload passengers in transfer stations is becoming increasingly serious, which leads to serious threat to the operation safety of urban rail transit. Therefore, it is urgent to establish a passenger flow control method to solve the problem of passenger flow crowded at peak hour in transfer stations.

---

H. Zhou (✉) · Q. Zhang · Y. Liu · G. Zheng  
Beijing Key Lab of Urban Road Transportation Intelligent Control Technology,  
North China University of Technology, No. 5 Jinyuanzhuang Road,  
Shijingshan District, Beijing 100144, People's Republic of China  
e-mail: zhouhuijuan@ncut.edu.cn

Y. Feng  
Hisense Trans Tech Co., Ltd., Qingdao 266071, China

Probing into the passenger flow control of rail transit, recent researches mainly cover three layers including station, rail line and rail network [1]. And there are two kinds of methods about passenger flow control. One kind is to build optimal passenger flow model using mathematical programming methods and acquire the optimal passenger flow to enter station. Zhao Peng built a combined passenger flow control model with linear programming under minimizing the passengers' delay time and maximizing the passenger traffic volume from the aspect of rail line [2], and verified this model by taking Beijing metro line 5. Yao Xiangming built a cooperative passenger flow control model of rail network on condition that the model satisfied the minimum passenger's delay time and the maximum matching between supply and demand [3]. The limit time aimed at rail line and station of Beijing rail network are determined by calculating the control rate of passenger flow. Wang Shuwei built a linear programming model about minimum passenger density inside station and validated it by simulation of Sihui East station [4]. The other kind is based on system dynamics theory. That is, the subway station is considered as a dynamic system and its evolution model of passenger flow is established using system dynamics theory [5, 6]. Xue Fei and Li Man studied the evolution and control of subway station [7].

Above all, the researches about passenger flow control focused on more on mathematical model or system dynamics but less on control theory. Based on linear quadratic optimal control for discrete systems, the paper constructs a passenger flow control model for urban rail transfer stations at peak hour under minimizing passenger flow density on platform. By solving this model, the optimal control sequence for the passenger flow flowing into platform at peak hour.

## 2 Passenger Flow Analysis on Platform

In order to build the model of passenger flow control, the process of aggregating and dispersing passenger flow on platform should be analyzed to determine the sampling period and sampling time. Then all kinds of passengers on platform would be classified during a sampling period for determining the model's control variables and stating variables.

### 2.1 Analysis of Passenger Flow on Platform

In this paper, we only consider the side platform and do not consider island platform in transfer stations. There is an assumption that subway trains run their schedules strictly. The departure interval of two adjacent trains is regarded as a sampling period  $T$ . The relation and trend of train's running and stop and the passenger flow can be described as shown in Fig. 1.

According to the train running state, the sampling period is divided into stop period  $\tau_{sk}$  and interval period  $\tau_{tk}$ , thus  $T = \tau_{sk} + \tau_{tk}$ . The passengers follow the



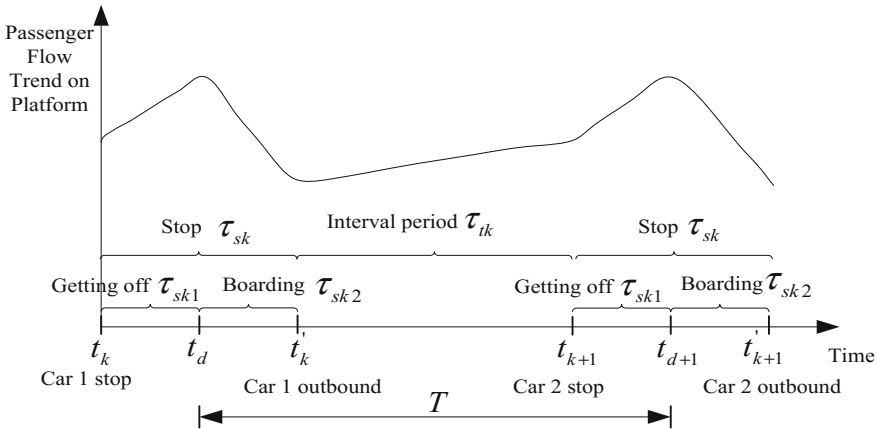
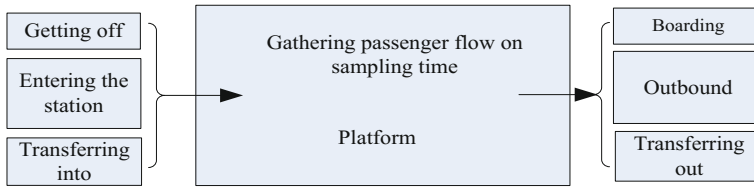


Fig. 1 Train state and passenger flow trend on platform

principle of “departing passengers getting off the train first”. All of alighting passengers get off the train at the moment of  $t_d$ . Taking  $t_d$  as a dividing point, stop period  $\tau_{sk}$  can be divided into two periods: getting off period  $\tau_{sk1}$  and boarding period  $\tau_{sk2}$ , that is  $\tau_{sk} = \tau_{sk1} + \tau_{sk2}$ , so  $T = \tau_{sk1} + \tau_{sk2} + \tau_{tk}$ . As shown in Fig. 1, after the train 1 stops, with the alighting passengers getting into the platform, the number of passengers on the platform is increasing gradually during the getting off period  $\tau_{sk1}$ . However, during the boarding period  $\tau_{sk2}$ , the number of passenger flow is reducing gradually with passengers boarding the train. In general, the number of passenger flow on platform is bigger than the carrying capacity of the train in the station, which results in partial passengers stayed on platform for waiting the next train. After the train 1 out of the station, during the interval period  $\tau_{tk}$ , the alighting passengers on train 1 leave the platform, at the same time, there are new passengers getting into the platform and waiting for train 2, the total number of passenger flow on platform is increasing during the period. The passenger flow distribution occurs repeatedly like this. According above analysis, the number of gathering passengers on platform is the largest at the moment of  $t_d$  and  $t_{d+1}$  [8]. In order to ensure the operation safety of subway station, the moment with maximum passenger density is the sampling time of the passenger flow control model and sampling cycle  $T$  is the departure interval of two adjacent trains.

## 2.2 Classification of Passenger Flow on Platform

In the process of passengers boarding and getting off, the collection and evacuation of passenger flow must be completed on the platform. According to the behavior of passengers, the classification of passenger flow on platform in transfer stations is shown in Fig. 2 [9].



**Fig. 2** Classification of passenger flow in transfer stations

The passenger flow on platform is divided into three categories during a sampling cycle:

- (1) The passenger flow gathering on platform at previous sampling time.
- (2) The passenger flow entering the platform during the sample cycle, including getting off, entering the station and the transferring into.
- (3) The passenger flow leaving the platform during the sample cycle, including the boarding, outbound through the gate and the transferring out.

Based on the linear quadratic optimal control theory of discrete system, the number of gathering passengers on platform and the passenger flow getting into the platform are taken as the state variable and the control variable respectively.

### 3 Passenger Flow Control Model Based on Linear Quadratic Optimal Theory

#### 3.1 Model Assumptions

In order to simplify the model, there are some relevant assumptions as follows.

- (1) Transfer stations operate in good condition without sudden accident and the key facilities are in normal.
- (2) The train runs on schedule strictly. The time of boarding, alighting and interval are similar for different trips and different platforms.
- (3) Passengers obey the rule “departing passengers getting off the train first” strictly [10].

#### 3.2 Model Building

##### 3.2.1 Definitions of Variables and Parameters

Assuming the passenger flow into platform through the ticket gate  $U_1(k)$ , transferring into the platform  $U_2(k)$  and passenger flow for alighting  $U_3(k)$ , then the passenger flow flowing into platform  $U(k)$  in one cycle can be represented by:

$$U(k) = U_1(k) + U_2(k) + U_3(k) \tag{1}$$

Assuming the passenger flow from platform to ticket gate  $Q_1(k)$ , transferring out the platform  $Q_2(k)$  and passenger flow for boarding  $Q_3(k)$ , then the passenger flow out of the platform  $Q(k)$  is acquired by:

$$Q(k) = Q_1(k) + Q_2(k) + Q_3(k) \tag{2}$$

Assuming the gathering passengers number on platform is  $N(k)$  on sample time  $k$ , according to Fig. 2, the passengers number on platform at time  $k + 1$  is:

$$N(k + 1) = N(k) + U(k) - Q(k) \tag{3}$$

According to the analysis in Sect. 2.1,  $N(k)$  is the maximum during one cycle, so  $Q(k) > N(k)$ . In general,  $N(k)$  and  $Q(k)$  are stable relatively at peak hour, so the ratio of  $Q(k)$  and  $N(k)$  is represented as  $\alpha$  to simplify the model. The relationship between  $Q(k)$  and  $N(k)$  is as blow.

$$Q(k) = \alpha \cdot N(k) (0 < \alpha \leq 1) \tag{4}$$

Taking Eqs. (3–4),  $N(k + 1)$  can be defined as:

$$N(k + 1) = (1 - \alpha)N(k) + U(k) \quad (0 < \alpha \leq 1) \quad k = 0, 1, \dots, N - 1 \tag{5}$$

The number of gathering passengers flow on platform  $N$  is replaced by the state variable  $x_i$ , and the number of passenger flow enter the platform  $U$  is replaced by the control variable  $u_i$ , we can get the one-dimensional linear time discrete control system expression is

$$x_i(k + 1) = (1 - \alpha)x_i(k) + u_i(k) \quad (0 < \alpha \leq 1) \quad k = 0, 1, \dots, N - 1 \tag{6}$$

If up and down direction platform are regarded as objects of the study, then the state space expression is:

$$X(k + 1) = AX(k) + BU(k) \quad k = 0, 1, \dots, N - 1 \tag{7}$$

where  $X(k)$  and  $U(k)$  indicate two dimensional state variables and control input vector. The ratio of  $Q(k)$  and  $N(k)$  in each sampling period of two platforms are  $\alpha$  and  $\beta$ , then  $A = \begin{bmatrix} 1 - \alpha & 0 \\ 0 & 1 - \beta \end{bmatrix}$ ,  $B$  is  $2 \times 2$  identity matrix.

### 3.2.2 Constraints and Objective Function of Model

The formula of maximum carrying capacity on platform is:

$$C_{z,\max} = \rho_{z,\max} \cdot S_E \tag{8}$$

where  $\rho_{z,\max}$  is the largest passenger density of the platform, in order to ensure the safety of subway operations, the largest number of gathering passengers can't excess  $C_{z,\max}$ . We can derive that:

$$0 \leq x_i(k) < C_{z,\max} \tag{9}$$

The distribution of passengers on platform is unbalanced at peak hour. In this paper, defining the area of gathering passengers centrally as waiting area, and the effective area of the platform  $S_E$  can be written as:

$$S_E = S_T - (S_F + S_R + S_R + S_O) \tag{10}$$

The relationship between waiting area and effective area of the platform is:

$$S_W = f \cdot S_E \tag{11}$$

where  $f$  is waiting coefficient. The objective function is established based on the minimum density of passenger flow on platform, then

$$\min J = \sum_{k=0}^{N-1} (X^T(k)QX(k) + U^T(k)RU(k)) \tag{12}$$

In the formula,  $Q$  and  $R$  are positive definite diagonal matrices. In the first term, when the diagonal element of  $Q$  is taken as the inverse of  $S_W^2$ , the square of the density of passenger flow on platform is minimum; the capability of control is affected by the matrix  $R = rI$  ( $I$  is identity matrix), in order to match the actual flow of passenger flow on platform, the value of  $r$  can be obtained by testing repeatedly in order to adapt to the actual passenger flow on platform [11].

### 3.3 Model Solution

At peak hour,  $\bar{X}$  is defined as the ideal number of gathering passengers on platform, and  $\bar{U}$  is defined as ideal number of passengers entering the platform. The value of  $\bar{X}$  is determined by the density of passenger flow and the actual waiting area of platform, the value of  $\bar{U}$  is determined by the ratio of all passenger flow entering the platform and ideal gathering passengers at the sampling time on platform.  $\bar{X}$  can be acquired by:

$$\bar{X} = A\bar{X} + B\bar{U} \tag{13}$$

Combining Eqs. (7) and (12), we can derive that:

$$X(k+1) - \bar{X} = A(X(k) - \bar{X}) + B(U(k) - \bar{U}) \tag{14}$$

Based on the theory of linear quadratic optimal control of discrete systems, the optimal control rule of Eq. (7) is:

$$U^*(k) = \bar{U} - K(X^*(k) - \bar{X}) \tag{15}$$

Assuming the waiting area of transfer stations on up and down platform are  $S_1$  and  $S_2$ , then the model of passenger flow control based on linear quadratic optimal theory at peak hour are as follows. The equation of state can be defined as:

$$\begin{bmatrix} x_1(k+1) \\ x_2(k+1) \end{bmatrix} = \begin{bmatrix} 1 - \alpha & 0 \\ 0 & 1 - \beta \end{bmatrix} \begin{bmatrix} x_1(k) \\ x_2(k) \end{bmatrix} + \begin{bmatrix} 1 & 0 \\ 0 & 1 \end{bmatrix} \begin{bmatrix} u_1(k) \\ u_2(k) \end{bmatrix} \tag{16}$$

The objective function can be defined as:

$$J = \min \sum_{k=0}^{N-1} \left[ \begin{bmatrix} x_1(k) \\ x_2(k) \end{bmatrix}^T \begin{bmatrix} \frac{1}{S_1^2} & 0 \\ 0 & \frac{1}{S_2^2} \end{bmatrix} \begin{bmatrix} x_1(k) \\ x_2(k) \end{bmatrix} + \begin{bmatrix} u_1(k) \\ u_2(k) \end{bmatrix}^T \begin{bmatrix} r_1 & 0 \\ 0 & r_2 \end{bmatrix} \begin{bmatrix} u_1(k) \\ u_2(k) \end{bmatrix} \right] \tag{17}$$

$0 \leq X_i(k) < C_{z,\max}$

The optimal control regular pattern can be defined as

$$\begin{bmatrix} u_1^* \\ u_2^* \end{bmatrix} = \begin{bmatrix} \bar{U}_1 - k_1(x_1^* - \bar{X}_1) \\ \bar{U}_2 - k_2(x_2^* - \bar{X}_2) \end{bmatrix} \tag{18}$$

## 4 Simulation and Case Verification

### 4.1 Building Anylogic Simulation Model

Huixinxijenankou Station is the transfer station of lines 5 and 10 in Beijing subway. A lot of passengers gather on platform at peak hour. Based on the actual physical environment of this station and the walking route of passenger flow, a simulation model is built in Anylogic simulation software. The model is used to simulate the passenger flow on up and down of line 10 during morning peak. According to the analysis of the train behavior in Sect. 2.1, taking the train of up direction as an example, the train logic module is built as shown in Fig. 3 [12].

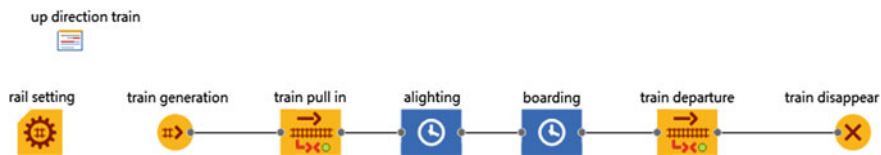


**Fig. 3** The train logic module of up direction

As shown in Fig. 3, the logic module includes train generation, train pulling in, alighting, boarding, train departure, train disappear and rail setting [13]. The departure timetable is set in “up direction train”.

In the software, the parameters of all key facilities are set, which includes ticket gate, transfer corridor and staircase. Then we can get the results of 3D simulation (Fig. 4) [14].

### 4.2 Model Calculation and Simulation Analysis

The effective area of up and down platform in this station are 137,296 and 133,368 m<sup>2</sup> respectively. Letting waiting coefficient  $f_1 = f_2 = 0.35$ , then the waiting area in up and down platform are 480.5 and 466.8 m<sup>2</sup> according to Eq. (10). As the field observation, the ratio of flowing out passengers and passengers at sampling time in up and down platform are  $\alpha = 0.9$ ,  $\beta = 0.95$ . The

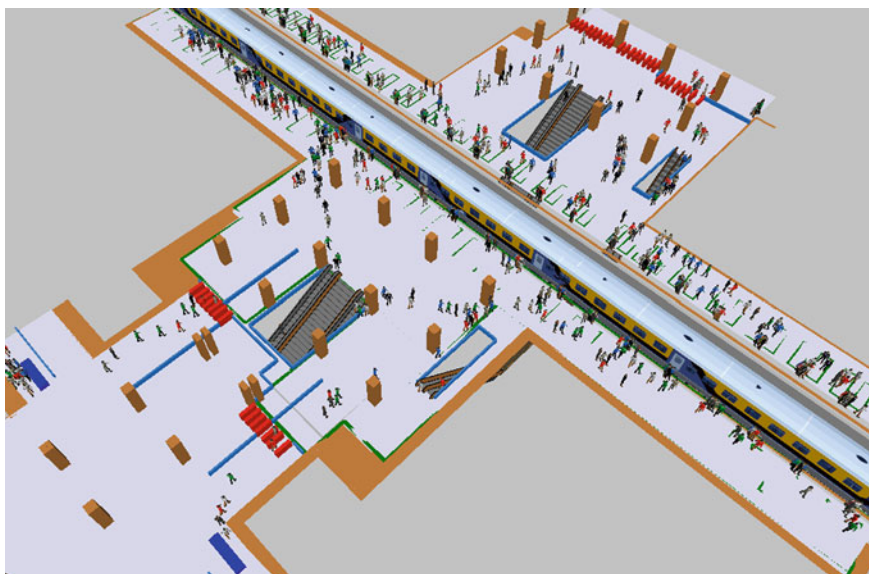


**Fig. 4** 3D simulation of Huixinxijianankou Station on line 10

passengers on up platform are more than on down platform. The appropriate passengers number flowing into up and down platform are  $\overline{U}_1 = 692$  and  $\overline{U}_2 = 665$ . Taking  $\overline{U}_1, \overline{U}_2, \alpha, \beta$  into Eq. (12), the appropriate passengers on up and down platform are  $\overline{X}_1 = 769, \overline{X}_2 = 700$ . And then the passenger density are  $\rho_1 = 1.6(\text{person}/\text{m}^2), \rho_2 = 1.5(\text{person}/\text{m}^2)$ . These results are suitable to the fact.

The function `dlqr()` is invoked in MATLAB to obtain the optimal control rule, adjusting the  $R$  matrix repeatedly, when  $R = \begin{bmatrix} 1.78 \times 10^{-5} & 0 \\ 0 & 1.12 \times 10^{-5} \end{bmatrix}$ , the results of simulation are in good agreement with the actual situation, meanwhile  $K = \begin{bmatrix} 0.0197 & 0 \\ 0 & 0.0167 \end{bmatrix}$ , we can rewrite Eq. (13) with  $K$ , such that:

$$\begin{bmatrix} u_1^*(k) \\ u_2^*(k) \end{bmatrix} = \begin{bmatrix} \overline{U}_1 - 0.0197(x_1^*(k) - \overline{X}_1) \\ \overline{U}_2 - 0.0146(x_2^*(k) - \overline{X}_2) \end{bmatrix} \tag{19}$$

According to Eq. (19), the number of passenger flowing into up and down direction platform is calculated by procedures in the simulation environment. The actual observation shows that the ratio of passenger flowing into platform through fare gate and transferring into is 1:5. The passengers getting off train are random. Each door would produce 3–4 or 2–3 person randomly on up or down direction at each sample cycle in accordance with the scene. Based on the field data and simulation data, the aggregation passengers on platform and the optimal control sequence of all kinds of flowing into platform can be got between 7:30 and 8:30 during morning peak hour (Fig. 5a, b).

For proving the simulation rationality, importing the AFC(Automatic Fare Collection System) and observation data from 7:30 to 8:30 during morning peak on January 27, 2016 to the same simulation environment, the aggregation passengers at the sampling time on up and down platform are obtained as Fig. 6a, b.

Comparing Fig. 6 with Fig. 7, based on the model in this paper, the number of gathering passengers on platform fluctuates in near of the ideal number of passengers gathering on the platform (up direction: 769 passengers, down direction: 700 passengers), and the range is smaller. It shows that the maximum gathering passengers on platform during the control period can be controlled near of the ideal number. But the simulation data obtained under the actual situation, the gathering passengers on platform is higher than the ideal number of gathering passengers, which is harm to safe operation of the subway.

The curve of gathering passengers on platform in Figs. 5 and 6 is converted into passenger density in waiting area. Then we can get the passenger density contrast diagram in Fig. 7.

As we can see from Fig. 7, compared with the actual situation, the control model presented in this paper can maintain the density of passenger flow in the waiting area of the platform near to the ideal density. The actual situation of the passenger flow density on platform is higher than the ideal density value. Compared with the fluctuation of passenger flow density, passenger flow density on platform

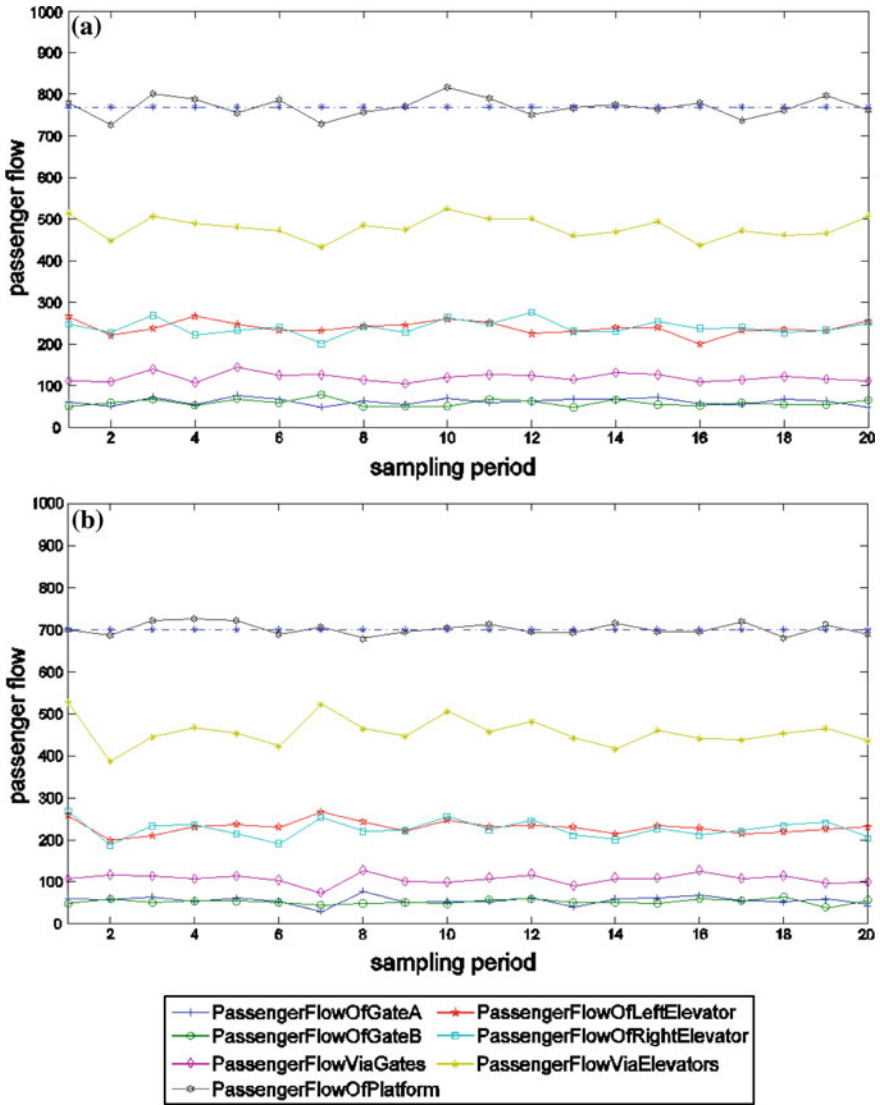


Fig. 5 a Simulation results of passenger flow on up platform. b Simulation results of passenger flow on down platform

fluctuation is much higher without control. Thus, the control model built in this paper can reduce the passenger flow density at sampling time on platform area obviously, and it also can maintain the passenger flow density on platform near to the ideal density. It shows that the method can decrease the passenger crowd on platform in transfer stations at peak hour effectively.



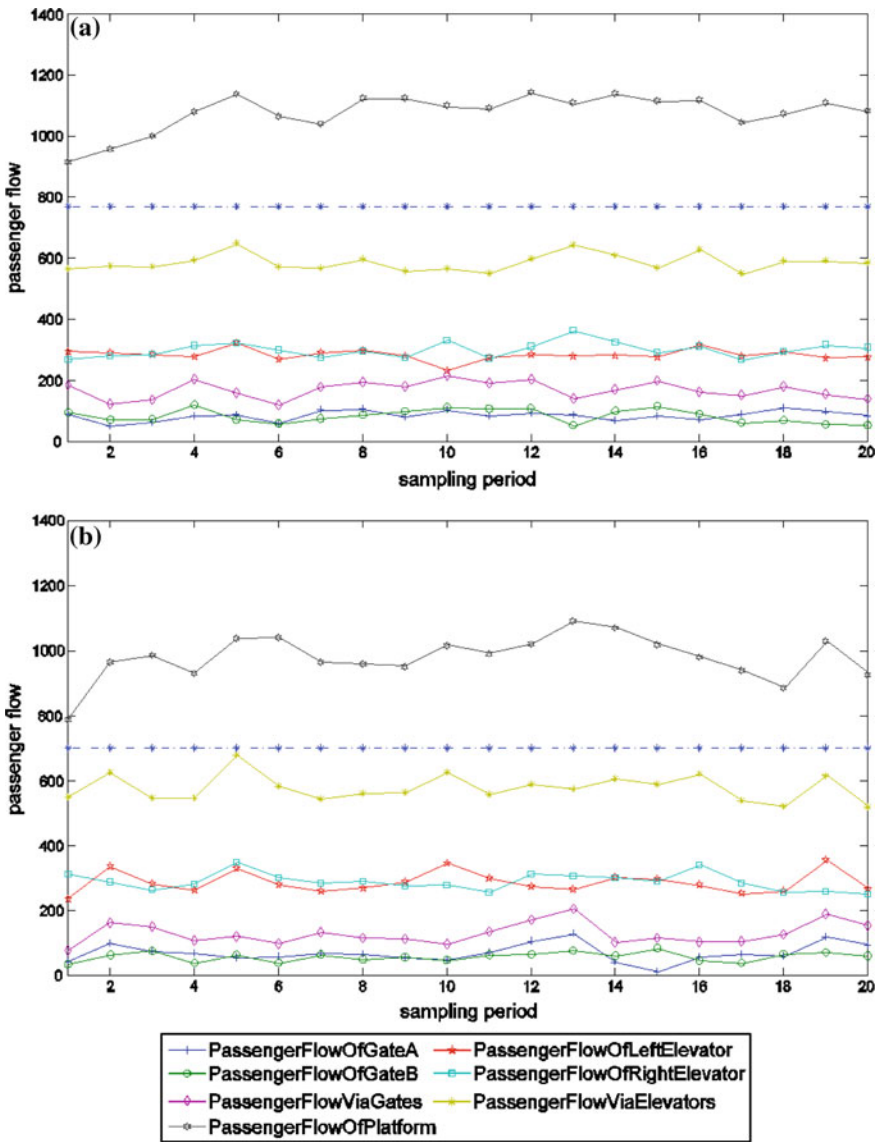


Fig. 6 a Simulation results of up platform according to the actual data. b Simulation results of down according to platform actual data

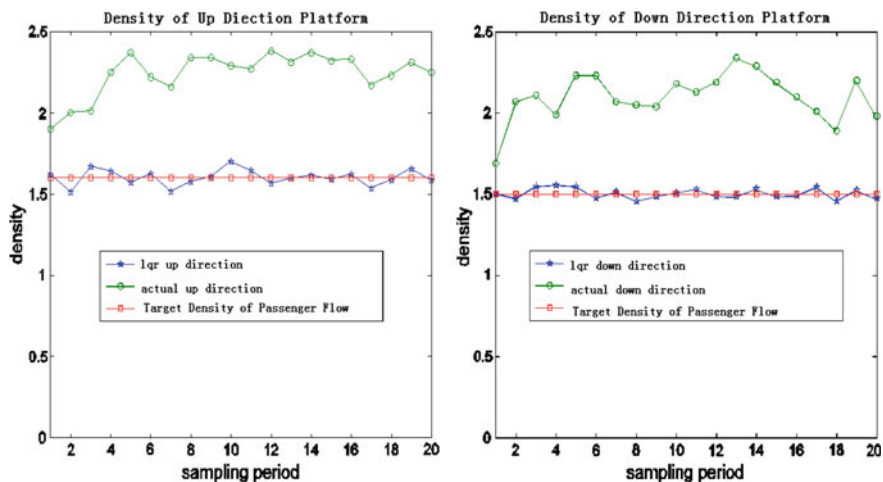


Fig. 7 Comparison of density on platform with or without control

## 5 Conclusion

Based on the control theory, this paper builds a linear quadratic optimal passenger flow control model. Taking Huixinxijienankou Station in Beijing subway as an example, the control model is simulated and proved to be suitable and effective by Anylogic software. The main findings are listed below:

- (1) The optimal control sequence of passengers through fare gate and transferring passageway can be calculated, which would provide a scientific quantitative basis for boarding limit measures at peak hour.
- (2) The model can make the largest number of gathering passengers on platform near to the ideal number during control period, which can reduce the crowd on platform effectively and ensure operation safety at transfer stations.

**Acknowledgements** The authors would like to acknowledge the support of National Key R&D Program of China (2016YFB1200402) and Scientific Research Project of Beijing Education Committee (PXM2017-014212-000031, PXM2017-014212-000033).

## References

1. Liu L, Jiang L (2011) Research on inflow control for urban mass transit network. *Railway Transp Econ* 33(5): 51–55 (in Chinese)
2. Zhao P, Yao X, Yu D (2014) Cooperative passenger inflow control of urban mass transit at peak hour. *J Tongji Univ (Nat Sci)* 42(9):1340–1346 (in Chinese)
3. Yao X, Zhao P, Qiao K et al (2015) Passenger flow coordination control model of urban rail transit network. *J Central South Univ (Nat Sci)* (1):342–350 (in Chinese)

4. Shuwei W, Lishan S, Jian R (2014) Study on the control measures of rail transit large passenger flow. *Urban Rapid Rail Transit* 27(1):16–18
5. Fruin JJ (1971) Pedestrian planning and design. *Metrop Assoc Urban Designers Environ Planners*
6. Hankin BD, Wright RA (1958) Passenger flow in subways. *J Oper Res Soc* 9(2):81–88
7. Li M, Wang Y, Jia L (2015) Passenger flow modes and control strategies in urban rail transit station. *J Southeast Univ (Nat Sci)* (6):1203–1208 (in Chinese)
8. Zhao Y, Mao B, Yang YZ et al (2011) Methods of calculating the maximum assembling on urban rail transit platforms. *J Transp Syst Eng Inf Technol* 4(1):30–35 (in Chinese)
9. Zhao M (2011) Research on the relationship between the urban rail transit platform and the departure intervals. Beijing Jiaotong University (in Chinese)
10. Helbing D (1991) A mathematical model for the behavior of pedestrians. *Behav Sci* 36(4):298–310
11. Laxman KK, Rastogi R, Chandra S (2015) Pedestrian flow characteristics in mixed traffic conditions. *J Urban Plan Dev* 136(1):23–33
12. Xie W (2012) Passenger control scheme for urban rail transit station. Beijing Jiaotong University (in Chinese)
13. Liang YJ, Yuan ZZ (2014) Assignment performance at Beijing south railway station based on Anylogic simulation. *Adv Mater Res* 989–994:2283–2287
14. Zhao L, Zheng Y, Xie J (2016) Simulation of urban transit station based on Anylogic. *Railway Comput Appl* 25(3):62–66 (in Chinese)

# RUL Prediction for Bearings Based on Fault Diagnosis

Dong Yan and Xiukun Wei

**Abstract** In recent years remaining useful life of rolling bearings is paid much more attention. In this paper, the remaining useful life prediction based on fault diagnosis is proposed. Based on the real-time fault diagnosis results of the bearing, the remaining life is predicted and a set of bearing life expectancy prediction system is established by obtaining the vibration signal. In order to solve the problem that the whole life fault data is difficult to obtain, make full use of the bearing information contained in unlabeled data and take into account the advantages of each algorithm, the remaining useful life prediction of bearing is studied based on a semi supervised co-training method. The effectiveness and prediction accuracy of this method are demonstrated by a case study.

**Keywords** Bearing · Remaining useful life prediction · Fault diagnosis  
Semi supervised co-training

## 1 Introduction

Bearings are important component of mechanical, which works in severe conditions and its life is often much less than the expected and desired life. The bearing fault is one of the foremost causes on mechanical breakdowns. And such fault will result in costly downtime and life safety are under serious threat [1]. Therefore, it is vitally important to diagnose the faults and predict the remaining useful life (RUL).

In recent years, scholars have made some achievements in the study of mechanical remaining useful life prediction methods. The mechanism model of running state is designed based on the model with the crack growth law [2], however, the residual life prediction method based on mechanism has a higher requirement on the professional research. Zio [3] has studied the similarity degree

---

D. Yan · X. Wei (✉)

State Key Laboratory of Rail Traffic Control and Safety,  
Beijing Jiaotong University, Beijing, China  
e-mail: xkwei@bjtu.edu.cn

© Springer Nature Singapore Pte Ltd. 2018

L. Jia et al. (eds.), *Proceedings of the 3rd International Conference on Electrical and Information Technologies for Rail Transportation (EITRT) 2017*, Lecture Notes in Electrical Engineering 482, [https://doi.org/10.1007/978-981-10-7986-3\\_102](https://doi.org/10.1007/978-981-10-7986-3_102)

1013

of the equipment characteristics, but the prediction accuracy will be affected even if the similar products are used to predict the remaining life. In addition, artificial intelligence and hybrid algorithm are the research directions of remaining useful life prediction.

Traditional data-driven prognostics often requires amount of fault data for the offline training in order to achieve better accuracy of the online prediction. In many experiments, it is hard to get enough fault data. So it becomes essentially critical to utilize unlabeled data which may carry rich information regarding the degradation trend and help achieve more accurate RUL prediction [4, 5]. Unlabeled data (UL) refer to the condition monitoring data acquired from the beginning of an engineered system's lifetime till planned inspection or maintenance when the system is broken down. Disagreement-based semi-supervised learning is used in the RUL prediction, which uses multiple learning algorithms to make use of unlabeled data, and the "disagreement" among the algorithms is crucial.

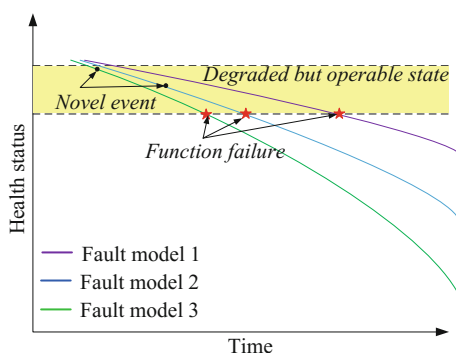
The rest of this paper is organized as follows. The problem statement is introduced in Sect. 2. Remaining life prediction of bearing based on fault diagnosis in this paper is primarily focused in Sect. 3. Section 4 has shown a case study of this method. Finally, some conclusions and prospects are given in Sect. 5.

## 2 Problem Statement

The change of the operating environment leads to a difficult RUL predict of a normal railway bearing. When the bearing fault occurs, the available life of the bearing is shortened and it is more meaningful to predict the RUL. There is a close relationship between the RUL estimation and the fault type of the bearing. The deteriorative curves for different fault types are shown in Fig. 1 [6], different faults have different prediction models. Hence predicting the RUL of the bearing accurately, it is important to identify fault type first.

In this paper, the RUL prediction of the bearing based on fault diagnosis is considered. Data processing as a preparation for diagnosis and RUL prediction in

**Fig. 1** Health status deteriorative curves for different fault model



the first place. The RUL prediction issue based on semi-supervised co-training method is considered. The frame of the whole process is shown in Fig. 2. In Fig. 2 the back propagation (BP), principal component analysis (PCA) are used.

The working principle of fault diagnosis is as follows: Put the bearing signal into the fault diagnosis system, determine the time and degree of failure. At the same time, put the original data into the processor system to extraction the feature, then separate the different type of fault. And the fault time, fault degree and fault type are used as the output of the fault diagnosis device.

The principle of RUL prediction: The extracted feature values are fused and PSO-BP and SVR are used to perform semi supervised training for different fault data. The fault type of the fault diagnosis system is used as the input of the RUL prediction system, according to this value, management and maintenance decision for the parts with current faults can make timely and accurately.

There are a lot of researches on fault diagnosis, and the semi supervised cooperative residual life prediction algorithm is introduced in detail in this paper.

### 3 Semi Supervised Co-training

This section focuses on the RUL prediction based on the fault diagnosis. The semi-supervised co-training-based approach is used for bearing RUL prediction, as a promising research aiming to exploit simultaneously the benefits from labeled and unlabeled data. And two prediction algorithms are used for algorithms integration, which can combine with different algorithms models, different forecasting process and different prediction results. The simple process of semi supervised co-training is shown in Fig. 3, and the fake code of main process is shown in Table 1, which is

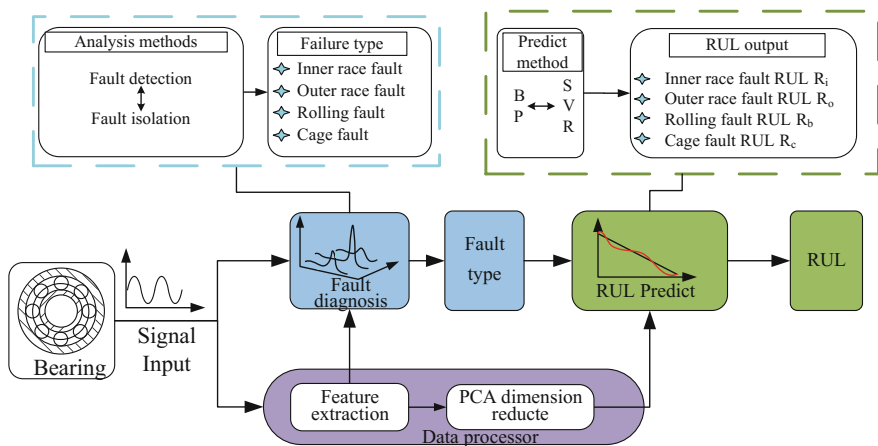


Fig. 2 The progress of residual life prediction based on fault diagnosis

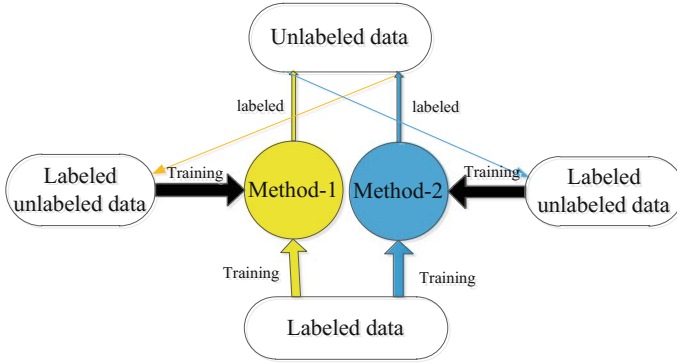


Fig. 3 Process of co-training semi-supervised algorithm

Table 1 Parameters of the bearing test platform

Input fault training data set
$D_l = \{(\langle x_1^1, x_1^2 \rangle y_1), \dots, (\langle x_l^1, x_l^2 \rangle y_l)\}$ ,
unlabeled training data set (U),
$D_u = \{\langle x_{l+1}^1, x_{l+1}^2 \rangle, \dots, \langle x_{l+u}^1, x_{l+u}^2 \rangle\}$ ;
maximum number of co-training iterations (T),
unlabeled pool size (S)
Training process
$h1 = \text{TrainFun}(D_l, 1); h2 = \text{TrainFun}(D_l, 2);$
for j = 1, 2 do
for each $D_u$
$y_u^p = h_j(D_u)$
$D_j' = \{D_l \cup (x_{i_u}, y_u^p), j\}, h_j' = \text{TrainFun}(D_j')$
end
if there exists an $\Delta_{j,x_u} > 0$
$x_j' = \arg \max \Delta_{j,x_u}, y_j' = h_j(x_j')$ ,
$\alpha_j = \{(x_j', y_j')\}; D' = D' \setminus \alpha_j$
else
$\alpha_j = \phi$
end
end
if $\alpha_1 == \phi$ & $\alpha_2 == \phi$ exist
else $D_1 = D_1 \cup \alpha_2; D_2 = D_2 \cup \alpha_1$
Training the two networks
end
$x_1^1, x_1^2$ : The characteristic values of the first sample, $y_1$ : Output value of first sample

taking the two characteristic values as an example. After the training process, the optimal algorithm is obtained. Then loading the testing data, the RUL will be exported. And method 1 and method 2 are RUL prediction method.

BP neural network is one of the algorithms, which can fit any finite input–outputs mapping with a sufficient number of neurons in the hidden layer. The exact parameters and function selection and more information about BP will be introduced in the [7] another algorithms is support vector regression (SVR). It is improved on the basis of support vector machine (SVM) by introducing the loss function  $\epsilon$  into the SVM. It can be approximated any nonlinear function by control the precision and the generalization ability. And SVR has a good global optimum ability and stability [8].

## 4 Case Analysis

### 4.1 Data Sources

To validate the efficiency of this method, data from the bearing experimental platform of the NSF/UCR intelligent maintenance center in the United States are used. Four Rexnord ZA-2115 double row bearings are installed on one shaft. The parameters of the bearing are shown in Table 2.

There are three groups of this experiment, each group has 4 bearings to test, and the data sampling rate is 20 kHz. RUL prediction results for different unlabeled number are compared to show the relation between unlabeled number and prediction accuracy. The data settings are shown in Table 3.

There are 12 input vectors, composed by the normalized age value of bearing and PCA features at the current and previous points, and RUL as the output.

**Table 2** Parameters of the bearing test platform

Name	Parameter	Name	Parameter
Number of rollers	16	Roller diameter	0.331 in
Pitch diameter	2.815 in	Contact angle	15.17°

**Table 3** Bearing data distribution

The first group	The type of data in the net	The second group	The type of data in the net	The third group	The type of data in the net
B-1	UL samples	B-5	Test samples	B-9	UL samples
B-2	UL samples	B-6	UL samples	B-10	UL samples
B-3	–	B-7	UL samples	B-11	Training samples
B-4	–	B-8	UL samples	B-12	UL samples



In BP network algorithm, the number of hidden layer neurons is 8, the output layer function is linear, trainlm as training function and sigmoid as hidden layer transfer function, the network is trained for 1000 times and the expected error value of this net is  $10e-5$ . The other algorithm is SVR, the center function is RBF, the parameter of C is 0.503, and is 0.016. The weight of each network is 0.5.

The RUL prediction result compared with other methods are shown in Fig. 4, which UL is mean the semi supervised co-training method when the unlabeled sets are 8. All of the results has shown a typical recession characteristic of rotating machinery. The prediction curve is gentle in the early stage. When the fault occurs, the curve shows a decreasing trend, and the slope is much larger than the initial stage. It can be seen that the result of semi-supervised cooperative algorithm are better than BP and SVR in the whole forecasting process.

To verify the effect of the unlabeled data to the prediction accuracy of the algorithm, four error indexes are calculated, which are the root mean square error, the mean absolute error, the hill coefficient of the inequality and the average relative change, respectively.

The RUL prediction result compared with different number of unlabeled data is shown in Fig. 5. Take 2, 5 and 8 as example. The trend of the prediction curve is the same, the recession curve is stable at the early stage, and the curve decreases when the fault occurred and the slope increases. The error values of different unlabeled data method are calculated as Table 4. With the increase of the number of unlabeled data, the accuracy of the model is generally improved, indicating that the increase of the number of unlabeled data can improve the prediction accuracy of the algorithm.

Considering the situation that RUL is predicted when fault occurs, Fig. 6 shows the RUL prediction from 118 to 164 h, which is in fault stage. When the unlabeled data is 8, the curve is closer to the actual value than others. And the error values are

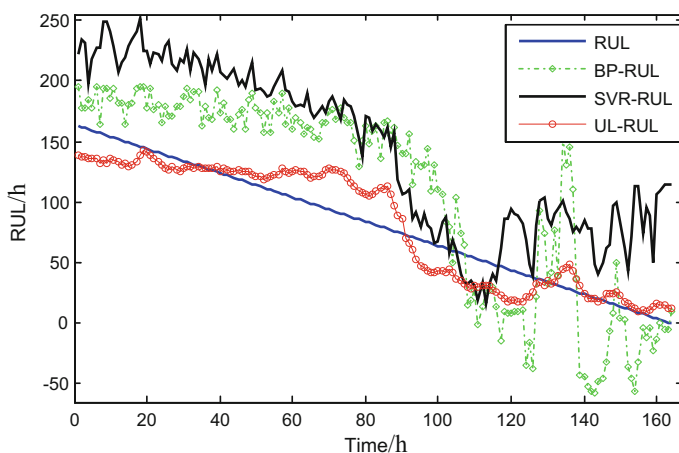


**Fig. 4** Different number of unlabeled data for RUL prediction

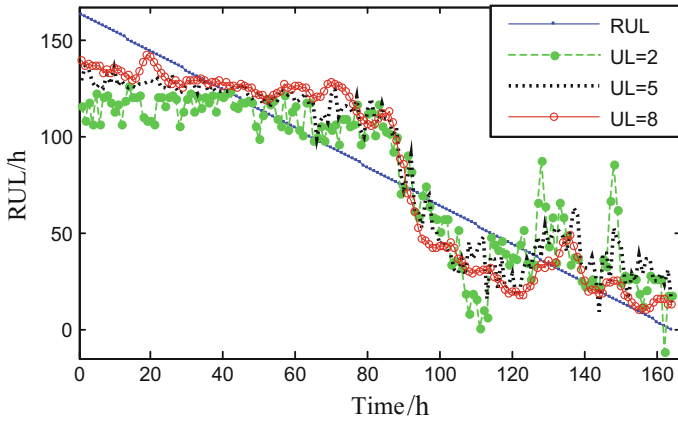


Fig. 5 Different number of unlabeled data for RUL prediction

Table 4 Bearing data distribution

Number of unlabeled data	Root mean square error	Mean absolute error	Hill inequality coefficient	Average relative change
PSO-BP	54.202	0.2326	0.517	1.308
SVR	69.947	0.3806	0.656	2.179
UL = 2	22.985	0.0574	0.227	0.235
UL = 5	19.434	<b>0.0172</b>	0.192	0.168
UL = 8	<b>17.839</b>	0.0175	<b>0.175</b>	<b>0.147</b>

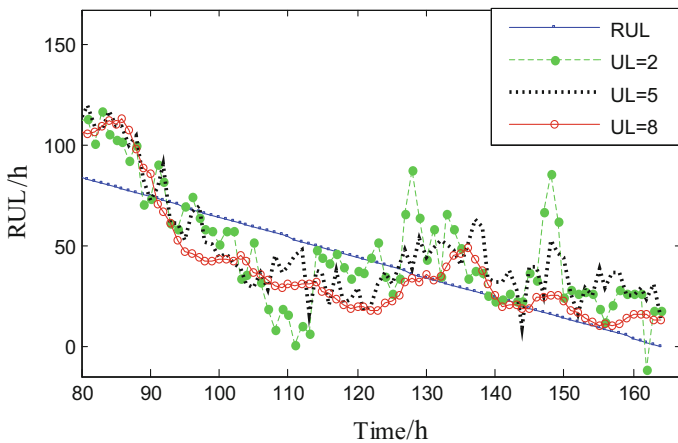


Fig. 6 Different number of unlabeled data for RUL prediction

**Table 5** Bearing data distribution

Number of unlabeled data	Root mean square error	Mean absolute error	Hill inequality coefficient	Average relative change
UL = 2	15.749	0.094	0.455	0.952
UL = 5	13.898	0.024	0.403	0.741
UL = 8	<b>11.798</b>	<b>0.022</b>	<b>0.345</b>	<b>0.534</b>

calculated for this period either, the error values are listed in Table 5. All error values reach the minimum when unlabeled data is 8.

## 5 Conclusions

This paper presents a RUL prediction method based on fault diagnosis and fault isolation at the early stage. For early fault diagnosis, spectral correlation density combination slice method is used, which fully considers the cycle characteristics of the rotating machine. VPMCD can verify the bearing's fault type even though the integrated fault. And semi supervised co-training-based approach combines the two models, and the unlabeled data is fully used in this method. The case study has proved the effectiveness of the method convincingly. A further study and application of the prediction method for practical mechanical systems would be our future work.

**Acknowledgements** This work is also partly supported by State Key Lab of Rail Traffic Control & Safety (Contract No. RCS2016ZT006). This work is also partly supported by National Key R&D Program of China (Contract No. 2017YFB1201201).

## References

1. Jianwei Y (2015) Fault diagnosis of railway bearing based on FIR-wavelet packet and LVQ neural network. *Open Autom Control Syst J* 7:303–313
2. Oppenheimer CH, Loparo KA (2002) Physically based diagnosis and prognosis of cracked rotor shafts. In *Aerosense international society for optics and photonics*
3. Zio E, Maio FD (2010) A data-driven fuzzy approach for predicting the remaining useful life in dynamic failure scenarios of a nuclear system. *Reliab Eng Syst Safety* 95(1):49–57
4. Hu C (2015) A co-training-based approach for prediction of remaining useful life utilizing both fault and suspension data. *Mech Syst Signal Process* 62–63:75–90
5. Zhou Z (2013) Disagreement-based semi-supervised learning. *Acta Automatica Sinica* 39(11)
6. Sikorska JZ, Hodkiewicz M, Ma L (2011) Prognostic modelling options for remaining useful life estimation by industry. *Mech Syst Signal Process* 25:1803–1836
7. Chen Yuhao (2010) Review of neural network BP algorithm. *Comput Knowl Technol* 6(36): 10364–10365
8. Dvaid M, Alexnader F (2004) Active set support vector regression. *IEEE Trans Neural Netw* 15(2)

# Two-Objective Optimization Reinforcement Learning Used in Single-Phase Rectifier Control

Ande Zhou, Bin Liu, Yunxin Fan and Libing Fan

**Abstract** Regarding the single-phase rectifier control as a Markov Decision Process (MDP) with continuous state space and discrete action space and in the meantime, we introduced a new two-objective optimization reinforcement learning framework and proposed a genetic algorithm to train the learning agent in order to optimize power factor and output DC voltage. This article analyzed the convergence of our new algorithm and presented favorable performance of numerical simulation.

**Keywords** Single-phase rectifier · Markov decision process · Reinforcement learning · Genetic algorithm

## 1 Introduction

The single-phase voltage source PWM rectifier (VSR) [1] is used to realize bidirectional power flow between AC net and DC-link and guarantee that the DC-link voltage maintains constant and power factor of AC net approaches 1 simultaneously. There are many rectifier control methods. Most of which, whether it is direct or indirect, in order to get a high power factor, phase loop lock (PLL) is required. Furthermore, control parameters have to be adjusted manually to make controllers act perfectly [2–4].

If we regard the rectifier control process as a Markov Decision Process (MDP) [5], which has continuous state space and discrete action space, the rectifier control could be achieved by reinforcement learning methods [6]. Nevertheless, the current reinforcement learning algorithms can not be implemented directly in single-phase rectifier control. For optimizing the power factor of rectifier and making the set value of DC voltage approach as quickly as possible at the same

---

A. Zhou (✉) · B. Liu · Y. Fan · L. Fan  
EMU Development Department, Zhuzhou Electric Locomotive Company Ltd.  
CRRC, Zhuzhou, Hunan, China  
e-mail: andel.zhou@163.com

time, we introduced a two-objective optimization reinforcement learning framework and gave a common algorithm to solve this problem.

In Sect. 2, we recommended how to use MDP to explain the single-phase rectifier control. Then the two-objective optimization reinforcement learning framework is put forward. In Sect. 4, the convergence of the proposed algorithm is analyzed. Finally, experiment results are presented.

## 2 Markov Decision Process

The MDP framework consists of 4 elements (S, A, R, P), where S is state space of an agent, which can be continuous state or finite discrete [7]. A denotes the action space of an agent, and it also can be continuous or discrete. R is the immediate reward of an agent after an action is done, which is defined  $R: S \times A \rightarrow R$ , P is the transition model, where  $P(s|s', a)$  with  $\sum_{s'} \epsilon_S P(s'|s, a) = 1$ . The objective is to estimate the optimal policy  $\pi^*$  satisfying the following:

$$Q^{\pi^*}(s, a) = \max_{\pi} E^{\pi} \left[ \sum_{t=0}^{\infty} \gamma^t r_t | s_0 = s, a_0 = a \right] \tag{1}$$

where the parameter  $\gamma \in [0, 1]$  is the discount factor. Figure 1 shows a typical single-phase rectifier electric circuit diagram.  $U_s(t)$  is source voltage,  $I_s(t)$  source current,  $U_c(t)$  DC voltage.  $L$ ,  $C_d$  and  $R_L$  indicate inductance, capacitor and DC load respectively.  $S_1$  and  $S_3$  are at the top IGBTs of rectifier bridge, and  $S_2$  and  $S_4$  are at the bottom.

The single-phase PWM rectifier control can be regarded as a MDP, which is composed of continuous state space and discrete action space [8]. The state space of rectifier can be defined as  $\{U_s(t_1), U_s(t_2), I_s(t_1), I_s(t_2), U_c(t_1), U_c(t_2)\} S$ , where  $t_2 = t_1 + \Delta t$ .  $U_s(t_1), U_s(t_2), I_s(t_1), I_s(t_2)$  and  $U_c(t_1), U_c(t_2)$  are the adjacent two

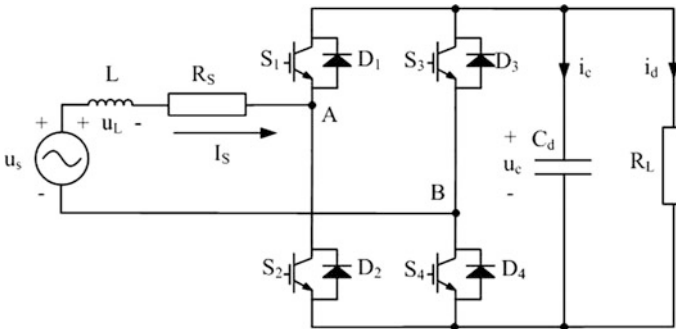


Fig. 1 Framework of SIngle-phase AC rectifier

samples of source voltage, current and DC link voltage, the sampling frequency is  $\frac{1}{\Delta t}$ . The purpose of using two adjacent samples of source voltage and current is to make source current waveform automatically change with voltage waveform, which can omit voltage phase and frequency detector in rectifier controller. The action space is discrete and only consists of 4 action pairs,  $\{(0, 0), (1, 0), (0, 1), (1, 1)\} \in A$ , where the first number  $x_i$  of the action pair  $(x_i, y_i)$  denotes open and close statuses of the first top IGBT  $S_1$ , and the second number  $y_i$  represents open and close statuses of the second top IGBT  $S_3$ .

The statuses of two bottom IGBTs of two bridges are opposite to the top ones.

For the immediate reward of the single-phase rectifier control, following aspects (Rectifier used for boosting is only involved here) are considered:

1. When source voltage increases, source current should increase as well, that is, source current should variate following source voltage. Therefore, the product with change rates are used to source current and source voltage to indicate the reward of one action.
2. If DC link voltage deviates from the set value more, the reward of the action should be smaller.

Based on the above 2 considerations, one of the possible immediate reward can be described as follows:

$$r_t = \alpha \frac{\Delta U_n(t) \times \Delta I_n(t)}{\Delta t^2} - \beta (U_d(t) - U_d^*)^2 \quad (2)$$

where

$$\begin{aligned} \Delta U_n(t) &= (U_n(t_2) - U_n(t_1)) \\ \Delta I_n(t) &= (I_n(t_2) - I_n(t_1)) \\ \Delta t &= t_2 - t_1 \end{aligned} \quad (3)$$

$U_d^*$  is the set value of the DC link, however the above reward function exists following issues:

1. The criterion is to assess the performance of power factor and whether the DC link voltage is near to the set value or different. If we want to combine them, two weight parameters have to be set manually.
2. The above two purposes are sometimes contradictory, in other words, when the source current follows the voltage, the DC link voltage may deviate from the set value more.

Simply combining two incompatible objectives together may not be a good solution. Therefore a new reinforcement learning framework is proposed to solve the above problem.

### 3 Two-Objective Optimization Reinforcement Learning

For a MDP, if there are two incompatible objectives required to be optimized concurrently, we need to find a best control policy  $\pi^*$  to make the following two Q functions to be maximum [9].

$$Q_1^{\pi^*}(s, a) = \max_{\pi_1} E^{\pi_1} \left[ \sum_{t=0}^{\infty} \gamma^t r_t^1 | s_0 = s, a_0 = a \right] \quad (4)$$

$$Q_2^{\pi^*}(s, a) = \max_{\pi_2} E^{\pi_2} \left[ \sum_{t=0}^{\infty} \gamma^t r_t^2 | s_0 = s, a_0 = a \right] \quad (5)$$

The above problem comes from the rectifier control, where we need to find a control scheme to maintain DC link voltage stable, meanwhile guarantee power factor approach 1. This is a multi-objective optimization problem, which only has a set of Pareto-optimal solutions. The Pareto-optimal is defined as follows:

**Definition 1** Consider the following multiple-objective optimization problem:

$$\min F(X) = \{f_1(X), f_2(X), \dots, f_m(X)\} \quad (6)$$

A solution  $X$  is said to dominate a solution  $Y$  if  $\forall j = 1, 2, \dots, m, f_j(X) \leq f_j(Y)$ , and there exists  $k \in \{1, 2, \dots, m\}$  such that  $f_k(X) < f_k(Y)$ .

Solution  $X$  is said Pareto-optimal if it is not dominated by any other feasible solutions.

Our goal is to use some algorithm to find a Pareto-optimal vector  $\theta$  of the vector function  $F(\theta) = \{\hat{q}_1, \hat{q}_2\}$ , where  $\hat{q}_1$  and  $\hat{q}_2$  are the approximate functions of (4 and 5).

Based on the idea of the Strength Pareto Evolutionary Algorithm (SPEA2) [10], a new Two-objective Optimization Reinforcement Learning Algorithm (TOORL) was proposed in this article, which is a genetic algorithm using  $Q(s, a)$  function and action function  $\pi(s, a)$  approximation [11]. Partially different from the SPEA2, we proposed a new crossover and mutation scheme that can guide the genetic algorithm search along with the direction to the optimal solution.

Our algorithm can be divided into two steps. The first step is to use random policy iteration to get the two  $Q(s, a)$  functions (4,5) approximation, then we use two approximate  $Q(s, a)$  functions as the objective functions to get the optimal policy function approximation  $\pi(s, a, \theta)$  through SPEA2. Although in this article only the SPEA2 algorithm is analyzed, other genetic algorithms, such as MOGA, NPGA, and NSGA II, can also be used in our framework [12–14].

**Algorithm: TOORL-Algorithm**

1. Given:

- A sample data set  $\{(x_i, a_i, x'_i, a'_i)\}$  ( $i = 1, 2, \dots, N$ )
- Two functions  $\hat{q}_1(s, a, w_1)$ ,  $\hat{q}_2(s, a, w_2)$  to approximate  $Q_1(s, a)$ ,  $Q_2(s, a)$ ,  $\pi(s, a, \theta)$  to approximate the policy function  $\pi(s, a)$
- Initial the iterative index  $K$ , accuracy threshold  $\epsilon$
- Select population size  $N$  and archive size  $\bar{N}$ , generate the initial population  $\Omega(0) = \{\theta_0^k, \dots, \theta_n^k\}$  and archive  $\bar{\Omega}(0) \neq \phi$
- Initial the  $w_1^k$ ,  $w_2^k$  with random small numbers, and use the policy function  $\{\pi(s, a, \theta_i^k)\}_{i=1}^n$  to generate the start policy  $\{\pi_i^k\}_{i=1}^n$

2. If  $\|w_1^{k+1} - w_1^k\|_2 \leq \epsilon$  and  $\|w_2^{k+1} - w_2^k\|_2 \leq \epsilon$ ,  $\hat{q}_1(s, a, w_1^{k+1}) = \hat{q}_1(s, a, w_1^*)$ ,  $\hat{q}_2(s, a, w_2^{k+1}) = \hat{q}_2(s, a, w_2^*)$  goto step 3, else For  $i = 1$  to  $n$ :

- Use  $\pi_i^k$  to update the  $\hat{q}_1(s, a, w_1^{k_i})$  to  $\hat{q}_1(s, a, w_1^{(k+1)_i})$ ,  $k_i \leftarrow (k+1)_i$ .
- Use  $\pi_i^k$  to update the  $\hat{q}_2(s, a, w_2^{k_i})$  to  $\hat{q}_2(s, a, w_2^{(k+1)_i})$ ,  $k_i \leftarrow (k+1)_i$ .

Until  $\hat{q}_1(s, a, w_1^k)$  update to  $\hat{q}_1(s, a, w_1^{k+1})$ ,  $\hat{q}_2(s, a, w_2^k)$  update to  $\hat{q}_2(s, a, w_2^{k+1})$ .  $\bar{\Omega}(k+1) = \Omega(k)$  goto step 6.

3. **Fitness assignment:** Use  $\hat{q}_1(s, a, w_1^*)$  and  $\hat{q}_2(s, a, w_2^*)$  to calculate fitness values of individuals in  $\Omega(k)$  and  $\bar{\Omega}(k)$ .
4. **Environment Selection:** Copy all non-dominated individuals in  $\Omega(k)$  and  $\bar{\Omega}(k)$  to  $\bar{\Omega}(k+1)$ . If size of  $\bar{\Omega}(k+1)$  exceeds  $N$  then reduce  $\bar{\Omega}(k+1)$  by means of the truncation operator, otherwise if size of  $\bar{\Omega}(k+1)$  is less than  $N$  then fill  $\bar{\Omega}(k+1)$  with dominated individuals in  $\Omega(k)$  and  $\bar{\Omega}(k)$ .
5. **Termination:** If  $k \geq K$  or another stopping criterion is satisfied then output the set of decision vectors represented by the non-dominated individuals in  $\bar{\Omega}(k+1)$ . Stop.
6. **Mating selection:** Perform binary tournament selection with replacement on  $\bar{\Omega}(k+1)$  in order to fill the mating pool
7. **Variation:** Apply recombination and mutation operators to the mating pool and set  $\bar{\Omega}(k+1)$  to the resulting population. Increment generation counter  $k = k + 1$  and go to Step 2



### 3.1 Q Function Updating Methods

The updated algorithm can be any existing methods, such as  $TD(0)$ ,  $TD(\lambda)$ , Monte Carlo methods [15, 16]. For Monte Carlo methods, the target is the return  $G_t$ , we used the following equation to update the parameter vector  $w$

$$\Delta w = a(G_t - \bar{q}(s, a, w)) \nabla_w \hat{q}(s, a, w) \quad (7)$$

where  $G_t$  is

$$G_t = r_{t+1} + \gamma r_{t+2} + \dots + \gamma^{T-t} r_T \quad (8)$$

For  $TD(0)$ , the target is the  $TD$  target

$$\begin{aligned} & r_{t+1} + \gamma Q(s_{t+1}, a_{t+1}) \\ \Delta w &= a(r_{t+1} + \gamma \bar{q}(s_{t+1}, a_{t+1}, w) - \hat{q}(s_t, a_t, w)) \nabla_w \hat{q}(s_t, a_t, w) \end{aligned} \quad (9)$$

For forward-view  $TD(\lambda)$ , target is the action-value  $\lambda$ -return

$$\Delta w = a(q_t^\lambda - \hat{q}(s_t, a_t, w)) \nabla_w \hat{q}(s_t, a_t, w) \quad (10)$$

For the Bellman Residual Gradient algorithm [17], the target is the minimum the mean squared Bellman residual

$$E = \frac{1}{n} \sum_x [E^\pi(r^t + \gamma \hat{q}(s_{t+1}, a_{t+1}, w)) - \hat{q}(s_t, a_t, w)]^2 \quad (11)$$

The update equation for  $\Delta w$  is

$$\begin{aligned} \Delta w &= -\alpha [r^t + \gamma \hat{q}(s_{t+1}, a_{t+1}, w)] \\ & \left[ \frac{\partial}{\partial w} \gamma \hat{q}(s_{t+1}, a_{t+1}, w) - \frac{\partial}{\partial w} \hat{q}(s_t, a_t, w) \right] \end{aligned} \quad (12)$$

In this article, we chose Monte Carlo method to estimate the Q function  $Q(s, a)$ .

### 3.2 Fitness Assignment

Before calculating the fitness of each individual in  $\Omega(k)$  and  $\bar{\Omega}(k)$ , the SEPA2 algorithm has to assign a strength value  $S(i)$  for each individual using the following equation:

$$S(i) = |\{j|j \in \Omega(k) + \bar{\Omega}(k) \text{ and } i \succ j\}| \tag{13}$$

where  $|\dots|$  is the cardinality of a set,  $+$  stands for multiset union and the symbol  $\succ$  corresponds to the Pareto dominance relation. Then the raw fitness of each individual is calculated by:

$$R(i) = \sum_{j \in \Omega(k) + \bar{\Omega}(k), j \succ i} S(j) \tag{14}$$

If  $R(i) = 0$ , that means  $i$  is a non-dominated individual, and the smaller  $R(i)$  means  $i$  dominated more individuals, but if most of the individuals have the same raw fitness, then the Pareto dominate relation cannot be confirmed, so the density of individuals is imported to discriminate the individuals.  $k$ -nearest neighbour method is always used as density estimation [9], where the distances from individual  $i$  to individual

$j, i, j \in \{\Omega(k) + \bar{\Omega}(k)\}$ , are sorted:  $d_1(i) \leq d_2(i) \leq \dots \leq d_{N+\bar{N}}(i)$ , and the  $k$ -nearest neighbour is estimated by  $\delta_i^k = k/[2(N + \bar{N}) \cdot d_k(i)]$ , usually  $k \approx \sqrt{N + \bar{N}}$  and then the fitness is calculated by  $F(i) = R(i) + D(i)$ .

### 3.3 Environment Selection

First copy the non-dominated individuals in  $\Omega(k)$  and  $\bar{\Omega}(k)$  into  $\bar{\Omega}(k+1)$ . If  $|\bar{\Omega}(k+1)| = \bar{N}$ , then the environment selection stop. If  $|\bar{\Omega}(k+1)| \leq \bar{N}$  then copy  $\bar{N} - |\bar{\Omega}(k+1)|$  individuals in  $\Omega(k) + \bar{\Omega}(k)$ , whose fitness value is smaller than the

Left individuals, if  $|\bar{\Omega}(k+1)| \geq \bar{N}$  then use the following truncation algorithm to make  $|\bar{\Omega}(k+1)| = \bar{N}$ .

$$\begin{aligned} & i \leq j : \Leftrightarrow, \forall k, 0 < k < |\bar{\Omega}(k+1)| : \delta_j^k = \delta_i^k \vee \\ & \exists k, 0 < k < |\bar{\Omega}(k+1)| : \\ & \left[ \forall l, 0 < l < k : \delta_j^k = \delta_i^k \right] \wedge \delta_j^k \wedge \delta_i^k \end{aligned} \tag{15}$$

where  $k = 1, 2, \dots, \bar{N}; l = 1, 2, \dots, k - 1$ .

### 3.4 Crossover and Mutation Based on Chromosome and Gene Importance

In this article, we provided a new chromosome and gene importance based on crossover and mutation methods, which can guide our algorithm to search along

with the direction to the optimal solution. The main idea is that, through environment selection and fitness assignment, we can get the information that chromosomes are more important than others, and also genes are more important than others in important chromosomes. Using the information we got, we can make the more important chromosomes and genes have more chances to do crossover and mutation in reproduction step. This, in positive probability, can reduce the chance of useless crossover and mutation in reproduction step.

Assume each individual (vector)  $\theta_i^{k+1}$  in archive set  $\overline{\Omega}(k+1)$  has  $N_1$  elements, that is  $\theta_i^{k+1} = \left\{ \theta_{ij}^{k+1} \right\}_{j=1}^{N_1}$ , and each element can be coded by  $N_2$  genes, that is  $\theta_{ij}^{k+1} = \{g_1, g_2, \dots, g_{N_2}\}$ . The vector  $P^s = \left\{ P_j^s \right\}_{j=1}^{N_1}$  is the probability to select  $j$ th element of each vector to do crossover, the matrix  $P^c = \left\{ P_{ij}^c \mid 1 \leq i \leq N_1, 1 \leq j \leq N_2 \right\}$  is the probability to select  $j$ th gene in  $i$ th element of each individual to do crossover, and the matrix  $P^m = \left\{ P_{ij}^m \mid 1 \leq i \leq N_1, 1 \leq j \leq N_2 \right\}$  is the probability to select  $j$ th gene in  $i$ th element of each individual to do mutation.

The chromosome and gene importance based on crossover and mutation algorithm (CGCM) is that:

#### Algorithm: CGCM-Algorithm

1. Given:

- Archive set  $\overline{\Omega}(k+1)$  and mating pool set  $M(k+1) = \left\{ \left( \theta_i^{k+1}, \theta_j^{k+1} \right) \right\}_{i,j \leq |M|}$
- Initial the element select probability vector  $P^s$  and the gene crossover and mutation matrix  $P^c$  and  $P^m$  with equal probability
- Initial the record vector  $R^s$ , and matrix  $R^c$ ,  $R^m$  with zero vector and zero matrix
- Crossover and mutation modify probability  $p_k = e^{-\frac{k}{T}}$ , where  $T$  is constant value

2. Using the element select vector  $P^s$  and gene crossover and mutation probability matrix  $P^c$  and  $P^m$  to do the crossover and mutation in mating pool set  $M(k+1)$

3. Record the selection, crossover and mutation information of  $i$ th individual  $\theta^i \in \Omega(k+1)$ ,  $\{s_{i,j} \in [0, 1]\}$ ,  $i = 1, \dots, N$ ,  $j = 1 \dots N_1$  denotes whether the  $j$ th element of  $i$ th individual has been done selection, and  $c_{i,j,k} \in [0, 1]$ ,  $i = 1, \dots, N$ ,  $j = 1 \dots N_1$ ,  $k = 1 \dots N_2$  denotes whether the  $k$ th gene in  $j$ th element of  $i$ th individual has done crossover, and  $m_{i,j,k} \in [0, 1]$ ,  $i = 1, \dots, N$ ,  $j = 1 \dots N_1$ ,  $k = 1 \dots N_2$  denotes whether the  $k$ th gene in  $j$ th element of  $i$ th individual has done mutation.

4. Running the TOOR-algorithm to get the next generation of  $\bar{\Omega}(k+1)$
5. Collect statistics of the selection, crossover and mutation in survived non-dominated vector  $\theta_i^{k+1}$ , to get information that elements and genes are more important.
6. Update the selection probability vector, crossover and mutation probability matrix according to the statistics collecting from step 5 with probability  $p(k)$ , goto step 2.

## 4 Convergence Analysis

Our algorithm can be divided into 2 steps, the first step is to use policy iteration methods to get two approximate action-value functions  $\{\hat{q}_i(s, a, w)\}_{i=1}^2$ , then using the SPEA2 algorithm to obtain the Pareto-optimal solution.

Firstly, we discussed the convergence of the action-value function  $\hat{q}_i(s, a, w)$ , suppose

$$\hat{q}_i(s, a, w) = \sum_{i=1}^M \psi_i(s, a) \omega_i = \Psi^T w \quad (16)$$

where  $\psi(s, a)$  is the basis function. Suppose the real Q function  $Q(s, a)$  can be written as

$$Q(s, a) = \sum_{i=1}^M \psi_i(s, a) \omega_i^* = \Psi^T w^* \quad (17)$$

Suppose  $k$  is the number of iterations and  $w^k$  is  $w$  value of  $k$ th iteration.  $w^0$  is the initialization. For gradient method, the next iteration is  $w_{k+1} = w^k + \Delta w^k$  where  $\Delta w^k = \alpha_k (Q(s, a) - \hat{q}(s, a, w^k)) \nabla \hat{q}(s, a, w)$ . With properly select  $\alpha_k$ , the convergence can be guaranteed.

$$\begin{aligned} \|w^{k+1} - w^*\| &= \|w^k + \Delta w - w^*\| \\ &= \|w^k + \alpha_k (Q(s, a) - \hat{q}(s, a, w^k)) \nabla \hat{q}(s, a, w) - w^*\| \\ &= \|w^k - w^* + \alpha_k (\Psi^T w^* - \Psi^T w^k) \Psi\| \\ &= \|(1 - \alpha_k \Psi^T \Psi)(w^k - w^*)\| \\ &\leq \|(1 - \alpha_k \Psi^T \Psi)\| \|w^k - w^*\| \\ &\leq \{1 - \alpha_k \mu\} \|w^k - w^*\| \end{aligned} \quad (18)$$

where  $\mu \leq \Psi^T \Psi \leq L$ . If we choose  $\alpha_k = \frac{1}{L}$  then

$$\begin{aligned} \|w^{k+1} - w^*\| &\leq \left(1 - \frac{\mu}{L}\right) \|w^k - w^*\| \\ &\leq \left(1 - \frac{\mu}{L}\right)^{k+1} \|w^0 - w^*\| \end{aligned} \tag{19}$$

So  $\lim_{k \rightarrow \infty} w^k = w^*$ , and the best linear convergence rate can be achieved with

$$\begin{aligned} \alpha_k &= \frac{2}{\mu + L} \\ \|w^{k+1} - w^*\| &\leq \frac{L - \mu}{L + \mu} \|w^k - w^*\| \end{aligned} \tag{20}$$

In this paper, we chose Monte Carlo method to estimate the Q function  $Q(s, a)$ , according to Eq. (8), then difference between  $Q(s, a)$  and  $G_t$  is

$$Q(s, a) - G_t = \sum_{t=1}^{\infty} \gamma^{-t} r_t - \sum_{t=1}^T \gamma^{-t} r_t = \sum_{t=T+1}^{\infty} \gamma^{-t} r_t \tag{21}$$

Combine Eqs. 18 and 21, then we can analyze the convergence of the Monte Carlo method.

$$\begin{aligned} \|w^{k+1} - w^*\| &= \|w^k + \Delta w - w^*\| \\ &= \left\| w^k + \alpha_k (Q(s, a) - \sum_{t=T+1}^{\infty} \gamma^{-t} r_t - \hat{q}(s, a, w^k)) \nabla \hat{q}(s, a, w) - w^* \right\| \\ &= \left\| w^k - w^* + \alpha_k (\Psi^T w^* - \Psi^T w^k - \sum_{t=T+1}^{\infty} \gamma^{-t} r_t) \Psi \right\| \\ &= \left\| (1 - \alpha_k \Psi^T \Psi) (w^k - w^*) - \alpha_k \Psi^T \Psi \sum_{t=T+1}^{\infty} \gamma^{-t} r_t \right\| \\ &\leq \|(1 - \alpha_k \Psi^T \Psi)\| \|w^k - w^*\| + \alpha_k \left\| \Psi^T \Psi \sum_{t=T+1}^{\infty} \gamma^{-t} r_t \right\| \\ &\leq \{1 - \alpha_k \mu\} \|w^k - w^*\| + \alpha_k \mu |A| \sum_{t=T+1}^{\infty} \gamma^{-t} \end{aligned} \tag{22}$$

where  $\mu \leq \Psi^T \Psi \leq L$ . Let  $|A|$  be the maximum value of action return  $r_t$ , then  $\lim_{t \rightarrow \infty} \sum_{t=T+1}^{\infty} \gamma^{-t} r_t = |A| \frac{\gamma^{-T+1}}{1-\gamma}$ .  $\forall \varepsilon > 0, N > 0, \exists T^* > N, \alpha_k |A| \frac{\gamma^{-T+1}}{1-\gamma} < \varepsilon$ , so the convergence of the Monte Carlo method can be guaranteed and the error between the estimated function  $\hat{q}$  and  $Q(s, a)$  can be controlled.

After that, we discussed the convergence of the approximate action function  $\pi(s, a, \theta)$ . The approximate action function  $\pi(s, a, \theta)$  can be converged to the optimal solution sets, if some conditions are satisfied.

**Definition 2** For two function vector parameters  $x$  and  $x^*$  and function  $f(x)$ , Two vectors  $x$  and  $x^*$  are said to be  $\epsilon$  reachable with respect to function  $f(x)$ , if  $f\|x - x^*\|_\infty \leq \epsilon$ , then  $\|f(x) - f(x^*)\| \leq \epsilon$ .

**Theorem 1** If any two function parameters  $\theta_1$  and  $\theta_2$  are reachable with respect to approximate objective functions  $\hat{q}_1$  and  $\hat{q}_2$ , then, for any initial population  $\Omega(0)$ , as  $k \rightarrow \infty$ ,  $\bar{\Omega}(\theta^k) \rightarrow \bar{\Omega}(\theta')$  with probability 1, where  $\theta'$  is  $\epsilon$  reachable to the optimal solution  $\theta^*$ .

*Proof* The proof is very simple, using the condition, then in any  $k$ th generation, the probability to generate the  $\theta'$  which is reachable to the optimal solution  $\theta^*$  is positive, and let the probability be  $\alpha$ . Then in  $k$ th generation the probability of not generating  $\theta'$  is  $(1 - \alpha)^k \in (0, 1)$ , if  $k \rightarrow \infty$  then  $\lim_{k \rightarrow \infty} (1 - \alpha)^k = 0$ .

But the objective functions  $\hat{q}_1$  and  $\hat{q}_2$  can not satisfy the reachable condition, so for any objective functions, our algorithm can not guarantee that with any initial condition, the optimal solution will be converged.

## 5 Experiments

In order to verify our algorithm's performance, we train the agent using iteration times  $K = 50$ , but in fact when  $K = 30$ , the Pareto-optimal solution sets remains stable, the convergence is very fast. Figure 2 shows the Pareto-optimal action-value.

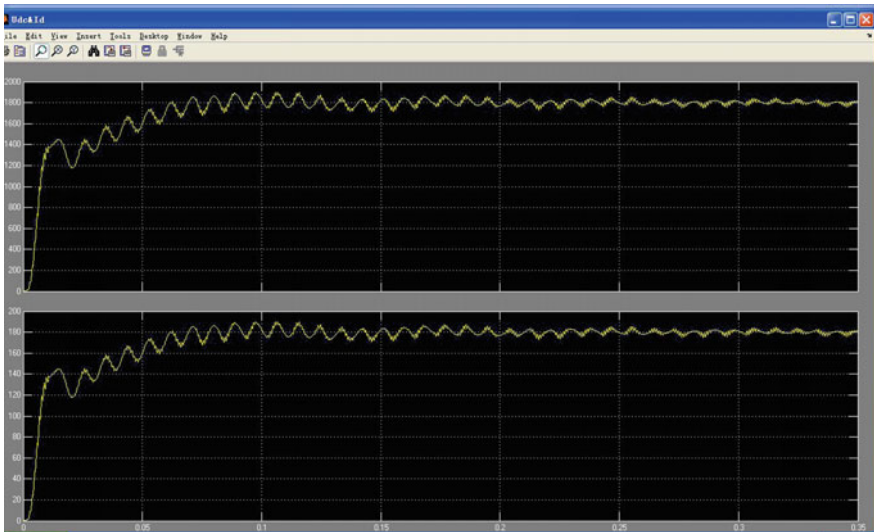


**Fig. 2** TOOR-algorithm simulation results-DC voltage response

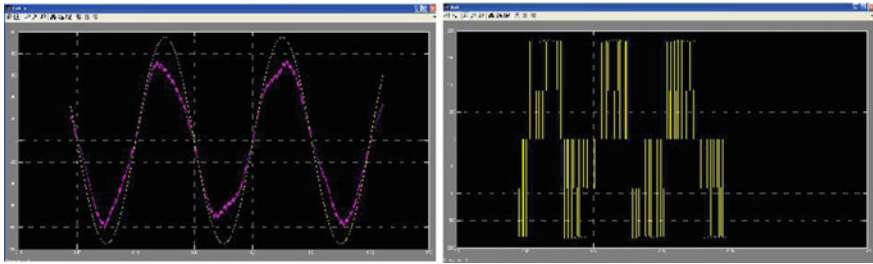


**Fig. 3** TOOR-algorithm simulation results- $U_s(t)$ ,  $I_s(t)$  and  $U_{ab}(t)$  response

Function  $\{\hat{q}_i^*\}$  simulation result of DC-Link voltage and current response. Figure 3 shows simulation results of input voltage  $U_s(t)$  and current  $I_s(t)$ , and the simulation result of input voltage of single-phase rectifier  $U_{ab}(t)$ . All simulation results indicate good performance of our training agent.

## References

1. Stihl O, Ooi BT (1988) A single-phase controlled-current PWM rectifier. *Power Electron IEEE Trans* 3(4):453–459
2. Giri F, Abouloifa A, Lachkar I, Chaoui FZ (2010) Formal framework for nonlinear control of PWM AC/DC boost rectifiers—controller design and average performance analysis. *IEEE Trans Control Syst Technol* 18(2):323–335
3. Kim GT, Lipo TA (1995) VSI-PWM rectifier/inverter system with a reduced switch count. *IEEE Trans Ind Appl* 32(6):1331–1337
4. Song HS, Keil R, Mutschler P, Van der Weem J (2003) Advanced control scheme for a single-phase PWM rectifier in traction applications. In: *Conference record of the industry applications conference, 2003. Ias Meeting*, vol 3 pp 1558–1565
5. Bellman RE (1957) A markov decision process. *J Math Fluid Mech* 6(1):65–73
6. Sutton RS (1998) Reinforcement learning. 11(5):126–134
7. Kaelbling LP, Littman ML, Moore AW (1996) Reinforcement learning: a survey. *J Artif Intell Res* 4(1):237–285
8. Doya K (2000) Reinforcement learning in continuous time and space. *Neural Comput* 12(1):219–245
9. Gaskett C, Wettergreen D, Zelinsky A (1999) Q-learning in continuous state and action spaces. *Lect Notes Comput Sci* 1747:417–428
10. Zitzler E, Laumanns M, Thiele L (2001) Spea2: improving the strength Pareto evolutionary algorithm
11. Sutton RS, Mcallester D, Singh S, Mansour Y (1999) Policy gradient methods for reinforcement learning with function approximation. *Adv Neural Inf Syst* 12:1057–1063
12. Fonseca CM (1993) Genetic algorithms for multiobjective optimization: formulation, discussion and generalization. In: *Proceedings of international conference on genetic algorithms*, pp 416–423
13. Horn J, Nafpliotis N, Goldberg DE (1994) A niched Pareto genetic algorithm for multiobjective optimization. In: *IEEE world congress on computational intelligence, proceedings of the first IEEE conference on evolutionary computation, 1994*, vol 1, pp 82–87
14. Deb K, Agrawal S, Pratap A, Meyarivan T (2000) A fast elitist non-dominated sorting genetic algorithm for multi-objective optimization: NSGA-II. Springer, Berlin Heidelberg

15. Cichosz P (1995) Truncating temporal differences: on the efficient implementation of td ( $\lambda$ ) for reinforcement learning 2:287–318
16. Bouzy B, Chaslot G (2006) Monte-carlo go reinforcement learning experiments. 187–194
17. Baird III LC (1995) Residual algorithms: reinforcement learning with function approximation. In: Machine learning, proceedings of the twelfth international conference on machine learning, Tahoe City, California, USA, July, pp 30–37



# Optimization Design and Research of LEACH Algorithm in Large Region of Rail Transportation

Chongjun Liu, Kuangang Fan, Pingchuan Liu and Gaoxing Ding

**Abstract** An improved LEACH algorithm is proposed to address the limitation of randomly selected cluster heads in an application environment with a large area of rail transportation. Through division, the number and selection of regional cluster heads are optimized to improve the robustness of the LEACH protocol in large areas of rail transportation. Simulation results show that the new algorithm exhibits significant improvement in terms of node survival number, data transmission, and network survival cycle compared with the LEACH algorithm, and thus, the lifetime of wireless sensor networks is prolonged.

**Keywords** Wireless sensor network · LEACH protocol · Cluster Network lifetime

## 1 Introduction

Wireless sensor network (WSN) technology is one of the supporting technologies of the Internet of things [1].

A WSN is composed of plenty of sensor nodes and base stations; it has extensive application prospects in national defense, industrial and environmental monitoring, and many other areas. The routing algorithm, which can extend the life cycle of a WSN, is a recent hot spot in local and overseas research [2]. To improve the shortcomings of the random selection of cluster heads in the LEACH algorithm, literature [3] compared the optimized cluster head LEACH protocol and the

---

C. Liu (✉)

System and Electronic Control Unit(NE1), United Automotive Electronic Systems Co., Ltd, Shanghai, China  
e-mail: kuangangfriend@163.com

K. Fan · P. Liu · G. Ding

School of Mechanical and Electrical Engineering, Jiangxi University of Science and Technology, Ganzhou, Jiangxi, China

© Springer Nature Singapore Pte Ltd. 2018

L. Jia et al. (eds.), *Proceedings of the 3rd International Conference on Electrical and Information Technologies for Rail Transportation (EITRT) 2017*, Lecture Notes in Electrical Engineering 482, [https://doi.org/10.1007/978-981-10-7986-3\\_104](https://doi.org/10.1007/978-981-10-7986-3_104)

1035

LEACH protocol based on a genetic algorithm; it concluded that the life cycle of the latter is longer than that of the former, thereby saving network energy. In literature [1], an energy prediction path based on the ant colony algorithm was proposed. The multi-hop path can be selected and the possible energy consumption of a node when the next jump is chosen can be predicted by using the ant colony algorithm. The results of the simulation illustrate that the ant colony algorithm can effectively reduce the energy consumption of a cluster head and prolong network survival time.

The preceding protocol mainly uses an intelligent algorithm to optimize the LEACH protocol but does not consider the applicability of the LEACH protocol to a large area of rail transportation.

In view of the shortcomings in the aforementioned application environment, this study proposes an improved LEACH routing algorithm, namely, the large-field LEACH (LF-LEACH) routing algorithm, which exhibits better applicability to a large area of rail transportation than the original LEACH protocol.

## 2 LEACH Protocol

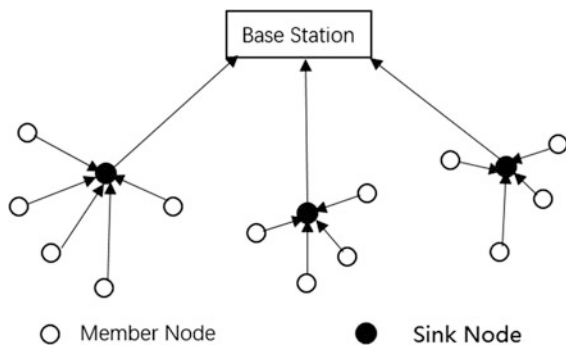
### 2.1 LEACH Network Model

The LEACH protocol is the first clustering routing protocol proposed by MIT scholars Heinzelman et al. Simulation experiments in WSNs show that compared with the direct transmission of the energy routing protocol, the energy cost of the LEACH protocol is decreased eight times and the network life cycle is increased by 15% [4]. The network topology of the LEACH protocol is shown in Fig. 1.

Several assumptions proposed in the LEACH protocol are as follows [5].

- (1) The sensor nodes in the transmission process have the same structure, and energy is limited.
- (2) The original energy of the nodes is the same, and the energy is also equal.

**Fig. 1** LEACH protocol network topology diagram



- (3) The base station and the node are far from each other, and their location is constant.
- (4) Nodes have extensive signal analysis and calculation functions.

The LEACH protocol uses the concept of rounds, and given that the LEACH protocol is periodic, one cycle can be defined as a round that consists of the cluster establishment and data transmission phases [6].

In processing cluster establishment, the node will form a cluster according to its location. First of all, we set a threshold  $T(n)$ . Then, the nodes in the network will generate a digit from 0 to 1, randomly. If this digit is smaller than the threshold  $T(n)$  and the node in the last round has not served as the cluster head, this node will be chosen as the cluster head in the next round. It will spread the message to neighboring nodes, thereby enabling the nodes around it to send information to it in a timely manner. The calculation method for  $T(n)$  is given in Formula (1):

$$T(n) = \begin{cases} \frac{p}{1-p \times (r \bmod \frac{1}{p})} & \text{if } n \in G \\ 0 & \text{otherwise} \end{cases} \quad (1)$$

where  $r$  represents the current number of rounds,  $p$  denotes the percentage of the cluster head in the node,  $n$  represents the total quantity of WSN nodes, and  $G$  denotes the summation of the nodes which are not chosen as the cluster head in the previous  $1/p$  round.

When  $r = 0$ , the nodes exhibit the probability that  $p$  will be selected as the cluster head. In the latter  $[1/p - r]$  round,  $p$  can no longer serve as the cluster head, thereby improving the possibility of other nodes to be selected as the cluster head. After  $1/p$  rounds, a node will have  $p$  possibility to be chosen as the cluster head. After the cluster head is determined, it sends a message with the same power. Normal nodes rely on the signal strength that it took to select a cluster to enter and inform the cluster head.

The cluster head uses time-division multiple access to allocate the transmission time gap to the nodes in the cluster. Once a cluster is formed, it enters a stable transmission phase. The node continuously collects detection data information and leads it to one cluster head with the smallest energy in its corresponding time slot. When data are not transmitted, the node can turn off the transmitter to conserve energy. When the entire data is accepted, the cluster head must perform data fusion and then send the results to the base station in a monotonic manner. After a certain period, the entire network will proceed to the next round and restart the selection of the cluster head [6].

## 2.2 LEACH Physical Energy Model

The LEACH protocol uses the first radio model [7], which is shown in Fig. 2.

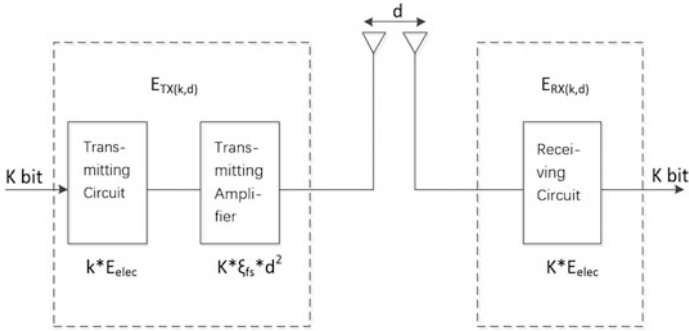


Fig. 2 Network channel energy loss model

A node loses its energy mainly because of the collection and sending of information. In the radio model, the attenuation extent of a signal is related to the distance  $d$  between the data receiver and the transmitter. Energy consumption is calculated by comparing the magnitude relationship between  $d$  and  $d_0$ . The calculation of  $d_0$  is given in Formula (2).

$$d_0 = \sqrt{\xi_{fs} / \xi_{mp}} \tag{2}$$

When the transmission distance  $d$  is shorter than  $d_0$ , the energy cost of the node transmission is proportionate to  $d^2$ , which uses a free interspace former, where  $\xi_{fs}$  is the magnification of the power amplifier of the free interspace former. When the distance  $d$  is longer than  $d_0$ , the energy cost of the node is proportionate to  $d^4$ , which uses a multipath attenuation model, and  $\xi_{mp}$  denotes the magnification of its power amplifier [6].

### 2.3 Limitations of the LEACH Protocol

Although the LEACH protocol has an advantage over the plane routing protocol in terms of balancing network energy consumption, it still has several limitations [8].

- (1) In the LEACH protocol, the cluster head will be randomly selected and the remnant energy factor of the nodes is not considered. If a node which has low energy is chosen as the cluster head, then this node will quickly die and affect the life cycle of the whole network.
- (2) In an application environment with a large area, the applicability of the LEACH protocol is considerably reduced because it has to choose a cluster head randomly. The spacing between one cluster head and one base station or the spacing between one ordinary node and one cluster head may be far, which will consume a considerable amount of energy because of the long data transmission distance. Consequently, the life cycle of the entire network will be significantly shortened.

### 3 LF-LEACH Algorithm

On the basis of the limitations of the LEACH algorithm, this study improves the LEACH algorithm in two aspects: regional division and cluster head selection in a large application environment with a large area of rail transportation. The improved algorithm is called the LF-LEACH algorithm.

#### 3.1 Breakdown of a Large Area

In an application environment with a large area, the first step is to make the large area divided into smaller areas of the same size. Then, the LEACH protocol communication model for data transmission is used in the small areas. Each individual small area can autonomously transfer data to sink nodes or base stations.

#### 3.2 Node Deployment in a Small Area

In an application environment with a large area of rail transportation, more monitoring nodes are deployed in the entire network to ensure that nodes are distributed well. Well-distributed nodes can be deployed in a small area, which is conducive to achieving energy balance consumption in the network cluster head selection and data transmission phases.

#### 3.3 Optimal Cluster Heads Number in a Region

To obtain the optimal cluster heads number in a region of rail transportation, we first presume that  $n$  nodes are deployed in region  $A$  of  $a \times a$ . Then we presume that the number of cluster heads is  $c$  and decide that  $c$  clusters exist in the region and all the nodes are distributed well. Thus,  $(n/c - 1)$  nodes exist in each cluster. Subsequently, analyses of energy cost of cluster heads and common nodes are separately conducted.

Energy cost of a cluster head that accepts data from ordinary nodes and performs data fusion:

$$E_{CH} = kE_{elec}(n/c - 1) + kE_{DA}n/c \quad (3)$$

The entire energy cost of a cluster head is expressed as:

$$E_{CH} = kE_{elec}(n/c - 1) + kE_{DA}n/c + kE_{elec} + k\xi_{mp}d_{toBS}^4 \quad (4)$$

or

$$E_{CH} = kE_{elec}(n/c - 1) + kE_{DA}n/c + kE_{elec} + k\xi_{fs}d_{toBS}^2 \quad (5)$$

where  $E_{DA}$  is considered the energy cost of the unit length data;  $E_{elec}$  is the energy cost of the transceiver; and  $d_{toBS}$  is the average distance between the cluster head and the base station, which can be expressed as:

$$d_{toBS} = \int_A \sqrt{x^2 + y^2} \cdot \frac{1}{A} dA = 0.765a/2 \quad (6)$$

The energy consumption of an ordinary node is expressed as:

$$E_{NOM} = kE_{elec} + k\xi_{mp}d_{toCH}^4 \quad (7)$$

or

$$E_{NOM} = kE_{elec} + k\xi_{fs}d_{toCH}^2 \quad (8)$$

We regard  $d_{toCH}$  as the average distance of a common node to the cluster head, which can be expressed as:

$$d_{toCH}^2 = \int_0^{x_{max}} \int_0^{y_{max}} (x^2 + y^2) \rho(x, y) dx dy = a^2/2\pi c \quad (9)$$

Then, the total energy cost is:

$$E = cE_{CH} + (n - c)E_{NOM} \quad (10)$$

The cluster head is away from the base station in an application environment with a large area of rail transportation, and thus, the multi-path attenuation space model is adopted. By contrast, the distance between cluster nodes and the cluster head is generally close, and thus, the free space model is adopted. The total energy cost of the network is:

$$E = kE_{elec}n + kE_{DA}n + ckE_{elec} + ck\xi_{mp}d_{toBS}^4 + nkE_{elec} + n\xi_{fs} \frac{1}{2\pi} \frac{a^2}{c} \quad (11)$$

Subsequently, we search for the derivative of the total energy cost and the cluster head number  $c$ . We set the derivative as zero, i.e.,

$$\frac{dE}{dc} = 0 \quad (12)$$

The optimal number of cluster heads is expressed as:

$$c = \sqrt{\frac{n}{2\pi}} \times d_0 \times \frac{a}{d_{toBS}^2} \tag{13}$$

Through the preceding formulas, we can calculate the optimal cluster head number in the monitoring area, and thus, obtain the smallest entire energy consumption of the network [9].

### 3.4 Optimization of Cluster Head Selection

First, a threshold  $T(n)$  is set, which is similar to the LEACH protocol. Then, the nodes in the network randomly generate a number from 0 to 1. When the number is less than the threshold  $T(n)$ , it can be selected as the cluster head. During this procedure, the influencing factor of residual energy is added to the selection formula of the cluster head. The calculation method for  $T(n)$  is expressed by Formula (14):

$$T(n) = \begin{cases} \frac{p}{1-p \times (r \bmod \frac{1}{p})} & \text{if } n \in G \\ 0 & \text{otherwise} \end{cases} \tag{14}$$

where  $Q$  is the influencing factor, and the expression is as follows:

$$Q = \sqrt{\frac{E_C(r) + 1}{E_O(r) + 1}}$$

In Formula (14),  $p$  is the rate of the cluster head to the entire number of nodes according to the optimal cluster number,  $r$  is the present number of rounds,  $E_C(r)$  is the remaining energy of the  $r$ -th node,  $E_O(r)$  is the initial energy of this node, and  $p$  is the rate of the cluster head to the total number of nodes. Under the same conditions, when the remaining energy of a node is greater, the possibility that this node will become a cluster head is higher. Therefore, the premature death of nodes with low residual energy is avoided due to such selection of cluster heads, and the lifetime of the network is prolonged.

## 4 Simulation and Performance Analysis

Experiments were conducted using MATLAB to simulate the comparison of the performance of the LEACH and LF-LEACH algorithms.

#### 4.1 Comparison of Node Deployment Simulation

##### (1) Node deployment simulation of the original LEACH protocol algorithm

In the  $1000\text{ m} \times 1000\text{ m}$  range of an arbitrary deployment of 2000 nodes, the base station coordinates (500, 500) are set, and the random distribution of the nodes is shown in Fig. 3.

##### (2) Node deployment simulation of the improved LF-LEACH protocol algorithm

A large area of  $1000\text{ m} \times 1000\text{ m}$  is divided equally into 100 small areas of  $100\text{ m} \times 100\text{ m}$ , and then, 20 nodes are arbitrarily deployed. The base station coordinates (500, 500) are set, and the random distribution of the nodes is shown in Fig. 4.

#### 4.2 Analysis and Comparison of Network Performance Simulation Results

The simulation parameters used in the LEACH protocol are presented in Table 1:

##### (1) Life cycle comparison of the entire network

The network lifetime of a routing protocol can reflect its persistence, i.e., when surviving nodes are more, network lifetime is longer. The life cycle comparison of the whole network is shown in Fig. 5.

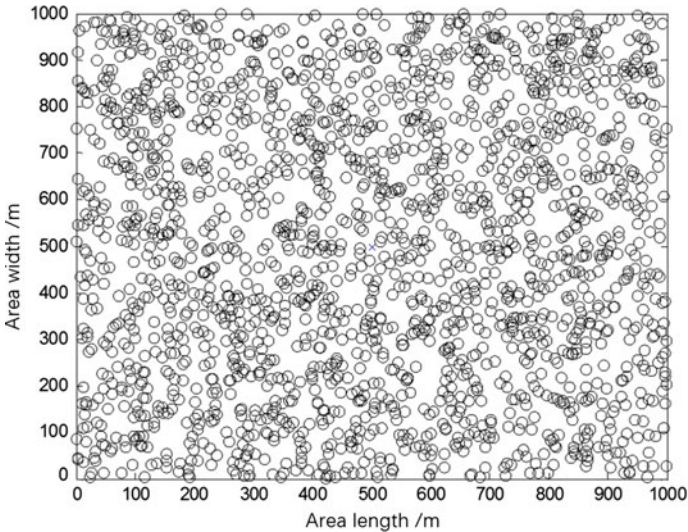


**Fig. 3** Regional node deployment diagram of LEACH protocol algorithm



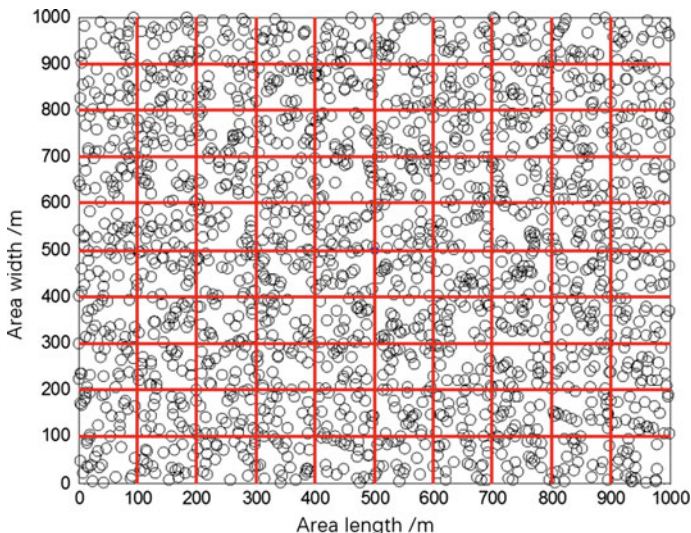


Fig. 4 Regional node deployment diagram of LEACH protocol algorithm

Table 1 LEACH protocol simulation parameters

Simulation parameters	Numerical values
Network area size	1000 m × 1000 m
Base station coordinates	(500, 500)
Number of nodes in the area	2000
Initial energy of the node	0.5 J
Energy consumption for sending and receiving 1bit data $E_{elec}$	50 nJ/bit
Times of free space power magnification $\zeta_{fs}$	10 pJ/bit/m*m
Times of attenuation space power magnification $\zeta_{amp}$	0.0013 pJ/bit/m*m
Energy consumption of fusion of 1bit data $E_{df}$	5 nJ/bit

In the LEACH routing protocol, the entire network dies after 1118 rounds, whereas in the improved LF-LEACH routing protocol, nearly 129 nodes still survive. These nodes can continue transferring data to the base station. The failure rate of LF-LEACH nodes is considerably slower than that of LEACH nodes, and life cycle is improved by 168%.

(2) Residual energy comparison of the entire network

The LF-LEACH routing protocol uses the method for region division, and thus, the remaining energy of the network is more than that in the LEACH routing protocol. Figure 6 shows the residual energy contrast between the two routing protocols. As time passes, the improved routing protocol has more remaining energy than the original protocol. After 1118 rounds, the remaining network energy increased by 7.2%.

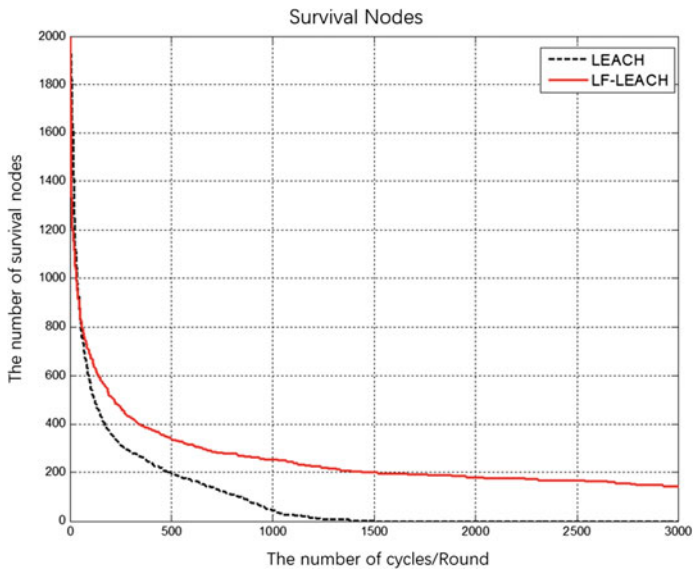


Fig. 5 Comparison of network life cycle

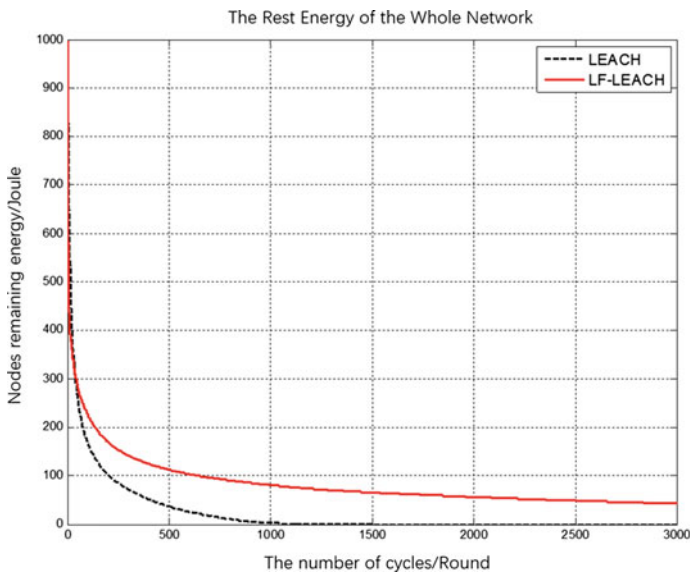


Fig. 6 Comparison of network residual energy

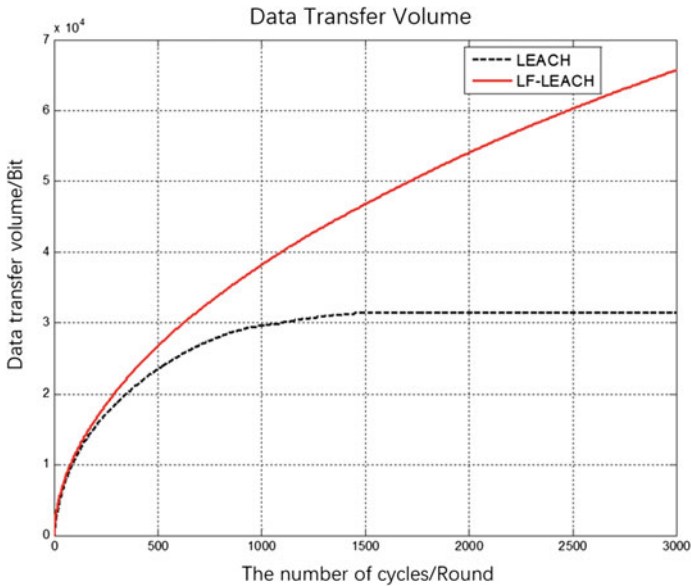


Fig. 7 Comparison of date transmission

(3) Comparison of data transmission of nodes

The improved routing protocol ensures that the residual energy of the network is higher than that of the original protocol; inevitably, the data throughput of the nodes is considerably higher than that of the former. Figure 7 shows the ratio of data transmission between the two routing protocols. The data transmission of the improved routing protocol can be increased by 105% with an increase in the number of cycle wheels.

## 5 Conclusion

After the analysis of the LEACH routing protocol, the LF-LEACH routing protocol is proposed to overcome the shortcomings in an application environment with a large area of rail transportation. In LF-LEACH, new measures, such as large area division, small area node deployment, cluster head number optimization, and the cluster head selection formula, are implemented to increase node residual energy. The results of MATLAB simulation show that the improved LF-LEACH routing protocol algorithm saves network energy, increases the amount of data transmission by 1.05 times, and prolongs network life cycle by 168% compared with the LEACH routing protocol.

**Acknowledgements** This work is supported by the Support Program of China National Science and Technology (No. 61763018, No. 2006BAK03A21, No. 2009BAK58B03,) and Jiangxi Provincial Department of Science and Technology (No. 20171BAB206030) and the Foundation of Education Committee of Jiangxi(GJJ150674) and the Key Program of Nature Foundation of Jiangxi University of Science and Technology (NSFJ2015-K09).

## References

1. Liao M, Zhang H, Xie J (2012) Energy forecast routing protocol in wireless sensor network based on ant colony algorithm. *Computer Eng* 38(3):88–90 (in Chinese)
2. Sun L, Li J, Chen Y (2005) *Wireless sensor networks*. Tsinghua University Press, Beijing, pp 1–3 (in Chinese)
3. Kaur L, Talwar R (2014) Review for leach protocol in WSN. *Int J Adv Sci Technol* 2(4):31–33
4. Zhao F, Gao Y (2011) Improvement and simulation based on LEACH routing protocol for wireless sensor networks. *Electronic Test* 3(3):47–50 (in Chinese)
5. Li H, Shi J, Yang Q, et al (2010) An Energy—efficient hierarchical routing protocol for long range transmission in wireless sensor networks. *Education technology and computer*. In: 2010 2nd international conference on IEEE, 4:45–48
6. Heinzelman WB, Chandrakasan AP, Balakrishnan H (2002) An application specific protocol architecture for wireless micro sensor networks. *IEEE Trans Wireless Commun*, 1(4)
7. Hou YT, Shi Y, Sherali HD et al (2005) On energy provisioning and relay node placement for wireless sensor networks. *IEEE Trans Wireless Commun* 4(5):2579–2590
8. Hara Shinsuke, Yomo Hiroyuki, Popovski Petar, Hayashi Kazunori (2006) New paradigms in wireless communication systems. *Wireless Pers Commun* 37(3–4):233–241
9. Fu Y, Li Y (2015) Optimization of cluster head multihop and selection in LEACH. *J Hunan Univ (Nat Sci)* 42(2):121–125 (in Chinese)